PROCEEDINGS OF THE

LEPTON PHOTON 2009
CONFERENCE

Edited by
TIES BEHNKE, JOACHIM MNICH

Introduction

The Lepton Photon Symposium 2009 took place in Hamburg, Germany, from August 16-22, 2009. It was the fifth time that this meeting came to Hamburg, after 1965, 1977, 1987, 1997.

DESY celebrated its 50th aniversary this year, which made it particularly approriate to have this important meeting in Hamburg. Starting as a national laboratory for German universities DESY has developed to a nationally operated and internationally used accelerator complex serving a wide community of scientists from around the world in fields as diverse as particle physics and molecular biology. Even though after the end of HERA DESY is no longer hosting an accelerator at the energy frontier, it remains a major player in particle physics, and in accelerator development for particle physics and synchroton sources.

For Lepton Photon 2009 some 400 physicist from around the world assembled in Hamburg to discuss the latest results from particle and related fields. The conference took place at a time where the LHC was just about to start again after a long shutdown to repair damages which were incurred in an accident during the first commissioning in 2008. No data from the LHC experiments were available yet, but the experiments were eagerly awaiting the turn-on of the accelerator, and reported on their already very advanced state of preparation.

The Tevatron, the only running high energy collider at this time, was turning out new results at a great rate. It narrowed down the allowed range for the Higgs particle, and new results were a highlight for the conference. The HERA experiments, which had stopped taking data two years earlier, presented many new results.

Another focus of the conference were results from experiments not at the intensity frontier. 2009 was the final year of operation for Babar, and lots of new results were presented.

Astroparticle physics has seen in enormous wealth of new data over the past few years, with many new experiments coming online. Among the most spectacular is the Fermi satellite, from which first results were reported.

Accelerators are a central tool for much of the physics talked about at this conference, and presentation on current and future facilities drew a picture of the field and its possible developments into the next decade. While a linear collider complementing the LHC remains at the top of the list of future projects, other smaller projects have gathered momentum like ultra high intensity Super B-factories, charm factories, and others.

Talks on theoretical deveklopments in a number of areas provided a broad background for the more experimental talks, and covered all aspects of modern particle and astroparticle physics.

The conference closed by a visionary outlook talk by Guido Altarelli, who summarised the newsest results, and pointed the attentees to the exciting times ahead with

the immediate turnon on the LHC. At the next Lepton Photon symposium, first results from this facility should be available, and might be good for some surprises.

Traditionally the Lepton Photon symposia are all plenary talks. The papers accompanying these presentations are collected in the first volume. In addition a limited number of posters could be presented during the conference, which allowed in particular younger physicists to present their work to an international audience. The posters are collected in the second volume of these proceedings.

The conference was opened by short speeches by Dr. B. Vierkorn-Rudolph from the German Ministry of Research, from Staatsrat B. Reinert, from the free and hanseatic city of Hamburg, and from Prof. Dr. H. Graener, the dean of the natural sciences at the University of Hamburg. All three speakers expressed their support for basic science and for DESY as a worldwide recognised center for particle physics.

In addition to the scientific program participants enjoyed a reception at the Hamburg town hall. The traditional conference dinner took part in the harbour of Hamburg, utilizing a former storage hall right on a pier. Participants were brought to the dinner by ship, and were treated to traditional Hamburg cuisine in a typical harbour athmosphere. Even the weather cooperated, and allowed for a reception at the dinner outside on the pier.

I would like to thank first of all the speakers for the excellent talks which created an inspiring athmoshere. The international advisory committe and the local organising comittee played key roles in shaping the scientific program. The symposium would not have been possible without the strong and enthusiastic support by numerous DESY staff.

The symposium was sponsored by DESY and the International Union of Pure and Applied Physics and by the German Research Council, DFG.

Joachim Mnich, Chair

Figure 1: Participants of the Lepton Photon Symposium 2009 gather in front of conference location.

Contents: Plenary Session

Contents: Poster Session

x

PROCEEDINGS OF THE

LEPTON PHOTON 2009
CONFERENCE

PART I: PLENARY SESSION

Status of the LHC and commissioning plans

Helmut Burkhardt[1]

[1]CERN, 1211 Geneve 23, Switzerland

The LHC is expected to provide first collisions soon. The current machine status and prospects for the near future are reviewed.

1 Introduction

The 27 km long LHC machine is starting operation at CERN in Geneva. The LHC is the worlds largest and most energetic particle collider. It took many years to plan and built this complex machine, which promises exciting, new physics results with an excellent potential for major discoveries.

The status of the LHC as presented in this conference in August 2009, will have significantly changed by the time that these proceedings will be published. Therefore, only a short overview over some of the most challenging aspects of the LHC and a brief summary of the status together with future prospectives are given here. More detailed information on the LHC machine can be found in the design report [1] and a more pedagogical description in the book [2].

2 LHC challenges and critical issues

The LHC is made of two rings which are horizontally separated by 19.4 cm over most of the circumference and brought together in four interaction regions, as schematically shown in Fig.1.

The main LHC parameters are listed in Table 1 and compared to LEP. The parameters for the magnetic field and beam intensity are particularly ambitious. The aim is to get the maximum energy and luminosity reachable with current technology.

A major challenge in the LHC is the large amount of energy stored in the superconducting magnets (10 GJ) and the beams (360 MJ at design parameters). For comparison, the energy required to heat and melt 1 kg of copper is 0.7 MJ.

The LHC is equipped with a machine protection system designed to automatically turn off and safely dump the energy in the magnets and the beams in case of problems.

The LHC relies on high quality, high intensity beams from its injectors, the CERN proton LINAC, the Booster, the PS and the SPS. A schematic view of the LHC with its injectors is shown in Fig. 2. Different from electron beams, which were strongly damped by synchrotron radiation and accumulated in LEP, the *proton beam density* (the normalized emittance) and bunch intensities in the LHC are determined by the corresponding parameters of the injected beams.

The LHC construction already was very challenging and required to diagnose and solve several critical issues. Some of these looked like a real headache when they were discovered, risking to delay the whole project. Among the earlier, solved issues were
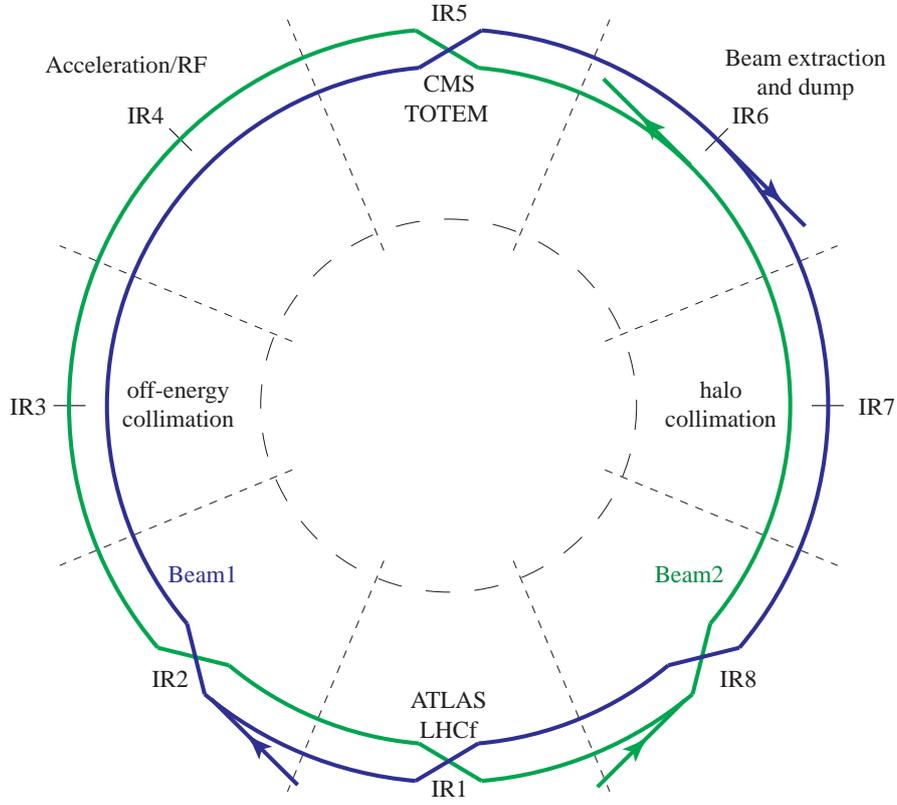
Figure 1: Schematic layout of the LHC collider.

Table 1: Design beam parameters at top energy. LHC compared to LEP.

	LHC	LEP2
Beam energy, E_b, TeV	7	0.1
Nominal design luminosity, $\mathcal{L}$, $\mathrm{cm}^{-2}\,\mathrm{s}^{-1}$	10^{34}	10^{32}
Dipole field at top energy, T	8.33	0.11
Number of bunches, each beam	2808	4
Particles / bunch	1.15×10^{11}	4.2×10^{11}
Typical beam size in the ring, μm	$200 - 300$	1800/140 (H/V)
Beam size at IP, μm	16	200 / 3 (H/V)
Total energy stored in each beam, Mega Joule	360	0.03
Total energy stored in the magnet system, Giga Joule	10	0.016

Figure 2: Schematic view of the LHC with its injectors.

Figure 3: View of a "ping-pong" ball, used to find aperture obstructions in the LHC. Equipped with a small battery, it can emitting a signal at 40 MHz for 2 hours. The passage of a ball within the vacuum chamber is recorded by the LHC beam-position monitors, which are sensitive to 40 MHz, matching the nominal LHC bunch spacing of 25 ns.

- QRL, the cryo-line for the Helium supply

- DFB, the high power electrical connections with warm cold transitions

- Triplet quadrupole cryostat - resistance to differential pressure

and among the more recent and present issues

- PIM, plug in modules with bellows and rf-fingers

- vacuum leaks

- condensation, humidity and corrosion in the tunnel

- magnet powering - cable, connections and polarity checks

- radiation to electronics, single event upset

- magnet re-training, magnets quenching in the tunnel below what was reached in the Lab (SM18)

- magnet interconnects, splices

Some of these issues were solved with rather ingenious methods and delays absorbed or minimized by re-scheduling. An example are the "ping-pong" balls, equipped with radio transmitters, which could be "blown" through the beam pipe. One of them is shown open in Fig. 3. They were quickly developed to check and locate faulty PIM module. In addition to making sure that there are no aperture obstructions for the beams, they were also useful to check the beam position monitors and data acquisition.

3 First operational experience

Over two week-ends in August 2008, beams were injected in parts of the LHC. This allowed to test and adjust injection and check out with beams 3 of the 8 sectors of the LHC.

On the 10th of September 2010, commissioning of the whole LHC with beams started. The injection and beam position monitoring systems performed very well. By measuring and correcting beam positions, it was possible within a couple of hours, to get beams around the full circumference of the LHC, see Fig. 4. The next crucial step was to bring on and synchronize the radio frequency system of the LHC to capture and stabilize the particle bunches (rf-capture). This also worked beautifully. Beam lifetimes of several hours were achieved within three days of commissioning the LHC with beams. This can be considered as a major milestone, demonstrating that there was no major fault in the optics and magnetic lattice.

Just a few days after the start of the commissioning of the LHC with beams in 2008, operation was interrupted by an incident. It occurred in training magnets to higher currents and resulted in a local loss of the energy stored in the magnets, rapid evaporation of Helium and pressure built-up in the insolation tanks, causing significant collateral damage. A poor contact in a splice in a magnet interconnect was identified as initial cause of this incident [3].

The repair and consolidation program which followed is progressing well [4]. Details of the repairs are shown in Fig.5. Fourteen quadrupole and thirty nine dipole magnets had to be removed from the tunnel and replaced or repaired. The last of these magnets was re-installed
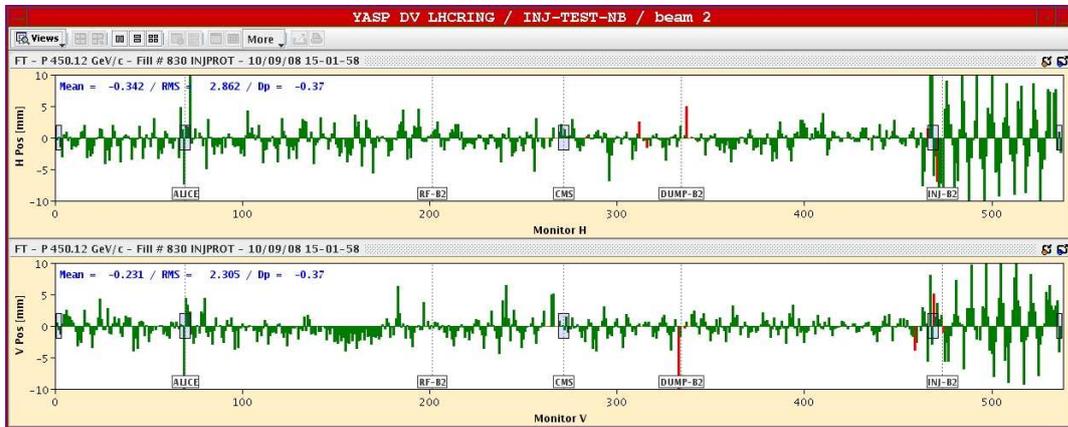
Figure 4: Vertical and horizontal beam positions recorded around the full circumference of the LHC on the 10 Sep. 2008, observed for beam 2 (anti-clockwise beam).
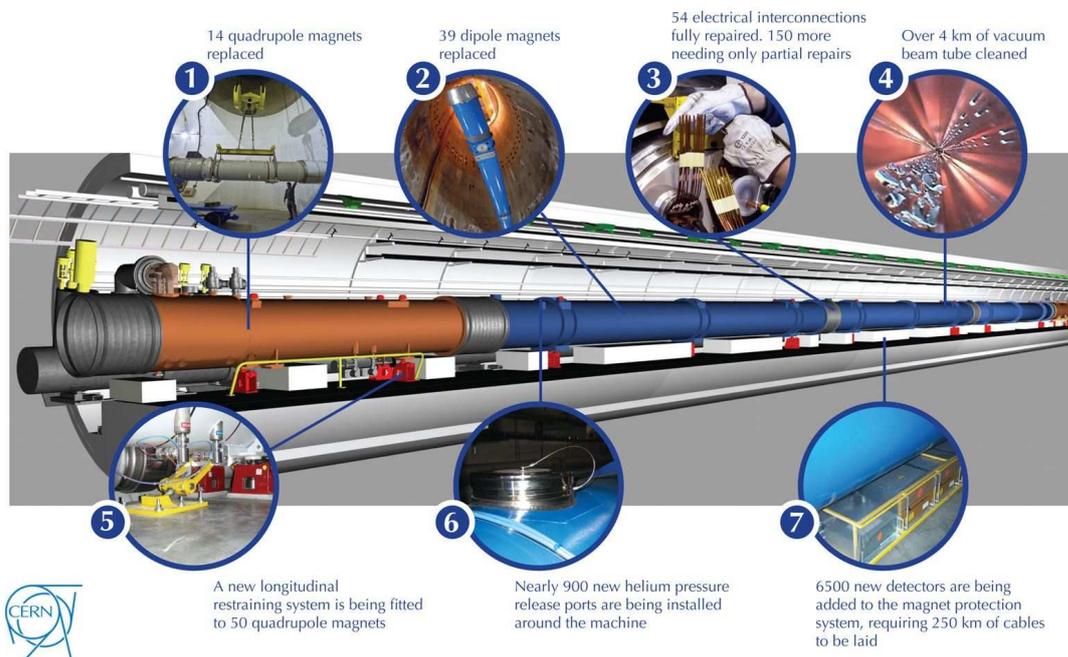
Figure 5: The LHC repairs in detail.

in the LHC on the 30/04/2009 and electrical connections finished on the second June 2009. Methods to diagnose and localize faulty splices were developed and have already been applied to a large fraction of the LHC. In addition to the measures taken to avoid any reoccurrence of such an incident, pre-cautions are also taken to minimize the risk for collateral damage, if this would nevertheless ever happen again. For this, magnet support structures were strengthened and 900 pressure release ports installed to avoid pressure built-up by accidental Helium release.

4 Next steps

The LHC is scheduled to restart for operation with beams in November 2009 and to provide first proton-proton collisions at the injection energy ($2\times450\,$GeV) before christmas. Initial transverse beams sizes are expected to be $\sigma_{x,y}^* \approx 300\,\mu$m. It is planned to use the beam position and orbit correction system to measure beam positions around the interaction regions (with an expected precision of $200\,\mu$m including electronic offsets) to steer the beams into collisions. Fine tuning of collisions will then be done using transverse luminosity scans and will have to rely on luminosity information from the experiments, since the very forward machine luminosity monitors cannot be expected to work at the injection energy. For collisions at higher energies, it is planned to use more extended luminosity scans to measure the transverse beam sizes to obtain an absolute luminosity calibration [5].

For the initial operation in 2009, currents in the LHC magnets will be limited to $2\,$kA which corresponds to a maximum centre of mass energy of just over $2\,$TeV. After a short technical stop in the winter 2009/2010, it is planned to restart the LHC early in 2010, to step up in intensity to roughly 10% of the design values, and to deliver several hundred pb^{-1} integrated luminosity at $7\,$TeV c.m.s. in proton proton collisions within the year. Before the winter shutdown 2010/2011, a run with lead-ion collisions in the LHC is foreseen.

For the last months with proton collisions in 2010 or early in 2011, it is planned to increase the c.m.s. energy to $10\,$TeV. Several winter shutdowns may be required to consolidate magnet interconnects and perform magnet training to allow for safe operation of the LHC at the full design energy of $14\,$TeV. Similarly, ramping up beam intensities and squeezing down beam sizes to increase the luminosity in proton proton collisions towards the very challenging design luminosity of 10^{34} cm^{-2}s^{-1} will be done gradually, over several years.

References

[1] O. Brüning (Ed.) et al., *LHC design report. Vol. 1: The LHC main ring*, CERN-2004-003-V-1.

[2] L. Evans, *The Large Hadron Collider: a Marvel of Technology*. EPFL Press, 2009.

[3] M. Bajko et al., *Report of the task force on the incident of 19th September 2008 at the LHC*, CERN-LHC-PROJECT-REPORT-1168, CERN, March 2009.

[4] M. Lamont, *LHC: status and commissioning plans*, `arXiv:0906.0347`, CERN, June 2009.

[5] H. Burkhardt and P. Grafstrom, "Absolute luminosity from machine parameters", CERN-LHC-PROJECT-REPORT-1019, CERN, May 2007

Discussion

Mel Shochet (University of Chicago): Steve Myers said at CERN that in order to safely reach 14 TeV, all of the splices would have to be clamped. I have heard two models for carrying this out. In one, there would be a long shutdown after the first run to install all of the clamps. In the other, the installation would be carried out over a few years during the annual shutdowns planned for other reasons. Has the decision been made on which model to follow?

Answer: Not to my knowledge.

Status of the ATLAS Experiment

Kerstin Jon-And[1]
On behalf of the ATLAS Collaboration

[1]Stockholm University, The Oskar Klein Centre for Cosmoparticle Physics, Department of Physics, AlbaNova, SE-106 91 Stockholm, Sweden

The ATLAS detector, which has been under construction and installation for close to 20 years, is now fully installed and running at the CERN Large Hadron Collider. In this paper the detector will be described. Some results from commissioning the detector with first single beam data from 2008 as well as cosmic ray data will be presented. Some physics expectations from the coming first year of LHC collision data will also be given.

1   Introduction

ATLAS is one of the two general-purpose detectors at the Large Hadron Collider (LHC), a proton collider designed to produce proton-proton collisions at a centre-of-mass energy of 14 TeV. The LHC started successfully circulating proton beams at the injection energy of 450 GeV per beam in September 2008. However, an incident involving a superconducting bus bar between two dipole magnets led to a shut-down period of more than one year for repair and consolidation work. At the time of writing these proceedings (January 2010) the LHC has successfully restarted, and proton-proton collisions at the world energy record of 2.36 TeV were already achieved at the end of 2009 before the short winter stop. During 2010 the plans are to restart in mid February going as fast as possible to a centre-of-mass energy of 7 TeV, possibly increasing towards 10 TeV during the year. An integrated luminosity of a few hundred pb^{-1} of collision data is expected to be delivered.

The ATLAS Collaboration comprises around 2800 physicists from 169 institutions in 37 countries (at the time of writing the number of institutions has increased to 172). After close to 20 years of construction and installation work the ATLAS detector was installed and working well for the first beam in 2008. Since then it has been further improved and commissioned with cosmic ray data. This paper will describe the status of the detector, some results obtained with single beam and cosmic ray data from 2008 as well as some expectations of first physics with high energy collision data.

2   The ATLAS Detector

The ATLAS detector [1, 2] is designed to have excellent tracking, calorimetry and muon detection over the full energy range available at the LHC. A schematic view of the detector, where the different parts are labelled, can be found in Figure 1. The huge detector has a cylindrical shape of 44 m length and 25 m diameter. It weighs around 7000 tons.
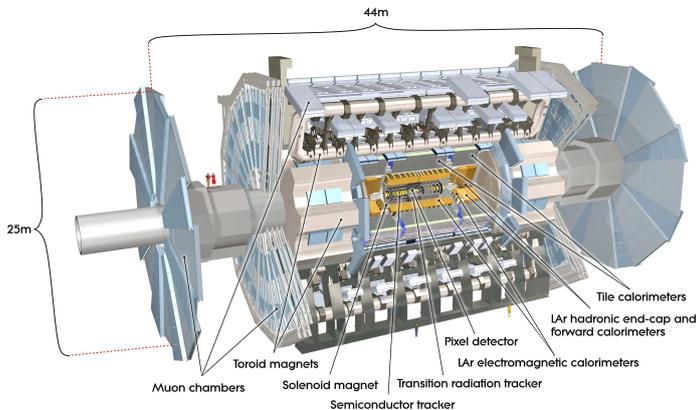
Figure 1: Schematic view of the ATLAS detector.
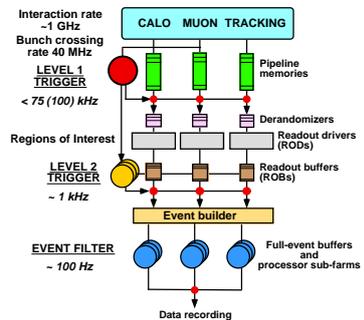
Figure 2: Schematic view of the ATLAS trigger and DAQ systems.

The innermost detector part is the Inner Detector (ID). It consists of three subdetectors, the pixel detector, the Semi-Conductor Tracker (SCT) and the Transition Radiation Tracker (TRT).

The ID covers a pseudorapidity region of $|\eta| < 2.5$. It is enclosed by a solenoid magnet providing an axial field of 2 T. The pixel detector has three layers of pixels both in the barrel and the endcap regions and has 80 million channels. The SCT consists of four double layers of silicon strips in the barrel region and nine in the endcap. It has around 6 M channels. The TRT, which is made of straw tube layers interleaved with transition radiation material, provides $e - \pi$ separation in the energy range of $0.5 < E < 150$ GeV. The TRT has 3.5×10^5 channels. The momentum resolution provided by the combined inner detector is $\sigma(p_T)/p_T \simeq 3.4 \times 10^{-4} p_T/\text{GeV} \oplus 0.015$.

The calorimeter system is situated outside the solenoid magnet. The calorimeters have a coverage up to $|\eta| = 5$. The electromagnetic (EM) calorimeter uses a sampling technique with accordion shaped lead plates as absorbers and Liquid Argon (LAr) as sensitive material both in the barrel and in the endcap regions ($|\eta| < 3.2$). The EM energy in the forward region is measured by the first layer of the forward calorimeter (LAr/copper). The hadron calorimeter is a sampling iron - scintillating tiles calorimeter (Tilecal) in the barrel region, $|\eta| < 1.7$. In the endcap and forward regions there are LAr calorimeters with copper/tungsten as absorber material respectively. The relative energy resolution of the electromagnetic calorimeter is $\sim 10\%\sqrt{E}$. In the hadron barrel region the relative jet resolution is $\sim 50\%/\sqrt{E} \oplus 0.03$.

The outermost system is the huge muon spectrometer. Two different technologies are used for the precision chambers. For most regions Monitored Drift Tubes (MDT) are used. In the endcap inner region Cathode Strip Chambers (CSC) are used since they are able to cope with higher background rates. Also the trigger chambers are made with two different technologies. Resistive Plate Chambers (RPC) are used in the barrel and Thin Gap Chambers (TGC) in the endcap regions. The barrel muon detectors are surrounded by eight huge air-filled toroid coils providing a bending field of $1.5 - 5.5$ Tm in the central region ($|\eta| < 1.4$). In each endcap there is also a toroidal magnet system with eight coils in a common cryostat providing approximately $1 - 7.5$ Tm ($1.6 < |\eta| < 2.7$). The standalone muon momentum resolution is designed to be $\Delta p_T/p_T < 10\%$ up to $E_\mu \sim 1$ TeV.

ATLAS has a three-level trigger system successively reducing the rate from the bunch crossing rate of 40 MHz to the rate of events being written to tape of around 200 Hz. The trigger and data acquisition (DAQ) system is schematically shown in Figure 2. The level 1 trigger is implemented in hardware based on the calorimeter and muon systems. The high level triggers (level 2 and the event filter) use computer farms with around 500 and 1800 multi-core processors respectively, analysing full granularity data. At level 2 only full readout granularity data from so called "regions of interest" are analysed. Only 35% of the high level trigger hardware is currently installed. This is completely adequate for the first year of data taking.

To cope with the massive need for computing infrastructure a world-wide computing network, the World-wide LHC Computing Grid, has been built. ATLAS has around 70 computing sites distributed over the world. The operational challenges (e.g. $\sim$50 PByte of data to be moved across the world every year, 10^9 raw events per year to be processed and reprocessed) and the complex Computing Model have been stress-tested and refined over the last years through functional tests and data challenges of increasing functionality, size and realism.

3 Commissioning with single beam data

During the short single beam run in September 2008 ATLAS collected data from beam halo events and so called beam-splash events, which were produced when bunches of around 2×10^9 protons at 450 GeV were stopped by closed collimators upstream of the experiment. An example of such a beam-splash event is shown in Figure 3. The whole detector was lit up, mainly by the muons resulting from the "splash", depositing around 100 TeV in the detector. The first beams on September 10-12 were very useful to synchronize the various sub-detectors, in particular to start timing-in the trigger. The timing of the various components (sub-detectors, trigger system) was synchronized with respect to the so called ATLAS beam pick-ups (BPTX) reference. An adjustment to within one bunch crossing, 25 ns, was achieved in these two days. The detection of the single beam data showed that ATLAS was ready for data taking in September 2008.
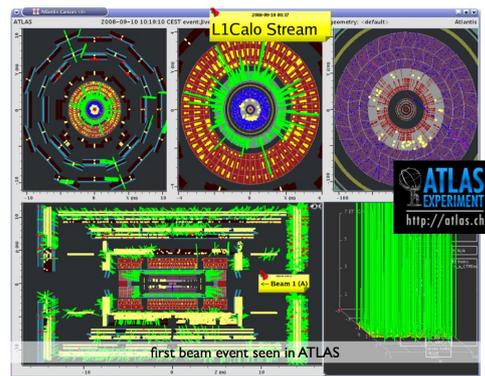
Figure 3: First beam in ATLAS.

4 Commissioning with cosmic ray data

After the LHC incident on 19 September 2008 ATLAS has made good use of the extra time to commission and validate all aspects of the detector. Global cosmics runs with the full detector operational were performed in the autumn of 2008. Around 500 M events were collected in August − October 2008 producing around 1.2 PByte of raw data. Over 200 M events were collected with the full detector being read out. Data were taken both with and without the magnetic field being switched on. The cosmic ray data were very useful to debug the experiment,

to study and validate the calibration and alignment and to gain in situ experience with the global detector operation. The detector was opened in October 2008 for maintenance, consolidation and a few repairs. In the beginning of June 2009 the detector was closed again and global cosmics runs were restarted at the end of June. In this section some results from the cosmic runs in the autumn of 2008 will be discussed.

4.1 The inner detector

To achieve the precise measurements of tracks and knowledge of the absolute momentum scale to $<< 0.1\%$, needed e.g. for a measurement of the W mass, a precise alignment of the detectors is required. Alignment of the inner detector was studied with the cosmic ray data. An example is given in Figure 4, where the pixel residual distribution is shown. The residual is defined as the difference between the measured hit position and the expected hit position from the track extrapolation. The broadest distribution corresponds to the residuals with nominal geometry. The distribution with the filled circles corresponds to the residuals after alignment with cosmic rays and the most narrow distribution, with the open circles, to a Monte Carlo (MC) simulation with perfect geometry. Both for the pixel and for the SCT detectors a precision of around 20 μm was achieved close to the ultimate goal of $5 - 10$ μm.
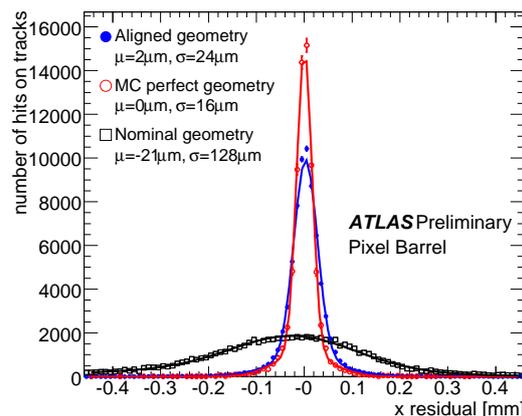
Figure 4: Pixel detector alignment with cosmic ray data compared to the MC expectation.
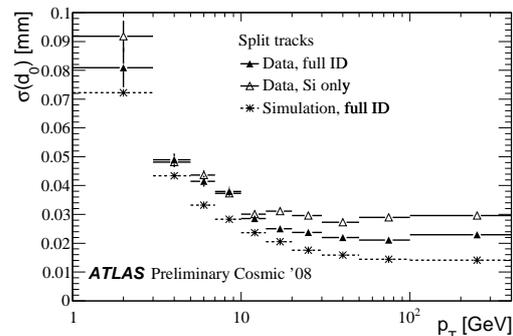
Figure 5: Impact parameter resolution plotted versus p_T
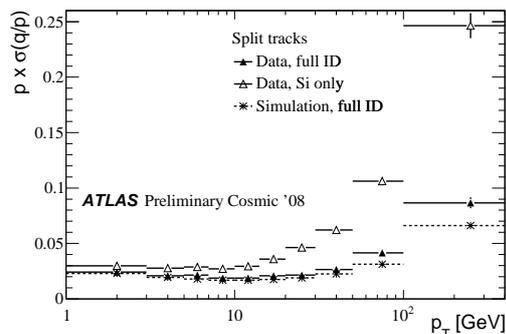
Figure 6: Momentum resolution plotted versus p_T.

Cosmic ray tracks crossing the whole inner detector were used to measure the track parameter resolution. The tracks were split in the center and refitted separately. By comparing the parameters of the two collision-like tracks originating from the same cosmic muon the res-

olution could be measured. In Figure 5 the transverse impact parameter resolution is plotted as a function of p_T. The plot shows comparisons of tracks using the full ID (closed triangles), only the silicon sub-detecors (open triangles) and tracks from cosmic simulation using the full ID (stars). In the low p_T region, the resolution is dominated by multiple scattering effects. Taking into account the TRT information improves the resolution. In Figure 6 the corresponding plot for the relative momentum resolution is shown. The relative momentum resolution increases with higher p_T due to stiffer tracks and a more difficult measurement of the sagitta. Including information from the TRT extends the lever arm and helps improve the resolution. The obtained resolution is already quite close to the ideal MC simulation.

Figure 7: Turn-on of transition radiation in the TRT barrel.

Studies of the transition radiation in the TRT were also performed. The transition radiation intensity is proportional to the particle γ-factor. In Figure 7 the turn-on of the transition radiation at values of the γ-factor of around 1000 is shown. For muons this corresponds to a momentum of around 100 GeV. On the y-axis the probability of a high-threshold hit, which is an indicator of transition radiation, is given. The data points are shown for cosmic muons separately for both charges and are compared to the results obtained in the ATLAS Combined Test Beam in 2004 (black thin line). The turn-on of the transition radiation is nicely seen and the identical behaviour of the detector to cosmic tracks and data recorded at the test beam demonstrates that the TRT is working properly.

4.2   The muon spectrometer

A very good momentum resolution for muons is important for the possibility to e.g. discover new heavy resonances decaying to a muon pair as a "narrow" peak. The muon p_T resolution varies from 5% at 10 GeV up to about 10% at 1 TeV. The latter can be achieved provided that the muon chambers will be aligned to about 30 μm. Cosmic ray data taken without the magnetic field were used for alignment studies. In Figure 8 are shown the measured residuals for cosmic data taken without magnetic field. For a properly aligned muon chamber tower the mean value of the residual is expected to be within the required 30 μm. The three plots show the residual distributions for tracks going through a particular muon chamber for three different geometries: the top distribution is obtained using nominal geometry, the middle one using the geometry based on the optical alignment system and the bottom one is obtained after alignment with straight tracks. The improvement between the steps is clearly seen and the result is very promising.

Studies have also been made checking the correlation between track measurements in the inner detector and the muon spectrometer. In Figure 9 the difference between the measurements of the momentum of a track in the lower part of the detector using the ID and using the muon spectrometer is shown. The peak value of around 3 GeV/c corresponds to the expected energy loss of the muon in the calorimeter. The measurements agree well with a Monte Carlo simulation.
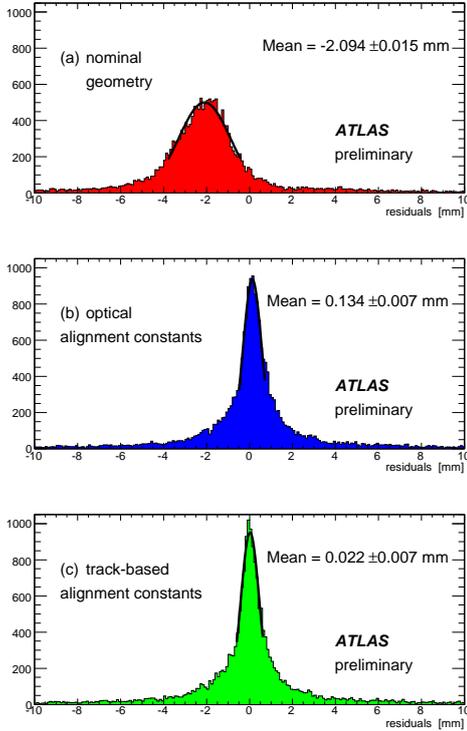
Figure 8: Alignment of the Muon Spectrometer.
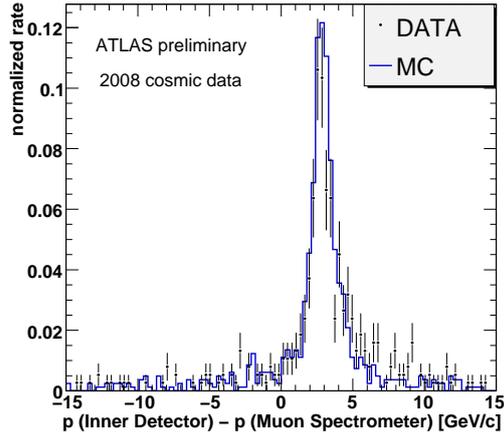
Figure 9: The difference of the momentum measured in the ID and the muon spectrometer for tracks in the bottom part of the detector.

4.3 The calorimeter system

Many studies of calorimeter performance were made with cosmic ray data. Here will be shown examples of how noise studies and studies of cosmic ray data can be used to study backgrounds of fake missing energy.

The ATLAS LAr calorimeter system has recorded several millions of cosmic ray and random trigger events. Detailed understanding and improvement of the signal reconstruction has made it possible to study the performance on these events of higher level quantities such as the missing transverse energy, E_T^{miss}. The performance of the standard calorimeter E_T^{miss} algorithms, as planned to be used for the analysis of the collision data, is shown in Figure 10. The missing transverse energies in the LAr calorimeter are reconstructed using all cells above a noise threshold of two standard deviations ($|E| > 2 \times \sigma_{noise}$). The width of the energy distribution in each cell, σ_{noise}, has been estimated on a cell by cell basis for all LAr sub-detectors as the RMS of the energy distribution in a calibration run. The analysis is performed with random and first level calorimeter (L1Calo) triggered events. Inclusive distributions of E_T^{miss} for both types of events are shown together with a simple MC simulation, which is based on randomisation of the cell energy with a gaussian noise. L1Calo events, triggered by hard bremsstrahlung photons from muons, are mainly originating from the Tilecal. Consequently the E_T^{miss} distribution in
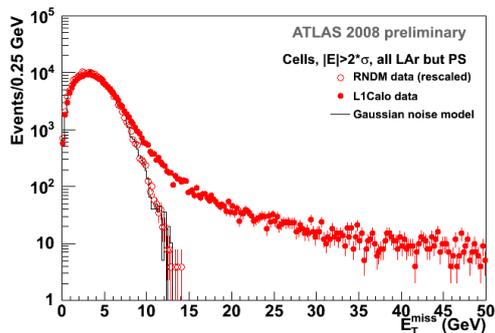
Figure 10: Distribution of the missing energy in events triggered by the calorimeter. The noise from random events is described in the text.
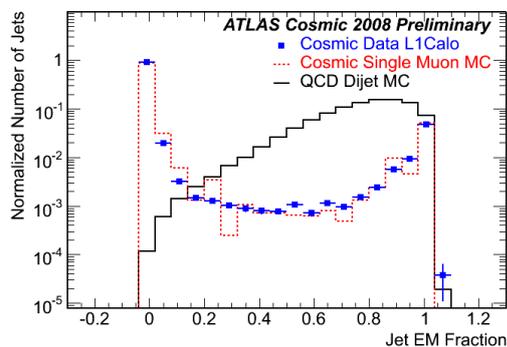
Figure 11: The distributions of the EM fraction of jets for cosmic data and QCD dijet MC.

most cases corresponds to the random event distribution. The high energy tail corresponds to real energy deposit in one of the LAr sub-detectors.

Jets and large missing transverse energy can originate from high energy cosmic muons passing the ATLAS calorimeter. The aim of the study shown in Figure 11 is to investigate the performance of cleaning cuts against cosmic rays. The jet EM fraction is the ratio of the energy deposited in the EM calorimeter and the whole calorimeter. The jet EM fraction from the cosmic L1Calo data stream, a cosmic MC simulation, and QCD di-jet MC samples simulating proton-proton collisions are shown. Only jets with $E_T > 20$ GeV are included. The distributions were normalized by the total number of jets. The most likely value for the EM fraction is 0 or 1 for fake jets from cosmics, since the high energy deposit from photons originating from high energetic muons will localize either in the EM or the hadronic calorimeter. The QCD jets have a broad distribution of the EM fraction peaking around 0.8. A good separation between real QCD jets and fake jets from cosmics is observed. Selection cuts around 0 and 1 can remove most of the fake jets while keeping most of the jets produced in proton-proton collisions.

4.4   First electrons seen in ATLAS

A study has been made to identify electrons in cosmic ray data. The electrons are expected to be produced as δ-rays from ionisation of cosmic muons. The analysis was performed on a sample of 3.5 million events selected by the level-two track trigger. The tracks used were required to have a loose association to an EM calorimeter cluster with a transverse energy above ~ 3 GeV and after some further cuts the events were split into two categories. One sample consisted of 1229 muon bremsstrahlung candidates with only one track reconstructed in the barrel inner detector. The other sample consisted of 85 ionisation electron candidates with at least two tracks reconstructed in the barrel inner detector. In Figures 12 and 13 scatter plots are shown for the two event categories respectively, where the TRT signal, expressed as the ratio of the number of high to to the number of low threshold hits in the TRT, is plotted versus the ratio of the energy measured in the EM calorimeter and the momentum measured in the ID. The dashed lines in the figures indicate the electron signal region: $0.8 < E/p < 2.5$ and the high to low threshold TRT hit ratio
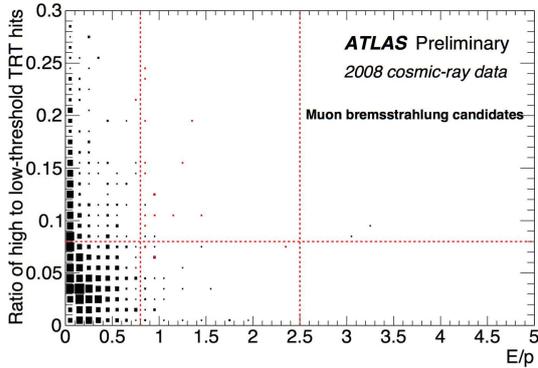
Figure 12: Ratio of high to low threshold TRT hits plotted versus E/p, where E is measured in the EM calorimeter and p in the inner detector, for bremsstrahlung candidates.
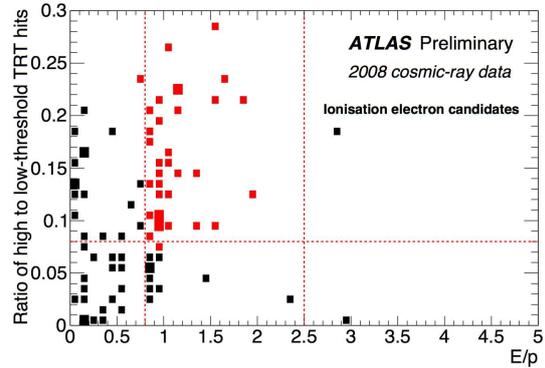
Figure 13: Ratio of high to low threshold TRT hits plotted versus E/p, where E is measured in the EM calorimeter and p in the inner detector, for ionisation electron candidates.

> 0.08 (indicating the detection of transition radiation produced only by relativistic particles). Most of the events in Figure 12 have small E/p ratio and few high threshold TRT hits. Only 19 of the 1229 events satisfy the signal criteria. In contrast, in the event sample shown in Figure 13, a large fraction of events, 36 out of the total of 85, satisfy the signal criteria. These events are interpreted as high energy δ-rays produced in the inner detector volume by the incoming cosmic muons. In Figure 14 the distribution of the energy to momentum ratio for the electron candidates of Figure 13, after applying the cut indicated on the ratio of high to low threshold TRT hits, is displayed. The background curve is estimated using both the electron candidates outside the signal region in Figure 13 and the muon bremsstrahlung candidates in Figure 12. A clear accumulation of signal events around $E/p = 1$ is observed, as expected for electrons. Out of the 36 signal candidates, 32 have a measured negative charge, and these constitute the final sample. This is the first observation of electrons in the ATLAS detector.
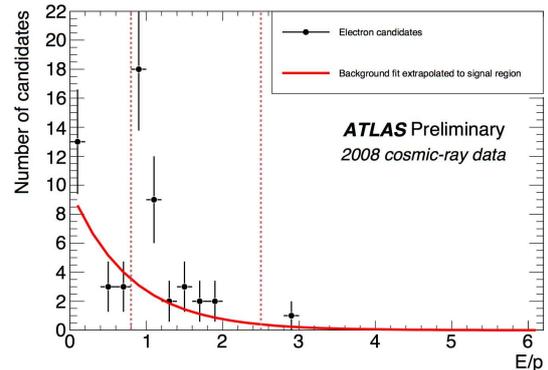
Figure 14: The distribution of the E/p ratio for the electron candidates of Figure 13 after applying the cut indicated on the ratio of high to low threshold TRT hits.

5   Detector status after the winter 2008-2009 shut-down

Only a few examples of commissioning results were discussed in the previous section. Also the trigger and DAQ systems as well as the computing system were successfully commissioned. For example comparisons between the trigger and the full readout gave very good results.

After the commissioning runs with cosmic rays in 2008 and the repair and consolidation work in the winter 2008-2009 shut-down the detector was efficient to the few per mille level as can be seen in Table 1. The overall data taking efficiency, calculated over dedicated 6-14 hour long simulated LHC stores, has already reached $\sim 83\%$. Some concerns are the long-term reliability of some components: the low-voltage power supplies of the LAr and Tile calorimeters, the LAr calorimeter readout optical links, and the inner detector cooling. Back-up solutions are being prepared for installation in future shut-down periods.

Sub-detector	Number of channels	Operational fraction(%)
Pixels	80 M	98.5
SCT	6 M	99.5
TRT	350 k	98.2
LAr EM calo	170 k	99.1
Tile calo	9800	99.5
LAr Hadronic endcap	5600	99.9
LAr Forward calo	3500	100
MDT	350 k	99.3
CSC	31 k	98.4
RPC	370 k	$\sim$95.5 (aim >98.5)
TGC	320 k	99.8

Table 1: Detector status after the winter 2008-2009 shut-down.

6 Examples of physics with first LHC data

When high-energy collision data will become available the commissioning and calibration of the detector in situ will be done using well-known physics samples. When the first tens of pb^{-1} are collected already a few hundred thousand J/ψ and several thousand Υ decays to muon pairs will be available. Further very useful event samples will be e.g. Z decays to muon and electron pairs and W decays to jets. These samples will be used for alignment and calibration of the muon spectrometer and the ID, for the EM calorimeter calibration, for the energy/momentum scale of the full detector, for lepton trigger and reconstruction efficiency etc.

The next step before searching for discoveries is to measure Standard Model processes, e.g. production of Z, W, $t\bar{t}$, QCD jets. In Figure 15 an example of simulated top pair production is shown [3]. Events with top pairs where one top quark decays to a b-quark, a lepton and a neutrino and the other to a b-quark and two light quarks are selected. The requirements are thus to have an event with four high p_T jets, a high p_T lepton and missing transverse energy. The lepton is used for triggering and the plot shows the invariant mass of the combination of three jets with the highest p_T. The analysis is relatively simple and requires no b-tagging. The plot contains events in the muon decay channel and corresponds to an integrated luminosity of 200 pb^{-1} at a collision energy of 10 TeV. After cuts the estimated number of events in the muon decay channel is around 1600. An analysis at 7 TeV with the same integrated luminosity would have yielded around 600 events. Event samples of this size should be available during the 2010 LHC run. The expected uncertainty on the measured top cross section at $\sqrt{s} =10$ TeV is less than 20% not including the luminosity uncertainty. The top measurement requires good understanding of most signatures essential for searching for new physics e.g. leptons, jets, missing transverse energy, b-jets. Also top will constitute an important background to most searches for new physics. When the top is measured the experiment is ready for the discovery phase.
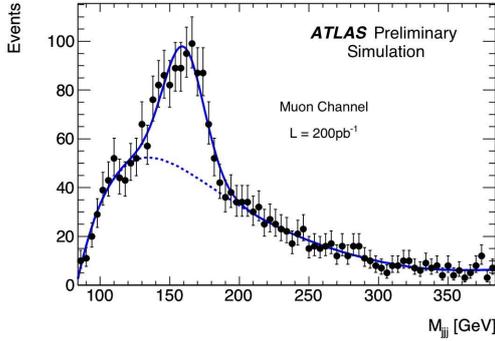
Figure 15: Invariant mass spectrum for the combination of three jets with highest p_T in events with top pairs, one top decaying leptonically in the muon channel and the other decaying hadronically.
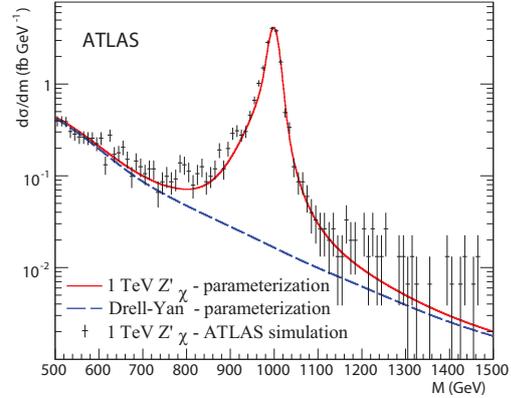
Figure 16: Mass spectrum for a $m = 1$ TeV $Z'_\chi \to e^+e^-$ obtained with ATLAS full simulation.

A possibility of an early physics surprise could be a narrow mass peak in the dilepton invariant mass spectrum. An example is given in Figure 16 [2]. The figure results from a simulation of Z'_χ with a mass of 1 TeV decaying to e^+e^- pairs. Z' particles appear in many models beyond the Standard Model. This particular simulation refers to production of a sequential Standard Model-like Z'. The signal is nicely seen above a small and smooth SM background. This analysis does not require the ultimate EM calorimeter performance. The analysis is made at $\sqrt{s} = 14$ TeV. A discovery at the level of 5σ at this energy would require an integrated luminosity of around 50 pb^{-1}. At $\sqrt{s} = 7$ TeV the estimated integrated luminosity to reach a sensitivity just beyond the current Tevatron limits of around 1 TeV is around 200 pb^{-1} (around 100 pb^{-1} at 10 TeV). This should be possible to achieve during the 2010 LHC run.
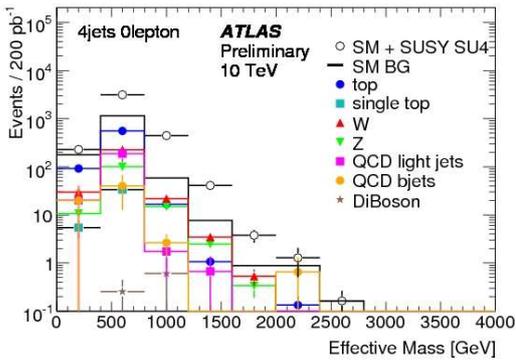
Figure 17: Effective mass distribution for the 4 jets channel with 0 leptons.
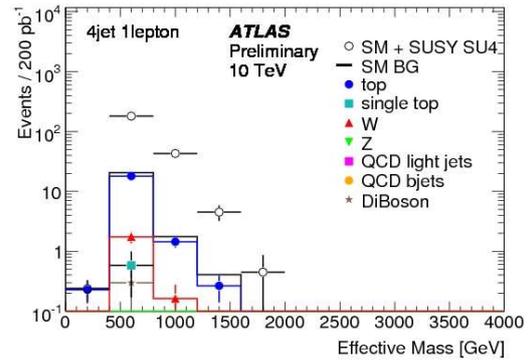
Figure 18: Effective mass distribution for the 4 jets channel with 1 lepton.

If supersymmetry (SUSY) exists with a mass scale of squarks and gluinos of around 1 TeV

it could be one of the first discoveries at the LHC. A huge production cross-section could be expected. The decay chains of the squarks or gluinos are expected to give rise to spectacular final states with many jets, leptons, and, in particular for R-parity conserving models, missing transverse energy. Of particular interest is of course that the stable lightest SUSY particle, the neutralino, is a dark matter candidate. Figures 17, 18 and 19 are based on a simulation study of inclusive SUSY searches in the minimal Supergravity model made at a centre-of-mass energy of 10 TeV assuming an integrated luminosity of 200 pb^{-1} [4]. Figures 17 and 18 show examples of distributions of the effective mass for signal and background events. The effective mass is the scalar sum of the transverse momenta of the main objects like leading jets, leptons, missing E_T. It is one of the variables used for sample defining cuts. These figures are

Figure 19: 5σ discovery reach as a function of m_0 and $m_{1/2}$ for the mSUGRA model with $\tan\beta = 10$.

produced for squark and gluino masses around 410 GeV. Figure 17 shows the effective mass distribution for the 4 jets channel with zero leptons and Figure 18 shows the distribution for the channel including one lepton. It can be seen from the figures that the jets and missing E_T channel gives highest reach, whereas the channel including one lepton in the final state is more robust against background. In Figure 19 the 5σ discovery reach as a function of m_0 and $m_{1/2}$ for channels with 0, 1 and 2 leptons is shown. The particular model used here is mSUGRA with $\tan\beta = 10$. The full, green line corresponds to the channel with 4 jets and no leptons, and the dashed-dotted, black line to the channel with 4 jets and 1 lepton. The discovery reach is squark and gluino masses of around 750 GeV. Going to $\sqrt{s} = 7$ TeV, the discovery reach for 200 pb^{-1} is still expected to be beyond the expected Tevatron reach of around 400 GeV. It will however take some time to understand the tricky backgrounds, in particular fake missing transverse energy. The ultimate discovery reach at LHC is expected at masses around 3 TeV.

7 Conclusions

The ATLAS experiment is in excellent shape. The fraction of non-working channels is on the few per mille level. Analysis of ∼600 M cosmics events, as well as single beam data in Sept 2008, shows better detector performance than expected at this stage. Software and computing have proved to be able to cope with simulation, analysis and world-wide distribution of massive amounts of data. After 20 years of efforts building all aspects of the experiment ATLAS is ready for LHC collisions data.

At the time of writing, January 2010, ATLAS has in fact taken around 1 M collision events provided by LHC late 2009. The preliminary analysis shows that all aspects of ATLAS work very well and that ATLAS is ready for the next phase of high energy collisions.

Acknowledgements

References

[1] The ATLAS Collaboration, G. Aad *et al.*, *The ATLAS Experiment at the CERN Large Hadron Collider*, JINST **3** S08003 (2008).

[2] The ATLAS Collaboration, G. Aad *et al.*, *Expected Performance of the ATLAS Experiment, Detector, Trigger and Physics*, CERN-OPEN-2008-020 (2008).

[3] The ATLAS Collaboration, *Prospects for the Top Pair Production Cross-section at $\sqrt{s} = 10$ TeV in the Single Lepton Channel in ATLAS*, ATL-PHYS-PUB-2009-087 (2009)

[4] The ATLAS Collaboration, *Prospects for SUSY and UED discovery based on inclusive searches at a 10 TeV centre-of-mass energy with the ATLAS detector*, ATL-PHYS-PUB-2009-084 (2009)

Discussion

Dmitri Denisov (FNAL): What are major factors defining 20% expected data taking inefficiency during initial ATLAS operation?

Answer: The factors affecting the initial data taking efficiency for cosmic muons are being evaluated in detail at the moment. I don?t know of any single large factors.

Vera Lüth (SLAC): At present, how long does it take to produce a typical high-pT event on a multi-core CPU unit (simulation)?

Answer: I don not have this number at the top of my head. It is not a limiting factor in our analysis. (Afterwards I have found out that the time for a full simulation is of the order of 2000 kSI2Kseconds depending on the type of event.)

Eckhard Elsen (DESY): Is the noise contributing to the ET-miss measurement already at the experimentally expected limit? What is the contribution from coherent noise etc...?

Answer: We are already in a rather good shape describing the noise. We continue to investigate the issue, in particular the tails of the noise distributions.

Vali Huseynov (Nakhchivan State University): One of the main mission of the ATLAS experiment is to test the existence of additional dimensions. How many additional dimensions do you expect from this experiment?

Answer: This is of course hard to tell. We certainly have strategies to investigate different models including extra dimensions. I mentioned one example. A spin analysis of a potential discovery of a narrow mass peak in the di-lepton invariant mass spectrum might disentangle a Z with spin one from a graviton resonance of spin two, the latter being a manifestation of extra dimensions.

Ahmed Ali (DESY): This is about the discovery potential of the SM Higgs boson at the LHC. Since the data taking will take place in the first stage at 7 to 10 TeV and the luminosity of the LHC is also scaled down in this phase, how long will it take the experiment at the LHC to be competitive with the ongoing experiments at the TeVatronin the SM Higgs search?

Answer: Considering that at 7 TeV the cross section for a Higgs boson, just above the mass limit set by LEP, is expected to be around 30cross section at 14 TeV, it will most likely take a couple of years until LHC is fully competitive.

Status of the CMS Experiment

Robert Cousins on behalf of the CMS Collaboration

Dept. of Physics and Astronomy, Univ. of California, Los Angeles, California 90095, USA

This talk provides an overview of many facets of the Compact Muon Solenoid (CMS) experiment, which was commissioned and ready for first beams in September 2008. Muons from beam splash, beam halo, and cosmic rays have provided valuable data for alignment and calibration, and for testing numerous aspects of offline software and computing. The first maintenance cycle is complete, and while eagerly anticipating for first LHC collisions, we also recall the CMS collaboration's physics studies based on simulated data to remind us of the exciting possibilities in the near future.

1 Introduction

The Compact Muon Solenoid (CMS) Collaboration consists of over 2500 scientists and engineers from 38 countries. After almost 20 years of work by collaborators and associated institutional and industrial partners, from the conception and design, through the construction, installation, and commissioning, CMS became a working experiment in September 2008. In this talk I review some of the highlights of installation and commissioning underground; the useful data taken during the brief period of single beams; the very productive month-long cosmics data-taking run after the LHC incident of September 19; the first maintenance cycle during the 2008-2009 shutdown; and a second cosmics run underway at the time of this conference. I also describe some of the many preparations and tests of software and computing, and end with a quick overview of some of the many physics analyses which have been prepared and extensively exercised on simulated data. These serve as reminder of the exciting possibilities in the months and years ahead of us.

For more information, the CMS main public page [1] has links to extensive public web pages including outreach information, continuously updated physics results for physicists, and an e-commentary during LHC beam periods.

2 The CMS detector

The central feature of the Compact Muon Solenoid (CMS) detector [2], illustrated in Fig. 1 alongside a transverse view of a cosmic muon traversing CMS, is a superconducting solenoid, of 6 m internal diameter, providing a field of 3.8 T. Within the field volume are the silicon pixel and strip tracker, the lead-tungstate crystal electromagnetic calorimeter (ECAL), and the brass/scintillator hadron calorimeter (HCAL). Muons are measured in gas-ionization detectors embedded in the steel return yoke. In addition to the barrel and endcap detectors, CMS has
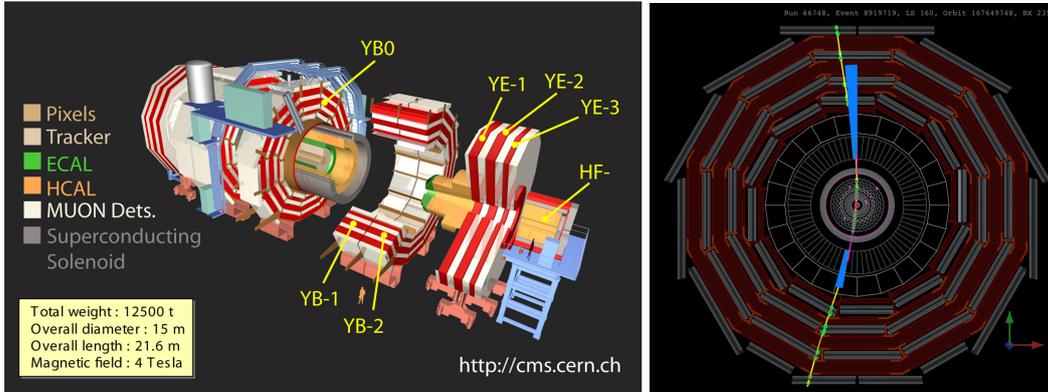
Figure 1: Left: The CMS detector. The z-axis, defined along the nominal LHC beams, has $+z$ direction pointing counter-clockwise. Right: Display of a cosmic muon (recorded during the CRAFT run, Sec. 6) that enters and exits through the muon system, leaves deposits in the HCAL and ECAL, and crosses the silicon strip and pixel tracking systems.

extensive forward calorimetry. CMS has an overall length of 22 m, a diameter of 15 m, and weighs 12 500 tonnes.

With 75 848 lead tungstate (PbWO$_4$) crystals (25.8 X_0 long in the barrel, 24.7 X_0 long in the endcaps), the ECAL has an energy resolution of better than 0.5 % above 100 GeV. The 15K-channel HCAL, when combined with the ECAL, measures jets with a resolution $\Delta E/E \approx 100\,\%/\sqrt{E} \oplus 5\,\%$. The CASTOR (5.3 $< |\eta| <$ 6.6) and Zero Degree ($|\eta| > 8.3$) calorimeters (made of quartz fibers/plates embedded in tungsten absorbers) cover very forward angles.

Muons with pseudorapidity in the range $|\eta| < 2.4$ are measured with detection planes made of three technologies: about 250 Drift Tube chambers (DT), 450 Cathode Strip Chambers (CSC), and 900 Resistive Plate Chambers (RPC). The readout has nearly 1 million electronic channels. Matching the muons to the tracks measured in the silicon tracker should result in a transverse momentum resolution between 1 and 5 %, for p_{T} values up to 1 TeV/c.

The inner tracker measures charged particles within the $|\eta| < 2.5$ pseudorapidity range. It consists of 1440 silicon pixel and 15 148 silicon strip detector modules. It provides an impact parameter resolution of ~ 15 μm and a transverse momentum (p_{T}) resolution of about 1.5 % for 100 GeV/c particles.

The first level (Level-1) of the CMS trigger system, composed of custom hardware processors, is designed to select the most interesting events in about 1 μs, using information from the calorimeters and muon detectors. The High Level Trigger (HLT) processor farm further decreases the event rate from up to 100 kHz to 100 Hz (initial DAQ system is 50 kHz), before data storage. On the Worldwide LHC Computing GRID (WLCG), some 50k cores dedicated to CMS run more than 2M lines of source code.

3 Installation of CMS components underground

The heavy elements of CMS began to be lowered into the experimental cavern in November 2006, starting with the forward calorimeters and continuing shortly thereafter with the $+z$ endcap disks and barrel wheels, complete with muon detectors and services. The central yoke wheel (YB0), which holds the cryostat, was lowered in February 2007, and by January 2008 the last heavy elements of the $-z$ endcap were successfully lowered into the cavern.

The campaign to connect services for the detectors within the central portion of CMS included the installation of more than 200 km of cables and optical fibres (about 6000 cables). Additionally, more than 20 km of cooling pipes (about 1000 pipes) were installed. The whole enterprise took place over a 5 month period and required more than 50 000 man-hours of effort. The silicon strip tracker was inserted in December 2007, its cabling was completed in March 2008, and its cooling was operational by June 2008. In the same month, the beryllium central beam pipe was installed and baked out.

The silicon pixel tracking system and the endcaps of the ECAL were the last components to be installed, in August 2008. The mechanics and the cabling of the pixel system have been designed to allow relatively easy access or replacement if needed. The preshower detector for the endcap electromagnetic calorimeter was the only major subsystem not installed prior to the 2008 data-taking with beam and cosmics. It was installed in March 2009.

4 Global run commissioning and final closing of CMS

A series of global commissioning exercises using the final detectors and electronics installed in the underground caverns, each lasting 3–10 days and occurring monthly or bimonthly, commenced in May 2007 and lasted until the experiment was prepared for LHC beams, by the end of August 2008. The scale of these "global runs" steadily increased to include all of CMS, while balancing the need to continue installation and perform extensive detector subsystem commissioning with the need for global system tests.

Many detector subsystems were available in their entirety for global commissioning by May 2008, and thus a series of four week-long exercises, each known as a Cosmics RUn at ZEro Tesla (CRUZET), were conducted to accumulate sizable samples of cosmic muon events from which to study the overall detector performance. By July (for the third CRUZET exercise) the silicon strip tracker was in the data-taking with about 75% of the front-end modules. In the fourth CRUZET exercise, in August, the complete silicon pixel tracker was introduced, along with the both endcaps of the ECAL, thus constituting the first global run with the CMS detector to be used for the September LHC beam. The total accumulated cosmic triggers at zero field exceeded 300 million, including the triggers recorded in September 2008 when the experiment was live for the first LHC beams. These global runs regularly exercised the full data flow from the data acquisition system at the experimental site to the reconstruction facility at the CERN Tier-0 computing facility, followed by the subsequent transfer of the reconstructed data to all seven of the CMS Tier-1 centres and to some selected Tier-2 centres.

The final sequence of closing the steel yoke was completed on August 25, 2008, and the last pieces of shielding were in place on September 3. After almost 20 years, from conception, design, construction and commissioning, CMS became a working experiment.
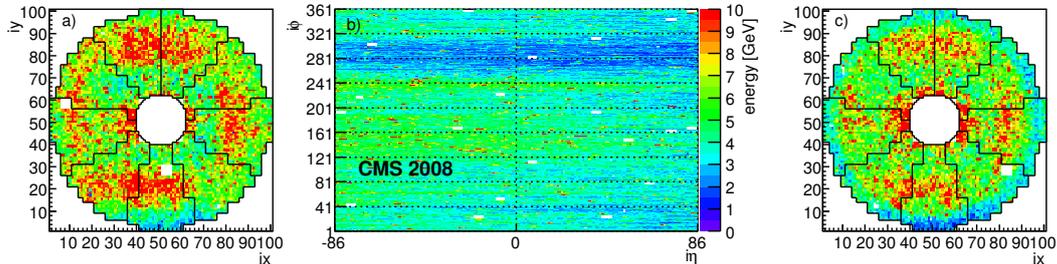
Figure 2: ECAL average energy deposit per crystal for a typical beam splash event with muons coming from the $-z$ side. (a) Occupancy of the $-z$ endcap, where ix and iy are indices of the crystals in the horizontal (x) and vertical (y) coordinates, respectively. (b) Occupancy of the barrel, where iη and iϕ are indices of the crystals in the η-ϕ coordinates. (c) Occupancy of the $+z$ endcap. The white regions correspond to channels masked in the readout, less than 1% of the total channels in that run. Many of these channels have been recovered subsequently.

5 LHC beam operations in 2008

The CMS experiment recorded data associated with activity from the first LHC beams in September 2008. This activity began with single shots of the beam onto a collimator 150 m upstream of CMS, which yielded sprays (so-called "beam splashes") containing $\mathcal{O}(10^5)$ muons crossing the cavern synchronously. With first circulating LHC beams beginning on September 10, CMS recorded beam-halo muons, first from the uncaptured beam, and then (at dramatically reduced rate) from the RF-captured beams. The CMS solenoid was off at the LHC's request, and the silicon pixel and strip tracking systems were powered off for safety reasons.

The first beam splash events were used to synchronize the beam triggers from several sources, and to commission the diamond beam condition monitors. The data collected from the beam splash events also proved useful for diagnostic occupancy plots and for adjusting the inter-channel timing of the ECAL and HCAL readout channels (Figs. 2 and 3), as the synchronous wave of crossing muons has a characteristic time-of-flight signature. CMS also recorded nearly 1 million beam-halo triggered events during the 2008 beam operations. For the endcap CSC's, beam halo muons were also valuable for making up for the lack of horizontal cosmics; by using them, local alignment precision of $270\,\mu$m was achieved within each ring of CSCs.

6 CRAFT 2008

Following the LHC incident of September 19 and end of LHC beams for 2008, in October and November CMS conducted a data-taking exercise known as the Cosmic Run At Four Tesla (CRAFT). In addition to commissioning the experiment operationally for an extended period, the cosmic muon dataset collected during CRAFT has proven invaluable for understanding the performance of the CMS experiment as a whole. The objectives of the CRAFT exercise were (1) to test the solenoid magnet at its operating field (3.8 T), with the CMS experiment in its final configuration underground; (2) to gain experience operating CMS continuously for one month; and (3) to collect approximately 300 million cosmic triggers for performance studies of the CMS subdetectors.
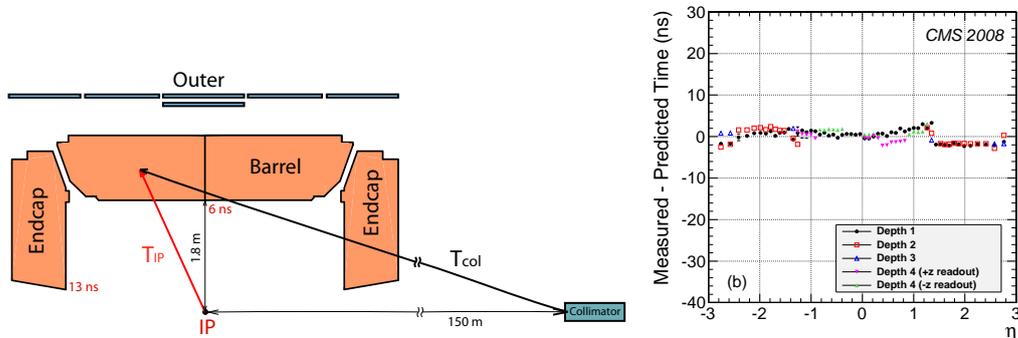
Figure 3: Left: A schematic view of the geometry of beam splash events. This geometry was used to predict the timing of energy deposits and thereby highlight channels in the HCAL that required synchronization. Right: Difference between measured and predicted time as a function of η from LHC beam splash events, after compensating sample delay settings were loaded for all three calorimeters, barrel, endcap and outer.

These goals were successfully met: over the course of 23 days during the most stable part of CRAFT, the experiment collected 270 million cosmic-triggered events with the solenoid at its operating central field of 3.8 T and with at least the silicon strip tracker and drift tube muon system operating at nominal conditions. These data were processed offline and then analyzed by teams dedicated to the calibration, alignment, and characterization of the detector subsystems. The precision achieved in detector alignment (equivalent to that foreseen after 10 pb^{-1} of LHC beam!), detector calibration, noise cleanup algorithms, as well as running the experiment for an extended period of time, gave confidence that the CMS experiment was ready for LHC beam operations. In the subsequent year 23 papers were written on performance and understanding of the detector, posted at arxiv.org, and submitted to JINST [3].

The infrastructure and services met the demands of running the experiment continuously for one month, although the exercise indicated areas needing further improvement. Several cooling failures did occur, resulting in the shutdown of some equipment during CRAFT. Leaks were detected on the barrel yoke circuit for wheels YB−2 and YB−1. The leak detection system on one of the cooling circuits fired unnecessarily a few times resulting in three automatic slow dumps of the magnet; the threshold has been subsequently adjusted. The cooling plants for the silicon strip tracker also suffered a few trips. The leak rate of the system was also higher than expected, necessitating a major revision in the ensuing shutdown. In total, about 70 hours of downtime were caused by general infrastructure related incidents, about 10% of the duration of CRAFT. This time was dominated by the downtime of the magnet. Aside from this, the typical data collection efficiency of CMS was about 70% during CRAFT, including periods used to conduct detector calibrations, pedestal runs, and diagnostics to further advance the commissioning of the experiment.

The data from cosmic muons was used to refine the timing of the Level-1 trigger, both in further cross-timing the elements within each subdetector beyond that performed with splash events, as well as synchronising across subsystems. As an example, trigger signals from the three muon systems are processed by the Global Muon Trigger (GMT), so it is necessary to
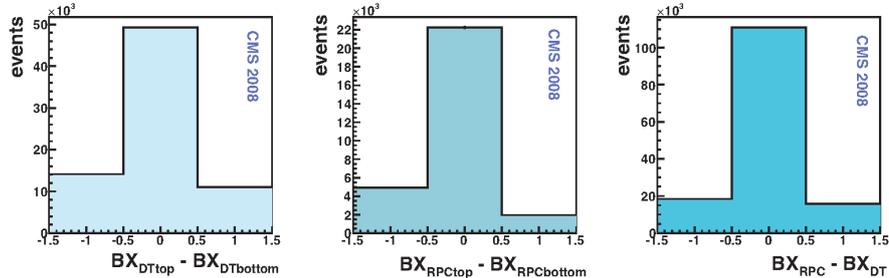
Figure 4: Time differences at the Global Muon Trigger (in units of 25-ns bunch crossing, BX) between Level-1 muon candidates - created in most cases by the same cosmic ray muon - from the top half and the bottom half of the DT system (left) and the RPC (middle) and between the RPC and DT system (right). The majority of the signals are synchronised and the skew at the clock edges is balanced.

ensure that the signal created by the same muon in different detectors enters the GMT in the same clock cycle. With cosmic rays (which, unlike eventual collision events, arrive at random phases within the LHC clock cycle, and do not originate from the beam collision plot), this was possible only to a limited extent. One method for fine-tuning of the timing delays involved measuring the signal arrival time from a particular subdetector with respect to triggers from another. A direct comparison is possible using the readout of the GMT, which records all input muon candidates and reads 3 consecutive clock cycles centered at the trigger. Fig. 4 shows that in most cases Level-1 muon candidates from different muon systems, induced by the same cosmic ray muon, arrive at the same BX. Occasional difference by 1 BX is unavoidable due to the fact that cosmic rays are asynchronous to the clock of the experiment and because the relative synchronisation between different detector parts obtained with cosmic rays has a finite precision of several ns. Such plots were used to fine-time the CSC timing during CRAFT, and similarly, delays of the various calorimeter trigger inputs to the Global Trigger were adjusted to provide the highest coincidence rate above the noise continuum.

Data were promptly reconstructed at the Tier-0 computing centre at CERN to create high-level physics objects with a job latency of about 8 hours, but with a broad distribution. These data were transferred to the CMS Analysis Facility (CAF) at the CERN Meyrin site and to several Tier-1 and Tier-2 centres worldwide for prompt analysis by teams of physicists. The average export rate from the Tier-0 centre to the Tier-1 centres during CRAFT was 240 MB/s, and the total volume transferred was about 600 TB.
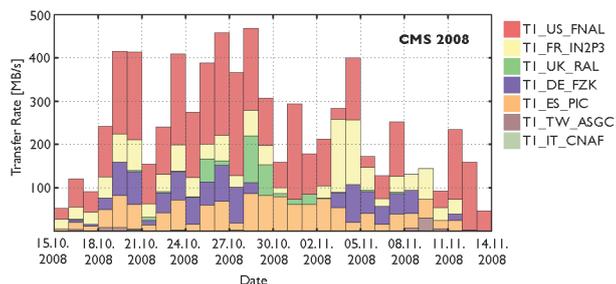
Figure 5: Transfer rates from Tier-0 to Tier-1 centres during CRAFT. The average was about 240 MB/s.

7 Data analysis results from CRAFT data

The data collected during CRAFT facilitated a wide range of analyses on the performance of the CMS subdetectors, the magnitude of the magnetic field in the return yoke, as well as the calibration and alignment of sensors in preparation for physics measurements. Alignment of the silicon strip and pixel sensor modules was improved significantly from initial survey measurements by applying sophisticated track-based alignment techniques to the data recorded from approximately 3.2 million tracks selected to cross the sensitive tracking region (with 110 000 tracks having at least one pixel hit). The precision achieved for the positions of the detector modules with respect to particle trajectories, derived from the distribution of the median of the cosmic muon track residuals, is 3–4 μm in the barrel and 3–14 μm in the endcaps for the coordinate in the bending plane. Other silicon tracking measurements performed with the CRAFT data include calibration of the absolute energy loss in silicon strip sensors, Lorentz angle measurements, hit efficiencies and position resolutions, track reconstruction efficiencies, and track parameter resolutions.

While the accuracy of the magnetic field map (calculated using TOSCA) had been previously confirmed to be better than 0.1% in the tracker region (where it is extremely uniform), the accuracy in the barrel steel yoke, used in muon reconstruction, was checked carefully for the first time using CRAFT 2008 DATA. The muon bending measured by DT chambers should agree with that predicted by extrapolating the track parameters measured by the inner tracking system. During CRAFT a discrepancy was noted: the measurement in the yoke was too high by up to 20%.

This was later traced to boundary conditions that had been set too restrictively in the TOSCA calculation, causing the magnetic field to be overestimated in the iron. The analysis also suggested improving the treatment of asymmetric features in the map. A field map based on these results has residual differences between data and the calculation reduced to about 4.5% in the middle station of the barrel yoke and 8.5% in the outer station; it is empirically corrected to better then 2% using the CRAFT measurements.

Figure 6: CMS magnetic field map.

Measurements of the cosmic muon energy loss, dE/dx, in the ECAL and HCAL barrel compartments validated the initial calibration of individual channels obtained prior to CRAFT. (The endcap studies suffered from small sample sizes.) The measured dE/dx as a function of muon momentum agrees well with first-principles calculations, as shown in Fig. 7.

Track-based alignment techniques using cosmic muons were also applied to align the DT muon detectors in the barrel region of the experiment. An alignment precision of better than 700 μm was achieved along the higher precision coordinate direction (approximately ϕ) for the first three DT stations as estimated by a cross-check of extrapolating muon segments from one detector to the next. A few lower-level resolution plots for CSC and DT position measurements were in my talk, and many more are in the CRAFT papers [3].

Figure 8 shows a higher-level result made possible by all this work: muon momentum

Figure 7: Left: Muon stopping power measured in PbWO$_4$ (dots) as a function of muon momentum compared to expectations (continuous black line). The expected contributions from collision and radiative processes are plotted as well (red dotted line and blue dashed line respectively). Right: (top) Energy loss of cosmic ray muons in the barrel HCAL after correcting the signal mean value for the muon path length and normalizing to the thickness at $\eta = 0$; (bottom) ratio of data and Monte Carlo simulation predictions (arbitrary scale) for the bottom half of the calorimeter.

resolution as determined from muons such as the one in Figure 1, for which one can compare the position and momentum measurements made independently using hits in the two halves of the track. In the p_T region below approximately 200 GeV/c, where the resolution is dominated by multiple-scattering effects, the inclusion of muon hits does not improve the resolution beyond that obtained with the tracker-only fits. In the high-p_T region, the resolution obtained with the dedicated high-p_T muon reconstructors (labeled as TPFMS and TMR) is better than that of global muons and of tracker-only tracks, as expected.

8   Activities during the 2008-2009 LHC shutdown

After the cosmics run ended, the detector was opened for carefully selected maintenance, consolidation, and repair activities, as well as the installation of the preshower subdetector and the CASTOR calorimeter. Work progressed according to the schedule laid down in Nov. 2008. After this seven-month long, successful maintenance period (resulting in only a few/mille channels not functioning), at the time of this talk in August 2009, CMS was closed once again and the CRAFT-2009 run was underway, once again taking cosmics data at the operating field of 3.8 T. The plan (since implemented) was to be smoothly taking data in a "beam-ready" state by the time of the first LHC beams of 2009.

Some highlights of the shutdown work on the hardware included: the installation and commissioning of the preshower on both endcaps; the removal, repair, and re-insertion of the forward pixel system; the installation of CASTOR ($5.2 < \eta < 6.6$) calorimeter; maintenance and (small) repairs involving many sub-systems; and the major revision of the tracker cooling plant to re-

duce leaks and improve reliability. As repaired components came online, re-commissioning of CMS proceeded with resumption of Mid-Week Global Runs and CRUZET-2009, interspersed with final maintenance and consolidation activities. Open, inclusive Level-1 and High-Level Triggers menus for early LHC running have passed tests at high throughput rates. (> 100 kHz for the full DAQ system except the HLT filter farm at 50 kHz).

In parallel to several re-reconstructions of the CRAFT data, large Monte Carlo simulation productions were produced and reconstructed (e.g., about 250M fully simulated events at 10 GeV begun at the end of 2008 were completed in February 2009). At the time of the talk, another large MC production was about to begin with CMSSW 3 (since completed).

Meanwhile, there was a large effort to prepare software for 2009 data taking, including improving stability and reliability of the computing infrastructure. Of course all of the results discussed here depend on extensive offline software (SW) (much of which also runs online for monitoring and high-level-triggering). During 2009, the major annual release known as CMSSW version 3 was developed and released in a sequence of updates converging on the version used for the major simulations and data-taking, and the respective analyses thereof. Among the many features added or refined, in many cases based on input from CRAFT08 and analysis exercises, were: GEANT4 and ROOT major updates; mixing of event data from more than one source, including simulated pileup; more realistic detector response, including dead/noisy channels; numerous improvements and innovations in reconstruction (such as track-corrected jets and missing E_T, and particle flow approach to event analysis); the new magnetic field map and empirical corrections to it; and the new version of Physics Analysis Toolkit used across the collaboration as a common language for analysis objects.

Figure 8: Widths of Gaussian fits to the distributions of the relative differences of measurements of charge over transverse momentum (q/p_T) made on the upper and lower halves of tracks such as that in Fig. 1 (divided by $\sqrt{2}$ to obtain single-track resolution), for various muon reconstruction algorithms, as a function of p_T of the reference track.

Much work also paid off in improving workflows, converting many manual operations to be more automatic, and reducing elapsed time, for example by pre-staging tapes to disk when re-reconstructing at Tier-1 centers. First analyses of the 2008 data used the WLCG infrastructure and the software release (CMSSW 2) that had been destined for 2008 data-taking. Re-reconstruction and further analyses proceeded quickly using updated alignment and calibration and refined CMSSW 2, and then CMSSW 3 after it was available.

All the the software usage in turn depends on the enormous computer infrastructure at CERN and on the WLCG, which has been scaled up in previous years and routinely exercised, with each exercise pointing to some needed improvements which had been subsequently implemented. In addition to participating successfully in extensive WLCG-wide tests as the Scale Testing for the Experimental Program (STEP'09) in spring, CMS made a concerted effort to

increase the site readiness of all Tier-1 and Tier-2 centers. As first LHC collisions approached, CMS computing was ready.

9 Physics commissioning

In parallel with installation and commissioning of the CMS detector, numerous physics analysis strategies have been "commissioned", necessarily using simulated data, but attempting wherever possible to exercise the eventual "data-driven" methods to extract detector resolutions, scale calibrations, and physics backgrounds from the data themselves. With simulated data, such results can be compared with "Monte Carlo truth", i.e. the assumed true values of resolution and backgrounds underlying the simulation.

Already two years ago, Tag and Probe (T&P) methods (such as those used in Tevatron experiments) were demonstrated in CMS simulations assuming 14 TeV LHC energy, to identify a physics object in an unbiased way in order to study efficiencies. E.g. , in $Z^0 \rightarrow e^+e^-$ events, using one tight electron as the tag, the other electron can be the probe, provided the invariant mass of the pair is M_Z. In a typical example of such an exercise, the measured efficiency from T&P was 94.36 ± 0.24, compared to MC truth of 94.63 ± 0.24 for 10 pb^{-1} at 14 TeV.

A brief sketch of the (extensively developed) plan for first physics analysis as the LHC increases intensity and energy is as follows. As emphasized above, much detector commissioning has already been achieved in the CRAFT run, supplementing earlier major test beam campaigns. After the LHC restart, splash events will be used for quick checks, and then first collisions at injection energy will be a long-anticipated next step, providing not only particles
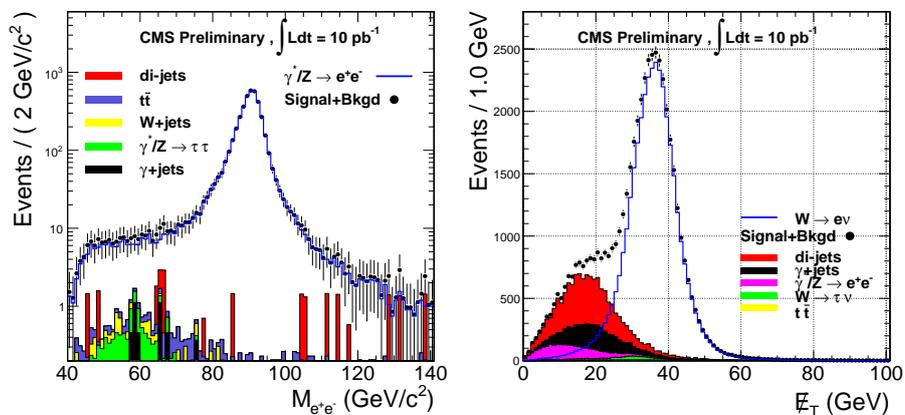
Figure 9: The M_{ee} distribution (left) for the $\gamma^*/Z \rightarrow e^+e^-$ signal, and the $\not{E}_T$ distribution (right) for the $W \rightarrow e\nu$ signal, each also showing the considered backgrounds, and each after selection cuts applied for 10 pb^{-1} of integrated luminosity.
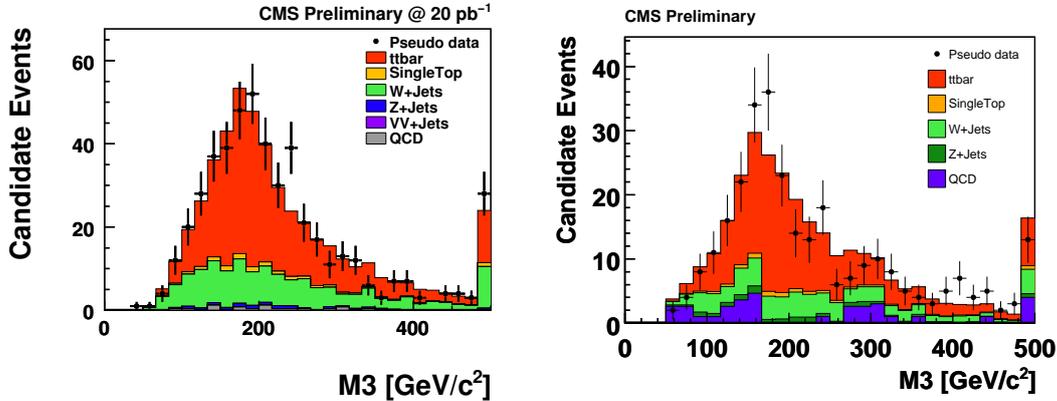
Figure 10: In the simulated search for $t\bar{t} \to \mu+ \geq 4$ jets (left) and $t\bar{t} \to e+ \geq 4$ jets (right) for 20 pb^{-1} at 10 TeV, the invariant mass of the three jets with the highest vectorially summed ET for the final selection. The pseudodata are a set of randomly selected, Poisson fluctuated, simulated events drawn from each process.

emerging from the interaction point for synchronization and alignment refinement, but also the first copious supplies of hadrons, including resonances which can demonstrate the performance of the ECAL (π^0) and tracking (K$_S^0$, Λ^0). (This in fact occurred [1].)

In the next step (scheduled for spring 2010), with 10-20 pb^{-1} at 7 TeV total LHC beam energy, the trigger will continue to be commissioned and refined, and more complex "physics commissioning" can proceed to "rediscover" the heavier objects of the Standard Model, and as luminosity becomes sufficient, measure rates of yet higher-p_T jets, leptons, and W, Z, and top (while of course being watchful for any extraordinary new signatures). At 7 TeV total energy, the approximate yields for detection of particles per inverse pb are 3000 W decays to electron or muon; 300 Z decays to ee or $\mu\mu$, and 5 $t\bar{t}$ events with at least one e or μ from the W decays. Some examples simulated at 10 TeV are in Figs. 9 and 10. Improved understanding of physics objects will result in, e.g., the jet energy scale from $W \to jj$, and extensive use (and understanding) of b-tagging. In parallel there will be extensive efforts to measure and understand backgrounds to SUSY and Higgs searches. As data accumulates, one can look for excesses such as those from SUSY and Z$'$ resonances. The search for new physics can then be significantly expanded as the luminosity increases and in particular as the energy increases towards 10 TeV total beam energy. With about 1000 pb^{-1}, CMS can enter the Higgs discovery era.

Fig. 11 can serve to remind the audience of some discovery possibilities which have been simulated. My talk contained a number of other plots, for example those showing the dramatic improvement in jet transverse energy and missing transverse energy resolutions in the reconstruction of simulated high-p_T events if a complete "particle flow" algorithm is applied; it is of course of great interest to see how such sophisticated algorithms perform in real LHC high-p_T data. Other plots pointed to the early potential to see high-mass dilepton resonances (Z$'$) if they exist just beyond current limits.
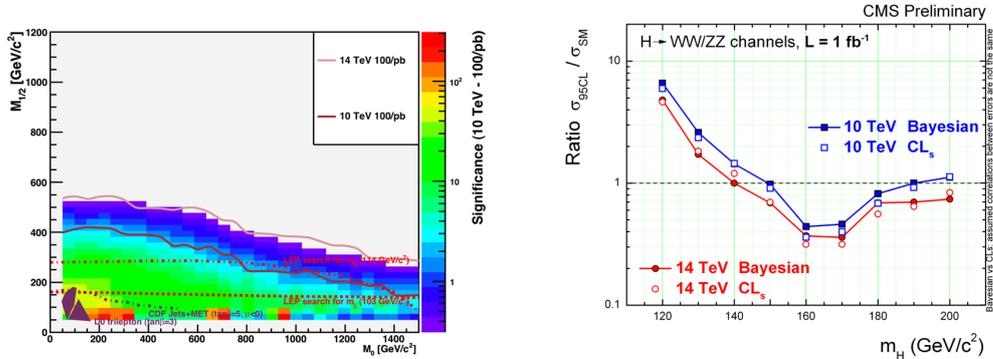
Figure 11: Left: Comparison of 5-sigma reach curves for search for SUSY in $\geq$ 3jets + $E\!\!\!/_T$ channel for 100 pb^{-1} of data collected at 14 and 10 TeV; the color maps gives the significance in each point at 10 TeV. Right: Projected exclusion limits for the SM Higgs boson at 14 and 10 TeV center of mass energies, using only H $\rightarrow$ WW$^{(*)} \rightarrow 2\ell2\nu$ and H $\rightarrow$ ZZ$^{(*)} \rightarrow 4\ell$ channels.

10 Summary

During the autumn 2008 LHC beam and cosmics runs, the sub-detectors, online, offline, computing, and analysis systems all performed well. The ensuing shutdown included maintenance activities and repairs interleaved with installation of the preshower detector. Much very useful information has been extracted from the 2008 CRAFT data, summarized in 23 papers [3].

At the time of the talk, the software, computing systems, and analysis systems were being exercised with newly taken cosmics data and by generating, distributing, and analysing 200M events to update 10 TeV "physics analyses" (and subsequently 7 TeV) using the software release intended for data taking. The experiment was being closed and another long magnet-on cosmics run (CRAFT 2009) was underway to put CMS once again into "beam-ready" state. CMS was (again) be ready, and eager, for LHC beam. Indeed, after the talk, circulating beams were quickly followed by collisions at injection energy and up to 2.36 TeV total beam energy – that story is unfolding on the CMS web site [1].

Acknowledgments

I thank the U.S. Dept. of Energy and the National Science Foundation for their support of my work on CMS. Acknowledgments of support of all CMS are given in Refs. [2, 3].

References

[1] CMS Public and Outreach web pages, `http://cms.cern.ch`. This includes a link to the real-time CMS "e-commentary" during the runs following this talk.

[2] CMS Collaboration, "The CMS experiment at the CERN LHC", JINST 0803:S08004, 2008.

[3] CMS Collaboration, "Commissioning of the CMS Experiment and the Cosmic Run at Four Tesla," arXiv:0911.4845v1, and 22 other papers posted at arxiv.org, submitted to JINST.

Discussion

Joel Feltesse (IRFU, CEA): Now that your detector has become reality, and that you better know the performances, have you identified a few physics processes where you are in a better or worse place than ATLAS? Of course the previous speaker (Kerstin Jon-And) can also comment about it.

Answer: I think that the detectors are fairly well matched in capabilities, each being well-designed for the the broad physics program. Now the key for each collaboration going forward is to understand well the calibration, alignment, and performance of the detector that they have built. That will determine which discoveries are seen or missed (and when) more than anything else. Both collaborations have a very good start on this by using test beams, beam splash events, and cosmics, as we have described.

Dimitri Denisov (FNAL): With the 2010 data set consisting of 7 TeV and 10 TeV samples: What is the strategy of combining these two samples for physics studies? Or is the 7 TeV sample expected to be mainly used for physics commissioning?

Answer: Of course, the first thing will be to analyze each set separately, so that a consumer can judge the reasonableness of any answer coming out of a combination. When I think about combining, I conclude that transparency of the combination may put a constraint on how fancy one should get in combinations in our first data sets. But if, as we hope, most of the running is at the higher energy (10 TeV is an upper bound, but it could be lower), then one might see hints at 7 TeV but the more compelling evidence at the higher energy without needing to combine them formally.

Bennie Ward (Baylor University): The previous speaker quoted ATLAS efficiency (data taking eff.) at 83You showed CMS's at 70%. What is the main reason for the difference in the two?

Answer: I would first mention that in quoting an efficiency there are choices to be made regarding which time interval to average over, which types of one-off failures (such as CERN site-wide power cut) to include, etc., if you want to make a relevant inference about future running efficiency. So I do not know if the numbers are directly comparable. In our case, the number is a rather inclusive number for several weeks. We have days (when we are not interrupting for tests) in which the efficiency is over 90%.

Sakue Yamada (KEK): You mentioned about PFA and said MC gives much better result. Did you try to find the reason?

Answer: A lot of it goes back to design choices: the CMS design has a high magnetic field and emphasizes excellent tracking and high-precision extremely-fined-grained electromagnetic calorimetry, which in turn forced some compromises (most obviously non-compensation) in CMS jet calorimetry. So, as you saw, the ATLAS calorimeter has better intrinsic jet resolution than that of CMS. The particle flow algorithm takes advantage of the superb CMS resolution in the tracker and ECAL, and substantially reduces the dependence on the HCAL for measuring hadrons (as neutral hadrons ac-

count for only about 10% of the energy of a jet), except at higher energy where the HCAL resolution is better and tracking resolution worsens. The result is a much smaller correction factor from raw (observed) jet energy to estimated (corrected) jet energy.

Recent Results from HERA

S. Glazov

DESY, Notkestraße 85, 22607 Hamburg, Germany

HERA *ep* collider provides unique information on the proton structure. High center-of-mass energy $s = 320$ GeV gives access to both the low Bjorken-x domain and regime of high momentum transfers Q. An ultimate precision for the deep inelastic scattering cross section is achieved by combining the measurements of the H1 and ZEUS collaborations. The combined data are used as a sole input to a QCD fit to obtained HERAPDF set. Both collaborations report measurements of the structure function F_L which provides important check of the QCD evolution. Semi-inclusive analyzes give additional information on the strong couplin constant α_S and heavy flavor contribution.

1   Introduction

Deep inelastic lepton-hadron scattering (DIS) is important for the understanding of the structure of the proton and of the dynamics of parton interactions. The discovery of Bjorken scaling [1] and its violation [2] at fixed target experiments triggered the development of the theory of strong interactions, Quantum Chromodynamics (QCD). Significant progress in the exploration of strong interactions has been achieved at the electron-proton collider HERA.

The high center-of-mass energy of the *ep* scattering at HERA leads to a wide kinematic range extending to large values of the absolute of the four-momentum transfer squared, Q^2, and to very small values of the Bjorken x variable. Electron (proton) beam energy of $E_e = 27.6 \, \text{GeV}$ ($E_p = 920 \, \text{GeV}$) give access to Bjorken x values as small as 10^{-4} for Q^2 of $10 \, \text{GeV}^2$ and Q^2 values as high as $30000 \, \text{GeV}^2$ for high x. A QCD analysis of the inclusive cross-section data allows to determine parton distribution functions (PDFs).

HERA operation spanned over 15 years, from 1992 until 2007, with a shutdown in $2000-2002$ to upgrade luminosity and instal spin rotators, to enable longitudinal beam polarization for the colliding experiments. The two colliding experiments, H1 and ZEUS, collected the DIS data for the whole HERA running period. The data before the luminosity upgrade is used for high precision measurements at low Q^2 and low x, where the scattering cross section is high. The data after the luminosity upgrade is focused more on high Q^2 analyzes and polarization studies. For the last three months of its operation HERA run at reduced proton beam energy to measure the proton structure function F_L.

2   DIS Cross Section

The neutral current deep inelastic $e^{\pm}p$ scattering cross section, at tree level, is given by a linear combination of generalized structure functions. For unpolarized beams it can be expressed as

$$\sigma_{r,\text{NC}}^{\pm} = \frac{\text{d}^2\sigma_{\text{NC}}^{\pm}}{\text{d}x\text{d}Q^2} \cdot \frac{Q^4 x}{2\pi\alpha^2 Y_+} = \tilde{F}_2 \mp \frac{Y_-}{Y_+}x\tilde{F}_3 - \frac{y^2}{Y_+}\tilde{F}_L, \tag{1}$$
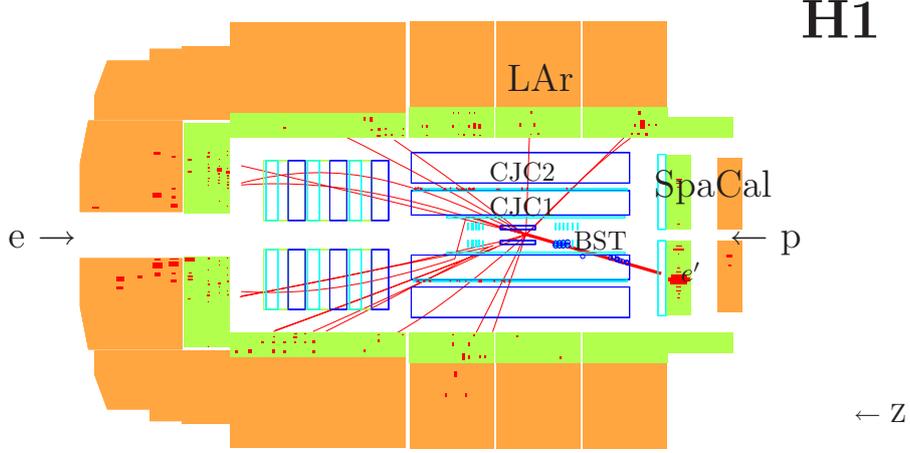
Figure 1: A view of a high y event reconstructed in the H1 detector. The positron and proton beam directions are indicated by the arrows. For the coordinate system used at HERA the z axis points in the direction of the proton beam. The interaction vertex is reconstructed using the hadronic final state (thin lines) and the scattered positron (thick line) tracks in the central tracker. The central tracker consists of (from the beam line outwards) the silicon tracker, the drift chambers CJC1 and CJC2, it is surrounded by the liquid argon (LAr) calorimeter. The detector operates in a solenoidal magnetic field of 1.16 T. The scattered positron trajectory is reconstructed in the backward silicon tracker BST and the CJC1. The charge of the particle is determined using the track curvature. The positron energy is measured in the electromagnetic part of the SpaCal calorimeter.

where the electromagnetic coupling, the photon propagator and a helicity factor are absorbed in the definition of a reduced cross section $\sigma_{r,\mathrm{NC}}^{\pm}$, and $Y_{\pm} = 1 \pm (1-y)^2$. The functions $\tilde{F}_2$, $\tilde{F}_L$ and $x\tilde{F}_3$ depend on the electroweak parameters as:

$$
\begin{aligned}
\tilde{F}_2 &= F_2 - \kappa_Z v_e \cdot F_2^{\gamma Z} + \kappa_Z^2 (v_e^2 + a_e^2) \cdot F_2^Z, \\
\tilde{F}_L &= F_L - \kappa_Z v_e \cdot F_L^{\gamma Z} + \kappa_Z^2 (v_e^2 + a_e^2) \cdot F_L^Z, \\
x\tilde{F}_3 &= \kappa_Z a_e \cdot x F_3^{\gamma Z} - \kappa_Z^2 \cdot 2 v_e a_e \cdot x F_3^Z.
\end{aligned}
\tag{2}
$$

Here v_e and a_e are the vector and axial-vector weak couplings of the electron to the Z boson and $\kappa_Z(Q^2) = Q^2/[(Q^2 + M_Z^2)(4\sin^2\Theta\cos^2\Theta)]$. At low Q^2, the contribution of Z exchange is negligible and $\sigma_{r,\mathrm{NC}} = F_2 - y^2 F_L/Y_+$. The contribution of the term containing the structure function F_L is only significant for large values of y.

In the Quark Parton Model (QPM) the structure function F_L is zero [3] and the other functions in equation 2 are given as

$$
\begin{aligned}
(F_2, F_2^{\gamma Z}, F_2^Z) &= [(e_u^2, 2e_u v_u, v_u^2 + a_u^2)(xU + x\bar{U}) \\
&+ (e_d^2, 2e_d v_d, v_d^2 + a_d^2)(xD + x\bar{D})], \\
(xF_3^{\gamma Z}, xF_3^Z) &= 2x[(e_u a_u, v_u a_u)(xU - x\bar{U}) \\
&+ (e_d a_d, v_d a_d)(xD - x\bar{D})],
\end{aligned}
\tag{3}
$$
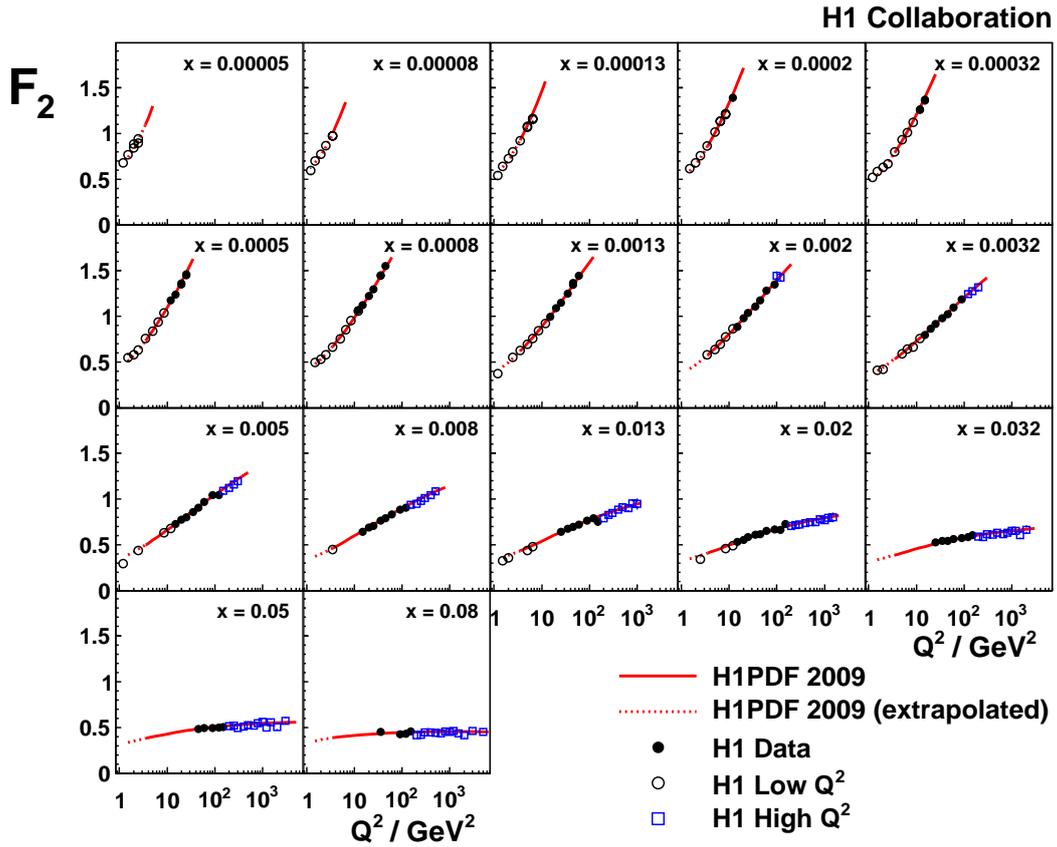
Figure 2: Measurement of the structure function F_2 as a function of Q^2 at various values of x by the H1 collaboration. The error bars represent the total measurement uncertainties. The solid curve represents the H1PDF 2009 QCD fit for $Q^2 \geq 3.5$ GeV^2, which is also shown extrapolated down to $Q^2 = 1.5$ GeV^2 (dashed).

where e_u, e_d denote the electric charge of up- or down-type quarks while $v_{u,d}$ and $a_{u,d}$ are the vector and axial-vector weak couplings of the up- or down-type quarks to the Z boson. Here xU, xD, $x\overline{U}$ and $x\overline{D}$ denote the sums of up-type, of down-type and of their anti-quark distributions, respectively. Below the b quark mass threshold, these sums are related to the quark distributions as follows

$$
\begin{aligned}
xU = xu + xc, \qquad x\overline{U} = x\overline{u} + x\overline{c}, \\
xD = xd + xs, \qquad x\overline{D} = x\overline{d} + x\overline{s},
\end{aligned}
\tag{4}
$$

where xs and xc are the strange and charm quark distributions. Assuming symmetry between sea quarks and anti-quarks, the valence quark distributions result from

$$
xu_v = xU - x\overline{U}, \qquad xd_v = xD - x\overline{D}.
\tag{5}
$$

A reduced cross section for the inclusive unpolarized charged current $e^{\pm}p$ scattering is

$$
\sigma_{r,\mathrm{CC}}^{\pm} = \frac{2\pi x}{G_F^2} \left[\frac{M_W^2 + Q^2}{M_W^2} \right]^2 \frac{\mathrm{d}^2\sigma_{\mathrm{CC}}^{\pm}}{\mathrm{d}x\mathrm{d}Q^2}.
\tag{6}
$$

At leading order, the e^+p and e^- charged current scattering cross sections are

$$
\begin{aligned}
\sigma_{r,\mathrm{CC}}^{+} &= x\overline{U} + (1-y)^2 xD, \\
\sigma_{r,\mathrm{CC}}^{-} &= xU + (1-y)^2 x\overline{D}.
\end{aligned}
\tag{7}
$$

The NC and CC measurements may be used to determine the combined sea quark distribution functions, $\overline{U}$ and $\overline{D}$, and the valence quark distributions, u_v and d_v. A QCD analysis in the DGLAP formalism [4] also allows the gluon momentum distribution xg in the proton to be determined from the scaling violations of the data.

For NC scattering, event kinematics can be reconstructed using the scattered electron as well as the hadronic final state particles. A typical low Q^2, high y event measured by the H1 detector is shown in figure 1. For CC scattering, kinematics is reconstructed using the hadronic final state.

3 Measurements of DIS Cross Section at low Q^2 by H1

Recently the H1 collaboration reported new measurements of the NC cross section at low $0.2 \leq Q^2 \leq 150$ GeV^2 [5, 6] based on data collected in 1999-2000. The precision of the data reaches 1.3% for intermediate values of Q^2. Figure 2 shows the structure function F_2 for fixed values of x as a function of Q^2 obtained from these cross-section results. For low x, there is a strong Q^2 dependence of the structure function. For highest x, the data show approximate scaling behavior. The data are compared to an next-to-leading order (NLO) QCD fit, termed H1PDF2009, which describes the data very well.

4 Combination of the H1 and ZEUS data

The highest precision of the cross-sections measurements at HERA is obtained by combining the results from the H1 and ZEUS experiments. The combination of the results is performed
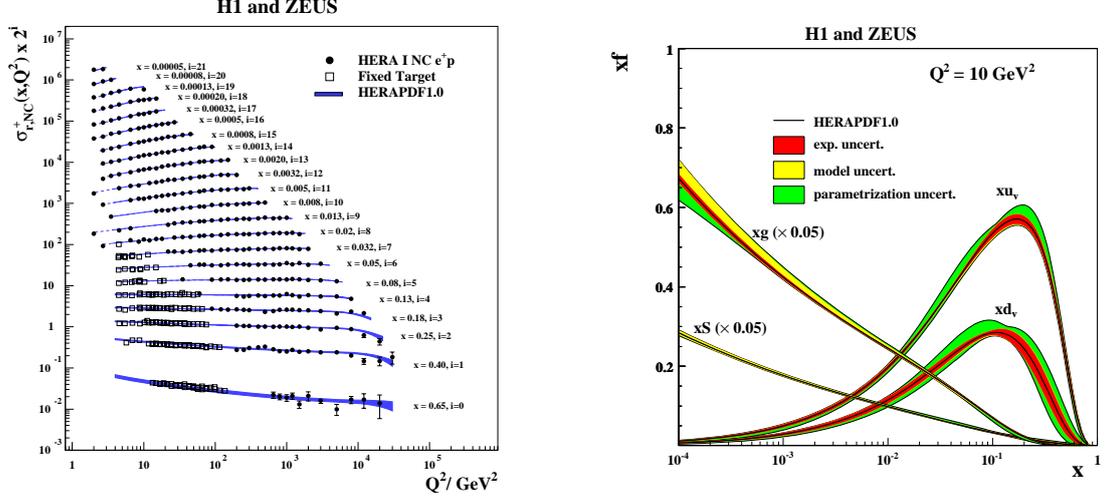
Figure 3: Measurement of the e^+p NC scattering cross section based on the combination of the H1 and ZEUS data compared to the fit to these data and measurements from fixed-target experiments.

taking into account the correlated systematic uncertainties [5, 11]. The starting point is the χ^2 function for individual measurement which is defined as

$$\chi^2_{\text{exp}}\left(\boldsymbol{m}, \boldsymbol{b}\right) = \sum_i \frac{\left[m^i - \sum_j \gamma_j^i m^i b_j - \mu^i\right]^2}{\delta^2_{i,\text{stat}}\, \mu^i \left(m^i - \sum_j \gamma_j^i m^i b_j\right) + \left(\delta_{i,\text{uncor}}\, m^i\right)^2} + \sum_j b_j^2. \tag{8}$$

Here μ^i is the measured value at a point i and γ_j^i, $\delta_{i,\text{stat}}$ and $\delta_{i,\text{uncor}}$ are relative correlated systematic, relative statistical and relative uncorrelated systematic uncertainties, respectively. The function χ^2_{exp} depends on the predictions m^i for the measurements (denoted as the vector $\boldsymbol{m}$) and the shifts of correlated systematic error sources b_j (denoted as $\boldsymbol{b}$). For the reduced cross-section measurements $\mu^i = \sigma^i_r$, i denotes a (x, Q^2) point, and the summation over j extends over all correlated systematic sources. The predictions m^i are given by the assumption that there is a single true value of the cross section corresponding to each data point i and each process, neutral or charged current e^+p or e^-p scattering. Under the assumption that the statistical uncertainties are proportional to the square root of the number of events and that the systematic uncertainties are proportional to $\boldsymbol{m}$, the minimum of equation 8 provides an unbiased estimator of $\boldsymbol{m}$.

Several data sets providing a number of measurements are represented by a total χ^2 function, which is built from the sum of the χ^2_{exp} functions for each data set e The data averaging procedure allows the rearrangement of the total χ^2 such that it takes a form similar to equation 8.

The averaging procedure is applied to the H1 and ZEUS inclusive data from the HERA-I running period. All the NC and CC cross-section data from H1 and ZEUS are combined in one simultaneous minimization[12]. Therefore resulting shifts of the correlated systematic
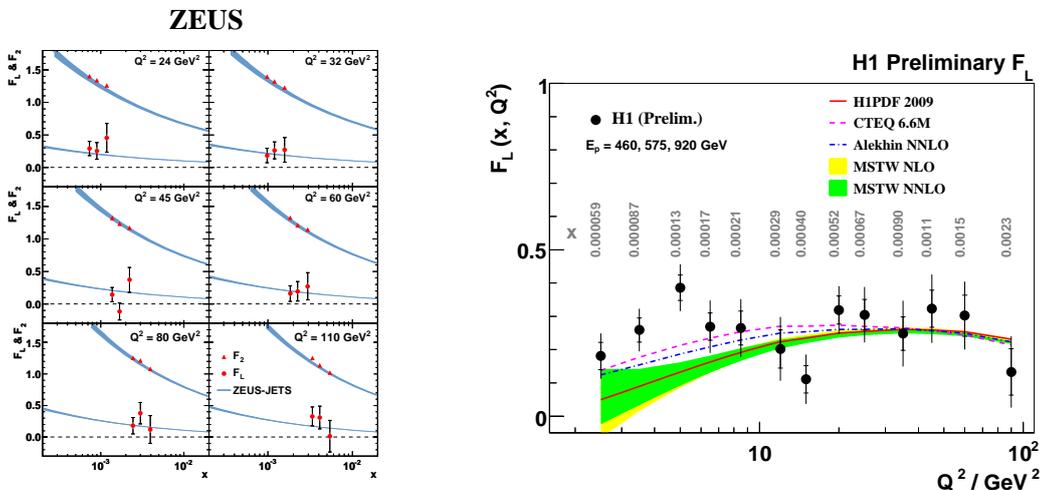
Figure 4: Left: measurement of the structure functions F_L and F_2 by the ZEUS collaboration compared to the prediction of ZEUS-JETS fit. Right: Preliminary measurement of the structure functions F_L and F_2 by the H1 collaboration. The data are quoted at fixed values of Q^2 and x indicated in grey and compared to predictions based on various models.

uncertainties propagate coherently to both CC and NC data. In total 1402 data points are combined to 741 cross-section measurements. The data show good consistency, with $\chi^2/n_{\mathrm{dof}} = 637/656$. In figure 3 left, the NC reduced cross section, for $Q^2 > 1\,\mathrm{GeV}^2$, is shown as a function of Q^2 for the HERA combined e^+p data and for fixed-target data [13, 14] across the whole of the measured kinematic plane. The data precision reaches 1.1% for $10 \leq Q^2 \leq 100\ \mathrm{GeV}^2$.

The combined data uses as a sole input for the NLO QCD analysis. The result of the fit is compared to the data in figure 3, left. There is a good agreement between the extrapolation of the fit to lower Q^2 and fixed-target data in this kinematic domain. The parton distribution densities obtained in this fit are shown in figure 3, right for $Q^2 = 10\ \mathrm{GeV}^2$. The QCD analysis considers various sources of the uncertainties which arise from experimental data, model assumptions and parameterization form of the PDFs. A prominent features of the parton densities is the dominance of the gluon and sea at low x.

5 Measurements of the Structure Function F_L

Large gluon density, determined from scaling violation of the F_2 data using QCD fits implies that the structure function F_L must be significant at low x. Direct measurements of F_L allow to test this prediction providing a check of the QCD and adding an extra constraint for the gluon density.

To determine the two structure functions $F_2(x, Q^2)$ and $F_L(x, Q^2)$ from the reduced cross section it is necessary to perform measurements at the same values of x and Q^2 but different y. This is achieved at HERA by reducing the proton beam energy. Two e^+p runs at reduced proton beam energy $E_p = 460$ GeV and $E_p = 575$ GeV were performed with an integrated luminosity of about 13 pb^{-1} and 6 pb^{-1}, respectively. The run at $E_p = 460$ GeV gives highest sensitivity
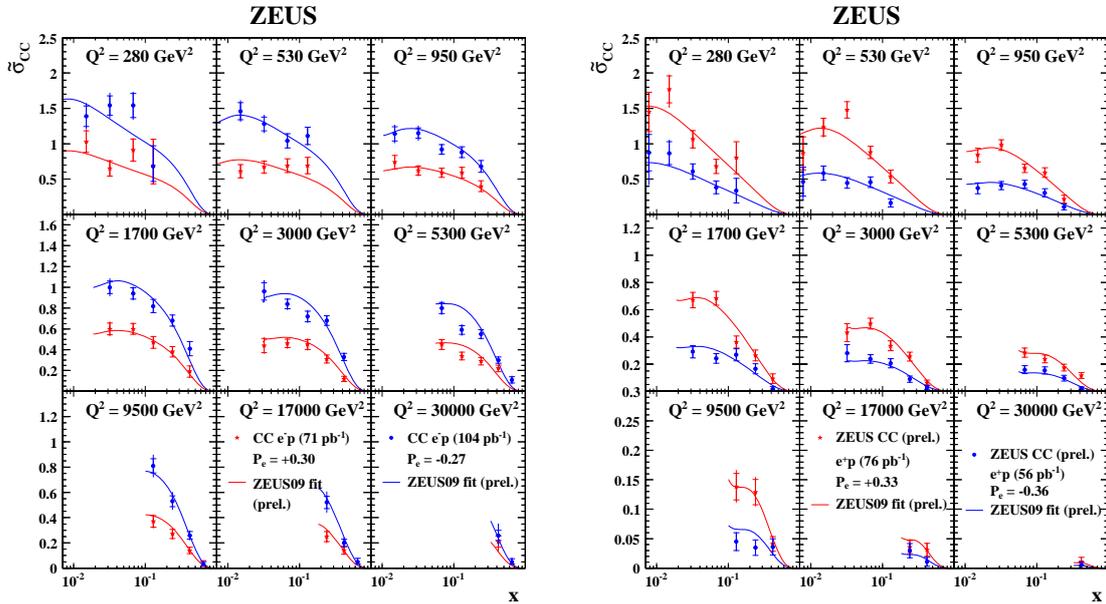
Figure 5: CC e^-p (left) and e^+p (right) scattering cross section measured by the ZEUS collaboration. Data for positive (red stars) and negative (blue dots) polarization are compared to the fit.

to F_L while the run at $E_p = 575$ GeV extends the kinematic range of the measurement and provides an important cross check.

The measurement must extend to as high y as possible to increase sensitivity to F_L. A high y kinematic domain at low Q^2 corresponds to low energies of the scattered positron E'_e. Measurement at low E'_e is challenging primarily because of high hadronic background.

The ZEUS collaboration uses Monte Carlo (MC) simulation to estimate the background. The MC prediction is normalized to the data using a sub-sample of tagged background events. The results of the ZEUS analysis [15] are shown in figure. 4, left. ZEUS report measurement of both structure functions F_2 and F_L obtained from a linear fit of the reduced cross section as a function of y^2/Y_+. The structure function F_L is found to be in a good agreement with the prediction of the ZEUS-JETS PDF set [16].

To reduce and estimate the hadronic background, H1 demand the scattered positron candidate to have a reconstructed track with well measured curvature. The curvature is used to determine the candidate charge. For the signal, positive charge is expected. The background is approximately charge symmetric, i.e. the number of background events with different charges is about equal. Using this, the background is estimated from the negative charge sample, corrected for a small charge asymmetry and then subtracted from the positive charge sample. The charge asymmetry of the background is determined directly from the data by comparing negatively and positively charged candidates from e^+p and e^-p data taking periods, respectively. Therefore, the background determination is purely data driven for the H1 analysis.

H1 published the first measurement of F_L at HERA using drift chambers CJC1 and CJC2 together with the SpaCal calorimeter for $12 \leq Q^2 \leq 90 \text{ GeV}^2$[17] and also reported a preliminary result at higher Q^2 using the LAr calorimeter [18]. These measurements were recently extended to lower $2.5 < Q^2 < 12 \text{ GeV}^2$ by using the backward silicon tracker BST [19].

The H1 measurement of the structure function F_L is shown in figure 4, right. The data are compared to the predictions from various models. The predictions agree among each other and with the data for $Q^2 > 10 \text{ GeV}^2$. For lower Q^2, there is a notable difference between the NLO predictions of MSTW and CTEQ. This difference is traced down to the difference in accounting for α_S^2 corrections. The data are somewhat higher than both predictions and agree better with the CTEQ calculations.

6 Charged Current $e^{\pm}p$ DIS Cross Section

In the standard model, the CC cross section depends linearly on the longitudinal electron beam polarization. Figures 5, left and figures 5, right show published [21] and preliminary analyzes of e^-p and e^+p CC cross sections performed by the ZEUS collaboration. For the published e^-p sample, the same 2005-2006 data are used as for the published NC sample, the preliminary e^+p analysis is based on data collected in 2003-2004 and 2006-2007. The data agree well with the expectations of the QCD fit. The e^+p CC data are of additional value for the QCD analyzes because they are sensitive to the d and s quark densities which are less constraint by the NC data, see equations 3 and 7.

7 Jet Cross Section and Determination of α_S

The production of jets in DIS can be used to determine the gluon density and to measure the strong coupling constant α_S. Recently H1 have performed a measurement of inclusive, 2-jet and 3-jet cross sections [22] as a function of Q^2 using HERA data collected in 1999-2007 with an integrated luminosity of $395 \ pb^{-1}$. The measurements are well described by NLO QCD calculations, corrected for hadronization effects.

Using these data, H1 determine the strong coupling constant α_S. The measurement is performed separately for different Q^2 bins and different processes. These measurements are combined together and the evolution of α_S as a function of Q is compared to the theory prediction in figure 6. A good agreement is observed between the data and theory. The theoretical uncertainty is dominated by the higher order corrections. The value of α_S at M_Z

$$\begin{aligned} \alpha_S(M_Z) &= 0.1176 \pm 0.0020(\text{exp.})^{+0.0046}_{-0.0030}(\text{th.}) \\ &\pm 0.0016(\text{PDF}) \end{aligned} \tag{9}$$

agrees well with the world average. The experimental error on α_S is about 0.6%. The total uncertainty is dominated by the theory, it may be improved with calculation of NNLO corrections.
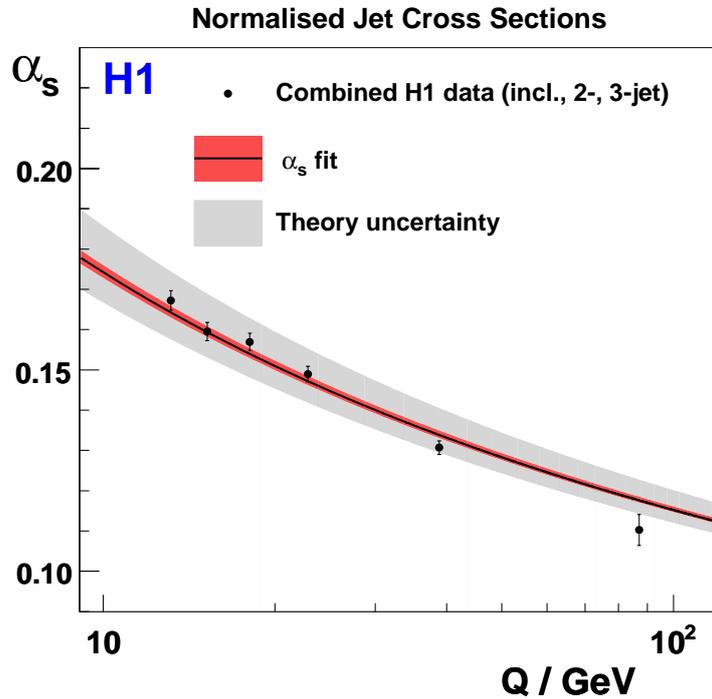
Figure 6: α_S as a function of Q obtained by H1 by a simultaneous fit of all normalized jet cross sections.

8 Measurements of Strange, Charm and Bottom Quark Densities

Inclusive NC cross section at low Q^2 and low x are dominated by the structure function F_2 and do not allow to separate contributions of individual quark flavors. The flavor separation can be achieved in semi-inclusive scattering by tagging the struck quark flavor. For HERA kinematics, tagging production of a charmed meson, e.g. D^*, almost certainly corresponds to a scattering off a c-quark. Samples with secondary vertices are enriched with scattering off c and b-quarks.

To measure b and c structure functions using secondary vertices, it is essential to have high precision tracking detector installed close to the interaction point. Recently the H1 collaboration reported the measurement of c and b reduced cross sections [23], using secondary vertex technique, based on complete sample for which the central silicon tracker was installed. These data are shown in figure 7 and compared to the H1PDF2009 fit. For all Q^2 bins there is a strong rise of the reduced cross section to low x values which increases with increasing Q^2. This is a direct indication of the large gluon density. The data are in a good agreement with the H1PDF2009 fit. The uncertainty of the fit is dominated by the model uncertainty due to the variation of the heavy quark masses. Therefore, these data allow to check the model and determine these parameters.

The fixed-target experiment HERMES, which operated using HERA $e^{\pm}$ beams, recently

H1 CHARM CROSS SECTION IN DIS

H1 BEAUTY CROSS SECTION IN DIS
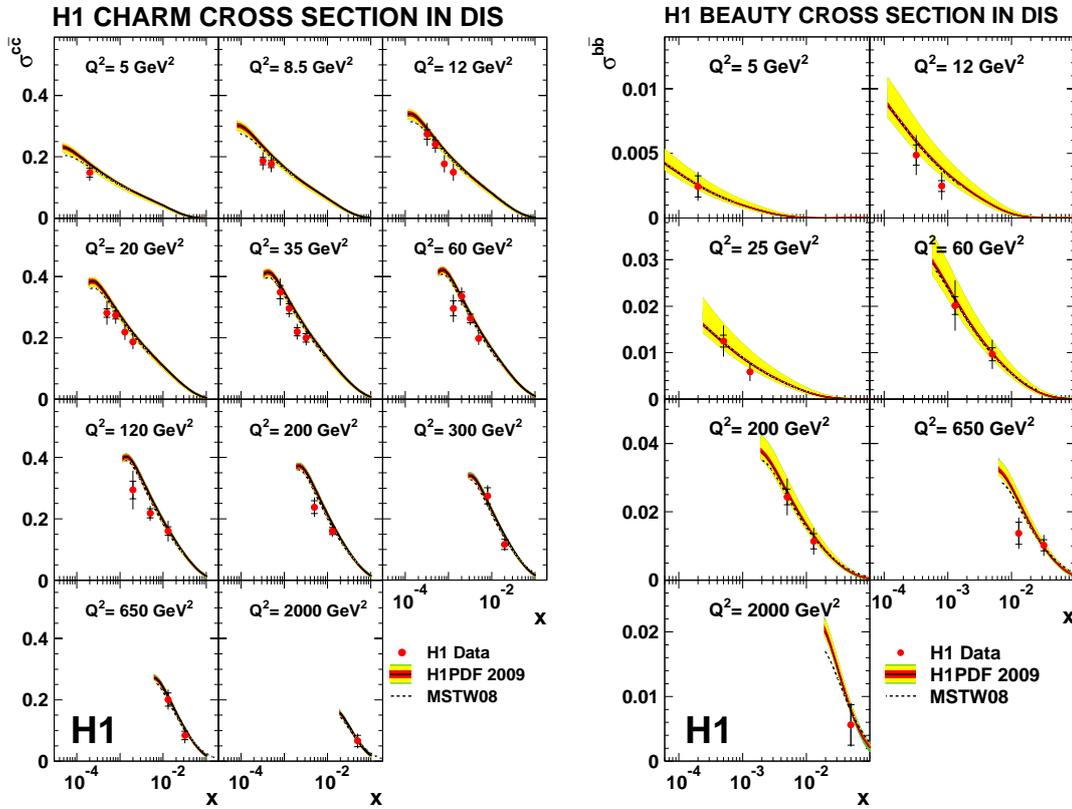
Figure 7: The reduced cross section $\sigma^{c\bar{c}}$ (left) and $\sigma^{b\bar{b}}$ measured by H1 and shown as a function of x for different Q^2 bins. The predictions of H1PDF 2009 and MSTW08 NLO fits to inclusive data are also shown.
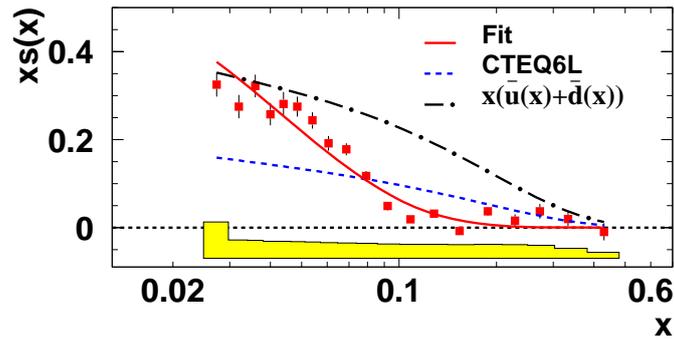
Figure 8: The strange parton distribution $xs(x)$ from the measured HERMES multiplicity for charged kaons evolved to $Q_0^2 = 2.5$ GeV^2 . The solid curve is the HERMES fit to the data, the dashed curve gives $xs(x)$ from the CTEQ6L set, and dot-dashed curve us the sum of light antiquarks from the CTEQ6L set.

46

reported a measurement of the momentum distribution of the strange quark sea, $xs(x)$, in scattering off deuteron. The strange density is extracted from $K^{\pm}$ multiplicities by correcting for the u, d and s fragmentation. The result is shown in figure 8 and compared to the CTEQ6L expectation. The HERMES data shows softer behavior of $xs(x)$ compared to the CTEQ6L fit: at high x the data is below the fit and at low x the data are above the fit. At low x the strange sea is comparable to the light sea density.

9   Summary

Recent results from HERA provide new precise data for determination of the proton structure at low x. The combination of the H1 and ZEUS results reaches 1.1% for the $10 \leq Q^2 \leq 100$ GeV^2 kinematic domain. The data are well described by the NLO QCD fit. This fit has impressively small experimental uncertainties for the PDFs, the total uncertainties are dominated by the model and parameterization errors.

The conventional QCD picture is checked by the measurements of the structure function F_L performed by H1 and ZEUS. Good agreement between the theory and the measurements is observed for $Q^2 \geq 10$ GeV^2. For lower $2.5 \leq Q^2 < 10$ GeV^2, the preliminary data from H1 are somewhat above the expectations.

Measurements at high Q^2 using the polarized HERA-II data performed by ZEUS check the Standard Model and provide constraints for the parton densities at high x. The flavor decomposition at high x is achieved by using the charged current data.

The flavor decomposition at low x and low Q^2 is performed by measuring semi-inclusive processes: tagged heavy flavor production at H1 and $K^{\pm}$ production at HERMES. The H1 data for the charm and bottom quark parton densities agree well with the predictions from the QCD fit to the inclusive data. The HERMES data are softer than prediction of the CTEQ6L analysis.

Further results from HERA are expected as the data analysis are being finalized. In particular, combined H1 and ZEUS measurements of the inclusive HERA-II cross sections and combined measurement of the charm and bottom production will have significant impact on PDFs for the kinematic range important for the future measurements at the LHC.

References

[1] E.D. Bloom *et al.*, Phys. Rev. Lett. 23 (1969) 930.

[2] D.J. Fox *et al.*, Phys. Rev. Lett. 33 (1974) 1504.

[3] C.G. Callan and D.J. Gross. Phys. Rev. Lett. **22**, 156 (1969).

[4] V.N. Gribov and L.N. Lipatov, Sov. J. Nucl. Phys. 15 (1972) 438;
V.N. Gribov and L.N. Lipatov, Sov. J. Nucl. Phys. 15 (1972) 675;
L.N. Lipatov, Sov. J. Nucl. Phys. 20 (1975) 94;
Y.L. Dokshitzer, Sov. Phys. JETP 46 (1977) 641;
G. Altarelli and G. Parisi, Nucl. Phys. B 126 (1977) 298.

[5] F. Aaron *et al.* [H1 Collaboration] (2009), [arXiv:0904.0929].

[6] F. Aaron *et al.* [H1 Collaboration] (2009), [arXiv:0904.3513].

[7] C. Adloff *et al.* [H1 Collaboration], Eur. Phys. J. C **30**, 1 (2003).

[8] M. Botje, QCDNUM version 17β.

[9] R.S. Thorne and R.G. Roberts, Phys. Rev. **D57**, 6871 (1998).

[10] R.S. Thorne, Phys. Rev. **D73**, 054019 (2006).

[11] A. Glazov, AIP Conf. Proc. **792**, 237 (2005) [doi:10.1063/1.2122026].

[12] F.D. Aaron *et al.* [H1 and ZEUS Collaborations], Submitted to JHEP (2009), [arXiv:0911.0884].

[13] A. Benvenuti *et al.* [BCDMS Collaboration], Phys. Lett. **B223**, 485 (1989).

[14] M. Arneodo *et al.* [NMC Collaboration], Nucl. Phys. **B483**, 3 (1997).

[15] S. Chekanov *et al.* [ZEUS Collaboration], Phys. Lett. **B26255**, (2009).

[16] S. Chekanov *et al.* [ZEUS Collaboration], Eur. Phys. J. **C42**, 1 (2005).

[17] F. Aaron *et al.* [H1 Collaboration], Phys. Lett. B 665 (2008) 139.

[18] V. Chekelian [for the H1 Collaboration], Proc. of XVI Int. Workshop on Deep-Inelastic Scattering and Related Topics, London, England, April 2008 `doi: 10.3360/dis.2008.39`.

[19] S. Glazov [for the H1 Collaboration], Proc. of XVII Int. Workshop on Deep-Inelastic Scattering and Related Topics, Madrid, Spain, April 2009.

[20] S. Chekanov *et al.* [ZEUS Collaboration], EPJ **C62** 625 (2009).

[21] S. Chekanov *et al.* [ZEUS Collaboration], EPJ **C61** 223 (2009).

[22] F.D. Aaron *et al.* [H1 Collaboration], Submitted to EPJC, arxiv:0904.3870.

[23] F.D. Aaron *et al.* [H1 Collaboration]. Accepted by EPJC. arxiv:0907.2643.

[24] A. Airapetian *et al.* [HERMES Collaboration], Phys. Lett. **B666** 446 (2008).

Discussion

Benny Ward (Baylor University): What is the ultimate experimental precision on PDF's that you will achieve from all HERA data?
Answer: The expected precision is about 1%.

Quantum Chromodynamics on the Lattice 2009

Akira Ukawa

University of Tsukuba, 1-1-1 Tennodai, Tsukuba, Ibaraki 305-8577, Japan

Lattice QCD is entering a new era as a theoretical machinery to elucidate the physics of strong interactions. We review the algorithmic progress over the past decade behind this advance, and the physics progress powered by it emphasizing flavor physics most relevant for the Lepton Photon Conference series.

1 Introduction

Lattice QCD has been turning a corner in the last couple of years since the time of Lepton-Photon 2007 [1]. Previously, despite the premise, it remained an approximate method requiring extrapolations in a number of ways to extract physical information. For example, "quenching" the quark determinant ignored the vacuum polarization effects of quarks, and unphysically large values of quark masses in the simulations required help from phenomenological models to estimate values for the physical quark masses.

Progress over years has been removing these restrictions one by one. Most recently, a class of algorithms has been developed which, coupled with deepened understanding of the dynamics of gluon and quark fields, has enabled the reduction of up and down quark masses almost down to the physical point of a few MeV. Thus, lattice QCD is becoming a real first principle method, not only in principle but also in practice, for calculating physical quantities directly at the physical point.

We begin this review with a brief description of the recent algorithmic progress. We next describe the status of lattice studies of flavor physics. Reflecting the algorithmic progress, these studies are increasingly based on the physical point simulations. The topics center around the precision determination of the Cabibbo-Kobayashi-Maskawa mixing matrix, and the light and heavy quark quantities relevant for this task. We shall also make a sojourn into thermodynamics of QCD matter and discuss high density region of QCD; there has been some potentially interesting progress reported this summer.

Lattice QCD in research style has much in common with high energy accelerator experiment; supercomputer installations are costly and need to be planned well ahead, and research groups, either small or large, are generally needed to secure necessary supercomputers time allocations. In particular, generation of gluon configurations is an expensive affair both in terms of computing resources and researcher power. Once generated, however, they can be exploited in more than one ways to tap physical information buried in them. The international lattice QCD community has been working since the summe of 2002 to develop an international data grid infrastructure so that researchers worldwide can benefit from generated configurations. We briefly describe this activity before concluding this review.

2 Going to the Physical Point

Lattice QCD calculations have to deal with four systematic errors, namely, (i) inclusion of quark vacuum polarization effects, (ii) small enough lattice spacing, (iii) large enough lattice size, and (iv) physically light values for the up, down and strange quarks. Of these four, the quenching approximation which ignores (i) became obsolete around 2000 due to the development of dynamical quark algorithms and computer power. Simulations including a degenerate pair of up and down quarks, and a heavier strange quark, often dubbed $N_f = 2 + 1$ simulations, have become routine since then. For (ii), a variety of improvement schemes have been developed, with a variable degree of success, and are embodied in today's simulations in one way or another. In essence one adjusts the form of the lattice action and operators for observables by terms higher order in the lattice spacing so that the finite lattice spacing errors in the physical observables are reduced as much as possible. Against (iii) we have had no remedy other than to use large enough volume, relying on increase of computing power. Finally the issue (iv) of using the light enough quark masses has been the most difficult computational problem in lattice QCD. Until quite recently lattice QCD simulations had to be run at the pion mass as heavy as 500MeV, and effective theories such as chiral perturbation theory have to be evoked to carry out a long and unreliable extrapolation to the physical point with $m_\pi = 135$ MeV.

Figure 1: Computational cost for generating 100 independent gluon configurations with the conventional and improved HMC algorithm for $N_f = 2 + 1$ QCD with the Wilson-clover quark action.

The reason behind this difficulty is the necessity to invert the lattice Dirac operator D. The computational cost for the inversion increases as the inverse of the minimum eigenvalue, *i.e.,* the quark mass, and so $1/m$. In the hybrid Monte Carlo algorithm, which is standard for dynamical quark simulations, this inversion is carried out $1/\delta\tau \propto 1/m$ times for every gluon configuration generated. Hence the computational cost blows up at least as fast as $1/m^2$ for small quark masses, and more like $1/m^3$ if one includes autocorrelation between successive configurations. In Figure 1 the solid line on the right shows an estimate in 2001 [2] for generating 100 independent gluon configurations for a lattice of physical size $L = 3$ fm at the lattice spacing $a = 0.1$ fm using the standard hybrid Monte Carlo algorithm in $N_f = 2 + 1$ lattice QCD with the Wilson-clover quark action. The computational cost soars far above the 10 Tflops*year mark well before the physical pion mass. The figure shows that even if one uses a computer which executes the lattice QCD code at the speed of 10Tflops, a full 1 year is needed just to do simulations at an unphysically heavy pion of 260 MeV.

The recent progress came from the realization that the magnitude of gluon and quark contributions to the force term in the hybrid Monte Carlo algorithm is stratified [3]: the gluon contribution F_g has the largest magnitude and has short-range contributions only, next comes in magnitude the short-range contributions of the quark force F_q^{UV}, and finally the long-distance part of the quark force F_q^{IR}. There is a clear separation in the magnitude of the three terms,

Collaboration	quark action	a(fm)	$m_\pi L$	m_π (MeV)	ref
MILC	staggered	0.06	4.0	180	[6]
PACS-CS	wilson-clover	0.09	2.3	155	[7]
BMW	wilson-clover	0.09	4.0	190	[8]
RBC-UKQCD	domain-wall	0.09	4.0	290	[9]
JLQCD	overlap	0.11	2.8	320	[10]
ETM	twisted mass($N_f = 2$)	0.07	3.0	250	[11]

Table 1: Recent large-scale $N_f = 2 + 1$ simulations.

typically of order $||F_g|| : ||F_q^{UV}|| : ||F_q^{IR}|| \approx 25 : 5 : 1$ in simulations done today. In such a situation, one can invoke a multi-time step evolution in the hybrid Monte Carlo algorithm using different step sizes for the three force terms in proportion of $\delta\tau_g : \delta\tau_q^{UV} : \delta\tau_q^{IR} \approx 1 : 5 : 25$. In the standard single time step algorithm, one uses the smallest step size $\delta\tau_g$ as the common step size for all three forces. Since the inversion of the lattice Dirac operator is computationally dominated by the long-distance part, the multi-time step evolution can speed up the computation roughly by a factor $\delta\tau_q^{IR}/\delta\tau_g \approx 25$ simply because the number of Dirac inversions is reduced by this factor.

Concrete implementation of the algorithm has a variety of forms. One way to separate the ultraviolet and infrared quark modes is the Schwarz domain decomposition [3]. An alternative is to apply the idea of mass preconditioner [4] to the quark force in the hybrid Molecular dynamics [5]. The solid line on the left in Figure 1 shows the cost for domain-decomposed hybrid Monte Carlo algorithm [7] as compared to that for the standard algorithm. Clearly, reaching the physical point has become reality with 10 Tflops-class computers for the lattice parameters given.

In Table 1 we list the parameters of representative large-scale simulations pursued today. Except the last entry from the ETM Collaboration using the twisted mass formalism, these are all $N_f = 2 + 1$ simulations fully incorporating dynamical effects of up, down, and strange sea quarks. They utilize the algorithmic progress described above so that the pion mass is reaching down to $m_\pi \approx 200 - 300$ MeV. There has even been a conscious attempt by the PACS-CS Collaboration to reach the physical point at $m_\pi = 135$ MeV, and this trend is accelerating.

We emphasize that this progress is pushing lattice QCD to an entirely new stage. The quark mass dependence of physical observables is difficult to control because of potential logarithmic singularities reflecting the infrared divergences at the chiral limit. With the possibility of making calculations directly with the physical pion mass, we no longer have to worry about this issue. In addition, there certainly is esthetic appeal in the ability to work with the physical pion mass since we shall no longer be simulating but actually calculating the strong interaction as it is taking place in Nature.

3 Fundamental Constants

The values of quark masses are one of the fundamental quantities of Nature which require lattice QCD to pin down. Accurate control of the behavior of hadron masses at physically small up and down quark masses as well as that of renormalization factors is required for a reliable calculation here. Recent advance of $N_f = 2 + 1$ simulations toward the physically light pion mass and non-perturbative estimates of renormalization factors help improve those two aspects.

In the $\overline{MS}$ scheme at $\mu = 2$ GeV, recent $N_f = 2 + 1$ data as reviewed in [12] are indicative of a value $\overline{m} = (m_u + m_d)/2 \approx 3$ MeV for the average up and down quark and $m_s \approx 90$ MeV for strange quark.

Another fundamental constant characterizing the strong interaction is the value of the QCD coupling constant. In Figure 2 we show a comparison of $\alpha_s^{\overline{MS}}(\mu = M_Z)$ from experimental determinations based on perturbative QCD and from lattice QCD. The experimental average this year [13] is given by $\alpha_s^{\overline{MS}}(\mu = M_Z) = 0.1186 \pm 0.0011$. The most elaborate lattice determination is from HPQCD whose value in 2008 [14] has been updated this year to $\alpha_s^{\overline{MS}}(\mu = M_Z) = 0.1184 \pm 0.0004$ [15] . Again the lattice value is based on $N_f = 2 + 1$ simulations, continuum extrapolated, and includes estimate of systematic errors. The agreement is quite remarkable, and attests to the fact that the single coupling of QCD describes the dynamics of strong interaction from ultraviolet to infrared scales.

Figure 2: QCD coupling constant as determined from experiment and lattice QCD. The vertical band is the 2009 experimental average [13].

4 Exploring Flavor Physics

4.1 Constraints on the Cabibbo-Kobayashi-Maskawa Matrix elements

quantity	value	error
$\hat{B}_K$	0.725 ± 0.028	4%
ξ	1.243 ± 0.028	2%
$|V_{ub}|_{excl}$	$3.42 \pm 0.37 \times 10^{-3}$	11%
$|V_{cb}|_{excl}$	$38.6 \pm 1.2 \times 10^{-3}$	3%
f_K	155.8 ± 1.7 MeV	1%

Table 2: Lattice QCD inputs as of summer 2009 for constraining the CKM matrix as compiled in [16]. Here $\xi = f_{B_s}\sqrt{B_{B_s}}/f_{B_d}\sqrt{B_{B_d}}$.

Application of lattice QCD toward flavor physics has centered around the constraints imposed on the Cabibbo-Kobayashi-Maskawa mixing matrix elements. In Table 2 we quote the values of representative observables relevant for this purpose as reported by Van de Water at the Lattice 2009 Symposium this summer [25]. It is worth noting that these numbers all come from $N_f = 2 + 1$ simulations, and that all errors, either statistical or systematic, the latter arising from chiral extrapolations, finite volumes, or finite lattice spacings, were either calculated or estimated.

We now make some specific comments.

4.1.1 Kaon B parameter

The Kaon box parameter B_K enters into the determination of the CKM matrix through the direct CP violation parameter ϵ_K. In Figure 3 we show how lattice determination of B_K has progressed over the years. The three points on the left show a tracking through the plenary reports at the annual lattice symposia in the year 1996 [17], 2000 [18], and 2005 [19]. The inner

error bars show statistical error, and the outer error bars estimates of systematic errors.

The report in 1996 reflects the calculation by the JLQCD Collaboration published next year [20] in which the continuum limit was taken for the first time, albeit in the quenched approximation. The staggered quark action was employed, and a large error is due to a non-linear dependence on the lattice spacing expected for the staggered action.

The box parameter is particularly sensitive to the chiral property of the underlying lattice action. For this reason it became the first natural target of simulations with the domain wall quark action pursued vigorously by the RBC-UKQCD Collaboration. The first results in quenched QCD came in around 2000 [21, 22], and by 2005 an $N_f = 2$ estimate with dynamical up and down quarks was available [23].

The two points on the right are the most recent calculations, finally in $N_f = 2 + 1$ QCD. The result in 2008 was reported with the domain-wall quark action at a single lattice spacing [24]. This year a new calculation using the overlap fermion formalism on $N_f = 2 + 1$ dynamical gluon configurations generated with staggered sea quarks was reported [25]. The 2009 result is continuum extrapolated based on two lattice spacings. The 4% error in the latest results for B_K is smaller than the 10% error due to $|V_{cb}|^4$ which enters into ϵ_K.
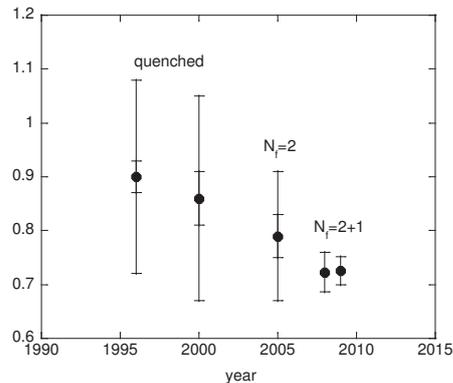
Figure 3: Renormalization group invariant B_K over the years. See text for explanation.

4.1.2 A non-lattice comment on ϵ_K

Buras and Guadagnoli [26] made an important comment on the numerical value connecting the experimental ϵ_K and theoretical B_K. In the expression

$$\epsilon_K = e^{i\phi_\epsilon} \sin \phi_\epsilon \left(\frac{\text{Im} M_{12}^K}{\delta M_K} + \frac{\text{Im} A_0}{\text{Re} A_0} \right) = \kappa_\epsilon \frac{\text{Im} M_{12}^K}{\delta M_K}, \tag{1}$$

the second term $\text{Im} A_0 / \text{Re} A_0$, being small, is usually neglected. However, with increasingly improved estimates of B_K and V_{cb}, this correction is significant. Buras and Guadagnoli estimates that

$$\kappa_\epsilon \approx \sqrt{2} \sin \phi_\epsilon \left(1 - \frac{1}{\omega} \text{Re} \left(\frac{\epsilon_K'}{\epsilon_K} \right) + \frac{1}{\sqrt{2}|\epsilon_K|} \frac{\text{Im} A_s}{\text{Re} A_2} \right) = 0.92 \pm 0.02. \tag{2}$$

This implies that the ϵ_K band in the $\rho - \eta$ plane for the CKM matrix might move up by about 10%.

4.1.3 Inclusive *vs* exclusive determination of V_{cb} and V_{ub}

The V_{cb} matrix element can be determined by combining the experimental $B \to D^*$ rate with a lattice determination of the corresponding form factor [27], and similarly for the V_{ub} matrix element *via* the $B \to \pi$ decay [28]. The lattice numbers have not changed since 2008, and the

values for V_{cb} and V_{ub} still differ from the estimates [29] combining the inclusive decay rates with non-lattice calculations of decay amplitudes at a two σ level. The situation is illustrated in Figure 4.
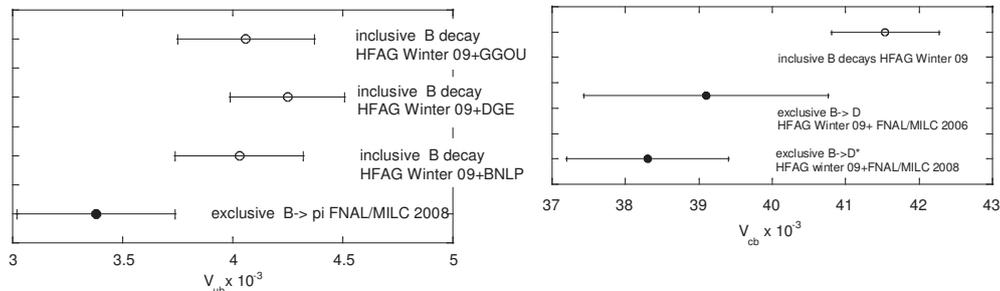
Figure 4: V_{cb} and V_{ub} matrix element as determined from exclusive rates and lattice form factor (filled circles) and inclusive rates and non-lattice transition amplitude estimates (open circles).

4.1.4 D meson decay constants

In Figure 5 we compare lattice results for the D and D_s meson decay constant against experiment. The latest 2009 experimental numbers from CLEO [30] are $f_D = 205.8 \pm 8.9$ MeV and $f_{D_s} = 259.5 \pm 7.3$ MeV.

On the lattice, there has been no change in the value from HPQCD Collaboration [31] who uses the HISQ form of the staggered quark action for the charm quark. The discrepancy in f_{D_s} still remains.

The estimates from Fermilab-MILC Collaboration who uses the Wilson-clover quark action has been updated this summer [32] due to a 2.3% revision in the lattice scale in physical units, and the numbers have gone up. Within the relatively large error of about 4%, they are consistent with experiment. Lattice QCD has to resolve the difference between the HISQ and Wilson-clover determinations which is a systematic effect.
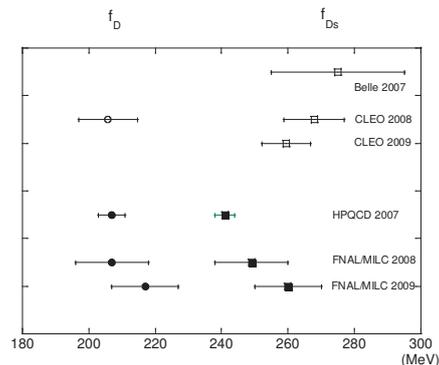
Figure 5: Lattice (filled symbols) and experimental (open symbols) determination of D and D_s meson decay constant from 2007 to 2009.

4.2 CKM unitarity

In Table 3 we present the status with the unitarity check of the CKM matrix using as much lattice input as possible. For the first row, the very precise value for V_{ud} comes from a non-lattice analysis of the nuclear transition rates [33]. The V_{us} is calculated from experimental $K \to \pi$ decay rate and an $N_f = 2 + 1$ lattice QCD determination of the form factor [34], and

V_{ub} is taken from the lattice determination from the exclusive $B \to \pi$ decay [28] as discussed in Subsection 4.1.3. The first row unitarity holds to within 0.1%.

V_{ud}	V_{us}	V_{ub}	$\sum_j |V_{uj}|^2 - 1$
0.97425	0.2246	0.00342	-0.0004
$\pm$0.00022	$\pm$0.0012	$\pm$0.00037	$\pm$0.0013
V_{cd}	V_{cs}	V_{cb}	$\sum_j |V_{cj}|^2 - 1$
0.239	0.969	0.039	-0.002
$\pm$0.032	$\pm$0.105	$\pm$0.001	$\pm$0.110

Table 3: First and second row unitarity of the CKM matrix

The status with the second row is far less satisfactory. The numbers for V_{cd} and V_{cs} are from 2004 [35], which have not been superceded since then, and V_{cb} from 2008 [27]. Clearly charm physics on the lattice has to improve by at least an order of magnitude in precision. The trouble has been that the charm quark mass of $m_c \sim 1.5$ GeV is uncomfortably close to the lattice spacing $a^{-1} \sim 2$ GeV which has been typically used in lattice calculations. In order to control systematic errors coming from $m_c a$ being not small, $N_f = 2 + 1$ simulations at smaller lattice spacings are required. Large-scale simulations are moving in this direction, so hopefully there will be progress here in the near future.

4.3   Lattice calculation of ϵ'/ϵ

Successful calculation of the CP violation parameter ratio ϵ'/ϵ has been a major challenge in lattice QCD since the middle of 1980's. Chiral symmetry turned out crucial to control renormalization and large fluctuations of ultraviolet origin in the Penguin contributions. It was only in 2003 that results with meaningful error estimations were obtained with domain-wall QCD [36, 37]. The calculations relied on the rewriting of the two-body $K \to \pi\pi$ amplitude in terms of the one-body $K \to \pi$ and $K \to$ vacuum amplitude to lowest order of chiral perturbation theory. It was quite a disappointment to find that the results do not agree with experiment even in sign. While it was not clear if quenching was the cause or possible failure of chiral perturbation theory in the range of pion mass $m_\pi \approx 0.5$ MeV is to be blamed, the severe lesson taught us that full QCD calculations directly addressing the two-body decay amplitude is needed.

The theoretical framework for this purpose was laid down in 2001 [38]; one chooses a lattice volume L^3 such that the K meson energy $E_K(L)$ on this volume matches the two-pion energy at the same volume $E_{\pi\pi}(L)$. One can then prove that the lattice value for the two-body decay amplitude $\langle K|H_W|\pi\pi\rangle_{lattice}$ calculated on this volume is proportional to the physical amplitude $\langle K|H_W|\pi\pi\rangle_{physical}$ up to a calculable factor.

This framework was applied to the isospin $I = 2$ sector last year using the domain wall QCD in the quenched approximation [39]. In this isospin channel, the troublesome Penguin contribution is absent, and previous attempts have already yielded values in agreement with experiment. The advance achieved by the new calculation is the working proof that the finite-volume method works for the K meson decay.

The calculation in the isospin $I = 0$ channel is much harder, but we can expect progress as $N_f = 2 + 1$ full QCD calculations are steadily progressing toward large volume and physical pion mass.

5   Exploring High Density

Temperature and density are two dials which allow us to explore the dynamics of QCD relevant under the extreme conditions in the Early Universe or in relativistic heavy ion collision experiments. At zero density the phase diagram as a function of temperature and the number of quarks has been studied extensively in the past. Theoretically the order of the transition from hadron gas to quark gluon plasma is sensitively dependent on the up, down and strange quark masses. The most recent calculation in 2006 [40] using finite-size scaling analyses made a strong case that the transition is a crossber at a temperature range $T_c \approx 150 - 170$ MeV for the physical quark mass. There has been no major change since this work.

On the other hand, much less is known on the phase diagram of QCD at finite density. This is due to the difficulty, in spite of many attempts, to resolve the sign problem, *i.e.,* the quark determinant for non-zero quark chemical potential μ_q becomes complex, and hence Monte Carlo methods break down. There are indications, based on the reweighting technique [41] and the method of Taylor expansion in μ_q [42] that the crossover behavior at zero density continues into the region of non-zero density but turns into a first-order phase transition through a critical point.

Most simulations for non-zero density have been attempted with the chemical potential formalism, *i.e.,* using the grand partition function. In principle one can equally well use the canonical partition function in which the number of quarks N_q or baryon number $n_B = N_q/3$ is fixed. The relation between the two partition functions are given by

$$Z_{grandcanonical}(T, m_q, \mu_B) = \sum_{n_B} e^{n_B \mu_B/T} Z_{canonical}(T, m_q, n_B) \tag{3}$$

and hence the path integral for the canonical partition function is given by

$$Z_{canonical}(T, m_q, n_B) = \int [dU] \left[\int_0^{2\pi} d\phi e^{-i3n_B \phi} \det D(U, m_q, \mu = i\phi T) \right] e^{-S_{gluon}(U)} \tag{4}$$

Since the quark determinant is an extensive quantity, it is important to accurately estimate the projection of the quark determinant in this equation. An exact evaluation of the projection [43] is computationally expensive and hence not very practical for large lattices. An interesting idea is to apply saddle point approximation expected to be valid for large spatial volume [44]. A quantitative measure of control of the approximation is needed for this method.

This year a new attempt was made to control the projection [45].. The direct projection has an apparent problem that cancellation of oscillations whose magnitude becomes exponentially large in volume has to be controled. Numerically this is a difficult task, and hence the idea is to carry out the projection to the logarithm of the determinant *via*

$$\log \det D(U, m_q, \mu) = \sum_{n_B} e^{n_B \mu_B/T} A(U, m_q, n_B) \tag{5}$$

Figure 6 shows the result [45] for the chemical potential as a function of baryon number (left panel) and the phase diagram (right panel) for $N_f = 3$ QCD with Wilson quark action on a $6^3 \times 4$ lattice. The cubic variation on the left panel indicates a first-order phase transition, and the familiar Maxwell construction yields the boundary of the two-phase coexistence region plotted on the right on the $T - \mu$ plane. We see that the coexistence region becomes narrower
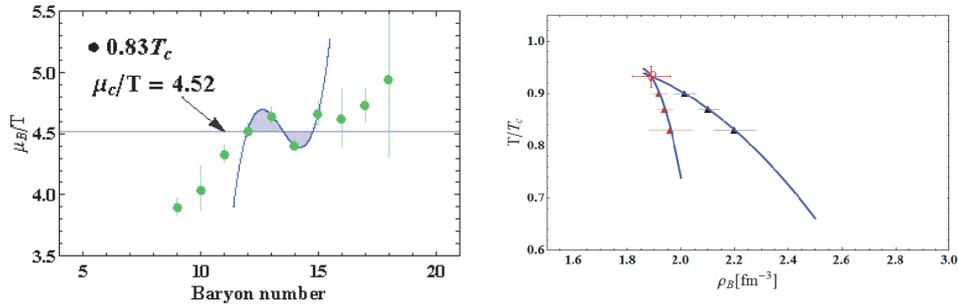
Figure 6: Chemical potential calculated as a function of baryon number (left panel) and the two-phase coexistence region on the $T - \rho_B$ ($\rho_B = n_B/V$) plane (right panel) calculated by a microcanonical approach [45].

as the temperature increases, likely terminating at the estimated endpoint marked by an open circle.

It may well be that the sign problem has not manifested itself in this calculation because of the heavy pion mass ($m_\pi \approx 700$ MeV) and the small lattice size ($6^3 \times 4$). It is nonetheless an encouraging result and is worth pursuing as an alternative to the grand canonical approach.

6   Collaborating World-wide

Lattice QCD is practiced across the globe. There are about a dozen major centers scattered in Japan, Australia, EU countries (including Germany, France, United Kingdom, Italy, and Spain), USA and Canada. As of 2009 the total computing capacity employed for lattice QCD is about half a petaflops, which is about 3% of the total world high performance computing resources.

The most time consuming element in lattice QCD calculation is the generation of gluon configurations with dynamical quarks. Once generated those configurations can be used by anyone to calculate physical observables of one's interest. Since 2002, this has motivated the lattice QCD community to make an effort toward a world-wide collaboration called *International Lattice Data Grid (ILDG)* to organize and run a data grid for gluon configurations [46].

ILDG consists of a number of regional grids, each operating on its own. For a world-wide sharing of configurations, a standardized xml called qcdml has been defined to describe gluon data, and standard middleware has been designed for interoperability of the regional grids through ILDG. After 4 years of preparation, ILDG started service in June 2006 [47]. The number of gluon ensembles (set of configurations) and downloads have been steadily increasing over the years as shown in Figure 7. ILDG has become an established infrastructure in the lattice QCD community, and its role will continue to increase in the years to come.

7   Conclusions

Over the last couple of years, realistic calculations directly at the physical point have finally become reality in lattice QCD. This is a fruit of continuous effort over 25 years toward better
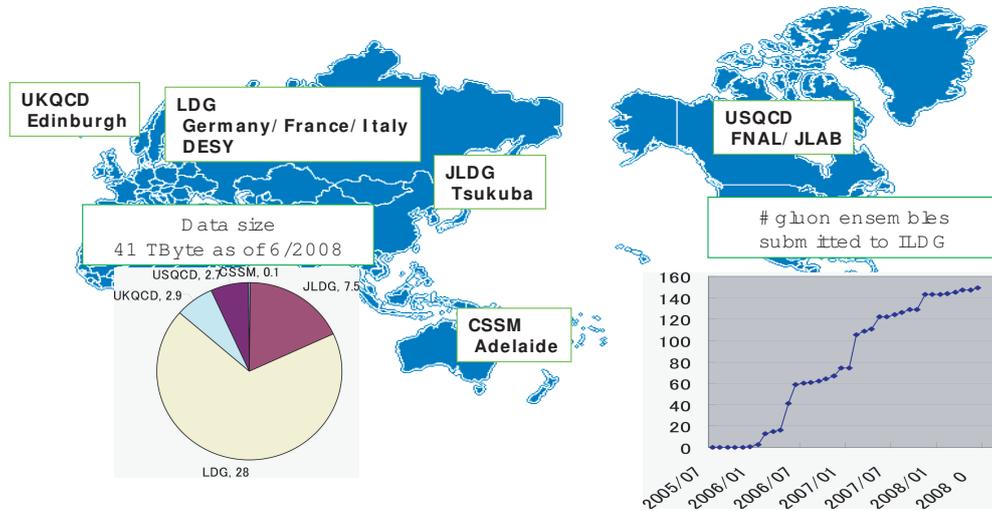
Figure 7: International Lattice Data Grid for a world-wide sharing of gluon configurations.

physics understanding, better algorithms and more powerful computers. Personally I believe that this entails a change of philosophy from "simulation" to "calculation": if lattice spacing is sufficiently small, there are no more approximations or extrapolations, and gluon configurations produced on the computer is strong interaction in Nature itself.

Armed with this tool, I expect that the fundamental issues of lattice QCD as particle theory make major progress over the next five-year range. Those include single hadron properties and fundamental constants, precision flavor physics with errors bound below 1% level and resolution of old issues such as $K \to \pi\pi$ decays, and hot/dense QCD explored with chiral lattice action on large lattices.

And there lies beyond the vast area of multi-hadron systems and atomic nuclei for our nuclear physics colleagues to explore, *e.g.,* nuclear force from lattice QCD, exotic nuclei with unusual neutron/proton ratios and/or strangeness, and element synthesis in supernovae and so on.

Acknowledgments

References

[1] C. T. H. Davies, *Proceedings of Lepton-Photon 2007*, arXiV:0807.1402 (hep-ph)(2007).

[2] A. Ukawa, Nucl. Phys. B(Proc. Suppl.), **106**, 195 (2002).

[3] M. Lüscher, Comput. Phys. Commun., **165**, 199 (2005).

[4] M. Hasenbusch, Phys. Lett. B **519**, 177 (2001).

[5] C. Urbach, K. Jansen, A. Shindler, U. Wenger, Comput. Phys. Commun. **174**, 87 (2006).

[6] MILC Collaboration, A. Bazavov *et al.*, arXiv:0903.3598 (2009).

[7] CP-PACS Collabortion, S. Aoki *et al*, Phys. Rev. D **79**, 034503 (2009).

[8] S. Durr *et al.*, Science, **322**, 1224 (2008).

[9] RBC and UKQCD Collaboration, R. Mawhinney *et al.*, arXiv:0910.3194 (2009).

[10] JLQCD Collaboration, H. Fukaya *et al.*, Phys. Rev. Lett. **104**, 122002 (2010).

[11] ETM Collaboration, C. Alexandrou *et al.*, Phys. Rev. D **78**, 014509 (2008).

[12] E. Scholz, Plenary talk at *Lattice 2009*, arXiv:0911.2191 (2009).

[13] S. Bethke, arXiv:0908.1135 (2009).

[14] HPQCD Collaboration, C. T. H. Davies *et al.*, Phys. Rev. D **78**, 114507 (2008).

[15] C. T. H. Davies, private communication (2009).

[16] R. Van de Water, Plenary talk at *Lattice 2009*; see, for details, J. Laiho, E. Lunghi, R. Van de Water, Phys. Rev. D **81**, 034503 (2010).

[17] S. Sharpe, at *Lattice 1996*, Nucl. Phys. B(Proc. Suppl.) **53**, 181 (1997)

[18] C. Lellouch, at *Lattice 2000*, Nucl. Phys. B(Proc. Suppl.) **94**, 142 (2001)

[19] C. Dawson, at *Lattice 2005*, PoS LAT2005, 007 (2006).

[20] JLQCD Collaboration, S. Aoki *et al.*, Phys. Rev. Lett. **80**, 5271 (1998).

[21] RBC Collaboration, Phys. Rev. D **68**, 114506 (2003).

[22] CP-PACS Collaboration, S. Aoki *et al*, Phys. Rev. D **64**, 114506 (2001).

[23] RBC Collaboration, Y. Aoki *et al.*, Phys. Rev. D **72**, 114505 (2005).

[24] RBC and UKQCD Collaboration, Phys. Rev. Lett. **100**, 0321001 (2008)

[25] C. Aubin, J. Laiho, R. Van de Water, Phys. Rev. D **81**, 014507 (2010).

[26] A. Buras and D. Guadagnoli, Phys. Rev. D **78**, 033005 (2008).

[27] Fermilab Lattice and MILC Collaborations, C. Bernarad *et al*, Phys. Rev. D **79**, 014506 (2009). See also M. Okamoto *et al*, Nucl. Phys. B (Proc. Suppl.) **140**, 461 (2005)

[28] Fermilab Lattice and MILC Collaborations, J. A. Bailey *et al*, Phys. Rev. D **79**, 054507 (2009).

[29] Heavy Flavor Averaging Group, http://www.slac.stadoford.edu/xorg/hfag/semi/ (2009).

[30] CLEO Collaboration, Liming Zhang, arXiv:0810.2328 (2009); CLEO Collaboration, B. I. Eisenstein *et al.*, Phys. Rev. D **78**, 052003 (2008).

[31] E. Follana *et al*, Phys. Rev. Lett. **100**, 062002 (2008).

[32] A. Bazavov *et al.*, PoS LAT2009, 249 (2009).

[33] J. C. Hardy and I. S. Towner, Phys. Rev. C **79**, 055502 (2009).

[34] P. Bopyle *et al.*, Phys. Rev. Lett. **100**, 141601 (2008).

[35] Fermilab Lattice, MILC, and HPQCD Collaborations, C. Aubin *et al.*, Phys. Rev. Lett. **94**,11601 (2005).

[36] T. Blum *et al.*, Phys. Rev. D **68**, 114506 (2003).

[37] CP-PACS Collaboration, J. Noaki *et al/*, Phys. Rev. D **68**, 14501 (2003).

[38] L. Lellouch and M. Lüscher, Commun. Math. Phys. **219**, 31 (2001).

[39] T. Yamazaki, Phys. Rev. D **79**, 094506 (2009).

[40] Y. Aoki *et al.*, Nature **443**, 675 (2006).

[41] Z. Fodor and S. Katz, JHEP **0404**, 050 (2004).

[42] C. Allton *et al.*, Phys. Rev. D **71**, 054508 (2005).

[43] P. de Forcrand and S. Kratochivila, Nucl. Phys. B (Proc. Suppl.) **153**, 62 (2006).

[44] S. Ejiri, Phys. Rev. D **78**, 074507 (2009).

[45] Anyi Li, talk at *Lattice 2009*, arXiv:1002.4459 (2009).

[46] C. T. H. Davies *et al.*, Nucl. Phys. B (Proc. Suppl.) **119**, 225 (2003).

[47] http://ildg.sasr.edu.au/Plone

Discussion

Bruno Stella (Universita Roma Tre): I think for the first time the rapporteur of Lattice QCD does not mention glueballs. Why? Could you say something more?

Answer: I do not think there has been substantial progress in recent years, especially on the difficult issue of a reliable estimate of mixing of pure glue states with quark states. Full QCD simulations necessary for this has not reached sufficient statistics so far.

Guido Altarelli (Roma III and CERN): Concerning the discrepancies between the lattice determinations of f_{D_s} and the data, is the smallness of the quoted error by HPQCD really justified, also in view of the FNAL/MILC more recent central values and quoted errors?

Answer: This is a difficult question to answer. I suppose they have a large number of data points in quark masses and lattice spacings to estimate the value for physical quark masses and the continuum limit, which helps reduce the error. Their light quark mass also goes down to a fairly small value so that the ambiguity of chiral extrapolation is smaller.

Markus Wobisch (FNAL): You mentioned the possibility of computing properties of hadrons. Could you also compute the distributions of partons inside hadrons?

Answer: Yes, lattice methods can compute the moments of structure functions. The computations becomes progressively difficult for higher moments, however, so only several moments are feasible so far.

Vera Lüth (SLAC): Current lattice calculations are $N_F = 2 + 1$. Can we hope to extend calculations to include charm and eventually beauty? At present the dominant error on V_{ub} determinations are quark masses, especially m_b.

Answer: Dynamical charm is already withing the scope of full QCD simulations. Dynamical beauty is still a future problem since the lattice spacing of larger than 5GeV necessary for this requires larger than petaflops scale computing resources. However, the estimate of m_b will not be affected much by dynamical beauty effects since the b quark is much heavier than the typical QCD scale.

Bennie Ward (Baylor University): In your plot of the hadron spectrum you only show a small subset of what is in the PDG. Are you cherry-picking? Can you predict glueballs, hybrids, molecules, pentaquarks, etc?

Answer: Confirming the ground state spectrum, though a small subset of PDG, is a basic step to establish the validity of QCD and the predictive capability of lattice QCD. Predictions of other states including exotics will come step by step.

Ahmed Ali (DESY): This question concerns chiral extrapolation on the lattice. Are the pion mass and the light quark masses for which lattice simulations are currently being done at a stage that the chiral perturbation theory can be checked in the sense that some of the constants in chiral pert. theory are now determined by lattice?

Answer: Yes, the low energy constants such as l_3 and l_4 have been determined with

reasonable precision. Further the convergence of ChPT has been examined. At present SU(3) ChPT does not seem to be convergent at the physical strange quark mass, while SU(2) ChPT seems to be convergent for physical up-down quark mass in the pseudoscalar sector. The situation may depend on the quantity.

Nucleon structure at low energies

Delia Hasch

Istituto Nazionale di Fisica Nucleare, Laboratori di Frascati, Italy
email:delia.hasch@lnf.infn.it

Understanding the structure of the nucleon in terms of quark and gluon degrees of freedom is one of the key objectives of nuclear physics. Over the last decade, theoretical breakthroughs lead to the new concepts of Generalized Parton Distributions (GPDs) and Transverse Momentum Dependent parton distributions (TMDs), which offer a means to unravel the true 3-dimensional nucleon structure and to shead new light on the yet unsolved 'nucleon spin crises'. After reviewing our current understanding of the spin structure of the nucleon, novel and pioneering measurements of hard exclusive processes and transverse spin phenomena are presented, which may provide access to the GPDs and TMDs, respectively. The measurements have been performed at second generation polarised lepton-nucleon and proton-proton scattering experiments at CERN, DESY, JLAB and RHIC.

1 Introduction

Over the past 40 years, an understanding of the nucleon in terms of elementary constituents (partons, i.e., quarks and gluons) has gradually and successfully emerged from experiments that scatter high energetic leptons (l) off protons or nuclear targets (N) with large four-momentum transfer from the initial to the final lepton, Q. Such deep-inelastic scattering (DIS) experiments have been successfully interpreted within the QCD parton model introducing parton distribution functions (PDFs). The universality property of these functions allows their measurement in various different hard processes such as lepton-nucleon and proton-proton scattering.

The parton distributions $f_{q/g}(x_B, Q^2)$, describing the distribution of quarks and gluons in terms of their longitudinal momentum fraction x_B, known as the Bjorken variable, are well mapped in a kinematic range that spans five orders of magnitude in both x_B and Q^2 [1]. In contrast, a detailed decomposition of the spin of the nucleon in terms of parton *helicity* distributions, $\Delta f_{q/g}(x_B, Q^2)$, including a measure of the contribution from orbital angular momenta (OAM) of quarks and gluons, remains elusive. Here, $\Delta f_{q/g}(x_B, Q^2) = f_{q/g}^+(x_B, Q^2) - f_{q/g}^-(x_B, Q^2)$ is the difference of partons with their spin aligned (+) or anti-aligned (−) to the spin of the nucleon. The striking result that only an unexpectedly small fraction, about a quarter, of the nucleon's spin can be attributed to the spins of quarks and anti-quarks is famously dubbed the 'nucleon spin crises'. Moreover, unravelling the true 3-dimensional nucleon structure requires to answer long-standing questions concerning the spatial distribution of quarks and gluons inside the nucleon, their orbital motion and a possible connection between their orbital motion, their spin and the spin of the nucleon.

In the last decade, theoretical breakthroughs lead to the new concepts of Generalized Parton Distributions (GPDs) and Transverse Momentum Dependent parton distributions (TMDs),
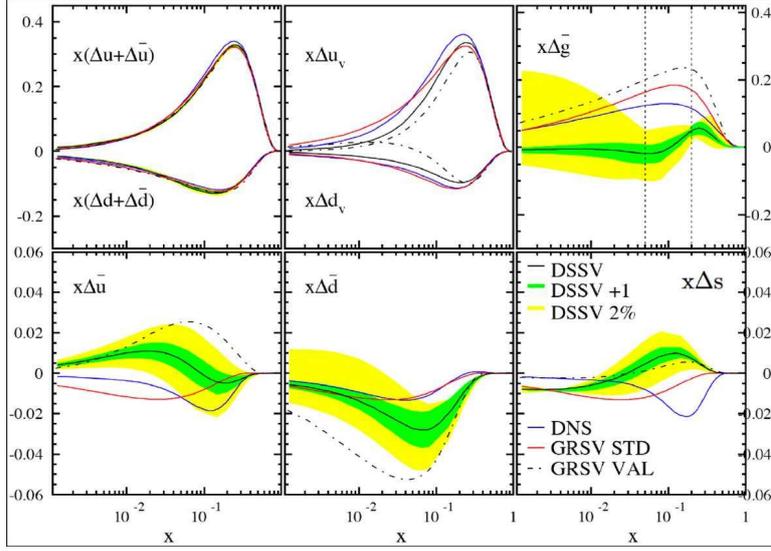
Figure 1: Parton helicity distributions of the nucleon obtained in NLO analyses of data from inclusive and semi-inclusive DIS (DNS [5]) as well as from proton-proton scattering (DSSV [3]). The figure is taken from [3] where also complete reference to all data is given.

which offer a multi-dimensional space and momentum resolution of the nucleon structure. These new functions allow studying a completely new aspect of nucleon structure: the localisation of partons in the plane transverse to the motion of the nucleon. As such GPDs and TMDs are excellent tools for nucleon tomography.

Modern experiments aim to obtain information about all contributions to the spin of the nucleon and to explore its multi-dimensional structure by measuring polarized inclusive, semi-inclusive and exclusive deep-inelastic scattering processes (Compass at CERN, HallA-C at JLab, Hermes at DESY) as well as by exploring polarized high energy proton-proton scattering (Brahms, Phenix and Star at RHIC, BNL).

2 The spin budget of the nucleon

The spin contribution of a quark or gluon to the nucleon spin is given by the intregral $\Delta f^1_{q/g}(Q^2) = \int_0^1 f_{q/g}(x_{\mathrm{B}}, Q^2)dx$. The helicity distributions $\Delta f_{q/g}(x_{\mathrm{B}}, Q^2)$ can be extracted from double-spin asymmetries

$$A_{\mathrm{LL}} \equiv \frac{d\Delta\sigma}{d\sigma} \equiv \frac{d\sigma^{++} - d\sigma^{+-}}{d\sigma^{++} + d\sigma^{+-}} \tag{1}$$

measured over a wide kinematic range in x_{B} and Q^2. Here, both beam and target have to be longitudinally polarized with helicity settings $\pm$. Analyses of such asymmetries measured over the past three decades in inclusive DIS, where only the scattered lepton is observed, revealed that surprisingly little of the nucleon spin is carried by the quark spins [2]. This finding has triggered much theoretical progress and new experiments dedicated to unraveling the nucleon spin structure.

From experimental side, the measurement of less inclusive observables in DIS (by Hermes and Compass) and of hadron production in polarized proton-proton collisions (by Phenix and Star) have opened a new stage in the quest for the spin of the nucleon. Semi-inclusive DIS (SIDIS), where a hadron is observed in the final state along with the scattered lepton, is a powerful tool to determine the individual spin contributions of quarks and antiquarks to the total spin of the nucleon. The production of hadrons with large transverse momentum in polarized proton-proton scattering provides unprecedented constraints on the gluon helicity distribution.

Figure 1 shows the helicity distributions obtained in a recent *global* next-to-leading order (NLO) analysis (labeled as DSSV) of available data from polarized inclusive and semi-inclusive DIS as well as from polarized proton-proton scattering [3]. They are compared with earlier fits of inclusive [4] (labeled as GRSV) and semi-inclusive DIS data only [5] (labeled as DNS). The DSSV analysis consequently utilizes new fragmentation functions (DSS) [6], which, for the first time, provide a good description of identified hadron yields over the entire kinematic range relevant for the analysis of polarized SIDIS and *pp* scattering data.

The total up and down quark helicity distributions, which are primarily probed in inclusive DIS, are by far the best determined distributions. Their uncertainty bands are very narrow and results from verious different analyses agree very well and are also in good agreement with recent lattice calculations for the first moments [7]. The light sea quark and antiquark helicity distributions are mainly constraint by the semi-inclusive DIS data. As shown in Ref. [3], differences in the light sea quark distributions between the DSSV and DNS extractions, which both use inclusive and semi-inclusive DIS data, can be fully attributed to the use of different sets of fragmentation functions. Of particular interest is a possible flavour symmetry breaking in the light sea, i.e., $\Delta \bar{u} \neq \Delta \bar{d}$, given the well-established flavour asymmetry in the spin-averaged case. In fact, Fig. 1 demonstrates a slightly positive $\Delta \bar{u}$ and a negative (with larger magnitude) $\Delta \bar{d}$ yielding a non-zero difference in agreement with various model calculations.

The polarization of strange quarks has been a focus since the very beginning of the nucleon spin crises. Assuming SU(3) symmetry, the small value found for the total quark spin contribution to the nucelon spin implies - within the parton model - a significant negative polarization of strange quarks. Indeed, most fits to only inclusive DIS data prefer a sizeable negative strange quark polarization, even if the commonly assumed SU(3) symmetry is not enforced. In contrast to these results, Fig. 1 shows a strange quark polarization for DSSV that is positive at larger x_{B} and turns negative around $x_{\mathrm{B}} = 0.02$. This result is fully driven by the kaon data from semi-inclusive DIS used for both the PDF fits (DSSV) and the fragmentation function fits (DSS). It is also in agreement with LO extractions of the strange helicity distribution by Hermes [8] and Compass [9] from their kaon data.

In view of the small contribution of quarks to the nucleon spin, an understanding of the role of gluons and the determination of their polarization has become a major focus of the field. A large polarization of gluons was expected from investigations of the QCD axial anomaly that tried to attribute the lacking spin contribution by quarks to Q^2 dependent contributions by gluons. Experimentally, the gluon helicity distribution remains the most elusive one. The available inclusive DIS data cover a kinematic range in x_{B} and Q^2 that is yet unsufficient to constrain the gluon helicity distribution from scaling violation of the polarized structure function. More direct probes are indispensable for gaining more knowledge about the gluon polarization. As shown in Fig. 1, the gluon polarization obtained by DSSV is small with a possible node in the

distribution. This is driven largely by the RHIC data, which strongly constrain Δg in the range $0.05 \leq x_{\mathrm{B}} \leq 0.2$ but cannot determine its sign as they mainly probe Δg squared. A small gluon polarization at x_{B} around 0.1-0.2 is also found in LO analyses of lepton-nucleon scattering data that dominantly select the photon-gluon fusion process in reactions like $lN \rightarrow hX$ or $lN \rightarrow h^+h^-X$ and in heavy flavour production [10].

Due to the lack of data in the small x_{B} region, it is yet not possible to reliably evaluate the full integral of $\Delta g(x_{\mathrm{B}}, Q^2)$. However, a very large gluon polarization as proposed in the context of the QCD axial anomaly is clearly ruled out by the data. Current and future measurements at RHIC focus on the golden channels of two-particle, jet-jet and γ-jet correlations which provide direct access to the hard-scattering subprocess kinematics. The spin asymmetry for prompt photon production is linear in Δg and therefore determines the sign of the distribution. However, the investigation of the region $x_{\mathrm{B}} < 10^{-3}$ will only be possible at a high-energy polarized electron-proton collider [11].

Figure 2: [colour online] Clas measurements of the DVCS beam-helicity asymmetry [14]. Left: kinematic coverage and binning in (x_{B}, Q^2) space, which is further subdivided into t bins. Right: For each bin in x_{B}, Q^2 and t the ϕ dependence of the cross section asymmetry w.r.t. the beam helicity is determined (red long-dashed curve). The data is compared to model calculations: the black dashed curves correspond to a Regge calculation [16]; the blue curves correspond to a GPD calculation [17], at twist-2 (solid) and twist-3 (dot-dashed) levels, with H contribution only.

Then, the remaining big piece in the puzzle is the contribution from quark and gluon orbital angular momenta (OAM) to the nucleon spin. For the first time, the newly developed formalism of GPDs offers a means to address this outstanding question.

3 Nucleon tomography and the quest for the OAM

Information towards a genuine multi-dimensional representation of the nucleon structure is offered by the so-called Generalized Parton Distributions (GPDs). GPDs unify the momentum-space parton distributions measured in inclusive DIS with the spatial distributions (form factors) measured in elastic lepton-nucleon scattering, which appear as kinematic limits and moments of GPDs, respectively. This new formalism provides a coherent and homogenous description of the nucleon structure as it reveals simultaneously (transverse) position and (longitudinal) momentum distributions of partons and describes their *correlations*. As such, GPDs are the basis for novel representations of the nucleon as an extended object in space (nucleon tomography) and provide access to fundamental static properties like the orbital angular momentum of partons in the nucleon - a question of fundamental importance for the understanding of nucleon structure. Generalized parton distributions depend on the squared four-momentum transfer t to the nucleon and on x and ξ, which represent respectively the average and half the difference

Figure 3: [colour online] Hermes measurement of the DVCS beam-charge (upper panel) and beam-helicity asymmetries [18]. The analysis of yield asymmetries w.r.t. the combined dependence of the cross section on beam helicity and charge allows for an experimental separation of the contribution from DVCS (middle panel) and its interference with the Bethe-Heitler process (lower panel). The data is compared to a GPD model (labeled VGG) [17] using a Regge-motivated t-dependence.

of the longitudinal momentum fractions carried by the probed parton in initial and final states. The skewness parameter ξ is related to the Bjorken variable x_B in the Bjorken limit. Most often discussed are the four twist-2 quark-helicity-conserving GPDs for each quark species in the nucleon: the quark-polarization averaged distributions H and E and the quark-polarization related distributions $\widetilde{H}$ and $\widetilde{E}$.

The crucial new information about the correlation of the spatial and momentum distributions is provided from measurements of exclusive processes at large momentum transfer, namely deeply-virtual Compton scattering (DVCS, $lN \to lN\gamma$) and meson production ($lN \to lN\pi(\rho, \phi, \text{etc.})$). The theoretically cleanest way to access GPDs appears to be the DVCS process. Since GPDs carry information about longitudinal and transverse degrees of freedom, the DVCS amplitudes need to be known completely, i.e., by magnitude and phase. This is possible through a measurement of the interference between the DVCS and the Bethe-Heitler processes, where the photon is radiated from a parton in the former and from the lepton in the latter process. Their interference has the potential to reveal the 3-dimensional structure of the nucleon at parton level. In order to isolate the real part of the interference term in a measurement, lepton beams of both charges are needed. The imaginary part can be accessed by measuring the angular dependence of the produced photon if polarized lepton beams or polarized targets are available. A determination of all relevant moments of the angular dependence in beam-charge,

beam-spin and target-spin asymmetry measurements allows one to perform a global analysis of all observables to obtain detailed information on GPDs.

Hard exclusive processes are very challenging to measure as they require high beam energies (to ensure the hard regime), very high luminosities (due to the small cross sections) and an excellent resolution of the spectrometer (to ensure the exclusivity of the process). Pioneering measurements have been performed at DESY (Hermes, H1, Zeus) and JLAB (Clas, HallA). After the first signals for GPDs from Hermes [12] and Clas [13], dedicated measurements have been and are going to be performed and a new quality of data analysis is reached. While measurements at Jlab focus on high statistics allowing for a multidimensional analysis of data (see Fig. 2), Hermes concentrates on new analysis methods making simultaneous use of polarization observables and data taken with different beam charges thereby providing full experimental separation of the different contributions to the measured cross section asymmetries (see Fig. 3).

Figure 4: Hall-A extraction of the interference term from the DVCS beam-spin cross section difference for the neutron [19]. The curves are calculations of GPD models with different values for the up and down quark total angular momenta J_u and $J_d = 0$.

The ability to describe longitudinal momentum distributions at a fixed transverse localization is a prerequisite for studying the so-called Ji relation [15], which links a certain combination of GPDs (H and E) to the total angular momentum ($J_{q,g}$) of a parton in the nucleon. Only few observables show a substantial sensitivity to the total angular momentum of quarks, mainly to J_u and J_d. Among them are the DVCS beam-helicity cross section difference for a neutron target (see Fig. 4) and the DVCS asymmetries w.r.t. transverse target polarization (see Fig. 5). Both measurements are compared to GPD model calculations [17] that embody explicitly the quark total angular momenta J_u and J_d in the parameterization of the spin-flip GPD E. Hence *model dependent* constraints on J_u and J_d can be derived by fitting them to the observables in Figs. 4 and 5.

These first attempts of extracting information about the total angular momentum of quarks reveal the potential of the data to provide quantitative information. Obviously, much more data and theoretical developments are needed to obtain GPD parameterization that allow for a description of all available DVCS data. By then, the model dependence of the above extractions might get under control.

4 Transverse spin phenomena and spin-orbit correlations

In addition to the quark momentum $f(x)$ and helicity $\Delta f(x)$ distributions discussed before a third independent quark distribution, the so-called transversity distribution $\Delta_T f(x)$, exists because of the relativistic nature of bound quarks. Transversity describes the distribution of transversely polarized quarks in a transversely polarized nucleon. In the non-relativistic limit
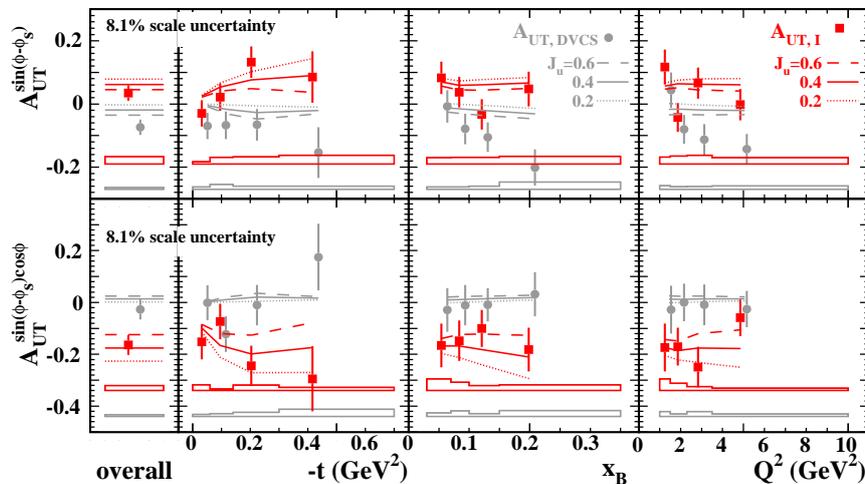
Figure 5: Hermes asymmetries describing the dependence of the squared DVCS amplitude (circles, $A_{UT,DVCS}$) and the interference term (squares, $A_{UT,I}$) on the transverse target polarization [20]. The curves are calculations of a GPD model [17] with three different values for the up quark total angular momentum J_u with fixed value for the down quark, $J_d = 0$.

$\Delta_T f(x)$ and $\Delta f(x)$ are identical as both functions describe the orientation of the quark spins relative to the nucleon spin, $\Delta f(x)$ in the helicity basis and $\Delta_T f(x)$ in a basis of transverse spin eigenstates. However, transversity and helicity distributions differ because quarks inside the nucleon move relativistically, hence boosts and rotations do not commute. They are therefore independent quantities which probe different QCD properties. Any experimental evidence for a deviation of $\Delta_T f(x)$ from $\Delta f(x)$ would be a measure of relativistic effects.

Viewed in the helicity basis, transversity is related to a forward scattering amplitude involving a *helicity flip* of both quark and target nucleon. Due to this chiral-odd nature, transversity - unlike the other two basic quark distributions - cannot be measured in inclusive DIS but only in a process in which it combines with another chiral-odd quantity. The most direct approach is to measure double transverse-spin asymmetries in polarized Drell-Yan processes which couple two transversity distributions. This approach is however experimentally not yet feasible. Another possibility is the semi-inclusive DIS process where fragmentation functions enter the cross section in conjunction with the distribution functions. Such a mechanism has been proposed by Collins [21] where the chiral-odd *Collins* fragmentation function relates the transverse polarization of the struck quark with the transverse momentum $P_{h\perp}$ of the produced hadron. This mechanism manifests itself in a single-spin asymmetry, i.e., a left-right asymmetry in the production of hadrons in the plane transverse to the direction of the virtual photon.

Single-spin asymmetries in semi-inclusive DIS on a transversely polarized target can also originate from the *Sivers mechanism* [22]: it emerges from the combination of the ordinary spin-averaged fragmentation function with the Sivers distribution. This naive time-reversal odd function, i.e., time-reversal without interchange of initial and final state, can be related to the interference of wave functions for different orbital momentum states. As such it parameterizes
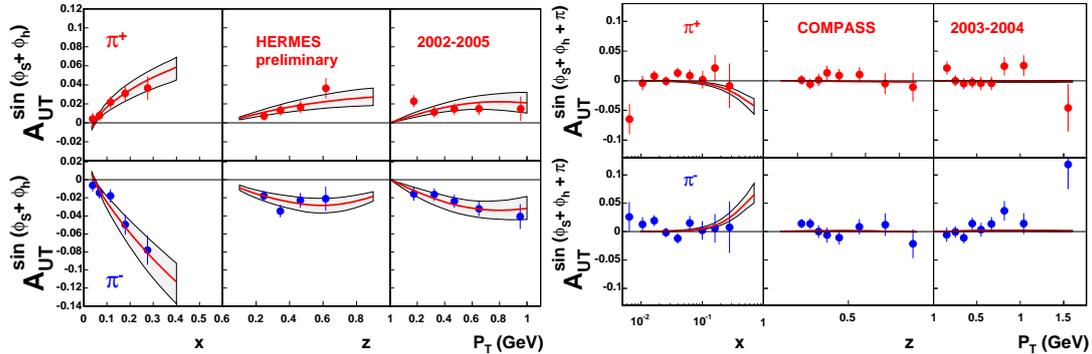
Figure 6: Left: most recent Hermes results for the Collins asymmetry for π-mesons. The strikingly non-zero amplitudes for charged pions demonstrated for the first time that both transversity and the Collins fragmentation function exist and are sizeable. Right: Compass results for the Collins asymmetry for π-mesons measured with a deuterium target. Both figures are taken from [28].

the correlations between the transverse momentum of quarks and the spin of the transversely polarized nucleon. The information on these spin-orbit correlations will be a key to construct a complete picture of the internal structure of hadrons beyond the collinear approximation.

Single-transverse spin asymmetries have a long history, starting from the 70s and 80s when surprisingly large asymmetries were observed in hadron reactions such as $p^\uparrow p \to \pi X$ at forward angles of the produced pion [23]. Experiments at RHIC found that large single-spin effects at forward rapidity persist even at very high energies up to $\sqrt{s} = 200$ GeV [23]. Such asymmetries could arise from both Collins or Sivers effect or from twist-3 contributions (Qui-Sterman effect). Experimentally, these mechanisms cannot be distinguished with the observables measured so far at RHIC but will become feasible in studies of Drell-Yan processes, di-jet or jet-jet correlations which, however, require high luminosities.

In contrast, semi-inclusive DIS on a *transversely* polarized target provide an additional degree of freedom due to the two azimuthal angles ϕ and ϕ_S involved, which are the azimuthal angle of the produced hadron and of the transverse target polarization vector, respectively, with respect to the virtual photon direction. These provide a distinct angular signature for the Collins and Sivers effects, which appear as $\sin(\phi + \phi_S)$ and $\sin(\phi - \phi_S)$ modulation of the SIDIS cross section, respectively. Both mechanisms were studied at Hermes with a proton target [24] and at Compass with deuterium and proton targets [25]. Figure 6 (left) shows the Collins amplitudes for pions measured by Hermes. These results are milestones in the field as the significant non-zero asymmetries for charged pions demonstrated for the first time unambiguously that both the transversity distribution and the Collins fragmentation function exist and are non-zero! Recent Compass asymmetries are in very good agreement with the Hermes data in the kinematic region of overlap and go to zero for smaller values of x_B. The asymmetries measured with a deuterium target are all compatible with zero, which can be understood as a cancellation of the contribution from up and down quarks when measuring on a isoscalar target. These data in combination with further information from jet asymmetries in e^+e^- scattering studied at Belle (KEK) [26], shown in Fig. 7 (left), which are sensitive to the Collins fragmentation function, allowed for the first extraction of the up and down quark
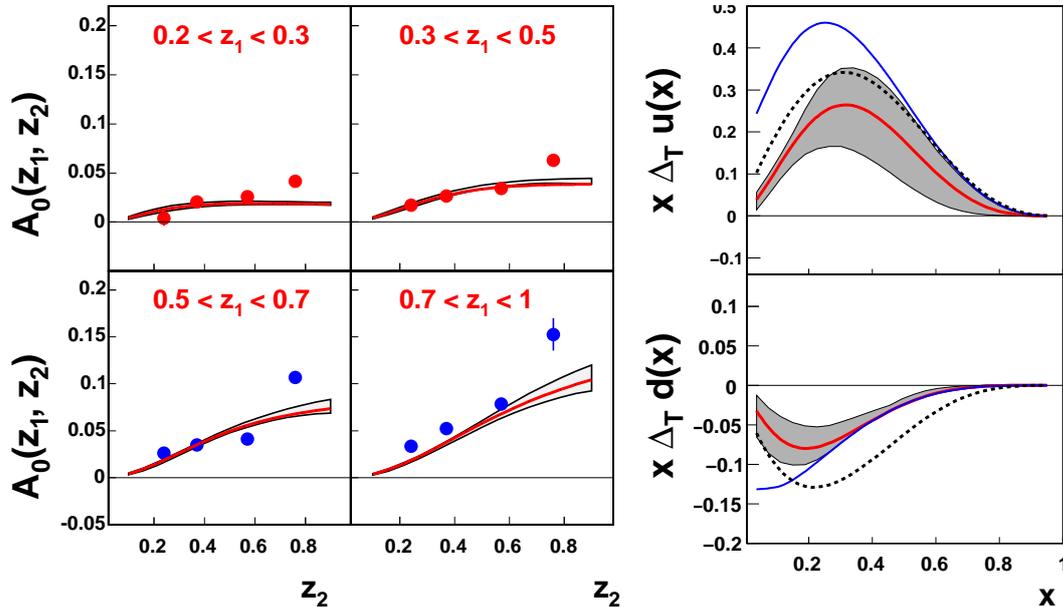
Figure 7: [colour online] Left: most recent BELLE results for jet asymmetries sensitive to the Collins fragmentation function [26]. The curves are results of a global fit [28] to these data as well as to Hermes and Compass data [25]. Right: As a result of the global fit the up and down quark transversity distributions are obtained and compared to the helicity distributions (dashed line). The blue line represents an upper bound for the transversity distribution. Both figures are taken from [28].

transversity distributions (see Fig. 7, right) [28] [1].

A measurement of the Siver asymmetries from Hermes [27] is presented in Fig. 8 (left). Also these results constitute milestones in the field as the significant non-zero asymmetries for π^+ and K^+ demonstrated for the first time that T-odd distribution functions indeed exist in DIS. Compass asymmetries measured with a deuterium target are compatible with zero [25]. The middle panel of Fig. 8 shows, as examples, two different extractions of the up and down quark Sivers distributions [29, 30] using parameterizations of the usual unpolarized fragmentation functions. These extractions are in agreement with recent lattice calculations of the Sivers distribution [7] shown in the right panel (note that the is a factor -1 in the definitions of the Sivers distribution). The oposite sign found for the Sivers up and down quark distributions indicates orbital angular momenta for up and down quarks of opposite sign.

The existence of such functions depending on the transverse momentum of quarks inside the nucleon implies that quarks also carry non-vanishing orbital angular momentum which is one of the still missing pieces in the *spin puzzle*. A direct relation, however, between the Sivers function or other similar functions that describe spin-orbit correlations and the angular momentum contribution of the quarks to the nucleon spin could not yet be established.

The most crucial test of our current understanding of azimuthal single-spin asymmetries in

---

[1]The updated analysis of [28] makes use of the new, high statistics data from Belle and Hermes but does not yet incorporate the Compass proton asymmetries.
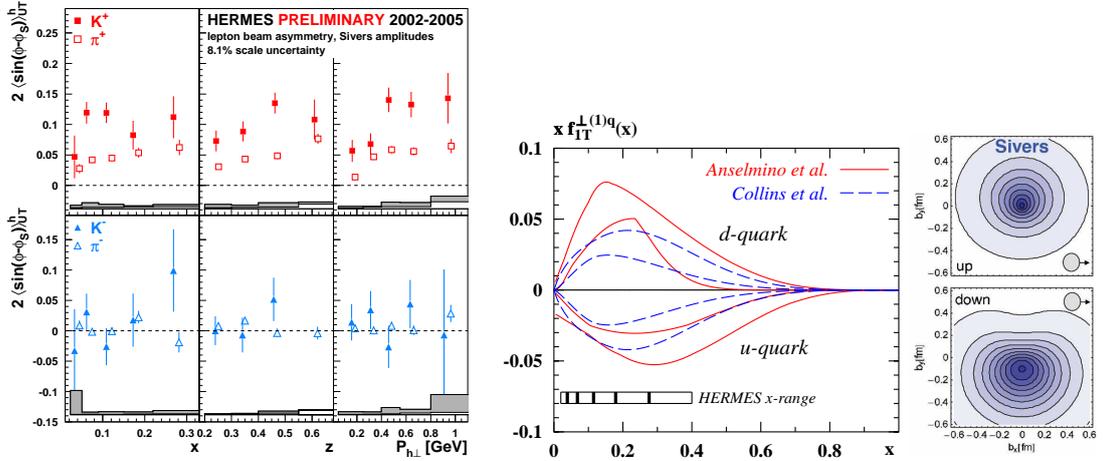
Figure 8: Left: Hermes results for the Sivers amplitudes for charged pions and kaons [27]. The striking non-zero asymmetries for π^+ and K^+ demonstrated for the first time that T-odd distribution functions indeed exist in DIS. Middle: Sivers up and down quark distributions extracted from the Hermes data (and for the full line also from Compass deuteron data) using two different parameterizations [29, 30]. The curves indicate the 1-sigma regions of the various parameterizations. The oposite sign found for the Sivers up and down quark distributions agrees with recent lattice calculation (right panel) [7] and indicates orbital angular momenta for up and down quarks of opposite sign.

terms of pertubative QCD will be the experimental verification of the predicted sign change of T-odd distribution functions, like the Sivers function, when being measured in DIS or in Drell-Yan processes. Such measurements of T-odd distribution functions in Drell-Yan processes are planned by Compass when running in the hadron-beam mode and by the proposed PAX experiment at the future FAIR facility at GSI [31].

5 Prospects of spin physics

Exciting new information has been obtained on the nucleon spin structure from polarized lepton-nucleon and proton-proton scattering. However, a detailed measurement of the gluon polarization remains one of the most important issues in spin physics. Running RHIC at higher energy ($\sqrt{s} = 500$ GeV) will shed more light on this issue.

The new concepts of Generalized Parton Distributions (GPDs) and Transverse Momentum Dependent parton distributions (TMDs) offer for the first time a multi-dimesional space and momentum resolution of the nucleon structure. Polarization observables serve as a very powerful tool to access the different GPDs and TMDs. The interplay between spin degrees of freedom and parton orbital angular momentum will be a key to understand the spin structure of the nucleon. The first extractions of transversity and of transverse momentum dependent distribution and fragmentation functions like the Sivers distribution and the Collins fragmentation function are milestones in the field. They constitute the first step towards a complete description of the partonic structure of hadrons beyond the collinear parton model.

The mapping of the nucleon GPDs and TMDs has been widely recognized as one of the key objectives of nuclear physics in the next decades. This requires a comprehensive programme, combining dedicated experiments at new facilities that provide high energy, high luminosity and polarization [11] with intense theoretical studies and lattice QCD simulations.

References

[1] PARTICLE DATA GROUP, Phys. Lett. **B667** 1 (2008).

[2] For a review see, e.g., S.D. Bass, Rev. Mod. Phys. **77** 1257 (2005); recent results can be found in: Hermes Collab., A. Airapetian *et al*, Phys. Rev. **D71** 012003 (2005), **D75** 012007 (2007); CLAS Collab., K.V. Dharmawardane *et al*, Phys. Lett. **B641** 11 (2006); Compass Collab., V.Yu. Alexakhin *et al*, Phys. Lett. **B647** 8 (2007), **B660** 458 (2008).

[3] D. De Florian, R. Sassot, M. Stratmann, W. Vogelsang, Phys. Rev. Lett. **101** 072001 (2008); Phys. Rev. **D80** 034030 (2009).

[4] M. Gluck, E. Reya, M. Stratmann, W. Vogelsang, Phys. Rev. **D63** 094005 (2001).

[5] D. De Florian, G. Navarro, R. Sassot, Phys. Rev. **D71** 094018 (2005).

[6] D. De Florian, R. Sassot, M. Stratmann, Phys. Rev. **D75** 114010 (2007); **D76** 074033 (2007).

[7] LHPC Collab., P. Hägeler *et al.*, Phys. Rev. **D77** 094502 (2008); P. Hägeler arXiv:0912.5483 [hep-lat].

[8] Hermes Collab., A. Airapetian *et al.*, Phys. Lett. **B666** 446 (2008).

[9] Compass Collab., M. Alekseev *et al.*, arXiv:0905.2828 [hep-ex].

[10] Hermes Collab., A. Airapetian *et al*, Phys. Rev. Lett. **84** 2584 (2000) and AIP Conf. Proc **915** 331 (2007); Smc Collab., B. Adeva *et al.* Phys. Rev. **D70** 012002 (2004); Compass Collab., E. Ageev *et al.*, Phys. Lett. **B633** 25 (2006) and arXiv:0802.3023.

[11] A. Deshpande, R. Milner, R. Venugopalan, W Vogelsang, Ann. Rev. Nucl. Sci. **55**, 165 (2005).

[12] Hermes Collab., A. Airapetian *et al.*, Phys. Rev. Lett. **87** 182001 (2001).

[13] Clas Collab., S. Stepanyan *et al.*, Phys. Rev. Lett. **87** 182002 (2001).

[14] Clas Collab., F.X. Girod *et al.*, Phys. Rev. Lett. **100** 162002 (2008).

[15] X.-D. Ji, Phys. Rev. Lett. **78** 610 (1997).

[16] J. M. Laget, Phys. Rev. **C76** 052201 (2007).

[17] M. Guidal, P. Guichon, M. Vanderhaeghen, Phys. Rev. **C62** 025501 (2000), code adapted to DVCS with GPD model by P. Guichon (2007); K. Goeke, M. Polyakov, M. Vanderhaeghen, Prog. Part. Nucl. Phys. **47** 401 (2001); M. Guidal, M. Polyakov, A.V. Radyushkin, M. Vanderhaeghen, Phys. Rev. **D72** 054013 (2005).

[18] Hermes Collab., A. Airapetian *et al.*, JHEP **11** 083 (2009).

[19] Hall-A Collab., M. Mazouz *et al.*, Phys. Rev. Lett. **99** 242501 (2007).

[20] Hermes Collab., A. Airapetian *et al.*, JHEP **06** 66 (2008).

[21] J.C. Collins, Nucl. Phys. **B396** 161 (1993).

[22] D.W. Sivers, Phys. Rev. **D41** 83 (1990).

[23] For a recent review see U. D'Alesio, F. Murgia, Prog. Part. Nucl. Phys.**61** 394 (2008).

[24] Hermes Collab., A. Airapetian *et al.*, Phys. Rev. Lett. **94** 012002 (2005); Hermes Collab., M. Diefenthaler *et al.*, arXiv:0706.2242 [hep-ex];

[25] Compass Collab., E. Ageev *et al.*, Nucl. Phys. **B765** 31 (2007); Phys. Lett. **B673** 127 (2009); arXiv:0907.5508 [hep-ex].

[26] BELLE Collab., R. Seidl *et al.*, Phys. Rev. Lett. **96** 232002 (2006); BELLE Collab., R. Seidl *et al.*, Phys. Rev. **D78** 032011 (2008).

[27] The final results (not shown here) are published in Hermes Collab., A. Airapetian *et al.*, Phys. Rev. Lett. **103** 152002 (2009).

[28] M. Anselmino *et al.*, Phys. Rev. **D75** 054032 (2007); M. Anselmino *et al.*, arXiv:0812.4366 [hep-ph].

[29] M. Anselmino *et al.*, Phys. Rev. **D72** 094007 (2005).

[30] J.C. Collins *et al.*, Phys. Rev. **D73** 014021 (2006).

[31] A. Efremov *et al.*, Phys. Lett. **B612** 233 (2005).

Discussion

Tom LeCompte (Argonne National Laboratory): The questioner found the quark orbital motion and nucleon tomography discussion interesting. Could such a correlation between quarks in a nucleon show up in the unpolarized double parton scattering measurements described in Markus' talk? What constraints can double parton scattering put on orbital angular momentum of quarks?

Answer: This is an very interesting question. In principle, a measurement of the correlation of quarks in a proton should carry information about their relative orbital motion. One would have do find an observable that is sensitive to this relative orientation. The fractions of double parton production measured so far by CDF and D0 do not carry such information. Possibly, azimuthal dependences of the produced jets could be investigated. Thank you for this interesting point.

V. Braun (University of Regensburg): What is the relation between unintegrated parton distributions and Fourier transforms of GPDs? Does this relative exist in QCD?

Answer: Till now, only model dependent relations between TMDs and GPDs could be established. There is for example the pioneering work of Matthias Burkhardt who showed a relation between the Sivers fct. and the GPD E within a quark-diquark model. More recently, Andreas Metz and collaborators are investigating such relations in a systematic way. However, it's not clear if model independent relations might exist in principle.

Recent Results from RHIC

Thomas Peitzmann

Utrecht University, P.O.Box 80000, 3508 TA Utrecht, The Netherlands

I review recent results from the Relativistic Heavy-Ion Collider with particular emphasis on gluon saturation, elliptic flow and parton energy loss. While studies of gluon saturation are still in an early stage, and as such are not yet conclusive, more results are eagerly awaited, both because of a general interest in saturation physics and because it defines the initial state of high-energy hadronic collisions. Elliptic flow measurements have shown the collective behaviour of the matter produced and are particularly interesting because of the fact that the matter appears to have an extremely low viscosity. The much higher beam energy at RHIC has for the first time given access to jet-related physics in heavy-ion collisions. A strong jet suppression has been observed and is now being studied in detail to unravel the physics mechanisms behind and obtain estimates of the medium density.

1 Introduction

Quantum chromodynamics predicts a phase transition in strongly interacting matter between the confined phase of hadrons at low temperature to a deconfined phase of quarks and gluons at high temperature. The goal of experiments with high-energy nuclear collisions at the Relativistic Heavy-Ion Collider (RHIC) is to study strongly interacting matter at high temperature, and in particular the properties of the partonic phase. The RHIC program, which consisted of four experiments in its initial phase, is now continued with the two major experiments PHENIX and STAR. A wealth of experimental results have been obtained, which go significantly beyond earlier results of the heavy-ion program at the CERN SPS because of the much higher available energy. Due to the huge amount of experimental data, I will in this paper only be able to review a selection of those results, and will in particular concentrate on data related to gluon saturation, elliptic flow, and parton energy loss. For an overview of other results see e.g. [1].

2 The initial state: gluon saturation

Another new state of strongly interacting matter, the *color glass condensate*, has been predicted recently. The number density of quarks and gluons seen in a proton or nucleus is known to increase at large momentum transfer Q^2 (i.e. high spatial resolution), when the momentum fraction x they carry decreases. This linear evolution can successfully be described within perturbative QCD. This increase can however not continue indefinitely. At some point the large number density of gluons would violate fundamental unitarity bounds, and in fact, for large densities non-liner effects become important and compensate the increase with a corresponding decrease due to gluon fusion processes. This balance of creation and annihilation leads to *gluon saturation*. Gluon saturation is a small x phenomenon and is expected to set in below a certain

characteristic scale in Q, the *saturation scale*,

$$Q_s \approx \frac{\alpha_s}{\pi R^2} x G(x, Q^2) \propto A^{1/3} \cdot x^{-\lambda},$$

where $\lambda \approx 0.3$.

At this saturated density the occupation number should be large enough that the gluons can be treated as a classical field. The state is often called the *color glass condensate* (CGC): a *color* field, *condensed* in a high density classical state, and slowly varying like a *glass*. In addition to being a fascinating new state of elementary particles in itself, it plays an important role in defining the initial conditions for any high energy hadronic interaction. Knowledge on gluon saturation will therefore have far reaching consequences in high-energy physics. (For a general introduction see e.g. [2].)

Gluon saturation is able to explain the observed particle multiplicities at RHIC, which turned out to be much smaller than previously expected. The behaviour of multiplicities by itself is however not conclusive as a signal of this physics mechanism. In addition, gluon saturation should be observable as a suppression of particle production at forward rapidities in p+A or d+A collisions relative to $p + p$ collisions, in particular via measurements of

- a suppression of inclusive hadron yields in a momentum range where parton scattering is dominant and

- a decrease and/or broadening of the azimuthal correlation related to recoil jets from parton-parton scattering.

Such studies have been performed at RHIC, and first results in particular on the suppression in inclusive hadrons at forward rapidities have been obtained by BRAHMS and STAR (see Fig. 1). The measurements show a significant suppression of the yield in d+Au collisions, qualitatively consistent with gluon saturation. However, no full calculation from a CGC-model has been performed yet. Preliminary studies of azimuthal correlations have been performed by STAR and PHENIX, they do however not yet show results

Figure 1: (colour online) Nuclear modification factor R_{dAu} for hadron production in d+Au collisions at forward rapidities as measured by STAR (π^0) and BRAHMS (negative hadrons). The inset illustrates that conventional calculations including shadowing effects are not able to describe the suppression shown in the STAR data (from [3]).

significant for gluon saturation searches. Moreover, questions remain whether the p_T region studied at RHIC allows the use of p+p measurements as a reference for the incoherent limit of perturbative QCD.

3 Elliptic flow: equilibration, viscosity, and partonic collectivity

One of the most important findings of the RHIC experiments is the strong collectivity, in particular the large values of elliptic flow. The created system in non-central heavy-ion collisions has an azimuthal anisotropy in coordinate space which leads via multiple interactions to an anisotropy in momentum space. Elliptic flow v_2 is defined as the coefficient of the second order Fourier component of this azimuthal anisotropy [4]. Large values of v_2 are generally considered to be signs of hydrodynamic behaviour, which in turn requires local equilibration of the produced matter. v_2 shows a straightforward dependence on the collision geometry, for ideal hydrodynamics it is proportional to the initial spatial eccentricity. Beyond that, its magnitude depends on the equation of state (EoS) of the matter produced. To extract this information from elliptic flow measurements knowledge of the initial distributions, which determine the eccentricity, is important. This makes the studies of gluon saturation significant for the interpretation of elliptic flow.

Figure 2 shows results of elliptic flow measurements as obtained by the STAR experiment [5, 6]. On the left hand side the measurements are compared to the expectation from ideal hydrodynamic calculations for different centralities. While there are discrepancies for the more peripheral reactions, the results have reached the values for the ideal fluid in central collisions. This behaviour has lead to the conclusion that the system created at RHIC behaves like a perfect liquid with very low viscosity [7].
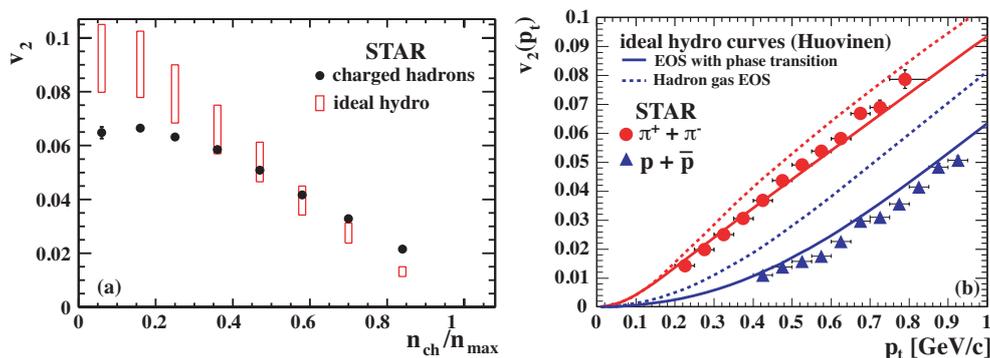
Figure 2: (colour online) (a) Elliptic flow (solid points) as a function of centrality n_{ch}/n_{max}. The open rectangles show a range of values expected for v_2 in the ideal hydrodynamic limit [5]. (b) Elliptic flow of pions and protons as function of transverse momentum [6]. The curves are hydrodynamical model calculations using a hadron gas EoS (dashed curve) and an EoS which incorporates the QCD phase transition (full curve).

These findings have lead to a number of theoretical activities on how to incorporate effects of viscosity in the calculations. The deviations for more peripheral reactions can be understood from the influence of viscous corrections due to the hadronic phase. However, the real behaviour of even the hot and dense phase should show a finite viscosity. It has been shown [8] using the so-called AdS/CFT correspondence that conformal field theories with gravity duals have a

shear viscosity normalized to the entropy density of $\eta/s = 1/4\pi$. The authors conjecture that this is a lower bound for any relativistic thermal field theory.

While in early analyses the normalization of v_2 to the initial eccentricity was performed using Glauber calculations, it has now been realized that estimates based on e.g. colour glass condensate model calculations yield significantly different results, which is relevant for the determination of the most likely viscosity of the matter. Different approaches are employed to obtain estimates of η/s, either by performing viscous hydro calculations as e.g. in [9] or to exploit the centrality dependence via a parameterization of v_2 inspired by transport calculations [10, 11]. Both approaches lead to the conclusion that the viscosity is in fact small, but slightly larger than (of the order of a few times) the theoretical bound of 0.08.

The right hand side of Fig. 2 shows v_2 for pions and protons as a function of transverse momentum. In this low momentum region there is a strong mass ordering, where the rise of v_2 with p_T occurs at higher values for the heavier particles. This behaviour can qualitatively be described by hydrodynamic calculations using hadronic degrees of freedom, where the mass ordering is related to the strong collective radial motion in the system, which affects the heavier particles more. A quantitatively satisfactory description is however only obtained in calculations using an EoS incorporating the QCD phase transition (solid lines in the figure).

At higher p_T the mass ordering is reversed, and as a general trend a scaling with the number of constituent quarks in the corresponding hadron has been observed [12]. More recently this has been confirmed with many hadron species. As an example Fig. 3 shows v_2 for pions and protons (left) and for ϕ mesons and Ω baryons (right). The constituent quark scaling works best when using transverse mass instead of transverse momentum and can nicely be demonstrated by comparing flow results for different hadrons when both v_2 and $m_T - m_0$ are normalized to the number of quarks as shown in Fig. 4 for Au+Au and Cu+Cu collisions. Such a behaviour is very naturally obtained if hadron production proceeds via coalescence [13] or recombination [14] from a deconfined phase and the hadron collective motion is determined from the collective motion of the quarks. The phenomenon of constituent quark scaling is thus seen as a strong hint of partonic collectivity.
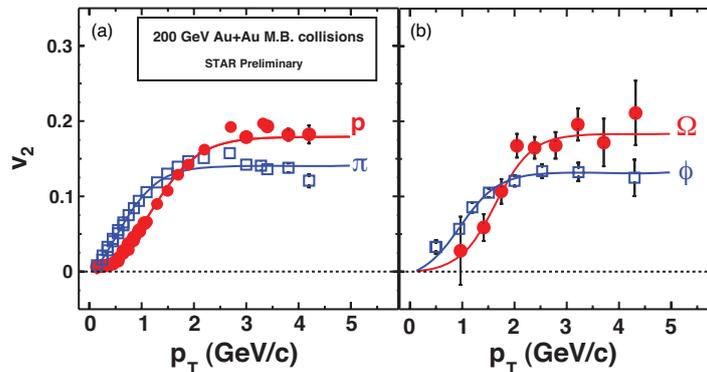
Figure 3: (colour online) Elliptic flow as function of transverse momentum in Au+Au collisions at 200 GeV for pions and protons (a) and ϕ mesons and Ω baryons (b).

There are obvious situations, where this scaling is not expected to work, e.g. at very low

momentum, where momentum distributions are strongly modified in the hadronic phase and the hadron mass is thus more important than the number of quarks, or at high momentum, where particles originate from jet fragmentation and azimuthally dependent parton energy loss (see next section) is responsible for the observed anisotropy. In addition, also the details of recombination/coalescence models may lead to differences with respect to how well and in what momentum ranges the constituent quark scaling will be realized. Studies of the details of the scaling properties of v_2 are being performed – they should profit much from further increased statistics and better understanding of non-flow effects.
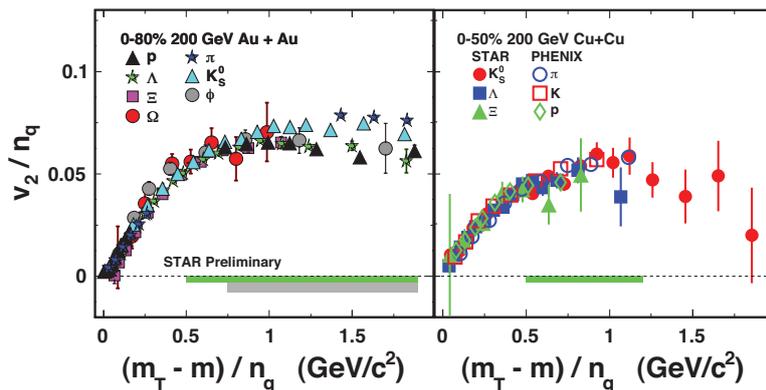
Figure 4: (colour online) Elliptic flow per quark as function of transverse mass per quark for different hadron species in collisions of Au+Au (a) and Cu+Cu (b) at 200 GeV.

4 Parton energy loss: jet quenching and medium response

Jet quenching, which dates back to original ideas from Bjorken in 1982 [15], has been established as a powerful tool to study the early density of the matter produced in heavy-ion collisions and its evolution. It was first observed in the study of inclusive hadron suppression. The inclusive yield of hadrons at high p_T, which are expected to originate from hard parton scattering, is suppressed in central heavy-ion collisions by a factor of ≈ 5 compared to expectations from p+p collisions [16, 17, 18, 19]. This is usually displayed as the nuclear modification factor:

$$R_{AA} = \frac{1/p_T dN_{AA}/dp_T}{\langle N_{coll}\rangle 1/p_T dN_{pp}/dp_T}.$$

The suppression is evident as a deviation from $R_{AA} = 1$.

The PHENIX experiment has now measured the suppression of neutral pions out to transverse momenta as large as $p_T \approx 20\,\text{GeV}/c$, and in more limited ranges for a number of other particle species. A selection of results is displayed in Fig. 5. Neutral pions are suppressed by about a factor of 4-5 in central Au+Au collisions up to very high momenta. η mesons show a similar behaviour albeit with larger statistical errors. Other particles like the ϕ or ω do not show such a strong suppression, they are, however, only measured with much larger errors, or at somewhat lower momenta, where production mechanisms other than jet fragmentation,
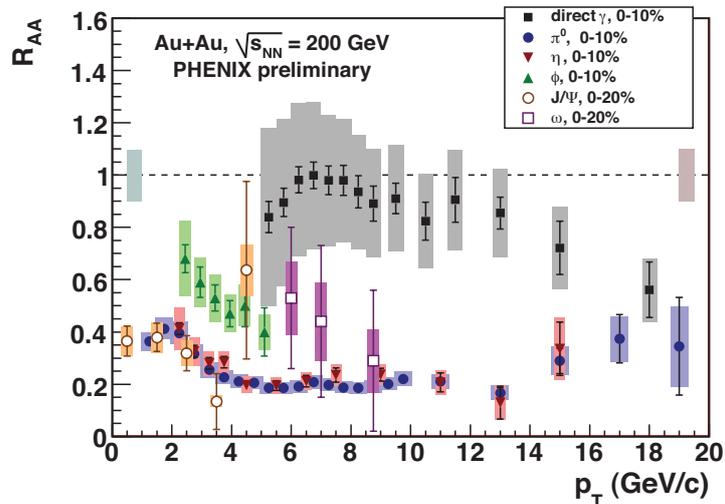
Figure 5: (colour online) Nuclear modification factor for different particle species in central Au+Au collisions at $\sqrt{s_{NN}} = 200$ GeV from PHENIX [20].

e.g. the above-mentioned coalescence/recombination, may have a significant influence. It is noteworthy that direct photons do not show a similar suppression. There is a decrease of the photon R_{AA} at very high p_T, but this can be explained e.g. from isospin differences between Au nuclei and protons.

The non-suppression for photons in central Au+Au collisions [21], which do not interact strongly, together with the absence of suppression for hadrons in d+Au collisions [22, 23, 24, 25], where no significant matter in the final state is produced, demonstrates that final state effects involving the strong interaction must be responsible. The most likely interpretation of the suppression is thus medium-induced energy loss of fast partons.

Additional information can be obtained from recent measurements by the STAR experiment. Figure 6 shows the nuclear modification factor R_{AA} for identified pions, kaons, and protons for central Au+Au collisions. There is a similarly strong suppression of the pion yield at high p_T and a distinctly different behavior of protons and kaons over the full momentum range. Kaons show less suppression than pions, and protons in turn again

Figure 6: (colour online) Nuclear modification factor (R_{AA}) for pions, kaons, and protons in central collisions of Au+Au at $\sqrt{s_{NN}} = 200$ GeV from STAR [26].

a weaker suppression than kaons. This contradicts a naïve expectation related to the origin of

the different particle species. Compared to pions, both kaons and protons should originate for a larger fraction from the fragmentation of gluons relative to quarks. As gluons have a larger colour factor, they should suffer a stronger effect from parton energy loss, which is however not seen in the data. It has been suggested that jet conversion may be able to explain this observation – in any case this demonstrates that the physics of parton energy loss is not completely unravelled.
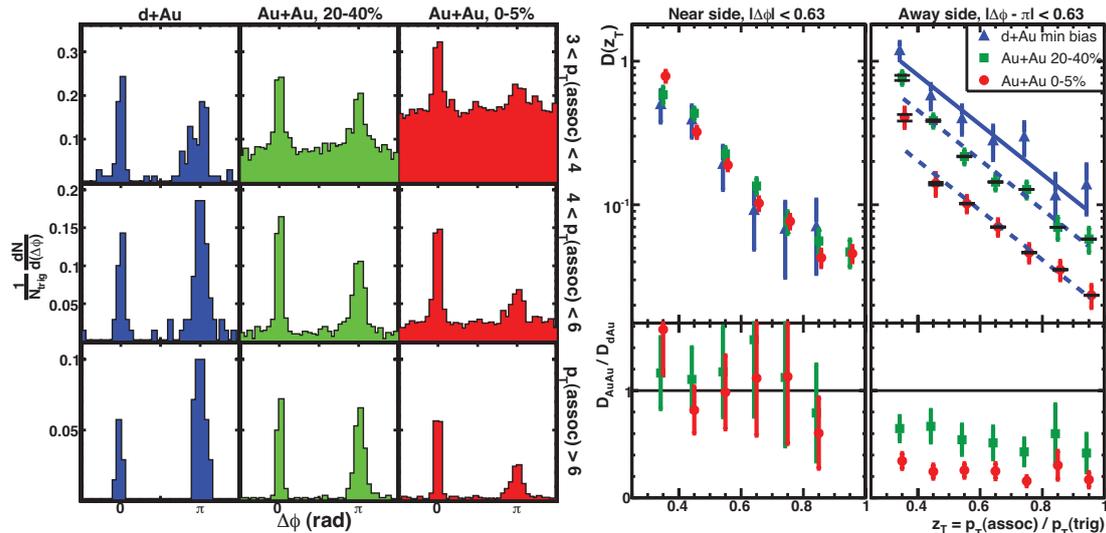
Figure 7: (colour online) left: Per-trigger yields of associated hadrons as a function of relative azimuthal angle for a trigger of $p_T > 8\,\text{GeV}/c$ for d+Au, semi-central Au+Au and central Au+Au at different values of p_T of the associated hadrons. right: Per-trigger yields of correlated hadrons as a function of the momentum fraction z_T (definition see text) for the near side (left) and for the away side)right). The bottom panels show ratios of the upper distributions for Au+Au collisions to those for d+Au. (From[28])

More directly jet suppression is observed in the modification of the characteristic correlation structure in azimuthal angle. For a high-p_T hadron trigger there is a prominent back-to-back correlation peak of associated hadrons with intermediate p_T in elementary reactions. In the earliest studies the same peak is essentially absent in central heavy-ion collisions [27]. Again d+Au collisions do not show a suppression effect. These studies have later been extended to truly high p_T [28]. On the left side of Fig. 7 the yields of hadrons associated with a very high-momentum trigger hadron is shown as a function of azimuthal angle for different systems and different p_T-ranges of the associated particles. In d+Au collision peaks are observed both at $\Delta\phi = 0$ and at $\Delta\phi = \pi$, related to the back-to-back two-jet structure of hard scatterings. In central Au+Au collisions at the lowest p_T the near-side peak is clearly visible, while on the away side there is only an indication of a correlation structure. At the highest p_T both correlation peaks are, however, clearly visible again, but the away-side peak is much smaller in magnitude than for d+Au collisions. This can be studied more quantitatively via the *trigger-normalized*

fragmentation functions

$$D(z_T) = \frac{1}{N_{trigger}} \frac{dN}{dz_T},$$

where $z_T \equiv p_T(assoc)/p_T(trigger)$, which are displayed in figure 7 on the right. All distributions have an approximately exponential shape with a similar slope parameter. This can best be seen directly from the ratios shown in the lower panels. The ratios are seen to be independent of z_T for both the near and the away side. The near side yield is even compatible with 1, i.e. no modification of these distributions in central Au+Au compared to d+Au, while the away side shows a further suppression by a factor $4 - 5$. Detailed analysis of the peak structures shows in addition that the peak widths for the higher p_T ranges is similar for all systems.

These findings can most easily be interpreted as follows: The suppression of hadrons at very high p_T is due to energy loss of partons. These partons emerge from the medium with a considerable momentum so that they still fragment in the vacuum as usual into several hadrons. On the near side the trigger requirement selects events which develop an ordinary jet. Energy-independent energy loss would preserve the shape of the distributions. On the away side of the trigger, the other parton suffers additional energy loss, such that the probability to observe a second jet is greatly reduced. Still, if a high-p_T hadron emerges on the away side it is part of a similar jet structure.

In Fig. 8 the measured values of the nuclear modification factor R_{AA} of neutral pions is compared to the expectations for different densities from one energy loss model [29]. The right panel shows the modified χ^2 (which accounts for systematic effects, see [32]) as a function of the medium density which is here given as the mean transport coefficient $\langle \hat{q} \rangle$. The transport coefficient $\hat{q}$ is the squared momentum transfer per unit path length which characterises the energy loss properties of the medium. The mean energy loss $\Delta E \propto \alpha_s \hat{q} L^2$ for a static medium [33]. The extracted value of the mean transport coefficient $\langle \hat{q} \rangle = 13.2^{+2.1}_{-3.2}$ GeV^2/fm, based on this model. A number of other models have also been compared to the data [32, 34] and tend to give lower estimates of the (equivalent) medium density.
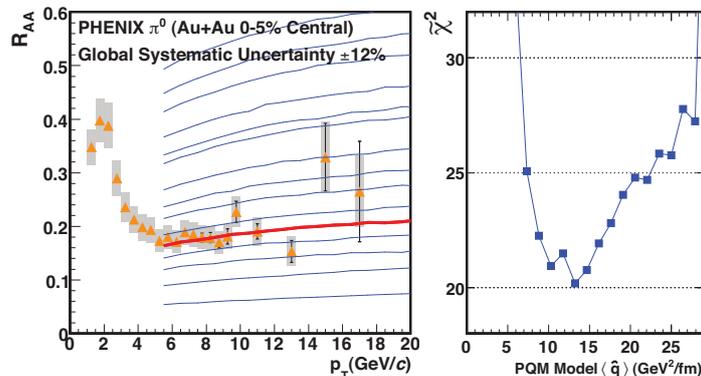
Figure 8: (colour online) Measured nuclear modification factor for π^0, compared to model calculations [29] based on the BDMPS formalism. The right panel shows the modified χ^2 of the comparisons [30].

Figure 9 (left panel) shows the away-side trigger-normalized fragmentation functions – also called the recoil yield – for trigger particles with $8 < p_{T,trig} < 15$ GeV/c in d+Au and Au+Au
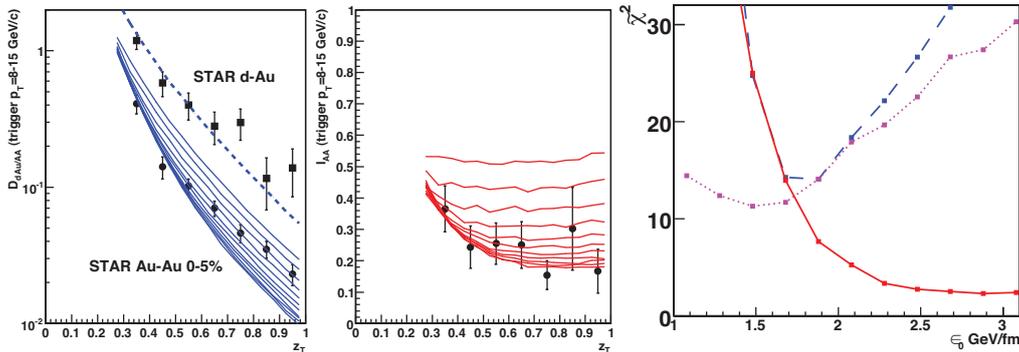
Figure 9: (colour online) Trigger-normalized fragmentation functions $D_{AA}(z_T)$ on the away side for d+Au and Au+Au collisions (left) and the suppression ratio I_{AA} (middle) for trigger particles with $8 < p_{T,trig} < 15$ GeV/c compared to model calculations [31]. The right panel shows the modified χ^2 of the comparisons (see text), including systematic effects [34].

collisions compared to model curves with different medium density. The right panel shows again the modified χ^2 as a function of density. The model used in this case is a higher twist model, because the full set of calculations for the recoil yield has so far only been performed for that model [31]. The parameter describing the medium density in this model is the typical energy loss ϵ_0. Because the d+Au reference measurement for this observable has only limited statistical precision, a few different approaches were taken for the theory fit. Firstly, one can fit the recoil yield using a NLO calculation to describe the p+p result. The resulting χ^2 is shown by the blue dashed curve in Fig. 9. The best-fit value for $\epsilon_0 \approx 1.9$ is compatible with the value extracted using the single-hadron data with this same model $\epsilon_0 = 1.9^{+0.2}_{-0.5}$ GeV/fm [34]. Adding the scale uncertainty on the calculated d+Au reference yield gives the magenta dotted curve. When the d+Au measurement is used to calculate the recoil suppression I_{AA}, the red solid curve is obtained. This last procedure is the least model dependent, but it gives the weakest constraint on ϵ_0. Future high-statistics measurements of di-hadron correlations in p+p and d+Au collisions at RHIC will further constrain the theory in this area.

The energy lost by the hard-scattered parton is expected to be carried by softer particles, and in fact di-hadron correlation studies at lower p_T show large qualitative differences between p+p reference measurements and Au+Au results. Two particularly remarkable feature have emerged. One effect is the observation of a significant associated yield on the near side at larger pseudo-rapidity difference $\Delta\eta \gtrsim 0.7$, which is not expected from jet fragmentation. The other observation is a large broadening of the recoil distribution at low p_T, to the point where the distribution exhibits a double-peak structure.

Figure 10 shows the distribution of associated hadrons with $2 < p_{T,assoc} < 3$ GeV/c in pseudo-rapidity η and azimuthal angle ϕ with respect to a trigger particle with $3 < p_{T,trig} < 4$ GeV/c in central Au+Au collisions at RHIC [35]. At these p_T, the associated hadrons show not only the jet-like peak around $(\Delta\eta, \Delta\phi) = (0,0)$, but also significant additional associated yield at larger $\Delta\eta$. The additional yield is approximately uniformly in $\Delta\eta$ and the effect is therefore referred to as the *ridge*. The ridge-effect is unique to heavy ion collisions and is found to be present for trigger hadrons over the entire accessible p_T-range (up to 7 GeV/c at present) [35]. The long range of the correlation in $\Delta\eta$ very likely requires a production mechanism at work

at very early times. A number of different possible mechanisms have been proposed, such as coupling of radiated gluons to longitudinal flow [36, 37, 38], medium heating by the passage of a hard parton combined with longitudinal flow [39] and a radial flow boost to the underlying p+p event, combined with trigger bias [40, 41]. Further experimental work is going on to distinguish the different scenarios.

Another striking finding from di-hadron correlations at intermediate p_T is that the away-side peak is strongly broadened. This is illustrated in Figure 11, which shows associated hadron distributions with $1 < p_{T,assoc} < 2.5$ GeV/c for three different ranges of $p_{T,trig}$ in central Au+Au collisions [42] (full symbols). The open symbols in the Figure show d+Au results for reference. Clearly, the away-side distribution is strongly broadened in the Au+Au collisions, compared to d+Au collisions. For lower $p_{T,trig}$, there might even be a minimum in the distribution at $\Delta\phi = \pi$. This observation has lead to the suggestion that partons propagating through the strongly interaction medium may give rise to Mach-Cone shock waves [43, 44]. The width of the away-side distribution would then measure the opening angle and thus the velocity of sound in the medium. However, it has also been pointed out that gluon radiation in combination with the kinematic constraint $p_{T,trig} \approx p_{T,assoc}$ may give rise to a broadened away-side as well [45]. It is also important to realize that the raw signal sits on a large background which is not constant, but has a $\cos(2\Delta\phi)$ modulation due to elliptic flow.

Figure 10: Distribution of associated hadrons with $2 < p_{T,assoc} < 3$ GeV/c in pseudo-rapidity η and azimuthal angle ϕ with respect to a trigger particle with $3 < p_{T,trig} < 4$ GeV/c in central Au+Au collisions at RHIC [35].

The background has been subtracted in Fig. 11 and the uncertainty on the extracted signal from the uncertainty in the strength of elliptic flow is indicated by the shaded band. However, possible correlations between elliptic flow and the jet-structure are not taken into account in this estimate. Three-particle correlation measurements are currently being developed to further explore the away-side shapes.

The interpretation of the single hadron and di-hadron suppression suffers from the fact, that the initial jet energy is unknown, and that theoretical descriptions thus have to perform averages over initial parton energy distributions in addition to the necessary averages over the spatial distributions of the production points. This significantly limits the discrimination power of the above measurements. Two types of more advanced measurements are currently under study that should provide access to the initial parton energy. One method uses γ-jet events, where the transverse momentum of the direct photon is equal to the initial parton transverse momentum, the other method attempts to perform jet reconstruction in heavy-ion events. First studies using the former method have already been performed [46, 47] but are limited from low statistics due to the small cross section for photon production. The latter has a potentially
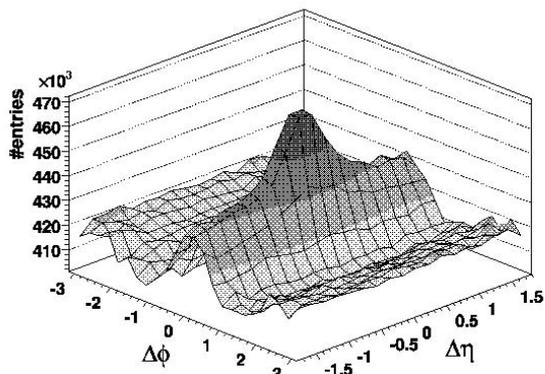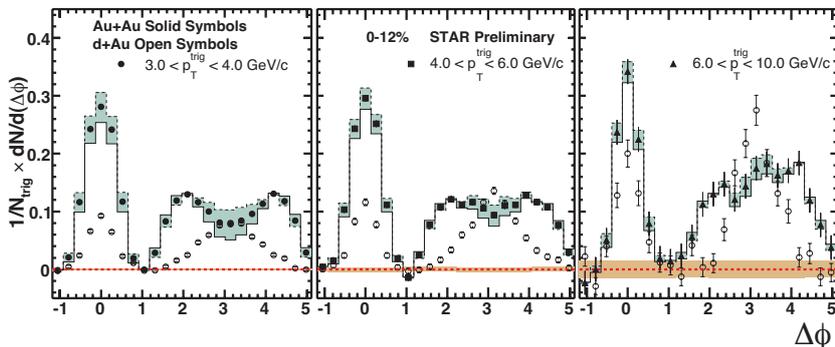
Figure 11: (colour online) Background-subtracted distribution of associated hadrons with $1 < p_{T,assoc} < 2.5$ GeV/c for three different ranges of $p_{T,trig}$, in central Au+Au collisions at $\sqrt{s_{NN}}$=200 GeV (full symbols) and d+Au collisions (open symbols)[42]. The lines indicate the uncertainty on the signal shape due to the uncertainty in the elliptic flow of the background. The shaded bands around 0 indicate the statistical uncertainty on the background level.

large cross section, but suffers from a large background of the high-multiplicity events in heavy ion collisions. Preliminary results of such an analysis have been presented in [48]. In the near future, differential measurements of the suppression as a function of hadron p_T will allow to further constrain parton energy loss in the medium.

5   Summary

The RHIC experimental program has produced a large number of new, interesting results. First dedicated studies of gluon saturation at forward rapidities have been performed. The results are consistent with pictures of gluon saturation, but a full theoretical description and additional data on jet-like correlations are still needed. Elliptic flow analysis shows early equilibration of the system and a preference for an equation of state with a QCD phase transition. Studies of systematic errors and the influence of the initial state distribution are being done to be able to reliably extract values of the viscosity of matter. Current estimates show a small but finite viscosity of about a few times the theoretical lower bound. The analysis has progressed to include many different hadron species, and so far constituent quark scaling has been confirmed in a reasonable momentum range.

Strong jet quenching has been demonstrated in single hadron yields up to transverse momenta of 20 GeV/c. The naïvely expected effects of different energy loss of gluons with respect to quarks have not been observed, pointing to a still not complete understanding of the physics of energy loss. A similar suppression is also observed in the recoil yield opposite to high p_T trigger particles. Both the suppression of single hadrons and of the recoil yield can successfully be described by QCD-based energy loss models, there is however still considerable uncertainty on the exact mechanisms. Strong modifications of the low and intermediate p_T jet-associated hadrons point to significant jet-induced effects on the medium, which are being studied by more advanced analysis methods. γ-jet correlations and full jet reconstruction are the observables of the future which should provide stronger constraints on parton energy loss.

References

[1] Proceedings of Quark Matter 2009, Nucl. Phys. A **830** (2009).

[2] E. Iancu, A. Leonidov, and L. McLerran (2002) `hep-ph/0202270`.

[3] J. Adams *et al.* (STAR collaboration), Phys. Rev. Lett. **97** 152302 (2006).

[4] S. Voloshin and Y. Zhang, Z. Phys. C **70**, 665 (1996).

[5] K. H. Ackermann *et al.* [STAR Collaboration], Phys. Rev. Lett. **86**, 402 (2001).

[6] C. Adler *et al.* [STAR Collaboration], Phys. Rev. Lett. **87**, 182301 (2001).

[7] T.D. Lee *et al.*, New Discoveries at RHIC: Case for the Strongly Interacting Quark-Gluon Plasma. Contributions from the RBRC Workshop held May 14-15, 2004. Nucl. Phys. A **750** (2005) 1-171

[8] P. Kovtun, D. T. Son and A. O. Starinets, Phys. Rev. Lett. **94** (2005) 111601

[9] M. Luzum and P. Romatschke, Phys. Rev. C **78**, 034915 (2008).

[10] H. J. Drescher, A. Dumitru, C. Gombeaud and J. Y. Ollitrault, Phys. Rev. C **76** (2007) 024905

[11] R. S. Bhalerao, J. P. Blaizot, N. Borghini and J. Y. Ollitrault, Phys. Lett. B **627** (2005) 49

[12] J. Adams *et al.* [STAR Collaboration], Phys. Rev. Lett. **92**, 052302 (2004).

[13] Z.W. Lin and C.M. Ko, Phys. Rev. Lett. **89**, 202302 (2002); D. Molnar and S.A. Voloshin, Phys. Rev. Lett. **91**, 092301 (2003).

[14] R.C. Hwa and C.B. Yang, Phys. Rev. C **67**, 064902 (2003); R.J. Fries, B. Muller, C. Nonaka and S.A. Bass, Phys. Rev. Lett. **90** 202303 (2003).

[15] J.D. Bjorken, Fermilab-Pub-82/59-THY (1982).

[16] K. Adcox *et al.* [PHENIX Collaboration], Phys. Rev. Lett. **88**, 022301 (2002).

[17] C. Adler *et al.* [STAR Collaboration], Phys. Rev. Lett. **89**, 202301 (2002).

[18] S.S. Adler *et al.* [PHENIX Collaboration], Phys. Rev. Lett. **91**, 072301 (2003).

[19] J. Adams *et al.* [STAR Collaboration], Phys. Rev. Lett. **91**, 172302 (2003).

[20] K. Reygers *et al.* [PHENIX Collaboration], J. Phys. G **35** 104045 (2008).

[21] S.S. Adler *et al.* [PHENIX Collaboration], Phys. Rev. Lett. **94**, 232301 (2005)

[22] B.B. Back *et al.* [PHOBOS Collaboration], Phys. Rev. Lett. **91**, 072302 (2003).

[23] S.S. Adler *et al.* [PHENIX Collaboration], Phys. Rev. Lett. **91**, 072303 (2003).

[24] J. Adams *et al.* [STAR Collaboration], Phys. Rev. Lett. **91**, 072304 (2003).

[25] I. Arsene *et al.* [BRAHMS Collaboration], Phys. Rev. Lett. **91**, 072305 (2003).

[26] J. Putschke *et al.* [STAR Collaboration], Nucl. Phys. A **830** 58c-65c (2009).

[27] C. Adler *et al.* [STAR Collaboration], Phys. Rev. Lett. **90**, 082302 (2003).

[28] J. Adams *et al.* [STAR Collaboration], Phys. Rev. Lett. **97**, 162301 (2006).

[29] A. Dainese, C. Loizides, G. Paic, Eur. Phys. J. C **38**, 461 (2005), `hep-ph/0406201`

[30] A. Adare *et al.* [PHENIX Collaboration], Phys. Rev. Lett. **101**, 232301 (2008).

[31] H. Zhang, J.F. Owens, E. Wang, X.N. Wang, Phys. Rev. Lett. **98**, 212301 (2007).

[32] A. Adare *et al.* [PHENIX Collaboration], Phys. Rev. C **77**, 064907 (2008).

[33] C.A. Salgado, U.A. Wiedemann, Phys. Rev. D **68**, 014008 (2003).

[34] J.L. Nagle (2008), `arXiv:0805.0299`

[35] J. Putschke *et al.* [STAR Collaboration], J. Phys. G **34**, S679 (2007).

[36] N. Armesto, C.A. Salgado, U.A. Wiedemann, Phys. Rev. Lett. **93**, 242301 (2004).

[37] A. Majumder, B. Muller, S.A. Bass, Phys. Rev. Lett. **99**, 042301 (2007).

[38] P. Romatschke, Phys. Rev. C **75**, 014901 (2007).

[39] C.B. Chiu, R.C. Hwa, Phys. Rev. C **72**, 034903 (2005).

Discussion

Guido Altarelli (Roma III and CERN): What is the physics programme at RHIC for the next future?

Answer: The upcoming heavy-ion measurements at RHIC will serve to collect significant luminosity for rare probes and should allow e.g. a quantitative characterization of jet quenching. This will profit in particular from the upgrade of the DAQ in STAR. Further detector upgrades already implemented or in progress will enhance the capabilities for particle identification, like the new TOF detector in STAR, the hadron-blind detector (HBD) in PHENIX, or the silicon vertex detector upgrades in both experiments. The latter should allow to obtain crucial information on the production of charm and bottom hadrons, and should help to elucidate the puzzles related to existing heavy flavor measurements at RHIC.

Benni Ward (Baylor University): String theorists have found model violations of the AdSICFT limit you reference as a quantum mechanical limit - quantum mechanics is not a model. Please comment.

Answer: The remark is relevant. In fact in the presentation I have shown a statement on a "quantum mechanical limit" of shear viscosity, which has been used by a number of colleagues in the field but which is strictly speaking not adequate. The limit has been derived from model calculations, which incorporate some aspects of quantum mechanics, but certainly not from first principles. There are some calculations in string theory that you probably refer to, which give a different answer. The purpose of the presentation was, however, to demonstrate that the shear viscosity of the matter produced at RHIC is very low, and possibly close to the AdS/CFT-limit - thus low compared to any other real system, independently of the conceptual status of this limit.

Theory of Heavy-Ion Collisions

Thorsten Renk[1]

[1]Department of Physics, P.O. Box 35, FI-40014 University of Jyväskylä, Finland

In high energy nucleus-nucleus (A-A) collisions, a transient state of thermalized, hot and dense matter governed by Quantum Chromodynamics (QCD) is produced. Properties of this state are reflected in the bulk low transverse momentum (P_T) hadron production which represent the remnant of the collective medium as well as in modifications of so-called probes which are not part of the thermalized medium, i.e. jets generated in high P_T processes or leptons and photons which do not participate in the strong interaction. Theory efforts aim at deducing the properties of QCD thermodynamics and collectivity from such observables.

1   Introduction

Often the aim of science is to understand the nature of a phenomenon in terms of its more fundamental constituents. This corresponds to a paradigm called 'reductionism', and the goal of high-energy physics can be understood from this paradigm as uncovering more fundamental building blocks of matter by probing ever decreasing distance scales. However, there are some phenomena in nature which require a different paradigm in order to understand them. Here, properties of a given system cannot be determined or explained by the sum of its fundamental constituents alone. Instead, the system as a whole determines in an important way how the parts behave. The corresponding paradigm has the name 'holism'.

An example in physics is Quantum Chromodynamics (QCD), the theory of strong interactions. While QCD at small distance scales is comparatively simple and can be understood using perturbation theory as the interaction of quarks and gluons as degrees of freedom, at large distance scales QCD shows phenomena like confinement and the appearance of hadrons as degrees of freedom which cannot easily be read off from the Lagrangean. Moreover, the thermodynamics of QCD matter appears quite complex in predicting a transition from a hadronic gas at low temperatures to a new state of matter with different degrees of freedom, the Quark-Gluon Plasma (QGP) above a transition temperature T_C of about 170 MeV. The properties of this transition are accessible experimentally in ultrarelativistic heavy-ion collisions (URHIC) where matter with peak energy densities corresponding to temperatures above T_C are reached for short times. Such experiments have been carried out at the CERN SPS at $\sqrt{s} = 17.6$ AGeV in the past, are currently being done at the Brookhaven National Lab RHIC collider at $\sqrt{s} = 200$ AGeV and will in the future be part of the CERN LHC program with Pb-Pb collisions at $\sqrt{s} = 5.5$ ATeV.

However, extracting these properties is not an easy task as always the system as a whole needs to be considered rather than an exclusive final state. Experimentally, this implies dealing with $O(10.000)$ particles in the detector while theoretically direct perturbative calculations from

the QCD Lagrangean cannot be done — even appropriate concepts to describe the system have to be found.

It has proven useful to analyze A-A collisions in terms of 'bulk' and 'probes'. Here, 'bulk' stands for the part of the system which exhibits collectivity and is approximately thermalized. In terms of a momentum scale, this typically implies $P_T = O(\text{few } 100 \text{ MeV})$, i.e. of the order of T_C. Particles at much higher momentum scales never thermalize and hence cannot be treated as part of the bulk matter. However, they nevertheless interact with the medium, and hence can serve as probes of the medium. Typically, the presence of the bulk medium implies either production channels of probes or final state interactions which are not present in more elementary reactions like p-p collisions, hence the modification of probes as compared to the suitably scaled p-p baseline carries information about the medium. Examples for important probes in heavy-ion physics are high P_T hadrons and jets, leptons and photons and heavy-quark bound states.

Using these concepts, one can examine heavy-ion collisions by looking at the bulk medium itself, by studying the modification of probes by the medium as compared to a p-p baseline, and finally also the modification of the bulk medium due to the interaction with a probe, i.e. its response to a local perturbation.

2   The bulk medium

Theoretical expectations about the thermodynamics of the bulk medium can be formed from lattice QCD simulations at finite temperature. While these can be done only for a static system, they allow to study thermodynamical properties of hot QCD. An example for such results [1] is shown in Fig. 1 in terms of normalized energy density ϵ and pressure p as a function of temperature T and the so-called interaction measure $(\epsilon - 3p)$ which measures deviations from an ideal gas behaviour.
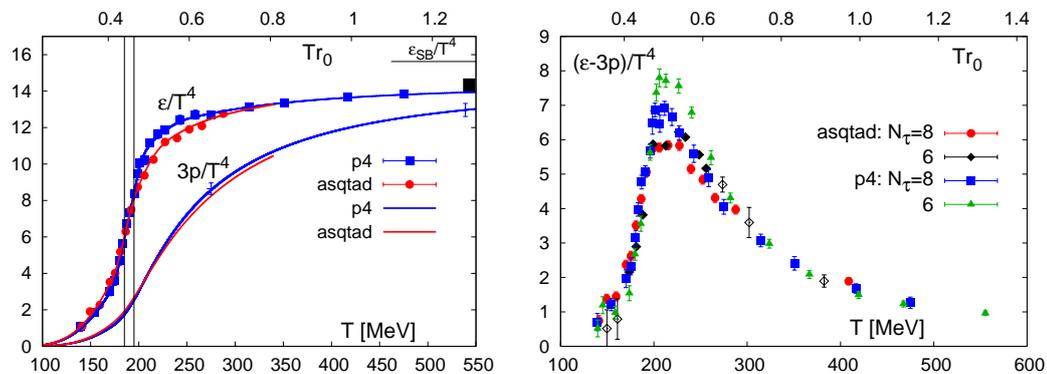
Figure 1: Lattice results [1] for equation of state (left) and interaction measure (right) of hot QCD.

These results, in particular the strong change of thermodynamical properties around $T = 170$ MeV, are indicative of a phase transition or a rapid crossover. The large value of the interaction measure indicates that the system is, at least close to T_C, far from an ideal gas and

instead strongly coupled. However, the applicability of lattice results, which describe a static medium in termal equilibrium to the highly dynamical situation in heavy-ion collisions is not *a priori* obvious. What is observed in the detector are free hadrons long after the breakup of any bulk medium created in the collision. Any conclusions as to the formation of a medium hence need to rely on indirect evidence, i.e. on the imprint of such a medium on the final distribution of hadrons.

First evidence for collectivity is found in the mass ordering of transverse mass m_T spectra (where $m_T = \sqrt{P_T^2 + m^2}$ with m the particle mass and P_T its transverse momentum). In Pb-Pb collisions at the CERN SPS [2] it was observed that transverse mass spectra of hadrons obey the formula

$$\frac{1}{m_T}\frac{dN}{dm_T} = \exp\left[-\frac{m_T}{T^*}\right] \quad \text{with} \quad T^* = T + m\langle v_T \rangle.$$

Such mass ordering in which heavier hadrons are characterized by harder spectra is difficult to understand in terms of direct hadron production, but has a natural explanation in terms of collective motion of a thermalized volume with average collective velocity $\langle v_T \rangle$, thus the apparent temperature T^* of the system has a part T due to random motion and a part $m\langle v_T \rangle$ due to collective motion. This interpretation naturally leads to a fluid picture of the bulk medium in which individual fluid elements are locally thermalized and the fluid pressure drives the collective expansion of the system, till eventually the mean free path of hadrons inside the fluid becomes larger than the dimensions of the system, and decoupling into a system of free hadrons occurs. Hydro-inspired parametrizations (e.g. [3, 4]) and later ideal relativistic hydrodynamical simulations (e.g. [5, 6]) have since been very successful at describing the various hadron spectra both in Pb-Pb collisions at the CERN SPS fixed target experiment at 17.3 AGeV and for Au-Au collisions at the Brookhaven RHIC collider at 200 AGeV.

Relativistic fluid dynamics is based on energy-momentum and current conservation,

$$\partial_\mu T^{\mu\nu} = 0 \qquad \partial_\mu j_i^\mu = 0 \quad \text{where} \quad T_{id}^{\mu\nu} = (\epsilon + p)u^\mu u^\nu - pg^{\mu\nu}$$

with j_i^μ a conserved current (like e.g. baryon number), u^μ the 4-velocity of a fluid element, ϵ its energy density and p its pressure, where properties of the medium enter in terms of the equation of state as e.g. the temperature dependence of the pressure $p(T)$. $T_{id}^{\mu\nu}$ here is the energy-momentum tensor of an ideal fluid with vanishing mean free path of the microscopic degrees of freedom. For finite mean free path, viscous corrections enter in the form $T^{\mu\nu} = T_{id}^{\mu\nu} + \Pi^{\mu\nu}$ where $\Pi^{\mu\nu}$ contains various gradients, e.g. a shear term which couples to velocity gradients. For a stable, causal result, gradients up to 2nd order have to be considered. In recent years, there has been tremendous numerical progress in the treatment of relativistic viscous hydrodynamics [7] going beyond the applicability of ideal hydrodynamics.

One of the most striking signatures of hydrodynamical behaviour is the so-called *elliptic flow*. If one makes a decomposition of the angular distribution of hadrons produced in a heavy-ion collision, elliptic flow appears as the second harmonic coefficient v_2,

$$\frac{dN}{d\phi} = \frac{1}{2\pi}\left[1 + 2v_1\cos\phi + 2v_2\cos 2\phi + \dots\right].$$

In a hydrodynamical system, v_2 arises because the fluid pressure converts initial anisotropies in position space (such as present in the shape of the overlap region in non-central A-A collisions) to anisotropies in momentum space. The impact parameter dependence of v_2 is therefore a direct

probe of pressure gradients in the system, and fluid dynamics must be able to give accurate predictions for v_2 as a function of impact parameter or P_T if it is a valid description of the dynamics.

Viscous hydrodynamical results for v_2 have been obtained in recent years, and examples are shown in Fig. 2. The key parameter characterizing viscous effects is the ratio of shear viscosity η over entropy density s.
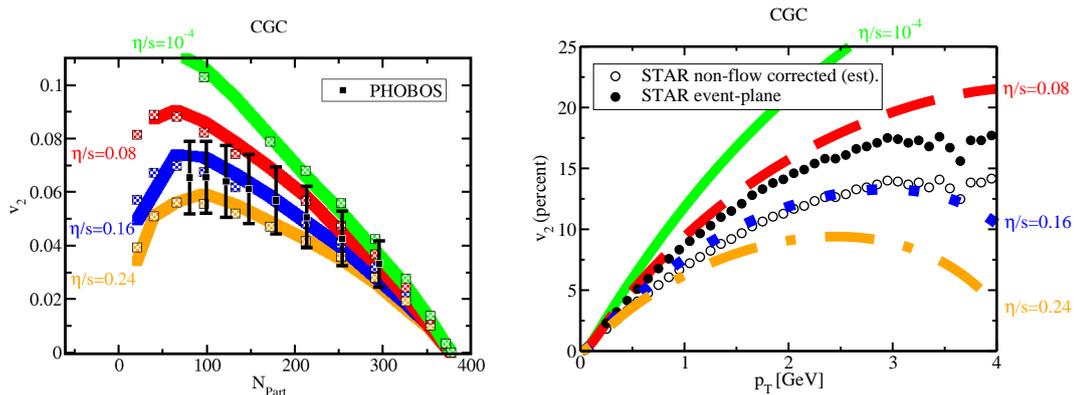
Figure 2: Relativistic viscous hydrodynamics results [8] for v_2 as a function of the number of collision participants (left) and P_T (right) for different values of η/s .

From the figures, it is apparent that the data can be well described with a range of about $\eta/s = [0.08..0.2]$. This implies that the system is not ideal. However, one may note that superfluid helium is characterized by a value of η/s about 10 times larger. This implies that the system created in heavy-ion collisions is very close to a perfect liquid, in fact it is the most perfect liquid known in nature, and that the mean free path in the medium is extremely small and the system hence exhibits strong collectivity.

3   Jet tomography

The fluid picture applies for P_T of $O(\text{few } T)$, however there are hadrons produced in heavy ion collisions with $P_T \gg T$. Such hadrons must come from hard, partonic processes. By arguments based on the uncertainty principle, one can establish that for typical kinematics the initial hard process takes place before a collective medium is produced and probes length scales at which collectivity is not relevant. Thus, the production of high p_T partons is unmodified by the medium. However, the subsequent QCD evolution from a highly virtual initial parton into a parton shower at lower virtuality scales probes length- and timescales comparable with the medium lifetime and extent, therefore the parton shower is likely to be medium modified. Finally, the non-perturbative hadronization process can be safely estimated to take place outside the medium, therefore it is again unmodified by any final state interaction. This leads to a picture in which a hard probe with known and calculable properties is created in the medium and subsequently modified by its passage through the medium. The idea to exploit this effect in order to characterize medium properties is known as *jet tomography*.

Experimentally, the final state interaction of hard partons with the medium leads to very striking phenomena, among them the suppression of single inclusice high P_T hadrons by a factor of about five in central 200 AGeV Au-Au collisions [9] as compared to the scaled expectation from p-p collisions or the appearance of monojets in events in which one parton of a back-to-back event is absorbed by the medium [10]. The most commonly discussed observable is the nuclear suppression factor R_{AA} of single high P_T hadrons. It is defined as the hadron yield in A-A collisions divided by the yield in p-p collisions scaled with the number of binary collisions,

$$R_{AA}(P_T, y) = \frac{d^2 N^{AA}/dp_T dy}{T_{AA}(0) d^2 \sigma^{NN}/dP_T dy}.$$

In the absence of any nuclear initial of final state effects, R_{AA} would hence be unity. Since the absence of strong initial state nuclear effects has been demonstrated in d-Au collisions, the strong deviation of R_{AA} from unity can almost exclusively be attributed to final state interations of produced partons with the bulk medium.

The likely mechanism for these modifications as compared to the p-p baseline expectation is medium-induced gluon radiation. The basic physics process is that gluons from the virtual gluon cloud surrounding a parton which propagates through the medium can decohere from the parent wave function if they pick up sufficient virtuality from the medium through interactions. A measure for the strength of the medium effect is the transport coefficient $\hat{q} = \frac{\langle q_\perp^2 \rangle_{med}}{\lambda}$ which measures the average momentum broadening per unit pathlength λ. Since the phase ϕ of a gluon relative to the parent parton needs to be $O(1)$ for decoherence, one can estimate $\phi = \langle \frac{k_\perp^2}{2\omega} \Delta x \rangle = \frac{\hat{q} L}{2\omega} L = \frac{\omega_c}{\omega}$ where $\omega_c = \frac{1}{2} \hat{q} L^2$ is the characteristic scale of energy loss. This typical scale grows in a constant medium quadratically with pathlength. Based on similar estimates, the spectrum of radiated gluons per unit pathlength can be computed to be $\omega \frac{dI}{d\omega dz} \sim \sqrt{\frac{\omega_c}{\omega}}$.
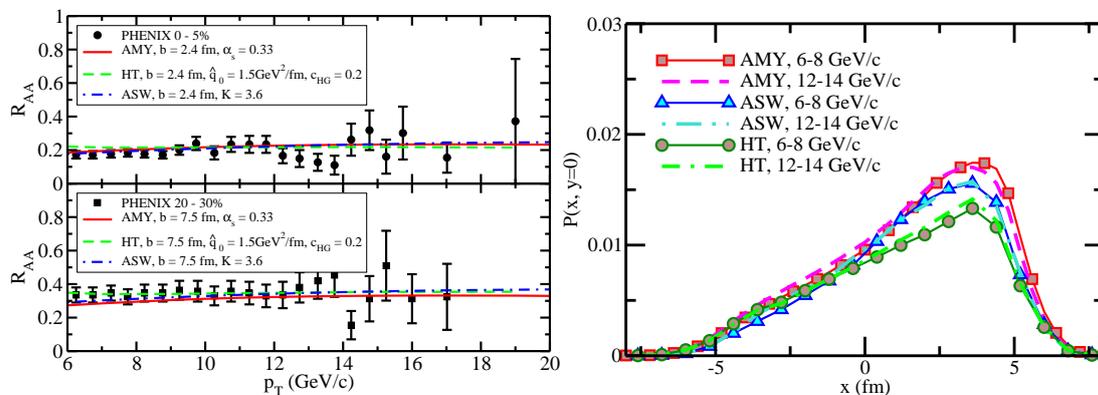
Figure 3: Nuclear suppression factor R_{AA} in 200 AGeV Au-Au collisions (left) and distribution of vertex of origin inside the medium for observed high P_T hadrons (right) for various models of radiative energy loss [11] in comparison with PHENIX data [9].

As mentioned above, hard partonic processes typically lead to the creation of highly virtual partons which evolve into a parton shower. However, for measurements which focus on the observation of high P_T hadrons there is a substantial bias towards events in which most of the energy within the shower is carried by a single hard parton. In this situation, it is justified to

approximate the situation of a shower which develops inside the medium by a parton which loses energy into the medium while traversing it, i.e. subleading shower partons are not explicitly tracked in this approximation. Calculations utilizing this energy-loss picture in which hard parton trajectories are embedded into a full 3+1 dim fluid dynamical model for the bulk medium have reached a high degree of sophistication (see e.g. [11]). As apparent from Fig. 3, they can reproduce both P_T dependence and centrality dependence of R_{AA} quite well and currently allow the extraction of information about the transport coefficient $\hat{q}$ from the medium with an accuracy of $\sim 50\%$.

The obvious next goal is to establish where the energy lost from the leading parton is recovered, and thus to confirm or disprove the picture of radiative energy loss. One possibility is a perturbative redistribution of energy within the parton shower — energy lost from the leading shower parton would then lead to increased production of partons at low momenta. Currently, several Monte Carlo (MC) codes based on known vacuum shower codes like PYTHIA [12] or HERWIG [13] are being developed [14]. They compute the whole medium-modified shower by including the possibility to have the parton kinematics or their branching probability modified by the interaction with the medium. Since one of the aims of jet tomography is to establish the relevant microscopic dynamics in the medium, currently the shower MC codes all include an assumption about the nature of the medium effect which eventually needs to be tested against data. However, there are consistent prescriptions to include generic quantum effects like the LPM suppression into the computation. Presumably, the LHC kinematic range is needed to observe clear jets and perturbative redistribution of energy.

Using such MC codes, the modification of typical jet observables like thrust, the subjet fraction, the jet shape or the longitudinal momentum distribution in the jet by the medium can be computed. Examples for the medium effect on such observables are shown in Fig. 4. However, jet finding in the environment of a heavy-ion collision is very difficult due to the high level of background created by the bulk medium, therefore the bias introduced by the jet definition must be carefully studied before such medium effects can actually be observed and a comparison of the model results with data can be made.
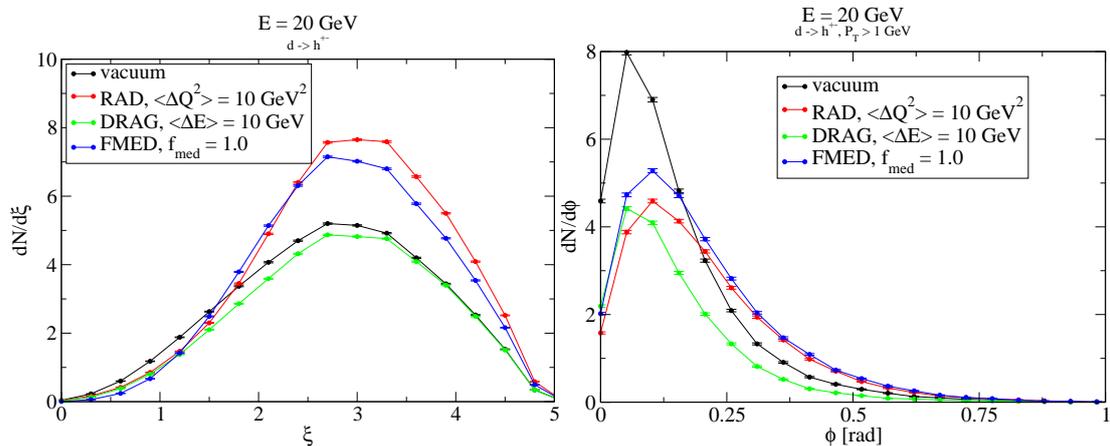
Figure 4: Modification of the so-called hump-backed plateau $dN/d\xi$ where $\xi = \ln(1/x)$ and $x = p/E_{jet}$ (left) and of the angular distribution of hadrons in the jet (right) by various models for the jet-medium interaction [15].

Experimentally, at least the onset of the characteristic enhancement of low P_T particle production induced by perturbative energy redistribution inside the jet cone should have been observable in γ-hadron correlations. The fact that this has not been seen so far points towards a different mechanism of energy redistribution being relevant at RHIC kinematics.

4 Medium response

Measurements of the correlation strength of hadrons associated with a high P_T trigger hadron have shed some light on a possible non-perturbative mechanism of energy redistribution. From these results (see Fig. 5) it is apparent that without a medium (i.e. in d-Au collisions) the correlations reflect back-to-back jet events. However, especially at low P_T, the away side ($\Delta\phi = \pi$) correlation function in Au-Au collisions does not resemble a jet-like structure at all, rather it exhibits a characteristic double-hump structure, and only at significantly higher momenta is a jet-like correlation recovered.
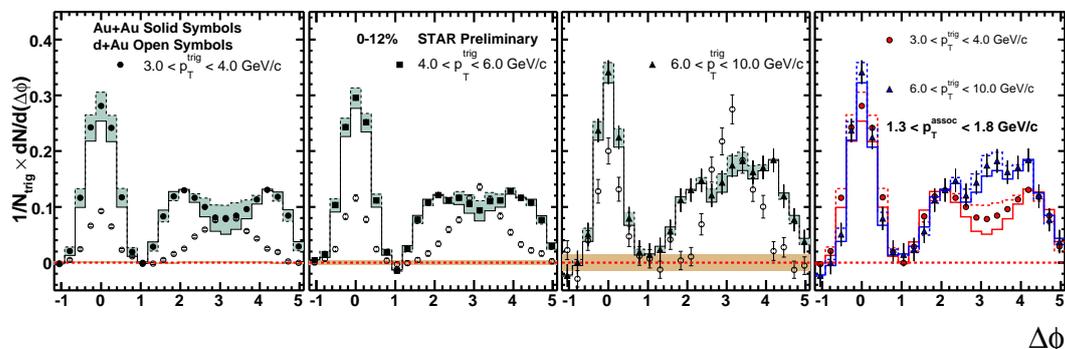
Figure 5: Correlations of particles with a high P_T trigger hadron (defining $\Delta\phi = 0$) as a function of angle for d-Au collisions (open symbols) and 200 AGeV Au-Au collisions (solid symbols) at RHIC [16] for rising values of associate hadron P_T.

These results have been widely interpreted as reflecting the recoil of the bulk medium from the hard probe. In this scenario, at least part of the energy lost from hard partons is contained in the medium in the form of a shockwave, where the characteristic cone structure of the shockwave leads to the double-hump structure in the angular correlation function. Note that if a fluid description of the medium is valid, shockwaves arise quite naturally from local perturbations of the medium.

Hydrodynamical calculations carried out under the assumption that the energy lost from a hard parton acts as a local source term of energy and momentum in the fluid dynamical equations have established that shockwaves leading to a characteristic double-hump structure in the correlation function can indeed be created (see e.g. [17]). However, at present these calculations are just a proof of concept — in order to compare with the measured correlations, it is not sufficient to compute the energy deposition of a single parton. Rather, the bias for the production point of the trigger hadron in the medium must be determined from an energy loss calculation, based on this information energy deposition into the medium must then be computed, taking also into account the distortion of any shockwave by the collective expansion

of the medium and the resulting bias for detecting the shockwave.

To date, no full hydrodynamical calculation has included these effects, but there is a phenomenological hydro-inspired model which has a proper averaging over the bias induced by energy loss and shockwave distortion by flow [18] which reproduces the two-particle correlations shown above.

A crucial test for the assumption that the observed signal is a shockwave is then a measurement of three particle correlations. Since the correlation measurement represents an average over many events, it is not evident that the double hump structure is created by the dynamics of a single event — a situation in which a jet peak is displaced to one side in a single event could average to the same correlation. However, the three particle correlation signal is different. In particular, if the correlation function is plotted as a function of ϕ_1 and ϕ_2 where ϕ_i is the angle of a measured hadron with the trigger, for a displaced peak scenario correlation strength is only created on the diagonal $\phi_1 \approx \phi_2$, whereas a shockwave cone leads to characteristical off-diagonal structures.
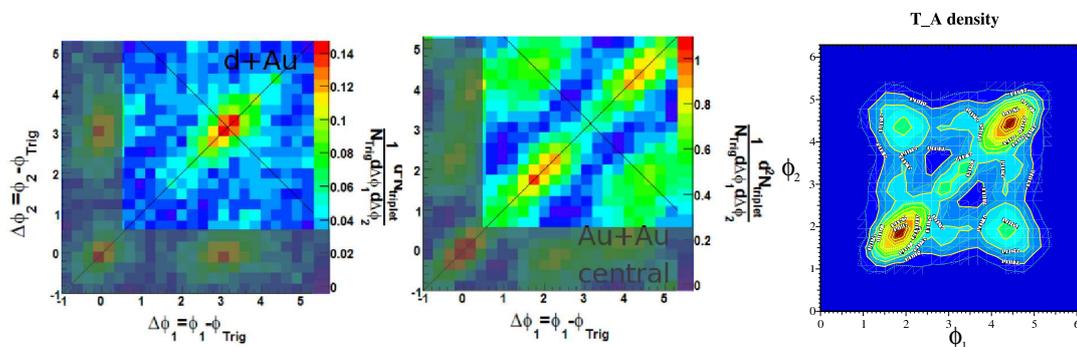
Figure 6: Left: Correlations of two particles with a high P_T trigger as measured in d-Au collisions (near side region is greyed out). Middle: Correlations of two particles with a high P_T trigger as measured in central Au-Au collisions (near side region is greyed out) Right: Calculated correlation of two particles with a trigger in the away side region [19].

In Fig. 6, a comparison between three-particle correlations measured by the STAR collaboration in d-Au and Au-Au at 200 AGeV and a calculation for Au-Au [19] for the away side is shown. While the d-Au measurement shows a signal very consistent with a back-to-back jet event, the correlation function in the Au-Au case exhibits a complicated structure on and off the diagonal. At least qualitatively the calculation manages to describe the observed signal well.

From these investigations can be inferred that the non-perturbative mechanism of shockwave excitation in the medium is a major channel absorbing energy lost from a leading parton. Conceptually, this is very interesting, as it offers in principle the possibility to measure various transport coefficients of the medium by observing its reaction to a localized perturbation. However, current theory efforts are still far away from this eventual goal.

Unlike at RHIC, at LHC energies multiple jet production per event is rather likely. Thus, shockwaves generated by the passage of hard partons through the bulk medium may actually become a major part of LHC bulk medium dynamics — surprises are rather likely.

5 Other major topics of interest

Characterizing properties of the bulk medium via direct observation of bulk matter, jet tomography and medium recoil are however not the only interesting areas of research in theoretical heavy-ion physics. Another key questions is, that if the medium can be described as an almost perfect liquid, how it reached this state at all? In other words, by what interaction mechanism can a nuclear initial state equilibrate on a very short timescale? This question leads to topics like the description of the initial state in terms of low x gluon saturation and the so-called Color-Glass-Condensate (CGC), which is believed to be the relevant state in the nuclear wave function. The subsequent 'shattering' of the CGC in the collision process next leads to a system with a very anisotropic distribution of particles in momentum space, which needs to isotropize before it can thermalize. Here, the physics of anisotropic coloured plasmas and plasma instabilities are research goals, with the ultimate aim to understand the onset of collectivity and to compute the initial state for hydrodynamical models.

A different set of questions is centered around the restoration of chiral symmetry, which in lattice QCD simulations takes place at the same temperature as the deconfinement transition from a hadron gas to a QGP. The chiral restoration requires that the vector correlator becomes degenerate with the axial correlator, but in what way this takes place is an open question. Experimentally, the vector mesons ρ, ω and ϕ as resonances in the vector correlator are most easily accessible, and their electromagnetic decays into dileptons offer the possibility to study their in-medium modifications. Such modifications may involve a shift in pole mass, as suggested by the so-called Brown-Rho scaling scenario, as well as a broadening of the meson widths. Theoretical studies of dilepton production within a fluid-dynamical model for the bulk medium in comparison with data suggest that chiral restoration is realized by dissolving resonance structures into a flat, featureless continuum. However, such calculations are rather involved and there is no clear consensus as to details yet.

Finally, in recent years the AdS/CFT correspondence discovered from String Theory has provided a new tool to compute properties of particular gauge theories in the strong coupling limit. In QCD, the strong coupling limit is very hard to access, thus the arrival of such methods has generated a lot of excitement. However, it remains to be seen how closely the gauge theories tractable by AdS/CFT methods resemble QCD, as present calculations are done for an $N = 4$ SYM theory which does not exhibit running coupling, a chiral transition or a deconfinement transition, i.e. which omits almost all the interesting features of QCD whose study is the aim of heavy-ion physics in the first place.

A good overview over topics currently relevant for heavy-ion physics can be found in the program of the Quark Matter 2009 conference [20].

6 Collectivity in QCD and the LHC

If the aim of ultrarelativistic heavy-ion physics is the study of collectivity in QCD, and hence phenomena which take place mainly at a momentum scale of $O(T_C) \sim 0.2$ GeV, one may ask why this needs to be studied at the LHC which will provide collisions between lead ions at 5.5 ATeV, i.e. at a momentum scale several orders of magnitude above the scale at which collective phenomena take place.

Part of the answer to the question is apparent from what has been said above: Techniques like jet tomography rely on the presence of hard processes in an event, and the abundance of

high P_T probes increases significantly with increased $\sqrt{s}$. However not only the quantity of hard probes increases, but also their quality: While reliable jet finding and the characterization of jet properties is difficult in a kinematic region where the jet energy is $O(20)$ GeV while the background is $O(1)$ GeV, this is no longer the case at LHC kinematics where jets with energies $O(500)$ GeV can be observed above a background with momentum scales $O(2-3)$ GeV. In addition, the kinematic range of the LHC offers access to processes like Z^0-jet back-to-back events, which are very clean probes as the narrow Z^0 decay signal can be detected practically background-free. Such probes allow a complete characterization of the jet kinematics independent from jet finding in the background, and hence can be used for precision calibration of the models.

However, jet tomography is not the only reason that collider kinematics is useful to probe collectivity in QCD — the excitation function of the bulk medium itself. An example is shown in Fig. 7.
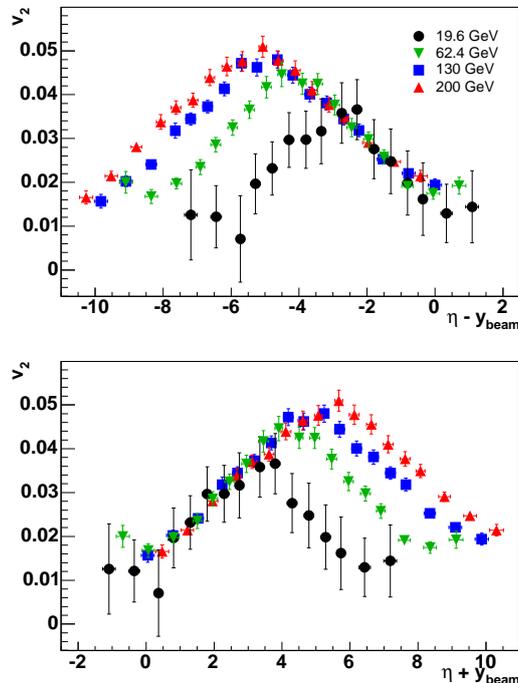
Figure 7: Elliptic flow coefficient v_2 as a function of rapidity difference to the beam rapidity for various values of $\sqrt{s}$ as obtained by the PHOBOS collaboration [21].

Here, the elliptic flow coefficient v_2 is shown as a function of the rapidity difference with the beam rapidity for various values of the collision energy $\sqrt{s}$. It is evident that $v_2(\eta \pm y_{beam})$ exhibits a characteristic triangular shape and a striking scaling behaviour. The change in this quantity is a very slow function of $\sqrt{s}$ — while the excitation function of hard probes is given by $\sqrt{s}/2$, collective phenomena typically scale like $\log \sqrt{s}$, i.e. one needs a large kinematic lever-arm to observe the excitation function of collective phenomena at all.

For the particular observable $v_2(\eta - y_{beam})$, the question is if the scaling persists at LHC

energies. The hydrodynamical picture predicts that the scaling will *not* be observed — yet the scaling behaviour in itself looks simple and compelling. The (dis-)agreement of the measured excitation function of this observable will therefore play a crucial part in either confirming or disproving ideas about the dynamical picture underlying heavy-ion collisions. However, to make such an argument, the large extension in kinematical range provided by LHC is absolutely crucial.

7 Outlook

What can be expected from future heavy-ion physics at the LHC? First of all, the huge extension in the kinematic range will help in our understanding of both bulk phenomena and jet tomography. Especially the physics of the interaction of hard probes with the medium will benefit enormously from the abundant production of high P_T particles and from the access to very clean channels.

In a broader sense, while qualitatively the dynamics of a collective QCD medium can be understood in terms of the near-perfect liquid, quantitatively many features of the dynamical evolution are not yet well understood, and in many areas even qualitative tests of our understanding of the relevant physics mechanisms are needed. LHC results will, from the first day on, have a large impact on heavy-ion theory in terms of ruling out or confirming existing ideas.

Clearly, there may be some surprises, for example there are hints that the dynamics of bulk recoil from hard probe energy loss may be an important feature of bulk dynamics at LHC, something that is not appreciated in predictions so far. But finally, there may be also genuinely new phenomena of collectivity in QCD to be discovered.

Acknowledgements

References

[1] A. Bazavov *et al.*, Phys. Rev. D **80** (2009) 014504.

[2] I. G. Bearden *et al.*, [NA44 Collaboration], Phys. Rev. Lett. **78** (1997) 2080.

[3] F. Retiere and M. A. Lisa, Phys. Rev. C **70** (2004) 044907.

[4] T. Renk, Phys. Rev. C **70** (2004) 021903.

[5] P. F. Kolb, J. Sollfrank and U. W. Heinz, Phys. Rev. C **62** (2000) 054909; K. J. Eskola, H. Honkanen, H. Niemi, P. V. Ruuskanen and S. S. Rasanen, Phys. Rev. C **72** (2005) 044904.

[6] T. Hirano, Phys. Rev. C **65** (2002) 011901; C. Nonaka and S. A. Bass, Phys. Rev. C **75** (2007) 014902.

[7] P. Romatschke and U. Romatschke, Phys. Rev. Lett. **99** (2007) 172301; K. Dusling and D. Teaney, Phys. Rev. C **77** (2008) 034905; H. Song and U. W. Heinz, Phys. Lett. B **658** (2008) 279; D. Molnar and P. Huovinen, J. Phys. G **35** (2008) 104125.

[8] M. Luzum and P. Romatschke, Phys. Rev. C **78** (2008) 034915 [Erratum-ibid. C **79** (2009) 039903].

[9] M. Shimomura [PHENIX Collaboration], Nucl. Phys. A **774** (2006) 457.

[10] J. Adams *et al.* [STAR Collaboration], Phys. Rev. Lett. **97** (2006) 162301.

[11] S. A. Bass, C. Gale, A. Majumder, C. Nonaka, G. Y. Qin, T. Renk and J. Ruppert, Phys. Rev. C **79** (2009) 024901.

[12] T. Sjostrand, Comput. Phys. Commun. **82** (1994) 74.

[13] G. Corcella *et al.*, JHEP **0101** (2001) 010.

[14] K. Zapp, G. Ingelman, J. Rathsman, J. Stachel and U. A. Wiedemann, Eur. Phys. J. C **60** (2009) 617; T. Renk, Phys. Rev. C **78** (2008) 034908; T. Renk, Phys. Rev. C **79** (2009) 054906; N. Armesto, L. Cunqueiro and C. A. Salgado, Eur. Phys. J. C **61** (2009) 775.

[15] T. Renk, Phys. Rev. C **80** (2009) 044904.

[16] M. J. Horner [STAR Collaboration], J. Phys. G **34** (2007) S995.

[17] B. Betz, J. Noronha, G. Torrieri, M. Gyulassy, I. Mishustin and D. H. Rischke, Phys. Rev. C **79** (2009) 034902;R. B. Neufeld and B. Muller, Phys. Rev. Lett. **103** (2009) 042301.

[18] T. Renk and J. Ruppert, Phys. Rev. C **73** (2006) 011901; T. Renk and J. Ruppert, Phys. Lett. B **646** (2007) 19.

[19] T. Renk and J. Ruppert, Phys. Rev. C **76** (2007) 014908.

[20] `http://qm09.phys.utk.edu/indico/conferenceOtherViews.py?confId=1`

[21] B. B. Back *et al.* [PHOBOS Collaboration], Phys. Rev. Lett. **94** (2005) 122303.

Discussion

Poonam Mehta (Raman Research Institute): Hanbury-Brown-Twiss (HBT) interferometry was mentioned in the beginning of the talk. How this effect is relevant in the context of heavy ion collisions. Please elaborate a bit on this.

Answer: HBT interferometry in the context of heavy-ion collisions utilizes two-particle quantum correlations between identical particles (usually pions and hence Bose-Einstein correlations, but HBT correlation measurements have also been done for protons or photons). For any given particle pair in the final state of the collision, total pair momentum and relative pair momentum are measured and the correlation function is determined as a function of relative momentum. This correlation can be inverted by a Fourier transformation to provide information on the spatial structure of the emission source. In particular, one finds, as a function of total momentum, the typical size scales of regions from which correlated emission occurs. This allows to make conclusions with regard to the geometry of the system and flow gradients in the system at the moment of the last interaction of particles.

Less technically, HBT interferometry provides a snapshot of the system created in a heavy-ion collision just at the moment of decoupling, i.e. before the hadrons cease to interact and freely move towards the detector. As such, it provides constraints for medium evolution models such as relativistic fluid dynamics which have to reproduce this final state as the endpoint of the medium evolution.

Bennie Ward (Baylor University):

In the talk you did not mention whether you are dealing with a hadron gas or a quark-gluon plasma? Is there no hadron gas model that explains the current data?

Answer: There is a broad consensus in the community of heavy-ion theory that we're indeed observing the production of a quark-gluon plasma and not with a hadron gas. This is based on a number of observations:

a) Measured hadron ratios indicate a high degree of equilibration in the system, in particular strangeness is substantially enhanced in A-A collision as compared to p-p collisions, consistent with the idea of thermal excitation of strange quarks, but not consistent with known hadronic strangeness production mechanisms. The measured transverse momentum spectra and in particular the elliptic flow indicate a system with a high degree of collectivity in which pressure is well defined. Thus, it can be inferred that we observe a system in thermal equilibrium for which a temperature can be defined.

b) Measurements of thermal photons and dileptons reveal that the initial temperature of the produced system is substantially above 200 MeV. This is not consistent with hadron gas models (which would reach a Hagedorn temperature of about 170 MeV). At the same time, dilepton invariant mass spectra show a structureless electromagnetic correlator, i.e. the resonance structure which characterizes this correlator in a hadronic system, i.e. chiefly the rho, the omega and the phi is absent. The correlator is instead compatible with a qqbar continuum coupling to the photon.

c) A scaling of the flow parameter v_2 with the quark number of the hadronic state is observed. This explicitly points to the presence of partonic, rather than hadronic, degrees of freedom in the system.

d) The suppression of high P_T processes in A-A collisions as compared to the scaled expectation from p-p collision indicates a substantial density of the system. At such a density, the concept of a hadron gas would be ill-defined as individual hadrons would substantially overlap. No hadronic model has so far been able to explain the suppression of high P_T probes.

In summary, there is good evidence for a system with the properties suggested for a quark-gluon plasma, whereas on the other hand no hadronic model has so far succeeded in describing all the observables outlined above.

Vali Huseynov (Nakhchivan State University):

At the beginning of your presentation you have mentioned about a hot dense medium. One of the characteristics of the medium is a chemical potential. At very high densities a chemical potential can be in order of the nuclear temperature (10^11 K). For example, it is possible in the neutron star medium (e.g. in magnetars). May be for the LHC experiments it does not take any importance. Do you take into account a chemical potential in your investigations?

Answer: The relativistic fluid-dynamical models used to describe the evolution of the bulk medium explicitly conserve the baryon number current, so the effect of finite baryon number is taken into account. It has to be stated though that the net baryon number, i.e. baryons minus antibaryons, is expected to be small at LHC - due to the high collision energy most baryons in the system come from pair production and are not baryons from the initial state, i.e. the baryochemical potential at LHC at midrapidity is expected to be extremely low.

Ahmed Ali (DESY):

If I understood correctly, the entire program of physics at RHIC abd heavy ion collisions at the LHC, one is studying experimentally the physics of the QCD lagrangian. The question is the potential of heavy ion collisions in discovering physics beyond the standard model. Could the coherent multigluon states (or other such collective systems) play a role in uncovering new phenomena which we can not study using, for example, the pp collisions?

Answer: The main problem with this idea is that collectivity in QCD is in essence new physics - there is no first principles calculation which would be able to predict even the growth in average particle multiplicity reliably and accurately. For any new physics process embedded in a heavy-ion event, it is thus extremely difficult to define the background. In addition, any particular new physics final state is embedded into a high multiplicity event, and this makes the identification of any rare channel very challenging.

In principle, one might think of coherent multigluon states as a situation which may allow for the observation of new physics in A-A collisions but not in p-p collisions -

but again, this requires that the QCD part is sufficiently understood. At present, it does not seem as if A-A collisions would have any advantage over p-p collisions in new physics searches - this may change once collectivity in QCD is better understood.

Thomas Peitzmann (Utrecht University):

Heavy-ion reactions can serve as a laboratory for many more physics questions beyond quark-gluon plasma studies. The strong fields created in these collisions could create a number of non-trivial effects not accessible in pp. One example is the search for local strong parity violation, which could arise from changes in topological charge. In this case, heavy-ion collisions have the additional advantage of a well-defined direction established from elliptic flow, which can be used to define a sensitive variable involving charge separation. In fact, preliminary results on this from the STAR experiment have been presented at the last Quark Matter conference and are qualitatively consistent with the predicted parity violation.

New physics: theoretical developments

Christophe Grojean

CERN, Physics Department, Theory Unit, CH–1211 Geneve 23, Switzerland
Institut de Physique Théorique, CEA–Saclay, F–91191 Gif–sur–Yvette Cedex, France

Electroweak interactions need three Nambu–Goldstone bosons to provide a mass to the $W^\pm$ and the Z gauge bosons but they also need an ultra-violet (UV) moderator or new physics to unitarize the gauge boson scattering amplitudes. I will present various recent models of physics at the Fermi scale, elaborate on the idea that the Higgs boson can be a composite bound state emerging from a strongly interacting sector, and argue that such composite Higgs scenarios offer a continuous interpolation between the Standard Model and models like technicolor.

1 The Standard Model and the mass problem

The strong, weak and electromagnetic interactions of elementary particles are described by gauge interactions based on a symmetry group $SU(3)_c \times SU(2)_L \times U(1)_Y$. Gauge theory is not only a way to classify particles and assign quantum numbers to them but it is also a dynamical principle that predicts particular couplings among particles. And the structure of these interactions has been well tested at LEP, for instance in the process $e^+e^- \to W^+W^-$. While this is certainly true at least for the 3-point functions, namely the interactions involving at least three particles, the gauge structure is actually badly violated at the level of the 2-point functions, namely in the mass spectrum: the observed mass terms for the leptons and the gauge bosons are not gauge invariant since the gauge group is chiral and also acts non-linearly on the gauge fields. This apparent clash calls for a spontaneous breaking of the gauge symmetry.

In the broken phase, a (massive) spin one particle describes three different polarizations: two transverse ones plus an extra longitudinal one which decouples in the massless limit. In the Standard Model (SM), the longitudinal degrees of freedom associated to the $W^\pm$ and Z^0 gauge bosons correspond presumably to the eaten Nambu–Goldstone bosons [1, 2] resulting from the breaking of the global chiral symmetry $SU(2)_L \times SU(2)_R / SU(2)_V$. This picture still leaves us with the question of the source of the Nambu-Goldstone bosons: What is the sector responsible for the breaking $SU(2)_L \times SU(2)_R \to SU(2)_V$? What is the dynamics of this sector? What are its interactions with the SM particles? The common lore [3, 4] is that these extra degrees of freedom are part of a fundamental scalar field transforming as a weak doublet. This Higgs doublet corresponds to 4 real scalar fields: the 3 eaten Nambu–Goldstone bosons and one physical real scalar degree of freedom, the notorious Higgs boson. While this picture is in very good agreement with Electroweak (EW) data [5, 6, 7] (for a review on the Higgs boson phenomenology, see Ref. [8]), the very fact that its unique prediction, namely the existence of the Higgs boson, has not been verified experimentally yet leaves open the possibility for other origins of the Nambu–Goldstone bosons: e.g., condensates of techniquarks, components of some

gauge fields along an extra dimension ... (see Refs. [9, 10] for recent reviews.)

2 The Higgs boson: a simple picture that calls for new physics

The Higgs mechanism is at best a description, but certainly not an explanation, of electroweak symmetry breaking (EWSB) since there is no dynamics that would explain the instability of the Higgs potential at the origin. Moreover, it also jeopardizes our current understanding of the SM at the quantum level since the Higgs potential suffers from two sources of radiative instabilities: (i) the mass term is quadratically divergent while (ii) the quartic Higgs-self interactions could easily be driven to a Landau pole or to a rolling vacuum at very large value of the Higgs field if the Higgs mass does not lie in the window around 130 and 170 GeV. New physics is required to solve these "naturalness" [11, 12, 13], "triviality" [14, 15] and "(meta)stability" [16, 17] problems. In particular the naturalness problem, also known as gauge hierarchy problem, has been the main source of inspiration/excuse for theoretical speculations on the structure of new physics above the weak scale. In the presence of generic new physics, the Higgs mass becomes UV sensitive unless a symmetry prevents it, in which radiative corrections will generate a contribution that is screened by this symmetry breaking scale and not by the UV scale of new physics. Such a symmetry should act non-linearly on the Higgs field and examples include (i) supersymmetry (SUSY), (ii) global symmetry when the Higgs appears as a pseudo Nambu–Goldtsone bosons, (iii) gauge symmetry when the Higgs appears as a component of the gauge field along an extra spatial dimension [18, 19] (see Refs. [20, 21] for modern realizations of this idea in the context of branes and orbifold symmetry breaking and see Ref. [22] for a recent review), ...

There are of course additional arguments for the existence of new physics beyond the SM: (i) at the level of $2 \div 3$ standard deviations, there are a few discrepancies between EW data and the SM predictions for quantities like $g_\mu - 2$ or the left-right asymmetries in the hadronic and leptonic sectors; (ii) the neutrino masses can be generated only if new states are added to the SM or if a new scale is introduced; (iii) the SM does not provide any dynamics to generate the observed matter-antimatter asymmetry; (iv) no SM particle can account for the dark matter (DM) relic abundance; (v) with may be the exception of the Higgs boson itself [23], no SM particle can drive inflation; (vi) there is no rationale for the pattern of fermion masses and mixing angles; (vii) the strong CP problem remains unexplained; (viii) the charge quantization most likely requires an embedding of the SM gauge group into a bigger symmetry which would unify all the fundamental interactions; (ix) gravity is left aside.

3 Elementary vs. composite Higgs boson. Strong vs. weak EWSB

What is unitarizing the WW scattering amplitude? Supersymmetric models, Little Higgs models and many other models take for granted that the Higgs boson provides the answer to this pressing question of the origin of EWSB. I said earlier that the masses of the $W^\pm$ and Z gauge bosons break the gauge symmetry. Actually, in the presence of these masses, the gauge symmetry is realized non-linearly: the longitudinal $W_L^\pm, Z_L$ can be described by the Nambu–Goldstone bosons, or pions, associated to the coset $SU(2)_L \times SU(2)_R/SU(2)_{\text{isospin}}$ and

the gauge boson mass terms correspond to the pions kinetic term (σ^a, $a = 1, 2, 3$, are the usual Pauli matrices):

$$\mathcal{L}_{\mathrm{mass}} = \frac{v^2}{4}\mathrm{Tr}\left(D_\mu\Sigma^\dagger D^\mu\Sigma\right) \quad \text{with} \ \Sigma = e^{i\sigma^a\pi^a/v}. \tag{1}$$

Thanks to this Goldstone boson equivalence [25], the non-trivial scattering of the longitudinal W's (W generically denotes $W^\pm$ as well as Z) now simply follows for the contact interactions among four pions obtained by expanding the Lagrangian (1) and leads to amplitudes that grow with the energy:

$$\mathcal{A}(W_L^a W_L^b \to W_L^c W_L^d) = \mathcal{A}(s)\delta^{ab}\delta^{cd} + \mathcal{A}(t)\delta^{ac}\delta^{bd} + \mathcal{A}(u)\delta^{ad}\delta^{bc} \quad \text{with} \ \mathcal{A}(s) \approx \frac{s}{v^2}. \tag{2}$$

In the absence of any new weakly coupled elementary degrees of freedom canceling this growth, perturbative unitarity will be lost around[1] 1.2 TeV and new strong dynamics will kick in and soften the UV behavior of the amplitude, for instance via the exchange of massive bound states similar to the ρ meson of QCD. In any circumstances, by measuring the $W^\pm$ and Z masses, we have been guaranteed to find new physics around the Fermi scale to ensure the proper decoupling of the longitudinal polarizations at very high energy.

The simplest example of new dynamics that can restore perturbative unitarity consists of a single scalar field, h, singlet under $SU(2)_L \times SU(2)_R/SU(2)_V$ and coupled to the longitudinal W's as [26]:

$$\mathcal{L}_{\mathrm{EWSB}} = \frac{1}{2}\partial_\mu h\partial^\mu h - V(h) + \frac{v^2}{4}\mathrm{Tr}\left(D_\mu\Sigma^\dagger D^\mu\Sigma\right) \times \left(1 + 2a\frac{h}{v} + b\frac{h^2}{v^2}\right). \tag{3}$$

Via its linear coupling, a, to the W_L's, the scalar gives an additional contribution to the WW scattering amplitude

$$\mathcal{A}_{\mathrm{scalar \ exchange}}(s) = -\frac{a^2\,s^2}{v^2(s - m_h^2)}, \tag{4}$$

which, for $a = 1$, cancels the leading contact term at high energy. This is not the end of the story yet: perturbative unitarity should be maintained in inelastic channels too, like $W_L W_L \to hh$. Both the linear and quadratic couplings, a and b, contribute to this amplitude and the terms growing with the energy are canceled for the particular choice $b = a^2$. The point $a = b = 1$ defines the SM Higgs boson and it can be shown that the scalar resonance and the pions then combine together to form a doublet transforming *linearly* under $SU(2)_L \times SU(2)_R$.

The Lagrangian (3) describes either an elementary or a composite Higgs boson. As soon as the couplings deviate from $a = b = 1$, the Higgs exchange alone will fail to fully unitarize the WW scattering amplitude irrespectively whether or not the effective Lagrangian (3) emerges from a perturbative theory (see for instance Refs. [?, 27]) or from a strongly interacting dynamics. Therefore and contrary to a general belief, the question of strong vs weak dynamics at the origin of the EWSB is decoupled from the question of the existence of a light and narrow Higgs-like scalar. In composite Higgs models, the deviations from $a = b = 1$ are controlled (see Section 4) by the ratio of the weak scale over the Higgs compositeness scale, f, which can be rather low (a few hundreds of GeV), and strong WW scattering above the Higgs mass is therefore expected.

---

[1]Defining the breakdown of perturbativity is subject to arbitrary choices: the 1.2 TeV($= 2\sqrt{2\pi}v$) number follows from requiring that the real part of the partial waves of the iso-amplitudes remains smaller than $\frac{1}{2}$, while demanding that the tree-level amplitude remains bigger than the one-loop one leads to the more conventional scale, $4\pi v(\approx 3.1$ TeV$)$, associated to a non-linear σ-model with a breaking scale v.

4 (Pseudo Nambu–Goldstone) composite Higgs models

Notwithstanding its simplicity, the appeal of the SM Higgs picture comes from its successful agreement with EW precision data, provided that the Higgs boson is rather light. In this regard, being an elementary scalar is not a virtue but rather a flaw because of the quadratic divergence destabilizing the Higgs mass. It is thus tantalizing to consider the Higgs boson as a composite bound state emerging from a strongly-interacting sector. In order to maintain a good agreement with EW data, it is sufficient that a mass gap separates the Higgs resonance from the other resonances of strong sector (the resonances that will ultimately enforce a good behavior of the WW scattering amplitudes). Such a mass gap can naturally follow from dynamics if the strongly-interacting sector possesses a global symmetry, G, spontaneously broken at a scale f to a subgroup H, such that the coset G/H contains a fourth Nambu–Goldstone bosons that can be identified with the Higgs boson. Simple examples of such coset are $SU(3)/SU(2)$ or $SO(5)/SO(4)$, the latter being favored since it is invariant under the custodial symmetry (some non-minimal models with extra Nambu–Goldstone bosons have also been constructed [28]). Attempts to construct composite Higgs models in 4D have been made by Georgi and Kaplan (see for instance Ref. [29]) and modern incarnations have been recently investigated in the framework of 5D warped models where, according to the principles of the AdS/CFT correspondence, the holographic composite Higgs boson now originates from a component of a gauge field along the 5th dimension with appropriate boundary conditions[2].

The composite Higgs models offer a nice and continuous interpolation between the SM and technicolor type models. The dynamical scale f defines the compositeness scale of the Higgs boson: when $\xi = v^2/f^2 \to 0$, the Higgs boson appears essentially as a light elementary particle (and its couplings approach the ones predicted by the SM) while the other resonances of the strong sector become heavier and heavier and decouple; on the other hand, when $\xi \to 1$, the couplings of the Higgs boson to the W_L's go to zero and unitarity in gauge boson scattering is ensured by the exchange of the heavy resonances.

At the eve of the LHC operation, I would like to give a description of the physics of such a composite Higgs boson rather than presenting the details of the construction of an explicit model. In the same way that we do not need the refinements of QCD to describe the physics of the pions, I will rely on an effective Lagrangian to capture the relevant physics. This effective Lagrangian involves higher dimensional operators for the low energy degrees of freedom (the SM particles and a unique Higgs boson in the minimal case) and the strong sector will be broadly parametrized by two quantities: the typical mass scale, m_ρ, of the heavy resonances and the dynamical scale, f, associated to the coset G/H (for maximally strongly coupled sectors, we expect $m_\rho \approx 4\pi f$; here, I will simply assume that m_ρ is parametrically larger than f). There are two classes of higher dimensional operators: (i) those that are genuinely sensitive to the new strong force and will affect qualitatively the physics of the Higgs boson and (ii) those that are sensitive to the spectrum of the resonances only and will simply act as form factors. Simple rules control the size of these different operators, see Ref. [33], and the effective Lagrangian generically takes the form (g, g' are the SM EW gauge couplings, λ is the SM Higgs quartic

---

[2]A Higgs localized on the IR brane of a warped model, like in the original models of Randall–Sundrum [30], would also correspond to a 4D composite Higgs boson in the dual interpretation [31, 32]. However, this composite Higgs state would not be a pseudo Nambu–Goldstone boson and there is no reason why it would be lighter than the other resonances of the strong sector (in other words, the original Randall–Sundrum models solve the gauge hierarchy problem but they do not address the little hierarchy problem. Hence the need to rely on the A_5 degree of freedom.

coupling and y_f is the SM Yukawa coupling to the fermions $f_{L,R}$)[3]:

$$\mathcal{L}_{\text{SILH}} = \frac{c_H}{2f^2} \left(\partial_\mu \left(H^\dagger H\right)\right)^2 + \frac{c_T}{2f^2} \left(H^\dagger \overleftrightarrow{D}_\mu H\right)^2 - \frac{c_6 \lambda}{f^2} \left(H^\dagger H\right)^3 + \left(\frac{c_y y_f}{f^2} H^\dagger H \bar{f}_L H f_R + \text{h.c.}\right)$$

$$+ \frac{ic_W g}{2m_\rho^2} \left(H^\dagger \sigma^i \overleftrightarrow{D^\mu} H\right) (D^\nu W_{\mu\nu})^i + \frac{ic_B g'}{2m_\rho^2} \left(H^\dagger \overleftrightarrow{D^\mu} H\right) (\partial^\nu B_{\mu\nu}) + \dots \tag{5}$$

All the coefficients, $c_H, c_T \dots$, appearing in Eq. (5) are expected to be of order one.

Some oblique corrections are generated, at tree-level, by the operators of this effective Lagrangian: (i) the operator c_T gives a contribution to the T Peskin–Takeuchi parameter, $\hat{T} = c_T v^2/f^2$, which would impose a very large compositeness scale; however, assuming that the custodial symmetry is preserved by the strong sector, the coefficient of this operator is vanishing automatically; (ii) a contribution to the S parameter is generated by the form factor operators only, $\hat{S} = (c_W + c_B) m_W^2/m_\rho^2$, and will simply impose a lower bound on the mass of the heavy resonances, $m_\rho \geq 2.5$ TeV. At the loop level, the situation is getting a bit more complicated: as I am going to show below, the couplings of the Higgs to the SM vectors receive some corrections of the order v^2/f^2, and these corrections prevent the nice cancelation occurring in the SM between the Higgs and the gauge boson contributions and S and T are logarithmically divergent [34] (the divergence in T will eventually be screened by resonance states if the strong sector is invariant under the custodial symmetry). Typically, this one-loop IR contribution imposes [35, 36] $f^2/v^2 \geq 3 \div 4$ (see Refs. [37, 38, 39, 40] for careful discussions of electroweak precision tests in composite models built in 5D). Overall, $\xi = v^2/f^2$ is a good estimate of the amount of fine-tuning of these models [41].

One may worry that because of the modified Yukawa interactions induced by the operator c_y, the mass matrices and the Yukawa interaction matrices are not simultaneously diagonalizable, leading to potentially dangerous flavor changing neutral currents (FCNC). Actually, the coefficient c_y is flavor universal (at least among the light fermions) and the flavor structure of the higher dimensional Yukawa interactions are proportional to the SM Yukawa interactions. In other words, the effective Lagrangian (5) satisfies the minimal flavor violation hypothesis [42]. And therefore no Higgs-mediated FCNC is generated at the leading level (see however Refs. [43, 44] for a detailed discussion on this subject). Besides the Higgs boson, the other resonances of the strong sector can generate too large flavor violating amplitude. The extra dimensional realizations of the composite Higgs models provide some clues on this issue. In these setups, the hierarchy among the fermion masses and mixing angles is the result of flavor dependent wavefunctions [45, 46] (the dual interpretation is that the light fermions are only *partially* composite [47]). At the same time, a built-in RS–GIM mechanism [48, 49] highly suppress the FCNC processes and the KK scale, equivalent to m_ρ, can be lowered to 20 TeV [50] or even to 5÷6 TeV [51] (to be compared to the generic $10^{4 \div 5}$ TeV scale in the absence of any suppression), the stringent constraint actually coming for CP violation in the kaon sector [52].

The effective Lagrangian (5) does induce some corrections to the Higgs couplings to the SM particles. In particular, the operator c_H gives a correction to the Higgs kinetic term which can be brought back to its canonical form at the price of a proper rescaling of the Higgs field

---

[3]This effective Lagrangian captures the physics of a Higgs boson identified as pseudo Nambu–Goldstone boson emerging from a *strongly* interacting sector. The scaling of the operators will be different in perturbative theories. For instance, in Little Higgs models with a product group gauge symmetry, there will be sizable corrections to the non-linear σ-model structure when none of the gauge couplings is strong. The Higgs potential, in the case of a strongly interacting light Higgs (SILH), is also fully saturated by quantum effects, i.e., generated radiatively, while in Little Higgs models, the quartic interactions can be larger [33].
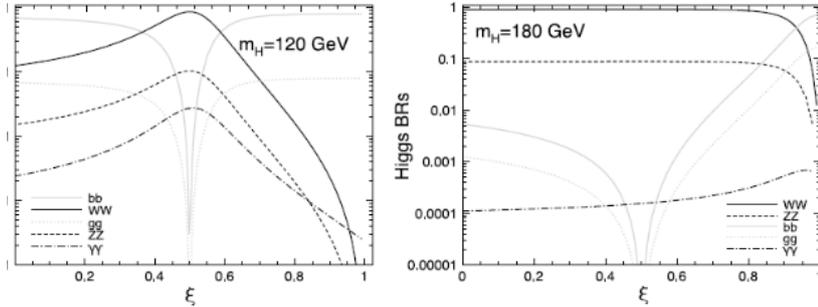
Figure 1: Higgs decay branching ratios as a function of $\xi = v^2/f^2$ for SM fermions embedded into fundamental representations of $SO(5)$ for two benchmark Higgs masses: $m_h = 120$ GeV (left plot) and $m_h = 180$ GeV (right plot). For $\xi = 0.5$, the Higgs is fermiophobic, while in the technicolor limit, $\xi \to 1$, the Higgs becomes gaugephobic. From Ref. [26].

inducing an universal shift of the Higgs couplings by a factor $1 - c_H\, v^2/(2f^2)$. For the fermions, this universal shift adds up to the modification of the Yukawa interactions:

$$g_{hf\bar{f}}^{\xi} = g_{hf\bar{f}}^{\text{SM}} \times (1 - (c_y + c_H/2)v^2/f^2),\tag{6}$$

$$g_{hWW}^{\xi} = g_{hWW}^{\text{SM}} \times (1 - c_H\, v^2/(2f^2)).\tag{7}$$

All the dominant corrections, i.e. the ones controlled by the strong operators, preserve the Lorentz structure of the SM interactions, while the form factor operators will also introduce couplings with a different Lorentz structure.

The effective Lagrangian (5) should be viewed as the first terms in an expansion in $\xi = v^2/f^2$. When departing significantly from the SM limit, $v^2/f^2 \sim \mathcal{O}(1)$, the series has to be resummed. Explicit models, like the ones constructed in 5D warped space [53], provide examples of such a resummation, allowing to study the effects of the anomalous Higgs couplings up to the technicolor limit. Figure 1 shows the modification in the branching ratios for the Higgs decays to SM particles in the minimal composite Higgs model with fermions embedded into fundamental representations of $SO(5)$.

The Higgs anomalous couplings affect the decay rates as well as the production cross sections of the Higgs [33, 54, 55]. Therefore, the searches for the Higgs boson at the LHC, as well as the LEP/Tevatron exclusion bounds are modified as compared to the SM case (see Ref. [56] and Answers to questions).

Will the LHC be able to probe these deviations in the couplings[4] of the Higgs? The contribution of the operator c_H is universal for all Higgs couplings and therefore it does not affect

---

[4]The physics of the composite models, as captured by the effective Lagrangian (5), selects the operators c_H and c_y as the most important ones for LHC studies, as opposed to totally model-independent operator analyses [57, 58] which often lead to the conclusion that the dominant effects should appear in the vertices $h\gamma\gamma$ and hgg, since their SM contribution occurs only at loop level.

the Higgs branching ratios, but only the total decay width and the production cross section. The measure of the Higgs decay width at the LHC is very difficult and it can be reasonably done only for rather heavy Higgs bosons, well above the two gauge boson threshold, a region which is not of particular interest since we consider the Higgs as a pseudo-Goldstone boson, and therefore relatively light. However, for a light Higgs, LHC experiments can measure the product $\sigma_h \times BR_h$ in many different channels: production through gluon, gauge-boson fusion, and top-strahlung; decay into b, τ, γ and (virtual) weak gauge bosons. At the LHC with about 300 fb^{-1}, it is possible to measure Higgs production rate times branching ratio in the various channels with 20–40 % precision [59, 60]. For c_H and c_y of order one, this will translate into a sensitivity on the compositeness scale of the Higgs, $4\pi f$, up to $5 \div 7$ TeV.

Deviations from the SM predictions of Higgs production and decay rates could be a hint towards models with strong dynamics, especially if no new light particles are discovered at the LHC. However, they do not unambiguously imply the existence of a new strong interaction. The most characteristic signals of a composite Higgs model have to be found in the very high-energy regime. Indeed, as already announced in Section 3, a peculiarity of a composite Higgs boson is that it fails to fully unitarize the $W_L W_L$ scattering amplitudes which have thus a residual growth with energy and the corresponding interaction becomes strong, eventually violating tree-level unitarity at the cutoff scale. Indeed, the extra contribution to the Higgs kinetic term from the c_H operator prevents Higgs exchange diagrams from accomplishing the exact cancellation, present in the SM, of the terms growing with energy in the amplitudes. Therefore, although the Higgs is light, we obtain strong WW scattering at high energies.

From the operator c_H, using the Goldstone equivalence theorem, it is easy to derive the following high-energy limit of the scattering amplitudes for longitudinal gauge bosons

$$\mathcal{A}(W_L^a W_L^b \to W_L^c W_L^d) = \mathcal{A}(s)\delta^{ab}\delta^{cd} + \mathcal{A}(t)\delta^{ac}\delta^{bd} + \mathcal{A}(u)\delta^{ad}\delta^{bc} \quad \text{with} \quad \mathcal{A}(s) \approx \frac{s}{f^2}. \quad (8)$$

The growth with energy of the amplitudes is strictly valid only up to the maximum energy of our effective theory, namely m_ρ. The behaviour above m_ρ depends on the specific model realization. In 5D models, the growth of the elastic amplitude is softened by Kaluza–Klein modes exchange [61], but the inelastic channels dominate and strong coupling is reached at a scale $\sim 4\pi f$. Notice that the amplitudes (8) are exactly proportional to the scattering amplitudes obtained in a Higgsless SM, the growth being controlled by the strong coupling scale, f, and not the weak scale itself, v.

Will the LHC be able to measure the growth of these scattering amplitudes? Contrary to a naive belief, it is a notoriously difficult measurement which requires some large integrated luminosity [62]. The most promising channels correspond to purely leptonic decays of the W's, though semileptonic decay channels have also been considered recently [63, 64]. The rapid falloff of the W luminosity inside the proton and the numerous SM backgrounds that can fake the signal certainly make the measurement harder, but, as a matter of fact, already at the partonic level, the onset of the strong scattering is delayed to higher energies due to a large pollution from the scattering of the transverse polarizations [26].

In composite Higgs models, another direct probe of the strong dynamics at the origin of EWSB is the cross section for the double Higgs production. Indeed, the Higgs boson appears as a pseudo Nambu–Goldstone boson and its properties are directly related to those of the other exact (eaten) Goldstones, corresponding to the longitudinal W, Z gauge bosons. Thus, a generic prediction is that the strong gauge boson scattering is accompanied by strong production of Higgs pairs. The amplitudes for double Higgs production grow with the center-of-mass energy

as

$$\mathcal{A}\left(Z_L^0 Z_L^0 \to hh\right) = \mathcal{A}\left(W_L^+ W_L^- \to hh\right) = \frac{c_H s}{f^2}. \tag{9}$$

Therefore a significant enhancement over the (negligible) SM rate for the production of two Higgs bosons at high p_T, along with two forward jets associated with the two primary partons that radiated the $W_L W_L$ pair, is expected. An explorative analysis [26] has shown that the best channel for discovery involves 3 leptons in the final states, with both Higgs bosons decaying to W^+W^-: $pp \to hhjj \to 4Wjj \to l^+l^-l^\pm \not{E}_T 4j$. The final states are undeniably more complicated than in the analyses of gauge boson scattering and come with smaller branching ratios, but at least the double Higgs production does not suffer from pollution from the transverse modes and it is the only process that gives access to the quadratic coupling b of the Lagrangian (3) and allows to test its relation to the linear coupling, a, as predicted by the structure of the higher dimension operators (5): $a = 1 - c_H v^2/(2f^2), b = 1 - 2c_H v^2/f^2$. A Monte-Carlo simulation with simple kinematic cuts concludes [26] that the signal significance at the LHC operating at $\sqrt{s} = 14$ TeV with 300 fb^{-1} will be limited to about 2.5 standard deviations for $v^2/f^2 = 0.8$. With an upgrade of the LHC luminosity (sLHC program), a 5σ discovery can be reached with less than 1 ab^{-1} of integrated luminosity.

While the effective Lagrangian 5 elegantly captures the LHC physics of composite Higgs models up to a scale of the order of 10 TeV, explicit holographic models constructed in 5D warped space provide a valid description in the far UV up to the energies close to the Planck scale and give a new and interesting twist to the question of gauge coupling unification. Not only the running of the gauge couplings receives a contribution from all the resonances of the strong sector (the KK states in the 5D picture) but it also loses the contribution of the Higgs (and the top) above the weak scale. And an appealing unification seems to follow from this minimal set-up with a degree of accuracy comparable to the one reached in the MSSM [65].

While my presentation has been focussed on the gauge sector, the fermionic sector of composite Higgs models, in particular in the top sector, provides also very interesting signatures easily accessible at the first stages of the LHC operation [35, 39, 66, 67, 68, 69, 70, 71]. In particular the same-sign dilepton final states offer a sensitive probe to the top partners [67, 71] with a discovery potential up to 500 GeV (resp. 1 TeV) with about 50 pb^{-1} (resp. 15 fb^{-1}).

In conclusion, in the plausible situation that the LHC sees a Higgs boson and no other direct evidence of new physics, it will not be immediate to determine the true nature of this Higgs boson and tell for sure if it is an elementary particle or a composite bound state emerging from a strongly interacting sector. In that situation, a physics case for a linear collider [72] together with the sLHC [73] can be easily made.

5 5D Higgsless models

In composite models, when the compositeness scale gets close to the weak scale, the Higgs boson effectively decouples. This Higgsless limit is easily reached in 5D dimensional setups and offers a new point of view on the mass problem. In a sense, the EWSB itself is achieved via boundary conditions (rather than by a Higgs vacuum expectation value). According to the Einstein's relation between the mass and the momentum ($\vec{p}_3$ denotes the momentum along the usual 3 spatial dimension and $p_\perp$ is the momentum along the extra dimension):

$$m^2 = E^2 - \vec{p}_3^2 - p_\perp^2, \tag{10}$$

a transverse momentum, $p_\perp$, simply appears as a mass from the 4D point of view. And the mass problem reduces to a problem of quantum mechanics in a box: suitable boundary conditions will generate a transverse momentum for the appropriate particles. Nonetheless, an immediate question arises: is it better to generate a transverse momentum than to introduce by hand a symmetry breaking mass for the gauge field? In other words, how is unitarity restored? In full generality, the elastic scattering amplitude of a massive Kaluza–Klein (KK) gauge field would have terms that grow with the fourth and the second powers of the energy

$$\mathcal{A} = \mathcal{A}^{(4)} \left(\frac{E}{M} \right)^4 + \mathcal{A}^{(2)} \left(\frac{E}{M} \right)^2 + \mathcal{A}^{(0)} + \ldots \tag{11}$$

In the SM, $\mathcal{A}^{(4)}$ is automatically vanishing due to gauge invariance, while $\mathcal{A}^{(2)}$ vanishes via the exchange of the physical Higgs boson. In 5D Higgsless models [74, 75], the unitarization of the WW scattering amplitudes follows from the exchange of all the KK excitations of the W. In order for this unitarization to actually happen, the couplings and the masses of the KK excitations have to obey the following sum rules[5] [74]:

$$g_{WWWW}^2 = g_{WW\gamma}^2 + g_{WWZ}^2 + \sum_n g_{WWZ^{(n)}}^2$$
$$4g_{WWWW}^2 M_W^2 = 3g_{WWZ}^2 M_Z^2 + 3\sum_n g_{WWZ^{(n)}}^2 M_{Z^{(n)}}^2. \tag{12}$$

The effective couplings among the KK states are dictated by the gauge structure of the 5D theory and it is easy to show that the two sum rules are automatically satisfied, provided there is no hard breaking of gauge invariance, i.e., if the 5D gauge fields obey Dirichlet or Neumann boundary conditions at the end points of the 5th dimension.

The most distinctive feature of the Higgsless models is, of course, the absence of a physical scalar state in the spectrum. Yet, *the absence of proof is not the proof of the absence* and some other models exist in which the Higgs is unobservable at the LHC (for a recent review, see for instance Ref. [76]). Fortunately, Higgsless models are characterized by other distinctive features, such as (i) the presence of spin-1 KK resonances with the W, Z quantum numbers, (ii) some slight deviations in the universality of the light fermion couplings to the SM gauge bosons and (iii) some deviations in the gauge boson self-interactions compared with the SM. References [77, 78] studied the production of the lightest KK excitations of the W and the Z via vector boson fusion. The most recent study [79] included also the more model-dependent possibility of Drell–Yan production. At the LHC, about 10 fb^{-1} of luminosity will be necessary for the discovery of the resonances in the 700 GeV mass range. A precise measurement of the couplings of these resonances or the search for some deviations in the SM couplings will require a more precise machine, such as an ILC or CLIC.

6 Conclusion

The SM has emerged as a successful description, at the quantum level, of the interactions among the elementary particles but it is at odds in what concerns the masses of these elementary

---

[5]g_{WWWW}^2 is the quartic W self-coupling, g_{WWX} is the cubic coupling between two W's and X and $Z^{(n)}$ denote the KK excitations of the Z. The two sum rules (12) correspond to the $W^\pm W^\pm \to W^\pm W^\pm$ channel and similar sum rules will apply to other WZ channels.

particles. EW interactions certainly need three Nambu–Goldstone bosons to provide a mass to the $W^{\pm}$ and the Z gauge bosons. But they also need new dynamics to act as a UV moderator and ensure a proper decoupling at high energy of the extra polarizations associated to the mass of these spin-1 fields. After many years of theoretical speculations and in the absence of any direct experimental evidences, it is not yet possible to tell whether the strength of this new dynamics is weak or strong. In many regards, this question is equivalent to asking whether a light Higgs boson exists or not. However it is also possible and plausible that a light and narrow Higgs-like scalar does exist but it is actually a bound state from some strong dynamics not much above the weak scale. Such composite models provide a continuous dynamical deformation of the SM, with the same spectrum as the SM up to 2÷3 TeV.

The LHC is prepared to discover the Higgs boson or whatever replaces it. To this end, the collaboration between experimentalists and theorists is more important than ever to make sure, for instance, that no unexpected physics is missed because of triggers and cuts. In this regards, signature-motivated approaches like 'unparticles' [80], 'hidden valleys' [81] or 'quirks' [82] should be encouraged.

Also, it should not be forgotten that the LHC will be a top(-quark) machine. And there are many reasons to believe that the top quark can be an important agent in the dynamics triggering the electroweak symmetry breaking.

Finally, it is also worth mentioning that most theories for the Fermi scale can be probed outside of colliders. The numerous experiments searching for Dark Matter nicely exemplify the strong cosmo-astro particle connection, and, for sure, if weakly interacting massive particles (WIMPs) are part of the dynamics of EWSB, their direct or indirect detections would provide valuable information. An intriguing signature [83] arises when the WIMPS can annihilate directly into a photon and a Higgs boson, giving rise to a line in the gamma ray spectrum whose position reflects the Higgs mass: the observation of such a line would be the first direct observation of a Higgs production process! The complementarity between astrophysics and collider physics is not restricted to Dark Matter. Another compelling example concerns gravitational waves: a background of stochastic gravitational waves peaked around mHz frequencies would be an indication of a strong EW phase transition due for instance to enhanced Higgs self-couplings [84, 85].

In any case, more than ever, experimental data are eagerly awaited to disentangle what may be the most pressing question faced by particle physics today: How is electroweak symmetry broken?

Acknowledgements

References

[1] Y. Nambu, Phys. Rev. Lett. **4** (1960) 380.

[2] J. Goldstone, Nuovo Cim. **19** (1961) 154.

[3] F. Englert and R. Brout, Phys. Rev. Lett. **13** (1964) 321.

[4] P. W. Higgs, Phys. Rev. Lett. **13** (1964) 508.

[5] R. Barate *et al.* [LEP Working Group for Higgs boson searches], Phys. Lett. B **565** (2003) 61 [arXiv:hep-ex/0306033].

[6] C. Amsler *et al.* [Particle Data Group], Phys. Lett. B **667** (2008) 1.

[7] A. Hoecker, arXiv:0909.0961 [hep-ph].

[8] A. Djouadi, Phys. Rept. **457** (2008) 1 [arXiv:hep-ph/0503172].

[9] C. Grojean, arXiv:0910.4976 [hep-ph].

[10] D. E. Morrissey, T. Plehn and T. M. P. Tait, arXiv:0912.3259 [hep-ph].

[11] V.F. Weisskopf, Phys. Rev. **56**, 72 (1939).

[12] G. 't Hooft, NATO Adv. Study Inst. Ser. B Phys. **59** (1980) 135.

[13] M. J. G. Veltman, Acta Phys. Polon. B **12** (1981) 437.

[14] K. G. Wilson and J. B. Kogut, Phys. Rept. **12** (1974) 75.

[15] M. Luscher and P. Weisz, Nucl. Phys. B **295** (1988) 65.

[16] A. D. Linde, JETP Lett. **23** (1976) 64 [Pisma Zh. Eksp. Teor. Fiz. **23** (1976) 73].

[17] S. Weinberg, Phys. Rev. Lett. **36** (1976) 294.

[18] N. S. Manton, Nucl. Phys. B **158** (1979) 141.

[19] Y. Hosotani, Phys. Lett. B **126** (1983) 309.

[20] I. Antoniadis, K. Benakli and M. Quiros, New J. Phys. **3** (2001) 20 [arXiv:hep-th/0108005].

[21] C. Csaki, C. Grojean and H. Murayama, Phys. Rev. D **67** (2003) 085012 [arXiv:hep-ph/0210133].

[22] M. Serone, arXiv:0909.5619 [hep-ph].

[23] F. L. Bezrukov and M. Shaposhnikov, Phys. Lett. B **659** (2008) 703 [arXiv:0710.3755 [hep-th]].

[24] C. Grojean, Phys. Usp. **50** (2007) 1 [Usp. Fiz. Nauk **177** (2007) 3].

[25] M. S. Chanowitz and M. K. Gaillard, Nucl. Phys. B **261** (1985) 379.

[26] R. Contino, C. Grojean, M. Moretti, F. Piccinini and R. Rattazzi, to appear.

[27] B. Bellazzini, S. Pokorski, V. S. Rychkov and A. Varagnolo, JHEP **0811** (2008) 027 [arXiv:0805.2107 [hep-ph]].

[28] B. Gripaios, A. Pomarol, F. Riva and J. Serra, JHEP **0904** (2009) 070 [arXiv:0902.1483 [hep-ph]].

[29] H. Georgi and D. B. Kaplan, Phys. Lett. B **145** (1984) 216.

[30] L. Randall and R. Sundrum, Phys. Rev. Lett. **83** (1999) 3370 [arXiv:hep-ph/9905221].

[31] N. Arkani-Hamed, M. Porrati and L. Randall, JHEP **0108** (2001) 017 [arXiv:hep-th/0012148].

[32] R. Rattazzi and A. Zaffaroni, JHEP **0104** (2001) 021 [arXiv:hep-th/0012248].

[33] G. F. Giudice, C. Grojean, A. Pomarol and R. Rattazzi, JHEP **0706** (2007) 045 [arXiv:hep-ph/0703164].

[34] R. Barbieri, B. Bellazzini, V. S. Rychkov and A. Varagnolo, Phys. Rev. D **76** (2007) 115008 [arXiv:0706.0432 [hep-ph]].

[35] C. Anastasiou, E. Furlan and J. Santiago, arXiv:0901.2117 [hep-ph].

[36] R. Contino, arXiv:0908.3578 [hep-ph].

[37] K. Agashe and R. Contino, Nucl. Phys. B **742** (2006) 59 [arXiv:hep-ph/0510164].

[38] M. S. Carena, E. Ponton, J. Santiago and C. E. M. Wagner, Phys. Rev. D **76** (2007) 035006 [arXiv:hep-ph/0701055].

[39] M. Gillioz, Phys. Rev. D **80** (2009) 055003 [arXiv:0806.3450 [hep-ph]].

[40] C. Bouchart and G. Moreau, Nucl. Phys. B **810** (2009) 66 [arXiv:0807.4461 [hep-ph]].

[41] R. Contino, L. Da Rold and A. Pomarol, Phys. Rev. D **75** (2007) 055014 [arXiv:hep-ph/0612048].

[42] G. D'Ambrosio, G. F. Giudice, G. Isidori and A. Strumia, Nucl. Phys. B **645** (2002) 155 [arXiv:hep-ph/0207036].

[43] K. Agashe and R. Contino, arXiv:0906.1542 [hep-ph].

[44] A. Azatov, M. Toharia and L. Zhu, Phys. Rev. D **80** (2009) 035016 [arXiv:0906.1990 [hep-ph]].

[45] N. Arkani-Hamed and M. Schmaltz, Phys. Rev. D **61** (2000) 033005 [arXiv:hep-ph/9903417].

[46] Y. Grossman and M. Neubert, Phys. Lett. B **474** (2000) 361 [arXiv:hep-ph/9912408].

[47] D. B. Kaplan, Nucl. Phys. B **365** (1991) 259.

[48] S. J. Huber, Nucl. Phys. B **666** (2003) 269 [arXiv:hep-ph/0303183].

[49] K. Agashe, G. Perez and A. Soni, Phys. Rev. Lett. **93** (2004) 201804 [arXiv:hep-ph/0406101].

[50] C. Csaki, A. Falkowski and A. Weiler, JHEP **0809** (2008) 008 [arXiv:0804.1954 [hep-ph]].

[51] K. Agashe, A. Azatov and L. Zhu, Phys. Rev. D **79** (2009) 056006 [arXiv:0810.1016 [hep-ph]].

[52] A. J. Buras, these conference proceedings, arXiv:0910.1032 [hep-ph].

[53] K. Agashe, R. Contino and A. Pomarol, Nucl. Phys. B **719** (2005) 165 [arXiv:hep-ph/0412089].

[54] A. Djouadi and G. Moreau, Phys. Lett. B **660** (2008) 67 [arXiv:0707.3800 [hep-ph]].

[55] A. Falkowski, Phys. Rev. D **77** (2008) 055018 [arXiv:0711.0828 [hep-ph]].

[56] J.R. Espinosa, C. Grojean and M. Muehlleitner, to appear.

[57] A. V. Manohar and M. B. Wise, Phys. Lett. B **636** (2006) 107 [arXiv:hep-ph/0601212].

[58] A. Pierce, J. Thaler and L. T. Wang, JHEP **0705** (2007) 070 [arXiv:hep-ph/0609049].

[59] M. Duhrssen, ATL–PHYS–2003–030.

[60] M. Duhrssen, S. Heinemeyer, H. Logan, D. Rainwater, G. Weiglein and D. Zeppenfeld, Phys. Rev. D **70** (2004) 113009 [arXiv:hep-ph/0406323].

[61] A. Falkowski, S. Pokorski and J. P. Roberts, JHEP **0712** (2007) 063 [arXiv:0705.4653 [hep-ph]].

[62] J. Bagger *et al.*, Phys. Rev. D **52** (1995) 3878 [arXiv:hep-ph/9504426].

[63] J. M. Butterworth, B. E. Cox and J. R. Forshaw, Phys. Rev. D **65** (2002) 096014 [arXiv:hep-ph/0201098].

[64] A. Ballestrero, G. Bevilacqua, D. B. Franzosi and E. Maina, arXiv:0909.3838 [hep-ph].

[65] K. Agashe, R. Contino and R. Sundrum, Phys. Rev. Lett. **95**, 171804 (2005) [arXiv:hep-ph/0502222].

[66] M. Carena, A. D. Medina, B. Panes, N. R. Shah and C. E. M. Wagner, Phys. Rev. D **77** (2008) 076003 [arXiv:0712.0095 [hep-ph]].

[67] R. Contino and G. Servant, JHEP **0806** (2008) 026 [arXiv:0801.1679 [hep-ph]].

[68] P. Lodone, JHEP **0812** (2008) 029 [arXiv:0806.1472 [hep-ph]].

[69] A. Pomarol and J. Serra, Phys. Rev. D **78** (2008) 074026 [arXiv:0806.3247 [hep-ph]].

[70] H. de Sandes and R. Rosenfeld, J. Phys. G **36** (2009) 085001 [arXiv:0811.0984 [hep-ph]].

[71] J. Mrazek and A. Wulzer, arXiv:0909.3977 [hep-ph].

[72] G. Aarons *et al.* [ILC Collaboration], arXiv:0709.1893 [hep-ph].

[73] F. Gianotti *et al.*, Eur. Phys. J. C **39** (2005) 293 [arXiv:hep-ph/0204087].

[74] C. Csaki, C. Grojean, H. Murayama, L. Pilo and J. Terning, Phys. Rev. D **69** (2004) 055006 [arXiv:hep-ph/0305237].

[75] C. Csaki, C. Grojean, L. Pilo and J. Terning, Phys. Rev. Lett. **92** (2004) 101802 [arXiv:hep-ph/0308038].

[76] A. De Roeck *et al.*, arXiv:0909.3240 [hep-ph].

[77] A. Birkedal, K. Matchev and M. Perelstein, Phys. Rev. Lett. **94** (2005) 191803 [arXiv:hep-ph/0412278].

[78] C. Englert, B. Jager and D. Zeppenfeld, JHEP **0903** (2009) 060 [arXiv:0812.2564 [hep-ph]].

[79] A. Martin and V. Sanz, arXiv:0907.3931 [hep-ph].

[80] H. Georgi, Phys. Rev. Lett. **98** (2007) 221601 [arXiv:hep-ph/0703260].

[81] M. J. Strassler and K. M. Zurek, Phys. Lett. B **651** (2007) 374 [arXiv:hep-ph/0604261].

[82] J. Kang and M. A. Luty, arXiv:0805.4642 [hep-ph].

[83] C. B. Jackson, G. Servant, G. Shaughnessy, T. M. P. Tait and M. Taoso, arXiv:0912.0004 [hep-ph].

[84] C. Grojean, G. Servant and J. D. Wells, Phys. Rev. D **71** (2005) 036001 [arXiv:hep-ph/0407019].

[85] C. Grojean and G. Servant, Phys. Rev. D **75** (2007) 043507 [arXiv:hep-ph/0607107].

Discussion

Majid Hashemi (University of Antwerp): What changes at the LHC if there are additional contributions from coupling constant terms in the Higgs sector? Is it only branching ratios or kinematics?

Answer: Obviously, when the Higgs couplings are modified compared to the Standard Model, the Higgs production cross sections and the Higgs decay branching ratios are affected [1]. Therefore, the searches for the Higgs boson at the LHC, as well as the LEP/Tevatron exclusion bounds are modified [2]. Figure 2 for instance reports the amount of luminosity needed for discovery in the most promising channels for the minimal composite Higgs models of Ref. [3]. Notwithstanding the fact that, in composite Higgs models, the Higgs boson emerges from a strongly interacting sector, in processes with a single Higgs boson involved the kinematics of the signal is not modified. As example, the p_T distribution in the gluon fusion process will be exactly the same as in the SM model up to an overall normalization factor. The reason is that the p_T distribution is obtained from the three processes: (i) $gg \to h + g$, (ii) $gq \to h + q$ and $g\bar{q} \to h + \bar{q}$ and (iii) $q\bar{q} \to h + g$. The three processes will rescaled the same way and therefore the overall normalization of the p_T distribution will change but not its shape. The situation is totally different when two particles from the strong sector are involved [1, 4, 5]. Two typical examples are the scattering of longitudinally polarized massive gauge bosons or the double Higgs production via vector boson fusion. The strong sector makes the signal much harder. Figure 3 depicts the differential cross section for $pp \to WWjj$ as function of the invariant mass of the WW pair for the SM model ($\xi = 0$) and for the technicolor limit of composite Higgs model ($\xi = 1$).

Guido Altarelli (University of Roma III and CERN): In composite Higgs models you have bounds on the couplings of new operators from precision tests, flavour physics and so on. This implies the need for fine-tuning. How would you quantify the amount of necessary fine-tuning in these models? How does it compare with SUSY?

Answer: Electroweak precision tests and flavor data certainly restrict the parameter space of any composite Higgs models. The dominant effects arise at tree-level from the exchange of the resonances of the strong sector. For instance, the vector spin-1 resonances give rise to a contribution to the Peskin–Takeuchi parameter[1] S scaling like m_W^2/m_ρ^2, $m_\rho = g_\rho f$ being the mass scale of the resonances (g_ρ is the typical coupling of the strong sector and f is the decay constant of the strong sector the Higgs is emerging from). The scale that controls the Higgs physics is the strong decay constant f and not the mass scale of the resonances, so that the large UV dominated contribution to S can be screened by increasing the coupling of the strong sector: this is a huge advantage

---

[1]T can always be protected by custodial symmetry in the strong sector. Actually, a careful analysis [6] of complete electroweak constraint reveals that the deviation of the coupling of the left-handed b quark to the Z gauge boson gives more stringent constraints than corrections to the oblique parameters. A particular realization of the custodial symmetry [7] can however relax significantly this constraint [8].

of composite Higgs models over regular technicolor models. However, there is a second contribution to S emerging at one-loop from the IR degrees of freedom as a result of the modifications of the Higgs couplings: the cancellation occurring in the SM between the gauge and the Higgs contributions to S does not hold anymore and it results in a logarithmic divergence proportional to the Higgs anomalous coupling [9]. Typically, this IR contribution imposes a lower bound on the compositeness scale of the Higgs: $\xi = v^2/f^2 \approx 0.2 \div 0.3$. Since the ratio ξ is the result of the dynamics generating the Higgs potential, forbidding larger values of ξ certainly restricts the allowed parameter space compatible with data. For instance, a typical Higgs potential has the form $V(h) = A \sin^2 h/f - B \sin^2 h/f \cos^2 h/f$ which, for $B > |A|$, has a global minimum at $\xi = \langle \sin^2 h/f \rangle = (1 - A/B)/2$. This certainly amounts to some level of fine-tuning in any particular model. For instance, Fig. 4 displays the region of parameter space fulfilling the electroweak constraints in a concrete model built in warped 5D: it gives a feeling of the fine-tuning necessary in these models, which can be estimated to be of the order of 20÷30%, compared to a typical $\mathcal{O}(1\%)$ fine-tuning in SUSY models. But it is also true that the outcome of the SUSY models are more predictive while the composite Higgs models do not offer a complete description of the strong sector at the origin of EWSB above the scale $4\pi f$.

References

[1] G. F. Giudice, C. Grojean, A. Pomarol and R. Rattazzi, JHEP **0706** (2007) 045 [arXiv:hep-ph/0703164].

[2] J.R. Espinosa, C. Grojean and M. Muehlleitner, to appear.

[3] K. Agashe, R. Contino and A. Pomarol, Nucl. Phys. B **719** (2005) 165 [arXiv:hep-ph/0412089].

[4] R. Contino, C. Grojean, M. Moretti, F. Piccinini and R. Rattazzi, to appear.

[5] C. Grojean, arXiv:0910.4976 [hep-ph].

[6] K. Agashe and R. Contino, Nucl. Phys. B **742** (2006) 59 [arXiv:hep-ph/0510164].

[7] K. Agashe, R. Contino, L. Da Rold and A. Pomarol, Phys. Lett. B **641** (2006) 62 [arXiv:hep-ph/0605341].

[8] R. Contino, L. Da Rold and A. Pomarol, Phys. Rev. D **75** (2007) 055014 [arXiv:hep-ph/0612048].

[9] R. Barbieri, B. Bellazzini, V. S. Rychkov and A. Varagnolo, Phys. Rev. D **76** (2007) 115008 [arXiv:0706.0432 [hep-ph]].
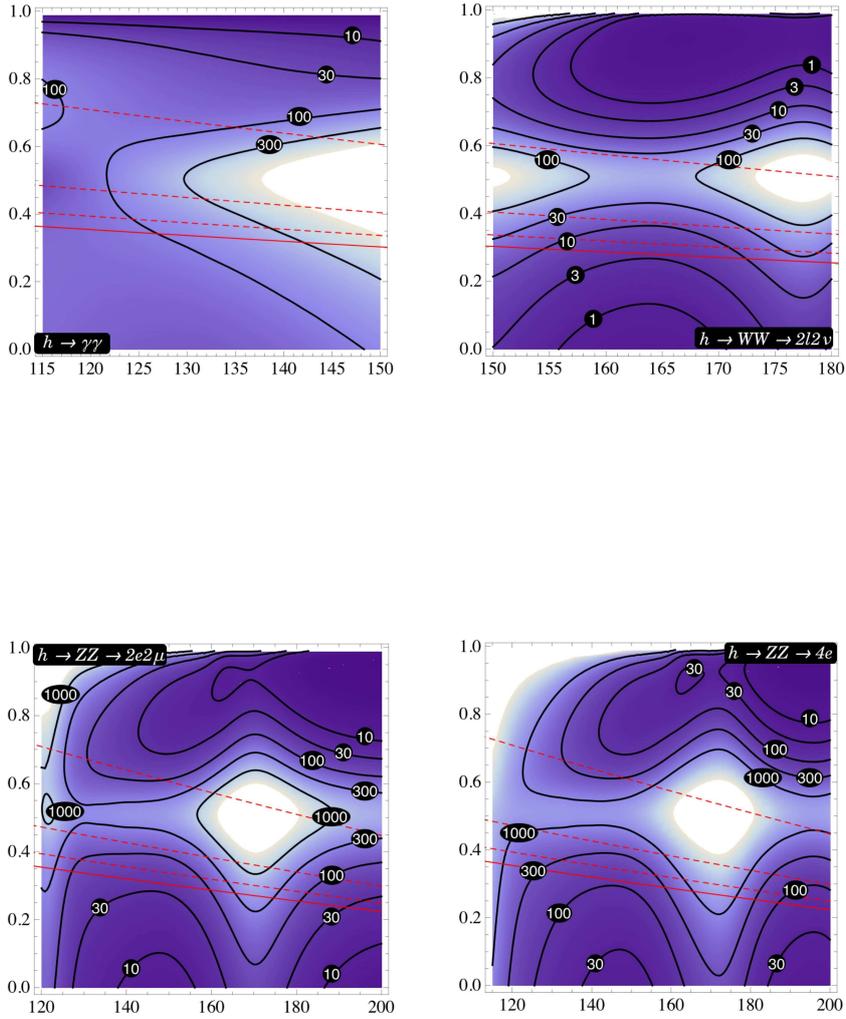
Figure 2: Luminosity (in fb^{-1}) needed for discovery in the most promising channels with the CMS detector as a function of the Higgs mass (horizontal axis, in GeV) and the parameter $\xi = v^2/f^2$ (vertical axis), measuring the amount of compositeness of the Higgs boson. From Ref. [2].
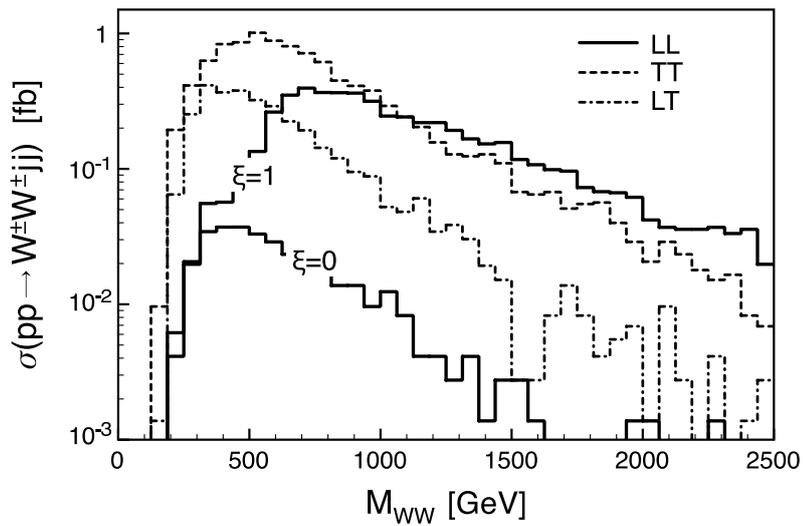
Figure 3: The differential cross section for $pp \to WWjj$ as function of the invariant mass of the WW pair for the SM model ($\xi = 0$) and for the technicolor limit of composite Higgs model ($\xi = 1$). The strong interaction makes the signal much harder. From Ref. [4].
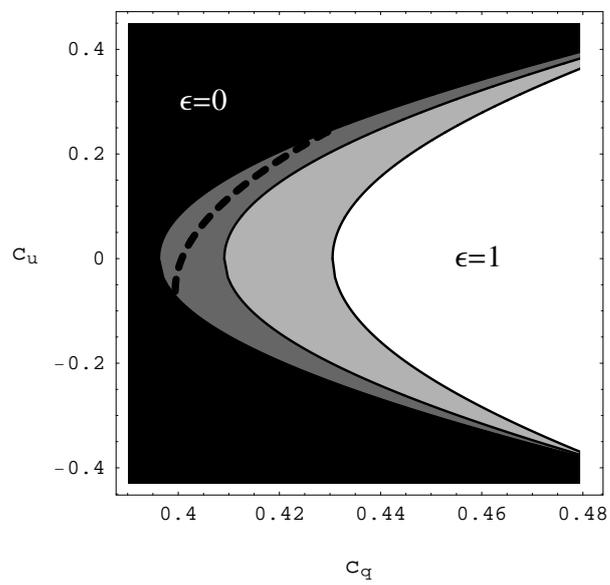
Figure 4: The electroweak precision data exclude large portions of the parameter space of a typical composite Higgs models built in warped 5D: in the dark region, no EWSB occurs, while in the white region EWSB is maximal ($v \sim f$). Only the dark-grey area is compatible with all electroweak constraints. From Ref. [8].

Higgs boson searches at the Tevatron

Gregorio Bernardi[1]
(on behalf of the CDF and DØ collaborations)

[1]*LPNHE, Universités Paris VI et VII, Paris, France*

We report on the searches for the Higgs boson(s) at the Tevatron as of Summer '09 . For the standard model Higgs we present searches in several decay modes, and the combination of all the channels analyzed by the CDF and DØ collaboration. A standard model Higgs having a mass between 160 and 170 GeV is excluded at 95% C.L. We also present searches for Higgs bosons appearing in theories beyond the standard model (SM). With the current datasets analyzed, in all tested models no evidence for Higgs bosons is found. Projections of the sensitivity to the SM Higgs boson at high luminosity are summarized.

1 Introduction

The search for the Higgs boson(s) has been of major importance for fundamental physics for many years, and is a central part of the Fermilab Tevatron physics program. Both the CDF and DØ experiments are reporting new results in different channels, which can then be combined to reach higher sensitivity. The new searches include more data and improved analysis techniques compared to previous analyses. The sensitivity of the current SM Higgs [1] combination significantly exceed previous combinations, while a Tevatron MSSM Higgs combination is reported here for the first time [2].

We report on the search for the standard model in the low mass channels, in which the Higgs boson is produced in association with a W or a Z and decays mostly in $b\bar{b}$ pairs, and in the high mass channels, in which the Higgs is produced mostly by gluon-gluon fusion and decays to WW pairs. We then present the combination of the results in all these channels obtained by the two collaborations. We also present searches for the Higgs bosons in beyond the standard model theories, mostly in supersymmetric (SUSY) models, and their combination.

All standard model Higgs boson signals are simulated using PYTHIA [3], and CTEQ5L or CTEQ6L [4] leading-order (LO) parton distribution functions. The $gg \to H$ production cross section is calculated at NNLL in QCD and also includes two-loop electroweak effects; see Refs. [5, 6] and references therein for the different steps of these calculations. The $gg \to H$ production cross section depends strongly on the PDF set chosen and the accompanying value of α_s. The cross sections used here are calculated with the MSTW 2008 NNLO PDF set [7]. All Higgs production modes are included in the high mass search: besides gluon-gluon fusion through a virtual top quark loop (ggH), are the production in association with a W or Z vector boson (VH) [8, 9, 10], and vector boson fusion (VBF) [8, 11]. The SM Higgs boson decay branching ratio predictions are calculated with HDECAY [12]. For both CDF and DØ, events from multijet (instrumental) backgrounds are measured in data with different methods, in orthogonal samples. For CDF, backgrounds from other SM processes were generated using PYTHIA,

ALPGEN [13], MC@NLO [14] and HERWIG [15] programs. For DØ, these backgrounds were generated using PYTHIA, ALPGEN, and COMPHEP [16], with PYTHIA providing parton-showering and hadronization for all the generators. These background processes were normalized using either experimental data or highest order calculationscalculations available (from MCFM [17] for $W+$ heavy flavor process).

For supersymmetric Higgs bosons, the acceptance for signal is determined from Monte-Carlo simulations, using the PYTHIA event generator with CTEQ5L (CDF) and CTEQ6L (DØ) parton sets and TAUOLA [18] to simulate the decays of the taus if present in the final state.

Two production modes, $gg \rightarrow \phi$ and $b\bar{b}\phi$ are considered by CDF while only $gg \rightarrow \phi$ is considered by DØ but the acceptances are seen to be similar for both production modes. In the interpretation of the results in the framework of the MSSM as limits in the $\tan\beta - M_A$ plan,e both production modes are taken into account as well as an additional factor of two on the cross section due to the near degeneracy of two of the three neutral Higgs bosons. The signal cross sections and branching fractions within each scenario have been calculated using FEYNHIGGS[19] with no theoretical uncertainties considered. All these searches are statistically limited, so the performance of the Tevatron is a crucial ingredient for the sensitivity which can be reached. The Tevatron continues to perform excellently and, as of August 2009, 6.8 fb^{-1} of data have been delivered, and 6.0 fb^{-1} have been recorded by each experiment. The analyses presented here are based on up to 5 fb^{-1} of data.

2   Searches for Standard Model Higgs bosons at low mass

The searches for the Higgs boson at the Tevatron are now in a rather mature state, so event selections are similar for the corresponding CDF and DØ analyses. The description for each low mass ($m_H < 135$ GeV) analysis are detailed in Refs. [20] to [31], and briefly described below.

For the $WH \rightarrow \ell\nu b\bar{b}$ channel, an isolated lepton (ℓ = electron or muon) and two (and three in the DØ analysis) jets are required, with one or more b-tagged jet. Selected events must also display a significant imbalance in transverse momentum (missing transverse energy or $\not{E}_T$). Events with more than one isolated lepton are vetoed. For the DØ $WH \rightarrow \ell\nu b\bar{b}$ analyses, the two and three jet events are analyzed separately, and in each of these samples two non-overlapping b-tagged samples are defined, one being a single "tight" b-tag (ST) sample, and the other a double "loose" b-tag (DT) sample. The tight and loose b-tagging criteria are defined with respect to the mis-identification rate that the b-tagging algorithm yields for light quark or gluon jets ("mistag rate") typically $\leq 0.5\%$ or $\leq 1.5\%$, respectively. The final variable is a neural network (NN) output for the two-jet sample, while for the three-jet sample the dijet invariant mass is used. DØ also performs a $WH \rightarrow \tau\nu b\bar{b}$ analysis in which the τ is identified through its hadronic decays. This analysis is sensitive to $ZH \rightarrow \tau\tau b\bar{b}$ as well, in those cases where a τ fails to be identified. The analysis is carried out according to the type of reconstructed τ. A boosted decision tree is used as the final discriminant.

For the CDF $WH \rightarrow \ell\nu b\bar{b}$ analysis, the events are grouped into six categories. In addition to the selections requiring an identified lepton, events with an isolated track failing lepton selection requirements are grouped into their own categories. This provides acceptance for single prong tau decays. Within the lepton categories there are three b-tagging categories – two tight b-tags (TDT), one tight b-tag and one loose b-tag (LDT), and a single, tight, b-tag (ST). These b-tag category names are also used in the $\not{E}_T b\bar{b}$ and $\ell^+\ell^- b\bar{b}$ channel descriptions. In each category, two discriminants are calculated for each event. One NN discriminant is trained at each m_H in

the test range, separately for each category. A second discriminant is a boosted decision tree, featuring not only event kinematic and b-tagging observables, but matrix element discriminants as well. These two discriminants are then combined together using another NN to form a single discriminant with optimal performance. In Figures 1a-d we display one dijet mass distribution and one of the discriminants obtained by each collaboration.
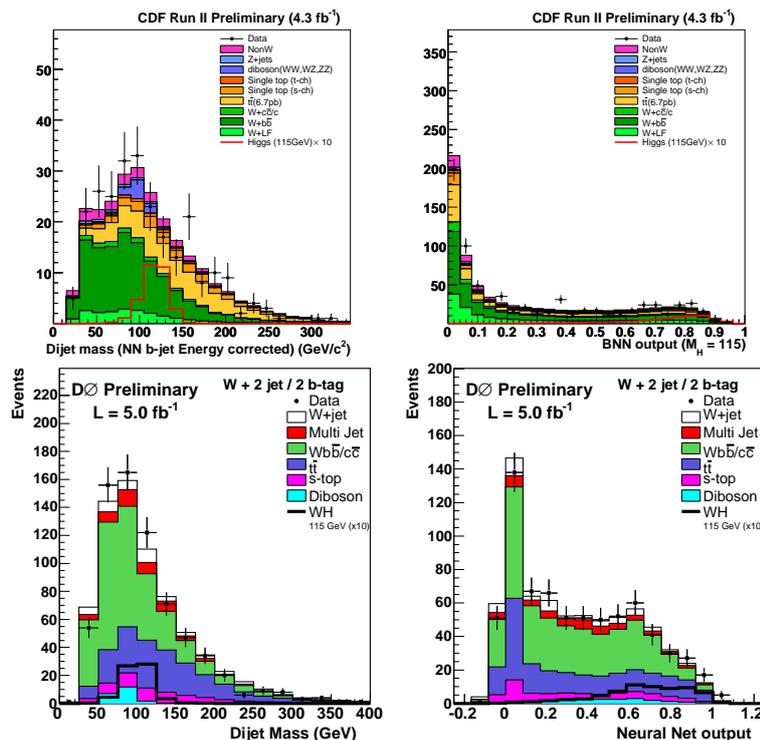
Figure 1: Dijet distributions (a,c) and discriminant output for events with two identified b-jets

For the $ZH \rightarrow \nu\bar{\nu}b\bar{b}$ analyses, the selection is similar to the WH selection, except all events with isolated leptons are vetoed and stronger multijet background suppression techniques are applied. Both CDF and DØ analyses use a track-based missing transverse momentum calculation as a discriminant against false $\not{E}_T$. In addition DØ train a boosted decision tree against the multijet background. There is a sizeable fraction of $WH \rightarrow \ell\nu b\bar{b}$ signal in which the lepton is undetected, that is selected in the $ZH \rightarrow \nu\bar{\nu}b\bar{b}$ samples, so these analyses are also refered to as $VH \rightarrow \not{E}_T b\bar{b}$. The CDF analysis uses three non-overlapping samples of events (TDT, LDT and ST as for WH). DØ uses one DT channel, but with one tight and one loose requirements on the b-identification of the two jets. CDF used NN discriminants as the final variables, while DØ uses boosted decision trees as advanced analysis technique.

The $ZH \rightarrow \ell^+\ell^- b\bar{b}$ analyses require two isolated leptons and at least two jets. They use non-overlapping samples of events with one tight b-tag and two loose b-tags. For the DØ analysis boosted decision trees are the final variables for setting limits, while CDF uses the output of a two-dimensional NN. For this combination CDF and DØ have increased the signal acceptance by

loosening the selection criteria for one of the leptons. In addition a kinematic fit is now applied to the $Z-$boson and jets. CDF corrects jet energies for $\rlap{E}{\,/}_T$ using a NN approach. In the CDF analysis the events are divided into three tagging categories: TDT, LDT, ST. Both CDF and DØ further subdivide the channels into lepton categories with different signal-to-background characteristics.

The DØ collaboration also searched for:

– direct Higgs boson production decaying to a photon pair. In this analysis, the final variable is the invariant mass of the two-photon system. At the Tevatron, this channel is not very sensitive due to the low branching ratio, but it is included in the combination and can gain sensitivity in beyond the standard model scenarios, as described in section 6.

$-t\bar{t}H \rightarrow t\bar{t}b\bar{b}$. Here the samples are analyzed independently according to the number of b-tagged jets (1,2,3, i.e. ST,DT,TT) and the total number of jets (4 or 5). The total transverse energy of the reconstructed objects (H_T) is used as discriminant variable.

– the final state $\tau\tau$ jet jet, which is sensitive to the $VH \rightarrow jj\tau\tau$, $ZH \rightarrow \tau\tau b\bar{b}$, VBF and gluon gluon fusion (with two additional jets) mechanisms. A NN output is used as discriminant variable for the first fb^{-1} of data; a boosted decision tree is used subsequently.

The CDF collaboration also searched for:

– Higgs bosons decaying to a tau lepton pair, in three separate production channels: direct $gg \rightarrow H$ production, associated WH or ZH production, or vector boson production with H and forward jets in the final state. Two jets are required in the event selection. The final variable for setting limits is a combination of several NN discriminants.

Table 1: Luminosity, explored mass range, 95% C.L. limits normalized to the SM expectation for $m_H = 115$ GeV, and references for the different low mass channels ($\ell = e, \mu$), for CDF.

Channel (CDF analyses)	Lumi. (fb^{-1})	m_H range (GeV)	Expected limit	Observed limit	Reference
$WH \rightarrow \ell\nu bb$ 2×(TDT,LDT,ST)	4.3	100-150	4.0	5.3	[20]
$ZH \rightarrow \nu\bar{\nu}b\bar{b}$ (TDT,LDT,ST)	3.6	105-150	4.1	6.9	[21]
$ZH \rightarrow \ell^+\ell^- b\bar{b}$ (low,high s/b)					
× (TDT,LDT,ST)	4.1	100-150	6.8	5.9	[22]
$H + X \rightarrow \tau^+\tau^- + 2$ jets	2.0	110-150	27	24	[23]
$WH + ZH \rightarrow jjb\bar{b}$	2.0	100-150	37	38	[24]

Table 2: Luminosity, explored mass range, 95% C.L. limits normalized to the SM expectation for $m_H = 115$ GeV, and references for the different low mass channels ($\ell = e, \mu$), for DØ.

Channel (DØ analyses)	Luminosity (fb^{-1})	m_H range (GeV)	Expected limit	Observed limit	Reference
$WH \rightarrow \ell\nu bb$ 2×(ST,DT)	5.0	100-150	5.1	6.9	[25]
$WH \rightarrow \tau\nu b\bar{b}$ (ST,DT)	0.9	100-150	42	35	[26]
$VH \rightarrow \tau\tau b\bar{b}/q\bar{q}\tau\tau$	4.9	105-145	18	27	[27]
$ZH \rightarrow \nu\bar{\nu}b\bar{b}$ (DT)	2.1	100-150	8.4	7.5	[28]
$ZH \rightarrow \ell^+\ell^- b\bar{b}$ 2×(ST,DT)	4.2	100-150	8.0	9.7	[29]
$H \rightarrow \gamma\gamma$	4.2	100-150	18	13	[30]
$t\bar{t}H \rightarrow t\bar{t}b\bar{b}$ 2×(ST,DT,TT)	2.1	105-155	45	64	[31]

– the all-hadronic channel, $WH + ZH \rightarrow jjb\bar{b}$. Events are selected with four jets, at least

two of which are b-tagged with the tight b-tagger. The large multijet backgrounds are estimated with the use of data control samples, and the final variable is a matrix element signal probability discriminant.

The limits obtained for $m_H = 115$ GeV in all these analyses together with the luminosity and mass range searched for, are summarized in Tables 1 and 2 for CDF and DØ.

3 Searches for Standard Model Higgs bosons at high mass

At high mass ($m_H > 135$ GeV), the Higgs boson decays predominantly in a WW pair, so by using the leptonic decays it is possible to also use the dominant direct gluon-gluon fusion production (all production modes are included in the high mass analyses). Event selections are similar for the corresponding $H \to W^+W^-$ CDF and DØ analyses. DØ has a dedicated analysis for the $WH \to WW^+W^-$ channel, while it is included in the $H \to W^+W^-$ analysis in the CDF case. The luminosity and mass range searched for these analyses, together with their sensitivity are summarized in Table 3. The description for each analysis are detailed in Refs. [32] to [34], and briefly described below.

Table 3: Luminosity, explored mass range, 95% C.L. limits normalized to the SM expectation for $m_H = 165$ GeV, and references for the different high mass channels ($\ell = e, \mu$), for the CDF and DØ analyses.

Channel	Luminosity (fb^{-1})	m_H (GeV)	Expected limit	Observed limit	Refs
CDF: $H \to W^+W^-$ (low,high s/b)					
$\times$ (0,1 jets)+(2+ jets)+Low-$m_{\ell\ell}$	4.8	110-200	1.2	1.2	[32]
DØ: $H \to W^+W^- \to \ell^\pm\nu\ell^\mp\nu$	4.2	115-200	1.7	1.3	[33]
DØ: $WH \to WW^+W^- \to \ell^\pm\nu\ell^\pm\nu$	3.6	120-200	11	18	[34]

For the $H \to W^+W^-$ analyses, signal events are characterized by a large $\not{E}_T$ and two opposite-signed, isolated leptons. The presence of neutrinos in the final state prevents the reconstruction of the candidate Higgs boson mass. DØ selects events containing electrons and muons, dividing the data sample into three final states: e^+e^-, $e^\pm\mu^\mp$, and $\mu^+\mu^-$. CDF separates the $H \to W^+W^-$ events in six non-overlapping samples, labeled "high s/b" and "low s/b" for the lepton selection categories, and also split by the number of jets: 0, 1, or 2+ jets. The sample with two or more jets is not split into low s/b and high s/b lepton categories. The sixth CDF channel is a new low-$m_{\ell^+\ell^-}$ channel, which accepts events with $m_{\ell^+\ell^-} < 16$ GeV. This channel increases the sensitivity of the $H \to W^+W^-$ analyses at low m_H, adding 10% additional acceptance at $m_H = 120$ GeV. CDF's division of events into jet categories allows the analysis discriminants to separate three different categories of signals from the backgrounds more effectively. The signal production mechanisms considered are $gg \to H \to W^+W^-$, $WH + ZH \to jjW^+W^-$, and the vector-boson fusion process.

The final discriminants are neural-network outputs for DØ and neural-network outputs including likelihoods constructed from matrix-element probabilities (ME) as input to the NNs, for CDF, in the 0-jet bin, else the ME are not used. All analyses in this channel have been updated with more data and analysis improvements.

The DØ collaboration analyzes separately the $WH \to WW^+W^-$ channel, where the associated W boson and the W boson from the Higgs boson decay which has the same charge

are required to decay leptonically, thereby defining three like-sign dilepton final states ($e^{\pm}e^{\pm}$, $e^{\pm}\mu^{\pm}$, and $\mu^{\pm}\mu^{\pm}$) containing all decays of the third W boson. In this analysis the final variable is a likelihood discriminant formed from several topological variables. CDF analyzes the $WH \to WW^+W^-$ channel using a selection of like-sign dileptons and a NN to further purify the signal.

4 Combination of the standard model Higgs results

Using the combination procedures described in Refs. [35, 36, 37, 38], we extract limits on SM Higgs boson production $\sigma \times B(H \to X)$ in $p\bar{p}$ collisions at $\sqrt{s} = 1.96$ TeV for m_H between 100 and 200 GeV. The analyses used in the combination have sometimes lower luminosity than presented above, since the combination presented here was performed in March 2009, i.e. before the latest updates presented at this conference became available. See Reference [1] for details of the differences. In short, the low mass channels had an average luminosity of about 2.5 fb^{-1} for the current combination, while the updated analyses have an average closer to 4 fb^{-1}.

The results are presented in terms of the ratio of obtained limits to cross section in the SM, as a function of Higgs boson mass, for test masses for which both experiments have performed dedicated searches in different channels. A value of the combined limit ratio which is less or equal to one would indicate that that particular Higgs boson mass is excluded at the 95% C.L. The expected and observed limit ratios are shown in Figure 2 for the combined CDF and DØ analyses. The observed and median expected ratios are listed for some typical Higgs boson masses in Table 4 with observed (expected) values of 2.5 (2.4) at $m_H = 115$ GeV, 0.99 (1.1) at $m_H = 160$ GeV, 0.86 (1.1) at $m_H = 165$ GeV, and 0.99 (1.4) at $m_H = 170$ GeV. The Tevatron experiments exclude at 95% C.L. the production of a standard model Higgs boson with mass between 160 and 170 GeV.
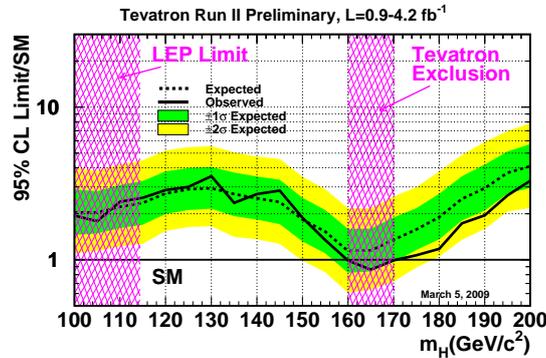
Figure 2: Observed and expected 95% C.L. upper limits on the ratios to the SM cross section, as functions of the Higgs boson mass for the combined CDF and DØ analyses. The limits are expressed as a multiple of the SM prediction. The bands indicate the 68% and 95% probability regions where the limits can fluctuate, in the absence of signal.

Table 4: Ratios of median expected and observed 95% CL limit to the SM cross section for the combined CDF and DØ analyses as a function of the Higgs boson mass in GeV.

	105	115	125	135	140	150	155	160	165	170	175	180	190	200
Expected	2.0	2.4	2.9	2.7	2.5	1.8	1.5	1.1	1.1	1.4	1.6	1.9	2.7	4.2
Observed	1.8	2.5	3.0	2.4	2.7	1.9	1.4	0.99	0.86	0.99	1.1	1.2	2.0	3.3

5 Search for MSSM Higgs bosons

The most appealing extensions of the SM are the supersymmetric models. In the minimal (MSSM) extension [39], there are three neutral Higgs bosons, and two charged ones. Searches for the MSSM neutral Higgs bosons decaying into tau lepton pairs ($\phi = H, h, A \rightarrow \tau\tau$) have been performed by the CDF and D0 Collaboration with integrated luminosities of 1.8 and 2.2 fb-1 of Run II data, respectively. The searches require the tau pairs to decay into $\tau_e\tau_\mu$, $\tau_e\tau_{had}$, and $\tau_\mu\tau_{had}$, where τ_e, τ_μ are the leptonic decays of the tau and τ_{had} represent the hadronic decay modes. The searches are described in detail in [40, 41, 42]. The visible mass spectrum, with an example shown in Fig. 3a and defined in [42], is used in the limit calculation. Correlations in systematic uncertainties between the different tau decay channels are taken into account. No signicant excess in signal over background has been observed and thus CDF-DØ combined limits on the production cross section for neutral Higgs boson times the branching fraction into tau leptons are given for neutral Higgs bosons in the range $100 < M_A < 200$ GeV. The results are shown in Figure 3b.

Though at leading order the Higgs sector of the MSSM can be described with just two parameters, with higher order corrections comes a dependence on other model parameters. To interpret the exclusion within the MSSM, these parameters are fixed in four benchmark scenarios [43]. The four scenarios considered are defined in terms of: M_{SUSY}, the mass scale of squarks, μ, the Higgs sector bilinear coupling, M_2, the gaugino mass term, A_t, the trilinear coupling the stop sector, A_b, the trilinear coupling of the sbottom sector and $m_{\tilde{g}}$ the gluino mass term. The maximal-mixing, m_h^{max}, scenario is defined as:

$$M_{\text{SUSY}} = 1 \text{ TeV}, \mu = 200 \text{ GeV}, M_2 = 200 \text{ GeV},$$
$$X_t = 2M_{\text{SUSY}}, \ A_b = A_t, \ m_{\tilde{g}} = 0.8 M_{\text{SUSY}}.$$

and the no-mixing scenario - with vanishing mixing in the stop sector and a higher SUSY mass scale to avoid the LEP Higgs bounds:

$$M_{\text{SUSY}} = 2 \text{ TeV}, \mu = 200 \text{ GeV}, M_2 = 200 \text{ GeV},$$
$$X_t = 0, \ A_b = A_t, \ m_{\tilde{g}} = 0.8 M_{\text{SUSY}}.$$

Four scenarios are constructed from these two by the consideration of both + and - signs for μ. The results are shown in Figure 4b,c for two of the four scenarios.
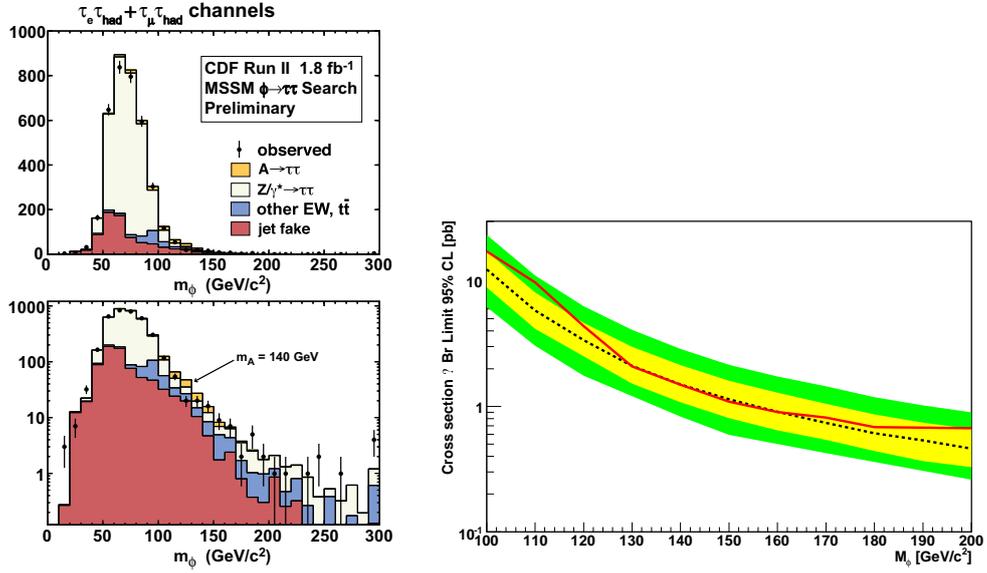
Figure 3: a) Visible mass distribution in the CDF $h \rightarrow \tau\tau$ analysis ; b) 95% C.L. limits on cross section × branching ratio in the $h \rightarrow \tau\tau$ CDF-DØ combination. The solid red and dashed black lines show the observed and expected limits respectively. The yellow and green shaded bands show the 1 and 2σ deviations from the expectation.
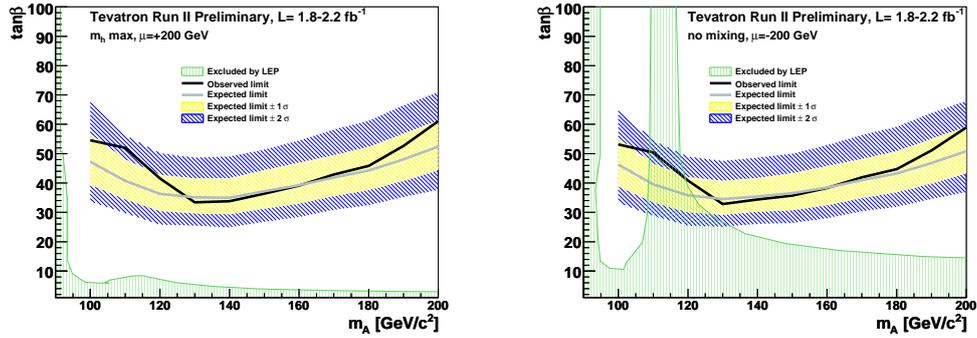
Figure 4: 95% C.L. limits obtained from the $h \rightarrow \tau\tau$ CDF-DØ combination in the tanβ-M_A plane for two benchmark scenarios: maximal mixing (a) and no mixing (b) for $\mu > 0$ and $\mu < 0$ respectively. The black line denotes the observed limit, the grey line the expected limit.

For this result the signal cross sections and branching fractions within each scenario have been calculated using FEYNHIGGS with no theoretical uncertainties considered. Tanβ dependent width effects have not been included, though in the region of the tanβ-M_A plane where limits have been set these are not expected to strongly impact on the limit.

The DØ collaboration has also done a combination of its 2.2 fb^{-1} $h \to \tau\tau$ channel with the $bh \to b\tau\tau$ channel (1.2 fb^{-1}[44]) and the $bh \to bbb$ channel (2.6 fb^{-1}[45]). This last analysis is divided into three channels with 3, 4 or 5 jets in the final state and the final discriminant is the invariant mass of the 2 b-jets of highest p_T. The results are displayed in Figure 5 for the two same benchmark scenarios, and show that the $bh \to b\tau\tau$ channel provides a visible gain in sensitivity at low m_A.
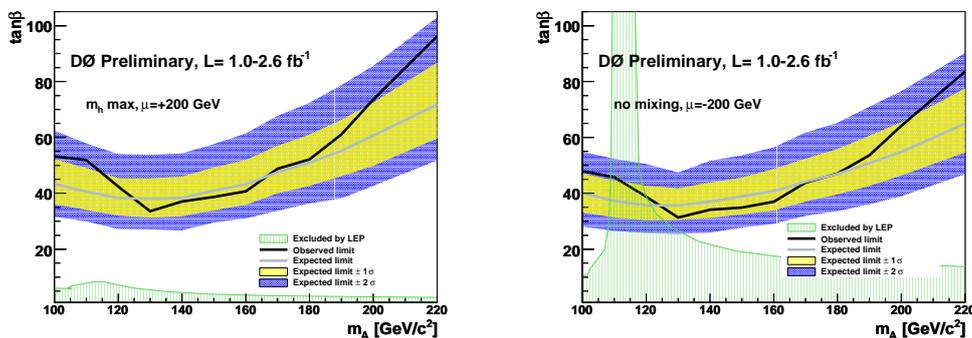
Figure 5: 95% C.L. limits obtained from the DØ combination ($h \to \tau\tau$, $bh \to b\tau\tau$, $bh \to bbb$) in the tanβ-M_A plane for two benchmark scenarios: maximal mixing (a) and no mixing (b) for $\mu > 0$ and $\mu < 0$ respectively. .

6 Beyond MSSM Higgs

Searches are also performed in models beyond the MSSM. In the next-to-MSSM model, the Higgs sector has three neutral CP-even Higgs (h), two CP-odd Higgs bosons (a). A scenario not excluded by LEP is a light Higgs boson with m_h between 100 and 130 GeV and m_a of a few GeV. In such configuration the Higgs boson h would decay preferentially in aa pairs, which are difficult to detect. DØ performed a search in this mode, assuming a decays in muon or tau pairs, with 4.2 fb^{-1} of data. In the case where $2m_\mu < m_a < 2m_\tau$, DØ sets a limit on the production cross section time branching ratio $\sigma(p\bar{p}) \to h \times \mathrm{BR}(h \to aa \to 4\mu) <\simeq 10$ fb [46].

In fermiophobic models, the Higgs boson decays only in bosons, and at low mass such decay is dominated by diphoton pairs. A higgs boson would appear as a "bump" in the diphoton invariant mass spectrum shown in Figure 6a. We can thus reinterpret the diphoton SM analyses, and derive limits as a function of the $h \to \gamma\gamma$ branching ratio, as shown in Figure 6b. Both CDF and DØ have reached sensitivity similar to LEP, excluding fermiophobic Higgs bosons below $\simeq 105$ GeV, and with more luminosity and improved analysis techniques are expected to reach sensitivity up to $\simeq 125$ GeV.
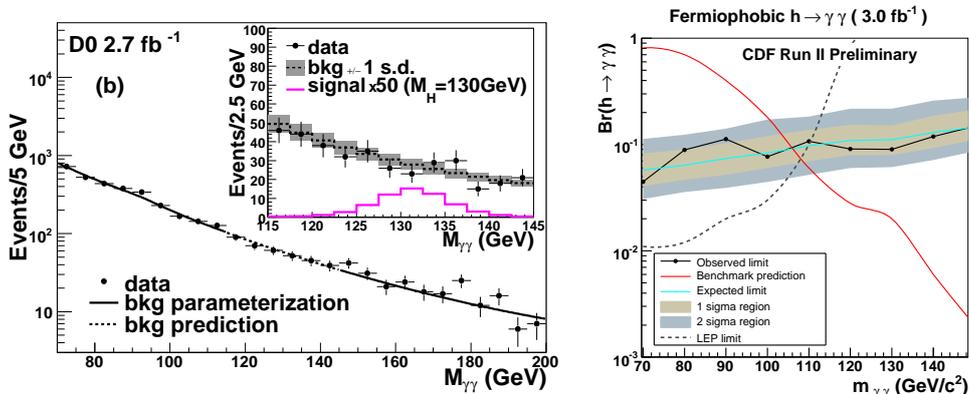
Figure 6: a) invariant diphoton invariant mass distribution in the DØ analysis, compared to the background prediction and to a simulated signal at $m_h = 130$ GeV increased by a factor of 50; b) 95% C.L. limit on the $h \to \gamma\gamma$ branching ratio as a function of the Higgs mass. The Fermiophobic scenario (red line) is excluded for m_h below approximately 105 GeV, both by CDF and, independently, by DØ(not shown).

7 Projections at high luminosity for the sensitivity to a SM Higgs boson

The Tevatron,CDF and DØ being now in a mature state, it is possible to estimate what will be the sensitivity to a SM Higgs boson by the end of 2011. At that time, the machine is expected to have delivered 12 fb^{-1}. Taken into account the recording efficiency and the data quality criteria currently applied by both experiments, this will result in analyses being done with 10 fb^{-1} of data. The analyses are being improved on several aspects (trigger and lepton detection efficiency, improvement in multivariate techniques, and, for low mass Higgs searches, b-tagging efficiency and dijet mass resolution), which lead to an expected improvement of approximately 50% in intrinsic sensitivity (i.e. outside the gain due to the luminosity increase). Injecting the luminosity increase and the analysis improvements in the current CDF-DØ combination, we can derive the probability to observe a Higgs signal at the 3 standard deviation level, depending on the Higgs mass, as shown in Figure 7. The projection shows that for masses close to two times the W mass the Tevatron has excellent sensitivity (which explain why this mass region is already excluded at 95% C.L.), but also that for $m_H = 115$ GeV, the probability to have evidence for the Higgs boson is about 50%. Such an evidence would be particularly important since the observation of a low mass Higgs boson in the dominant $b\bar{b}$ decay mode is not foreseen at the LHC before many years, if at all possible. Similarly, the reach for beyond the standard model Higgs bosons will increase significantly with luminosity and analysis improvements. In conclusion, with the complete dataset of the Tevatron Run II, whose end has already been postponed several times given the Higgs sensitivity potential and the LHC ramp-up schedule, we expect to have a first sight of this elusive particle, if it is indeed of the standard model type, or if it is supersymmetric with favorable SUSY phase space parameters.
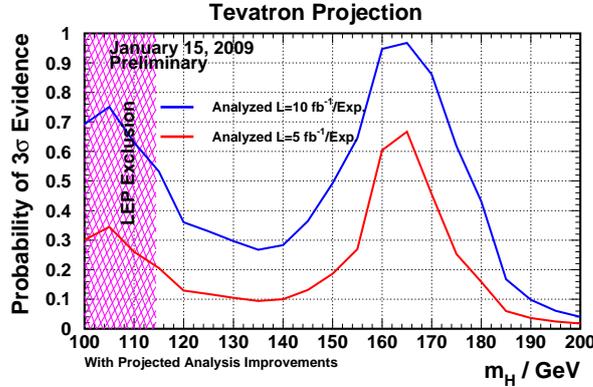
Figure 7: Probability to have evidence at the 3σ level for a SM Higgs boson between 100 and 200 GeV, for 5 and 10 fb^{-1} of data analyzed by CDF and DØ and subsequently combined.

References

[1] The CDF and DØ Collaborations and the TEVNPHWG Working Group, "Combined CDF and DZero Upper Limits on Standard Model Higgs-Boson Production with up to 4.2 fb^{-1} of Data", FERMILAB-PUB-09-060-E, CDF Note 9713, DØ Note 5889, arXiv:0903.4001v1 [hep-ex] (2009).

[2] The CDF and DØ Collaborations and the TEVNPHWG Working Group, "Combined CDF and D0 upper limits on MSSM Higgs boson production in tau-tau final states with up to 2.2 fb^{-1} of data", FERMILAB-PUB09-394-E, CDF Note 9888, DØ Note 5980.

[3] T. Sjöstrand, L. Lonnblad and S. Mrenna, "PYTHIA 6.2: Physics and manual," arXiv:hep-ph/0108264.

[4] H. L. Lai *et al.*, "Improved Parton Distributions from Global Analysis of Recent Deep Inelastic Scattering and Inclusive Jet Data", Phys. Rev D **55**, 1280 (1997).

[5] C. Anastasiou, R. Boughezal and F. Petriello, "Mixed QCD-electroweak corrections to Higgs boson production in gluon fusion", arXiv:0811.3458 [hep-ph] (2008).

[6] D. de Florian and M. Grazzini, "Higgs production through gluon fusion: updated cross sections at the Tevatron and the LHC", arXiv:0901.2427v1 [hep-ph] (2009).

[7] A. D. Martin, W. J. Stirling, R. S. Thorne and G. Watt, "Parton distributions for the LHC", arXiv:0901.0002 [hep-ph] (2009).

[8] K. A. Assamagan *et al.* [Higgs Working Group Collaboration], "The Higgs working group: Summary report 2003," arXiv:hep-ph/0406152.

[9] O. Brein, A. Djouadi, and R. Harlander, "NNLO QCD corrections to the Higgs-strahlung processes at hadron colliders", Phys. Lett. B579, 2004, 149-156.

[10] Ciccolini, M. L. and Dittmaier, S. and Kramer, M., "Electroweak radiative corrections to associated W H and Z H production at hadron colliders", Phys. Rev. D68 (2003) 073003.

[11] E. Berger and J. Campbell. "Higgs boson production in weak boson fusion at next-to-leading order", Phys. Rev. D70 (2004) 073011,

[12] A. Djouadi, J. Kalinowski and M. Spira, "HDECAY", Comput. Phys. Commun. **108**, 56 (1998) [arXiv:hep-ph/9704448].

[13] M. L. Mangano, M. Moretti, F. Piccinini, R. Pittau and A. D. Polosa, "ALPGEN", JHEP **0307**, 001 (2003) [arXiv:hep-ph/0206293].

[14] S. Frixione and B.R. Webber, "MC@NLO", JHEP 06, 029 (2002) [arXiv:hep-ph/0204244]

[15] G. Corcella *et al.*, "HERWIG 6", JHEP **0101**, 010 (2001) [arXiv:hep-ph/0011363].

[16] A. Pukhov *et al.*, "CompHEP", [arXiv:hep-ph/9908288].

[17] J. Campbell and R. K. Ellis, "MCFM", http://mcfm.fnal.gov/.

[18] S. Jadech *et al.*, "TAUOLA", Comput. Phys. Commun. 76 (1993) 361

[19] S. Heinemeyer, W. Hollik, and G. Weiglein, Eur. Phys. J. C **9**, 343 (1999); Comput. Phys. Commun. **124**, 76 (2000); G. Degrassi *et al.*, Eur. Phys. J. C **28**, 133 (2003), M. Frank *et al.*, JHEP **0702**, 047 (2007). FEYNHIGGS version 2.6.3.

[20] CDF Collaboration, "Search for Higgs Boson Production in Association with $W^\pm$ Boson with 4.3 fb^{-1}", CDF Conference Note (2009).

[21] CDF Collaboration, "Search for the Standard Model Higgs Boson in the $\not{E}_T$ Plus Jets Sample", CDF Conference Note (2009).

[22] CDF Collaboration, "A Search for $ZH \to \ell^+\ell^- b\bar{b}$ in 2.7 fb^{-1} using a Neural Network Discriminant", CDF Conference Note 9665 (2009).

[23] CDF Collaboration, "Search for SM Higgs using tau leptons using 2 fb^{-1}", CDF Conference Note 9179.

[24] CDF Collaboration, "A Search for the Standard Model Higgs Boson in the All-Hadronic channel using a Matrix Element Method", CDF Conference Note 9366.

[25] DØ Collaboration, "Search for WH associated production using neural networks with 5.0 fb^{-1} of Tevatron data," DØ Conference Note 5972.

[26] DØ Collaboration, "Search for the standard model Higgs boson in $WH \to \tau\nu b\bar{b}$ channel in 0.94 fb^{-1} of $p\bar{p}$ collisions at $\sqrt{s} = 1.96$ TeV", DØ Conference note 5669.

[27] DØ Collaboration, "Search for the standard model Higgs boson in τ final states", DØ Conference note 5883; "Search for the standard model Higgs boson in the $\tau^+\tau^- q\bar{q}$ final state", DØ Conference note 5485.

[28] DØ Collaboration, "Search for the standard model Higgs boson in the $ZH \to \nu\nu b\bar{b}$ channel in 5.2 fb^{-1} of $p\bar{p}$ collisions at $\sqrt{s} = 1.96$ TeV", DØ Conference note 5872.

[29] DØ Collaboration, "A Search for $ZH \to e^+e^- b\bar{b}$ and $ZH \to \mu^+\mu^- b\bar{b}$ Production in 4.2 fb^{-1} of data with the DØ detector in $p\bar{p}$ Collisions at $\sqrt{s} = 1.96$ TeV", DØ Conference Note 5876.

[30] DØ Collaboration, "Search for the Standard Model Higgs boson in $\gamma\gamma$ final states at DØ with 4.2 fb^{-1} of data", DØ Conference Note 5858.

[31] DØ Collaboration, "Search for the standard model Higgs boson in the $t\bar{t}H \to t\bar{t}b\bar{b}$ channel", DØ Conference note 5739.

[32] CDF Collaboration, "Search for $H \to WW^*$ Production Using 4.8 fb^{-1} of Data", CDF Conference Note (2009).

[33] DØ Collaboration, "Search for the Higgs boson in $H \to WW^* \to l^+l^- (\ell, \ell' = e\mu)$ decays with 1.7 fb^{-1} at DØ in Run II", DØ Conference Note 5537.

[34] DØ Collaboration, "Search for associated Higgs boson production $WH \to WWW^* \to \ell^\pm \nu \ell'^\pm \nu' + X$ in $p\bar{p}$ collisions at $\sqrt{s} = 1.96$ TeV", DØ Conference Notes 5485 and 5873.

[35] T. Junk, Nucl. Instrum. Meth. A **434** (1999) 435.; R. Barate *et al.*, Phys. Lett B **565** (2003).

[36] W. Fisher, FERMILAB-TM-2386-E (2007).

[37] CDF Collaboration, "Combined Upper Limit on Standard Model Higgs Boson Production for Winter 2009", CDF Conference Note 9674 (2009).

[38] DØ Collaboration, "Combined Upper Limits on Standard Model Higgs Boson Production from the DØ Experiment with up to 4.2 fb^{-1} of data" DØ Conferenve Note 9674 (2009).

[39] H.P. Nilles, Phys. Rep. **110**, 1 (1984); H.E. Haber and G.L. Kane, Phys. Rep. **117**, 75 (1985).

[40] CDF Collaboration, CDF Note 9071.

[41] V.M. Abazov *et al.* (D0 Collaboration), Phys. Rev. Lett.**101**, 071804 (2008).

[42] D0 Collaboration, D0 Note 5740-CONF.

[43] M. Carena, S. Heinemeyer, C. E. M. Wagner, and G. Weiglein, Eur. Phys. J. C **45**, 797 (2006).

[44] D0 Collaboration, D0 Note 5727-CONF.

[45] D0 Collaboration, D0 Note 5726-CONF.

[46] V.M. Abazov *et al.* (D0 Collaboration), Phys. Rev. Lett.**103**, 061801 (2009)

Discussion

Guido Altarelli, CERN/ Roma Tre: You said that from the new improved results from CDF and D0 in the SM Higgs search we can extrapolate and guess what the new combined result would be. What is your guess then on the new excluded region for the SM Higgs?

Answer: Since I am speaking on behalf on CDF and D0, I prefer not to provide personal guesses in this forum, but we expect these new combined limits to be available in the fall. Besides, note that there also improvements on the Higgs theoretical cross-sections which will have some influence on the next exclusion region we will provide.

Majid Hashemi (University of Antwerp): Is there any update of charged Higgs search from Tevatron?

Answer: Not yet, those are expected for fall 2009.

Status of Experimental Searches at Colliders

O. González[1]

(On behalf of the CDF, DØ, H1 and ZEUS Collaborations)
[1]*CIEMAT Avda. Complutense 22, E-28040 Madrid (Spain)*

This document reports on the current status of the searches for Physics beyond the standard model performed by the high-energy-physics experiments located at the Tevatron and the HERA colliders. The main results from the analyses and their connection with possible extensions of the Standard Model are discussed.

1   Introduction

The standard model (SM) of elementary particles and fundamental interactions, however successful, is incomplete, since it does not explain the origin of electroweak symmetry breaking or the gauge hierarchy problem [1]. In addition some experimental observation are not included in the SM, as the gravitational interaction, the neutrino masses and the non-barionic content of the Universe (Dark Matter). These limitations lead to the need of introducing some additional components to the theory, extending the SM beyond its current structure. This extension is referred as *New Physics* and requires the presence of new particles and/or new interactions which would help to expand our knowledge about Nature by solving the limitations of the SM.

In order to test the possible existence of the New Physics, experiments taking place at the highest available energies are required. For this purpose, analyses performed at the LEP, HERA and Tevatron colliders are the most sensitive to the presence of interactions beyond the SM. The LEP accelerator, colliding e^- and e^+ finished operations in 2000 and therefore the results from the experiments have been extensively covered in the past. This report would not describe directly the analyses of the LEP data, but some of the results are still relevant and will be shown in comparison with the more recent updates from Tevatron and HERA.

The Tevatron accelerator has been during several years the most energetic collider in the world. Currently in operation for the run II, it collides protons and antiprotons at a center-of-mass energy of 1.96 TeV and has provided more than 7 fb^{-1} of data to the two experiments, CDF and DØ. With the current data sample, the analyses are sensitive to previously unexplored regions and being sensitive to very different new physics.

The HERA collider, in which interactions between protons and $e^\pm$ at a center-of-mass energy of 300/318 GeV were studied, finished operations in 2007. During two run periods, it provided 0.5 fb^{-1} of data to the two collider experiments, H1 and ZEUS. Due to the unique initial state at such energies, the searches for new physics and particles performed in this collider are competitive/complementary to LEP and Tevatron.

This report summarizes the status of the searches performed at the collider experiments in these accelerators. Due to space limitation it does not provide a full report on the current status on searches. The interested reader may check the specific references and web-pages of

the experiments for that purpose.

2 Searches for supersymmetric particles

A proposed extension of the SM, supersymmetry (SUSY) [2] solves some of the indicated limitations of the SM by introducing a symmetry that relates particles of different spin. In these models, a new multiplicative quantum number, R-parity, is introduced to distinguish SUSY and SM particles, with R-parity = $(-1)^{3(B-L)+2S}$ where B and L are the baryon and lepton numbers, and S is the spin. In case of R-parity conserving scenarios, SUSY particles are produced in pairs and ultimately decay into the lightest supersymmetric particle (LSP), which constitutes a valid candidate for cold dark matter. If unbroken, SUSY would predict the existence of partners of the SM particles sharing the same properties but the spin. Since no such particles have been observed, SUSY must be a broken symmetry, and more than a hundred new parameters enter the theory even in the minimally supersymmetric extension of the SM (MSSM [3]). The choice of mechanism for the SUSY breaking mediation and of the soft SUSY breaking terms determines the phenomenology and therefore the search strategies at colliders.

The most widely studied SUSY models involve mediation by gravitational interactions. In the minimal model of supergravity (mSUGRA), the vast SUSY parameter space is reduced to only five parameters that determine the low energy phenomenology from the scale of Grand Unification (GUT): the common scalar mass m_0, the common gaugino mass $m_{1/2}$, the common soft trilinear SUSY breaking parameters A_0, the ratio of the Higgs vacuum expectation values at the electroweak scale $\tan\beta$, and the sign of the Higgsino mass term $\mathrm{sgn}(\mu)$. In most of the mSUGRA parameter space, the LSP is the lightest neutralino, sleptons are lighter than squarks, and the relation among gaugino masses is given by: $m_{\tilde{g}}/3 \simeq m_{\tilde{\chi}^\pm} \simeq 2m_{\tilde{\chi}_1^0}$. At hadron colliders, standard-SUSY searches based on these models focus on production of electroweak gauginos (chargino and neutralino), and on the search for squarks and gluinos.

In gauge-mediated SUSY breaking models (GMSB), the LSP is the gravitino, $\tilde{G}$, which has very low mass ($\ll$ keV). The phenomenology depends on the nature of the next-to-lightest SUSY particle (NLSP), typically the lightest neutralino or the lightest stau, and on its lifetime. GMSB scenarios are defined by six parameters: the effective SUSY breaking scale Λ, the number of messenger fields N, the mass of the messenger field m_M, the gravitino mass factor C_G, $\tan\beta$ and the sign of μ. In the context of standard GMSB models, coloured SUSY sparticles and first and second generation sleptons are expected to be heavy ($>$1 TeV), and gaugino pair production dominates.

As a consequence of the electroweak symmetry breaking, higgsinos and electroweak gauginos mix with each other to form four neutral and two charged mass eigenstates (neutralinos and charginos, respectively). For a large fraction of parameter space, these sparticles have low mass and the cross section of the associated production of chargino and neutralino is sizable. If sleptons are sufficiently light, leptonic decays such as $\tilde{\chi}^\pm \to \tilde{l}^*\nu \to l\nu\tilde{\chi}_1^0$ and $\tilde{\chi}_2^0 \to \tilde{l}^*l \to l^+l^-\tilde{\chi}_1^0$ are enhanced, leading to very clean final states containing three isolated leptons and missing transverse energy ($\not{E}_T$). This signature has a very low expected background in the SM, but can be particularly challenging in regions of parameter space where lepton momenta are soft due to small mass differences of the SUSY particles. As a consequence, CDF and DØ search strategy is to require three charged leptons l ($l = e, \mu$) with minimum transverse momenta as low as possible, or two identified l and one isolated track ($t = e, \mu, \tau$). In the DØ search [6], additional categories of events including one identified μ, one hadronic τ and one isolated track or a
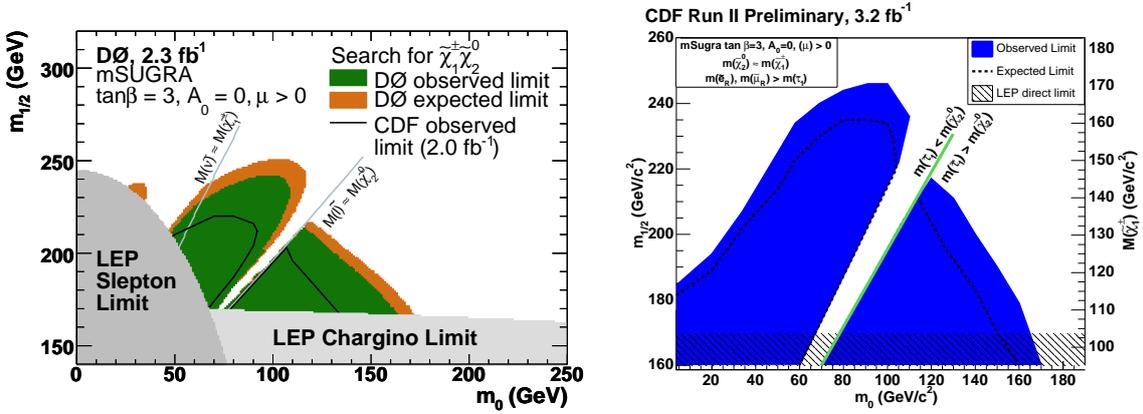
Figure 1: Limits obtained from the trilepton-signature searches performed by the DØ (left) and CDF (right) collaborations. Limits from LEP analyses are also shown.

second hadronic τ are considered, to enhance the sensitivity at large $\tan\beta$, where $\mathrm{m}(\tilde\tau)\ll\mathrm{m}(\tilde{l})$ and several τs are expected in the final state. The observed data are found to be consistent with SM predictions. In the CDF search [7], based on 3.2 fb^{-1} of data, one trilepton event passes all the stages of the selection, with a background expectation of 1.47 ± 0.21 events; 6 events are observed in the leptons+track categories, with expectation of 9.38 ± 1.44 events. Similarly, agreement between data and SM predictions is found for all lepton categories considered by the DØ analysis, based on 2.3 fb^{-1} of data. The results are translated into 95% confidence-level (C.L.) exclusion limits on the product of production cross section and leptonic branching fraction ($\sigma \times BR$). Within minimal supergravity, these limits translate into bounds on m_0 and $m_{1/2}$, for parameter $\tan\beta=3$, $A_0=0$, $\mu > 0$ and they are shown in Figure 1 (left). The gap between the two lobes in the plane corresponds to the parameter space regions where slepton masses are similar to neutralino masses and one of the leptons arising from $\tilde\chi_2^0 \to \tilde{l}^*l$ is too soft to be detected. Figure 1 (right) shows CDF upper limits on $\sigma \times BR$ as a function of the chargino mass, for $m_0=60$ GeV/c^2: chargino masses below 164 GeV/c^2 are excluded for this benchmark configuration.

The CDF collaboration recently reported on a search [8] for gaugino pairs using events with Z bosons, two or more jets and missing transverse energy. In regions of the parameter space where the mass of $\tilde\chi_2^0(\tilde\chi_1^\pm)$ is larger than the lightest neutralino by at least the mass of the $Z(W)$ boson, chargino-neutralino pairs decay into real W/Z bosons. The analysis, based on an integrated luminosity of 2.7 fb^{-1}, requires two electrons to reconstruct Z boson candidates, while W boson candidates are searched for in the di-jet invariant mass spectrum. The selection on the missing transverse energy is optimized to maximize the expected exclusion limit. Results are found in agreement with SM predictions. The extracted upper limits at 95% C.L. on $\sigma \times BR$ are between 3 and 1 pb as the $\tilde\chi_2^0$ mass increases.

The production of squarks ($\tilde{q}$) and gluinos ($\tilde{g}$), superpartners of quarks and gluons and therefore strongly-interacting particles, constitutes one of the most promising channels at the Tevatron. The cascade decay of gluinos and squarks into quarks and gluons will result in a final state consisting of several jets plus missing transverse energy coming from the undetected neutralinos. At low $\tan\beta$, depending on the relative masses of squarks and gluinos, different

event topologies are expected. If squarks are significantly lighter than gluinos, $\tilde{g}$ production is enhanced. The squark tends to decay according to $\tilde{q} \to q\tilde{\chi}_1^0$, and a dijet+$\not{E}_T$ topology is favored. If gluinos are lighter than squarks, $\tilde{g}\tilde{g}$ process dominates. Gluinos decay via $\tilde{g} \to q\bar{q}\tilde{\chi}_1^0$, leading to topologies containing a large number of jets (≥ 4) and moderate $\not{E}_T$. For $m_{\tilde{g}} \approx m_{\tilde{q}}$, a topology with at least three jets in the final state is expected. As a result, CDF and DØ collaborations have optimized three different analyses, requiring at least 2, 3 or 4 jets in the final state and missing transverse energy. No significant deviation from SM predictions is found by the CDF [9] and DØ [10] searches, carried out using 2 and 2.1 fb^{-1} of data, respectively. The results are translated into 95% C.L. upper limits on the cross section for squark and gluino production in different regions of the squark-gluino mass plane. The CDF search excludes masses up to 392 GeV/c^2 at 95% C.L. in the region where gluino and squark masses are similar and gluino masses up to 280 GeV/c^2 for every squark mass. Similar exclusion limits are found by the DØ collaboration.

If tanβ is large, then there can be a large mass splitting in the scalar bottom sector, yielding a mass to the lightest state ($\tilde{b}$) in the reach of the Tevatron center of mass energy. Assuming R-parity conservation the only particle lighter than the $\tilde{b}$ is the LSP. At Tevatron, two different searches for sbottom are performed depending on its production mechanism. Direct $\tilde{b}$ production with the subsequent sbottom decay to a b-quark and the lightest neutralino ($\tilde{\chi}^0$), leads to the main signature for $\tilde{b}$ detection which includes two b jets and $\not{E}_T$. Due to the presence of these b jets in the final state, applying a b tagging algorithm is a mandatory tool to enhance the sensitivity by reducing backgrounds. The B hadrons in jets coming from b quark fragmentation have an average flight path of about 500 μm, yielding secondary vertices relative to the inter-action point (primary vertex). The tagging algorithms are optimized to find these sencondary vertices using different approaches in each experiment.

Recent analyses by the CDF [11] and DØ [18] collaborations have exploited the properties of these final states to increase the sensitivity of the search for sbottom and have extended previous limits.

The CDF analysis was performed optimizing the selection of events with cuts on $\not{E}_T$ and in the scalar sum of the transverse energy of the jets in a dijet sample with the two jets tagged as coming from a bottom quark. Several optimization were performed in order to increase sensitivity in different regions of the phase space, basically identified with the mass difference between the sbottom and the neutralino. No significant discrepancy was observed between the observed number of events and the expectations from the SM. Plot on the right-side in Figure 2 show the obtained limit in the sbottom-neutralino mass plane. The DØ sbottom search was done as part of the analysis searching for third-generation leptoquarks decaying into bottom+neutrino, which yields a very similar topology (see below). 95% C.L. limit on sbottom mass was extended to $m(\tilde{b}) > 240$ GeV/c^2 for a neutralino mass smaller than 80 GeV/c^2, as shown in the left-side plot in Figure 2.

A parallel approach at Tevatron is to search for the $\tilde{b}$ production through gluino ($\tilde{g}$) decays. Under the assumption that mass of the $\tilde{g}$ is smaller than mass of the $\tilde{q}$, but larger than mass of the lightest $\tilde{b}$, the gluino pair production, $p\bar{p} \to \tilde{g}\tilde{g}$ is one of the dominant SUSY processes. After production the gluino decays to $\tilde{g} \to b\tilde{b}$ with the subsequent sbottom decay to a b-quark and $\tilde{\chi}^0$, $\tilde{b} \to b\tilde{\chi}^0$. Although involving more particles and constraints in the SUSY spectrum, this last approach is stronly motivated by the fact that the gluino pair production cross section is large ($\sigma(g\tilde{g}) \sim 10 \times \sigma(b\tilde{b})$) compared to direct sbottom pair production of similar mass. The analysis by the CDF collaboration [12], requiring large $\not{E}_T$ and at least two b-tagged jets finds a very good agreement with the SM predictions and the obtained limit excludes the presence
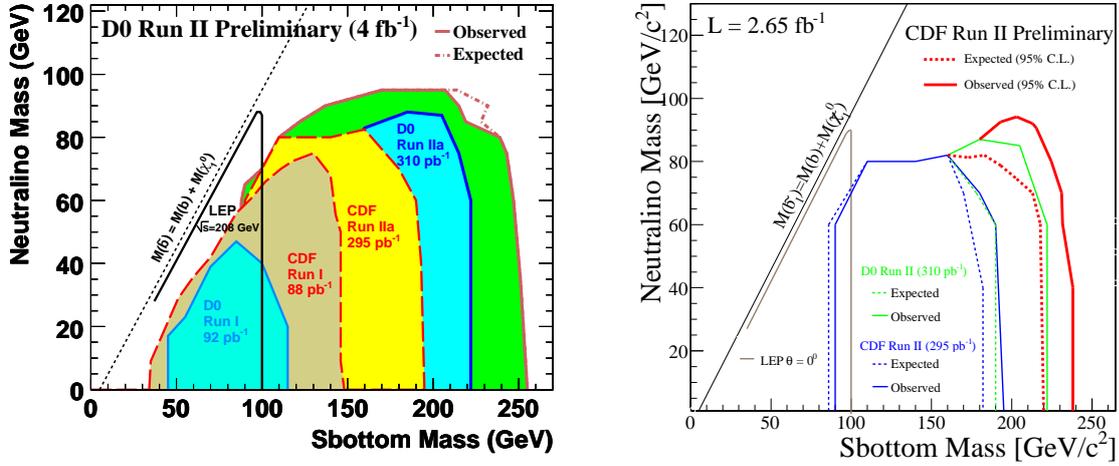
Figure 2: Limits on sbottom pair production at the Tevatron by the DØ (left) and CDF (right) collaborations. Limits from LEP analyses are also shown.

of gluinos with $m(\tilde{g}) < 350$ GeV/c^2 at 95% C.L. nearly independent of the $\tilde{b}$ mass.

As in the case of the sbottom, the mass splitting between the two stop quarks states $(\tilde{t}_1, \tilde{t}_2)$ may be large due to the large mass of the top quark. This gives the possibility that the lightest stop state, $\tilde{t}_1$, might be the lightest squark, and even lighter than the top quark.

Three different seaches for $\tilde{t}_1$ particles are performed at Tevatron depending on their decay mode. The first scenario is accessible in the range $m_{\tilde{t}_1} < m_b + m_{\tilde{\chi}^+}$ and $m_{\tilde{t}_1} < m_W + m_b + m_{\tilde{\chi}^0}$. The dominant $\tilde{t}_1$ decay mode in this model is the flavor changing process $\tilde{t}_1 \to c\tilde{\chi}^0$ which is typically assumed to occur with 100% branching fraction. The $\tilde{t}_1 \to t\tilde{\chi}^0$ decay is kinematically forbidden over the $\tilde{t}_1$ mass range currently accessible at Tevatron, and the tree level four-body decays $\tilde{t}_1 \to b f f' \tilde{\chi}^0$ may be neglected. In this particular case the experimental signature consists of two c-jets and $\not{E}_T$ from the undetected $\tilde{\chi}^0$ [13]. A recent analysis by CDF [14] exploited the properties of jets originating from charm in order to reduce the background coming from bottom and light jets while enhancing the signal and the sensitivity of the analysis. This was achieved with a Neural-Network based discriminant using the displaced vertex and track properties of the jets tagged as originating from heavy-flavour jets. The use of this discriminant allows to increase the sensititivy of this search far beyond the increase in luminosity.

In the second scenario one assumes that $BR(\tilde{t}_1 \to bl\tilde{\nu}) = 1$, where $\tilde{\nu}$ is the scalar neutrino (sneutrino). Among possible stop decays, this final state is one of the most attractive from the experimental point of view; in addition to a b quark, it benefits from the presence of a lepton with high transverse momentum with respect to the beam axis. The sneutrino is either the LSP or decays invisibly: $\tilde{\nu} \to \nu\tilde{\chi}^0$ or $\nu\tilde{G}$ where the lightest neutralino, $\tilde{\chi}^0$, or the gravitino, $\tilde{G}$, is the LSP. The signal topology consists of two isolated leptons, $\not{E}_T$, coming mainly from undetected sneutrinos, and jets [15].

The third scenario happens when $\tilde{t}_1 \to b\tilde{\chi}^+ \to b\tilde{\chi}^0 l\nu$ assuming a 100% branching ratio of the stop squark into a b quark and chargino, and allow for the chargino to dileptons through a variety of channels. These stop events produce signatures similar to those of SM top quark
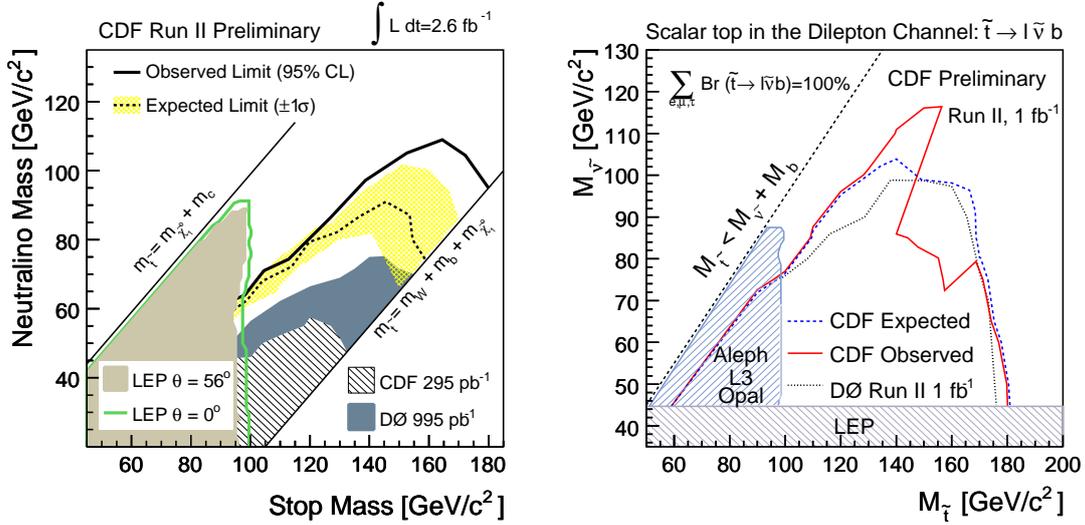
Figure 3: Limits for stop pair production at the Tevatron for the charm+LSP (left) and the lepton+bottom+LSP (right) decays.

decays, and could potentially be hiding in the top samples of the Tevatron data.

No significant deviation from the SM prediction was observed in any of the previous searches, and the results were used to extract exclusion limits for the cross section of the described process. Plots in Figure 3 show the exclusion limits at 95% C.L in the neutralino-stop mass plane for stop decaying into charm+neutralino, the exclusion limits at 95% C.L in the sneutrino-stop mass plane for stop decaying into $bl\tilde{\nu}$. Limits extracted in the third scenario may be found in reference [16].

3 SUSY Searches with photons

Gauge-Mediated Supersymmetry Breaking (GMSB) Models usually allow the neutralino to decay in a photon and a gravitino, which is the LSP as mentioned before. Under these assumptions the production of neutralinos that would eventually decay into gravitino and photon would provide a final state with two photons and $\not{E}_T$ from the escaping gravitinos. CDF has performed the search for this process [17] using the timing of the electromagnetic calorimeter to reject events that are out-of-sync with the interactions, which are mostly related to background such as cosmics. The analysis was performed by electing events containing two photons, large $\not{E}_T$ and having large H_T defined as the scalar sum of transverse energy of all objects.

The sensitivity was increased by using a probabilistic model to assign a significance of the observed $\not{E}_T$ in the event. The model accounts for resolution effects expected for the observed objects and provides a new handle to reject events in which the $\not{E}_T$ is originated by a mismeasured object. This tool also allows to estimate the QCD background from data, as done in this analysis.

With all the tools in hand, and after the final optimization, no events were observed, consistent with a standard model background expectation of 1.4±0.4 events. This results extend the sensitivity to previously unexplored regions and the good agreement in the final selection between data and SM expectation translates into a 95% C.L. limit set to a mass of the neutralino larger than 149 GeV/c^2 for a lifetime smaller than 2 ns. It should be noted that the use of timing to reject background makes this search insensitive to long-lived neutralinos.

4 Searches for leptoquarks

Other possible extensions of the SM suggests the existence of a new kind of particle, generically known as *leptoquarks* having both barion and lepton number different from zero. These particles are scalar or vector bosons which would mediate lepton-quark transitions in the different GUT or compositeness models, among others. At colliders, the searches are optimized for different final states, depending on the generation of the leptoquark, which determines to which families they couple. For this reason, interpretation of the results are commonly done in different parameter planes.

Related to the third generation, DØ has performed a recent search [18] of leptoquarks decaying to bottom and neutrino by requiring bottom tagging of the final jets. The analysis did not find a significant excess in the data that might be attributed to leptoquarks and therefore a limit was set which excludes at the 95% C.L. third generation scalar leptoquarks with masses smaller than 252 GeV/c^2.

Regarding leptoquarks, the experiments at the HERA collider are very competitive since HERA is the most efficient collider to produce leptoquarks that couple to the first generation, since they are produced in resonance. A recent analysis by H1 [19] of the full data sample look for leptoquarks as a resonance in the invariant mass of the final lepton and the leading jet. Good agreement with the SM expectation is observed, as shown in the upper plots in Figure 4 for the electron and positron data samples and for neutral-current (left plots) and charged-current (right plots) interactions. Out of this agreement, 95% C.L. limits were obtained and are shown in the lower plots in Figure 4 compared to the limits obtained at LEP and at Tevatron. The current best limit obtained by the ZEUS collaboration is $m/\lambda > 0.41$ 1.88 TeV/c^2 done in the analysis searching for contact interactions [20].

It should be noted that the limits at HERA goes beyond the actual kinematic limit due to the additional sensitivity achieved by the u channel.

5 Searches for resonances

Some extensions of the SM suggest the existence of new resonances which would eventually decay into known SM particles. In the case that the width is much smaller than the detector resolution related to the corresponding objects, the search may be performed in a model-independent way and just search for the presence of a resonance over the continuous spectrum. CDF [24] and DØ [25] have studied the distribution of the dielectron invariant mass in a clean event selection. The distributions in Figure 5 show the results from the two collaborations, in which no significant discrepancy has been found, although the CDF distribution shows a visible excess around $M(ee) > 240$ GeV/c^2 which is not confirmed by the DØ analysis with a larger dataset.
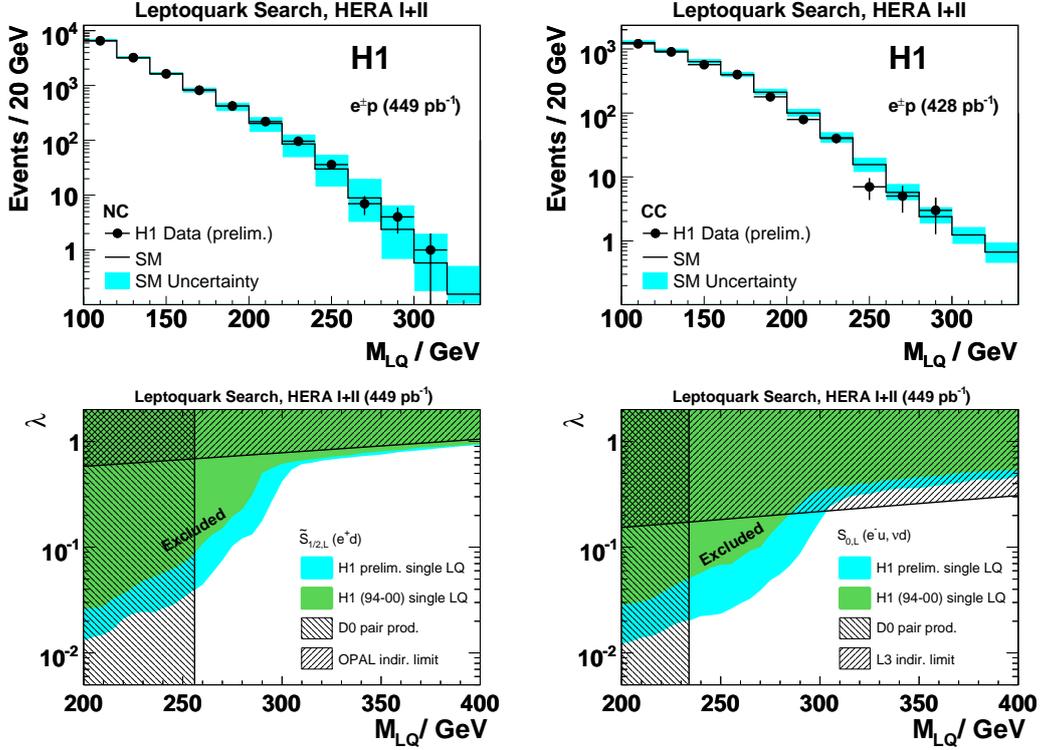
Figure 4: Distribution of the lepton+jet invariant mass and current leptoquark limits by the H1 search. See text for details.

Similar searches are done in the dimuon channel where the resolution commonly gets worse as the mass improves. For this reason, the CDF collaboration has performed the analysis [26] by looking for an excess in the distribution of the $1/m(\mu\mu)$ variable, for which the resolution is constant. In this analysis, done with 2.3 fb^{-1} of data, measurements are in good agreement with the SM predictions and no excess is observed. Limits are set for different models, and especifically a limit on the mass of a SM-like Z' of $m(Z') > 1.03$ TeV/c^2 at 95% C.L.

6   Searches for large extra-dimensions

If gravity propagates in $4 + n$ dimensions (as a difference to the other interactions, confined in 3+1 dimensions), the effective Planck scale could be small (perhaps of the order of ~ 1 TeV and gravity becomes comparable in strength to the electroweak interaction. The typical golden channel for this at Tevatron is the production of a single high-ET photon and $\not{E}_T$ from the undetected graviton, which is typically a Kaluza-Klein mode. Analyses looking for this signature have been performed by CDF [21] and DØ [22] using the Tevatron data. Good agreement with the SM expectations has been observed in both cases and the results were used to set limits on the extradimension scale at the order of 1 TeV. These limits are more stringent than those obtained at LEP for a number of extra dimensions larger than 3.
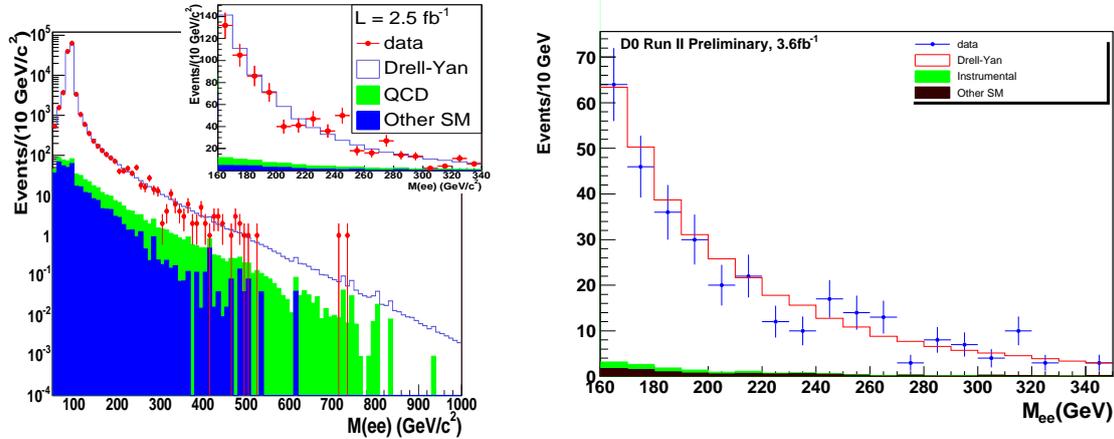
Figure 5: Invariant mass distribution for electron+positron pairs in the resonance search performed by the CDF (left) and DØ (right) Collaborations. See text for details.

At HERA the presence of extra dimensions may be observed as a deviation of the total ep cross section at high energies where gravity effects become comparable to the electroweak interaction. The contribution of the graviton exchange is described in the model as a coupling depending on the effective Planck scale (M_s), which sets the energy scale of the extra dimensions. The study of the high Q^2 distribution the ZEUS Collaboration [20] shows a good agreement with the SM expectations, as shown in Figure 6. A limit of $M_s > 0.94$ TeV at 95% C.L. has been set with the full dataset. Previous limits by H1 based on the Run I dataset the limit of $M_s > 0.48$ (0.72) TeV/c^2 [23] for a constructive (destructive) interference between the graviton and the electroeweak boson exchange.

7   Multileptons at HERA

In the context of signature-based searches, the experiments are also performing analyses which are intended to look for striking final states for which the SM processes have very small cross section.

For this one of the most interesting signatures is the multilepton production at HERA, in which the HERA sample shows an excess in the positron data. Recently the two collaborations have performed a combined analysis [27] with their full data samples to extract the highest sensitivity to this final state.

In the analysis the data shows an excellent agreement for the electron data. As a function of the sum of the p_T of the leptons, the positron data shows good agreement for small values of that variable, but a clear excess of events for which that sum is larger than 100 GeV/c^2. Numbers in Table 1 summarizes the comparison in that region for the two data samples.

Final statistical significance of the excess in the positron data is 2.6σ but it should be remarked that most of the significance is coming from the H1 dataset.

Multi-Leptons at HERA (0.94 fb^{-1})				
$\sum P_T > 100/c^2$ GeV				
Data sample	Data	SM	Pair Production (GRAPE)	NC DIS + QEDC
e$^+$p (0.56 fb^{-1})	7	1.94 ± 0.17	1.52 ± 0.14	0.42 ± 0.07
e$^-$p (0.38 fb^{-1})	0	1.19 ± 0.12	0.90 ± 0.10	0.29 ± 0.05
All (0.94 fb^{-1})	7	3.13 ± 0.26	2.42 ± 0.21	0.71 ± 0.10

Table 1: Number of observed and expected events containing two or more high-p_T isolated leptons in the full HERA data. Events in which the sum of the p_T of the leptons is larger than 100 GeV/c^2 are counted and organize according to the charge of the initial lepton. The grand totals are also listed.

8   Searches of Hidden-Valley signatures

Hidden valley models – some of them including SUSY – introduce a new "hidden" sector, which is very weakly coupled to the SM particles. A recent DØ analysis [28] searches for a new light gauge boson, a dark photon (γ_D), considering a scenario in which SUSY particles are pair-produced and decay into SM particles and the lightest neutralino. The $\tilde{\chi}_1^0$ can decay into the hidden sector state (darkino, $\tilde{X}$) plus either a photon or a dark photon, the latter decaying through its mixing with a photon into fermion pairs. The branching fraction (BR) of $\tilde{\chi}_1^0 \to \gamma_D \tilde{X}$ is a free parameter of the model. If it is small, decays into γ dominate, and the signature is the same as in GMSB models. Due to the overwhelming SM jet backgrounds, dark photons are searched for in isolated electron or muon pairs. Events are required to contain two spatially close leptons, a photon and $\not{E}_T$ arising from the escaping darkinos. No evidence of dark photon signal is found. Limits are set on γ_D production cross section and interpreted as limits on the lightest chargino mass as a function of the dark photon mass and the neutralino branching fraction. Figure 7 shows the exclusion limit set by this analysis. It should be noted that the sensitivity gets worse when the branching ratio of the neutralino decaying to photon and darkino is small dure to the requirement of a photon in the final state. It also gets worse when that branching ratio approaches 100%. In this case this search is in fact less competitive when compared to the standard diphoton+$\not{E}_T$ GMSB seach.

In Hidden-Valley models another possible final state is given by the existence of long-lived particles which decay into a bottom-antibottom quark pair. This decay takes place inside the detector volume and further from the beam-axis than it is commonly used to reconstruct B-hadron decays and for that reason this kind of topology might have been missed in previous searches which include displaced vertices and decays. On the other hand this kind of analysis is very challenging since it require a good understanding of the material and the background due to particle-detector interactions (conversions, inelastic interaction with nuclei) or decays in flight of kaons (and others). The results of the search performed by DØ [29] were interpreted in a model in which the Higgs boson decays into the Hidden-Valley particles producing the b-quark pair. No significant discrepancy was observed in the properties of the two secondary vertices when comparing the data to the SM expectations and therefore limits were set that represent the first constraints at a hadron collider on pair-production of neutral long-lived particles decaying in distances of 1.6-2.0 cm.
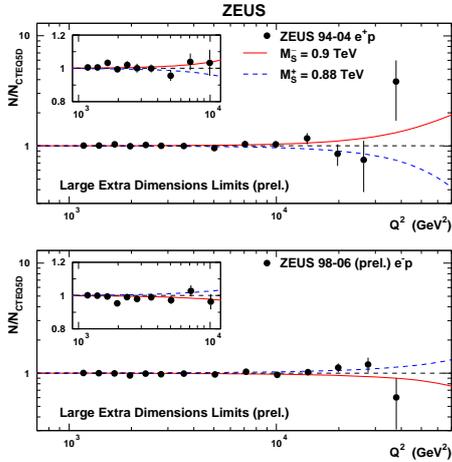
Figure 6: Ratio of the measurements to the SM expectation for the High-Q^2 cross section as measured by the ZEUS Collaboration in the positron (above) and electron (below) data samples.
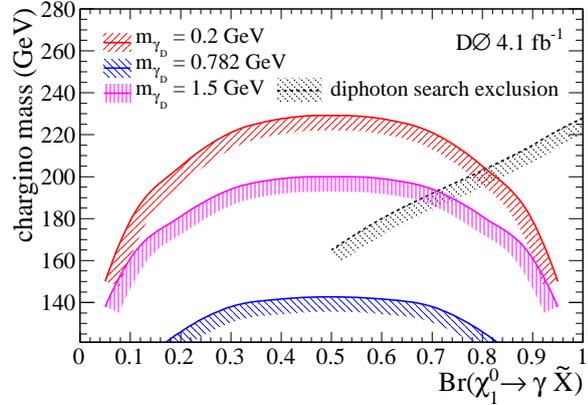
Figure 7: Limit in the chargino mass obtained from the Dark Photon search by the DØ Collaboration. Limit is plotted as a function of the neutralino branching ratio to photon+LSP and compared to the standard GMSB-based diphoton+$\not{E}_T$ search.

9   Global searches of New Phenomena

In order to avoid any possible bias from the assumed model and signature, a different strategy has been put in place which looks for discrepancies in all possible final states (and relevant variables). The advantage of this kind of studies is that they are completely independent of the model, and therefore avoid any bias from the assumptions on the structure of the New Physics. On the other hand, the interpretation of any observed discrepancy must be interpreted taking into account the large number of observables (as trial factors) and therefore the significance must be properly corrected.

H1 performed a global analysis of the full dataset studying all the possible final states [30] and found no significant discrepancy with the standard model prediction in the electron and positron data.

Both Tevatron experiments have performed these studies in their datasamples [31]. Although some discrepancies have been found, the related significances is not high enough to claim a deviation that cannot be explained by the SM predictions. Studies of the larger dataset currently being collected will be very helpful to clarify the situation in the distributions that are not correctly described by the predictions.

10   Conclusions

The most recent results on searches for physics beyond the SM at the HERA and Tevatron experiments have been reported. No evidence of New Physics has been found yet in both direct

analysis and more inclusive searches. Out of these studies stringent exclusion limits have been extracted in several models.

Further analyses of the HERA and the Tevatron data could reveal hints of New Physics, or place more severe limits on the vast SUSY parameter space as we come into the LHC era.

I acknowledge the dedicated efforts of the working groups of the four collaborations, reflected in the results presented here, in particular the conveners and the physics coordinators for all the help and support in prparing the talk and these proceedings. I also thank the organizing committee for the oportunity to present all these results at the conference.

References

[1] E. Gildener, Phys. Rev. **D14** 1667 (1976).

[2] J. Wess and B. Zumino, Nucl. Phys **B70** 39 (1974);
For a review of SUSY, see S.P. Martin, hep-ph/9709356, and references therein.

[3] J. R. Ellis, S. Kelley, and D.V. Nanopolous, Phys. Lett. **B260** 131 (1991).

[4] A.H. Chamseddine, R. Arnowitt, and P. Nath, Phys. Rev. Lett. **49** 970 (1982).

[5] S. Ambrosiano, G.L. Kane, G.D. Kribs, S.P. Martin and S. Mrenna, Phys. Rev. **D54** 5395 (1996).

[6] DØ Collaboration, V.M. Abazov *et al*, Phys.Lett. **B680** 34 (2009).

[7] CDF Collaboration, Public Note 9817 (2009);
All CDF public results and notes are listed in *http://www-cdf.fnal.gov/physics/exotic/exotic.html*

[8] CDF Collaboration, Public Note 9791 (2009).

[9] CDF Collaboration, T. Aaltonen *et al*, Phys. Rev. Lett. **102** 121801 (2009).

[10] DØ Collaboration, V.M. Abazov *et al*, Phys. Lett. **B660** 449 (2008).

[11] CDF Collaboration, Public Note 9969 (2009).

[12] CDF Collaboration, T. Aaltonen *et al*, Phys. Rev. Lett **102** 221801 (2009).

[13] DØ Collaboration, V.M. Abazov *et al*, Phys. Lett. **B665** 1 (2008).

[14] CDF Collaboration, Public Note 9834 (2009).

[15] DØ Collaboration, V.M. Abazov *et al*, Phys. Lett. **B675** 289 (2009);
CDF Collaboration, Public Note 9775 (2009).

[16] CDF Collaboration, Public Note 9439 (2009).

[17] CDF Collaboration, arXiv:0910.3606v2, submitted to Phys. Rev. Lett.

[18] DØ Collaboration, Conference Note 5931-CONF (2009).

[19] H1 Collaboration, Public Note H1Prelim-07-164.

[20] CDF Collaboration, Public Note ZEUS-prel-09-013 (2009).

[21] CDF Collaboration, T. Aaltonen *et al*, Phys. Rev. Lett **101** 181602 (2008).

[22] DØ Collaboration, Conference Note 5729-CONF (2008).

[23] H1 Collaboration, C. Adloff *et al*, Phys.Lett. **B479** 358 (2000).

[24] CDF Collaboration, T Aaltonen *et al*, Phys. Rev. Lett. **102** 031801 (2009).

[25] DØ Collaboration, Conference Note 5923-CONF (2009).

[26] CDF Collaboration, T Aaltonen *et al*, Phys. Rev. Lett. **102** 091805 (2009).

[27] H1 Collaboration and ZEUS Collaboration, F.D. Aaron *et al*, JHEP 0910:013 (2009).

[28] DØ Collaboration, V. Abazov *et al*, Phys. Rev. Lett. **103** 081802 (2009).

[29] DØ Collaboration, V. Abazov *et al*, Phys. Rev. Lett. **103** 071801 (2009).

[30] H1 Collaboration, F.D. Aaron *et al*, Phys. Lett. **B674** 257 (2009).

[31] CDF Collaboration, T Aaltonen *et al*, Phys. Rev. **D79** 011101 (2009);
DØ Collaboration, Conference Note 5777-CONF (2009).

Linear Collider

Eckhard Elsen[1]

[1]DESY, Notkestraße 85, 22607 Hamburg, Germany

Abstract

A linear collider is the next large project of particle physics following the commissioning of the LHC. By 2012 feedback can be expected from the LHC on the spectrum of *new physics* below 1 TeV. This information will be timely for a revision of the European Strategy for particle physics and the possible decision for a linear collider for which the ILC is the only contender that could promptly be realized. Similar strategic considerations are made in Japan so that currently two regions are exploring the implications of hosting the ILC. A multi-TeV collider would require considerable R&D, which is well under way for the CLIC project. The status of these two projects is described.

1 Introduction

Since a long time the key elements of the strategy of particle physics have been clearly laid out: following the commissioning of the *Large Hadron Collider* LHC a linear collider will be the next large project of particle physics. This strategy has most recently been formulated in 2006 in the European Strategy issued by the CERN Council [1, 2] when it assumed its role for coordination of the programmes in Europe. The outcome of that strategy process culminated in a list of recommendations. Explicitly, the first three recommendations read:

- The LHC will be the energy frontier machine for the foreseeable future, maintaining European leadership in the field; the highest priority is to fully exploit the physics potential of the LHC, resources for completion of the initial programme have to be secured such that machine and experiments can operate optimally at their design performance. A subsequent major luminosity upgrade (SLHC), motivated by physics results and operation experience, will be enabled by focussed R&D; to this end, R&D for machine and detectors has to be vigorously pursued now and centrally organized towards a luminosity upgrade by around 2015.

- In order to be in the position to push the energy and luminosity frontier even further it is vital to strengthen the advanced accelerator R&D programme; a coordinated programme should be intensified, to develop the CLIC technology and high performance magnets for future accelerators, and to play a significant role in the study and development of a high-intensity neutrino facility.

- It is fundamental to complement the results of the LHC with measurements at a linear collider. In the energy range of 0.5 to 1 TeV, the ILC, based on superconducting technology, will provide a unique scientific opportunity at the precision frontier; there should be

a strong well-coordinated European activity, including CERN, through the Global Design Effort, for its design and technical preparation towards the construction decision, to be ready for a new assessment by Council around 2010.

At the same time there is considerable interest in Japan to host the ILC and correspondingly a similar plan for particle physics has been developed.

Following the magnet incident at the LHC start-up in 2008 these time lines will have to be somewhat revised. As the LHC turns on for physics production the machine performance will be better understood. The upgrade requirements will become clearer and so does the schedule that can be associated with this upgrade. Both the evolution of the luminosity at the LHC and of the centre of mass energy will have to be folded in to arrive at reasonable predictions for the upgrade needs of the LHC.

While the physics programme of a linear collider operating in the energy range up to 500 GeV [3, 4, 5, 6] has been fully worked out it will be helpful to receive guidance from the Large Hadron Collider: there is a good chance that the LHC may discover a light Higgs particle. Likewise will the spectrum of "low energy" SUSY particles – if realized in nature – define the homework for a linear collider. The physics potential at high energies above 1 TeV is largely uncertain; too little is known of the mass spectrum of new particles, their signatures and width and too large is the variety of options for firm predictions.

Given this uncertainty the technical development for the linear collider follows a dual approach: a strong emphasis on the R&D for a linear collider reaching well into the TeV region for which the *Compact Linear Collider* CLIC provides a proposal for technical realization and the preparation of the construction of the *International Linear Collider* ILC, initially targeted to operate at energies up to 500 GeV with an upgrade option up to 1 TeV, where a full physics case has been developed.

2   Brief Reminder of the Physics Case for a Linear Collider

The physics case for the linear collider has often been made and is summarized in [6]. The advantage lies in the simplicity of the initial state, the well-defined quantum numbers for the hard interaction and the well defined centre of mass energy of the hard interaction. As an often quoted example Figure 1 displays the recoil mass spectrum of the two muons from the decay $e^+e^- \rightarrow ZH$ with $Z \rightarrow \mu^+\mu^-$ for an assumed Higgs mass of 120 GeV and a centre of mass energy of 350 GeV. It is obvious that even for an invisibly decaying Higgs particle the mass can be well reconstructed if the detector provides the appropriate resolution. It is thus clear that the detector performance has to be fully optimized and that these detectors will be high precision instruments, in line with the theme of high precision for the layout of the collide proper.

3   Linear Colliders

It has long been recognized [7] that linear colliders provide an alternate way to circular colliding beam machines. They are more power efficient and hence more cost-effective at high energies where synchrotron radiation becomes prohibitive for circular machines. They are challenged to provide a respectable luminosity where beams of minute dimensions are required. The only high-energy e^+e^--collider built to date is the SLAC Linear Collider SLC, which operated at
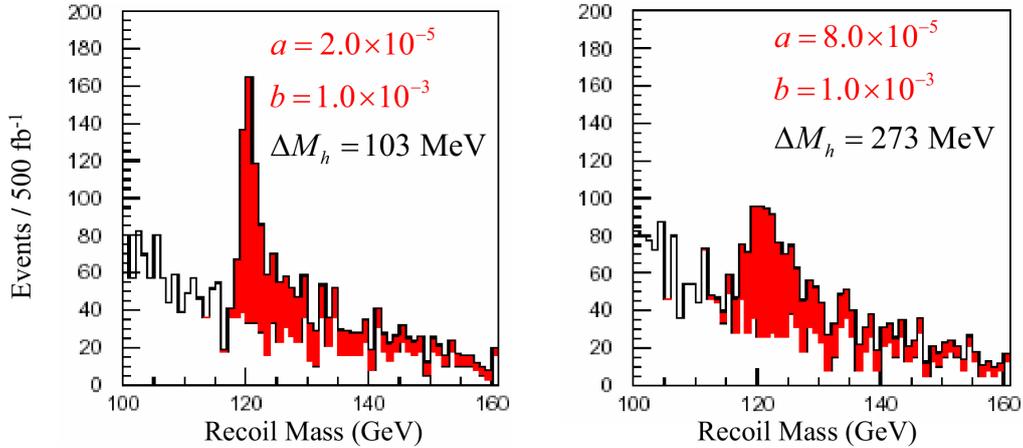
Figure 1: The Higgs boson recoil mass spectrum for two assumed resolutions for decays $e^+e^- \rightarrow ZH$, where the Z decays into 2 muons. The quantities a and b refer to the terms in the transverse momentum resolution $\sigma p_t/p_t = ap_t \bigoplus b/\sin\theta$ (from ref, [6]

the centre of mass energy around the Z-mass and provided highly polarized electrons. (With polarization of only one beam the case could be made that precise knowledge of yet another initial state quantity provides almost an order of magnitude more sensitivity in electroweak measurements.

Two technologies based on this radio-frequency cavities have been developed: a traveling wave accelerator with fully loaded structures operated in the *X-band* at 12 GHz and a standing wave accelerator using 1.3 GHz *L-band*-technology. The *X-band*-technology, originally explored for klystron operation [4, 5], has now become the baseline for the *Compact Linear Collider* design, which is the key linear collider project at CERN in the framework of the CLIC collaboration. The *L-band* technology based on superconducting RF structures constitutes the state of the art for a high-energy collider that could be built today.

Compact Linear Collider

The Compact Linear Collider (CLIC) is a linear collider design study that has emerged from acceleration ideas developed in the 80ies [8]. It uses high-frequency, high-gradient copper structures to accelerate the beam; the copper structures are excited by a high-current drive beam that runs parallel to the accelerator. The wakefields of the drive beam are transferred to the main beam. Following an optimization study [9] of the parameters the frequency has now been lowered to 12 GHz (from the original 30 GHz). The layout of the facility is shown in Figure 2.

The main e^+- and e^--beams are injected at 2.4 GeV into a predamping ring (PDR) and transferred to a subsequent damping ring (DR) to achieve the low emittance. A bunch compressor reduces the bunch length before the beam is accelerated to 9 GeV in a booster linac. These beams are transferred over roughly 21 km to the start of the respective linac section to be accelerated to 1.5 TeV in the actual linac. The RF power for the linac is extracted from the
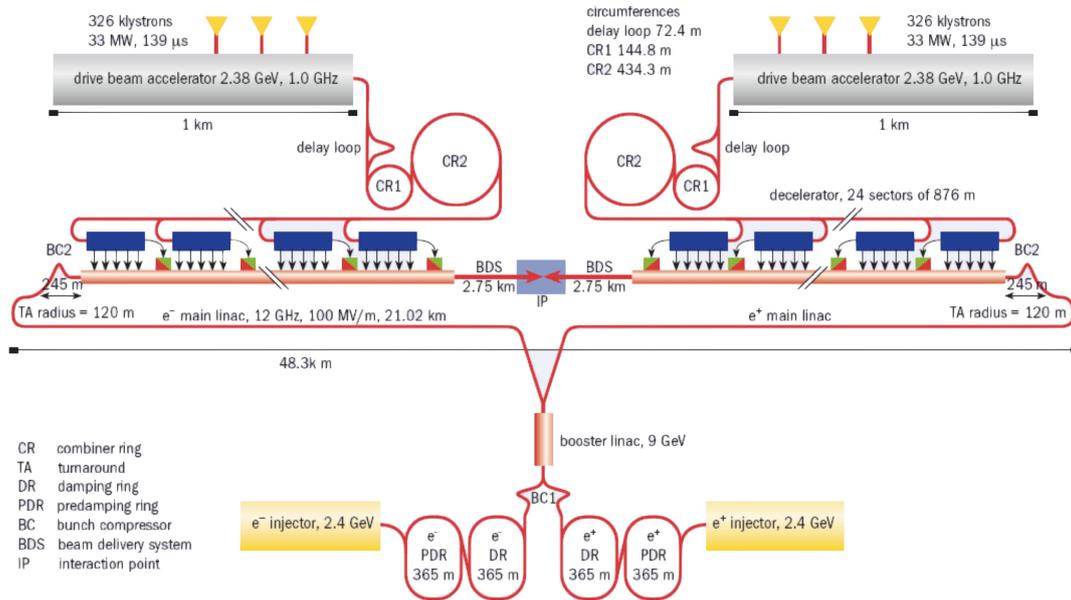
Figure 2: The layout of the Compact Linear Collider for operation at 3 TeV. The lower part shows the generation of the high-energy beam; the upper part describes the generation of drive beams.

drive beam.

The drive beams are generated in 1 km long conventional linacs operating at 1 GHz. Each of these high power linacs is equipped with 326 klystrons that accelerate a $139\,\mu$s pulse to 2.4 GeV. These linacs are highly efficient so that essentially no power is reflected under full beam loading. The 1 GHz bunch pattern is compressed to a 12 GHz train by using a delay loop and a two combiner rings that place subsequent bunches onto the adjacent empty bunch location and thus achieve a time compression by a factor two, three and four respectively. At the same time the current increases to 100 A. These trains are transferred to the respective acceleration section of $\sim$900 m length, where the drive beam power is extracted in the Power Extraction Structures (PETS), cf. Figure 3.

The wakefield is coupled into the accelerating structures of the main beam. Note that while it is the wakefield of the drive-beam that excites the RF in accelerating structure the principle should not be confused with the wakefield acceleration that uses the wakefield directly to accelerate particles, eg. in a plasma. Instead, the principle is better thought of as a very long klystron in which the RF power is delivered when and where it is needed. It is in fact this principle that results in the power efficiency of the two-beam acceleration.

Many aspects of the CLIC principle have been tested over the past decades [10]. The CTF3 test facility at CERN has demonstrated amongst others the successful time compression from 1 GHz to 12 GHz and the highly efficient power transfer from klystron to the drive beam. The beam has been extracted into the CLEX facility where the deceleration of the beam will be tested while the beam quality can be monitored. In addition the CLEX facility will enable tests of the power extraction onto a dedicated witness bunch.
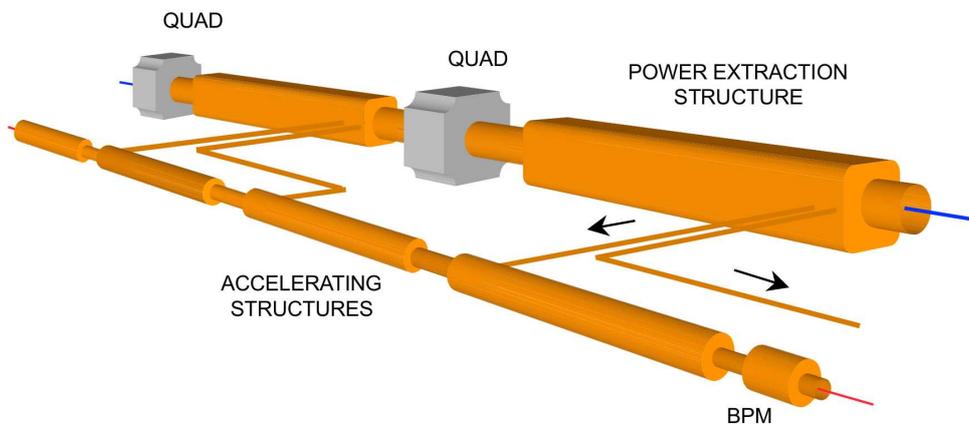
Figure 3: Principe of two-beam acceleration: as the high-current drive beam travels through the Power Extraction Structure the wakefield is coupled into the accelerating structures of the main beam.

The success of the CLIC concept hinges on several aspects that need to be demonstrated on a system level. At this time these challenges are the *high accelerating gradient* and the *beam stability*. CLIC is to operate at accelerating gradients of $100\,\mathrm{MV/m}$. At these peak fields electric breakdowns become serious. Given the large number of accelerating structures the smallest possible breakdown rate is required. Figure 4 demonstrates proof of existence for a structure that yielded a breakdown rate below 10^{-6} after sufficient training of $1200\,\mathrm{h}$. Note, however, that *Higher Order Modes* (HOM) were not damped in this structure and evidently no beam was traversing the structure.

The beam stability is tightly coupled to the stability of the entire accelerator structure. Given the high frequency of CLIC all dimensions are small; in particular the iris of the structure. A beam that propagates only slightly off-axis will be transversely deflected over its longitudinal dimensions. The CLIC structures are hence actively stabilized to maintain the required spatial accuracy.

The long-term optimistic schedule fro CLIC, only technically constraint, foresees to provide a Conceptual Design Report by the end of 2010. A Technical Design Report is to be issued by 2015, which would formally allow the project to proceed. It should be noted however, that a system test of the individual components will not have been possible by that time. In particular, the handling of the drive beam of $2.4\,\mathrm{GeV}$, which is exhausted down to 10% of its energy over a length of $\sim 900\,\mathrm{m}$ will not have been demonstrated. In addition, the power transfer onto the main beam will not have been tested under operational conditions. The CLIC collaboration is developing concepts to circumvent these challenges. – The construction time for CLIC is canonically assumed to be 7 to 8 years.

In addition the viability of the entire concept hinges on the mandatory progress of the high gradient programme for the CLIC structures. To date only small scale tests have been carried out and the actual operational gradient under beam loading needs to be demonstrated.
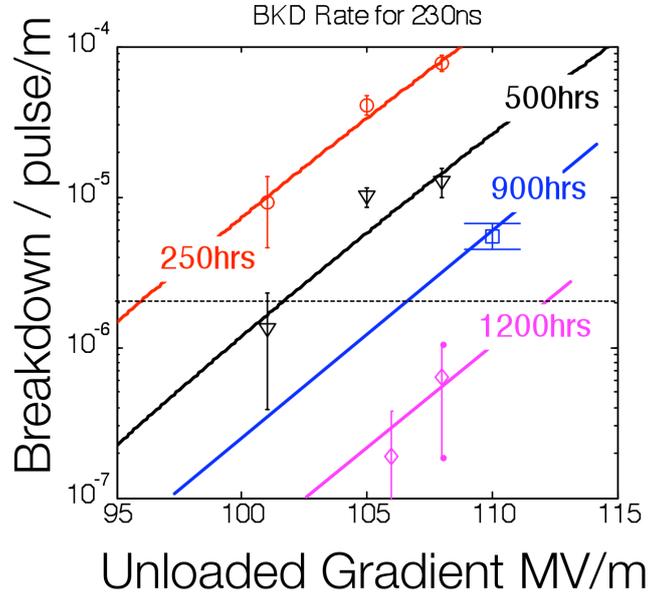
Figure 4: The breakdown rate of a unloaded 12 GHz CLIC structure after a considerable training time. After 1200 h the structure satisfies the breakdown requirement for gradients above 100 MV/m.

International Linear Collider

The International Linear Collider (ILC) is the technical solution to building an e^+e^--collider operating in the energy range from 100 GeV up to 500 GeV with an upgrade option to 1 TeV. It is based on superconducting RF technology which has been selected as the most suitable technology for such a machine following the deliberations of the ITRP in 2004 [11]. This decision led to the creation of the *Global Design Effort* (GDE) that brought together all experts and laboratories to design such a collider and eventually realize the machine. The GDE under the leadership of Prof.B. Barish is a virtual organization that prepares the machine independent of the site so that all regions are enabled to bid for the project.

The GDE has led to a reference design report (RDR) that was published in 2007 [12]. It includes a cost estimate of the ILC and forms the basis for further optimization. The layout resulting from the RDR is depicted in Figure 5.

The ILC extends over a length of ∼30 km and is laid out around a central campus that houses the beam sources and the damping ring and the interaction point of the two beams. Two detectors are foreseen at the interaction point. These detectors will be operated in a *push-pull* configuration[1], which is housed in the same experimental hall. The experimental hall also

---

[1]This configuration has been chosen over two separate beam delivery systems which seem more demanding to realize and yield effectively the same integrated luminosity. Note that the switch-over time needs to be small.
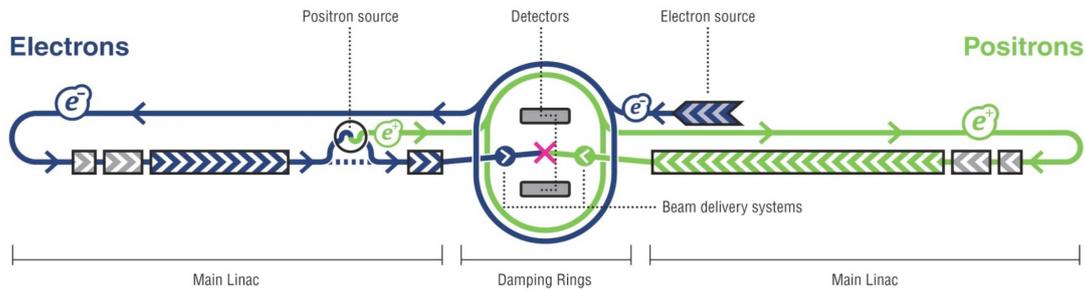
Figure 5: Schematic layout of the ILC according to the Reference Design Report. The whole complex stretches over length of 30 km

houses the final quadrupole triplet which is needed to focus the beam to the small dimensions at the interaction point.

Superconducting linacs are more efficient the longer the pulse train of bunches. Standing wave accelerators profit from the stored energy in the cavities of which only a small fraction is transferred to the individual bunch. The extracted energy is replenished in between bunches to maintain a constant accelerated field. Were it not for the overall cryogenic load such a collider would best be operated in continuous mode. To pick a compromise a train duration of 1 ms has been chosen for the ILC with a repetition rate of 5 Hz. This is also well matched to the power output of currently operating klystrons. At 1.3 GHz such a train is composed of ∼3000 bunches (3MHz). The train hence has a length of 300 km.

The electron source provides highly polarized electrons which are accelerated to 5 GeV before they enter the damping ring with a circumference of 6 km. They are cooled to the final emittance within 200 ms. Since the bunches have a 6 ns separation in the damping ring a fast kicker is required to extract the particles and transfer them along the length of the linac where the enter a two stage bunch compressor that reduces the bunch length and accelerates the particles to 15 GeV at which point the electrons enter the main linac. The main linac accelerates the particles with a gradient of 31.5 MV/m and has a RF-fill factor of ∼0.7. At an energy of 150 GeV the electron traverse a helical undulator of ∼150 m length to produce polarized photons. These photons impinge on a thin rotating target to create e^+e^--pairs. The positrons are captured and accelerated to 5 GeV. They then enter their damping ring where they are cooled. A transfer line takes them to the beginning of the positron linac, where they proceed for acceleration analogous to the electrons.

A ∼5 km *final focus* section is required to squeeze the beams to the dimensions required for the collisions.

Superconducting RF-cavities have seen a dramatic technological development in the 90ies, when the accelerator gradient was pushed from 5 MV/m to 25 MV/m for niobium cavities whilst there was a similar decrease in cost. The technology was first applied at high gradients in the TESLA Test Facility at DESY, which subsequently turned into the FLASH facility for user operation as a Free Electron Laser. The Global Design Effort for the ILC made an early decision for a more ambitious average accelerating field of 31.5 MV/m. The technical limit for superconducting cavities at 1.3 GHz lies above 50 MV/m when the peak magnetic field exceeds

Electropolished 9-cell cavities
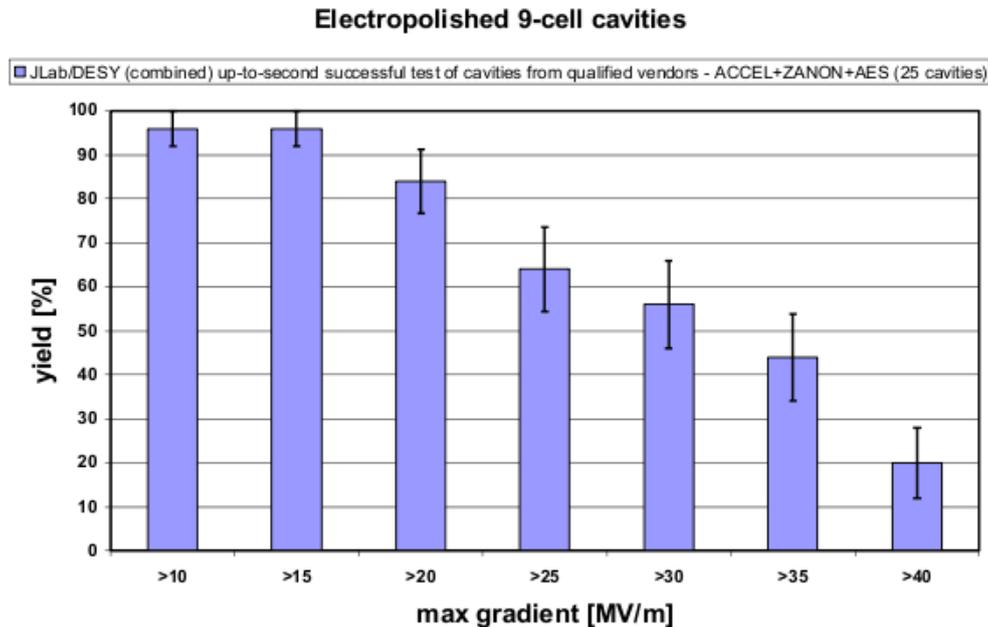
Figure 6: The production yield for cavities in the vertical test. The ILC requirement for this test is 35 MV/m. The cavities originate from two vendors.

the critical field for Nb and hence is far away from the envisaged operational field. Individual cavity cells (single resonators) have been manufactured that withstand fields of 50 MV/m. Hence there is no physics limitation for achieving the ambitious operational gradient. Instead the production technology has to be prepared for mass production. This is a field of particular R&D for the ILC.

The limitation results predominantly from two effects: *field emission* from impurities on the Nb surface and *quenches* that occur when local features in the Nb surface lead to field enhancement that exceeds the critical field. Once a quench is locally induced it spreads quickly and affects the entire bunch train. Such quenches are likely to occur near the equator of a resonator where the field is highest and the electro-beam welding affects the surface homogeneity. Big progress has been made in removing field emission as a primary source of breakdown by removing sulphur remnants from the electro-polishing in a dedicated rinsing cycle. Subsequent surface annealing at 800°C improves the surface structure. The state of the art in this world-wide endeavour is shown in Figure 6. More than 40% of the cavities exceed a gradient of 35 MV/m in a so-called vertical test[2] and meet the acceptance criteria for the ILC. A 10% degradation for beam operation is allowed for so that an average gradient of 31.5 MV/m can be envisaged.

Quenches can typically be traced to features of the surface. They have typically a size of 10 μm to several 100 μm and can hence be identified using appropriate optical inspections.

---

[2]This low-power test is carried out with a provisional antenna inserted in place of the high-power coupler in actual beam operation.
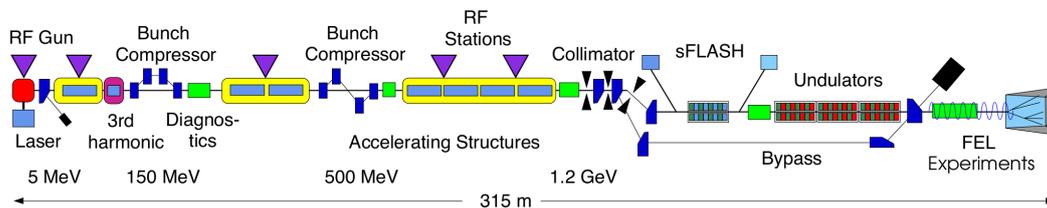
Figure 7: The first section of the FLASH linac. The RF-structures much resemble those of the ILC, where a cryomodule holds three 9-cell cavities.

	European XFEL	ILC	FLASH design	FLASH experiment
Bunch charge [nC]	1	3.2	1	3
# bunches	3250	2625	7200	2400
Pulse length [μs]	650	970	800	800
Current [mA]	5	9	9	9

Table 1: Comparison of operational parameters for the European XFEL, ILC and FLASH. The numbers shown for the FLASH experiment refer to the actual test that has been carried out.

Such tools are under development and are expected to provide the feedback to the cavity manufacturer for proper surface treatment, in particular during electro-beam welding. The ILC goal for cavity production yield is better than 50% for 2010 and better than 90% for 2012 for a gradient of 35 MV/m and above. The results are coming from all three regions: Asia, America and Europe. All regions invest heavily in the technology and infrastructure.

By now superconducting cavities have long been used at the FLASH facility which naturally much resembles the planned accelerator infrastructure for the ILC from the RF point of view. A layout of the injector section and the first acceleration stage is shown in Figure 7 together with the subsequent FEL undulator section. Even though in typical operation FLASH runs with a small number of bunches per train to respond to the wishes of the FEL users FLASH is also able to emulate the high power operation of the ILC: using long trains, high gradients and large number of bunches FLASH basically reproduces the envisaged operational environment for the ILC, cf. Table 1. This environment provides ample opportunity to study the performance of the superconducting accelerating structures in a real environment. It is also very demanding since e.g. the variation of maximum gradients and the gradient spread in FLASH are large. It is hence a demanding task to set up the so called *low level RF* to control the RF distribution that all cavities can perform maximally. The GDE is fortunate to have a test facility routinely operational at this early stage.

A veritable systems test for the ILC will be carried by the European XFEL project at DESY, which features a 1.2 km superconducting linac that serves the undulator beam lines. The construction of the the European XFEL is imminent. The ILC will profit from the understanding of the industrial production of the high-technology components and will gain valuable experience from the operation of the linac, which in effect constitutes a 5% prototype for the ILC.

While the superconducting infrastructure for the ILC is the largest single cost driver and

hence warrants the concentrated effort there are other aspects of the project that are subject to optimization. The GDE is hence launching an assessment process that scrutinizes the assumptions of the RDR. As an example the underground tunnel layout of the ILC may offer potential for simplification and cost savings. The RDR assumes a two-tunnel main linac; one tunnel would be used to accelerate the beam whereas the other tunnel would accommodate the high power infrastructure which would remain accessible during operation. It may well be possible to obtain high availability of the ILC with even a single tunnel. Topological simplifications of the tunnel layout at the central campus may well be possible. The damping rings are large; progress in kicker technology allows for a 3 ns bunch spacing and consequently a 3 km ring could suffice. However, such a high-current positron ring may experience instabilities due to the electron cloud effect, which needs to be studied. The intensity requirements on the undulator based positron source are large and hence constitute a risk. – A corresponding research programme for risk mitigation and cost containment has thus been launched for the ILC. It profits from the availability of dedicated tests at facilities such as KEK, CesrTA and FLASH.

Results of this intense R&D programme will form the basis of the Technical Design Report (TDR) that will be released in 2012.

4 Conclusions

With the start of the LHC the exploration of the Terascale will begin. By 2012 considerable feedback will have been obtained on the existence of a low mass Higgs boson and the mass spectrum of particles from *new physics*. That input will bode well for a reassessment of the CERN Council strategy that is foreseen at the same time. The ILC will have completed its technical design phase with the publication of the Technical Design Report. It is expected that the TDR documents the construction of the machine to sufficient details so that there is minimal uncertainty in the estimated remaining engineering and cost. With this approach the ILC construction could begin soon after.

Should the community foresee immediately to concentrate on the multi-TeV energy range a linear collider will only be realized considerably later when the R&D for CLIC will have been successfully concluded. In an optimistic scenario all technical hurdles may have been overcome by the mid of the next decade. However, the demonstration of the technology at a large scale, which is no small endeavour itself, will not have been possible by that time.

Acknowledgments

References

[1] The key statements of the CERN Council on the European Strategy are available at `http://council.web.cern.ch/council/en/EuropeanStrategy/ESStatement.pdf` and the full broschure `http://council.web.cern.ch/council/en/EuropeanStrategy/ESBrochure.pdf`.

[2] T. Akesson, R. Aleksan, B. Allanach *et al.*, Eur. Phys. J. **C51** (2007) 421-500. [hep-ph/0609216].

[3] R. Brinkmann *et al.*, eds., "TESLA Technical Design Report", DESY-2001-011 (March, 2001).

[4] T. O. Raubenheimer *et al.*, eds., "Zeroth Order Design Report for the Next Linear Collider," SLAC-R-474 (1996); N. Phinney, ed., "2001 report on the Next Linear Collider: A report submitted to Snowmass 01," SLAC-R-571 (2001).

[5] "GLC project: Linear Collider for TeV Physics," KEK-Report-2003-7, `http://lcdev. kek.jp/Roadmap/` (2003)

[6] Aarons, G. *et al.*, "International Linear Collider Reference Design Report", Volume 2: Physics at the ILC, 2007, `arXiv/hep-ph/0709.1893`. This is one volume of ref. [12].

[7] M. Tigner, Nuovo Cimento **37** (1965) 1228.

[8] W. Schnell, CERN CLIC Note 13 (1986) and Proc. of Symposium on Advanced Accelerator Concepts, Madison, Aug. 86, ed. F.E. Milles (Am. Inst. of Phys., New York, 1987, p. 17).

[9] H. Braun *et al.*, "Updated CLIC parameters 2005", CERN-OPEN-2006-022, CLIC-Note-627, (2006).

[10] CLIC Test Facility 3 (CTF3), `http://ctf3.home.cern.ch/ctf3/CTFindex.htm`.

[11] ITRP Recommendation, `http://www.fnal.gov/directorate/icfa/ITRP_Report_Final.pdf` (2004).

[12] ILC Reference Design Report, `http://www.linearcollider.org/about/Publications/Reference-Design-Report` (2007).

Discussion

Cheng-Ju Lin (LBNL): What do you think are the deciding factor to choosing between ILC or CLIC?

Answer: Timing and physics interest: The ILC can be built now and will deliver e.g. on resolving the issue of electroweak symmetry breaking. Its energy reach can be extended to 1 TeV. If the interest were focussed on the multi-TeV region from the start CLIC is currently the most viable approach. Verification of its technology on a system scale will however consume a number of years.

The most complete and timely physics return would come from an early ILC implementation compatible with an upgrade option to multi-TeV using CLIC technology.

The super-LHC, a luminosity upgrade

Marzio Nessi

CERN, 1211 Geneve 23, Switzerland

The prospects for a long-term upgrade programme for the Large Hadron Collider, CERN's new proton-proton collider, are presented. While the final physics motivation and the exact schedule of operations depends on the coming LHC findings, it is clear today that a major consolidation and upgrade of the existing detectors and of the CERN accelerators complex will be necessary.

1 Motivation

The Large Hadron Collider (LHC) is the new particle accelerator which just started operations at CERN. It will collide protons on protons, at a centre-of-mass energy of 14 TeV. Its primary goal is to answer one of today's deepest questions of physics, namely what is the origin of the elementary particles' masses. The Higgs boson is a hypothised particle which, if it exists, would give the mechanism by which particles acquire mass. The mass of the Higgs boson is a free parameter in the Standard Model.

The design of the LHC [1] collider and of its two largest experiments, ATLAS [2] and CMS [3], has been tuned to enable the full exploration of this mass range, searching for a broad variety of the Higgs production and decay processes predicted by the Standard Model. The
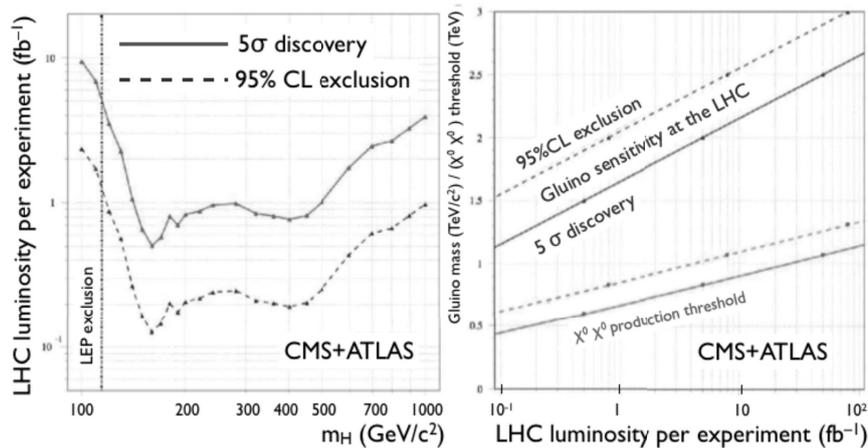
Figure 1: LHC Higgs and Gluino discovery potential at 10 fb^{-1} [4]

timeline for these searches is outlined in the left plot of figure 1. This shows the amount of data needed by each of the two experiments to establish a 5σ discovery, or a 95% CL exclusion, as a function of the Higgs mass. The present planning of LHC operations foresees the delivery of a few 100 pb^{-1} of data during 2010, which will not be enough to fulfill this task. Instead, with 10 fb^{-1} of delivered integrated Luminosity, the LHC will either discover or exclude the SM Higgs and this, probably, after 2-3 years of running at 14 TeV and at 10^{33} cm^{-2}sec^{-1}.

Whatever the results will be, we will be left with a lot of new questions and problems to solve [4]. There will be no limit to the need of accuracy after that! If the Higgs is discovered, among the possible open questions there is: Are there more particles in the Higgs sector? Is the Higgs boson elementary or composite? What is the origin of fermion masses?

Following the discovery, the main focus will become the quantitative study of the Higgs properties.
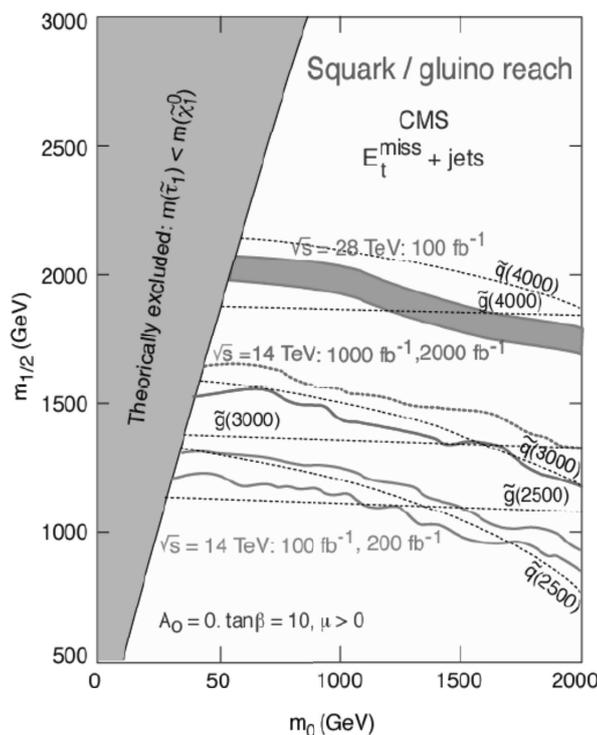
Figure 2: LHC SUSY mass reach for different luminosity and energy scenari

At some point, with high statistics, rare decay modes of the SM Higgs will become accessible ($H \to \mu_+\mu_-, H \to Z\gamma$). Hb,Ht, HZ, HW couplings might be measured to 10% for $m_H < 200$ GeV.

If the Higgs boson is not found, a radical departure from the Standard Model will be needed, and the searches to understand what other mechanism is responsible for the electroweak symmetry breaking will begin.

Dark matter is an additional puzzle that today's experimental particle physics tries to

reveal. Various models anticipate the existence of a higher level of symmetry in nature. In a theory with unbroken supersymmetry, for every type of boson there exists a corresponding type of fermion with the same mass and internal quantum numbers, and vice-versa. Once the discovery of supersymmetry is achieved, then it will be important to extend the mass reach for new particles. In general one will need to continue in the determination of SUSY masses and parameters.

An increase of a factor 5 to 10 in integrated luminosity will buy an additional 500 GeV on the mass reach. In the same way, the mass reach for new gauge bosons, or signatures of extra-dimension models will be increased by 30%.

All this has justified the need to start defining a project for running LHC for a longer period (at least until 2030). A luminosity upgrade (superLHC or sLHC [5]) will have a strong impact on the machine and on the experiments.

2 The CERN accelerator complex

In the LHC, at the interaction point the number of beam collision directly scales with the LHC luminosity (L), defined as :

$$L = \frac{f_r \cdot \gamma}{4\pi} \frac{N_b^2 \cdot n_b}{\epsilon_n \cdot \beta^*} \cdot F$$

Here f_r is the LHC revolution frequency, N_b is the number of protons per bunch, n_b is the number of bunches, β^* is the value of the betatron function at the interaction point (IP), and $F < 1$ is a factor measuring the geometric loss of overlap between two bunches as they cross at a given crossing angle. The luminosity can therefore be increased by increasing the bunch current (N_b), the number of bunches (n_b) and the geometric overlap (F), or by reducing the normalised emittance ϵ_n or β^*.

The LHC injector chain is shown in figure 3. The first stage of the acceleration takes place in the Linac2, a linear accelerator where protons reach an energy of 50 MeV. The proton-booster synchrotron (PSB) increases their energy up to 1.4 GeV, injecting them into the 51-years old proton synchrotron (PS). This one accelerates the beam to 25 GeV, and sends it into the super proton synchrotron (SPS), out of which 450 GeV protons are transferred to the LHC for the start of the ramp-up to the nominal energy of 7 TeV.

There are 2 fundamental parameters which define the characteristic and quality of the accelerator chain: the normalised emittance and the allowed number of protons per bunch. Both parameters enter into the definition of the beam brightness which is proportional to N_b/ϵ_n. The normalized emittance, $\epsilon_n = \beta \cdot \epsilon \cdot \gamma$, where β and γ are the relativistic functions, is constant across the full beam acceleration and storage path. Its value is defined at the earliest stage of the acceleration process, and is inherited by the high-energy components of the accelerator chain. The beam emittance is the extent of space and momentum phase space occupied by the particles as it travels, and in practice it determines, together with the β function, the transverse dimensions of the beam at a given point of its trajectory.

CERN is in the process of analysing the entire injection chain, trying to define possible bottlenecks that might limit the final LHC luminosity. Presently, the LHC brightness is limited by the characteristics of the Linac2 and of the PSB. For this reason CERN has already approved a new project, which consists in building a new linac accelerator (Linac4). The Linac4, whose construction has started and should be completed by 2014, will raise the injection energy into the PSB from 50 to 160 MeV. The factor of two gain in $\beta\gamma^2$ allows to double the beam intensity

at constant tune shift, providing a better match to the space charge limitations of the PSB. The early stages of the acceleration make use of a H^- beam, whose two electrons will be eventually stripped off. This step eludes the constraints of the Liouville theorem, and reduces the beam emittance. Beam losses at the injection in the PSB will be reduced also via a chopper, which will remove the low-energy tail of the proton momentum distribution. Overall, the improved beam quality will allow to increase N_b from the nominal value of $1.15 \cdot 10^{11}$ to at least $1.7 \cdot 10^{11}$, leading to the so-called ultimate luminosity of $2.3 \cdot 10^{34} cm^{-2} s^{-1}$ in the LHC phase I upgrade.

The next steps in the chain are the PSB and the proton synchrotron. Higher energy out of the PS gives smaller transverse emittances and beam sizes, and therefore reduced injection losses in the next injection stage: the SPS.

A stage-2 upgrade project study was set up a few years ago with the goal of technically and financially defining the impact of constructing a new superconducting PS (PS2), with the goal of having it operational around 2020 -2022 (sLHC upgrade phase II). The PSB would then be replaced by a low-power superconducting linear accelerator (SPL), increasing the injection energy into the PS from 1.4 to 4 GeV thus greatly reducing the filling time. The increase in output energy of the SPL will allow to increase also the output energy of the PS2. The PS2 will deliver protons to the SPS at 50 GeV, well above the 22 GeV transition energy of the SPS, easing the handling of higher intensities. Injection into the SPS at 50 GeV will reduce the space-charge tune spread, to allow the bunch intensity to reach, if needed, $N_b = 4 \cdot 10^{11}$. Higher energy also gives smaller emittance, and less beam losses at injection. Shorter injection and acceleration times, finally, reduce the filling time, with a greater operational efficiency.

Recently this 1.3 billion CHF project has been questioned, given the uncertainties related to the real limitations of the SPS and of the LHC itself. Such a large investment makes sense if both accelerators will be able to accept the new delivered beam brightness or if it will serve
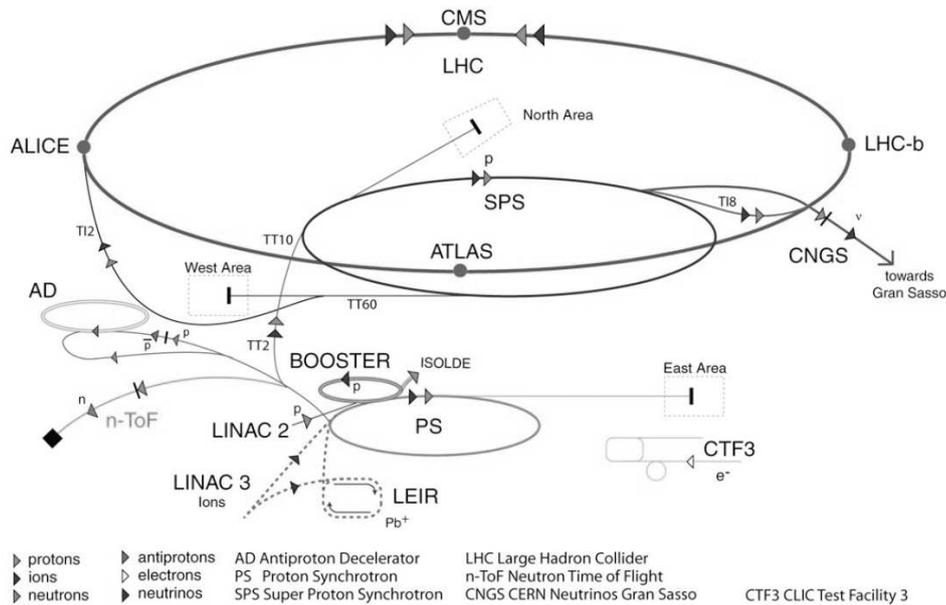
Figure 3: The CERN accelerator complex

the need of other projects at CERN beyond the sLHC. This debate is still open and mostly depends for its technical part from the knowledge of the limitations related to the SPS that will be gained over time. Today it is known that the SPS will need to be first upgraded to accept $1.7 \cdot 10^{11}$ protons per bunch. The electron cloud effect must be first mitigated. Beam losses which today account for about 10% of the total will have to be understood and reduced. The RF system will need a major upgrade to cope with high intensity beams. A study group has been set up and is operational since March 2007. Since then, progresses have been made on many fronts. The recent work has mainly focused on e-cloud mitigation, a-C coating of the vacuum chambers is the best candidate for implementation before 2014. E-cloud mitigation, impedance reduction and RF upgrade would help even for nominal and for sure for ultimate LHC beam operation and can be implemented earlier than in phase II.

If the SP2 phase II upgrade will not take place, the existing PS accelerator will need in any case to go through major consolidation work, to grant stability and reliability during the next 20 years of LHC operation.

3   The superLHC accelerator

Once enough beam brightness can be injected into the LHC, to obtain the necessary luminosity for sLHC, one has to optimise and upgrade the interaction regions (IRs).

Four schemes are presently under consideration: early separation (ES) of the beams, full crab crossing (FCC), large Piwinski angle (LPA) and low emittance (LE). The schematics of their layouts are shown in figure 4.

In the ES scheme, the relative positions of the quadrupoles and of the innermost dipole
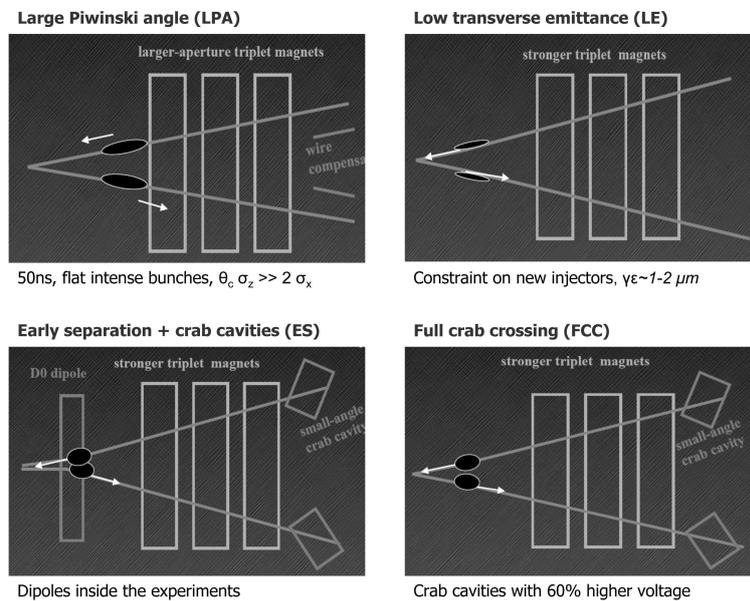
Figure 4: Four different and still possible interaction regions upgrade schemes

are swapped; the dipole is brought closer to the IP, and will reside within the detectors. This allows to keep the bunches separated up to the final dipoles. Small-angle crab cavities, located outside the quadrupoles, would allow for a total overlap at the collision. Introducing additional beam elements inside the detectors area is a major concern. It will complicate enormously the present detectors layout and might imply additional radiation background closer to the sensitive part of the detectors. The FCC scheme relies solely on crab cavities to maximise the bunch overlap (figure 5). The LPA scheme allows for much more intense beams, requiring a longer bunch spacing, of 50 ns, and a larger crossing angle, limiting the geometric loss with a flat beam profile. Long-range beam-beam interactions need to be screened with compensating wires. The LE scheme provides much thinner bunches, at a cost of a larger geometric loss. The LPA and LE schemes will require a full upgrade of the injector chain, including PS2 and SPL.

Certainly, the FCC scheme is the most attractive one. It does not require any major changes in the interface between machine and experiments, nor adds it requirements to the injection chain. RF crab cavities [6] deflect head and tail in opposite direction so that collisions are effectively "head on" for luminosity and tune shift. Bunch centroids still cross at an angle (easy separation). Crab cavities can increase the LHC luminosity without an accompanying increase in beam intensity, thereby avoiding negative side effects associated with high intensity and high stored beam energy.

Both "local" and "global" crabbing schemes are still under consideration for the LHC upgrade phase II. In the global solution a set of cavities is positioned at IR4, in the local solution crab cavities are placed on each beam around the ATLAS and CMS IR.

Over the last few years, major progresses have been made in the field of crab cavities. Recent KEK-B results have shown that crab cavities work and improve luminosity. Worries relate to machine protection, reliability and possible induced phase noise. A vigorous R&D program has started in various accelerator labs related to LHC. A test in the SPS could be prepared for 2012.

In addition, luminosity can be improved by a proper focusing of the beam around the interaction regions. While the overall behaviour of $\beta(s)$ around the full ring is constrained by global stability requirements, like the value of the tune, its value at a specific point (IP for
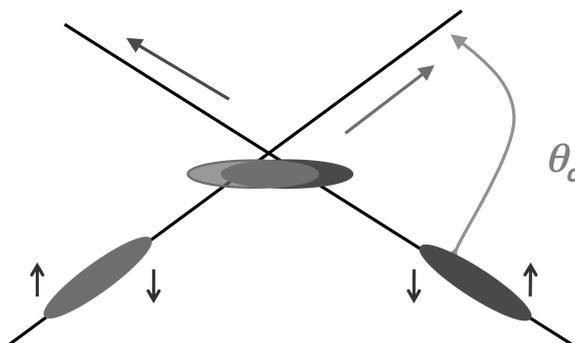
Figure 5: RF crab cavity scheme at the interaction point

example) depends on the local machine optics. The price to pay for a beam squeeze at the IP is a growth of the beam size before and after the minimum of β^*. The internal aperture of the quadruple magnets surrounding the IR must match this growth, to prevent the beam hitting their inner surface. An increase in the quadrupole aperture, on the other hand, requires a larger field, in order to maintain the constant field gradient necessary to focus the beam. Today the plan is to have new large aperture triplets already for phase I and high field ones based on Ni_3Sn technology for phase II. In both cases the installation of such devices in the straight sections in front of the experiments will require major shutdowns of the order of 9-12 months.

Recently it became evident that not just the value of the peak luminosity is a fundamental parameter for the sLHC, but also a decent life time of the beam luminosity is very important. What really counts, at the end, is to be able to maximise the integrated luminosity delivered to the experiments over a reasonable time span. Figure 6 shows that at a peak luminosity of $10^{35}cm^{-2}s^{-1}$, the typical life time, independently from the bunch intensity, is of the order of 3 to 4 hours. Its time evolution is exponential. Therefore it might not be optimal to continuously fill the machine to optimise the delivered integral luminosity. The drop in luminosity is proportional to the increase in interaction rate, and is just due to the loss of protons due to the collisions. With a bunch-bunch crossing every 25 ns, 300 or 400 pp collisions at each crossing, and two active experiments (ATLAS and CMS), a number of the order of 10^{14} p/h is simply disappearing, out of a total of about $5 \cdot 10^{14}$ stored in the initial beam.

The obvious solution is luminosity levelling, starting from an initial peak luminosity of $5 \cdot 10^{35}cm^{-2}s^{-1}$. The luminosity can be expressed as:

$$L \propto \frac{1}{\beta^*\sqrt{1 + \frac{\theta^2\sigma^2}{4\beta^*\epsilon}}}$$

Here the idea is to to tune the various parameters as a function of time to keep the luminosity constant as long as possible. Three possibilities in LHC, specific to crossing at an angle: 1)
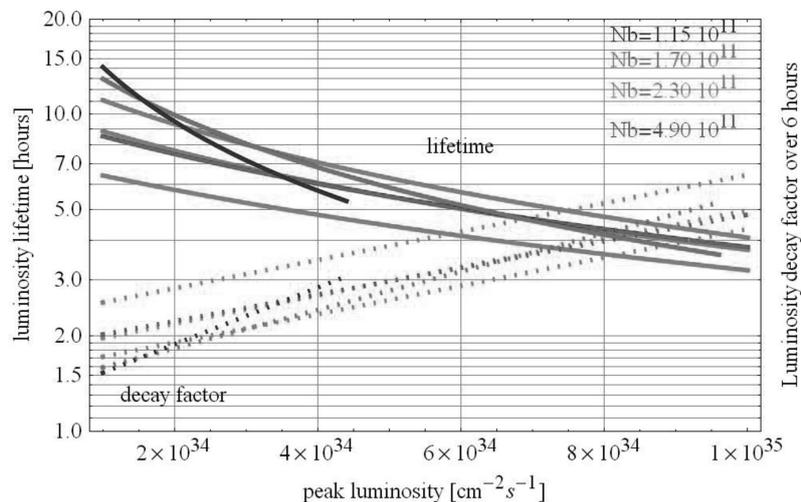
Figure 6: Luminosity lifetime as a function the peak luminosity, no levelling

levelling via dynamic β^* adjustments, 2) Levelling via dynamic crossing angle adjustments (θ) and 3) Levelling via dynamic bunch length adjustments (σ).

Levelling via the crossing angle (2) appears to have the best potential (performance, complexity) but requires the crab cavities solution to work. If the method works, one could keep an average luminosity of $5 \cdot 10^{35} cm^{-2} s^{-1}$ over 7 to 8 hours. This could be translated into a yearly integrated luminosity of $200 - 250 fb^{-1}$. Hence, luminosity levelling could be imposed as a requirement for all scenarios. Levelling is also useful for the machine in terms of peak energy deposition, beam-beam effect, operation efficiency.

4 Detectors requirement and detectors upgrade plans

The requirements on the experiments are driven by the nature of the observables that will be of interest at the sLHC. These will be defined by the discoveries or lack thereof that will emerge after the first few years of data taking and once the nature of any new phenomena will be more evident.
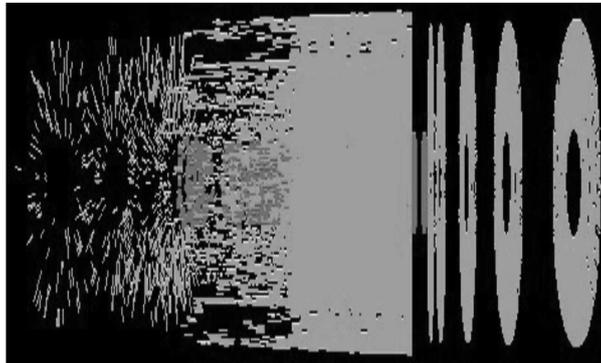
Figure 7: Tracks simulation in the new ATLAS inner tracker with 400 pile-up events

At this stage of the project, one can not relax any of the initial experimental requirements. Whatever the discovery scenario will be, the experiments will be required to perform lepton and photon identification down to rapidities of 3. Jet tagging in the very forward region will remain a must, in particular if the Higgs is not found. Missing energy will be a fundamental parameter for any search for new physics.

On top of that, luminosity above or equal $4 \cdot 10^{34} cm^{-2} s^{-1}$ implies many overlapping hard collisions in the same bunch crossing (pile-up). For example, the PA scheme at $10^{35} cm^{-2} s^{-1}$ implies a pile-up of about 400 hard collisions in the same bunch crossing.

This imposes a very high density of tracks and photons in the inner detector regions, far beyond what the existing ATLAS and CMS trackers can effort. The detector occupancy would be very high, the challenge being to find all the tracks, without also finding many fake tracks from random combinations of hits. Picture 7 shows hits in the newly designed sLHC ATLAS inner tracker from one bunch crossing with 400 pile-up events; only tracks in the forward half of the detector were generated. The inner tracker gets about 15,000 tracks per bunch crossing and a similar number of photons which can produce e+e- pairs. A sufficient number of hits per tracks must be recorded, the detector granularity will be increased by almost a factor 10 to

keep occupancy at the $1 - 2\%$ level for an efficient pattern recognition. This can be achieved by reducing pixel size, strip dimensions for silicon counters, and by adding more detector layers to increase the number of precision points per track. The ability to reconstruct displaced vertices will also deteriorate, with a reduced efficiency to tag b quarks and leptons and a larger rate of fake tags.

In any case, before one moves to the sLHC regime (upgrade phase II), the existing ATLAS and CMS inner detectors will need to be replaced, because fully damaged by the accumulated radiation dose during the initial LHC discovery period (600-700 fb^{-1} acquired on tape). Whatever the sLHC scenario will be, beyond this integrated luminosity, both experiments will require new inner detector trackers. ATLAS in particular will have to abandon the concept of a TRT tracker detector and fully rely on semiconductor sensors.

Other components might not survive beyond the agreed LHC luminosity period. ATLAS might loose the front-end electronics placed on the forward hadron calorimeter. The functioning of the forwards calorimeters might be compromised. As an example, the ATLAS LAr forward calorimeter might suffer from space charges which might break down the original ionization signal and even cause boiling of the liquid at the innermost radii. Similarly, the CMS endcap and forward calorimeters might suffer from radiation damage.

ATLAS has estimated the need for at least 18 months of shutdown before moving to phase II, to replace and commission its new inner detector and eventually upgrade its forward calorimeter and change the hadronic calorimeter front-end electronics.

Even before worrying about physics performance, the experiments will have to worry about the operability of their innermost detectors. Already during the phase I shutdown, needed to install the Linac4 and the new large aperture triplets, ATLAS and CMS plan to upgrade their pixel detectors. ATLAS will add a new pixel layer, built around a new beam pipe, sliding inside the previous pixel detector. CMS will replace the entire pixel detector with a new low-mass, 4-layers one. Layout drawings of both pixel detectors are shown in figure 8.

The performance of the level 1 trigger (LVL1) system, fully based on hardware today , will be the real challenge. The emphasis will therefore be on the first trigger levels, where one may need to incorporate tracking information to supplement the reduced rejection power of muon and calorimeter triggers, and to maintain acceptable efficiency and purity for electrons, affected by the degradation of isolation criteria.
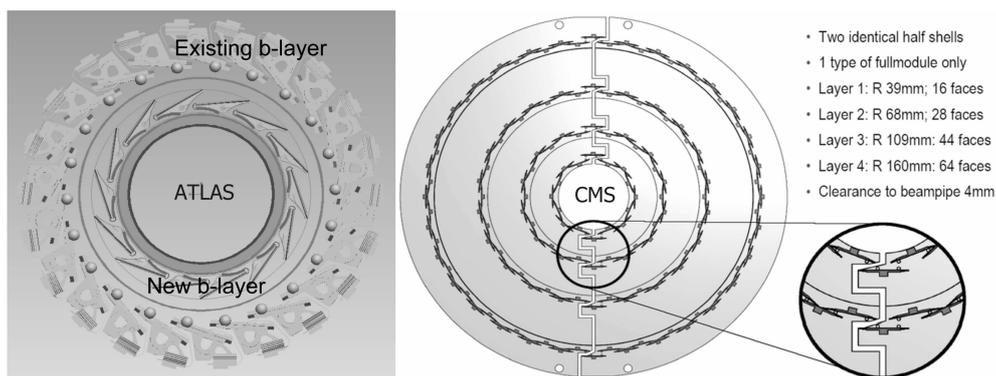
Figure 8: ATLAS (left) and CMS (right) new phase I pixel detectors

One needs to keep the stored event rate roughly the same as now : ~ 200 events per bunch crossing. The events are much bigger at high luminosity, so this is quite a challenge. It means rejecting 10 to 20 times as many events as now, each of which is about 10 times as big. To meet this challenge, one can increase the latency at level-1 and move some of what is done in software at high level, such as combining trigger objects.

Today ATLAS and CMS consider introducing new elements at LVL1, including a track-trigger. First studies in this direction are just starting, but the community is lacking experience in this field.

Full granularity of the calorimeters at trigger level will allow better particle identification.

The muon trigger needs better resolution to allow higher momentum thresholds to reduce the muon trigger rate. Adding some new chambers can achieve this, or at least trying to use the existing precision chambers granularity at the trigger level.

It is not known how the very important forward calorimeter trigger will perform at these sLHC high rates.

The upgrade of the LHC experiments will require major R&D and construction work, with a likely time line of at least 8-9 years for construction and integration. The planning has to assume the worst possible scenarios in terms of pile-up and radiation environment. While getting the financial green light for this new enterprise will probably take a few years and will be triggered by the first LHC discoveries, the detector community has to act now, preparing technology, making choices, testing prototypes and going deeply into the engineering design.

5   Outlook

Whatever the LHC will discover, it will set the path of future research in particle physics. After the first moments of assessments of the new landscape, the next step will be the precise measurement of the spectra, mixings and couplings of the new particles. The existence of supersymmetry, if confirmed, will open a completely new world of mass spectroscopy at high masses. For years one will be far from the dominance of systematics, and statistics will undoubtedly remain the most important factor.

Defining from now on a programme of high luminosity, beyond the initial LHC mandate, remains the only logical solution. It will take time until more dedicated machines, like linear colliders or more energetic hadron colliders, will become a reality.

Planning from now on a LHC luminosity upgrade program is a must.

References

[1] LHC machine, L. Evans and Ph. Bryant Eds., 2008 JINST 3, S08001.

[2] G. Aad et al. [ATLAS Collaboration], The ATLAS Experiment at the CERN Large Hadron Collider, JINST 3 (2008) S08003.

[3] S. Chatrchyan et al. [CMS Collaboration], The CMS Experiment at the CERN Large Hadron Collider, JINST 3 (2008) S08004.

[4] The super-LHC, M.Mangano, arXiv:0910.0030, to appear in Contemporary Physics.

[5] Scenarios and Technological Challenges for a LHC Luminosity Upgrade, 8 lectures delivered as part of CERNs 2009 Academic Training programme, S. Gobba and J.-P. Koutchouk eds., 8-12 June 2009, available at http://indico.cern.ch/conferenceDisplay.py?confId=55041.

[6] K. Oide and K. Yokoya, The crab crossing scheme for storage ring colliders, Phys. Rev. A 40 (1989) 315.

Discussion

Majid Hashemi (Antwerp University): One of the main concerns of SLHC would be the amount of the pile up. Are the current physics results shown in the talk based on rescaling or simulation including pile-up?

Answer: Not all. Today it is still very difficult to work with 400 pile-up events in full simulation. For the moment we have that just for special optimization studies related to the inner tracker detector.

Joel Feltesse (IRFU, CEA): We all know how old is the PS. Reliability is more and more a problem. Have you already an estimate of the cost and the schedule of a new PS?

Answer: I did not give a number. But I forwarded the question to the CERN DG, who was better qualified. The number was not given, but today (end of 2009) we know that the estimation is of the order of 1.2BCHF

Dimitri Denisov (FNAL): Energy is in many cases more important than luminosity for physics reach: 1. Are there any substantial upgrades expected to be needed to reach 14 TeV?

Answer: More then upgrade we speak about consolidation work, to repair the warm splices and retune the dipole magnets. This is part of the plans of CERN for the next few years. It is a major piece of work.

: What are options to go above 14 TeV?

Answer: We speak about DLHC. Here the possible idea is to double the field strength of the dipoles by using new superconducting material (Ni3Sn). This technology is no yet at the stage to be rescaled to mass production. A substantial R&D would need to be launched.

Future B-Factories

Marcello A. Giorgi
INFN and Dipartimento di Fisica "E.Fermi" Universita' di Pisa
Largo B. Pontecorvo 3, Pisa. Italy

This paper presents the scientific motivations for future Super Flavor Factories. An update on the status of the projects of High Luminosity B-factories $SuperB$ and $SuperKEKB$ is presented, together with the approval process.

1 Introduction

The experiments $BABAR$ and $Belle$ at the e^+e^- asymmetric colliding beam machines $PEPII$ and $KEKB$, have run for about a decade with a remarkable success, contributing to the elucidation of the Cabibbo-Kobayashi-Maskawa (CKM) paradigma [1] of flavor physics in the framework of the Standard Model of fundamental interactions (SM) that has been one of the most tested theories of all time. Nonetheless the SM can not explain many physical observations and crucial questions are still left unanswered as how can we explain the still unobserved original antimatter in the Universe or the nature of dark matter, whose existence can be inferred from the cosmological observations. The beautiful results on neutrinos from SuperKamiokande [2] Are now suggesting that NP is at hand and Lepton Flavor Violation(LFV) would be one of the most clear signals of it. There are two complimentary ways to search for new physics effect in elementary interaction. A *direct* way is pursued presently at LHC, where the energy available for the interaction is the largest available at present, and new particles not predicted by the SM are searched for. The other way to search for NP is by looking at the *indirect* effects of NP in interference processes (as CP-Violation in quark sectors) and rare or forbidden decays (like lepton flavor violation processes in μ and τ decays).

It is a general opinion that a new experimental exploration beyond SM is needed to discover New Physics (NP). Higher luminosity B factories can help today to improve precision in the CKM measurements looking for little small discrepancies from SM predictions. A crucial question today is: how precision measurements at low energy in flavor sector can help in discovering New Physics (NP) Beyond the Standard Model (BSM) in the era of LHC [3]. The answer to this very legitimate question can be given by focusing the attention on a few specific points showing the clear complementarity between high luminosity flavor factory potential and the energy frontier colliding beam machines.

1. Flavor precision measurements are sensitive to NP through:

   - measurement of symmetries due to interference effects in known processes
   - measurement of decay rates for very rare or SM forbidden modes.

2. NP effects are governed by :

- NP scale Λ

- effective coupling reflecting on different intensity (coupling effect) or different patterns (from symmetries).

3. The aim of Future Factories is to collect between 5 and 10 $\times 10^{10}$ b $\overline{b}$, c $\overline{c}$, $\tau^+\tau^-$ pair thanks to an integrated luminosity between 50 and 100 ab^{-1}. Clear signals of NP from:

- Lepton Flavor Violation in τ decay
- Discovery of CP violation in charm decay.

If the NP scale Λ is found at LHC, the future flavor factories will study the flavor structure of NP, contributing to the determination of couplings Flavor Violating (FV) and CP violating of NP. If instead the NP scale Λ is not found at LHC, indirect signals of NP could be looked for at Super Flavor Factories and linked to NP models. Regions in parameter space can be constrained with NP(Λ) sensitivity higher than TeV up to order of tens or even hundreds of TeV. In what follows a very quick summary of the flavor physics results and the perspective for dedicated experiments with single beam for experiments at colliding beam super flavor factories are presented. The Super Flavor machine, the Detector and the experimental tools are strongly correlated to make possible hitting the target of NP.

2   Present Status

The physics of quark b has been the most studied topics in the past few years with two B-factories operating in USA and in Japan, it was in actual fact the main motivation for the construction of $PEPII$ and $KEKB$. The contribution to b physics has come from $BABAR$ and $Belle$ that have recorded more than almost 1.5 ab^{-1} at the $\Upsilon(4S)$ resonance, and from CDF and D0 experiments with the study of B_S system at Tevatron. B-factories made measurement of almost all elements involving third generation quarks of the CKM matrix, strictly constraining the space parameters for NP insertions in the weak sector. Many different measurements were made, even beyond the original goals, spanning from precision measurements of CKM elements, spectroscopy of unexpected states, and measurements of rare decays which constrained MSSM models such as $B \to \tau\nu$ decays.

With further increase of statistics, the sensitivity to new physics will become higher, and the new measurement of CKM unitarity triangle could in principle lead to inconsistencies with SM, which can not be observed with the present result. In Fig. 2 we show the achievable sensitivity to the unitarity triangle using the statistics expected at Super-Flavor factories.

3   B-τ-Charm Perspectives

The search for new physics through the use of very high luminosity machines, leading to high sensitivities for rare processes is complimentary with the choice of pursuing new physics by opening new energy thresholds, as done at LHC. Understanding the NP flavor structure during LHC operations by means of Super Flavor Factories is described in various papers (see for example $SuperB$ CDR [4] and $Belle$ Physics document [5] and [6]) . In what follows the sensitivities for Super-Flavor factories will be shown considering samples consisting of integrated luminosities $\geq$ 75ab^{-1}, corresponding to 5 years run of an e^+e^- asymmetric machine running
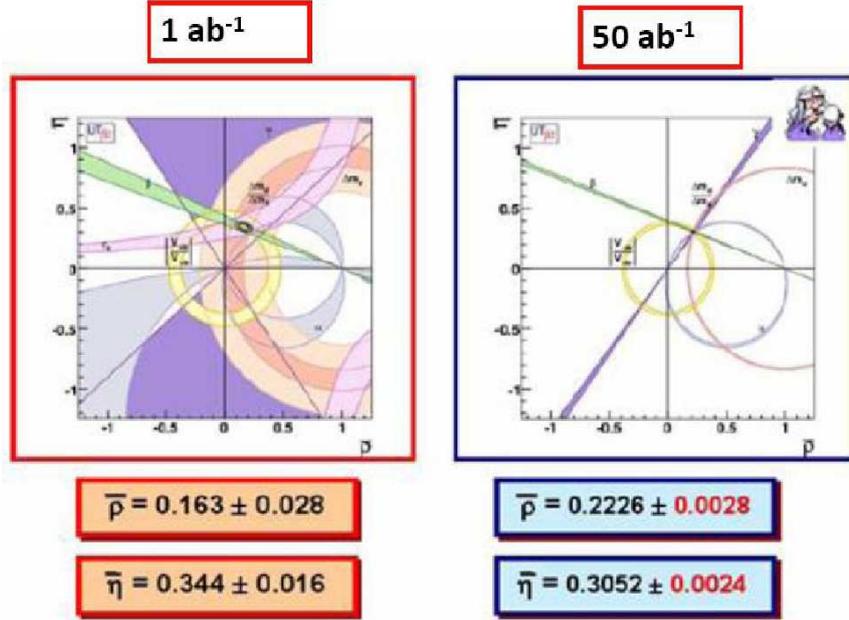
Figure 1: Present results on unitarity triangle measurement (on the left) and predicted results achievable with 50 ab^{-1} statistics (on the right)as from a general fit by UTfit group [1]

with a peak luminosity of 10^{36}cm^{-2}s^{-1}. Only a small selection of observables for the above integrated luminosity are shown here, a more detailed description is in [11].

3.1 B physics

Super-Flavor facilities will produce the largest samples of B mesons available, improving the sensitivities for many of the rare processes already studied at B-factories, and would provide novel measurement for channels presently beyond experimental reach. Many searches for small deviations, a brief references about the reaches for a foreseeable $SuperB$ factory are reported in table 1.

For the channel $b \rightarrow s\ell^+\ell^-$ Super-B can use inclusive modes, therefore it can provide a precise and theoretically clean measurement, not affected by systematics coming from the hadronic correction affecting the study of exclusive channels as $B \rightarrow K^*\ell^+\ell^-$.

Such channels are also accessible with high statistics at LHC. Nonetheless several interesting rare decay modes, such as $B \rightarrow K\nu\bar{\nu}$, can only be observed with high integrated luminosity ≥ 75 ab^{-1}, and need a clean environment not compatible with LHC backgrounds. Other channels can also be accessible as $B \rightarrow \gamma\gamma$ and $B \rightarrow \nu\bar{\nu}$ decays which are sensitive to New Physics models with extra-dimensions. The sensitivity in the high luminosity Super Flavor Factory $SuperB$ can be seen in fig. 2, where by reducing the statistical error, which is the main contributor to the experimental error, the Standard Model can be severely challenged.

In addition to CKM measurements $Super-B$-factories would be able to measure CP viola-

Table 1: Super-B **Some channels sensitive to new physics.**

Parameter	Baseline	Upgrade
$B(B \to X_s \gamma)$	7%	3%
$A_{CP}(B \to X_s \gamma)$	0.037	0.004-0.005
$B(B^+ \to \tau^+ \nu)$	30%	$3-4\%$
$B(B^+ \to \mu^+ \nu)$	No	5-6 %
$B(B \to X_s l^+ l^-)$	23%	4-6%
$A_{FB}\ (B \to X_s l^+ l^-)_{s_0 xing}$	No	4-6%
$B(B \to K \nu \bar{\nu})$	No	16-20%
$S_{CP}(B \to K_S \pi^0 \gamma \nu \bar{\nu})$	0.24	0.02-0.03
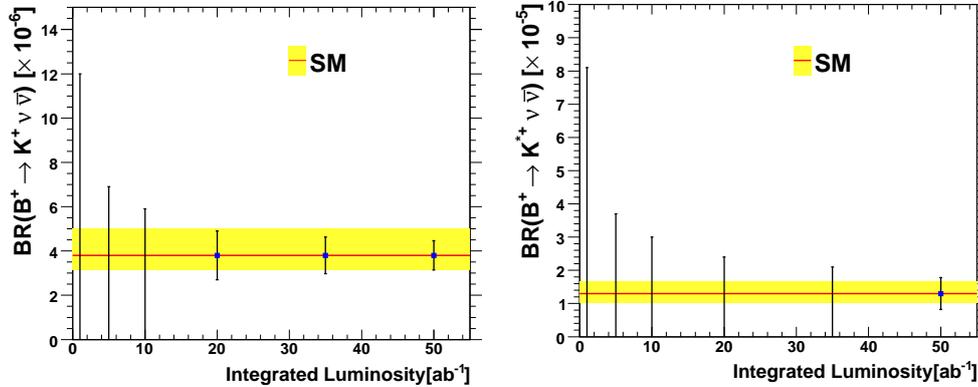
Figure 2: Test the mechanism of direct CP violation is based on the presence of a weak phase ϕ that shows opposite sign in the decay of B^0 $\bar{B}^0$ and a strong phase δ that doesn't change sign.

tion asymmetries in branching fractions and in B meson leptonic decays for a SUSY mass scale below 1 TeV, that would be complimentary with direct observations at LHC. The sensitivity needed to study the SUSY structure for such low energies would be reached after five years of data taking at new machines allowing to extend the sensitivity for SUSY well beyond the TeV scale, allowing to see NP contribution coming from a 10-TeV-scale SUSY, which would not be discovered by LHC.

3.2   tau physics

The τ physics will assume great importance to probe new physics beyond Standard Model. The τ-sector, with the use larger integrated luminosities available at $SuperB$ and $SuperKEKB$, will provide precise measurement of both direct effects, via LFV processes, and indirect effects, visible in g-2 [7] and electric dipole moment (EDM) of τ [8].

The use of polarized beams, as in the baseline design of $SuperB$, would help reducing

backgrounds to $\tau \to \mu\gamma$ decay, which is expected to be the most sensible to new physics, in fact polarized beams would allow to reduce backgrounds coming from $e^+e^- \to \mu\mu\gamma$ processes. The sensitivities achieved after few years of data taking with $SuperB$ would be as high as 2×10^{-9} for $\tau \to \mu\gamma$ and 2×10^{-10} for $\tau \to \mu\mu\mu$ [9]. Due to the lack of polarization option $SuperKEKB$ the angular distribution of muons coming from $\tau \to \mu\gamma$ can not be used to reject backgrounds leading to sensitivities worse by a factor of 2.5.

The other hint for New Physics come from g-2 measurement : at present muon g-2 is measured to be $\Delta a_\mu = a_\mu^{SM} - a_\mu^{exp} = (3 \pm 1) \times 10^{-9}$ and any effect on τ's would at least scale with the ratio between the tau and muon mass, making the effect within reach of future flavor factories $SuperB$ and $SuperKEKB$. The two machine have different design , only $SuperB$ will have a high polarized beam ($\geq 80\%$) and the capability of running at charm threshold. The polarization and an integrated luminosity $\geq 75ab^{-1}$ will allow to investigate the magnetic structure of τ , combining the measurements of total cross section angular distribution and Forward-Backward asymmetry with a sensitivities up to 0.6×10^{-6} [7], equivalent to the sensitivity for muons in g-2 experiments.

3.3   Charm physics

Major improvements are foreseen in the charm sector as well.The recent observation of large $D^0\bar{D}^0$ mixing [10] raises the exciting possibility of finding CP violation in charm decay, which would be a major hint for physics beyond the Standard Model. Future flavor factories $SuperB$ and $SuperKEKB$ will be able to make comprehensive studies in the charm-sector, taking data with high luminosity 10^{36} at the $\Upsilon(4S)$ resonance. $SuperB$ could also take data at a lower center-of-mass energy corresponding to $\psi\prime$ (3770) resonance, still with a remarkable high luminosity 10^{35} , that is the same design luminosity of the future $Super\ \tau - charm$ that is planned at Novosibirsk.

Both future B-Factories show common distinctive features useful to study rare processes in the charm sector. The experimental environment is very clean, both at production threshold, where the backgrounds contribution are small with respect to great rate of production of D mesons, and at $\Upsilon(4S)$ energy, where D's can be efficiently tagged through $D^\star \to D\pi^\pm$ decay, which make possible also a flavor tag on the produced D. On the other side, D production at $\Psi\prime$ would allow a coherent production of $D^0\bar{D}^0$ pairs, opening novel ways to measure CPV processes and allowing the measurement of the phase related to CPV in the up sector. While running at threshold offer lower background and access to the measurement of both direct and indirect CPV, it comes at the expense of statistics, and although having larger cross section (by a factor 3) suffers from lower luminosities. In Figure 3 present and future precision for CPV parameters are shown.

3.4   Summary of the physics goals

The expected precision of some of the most important measurements that can be performed at Super Flavor Factories are contained and compared in
fully comprehensive tables where the reach of the B Factories at 2 ab^{-1} and at 75 ab^{-1} are reported in the above quoted $SuperB$ CDR [4].

The physics program for the future Flavor Factories can be summarized:

1. Increase by O(10) the precision of $BABAR$ and $Belle$ in Flavor sector
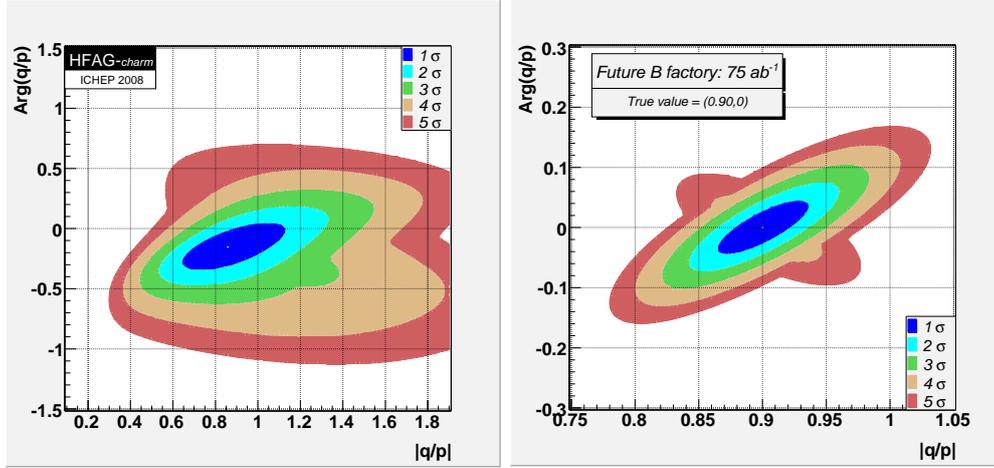
Figure 3: Two dimensional contours Charm mixing and CP violation as a function of $\frac{q}{p}$ a strong phase δ that doesn't change sign, at present (left) and after 5 years of datataking from one of the Super Flavor Factories under design.

2. Challenge CKM in $(\rho.\eta)$ plane at 1% level.

3. Explore CP violation in charm sector

   - CP violation in $D^0 \overline{D}^0$ mixing at $\Upsilon(4s)$ and at chatm threshold (3770 MeV)
   - Explore the measurement of violating phase

4. τ Physics (LFV), also with the addition of beam polarization:

   - Reduce the irreducible background in LFV channel $\tau \to \mu\gamma$.
   - Explore T Violation.
   - Search for magnetic structure of τ .

5. Explore New Spectroscopy in a clean environment with extremely high statistics.

   All these goals can be achieved by a machine with a peak luminosity of $10^{36} cm^2 s^{-1}$ in 5 years run at $\Upsilon(4s)$, with one polarized beam and possibility to operate at charm threshold for a few months and with a peak luminosity of $10^{35} cm^2 s^{-1}$.

4 e^+e^- colliders

The present status of e^+e^- factories shows $KEKB$ in Tsukuba as the only B-Factory running after the shut down of $PEPII$, the Φ-Factories $Da\Phi ne$ in Frascati ready for restart after the upgrades and $VEPP2000$ in Novosibirsk and the tau-charm-Factory $BEPCII$ in Beijing. The

luminosity needed to accomplish the challenging Physics program of the future B-factories is 10^{36}cm^{-2}s^{-1}. The luminosity $\mathcal{L}$ of a collider is given by the superposition integral:

$$\mathcal{L} = f_c \int d^3\vec{\mathbf{x}}\, dt\, \rho_1(\vec{\mathbf{x}}, t)\rho_2(\vec{\mathbf{x}}, t) \cdot 2c \tag{1}$$

where f_c is the bunch collision frequency, $\rho_i(\vec{\mathbf{x}}, t)$ are the local spatial densities of particles in a bunch of the the beam i at the position $\vec{\mathbf{x}}$ at time t and c is the speed of light. The luminosity is readily maximized by increasing f_c and the local spatial densities ρ.

The upper limit on f_c is set by the available number of stable buckets in the ring and by the minimum distance d between two adjacent bunches necessary to impede parasitic collisions, in this respect a quick separation of the low and high energy beams is necessary to reduce d. The $BABAR$ approach was to implement an head on collision scheme and to exploit the energy asymetry and a pair of Halbach dipoles placed at ±20cm from the IP to separate the HER from the LER before the occurence of parasitic collisions. KEKB renounced to the advantages of an head on collision scheme in favour of a crossing angle one. The advantage of this approach is that the beam lines separates in the straight drift section between the IP and the first vertical focusing quadrupole of the final doublet. The disadvantage of this aproach is that the superposition of the head of a colliding beam with the tail of the opposite one is not optimal so that the luminosity is reduced. As a mater of fact the general formula (1) can be expressed in a closed form assuming gaussian bunches and neglecting the bunch length by

$$\mathcal{L} \sim f_c \frac{N_1\, N_2}{4\pi\, \sigma_y\sigma_x} \frac{1}{\sqrt{1 + \varphi_{\mathbf{Piwi.}}^2}} \tag{2}$$

where σ_y,σ_x and σ_z are respectively the RMS vertical, radial and longitudinal bunch length, and N_i is the total number of particles contained in a bunch of the beam i. The finite crossing angle effect on the luminosity is contained in the Piwinsky angle factor $\varphi_{\mathbf{Piwi.}}$ defined as

$$\varphi_{\mathbf{Piwi.}} = \frac{\sigma_z\, \tan\chi/2}{\sigma_x} \tag{3}$$

where χ is the full crossing angle. The $SuperB$ path to reach 10^{36}cm^{-2}s^{-1} is the "large Piwinsky angle with crab waist collisions" scheme. The first key ingredient is to increase the Piwinsky factor by reducing σ_x. Doing that almost all the advantages of the short bunches collision scheme are kept without the burden of the actual bunch shortening. The most important effect of this choice is that the length of the bunch overlap region is reduced to σ_x/χ so that the vertical beta function at the collision point can be reduced to

$$\beta_y^\star \sim \frac{\sigma_x}{\chi} \sim 300\mu\text{m} \ll \sigma_z \sim 6\text{mm}$$

thus allowing the vertical beam size to be reduced to 40 nm, moreover the vertical tune shift is reduced and the vertical synchrobetatron resonances are suppressed [13] However, a large Piwinski angle itself introduces new beam-beam resonances that may strongly limit the maximum achievable luminosity. The second key ingredient, that is the "crab waist transform" [14], reduces the strenght of the betatron and synchrobetatron resonances increasing the beam beam limit. This concept was successfully tested in collisions at DaΦne [15].

SuperKEKB original path to high luminosity was to increase the beam current by a factor 4(2) for the LER(HER) and to push the beam beam tune shift parameter by the short bunches

(σ_z 3mm) "crab crossing" collision scheme. The main issues of this configuration are the wall-plug power needed to store such high current beams, the detector background component that scales with the currents and the head tail fast instability that limit the luminosity attainable with this scheme to $5 \cdot 10^{35} \mathrm{cm}^{-2} \sec^{-1}$

To overcome these problems the SuperKEKB collaboration proposed a new approach 'called 'nano beam italian scheme" based on low emittance lattice (like $SuperB$), crab crossing collisions with traveling focus whose parameters are presented, together with the $SuperB$ ones, in table 2.

Table 2: Machine parameters for $SuperB$ and superKEKB

Parameter	units	$SuperB$	superKEKB
Energy (HER/LER)	GeV	4/7	3.5/8
Luminosity	$10^{36}\mathrm{cm}^{-2}\mathrm{s}^{-1}$	1.0	0.8
Beam Current (HER/LER)	A	2.7/2.7	3.8/2.2
N$_{bunches}$		1740	2230
ε_y (LER/HER)	pm	7/4	34/11
ε_x (LER/HER)	nm	2.8/1.6	2.8/2
β_y (LER/HER)	μm	210/370	210/370
β_x (LER/HER)	cm	3.5/2.0	4.4/2.5
σ_z	mm	5	5
Crossing angle χ	mrad	60	60
RF power (AC line)	MW	26	¿ 50
beam beam hor. tune shift (LER/HER)	%	0.4/0.13	8.1 /8.1
beam beam ver. tune shift (LER/HER)	%	9.4/9.5	9.0 /8.7

For a complete view of the e^+e^- colliders including future machines see Fig. 4.

5   Basics of Detectors

For both future B-Factories $SuperB$ and $SuperKEKB$ the communities of experimenters are planning the reuse of large part of the existing apparatus of $BABAR$ and $Belle$. The detectors for both colliders will be asymmetric reflecting the asymmetry of machines needed for boosting the center of mass (typically the $\Upsilon(4s)$ to determine the decay time of B^0 and $\overline{B}^0$ allowing the measurement of their time decay asymmetry. Detectors have to be as hermetic as possible and their main requirements are:

- Good measurement of decay vertices by means of precise multilayer Silicon Vertex Detector.

- A central tracking chamber almost transparent for a good direction and p_T in an intense magnetic field.

- A Cherenkov particle identifier, to identify distinguish pions, kaons and protons in a quite wide range with high efficiency.
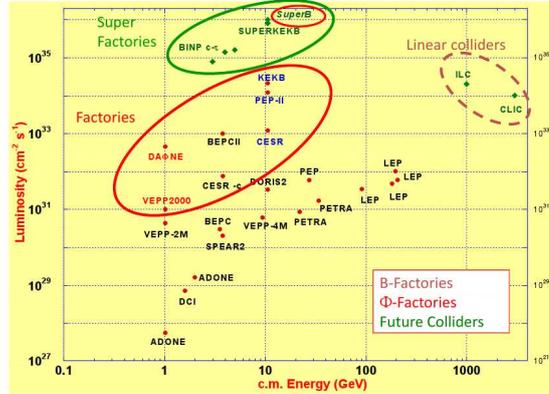
Figure 4: e^+e^- colliders

- An electromagnetic calorimeter with high energy resolution for soft photons and a good identification of electrons.

- a good detector for muon and neutral hadrons

They should be upgraded version of $BABAR$ and $Belle$.

5.1 the $SuperB$ detector

The baseline of the apparatus that is under study for $SuperB$ is largely based on the reuse of $BABAR$ detector as presented in details in the $SuperB$ Conceptual Design Report (CDR) [4] It reuses the:

- Fused Silica bars of the internal reflecting Cherenkov Detector (DIRC) that has shown high efficiency in kaon identification.

- Mechanical support of DIRC and drift chamber(DCH) .

- The barrel of the electromagnetic calorimeter (EMC), the mechanical structure and the scintillating crystals of CsI(Tl).

- The magnet with the Superconducting coil and the magnetic flux return (that needs some redesign).

Some elements of $BABAR$ have aged and therefore their replacement would be needed. Others require moderate improvements to cope with the high luminosity environment, a factor (100 higher the in $BABAR$), with a reduced the center of mass boost at $\Upsilon(4s)$: $\beta\gamma = 2.83$ as from the energy choice of $SuperB$, where the positron energy is 4 GeV and electron energy is 7
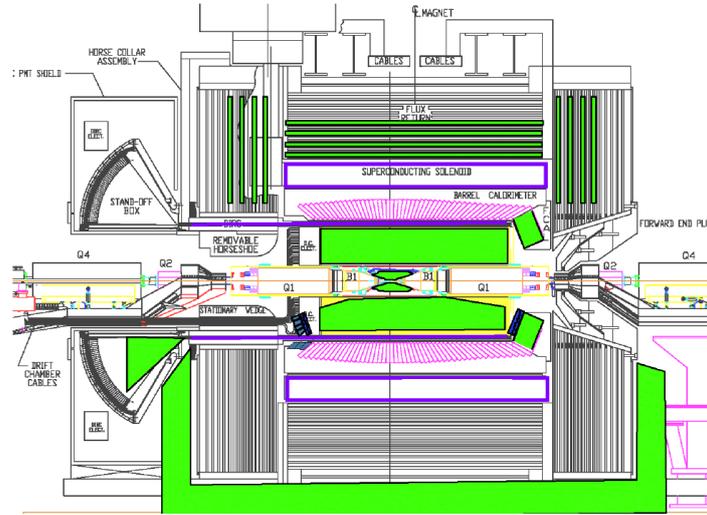
Figure 5: The *SuperB* Detector . In green are the detector component to be rebuilt in the baseline and in the optimal design

GeV (4×7 GeV)[1]. , and the high DAQ rates and with the expected very high darta acquisition (DAQ) rate.Then within respect to $BABAR$ are considered the following changes:

- A small (≤ 1.2 cm radius) beam pipe technology.

- A new very thin 6 layer Silicon Vertex Tracker. *The optimal choice should be a thin pixel first layer L0 and double sided detectors in the remaining 5 layers.*

- A new DCH with a carbon fiber mechanical structure, with modified gas mixture and cell size.

- About DIRC an optimized Photon detection for fused silica bars.

- The possible addition of a forward PID system (TOF in Baseline option)

- A rebuilt Forward EMC , made with crystals of LYSO and an additional Backward EMC endcap mainly for vetoing.

- The instrumented flux return for muon and neutral hadron detection based in $BABAR$ on Limited Streamer Tubes and RPC's would be changed to the extruded plastic scintillator bars.

- The electronics, the trigger and DAQ will be updated to cope with real event rate 100 times higher than in $BABAR$.

- Computing upgrade is needed for a massive data volume similar to the LHC experiments.

---

[1]In $PEPII$ the beam energies were 3.11 and 9.0 GeV with a $\beta\gamma$ of 0.556 and in $KEKB$ 3.5 and 8.0 GeV with $\beta\gamma = 0.42$

Fig. 5.1 shows the side view of the $SuperB$ detector where the half above the beam is the baseline choice with small changes from the $BABAR$ design, where instead in the lower part improving options are clearly visible as the shaped DCH, the additional FOrward PID and Backward EMC.

5.2   *Belle* **Detector**
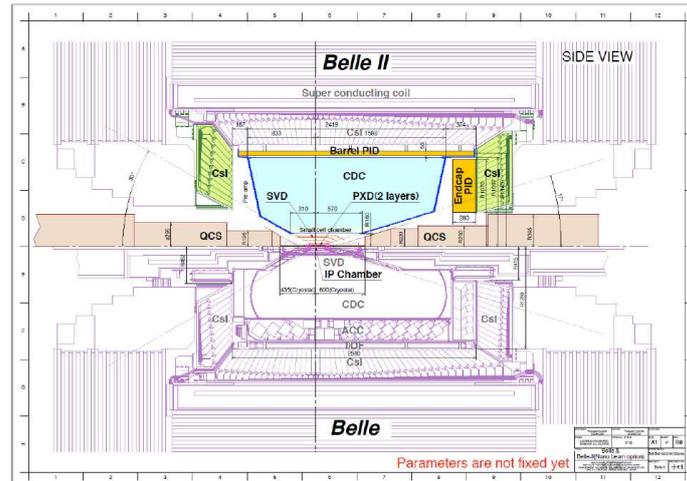
Figure 6: In the upper part of the figure the apparatus $BelleII$ modified for running at $SuperKEKB$ is shown. It has to be compared with the $Belle$ apparatus in the lower part of the figure.

In a very similar way for the $SuperKEKB$ project the Fig. 5.2 shows the evolution from the $Belle$ apparatus to the expected $BelleII$. Of course some problems are common to the two machines and therefore the solutions are quite similar.

*   *   *

The author would like to gratefully aknowledge Eugenio Paoloni for its skillful technical assistance, fighting against some of the LATEX idiosyncrasies.

References

[1] Cabibbo N, *Phys Rev. Lett.***10** (1963)
    Kobayashi M. and Maskawa T. *Prog. Theor.Phys.***49** (1973)

[2] Y. Fukuda *et al.* [Super-Kamiokande Collaboration], Phys. Rev. Lett. **81** (1998) 1562;
    Y. Ashie *et al.* [Super-Kamiokande Collaboration], Phys. Rev. Lett. **93** (2004) 101801.

[3] G. Isidori, arXiv:1001.3431 [hep-ph].

[4] M. Bona *et al.*, arXiv:0709.0451 [hep-ex].

[5] S. Hashimoto *et al.*, "Letter of intent for KEK Super *B* Factory," http://superb.kek.jp/documents/loi/img/LoI_physics.pdf.

[6] Proceeding of SuperB Workshop VI: http://www.pi.infn.it/SuperB/files/active/0/Valencia_Report.pdf.

[7] J. Bernabeu, G. A. Gonzalez-Sprinberg, J. Papavassiliou and J. Vidal, Nucl. Phys. B **790** (2008) 160 arXiv:0707.2496 [hep-ph].

[8] G. A. Gonzalez-Sprinberg, J. Bernabeu and J. Vidal, arXiv:0707.1658 [hep-ph].

[9] Y. Kuno, Y. Okada, arXiv:9604296 [hep-ph].

[10] B. Aubert et al. (BaBar Collab.), *Phys. Rev.* D **76**, 014018 (2007).

[11] Y. Ohnishi, SuperKEKB Meeting, Atami, Izu, Japan, January 24-26, 2008; K. Kinoshita, BEACH 2008, Columbia, SC, June 23-28, 2008; T. Browder, M. Ciuchini, T. Gershon, M. Hazumi, T. Hurth, Y. Okada and A. Stocchi, JHEP 0802 (2008) 110 , arXiv:0710.3799[hep-ph]; M. Bona *et al.*, arXiv:0709.0451[hep-ex].

[12] Y. Ohnishi, http://www.slac.stanford.edu/spires/find/hep/www?irn=5536120SPIRES entry *Prepared for 3rd Workshop on Higher Luminosity B Factory, Shonan Village, Kanagawa, Japan, 6-7 Aug 2002*

[13] D. V. Pestrikov, Nucl. Instrum. Meth. A **588**, 336 (2008).

[14] P. Raimondi, D. N. Shatilov and M. Zobov, arXiv:physics/0702033.

[15] P. Raimondi *et al.*, *In the Proceedings of 11th European Particle Accelerator Conference (EPAC 08), Magazzini del Cotone, Genoa, Italy, 23-27 Jun 2008, pp WEXG02.*

[16] K. Ohmi, M. Tawada, Y. Cai, S. Kamada, K. Oide and J. Qiang, Phys. Rev. ST Accel. Beams **7**, 104401 (2004).

Sect. A **336**, 427 (1993).

Discussion

Benny Ward (Baylor University: Are yoy saying that the Super KEK-B factory cannot do polarisation, or that they have chosen not to do polarization - I could not understand what you were saying.

Peter Chrisan Lublijana : I just have a comment. In fact for super keke b there is no principla reason to have polarisation, but we have not considered it up to now - it costs money and manpower.

Vera Lüth, SLAC: I think one thing we probably should have added to your table is that there is now an operating tau-charm factory in Beijung.

Toru Iijima: Do you think that you can achive the target luminosity with polarisation?

Mauro Savrie (University of Ferrara, INFN): You didn't make any coments on the possible time schedule of the two machines. Could you comment on that please?

Helena Abramowich (Tel Aviv University): I am hesitating to ask this question, but what warrants the need for two B-factory machines at this stage?

Benni Ward (Baylor University): What are the cost of these two machines?

Neutrino Telescopes

Per Olof Hulth[1]

[1]Oskar Klein Centre, Dept. of Physics, Stockholm University, 10691, Stockholm, Sweden

Three large optical Neutrino Cherenkov telescopes are now searching the sky for High Energy extraterrestrial neutrinos: the NT200+ in Lake Baikal, the ANTARES in the Mediterranean outside Toulon and the partially completed IceCube at the geographical South Pole, Antarctica. Tens of thousands of atmospheric neutrinos have been observed with energies up to several 100 TeV but so far no evidence for extraterrestrial neutrinos has been found. The IceCube neutrino telescope is approaching Gigaton size which is the expected minimum needed for observing extraterrestrial neutrinos. In the Northern hemisphere the KM3NeT collaboration is planning a Gigaton telescope in the Mediterranean and the Baikal collaboration is planning a Gigaton telescope for cascades in Lake Baikal.

1 Introduction

This paper discusses large neutrino Cherenkov telescopes using the optical Cherenkov technique with water and ice as detector medium.

1.1 Why neutrino astronomy?

Cosmic rays (CR) were discovered almost 100 years ago but we have not yet been able to identify any source by direct observation. The flux of cosmic rays has been measured up to an incredible energy of 10^{20} eV. The acceleration process for these energies is not completely understood. Figure 1 shows the observed cosmic ray flux for different particles compiled by Gaisser [1]. The spectrum is described by power-laws with different spectral index, $\gamma=2.7$ below 10^{15} eV (the so-called "knee"), and $\gamma=3$ for energies above 10^{15} eV. This can be interpreted as particles (mainly protons) leaking out from our galaxy. The spectrum changes again to a harder spectrum above $10^{18.5}$ eV (the "ankle") which is interpreted as due to an influx of extragalactic particles. The leading theory to explain the cosmic rays below
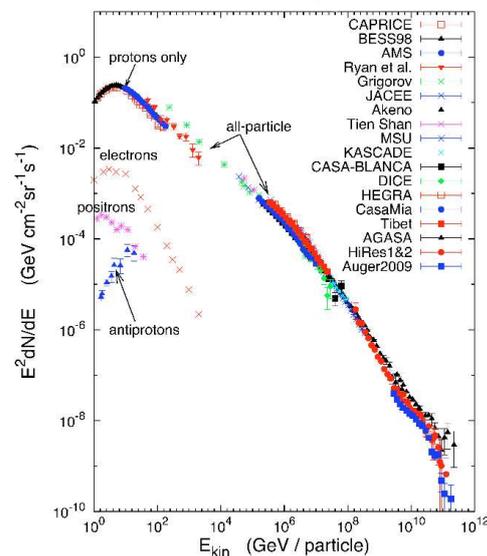
Figure 1: Cosmic ray flux as a function of energy [1].

10^{15} eV is Fermi acceleration in galactic super-
nova remnant (SNR) shocks. The sources for the extragalactic cosmic rays are believed to be
active galactic nuclei (AGN) and/or gamma ray bursts (GRB) which are the most energetic
objects observed in space. The reason for not being able to observe the cosmic ray sources
directly is that the cosmic rays are electrically charged and deflected by the magnetic field in
space. For ultrahigh energy cosmic rays, at energies where the magnetic field in space will
have a smaller bending effect, the Cosmic Microwave Background (CMB) from Big Bang will
reduce the mean free path in space for protons with energies above $10^{19.5}$ eV via the interaction
$p + \gamma_{CMB} \to \Delta^+$. The process is called GZK (after Greisen, Zatsepin, and Kuzmin) [2] and
limits the distance in the Universe observable via ultra high energy protons. Figure 2 shows
the range in space as a function of the energy of the protons. The GZK process will produce
UHE neutrinos via the $\pi^+ \to \mu^+ + \nu_\mu \to e^+ + \nu_e + \bar{\nu}_\mu$ from the decay of the Δ^+. The detection
of the "GZK neutrinos" is very important for the confirmation of the expected GZK process.

By using high energy photons the deflection by
magnetic fields in space is avoided. But the Uni-
verse is even less transparent for ultra high energy
photons than for high energy protons since these
will also interact with the photons from the Cos-
mic Microwave Background ($\gamma + \gamma_{CMB} \to e^+ e^-$).
A similar process occurs with infrared background
photons. Photons with energies about 10^{15} eV, for
example, will only reach us from sources within
our own galaxy. The observable distance in space
as a function of the energy of photons and pro-
tons [3] is shown in Figure 2. The maximum en-
ergy of photons observed is about 10^{13} eV limiting
the distances to the sources to be within 100 Mpc.
Photons are not suitable to transmit information
about very high energy processes far out in space.
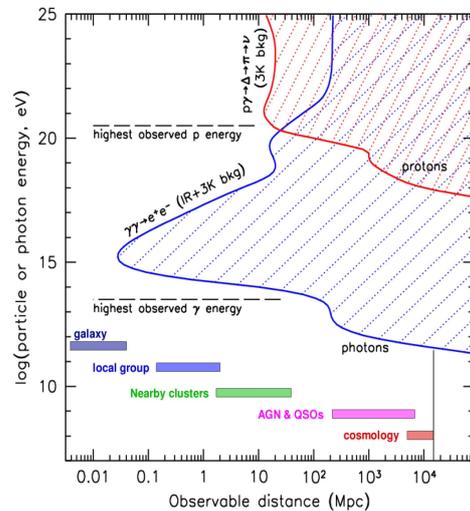
Figure 2: Observable distance for photons
as a function of energy.

Neutrinos from galactic and extra galactic
sources will not be absorbed by the microwave
background in space. It should be possible to iden-
tify the CR sources by large neutrino telescopes.
The flux ratios of neutrino flavors from pion and muon decays at the source are expected to be
1:2:0 ($\nu_e : \nu_\mu : \nu_t$) but due to neutrino oscillation, the flux ratios will be equal at Earth.

So far only two extraterrestrial sources of neutrinos have been seen, the Sun and the Super-
nova SN1987a in the Large Magellanic Cloud. Both are, however, low energy neutrino sources
of a few tens of MeV.

In addition there are scientific topics besides cosmic ray sources which can be studied by large
neutrino telescopes like indirect detection of dark matter particles (see section 3.4), magnetic
monopoles, nuclearites, atmospheric neutrinos with very high statistics up PeV energies, Lorentz
invariance tests etc.

2 High Energy Neutrino telescopes

The cosmic rays are expected to interact with matter or the radiation field in the vicinity of the source, producing hadrons and leptons decaying to neutrinos. When estimating the expected flux of neutrinos from the observed cosmic ray flux, one finds that detectors of Gigatons of target mass are needed [4]. For the optical Cherenkov detection technique there are mainly water and ice available. The transparent medium is equipped with a lattice of light sensors with a spacing depending on the optical transmission in the media and of the neutrino energies aimed for. The probability for a 1 TeV neutrino to interact in 1 km of water is only $4 \cdot 10^{-7}$. On the other hand the interaction length for neutrinos becomes the size of Earth at neutrino energies of $\sim$100 TeV. Neutrinos with PeV energies will mainly appear only close to the horizon and neutrinos at EeV energies even from above the horizon.

The neutrino telescopes are exposed to an intense flux of atmospheric muons (depending of the depth of the telescope) produced by the CR interactions in the atmosphere, and the atmospheric neutrinos produced in the same interactions will be a background for extraterrestrial neutrinos. The Earth is used as a muon filter and, therefor neutrinos below PeV energy, mainly upward-going neutrinos are used in the analysis.

High energy ν_μ's produce muons (via charge current interactions, CC) with a range in water or ice of several km (about 1 km at 300 GeV) allowing muons created far outside the instrumented detector volume to be detected. The mean angular difference between the incoming neutrino and the out-going muons falls approximately as $E^{-0.5}$ and is about 1° at 1 TeV. Electron neutrinos, tau neutrinos (at moderate energies) and neutral current (NC) interactions will produce "cascades" in which most of the secondary particles will interact and stop within a few tens of metres. The Cherenkov light will, to first order, come from a point source inside the large detector volume. The maximum intensity will, however, be at the Cherenkov angle (41°) around the shower axis allowing a crude determination of the neutrino direction. For ν_τ's at energies above several PeV the decay length for the tau will be hundreds of meters, allowing detection of the two cascades ("double bang events") from the primary interaction and the subsequent decay of the tau.

The neutrino telescopes in the Northern Hemisphere are sensitive to different areas of the sky than the ones in the Southern hemisphere and together they complement each other. The light in ice has shorter scattering length and longer absorption length compared to water. The angular resolution is better in water than in ice owing to the shorter scattering length. The photomultiplier (PM) noise rate in ice is about 1 kHz or less compared with 20-60 kHz (10 inch PM) in sea water due to ^{40}K decays and bioluminescence.

The expected energy spectrum for the neutrino flux from cosmic ray accelerators is E^{-2} due the assumed Fermi acceleration. The atmospheric neutrinos have a softer spectrum more like $E^{-3.7}$. The energy of the neutrino events will thus be useful when searching for extraterrestrial sources.

2.1 Baikal

The Baikal neutrino telescope was the first medium sized neutrino telescope successfully installed. It is situated in Lake Baikal in Russia. The existing NT-200+ telescope is deployed at a depth of 1100 m. It consists of a central part with eight strings with 192 optical modules arranged in pairs and is 72 m in height and 43 m in diameter. It has been taking data since 1998. In addition three outlier strings were installed in 2005 at 100 m radius with an additional
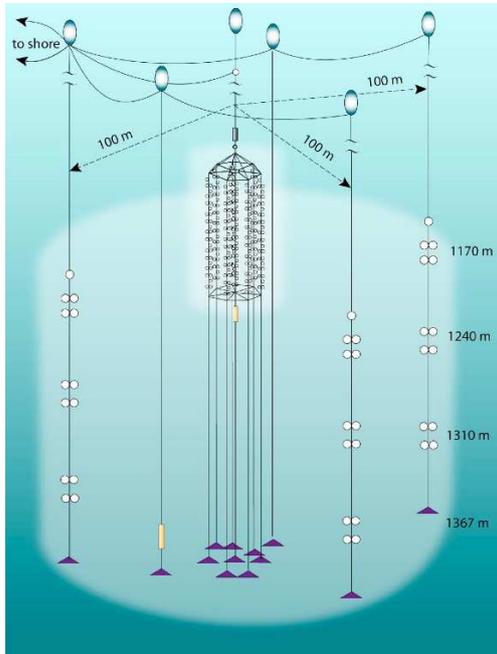
Figure 3: The Baikal NT200+
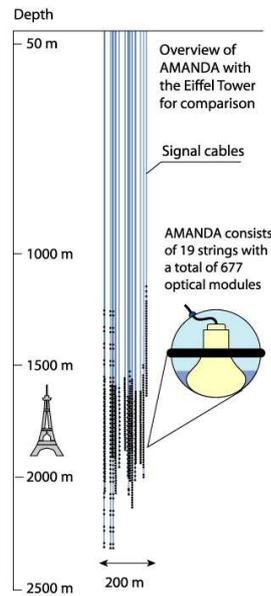
Figure 4: The AMANDA neutrino telescope.

38 modules. This extension is mainly for improving the efficiency for detecting cascades . The telescope has a total sensitive mass of 10 Mtons. The deployment (and repair) is done during winter when the ice of the lake is used as deployment platform. The angular resolution for muon tracks is about 4° and the energy threshold 15 GeV. In total ~400 up-going muon neutrinos have been detected. Figure 3 shows the existing telescope.

2.2 AMANDA

The AMANDA neutrino telescope is located 1500 m - 2000 m deep in the very optically transparent ice at the Amundsen-Scott base at the geographical South Pole in Antarctica. It was completed in 2000 with 19 strings with in total 680 optical modules. The diameter of the telescope is 200 m and it is about 350 m tall. It has an effective mass of 15 Mtons. The optical modules are deployed in water-filled holes made with a hot water drilling system. The energy threshold is about 50 GeV and the angular resolution for muon tracks about 2° - 3°. After nine years of successful running the telescope was closed down in May 2009. It will be replaced by the low energy extension DeepCore in IceCube. More than 6500 atmospheric neutrinos have been recorded between 2000 and 2006.

2.3 ANTARES

The ANTARES neutrino telescope is situated at 2050 m - 2400 m depth in the sea outside Toulon at the French Mediterranean coast. It consists of 12 strings with in total 900 optical modules. The strings are sepateted by 60 m - 75 m and the vertical instrumented size 350 m. It is comparable in size with the AMANDA telescope. The simulated angular resolution is about 0.3°. The first strings were deployed in 2006 and the final strings in 2008. The strings are deployed from a ship and connected to a junction box on the seabed with a Remotely Operated Vehicle (ROV).
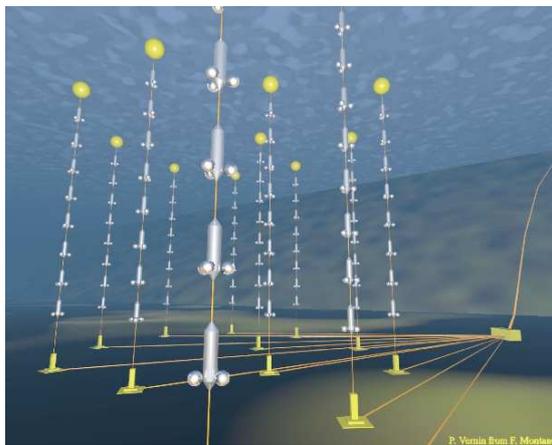
Figure 5: The ANTARES neutrino telescope
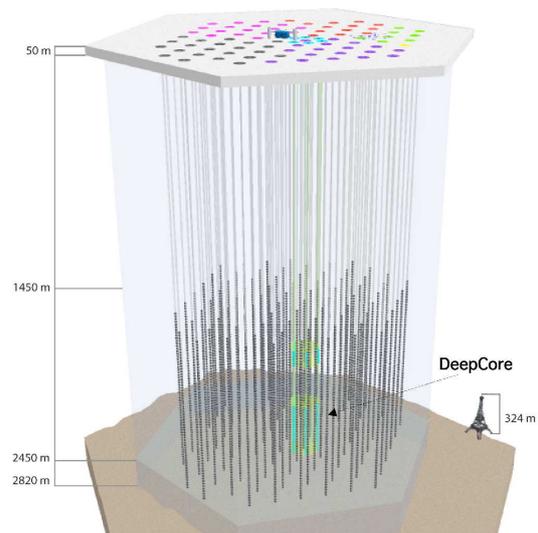
Figure 6: The IceCube neutrino telescope.

The telescope has so far recorded in total 759 upward going muon neutrinos using the first 5-string configuration (2007) and the completed 12 string configuration (2008).

2.4 IceCube

The IceCube neutrino telescope was designed based on the experience from AMANDA. It will be the first neutrino telescope to reach the expected necessary Gigaton scale. It will consist of 80 strings with 60 Digital Optical Modules (DOM) deployed between 1450 and 2450 m depth. The first string was installed in 2005 and the telescope will be completed in January 2011. In January 2010 the telescope consisted of 79 strings with 60 Digital Optical Modules (DOM) each. A cosmic ray air-shower telescope, IceTop, is situated at the surface with high efficiency for PeV - EeV energies. An IceTop station is situated close to the string hole and consists of two tanks with frozen water with two DOMs each. The combination of the neutrino telescope and the air-shower telescope is a unique feature of the South pole installation. It gives the possibility for absolute direction calibration of the neutrino telescope as well as for studies of the chemical components of the air-showers. IceCube has a low energy part called DeepCore with six additional strings deployed at the center of the main telescope where the transparency of the ice is the best. DeepCore will improve the low energy sensitivity for dark

matter searches and neutrino oscillation studies, and can use part of the outer IceCube strings for vetoing against atmospheric muons from above. The deployment of the IceCube modules is done as in AMANDA but with a much more efficient hot water drill. A 2450 m deep hole is completed within less than 35 h and the deployment of the string takes less than 10 h. The hole is completely frozen after about 1-2 weeks. The drilling and deployment is only possible during the austral summer, November - February. IceCube has been taking data with the partially completed telescope every year (with 1, 9, 22, 40 and 59 strings called IC1, IC9, IC22, IC40 and IC59) and in total about 13000 up-going muon neutrinos have been analyzed (up to half year of IC40). The median angular resolution is expected to be less than 0.5° for the final detector. Figure 6 shows the IceCube neutrino telescope with the air-shower IceTop on surface and the new DeepCore low energy sub-detector.

3   Recent results

The atmospheric neutrinos are very useful for testing and calibrating the neutrino telescopes. Figure 7 shows the observed muon rate as a function of the cosine of the zenith angle (-1 up-going and +1 down-going) for the Baikal and the ANTARES neutrino telescopes. The separation between atmospheric muons and atmospheric neutrinos is easily seen. Depending on the depth of the telescope the rate of down-going atmospheric muons is five to six orders of magnitude higher than the atmospheric neutrinos.
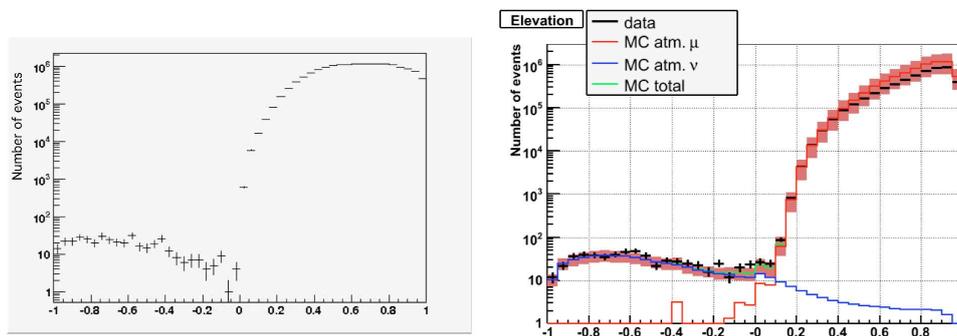
Figure 7: Cos(zenith) distributions of reconstructed muons in Baikal[5] (left) and ANTARES [6] preliminary (right). (Down going muons +1 and up going muons -1)

The four neutrino telescopes have recorded different amounts of atmospheric neutrinos reflecting the different sizes and exposure times. Baikal, 391 events, ANTARES 5+12 lines (2007-2008), 750 events, AMANDA (2000-2006) 6600 events and IceCube (up to half-year of IceCube with 40 strings) 13000 events. No extra-terrestrial neutrinos have been found so far but results have been presented giving improved limits for the extraterrestrial neutrino flux, magnetic monopoles, violation of Lorentz invariance, limits on dark matter and determination of the conventional atmospheric muon neutrino flux up to several 100 TeV.

3.1 Search for neutrino point sources

Neutrino telescopes have been using the Earth as a filter to reject down going atmospheric muons when searching for neutrino point sources. When demanding only up going muons, AMANDA and IceCube are sensitive to neutrino sources in the Northern Hemisphere only, owing to the position at the South Pole. Neutrino sources in the Northern sky are fully visible 24 h per day for AMANDA and IceCube. The neutrino telescopes in the Northern hemisphere have a larger fraction of the sky accessible but not for 24 h per day.

The IceCube collaboration has recently started [7] to search for high energy neutrino sources above the horizon. This can be done by a zenith dependent cut on muon energy reducing the flux of down going atmospheric muons by a factor of 10^{-5} to obtain a constant muon rate per solid angle. The flux limits in the Southern hemisphere for IceCube are mainly for neutrino energies above 100 TeV. The sensitivity for neutrinos from point sources is reduced but still very competitive to existing limits for E^{-2} neutrino sources.

The observed sky-maps for the four telescopes are shown in Figure 8 with the directions of the observed neutrino events, except for ANTARES where the directions still are scrambled. The true directions will be available when data is unblinded.
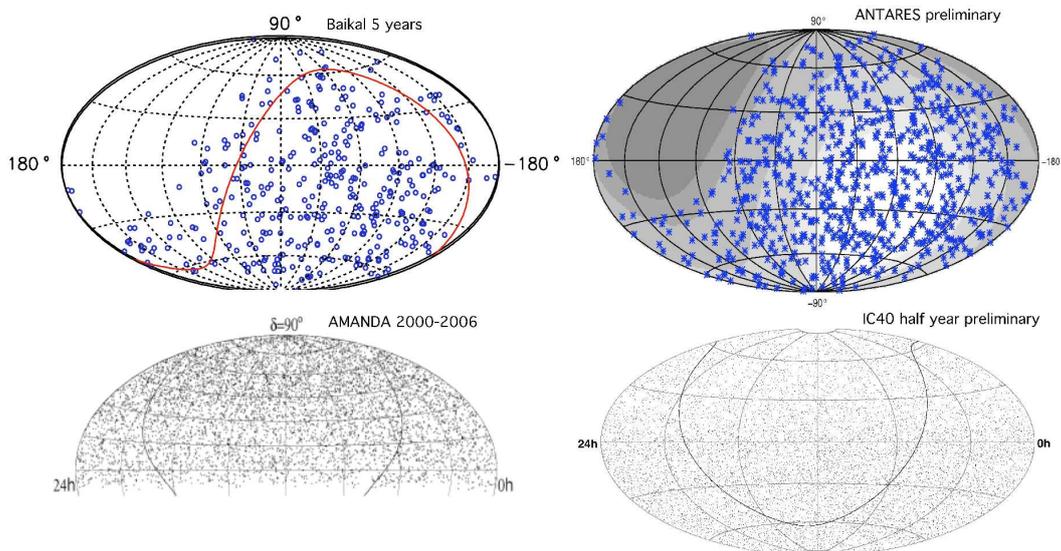
Figure 8: Sky maps from Baikal [5] upper left (391 events), ANTARES 5+12 lines [8] (preliminary) upper right (750 events), AMANDA 7 years [9] lower left (6600 events) and IC40 half-year [10] (preliminary) lower right (6796 events Northern Hemisphere and 10981 events Southern Hemisphere). Baikal and ANTARES maps are in galactic coordinates and AMANDA and IceCube in equatorial coordinates. The ANTARES sky map has the neutrino directions still scrambled. The events in the IceCube Southern hemisphere are mainly high energy atmospheric muons with a reduced rate by a factor of 10^{-5} by energy cut.

IceCube's most sensitive search so far is the half-year exposure of IC40 (2008), see Figure 8 (lower right) [10]. The "warmest" spot was at right ascension of 114.95° and declination of

15.35°. The *p*-value accounting for effective trials in scanning the sky was 61 % which is far from significant. ANTARES has presented their first preliminary results for 25 selected sources [11] using the 5 string telescope (2007) without any significant signal.

In Figure 9, neutrino flux upper limits (90 %) for predefined specific point sources as well as average upper limits and expected sensitivities are shown, assuming an E^{-2} energy dependence. The IC40 175 days (half year) exposure is used to predict the sensitivity and discovery potential (5σ) for IC40 345 days. The preliminary sensitivities for the completed IceCube [12] and KM3NeT [13] are also shown for one year exposure. The flux limits for IceCube above the horizon (negative declination) are based on very high energy events (above 100 TeV and in the PeV range) whilst ANTARES covers the GeV to TeV energy range. IceCube and ANTARES are sensitive to different parts of the E^{-2} spectrum for the negative declination.

3.2 GRB

Short transient neutrino sources have a much reduced background from atmospheric neutrinos. One type of potential transient sources for high energy cosmic rays are the Gamma Ray Bursts (GRBs). They are the most violent events observed in space. The search for neutrino events in coincidence in time and direction (given by satellites) with a GRB is almost free of background from atmospheric neutrinos. AMANDA [14], IceCube [15][16] and ANTARES [17] have presented limits for hundreds of GRBs but without any significant observation of coincident neutrinos. The GRBs are probably the most promising source for detection of extra galactic neutrinos. The sensitivity for Ice-Cube is expected to be high enough

Figure 9: Upper limits (90%) and sensitivities for E^{-2} neutrino sources as a function of declination. AMANDA [9], IC40 [10], Super Kamiokande [18], ANTARES 5 lines [11], ANTARES 365 days [11], KM3NeT [13], IceCube 365 days [12]. Courtesy T. Montaruli.

to exclude GRBs as the main sources for ultra high energy cosmic rays, if no signal is observed by IceCube within five years.

3.3 Search for a diffuse neutrino flux

If there is not a sufficient number of events from neutrino point sources to give individual significant observations, the sum of all neutrino sources in the sky could still be significant. However, the only way to distinguish these neutrinos from the atmospheric neutrinos is that we expect the astrophysical sources to have a harder energy spectrum E^{-2} compared to the atmospheric neutrinos $E^{-3.7}$. The signal for a diffuse astrophysical neutrino flux is then an excess of high energy neutrino events above the expected atmospheric neutrino energy distribution. Diffuse flux limits are normally given for the sum of all three neutrino flavors because the

large distance from an astrophysical source will give equal mixture due to neutrino oscillation.

Figure 10 shows the 90 % confidence level upper limits and expected sensitivities for diffuse flux of astrophysical neutrinos as a function of neutrino energy for a number of experiments. The unfolded atmospheric muon neutrino spectrum from AMANDA [19] and Ice-Cube [20] (preliminary) are also shown. New preliminary diffuse flux limits for astrophysical neutrinos from Baikal [21], AMANDA [22] and IceCube [23] [24] with 22 strings are included. No statistically significant observation of any astrophysical diffuse neutrinos has been observed. However, as can be seen in Figure 10 the preliminary flux sensitivity for IC40 [10] is now below the Waxman-Bahcall flux prediction [4], showing that with 50% of IceCube one has already reached a possible discovery region.
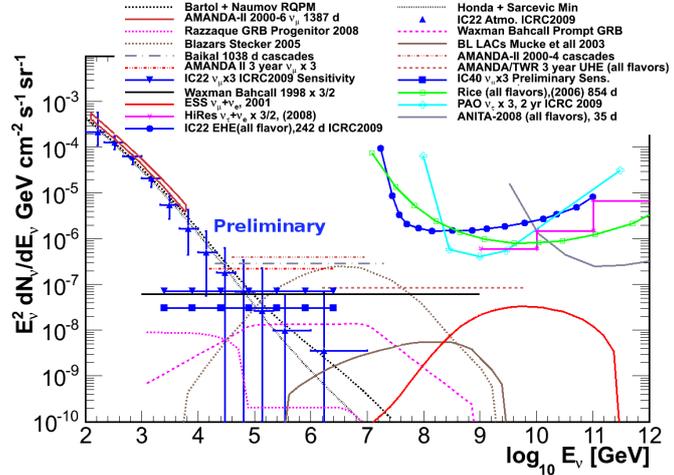
Figure 10: Experimental upper limits for diffuse extraterrestrial neutrino fluxes, estimated sensitivities and predictions for different theoretical models as a function of neutrino energies.

3.4 Dark matter search

If the dark matter consists of weakly interacting massive particles (WIMPs) like e.g. supersymmetric neutralinos, one expects these to be gravitationally captured by heavy objects like Sun, Earth, the center of the galaxy, etc. Since neutralinos are majorana particles, they annihilate and produce standard matter e.g. neutrinos. The observation of high energy neutrinos (GeV to TeV) from the centers of Sun or Earth or the centre of the galaxy might then be an indirect indication for dark matter particles. Baikal [25], ANTARES [26], AMANDA [28] and IceCube[29] have recently presented limits on muon flux generated by neutrinos from neutralino annihilation in the Sun. No excess of neutrinos from the Sun or the centre of the Earth has been observed.

The neutrino telescopes are especially sensitive for spin-dependent interactions between dark matter particles and standard matter since
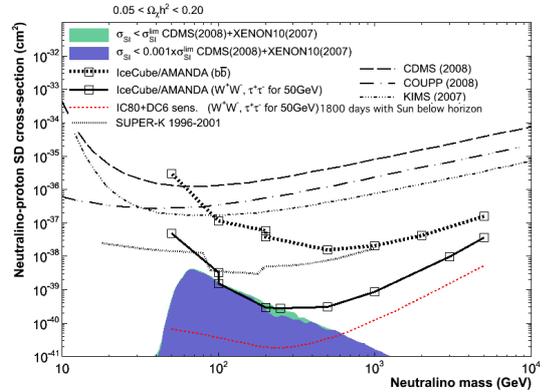
Figure 11: Upper limits at 90% confidence level on spin-dependent neutralino proton cross section for the hardest (W^+W^-) and softest $(b\bar{b})$ decay channels. The shaded area represents MSSM models not disfavored by direct dark matter experiments based on DarkSusy [34].

the capture in the Sun is sensitive to this cross section. This allows for comparison with direct detection experiments for models having equilibrium between capture and annihilation rates in the Sun. In Figure 11 the 90% upper limits on the spin-dependent neutralino-proton cross section are shown for the neutrino telescopes Super-Kamiokande [27], AMANDA [28] and IC22 [29]. The limits from the neutrino telescopes are far better than for the direct detection experiments CDMS [30], XENON-10 [31], KIMS [32] and COUPP [33]. The shaded area represents MSSM models not disfavored by direct dark matter experiments based on DarkSusy [34]. The IC80 + DeepCore sensitivity is given for 1800 days with the Sun below the horizion. As seen in Figure 11, IC80 with the DeepCore telescope will soon be able to test many interesting MSSM models. DeepCore is improving the sensitivity at the lowest neutralino masses.

3.5 Atmospheric muon anisotropy

The high flux of atmospheric muons recorded in IceCube opens up the possibility for studies of anisotropy in cosmic rays. IceCube [35] with 22 strings (2008) has reconstructed more than $4.3 \cdot 10^9$ down-going atmospheric muons from the CR interactions in the atmosphere. The median angular resolution is $3°$ and the median energy is 14 TeV. Figure 12 shows the Southern sky in equatorial coordinates with a large-scale anisotropy of amplitude $(6.4 \pm 0.2) \cdot 10^{-4}$. The explanation is not

Figure 12: The sky map of relative intensity of atmospheric muons in equatorial coordinates. In total $4.3 \cdot 10^9$ atmospheric muons have been recorded.

known but the anisotropy is probably due to the the local interstellar magnetic field. It is consistent with what has already been observed for the Northern hemisphere by Super-Kamiokande [36], MILAGRO [37] and the Tibet array [38] [39].

4 New neutrino telescopes

The KM3NeT [13] Consortium (joint effort by the ANTARES, NEMO [40] and Nestor [41] [42] collaborations) is working on a large Gigaton telescope in the Mediterranean. The aim is to have one large telescope in the Northern Hemisphere as a complement to IceCube in the Southern Hemisphere. They have published a Conceptual Design Report [43] and are working on a technical design report to be published early 2010. The KM3NeT consortium has broad experience with neutrino telescopes in the deep ocean. The sites discussed for the KM3NeT telescope are 1) 40 km outside Toulon France at 2500 m depth 2) 15 km - 48 km outside Pylos Greece at 3700-5200 m depth and 3) 70 km outside Sicily Italy at 3500 m depth. Of the three projects ANTARES is the only "complete" telescope running. NEMO and NESTOR have been using single telescope components for testing. The angular resolution aimed for is $0.1°$ at 100 TeV neutrino energies.

The Baikal collaboration is preparing a new telescope in the Lake Baikal called Gigaton Volume Detector (GVD). It will have 91-100 strings with 12-16 optical modules each. The

instrumented vertical size will be 350 m and the total horizontal area about two square kilometers. The effective volume for 100 TeV cascades will be 0.5 - 1.0 Gigaton. The muon threshold is expected to be 10 TeV. The construction is planned to start 2011 and the telescope to be completed in five years.

5 Conclusion

The partially completed IceCube telescope has already reached the sensitivity for testing "realistic" predictions of astrophysical neutrino fluxes. ANTARES is now fully operational and is the first running telescope in the Mediterranean. The planning for KM3NeT in Mediterranean and GVD in Lake Baikal are in progress. ln the near future it will be shown if telescopes of one Gigaton will be large enough to detect the neutrino flux from extraterrestrial sources.

6 Acknowledgments

I would like to thank the organizers for inviting me to the Lepton Photon 2009 conference in Hamburg. I am indebted to my colleagues in the different experiments for giving me information and for valuable discussions and to C. Finley, K. Hultqvist and C. Walck for reading and commenting the manuscript.

References

[1] T. Gaisser Private communication 2009.

[2] K. Greisen, *et al.,Phys. Rev. Lett.* 16 (1966) 748; G.T. Zatseptin and V.A. Kuzmin, JETP Lett. 5 (1966) 78.

[3] P. Gorham, 1st International Workshop on the Saltdome Shower Array (SalSA), SLAC, Feb 2005.

[4] E. Waxman and J.N. Bachall, Phys. Rev. **D59** (1999) 023002.

[5] V. Aynutdinov *et al.,*Nucl. Instr. and Meth. A602 (2009) 14.

[6] A. Heijboer for the ANTARES collaboration, *Reconstruction of Atmospheric Neutrinos in Antares*, Proc. of the 31st ICRC, arXiv:astro-ph/0908.0864 (2009).

[7] R .Abbasi *et al.,* Phys. Rev. Lett. **103**, 221102 (2009).

[8] P. Vernin, *et al., High Energy Neutrino astronomy with the ANTARES telescope.*Proceedings of the 4th International workshop on astronomy and relativistic astrophysics, Sao Paulo, Brasil, 4 august 2009. To be published in International Journal of Modern Physics D.

[9] R.Abbasi *et al.,* Phys. Rev. **D79**, 062001 (2009).

[10] A. Karle for the IceCube collaboration, *IceCube*, Proc. of the 31st ICRC, Lodz, Poland, July 2009.

[11] S. Toscano for the ANTARES collaboration, *Point source searches with the ANTARES neutrino telescope*, Proc. of the 31st ICRC, Lodz, Poland, July 2009, arXiv:astro-ph/0908.0864.

[12] J. Dumm, J.A. Aguilar, M. Baker, C. Finley, T. Montaruli for the IceCube collaboration, *All-Sky Point-Source Search with 40 Strings of IceCube* Proc. of the 31st ICRC, Lodz, Poland, July 2009, presented at the conference.

[13] J. P. Ernenwein on behalf of the Km3NeT consortium, *KM3NeT: a cubic-kilometre-scale deep sea neutrino telescope in the Mediterranean Sea*, Proc. of the 31st ICRC, Lodz, Poland, July 2009

[14] M. Duvoort and N. van Eindhoven, for the IceCube Collaboration, *Search for GRB neutrinos via a (stacked) time profile analysis*, Proc. of 31st ICRC, Lodz, Poland, July 2009.

[15] R. Abbasi *et al.,* Astrophys. J. **710** (2010) 346.

[16] K. Meagher *et al., Search for neutrinos from GRBs with IceCube*, Proc. of 31st ICRC, Lodz, Poland, July 2009.

[17] M. Bouwhuis on behalf of the ANTARES collaboration, *Search for gamma-ray bursts with the ANTARES neutrino telescope*, Proc. of 31st ICRC, Lodz, Poland, July 2009.

[18] E. Thrane *et al.,* Super-Kamiokande collaborationen arXiv:0907.1594v1 [astro-ph.HE]

[19] A. Abbasi *et al.,* Phys. Rev. **D79**, 102005, 2009.

[20] D. Chirkin *et al., Measurement of the atmospheric Neutrino Energy Spectrum with IceCube*, Proc. of 31st ICRC, Lodz, Poland, July 2009.

[21] A. Avrorin *et al. Search for a diffuse flux of high-energy neutrinos with the Baikal neutrino telescope NT200,* Proc. of 31st ICRC, Lodz, Poland, July 2009.

[22] A. Silvestri for the IceCube collaboration, *Search for Ultra High Energy Neutrinos with AMANDA*, Proc. of 31st ICRC, Lodz, Poland, July 2009.

[23] K. Hoshina *et al., Search for Diffuse High Energy Neutrinos with IceCube,* Proc. of 31st ICRC, Lodz, Poland, July 2009.

[24] K. Mase, A. Ishihara and Shigeru Yoshida for the IceCube Collaboration, *The extremely high energy neutrino search with IceCube*, Proc. of 31st ICRC, Lodz, Poland, July 2009.

[25] A. Avrorin *et al.,Search for Neutrinos from Dark Matter Annihilation in the Sun with the Baikal Neutrino Experiment,* Proc. of 31st ICRC, Lodz, Poland, July 2009, arXiv:0909.5589.

[26] G.M.A. Lim on the behalf of the ANTARES collaboration, *First results on the search for dark matter in the Sun with the ANTARES neutrino telescope,* Proc. of 31st ICRC, Lodz, Poland, July 2009, arXiv:1002.0701

[27] S. Desai *et al.,* Phys. Rev. **D70**, 083523 (2004) [Erratum-ibid. **D70**, 109901 (2004).

[28] J. Braun and D. Hubert for the IceCube Collaboration, *Searches for WIMP Dark Matter from the Sun with AMANDA*, Proc. of 31st ICRC, Lodz, Poland, July 2009.

[29] R. Abbasi *et al.,* Phys. Rev. Lett. **102**, 201302 (2009).

[30] Z. Ahmed *et al.,* Phys. Rev. Lett. **102**, 011301 (2009).

[31] J. Angle *et al.,* Phys. Rev. Lett. **100**, 021303 (2008).

[32] H. S. Lee *et al., Phys. Rev. Lett.* **99**, 091301 (2007).

[33] E. Behnke *et al.,* Science **319**, 933 (2008).

[34] P. Gondolo *et al.,* J. Cosmol. Astropart. Phys. **07**, (2004) 8.

[35] R. Abbasi and P. Desiati for the IceCube collaboration, *Large Scale Cosmic Rays Anisotropy With IceCube*, Proc. of 31st ICRC, Lodz, Poland, July 2009.

[36] G. Guillian *et al.* Super-Kamiokande collaboration, Phys. Rev. **D75** 062003 (2007).

[37] A. Abdo et al., ArXiv:astro-ph/0806.2293, 2008.

[38] M. Amenomori *et al., Science*, vol **314**, 439-443, 2006.

[39] M. Amenomori *et al., Large-scale sidereal anisotropy of multi-TeV galactic cosmic rays and the heliosphere,* Proc. of 31st ICRC, Lodz, Poland, July 2009.

[40] E. Migneco *et al.,* Nucl. Inst. Meth. A**588**, 111 (2008).

[41] NESTOR homepage, http://www.nestor.org.gr.

[42] G. Aggouras *et al.,* NESTOR collaboration, Nucl. Inst. Meth. A**552**, 420 (2005).

[43] KM3NeT Consortium, *Conceptual Design Report:* http//www.km3net.org.

Discussion

Frank Simon (MPI Munich: How is the connection between GRBs, high energy CRs and neutrinos made? Does it involve pinpointing the source in space with the neutrino signal?

Answer: The GRB are easy to study with a very small background of atmospheric neutrinos. The analysis is done off line using the information from GRB satellites about the exact time and direction. The expected background from atmospheric neutrinos is very small. E.g. the AMANDA GRB search mentioned, with more than 400 GRB studied, had in total less than two expected atmospheric neutrino events.

Giovanni Siragusa (Universiät Mainz): What are the prospectives for radio and acoustic detection for high energy neutrinos? Nemo is testing such a technology.

Answer: I do not know the status of the NEMO effort. There are several radio projects for ice which are looking promising. The prospect for acoustic detecting of high energy neutrinos in ice does not looks as promising at the moment.

Vali Huseynov (Nakhchivan State University): To detect neutrinos it would be better in the future to use the crystals with strong magnetic field. When inner effective magnetic fields are strong enough, the influence of the field on the neutrino interaction processes (e.g. Neutrino-electron scattering) is essential. In this case it is possible to detect neutrinos of very low energies and relic neutrinos.

Answer: I do not know enough in order to comment what you are saying. However, the detection of the relic neutrinos is the ultimate neutrino experiment.

Gravity Scale Particle Physics with Torsion Pendulums

Seth A. Hoedl, Eric G. Adelberger, Jens Gundlach, Blayne R. Heckel and Stephan Schlamminger
University of Washington, Seattle, WA, USA

Torsion pendulum experiments are used for precise tests of the strong and weak equivalence principle, the gravitational inverse square law and Lorentz symmetry. In addition, dedicated experiments can be constructed that are sensitive to axion-like particles. The fantastic sensitivity of these devices has many implications for gravity scale particle physics. Here we briefly summarize a few of the particle physics implications of four of the Eöt-Wash torsion pendulum experiments inspired by string theory and other extensions to the standard model.

1 Introduction

Starting with Cavendish, torsion balance experiments have been used for precision measurements of gravity and other forces. The fantastic sensitivity these devices can achieve motivates their continued use for testing fundamental symmetries and searching for new interactions. Modern efforts are inspired by theoretical work, such as string theory, that attempts to unify gravity with the standard model, explain the "dark energy" that constitutes most of the energy density of the universe and explain the very small CP violation in the strong interaction.

The principle of operation of our torsion balances is straight forward. We convert an oscillating differential acceleration (in the case of the equivalence principle) or an oscillating force (in the case of our other experiments) into an oscillating twist of a torsion pendulum. This twist is then observed by reflecting a collimated infrared laser beam off the pendulum onto a position sensitive light detector. At the room temperature thermal limit, our experiments experience a twist noise of 1 nano-radian/$\sqrt{\text{day}}$. In essence, we confine the motion of almost one mole of atoms to one degree of freedom. With this sensitivity, our torsion pendulums can place very interesting constraints on the exchange of very light scalar, pseudoscalar or vector particles, large extra dimensions, the chameleon mechanism, non-commutative spacetime geometry and Plank-scale Lorentz violation. A thorough review of the Eöt-Wash experiments and their theoretical motivations has recently been published [1]. Here we briefly summarize the particle physics implications of four pendulums devoted to testing the equivalence principle [2], looking for short range deviations from the inverse square law [3, 4], testing Lorentz symmetry [5] and searching for axion-like particles.
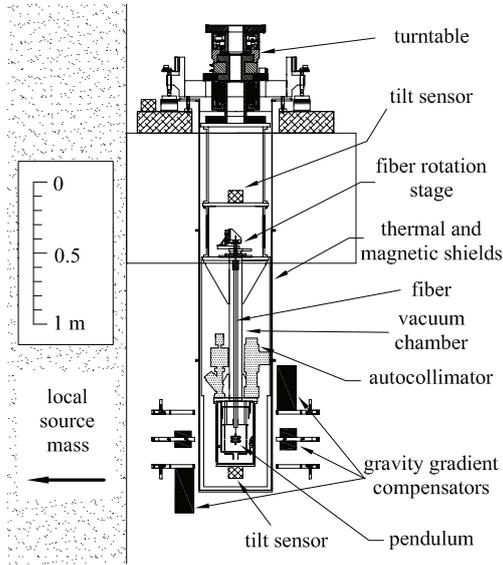
Figure 1: A cross section diagram of the equivalence principle torsion balance. The balance is suspended below a continuously rotating turntable. Gravity gradient compensator masses reduce the gravity gradients at the location of the pendulum.
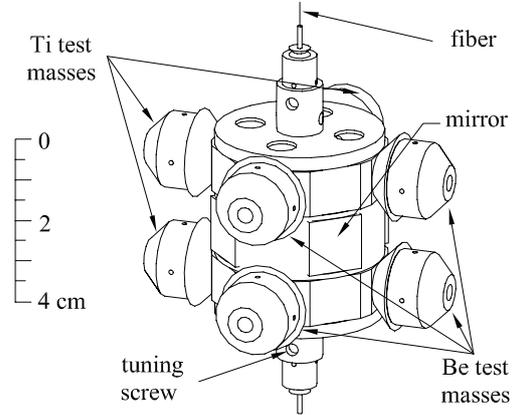
Figure 2: A diagram of the equivalence principle torsion pendulum. The four titanium and four beryllium test masses are arranged in a composition dipole. Their shape and location is chosen to minimize coupling to residual gravity gradients.

2 Test of the equivalence principle

Most theoretical attempts to unify general relativity with the standard model predict violation of the equivalence principle. In particular, string or M theory predicts hundreds of massless scalar particles with composition dependent gravitational strength couplings. Thus, the equivalence principle, which states that all objects, independent of composition, fall at the same rate in a *uniform* gravitational field is an ideal test of such forces.

Our equivalence principle torsion balance looked for a horizontal differential acceleration between test bodies composed of different materials. A differential acceleration would violate the equivalence principle. This torsion balance was continuously rotated by an air-bearing turntable with a period of ~ 20 min (See Fig. 1). The twist angle of the torsion pendulum was observed using

Source	Δa (cm/s^2)	$\Delta a/a_{source}$
Earth	$(+0.6 \pm 3.1) \times 10^{-13}$	$(+0.3 \pm 1.8) \times 10^{-13}$
Sun	$(-2.4 \pm 2.8) \times 10^{-13}$	$(-4.0 \pm 4.7) \times 10^{-13}$
Milky Way	$(-2.1 \pm 3.1) \times 10^{-13}$	$(-1.1 \pm 1.6) \times 10^{-5}$
CMB	$(-2.9 \pm 2.7) \times 10^{-13}$	$(-2.1 \pm 1.9) \times 10^{-3}$

Table 1: The differential acceleration of titanium and beryllium test bodies towards terrestrial and astronomical sources. The $1 - \sigma$ uncertainties are dominated by thermal noise in the fiber (statistical) and residual gravity gradients at the location of the pendulum (systematic).

a corotating autocollimator. The pendulum itself consisted of eight test bodies in a compo-

sition dipole orientation (See Fig. 2). In the most recent published experiment [2], the test bodies were made of titanium and beryllium. The interior volume of the less dense body is machined so that both the mass and the exterior geometry of each test body are well matched. The shape and location of each body on the pendulum were chosen to minimize the coupling of the pendulum to residual gravity gradients. Table 1 lists our most recent measurements of the differential acceleration of the titanium and beryllium test bodies towards both terrestrial and astronomical sources.

In grand unified theories, B-L number is exactly conserved, and thus one expects to observe Yukawa couplings to B-L number. We parameterize this possibility by looking for a potential of the form:

$$V(r) = -G\frac{m_1 m_2}{r}\left(1 + \widetilde{\alpha}\cdot\left[\frac{\widetilde{q}}{\mu}\right]_1\left[\frac{\widetilde{q}}{\mu}\right]_2 e^{-r/\lambda}\right),$$

where r is the distance between two point objects, λ is the Compton wavelength of the exchange particle, m_1 and m_2 are the masses of the two objects, μ represents the mass of each object in atomic mass units and $\widetilde{q}$ is the "charge" of each object. The coupling strength of the Yukawa interaction, $\widetilde{\alpha}$, is expressed in units of the gravitational interaction between the two point objects. Note that for electrically neutral matter, a B-L coupling implies that $\widetilde{q} = N$. Figure 3 shows our 2-σ exclusion plot for interactions coupled to B-L as a function of interaction range.
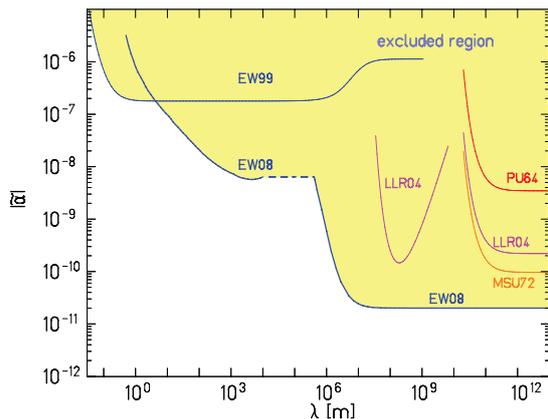
Figure 3: The 2-σ limit on EP-violating Yukawa interactions that couple to B-L. The labels link to the references as follows: PU64 –[7], MSU72 – [8], EW99 – [9], LLR04 –[10], EW08 – [11].

The EP-violating pendulum can also be used to constrain non-gravitational forces between matter and dark matter [6]. At the Earth's location in the galaxy, roughly three-quarters of the acceleration towards the center of the galaxy is due to normal matter, and the other quarter is due to dark matter. Thus, by looking for an equivalence principle violating acceleration towards the center of the galaxy we can constrain the differential acceleration of different elements towards the dark matter. Although the bound this analysis places on a non-gravitational interaction depends on the relative new "charge" of the proton, electron and neutron, by analyzing the differential acceleration of two pendulums with different composition dipoles we can state that, at most, 5% of the acceleration of neutral hydrogen towards the galactic center is due to a non-gravitational interaction.

3 Test of the gravitational inverse square law at short distances

A number of theoretical developments predict modifications to the gravitational inverse square law at short distance scales. The fat graviton scenario [19] and models with extra time dimensions [20] would *weaken* gravity at short distance scales. The extra space dimensions of M
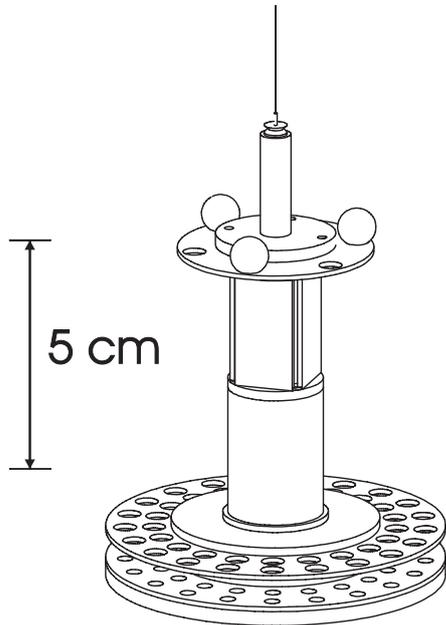
Figure 4: A scale drawing of the gravitational inverse square law torsion pendulum and attractor. The disks are explained in the text. The three small spheres were used for continuous gravitational calibration of the pendulum. An electrical shield between the pendulum and the attractor is not shown.
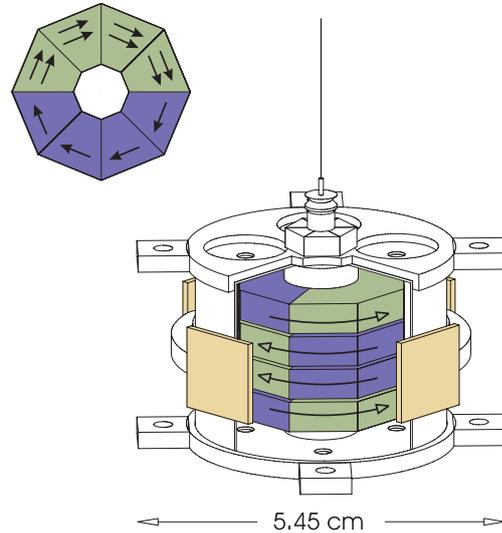
Figure 5: A scale diagram of the spin pendulum. The light green and dark blue volumes are AlNiCo and $SmCo_5$ magnets respectively. Arrows with filled heads show the relative densities and directions of the electron spins, open-headed arrows show the directions of B. Upper left: top view of a single "puck." Lower right: the pendulum with the magnetic shields removed to illustrate the orientation of the four pucks.

theory would cause gravity to *strengthen* at distance scales smaller than the size of the largest compactified dimension [21]. Tests of the inverse square law (ISL) at short distance scales using a torsion pendulum place very interesting constraints on these theories, as well as new forces generated by the exchange of proposed scalar or vector particles [4].

The most recent version of our ISL test [3] consisted of a torsion pendulum, the "detector," suspended above a rotating "attractor." (See Fig. 4). The detector's test bodies were 42 holes machined into a 1 mm thick molybdenum disk in a 21-fold rotationally symmetric pattern. The attractor consisted of two disks. The upper attractor disk had a hole pattern similar to the detector disk. The lower attractor disk was thicker and made of tantalum. 21 holes were machined into the lower disk and were displaced by $\pi/21$ rad from the holes in the upper attractor to cancel the Newtonian torque on the detector produced by the upper set of attractor holes. The gravitational interaction between the missing masses of the detector and the attractor holes applied a torque on the detector that oscillated 21 times for each revolution of the attractor. We monitored the twist of the pendulum with an autocollimator system.

We parameterize a deviation from the ISL by looking for a potential between two point
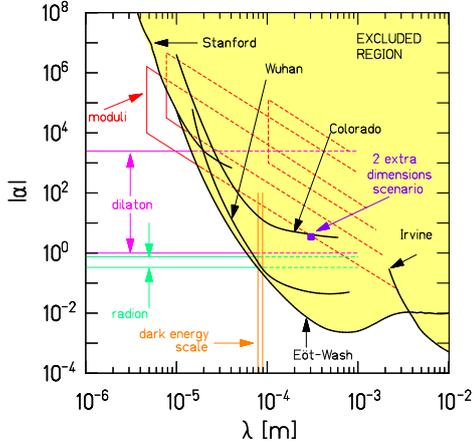
Figure 6: The 2-σ constraints on Yukawa violations of the gravitational inverse square law. Heavy lines labeled Eöt-Wash, Irvine, Wuhan, Colorado and Stanford show experimental constraints from Refs. [3, 12, 13, 14, 15] respectively. Lighter lines show theoretical expectations summarized in Ref. [16].
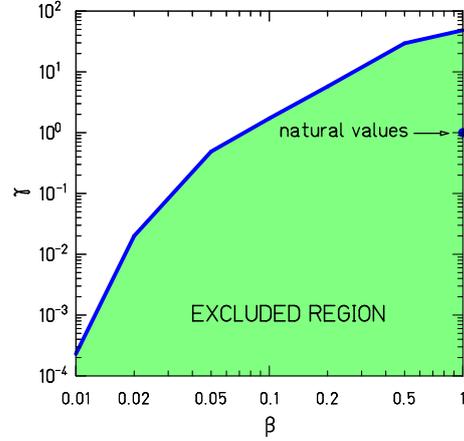
Figure 7: The 2-σ exclusion bound on the chameleon parameter γ as a function of β calculated from the data in Ref. [3]. In most chameleon theories, it is expected that both parameters are of order 1.

objects of the form:

$$V(r) = -G\frac{m_1 m_2}{r}\left(1 + \alpha \cdot e^{-r/\lambda}\right),$$

where λ and α parameterize respectively the range and strength of a Yukawa deviation. Figure 6 plots our most recent 2-σ exclusion on α as a function of λ. Our 2-σ exclusion bounds imply that the maximum size of any extra dimension must be less than 44 μm. If there are two extra dimensions, our result implies that the unification scale $M^* \geq 3.2$ TeV/c^2. In a six extra dimension scenario, our results imply that $M^* \geq 6.4$ TeV/c^2.

Our ISL pendulum can also make very interesting constraints on chameleons. In this model, the very strong constraints on gravitationally coupled low mass scalars can be evaded if the scalars are self-interacting. In the presence of matter, the scalars acquire an effective mass so that only a thin skin of material can generate long-range fields [22, 23]. The natural value of the parameters in this model, β and γ, are excluded by our 2-σ constraints (see Fig. 7).

The bounds on an ISL deviation also limit the exchange of scalar or vector particles. For example, through a second order interaction, the ISL pendulum is sensitive to a scalar/photon vertex [24]. For a scalar mass of 1 meV/c^2, our results constrain the coupling strength $g_{\phi\gamma\gamma} \leq 1.6 \times 10^{-17}$ GeV^{-1}. Note that this constraint is 10^{11} times smaller than the coupling that was claimed to explain the dichroism and birefringence of the vacuum initially observed by the PVLAS collaboration [25].

4 Spin pendulum experiment

Torsion pendulums can also be used to look for interactions that couple to intrinsic spin. Our most recent spin pendulum apparatus [5] employed a rotating torsion balance and a torsion pendulum consisting of four octagonal "pucks" (see Fig. 5). One half of each puck was made of AlNiCo, the other half was made of SmCo$_5$. The magnetic field of AlNiCo is created almost entirely by electron spin; in SmCo$_5$ roughly half of the field is created by electron spin and the balance is created by the orbital moment of the electrons. Thus, in each puck there was a net spin moment created by $\approx 10^{23}$ polarized electrons but minimal external magnetic fields. The four pucks were arranged in the pendulum to minimize coupling to gravity gradients and cancel a composition dipole that could make the pendulum sensitive to a violation of the equivalence principle.

By looking for a coupling of the pendulum's intrinsic spin to a preferred frame, we place an upper bound of 10^{-22} eV on the energy required to flip an electron spin about an arbitrary direction fixed in inertial space. The interested reader is directed to [5] for a thorough discussion of the impact of this constraint on CP violating forces and Lorentz violation. A preferred-frame can also occur in noncummutative space-time geometries predicted in some D-brane theories [26]. In these models, the space-time coordinates x_μ do not commute, but instead satisfy $[\hat{x}_\mu, \hat{x}_\nu] = i\Theta_{\mu\nu}$, where $|\Theta|$ represents the smallest "patch" of area. The noncommutative geometry is equivalent to a pseudo-magnetic field that defines a preferred direction, $\eta^i = \epsilon^{ijk}\Theta_{jk}$. Our preferred-frame constraints imply that the minimum observable area is $|\Theta| \leq 4.9 \times 10^{-59}$ m^2, which corresponds to a length scale $\ell = 350 l_{GUT}$, where $l_{GUT} = \hbar c/(10^{16}\text{GeV})$.

5 A search for axion-like particles

A wide variety of extensions to the standard model predict the existence of new pseudoscalar bosons. Conventionally, these pseudoscalars are the pseudo-Nambu-Goldstone bosons of a spontaneously broken symmetry, such as familons, majorons, arions, omions or axions. Pseudoscalars can also arise in the context of technicolor, superstring and Kaluza-Klein theories. The axion is perhaps the most studied pseudoscalar experimentally, and several searches are actively underway. We follow convention and refer to all light pseudoscalars as axion-like particles or ALPs.

Any sufficiently light ALP will mediate a macroscopic parity and time violating interaction between polarized electrons and unpolarized nucleons [27] given by the potential:

$$V(\hat{\sigma}, \hat{r}) = \frac{\hbar^2}{8\pi m_e} \left(\frac{g_s g_p}{\hbar c}\right) (\hat{\sigma} \cdot \hat{r}) \left(\frac{1}{\lambda r} + \frac{1}{r^2}\right) e^{-r/\lambda},$$

where λ is the Compton wavelength of the ALP, and $g_s g_p/\hbar c$ is a dimensionless measure of the strength of the interaction. Although the spin pendulum is very sensitive to a long range ($r > 1$ m) interaction, for short ranges a dedicated effort is needed. Length scales between 0.02 m and 20 μm are especially interesting because they correspond to the high mass end of the axion "window," where microwave cavity based axion searches are not sensitive.

17.8 μm thick
Tungsten Fiber

Cross Bar

Ultrapure Titanium Bar

Laser Cut
Silicon Wafer

Electromagnet

x

y
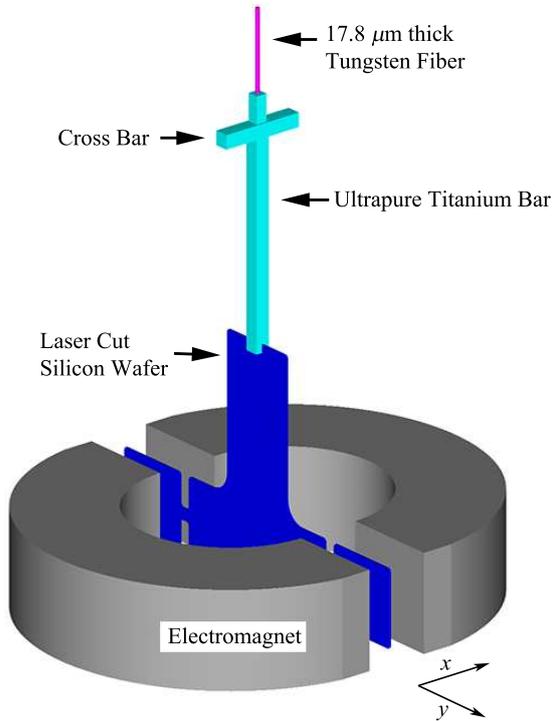
Figure 8: A scale diagram of the ALP pendulum suspended between the two magnet halves. The gap between the magnet halves is exaggerated for clarity.

Inspired by these considerations, we have constructed a dedicated experiment sensitive to a macroscopic parity and time violating force. The apparatus consists of two parts: a split toroidal electromagnet and a planar torsion pendulum that is suspended between the two magnet halves. The magnet halves are fixed to the apparatus; the pendulum is free to twist about the torsion fiber axis. The pendulum twist is observed with an autocollimator. The gap between the magnet halves is ≈ 3 mm, and the pendulum is a laser-cut 500 μm thick silicon wafer.

The signal of a macroscopic PT violating force is a change in the equilibrium angle of the pendulum when the magnetic field is switched from the clockwise to counterclockwise orientation. Because the pendulum is suspended in a region with a strong magnetic field (3.59 kG), systematic errors associated with the finite magnetic susceptibility of the silicon dominate the data. Nevertheless, a constraint on an ALP mediated force can still be obtained because an ALP force will *strengthen* when the pendulum is moved closer to either magnet half, whereas magnetic systematics depend only on the magnetic field. Thus, by measuring the ALP signal at different pendulum distances from the pole faces, we are able to constrain the PT violating force. Figure 9 plots our expected 2-σ exclusion region given our current understanding of the systematic errors.

6   Conclusion

Torsion balances have a long tradition of fundamental precision measurement. Our torsion balances can make many very interesting statements about particle physics. A few examples:

- Any infinite-range interaction that couples to B-L must be 2×10^{-11} times weaker than gravity.

- At most, 5% of the acceleration of hydrogen towards the center of the galaxy could be due to a non-gravitational force between luminous matter and dark matter.

- Any extra dimension must have a size less than 44 μm.

- The energy scale in a noncommutative geometry must be greater than 10^{13} GeV.
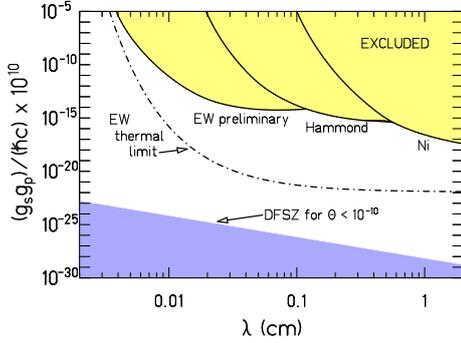
Figure 9: Current and prospective 2-σ bounds on the parity and time violating monopole-dipole force between polarized electrons and unpolarized nucleons as a function of the Compton wavelength of the exchanged ALP. Lines labeled Ni and Hammond show experimental constraints from Refs. [17] and [18] respectively. The EW preliminary limit shows the exclusion bound we expect to achieve with our current apparatus. The EW thermal limit line shows the ultimate sensitivity of the ALP pendulum if all systematic effects could be mitigated. The lower shaded region shows the allowed region in the DSFZ QCD axion model given that $\Theta_{QCD} \leq 10^{-10}$.

7 Acknowledgments

References

[1] E.G. Adelberger *et al.*, Progress in Particle and Nuclear Physics **62** 102 (2009).

[2] S. Schlamminger *et al.*, Phys. Rev. Lett. **100** 041101 (2008).

[3] D.J. Kapner *et al.*, Phys. Rev. Lett. **98** 021101 (2007).

[4] E.G. Adelberger *et al.*, Phys. Rev. Lett. **98** 131104 (2007).

[5] B.R. Heckel *et al.*, Phys. Rev. **D78** 092006 (2008).

[6] C.W. Stubbs *et al.*, Phys. Rev. Lett. **70** 119 (1993).

[7] P.G. Roll, R. Krotkov, R.H. Dicke, Ann. Phys. **26** 442 (1964).

[8] V.G. Braginsky, V.I. Panov, JETP **34** 463 (1972).

[9] G.L. Smith *et al.*, Phys. Rev. **D61** 22001 (2000).

[10] J.G. Williams, S.G. Turyshev, D.H. Boggs, Phys. Rev. Lett. **93** 261101 (2004);
C. Talmadge *et al.*, Phys. Rev. Lett. **61** 1159 (1988);
S.G. Turyshev, J.G. Williams, Int. J. Mod. Phys. **D16** 2165 (2007).

[11] T.A. Wagner, Ph.D. Thesis, University of Washington (in press).

[12] R. Spero *et al.*, Phys. Rev. Lett. **44** 1645 (1980).

[13] L.-C. Tu *et al.*, Phys. Rev. Lett. **98** 201101 (2007).

[14] J.C. Long *et al.*, Nature **421** 922 (2003).

[15] S.J. Smullin *et al.*, Phys. Rev. **D72** 122001 (2005).

[16] E.G. Adelberger *et al.* Ann. Rev. Nucl. Part. Sci. **53** 77 (2003).

[17] W.-T. Ni *et al.* Phys. Rev. Lett. **82** 2439 (1999).

[18] G. Hammond *et al.* Phys. Rev. Lett. **98** 081101 (2007).

[19] R. Sundrum, Phys. Rev. **D69**, 044014 (2004).

[20] G. Dvali, G. Gabadadze and G. Senjanovic, arXiv:hep-ph/9910207 (1999).

[21] N. Arkani-Hamed, S. Dimopoulis and G.R. Dvali, Phys. Lett. **B436** 257 (1998).

[22] J. Khoury and A. Weltman, Phys. Rev. Lett. **93** 171104 (2004).

[23] A. Upadhye *et al.* Phys. Rev. **D74** 104024 (2006).

[24] A. Dupays *et al.* Phys. Rev. Lett. **98** 131802 (2007).

[25] E. Zavattini *et al.* Phys. Rev. Lett. **96** 110406 (2006).
E. Zavattini *et al.* Phys. Rev. **D77** 032006 (2007).

[26] S.M. Carroll *et al.* Phys. Rev. Lett. **87** 141601 (2001).
I. Hinchliffe, N. Kersting and Y.L. Ma, Int. J. Mod. Phys. **A19** 179 (2004).
A. Anisimov *et al.* Phys. Rev. **D65** 085032 (2002).

[27] J. Moody and F. Wilczek, Phys. Rev. **D30** 130 (1984).

Discussion

Dimitri Denisov (FNAL): What are expected improvements in pendulum experiments which could substantially improve sensitivity?

Answer: We are pursuing two new torsion pendulums to test the Inverse Square Law. One is an "upgrade" to the ISL pendulum I described. It has 120 tungsten wedges instead of 42 holes in molybdenum. Here we hope to achieve a slightly smaller separation between the detector and the attractor (maybe a few 10's of microns closer). In addition, the 120-fold symmetry will generate a larger torque and thus perhaps a better S/N ratio. However, as with all torsion pendulums, the sensitivity will likely be limited by systematic errors, which are inherently hard to predict. The other pendulum for the ISL tests uses a completely different geometry. This torsion balance, what we call "Plate-Wash," attempts a true "null" type experiment to test for deviation from Newton's laws. Because this device is completely different, it is unclear how much better it will be able to do than the ISL tests I presented today.

For the equivalence principle we are exploring using a polyethylene/beryllium test body pair. This test pair should provide about a factor of ten improvement on the bounds on a non-gravitational coupling of hydrogen to dark matter. The challenge, however, is that the polyethylene must be coated with gold or enclosed in a metal housing. In addition, polyethylene is likely to distort due to temperature changes. This effect could in turn couple temperature fluctuations with gravity gradients (the source of the largest systematic errors).

More promising, and perhaps more adventurous, we are exploring using fused quartz as a torsion fiber. The advantage here is that the Q of a quartz fiber is much higher than a tungsten fiber and thus the noise should be lower at room temperature. This may offer a factor of ten improvement. The challenge here, however, is that the electric charge of the pendulum must be controlled via other means. It seems likely that by exposing an appropriate metal surface with UV light one can move charge on and off the pendulum.

In addition, we are constructing a cryogenic torsion pendulum. This can offer two advantages. First, one can immediately gain a factor of ten from the thermal noise in the torsion fiber alone. Second, the "patch field" I mentioned as the limiting source of noise in the ISL test, are likely to change much less frequently at lower temperatures and thus generate less noise.

Thomas Coan (SMU): The first part of your talk concerned measurements of matter interacting with matter. If you could measure interactions of matter with anti-matter, what level of sensitivity would be interesting?

Answer: Obviously one can not construct a torsion pendulum from anti-mater. Nevertheless, one can impose strong constraints on an EP violating force to anti-mater. There are two ways to see this. First, an EP violation that is sensitive to anti-mater would by necessity have to be mediated by a vector particle. (A particle and it's anti-

particle must have the same scalar charge). We can strongly constrain a new vector particle interaction, and thus, can also constrain a potential EP violation to anti-mater. A paper analyzing an early version of our experiment (PRL 66 850 (1991)) presents a limit of 10^-6 g, given our improvements since 1991, I think 10^-7 g is very reasonable. The second way to see how our torsion pendulum can constrain an EP violation to anti-mater is to realize that different elements will have different contributions to their mass generated by electrostatic or nuclear binding energy. Loops of electron/positron pairs will contribute part of this binding energy, and thus, different atoms have different fractions of anti-mater. This idea is discussed in a recent article by Alves et al (arxiv:0907.4110).

Electroweak and Top Physics at High Energies

Florencia Canelli[1,2]

[1]University of Chicago, 5640 S. Ellis Ave., Chicago, IL 60637, USA
[2]Fermi National Accelerator Laboratory, Batavia, P.O. Box 500, IL, 60510, USA

I present a summary of electroweak and top physics analyses from experiments at the Tevatron and HERA colliders, corresponding to the newest results acquired between Winter and Summer 2009. This includes progress in the precision measurement of the top quark and W boson masses and their constraint on the Higgs boson mass, establishing of processes with challenging signatures, measurements of top quark properties, as well as searches for new physics in data samples enriched with top quarks.

1 Introduction

This proceeding summarizes the latest results on electroweak and top quark physics. Most of the results included are from the Tevatron, while a few are from HERA. The Fermilab Tevatron has been colliding protons and antiprotons at a center-of-mass energy of $\sqrt{s} = 1.96$ TeV since 2002. By summer 2009, it had delivered about 7 fb^{-1} of data to its experiments, CDF and D0. The results presented in this talk use up to 5 fb^{-1} of the collected data. The HERA collider at DESY operated from 1992 to 2007, colliding electron/positrons with protons at a center-of-mass energy of 319 GeV. The H1 and ZEUS detectors collected data corresponding to an integrated luminosity of about 900 pb^{-1}. In this talk I present combined results from both HERA experiments.

This proceeding is divided into three main parts. The first part focuses on the efforts to establish top and electroweak signatures, including the very precise understanding of W and Z boson physics and the new observed signatures which include diboson and single top production. The second part includes the precision measurement of the top quark and W boson mass and their constraint on the Higgs boson mass. The third part is about top quark physics, the analysis of its properties and searches beyond the standard model (SM) using top based samples.

2 Establishing Signatures

Electroweak and top quark measurements at hadron colliders span a wide range of cross sections. Figure 1 shows the measured cross sections for different processes by the CDF and D0 experiments. The Tevatron has measured all the predicted SM processes. Until recently these processes had only been measured in relatively clean samples, with signatures where there are no jets in the final state and a very small expected background contribution. The measurements of these physics processes demonstrate a good agreement with the SM prediction and among CDF and D0.
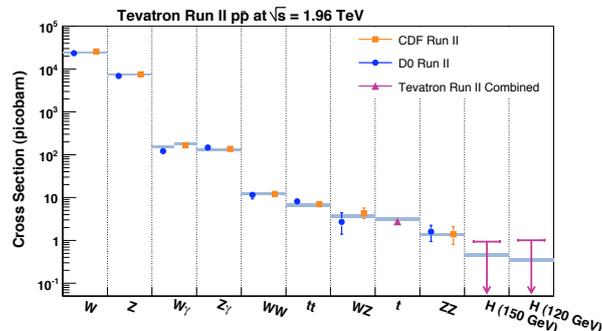
Figure 1: Measured cross sections by CDF and D0 experiments. Higgs boson limits are shown for m_{Higgs}=150 GeV and m_{Higgs}=120 GeV. Grey lines show the theory prediction.

In the past year the Tevatron experiments established these processes in more challenging environments, focusing on final states with jets, where the backgrounds are larger and topologically very similar. The main experimental reason why these difficult signatures are interesting is because they are a background to the unobserved Higgs boson. It is important to observe these processes to improve and establish analysis techniques. Moreover, establishing processes in different channels allows us to combine with the other channels to improve their precision, giving us confidence in their modeling and consistency between channels. Measuring cross sections could point to new physics through deviations from the SM.

In general, these processes have a large amount of background in comparison with signal. Moreover background are kinematically very similar. As these challenges arise the experiments introduce more sophisticated methods to analyze the data. Most of the results rely on multi-variate techniques, either matrix-element or machine-learning based approaches. The matrix element technique is based on an event-per-event probability density by using the signal and background matrix elements. The inputs to the calculation are the 4-vectors of the final state particles. Machine learning techniques correspond to different computing algorithms such as Artificial Neural Networks or Boosted Decision Trees. Although they are different in their signal discrimination algorithm they use the same concept. These computing algorithms correlate kinematic and angular variables of simulated signal and background events in order to classify events into events with varying signal to background ratios.

The next sections describe the new measurements of challenging processes at the Tevatron and HERA.

2.1 W production at HERA

The H1 and ZEUS experiments searched for events containing high energy isolated leptons and missing transverse momentum produced in electron/positron collisions at HERA. These events

are interesting as they may be a signature of physics beyond the SM. These experiments analyzed the full data set taken between 1994 and 2007 corresponding to an integrated luminosity of 0.98 fb^{-1}. In the SM, the production of single W bosons with subsequent leptonic decay gives rise to this topology (see Figure 2). An excess of electron and muon events with large missing transverse momentum containing a hadronic final state at high transverse momentum P_T^X was previously reported by H1. The observed event yield was found to be in agreement with the SM. The total single W boson production cross section is measured as 1.07±0.16(stat)±0.08(syst) pb. The differential single W production cross section is measured as a function of P_T^X, the results of which are displayed in Figure 2, and is in agreement with the SM prediction [1].
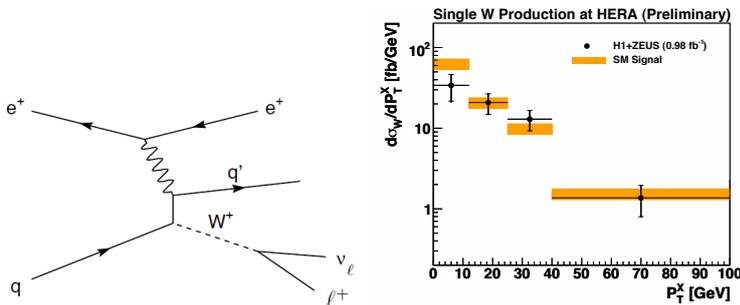
Figure 2: (left) W production at HERA. (right) The single W production cross section, measured by H1 and ZEUS in a common phase space as a function of the hadronic transverse momentum, P_T^X. The inner error bar represents the statistical error, which dominates, and the outer error bar indicates the statistical and systematic uncertainties added in quadrature. The shaded band represents the one standard deviation uncertainty in the SM prediction.

2.2   W and Z bosons at the Tevatron

At the Tevatron, the leptonic decays of W and Z bosons have been used extensively for precision measurements. Two of the more outstanding latest results in these samples are presented.

The W boson charge asymmetry has been measured using a new analysis method which directly reconstructs the W rapidity using an integrated luminosity of 1 fb^{-1} taken with the CDF detector. A precise measurement of the W asymmetry is a sensitive probe of the momentum fraction difference between u and d quarks in the $Q^2 \approx M_W^2$ region and is one of the best determinations of the proton d/u momentum ratio as a function of x. It also plays an important role in global fits. Figure 3 shows the measured asymmetry, A($|y_W|$), compared to an NLO prediction with CTEQ6.1M parton distribution functions (PDFs). Results are also compared to an NNLO prediction using MRST2006 PDFs and their corresponding error PDFs, and they were found to be in good agreement [2].

The forward backward charge asymmetry (A_{FB}) is also measured in Z→e$^+$e$^-$ events using 1.1 fb^{-1} of data collected with the D0 detector. A_{FB} is measured as a function of the invariant mass of the electron-positron pair, and found to be consistent with the SM prediction (see Fig.3). The A_{FB} measurement is used to extract the effective weak mixing angle, $\sin^2\theta_W = 0.2326\pm0.0018(\text{stat})\pm0.0006$ (syst). The precision of this measurement is comparable to that obtained from LEP measurements of the inclusive hadronic charge asymmetry and that of
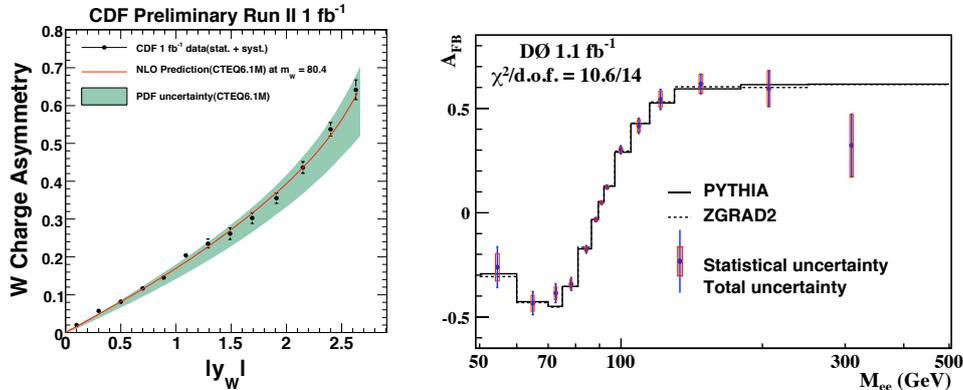
Figure 3: (left) The measured asymmetry, A($|y_W|$), compared to the NLO prediction with CTEQ6.1M PDFs. (right) Comparison between the unfolded AFB (points) and the Pythia (solid curve) and ZGRAD2 (dashed line) predictions. The inner (outer) vertical lines show the statistical (total) uncertainty.

NuTeV measurement. With about 8 fb^{-1} of data expected by the end of Run II, a combined measurement of A_{FB} by the CDF and D0 collaborations using electron and muon final states could lead to a measurement of $\sin^2\theta_W$ with a precision comparable to that of the current world average [3]

2.3 Dibosons

2.3.1 Z gamma

The first observation of the $Z\gamma \rightarrow \nu\bar{\nu}\gamma$ process at the Tevatron at 5.1 standard deviations significance was done using 3.6 fb^{-1} of integrated luminosity collected with the D0 detector. The measured Z cross section multiplied by the branching fraction of $Z\rightarrow \nu\bar{\nu}$ is 32±9(stat+syst)±2(lumi) fb for the photon $E_T > 90$ GeV. This result is in agreement with the SM prediction of 39±4 fb. Limits on anomalous triple gauge couplings are set by comparing the photon E_T spectrum in data with that from the sum of expected Z signal and background (see Fig.4). These are the most restrictive limits on anomalous trilinear $Z\gamma\gamma$ and $ZZ\gamma$ gauge boson couplings at a hadron collider to date [4].

2.3.2 WW

The direct production of WW pairs in proton-antiproton collisions is the primary background in searches for a high mass SM Higgs boson decaying to WW. A good understanding and modeling of WW production is thus essential to any Higgs to WW search. Studying WW production at the Tevatron also provides an opportunity to explore $\sqrt{s}$ energies higher than those available at the LEP collider. Both Tevatron experiments have measured the WW production cross section in the past, and the D0 experiment has recently released a new preliminary result. The most precise measurement to date of the WW production cross section using approximately 3.6 fb^{-1} of integrated luminosity collected by the CDF II detector is $12.1^{+1.8}_{-1.6}$ pb where the uncertainty
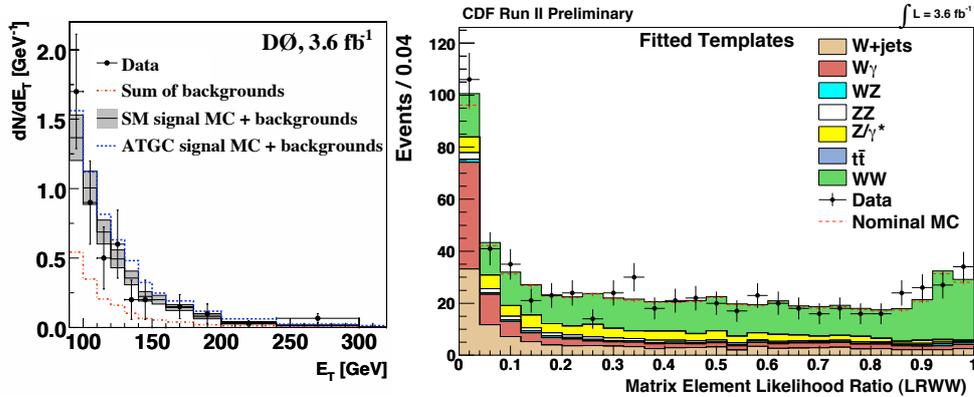
Figure 4: (right) Photon E_T spectrum in data (solid circles), sum of backgrounds (dash-dot line), and sum of MC signal and background for the SM prediction (solid line) and for the anomalous triple gauge coupling prediction with $h_{30}^{\gamma} = 0.09$ and $h_{40}^{\gamma} = 0.005$ (dashed line). The shaded band corresponds to the $\pm$ 1 s.d. total uncertainty on the predicted sum of SM signal and background. (left)

includes statistical, systematic, and luminosity uncertainties. This is in good agreement with the theoretical expectation of 11.66±0.66 pb. Figure 4 shows the matrix element likelihood ratio built from signal and background probability densities used to extract the number of WW events in data [5].

2.3.3 WW/WZ/ZZ with hadronic decays

The CDF experiment reported the first observation in hadronic collisions of the electroweak production of vector boson pairs (VV, V=W,Z) where one boson decays to a dijet final state using 3.5 fb^{-1} of integrated luminosity. The dijet mass is fitted using an unbinned maximum likelihood with the main systematic uncertainties treated as nuisance parameters and allowed to float in the fit within their predetermined uncertainties (see Fig. 5). The WW/WZ/ZZ cross section measured is 18±2.8(stat)±2.4(syst)±1.1(lumi) pb, in agreement with expectations from the SM. This results represents a 5.3 σ observation of the diboson production in the hadronic channel [6]. CDF has reached a similar observation in the WW/WZ production with an identified electron or muon, large missing transverse energy, and two jets in 2.7 fb^{-1} of integrated luminosity. The analysis employs a matrix element technique which calculates event probability densities for signal and background hypotheses. The probabilities are combined to form a discriminant variable which is evaluated for signal and background Monte Carlo events (se Fig.5). We measure a cross section of 17.7±3.9 pb which corresponds to a 5.4 σ significance [7]. The samples used on these results were shown to overlap by only 20%.

2.3.4 Top quark pairs

The top quark completes the third quark generation in the SM. Top quarks at the Tevatron are mainly produced in pairs via the QCD interaction about 3 times more often than singly via the
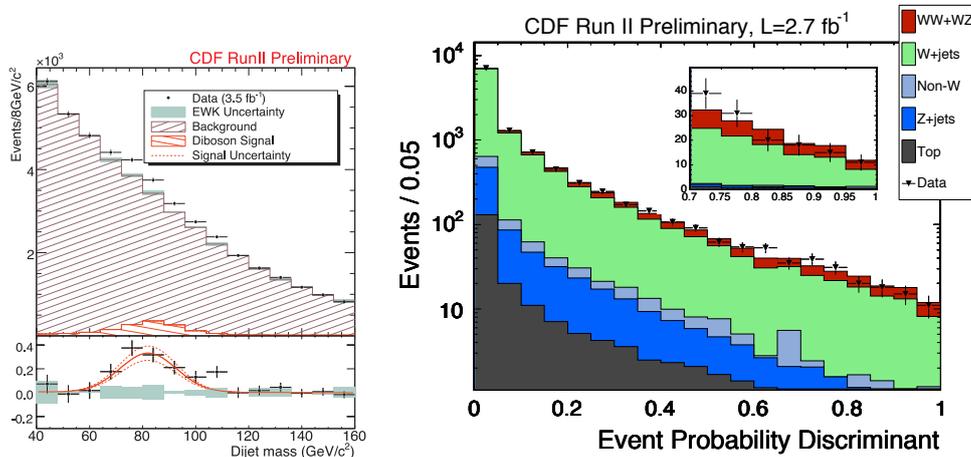
Figure 5: (left) Comparison of the diboson signal (solid line) with the background-subtracted data (points). The dashed lines represent the 1-σ statistical variations on the extracted signal. The gray band represents the systematic uncertainty due the EWK shape. (right) Observed event probability distribution distribution superimposed on distribution expected from simulated processes

electroweak interaction. Significant enhancements in the integrated luminosity and improvements to the sensitivity for detecting top quark decay products made the measurements of the $t\bar{t}$ production cross section no longer limited by statistical uncertainties. Current measurements have reached a comparable or better precision than of the theory.

The top quark decays predominantly to a W boson and a bottom quark. The decays of two W bosons define the final state topology which is referred to as "all-jets", "lepton+jets", and "dilepton" channels, respectively. In general, the lepton in the above processes refers to an electron or muon. The background composition in these three decay modes is very different. The dilepton channel has the best signal to background ratio, but the small branching ratio makes it statistically limited. On the contrary, the all-jets channel has a good branching ratio but large amount of background. The lepton+jets channel produces the most precise measurements since its background is smaller than in all-jets and has more signal than in dilepton modes.

Given that $t\bar{t}$ events have two b hadrons, whereas the backgrounds for each channel are dominated by jets of light flavor (u, d, s, g), top measurements rely on the use of techniques for the identification of b-jets, or b tagging which are based upon the fact that b hadrons have long lifetimes. If the b hadron decays to two or more charged stable particles, it can often be detected via a well-reconstructed vertex that is significantly displaced from the primary vertex.

In the dilepton channel there are two new measurements of the $t\bar{t}$ cross section, before and after b-tagging requirements are made. Candidate events are selected by requiring two leptons identified as electrons or muons. For the selection with b-jet identification we calculate background estimates using a parametrized tagging matrix prediction applied to normalized pretag samples. In a sample of about 4.47 fb^{-1} of data collected with the CDF detector

the measurement before b-tagging is $\sigma_{t\bar{t}}$-pre= 6.56±0.65(stat)±0.41(syst)±0.38(lumi) pb and after requiring at least one b-tagged jet is $\sigma_{t\bar{t}}$-tag = 7.27±0.71(stat)±0.46(syst)±0.42(lumi) pb. Both results are in agreement. Since these samples have a large signal content and very different backgrounds they show a good modeling of the signal (see Fig.6) [8].
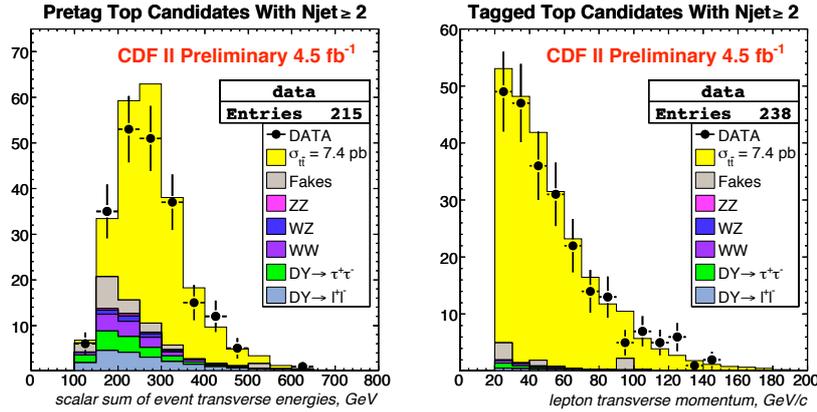
Figure 6: Data and simulation comparison of different variables before and after b-tagging in the dilepton channel.

The D0 experiment extracted a new measurement of the $t\bar{t}$ production cross section in the all-jets channel using 1 fb^{-1} of integrated luminosity. The cross section was extracted using high-multiplicity jet events, specifically selected with at least six jets, two of them b-tagged. To improve the signal purity a neural network b-tagger is used with inputs variables related to the characteristics of secondary vertices and tracks associated with b hadron decays. A model of the multijet background was created from lower jet-multiplicity data. The cross section was obtained from a likelihood fit to the discriminant distribution and the measurement is 7.9±2.2 pb assuming M_{top}= 170 GeV/c^2, and 6.9±2.0 pb assuming M_{top}= 175 GeV/c^2 [9].

The CDF experiment updated the measurement of the $t\bar{t}$ production cross section in the all-jets channel using about 2.9 fb^{-1} of data. Assuming M_{top}=172.5 GeV/^{2} and δJES=0 (the reference values for a CDF average over all channels) obtains a measurement of 7.2±1.3 pb. Both results are shown in Fig.7 and agree with theoretical expectations [10].

The most precise $t\bar{t}$ measurements are extracted in the lepton+jets channel. CDF updated a result using two complementary methods, one based on b-tagging, and the other a topological approach, which uses event kinematics to distinguish $t\bar{t}$ events from backgrounds. These analyses use datasets corresponding to an integrated luminosity of up to 4.6 fb^{-1}. By measuring the cross section ratio between $t\bar{t}$ and Z production and normalizing to the well-known theoretical Z cross section predicted by the SM, the extracted $t\bar{t}$ cross sections are effectively insensitive to the uncertainty on luminosity. The luminosity systematic uncertainty for both measurements has been replaced by a small uncertainty from the theoretical $Z\to ll$ cross section. The Best Linear Unbiased Estimate (BLUE) technique is used to combine both measurements with the result $\sigma_{t\bar{t}}$= 7.70±0.52 pb, for a top-quark mass of 172.5 GeV/c^2. Figure 8 shows a comparison of data and simulation in both measurements [11].

Figure 9 shows the combination of all the CDF results assuming M_{top}=172.5 GeV/c^2. For
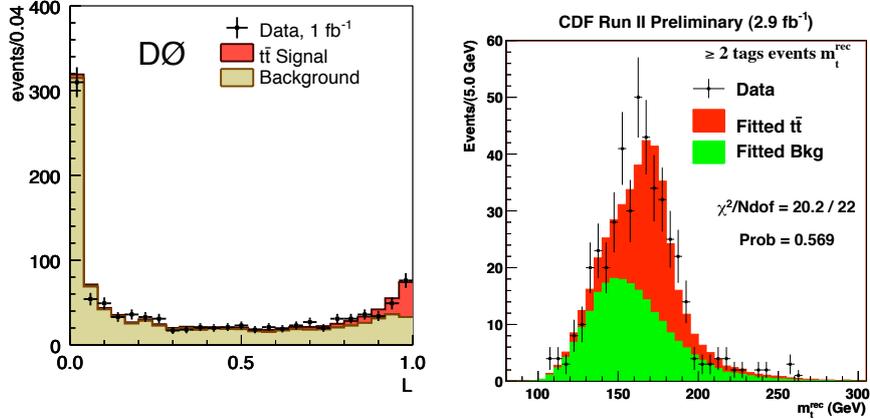
Figure 7: (left) Data and simulation comparison of the likelihood discriminant used all-jets channel $t\bar{t}$ cross section measurement. (right) Data and simulation comparison with events with 2 b-tagged jets in the all-jets channel.

each measurement, the statistical uncertainty is shown by the magenta line, which is superimposed on the black line which is the total uncertainty additionally including systematic and luminosity uncertainties. The four measurements carry the following weights in the combination: the lepton+jets channel with artificial neural network discriminant with a weight of 70%, the lepton+jets channel with secondary vertex b-tagging with 18%, the dilepton channel with 18%, and the all-jets channel with -6%. The combined measurement is $\sigma_{t\bar{t}} = 7.50\pm0.31(\text{stat})\pm0.33(\text{syst})\pm0.13(\text{Z-theory})\pm0.06(\text{lumi})$ pb. The result is in good agreement with the theoretical prediction.

2.3.5 Single Top

Observation of top quarks produced via the electroweak interaction was achieved by both Tevatron experiments in 2008. Each experiment used different multivariate techniques to separate signal from background. Following this discovery the two experiments report here a combination of the CDF and D0 measurements of the inclusive single top quark production cross section. The total integrated luminosity included in CDF's analysis is 3.2 fb^{-1} and D0's analysis is 2.3 fb^{-1}. A Bayesian analysis is used to extract the cross section from the distributions of multivariate discriminants provided by the collaborations. For a top quark mass M_{top}=170 GeV/c^2, the measured cross section is 2.76 $^{+0.58}_{-0.47}$ pb (see Figure 10). The extracted CKM matrix element is $|V_{tb}|$=0.88±0.07 with a 95% C.L. lower limit of $|V_{tb}|$ >0.77 [12].

Using the same data, the D0 collaboration reports direct evidence for electroweak production of single top quarks through the t-channel exchange of a virtual W boson. This is the first analysis to isolate an individual single top quark production channel. Three multivariate techniques optimized for the t-channel process to measure the t- and s-channel cross sections simultaneously are combined and measure a cross sections of 3.14$^{+0.94}_{-0.80}$ pb for the t-channel and 1.05±0.81 pb for the s-channel. The measured t-channel result is found to have a significance
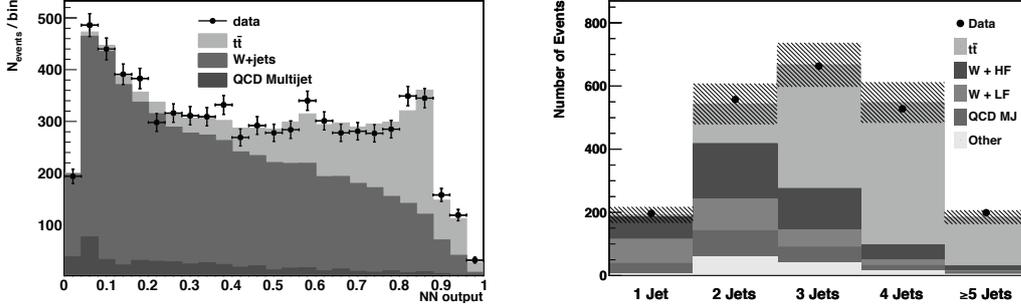
Figure 8: (left) The output of an artificial neural network (ANN), trained to distinguish $t\bar{t}$ events in the lepton+jets channel from background without using b-tagging, for simulated $t\bar{t}$ and background events, and data. The $t\bar{t}$ cross section is extracted from a fit of templates to the data. (right) Number of data and predicted background events as a function of jet multiplicity, with the number of $t\bar{t}$ events normalized to the measured cross section. The hashed lines represent the uncertainty on the predicted number of events.

of 4.8 standard deviations and is consistent with the SM prediction. Figure 10 shows these measurements [13].

2.4 Precision Measurements

The precision measurement of the W boson mass and top quark mass helps to tighten the constraints on the mass of the Higgs boson as determined from internal consistency of the SM. Improving the measurement of M_W and M_{top} is an important contribution to our understanding of the electroweak interaction, and, potentially, of how the electroweak symmetry is broken.

2.4.1 W-boson

The D0 experiment has measured the W boson mass in W→eν decays using 1 fb^{-1}. To determine M_W, fast simulation (FASTMC) template distributions for m_T (W boson transverse mass, shown in Fig.11), p_T^e(electron P_T), and MET (missing transverse energy) are fitted using a binned likelihood between data and each template. The results are combined to give the final result M_W =
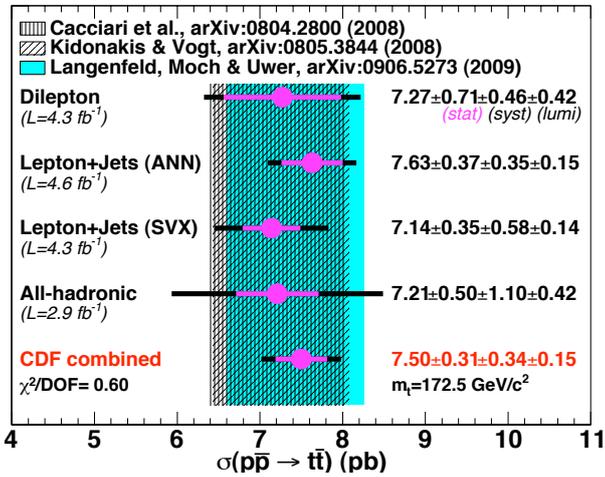
Figure 9: Combination of CDF $t\bar{t}$ cross section measurements assuming M_{top}=172.5 GeV/c^2.
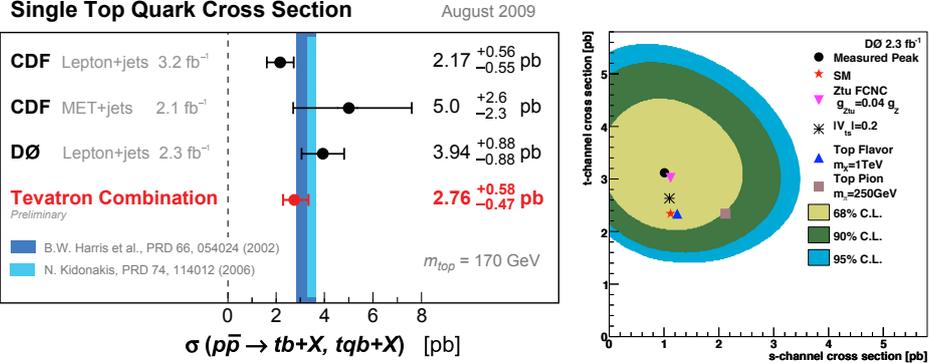
Figure 10: (left) Tevatron single top cross section measurements and their combination. (right) Posterior probability density for t-channel and s-channel single top quark production in contours of equal probability density. Also shown are the measured cross section, SM expectation, and several representative new physics scenarios.

80.401±0.043 GeV. This is the most precise measurement from a single experiment to date [14].

The dominant uncertainties arise from the available statistics of the W→eν and Z→ee samples. Thus, this measurement can still be expected to improve as more data are analyzed. The M_W measurement reported here agrees with other individual measurements. This result is combined with all the previous direct measurements of M_W boson in data collected by the Tevatron experiments, including the CDF 200 pb^{-1} published results from the first period of Run-II (2001-2004) (see Fig. 11). The resulting Tevatron average for the mass of the W boson is $M_W = 80.420\pm31$ MeV [15]

2.4.2 Top quark mass

A new update of the most precise measurement of the top quark mass has been done by the CDF experiment using 4.3 fb^{-1} of integrated luminosity. The measurement is done in the lepton+jets channel using a matrix element integration method with a Quasi-Monte Carlo integration to take into account finite detector resolution and quark mass effects. The events are required to have at least one b-tagged jet. The extracted measurement is $M_{top} = 172.6\pm0.9$ (stat)±0.7 (JES)±1.1 (syst) GeV/c^2 [16]. Results from the five published Run I measurements and six preliminary Run II measurements in different channels are combined. Taking into account the statistical and systematic uncertainties and their correlations, the preliminary world-average result is: $M_{top} = 173.1\pm1.3$ GeV/c^2, where the total uncertainty is obtained assuming Gaussian systematic uncertainties and adding them plus the statistical uncertainty in quadrature. The mass of the top quark is now known with a relative precision of 0.75%, limited by the systematic uncertainties, which are dominated by the jet energy scale uncertainty. It can be reasonably expected that with the full Run II data set the top-quark mass will be known to better than 0.75%. To reach this level of precision further work is required to determine more accurately the various correlations present, and to understand more precisely the b-jet modeling, signal, and background uncertainties which may limit the sensitivity at larger data sets [17].
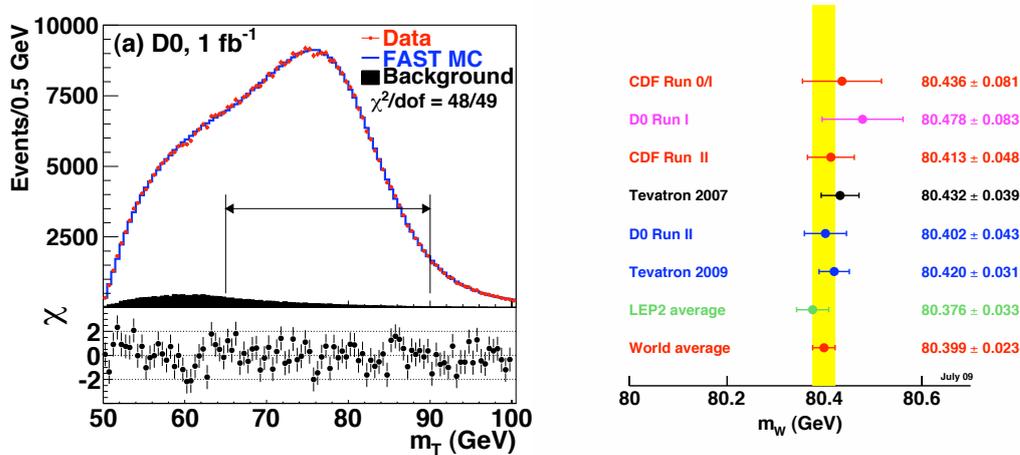
Figure 11: (left)The m_T distributions for data and FASTMC simulation with backgrounds. (right) Summary of the measurements of the W boson mass and their average as of July 2009. The result from the Tevatron corresponds to the values which include corrections to the same W boson width and PDFs. An estimate of the world average of the Tevatron and LEP results assuming no correlations between the Tevatron and LEP is included.

2.4.3 Electroweak Fit

The new measurements of the top quark mass and W boson mass allow to check the validity of the SM and, within its framework, to infer valuable information about its fundamental parameters. The accuracy of the W- and Z-boson measurements makes them sensitive to the mass of the top quark, and to the mass of the Higgs boson m_H through loop corrections. While the leading M_{top} dependence is quadratic, the leading m_H dependence is logarithmic. Therefore, the inferred constraints on M_{top} are much stronger than those on m_H. Figure 12 shows the most probable value of m_H using these measurements [18].

2.5 Top Quark Properties and Searches

Since the top quark has the strongerst coupling to the Higgs boson of all other fermions, it makes the study of top quark properties very interesting. It is an ideal place to study the interactions and to search for new physics related to electroweak symmetry breaking. In the past years the Tevatron has made huge progress in the measurements of many of these properties and also in searches for new physics contaminating the top quark sample. Due to length restrictions, these proceedings do not include details of these analyses. All of these results can be found in the CDF and D0 experiments public webpages at `http://www-cdf.fnal.gov/physics/new/top/top.html` and `http://www-d0.fnal.gov/Run2Physics/top/top_public_web_pages/top_public.html`.

3 Conclusions

The Tevatron is making precision measurements to help constrain the SM. Measurements like the W charge asymmetry and $\sin^2\theta_W$ are good examples. In teh past year, the Tevatron expanded its experimental reach on signatures. These processes give confidence in the experimental tools while establishing challenging processes on the way to the Higgs boson. The top quark cross section is now known to 6.5% (better than theory). The top quark mass known to 0.7%. The Tevatron should be able to reach 1 GeV/c^2. The new W boson mass Tevatron combination is now better than LEP2 average. The Tevatron is expected to reach 20 MeV precision. Top quark physics is beginning to have sensitivity to unexpected in particle properties and in the data samples In the near future.

The LHC will rediscover top and use it as most likely the most important stepping stone to find new physics

Figure 12: $\Delta\chi^2 = \chi - \chi_{min}$ vs. m_H curve. The vertical band shows the 95% C.L. exclusion limit on m_H from the direct searches at LEP-II (up to 114 GeV/c^2) and the Tevatron (160 GeV to 170 GeV/c^2).

References

[1] H1prelim-09-161, ZEUS-prel-09-014, July 2009.

[2] CDF public note 8942.

[3] D0 collaboration, Phys. Rev. Lett. **101**, 191801 (2008).

[4] D0 collaboration, Phys. Rev. Lett. **102**, 201802 (2009).

[5] CDF collaboration, Phys. Rev. Lett. **104**, 201801 (2010).

[6] CDF collaboration, Phys. Rev. Lett. **103**, 091803 (2009).

[7] CDF collaboration, Phys. Rev. Lett. **104**, 101801 (2010).

[8] CDF public note 9890.

[9] D0 collaboration, hep-ex:0911.4286.

[10] CDF collaboration, Phys. Rev. D **81**, 052011 (2010).

[11] CDF collaboration, Phys. Rev. Lett. **105**, 012001 (2010).

[12] hep-ex:0908.2171v1.

[13] D0 collaboration, Phys. Lett. B **682** (2010).

[14] D0 collaboration, Phys. Rev. Lett. 103, 141801 (2009).

[15] hep-ex:0908.1374.

[16] CDF public note 9880.

[17] hep-ex/0903.2503v1.

[18] CDF Note 9979 and D0 Note 6005.

Discussion

Tobias Haas (DESY): Could you please explain on the details of the systematic error on the W mass measurement. It seems to be dominated by the electron energy scale. If so, can it profit from a combination of the D0 and CDF results in the spirit if the HERA combinations?

Answer: The energy scale is treated differently in each experiment, experimentsdo not use a common energy scale.D0 uses the Z sample for scale and linearity. For CDFthe Z is a relatively minor scale determinant. The fact that they are different helps for decoupling in the combination.

Majid Hashemi (University of Antwerp): Related to anomalous top peak at HERA could the shape center shift related to MC shape be related to JES of b-jets

Answer: The position of the peak near 80 GeV is due to kinematic cuts applied in the analysis. Within statistical uncertainties, the position and shape of this peak are in agreement between data and prediction. This gives us confidence that the jet energy scale is well understood.he jet energy scale is known at a level of 1.5this analysis, controlled by independent high statistics neutral current event samples. The expected shape of single top is shown with arbitrary normalization. Masses above 150 GeVare interpreted as statistical fluctuation, not as a top mass peak.

Bennie Ward (Baylor University): If I understand correctly, you have an error of 1.2 GeV on m_t, which seems to imply that your statistical error is less than $1.2/173 = 4.94x10^-3$, which means $N > 20.8x10^4$. Do you have $20.8x10^4$ tops ?

Answer: The uncertainty on the top quark mass measurement comes from the uncertainty on the mean of the top mass distribution.Our resolution on the mass is more than 20 GeV. The uncertaintyon the mean decreases as $\sqrt{(Nevents)}$. Note that this number could be smaller than 1.2 GeV (top mass width).No, we don't have$20.8x10^4$ tops but we don't need this amount to achieve the current precision.

Electroweak physics at low energy

B.A.Shwartz[1]

[1]Budker Institute of Nuclear Physics, Novosibisrsk, 630090 Novosibirsk, Russia

Recent experimental results on the muon $(g-2)$ and τ-lepton decays including search for lepton flavour violation are discussed.

1   Introduction

In the last three decades the Standard Model (SM) was successfully used to describe variety of physical phenomena in the wide energy range from atomic transitions to the hundreds GeV scale. On the other hand, the word "model" in the title reflects the common feeling that some more fundamental theory can be hidden behind SM. At present many experiments are aimed to search for the SM boundaries. In this report the present status and recent results on muon anomalous magnetic moment and τ-lepton decays are considered.

2   Muon $(g-2)$ and R measurements

As it is well known, the magnetic moment of a particle with the charge e is:

$$\overrightarrow{\mu} = g\frac{e}{2m}\overrightarrow{s}, \quad a = (g-2)/2.$$

In Dirac theory for pointlike particles the gyromagnetic factor $g = 2$. However, higher-order QED effects (or new physics) can change it, $g \neq 2$. QED calculations of a provide a slightly (by 10^{-3}) higher value. A deviation of the experimental measurements from the theoretical calculations would be an evidence of the new physics.

2.1   Muon $(g-2)$ – experiment and theory

At present the a_μ value is measured with a $5 \cdot 10^{-7}$ relative accuracy [1]:

$$a_\mu = (11659208.0 \pm 6.3) \cdot 10^{-10}.$$

It should be noted that the value of anomalous magnetic moment for electron, a_e is measured with a $4.9 \cdot 10^{-10}$ relative accuracy. However, a_μ is much more sensitive to new physics effects: in most of the models the gain is proportional to $(m_\mu/m_e)^2 = 4.3 \cdot 10^4$.

Usually, the a_μ value is considered as a sum:

$$a_\mu^{SM} = a_\mu^{QED} + a_\mu^{EW} + a_\mu^{had},$$

where a_μ^{QED} – the QED contribution; a_μ^{EW} – the electroweak contribution; a_μ^{had} – the contribution of the vacuum polarization by hadrons. At present, terms up to α^3 are known analytically, a recent more accurate numerical calculation of the α^4 terms and the leading log α^5 terms was done in [2, 3]. From the latest value of a_e [4, 5] $1/\alpha = 137.035999710(96)$,

$$a_\mu^{QED} = (116584718.09 \pm 0.14 \pm 0.08) \cdot 10^{-11}.$$

The errors are due to higher-order terms, $O(\alpha^5)$ and precision of the α.

The electroweak contributions were calculated in the two-loop approximation [6] to be $(15.4 \pm 0.1 \pm 0.2) \cdot 10^{-10}$. The quoted errors are due to hadronic loops which were not taken into account, ambiguity in the Higgs-boson mass, precision of the t-quark mass and higher order effects. A contribution corresponding to the light-by-light scattering diagrams was calculated in [7] as $(10.5 \pm 2.6) \cdot 10^{-10}$.

The hadronic contribution in the leading order, a_μ^{had}, is given by the expression:

$$a_\mu^{had} = (\frac{\alpha m_\mu}{3\pi})^2 \int_{4m_\pi^2}^{\infty} ds \frac{R(s)\hat{K}(s)}{s^2},$$

$$R(S) = \frac{\sigma(e^+e^- \to hadrons)}{\sigma(e^+e^- \to \mu^+\mu^-)}, \quad \sigma(e^+e^- \to \mu^+\mu^-) = \frac{85.86\,\text{nb}}{s\,[\text{GeV}^2]}.$$

$\hat{K}(s)$ grows from 0.63 at $s = 4m_\pi^2$ to 1 at $s \to \infty$. The factor $1/s^2$ emphasizes the role of low energies, particularly important is the reaction $e^+e^- \to \pi^+\pi^-$ with a large cross section below 1 GeV. The results of the calculations in comparison with the experiment are presented in Table 1 [8].

Contribution	$a_\mu, 10^{-10}$
Experiment	11659208.0 ± 6.3
QED	11658471.8 ± 0.016
Electroweak	$15.4 \pm 0.1 \pm 0.2$
Hadronic	693.1 ± 5.6
Theory, total	11659180.3 ± 5.6
Exp. - Theory	$27.7 \pm 8.4 (3.3\sigma)$

Table 1: a_μ – experiment and theory

The calculations of a_μ^{had}, given in this Table, used the data on hadronic cross sections obtained in the direct measurements, mostly at the VEPP-2M collider.

2.2   Direct R measurements in e^+e^- annihilation

According to QCD, the quantity R is expressed as:

$$R_{QCD} = R^{(0)} \left[1 + \frac{\alpha_s}{\pi} + C_2 \left(\frac{\alpha_s}{\pi}\right)^2 + C_3 \left(\frac{\alpha_s}{\pi}\right)^3 + ... \right], R^{(0)} = 3\sum e_q^2,$$

where α_s is a strong coupling constant, e_q are quark charges, $C_2 = 1.411$, $C_3 = -12.8$.

Why is R Measurement Interesting?

- The experimental data on R provide tests of perturbative QCD as well as QCD sum rules, give information about quark masses and values of the quark and gluon condensates. Higher order QCD corrections depend on Λ_{QCD} and $\alpha_s(s)$.

- Precise knowledge of R values is necessary to derive the hadronic corrections to various fundamental parameters like the running fine structure constant - $\alpha(M_{Z^2})$ as well as mentioned above anomalous magnetic moment of the muon.

Depending on the problem, different energy ranges are important. In the energy range below 2 GeV the total hadronic cross section is obtained as a sum of the exclusive cross sections. For more than 25 years, VEPP-2M collider was the main supplier of the precise data on the hadronic cross section in the energy range below 2 GeV [9]. The results on the hadronic cross section
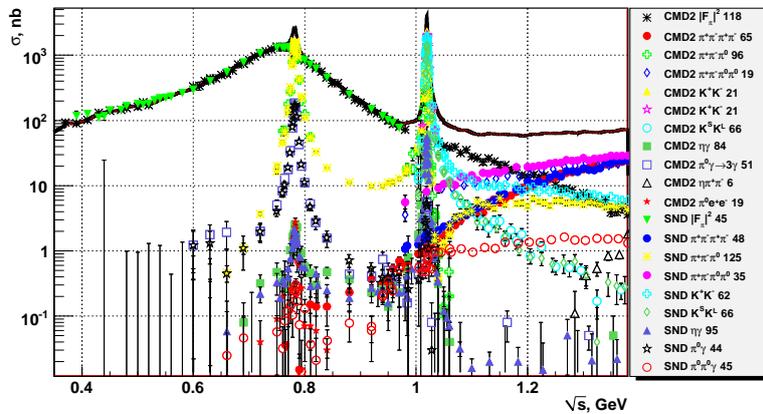
Figure 1: Overview of the results from the VEPP-2M e^+e^- collider.

obtained in the experiments at the VEPP-2M collider are shown in Fig. 1.

2.3 R measurement by ISR

In the last years a lot of new data were obtained at B- and ϕ-factories, at the BaBar, Belle and KLOE detectors, using initial state radiation (ISR) processes [10]. The idea of this approach is illustrated by the diagram shown in Fig. 2. After emission of hard photon e^+e^- pair can acquire
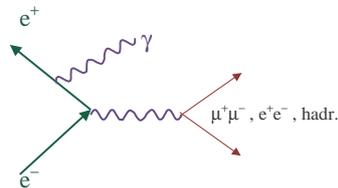
Figure 2: Diagram of the processes with initial state radiation.

any center-of-mass energy below the energy of the experiment. That means that one can study

the processes of e^+e^- annihilation in the entire range from the threshold to the experiment energy.

The BaBar collaboration has measured cross sections of many processes like $e^+e^- \rightarrow 3\pi, 4\pi, 6\pi, p\overline{p}$ and other [11, 12, 13] while Belle obtained valuable data on $D\overline{D}$ production [14].

Recently BaBar presented the results on the pion formfactor [15, 16]. A measurement of the cross section of the process $e^+e^- \rightarrow \pi^+\pi^-(\gamma)$ was performed in the energy range from threshold up to 3 GeV using 232 fb^{-1} of data collected with the BABAR detector at the center-of-mass energies near 10.6 GeV. For the normalization and cross-check the process $e^+e^- \rightarrow \mu^+\mu^-(\gamma)$ was used. The results of this study is presented in Fig. 3.
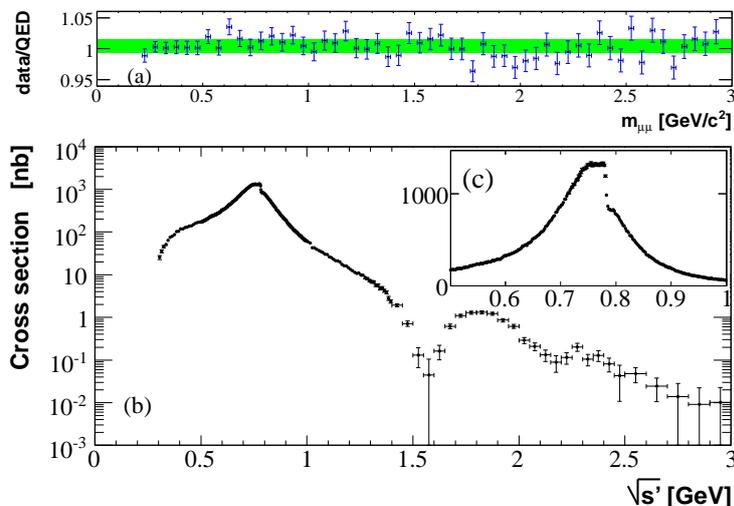
Figure 3: BaBar results on the study of the $e^+e^- \rightarrow \pi^+\pi^-$ process using ISR. The ratio of the measured $\mu^+\mu^-$ spectrum to QED calculation is shown in the upper plot.

The ratio of the measured $\mu^+\mu^-(\gamma)$ cross section to that calculated by QED is shown in upper part of the Figure. The average ratio is

$$\frac{\sigma_{\mu\mu\gamma}^{exp}}{\sigma_{\mu\mu\gamma}^{NLOQED}} = 1 + (4.0 \pm 2.0 \pm 5.5 \pm 9.4) \times 10^{-3},$$

where the first error is statistical, the second and third are systematic from the analysis and luminosity determination, respectively. Relative systematic uncertainties of the $\pi\pi\gamma$ cross section do not exceed 1% in the range from 0.4 to 1.3 GeV and increase to about 1.4% near $\pi\pi$ threshold. Obtained data were used to calculate the contribution to a_μ from $\pi^+\pi^-$ threshold to 1.8 GeV. This value, $(514.1 \pm 2.2 \pm 3.1) \times 10^{-10}$ is considerably higher than that based on all previous e^+e^- data: $(503.5 \pm 3.5) \times 10^{-10}$.

A comparison of the BaBar results with CMD-2 and KLOE data are presented in Fig. 4. The BaBar and CMD-2 data are in relatively good agreement while the former considerably differ from the results of KLOE.

KLOE is another experiment studying pion electromagnetic form factor via ISR. This experiment [17] has been conducted at DAPHNE e^+e^- collider near $\sqrt{s} = 1.019$ GeV center-of-mass
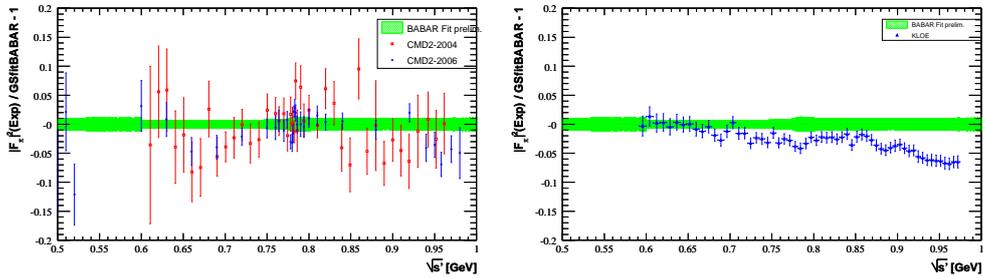
Figure 4: Ratio of the pion form factor squred values, $|F_\pi|^2$, measured by CMD-2 (left figure) and KLOE (right figure) to the BaBar fit. The bands correspond to systematic uncertainties.

with $L_{peak} = 1.3 \times 10^{32}\,\mathrm{cm}^{-2}\mathrm{s}^{-1}$. Results obtained by this experiment [18] are shown in Fig. 5. The systematic uncertainty shown in Fig. 5 by the grey band is approximately 1%. The com-
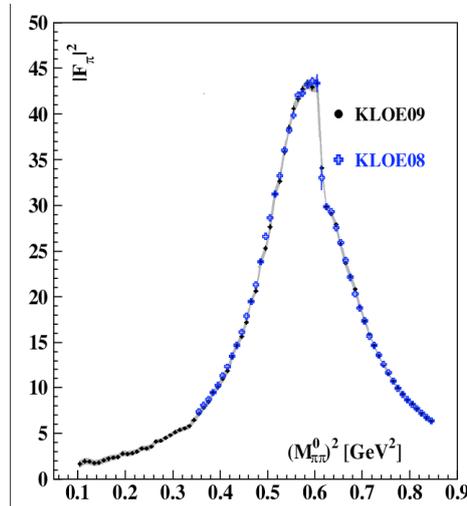
Figure 5: Results of the KLOE experiment.

parison of the KLOE results with CMD-2 and SND data is shown in Fig. 6.

The value of a_μ was calculated by KLOE using two sets of the results in the s range (0.35 – 0.85) GeV^2):

KLOE 08 (small angles): $a_\mu = (379.6 \pm 0.4(\mathrm{stat.}) \pm 2.4(\mathrm{sys.}) \pm 2.2(\mathrm{theo.})) \times 10^{-10}$
KLOE 09 (large angles): $a_\mu = (376.6 \pm 0.9(\mathrm{stat.}) \pm 2.4(\mathrm{sys.}) \pm 2.1(\mathrm{theo.})) \times 10^{-10}$

The value of a_μ obtained by KLOE can be compared with CMD-2 and SND results when the integration is performed over the same range, $0.397 < s < 0.918$ GeV^2:

KLOE 08 (small angles) $a_\mu = (356.7 \pm 0.4(\mathrm{stat.}) \pm 3.1(\mathrm{sys.})) \times 10^{-10}$;
CMD-2 $a_\mu = (361.5 \pm 1.7(\mathrm{stat.}) \pm 2.9(\mathrm{sys.})) \times 10^{-10}$;
SND $a_\mu = (361.0 \pm 2.0(\mathrm{stat.}) \pm 4.7(\mathrm{sys.})) \times 10^{-10}$.

Finally, KLOE strengthens the discrepancy 3.4 σ between the SM prediction and the BNL measurements.
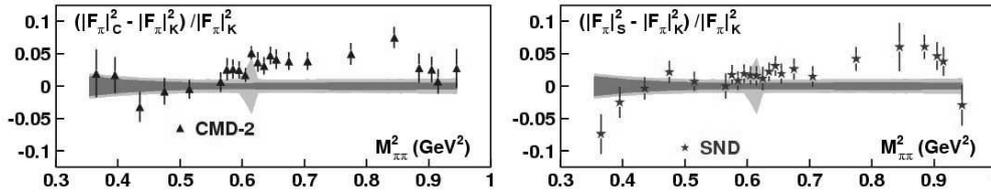
Figure 6: Comparison of the KLOE results with CMD-2 and SND data. The grey band shows the systematic uncertainty in the KLOE data.

3 Search for LFV in τ-lepton decays

Charged lepton flavour violation (LFV) would be a very clear manifestation of the new physics since in the Standard Model the lepton flavour violation decays are extremely small. Searches for $\mu - e$ LFV are performed in $\mu - e$ conversion and $\mu^- \to e^- \gamma$ decay [19] ($B < 1.2 \times 10^{-11}$), as well as in $\mu^- \to e^- e^- e^+$ decay [20] ($B < 1.0 \times 10^{-12}$).

Many models consider extensions of the Standard Model with enhanced LFV. Particularly popular are SUSY models, e.g. MSSM extension of SM, also discussed SUGRA, GUT, Higgs, little Higgs. The predicted $B(\tau \to \mu^- \gamma)$ reaches $10^{-8} - 10^{-7}$.

In the last years main contributions on tau decays study came from two B-factories. Both detectors, Belle [21] and BaBar [22], are forward/backward asymmetric detectors with high vertex resolution, magnetic spectrometry, excellent calorimetry and sophisticated particle ID ability. Total luminosity collected by both detectors is about 1.5 ab^{-1}, which corresponds to about 1 400 000 000 $\tau^+ \tau^-$ events.

At Belle and BaBar 44 different LFV modes were searched for. The most stringent limit is $B(\tau \to \mu^+ e^- e^-) < 1.5 \times 10^{-8}$ [23]. The sensitivity for different modes is limited by background suppression or statistics. The following results from Belle can be considered as examples:

- $\tau \to \mu^- \gamma, e\gamma$ [24]. The data sample included 535 fb^{-1} of integrated luminosity was used to the analysis. After event selection the number of events in the 2σ signal region was 10 (5) for $\mu\gamma$ ($e\gamma$) decays in agreement with the background expectation. This provides the upper limits $Br(\tau \to \mu^- \gamma) < 4.5 \times 10^{-8}$ and $Br(\tau \to e^- \gamma) < 1.2 \times 10^{-7}$ at 90% C.L. The sensitivity in this case is limited by the remaining background from $e^+ e^- \to \tau^+ \tau^- \gamma$ process.

- $\tau \to e/\mu(\eta, \eta\prime, \pi^0)$ [25]. The data sample included 401 fb^{-1} of integrated luminocity. One event was found in the signal region in agreement with expectation (0.–0.6 for different decay modes). The obtained upper limits are: $Br(\tau \to \mu\eta, \mu\eta\prime, \mu\pi^0) < (6.5 - 13) \times 10^{-8}$ $Br(\tau \to e\eta, e\eta\prime, e\pi^0) < (8.0 - 16) \times 10^{-8}$ at 90% C.L. In this case the sensitivity is clearly limited by the statistics.

In general, the improvement in upper limits on the LFV decays achieved by studies at the B-factories is ~ 100 compared to CLEO.

4 Hadronic τ-lepton decays

Main motivations to study tau hadronic decays:

234   *LP09*

- τ-lepton decays provide an excellent laboratory to study hadron physics up to 1.8 GeV. The main attractive feature is a clean initial state and low multiplicity of final hadrons decreasing combinatorial background and final state interaction effects.

- Tests of CVC and evaluation of the a_μ from spectral functions.

- Search for CP violation effects in the hadronic decays in hope to find new physics.

- Improvement of the limits on the τ-neutrino mass.

4.1 $\tau^- \rightarrow \pi^- \pi^0 \nu_\tau$ decay and CVC

$\tau^- \rightarrow \pi^- \pi^0 \nu_\tau$ decay has the largest branching fraction. The important feature is that the produced pions are in the vector state which means that their invariant mass distribution can be related to the cross section of the process $e^+ e^- \rightarrow \pi^+ \pi^-$ via CVC:

$$\frac{1}{N}\frac{dN_{\pi\pi}}{ds} = \frac{6\pi|V_{ud}|^2 S_{EW}}{m_\tau^2} \cdot \frac{B_e}{B_{\pi\pi}}\left[\left(1 - \frac{s}{m_\tau^2}\right)^2\left(1 + \frac{2s}{m_\tau^2}\right)\right]\nu^{\pi\pi}(s), \quad \nu^{\pi\pi}(s) = \frac{\beta_\pi^3(s)}{12\pi}|F_\pi|^2.$$

However, certain corrections to the Spectral Functions are needed [26]:
$S_{EW} = 1.0233 \pm 0.0006$
Real photons, loops; FSR;
$m_{\pi^\pm} \neq m_{\pi^0}$ – (phase space, Γ_ρ);
$m_{\rho^\pm} \neq m_{\rho^0}$;
$\rho - \omega$- interference;
Radiative decays ($\pi\pi\gamma$ amd other); $m_u \neq m_d$; and possible 2d class currents.

Recently the Belle collaboration presented the results of a study of the mentioned process based on 5.6×10^6 $\tau^- \rightarrow \pi^- \pi^0 \nu_\tau$ decays (72.2 fb^{-1}) [27]. The measured value of the branching fraction is: $Br_{2\pi} = (25.24 \pm 0.01(\text{stat.}) \pm 0.39(\text{sys.}))\%$. Systematics is dominated by the uncertainty of the π^0 efficiency and the background from other τ decays.

The quoted value is in good agreement with the previous measurements as well as with the PDG average [28] but it is considerably higher than that calculated via CVC using e^+e^- data. It should be noted that the branching from all groups is systematically higher than the CVC prediction, $< Br_{2\pi} > -Br_{CVC} = (0.92 \pm 0.21)\%$ or 4.5σ from 0. The discrepancy is a 3.6% effect, about twice the SU(2) correction.

The $\pi^+\pi^0$ spectral function evaluated in the Belle analysis is shown in Fig. 7 in comparison with the results of the previous ALEPH and CLEO experiments [29]. The systematic error varies from 0.7% at the ρ-meson mass to about 11% at the right end of the spectrum.

The contribution to a_μ, calculated with the Belle data, $a_\mu = (523.5 \pm 1.5(\text{exp.}) \pm 2.6(\text{br.}) \pm 2.5(\text{isospin})) \times 10^{-10}$, is in good agreement with the previous calculation based on combined ALEPH, CLEO and OPAL data [30]. It should be noted that the recent work [31] revisiting isospin corrections gave a lower value for a_μ in good agreement with the last BaBar results.

4.2 Search for the second class currents

The idea to separate hadronic currents in weak interactions to the first and second classes with different isospin properties was introduced by S.Weinberg [32]. The properties of the First Class Currents (FCC) and the Second Class Current (SCC) are defined as: FCC – $PG(-1)^J = +1$
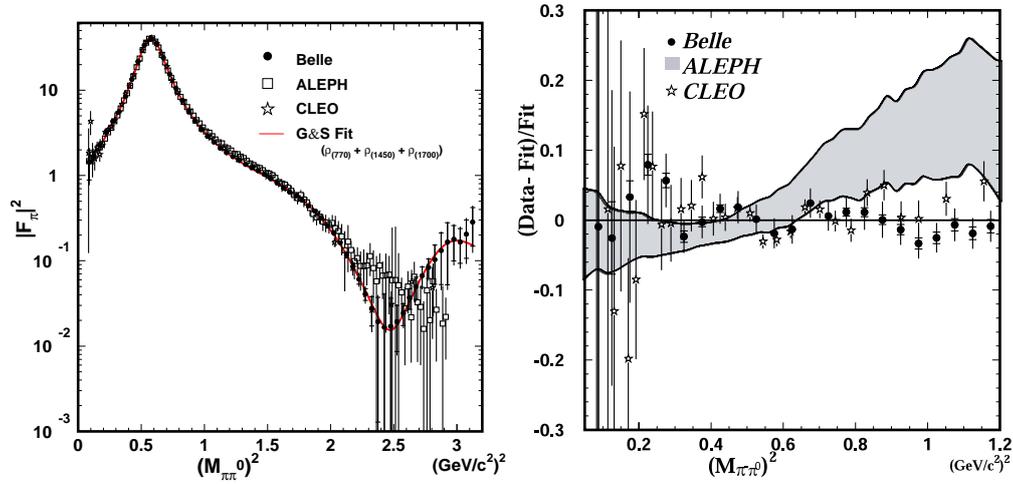
Figure 7: $|F_\pi|^2$ obtained by the Belle from the $\tau^- \to \pi^- \pi^0 \nu_\tau$ decay study in comparison with previous experiments (left plot). Detail comparison at the ρ-meson region is shown in the right plot. The grey band indicates the systematic umcertainties of the ALEPH data.

and SCC – $PG(-1)^J = -1$, where P is a parity, G – G-parity and J – spin of the hadronic system.

In SM the SCC should be suppressed by the difference of the light quark masses: $m_u - m_d$. In case of the perfect $SU(2)$ symmetry only FCC exists. Up to now no SCC were found in experiment.

The decay $\tau^- \to \eta \pi^- \nu_\tau$ has $JPG = 0^{+-}$. The theoretical prediction of its branching fraction is at the level: $B(\tau \to \eta \pi \nu_\tau) \sim 10^{-6} \div 10^{-5}$. Large background from $\tau^- \to \eta \pi^- \pi^0 \nu_\tau$ decay with $B = (1.77 \pm 0.24) \times 10^{-3}$ is one of the problems in a search of SCC decay.

Recently a search for this decay was performed at Belle experiment [33]. A studied sample contained 6.2×10^8 τ pairs. Each event had to include $\tau \to \eta \pi + \nu_\tau$, $\eta \to \pi^+ \pi^- \pi^0$ decay at the signal side while the tag side was required to be a leptonic τ decay – $\tau^- \to l^- \nu_l \nu_\tau + n\gamma$. An additional condition on invariant mass of four pions at the final state, $M(4\pi) < 1.2$ GeV was applied.

After background subtraction the number of signal events was found to be $N_{sig} = 190.9 \pm 68.6$ which corresponds to the $Br(\tau \to \eta \pi + \nu_\tau) = (4.4 \pm 1.6 \pm 0.8) \times 10^{-5}$ and to the upper limit $Br(\tau^- \to \eta \pi^- \nu_\tau) < 7.3 \times 10^{-5}$ at 90%CL. The obtained limit improved the previous results [34] by a factor of about 2.

In the same analysis the upper limit to the $\tau^- \to \eta\prime \pi^- \nu_\tau$ was set: $Br(\tau^- \to \eta\prime \pi^- \nu_\tau) < 4.6 \times 10^{-6}$ at 90%CL.

The BaBar experiment has also presented the results on the searches for $\tau^- \to \eta\prime \pi^- \nu_\tau$: $B(\tau^- \to \eta\prime(958)\pi^- \nu_\tau) < 7.2 \times 10^{-6}$ at 90% confidence level [35]. The other decay including SCC effects, which was studied recently by the BaBar, is $\tau^- \to \omega \pi^- \nu_\tau$. The hadronic current of this decay can contain both vector (FCC) and axial-vector (SCC) components. On the base of the integrated luminosity of 347 fb^{-1} (319 million $\tau^+ \tau^-$-pairs) BaBar evaluated an upper limit for the ratio: $N(\omega \pi, vector)/N(\omega \pi, non-vector) < 0.69\%$ at 90% C.L. and 0.85% at 95%

CL [36], which is about 10 times better than the previous results of CLEO [37] and ALEPH [38]

4.3 V_{us} evaluation from τ hadronic decays

A precise measurement of the τ-lepton branching fractions provides a basis for the determination of the V_{us} element of the CKM matrix [39]. The following relations are used for this:

$$R_\tau = \frac{\Gamma(\tau \to h\nu_\tau)}{\Gamma(\tau \to e\overline{\nu}_e\nu)} = R_s + R_{ns}, \quad |V_{us}|^2 = \frac{R_s}{R_{ns}/|V_{ud}|^2 - \delta R_\tau},$$

where R_s and R_{ns} are the ratios containing strange and non-strange final states respectively. The branching fractions and invariant mass distributions are the experimental input to determine $|V_{us}|$ while V_{ud} is well measured from superallowed beta decays. The δR_τ is determined from Finite Energy Sum Rules and is relatively small, so that even a large relative error can allow a precise measurement of $|V_{us}|$. The $|V_{us}|$ value obtained in [40], where the latest results on hadronic τ-decays from Belle and BaBar were included, is in the range from 0.2160 to 0.2190 depending on the parameters in FESR calculations. The experimental uncertainty is about 0.0030. $0.2144 \pm 0.0030 \pm 0.0017$ Thus, this value is about $2 - 3\sigma$ smaller than the quantity derived from the unitarity condition, 0.2262 ± 0.0011, obtained with $|V_{ud}| = 0.97408 \pm 0.00026$ as determined in [41].

An independent determination of $|V_{us}|$ is possible via the ratio

$$\frac{\Gamma(\tau \to K\nu_\tau)}{\Gamma(\tau \to \pi\nu_\tau)}.$$

Such a study was recently made by BaBar [43] which measured the $B(\tau \to K\nu)/B(\tau \to \pi\nu)$ ratio. Then, taking the ratio $f_K/f_\pi = 1.189 \pm 0.007$ from Lattice QCD [42] and $|V_{ud}| = 0.97408 \pm 0.00026$ from superallowed beta decays they obtained the value 0.2255 ± 0.0023 in a good agreement with the unitarity prediction.

5 Lepton universality and τ-lepton mass measurement

In the Standard Model all lepton decays are governed by the same weak constant:

$$G_F = \frac{g^2}{4\sqrt{(2)}M_W^2}, \quad g = g_e = g_\mu = g_\tau,$$

where G_F is Fermi constant. According to the present knowledge $g_e = g_\mu$ within at least 0.2% while the difference $g_\mu - g_\tau$ is less than 2%. Tests of the g_l equality were performed in W decays (ALEPH, DELPHY, L3 and OPAL), τ decays (ALEPH, DELPHY, L3, OPAL and CLEO), kaon decays (KLOE) and pion decays (TRIUMPH and PSI).

To test the g_τ/g_μ ratio the precise value of τ mass is important. Recently, new results on that came from KEDR, Belle and BaBar experiments.

In the KEDR experiment [44], which was performed at the VEPP-4M collider at BINP, the τ-lepton mass was derived from the measurements of $e^+e^- \to \tau^+\tau^-$ cross section near threshold [45]. The key problem for this approach is the precise energy determination. Two independent methods were used in this experiment. One of them was resonant depolarization

method which provided the accuracy of the energy determination of about 10 keV. The other one used Compton backscattering of the laser photons by the beam in the collider and determined the energy with the accuracy 50-70 keV. The τ mass value determined in this experiment is presented in Table 3.

In the Belle and BaBar experiments the τ mass values were determined by the fit of the pseudomass distribution of the hadronic decays. The pseudomass is defined by the formulae:

$$M_\tau^2 = (E_h + E_\nu)^2 - (\overrightarrow{p}_h + \overrightarrow{p}_\nu)^2 = M_h^2 + 2(E_\tau - E_h)(E_h - p_h \cos(\theta)) \geq M_p^2 = M_h^2 + 2(E_\tau - E_h)(E_h - p_h).$$

The results of the BaBar and Belle experiments, based on 389 and 370 million $\tau^+\tau^-$ pairs respectively [46, 47] are presented in the Table 3.

These measurements can be used to determine the difference between masses of the positive and negative τ leptons and test CPT theorem. The results are presented in the Table 2

Experiment	OPAL, 2000	Belle, 2007	BaBar, 2008
$N_{\tau^+\tau^-}, 10^6$	0.16	370	389
$\Delta m / m_\tau, 10^{-4}$	0.0 ± 18.0	0.3 ± 1.5	-3.5 ± 1.3
$\Delta m / m_\tau, 10^{-4}, 90\%$ CL	< 30.0	< 2.8	$-5.6 < \Delta m / m_\tau < -1.4$

Table 2: Experimental values of the $\Delta m = m_{\tau^+} - m_{\tau^-}$

6 Perspectives and conclusion

In the next 3-5, or even more years intensive analysis of about a 1.5 ab^{-1} data sample harvested by both B-factories will continue that providing new interesting results. New results from KLOE, BES-III and KEDR are expected as well.

Talking about future we can also hope that two new proposals for muon $(g-2)$ measurements intended for FNAL [48] and JPARC [49] will be accepted and start experiments. These two projects aim to improve the $(g-2)$ accuracy by a factor 3-4.

At present the VEPP-2000 e^+e^- storage ring at BINP is at the commissioning stage. Experiments at this collider with two detectors, CMD-3 and SND, in the energy range up to 2 GeV should provide new accurate data on the hadronic cross sections. The expected accuracy is 2-3 times better than the present one [?].

Rich information on the tau lepton properties will be obtained if, at least, one of the Super B-factory projects [50, 51] is accepted. The design luminosity of $8 \div 20 \times 10^{35}$ and upgraded detector have to provide improvement 10-100 times in a sensitivity.

In the last decade many new precise results were obtained in the considered class of experiments at low energies. We can see in some cases discrepancies with the calculations based on the SM at the level of 3 standard deviation. These can be hardly taken as the indications of a NP, however, we have to apply additional efforts to clarify these phenomena.

Hopefully, in the next 5-10 years we will receive new rich information on the these field of physics from new experiments and advanced theoretical approaches .

Group	m_τ, MeV
BES, 1996	$1776.96^{+0.18+0.25}_{-021-0.17}$
PDG, 2006	$1776.99^{+0.29}_{-0.26}$
KEDR, 2007	$1776.81^{+0.25}_{-0.23} \pm 0.15$
Belle, 2007	$1776.61 \pm 0.13 \pm 0.35$
PDG, 2008	1776.83 ± 0.18
KEDR, 2008	$1776.68^{+0.17}_{-0.19} \pm 0.15$
BaBar, 2008	$1776.68 \pm 0.12 \pm 0.41$

Table 3: Measurements of τ-lepton mass

Acknowledgments

References

[1] G.W. Bennett *et al.*, Phys. Rev. **D73** 072003 (2006).

[2] T. Kinoshita and M. Nio, Phys. Rev. **D73** 053007 (2006).

[3] A.L. Kataev, Phys. Rev. **D74** 073011 (2006).

[4] G. Gabrielse *et al.*, Phys. Rev. Lett. **D97** 030802 (2006).

[5] M. Passera, J. Phys. **G31** 75 (2005) M. Passera, Phys.Rev. **D75** 013002 (2007).

[6] A. Czarnecki *et al.*, Phys. Rev. **D67** 073006 (2003); T. Gribouk and A. Czarnecki, Phys. Rev. **D72** 053016 (2005).

[7] J. Prades, E. de Rafael, A. Vainshtein, arXiv:hep-ph/0901.0306 (2009).

[8] S. Eidelman, Nucl. Phys. B (Proc.Suppl.) **189** 208 (2009).

[9] I.B. Logashenko, Nucl. Phys. B (Proc.Suppl.) **189** 239 (2009).

[10] V.N. Baier, V.A.Khoze, Sov. Phys. JETP **21** 1145 (1965);
S. Binner, H.J. Kuhn, K. Melnikov, Phys. Lett.B **459** 279 (1999);
M.Benayoun *et al.*, Mod. Phys. Lett. A **14** 2605 (1999).

[11] B. Aubert *et al.*, Phys. Rev. D **70** 072004 (2004).

[12] B. Aubert *et al.*, Phys. Rev. D **71** 052001 (2005).

[13] B. Aubert *et al.*, Phys. Rev. D **73** 012005 (2006);
B. Aubert *et al.*, Phys. Rev. D **73** 052003 (2006).

[14] G. Pakhlova *et al.*, Phys. Rev. D **77** 011103 (2008).

[15] M. Davier, Nucl. Phys. B (Proc.Suppl.) **189** 222 (2009).

[16] B. Aubert *et al.*, Phys. Rev. Lett. **103** 231801 (2009).

[17] M. Adinolfi *et al.*, Nucl. Instr. Meth. A **488** 51 (2002);
M. Adinolfi *et al.*, Nucl. Instr. Meth. A **482** 364 (2002).

[18] F. Ambrosino *et al.*, Phys. Lett.B **670** 285 (2009).

[19] M.L. Brooks *et al.*, Phys. Rev. Lett., **83** 1521 (1999).

[20] U. Bellgardt *et al.* Nucl. Phys. B **299** 1 (1988).

[21] A. Abashian *et al.* Nucl. Instr. Meth. A **479** 117 (2002).

[22] B. Aubert *et al.*, Nucl. Instr. Meth. A **479** 1 (2002).

[23] Y. Miyazaki *et al.*, Phys. Lett. B **660** 154 (2008);
K.Hayasaka *et al.*, arXiv:hep-ex/1001.3221 (2010).

[24] K.Hayasaka *et al.*, Phys. Lett. B **666** 18 (2008).

[25] Y. Miyazaki *et al.*, Phys. Lett. B **648** 341 (2007).

[26] V. Cirigliano, G. Ecker, H. Neufeld, J. High Energy Phys. **08** 002 (2002).

[27] M. Fujikawa *et al.*, Phys. Rev. D **78** 072006 (2008).

[28] C. Amsler *et al.*, Phys. Lett. B **667** 1 (2008).

[29] S. Schael *et al.*, Phys. Rep. **421** 191 (2005);
S. Anderson *et al.*, Phys. Rev. D **61** 112002 (2000).

[30] M. Davier *et al.*, Eur. Phys. J. C **27** 497 (2003).

[31] M. Davier *et al.*, arXiv:hep-ph/0906.5443v1 (2009).

[32] S. Weinberg, Phys. Rev. **112** 1375 (1958).

[33] K. Hayasaka, PoS EPS-HEP 374 (2009).

[34] J.E. Bartelt *et al.*, Phys. Rev. Lett. **76** 4119 (1996).

[35] B. Aubert *et al.* Phys. Rev. D **77** 112002 (2008).

[36] B. Aubert *et al.* Phys. Rev. Lett. **103** 041802 (2009).

[37] K.E. Edwards *et al.*, Phys. Rev. D **61** 072003 (2000).

[38] D. Buskulic *et al.*, Zeit. Phys. C **74** 263 (1997).

[39] E. Gamiz *et al.*, Phys. Rev. Lett. **94** 011803 (2005).

[40] K. Maltman *et al.*, Nucl. Phys. B (Proc. Suppl.) **189** 175 (2009).

[41] T. Eronen *et al.*, Phys. Rev. Lett. **100** 132502 (2008).

[42] E. Follana *et al.*, Phys. Rev. Lett. **100** 062002 (2008).

[43] I.M. Nugent, Nucl. Phys. B (Proc. Suppl.) **189** 9 (2009)

[44] V.V. Anashin *et al.*, Nucl. Instr. Meth. A **478** 420 (2002).

[45] A.G. Shamov *et al.*, Nucl. Phys. B (Proc. Suppl.) **189** 21 (2009).

[46] B. Aubert *et al.* Phys. Rev. D **80** 092005 (2009).

[47] K. Belous *et al.*, Phys. Rev. Lett. **99** 011801 (2007).

[48] K.R. Lynch, Nucl. Phys. B (Proc. Suppl.) **189** 201 (2009).

[49] N.Saito, *g-2/EDM experiments at J-PARC*, Hints for new physics in flavor decays, KEK, Tsukuba, Japan (2009).

[50] T.E. Browder, Nucl. Phys. B (Proc. Suppl.) **185** 83 (2008).

[51] M.A. Giorgi, Nucl. Phys. B (Proc. Suppl.) **185** 88 (2008).

Discussion

Eckard Elsen (DESY): Could you comment on the discrepancy in R from $\pi^+\pi^-\gamma$?
Answer: The experiments with such a high accuracy are quite complicated. On the other hand, theoretical calculations which are used to obtain the experimental results, like radiation corrections calculations, are very complicated as well. So, at present, we cannot say where the source of these discrepancies can be. In short words - I have no answer to your question, but it is clear that more work is needed to reach an understanding.

Indirect Search Results for Signatures of Particle Dark Matter

W. B. Atwood

Santa Cruz Institute for Particle Physics Department of Physics
University of California
1156 High Street
Santa Cruz, 95064, USA

Recent astro-particle experiments have reported results of searches for signatures of particle dark matter (DM) other than the ubiquitious gravitational effects. Tantalizing hints of unexpected behavior in the cosmic-ray electron and positron spectra have been found by PAMELA, ATIC, and the *Fermi* LAT. However, these signatures, sometimes interpreted as coming from DM annihilation and/or decays, can have alternative – "standard" – astrophysical interpretations as well, and hence can be used to further constrain the mass, cross section, and distribution of DM. The forerunner experiment to the *Fermi* LAT, EGRET, detected excess diffuse γ-ray emission above 1 GeV, compared to standard astrophysical models for the diffuse Galactic γ-ray emission. However, this has not been confirmed by the *Fermi* LAT. Searches by the *Fermi* LAT for γ-rays from DM lines, clumps, and signals from nearby dwarf galaxies have also been performed. I will review the various experiments and discuss the new limits provided on the properties of particle DM.

1 Introduction

The existence of dark matter (DM) was first postulated by Zwicky and confirmed by astronomical rotation curves for stars within distant galaxies [1]. Stars at the periphery of galaxies have tangential velocities far in excess of that expected by estimating the gravitating mass of the galaxy within their orbits. And, this observation is repeated in essentially all galaxies for which this behavior has been looked for. More recently, in the collision of two galaxies known as the Bullet Cluster, the center of the luminous mass and the gravitational center are not co-located [2].

The existence of DM is not at issue, but rather its nature. The only observable trait found to date is the gravitational interaction. Many believe that this as-yet unobserved matter is particle in origin. Extensions to the Standard Model of particle physics often have enticing slots into which DM could fall, the idea being that it is a cosmological relic left over from the Big Bang. If indeed DM is particle in nature, then its interactions with ordinary matter as detailed by the Standard Model can be calculated. Signs of its presence could arise from either co-annihilation of two DM particles resulting in standard model particles, or these dark matter particles could simply decay into ordinary matter, albeit with a very long lifetime. A common expression for the resulting flux of γ-rays from DM particle co-annihilations is given by

$$F_\gamma(E, \psi) = \frac{<\sigma v>}{4\pi} \left[\sum_f \frac{dN_f}{dE} B_f \right] \int_{l.o.s} \frac{1}{2} \left(\frac{\rho(l)}{M_\chi} \right)^2 dl \qquad (1)$$

where F_γ is the flux of γ-rays, $<\sigma v>$ is the annihilation cross-section velocity average, the term in square brackets is the sum over possible final states where B_f is the branching fraction and dN_f/dE is the energy spectrum, and the integral in last term is along the line-of-sight for the observation with ρ the DM energy density and M_χ the DM candidate mass. The ratio of the energy density to mass is the number density and the co-annihilation means this appears as a squared term in the expression. The uncertainties for the contributing terms in equation 1 are large, particularly the number density. State-of-the-art N-body simulations predict DM clumps over all length scales. Since the annihilation rate depends quadratically on the number density, clumping essentially boosts the potential signal. However, current simulations are numerically limited in resolution of the clumping below a lower length scale. Below this, the assumptions of the scaling behaviour of the clumping introduce a significant uncertainty in the annihilation rate that can be several orders of magnitude. For the case of decaying DM particles, the quadratic dependence on density becomes linear and in place of $\langle \sigma v \rangle$ is the DM particle decay rate.

The same expression can be written for final state particles other than γ-rays. Recent measurements of cosmic-ray (CR) fluxes of antiprotons, positrons, and electrons have provoked a great deal of speculation as to whether or not we are finally seeing evidence for the particle origins of the DM. I will first review the status of these CR searches and follow with γ-ray searches.

2   Cosmic-Ray Flux Measurements

The first experimental result to be discussed is the ATIC (Advanced Thin Ionization Calorimeter) collaboration's measurement of the total CR electron + positron flux [3]. This balloon-borne experiment has had four flights from the NSF Antarctic balloon facility. The original motivation for these measurements was to obtain the spectrum of entering CRs not only for electrons, but for protons and heavier nuclei as well. The detector was not tuned to provide a high discrimination power between electrons and hadrons. In particular, in order to insure that a large fraction of incoming nuclei energy would be deposited in the calorimeter section, about 1.5 radiation lengths of carbon served as a converter target in front of the calorimeter. This is contrary to the usual practice in a dedicated electron detector that tries to accentuate the separation between the first interaction locations of electrons and hadrons. A diagram of the ATIC detector is shown in Fig. 1.

The ATIC collaboration has logged four balloon flights to date, the third of these however ended prematurely and resulted in no useful data. Over the course of these flights the apparatus was upgraded, particularly the depth of the calorimeter which was increased from 18 to 22 radiation lengths for the fourth and last flight. In order to measure the electron spectrum, an offline analysis capable of discriminating between electrons and hadrons at greater then 1000:1 had to be achieved. Initially, the ATIC collaboration published the results for the first two balloon flights and more recently added the data from the last flight. The spectra, multiplied by E^3 to compress the dynamic range, is shown in Fig. 2.

The prominent enhancement in the spectrum around 600 GeV caused a great deal of excitement in 2008 and was interpreted in more than a few papers as a signature of particle
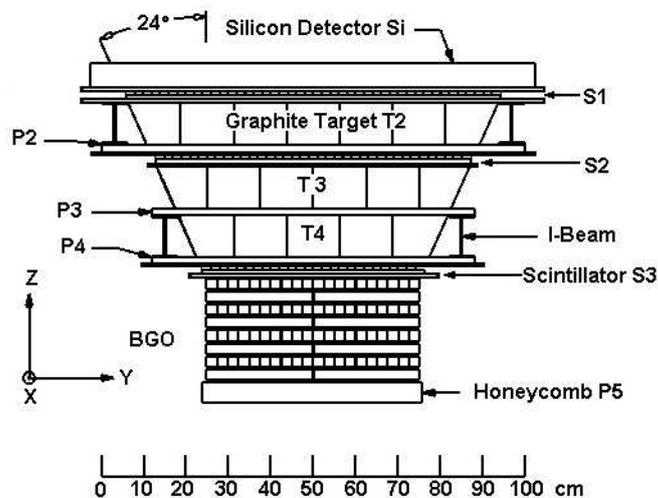
Figure 1: The ATIC detector. The top layer of silicon detectors is used to the determine the magnitude of the incoming charge. Three layers of graphite, interspersed with scintillation hodoscopes for tracking, enhance the early interaction of incoming hadronic CRs. A Bismuth-Germanium-Oxide calorimeter with 18–22 radiation lengths depth is located at the bottom of the instrument.

DM. However, it was also realized that the DM source for high-energy electrons would have to be quite close to the solar system, otherwise their energy would be significantly degraded via inverse Compton scattering of the interstellar radiation field and synchrotron cooling on the Galactic magnetic field.

During the same time period as the latter of the ATIC flights, a satellite-borne instrument has also been in operation: PAMELA, the Payload for Antimatter Matter Exploration and Light-nuclei Astrophysics[4]. The PAMELA apparatus distinguishes itself from other payloads by having a magnetic spectrometer that can determine the sign and magnitude of the charge of the incoming CRs. The primary motivation for PAMELA was to measure with high statistics the antimatter component in CRs. The relevance of PAMELA to DM searches is that annihilations (or decays) of DM particles will create equal amounts of matter and antimatter in the final state. A diagram of the PAMELA apparatus is shown in Fig. 3.

PAMELA was launched in June 2007 onboard a Russian satellite and has taken data continually since launch. The two results published in 2008 of interest for DM searches are shown in Fig. 4: the CR antiproton and positron fractions, respectively. The high statistics and energy coverage have resulted in a significant improvement for the measurements of these CR species.

The PAMELA measurement of the antiproton fraction is consistent with that expected from standard secondary production by CR nuclei interacting with the interstellar gas. The surprise was the dramatic rise in the positron fraction with increasing energy. This together with the ATIC results was the source of many papers in 2008. We currently await the publication of PAMELA results for the separate CR electron and positron spectra, which will provide deeper information than the positron fraction.

The newest experiment to provided data on the CR electron flux (hereafter I use the term
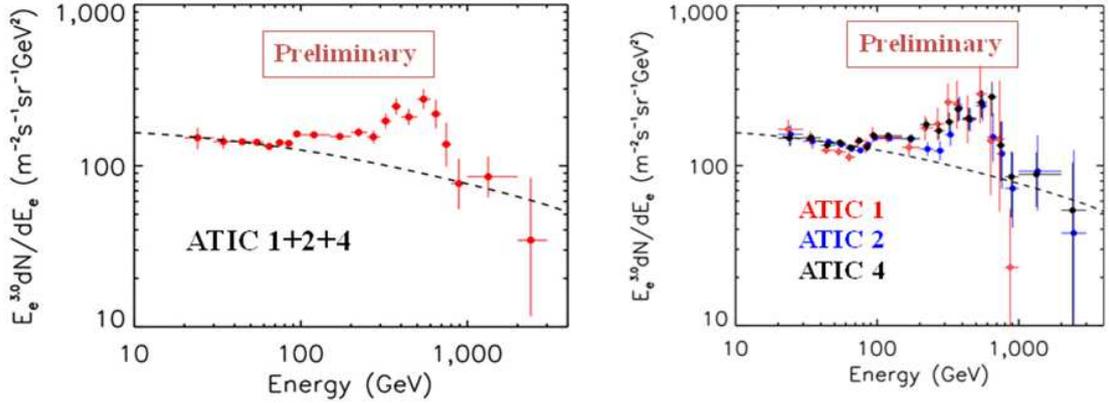
Figure 2: The total $e^+ + e^-$ spectrum measured by ATIC. The first and second flight (ATIC 1 & 2) showed an enhancement of 3.8σ centerd around 600 GeV. The fourth flight (ATIC 4) showed the same feature with increased statistics resulting in an overall significance of 5.1σ.

"electron" to mean electrons and positrons combined) is the Large Area Telescope (LAT) on the *Fermi Gamma-ray Space Telescope*. This instrument was originally conceived in 1992 as the next generation high-energy γ-ray satellite as a follow on to the Energetic Gamma-Ray Experiment Telescope (EGRET) on the *Compton Gamma-Ray Observatory*. It was realized early in the evolution of the then named GLAST (Gamma-ray Large Area Telescope) project, that an excellent γ-ray instrument would also measure the CR electron component. After the *Fermi* launch in June, 2008, a dedicated effort was mounted to develop the electron measuring potential of this instrument. The LAT instrument along with the satellite and the companion Gamma ray Burst Monitor (GBM) is shown in Fig. 5. Details of the LAT can be found in reference[5].

The LAT is a pair-conversion telescope comprised of a 4×4 modular array with each module comprising a precision converter-tracker section followed by a calorimeter (see Fig. 5). The active elements of the tracker are silicon-strip detectors. The calorimeter is a hodoscopic configuration of 8.6 radiation lengths of CsI crystals that allows imaging of the shower development in the calorimeter. This imaging capability enables making corrections to the energy estimate for the shower leakage fluctuations event by event. The total thickness of the tracker and calorimeter is 10.1 radiation lengths at normal incidence. A segmented, anticoincidence detector (ACD) covers the tracker array, and a programmable trigger and data acquisition system uses prompt signals available from the tracker, calorimeter, and ACD to form a trigger that initiates readout of these three subsystems. The onboard trigger is optimized for rejecting events triggered by CR background particles while maximizing the number of events triggered by γ-rays, that are transmitted to the ground for further processing.

To take full advantage of the LATs large field-of-view (FoV), the primary observing mode of Fermi is the so-called "scanning mode". In this mode the instrument axis is pointed to $+35°$ from the zenith and towards one pole of the orbit on alternate orbits and to $-35°$ from the zenith for the other orbits. Thus, after two orbits (or about 3 hours for the nominal orbit at 565 km and 25.5° inclination) the sky exposure is almost uniform. For autonomous re-points or for other targets of opportunity, the observatory can be inertially pointed as well. Building on
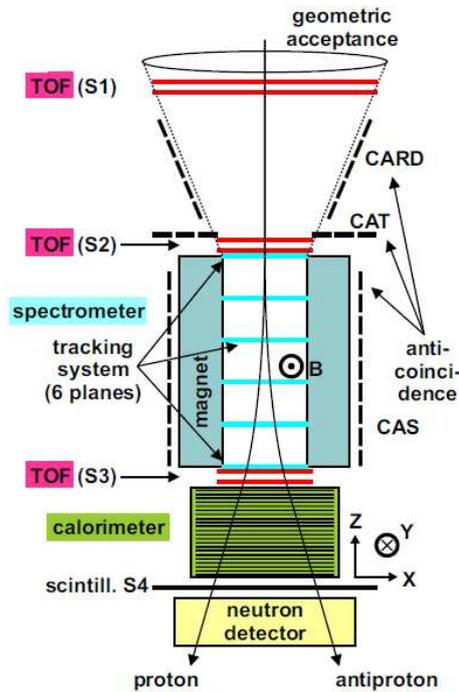
Figure 3: The PAMELA experiment. The magnetic spectrometer of this instrument is capable of of determining the sign of the charge of detected particles to energies > 200 GeV. PAMELA was launched in June 2007 onboard a Russian satellite and has taken data continually since launch.

the γ-ray analysis, the LAT Collaboration has developed an efficient electron detection strategy that provides sufficient background rejection for the measurement of the steeply falling electron spectrum up to 1 TeV[6]. Similar to ATIC, the LAT cannot directly distinguish electrons and positrons. Since the initial results above 20 GeV, the LAT results have been extended to below 10 GeV using an independent hardware trigger and analysis. Where the results overlap, the agreement is excellent. These results are shown in Fig. 6. Fits to this spectrum with a power law shows it falls with energy as $E^{-3.04}$ and does not exhibit prominent spectral features such as seen in the ATIC results. The energy resolution of the LAT calorimetry, verified by beam test and Monte Carlo, is sufficient that any prominent peak, such as seen by ATIC, would have been significantly detected by the analysis.

A standard diffusion-reacceleration CR propagation model [7, 8] based on the assumption that the CR electrons originate from a continuous distribution of sources, mainly associated with supernova remnants and pulsars, fits the LAT spectrum moderately well. This kind of model predicts a featureless spectrum from 10 GeV up to few hundreds of GeV. Above a few hundreds of GeV the assumptions for the sources in such a model break down. Due to the actual stochastic nature of CR electron sources in space and time, and to the strong synchrotron and inverse Compton energy losses, the spectrum should fall faster. Deviations from a featureless power law are likely to be caused by nearby sources [9, 11, 12, 13, 10]. The PAMELA results,
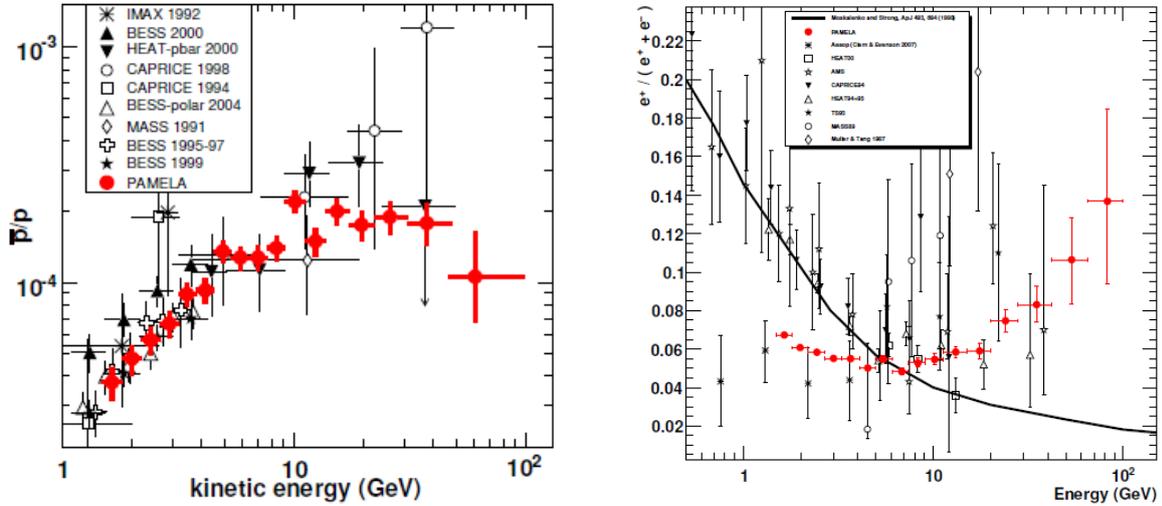
Figure 4: PAMELA results for the CR $\overline{p}/p$ ratio (left) and $e^+/(e^+ + e^-)$ ratio (right). Previous measurements are shown in black while the PAMELA data are shown in red. The dramatic improvement over earlier measurements is clear.

along with the Fermi and H.E.S.S. results [14, 15], may indicate the presence of a nearby primary source(s) of CR electrons and positrons, two classes of which stand out: nearby pulsar(s) [16, 11] and DM, either by annihilation [8] or decay, for example through grand unified interactions with a lifetime $\sim 10^{26}$ s [18].

3   Fermi-LAT Gamma-Ray Searches for Dark Matter

Gamma-ray signals from DM have been looked for using many different approaches with the first year of LAT data. These include searches for line signatures, excess emission from the Galactic Center, halo objects and galaxy clusters, together with studies of the diffuse Galactic and extragalactic γ-ray emission.

Galactic Diffuse Emission: The γ-ray sky is dominated by diffuse emission from the Milky Way. The diffuse Galactic emission (DGE) is generated by energetic CRs that interact with interstellar gas (π^0-decay and bremsstrahlung) and radiation fields (via inverse Compton scattering). An apparent excess in DGE spectrum was observed by EGRET > 1 GeV relative to conventional DGE models based on locally measured CR spectra [19]. The so-called EGRET "GeV excess" was proposed to be due to γ-rays from annihilating DM [20]. However, alternative explanations included variations in the CR spectra [12, 21] and instrumental effects [22, 23].

Based on analysis of data from the first year of observations, the *Fermi* LAT collaboration reported on measurements of the diffuse γ-ray emission from 100 MeV to 10 GeV for Galactic latitudes $10° \leq |b| \leq 20°$ [7]. The diffuse emission spectrum, shown in Fig. 7, is consistent with a DGE model that reproduces the local CR spectrum and does not require an additional component.

Extra-Galactic Diffuse Emission: The DGE presents a large forground signal to the much fainter
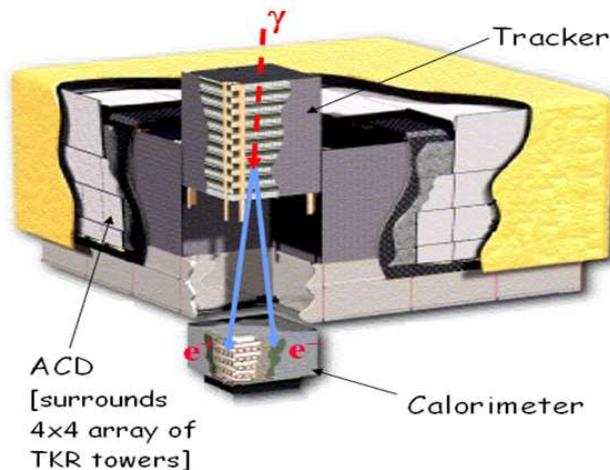
Figure 5: A cut-away diagram of the primary instrument on the *Fermi Gamma-ray Space Telescope*: the LAT. The LAT images the γ-ray sky in the energy band from ~ 20 MeV to more than 300 GeV. The LAT is comprised of 16 indentical tracker/calorimeter modules arranged in a 4×4 array. The tracker portion of the instrument is covered by the anti-coincidence detector (ACD) comprised of 89 scintillation veto tiles. The ACD helps discriminate incoming charged particles from neutrals, such as γ-rays.

diffuse Extra-Galactic Gamma-ray Background (EGB). The EGB is the sum of contributions from unresolved sources and truly diffuse emssion processes, e.g., from ultra-high energy CRs interacting with background light, large-scale structure formation, etc., as well as possibly from cosmological DM through annihilation or decay. The LAT Collaboration has reported a measurement of the spectrum of the isotropic diffuse γ-ray radiation from 200 MeV to 100 GeV [25]. The biggest challenge in the determination of the EGB is the subtraction of the various foregrounds and this is the source of the largest systematic uncertainty. Most important are the contributions from the DGE, the instrumental background from misclassified CRs, and from the resolved sources. The mis-identified CRs are suppressed by applying very stringent event selection criteria albeit at the expense of efficiency. The DGE and the contribution from point sources is obtained from a fit to the *Fermi* LAT dataset. The derived spectrum is shown in Fig. 8. It is a featureless power law, significantly softer than the one obtained from EGRET observations [26]. Also, the spectrum does not show the feaure $\gtrsim 2$ GeV found in a reanalysis of the EGRET data with an updated diffuse model [27], that had been suggested as a DM signal [28].

Dark Matter Line Searches: Perhaps the cleanest and most convincing DM signal the LAT might measure would be a monochromatic γ-ray line-like feature sitting on top of some continuum spectrum. Such a feature would arise from two-body final states from DM particle annihilations into either a pair of γ-rays or a γ-ray and Z^0 boson. However, most estimates for the branching fraction into such states are very small ($< .001$) and place them well below the flux sensitivity of the LAT. A search for γ-ray lines has been done using the first year of data. Data from two regions of the sky have been used: Region A excludes the Galactic Plane ($|b| > 10°$) and Region B includes the inner Galaxy ($|l| < 30°$) along with Region A. The
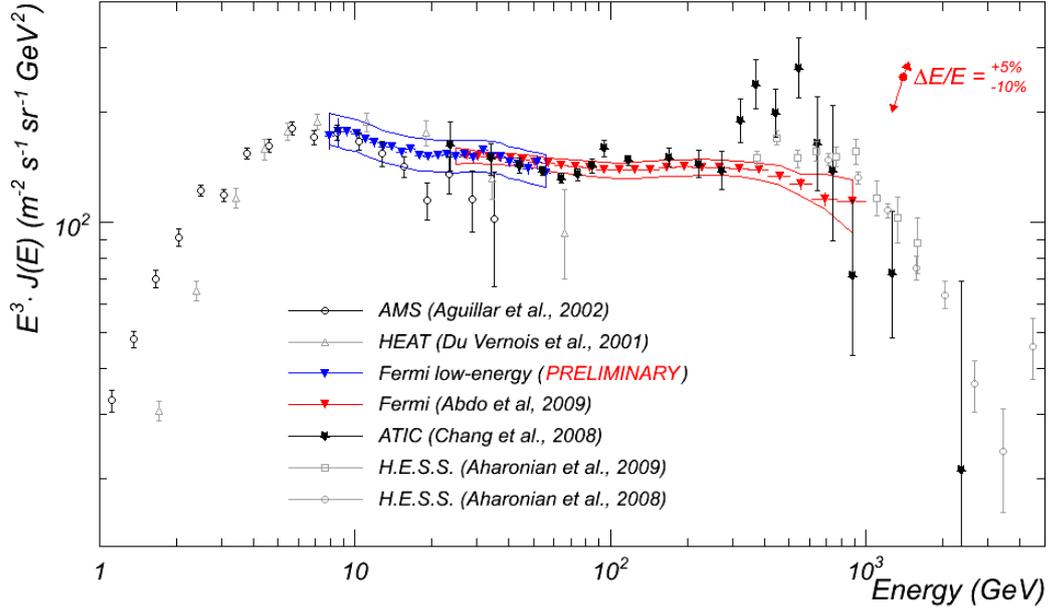
Figure 6: The Fermi-LAT measured total CR electron + positron spectrum (red and blue points). The two-headed arrow in the top-right corner of the figure gives the size and direction of the shift of the spectrum implied by a $+10\%/-5\%$ shift of the absolute energy scale of the LAT. This shift corresponds to the current estimate of the systematic uncertainty for the LAT energy scale.

motivation for Region B is this is where the largest concentration of DM is thought to be. After removing γ-rays from known sources by cutting out circular portions of the sky (ie., within $0.2°$ of the source position) the data was binned into energy intervals with relative widths of 20%. A line shape along with a polynomial background determined from the side bins is then fitted for each bin. No line signals have been found. Due to the large uncertainty in the branching fraction, this does not provide a significant result constraining the parameter space for DM models.

The Galactic Center: For the case of annihilating DM, the Galactic Center (GC) is a natural place to expect a large enhancement. Since the annihilation rate is proportional to the number density of the DM particles squared, and most particle DM models have the density increasing (sometime dramatically) in the vicinity of the GC, the potential signal would be strongest in this region. However the GC is a complex region with many nearby sources and a large DGE flux.

The LAT analysis uses data within $1°$ of the GC and is attempting to detect a spectral component the might be ascribed to DM annihilations. No attempt is made to subtract either the multitude of sources or the large DGE component. Fits are made to the spectra from this region using simple power laws, or broken power laws, as is common for standard astrophysical sources. These fits are compared to the same with an added DM spectral component determined from specific particle physics models (e.g., 50 GeV DM particles annihilating through the $b\bar{b}$–
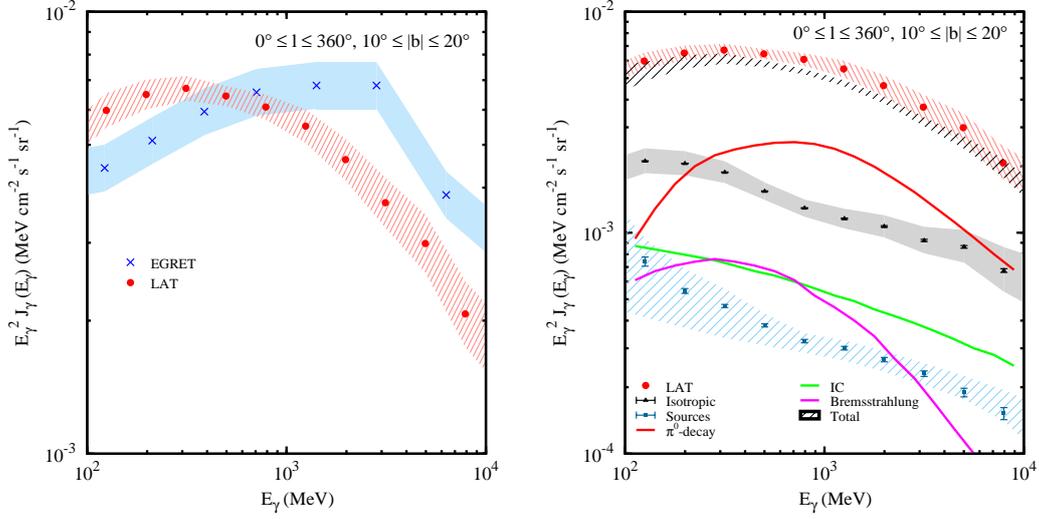
Figure 7: Diffuse emission intensity averaged over all Galactic longitudes for latitude range $10° \leq |b| \leq 20°$. Left panel: LAT (red dots) and EGRET (blue crosses) data. Systematic uncertainties: LAT, red; EGRET, blue. Right panel: LAT data with model, source, and unidentified background (UIB) components. Model (lines): π^0-decay, red; bremsstrahlung, magenta; IC, green. Shaded/hatched regions: UIB, grey/solid; source, blue/hatched; total (model + UIB + source), black/hatched. The UIB component was determined by fitting the data and sources with the model held constant using the latitude range $|b| \geq 30°$. For full details see [7].

quark channel). Typical broken power-law fits are adequate for this region to describe the combination of astrophysical sources and DGE, hence no spectral signature for DM annihilations (modulo the given assumptions) is claimed.

Halo Objects: There are two types of DM concentrations which have been searched for. The first are the dwarf spheroidal galaxies (dSphs) that circulate about the Milky Way and the second are DM clumps as predicted by various N-body simulations. The DM clumps are more speculative than the dSphs, since none have actually been observed in other wavebands, but do appear as a common feature in computer models [29, 30] trying to describe the evolution of Universe.

Nearby dwarf spheriodal galaxies present an excellent target for DM searches. These clusters of stars, self gravitate and form coherent objects in orbit about the Milky Way. By measuring the motion of the stars within a dSph, astronomers can determine the total gravitating mass and this can be compared with the mass estimate derived by simply counting the stars. This is often expressed by the mass-to-luminosity ratio (M/L). Hence the DM within a dSph is "calibrated". In the most promising candidates this ratio exceeds 1000:1 albeit sometimes with large errors and many have a ratio exceeding 100:1 [31].

The current LAT search for a DM signal in dSphs uses a selection of 10 dSphs [32]. These dSphs are located within 150 kpc of the Sun and are $> 30°$ from the Galactic plane. These criteria are imposed to maximize any signal as well as reduce the foreground from the DGE.
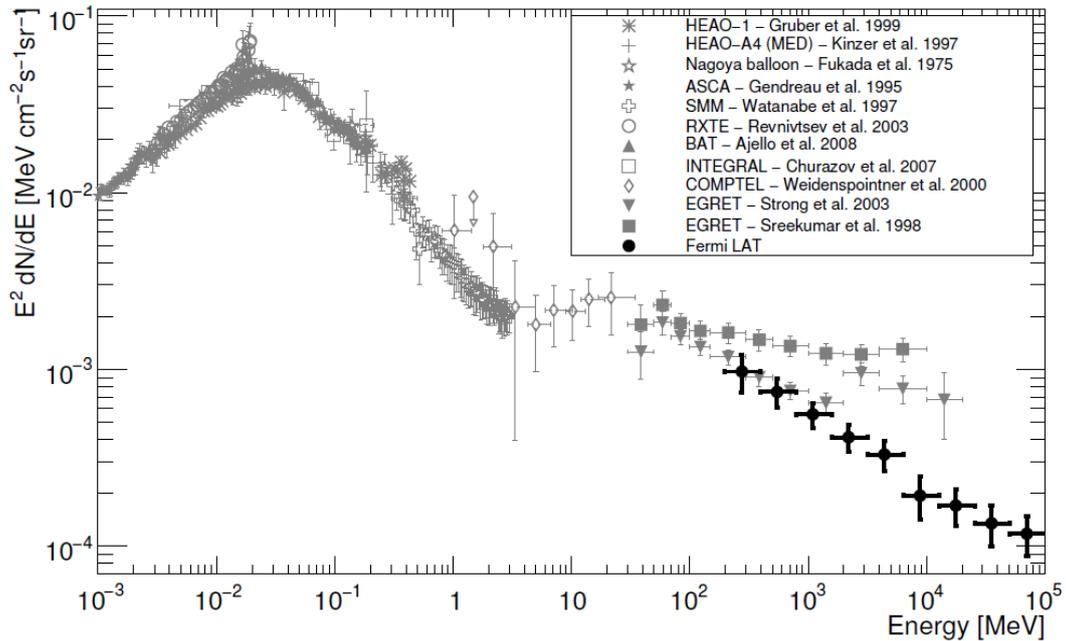
Figure 8: Spectral energy distribution of the extragalactic diffuse emission between 1 keV and 100 GeV measured by various instruments, including the *Fermi* LAT. Adapted from [24]. For full details of the LAT-derived spectrum see [25].

Using the first 9 months of data, no significant detection of these 10 objects is obtained, even before imposing a requirement that the spectra are DM-like. The 95% flux limits integrated above 100 MeV are at the $\sim 2-3 \times 10^{-9}$ ph cm^{-2} s^{-1} level and these will slowly improve over time.

Large *N*-body simulations predict that the distribution of DM will tend to clump as opposed to remain uniformly distributed within a galaxy. The simulations predict a distribution of masses for these clumps with the frequency of clumping increasing as the size of the clump becomes smaller. Overall, the predicted total rate for DM annihilations could be boosted by factors of a few, to more than an order of magnitude, over a uniform distribution. The rate at which these clumps might be found in γ-rays is very model dependent. Overall, 1-to-2 might be seen by the LAT with a one year exposure of the sky.

Such clumps would appear as unassociated γ-ray sources, with a spectrum characteristic of the annihilation process. If close by, they would also appear to be spatially extended. Currently, searches are under way with the LAT data for such occurances. The search criteria are 1) no counterpart observed close to the candidate location, 2) the emission is constant in time, 3) they be spatially extended ($\sim 1°$), and 4) their spectrum is consistent with expectations for γ-rays from DM. After 10 months of data, the most promising of such unidentified sources has started to become resolved into two nearby sources. Hence, no claims for a significant detection for DM clumps is made by the LAT Collaboration. As more data is accumulated, the same criteria will be applied to subsequently detected unidentified sources.

Galaxy Clusters: Another "calibrated" DM source are galaxy clusters. Galaxy clusters are the most massive collapsed structures in the Universe where, from measurements of the relative motion of the galaxies about each other, the presence of large amounts of matter not traced by the individual galaxies is inferred. The LAT Collaboration has searched for a DM signal in the Coma and Fornax clusters, respectively [33]. However, as with the other promising targets, no signal in γ-rays has been observed.

4 Summary

The search for DM remains just that: a search. Exciting hints of signals have not stood up to closer examination with new, high precision experiments. Exhaustive searches in what should be the most promising channel, γ-rays, have so far turned up nothing that cannot be explained within "standard" astrophysics. However, it is also the case that when the γ-ray searches are turned into limits, the excluded parameter space does not place strong excludsions on models of DM based on extensions to the Standard Model. The limits will improve slowly over time, but likely will only be extended by a factor of a few.

The resolution to the real nature of the unobserved gravitating matter that so dominates our universe still awaits us. Perhaps with the extended high-energy reach afforded by the Large Hadron Collider (LHC) at CERN, some answers will be forth coming. Prior to the launch of *Fermi* many of us thought that the LHC would find candidate DM particles, providing details as to mass, cross sections, and inclusive branching fractions. Then armed with this knowledge *Fermi* LAT would map out the role the DM plays in the cosmos. It could very well play out this way, in spite of the delays in the commencement of data taking at the LHC. It could also turn out that the LHC finds no candidates and if this should be the case it is essential to recall that one of the most important experiments in Physics was a null experiment: the Michelson–Morley experiment preformed in 1887 [34]!

5 Acknowledgments

References

[1] V. C. Rubin *et al.*, ApJ **238**, 471 (1980).

[2] M. Markevitch *et al.*, ApJ **606**, 819 (2004).

[3] J. Chang *et al.*, Nature **456**, 362 (2008).

[4] O. Adriani *et al.*, Nature **458**, 607 (2009).

[5] W. B. Atwood *et al.*, ApJ **697**, 1071 (2009).

[6] A. A. Abdo *et al.*, PRL **102**, 181101 (2009).

[7] A. A. Abdo *et al.* PRL **103**, 251101 (2009).

[8] D. Grasso *et al.* APh **32**, 140 (2009).

[9] J. Nishimura *et al.*, ApJ **238**, 394 (1980).

[10] T. Kobayashi *et al.*, ApJ **601**, 340 (2004).

[11] F. A. Aharonian *et al.*, A&A **294**, L41 (1995).

[12] T. A. Porter & R. J. Protheroe, J.Phys.G **23**, 1765 (1997).

[13] M. K. Pohl & J. A. Esposito *et al.*, ApJ **507**, 327 (1998).

[14] F. A. Aharonian *et al.*, PRL **101**, 261104 (2008).

[15] F. A. Aharonian *et al.*, ApJL **696**, 150 (2009).

[16] C. S. Shen, ApJL **162**, 181 (1970).

[17] S. Profumo, arXiv:0812.4457 (2008).

[18] A. Arvanitaki *et al.*, PRD **80**, 055011 (2009).

[19] S. D. Hunter *et al.*, ApJ **481**, 205 (1997).

[20] W. de Boer, A&A **444**, 51 (2005).

[21] A. W. Strong, I. V. Moskalenko, & O. Reimer, ApJ **537**, 763 (2000).

[22] I. V. Moskalenko *et al.*, NuPhS **173**, 44 (2007).

[23] F. W. Stecker *et al.*, APh **29**, 25 (2008).

[24] M. Ackermann, on behalf of the Fermi-LAT collaboration. Talk at TeVPA 2009.

[25] A. A. Abdo *et al.*, PRL (accepted) (2010).

[26] P. Sreekumar P *et al*, ApJ **494**, 523 (1998).

[27] A. W. Strong, I. V. Moskalenko, & O. Reimer, ApJ **613**, 956 (2004).

[28] D. Elässer & K. Mannheim, PRL **94**, 171302 (2005).

[29] V. Springel *et al.*, Nature **435**, 629 (2005).

[30] J. Diemand *et al.*, Nature **454**, 735 (2008).

[31] M. L. Mateo, ARA&A **36**, 435 (1998).

[32] A. A. Abdo *et al.*, ApJ (accepted) (2010).

[33] A. A. Abdo *et al.*, in preparation (2010).

[34] A. Michelson & E. Morley, Am.J.Sci **34**, 333 (1887).

Discussion

Guido Altarelli (Roma3/CERN): I heard that people were excited about the release of new results from FERMI in August 2009. Are those results included in your presentation?

Answer: The LAT worked immediately upon activation in orbit: when we turned it on - there was the gamma ray sky! Our ground simulations and analysis prior to launch were sufficient to begin science operations directly after the check out period. The easiest targets for early science are sources as they distinguish themselves by their location in the sky. There are now more then a dozen papers on sources. The fundamental science topics however, often involve pushing the instrument to its performance limit and understanding backgrounds, particularly when dealing with extended or diffuse signals. We are now just starting to produce results on these and this work is reflected in my presentation here. We expect however, that this is just the beginning.

Roger Wolf (Univ. Hamburg): Could you comment on the discrepancies between LAT and EGRET data?

Answer: The EGRET experiment was initially conceived in 1968 and used technologies contemporary with experimental techniques in particle physics of the 1960's, e.g. its trigger spark chamber. These made the on-orbit calibration difficult to monitor and track and lead to efficiency corrections which could vary by almost a factor of 3. In addition EGRET never had a complete monte-carlo simulation with which to study backgrounds and acceptance, and instead relied on extensive test beam data taken at SLAC and elsewhere. In short, there were systematic problems that limited the quantitative results. While acknowledging these short comings, we nevertheless emphasize that EGRET was the "path-finder" without which the enthusiasm and rapid development of the next generation gamma ray satellite would not have happened. Fermi-LAT on the other hand is representative of contemporary practice in high energy particle physics, from the choice of technologies to the extensive use of standard simulation packages (i.e. GEANT4). In addition the simulations were extensively cross-checked in beam tests at CERN and elsewhere.

Dark Energy and Dark Matter

Keith A. Olive[1]

[1]William I. Fine Theoretical Physics Institute, University of Minnesota, Minneapolis, MN 55455

A brief overview of our current understanding of abundance and properties of dark energy and dark matter is presented. A more focused discussion of supersymmetric dark matter follows. Included is a frequentist approach to the supersymmetric parameter space and consequences for the direct detection of dark matter.

1 The Energy Density Content of the Universe

The overall composition of the Universe can be conveniently described by the density parameter, Ω, defined as the average energy density of the Universe, ρ, relative to the critical density needed for a spatially flat Universe, ρ_c. One of the Einstein field equations leads to the expression for the expansion rate of the Universe, which we characterize by the Hubble parameter,

$$H^2 \equiv \left(\frac{\dot{R}}{R}\right)^2 = \frac{8\pi G_N \rho}{3} - \frac{k}{R^2} + \frac{\Lambda}{3}, \tag{1}$$

where $R(t)$ is the cosmological scale factor and k is the three-space curvature constant ($k = 0, +1, -1$ for a spatially flat, closed or open universe). Λ is the cosmological constant which is assumed here to contain all contributions from the vacuum energy density. One can define a critical energy density ρ_c such that $\rho = \rho_c$ for $k = 0$

$$\rho_c = 3H^2/8\pi G_N. \tag{2}$$

In terms of the present value of the Hubble parameter this is,

$$\rho_c = 1.88 \times 10^{-29} h_0{}^2 \mathrm{gcm}^{-3}, \tag{3}$$

where

$$h_0 = H_0/(100\mathrm{kmMpc}^{-1}\mathrm{s}^{-1}). \tag{4}$$

The cosmological density parameter is then defined by

$$\Omega \equiv \frac{\rho}{\rho_c}. \tag{5}$$

The composition of the Universe can be expressed by breaking down the density parameter into separate contributions,

$$\Omega = \Omega_r + \Omega_m + \Omega_\Lambda, \tag{6}$$

for contributions from radiation, matter and a cosmological constant/vacuum with $\Omega_\Lambda = \Lambda/3H^2$. The contribution to Ω_r from the cosmic microwave background (CMB) is small, of

order 10^{-4}. Precise determinations of the matter and vacuum contributions to Ω are obtained from the detailed power spectrum of CMB anisotropies as measured by WMAP [1]. When combined with other measurements such as high redshift supernova type Ia data [2] and baryon acoustic oscillations [3], one finds

$$h_0 = 0.71 \pm 0.01 \qquad \Omega_0 = 1.006 \pm 0.006. \tag{7}$$

WMAP data alone is sufficient for determining the individual contributions to Ω of

$$\Omega_m h_0^2 = 0.133 \pm 0.006 \qquad \Omega_\Lambda = 0.74 \pm 0.03. \tag{8}$$

The matter content of the Universe can be further broken down as WMAP also determines the baryon density of Universe [1]

$$\Omega_B h_0^2 = 0.0227 \pm 0.0006. \tag{9}$$

The contribution to Ω in neutrinos lies in the range

$$0.0005 < \Omega_\nu h_0^2 < 0.0076, \tag{10}$$

where the lower bound is obtained from the requirement of finite neutrino masses from oscillation data and the upper bound is again derived from WMAP data in conjunction with other large scale structure data.

2   Dark Energy

The biggest surprise of all of the recent determinations of contributions to Ω must be the realization that there is a substantial contribution from dark energy, namely that $\Omega_\Lambda \neq 0$. The WMAP value for Ω_Λ is moreover consistent with determinations from supernovae data and baryon acoustic oscillations. When all data are used, one finds $\Omega_\Lambda = 0.726 \pm 0.015$.

But now a bigger question arises: What is the physical nature of the dark energy? Different possibilities can be distinguished by their equation of state characterized by $w = p/\rho$. The equation of state parameter for radiation is simply $w_r = 1/3$, whereas for matter, it is $w_m = 0$.

The simplest solution for the dark energy remains either a cosmological constant or a constant vacuum contribution to the energy density with an equation of state, $w = -1$. This is indeed consistent with the central value determined by WMAP, which finds [1]

$$-0.33 < 1 + w_0 < 0.21, \tag{11}$$

for the value of w today (at 95 % CL). The numerical value for Λ, however, is extremely small, and when written as a dimensionless constant (as $G_N \Lambda$), it is of order 10^{-123}. This is the well known cosmological constant problem in cosmology [4].

There are, of course, other possibilities, the largest class of which is known as quintessence [5]. In this case, the dark energy may be a dynamical phenomenon described by an evolving scalar field. The energy density and pressure of a scalar field, ϕ, with potential, $V(\phi)$, can be written as (neglecting spatial gradient terms)

$$\rho = \frac{1}{2}\dot{\phi}^2 + V(\phi) \tag{12}$$

$$p = \frac{1}{2}\dot{\phi}^2 - V(\phi). \tag{13}$$

When the kinetic term is small compared to the potential, $\rho \approx V$ and $p \approx -V$, and we recover the constant solution with $w = -1$. In general, however, w_0 may differ from -1 and indeed may not even be a constant. Once again, WMAP (using supernovae and BAO data) place combined limits on w and its derivative with respect to redshift, w',

$$w = -1.06 \pm 0.14 \qquad w' = 0.36 \pm 0.62 \tag{14}$$

In short summary, we are left with the following puzzles regarding dark energy:

- There is the question of fine-tuning associated with the cosmological constant problem. Namely, we expect several contributions to the vacuum energy density

$$\Lambda = \Lambda_{GUT} + \Lambda_{EW} + \Lambda_{QCD} \cdots \tag{15}$$

  where the various contributions listed arise from possible sources such as grand unified theories $(G_N \Lambda_{GUT} \sim (10^{-3})^4)$, the Standard Model $(G_N \Lambda_{EW} \sim (10^{-16})^4)$, and QCD $(G_N \Lambda_{QCD} \sim (10^{-20})^4)$, yet sum to 10^{-123}.

- The coincidence problem. Here, we would like to understand why Ω_m is within a factor of a few of Ω_Λ today. This is one of the issues addressed by quintessence models and may be probed in observations testing the possibility of variability in fundamental constants.

3 Dark Matter

From the quoted contributions to Ω in matter and baryons from WMAP, we can obtain the density of cold dark matter from the difference between the total matter density and the baryon density [1]

$$\Omega_{CDM} h^2 = 0.1099 \pm 0.0062 \tag{16}$$

or a 2σ range of $0.0975 - 0.1223$ for $\Omega_{CDM} h^2$.

Evidence for dark matter in the universe is available from a wide range of observational data. In addition to the results from the CMB, there is the classic evidence from galactic rotation curves [6], which indicate that nearly all spiral galaxies are embedded in a large galactic halo of dark matter leading to rather constant rotational velocities at large distances from the center of the galaxy (in contrast to the expected $v^2 \sim 1/r$ behavior in the absence of dark matter). Other dramatic pieces of evidence can be found in combinations of X-ray observations and weak lensing showing the superposition of dark matter (from lensing) and ordinary matter from X-ray gas [7] and from the separation of baryonic and dark matter after the collision of two galaxies as seen in the Bullet cluster [8]. For a more complete discussion see [9].

In addition to being stable (or at least very long lived), the dark matter should be both electrically and color neutral. Indeed, there are very strong constraints, forbidding the existence of stable or long lived particles which are not color and electrically neutral as these would become bound with normal matter forming anomalously heavy isotopes. The limits on the abundances, relative to hydrogen, of nuclear isotopes [10], $n/n_H \lesssim 10^{-15}$ to 10^{-29} for 1 GeV $\lesssim m \lesssim 1$ TeV. A strongly interacting stable relic is expected to have an abundance $n/n_H \lesssim 10^{-10}$ with a higher abundance for charged particles.

Unfortunately, there are no viable candidates for dark matter in the Standard Model. As baryons and neutrinos have been excluded, one is forced to go beyond the Standard Model, and

here, I will focus on the possibilities which exist in the context of the minimal supersymmetric extension of the Standard Model (MSSM) [11]. In the MSSM, the lightest supersymmetric particle (LSP) is stable if R-parity ($R = -1^{3B+L+2s}$) is unbroken. There are several possibilities in the MSSM, specifically the sneutrino with spin zero, the neutralino with spin 1/2, and the gravitino with spin 3/2. However, a sneutrino LSP would have relatively large coherent interactions with heavy nuclei, and experiments searching directly for the scattering of massive dark matter particles on nuclei exclude a stable sneutrino weighing between a few GeV and several TeV [12]. The possible loophole of a very light sneutrino was excluded by measurements of the invisible Z-boson decay rate at LEP [13]. The gravitino is a viable candidate and often predicted in models based on supergravity [14, 15]. In this case, however, its probability for direct detection is negligible.

There are four neutralinos, each of which is a linear combination of the $R = -1$ neutral fermions [16]: the wino $\tilde{W}^3$, the partner of the 3rd component of the $SU(2)_L$ gauge boson; the bino, $\tilde{B}$; and the two neutral Higgsinos, $\tilde{H}_1$ and $\tilde{H}_2$. The mass and composition of the LSP are determined by the gaugino masses, M_1 and M_2, the Higgs mixing mass term, μ, and the ratio of the two Higgs vacuum expectation values expressed as $\tan\beta$. In general, neutralinos can be expressed as a linear combination

$$\chi = \alpha\tilde{B} + \beta\tilde{W}^3 + \gamma\tilde{H}_1 + \delta\tilde{H}_2. \tag{17}$$

The relic density of neutralinos depends on additional parameters in the MSSM beyond M_1, M_2, μ, and $\tan\beta$. These include the sfermion masses, $m_{\tilde{f}}$ and the Higgs pseudo-scalar mass, m_A. To determine the relic density it is necessary to obtain the general annihilation cross-section for neutralinos. In much of the parameter space of interest, the LSP is a bino and the annihilation proceeds mainly through sfermion exchange.

In its generality, the MSSM has over 100 undetermined parameters. There are good arguments based on grand unification [17] and supergravity [18] which lead to a strong reduction in the number of parameters. I will assume several unification conditions placed on the supersymmetric parameters. In all models considered, the gaugino masses are assumed to be unified at the GUT scale with value, $m_{1/2}$, as are the trilinear couplings with value A_0. Also common to all models considered here is the unification of all soft scalar masses set equal to m_0 at the GUT scale. With this set of boundary conditions at the GUT scale, we can use the radiative electroweak symmetry breaking conditions by specifying $\tan\beta$, and the mass, M_Z, to predict the values of μ and Higgs pseudoscalar mass, m_A. The sign of μ remains free. This class of models is often referred to as the constrained MSSM (CMSSM) [19, 20, 21, 22, 23]. In the CMSSM, the solutions for μ generally lead to a lightest neutralino which is very nearly a pure $\tilde{B}$.

I note that that while the name CMSSM is often used synonymously with mSUGRA, for minimal supergravity [18, 24]. The latter however, has two additional constraints: $m_{3/2} = m_0$ and $B_0 = A_0 - m_0$. The former sets the unification scale scalar masses equal to the gravitino mass. This condition often results in a gravitino LSP [14]. The latter condition sets a relation between the supersymmetry breaking bilinear, trilinear and scalar mass terms. Because of this condition, $\tan\beta$ is no longer a free parameter, but must be solved for through the radiative electroweak symmetry breaking relations.

In Fig. 1, an example of the renormalization group running of the mass parameters in the CMSSM is shown. Here, we have chosen $m_{1/2} = 250$ GeV, $m_0 = 100$ GeV, $\tan\beta = 3$, $A_0 = 0$, and $\mu < 0$. Indeed, it is rather amazing that from so few input parameters, all of the masses of

the supersymmetric particles can be determined. The characteristic features that one sees in the figure, are for example, that the colored sparticles are typically the heaviest in the spectrum. This is due to the large positive correction to the masses due to α_3 in the RGE's. Also, one finds that the $\widetilde{B}$, is typically the lightest sparticle. But most importantly, notice that one of the Higgs mass^2, goes negative triggering electroweak symmetry breaking [25]. (The negative sign in the figure refers to the sign of the mass squared, even though it is the mass of the sparticles which is depicted.)
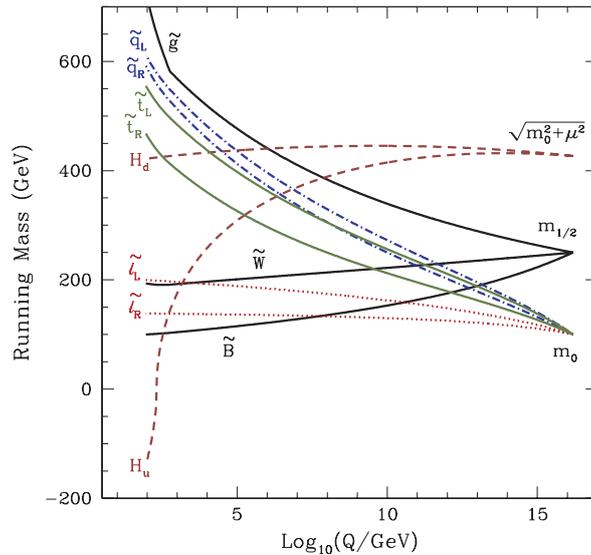
Figure 1: RG evolution of the mass parameters in the CMSSM. I thank Toby Falk for providing this figure.

For given values of $\tan\beta$, A_0, and $sgn(\mu)$, the regions of the CMSSM parameter space that yield an acceptable relic density and satisfy the other phenomenological constraints may be displayed in the $(m_{1/2}, m_0)$ plane. In Fig. 2a, the light shaded region corresponds to that portion of the CMSSM plane with $\tan\beta = 10$, $A_0 = 0$, and $\mu > 0$ such that the computed relic density yields the WMAP value given in eq. (16) [22]. The bulk region at relatively low values of $m_{1/2}$ and m_0, tapers off as $m_{1/2}$ is increased. At higher values of m_0, annihilation cross sections are too small to maintain an acceptable relic density and $\Omega_\chi h^2$ is too large. Although sfermion masses are also enhanced at large $m_{1/2}$ (due to RGE running), co-annihilation processes between the LSP and the next lightest sparticle (in this case the $\tilde{\tau}$) enhance the annihilation cross section and reduce the relic density. This occurs when the LSP and NLSP are nearly degenerate in mass. The dark shaded region has $m_{\tilde{\tau}} < m_\chi$ and is excluded. The effect of coannihilations is to create an allowed band about 25-50 GeV wide in m_0 for $m_{1/2} \lesssim 950$ GeV, or $m_{1/2} \lesssim 400$ GeV, which tracks above the $m_{\tilde{\tau}_1} = m_\chi$ contour [26].

Also shown in Fig. 2a are the relevant phenomenological constraints. These include the LEP lower limits on the chargino mass: $m_{\chi^\pm} > 104$ GeV [27] and on the Higgs mass: $m_h > 114$ GeV [28]. FeynHiggs [29] is used for the calculation of m_h. The Higgs limit imposes important constraints, principally on $m_{1/2}$ and particularly at low $\tan\beta$. Another constraint

is the requirement that the branching ratio for $b \to s\gamma$ be consistent with the experimental measurements [30]. These measurements agree with the Standard Model, and therefore provide bounds on MSSM particles [31], such as the chargino and charged Higgs bosons, in particular. The constraint imposed by measurements of $b \to s\gamma$ also exclude small values of $m_{1/2}$. Finally, there are regions of the $(m_{1/2}, m_0)$ plane that are favored by the BNL measurement [32] of the anomalous magnetic moment of the muon or $g_\mu - 2$. Here, we assume the Standard Model calculation [33] of $g_\mu - 2$, and indicate by dashed and solid lines the contours of 1- and 2-σ level deviations induced by supersymmetry.

At larger $m_{1/2}, m_0$ and $\tan\beta$, the relic neutralino density may be reduced by rapid annihilation through direct-channel H, A Higgs bosons, as seen in Fig. 2(b) [19, 21]. Finally, the relic density can again be brought down into the WMAP range at large m_0 (not shown in Fig. 2), in the 'focus-point' region close the boundary where electroweak symmetry breaking ceases to be possible and the lightest neutralino χ acquires a significant higgsino component [34].

As seen in Fig. 2, the relic density constraint is compatible with relatively large values of $m_{1/2}$ and m_0. However, all values of $m_{1/2}$ and m_0 are not equally viable when the available phenomenological and cosmological constraints are taken into account. A global likelihood analysis enables one to pin down the available parameter space in the CMSSM. One can avoid the dependence on priors by performing a pure likelihood analysis as in [35], or a purely χ^2-based fit as done in [36, 37]. Here, the results from one such analysis [38, 39] is presented, which used a Markov-Chain Monte Carlo (MCMC) technique to explore efficiently the likelihood function in the parameter space of the CMSSM. A full list of the observables and the values assumed for them in this global analysis are given in [37], as updated in [38, 39].

The best fit point is shown in Fig. 3, which also displays contours of the $\Delta\chi^2$ function in the CMSSM. The parameters of the best-fit CMSSM point are $m_0 = 60$ GeV, $m_{1/2} = 310$ GeV, $A_0 = 130$ GeV, $\tan\beta = 11$ and $\mu = 400$ GeV, yielding the overall $\chi^2/N_{\rm dof} = 20.6/19$ (36% probability) and nominally $M_h = 114.2$ GeV [39]. The best-fit point is in the coannihilation region of the $(m_0, m_{1/2})$ plane. The C.L. contours extend to slightly larger values of m_0 in the CMSSM. However, the qualitative features of the $\Delta\chi^2$ contours indicate a preference for small m_0 and $m_{1/2}$. It was found in [38] that the focus-point region was disfavored at beyond the 95% C.L. in the CMSSM. We see in Fig. 3 that this region is disfavored at the level $\Delta\chi^2 \sim 8$ in the CMSSM.

As noted above, there are several important cosmological and phenomenological constraints on the supersymmetric parameter space. Improvements in sensitivity have made it possible for direct detection experiments [40, 41] to be competitive as well. The elastic cross section for χ scattering on a nucleus can be decomposed into a scalar (spin-independent) and a spin-dependent part. Each of these can be written in terms of the cross sections for elastic scattering off individual nucleons. The scalar part of the cross section can be written as

$$\sigma_{\rm SI} = \frac{4m_r^2}{\pi} \left[Z f_p + (A - Z) f_n \right]^2, \tag{18}$$

where m_r is the χ-nuclear reduced mass and

$$\frac{f_N}{m_N} = \sum_{q=u,d,s} f_{T_q}^{(N)} \frac{\alpha_{3q}}{m_q} + \frac{2}{27} f_{TG}^{(N)} \sum_{q=c,b,t} \frac{\alpha_{3q}}{m_q}, \tag{19}$$

for N = p or n. The parameters $f_{T_q}^{(N)}$ are defined by

$$m_N f_{T_q}^{(N)} \equiv \langle N | m_q \bar{q} q | N \rangle \equiv m_q B_q^{(N)}, \tag{20}$$

and the α_{3q} contain the individual quark-neutralino scattering cross sections, see [42, 43, 44] for further details regarding the calculation of the cross section.

The elastic scattering of neutralinos on nucleons is very sensitive to the strangeness contribution to the nucleon mass and can be characterized by the parameter, y, which is also related to the π-nucleon sigma term $\Sigma_{\pi N}$ by

$$y \equiv \frac{2B_s}{B_u + B_d} = 1 - \sigma_0/\Sigma_{\pi N} \ . \tag{21}$$

where σ_0 is the change in the nucleon mass due to nonzero u and d masses and is estimated from octet baryon mass differences to be $\sigma_0 = 36$ MeV [45], and the latest determination of $\Sigma_{\pi N} = 64$ MeV. The effect of varying these assumptions are discussed in the context of the CMSSM in [43, 44]. Lattice calculations are now reaching the stage where they may also provide useful information on $\Sigma_{\pi N}$ [46], and a recent analysis would suggest a lower value $\Sigma_{\pi N} \lesssim 40$ [47].

In panel (a) of Fig. 4 the spin-independent neutralino-nucleon elastic scattering cross sections are shown as functions of neutralino mass for the regions of Fig. 2a that are cosmologically viable (i.e., those where the upper limit on the relic density of neutralinos is respected), and are not excluded by constraints from colliders. Here, however, parameter values corresponding to the focus point at high m_0 are also included. Also plotted are the limits on the spin-independent cross section from CDMS II [40] (solid black line) and XENON10 [41] (solid red line), as well as the sensitivities projected for XENON100 [49] (or a similar 100-kg liquid noble-gas detector such as LUX, dashed red line) and SuperCDMS at the Soudan Mine [50] (dashed black line).

There are two distinct regions in the (m_χ, σ) plane, that arising from the focus-point region at $m_\chi \lesssim 150$ GeV and relatively large σ, and that from the coannihilation strip. In the coannihilation strip, 50 GeV $< m_\chi < 400$ GeV, where the lower limit on m_χ is a result of the LEP constraint on the chargino mass, and the upper limit on m_χ corresponds to the endpoint of the coannihilation strip for $\tan\beta = 10$. In contrast, the end point of the focus-point region shown is due only to the cut-off $m_0 < 2$ TeV that has been assumed. In addition, for $m_{1/2} \lesssim 380$ GeV in the coannihilation strip ($m_\chi \lesssim 160$ GeV), the nominal calculated mass of the lighter scalar MSSM Higgs boson is less than the LEP lower bound. These points are indicated by lighter shadings.

The choices $\tan\beta = 10$ and $A_0 = 0$ do not yield viable direct detection cross sections that are completely representative of the range of possibilities within the CMSSM. Therefore, in Fig. 4b, we show CMSSM spin-independent neutralino-nucleon cross section, as obtained in a scan over all CMSSM parameters with $5 \leq \tan\beta \leq 55$, $100 \leq m_{1/2} \leq 2000$ GeV, 0 GeV $\leq m_0 \leq 2000$ GeV, and $-3m_{1/2} \leq A_0 \leq 3m_{1/2}$ [48]. We also allow both positive and negative μ, except for large $\tan\beta > 30$, where convergence becomes difficult in the $\mu < 0$ case. At low $m_\chi < 300$ GeV, cross sections generally exceed 10^{-9} pb, and the largest scalar cross sections, which occur for $m_\chi \sim 100$ GeV, are already excluded by CDMS II [40] and/or XENON10 [41]. These exclusions occur primarily in the focus-point region at large $\tan\beta$. On the other hand, for $m_\chi \gtrsim 400$ GeV scalar cross sections are well below 10^{-9} pb, and come from the coannihilation strip or the rapid-annihilation funnel that appears at large $\tan\beta$ in the CMSSM. The effective cross sections shown are suppressed for points with $\Omega_\chi \ll \Omega_{CDM}$, and there may be cancellations at larger m_χ that suppress the cross sections substantially. These regions of parameter space will not be probed by direct detection experiments in the near future [49, 50].

Finally, the frequentist analysis described above can also be used to predict the neutralino-nucleon elastic scattering cross section [39]. The value of σ_p^{SI} shown in Fig. 5a is calculated

assuming a π-N scattering σ term $\Sigma_N = 64$ MeV. We see in Fig. 5 that values of the $\tilde{\chi}_1^0$-proton cross section $\sigma_p^{\mathrm{SI}} \sim 10^{-8}$ pb are expected in the CMSSM, and that much larger values seem quite unlikely. The 2D χ^2 function is shown in Fig. 5b.

4 Acknowledgments

References

[1] J. Dunkley *et al.* [WMAP Collaboration], Astrophys. J. Suppl. **180**, 306 (2009) [arXiv:0803.0586 [astro-ph]]; E. Komatsu *et al.* [WMAP Collaboration], Astrophys. J. Suppl. **180**, 330 (2009) [arXiv:0803.0547 [astro-ph]].

[2] A.G. Riess *et al.*, A. J. **116**, 1009 (1998); P. Garnavich *et al.*, Astrophys. J. **509**, 74 (1998); S. Perlmutter *et al.*, Ap. J. **517**, 565 (1999); A. G. Riess *et al.*, *Ap. J.* **560** (2001) 49; J.L. Tonry *et al.*, Ap. J. **594**, 1 (2003); A.G. Riess *et al.*, Astrophys. J. **659**, 98 (2007); P. Astier *et al.* [The SNLS Collaboration], Astron. Astrophys. **447**, 31 (2006) [arXiv:astro-ph/0510447].

[3] D. Eisenstein *et al.*, Astrophys. J. **633**, 560 (2005); C. Blake *et al.*, Mon. Not. Roy. Astr. Soc. **374**, 1527 (2007); W. J. Percival, *et al.*, Mon. Not. Roy. Astron. Soc. **381**, 1053 (2007); M. Kowalski *et al.*, Astrophys. J. **686**, 749 (2008).

[4] S. Weinberg, Rev. Mod. Phys. **61**, 1 (1989); S. M. Carroll, Living Rev. Rel. **4**, 1 (2001) [arXiv:astro-ph/0004075]; P. J. E. Peebles and B. Ratra, Rev. Mod. Phys. **75**, 559 (2003) [arXiv:astro-ph/0207347].

[5] I. Zlatev, L. M. Wang and P. J. Steinhardt, Phys. Rev. Lett. **82**, 896 (1999) [arXiv:astro-ph/9807002]; C. Armendariz-Picon, V. F. Mukhanov and P. J. Steinhardt, Phys. Rev. D **63**, 103510 (2001) [arXiv:astro-ph/0006373].

[6] S. M. Faber and J. J. Gallagher, *Ann. Rev. Astron. Astrophys.* **17** (1979) 135; A. Bosma, *Ap. J.* **86** (1981) 1825; V. C. Rubin, W. K. Ford and N. Thonnard, *Ap. J.* **238** (1980) 471; V. C. Rubin, D. Burstein, W. K. Ford and N. Thonnard, *Ap. J.* **289** (1985) 81; T. S. Van Albada and R. Sancisi, *Phil. Trans. R. Soc. Land.* **A320** (1986) 447; M. Persic and P. Salucci, *Ap. J. Supp.* **99** (1995) 501; M. Persic, P. Salucci, and F. Stel, *MNRAS* **281** (1996) 27P.

[7] D. Wittman, *et al.*, Astrophys. J. **643**, 128 (2006) [arXiv:astro-ph/0507606].

[8] D. Clowe,*et al.*, Astrophys. J. **648** (2006) L109 [arXiv:astro-ph/0608407].

[9] K. A. Olive, arXiv:astro-ph/0301505.

[10] J. Rich, M. Spiro and J. Lloyd-Owen, *Phys.Rep.* **151** (1987) 239; T. Yamagata, Y. Takamori and H. Utsunomiya, Phys. Rev. D **47** (1993) 1231; T. K. Hemmick *et al.*, Phys. Rev. **D41** (1990) 2074; P. F. Smith, Contemp. Phys. **29** (1998) 159; D. Javorsek, D. Elmore, E. Fischbach, D. Granger, T. Miller, D. Oliver and V. Teplitz, Phys. Rev. D **65**, 072003 (2002).

[11] P. Fayet, Phys. Lett. **B64** (1976) 159; Phys. Lett. **B69** (1977) 489; Phys. Lett. **B84** (1979) 416; H.E. Haber and G.L. Kane, *Phys.Rep.* **117** (1985) 75.

[12] T. Falk, K. A. Olive and M. Srednicki, Phys. Lett. B **339**, 248 (1994) [arXiv:hep-ph/9409270]; C. Arina and N. Fornengo, JHEP **0711**, 029 (2007) [arXiv:0709.4477 [hep-ph]].

[13] LEP Collaborations, ALEPH, DELPHI, L3 and OPAL, LEP Electroweak Working Group, SLD Electroweak Group and SLD Heavy Flavor Group, hep-ex/0312023.

[14] J. R. Ellis, K. A. Olive, Y. Santoso and V. C. Spanos, Phys. Lett. B **573** (2003) 162 [arXiv:hep-ph/0305212]; J. R. Ellis, K. A. Olive, Y. Santoso and V. C. Spanos, Phys. Rev. D **70** (2004) 055005 [arXiv:hep-ph/0405110].

[15] J. R. Ellis, K. A. Olive, Y. Santoso and V. C. Spanos, Phys. Lett. B **588** (2004) 7 [arXiv:hep-ph/0312262]; J. L. Feng, A. Rajaraman and F. Takayama, Phys. Rev. Lett. **91** (2003) 011302 [arXiv:hep-ph/0302215]; J. L. Feng, S. Su and F. Takayama, Phys. Rev. D **70** (2004) 075019 [arXiv:hep-ph/0404231].

[16] J. Ellis, J.S. Hagelin, D.V. Nanopoulos, K.A. Olive and M. Srednicki, Nucl. Phys. B **238** (1984) 453; see also H. Goldberg, Phys. Rev. Lett. **50** (1983) 1419.

[17] J. R. Ellis, S. Kelley and D. V. Nanopoulos, Phys. Lett. B **249** (1990) 441 and Phys. Lett. B **260** (1991) 131; U. Amaldi, W. de Boer and H. Furstenau, Phys. Lett. B **260** (1991) 447; C. Giunti, C. W. Kim and U. W. Lee, Mod. Phys. Lett. A **6** (1991) 1745.

[18] For reviews, see: H. P. Nilles, Phys. Rep. **110** (1984) 1; A. Brignole, L. E. Ibanez and C. Munoz, arXiv:hep-ph/9707209, published in *Perspectives on supersymmetry*, ed. G. L. Kane, pp. 125-148.

[19] M. Drees and M. M. Nojiri, Phys. Rev. D **47** (1993) 376 [arXiv:hep-ph/9207234]; H. Baer and M. Brhlik, Phys. Rev. D **53** (1996) 597 [arXiv:hep-ph/9508321]; Phys. Rev. D **57** (1998) 567 [arXiv:hep-ph/9706509]; H. Baer, M. Brhlik, M. A. Diaz, J. Ferrandis, P. Mercadante, P. Quintana and X. Tata, Phys. Rev. D **63** (2001) 015007 [arXiv:hep-ph/0005027]; A. B. Lahanas, D. V. Nanopoulos and V. C. Spanos, Mod. Phys. Lett. A **16** (2001) 1229 [arXiv:hep-ph/0009065].

[20] J. R. Ellis, T. Falk, K. A. Olive and M. Schmitt, Phys. Lett. B **388** (1996) 97 [arXiv:hep-ph/9607292]; Phys. Lett. B **413** (1997) 355 [arXiv:hep-ph/9705444]; J. R. Ellis, T. Falk, G. Ganis, K. A. Olive and M. Schmitt, Phys. Rev. D **58** (1998) 095002 [arXiv:hep-ph/9801445]; V. D. Barger and C. Kao, Phys. Rev. D **57** (1998) 3131 [arXiv:hep-ph/9704403]; J. R. Ellis, T. Falk, G. Ganis and K. A. Olive, Phys. Rev. D **62** (2000) 075010 [arXiv:hep-ph/0004169]; V. D. Barger and C. Kao, Phys. Lett. B **518** (2001) 117 [arXiv:hep-ph/0106189]; L. Roszkowski, R. Ruiz de Austri and T. Nihei, JHEP **0108** (2001) 024 [arXiv:hep-ph/0106334]; A. B. Lahanas and V. C. Spanos, Eur. Phys. J. C **23** (2002) 185 [arXiv:hep-ph/0106345]; A. Djouadi, M. Drees and J. L. Kneur, JHEP **0108** (2001) 055 [arXiv:hep-ph/0107316]; U. Chattopadhyay, A. Corsetti and P. Nath, Phys. Rev. D **66** (2002) 035003 [arXiv:hep-ph/0201001]; J. R. Ellis, K. A. Olive and Y. Santoso, New Jour. Phys. **4** (2002) 32 [arXiv:hep-ph/0202110]; H. Baer, C. Balazs, A. Belyaev, J. K. Mizukoshi, X. Tata and Y. Wang, JHEP **0207** (2002) 050 [arXiv:hep-ph/0205325]; R. Arnowitt and B. Dutta, arXiv:hep-ph/0211417.

[21] J. R. Ellis, T. Falk, G. Ganis, K. A. Olive and M. Srednicki, Phys. Lett. B **510** (2001) 236 [arXiv:hep-ph/0102098].

[22] J. R. Ellis, K. A. Olive, Y. Santoso and V. C. Spanos, Phys. Lett. B **565** (2003) 176 [arXiv:hep-ph/0303043].

[23] H. Baer and C. Balazs, JCAP **0305**, 006 (2003) [arXiv:hep-ph/0303114]; A. B. Lahanas and D. V. Nanopoulos, Phys. Lett. B **568**, 55 (2003) [arXiv:hep-ph/0303130]; U. Chattopadhyay, A. Corsetti and P. Nath, Phys. Rev. D **68**, 035005 (2003) [arXiv:hep-ph/0303201]; . Munoz, Int. J. Mod. Phys. A **19**, 3093 (2004) [arXiv:hep-ph/0309346].

[24] R. Barbieri, S. Ferrara and C.A. Savoy, Phys. Lett. **119B** (1982) 343.

[25] L.E. Ibáñez and G.G. Ross, Phys. Lett. **B110** (1982) 215;
L.E. Ibáñez, Phys. Lett. **B118** (1982) 73;
J. Ellis, D.V. Nanopoulos and K. Tamvakis, Phys. Lett. **B121** (1983) 123;
J. Ellis, J. Hagelin, D.V. Nanopoulos and K. Tamvakis, Phys. Lett. **B125** (1983) 275;
L. Alvarez-Gaumé, J. Polchinski, and M. Wise, Nucl. Phys. **B221** (1983) 495.

[26] J. Ellis, T. Falk, and K.A. Olive, Phys. Lett. **B444** (1998) 367 [arXiv:hep-ph/9810360]; J. Ellis, T. Falk, K.A. Olive, and M. Srednicki, *Astr. Part. Phys.* **13** (2000) 181 [Erratum-ibid. **15** (2001) 413] [arXiv:hep-ph/9905481].

[27] Joint LEP 2 Supersymmetry Working Group, *Combined LEP Chargino Results, up to 208 GeV*, http://lepsusy.web.cern.ch/lepsusy/www/inos_ moriond01/charginos_pub.html.

[28] R. Barate *et al.* [ALEPH, DELPHI, L3, OPAL Collaborations: the LEP Working Group for Higgs boson searches], Phys. Lett. B **565**, 61 (2003) [arXiv:hep-ex/0306033]; D. Zer-Zion, *Prepared for 32nd International Conference on High-Energy Physics (ICHEP 04), Beijing, China, 16-22 Aug 2004*; LHWG-NOTE-2004-01, ALEPH-2004-008, DELPHI-2004-042, L3-NOTE-2820, OPAL-TN-744, http://lephiggs.web.cern.ch/LEPHIGGS/papers/August2004_MSSM/index.html.

[29] S. Heinemeyer, W. Hollik and G. Weiglein, *Comput. Phys. Commun.* **124** (2000) 76 [arXiv:hep-ph/9812320]; S. Heinemeyer, W. Hollik and G. Weiglein, *Eur. Phys. J. C* **9** (1999) 343 [arXiv:hep-ph/9812472]; G. Degrassi, S. Heinemeyer, W. Hollik, P. Slavich and G. Weiglein, Eur. Phys. J. C **28** (2003) 133 [arXiv:hep-ph/0212020].; M. Frank, T. Hahn, S. Heinemeyer, W. Hollik, H. Rzehak and G. Weiglein, JHEP **0702** (2007) 047 [arXiv:hep-ph/0611326]; http://www.feynhiggs.de/

[30] S. Chen *et al.* [CLEO Collaboration], Phys. Rev. Lett. **87** (2001) 251807 [arXiv:hep-ex/0108032]; P. Koppenburg *et al.* [Belle Collaboration], Phys. Rev. Lett. **93** (2004) 061803 [arXiv:hep-ex/0403004]. B. Aubert *et al.* [BaBar Collaboration], arXiv:hep-ex/0207076; E. Barberio *et al.* [Heavy Flavor Averaging Group (HFAG)], arXiv:hep-ex/0603003.

[31] C. Degrassi, P. Gambino and G. F. Giudice, *JHEP* **0012** (2000) 009 [arXiv:hep-ph/0009337], as implemented by P. Gambino and G. Ganis.

[32] [The Muon g-2 Collaboration], *Phys. Rev. Lett.* **92** (2004) 161802, hep-ex/0401008; G. Bennett et al. [The Muon g-2 Collaboration], *Phys. Rev.* **D 73** (2006) 072003 [arXiv:hep-ex/0602035].

[33] M. Davier, S. Eidelman, A. Höcker and Z. Zhang, *Eur. Phys. J.* **C 31** (2003) 503, hep-ph/0308213; see also M. Knecht, Lect. Notes Phys. **629**, 37 (2004) [arXiv:hep-ph/0307239]; K. Melnikov and A. Vainshtein, Phys. Rev. **D70** (2004) 113006 [arXiv:hep-ph/0312226]; J. F. de Troconiz and F. J. Yndurain, Phys. Rev. D **71**, 073008 (2005) [arXiv:hep-ph/0402285]; M. Passera, arXiv:hep-ph/0411168; K. Hagiwara, A. Martin, D. Nomura and T. Teubner, *Phys. Lett.* **B 649** (2007) 173 [arXiv:hep-ph/0611102]; M. Davier, Nucl. Phys. Proc. Suppl. **169**, 288 (2007) [arXiv:hep-ph/0701163]; F. Jegerlehner, Acta Phys. Polon. B **38**, 3021 (2007) [arXiv:hep-ph/0703125]; J. Miller, E. de Rafael and B. Roberts, *Rept. Prog. Phys.* **70** (2007) 795 [arXiv:hep-ph/0703049]; S. Eidelman, talk given at the ICHEP06, Moscow, July 2006, see: `http://ichep06.jinr.ru/reports/333_6s1_9p30_ Eidelman.pdf`; M. Davier, A. Hoecker, B. Malaescu, C. Z. Yuan and Z. Zhang, arXiv:0908.4300 [hep-ph].

[34] J. L. Feng, K. T. Matchev and T. Moroi, *Phys. Rev. D* **61** (2000) 075005 [arXiv:hep-ph/9909334].

[35] J. R. Ellis, K. A. Olive, Y. Santoso and V. C. Spanos, Phys. Rev. D **69** (2004) 095004 [arXiv:hep-ph/0310356].

[36] J. R. Ellis, S. Heinemeyer, K. A. Olive, A. M. Weber and G. Weiglein, JHEP **0708**, 083 (2007) [arXiv:0706.0652 [hep-ph]].

[37] O. Buchmueller *et al.*, Phys. Lett. B **657** (2007) 87 [arXiv:0707.3447 [hep-ph]].

[38] O. Buchmueller *et al.*, JHEP **0809** (2008) 117 [arXiv:0808.4128 [hep-ph]].

[39] O. Buchmueller *et al.*, Eur. Phys. J. C **64**, 391 (2009) [arXiv:0907.5568 [hep-ph]].

[40] Z. Ahmed *et al.* [CDMS Collaboration], Phys. Rev. Lett. **102**, 011301 (2009) [arXiv:0802.3530 [astro-ph]].

[41] J. Angle *et al.* [XENON Collaboration], Phys. Rev. Lett. **100**, 021303 (2008) [arXiv:0706.0039 [astro-ph]].

[42] J. Ellis, A. Ferstl and K. A. Olive, Phys. Lett. B **481**, 304 (2000) [arXiv:hep-ph/0001005]; J. Ellis, A. Ferstl and K. A. Olive, Phys. Rev. D **63**, 065016 (2001) [arXiv:hep-ph/0007113]; J. R. Ellis, A. Ferstl and K. A. Olive, Phys. Lett. B **532**, 318 (2002) [arXiv:hep-ph/0111064].

[43] J. R. Ellis, K. A. Olive, Y. Santoso and V. C. Spanos, Phys. Rev. D **71**, 095007 (2005) [arXiv:hep-ph/0502001].

[44] J. R. Ellis, K. A. Olive and C. Savage, Phys. Rev. D **77**, 065026 (2008) [arXiv:0801.3656 [hep-ph]].

[45] B. Borasoy and U. G. Meissner, Annals Phys. **254**, 192 (1997) [arXiv:hep-ph/9607432]; J. Gasser, H. Leutwyler and M. E. Sainio, Phys. Lett. B **253**, 252 (1991); M. Knecht, PiN Newslett. **15**, 108 (1999) [arXiv:hep-ph/9912443]; M. E. Sainio, PiN Newslett. **16**, 138 (2002) [arXiv:hep-ph/0110413].

[46] R. D. Young and A. W. Thomas, arXiv:0901.3310 [hep-lat].

[47] J. Giedt, A. W. Thomas and R. D. Young, arXiv:0907.4177 [hep-ph].

[48] J. Ellis, K. A. Olive and P. Sandick, arXiv:0905.0107 [hep-ph].

[49] E. Aprile, L. Baudis and f. t. X. Collaboration, arXiv:0902.4253 [astro-ph.IM].

[50] *SuperCDMS Development Project*, Fermilab Proposal 0947, October 2004.
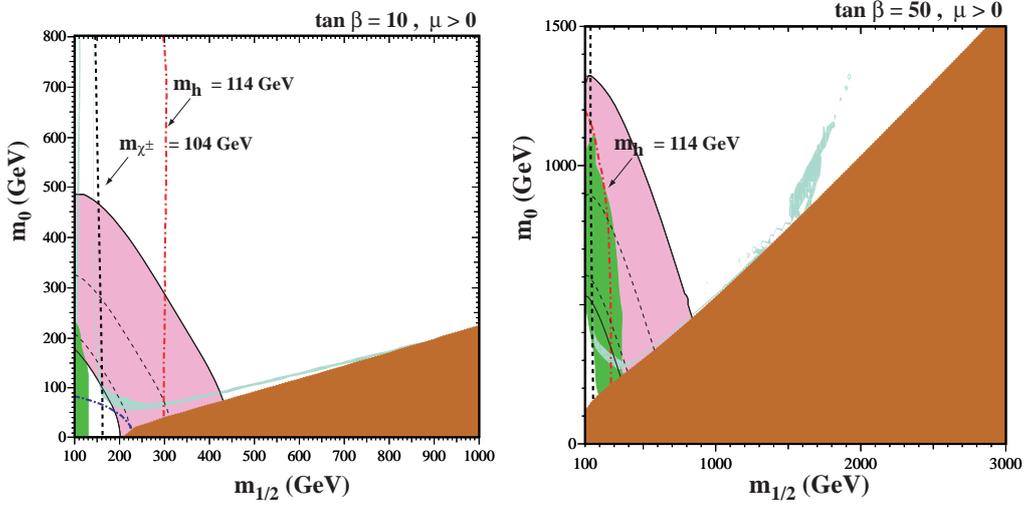
Figure 2: The $(m_{1/2}, m_0)$ planes for (a) $\tan\beta = 10$ and $\mu > 0$, assuming $A_0 = 0, m_t = 175$ GeV and $m_b(m_b)_{SM}^{\overline{MS}} = 4.25$ GeV. The near-vertical (red) dot-dashed lines are the contours $m_h = 114$ GeV, and the near-vertical (black) dashed line is the contour $m_{\chi^\pm} = 104$ GeV. Also shown by the dot-dashed curve in the lower left is the corner excluded by the LEP bound of $m_{\tilde{e}} > 99$ GeV. The medium (dark green) shaded region is excluded by $b \to s\gamma$, and the light (turquoise) shaded area is the cosmologically preferred region. In the dark (brick red) shaded region, the LSP is the charged $\tilde{\tau}_1$. The region allowed by the E821 measurement of a_μ at the 2-σ level, is shaded (pink) and bounded by solid black lines, with dashed lines indicating the 1-σ ranges. In (b), $\tan\beta = 50$.
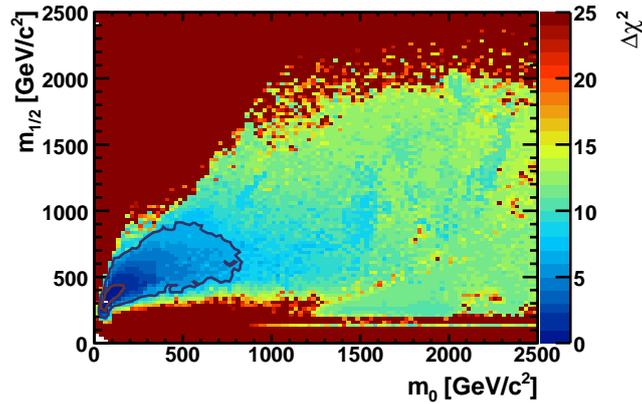
Figure 3: The $\Delta\chi^2$ functions in the $(m_0, m_{1/2})$ planes for the CMSSM. We see that the coannihilation region at low m_0 and $m_{1/2}$ is favored.
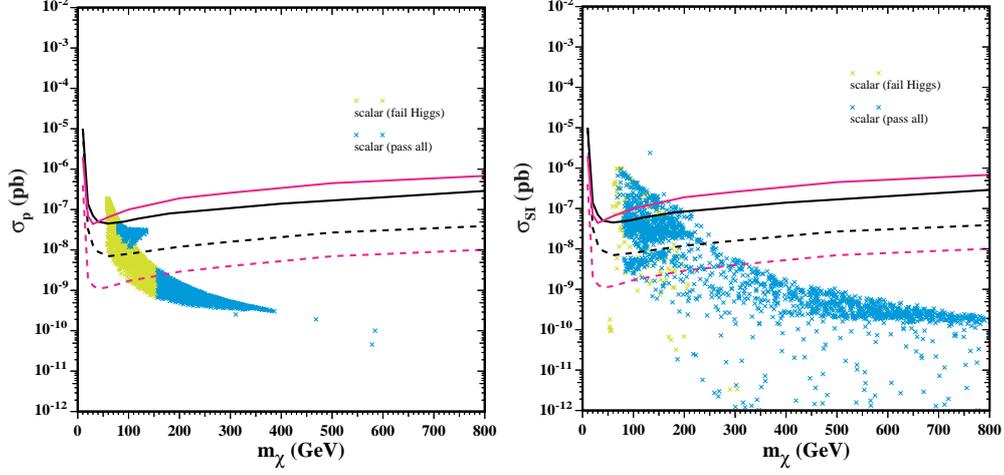
Figure 4: The neutralino-nucleon cross sections as functions of neutralino mass for the CMSSM with $\tan\beta = 10$. Also shown are upper limits on the cross section from CDMS II [40] (solid black line) and XENON10 [41] (solid pink line), as well as the expected sensitivities for XENON100 [49] (dashed pink line) and SuperCDMS at the Soudan Mine [50] (dashed black line). Panel (b) shows the neutralino-nucleon cross sections as functions of neutralino mass for the CMSSM, with $5 \leq \tan\beta \leq 55$, $0 \leq m_{1/2} \leq 2000$ GeV, 100 GeV $\leq m_0 \leq 2000$ GeV, and $-3m_{1/2} \leq A_0 \leq 3m_{1/2}$ We consider $\mu < 0$ only for $\tan\beta < 30$. Taken from [48].
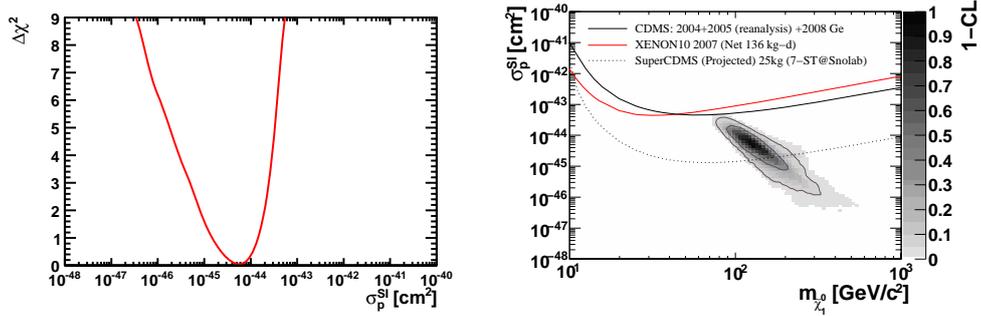
Figure 5: The likelihood functions for the spin-independent $\tilde{\chi}_1^0$-proton scattering cross section σ_p^{SI} (in cm^2) in the CMSSM (left panel). The correlation between the spin-independent DM scattering cross section σ_p^{SI} and $m_{\tilde{\chi}_1^0}$ in the CMSSM (right panel).

Discussion

Cheng-Ju Lin (LBNL Berkely): What are the current constraints from the experimental bound on $B_s \to \mu^+\mu^-$ on the CMSSM model?

Answer: The $B_s \to \mu^+\mu^-$ constraint is essentially non-existent for low values of $\tan\beta$. They are somewhat more important for large $\tan beta$. The current constraint on the branching ratio is 4.7×10^{-8} At high $\tan\beta$, there are departures from the standard model value of $B_s \to \mu^+\mu^- (= 3.4 \times 10^{-9})$. The current constraint would exclude the lower left portion of the plane at $\tan\beta = 50$ with $m_0 < 350$ GeV and $m_{1/2} < 400$ GeV. This region is also excluded by $b \to s\gamma$ as well as the LEP bound on the Higgs mass. It will become an intersting question as the experimental bound approaches the standard model value.

Guy Wormser (LAL Orsay): Could you comment on the recent press article mentioning the possibility of no dark energy at all?

Answer: I don't have too much to say on this. It would be attractive to have an alternative to dark energy. I don't know that it can be achieved consistently within the context of the concordance model known as ΛCDM which accounts for the growth of structure in the Universe and all of the other associated observations. It would be nice to get out of it, but I think currently we are stuck with the notion of dark energy or a cosmological constant.

Guy Wormser (LAL Orsay): A new BABAR result presented at this conference indicates a better agreement in the muon $g - 2$ between theory and experiment. This would reduce room for new physics. How would it affect your constraints?

Answer: The new result has been examined and the combined result using e^+e^- and τ data has been derived in Davier et al. (arXiv:0908.4300 [hep-ph]) yielding yielding a deviation (in units of 10^{-10}) of 24.6 ± 0.8 or a deviation of 3.1 σ. This represents only a small change from the results I have presented.

The g-2 result drives one to the conclusion that sparticle masses are small (and hence favorable for the LHC), but this is not the only observable driving in that direction. The W-mass also points to relatively low sparticle masses as well. If the g-2 result is weakened, the theory is certainly less constrained.

Vali Huseynov (Nakhchivan State University): You have reported about the dark matter candidates (neutralinos, axions, sneutrinos). Which of them is the best candidate for the cold dark matter? And, which one of them is the best candidate for the hot dark matter?

Answer: All of the candidates that I spoke about are cold dark matter candidates. The neutralino, snueutrino, and gravitino are all heavy particles which would be non-relativistic at the time of structure formation. The axion though it is light is also a cold dark matter candidate. A standard candidate for hot dark matter is the light neutrino. But this is excluded as dark matter as the neutrino mass is constrained. In addition, hot dark matter produces too much structure on large scales and is no longer

considered viable.

Experimental Status of the CKM Matrix

Sören Prell

Iowa State University, Department of Physics and Astronomy, Ames, Iowa 50011-3160, USA

We review the present status of experimental results on the magnitudes and phases of the elements of the Cabibbo-Kobayashi-Maskawa matrix. The matrix is found to be consistent with being unitary as predicted by the Standard Model. The matrix is also consistent with being the origin of the observed violations of CP-symmetry in K and B decays.

1 Introduction

In the Standard Model with three generations quarks and leptons are assigned to be left-handed doublets and right-handed singlets. The quark mass eigenstates are not the same as the weak eigenstates and the Cabibbo-Kobayashi-Maskawa (CKM) matrix relates these two bases:

$$\begin{pmatrix} d' \\ s' \\ b' \end{pmatrix} = \begin{pmatrix} V_{ud} & V_{us} & V_{ub} \\ V_{cd} & V_{cs} & V_{cb} \\ V_{td} & V_{ts} & V_{tb} \end{pmatrix} \begin{pmatrix} d \\ s \\ b \end{pmatrix}$$

The CKM matrix element V_{ij} describes the strength of the amplitude of the charged-current, flavor-changing quark transition $i \to jW^-$. Since the CP-conjugate decay $\bar{i} \to \bar{j}W^+$ depends on V_{ij}^*, the complex nature of the CKM matrix allows for violation of CP-symmetry in quark transitions.

The quark mixing matrix for three generations was first suggested by Makoto Kobayashi and Toshihide Maskawa in 1973 [1] for which they received the 2008 Nobel Prize in Physics (shared with Y. Nambu). In acknowledgement of Nicola Cabibbo's earlier work [2] on quark mixing with two generations we call the quark mixing matrix the CKM matrix V_{CKM}.

In the three-generation Standard Model V_{CKM} is a unitary 3×3 matrix. Observables are combinations of matrix elements that are invariant under arbitrary phase transformations:

- doublets $V_{ij}V_{ij}^*$, i.e. the magnitudes of the CKM matrix elements,

- quartets $V_{ij}V_{kl}V_{il}^*V_{kj}^*$, which give access to relative phases between matrix elements,

- sextets $V_{ij}V_{kl}V_{mn}V_{il}^*V_{kn}^*V_{mj}^*$ and higher $2n$-tets constructed in an analogous way.

Due to unitarity constraints the CKM matrix has only four independent parameters. Several parameterizations have been suggested. A common parameterization is the one from Wolfenstein [3], which is an expansion in the small parameter λ that reflects the hierarchy of the magnitudes of the matrix elements.

$$V_{CKM} = \begin{pmatrix} 1 - \lambda^2/2 & \lambda & A\lambda^3(\rho - i\eta) \\ -\lambda & 1 - \lambda^2/2 & A\lambda^2 \\ A\lambda^3(1 - \rho - i\eta) & -A\lambda^2 & 1 \end{pmatrix} + \mathcal{O}(\lambda^4)$$

The Standard Model makes no predictions about the values of the CKM matrix elements. However, the unitarity of the CKM matrix provides precise constraints on the relations between matrix elements. A deviation from unitarity would be evidence for physics beyond the Standard Model. The test of the unitarity of the CKM matrix has been a major goal of many flavor physics experiments over the last decade.

2 Magnitudes of the CKM matrix elements

The magnitudes of the CKM matrix elements of the first two rows are all determined from semileptonic decays in order to reduce as much as possible theoretical uncertainties arising from strong interactions between quarks. It is currently not possible to determine the CKM matrix elements which involve the top quark from semileptonic decays. These matrix elements are determined from processes involving virtual top quark pairs or weak production of single top quarks. The measurements of the magnitudes of the CKM matrix elements are limited by the understanding of the influence of the strong interaction in these weak weak processes.

2.1 $|V_{\text{ud}}|$ and $|V_{\text{us}}|$

The most precise determination of the magnitude of V_{ud} comes from super-allowed nuclear β-decays. These decays are pure vector, $0^+ \to 0^+$ transitions within the same isospin multiplet. A recent review [5] gives an average of $\mathcal{F}t = (3071.81 \pm 0.79 \pm 0.27)$ s for thirteen different transitions, where $\mathcal{F}t$ is the product of the Fermi function f, the half-life t and nucleus-dependent corrections for isospin symmetry breaking and internal bremsstrahlung. The magnitude of V_{ud} is obtained from

$$|V_{\text{ud}}|^2 = \frac{m_e^{-5}\pi^3 \ln 2}{G_F^2(1 + \Delta_R^V)\mathcal{F}t} \ ,$$

where m_e is the electron mass, G_F is the Fermi constant taken from muon decay, and Δ_R^V is the electroweak radiative correction. Uncertainties in the calculation of Δ_R^V have recently been reduced by a factor of two [6] and the current value is $\Delta_R^V = (2.361 \pm 0.038)\%$. However, Δ_R^V is still the dominant source of uncertainty for $|V_{\text{ud}}|$. The current world average [5] is given by $|V_{\text{ud}}| = 0.97425 \pm 0.00022$.

The magnitude of V_{us} is determined from semileptonic kaon decays ($Kl3$ decays). Their decay rate is given by

$$\Gamma(Kl3) = \frac{C_K^2 G_F^2 M_K^5}{192\pi^3} S_{\text{EW}}|V_{\text{us}}|^2|f_+(0)|^2 I_{Kl}\left(1 + \delta_K^{\text{SU}(2)} + \delta_{Kl}^{\text{EM}}\right),$$

where l refers to either e or μ, M_K is the kaon mass, S_{EW} is the short-distance radiative correction, δ_{Kl}^{EM} is the mode-dependent long-distance radiative correction, $f_+(0)$ is the transition form factor calculated at zero momentum transfer for the $l\nu$ system, and I_{Kl} is the phase-space integral, which depends on the measured semileptonic form factors. For charged kaon decay $\delta_K^{\text{SU}(2)}$ is the deviation from one of the ratio of $f_+(0)$ for the charged to neutral kaon decay. C^2 is 1 (1/2) for neutral (charged) kaon decays. Experimentally measured are the $Kl3$ decay widths (from the $Kl3$ branching fractions and K lifetimes) and form factors. The values of $S_{\text{EW}}, \delta_{Kl}^{\text{EM}}, \delta_K^{\text{SU}(2)}$, and $f_+(0)$ are provided by theory.

An average of $|V_{\text{us}}|f_+(0)$ including new measurements from KLOE, KTeV, ISTRA+ and NA48 has recently been presented at the KAON '09 conference [7]: $\langle|V_{\text{us}}|f_+(0)\rangle = 0.21660(47)$.

The uncertainty of the two most precise measurements in this average from $K_L l3$ decays are dominated by the K_L lifetime uncertainty. The most recent measurements of the K_L [8] and K_S [9] lifetimes from KLOE have not been used in the $|V_{us}|f_+(0)$ average. Using a recent lattice calculation of $f_+(0) = 0.964(5)$ [10] gives $|V_{us}| = 0.2246 \pm 0.0012$.

It is noteworthy that measurements of $|V_{us}|$ from τ decays have reached a comparable precision. From the ratio of branching ratios $BR(\tau \to K\nu)/BR(\tau \to \pi\nu)$ BABAR obtains $|V_{us}| = 0.2246 \pm 0.0023$ [11]. From inclusive τ decays to strange final states $|V_{us}|$ is determined with very small theoretical uncertainties: $|V_{us}| = 0.2165 \pm 0.0026(\text{exp}) \pm 0.005(\text{theo})$ [12]. However, the difference of about 2.6σ with respect to the result from $Kl3$ decays needs to be understood.

The ratio $|V_{us}/V_{ud}|$ is determined from the ratio of decay rates for $K \to \mu\nu$ [13] and $\pi \to \mu\nu$:

$$\left| \frac{V_{us}}{V_{ud}} \right| = 0.2387(4) \sqrt{\frac{\Gamma(K \to \mu\nu)}{\Gamma(\pi \to \mu\nu)}} \times \frac{f_\pi}{f_K} \ .$$

Using a recent calculation of the ratio of decay constants $f_\pi/f_K = 1.189(7)$ [14] gives $|V_{us}/V_{ud}| = 0.2321(15)$. From the direct determinations of $|V_{ud}|$ and $|V_{us}|$ and the ratio $|V_{us}/V_{ud}|$ the FlaviaNet collaboration calculates [7]:

$$|V_{ud}| = 0.97424 \pm 0.00022 \quad \text{and} \quad |V_{us}| = 0.2252 \pm 0.0009 \ .$$

2.2 $|V_{cd}|$ and $|V_{cs}|$

Di-muon production measurements by neutrinos on nuclei provide still the best measurement of $|V_{cd}| = 0.230 \pm 0.011$ [15]. However, new measurements of the rate for semileptonic $D \to \pi l\nu$ decays from CLEO-c have a smaller experimental error $|V_{cd}| = 0.234 \pm 0.007(\text{exp}) \pm 0.025(\text{theo})$ [16]. The theoretical error is dominated by the uncertainty of the lattice calculation of the $D \to \pi$ form factor. Our average of these two measurements is

$$|V_{cd}| = 0.231 \pm 0.010 \ .$$

The value $|V_{cs}|$ is determined from measurements of branching ratios of leptonic D_s^+ and semileptonic D decays by CLEO-c [17, 18], BELLE [19] and BABAR [20]. CLEO-c has published recently precise results for $|V_{cs}|f_{D_s}$ from their measurements of the $D_s \to \tau\bar\nu, \mu\bar\nu$ branching ratios [17]. In their paper CLEO-c quote their result in form of the D_s^+ decay constant. We turn this into a number for $|V_{cs}|$ by using $|V_{cs}| = (f_{D_s,\text{meas}}/f_{D_s,\text{LQCD}})|V_{ud}|$ where we use the value of $|V_{ud}|$ from above and an average of $\langle f_{D_s} \rangle = 242 \pm 5$ MeV (calculated from results in [14] and [21] with a scale factor of 1.6 for the error). One obtains $|V_{cs}| = 1.04 \pm 0.04$. CLEO-c measures a consistent result although with a somewhat larger theoretical error (dominated by the $D \to K$ form factor) from semileptonic $D \to Kl\bar\nu$ decays: $|V_{cs}| = 0.985 \pm 0.01(\text{exp}) \pm 0.10(\text{theo})$ [18]. Our average of these numbers is

$$|V_{cs}| = 1.03 \pm 0.04 \ .$$

2.3 Unitarity check of the udsc submatrix

Using the measurements of $|V_{ud}|$, $|V_{us}|$, $|V_{cd}|$, and $|V_{cs}|$ one can check the unitarity of the udsc 2×2 submatrix:

$$
\begin{aligned}
|V_{ud}|^2 + |V_{us}|^2 - 1 &= -0.0004 \pm 0.0007 \ (-0.6\sigma) \\
|V_{cd}|^2 + |V_{cs}|^2 - 1 &= +0.114 \pm 0.083 \ (+1.3\sigma) \\
|V_{ud}|^2 + |V_{cd}|^2 - 1 &= +0.003 \pm 0.005 \ (+0.6\sigma) \\
|V_{us}|^2 + |V_{cs}|^2 - 1 &= +0.112 \pm 0.082 \ (+1.4\sigma)
\end{aligned}
$$

The most precise unitarity test of the udsc matrix comes from the first row elements. The uncertainties of $|V_{ud}|^2$ and $|V_{us}|^2$ contribute roughly the same to the error of this unitarity check. The precision of the udsc submatrix elements is not yet sufficient to predict the existence of the third quark family. Tight constraints on new physics parameters such as the mass of a charged Higgs [22], the coupling to a fourth quark generation [23] and the inclusive branching ratio of exotic muon decays (through G_F) [23] can be obtained from these measurements.

The 2×2 matrix also gives

$$
\lambda_{CKM} = 0.2252 \pm 0.0009 \ .
$$

2.4 $|V_{cb}|$

The CKM matrix element $|V_{cb}|$ is determined from exclusive and inclusive semileptonic B decays to charmed final states. The differential decay rates for the exclusive $\bar{B} \to D^{(*)}l\bar{\nu}$ decays are given by

$$
\begin{aligned}
\frac{d\Gamma}{dw}(\bar{B} \to D^*l\bar{\nu}) &= \frac{G_F^2}{48\pi^3}|V_{cb}|^2 m_{D^*}^3 (w-1)^{1/2} P(w)(F(w))^2, \\
\frac{d\Gamma}{dw}(\bar{B} \to Dl\bar{\nu}) &= \frac{G_F^2}{48\pi^3}|V_{cb}|^2 (m_D + m_B) m_D^3 (w-1)^{3/2} (G(w))^2,
\end{aligned}
$$

where $m_{D^{(*)}}$ and m_B are the $D^{(*)}$ and B meson masses, w is related to the energy of the $D^{(*)}$ meson in the B rest frame, $P(w)$ is a phase space factor and $F(w)$ and $G(w)$ are the $B \to D^{(*)}$ form factors.

Experiments fit the differential decay rates for $|V_{cb}|F(1)$ and $|V_{cb}|G(1)$ using form factor parameterizations derived from HQET. There have been several new precision results [24] over the last few years from BABAR and BELLE. The latest averages from HFAG [25] calculated for this conference are $|V_{cb}|G(1) = (42.3 \pm 0.7 \pm 1.3) \times 10^{-3}$ and $|V_{cb}|F(1) = (35.75 \pm 0.42) \times 10^{-3}$.

The $|V_{cb}|F(1)$ average does not yet include the recent result $|V_{cb}|F(1) = (35.0 \pm 0.4 \pm 2.2) \times 10^{-3}$ from BELLE's study of $B^- \to D^{*0}l\nu$ decays [26]. Using recent calculations of the $B \to D^{(*)}$ form factors $G(1) = 1.074 \pm 0.018 \pm 0.016$ [27] and $F(1) = 0.921 \pm 0.013 \pm 0.020$ [28] from lattice calculations gives consistent values for $|V_{cb}|$ from $\bar{B} \to D^*l\bar{\nu}$ ($|V_{cb}| = (39.4 \pm 1.4(\text{exp}) \pm 0.9(\text{theo})) \times 10^{-3}$) and $\bar{B} \to Dl\bar{\nu}$ ($|V_{cb}| = (38.8 \pm 0.5(\text{exp}) \pm 1.0(\text{theo})) \times 10^{-3}$) decays.

The theoretical uncertainty in $|V_{cb}|$ from $\bar{B} \to D^{(*)}l\bar{\nu}$ decays due to the hadronization process can be avoided if $|V_{cb}|$ is determined from inclusive $b \to cl\nu$ transitions. Using HQET and Operator Product Expansion the inclusive $b \to cl\nu$ decay rate can be expressed by an expansion in powers of $1/m_b$. Non-perturbative corrections up to order $1/m_b^3$ are determined

from inclusive distributions in B decays such as the lepton energy spectrum and the hadronic mass spectrum in $b \to cl\nu$ decays and the photon energy spectrum in $b \to s\gamma$ decays. HFAG gives an average of $|V_{cb}|$ from inclusive $b \to cl\nu$ transitions of $|V_{cb}| = (41.67 \pm 0.44 \pm 0.58) \times 10^{-3}$ [25]. This value is about 2.3σ higher than the value from $\bar{B} \to D^{(*)}l\bar{\nu}$ decays. Averaging the two $|V_{cb}|$ values we obtain

$$|V_{cb}| = (40.6 \pm 1.3) \times 10^{-3} \ ,$$

which includes a scale factor for the error of 2.3 .

2.5 $\quad |V_{ub}|$

The B factories determine $|V_{ub}|$ from $B \to \pi l\nu$ decays and inclusive $b \to ul\nu$ decays. There have been several new results in the last few years. The total decay rate for $B \to \pi l\nu$ is now measured by BABAR [29], BELLE [30] and CLEO [31] with a precision of about 5%.

The product $|V_{ub}|f_+(q^2)$ is obtained from the differential decay rate

$$\frac{d\Gamma}{dq^2} = \frac{G_F^2}{24\pi^3} p_\pi^3 |V_{ub}|^2 |f_+(q^2)|^2 \ .$$

The $B \to \pi$ form factor $f_+(q^2)$ is calculated from lattice QCD [32] and light-cone sum rules [33]. The two methods are complementary since the lattice calculation is limited to large q^2 and light-cone sum rules provide information close to $q^2 = 0$. A recent review [34] quotes an average value for $|V_{ub}|$ from $B \to \pi l\nu$ decays of $|V_{ub}|_{\text{excl}} = (3.5^{+0.6}_{-0.5}) \times 10^{-3}$, where the error is dominated by the form factor calculations. This average does not include a new result of $|V_{ub}|_{\text{excl}} = (3.38 \pm 0.36) \times 10^{-3}$ obtained with an improved form factor calculation [35].

The magnitude of V_{ub} can also be determined from measurements of the total inclusive $B \to X_u l\nu$ decay rate:

$$\Gamma(B \to X_u l\nu) = \frac{G_F^2}{192\pi^3} |V_{ub}|^2 m_b^5 (1 + \ \Delta_{\text{hadr}}),$$

where m_b is the b quark mass and Δ_{hadr} are hadronic corrections. The two main challenges for the determination of $|V_{ub}|$ from inclusive decays are the strong dependence of the decay rate on the b quark mass and the large background from $B \to X_c l\nu$ decays, which is about fifty times larger than the $B \to X_u l\nu$ signal. In practice the experiments measure a partial $B \to X_u l\nu$ decay rate in regions of phase space where the background is comparatively small and then use so-called shape functions derived from the photon energy spectrum in $B \to X_s \gamma$ decays and theory to extrapolate the rate to the full phase space. Their have been several recent analyses by BABAR and BELLE with varying levels of signal purity and reconstruction efficiency [36]. The average of all measurements of $|V_{ub}|$ from inclusive $B \to X_u l\nu$ decays within one particular theoretical framework [37] gives $|V_{ub}| = (4.20 \pm 0.16^{+0.22}_{-0.23}) \times 10^{-3}$. However, there are several such frameworks [38] and their calculations for $|V_{ub}|$ vary between $(4.05 - 4.87) \times 10^{-3}$.

Taking the average of the $|V_{ub}|$ value from [37] and the $|V_{ub}|$ measurement from $B \to \pi l\nu$ decays gives

$$|V_{ub}| = (4.07 \pm 0.38) \times 10^{-3} \ .$$

This average does not account for the spread between theory frameworks for the value of $|V_{ub}|$ from inclusive $B \to X_u l\nu$ decays. However, the error is scaled by 1.5 to account for the difference between the values for $|V_{ub}|$ from inclusive and exclusive decays.

2.6 $|V_{\text{td}}|$ and $|V_{\text{ts}}|$

The large value of $|V_{\text{tb}}|$ and the relatively small size of currently available top samples do not allow the determination of $|V_{\text{td}}|$ and $|V_{\text{ts}}|$ from semileptonic top quark decays. Instead these CKM matrix elements are determined from the oscillation frequencies of B_d^0 and B_s^0 mesons, respectively. The $B\bar{B}$ oscillation process is dominated by a 2nd order weak box diagram involving a $t\bar{t}$ pair. The oscillation frequencies are given by

$$\Delta m_{d(s)} = \frac{G_F^2}{6\pi^2} m_{B_{d(s)}} f_{B_{d(s)}}^2 \hat{B}_{B_{d(s)}} \eta_{\text{QCD}} |V_{\text{td(ts)}}|^2 |V_{\text{tb}}|^2 S_0(m_t^2/m_W^2),$$

where $f_{B_{d(s)}}$ and $\hat{B}_{B_{d(s)}}$ are the $B_{d(s)}$ weak decay constant and bag parameter, respectively, η_{QCD} is a QCD correction factor and S_0 is a function that depends on the square of the ratio of the top quark mass and the W boson mass [39].

The B-factories BABAR and BELLE provide the most precise measurements of Δm_d [41] while CDF and D0 measure Δm_s best [42]. The current world averages [25] are given by $\Delta m_d = (0.507 \pm 0.004)\text{ps}^{-1}$ and $\Delta m_s = (17.78 \pm 0.12)\text{ps}^{-1}$. With new lattice results for $f_{B_{d(s)}} \sqrt{\hat{B}_{B_{d(s)}}}$ [40] one obtains

$$|V_{\text{td}}| = (8.1 \pm 0.6) \times 10^{-3} \quad \text{and} \quad |V_{\text{ts}}| = (38.7 \pm 2.3) \times 10^{-3} .$$

Since about half of the theoretical error budget cancels in the calculation of $(f_{B_d}/f_{B_s}) \sqrt{\hat{B}_{B_d}/\hat{B}_{B_s}}$, the ratio $|V_{\text{td}}/V_{\text{ts}}|$ has a correspondingly smaller relative error: $|V_{\text{td}}/V_{\text{ts}}| = 0.209 \pm 0.001 \pm 0.006$. BABAR [43] and BELLE [44] have measured this ratio also from radiative B decays to $K^*\gamma$ and $(\rho/\omega)\gamma$ final states to be $|V_{\text{td}}/V_{\text{ts}}| = 0.210 \pm 0.15 \pm 0.018$ [45], which is consistent with the value determined from the oscillation frequencies, but has a larger error.

2.7 $|V_{\text{tb}}|$

The value of $|V_{\text{tb}}|$ is determined from the production cross-section of single top events in $p\bar{p}$ collisions. CDF [46] and D0 [47] have both reported observations of this process with significances above 5σ. The experiments presented an updated average of $|V_{\text{tb}}|$ at this conference [48]:

$$|V_{\text{tb}}| = 0.91 \pm 0.08 .$$

2.8 Unitarity check of the CKM matrix element magnitudes

From the measurements of the magnitudes of all CKM matrix elements one can check the unitarity of the CKM matrix:

$$
\begin{aligned}
|V_{\text{ud}}|^2 + |V_{\text{us}}|^2 + |V_{\text{ub}}|^2 - 1 &= -0.0004 \pm 0.0007 \ (-0.6\sigma) \\
|V_{\text{cd}}|^2 + |V_{\text{cs}}|^2 + |V_{\text{cb}}|^2 - 1 &= +0.11 \pm 0.08 \ (+1.3\sigma) \\
|V_{\text{td}}|^2 + |V_{\text{ts}}|^2 + |V_{\text{tb}}|^2 - 1 &= +0.00 \pm 0.20 \ (+0.0\sigma) \\
|V_{\text{ud}}|^2 + |V_{\text{cd}}|^2 + |V_{\text{td}}|^2 - 1 &= +0.003 \pm 0.005 \ (+0.6\sigma) \\
|V_{\text{us}}|^2 + |V_{\text{cs}}|^2 + |V_{\text{ts}}|^2 - 1 &= +0.11 \pm 0.08 \ (+1.4\sigma) \\
|V_{\text{ub}}|^2 + |V_{\text{cb}}|^2 + |V_{\text{tb}}|^2 - 1 &= +0.00 \pm 0.20 \ (+0.0\sigma)
\end{aligned}
$$

The magnitudes of the CKM matrix fulfill the unitarity requirements well. From the matrix elements $|V_{cb}|$ and $|V_{ts}|$ one obtains

$$A\lambda_{CKM}^2 = (40.1 \pm 1.1) \times 10^{-3} \ .$$

3 Phases of the CKM matrix elements

Six unitarity constraints involving the relative phases between CKM matrix elements can be expressed by the products of one row (or column) of the CKM matrix with the complex-conjugate transpose of another row (or column) and graphically displayed as triangles in the complex plane. The triangle derived from the first and third column of the CKM matrix has become known as the Unitarity Triangle. The inner angles of the Unitarity Triangle α, β, and γ and a fourth phase, β_s related to B_s mixing are defined as

$$\alpha = \arg\left(\frac{-V_{td}V_{tb}^*}{V_{ud}V_{ub}^*}\right), \quad \beta = \arg\left(\frac{-V_{cd}V_{cb}^*}{V_{td}V_{tb}^*}\right), \quad \gamma = \arg\left(\frac{-V_{ud}V_{ub}^*}{V_{cd}V_{cb}^*}\right), \quad \beta_s = \arg\left(\frac{-V_{ts}V_{tb}^*}{V_{cs}V_{cb}^*}\right).$$

By dividing all sides by $V_{cd}V_{cb}^*$, the apex of the Unitarity Triangle is given by $(\bar{\rho}, \bar{\eta})$ where, for example, $\bar{\rho} = \rho(1 - \lambda^2/2)$. In the Wolfenstein convention γ is the phase of V_{ub} and $\beta_{(s)}$ is the phase of $V_{td(ts)}$. Experimental sensitivity to the phases of the CKM matrix elements comes from the interference of two decay amplitudes with different weak phases and from the comparison of CP asymmetries from B and $\bar{B}$ decays. Since hadronic uncertainties largely cancel in the ratios of amplitudes between B and $\bar{B}$ decays, the measured values of the CKM phases have small theoretical uncertainties and turn out to be experimentally limited.

3.1 β

The value of $\sin(2\beta)$ can be determined without large theoretical uncertainties [49] from the time-dependent CP asymmetries in B decays to final states with a charmonium meson and a neutral kaon. These decays proceed either through the direct $b \to (c\bar{c})s$ amplitude or through the $B\bar{B}$ mixing amplitude followed by $\bar{b} \to (c\bar{c})\bar{s}$. The most precise determination of $\sin(2\beta)$ comes from measurements by BABAR and BELLE of B decays to $J/\psi K^0$, $J/\psi K^{*0}$, $\psi(2S)K_S^0$, $\eta_c K_S^0$, and $\chi_{c1}K_S^0$ [50]. The world average [25] is given by $\sin(2\beta) = 0.672 \pm 0.023$.

Converting $\sin(2\beta)$ into β leaves a two-fold ambiguity for $\beta < 90°$. The solution with negative $\cos(2\beta)$ has been ruled out by measurements of the CP asymmetries in decays with contributions from CP-odd and CP-even amplitudes ($B \to J/\psi K^{*0}$, $B \to D^*D^*K_S^0$ and $B \to Dh^0$ (with $D \to K_S^0\pi^+\pi^-$)). This gives

$$\beta = (21.1 \pm 0.9)° \ .$$

A sensitive test of the predictions of the CKM theory regarding CP asymmetries comes from comparing the above value of $\sin(2\beta)$ with the CP asymmetry obtained from B decays through suppressed penguin loop diagrams. In the Standard Model the weak phase in $b \to (q\bar{q})s$ penguin loop decays, where $q\bar{q}$ is a light quark pair, is the same as in decays to charmonium final states. Therefore the time-dependent CP asymmetry in $b \to (q\bar{q})s$ decays, $\sin(2\beta_{eff})$, is expected to be close to $\sin(2\beta)$. Theoretical calculations give $\Delta\sin(2\beta) \equiv \sin(2\beta_{eff}) - \sin(2\beta)$ in the range of $0.01 - 0.1$. However, contributions from new physics processes to these rare decays could cause large $|\Delta\sin(2\beta)|$.

BABAR and BELLE have measured the time-dependent CP asymmetries for 9 rare $b \to (q\bar{q})s$ decays. All measurements are consistent with $\Delta \sin(2\beta) = 0$ and no direct CP violation. A few years ago the (naive) average of the $\sin(2\beta_{\text{eff}})$ for these rare modes differed by more than 3σ from zero [25]. With the latest measurements of $\sin(2\beta_{\text{eff}})$ this discrepancy has been been reduced to approximately 1σ [25].

The theoretical uncertainty in $\sin(2\beta_{\text{eff}})$ is believed to be relatively small for the modes $B \to \phi K^0$, $B \to \eta' K^0$ and $B \to K_S^0 K_S^0 K_S^0$. Our average for these modes is $\sin(2\beta_{\text{eff,clean}}) = 0.59 \pm 0.06$, which is 1.3σ way from $\sin(2\beta)$.

3.2 α

The time-dependent CP asymmetries in B^0 decays proceeding through a $b \to u$ tree amplitude are sensitive to α. The decay $B^0 \to \pi^+ \pi^-$, which is experimentally most accessible, suffers from the contribution of a relatively large $b \to d$ penguin amplitude. The time-dependent CP asymmetries of $B^0 \to \pi^+ \pi^-$ are sensitive to $\sin(2\alpha + \delta_{\pi\pi})$ and the phase $\delta_{\pi\pi}$ needs to be measured through an isospin analysis of the branching ratios of neutral and charged B decays to $\pi\pi$ final states [51]. The large size of the $B \to \pi\pi$ penguin amplitude and discrete ambiguities in the determination of $\delta_{\pi\pi}$ currently only allow to exclude the range of $12° < \alpha < 78°$ (at 95% C.L.) [54].

The decays $B \to \rho^+ \rho^-$ proceed through the same Feynman diagrams as $B \to \pi^+ \pi^-$ decays. The $\rho\rho$ final state consists of two vector mesons and thus separate isospin analyses are in principle required for each of the three polarization amplitudes. However, since the fraction of $B^0 \to \rho^+ \rho^-$ decays proceeding through the longitunal polarization amplitude is $f_L(\rho^+ \rho^-) = 0.978^{+0.025}_{-0.022}$ [25] in practice only one isospin analysis in needed. In addition, the penguin contribution to $B \to \rho^+ \rho^-$ is rather small as is evident from the small ratio of branching ratios for $BR(B \to \rho^0 \rho^0)/BR(B^+ \to \rho^+ \rho^0)$. As a result the discrete ambiguities for $\delta_{\rho\rho}$ all overlap. A recent update of the branching ratio of $B^+ \to \rho^+ \rho^0$ by BABAR constrains $\delta_{\rho\rho}$ further [52]. An average for α from the most recent measurements of time-dependent CP asymmetries in $B \to \pi\pi$, $\rho\rho$ and $\rho\pi$ [53] and corresponding branching fractions has been calculated by the CKMFitter group to be [54]:

$$\alpha = (89.0^{+4.4}_{-4.2})° \ .$$

A first determination of α by BABAR using B decays to the axial-vector final state $a_1 \pi$ of $\alpha = (79 \pm 7 \pm 11)°$ [55] is not yet included in this average.

3.3 γ

The angle γ is determined from the interference between $b \to c$ and $b \to u$ transition amplitudes in $B^\pm \to D^{(*)} K^\pm$ decays, where the $D^{(*)}$ meson decays to final states accessible to D^0 and $\bar{D}^0$. Several neutral D final states have been investigated by BABAR, BELLE and CDF including D decays to CP eigenstates [56], D decays to flavor states involving doubly Cabibbo-suppressed transitions [57] and D decays to three-body final states [58].

BABAR recently found evidence at 3.4σ for the decay $B^- \to \bar{D}^0 K^-$ [59], which proceeds through a doubly Cabibbo-suppressed D decay amplitude. The best sensitivity to γ comes from the time-dependent Dalitz analysis of $B^- \to D^{(*)0} K^-$ decays where the D^0 subsequently decays to a three-body $K_S^0 \pi^+ \pi^-$ or $K_S^0 K^+ K^-$ final state. BELLE recently updated their result and now includes also $D^{*0} \to D^0 \gamma$ decays in their analysis. They obtain $\gamma = (78^{+11}_{-12} \pm 3.6 \pm 9)°$ [60],

where the first errors is statistical, the second is systematical and the last one is due to the D^0 decay model. BABAR was able in their recent measurement of γ [61] to reduce the error due to the D^0 decay model to 5°, based on a study of their large sample of D^{*+}-tagged $D^0 \to K_S^0 \pi^+ \pi^-$, $K_S^0 K^+ K^-$ decays. This error can ultimately be reduced to about 2° using information from the phase in $\psi(3770) \to D\bar{D}$ decays obtained by CLEO-c [62]. An average of the γ measurements by the UTFit group gives [63]:

$$\gamma = (75.0 \pm 12)° \ .$$

An additional constraint on γ comes from the measurements of time-dependent CP asymmetries in $B^0 \to D^{(*)}\pi$ and $B^0 \to D\rho$ decays giving $\sin(2\beta + \gamma) = (\pm 90 \pm 32)°$ [63].

3.4 $\beta_{\rm s}$

The phase $\beta_{\rm s}$ is predicted to be very small in the Standard Model with a value of approximately 0.02 [15, 64], but can be much larger in new physics models. It can be extracted from the time-dependent CP asymmetries in B_s decays to the $J/\psi\phi$ final state. Both CDF and D0 extract simultaneously $\beta_{\rm s}$ and $\Delta\Gamma_s$, the width difference between the heavy and light B_s mass eigenstates, from the time and angular-dependent decay time distributions of $B_s \to J/\psi\phi$ [65]. The combined result from CDF and D0 allows a range for $\beta_{\rm s}$ between 0.10 and 1.42 at the 95% C.L. and differs from the Standard Model prediction by 2.0σ [65].

4 Global CKM matrix fits

A simple way to test the unitarity of the CKM matrix is to check the sum of the inner angles of the unitarity triangle. It is found to be consistent with 180°:

$$\alpha + \beta + \gamma = (185 \pm 13)° \ .$$

The error of this check is dominated by the experimental uncertainty on γ.

Global tests use all information on the sides and angles of the Unitarity Triangle to determine and overconstrain its apex position. The CKMFitter [54] and UTFit [63] groups use different statistical approaches. While the CKMFitter group uses a frequentist method, the UTFit group employs Bayesian statistics. As a result the uncertainties quoted by the CKMFitter group are often more conservative. The two groups determine the position of the apex of the unitarity triangle to be

$$\text{CKMFitter}: \quad \bar{\rho} = 0.139^{+0.025}_{-0.027}, \qquad \text{UTFit}: \quad \bar{\rho} = 0.154 \pm 0.022,$$
$$\bar{\eta} = 0.341^{+0.016}_{-0.015}, \qquad\qquad\qquad \bar{\eta} = 0.342 \pm 0.014 \ .$$

There is a "tension" at the 2σ level between $\sin(2\beta)$ and ϵ_K (the CP-asymmetry in neutral K decays) and the value of $|V_{\rm ub}|$ from inclusive $b \to ul\nu$ decays [67]. It would increase to close to 3σ if an 8% correction is applied to ϵ_K as proposed in [68]. Due to their more conservative treatment of the systematic errors the CKMFitter group obtains a p-value of 45% for their global CKM fit [69]. There is also a 2.4σ tension between the branching fraction $BR(B \to \tau\nu)$ and the result of global Unitarity Triangle fit without information from $B \to \tau\nu$ [66].

As of now there is no significant evidence from global CKM fits that the CKM matrix is not unitary. Comparisons between sets of measurements that might be sensitive to new physics such as quantities derived from tree processes versus quantities derived from loop processes, CP-conserving versus CP-violating processes, etc. do not shown any inconsistency either[54, 63].

5   Conclusions

There have been a wealth of new measurements regarding quark flavor mixing in the last few years that continue to constrain the CKM matrix elements with increasing precision. All current experimental results in quark mixing and CP violation are described by the CKM mechanism, which has proven to be the dominant mechanism for these phenomena. There are some intrinsic discrepancies that need to be resolved (e.g. V_{us} from inclusive versus exclusive tau decays and strange final states and V_{ub} and V_{cb} from inclusive versus exclusive B decays). There are also a few interesting tensions at the 2-3σ level (β versus ϵ_K and V_{ub}, β_s and $BR(B \to \tau\nu)$, which should be monitored closely in the future. This will be particulary exciting as with the turn on of new experiments such as LHCb and the Super B factories and improved lattice calculations significant improvements particulary for γ, β_s, $|V_{\text{ub}}|$ and $|V_{\text{td}}/V_{\text{ts}}|$ are expected.

Figure 1: Experimental constraints on the Unitarity Triangle.

References

[1] M. Kobayashi and T. Maskawa, Progr. Theor. Phys. **49** 652 (1973).

[2] N. Cabibbo, Phys. Rev. Lett. **10** 531 (1963).

[3] L. Wolfenstein, Phys. Rev. Lett. **51** 1945 (1983).

[4] Particle Data Group, C. Amsler *et al.*, Phys. Lett. **B667** 1 (2008).

[5] J.C. Hardy and I.S. Towner, Phys. Rev. **C79** 055502 (2009).

[6] W.J. Marciano and A. Sirlin, Phys. Rev. Lett. **96** 032002 (2006).

[7] M. Palutan, "Precision tests of the Standard Model with kaon decays", KAON '09, Tsukuba, Japan (2009) and references therein.

[8] S.S. Bocchetta, "Studies of the K_S and K_L lifetimes and BR($K^{\pm} \to \pi^{\pm}\pi^{+}\pi^{-}$) with KLOE", KAON '09, Tsukuba, Japan (2009).

[9] M. Dreucci, "Measurement of the K_S lifetime and CPT symmetry tests in the neutral kaon system with quantum interferometry at KLOE", 2009 Europhysics Conference on High Energy Physics, Krakow, Poland (2009).

[10] RBC and UKQCD Collaborations, P.A. Boyle *et al.*, Phys. Rev. Lett. **100** 141601 (2008).

[11] S. Banerjee, "Tau decays at BABAR", 34th International Conference on High Energy Physics, Philadelphia, USA (2008).

[12] "Flavor Physics in the Quark Sector", M. Antonelli *et al.*, arXiv:0907.5386 [hep-ph] (2009).

[13] KLOE Collaboration, F. Ambrosino *et al.*, Phys. Lett. **B632** 76 (2006).

[14] HPQCD and UKQCD Collaborations, E. Follana *et al.*, Phys. Rev. Lett. **100** 062002 (2008).

[15] A. Ceccucci, Z. Ligeti and Y.Sakai, review in [4].

[16] CLEO Collaboration, D. Besson *et al.*, Phys. Rev. **D80** 032005 (2009).

[17] CLEO Collaboration, J.P. Alexander *et al.*, Phys.Rev. **D79** 052001 (2009), CLEO Collaboration, P.U.E. Onyisi *et al.*, Phys.Rev. **D79** 052002 (2009).

[18] CLEO Collaboration, D. Besson *et al.*, Phys. Rev. **D80** 032005 (2009).

[19] BELLE Collaboration, K. Abe *et al.*, Phys. Rev. Lett. **100** 241801 (2008).

[20] BABAR Collaboration, B. Aubert *et al.*, Phys. Rev. Lett. **98** 141801 (2007).

[21] Fermilab Lattice and MILC Collaborations, J.N. Simone *et al.*, "The D_s and D^+ Leptonic Decay Constants from Lattice QCD", XXVII International Symposium on Lattice Field Theory – LAT2009, Bejing, China (2009).

[22] FlaviAnet Collaboration, http://ific.uv.es/flavianet/

[23] E. Blucher and W.J. Marciano, review in [4].

[24] BABAR Collaboration, B. Aubert *et al.*, Phys. Rev. **D77** 032002 (2008); BELLE Collaboration, I. Adachi *et al.*, arXiv:0810.1657 [hep-ex]; BABAR Collaboration, B. Aubert *et al.*, Phys. Rev. Lett. **100** 231803 (2008); BABAR Collaboration, B. Aubert *et al.*, Phys. Rev. **D79** 012002 (2009).

[25] Heavy Flavor Averaging Group, E. Barberio *et al.* arXiv:0808.1297 [hep-ex] (2008) and up-to-date averages at http://www.slac.stanford.edu/xorg/hfag/

[26] W. Dungel, "Semileptonic $b \to c$ Decays at Belle", 2009 Europhysics Conference on High Energy Physics, Krakow, Poland (2009).

[27] Fermilab Lattice and MILC Collaborations, M. Okamoto *et al.*, Nucl. Phys. Proc. Suppl. **140** 461 (2005).

[28] Fermilab Lattice and MILC Collaborations, C. Bernard *et al.*, Phys. Rev. **D79** 014506 (2009).

[29] BABAR Collaboration, B. Aubert *et al.*, Phys. Rev. Lett. **101**, 081801 (2008); BABAR Collaboration, B. Aubert *et al.*, Phys. Rev. Lett. **98**, 091801 (2007).

[30] BELLE Collaboration, T. Hokuue *et al.*, Phys. Lett. **B648** 139 (2007); BELLE Collaboration, I. Adachi *et al.* arXiv:0812.1414 [hep-ex].

[31] CLEO Collaboration, N.E. Adam *et al.*, Phys. Rev. Lett. **99** 041802 (2007).

[32] Fermilab Lattice and MILC Collaborations, M. Okamoto *et al.*, Nucl. Phys. Proc. Suppl. **140** 461 (2005); HPQCD Collaboration, E. Dalgic *et al.*, Phys. Rev. **D73** 074502 (2006), erratum ibid. **D75** 119906 (2007).

[33] T. Becher, H. Boos and E. Lunghi, JHEP **0712** 062 (2007).

[34] R. Kowalewski and T. Mannel, review in [4].

[35] Fermilab Lattice and MILC Collaborations, J.A. Bailey *et al.*, Phys. Rev. **D79** 054507 (2009).

[36] BABAR Collaboration, B. Aubert *et al.*, Phys. Rev. Lett. **100** 171802 (2008); BELLE Collaboration, P. Urquijo *et al.*, Phys. Rev. Lett. **104** 021801 (2010).

[37] B.O. Lange, M. Neubert and G. Paz, Phys. Rev. **D72** 073006 (2005) and references therein.

[38] J.R. Andersen and E. Gardi, JHEP **0601** 097 (2006); E. Gardi, arXiv:0806.4524 [hep-ph]; P. Gambino *et al.*, JHEP **0710** 058 (2007); U. Aglietti *et al.*, Eur. Phys. Jour. **C59** (2009); U. Aglietti, G. Ferrara and G. Ricciardi, Nucl. Phys. **B768** 85 (2007); C. Bauer, Z. Ligeti and M.E. Luke, Phys. Rev. **D64** 113004 (2001).

[39] T. Inami and C.S. Lim, Prog. Theor. Phys. **65** 297 (1981).

[40] HPQCD Collaboration, E. Gamiz *et al.*, Phys. Rev. **D80** 014503 (2009).

[41] BABAR Collaboration, B. Aubert *et al.*, Phys. Rev. Lett. **97** 201801 (2006); BABAR Collaboration, B. Aubert *et al.*, Phys. Rev. Lett. **88** 221802 (2002); BABAR Collaboration, B. Aubert *et al.*, Phys. Rev. Lett. **88** 201803 (2002); BELLE Collaboration, K. Abe *et al.*, Phys. Rev. **D71** 072003 (2005), erratum ibid. 079903 (2005); BELLE Collaboration, N.C. Hastings *et al.*, Phys. Rev. **D67** 052004 (2003); BELLE Collaboration, Y. Sheng, Phys. Rev. **D67** 092004 (2003).

[42] CDF Collaboration, A. Abulencia *et al.*, Phys. Rev. Lett. **97** 242003 (2006); D0 Collaboration, V.M. Abazov *et al.* Phys. Rev. Lett. **97** 021802 (2006).

[43] BABAR Collaboration, B. Aubert *et al.*, Phys. Rev. **D78** 112001 (2008).

[44] BELLE Collaboration, N. Taniguchi *et al.*, Phys. Rev. Lett. **101** 111801 (2008).

[45] B. Schumm, "New Results on $|V_{td}/V_{ts}|$ from Radiative Decays", CKM 2008: 5th International Workshop on the CKM Unitarity Triangle, Rome, Italy (2008).

[46] CDF Collaboration, T. Aaltonen *et al.*, Phys. Rev. Lett. **103** 092002 (2009).

[47] D0 Collaboration, V.M. Abazov *et al.*, Phys. Rev. Lett. **103** 092001 (2009).

[48] F. Canelli, these proceedings.

[49] A.B. Carter and A.I. Sanda, Phys. Rev. **D23** 1567 (1981); I.I. Bigi and A.I. Sanda, Nucl. Phys. **B193** 85 (1981).

[50] BABAR Collaboration, B. Aubert *et al.*, Phys. Rev. **D79** 072009 (2009); BABAR Collaboration, B. Aubert *et al.*, Phys. Rev. **D80** 112001 (2009); BABAR Collaboration, B. Aubert *et al.*, Phys. Rev. **D69** 052001 (2004); BELLE Collaboration, H. Sahoo, *et al.*, Phys. Rev. **D77** 091103 (2008); BELLE Collaboration, K.-F. Chen, *et al.*, Phys. Rev. Lett. **98** 031802 (2007).

[51] M. Gronau and D. London, Phys. Rev. Lett **65** 3381 (1990).

[52] BABAR Collaboration, B. Aubert *et al.*, Phys. Rev. Lett. **102** 141802 (2009).

[53] BABAR Collaboration, B. Aubert *et al.*, arXiv:0807.4226 (2008); BELLE Collaboration, H. Ishino *et al.*, Phys. Rev. Lett. **98** 211801 (2007); BABAR Collaboration, B. Aubert *et al.*, Phys. Rev. **D76** 012004 (2007); BELLE Collaboration, A. Kusaka *et al.*, Phys. Rev. Lett. **98** 221602 (2007); BABAR Collaboration, B. Aubert *et al.*, Phys. Rev. **D76** 052007 (2007); BELLE Collaboration, A. Somov *et al.*, Phys. Rev. **D76** 011104 (2007).

[54] CKMFitter Collaboration, J. Charles *et al.*, Eur. Phys. J. **C41** 1 (2005) and up-to-date averages at http://ckmfitter.in2p3.fr/ .

[55] V. Lombardo, "Measurements of charmless *B* Decays related to α at BABAR", 2009 Europhysics Conference on High Energy Physics, Krakow, Poland (2009).

[56] M. Gronau and D. London, Phys. Lett. **B253** 483 (1991); M. Gronau and D. Wyler, Phys. Lett. **B265** 172 (1991)

[57] D. Atwood, I. Dunietz and A. Soni, Phys. Rev. Lett. **78** 3257 (1997); D. Atwood, I. Dunietz and A. Soni, Phys. Rev. **D63** 036005 (2001).

[58] A. Giri *et al.*, Phys. Rev. **D68** 054018 (2003); BELLE Collaboration, A. Poluektov *et al.*, Phys. Rev. **D70** 072003 (2004).

[59] N. Lopez-March, "Hadronic decays related to γ at BABAR",2009 Europhysics Conference on High Energy Physics, Krakow, Poland (2009).

[60] A. Poluektov, "CPV measurement in *B* Decays at BELLE", 2009 Europhysics Conference on High Energy Physics, Krakow, Poland (2009).

[61] BABAR Collaboration, B. Aubert *et al.*, Phys. Rev. **D79** 072003 (2009).

[62] CLEO Collaboration, R.A. Briere *et al.*, Phys. Rev. **D80** 032002 (2009).

[63] UTFit Collaboration, M. Ciuchini *et al.*, JHEP **0107** 013 (2001) and up-to-date averages at http://www.utfit.org/

[64] S. Laplace, *et al.*, Phys. Rev. **D65** 094040 (2002).

[65] CDF/D0 $\Delta\Gamma_s, \beta_s$ Combination Working Group, "Combination of D0 and CDF Results on $\Delta\Gamma_s$ and the CP-Violating Phase $\beta_s^{J/\psi\phi}$", CDF/PHYS/BOTTOM/CDFR/9787, D0 Note 5928-CONF (2009).

[66] T. Iijima, these proceedings.

[67] E. Lunghi and A. Soni, Phys. Lett. **B666** 162 (2008).

[68] A. Buras and D. Guadagnoli, Phys. Rev. **D78** 033005 (2008).

[69] J. Ocariz,"The CKM matrix : Status and Sensitivity to New Physics", 2009 Europhysics Conference on High Energy Physics, Krakow, Poland (2009).

Discussion

Andrei Golutvin (CERN/ Imperial College, London/ ITEP, Moscow: A discrepancy between Vub determined from exclusive and inclusive measurements limits significantly the accuray of the comparison of beta with the opposite side of the unitarity triangle. Consequently, a sensitivity to a possible contribution from the phases of new particles, if any, to the angle beta is limited.

Rare B Decays

Toru Iijima

Department of Physics, Nagoya University, Chikusa, Nagoya, 464-8602, Japan

This paper reviews recent experimental results for rare B meson decays, in view of searching for new physics effects, based on data collected by Belle and BaBar at the B-factories, as well as CDF and D0 at the Tevatron.

1 Introduction

The success of B factories, both at KEK and SLAC, have brought the quantitative confirmation of the theory proposed by Kobayashi-Maskawa to explain the CP violation [1]. So far, all the measurements, relevant to the three internal angles and three sides of the Unitarity Triangle (UT), are consistent. It indicates that there is no $O(1)$ correction from New Physics (NP), however, there is still room for sub-leading contribution at $O(0.1)$. Decays of the B meson, the heaviest meson containing the third generation quark, involve a variety of Feynman diagrams sensitive to NP, such as penguin, box and annihilation diagrams. This paper reviews the present status of NP search in the following categories; a) B decays with missing energy($b \to \tau\nu, c\tau\nu, b \to \ell\nu(\gamma)$), b) electromagnetic ($b \to s\gamma$) and electroweak ($b \to s\ell\ell$) penguins, c) leptonic decays ($B_{s(d)} \to \ell\ell$) and d) gluonic penguin decays ($b \to sg$ and $b \to uq\bar{q}$). Relevant Feynman diagrams are shown in Figure 1. Results are taken from Belle and BaBar at the B factories, as well as CDF and D0 at the Tevatron. Throughout the paper, charge conjugate states are implied, and the first and second errors in numerical results represent statistical and systematic errors, respectively.

Studies of rare B decays, especially at the B-factories, rely on success of the accelerators. Figure 2 shows the integrated luminosity of the two experiments, KEKB/Belle and PEP II/BaBar. The achieved peak luminosity is $2.1 \times 10^{34} \mathrm{cm}^{-2}\mathrm{s}^{-1}$ for KEKB and $1.2 \times 10^{34} \mathrm{cm}^{-2}\mathrm{s}^{-1}$ for PEP II. The number of produced $B\overline{B}$ pairs exceeds 800 million for Belle and 470 million for BaBar. Such high luminosity data have enabled us not only to observe rare B decay modes but also to measure detailed information, i.e., distribution of decay quantities, such as decay angle, q^2 and so on.
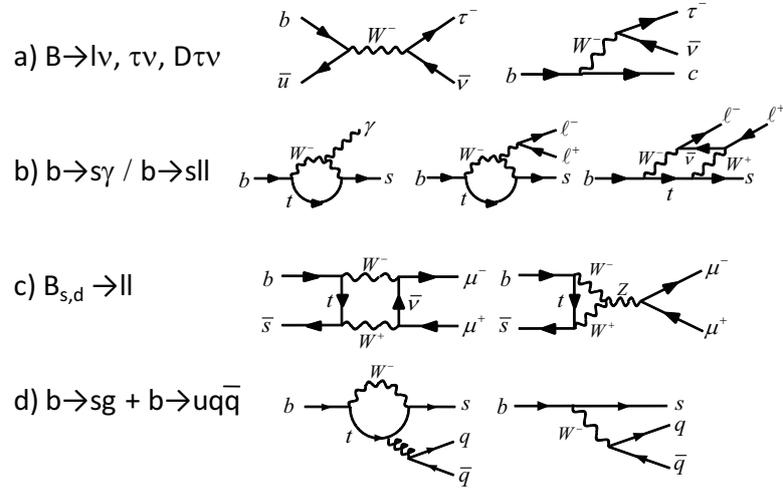
Figure 1: Feynman diagrams of rare B decays discussed in this paper.
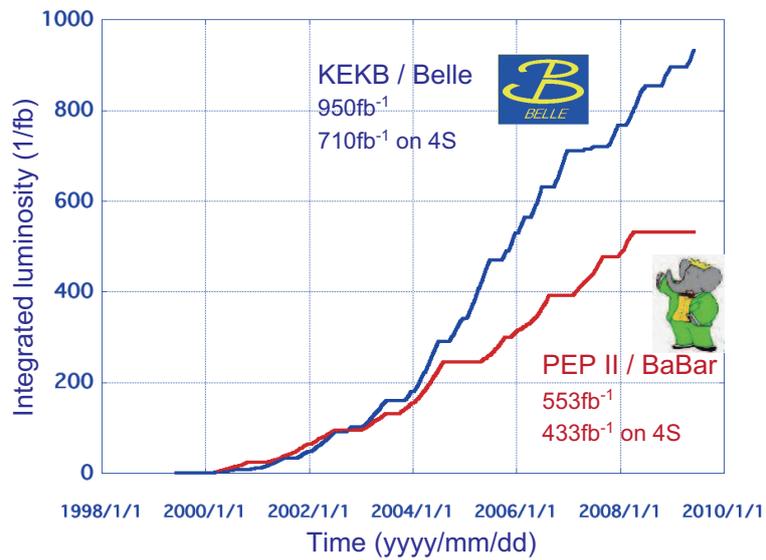
Figure 2: Integrated luminosity at the B factories.

2 B Decays with Missing Energy ($B \to \tau\nu, D\tau\nu, \ell\nu(\gamma)$)

2.1 $B \to \tau\nu$

In the Standard Model (SM), the purely leptonic decay $B^- \to \tau^- \bar{\nu}$ proceeds via annihilation of b and $\overline{u}$ quarks to a W^- boson (see Figure 1). The branching fraction is given by

$$\mathcal{B}(B^- \to \tau^- \bar{\nu}) = \frac{G_F^2 m_B m_\tau^2}{8\pi} \left(1 - \frac{m_\tau^2}{m_B^2}\right)^2 f_B^2 |V_{ub}|^2 \tau_B, \qquad (1)$$

where G_F is the Fermi coupling constant, m_B and m_τ are the B and τ masses, respectively, and τ_B is the B^- lifetime [2]. The expected branching fraction is $(1.20 \pm 0.25) \times 10^{-4}$ using $|V_{ub}| = (4.32 \pm 0.33) \times 10^{-3}$, determined by inclusive charmless semileptonic B decay data [3], and $f_B = 0.190 \pm 0.013$ GeV obtained from recent lattice QCD calculations [4]. Physics beyond the SM, such as supersymmetry or two-Higgs doublet models, could modify $\mathcal{B}(B^- \to \tau^- \bar{\nu})$ through the introduction of a charged Higgs boson [5]. The charged Higgs boson effect is given by $\mathcal{B}(B^- \to \tau^- \bar{\nu}) = \mathcal{B}(B^- \to \tau^- \bar{\nu})_{SM} \times r_H$, where the ratio r_H is given by $r_H = (1 - m_B \tan^2\beta/m_{H^\pm})^2$, using the charged Higgs mass $m_{H^\pm}$ and the ratio of the two Higgs vacuum expectation values $\tan\beta$.

Experimentally, it is challenging to detect decay modes including neutrinos in the final state, such as $B \to \tau\nu$ and $B \to D\tau\nu$ discussed in the following sub-section, since they cannot be kinematically constrained. In order to suppress background, the accompanying B mesons are reconstructed, by using hadronic decays, by using semileptonic decays, and also by calculating the four-vector sum of the PID tracks inclusively without reconstructing the intermediate mesons. Then, on the other side, signals are identified by detecting charged tracks from the signal decays, requiring no extra activities in the electro-magnetic calorimeter, and calculating the missing energy due to neutrinos.

Both Belle and BaBar collaborations have reported branching fractions using the hadronic and semileptonic tags, as summarized in Table 1. Figure 3-a) shows distributions of the extra energy in the electromagnetic colorimeter on the signal side (E_{ECL}), reported by Belle using the semileptonic tags, where one can see the excess due to $B \to \tau\nu$ signals near $E_{\mathrm{ECL}} = 0$. The naive average branching fraction is calculated to be $\mathcal{B}(B \to \tau\nu)_{AVG} = (1.73 \pm 0.35) \times 10^{-4}$, which is consistent with the above SM prediction, and leads to the ratio $r_H = 0.95 \pm 0.32$. Based on this result, the charged Higgs can be constrained in the $(\tan\beta, m_H)$ plane, as shown in Figure 3-b).

It should be noted here that there appears tension in this comparison, if the SM value is taken from the CKM fit rather than from Eq.(1) with inputs of f_B and $|V_{ub}|$. In this case, the average branching fraction $\mathcal{B}(B \to \tau\nu)_{AVG}$ is 2.4 σ higher than the prediction, $\mathcal{B}(B \to \tau\nu)_{\mathrm{CKMfit}} = (0.786^{+0.179}_{-0.083}) \times 10^{-4}$.

2.2 $B \to D\tau\nu$

The semileptonic B decay to the τ channel, $B \to D^{(*)}\tau\nu$, is also sensitive to the charged Higgs. In the SM, the decay occurs via an external W emission diagram with predicted branching fractions of $(0.69 \pm 0.04)\%$ and $(1.41 \pm 0.07)\%$ for $B^0 \to D^- \tau^+ \nu_\tau$ and $B^0 \to D^{*-}\tau^+\nu_\tau$, respectively [10]. On the other hand, if a charged Higgs boson ($H^\pm$) exists, it contributes to the decay amplitude at tree level, and the branching fraction can be modified significantly [11]. The charged Higgs can be constrained based on the ratio, $R(D) = \mathcal{B}(B \to D\tau\nu)/\mathcal{B}(B \to D\ell\nu)$.

Exp.	Tag	$N_{B\bar{B}}$ (10^6)	B (10^{-4})	Ref.
Belle	hadronic	449	$1.79^{+0.56+0.46}_{-0.49-0.51}$	[6]
Belle	semileptonic	657	$1.65^{+0.38+0.35}_{-0.37-0.37}$	[7]
BaBar	hadronic	383	$1.8^{+0.9}_{-0.8} \pm 0.4 \pm 0.2$	[8]
BaBar	semileptonic	459	$1.8 \pm 0.8 \pm 0.1$	[9]
Average			1.73 ± 0.35	

Table 1: Measured branching fractions for $B^- \to \tau^- \bar{\nu}$.

The $B \to D^{(*)}\tau\nu$ and $B^+ \to \tau^+\nu_\tau$ decays have similar sensitivity to $H^\pm$, but with different theoretical systematics; the former suffers from uncertainty in the form factor, while the latter requires knowledge of the B decay constant f_B. Therefore, they provide complementary approaches to searching for $H^\pm$ signatures in B decays.

The BaBar collaboration presented the first evidence of the $B \to D\tau\nu$ decay, by applying the hadronic tags to the 238M $B\bar{B}$ sample. As shown in Figure 3-c), both $B \to D\tau\nu$ and $B \to D^*\tau\nu$ signals are seen as excess of events in the large missing mass region [12]. When D^0 and D^+ modes are combined, the significance of the $B \to D\tau\nu$ signal is found to be 3.6σ, including systematics, and the ratio is found to be $R(D) = 0.42 \pm 0.12 \pm 0.05$. The Belle collaboration applied the inclusive tags, and reported the first observation of $B \to D^*\tau\nu$ [13]. More recently, they has reported preliminary results of $B \to D^{(*)}\tau\nu$ by using the hadronic tag methods, and obtained $R(D) = 0.60 \pm 0.14 \pm 0.08$ [14]. The naive average of the BaBar and Belle results for the ratio is found to be $R(D) = 0.49 \pm 0.10$. This provides a constraint on the charged Higgs, comparable to the one obtained by $B \to \tau\nu$, as shown in Figure 3.

2.3 $B \to \ell\nu(\gamma)$

The BaBar collaboration has presented results of search for purely leponic decays in the electron and muon channels, by applying the inclusive tags on the 468 M $B\bar{B}$ data set. [15]. Reported upper limits for the muon channel, $\mathcal{B}(B \to \mu\nu) < 1.0 \times 10^{-6}$ (90% C.L.), is about a factor of 2 larger than the SM value. They have also reported upper limits for the radiative leptonic decays [16].

3   Radiative Penguin Decays ($b \to s\gamma$)

The radiative penguin decay is one of the most powerful tool to constrain NP. The large data sample at the B factories enable us to measure not only the branching fractions, but also more detailed information such as isospin asymmetry, direct CP asymmetry, as well as the mixing induced time-dependent CP violation. The photon energy spectrum is also an ideal tool to determine the HQE parameters, which are required in deducing $|V_{cb}|$ and $|V_{nb}|$ from semileptonic B decays.

3.1   Exclusive $B \to X_s\gamma$

Figure 4-a) shows the new measurements of exclusive $B \to K^*(892)\gamma$ decays by BaBar, based on 383 M $B\bar{B}$ sample [17]. The figures demonstrate how precisely these decays are measured in the
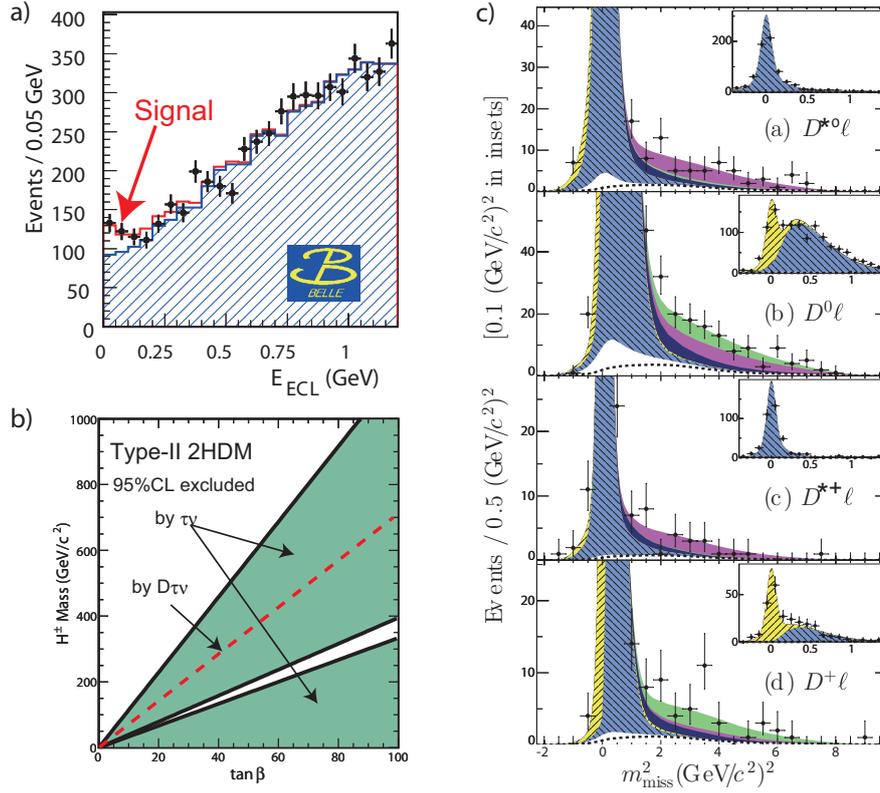
Figure 3: a) Distribution of residual energy E_{ECL} reported by Belle using semileptonic tags. $B^- \to \tau^- \bar{\nu}$ signals are seen near $E_{ECL} = 0$. b) Constraint on charged Higgs in the $(\tan\beta, m_H)$ plane in the type-II two Higgs doublet models. Hatched regions are excluded by $B \to \tau\nu$ at 95% confidence level. The similar exclusion limit by $B \to D\tau\nu$ is also shown by the dashed line. c) Distribution of the missing mass squared m^2_{miss} reported by BaBar using hadronic tags. $B \to D^{(*)}\tau\nu$ signals are seen in the large m^2_{miss} region.

B-factory era. The reported branching fractions are, $\mathcal{B}(B^0 \to K^{*0}\gamma) = (4.47 \pm 0.10 \pm 0.16) \times 10^{-5}$ and $\mathcal{B}(B^+ \to K^{*+}\gamma) = (4.22 \pm 0.14 \pm 0.16) \times 10^{-5}$, which lead to the isospin asymmetry,

$$\Delta_{0+}(B \to K^*\gamma) = \frac{\Gamma(\overline{B}^0 \to \overline{K}^{*0}\gamma) - \Gamma(B^- \to K^{*-}\gamma)}{\Gamma(\overline{B}^0 \to \overline{K}^{*0}\gamma) + \Gamma(B^- \to K^{*-}\gamma)} = 0.066 \pm 0.021 \pm 0.022 \ . \tag{2}$$

The result is consistent with the SM value $(2 - 10\%)$. They have also reported the direct CP asymmetry, $A_{CP}(B \to K^*\gamma) = -0.003 \pm 0.017 \pm 0.007$, and it is consistent with the SM value $(\sim 1\%)$.

The mixing-induced time-dependent CP violation in $b \to s\gamma$ processes is of particular interest as a sensitive probe to unknown right-handed currents. In the SM, photon polarization is flavor specific, and CPV is not expected. On the other hand, if non-SM right-handed current exists, CP violation may appear. The BaBar collaboration has reported such a measurement using the $B \to K\eta\gamma$ decay, based on the full data set (484M $B\overline{B}$) [18]. The reported results are, $\mathcal{B}(B^0 \to K_S^0\eta\gamma) = (7.1^{+2.1}_{-2.0} \pm 0.4) \times 10^{-6}$, $S_{Ks\eta\gamma} = -0.18^{+0.49}_{-0.46} \pm 0.12$, $C_{Ks\eta\gamma} = -0.32^{+0.40}_{-0.39} \pm 0.07$. They reported also the branching fraction and direct CP asymmetry for charged B decays, $\mathcal{B}(B^+ \to K^+\eta\gamma) = (7.7 \pm 1.0 \pm 0.4) \times 10^{-6}$, $A_{CP}(B^+ \to K^+\eta\gamma) = (-9.0^{10.4}_{-9.8} \pm 1.4) \times 10^{-2}$.

The Belle collaboration has reported the results of $B \to K\eta'\gamma$ decay; evidence for the charged B mode, and upper limit for the neutral B, based on the 657M $B\overline{B}$ sample, $\mathcal{B}(B^+ \to K^+\eta'\gamma) = (3.6 \pm 1.2 \pm 0.4) \times 10^{-6}(3.3\sigma)$, $\mathcal{B}(B^0 \to K^0\eta'\gamma) < 6.4 \times 10^{-6}(90\%\text{C.L.})$. [19] They also observed $B \to K\phi\gamma$ decays, based on the 772M $B\overline{B}$ sample [20]. These decay modes will be used for time-dependent CP violation measurements in the near future.

3.2 Inclusive $B \to X_s\gamma$

The Belle collaboration has reported a new result for the inclusive $B \to X_s\gamma$ branching fraction, based on 657M $B\bar{B}$ sample [21]. In the new result, the photon energy threshold is lowered to $1.7 \, \text{GeV}/c$, by which 97% of the decay phase space are covered. This leads to less systematic uncertainty when the result is extrapolated to the total branching fraction and compared to theoretical calculations. Two streams are used in the analysis; one is without tags (MAIN) and the other one with tags using leptons from B decays (LT), which is useful to suppress continuum background. Figure 4-b) shows the photon energy spectrum obtained by averaging the two results. The partial branching fraction in the photon energy range between 1.7 and 2.8GeV, is obtained as $\mathcal{B}(B \to X_s\gamma; 1.7 < E_\gamma(\text{GeV}) < 2.8) = (3.45 \pm 0.15 \pm 0.40) \times 10^{-4}$ with the systematic error dominated by uncertainty in the background estimation.

The new world average for the branching fraction above 1.6GeV is calculated to be $\mathcal{B}(B \to X_s\gamma; E_\gamma > 1.6GeV) = (3.57 \pm 0.24) \times 10^{-4}$, which shows marginal consistency with the most recent NNLO calculation, $(3.15 \pm 0.23) \times 10^{-4}$ [22]. The result constraints the charged Higgs mass above 300GeV. Search for charged Higgs in B decays, $B \to X_s\gamma$ as well as $B \to \tau\nu$ are complementary to the direct search at hadron colliders.

4 Electroweak Penguin Decays ($b \to s\ell\ell$)

The $b \to s\ell\ell$ decay proceeds via the electroweak penguin or box diagrams, to which NP can contribute significantly. There are many observables and distributions, which can be tested, such as the q^2 distribution, K^* longitudinal polarization (F_L), forward-backward asymmetry (A_{FB}), isospin asymmetry (A_I).
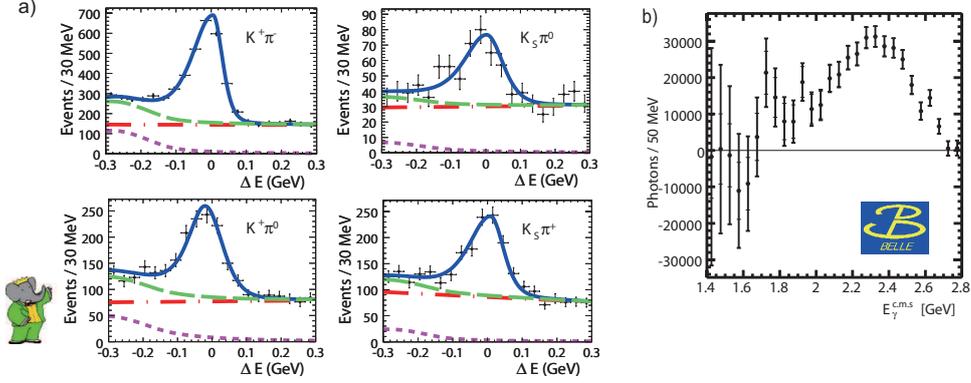
Figure 4: a) Updated results for the exclusive $B \to K^*(892)\gamma$ decays by BaBar. b) The photon energy spectrum for the $B \to X_s\gamma$ reported by Belle.

Table 2 summarized the branching fractions of exclusive $B \to K^*\ell\ell$ decays reported by the Belle, BaBar and CDF experiments. The average branching fraction is found to be $\mathcal{B}(B \to K^*\ell\ell) = (10.0 \pm 1.1) \times 10^{-7}$ and $\mathcal{B}(B \to K\ell\ell) = (4.3 \pm 0.4) \times 10^{-7}$. The q^2 distributions have also been measured, and they are found to be consistent with theoretical predictions within errors.

Exp.	$\mathcal{B}(B \to K^*\ell\ell)$ $[10^{-7}]$	$\mathcal{B}(B \to K\ell\ell)$ $[10^{-7}]$	Ref.
Belle	$10.7^{+1.1}_{-1.0} \pm 0.9$	$4.8^{+0.5}_{-0.4} \pm 0.3$	[23]
BaBar	$7.8^{+1.9}_{-1.7} \pm 1.1$	$3.4 \pm 0.7 \pm 0.2$	[24]
CDF	$8.1 \pm 3.0 \pm 1.0$	$5.9 \pm 1.5 \pm 0.4$	[25]
Average	10.0 ± 1.1	4.3 ± 0.4	

Table 2: Measured branching fractions for $B \to K^{(*)}\ell\ell$. Only $B \to K^{(*)}\mu\mu$ are measured in the CDF result.

The forward-backward asymmetry of the leptons from the $B \to K^*\ell\ell$ is generated by γ/Z interference, and is one of the most interesting observables to search for NP. In both Belle and BaBar analysis, in each q^2 bin, the K^* longitudinal polarization fraction (F_L) is measured by fitting the angular distribution of the kaon, and then the asymmetry (A_{FB}) is deduced by fitting the signal PDF, $\frac{3}{4}F_L(1 - \cos^2\theta_{B\ell}) + \frac{3}{8}(1 - F_L)(1 + \cos^2\theta_{B\ell}) + A_{FB}\cos\theta_{B\ell}$, to the distribution of the angle between the lepton and B meson ($\theta_{B\ell}$). Figure 5 shows the obtained A_{FB} as a function of q^2, compared to the SM prediction shown by blue lines. In the Belle result, the obtained A_{FB} exceeds the SM with a 2.7 σ significance.

Another interesting observable is the isospin asymmetry, defined as,

$$A_I \equiv \frac{(\tau_{B^+}/\tau_{B^0}) \times \mathcal{B}(K^{(*)0}\ell^+\ell^-) - \mathcal{B}(K^{(*)\pm}\ell^+\ell^-)}{(\tau_{B^+}/\tau_{B^0}) \times \mathcal{B}(K^{(*)0}\ell^+\ell^-) + \mathcal{B}(K^{(*)\pm}\ell^+\ell^-)}. \tag{3}$$

As shown in Figure 6, data present slight negative deviation in the low q^2 region below the J/ψ

veto region. The deviation is more significant in the BaBar result; 2.7 σ and 3.2 σ away from zero for $K^*\ell\ell$ and $K\ell\ell$ mode, respectively, and 3.9 σ when the two modes are combined.

It is of particular interest to see the results for A_{FB} and A_I using the full data sets from the two B-factory experiments, and also from the Tevatron experiments.
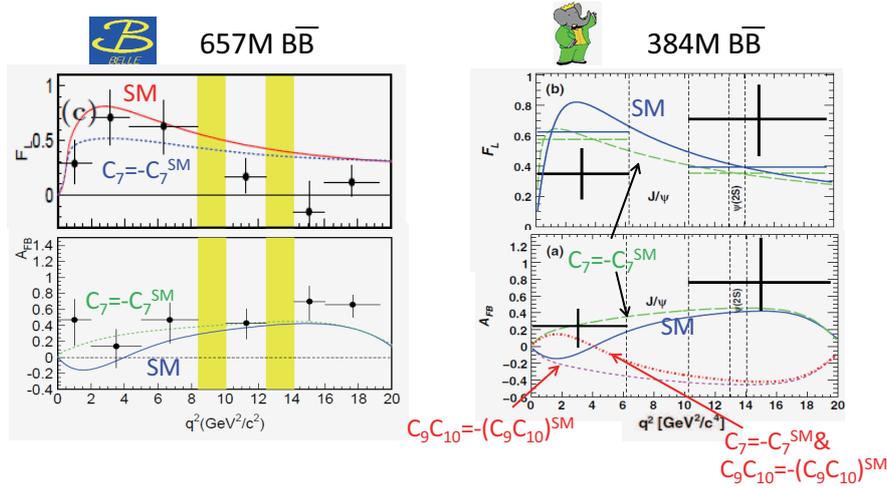
Figure 5: K^* longitudinal polarization fraction (F_L) and forward-backward asymmetry of the leptons (A_{FB}) for $B \rightarrow K^*\ell\ell$ measured by Belle (left) and BaBar(right).
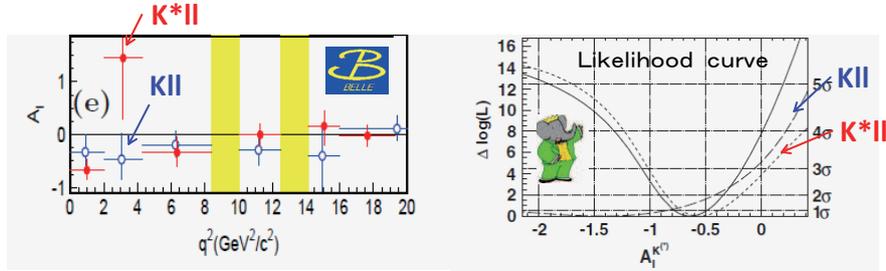
Figure 6: Isospin asymmetry (A_I) for $K^{(*)}\ell\ell$ measured by Belle (left) and BaBar(right).

The Belle collaboration has updated the result for the inclusive $B \rightarrow X_s\ell\ell$ process. The X_s system is reconstructed by one K^+ or K_S^0 plus up to four pions where number of π^0 is restricted to less than 1. The new results are obtained by using about 4 times more data and the improved background rejection than the previous measurement. Approximately, 240 decays are detected in the entire X_s mass region, and 56 decays in the mass region above K^*. The inclusive branching fraction for the entire mass region is deduced to be $(3.33 \pm 0.80^{0.19}_{-0.24}) \times 10^{-6}$.

5   Leptonic B decay $(B_{s(d)} \to \mu\mu)$

The leptonic B decays, $B_{s(d)} \to \mu\mu$, proceed via the diagrams shown in Figure 1-c). Within the SM, the branching fractions are predicted to be $O(10^{-9})$ for $B_s \to \mu\mu$ and $O(10^{-10})$ for $B_d \to \mu\mu$ [26]. The decay amplitude can be enhanced by several orders of magnitude in some SUSY models through the neutral Higgs exchange if the value of $\tan\beta$ is large.

Figure 7 shows the result updated by CDF with 3.7 fb^{-1} data, based on analysis technique identical to the previous one with 2 fb^{-1} data. No significant excess are seen, and upper limits at 95%C.L. are found to be 4.3×10^{-8} for B_s and 7.6×10^{-9} for B_d [27]. The D0 collaboration has reported the expected upper limit using 5 fb^{-1} data, 4.7×10^{-8} for B_s at 95% C.L., that is similar to the limited obtained by CDF [28].

The present upper limits from CDF and D0 are about 10 times above the SM prediction. By accumulating more data; 6 fb^{-1} already at hand, and two times more data expected by the end of the Tevatron Run-II, and also by improving the analysis, they will provide significantly tighter constraints on NP parameter space.
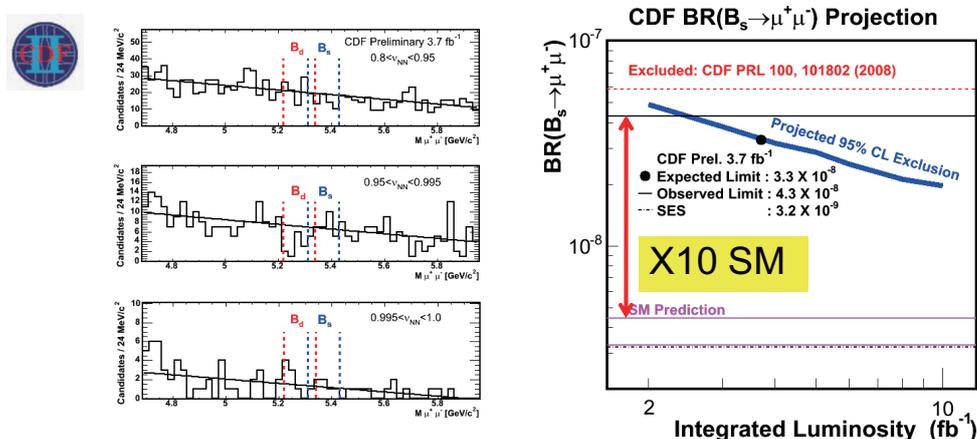
Figure 7: The di-muon invariant mass distribution in 3 NN(Neural Net) bins (left). Projected 95% C.L. exclusion limit as a function of the integrated luminosity (right).

6   Charmless Hadronic Decays

Charmless hadronic decays proceed via $b \to s$ gluonic penguin and/or $b \to u$ tree diagrams. The interference between the two diagrams induce direct CP violation. $B^+ \to \eta K^+$, $B^0 \to \rho^+\pi^-$, $B^+ \to \rho^0 K^+$, $B^+ \to D^{(*)0}K^+$.

6.1 $A_{CP}(K\pi)$ puzzle

The large luminosity data from the B factories have enabled us to measure the direct CP asymmetry (A_{CP}) for many charmless hadronic decay modes. Figure 8-a) summarizes the current status [3]. Up to now, direct CP violation has been observed in $K\pi$ and $\pi\pi$ decays, and evidence have been seen in 5 decay modes; $B^0 \to \eta K^{*0}$, The present average value for the

$B \to K\pi$ decay is $A_{CP}(K^+\pi^-) = -0.098^{+0.012}_{-0.011}$ and $A_{CP}(K^+\pi^0) = +0.050 \pm 0.025$, leading to the difference,

$$\Delta A_{CP}(K\pi) = A_{CP}(K^+\pi^0) - A_{CP}(K^+\pi^-) = 0.144 \pm 0.029 . \qquad (4)$$

The difference is more than 5 σ significant, therefore, very firm experimentally. On the other hand, since the charged B decay amplitude must be similar to the neutral B, up to sub-leading corrections, one expect $\Delta A_{CP}(K\pi) \sim 0$. The sub-leading corrections may arise from electroweak penguin amplitude and color-suppressed tree amplitude. Enhancement of the color-suppressed tree amplitude may change $\Delta A_{K\pi}$, however, it would have to be larger than the color-allowed tree amplitude [29]. The electroweak amplitude could be the source of difference. However, as a loop amplitude, it can pick up a CP violating phase from NP. In order to clarify the issue, one can test the isospin relation between $A_{K\pi}$ asymmetry for the four $K\pi$ decays, $A_{K^-\pi^+}, A_{K^-\pi^0}, A_{K^0\pi^+}$ and $A_{K^0\pi^0}$ [30]. If the isospin relation violates, it would indicates that contribution of the electroweak penguin was significant. This require even more data because of the lower detection efficiency of $B^0 \to K^0\pi^0$, and also the necessity of flavor tagging to measure $A_{K^0\pi^0}$.
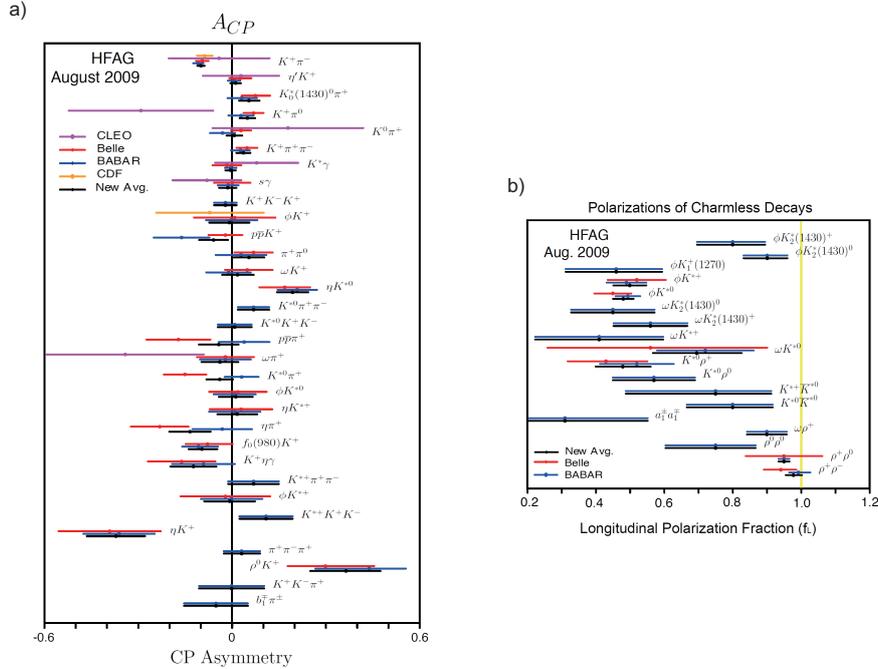
Figure 8: Current status of a) direct CP asymmetry and b) longitudinal polarization fraction in charmless hadronic B decays.

6.2 Modes including η and η'

The decay modes including η and η' have attracted much interests, since unexpectedly large branching fraction was measured at the CLEO experiment [31]. The BaBar collaboration has

published updates for many decay modes including η and $\eta^{'}$, using the full data set, and found evidence for CP asymmetry $A_{CP}(B^+ \to \eta K^+) = -0.36 \pm 0.11 \pm 0.03$, and evidence for the three decay modes; $B^0 \to \eta K^0, \eta\omega$, and $\eta^{'}\omega$ [32]. The Belle collaboration has reported inclusive branching fraction for $B \to X_s\eta$, based on the 657M $B\bar{B}$ sample. The partial branching fraction for the X_s mass region from 0.4 to 2.6 GeV/c^2 is found to be $\mathcal{B}(B \to X_s\eta; 0.4 < M_{X_s}(\text{GeV}/c^2) < 2.6) = (25.5 \pm 2.7 \pm 1.6^{+3.8}_{-14.2}) \times 10^{-5}$, where the last error is the modeling error [33].

6.3 $B \to VV$ modes

In the B meson decays to two vector mesons, $B \to VV$, we naively expect the longitudinal polarization factor is close to 1. However, the polarization factor for the penguin dominated $B \to \phi K^*$ decay was found to be about 0.5. Since then this problem has been known as the "polarization puzzle". On the other hand, the factor is close to one for the tree-dominated $B \to \rho\rho$ decay, and the vector-tensor decay mode $B \to \phi K_2^*(1430)$.

Improved understanding of these effects can come from data in decays such as $B \to \omega K^*$, which is related to $B \to \phi K^*$ via $SU(3)$ symmetry. The BaBar collaboration has reported measurements of B meson decays to the final states ωK^*, $\omega\rho$, and ωf_0, where K^* indicates a spin 0, 1 or 2 strange meson. The measured f_L is found to be near 1.0 for $B^+ \to \omega\rho^+$, as it is for $B \to \rho\rho$. On the other hand, for the vector-tensor $B\omega K_2^*(1430)$ decays, f_L is close to 0.5, as it is for $B \to \phi K^*$ decays, and about 4σ away from 1.0 for both charge states. They also measured the $b \to d$ penguin decays $B \to K^{*0}K^{*+}$ and its polarization [34].

7 Summary

In summary, the following points are addressed.

- The large data samples of B decays accumulated at the B experiments, Belle and BaBar, as well as the Tevatron experiments, CDF and D0, have made it possible to measure not only the branching fractions but also more detailed information (q^2 distribution, A_{CP}, A_{FB} etc. of rare B decays to probe NP.

- There are some hints of NP (puzzles) in the existing data; 1) $\mathcal{B}(B^- \to \tau^-\nu)$ larger than the prediction from the CKM fit, 2) $A_{FB}(B \to K^*\ell\ell)$ and $A_I(B \to K^*\ell\ell)$ in the low q^2 region deviated from the SM prediction, 3) Difference of CP asymmetry in $B \to K\pi$ decays between neutral and charged B decays, 4) Longitudinal polarization in $B \to VV$ decays smaller than the prediction.

- Search for $B_{s(d)} \to \mu\mu$ at Tevatron will be at critical corner in coming years.

- We need much more luminosity to clearly see the NP effects as the level of O(0.1) correction to the SM.

In the near future, more results with improved precision are expected from the B factories and the Tevatron experiments. Moreover, the next generation experiments, LHCb and Super B factories, will enable us measurements with much more improved precision. Let us prepare for exciting future in B physics !

Acknowledgments

References

[1] M. Kobayashi and T. Maskawa, Prog. Theor. Phys. **49**, 652 (1973).

[2] C. Amsler *et al.*(Particle Data Group), Phys. Lett. B **667**, 1 (2008).

[3] The average at ICHEP2008 calculated by the Heavy Flavor Averaging Group, http://www.slac.stanford.edu/xorg/hfag/semi/index.html

[4] Elvira Gamiz, Christine T. H. Davies, G. Peter Lepage, Junko Shigemitsu, Matthew Wingate, Phys. Rev. D **80**, 014503 (2009).

[5] W. S. Hou, Phys. Rev. D **48**, 2342 (1993).

[6] K. Ikado *et al.* (Belle Collaboration), Phy. Rev. Lett. **97** 251802 (2006).

[7] I. Adachi *et al.* (Belle Collaboration), arXiv:0809.3834.

[8] B. Aubert *et al.* (BaBar Collaboration), Phys. Rev. D **77**, 011107(R) (2008).

[9] B. Aubert *et al.* (BaBar Collaboration), arXiv:0809.4027.

[10] C.-H. Chen and C.-Q. Geng, J. High Energy Phys. 10, 053 (2006).

[11] B. Grzadkowski and W.-S. Hou, Phys. Lett. B **283**, 427 (1992); M. Tanaka, Z. Phys. C **67**, 321 (1995); K. Kiers and A. Soni, Phys. Rev. D **56**, 5786 (1997); H. Itoh, S. Komine and Y. Okada, Prog. Theor. Phys. **114**, 179 (2005); Ulrich Nierste, Stephanie Trine, Susanne Wesoff, arXiv:0801.4938.

[12] B. Aubert *et al.* (BaBar Collaboration), Phys. Rev. Lett. **100**, 021801 (2008); Phys. Rev. D **79**, 092002 (2009).

[13] A. Matyja, M. Rozanska *et al.* (Belle Collaboration), Phys. Rev. Lett. **99**, 191807 (2007).

[14] I. Adachi *et al.* (Belle Collaboration), arXiv:0910.4301.

[15] B. Aubert *et al.* (BaBar Collaboration), Phys. Rev. D **79**, 091101(R) (2009).

[16] B. Aubert *et al.* (BaBar Collaboration), Phys. Rev. D **80**, 111105(R) (2009).

[17] B. Aubert *et al.* (BaBar Collaboration), Phys. Rev. Lett. **103**, 211802 (2009).

[18] B. Aubert *et al.* (BaBar Collaboration), Phys. Rev. D **79**, 011102(R) (2009).

[19] R. Wedd *et al.* (Belle Collaboration), arXiv:0810.0804, to appear in Phys. Rev. D (RC).

[20] I. Adachi *et al.* (Belle Collaboration), arXiv:0911.1779.

[21] A. Limosani *et al.* (Belle Collaboration), Phys. Rev. Lett. **103**, 241801 (2009).

[22] M. Misiak *et al.*, Phys. Rev. Lett. **98**, 022002 (2007).

[23] J.-T. Wei, P. Chang *et al.* (Belle Collaboration), Phys. Rev. Lett. **103**, 171801 (2009).

[24] B. Aubert *et al.* (BaBar Collaboration), Phys. Rev. D **79**, 031102(R) (2009); B. Aubert *et al.* (BaBar Collaboration), Phys. Rev. D **73**, 092001 (2009).

[25] T. Aaltonen *et al.* (CDF Collaboration), Phys. Rev. D **79**, 011104(R) (2009).

[26] A.J. Buras, Phys. Lett. B **566**, 115 (2003).

[27] See http://www-cdf.fnal.gov/physics/S09CDFResults.html.

[28] D0 Note 5906-CONF.

[29] S. Baek and D. London, Phys. Lett. B **653**, 249 (2007); S. Baek *et al.* Phys. Rev. D **71**, 057502 (2005).

[30] M. Gronau and J. Rosner, Phys. Rev. D **74**, 057503 (2006).

[31] T.E. Browder *et al.* (CLEO Collaboration) Phys. Rev. Lett. **81**, 1786 (1998); G. Bonvicini *et al.* (CLEO Collaboration) Phys. Rev. D **68**, 011101 (2003).

[32] B. Aubert *et al.* (BaBar Collaboration), Phys. Rev. D **80**, 112002 (2009).

[33] I. Adachi *et al.* (Belle Collaboration), arXiv:0910.4751.

[34] B. Aubert *et al.* (BaBar Collaboration), Phys. Rev. D **79**, 052005 (2009).

Discussion

Achmed Ali (DESY): Your data seem to show some deviations in $K^* \to l^+l^-$ forward backward asymmetry and in the isospin asymmetry, but you did not show us the di-lepton mass spectrum itself. How does this spectrum compare to the existing models you have?

Answer: The dilepton mass spectrum is shown in the slide, and is consistent with the Standard Model within uncertainties.

Heavy Flavour Spectroscopy

Jolanta Brodzicka[1]

[1]Institute of Nuclear Physics Polish Academy of Sciences, Krakow, Poland

Study of heavy hadrons is a valuable test of QCD predictions and a search for exotic phenomena. In this review the recent experimental results on hadrons of heavy flavours are presented. These include measurements of properties of the known $c\bar{c}$ and $b\bar{b}$ quarkonium states, as well as observations of new hadrons, like charmed-strange mesons, beauty baryons and a ground bottomonium state, the η_b. Also charmonium-like XYZ resonances, being candidates for exotic particles, are reviewed.

1 Introduction and motivation

Study of heavy hadrons is a study of strong interactions and a test of QCD predictions. Forces binding quarks into hadrons of either meson or baryon configuration are described by QCD. Quarks are considered to be bound into hadrons by single-gluon exchange plus a linear confining potential. The potential models, incorporating the general features of QCD, describe the spectra and properties of the hadrons. This allows one to obtain a picture of hadron multiplets including masses of resonances, their electromagnetic and hadronic transitions, decays, fine and hyperfine splittings between the states, etc. Since the models give detailed predictions for such observables, they can be validated by comparing with experimental measurements. Measured variances from theoretical predictions could indicate new phenomena. Alternative way to generate QCD observables are numerical lattice QCD computations which also can be tested by experiments.

The QCD-motivated models predict also an existence of hadrons of more complex structure than conventional mesons or baryons, such as hybrids and multiquark states of either molecular or tetraquark configuration. Molecular state [1] consists of two mesons weakly bound through pion exchange. Because of a loose binding, the comprising mesons decay as if they are free. Tetraquark is a tightly bound four-quark state of for example diquark-diantiquark configuration where the comprising quarks group into colour-triplet clusters interacting by a gluon exchange [2]. In decay process the quarks rearrange to form colour-singlet mesons which subsequently dissociate. Some multiquarks can be easily distinguished from conventional states, for example ones with non-zero charge [$cd\bar{c}\bar{u}$] or strangeness [$cd\bar{c}\bar{s}$]. Hybrid mesons in addition to quark-antiquark component contain an excited gluon [3]. The lowest charmonium hybrids are predicted by lattice QCD to have masses of about $4.2\text{GeV}/c^2$. Some of the hybrids can have exotic quantum numbers like $J^{PC} = 0^{+-}, 1^{-+}, 2^{+-}$, not possible for conventional states. Observation of state with such a spin-parity would indicate existence of exotic resonance.

Model calculations for heavy hadrons are easier and more reliable than for light ones. Also spectra of heavy hadrons are much cleaner with regard to dense spectrum of light states. Therefore exotic states containing for example $c\bar{c}$ or $b\bar{b}$ are expected to be identified easier than

the ones predicted in the light spectrum. However no unambiguous evidence for exotic states has been found till recently when the XYZ particles were observed giving a hint of the exotic spectroscopy. All these make spectroscopy of heavy hadrons even more interesting.

2   Charmed-strange mesons

Charmed-strange mesons are heavy-light systems for which the potential models employ the heavy quark symmetry [4]; in this picture such mesons become similar to the hydrogen atom.

In the spectrum of $c\bar{s}$ multiplets there are two S-wave states, D_s^+ and D_s^{*+} with $J^{PC} = 0^-$, 1^-, whereas orbitally excited P-wave states are due to relativistic corrections split into four states with quantum numbers of 0^+, 1^+, 1^+, 2^+, and are respectively identified with $D_{s0}^*(2317)^+$, $D_{s1}(2460)^+$, $D_{s1}(2536)^+$ and $D_{s2}^*(2573)^+$. As properties of the states with masses at 2317 MeV/c^2 and 2460 MeV/c^2 contradict predictions of the most potential models, more exotic assignments have been also proposed for the new states, like DK molecules, multiquark states or mixtures of P-wave $c\bar{s}$ meson with $c\bar{s}q\bar{q}$ tetraquark; chiral partners of D_s and $D_s^\star$ [5]. Although some quark models already succeeded in reproducing the low masses of these states by considering both chiral and heavy quark symmetries [6], it is clear that our understanding of $c\bar{s}$ spectroscopy is incomplete.

Two more $c\bar{s}$ mesons, the $D_{s1}^*(2700)^+$ 1^- state [7] and the $D_{sJ}^*(2860)^+$ [8], observed in their decays into the DK final states, are candidates for either radial or higher orbital excitations. Additional measurements of their properties, especially of new decay modes, may help to distinguish between these two interpretations.

Recently BaBar has studied the mass spectrum of $D^{(*)}K$ inclusively produced in e^+e^- annihilation [9]. In the DK system the $D_{s1}^*(2700)^+$ and $D*_{sJ}(2860)^+$ states, are confirmed, whereas in the D^*K mass distribution, in addition to these two mesons also a new broad state has been found with mass of 3040 MeV/c^2 and width of about 240 MeV/c^2. Nonobservation of the $D_{sJ}(3040)^+ \to DK$ suggests unnatural parity (0^-, 1^+, 2^-, etc.) for this meson, whereas observation of the $D_{s1}^*(2700)^+$ and $D_{sJ}^*(2860)^+$ in both DK and D^*K final states rules out 0^+ assignment and implies natural parities (1^-, 2^+, 3^-) for them. Ratios of branching fractions have been measured to be: $\frac{\mathcal{B}(D_{s1}^*(2700)^+ \to D^*K)}{\mathcal{B}(D_{s1}^*(2700)^+ \to DK)} = 0.91 \pm 0.13 \pm 0.12$ and $\frac{\mathcal{B}(D_{sJ}^*(2860)^+ \to D^*K)}{\mathcal{B}(D_{sJ}^*(2860)^+ \to DK)} = 1.10 \pm 0.15 \pm 0.19$. This favours for the $D_{s1}^*(2700)^+$ an interpretation as first radial excitation of D_s^{*+}, the 2^3S_1 [10]. For the $D_{sJ}^*(2860)^+$ and the $D_{sJ}(3040)^+$ interpretations as radial excitations with respectively $J^P = 3^-$ and $J^P = 1^+$ are proposed [11].

3   Charmonia

All the $c\bar{c}$ states predicted to have masses below the threshold for open charm production have been observed. Discovery of the $\eta_c(2S)$ as well as of the most elusive state h_c, have completed the list of low lying charmonia. All these states have properties that agree quite well with the predictions of the potential models. As for the states above the $D\bar{D}$ mass threshold, despite recent experimental progress, situation is not well established and many resonances remain unobserved. The known charmonia above the $D\bar{D}$ mass threshold: $\psi(3770)$, $\psi(4040)$, $\psi(4160)$ and $\psi(4415)$ are 1^{--} states corresponding respectively to 1^3D_1, 3^3S_1, 4^3S_1 and 2^3D_1. Their parameters have been determined from the fit to the R_c spectrum defined as a ratio of the measured inclusive hadronic cross-section $e^+e^- \to c\bar{c}$ to the calculated cross-section for

$e^+e^- \rightarrow \mu^+\mu^-$. The R_c values measured by BES in energy scans at center-of-mass (cms) energies between 3.7 and 5.0 GeV have been recently refitted with interferences between the ψ states allowed [12]. As a result, some of the resonance parameters, especially of the $\psi(4160)$, have significantly changed with respect to the previous, incoherent approach [13]. However fitting such inclusive data is complicated and yields the resonant parameters being strongly model-dependent as there are many decay channels allowed, like $D^{(*)}\bar{D}^{(*)}$ and $D_s^{(*)}\bar{D}_s^{(*)}$. To reduce this effect, one could fit exclusive cross-sections for $e^+e^- \rightarrow D^{(*)}\bar{D}^{(*)}$ accessed through initial state radiation (ISR) process, once they are measured with statistics high enough.
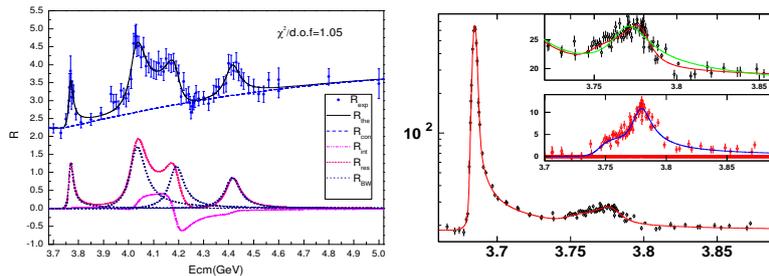
Figure 1: (Left) Fit to the R_c values. The solid curve shows the best fit, R_{BW} shows contributions from each resonance, R_{int} shows interference. (Right) Inclusive hadronic cross-section (in [nb]) versus the cms energies. In the upper sub-figure the fit for the one amplitude hypothesis (green line) is compared with the fit for hypothesis with two resonances (red line).

BES has also examined fine-grained R_c spectrum in the cms energy region between 3.70 and 3.87 GeV. While the $\psi(3770)$ resonance was believed to be the only structure in that region, BES found a line-shape of the $\psi(3770)$ to be anomalous [14]. The data significantly favour a fit with the two resonance hypothesis over the fit with a single $\psi(3770)$ resonance (Fig. 1). This new resonance structure, unless these are some dynamics effects distorting the pure Breit-Wigner line-shape (for example rescattering of $D\bar{D}$), may help to solve the puzzle related to non-$D\bar{D}$ decays of the $\psi(3770)$. Large inclusive non-$D\bar{D}$ branching fraction (15%), has not been confirmed by searches for exclusive decays; the summed non-$D\bar{D}$ decays are less than 2%.

Unobserved ground charmonia $1^3D_{c2,c3}$ and 1^1D_{c2} are predicted to have masses close to the $\psi(3770)$ mass, relatively small widths and are expected to decay to lower-lying charmonia. Therefore their observation is feasible. The next unseen multiplet are radially excited states $\chi_{c1,c2,c3}(2P)$ $(2^3P_{c1,c2,c3})$ and $h_c(2P)$ (2^1P_{c1}). They should lie in mass range of $3800 - 3980$ MeV/c^2 and have widths of $30 - 150$ MeV/c^2. The $Z(3930)$ observed in its decay to the $D\bar{D}$ and bearing quantum numbers of 2^{++}, is identified with the $\chi_{c2}(2P)$ [15]. Some of the other recently found charmonium-like states, the XYZ, could be candidates for the missing charmonia. However their properties are either unusual or forbidden for conventional $c\bar{c}$ states and, as such, are candidates for the exotic hadrons, although most of them still await confirmation and need their properties to be further studied before any decisive interpretation is made.

4 Charmonium-like states

4.1 $X(3872)$

Out of the XYZ states, the first and most famous one is the $X(3872)$ observed by Belle in the $M(J/\psi\pi^+\pi^-)$ spectrum in $B^+ \to J/\psi\pi^+\pi^- K^+$ decays and further confirmed by CDF and $D\slashed{0}$ to be produced in $p\bar{p}$ collisions, as well as by BaBar [16]. Mass of the $X(3872)$ has been recently precisely measured by CDF to be $m_{X(3872)} = 3871.61 \pm 0.16 \pm 0.19$ MeV/c^2 (Fig. 2) [17], its total width is $\Gamma_{X(3872)} < 2.3$ MeV/c^2. The $X(3872)$ mass is in close vicinity of the sum of the D^0 and D^{*0} masses (3871.81 ± 0.36 MeV/c^2). Whether the $X(3872)$ lies below or above that threshold still remains a question important to understand a nature of the $X(3872)$.

In addition to $J/\psi\pi^+\pi^-$ where dipion mass is consistent with originating from $\rho(770)$ [18], also evidence of the $X(3872) \to J/\psi\pi^+\pi^-\pi^0$ mode was found [19]; comparable rates of these decays suggest large isospin violation. An evidence of radiative decays to $J/\psi\gamma$ and $\psi(2S)\gamma$ [20] indicate C-parity$= +$ for the $X(3872)$. The mentioned properties along with results of the CDF angular analysis [21] strongly favour $J^{PC} = 1^{++}$.

Narrow near-threshold enhancement which could originate from the $X(3872)$, has been observed in the mass distribution of the $D^0\bar{D}^{*0}$ system produced in $B \to KD^0\bar{D}^{*0}$ decays (Fig. 2) [22]. New Belle measurement gives a position of the peak to be $3872.6^{+0.5}_{-0.4}\pm0.4$ MeV/c^2, thus is in good agreement with the $X(3872) \to J/\psi\pi^+\pi^-$ mass; the mass measured by BaBar, $3875.1^{+0.7}_{-0.5} \pm 0.5$ MeV/c^2, is slightly larger.
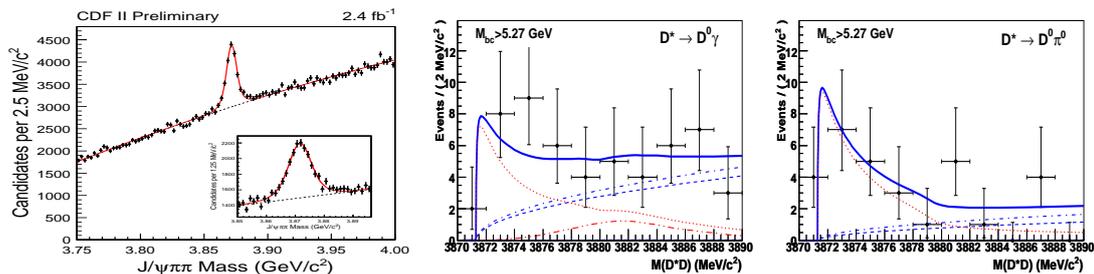
Figure 2: Left: $M(J/\psi\pi^+\pi^-)$ distribution from CDF. Middle and right: $M(D^0\bar{D}^{*0})$ distributions for $D^{*0} \to D^0\gamma$ and $D^{*0} \to D^0\pi^0$ from Belle. Red-dotted line is fit result with the Flatté parameterization, blue-solid line is fit using the Breit-Wigner function.

As finding 1^{++} charmonium fitting the $X(3872)$ failed, many theorists suggested that this particle may be a four-quark meson. A mass of the $X(3872)$ has triggered speculations that it is a molecular bound state of D^0 and $\bar{D}^{*0}$ lying just below the $D^0 D^{*0}$ threshold [23]. Large branching fraction of $X(3872) \to D^0\bar{D}^{*0}$, measured to be one order of magnitude larger than for $X(3872) \to J/\psi\pi^+\pi^-$, supports this interpretation. However the large partial width of $X(3872) \to \psi(2S)\gamma$ with respect to $J/\psi\gamma$ is problematic for the molecular scenarios, whereas can be naturally explained in the framework of quark models. To overcome this, an admixture of $c\bar{c}$ component in the $X(3872)$, in addition to the molecular components, was proposed [24]. Such a charmonium admixture could also explain a large cross-section for prompt production of the $X(3872) \to J/\psi\pi\pi$ seen by CDF and $D\slashed{0}$ [25]; formation of J/ψ from largely separated D^0 and $\bar{D}^{*0}$ constituents is far more difficult than from $c\bar{c}$ component.

Another four-quark interpretation suggests that the $X(3872)$ is a tightly bound diquark-diantiquark system [26]. In this scenario one expects a doublet, $X_u = [cu][\bar{c}\bar{u}]$ and $X_d = [cd][\bar{c}\bar{d}]$, produced respectively in charged $B^+ \rightarrow K^+ X_u$ and neutral $B^0 \rightarrow K^0 X_d$ decays and having masses which differ by a few MeV [28]. However studies by Babar and Belle have not revealed such a mass split [27]; CDF have found no evidence of two states either. In addition, an isospin partner state with quark composition $[cu][\bar{c}\bar{d}]$ is expected to exist and decay to the $J/\psi\pi^+\pi^0$. Nevertheless any charged partner of the $X(3872)$ has not been observed so far [29].

Thus, in view of the mentioned experimental results, interpretation of the $X(3872)$ as a mixture of the molecule with the conventional $c\bar{c}$ state seems to be favourable.

4.2   News on Y family

Another states which await understanding are $Y(4008)$, $Y(4260)$, $Y(4360)$ and $Y(4660)$. These are 1^{--} resonances observed in the $J/\psi\pi^+\pi^-$ and $\psi(2S)\pi^+\pi^-$ systems produced in the ISR reaction $e^+e^- \rightarrow \gamma_{ISR}Y$ [30]. Their parameters do not coincide with any of the vector charmonia observed so far and are inconsistent with the quark model calculations for charmonia. Although the masses of the Y states are above the threshold for decays to final states like $D\bar{D}$, $D\bar{D}^*$ or $D^*\bar{D}^*$, there are no clear peaks in the cross-sections for $e^+e^- \rightarrow D^{(*)}\bar{D}^{(*)}$ [31] that could originate from the Y states.

Recently BaBar has fitted invariant mass spectra of the $D^{(*)}\bar{D}^{(*)}$ systems produced in the ISR process. In addition to the ψ vector states, a contribution from the $Y(4260)$ resonance has been coherently added. No evidence of the $Y(4260)$ has been found; the corresponding upper limits are $\frac{\mathcal{B}(Y(4260)\rightarrow D\bar{D})}{\mathcal{B}(Y(4260)\rightarrow J/\psi\pi^+\pi^-)} < 1$, $\frac{\mathcal{B}(Y(4260)\rightarrow D\bar{D}^*)}{\mathcal{B}(Y(4260)\rightarrow J/\psi\pi^+\pi^-)} < 34$, $\frac{\mathcal{B}(Y(4260)\rightarrow D^*\bar{D}^*)}{\mathcal{B}(Y(4260)\rightarrow J/\psi\pi^+\pi^-)} < 40$ [32]. Instead, the partial decay widths for the hadronic transitions of the Y states to $J/\psi\pi\pi$ or $\psi(2S)\pi\pi$ are very large ($\mathcal{O}(\mathrm{MeV})$) and, as such, unlikely for the conventional $c\bar{c}$ states. Other possible interpretations of the Y states are: charmonium hybrids predicted in this mass region and expected to decay dominantly into $D\bar{D}_1$; $cq\bar{c}\bar{q}$ tetraquarks, $D^*\bar{D}^*$, $D\bar{D}_1$ and $D^*\bar{D}_0^*$ molecules or just S-wave charm meson thresholds [33]. More experimental information on the decay properties is needed to test these scenarios, such as searching for other close charm decay modes ($J/\psi\pi^0\pi^0$, $J/\psi\eta$, $\chi_c\omega$), as well as open charm channels, especially $D\bar{D}_1$ followed by $\bar{D}_1 \rightarrow \bar{D}^*\pi$. In a Belle search for the latter decay channel, amplitudes of the Y states obtained in the fit to the $M(D^0 D^{*-}\pi^+)$ spectrum are found to be consistent with zero. Upper limit $\frac{\mathcal{B}(Y(4260)\rightarrow D^0 D^{*-}\pi^+)}{\mathcal{B}(Y(4260)\rightarrow J/\psi\pi^+\pi^-)} < 9$ [34], although not stringent with currently available statistic, does not support the hybrid interpretation.

4.3   Y(4140)

An evidence of the $Y(4140)$ has been found nearby mass threshold of the $J/\psi\phi$ system produced in the $B^+ \rightarrow J/\psi\phi K^+$ decays exclusively reconstructed by CDF [35]. Mass and width of the structure (Fig. 3) have been measured to be $4143.0\pm2.9\pm1.2$ MeV/c^2 and $11.7^{+8.3}_{-5.0}\pm3.7$ MeV/c^2; the $Y(4140)$ signal yield 14 ± 5 has significance of 3.8σ. The $Y(4140)$ could be a candidate for a multiquark state of $[cs\bar{c}\bar{s}]$ composition, for example a $D_s^{*+}D_s^{*-}$ molecule [36].

Belle having four times larger sample of the $B^+ \rightarrow J/\psi\phi K^+$ decays reconstructed, have found a yield of the $Y(4140)$ to be only $7.5^{+4.9}_{-4.4}$ from the fit with the resonance parameters fixed to the CDF ones (Fig. 3) [37]. Because of low reconstruction efficiency close to the $M(J/\psi\phi)$ threshold, Belle data have sensitivity lower than the CDF one. The upper limit set by Belle

$\mathcal{B}(B^+ \to Y(4140)K^+) \times \mathcal{B}(Y \to J/\psi\phi) < 6 \times 10^{-6}$ remains in agreement with this branching fraction product measured by CDF to be $(9.0 \pm 3.4 \pm 2.9) \times 10^{-6}$.

Also Belle has investigated the $J/\psi\phi$ system produced in the $\gamma\gamma$ fusion processes [38]. Such a reaction allows states with $J^{PC} = 0^{++}$ and 2^{++} to be formed. No signal has been found in $M(J/\psi\phi)$ around 4.14 GeV/c^2; a narrow enhancement around 4.35 GeV/c^2 is seen instead (Fig. 3). Upper limit on the product of the two-photon decay width of the $Y(4140)$ and its branching fraction, $\Gamma_{\gamma\gamma}(Y(4140))\mathcal{B}(Y(4140) \to J/\psi\phi) < 41$ eV for $J^P = 0^+$ or < 6.0 eV for $J^P = 2^+$, are much lower than predicted for the $Y(4140)$ if it was the $D_s^{*+}D_s^{*-}$ molecule.
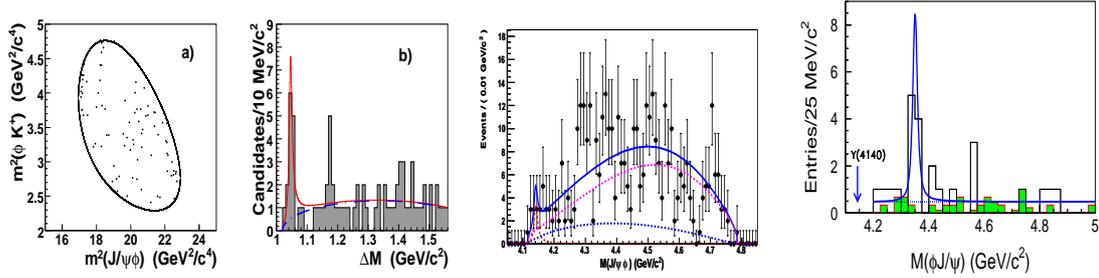
Figure 3: Left: Dalitz plot of $B \to J/\psi\phi K$ decays and $M(J/\psi\phi) - M(J/\psi)$ distribution from CDF. Middle: $M(J/\psi\phi)$ from B decays in Belle. Right: $M(J/\psi\phi)$ produced in $\gamma\gamma$ in Belle.

4.4 Y(3940)

The $Y(3940) \to J/\psi\omega$ in $B \to KJ/\psi\omega$ decays was observed by Belle and confirmed by BaBar [39], although its mass and total width measured by Belle ($m_{Y(3940)} = 3943 \pm 11 \pm 13$ MeV/c^2, $\Gamma_{Y(3940)} = 87 \pm 22 \pm 26$ MeV/c^2) and BaBar ($m_{Y(3940)} = 3914.6^{+3.8}_{-3.4} \pm 2$ MeV/c^2, $\Gamma_{Y(3940)} = 34^{+12}_{-8} \pm 5$ MeV/c^2) slightly differ. Large production rate in B decays ($\mathcal{O}(10^{-5})$) implies $\Gamma(Y(3940) \to J/\psi\omega) > 1$ MeV, thus larger than for any $c\bar{c}$ state above open charm threshold. However the $\chi_{c1}(2P)(\equiv Z(3930))$ charmonium assignment cannot be excluded.
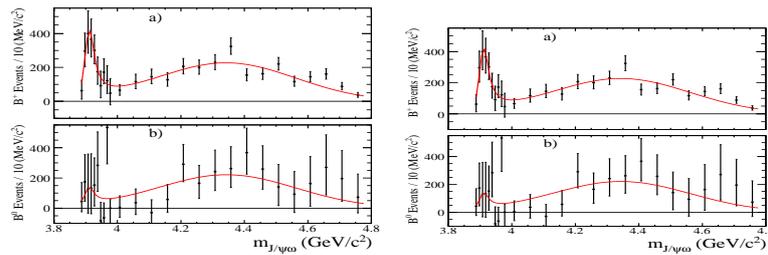
Figure 4: Left: $M(J/\psi\omega)$ distributions for charged (top) and neutral (bottom) $B \to KJ/\psi\omega$ decays from BaBar. Right: $M(J/\psi\omega)$ distributions from two-photon production in Belle.

In the recent study of the $J/\psi\omega$ produced in the $\gamma\gamma$ process, Belle have observed a significant peak in the $M(J/\psi\omega)$ distribution [40]. Its parameters, $m = 3915 \pm 3 \pm 2$ MeV/c^2 and $\Gamma = 17 \pm 10 \pm 13$ MeV/c^2, are consistent with the $Y(3940)$ (Fig. 4). Product of the two-photon

decay width and $J/\psi\omega$ partial width are $61 \pm 17 \pm 8$ eV for 0^+ and $18 \pm 5 \pm 2$ eV for 2^+ case. The 0^+ and 2^+ spin-parity assignments cannot be distinguished with the current data sample. Assuming two-photon width typical for an excited charmonia $\Gamma_{\gamma\gamma} \sim \mathcal{O}(1$ keV$)$ implies a partial width of $\Gamma(Y(3940) \to J/\psi\omega) \sim \mathcal{O}(1$ MeV$)$, which is again quite large for conventional charmonium assignment.

4.5 Charged Z states

The $Z^+(4430)$, the first charmonium-like state of non-zero electric charge, has been observed in the $\pi^+\psi(2S)$ decay channel in a study of $B \to K\pi^+\psi(2S)$ decays performed by Belle [41]. This observation, based on a simple fit to the $\pi^+\psi(2S)$ mass distribution, has been confirmed through the Dalitz-plot analysis of the $B \to K\pi^+\psi(2S)$ [42]. Being a charged state the $Z^+(4430)$ has minimum quark content $[c\bar{c}u\bar{d}]$, thus must be exotic. Theoretical explanations have suggested that it could be either an S-wave threshold effect or a $D^*\bar{D}_1(2420)$ molecule, whereas tetraquark hypothesis considers the $Z^+(4430)$ to be a diquark-antidiquark state with the $[cu][\bar{c}\bar{d}]$ configuration and predicts an existence of its neutral partner decaying to $\psi(2S)\pi^0$ or $\psi(2S)\eta$ [43]. In the molecular scenario the dominating decay modes should be $D^*\bar{D}^*\pi$ whereas in the tetraquark one: $D^{(*)}\bar{D}^*$ and $J\psi\pi$ decay channels in addition to $\psi(2S)\pi$.

Recently BaBar in a search for the $Z^+(4430)$ in the $\pi^+\psi(2S)$ and π^+J/ψ decays modes has not found significant $Z^+(4430)$ signal in any of these systems [44], but claims that both Belle and BaBar data remain statistically consistent. The upper limit on the branching fraction product measured by BaBar: $\mathcal{B}\left(\bar{B}^0 \to Z(4430)^+K^-\right)\mathcal{B}\left(Z^+ \to \psi(2S)\pi^+\right) < 3.1 \times 10^{-5}$ does not contradict Belle measurement of $3.2^{+1.8}_{-0.9}{}^{+5.3}_{-1.6} \times 10^{-5}$. This calls for further, high statistics studies of the $Z^+(4430)$. Two other charged resonance-like structures have been observed by Belle in the $\pi^+\chi_{c1}$ mass distribution near 4.1 GeV/c^2 in the $\bar{B}^0 \to K^-\pi^+\chi_{c1}$ decays through full analysis of the Dalitz plot [45]. Just like in the $Z^+(4430)$ case, both these states once confirmed will be certain candidates for exotic, most likely multiquark states.

5 Bottomonia

Experimental data on bottomonia remain incomplete. With respect to $c\bar{c}$ spectrum, studies of $b\bar{b}$ states require higher statistics, since resonances are expected to be broad, have many decay channels, and the cross sections are lower. In addition to completing the picture of conventional bottomonia also search for exotic states, $b\bar{b}$ analogues of the $c\bar{c}$-like exotic resonances would be a good test for the proposed interpretations.

Below the $B\bar{B}$ threshold the known states are $\Upsilon(1,2,3S)$, $\chi_{b1,b2,b3}(1P)$ and, since very recently also $\eta_b(1S)$ (reffered to as the η_b). The spin-singlet states, $\eta_b(2,3S)$ and $h_b(1,2,3P)$, are still missing and could be observed via magnetic or hadronic transitions from lower Υ states. The D-wave $b\bar{b}$ states $\psi_{b1,b2,b3}(1,2D)$ either have not been observed or need confirmation. Above the $B\bar{B}$ threshold only $\Upsilon(4,5,6S)$, vector states were found, though properties of the latter two are not measured precisely.

5.1 Discovery of the η_b

The ground state of bottomonium system, the η_b, has been discovered by BaBar in energy spectrum of the monochromatic photons from the radiative transition $\Upsilon(3S) \to \gamma\eta_b$ [46].

Such an inclusive approach suffers from a severe background; in addition to large non-peaking background from $e^+e^- \rightarrow q\bar{q}$ continuum and bottomonium decays, there is also a background peaking close to the signal region which is expected by theory around $E_\gamma = 900$ MeV. Such a background arises from two sources: double radiative decays $\Upsilon(3S) \rightarrow \gamma\chi_{bJ}(2P)$; $\chi_{bJ}(2P) \rightarrow \gamma\Upsilon(1S)$ producing a dominant peak around 760 MeV, and a production of the $\Upsilon(1S)$ via ISR $e^+e^- \rightarrow \gamma_{ISR}\Upsilon(1S)$ leading to a peak near 860 MeV (Fig. 5). From the fit to the E_γ spectrum, with the mentioned backgrounds properly modelled, the signal peak has been observed at $E_\gamma = 921.2^{+2.1}_{-2.8}\pm2.4$ MeV corresponding to the η_b mass of $9388.9^{+3.1}_{-2.3}\pm2.7$ MeV/c^2. This gives hyperfine mass splitting between the η_b and $\Upsilon(1S)$ about 71 MeV/c^2, slightly larger than most potential models predictions [47]. BaBar has found also an evidence for the radiative transition $\Upsilon(2S) \rightarrow \gamma\eta_b$ [48] using a procedure similar to the study of $\Upsilon(3S)$ sample. The η_b mass measured to be $9392.9^{+4.6}_{-4.8}\pm1.9$ MeV/c^2 is consistent with one from the discovery analysis.

Exclusive searches, which would allow one to measure the η_b width, will be difficult because dominant hadronic decays of the η_b are expected to proceed through OZI suppressed two gluons and, as such, will result in low branching fraction ($\mathcal{O}(10^{-5})$) and high multiplicity decays.
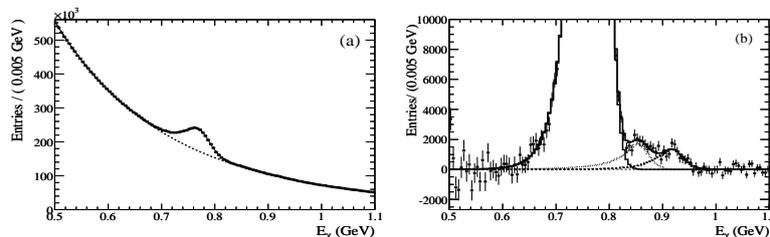
Figure 5: Inclusive spectrum of photons from $\Upsilon(3S) \rightarrow \gamma\eta_b$ before (left) and after (right) non-peaking background subtraction. The peaking components in right plot are from $\chi_{bJ}(2P)$, ISR $\Upsilon(1S)$ and η_b. In the left plot only the $\chi_{bJ}(2P)$ peak is visible.

5.2 Υ states

Recently new experimental data on the higher Υ states have been delivered by the B-Factories. Belle performed exclusive study of the $\Upsilon(5S)$ dipion transitions, whereas BaBar studied inclusive $b\bar{b}$ cross-section in the $\Upsilon(5S)$ and $\Upsilon(6S)$ mass region.

Belle has found unexpectedly large signals for the $\Upsilon(5S) \rightarrow \Upsilon(nS)\pi^+\pi^-$ $(n = 1, 2, 3)$ decays [49]. Their partial widths are of about $\mathcal{O}(100)$ keV, thus about two orders of magnitude larger than for the other Υ states. Similar relation observed between $\Gamma(Y(4260) \rightarrow J/\psi\pi^+\pi^-)$ and such partial widths for usual charmonia, has suggested that this might be a $b\bar{b}$ analogue of $Y(4260)$ (Y_b) overlapping the $\Upsilon(5S)$ and giving the anomalous dipion transitions. To check this, Belle performed an energy scan between 10.83 GeV and 11.02 GeV and measured energy dependent cross section for the $\Upsilon(nS)\pi^+\pi^-$ $(n = 1, 2, 3)$ production (Fig. 6). It has revealed an enhancement which cannot be described by a conventional, confirmed by the inclusive R_b fit, $\Upsilon(5S)$ line shape. Fit to the exclusive cross sections yields a peak mass of $10889.6 \pm 1.8 \pm 1.5$ MeV/c^2 and a total width of $54.7^{+8.5}_{-7.2}\pm2.5$ MeV/c^2 [50]. Explanation other than existence of the Y_b with mass of 10.89 GeV, suggests mixing of the conventional $b\bar{b}$ state with the threshold followed by rescattering to $\Upsilon(nS)\pi^+\pi^-$ [51].

BaBar has measured the R_b values in the range 10.54 to 11.20 GeV [52]. This measurement reveals a rich structure of $B^{(*)}\bar{B}^{(*)}$, and $B_s^{(*)}\bar{B}_s^{(*)}$ thresholds. To measure the parameters of the $\Upsilon(5S)$ and $\Upsilon(6S)$, one has performed a simplified fit with two Breit-Wigner resonances and a flat $b\bar{b}$ continuum added coherently (Fig. 6). The measured masses: $m_{\Upsilon(5S)} = 10.876 \pm 0.002\,\mathrm{GeV}/c^2$ and $m_{\Upsilon(6S)} = 10.996 \pm 0.002\,\mathrm{GeV}/c^2$ agree with the PDG values, whereas the widths: $\Gamma_{\Upsilon(5S)} = 43 \pm 4\,\mathrm{MeV}/c^2$, $\Gamma_{\Upsilon(6S)} = 37 \pm 3\,\mathrm{MeV}/c^2$ are significantly lower. However coupled channel effects and the thresholds mentioned, once taken properly into account, may modify the fit results. Also possible exotic extensions could be further tested in the fit model.
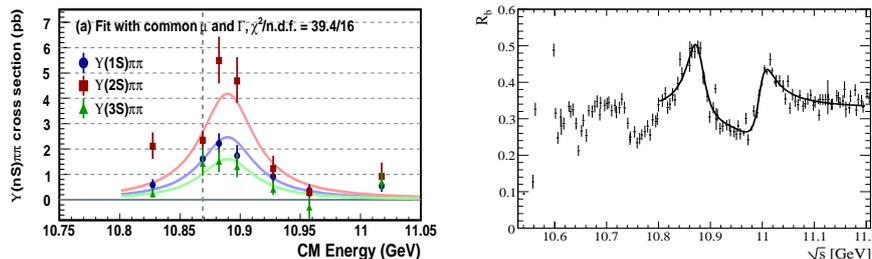
Figure 6: Left: Cross-section for $e^+e^- \to \Upsilon(nS)\pi^+\pi^-$ processes from Belle. The curves show fit result, the vertical line indicates the $\Upsilon(5S)$ mass. Right: Fitted R_b from BaBar.

6 Beauty baryons

In the pre-LHC era Tevatron is the unique facility to study baryons containing b quark. Till recently the only b-baryon observed was Λ_b^0 (quark content $[udb]$); large Tevatron data sample made possible the observation of the Ξ_b^- $[dsb]$, the $\Sigma_b^{(*)}$ $[uub]$, $[ddb]$ and recently the doubly-strange b-baryon Ω_b^- $[ssb]$. In studies of Ω_b^- its decay chain: $\Omega_b^- \to J/\psi\Omega^-$, $J/\psi \to \mu^+\mu^-$, $\Omega^- \to \Lambda K^-$ and $\Lambda \to p\pi^-$ was fully reconstructed. The $M(J/\psi\Omega^-)$ mass distribution measured for selected candidates by $D\emptyset$ is shown in Fig. 7 [53]. An observed peak, assumed to originate from the Ω_b^-, has a mass $6165 \pm 10 \pm 13\,\mathrm{MeV}/c^2$, slightly higher than a theory predicted Ω_b^- mass between $5.94 - 6.12\,\mathrm{GeV}/c^2$. The Ω_b^- production rate $f(b \to \Omega_b^-)\mathcal{B}(\Omega_b^- \to J/\psi\Omega^-)$, measured with respect to the production rate of baryon of similar topology $\Xi_b^- \to J/\psi\Xi^-$, is $0.80 \pm 0.32^{+01.4}_{-0.22}$. Position of a peak in the $M(J/\psi\Omega^-)$ obtained by CDF (Fig. 7) is measured to be $6054 \pm 7 \pm 1\,\mathrm{GeV}/c^2$ [54], thus significantly lower than the mass measured by $D\emptyset$. CDF also measured lifetime of the Ω_b^- to be $1.13^{+0.53}_{-0.40} \pm 0.02$ ps, in agreement with theory calculations giving $0.83 < \tau_{\Omega_b^-} < 0.67$ ps. The Ω_b^- production rate with respect to the Ξ_b^- has been measured to be $0.27 \pm 0.12 \pm 0.01$, thus lower than the one in $D\emptyset$ analysis.

Because of the different Ω_b^- mass measured by $D\emptyset$ and CDF, it is not clear whether both experiments see the same baryon. Further analysis for full Tevatron data sample is needed to resolve this discrepancy.
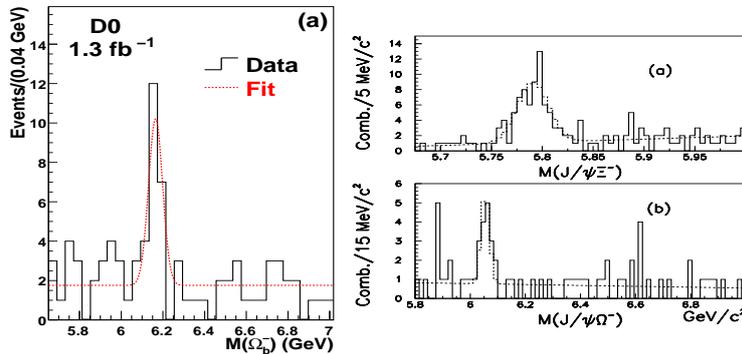
Figure 7: $M(J/\psi\Omega^-)$ distribution and fit result from $D\!\!\!/0$ (left) and CDF (bottom right). Top right plot shows reference $M(J/\psi\Xi^-)$ distribution from CDF.

7   Summary

Spectroscopy of heavy flavour hadrons has attracted significant interest in recent years due to many experimental facilities such as BaBar, Belle, BES, Cleo, CDF and $D\!\!\!/0$ reporting discoveries of new states, new production mechanisms and new decays. The XYZ particles, being candidates for exotic hadrons, may suggest that there is a new $c\bar{c}$ spectroscopy around 4 GeV mass region. Future experiments like BESIII, Panda, Super B-Factories will certainly bring new results in this field.

References

[1] M.B. Voloshin, L.B. Okun JETP Lett. **23**, 333 (1976); A. De Rujula, H. Georgi *et al.* Phys. Rev. Lett. **38**, 317 (1977); N.A. Tornqvist Z. Phys. C **61**, 525 (1994).

[2] L. Maiani, F. Piccinini *et al.* Phys. Rev. D **71**, 014028 (2005).

[3] T. Barnes, F.E. Close *et al.* Phys. Rev. D **52**, 5242 (1995).

[4] S. Godfrey and N. Isgur, Phys. Rev. **D32**, 189 (1985); E.Eichten, K.Gottfried *et al.* Phys. Rev. D **21**, 203 (1980).

[5] T.Barnes, F.Close *et al.*, hep/ph-0307012; T.E.Browder, S.Pakvasa *et al.*, hep/ph-0307054; M.A.Nowak, M.Rho *et al.*, Phys. Rev. **D48**, 4370 (1993); W.Bardeen and C.Hill, Phys. Rev. **D49**, 409 (1994).

[6] T. Matsuki, T. Morii, Phys. Rev. **D56**, 5646 (1997).

[7] J. Brodzicka *et al.* (Belle Collab.), Phys. Rev. Lett. **100**, 092001 (2008).

[8] B.Aubert *et al.* (BaBar Collab.), Phys. Rev. Lett. **97**, 222001 (2006).

[9] B.Aubert *et al.* (BaBar Collab.), Phys. Rev. **D80**, 092003 (2009).

[10] P. Colangelo, F. De Fazio *et al.* Phys. Rev. **D 77**, 014012 (2008).

[11] B. Zhang, X. Liu *et al.* Eur. Phys. J. C 50, 617 (2007); T. Matsuki, T. Morii *et al.*, Eur. Phys. J. A 31, 701 (2007). (2006).

[12] M. Ablikim *et al.* (BES Collab.) Phys. Lett. B 660 315 (2008).

[13] W.-M. Yao *et al.* J. Phys. **G33**, 1 (2006).

[14] M. Ablikim *et al.* (BES Collab.) Phys. Rev. Lett. **101** 102004 (2008).

[15] S. Uehara *et al.* (Belle Collab.) Phys. Rev. Lett. **96**, 082003

[16] S.K. Choi *et al.* (Belle Collab.) Phys. Rev. Lett. **91**, 262001 (2003); D. Acosta *et al.* (CDF Collab.) Phys. Rev. Lett. **93**, 072001 (2004); V.M. Abazov *et al.* D∅ Collab.) Phys. Rev. Lett. **93**, 162002 (2004); C. Amsler *et al.* (Particle Data Group) Phys. Lett. B **667** 1, (2008).

[17] T. Aaltonen *et al.* (CDF Collab.) Phys. Rev. Lett. **103**, 152001 (2009).

[18] A. Abulencia *et al.* (CDF Collab.) Phys. Rev. Lett. **96**, 102002 (2006).

[19] K. Abe *et al.* (Belle Collab.) arXiv:0505037

[20] B. Aubert *et al.* (BaBar Collab.) arXiv:0809.0042

[21] A. Abulencia *et al.* (CDF Collab.) Phys. Rev. Lett. **98**, 132002 (2007).

[22] B. Aubert *et al.* (BaBar Collab.) Phys. Rev. D **77**, 011102 (2008); I. Adachi *et al.* (Belle Collab.) arXiv:0810.0358

[23] E.S. Swanson Phys. Lett. B **588**, 189 (2004); F.E. Close, P.R. Page Phys. Lett. B **578**, 119 (2004); M.B. Voloshin Phys. Lett. B **579**, 316 (2004).

[24] Y. Dong, A. Faessler arXiV:0909.0380

[25] C. Bignamini, B. Grinstein *et al.* arXiV:0906.0882

[26] D. Ebert, R.N. Faustov *et al.* Phys. Lett. B **634**, 214 (2006).

[27] B. Aubert *et al.* (BaBar Collab.) Phys. Rev. D **77**, 111101 (2008); I. Adachi *et al.* (Belle Collab.) arXiv:0809.1224

[28] L. Maiani, A.D. Polosa *et al.* arXiv:0707.3354

[29] B. Aubert *et al.* (BaBar Collab.) Phys. Rev. D **71**, 031501 (2007).

[30] B. Aubert *et al.* (BaBar Collab.) Phys. Rev. Lett. **95**, 142001 (2005); Q. He *et al.* (Cleo Collab.) Phys. Rev. D **74**, 091104 (2006); C.Z. Yuan *et al.* (Belle Collab.) Phys. Rev. Lett. **99**, 182004 (2007); B. Aubert *et al.*(BaBar Collab.) Phys. Rev. Lett. **98**, 212001 (2007); X.L. Wang *et al.*(Belle Collab.) Phys. Rev. Lett. **99**, 142002 (2007).

[31] G. Pakhlova *et al.* (Belle Collab.) Phys. Rev. D **77**, 011103 (2008); G. Pakhlova *et al.* (Belle Collab.) Phys. Rev. Lett. **98**, 092001 (2007).

[32] B. Aubert *et al.*(BaBar Collab.) Phys. Rev. D **76**, 111105 (2007); B. Aubert *et al.*(BaBar Collab.) Phys. Rev. D **79**, 092001 (2009).

[33] For example: L. Maiani *et al.* Phys. Rev. D **72**, 031502 (2005); D. Ebert *et al.* Eur. Phys. J. C 58, 399 (2008); X. Liu *et al.* Phys. Rev. D **72**, 054023 (2005); G.-J. Ding, Phys. Rev. D **79**, 014001 (2009); S. L. Zhu, Phys. Phys. Lett. B **625**, 212 (2005); F. E. Close *et al.* Phys. Lett. B **628**, 215 (2005). E. Kou *et al.* Phys. Lett. B **631**, 164 (2005).

[34] G. Pakhlova *et al.* (Belle Collab.) Phys. Rev. D **80**, 091101 (2009).

[35] T. Aaltonen *et al.* (CDF Collab.) Phys. Rev. Lett. **102**, 242002 (2009).

[36] T. Branz, T. Gutsche *et al.* Phys. Rev. D **80**, 054019 (2009); F. Stancu, arXiv:0906.2485

[37] I. Adachi *et al.* (Belle Collab.) BELLE-CONF-0931.

[38] C. P. Shen *et al.* (Belle Collab.) arXiv:0912.2383

[39] S.K. Choi *et al.* (Belle Collab.) Phys. Rev. Lett. **94**, 182002 (2005); B. Aubert *et al.* (BaBar Collab.) Phys. Rev. Lett. **101**, 082001 (2008).

[40] S. Uehara *et al.* (Belle Collab.) arXiv:0912.4451

[41] S.K. Choi *et al.* (Belle Collab.) Phys. Rev. Lett. **100**, 142001 (2008).

[42] R. Mizuk *et al.* (Belle Collab.) Phys. Rev. D **80**, 031104 (2009).

[43] J.L. Rosner Phys. Rev. D **76**, 114002 (2007); C. Meng and K.T. Chao arXiv:0708.4222; X. Liu and Y.R Liu *et al.* arXiv:0711.0494; L. Maiani and A.D. Polosa arXiv:0708.3997

[44] B. Aubert *et al.* (BaBar Collab.) Phys. Rev. D **79**, 112001 (2009).

[45] R. Mizuk *et al.* (Belle Collab.) Phys. Rev. D **78**, 072004 (2008).

[46] B. Aubert *et al.* (BaBar Collab.) Phys. Rev. Lett.**101**, 071801 (2008).

[47] N. Brambilla *et al.* [QWG], CERN Yellow Report, CERN-2005-005 (2005).

[48] B. Aubert *et al.* (BaBar Collab.) Phys. Rev. Lett.**103**, 161801 (2009).

[49] K.F. Chen *et al.* (Belle Collab.) Phys. Rev. Lett. **100**, 112001 (2008).

[50] I. Adachi *et al.* (Belle Collab.) arXiV:0804.2063

[51] F.E. Close arXiv:0801.2646

[52] B. Aubert *et al.* (BaBar Collab.) Phys. Rev. Lett.**102**, 012001 (2009).

[53] V.M. Abazov *et al.* $D\emptyset$ Collab.) Phys. Rev. Lett. **101**, 232002 (2008).

[54] T. Aaltonen *et al.* (CDF Collab.) Phys. Rev. D **80**, 072003 (2009).

Discussion

Ahmed Ali (DESY): I would like to make two comments. My first comment is that there is an indirect theoretical argument against X(3872) as a DD* molecule based on the recent work by Grinstein at al. Assuming that X(3872) is a DD* molecule, their estimation of the upper limit of the cross section for PPbar- ¿X(3872) + X is at least two order of magnitude lower than the CDF measurement. My second comment is actually a suggestion to take a closer look in the energy range from ^{2} f(5S) to 12 GeV searching for bbbar -¿ states of the tetraquarks type.

Answer: As for the first comment from Prof. Ali, indeed if the X(3872) was a DD* molecule its prompt production from pp-bar annihilation should be very suppressed. Simply speaking, largely separated D and D* mesons would not have enough time to form a J/psipipi final state in which the X(3872) has been reconstructed by CDF. However an interpretation of X(3872) as a molecule with an admixture of charmonium component, proposed recently by theoreticians, might explain the large cross-section measured.

Regarding the second comment, in the inclusive bb-bar cross-section measured by BaBar there are couple of spikes sticking out of a line fitted with only the Upsilon states assumed. They can be either just statistical fluctuations or indicate an existence of new states below 11GeV. However the energy scans taken by Belle in new runs in 2010 do not confirm any narrow peaks in hadronic cross-section in the range from 10.7 to 11 GeV. Nevertheless studying of exclusive cross-sections might be more promising. An example is cross-section for bb-bar -¿Y(1,2,3S)pi+pi- around 10.9GeV, found by Belle to be far too large for being produced from conventional bb-bar state.

Rob Kutschke (FNAL): How do you tell the difference between the molecule state and the hybrid state? I am thinking of the case in which the isospin partners are not seen but in which there are reasons to believe that the isospin partners are unbound. Are there observables with which to distinguish the two interpretations?

Answer: In the mentioned case measuring of quantum numbers through study of angular distributions, could help to distinguish between molecules and hybrids. Hybrids are allowed to have exotic spin-parities. Studying certain final states could give some information as well; hadronic transitions should dominate for hybrids, whereas decays to constituent mesons are expected to be dominant for molecules. Moreover a final state with an unbalanced flavour, for example strangeness, is not allowed for hybrids but possible for molecules.

Status of the LHCb experiment

Andrey Golutvin

CERN, 1211 Geneve 23, Switzerland
Imperial Colllege London, Exhibition Road, SW7 2AZ London, United Kingdom

The status of the LHCb detector is presented. A particular emphasis is given to the LHCb strategy for New Physics searches in CP-violation and rare decay measurements. Prospects for early physics results are reviewed as well.

1 LHCb detector and its expected performance

The LHCb detector, described in detail elsewhere [1], has been designed and constructed in order to search for new physics beyond the Standard Model (SM) at the Large Hadron Collider (LHC) via precision measurement of CP-violation and rare decays of heavy flavours. The main advantages of heavy flavours studies at hadron collider is the accessibility to all b-hadrons, in particular B_s mesons, which being boosted allow for the possibility of time-dependent studies, and a large $b\bar{b}$ production cross-section. The cross section of $b\bar{b}$ pairs produced in proton-proton collisions at $\sqrt{s} = 14$ TeV is expected to be $\sim 500\mu b$. A total of 10^{12} $b\bar{b}$ pairs are produced per year running at the nominal LHCb luminosity of 2×10^{32} cm^{-2} s^{-1}, which corresponds to an annual integrated luminosity of 2 fb^{-1}.

To maximize the detector acceptance for flavour physics LHCb has been constructed as a forward angle spectrometer with an angular coverage of ~ 15 to 300(250) mrad in the bending (non-bending) plane. A side view of the LHCb detector is shown in Figure 1. The key features of LHCb are:

- Excellent vertexing capabilities and proper time resolution of ~ 40 fs, as provided by the Vertex Locator (VELO), the detectors of which approach to within 8 mm of the beam line during collisions;

- Particle identification capabilities provided by two RICH detectors which allow for good π/K separation in 2 - 100 GeV/c momentum range;

- Good momentum resolution $\delta p/p \sim 0.3 - 0.5\%$ depending on p, which together with precise track direction measurement, results in excellent invariant mass resolution of $\sim$ 10 - 20 MeV/c^2 depending on the B decay channel;

- A selective and flexible trigger system.

High performance trigger operation is a crucial requirement for the success of the LHCb physics programme since the $b\bar{b}$ cross-section constitutes less than 1% of the total inelastic cross-section and the typical branching fractions of B decays of interest are less than $\sim 10^{-5}$. A schematic of the LHCb trigger implementation is shown in Figure 2.
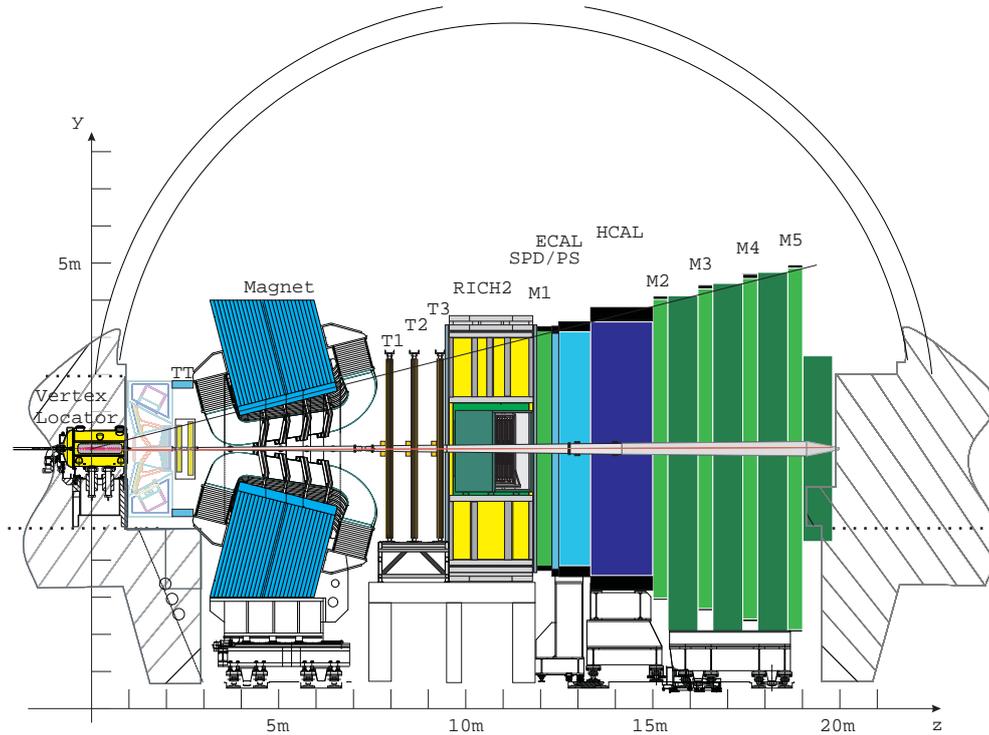
Figure 1: Schematic side view of the LHCb detector showing the following components: Vertex Locator (VELO), RICH1, Trigger Turicencis (TT), warm dipole magnet, three stations of the main tracker (T1,T2,T3), RICH2, Scintillating Pad Detector (SPD), PreShower (PS), Electromagnetic (ECAL) and Hadronic (HCAL) calorimeters and Muon detector stations (M1 - M5).

The trigger system is composed of two parts.The hardware Level-0 (L0) trigger is implemented in custom made electronics while a High Level Trigger (HLT) is a software based trigger, which currently runs on $\sim$ 4000 multi-core commercially available processors. In order to reduce the input rate down to $\sim$1 MHz, L0 searches for muon, electron, photon and hadron candidates with p_T significantly higher than in minimum bias events. The backwards planes of the VELO contribute as a Pile-up detector, identifying events with multiple interactions, which can then be rejected or triggered on with adjusted p_T thresholds. The HLT further reduces the rate down to $\sim$2 kHz by first confirming and refining the L0-candidates with more complete information on their impact parameter and lifetime, and then selecting partially or fully reconstructed B decay modes. After HLT, selected events are written to storage at $\sim$2 kHz rate for subsequent off-line analysis.

1.1   Commissioning of LHCb detector

The LHCb detector has been successfully commissioned using cosmic rays and beam induced events. Although the horizontal configuration of LHCb is not well suited for measuring cosmic
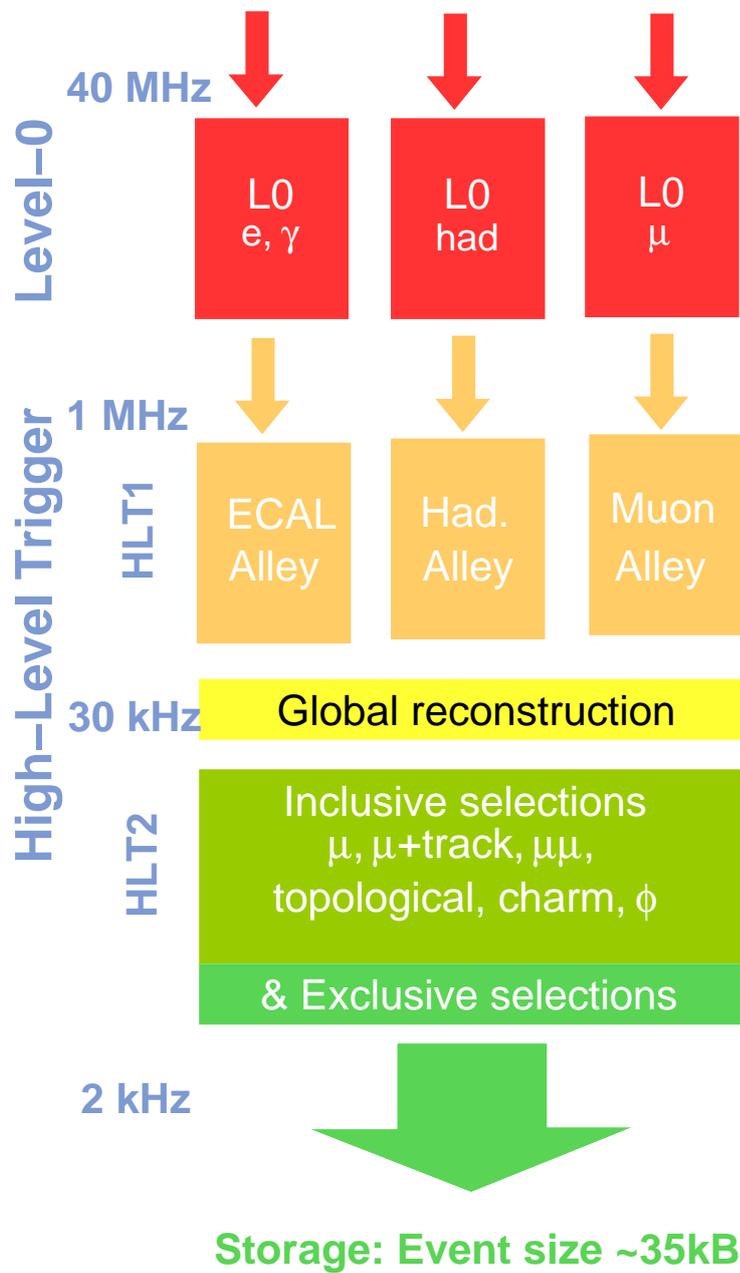
Figure 2: Conceptual diagram of the LHCb trigger

rays, several million cosmic events have been collected for the time and spatial alignment of large sub-systems, such as the calorimeter, muon and outer tracker. For the smaller area and fine granularity detectors, like Inner Tracker (IT), TT and VELO, LHC beam-induced events have been effectively utilized. Occasionally during the LHC injection tests the proton bunches from SPS were dumped onto a beam stopper located close to the LHC injection point and only about 340 m downstream of LHCb. The resulting high intensity flux of produced secondary particles, traveling almost parallel to the LHC beam line, have been reconstructed by the VELO, TT and IT sub-detectors. This data sample had a typical fluence of ~ 100 particles/cm^2 allowed a time alignment to be achieved with a precision better than 2 ns and to test *in situ* the alignment from metrology measurements. In particular, for the VELO detector the module alignment parameters have been found to be within 10 μm for translation and 200 μmrad for rotation with respect to their nominal position.

2 LHCb physics program

The main goal of LHCb physics programme is to search for the virtual contribution of New Particles (NP) to Flavour Changing Neutral Currents (FCNC) in reactions mediated by the loop diagrams involving beauty and charm quarks. A search strategy has been developed on an illustrative set of "key measurements" [2] sensitive to the phases and couplings of NP and even to their helicity structure. Loop mediated FCNC reactions described by box or penguin diagrams, shown in Figure 3, may have different sensitivity to various NP effects. Thus LHCb will search for NP effects in the box and penguin diagrams separately. In the following we
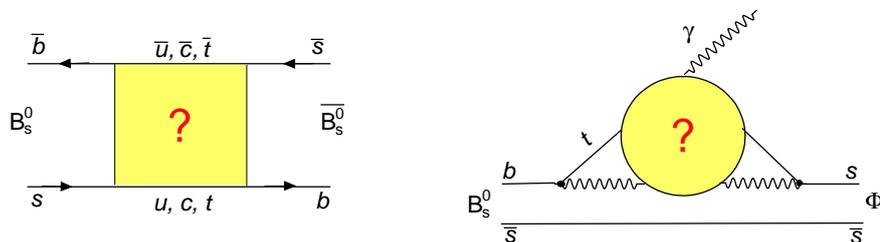
Figure 3: Box (left) and radiative penguin (right) diagrams. The internal lines may consist of either SM or new particles.

summarize in Sections 2.1 and 2.2 the status of some of the important observables in flavour physics, while in Section 2.3 we give the prospects for LHCb in this set of illustrative key measurements.

2.1 Measurements sensitive to the phases of NP

The most promising way to search for NP phases contributing to box diagrams is in the measurement of the B_s mixing phase ϕ_s. Within the SM this CP violating phase is predicted very accurately and expected to be very small: $\phi_s^{SM} = -2\beta_s = (0.0360^{+0.0020}_{-0.0016})$ [3]. Until now mea-

surements have had low sensitivity to this observable, but recent results from the Tevatron hint at a value far larger than the SM prediction, $2\beta_s \in [0.54,\ 1.18] \cup [1.94,\ 2.60]$ @ 68% CL [4, 5, 6].

Alternatively NP contributions to box diagrams can be searched for making a consistency test of the main Unitarity Triangle (UT), shown in Figure 4. This test requires the measurement of all the elements of the main Unitarity Triangle (UT) meaning that the exercise is more involved and less straightforward to interpret. Currently the precision of the UT elements is limited for the two non-trivial sides, on account of the uncertainties of the lattice QCD inputs, and by experimental errors for the three angles. Thanks to the B factories the angle β has been measured to a precision better than $\sim 1°$, $\beta = (21.65^{+0.91}_{-0.89}{}°)$ [3]. The accuracy of the other two angles, α and γ, is currently rather modest, in particular for γ, where the limited statistics lead to a $\sim 20°$ uncertainty [3].

Two of the five UT elements, the side opposite to the angle β and the angle γ can be extracted from the measurement of the reactions explicitly described by tree diagrams, which are insensitive to NP. In contrast, the other two elements, the angle β and the side opposite to the angle γ, can potentially receive virtual contribution from NP to the box diagrams.

Figure 4: Constraints from the global CKM fir in the $(\bar{\rho}\bar{\eta})$ plane

Due to the specific shape of the UT, with the angle α being close to $90°$, possible contributions from NP are mainly constrained by the comparison of the angles with the opposite sides, namely β with the side proportional to $\frac{|V_{ub}|}{|V_{cb}|}$ or γ with the side proportional to $\frac{|V_{td}|}{|V_{ts}|}$. As of today both tests suffer from rather limited accuracy. For the first pair of elements, the determination of the side is limited by $\sim 10\%$ accuracy of the $|V_{ub}|$ extraction methods [7] while for the second pair the statistical error of the angle γ measurement is by far the limiting factor. Indeed, the CKMFitter prediction for extracted from direct measurements, $\gamma = (73\pm^{22}_{25})°$ [3], is significantly less accurate than the value following from the global SM constraint: $\gamma = (67.9\pm^{4.3}_{3.8})°$ [3]. This SM constraint is mainly based on the measurement of the processes mediated by the box diagrams, such as the angle β, which gives the phase of the B_d oscillation, and the side opposite to the angle γ side, which is proportional to the ratio of the B_d to B_s oscillation frequencies.

2.2 Measurements sensitive to NP couplings and their helicity structure

Rare loop-induced B decays offer a set of experimental observables sensitive to the masses and couplings of NP. Current experimental sensitivity is limited by the statistics of the available data samples leaving room for sizable effects caused by NP contribution.

Assuming a generic coupling the inclusive measurement of $BR(b \to s\gamma)$ indirectly constraints the scale of NP masses to $\Lambda > 10^3$ TeV [8]. NP models with specific couplings can be effectively tested using exclusive rare B decays. The often cited example is the super-rare $B_s \to \mu^+\mu^-$ decay. In the SM this helicity suppressed decay has a branching ratio of $BR(B_s \to \mu^+\mu^-) = (3.35 \pm 0.32) \times 10^{-9}$ [9]. In the MSSM with an extended Higgs sector $BR(B_s \to \mu^+\mu^-)$ is proportional to $\frac{tan^6\beta}{M_A^4}$ [10] and so may significantly exceed the SM prediction for large values of the $tan\beta$ parameter. The best current limit from CDF, $BR(B_s \to \mu^+\mu^-) < 4.3 \times 10^{-8}$ @ 90% CL [11], is still an order of magnitude higher that the SM prediction.

Several strategies have been proposed to search for NP effects in the processes mediated by radiative and electroweak penguin diagrams through the measurement of the helicity structure of the inherent amplitudes. Owing to the $V - A$ structure of the W-boson coupling, the photon produced in $b \to s\gamma$ transition is predominantly left-handed up to corrections of order $\frac{m_s}{m_b}$, which arise from a chirality flip. A contribution of soft gluons to the penguin loop may further increase the fraction of right-handed photons; recent calculation [12] predict a $\sim 1\%$ increase.

The fraction of right-handed photons produced in $b \to s\gamma$ transition can be extracted from the measurement of the time-dependent CP-asymmetry in exclusive $B_s \to \phi\gamma$ decays (the corresponding diagram is shown in Figure 3). In general, the time-dependent rate of $B_s(\bar{B}_s)$ mesons decaying to a photon and the CP-eigenstate f^{CP} is given by:

$$\Gamma(B_s(\bar{B}_s)) \propto e^{-\Gamma_s t}\{\cosh\frac{\Delta\Gamma_s t}{2} - \mathcal{A}^\Delta \sinh\frac{\Delta\Gamma_s t}{2} \pm C\cos\Delta m_s t \mp S\sin\Delta m_s t\}.$$

Following the notations of [13, 14] in the SM $S \approx \sin 2\psi \sin\phi_s$, $\mathcal{A}^\Delta \approx \sin 2\psi \cos\phi_s$ and $C \approx 0$, where $\tan\psi \equiv |\frac{A(\bar{B}\to f^{CP}\gamma_R)}{A(B\to f^{CP}\gamma_L)}|$ is related to the fraction of the photons with "wrong" helicity. Since $\cos\phi_s \sim 1$ in the SM, a measurement of $\mathcal{A}^\Delta$ through the study of time-dependent rates of $B_s(\bar{B}_s) \to \phi\gamma$ provides a sensitive test of the $V - A$ structure of weak interactions in FCNC processes.

As shown in Figure 5, the decay $\bar{B}_d \to \bar{K}^{*0}\mu^+\mu^-$ proceeds via a combination of the electroweak penguin and box diagrams. The FCNC describing this $b \to s$ transition contains a right-handed component that is well calculable in the SM but can be affected by NP contributions resulting in modified angular distributions. As an example, the forward-backward asymmetry, $A^{FB}(q^2 = m_{\mu\mu}^2)$ [15, 16], is particularly sensitive to NP contributions at its zero-point, s_0, since the dominant theoretical uncertainty from hadronic form-factors cancels out at leading order.

At low values of q^2 the decay $\bar{B}_d \to K^{*0}e^+e^-$ is dominated by the contribution from the virtual photon and therefore is very sensitive to the photon helicity providing a complementary measurement to the time-dependent CP violation measurement in $B_s \to \phi\gamma$ decays.

2.3 LHCb performance for the key measurements

The LHCb key measurements include:
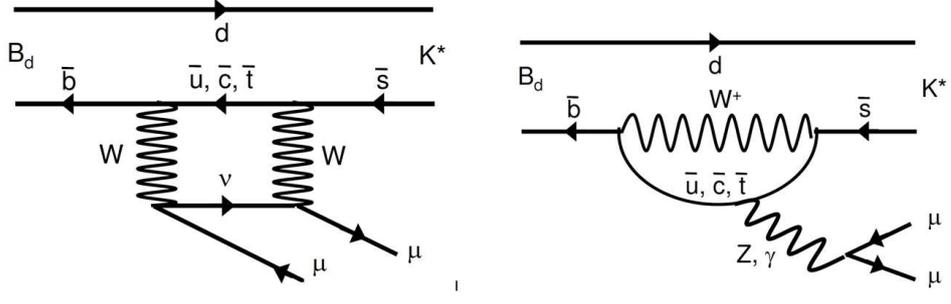
Figure 5: Box (left) and electroweak penguin (right) diagrams describing $\bar{B}_d \to K^* \mu^+ \mu^-$ decay

Key measurements	Accuracy in one nominal year $(2 fb^{-1})$
β_s	0.03
γ in trees	4.5°
γ in loops	7°
$B_s \to \mu\mu$	3σ measurement down to SM prediction
$B \to K^* \mu\mu$	$\sigma(s_0) = 0.5 \ GeV^2$
Polarization of photon in radiative penguin decays	$\sigma(H_R/H_L) = 0.1$(in $B_s \to \phi\gamma$) $\sigma(H_R/H_L) = 0.1$(in $B_d \to K^* e^+ e^-$)

Table 1: Expected LHCb sensitivities for the key measurements, achieved with the data sample of 2 fb^{-1} integrated luminosity.

- A measurement of the B_s mixing phase ϕ_s in $B_s^0 \to J/\psi(\mu\mu)\phi(KK)$ decays;

- A measurement of the UT angle γ in the processes mediated by tree diagrams, further referred to as γ *in trees*, using both CP-violation time-integrated and time-dependent measurements. These include studies of decays of the type $B_u \to D^0 K^+$, $B_d \to D^0 K^{*0}$, $B_d \to D\pi$ and $B_s \to D_s K$;

- A measurement of the UT angle γ in loop mediated processes, further referred to as γ *in loops*. The $B_{d,s}^0 \to h^+ h^-$ family of decays, where h stands for a pion or kaon, have decay rates with sizable contribution from penguin diagrams, making them sensitive to NP effects in penguin loops. Allowing for a 20% U-spin symmetry breaking, the UT angle γ can be extracted with a precision of 7° after one nominal LHCb year of data taking;

- A measurement of the super-rare $B_s \to \mu^+ \mu^-$ decay;

- A test of the $V - A$ helicity structure of the weak interaction in loop mediated $B_s \to \phi\gamma$ and $B_d \to K^{*0} \ell^+ \ell^-$ decays, where ℓ stands for an electron or muon.

The LHCb performance for the key measurements is described in detail in [2]. Expected sensitivities, achieved with the data sample of 2 fb^{-1} integrated luminosity, are summarized in Table 1.

3 Prospects for physics in 2010
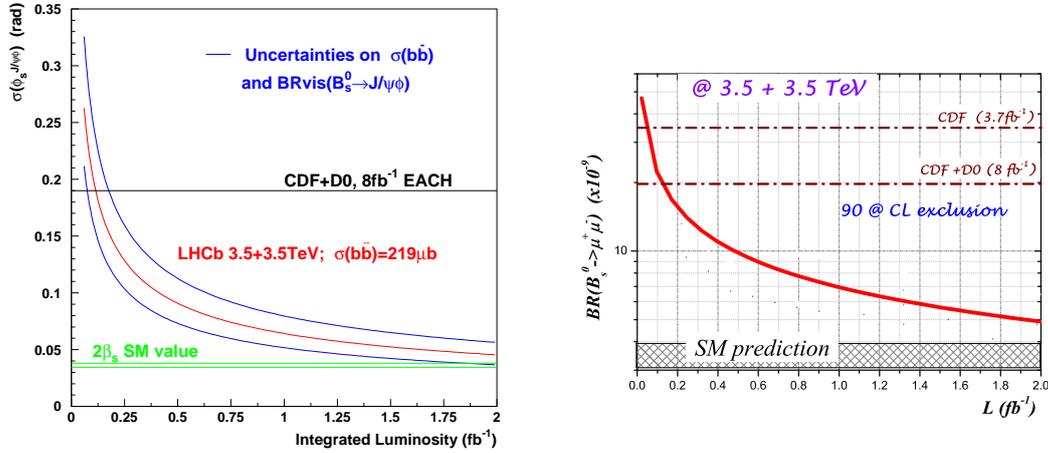
Figure 6: Left: Statistical uncertainty for the ϕ_s measurement as a function of the integrated luminosity. The outer lines indicate the uncertainties coming from the $b\bar{b}$ cross-section and visible branching ratio of $B_s \to J/\psi(\mu\mu)\phi(KK)$. Right: Exclusion limit for $\text{BR}(B_s \to \mu^+\mu^-)$ at 90% CL as a function of the integrated luminosity.

The current LHC plan foresees the two years physics run at the center-of-mass-energy of 7 TeV in order to collect the data sample of ~ 1 fb^{-1} integrated luminosity, of which ~ 200 pb^{-1} should be available for physics analysis already in 2010.

LHCb plans for early physics studies will evolve in accordance to the integrated luminosity delivered by LHC. Apart from using first data for an understanding of the track reconstruction and particle identification, inclusive V0 production will be studied, followed by the measurement of differential cross-section for the prompt J/ψ production as well as the $b\bar{b}$ production cross-section. High class measurements in the charm sector are feasible with ~ 200 pb^{-1} integrated luminosity. For example, LHCb expects to collect a data sample of $\sim 10^7$ flavour tagged $D^0 \to KK$ events that should improve significantly the sensitivity of D mixing and CP-violation studies compared to existing the B factories results.

With 200 pb^{-1} integrated luminosity LHCb, even when running at the reduced centre-of-mass-energy of $\sqrt{s} = 7$ TeV, has an excellent opportunity to improve on the Tevatron sensitivity in several key measurements in the beauty sector. Figure 6 for example shows LHCb prospects for the measurement of the phase ϕ_s and the search for the mode $B_s \to \mu^+\mu^-$ with integrated luminosity.

References

[1] B. Adeva *et al.*, (LHCb Collaboration) *"The LHCb Detector at LHC,"* JINST (2008) 3 508005.

[2] B. Adeva *et. al.*, (LHCb Collaboration) *"Roadmap for selected key measurements of LHCb,"* arXiv:0912.4179 [hep-ex].

[3] CKMfitter Group (J. Charles et al.), Eur. Phys. J. C41, 1-131 (2005) [hep-ph/0406184].

[4] T. Aaltonen *et al.* [CDF Collaboration], "First Flavor-Tagged Determination of Bounds on Mixing-Induced CP Violation in $B_s^0 \to J/\psi\phi$ Decays," Phys. Rev. Lett. **100** (2008) 161802 [arXiv:0712.2397 [hep-ex]]; CDF collaboration, "An updated measurement of the CP violating phase $\phi_s^{J/\psi\phi}$", CDF/ANAL/BOTTOM/PUBLIC/9458 (2008);

[5] V. M. Abazov *et al.* [D0 Collaboration], Phys. Rev. Lett. **101** (2008) 241801 [arXiv:0802.2255 [hep-ex]].

[6] CDF and D0 collaboration, "Combination of D0 and CDF results on $\Delta\Gamma_s$ and the CP-violationg phase $\beta_s^{J/\psi\phi}$", CDF/PHYS/BOTTOM/CDFR 9787, D note 59-28-CONF (2009).

[7] C. Amsler *et al.* [Particle Data Group], Phys. Lett. B **667** (2008) 1.

[8] Y. Nir, Nucl. Phys. Proc. Suppl. **117** (2003) 111 [arXiv:hep-ph/0208080].; S. Y. Nir Talk at the 2008 European School of High-Energy Physics, Herbeumontsur- Semois, Belgium, 8-21 June 2008.

[9] M. Blanke, A. J. Buras, D. Guadagnoli and C. Tarantino, JHEP **0610** (2006) 003 [arXiv:hep-ph/0604057].

[10] S. R. Choudhury and N. Gaur, Phys. Lett. B **451** (1999) 86 [arXiv:hep-ph/9810307]. C. S. Huang, W. Liao, Q. S. Yan and S. H. Zhu, Phys. Rev. D **63** (2001) 114021 [Erratum-ibid. D **64** (2001) 059902] [arXiv:hep-ph/0006250]. P. H. Chankowski and L. Slawianowska, Phys. Rev. D **63** (2001) 054012 [arXiv:hep-ph/0008046]. K. S. Babu and C. F. Kolda, Phys. Rev. Lett. **84** (2000) 228 [arXiv:hep-ph/9909476]. C. Bobeth, T. Ewerth, F. Kruger and J. Urban, Phys. Rev. D **64** (2001) 074014 [arXiv:hep-ph/0104284].

[11] CDF Collaboration, T. Aaltonen *et. al.*, (CDF Collaboration), Phys. Rev. Lett. 100 (2008) 101802 [0712.1708]; *"Search for $B_s^0 \to \mu^+\mu^-$ and $B_d^0 \to \mu^+\mu^-$ decays with $3.7fb^{-1}$ of $p\bar{p}$ collisions with CDF II."*

[12] P. Ball and R. Zwicky, Phys. Lett. B **642** (2006) 478 [arXiv:hep-ph/0609037].

[13] D. Atwood, M. Gronau and A. Soni, Phys. Rev. Lett. 79 (1997) 185 [arXiv:hep-ph/9704272].

[14] D. Atwood, T. Gershon, M. Hazumi and A. Soni, Phys. Rev. D 71 (2005) 076003 [arXiv:hep-ph/0410036].

[15] A. Ali, P. Ball, L. T. Handoko and G. Hiller, Phys. Rev. D **61** (2000) 074024 [arXiv:hep-ph/9910221].

[16] M. Beneke, T. Feldmann and D. Seidel, Nucl. Phys. B **612** (2001) 25 [arXiv:hep-ph/0106067].

Discussion

Bennie Ward (Baylor University: Do you have any sensitivity to the Higgs in scenarios wherein it decays to bbbar?
Answer: DespiteLHCb's excellent capability to trigger and reconstruct on b-jets the acceptance of the experiment limits its sensitivity to the Higgs masses below 135 GeV. The dominant background comes from ttbar decays. Currentlystudies yield a S/B ratio of about 1/300. Effort is ongoing to improve the S/B and to the jet energy calibration.
Vera Lüth (SLAC): Will LHCb be able to improve the measurement of the angle alpha? Or perform meaxurements of two-body decays including a neutrino?
Answer: In order to improve our knowledge of the angle alpha, LHCb will contribute with measurements of CP asymmetries in the final states with not more than one pi0 meson, such as $B \rightarrow \pi^{+}\pi^{-}$, $B \rightarrow \rho^{+}\pi^{-}$ and $B \rightarrow \rho\rho$. Measurements of leptonic two-body decays including neutrino are not feasible at LHCb.
John Wilson (University of Birmingham): There were some features (short dips) in the data on particle identification in the range $2 - 20$ GeV/c which you showed. Could you comment on the performance of aerogel in this momemtum range?
Answer: These dips are not related to the aerogel performance but ratherare an artifact of how thefigure is made. In the plot, identification efficiency is only evaluated for tracks above kaon threshold. This results in discontinuities as each radiator threshold is encountered.
Dmitri Denisov (FNAL): What are the expected upgrades and major challenges of the LHCb experiment for data sets above $10 - 100 fb^{-1}$?
Answer: The main goalof the LHCb upgrade is to ensurethe capability to collect a very large data sample using a trigger strategy which is software based at the earliest level, and therefore adaptable enough to select any channel of interest "interactively". Such anapproach will require the readout of LHCb at a rate of 40 MHz. The intention is to run at a luminosity of $10^{3}3cm^{-}2s^{-}1$, which is a factor 5 times higher than the design value of the present experiment. These running conditionswill require the replacement of several subdetectors, in particular the vertex detector.

Kaons - Recent Results and Future Plans

Takeshi K. Komatsubara

KEK, Oho, Tsukuba, Ibaraki 305-0801, Japan

Recent results and future plans of kaon physics are reviewed. Topics include CP violation, rare decays, light neutral-boson search, lepton flavor universality, and CPT and QM tests.

1   CP violation

This review article starts with the kaon-side story of CP violation. After the $K_L^0 \to \pi^+\pi^-$ decay was discovered [1] in 1964 and the CP asymmetry in the $K^0 - \overline{K^0}$ mixing was established [2], a long-standing problem has been its origin; the first question was whether it was due to the $\Delta S = 2$ *superweak* transition [3] or not. In 1973, Kobayashi and Maskawa [4] accommodated CP violation in the electroweak theory with six quarks (and single complex-phase). The Kobayashi-Maskawa theory [5], including the prediction of *direct* CP violation in the decay process from the CP-odd component (K_2) to the CP-even state ($\pi\pi$), was verified by the observations of Time-reversal non-invariance (CPLEAR [6] at CERN) and finite ϵ'/ϵ (NA48 at CERN and KTeV at FNAL) as well as the discoveries of top quark and CP-violating B decays.

The KTeV collaboration reported the final measurement of $Re(\epsilon'/\epsilon)$ with their entire data set: $(19.2\pm1.1(stat.)\pm1.8(syst.))\times10^{-4}$ [7]. Combining all the measurements including the final result from NA48: $(14.7 \pm 2.2) \times 10^{-4}$ [8], the world average is $(16.8 \pm 1.4) \times 10^{-4}$ [9]; it clearly demonstrates the existence of direct CP violation. However, due to theoretical uncertainties in the hadronic matrix elements, to get information on the Standard Model and New Physics beyond it from $Re(\epsilon'/\epsilon)$ is difficult and remains to be a challenge to lattice QCD calculations [10].

In the modern classification [11] CP violation is grouped into three: in *mixing*, *decay*, and *interference between decays with and without mixing*. All of these have been extensively studied in the B Factory experiments, while the study of CP violation in the charged-kaon decay modes started recently. The NA48/2 experiment at CERN performed charge asymmetry measurements with the simultaneous $K^\pm$ beams of 60 ± 3 GeV/c in 2003 and 2004. The asymmetries of the linear slope parameter in the matrix element expansion of the $K^\pm \to \pi^\pm\pi^+\pi^-$ decay and the $K^\pm \to \pi^\pm\pi^0\pi^0$ decay were measured to be $(-1.5 \pm 2.2) \times 10^{-4}$ and $(1.8 \pm 1.8) \times 10^{-4}$ with the data sets of 4G and 0.1G events, respectively [12]. The Standard Model expectation is in $10^{-5} \sim 10^{-6}$, and no evidence for CP violation in *decay* was observed at the level of 2×10^{-4}. NA48/2 also measured the asymmetries of K^+ and K^- decay-widths in $K^\pm \to \pi^\pm e^+e^-$ and $K^\pm \to \pi^\pm\pi^0\gamma$ to be $(-2.2\pm1.5(stat.)\pm0.6(syst.))\times10^{-2}$ [13] and $(0.0\pm1.0(stat.)\pm0.6(syst.))\times 10^{-3}$ [14] and set the upper limits of 2.1% and 0.15%, respectively.

The CP-violating processes in *mixing* and *decay* suffers from hadronic uncertainties. In contrast, the CP violation in *interference between decays with and without mixing* is theoretically clean, and the decay $K_L^0 \to \pi^0\nu\bar{\nu}$ [15] is known to be a golden mode in this category [16] because the branching ratio can be calculated with very small theoretical-uncertainties in the Standard

Model as well as in New Physics. Measurement of the branching ratios for $K^0 \to \pi^0 \nu\bar{\nu}$ and for the charged counterpart $K^+ \to \pi^+ \nu\bar{\nu}$ is the main issue in the near future plans of kaon physics, and is the topics of the next section.

2 Rare decays

The $K \to \pi\nu\bar{\nu}$ decay [17] is a Flavor-Changing Neutral Current (FCNC) process and is induced by the electroweak loop effects as Penguin and Box diagrams. The decay is suppressed in the Standard Model, and the branching ratios are predicted as $B(K_L^0 \to \pi^0\nu\bar{\nu}) = (2.76\pm0.40)\times10^{-11}$ and $B(K^+ \to \pi^+\nu\bar{\nu}(\gamma)) = (8.22\pm0.84)\times10^{-11}$ [18], in which the uncertainties are dominated by the allowed range of the quark-mixing matrix elements. Long-distance contributions are small, the hadronic matrix elements are extracted from the $K^+ \to \pi^0 e^+ \nu$ decay [19], and the next-to-next-to-leading order QCD corrections [20] and the QED and electroweak corrections [21] to the charm quark contribution to $K^+ \to \pi^+\nu\bar{\nu}$ have been calculated. New Physics could affect these branching ratios [22] and, by the measurement, the flavor structure in New Physics (operators and phases in the interactions of new particles) can be studied. The $K \to \pi\nu\bar{\nu}$ branching ratios beyond the Standard Model are presented in Fig. 1. A model-independent bound $B(K_L^0 \to \pi^0\nu\bar{\nu}) < 4.4 \times B(K^+ \to \pi^+\nu\bar{\nu})$ (Grossman-Nir bound [16]) can be extracted from their isospin relation.
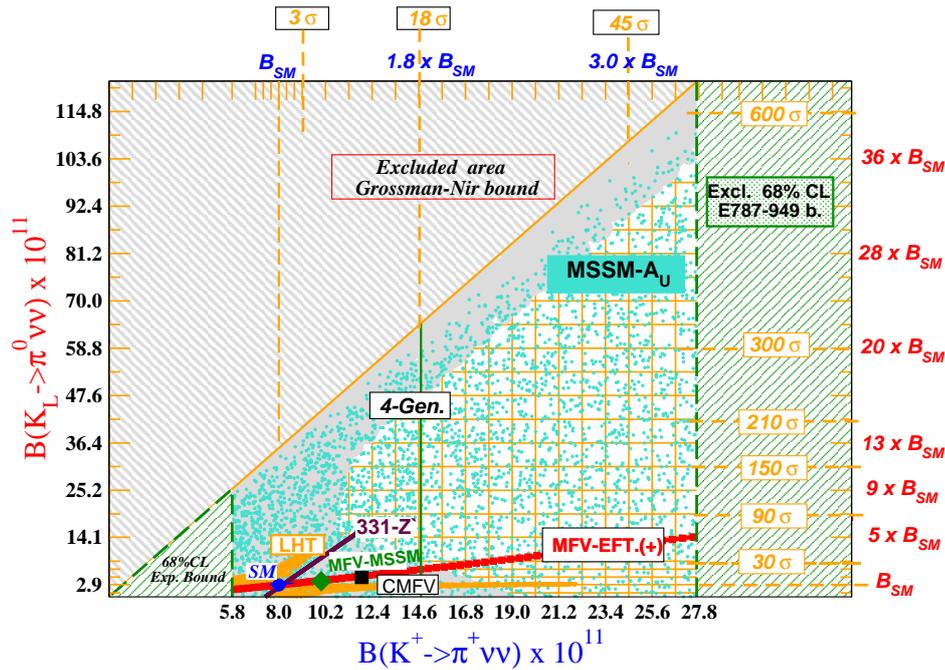
Figure 1: $K \to \pi\nu\bar{\nu}$ branching ratios beyond the Standard Model, by courtesy of F. Mescia and C. Smith [18].

The signature of $K \to \pi\nu\bar{\nu}$ is a kaon decay into *a pion plus nothing*. Background rejection is

essential in these experiments, and *blind analysis* techniques have been developed and refined to achieve a high level of confidence in the background measurements. To verify *nothing*, hermetic extra-particle detection by photon and charged-particle detectors, called the *veto*, is imposed to the hits in coincidence with the pion time and with the energy threshold less than a few MeV. Tight veto requirements are indispensable in order to achieve a low detection-inefficiency $< 10^{-3} \sim 10^{-4}$; good timing resolution for low energy hits is therefore essential to avoid acceptance loss due to accidental hits.

The E391a experiment at KEK was the first dedicated search for the $K_L^0 \to \pi^0 \nu \bar{\nu}$ decay. A small-diameter neutral beam (called a *pencil* beam [23]) was developed and constructed. The K_L^0 beam whose momentum peaked at 2 GeV/c was produced by the 12-GeV proton synchrotron (KEK-PS). The energy and position of the two photons from π^0 decays were measured by a downstream calorimeter. The K_L^0-decay vertex position along the beam line was determined from the constraint of π^0 mass, and a π^0 with a large transverse momentum (≥ 0.12 GeV/c) was the signal. The remaining part of the calorimeter not hit by the two photons and the other detector subsystems that covered the decay region were used as a veto, which was crucial to suppress the major background from $K_L^0 \to \pi^0 \pi^0$. The beam line and the collimation scheme were designed carefully to minimize the beam halo (mostly neutrons), which could interact with the counters near the beam and produce π^0's and η's.

Final results from E391a on $K_L^0 \to \pi^0 \nu \bar{\nu}$ were published recently [24]. Combining the data sets from February-April and October-December 2005, the single event sensitivity was 1.11×10^{-8} and no events were observed inside the signal region (Fig. 2, left). The upper limit on $B(K_L^0 \to \pi^0 \nu \bar{\nu})$ was set to be 2.6×10^{-8} at the 90% confidence level (C.L.). The E391a experiment has improved the limit from previous experiments by a factor of 20.
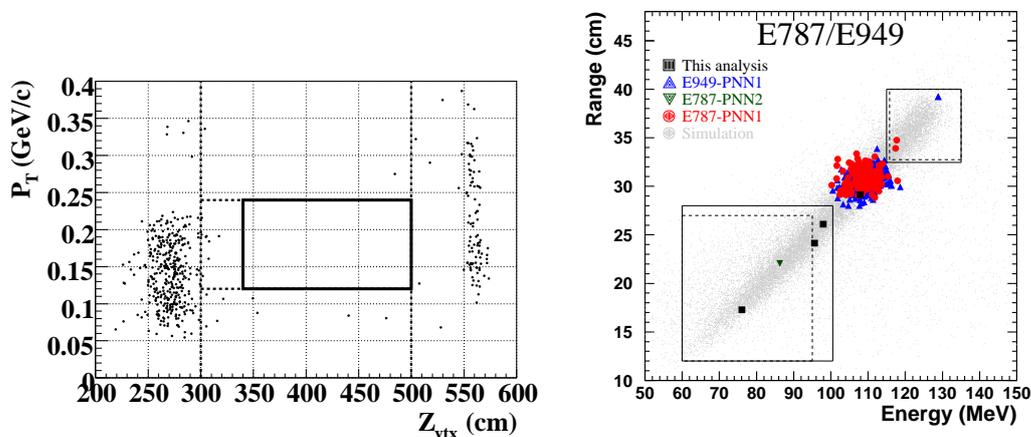
Figure 2: E391a result on $K_L^0 \to \pi^0 \nu \bar{\nu}$ [24] (left); E787/E949 result on $K^+ \to \pi^+ \nu \bar{\nu}$ [26] (right).

The E949 experiment at BNL measured the charged track emanating from $K^+ \to \pi^+ \nu \bar{\nu}$ decaying at rest in the stopping target. Charged-particle detectors for measurement of the π^+ properties were located in the central region of the detector and were surrounded by hermetic photon detectors. The π^+ momentum (P_{π^+}) from $K^+ \to \pi^+ \nu \bar{\nu}$ is less than 0.227 GeV/c, while

the major background sources of $K^+ \to \pi^+\pi^0$ and $K^+ \to \mu^+\nu$ are two-body decays and have monochromatic momentum of 0.205 GeV/c and 0.236 GeV/c, respectively. The π^+ momentum regions above and below the peak from $K^+ \to \pi^+\pi^0$ were adopted. Redundant kinematic measurement and μ^+ rejection were employed; the latter was crucial because the $K^+ \to \mu^+\nu$ background had the same topology as the signal. Pion contamination to the incident K^+ beam (0.7 GeV/c) was reduced by two stages of electrostatic particle separation in the beam line to prevent the background due to scattered beam pions.

The E949 experiment observed one $K^+ \to \pi^+\nu\bar{\nu}$ event in the kinematic region $0.211 < P_{\pi^+} < 0.229$ GeV/c (PNN1) [25] and three events in the region $0.140 < P_{\pi^+} < 0.199$ GeV/c (PNN2) [26]. Combining the results with the observation of two events in PNN1 and one event in PNN2 by the predecessor experiment E787 gave $B(K^+ \to \pi^+\nu\bar{\nu}) = (1.73^{+1.15}_{-1.05}) \times 10^{-10}$ (Fig. 2, right) [26], consistent with the Standard Model prediction.

The next generation of $K_L^0 \to \pi^0\nu\bar{\nu}$ is the E14 KOTO experiment [27] at the new high-intensity proton accelerator facility J-PARC (Japan Proton Accelerator Research Complex) [28]. The accelerators, consisting of a Linac, 3-GeV Rapid Cycle Synchrotron and Main Ring, succeeded in the acceleration to 30 GeV and slow and fast beam-extractions. The KOTO collaboration built the neutral beam line at the Hadron Hall of J-PARC and surveyed the beam in 2009. They started the detector construction in 2010 with the undoped CsI crystals used in the KTeV calorimeter. The next generation of $K^+ \to \pi^+\nu\bar{\nu}$ is the NA62 experiment [29] at CERN, which will use K^+ decays in flight from an un-separated beam of 75 GeV/c. The detector R&D with beam tests is close to the end, and the NA62 detector is being built. KOTO, as the first step in measuring $B(K_L^0 \to \pi^0\nu\bar{\nu})$ at J-PARC, aims at the observation of $K_L^0 \to \pi^0\nu\bar{\nu}$, and the goal of NA62 is to detect 100 $K^+ \to \pi^+\nu\bar{\nu}$ events. At FNAL, a new proposal [30] to measure $K^+ \to \pi^+\nu\bar{\nu}$ decays at rest has been submitted. Higher sensitivity kaon experiments based on a new high-intensity proton source at FNAL [31] are now under discussion.

At J-PARC, another new kaon experiment (E06 TREK) [32] is being prepared. In the $K^+ \to \pi^0\mu^+\nu$ decay, the transverse muon polarization (P_T) is a T-odd quantity and is a CP violation observable. New sources of CP violation may give rise to P_T as large as 10^{-3}. TREK is a successor to E246 at KEK-PS [33] and will measure the charged track and photons from the K^+ decay at rest with the E246 superconducting toroidal magnet, and aims at a P_T sensitivity of 10^{-4}. A low-momentum beam line is being built at the Hadron Hall.

3   Light neutral-boson search

Experimental searches for very light bosons have a long history, but a neutral boson whose mass is twice the muon mass has not yet been excluded. In 2005, the HyperCP collaboration at FNAL reported three events of the $\Sigma^+ \to p\mu^+\mu^-$ decay, and the dimuon mass may indicate a neutral intermediate state P^0 with a mass of 214.3 ± 0.5 MeV/c^2 [34]. Since the events were observed in an FCNC with a strange to down quark transition, P^0 should be confirmable with kaon decays. Dimuon masses in previous $K^+ \to \pi^+\mu^+\mu^-$ measurements were not observed in the narrow range around the P^0 mass; thus, P^0 should be a pseudo-scalar or axial-vector particle and be studied with the three-body decay $K \to \pi\pi P^0$.

The KTeV collaboration searched for the $K_L^0 \to \pi^0\pi^0\mu^+\mu^-$ decay for the first time [35] and set $B(K_L^0 \to \pi^0\pi^0\mu^+\mu^-) < 8.63 \times 10^{-11}$ and $B(K_L^0 \to \pi^0\pi^0P^0 \to \pi^0\pi^0\mu^+\mu^-) < 9.44 \times 10^{-11}$ (90% C.L.). The E391a collaboration searched for the decay $K_L^0 \to \pi^0\pi^0X$, $X \to \gamma\gamma$ in the mass range of X from 194.3 to 219.3 MeV/c^2, and set $B(K_L^0 \to \pi^0\pi^0P^0 \to \pi^0\pi^0\gamma\gamma) < 2.4 \times 10^{-7}$

(90% C.L.) [36]. Both results almost ruled out the predictions when P^0 is a pseudo-scalar particle [37, 38].

The E787/E949 results on $K^+ \to \pi^+ \nu \bar{\nu}$ have also been interpreted in the two-body decay $K^+ \to \pi^+ X$, where X is a massive noninteracting particle either in stable or unstable, and in $K^+ \to \pi^+ P^0$, $P^0 \to \nu \bar{\nu}$. The limits are presented in [26].

4   Lepton flavor universality

Investigation of the lepton-flavor violating (LFV) processes involving both quarks and charged leptons ($K_L^0 \to \mu^\pm e^\mp$ by E871 at BNL [39], $K^+ \to \pi^+ \mu^+ e^-$, $K^+ \to \pi^- \mu^+ \mu^+$, and $K^+ \to \pi^- e^+ e^+$ by E865 at BNL [40, 41], $K_L^0 \to \pi^0 \mu^\pm e^\mp$ and $K_L^0 \to \pi^0 \pi^0 \mu^\pm e^\mp$ by KTeV [42]) has achieved stringent limits on the branching ratios in $10^{-9} \sim 10^{-12}$. Continual efforts are made to search for the $\mu^+ \to e^+ \gamma$ decay and the $\mu^- N \to e^- N$ conversion with muons [43].

The LFV process in kaon decays is currently studied, intensively, in the context of high precision tests of Lepton Flavor universality. The ratio $R_K \equiv \Gamma(K^+ \to e^+ \nu(\gamma))/\Gamma(K^+ \to \mu^+ \nu(\gamma))$ is helicity suppressed in the Standard Model due to the V-A couplings and is predicted to be $R_K^{SM} = (2.477 \pm 0.001) \times 10^{-5}$ [44], in which the radiative decay $K^+ \to e^+ \nu \gamma$ ($K_{e2\gamma}$) via internal bremsstrahlung is included. Suppose a decay $K^+ \to e^+ \nu_\tau$ exists due to the process of an intermediate charged-Higgs particle and a LFV Supersymmetric loop (Fig. 3) [45]. Since the neutrino flavor is undetermined experimentally, deviations of

$$R_K = \frac{\Sigma_i \Gamma(K^+ \to e^+ \nu_i)}{\Sigma_i \Gamma(K^+ \to \mu^+ \nu_i)} \simeq \frac{\Gamma_{SM}(K^+ \to e^+ \nu_e) + \Gamma_{NP}(K^+ \to e^+ \nu_\tau)}{\Gamma_{SM}(K^+ \to \mu^+ \nu_\mu)}$$

from the Standard Model prediction, ΔR_K, in the relative size of $10^{-2} \sim 10^{-3}$ are suggested [46] as a function of the charged Higgs mass m_{H^+}, the ratio of the Higgs vacuum expectation values for the up- and down- quark masses (denoted as $\tan \beta$), and the effective $e - \tau$ coupling constant Δ_{13}:

$$\frac{\Delta R_K}{R_K^{SM}} = \frac{\Gamma_{NP}(K^+ \to e^+ \nu_\tau)}{\Gamma_{SM}(K^+ \to e^+ \nu_e)} = \left(\frac{m_{K^+}}{m_{H^+}}\right)^4 \left(\frac{m_\tau}{m_e}\right)^2 |\Delta_{13}|^2 \tan^6 \beta$$

and can be experimentally studied. The same physics goal is pursued by the PIENU experiment [47] at TRIUMF and the PEN experiment [48] at PSI to measure $\Gamma(\pi^+ \to e^+ \nu(\gamma))/\Gamma(\pi^+ \to \mu^+ \nu(\gamma))$ precisely.
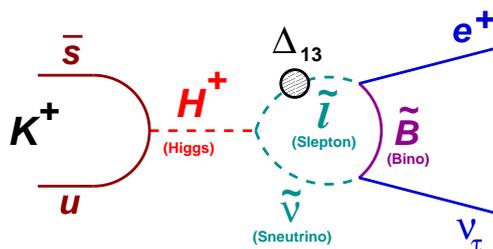
Figure 3: Diagram for the $K^+ \to e^+ \nu_\tau$ decay.

The KLOE collaboration at DAΦNE, the Frascati ϕ factory, measured R_K with 3.3G of the $K^+ K^-$ pairs from ϕ mesons with an integrated luminosity of 2.2 fb^{-1} collected during 2001-2005 [49]. The $K^\pm \to \ell^\pm \nu$ decay in flight ($\sim$0.1 GeV/c) was reconstructed by the tracks of a

kaon and a decay product with the same charge in the cylindrical drift chamber, and the squared mass m_ℓ^2 of the lepton for the decay was computed. To distinguish the $K^\pm \to e^\pm \nu$ events around $m_\ell^2 = 0$ from the tail of the $K^\pm \to \mu^\pm \nu$ peak, in addition to the track quality cuts, information about shower profile and total energy deposition in the electromagnetic calorimeter, combined with a neural network, and time-of-flight information were used for electron identification. The numbers of $K \to e\nu(\gamma)$ events were 7064±102 for K^+ and 6750±101 for K^-, respectively, 89.8% of which were $K \to e\nu$ events and the $K_{e2\gamma}$ events with $E_\gamma < 10$ MeV. The contribution from the $K_{e2\gamma}$ events with $E_\gamma > 10$ MeV, due to the direct-emission process, was studied [49, 50] by using a separate sample with photon detection requirement, and was subtracted. The numbers of $K \to \mu\nu(\gamma)$ events were 287.8M for K^+ and 274.2M for K^-, respectively. The difference between the K^+ and K^- counts was due to the larger cross section of K^- nuclear interaction in the material traversed. Finally, KLOE obtained $R_K = (2.493 \pm 0.025(stat.) \pm 0.019(syst.)) \times 10^{-5}$, in agreement with the Standard Model prediction. The regions excluded at 95% C.L. in the plane $M_{H^+} - \tan\beta$ are shown in Fig. 4, left, for different values of Δ_{13}.
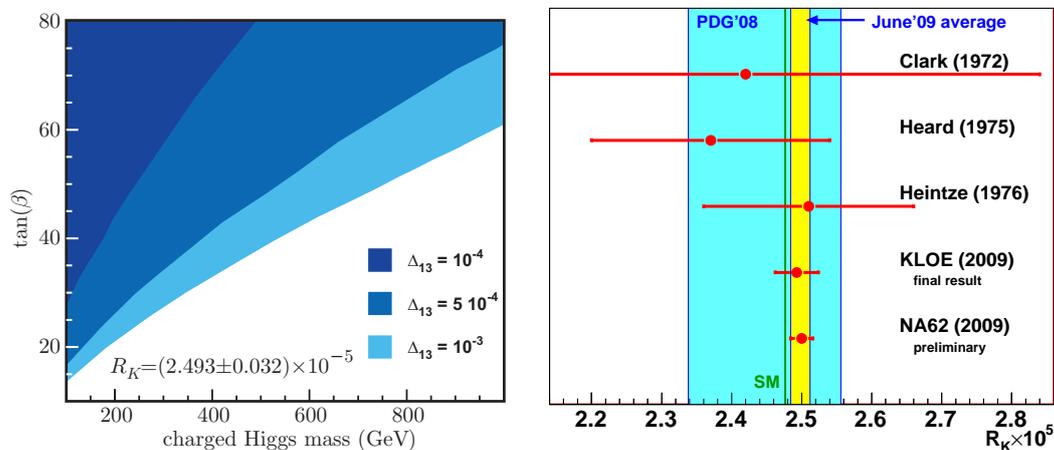
Figure 4: KLOE result on the excluded regions at 95% C.L. in the plane $m_{H^+} - \tan\beta$ for $\Delta_{13}=10^{-4}$, 5×10^{-4} and 10^{-3} [49] (left); summary of the R_K measurements including the report from NA62 [51] (right).

The NA62 collaboration, as the first phase, collected data to measure R_K during four months in 2007, and collected special data samples to study systematic effects for two weeks in 2008. The beam line and detector apparatus of NA48/2 were used; 90% of the data were taken with the K^+ beam of 74.0 ± 1.6 GeV/c, because the muon sweeping system provided better suppression of the positrons produced by beam halo muons via $\mu \to e$ decay. Preliminary results based on the analysis of 40% of the 2007 data collected with the K^+ beam only were reported in [51]. The number of $K^+ \to e^+\nu$ candidate events was 51089, and the number of $K^+ \to \mu^+\nu$ candidate events was 15.56M. The source of the main background, (6.28 ± 0.17) %, was found to be the $K^+ \to \mu^+\nu$ decay with muon identification as positron due to *catastrophic* bremsstrahlung in or in front of the liquid-Krypton electromagnetic calorimeter (LKr). The probability of the mis-identification was studied with pure muon samples, without positron contamination due to $\mu^+ \to e^+$ decays in flight, selected from the tracks traversing a $9.2X_0$-thick lead wall installed in front of LKr. R_K was obtained to be $(2.500 \pm 0.012(stat.) \pm 0.011(syst.)) \times 10^{-5}$, consistent

with the Standard Model prediction. Combining with other R_K measurements, the current world average is $(2.498 \pm 0.014) \times 10^{-5}$ as presented in Fig. 4, right. The final results from this 40% partial data will be available soon.

The R_K measurement will continue in the NA62 analysis of the full data sample as well as in the future KLOE-2 experiment, which is described in the next section.

5   CPT and QM tests

ϕ mesons decay into K^+K^- pairs with 49% and $K_L^0 K_S^0$ pairs with 34%. In the latter, the initial state is a coherent (and entangled) quantum state:

$$|i\rangle \;=\; \frac{1}{\sqrt{2}}\,[\,|K^0\rangle|\overline{K^0}\rangle \;-\; |\overline{K^0}\rangle|K^0\rangle\,] \;=\; \frac{N}{\sqrt{2}}\,[\,|K_S^0\rangle|K_L^0\rangle \;-\; |K_L^0\rangle|K_S^0\rangle\,]$$

where $N \simeq 1$ is a normalization factor. In the KLOE experiment, by tagging K_L^0 *crash* events in the calorimeter, a pure K_S^0 beam was available and there has been a major improvement in K_S^0 decay measurements [52]. With the results of various new measurements on neutral kaon decays, the Bell-Steinberger relation was used [53] to provide a constraint relating the unitarity of the sum of the decay amplitudes to the CPT observables. The latest limit on the mass difference between K^0 and $\overline{K^0}$ was 4.0×10^{-19} GeV at 95% C.L. [54].
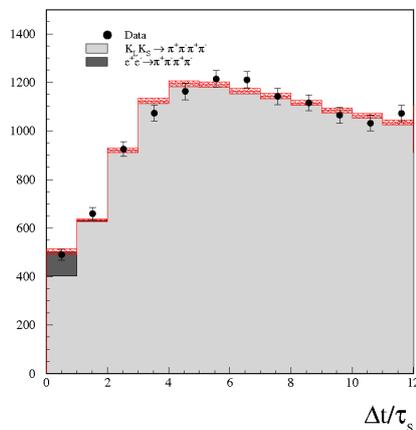
Figure 5: KLOE result on the fit to the measured $I(\Delta t)$ distribution of $\phi \rightarrow K_S^0 K_L^0 \rightarrow \pi^+\pi^-\pi^+\pi^-$ [56]. The black points with errors are data and the solid histogram is the fit result. The uncertainty arising from the efficiency correction is shown as the hatched area.

In the CP-violating process $\phi \rightarrow K_S^0 K_L^0 \rightarrow \pi^+\pi^-\pi^+\pi^-$, KLOE observed the quantum interference between two kaons for the first time [55]. The measured Δt distribution, with Δt the absolute value of the time difference of the two $\pi^+\pi^-$ decays, can be fitted with the

distribution in the $K_S^0 - K_L^0$ basis:

$$I(\Delta t) \quad \propto \quad e^{-\Gamma_L \Delta t} \; + \; e^{-\Gamma_S \Delta t} \; - \; 2(1-\zeta_{SL}) \; e^{-\frac{(\Gamma_S+\Gamma_L)}{2}\Delta t} \; \cos(\Delta m \Delta t)$$
$$\rightarrow \quad 2\zeta_{SL} \; \left(1 - \frac{(\Gamma_S + \Gamma_L)}{2}\Delta t\right) \qquad \Delta t \rightarrow 0$$

where Δm is the mass difference between K_L^0 and K_S^0. The interference term $e^{-\frac{(\Gamma_S+\Gamma_L)}{2}\Delta t} \cos(\Delta m \Delta t)$ is multiplied by a factor $(1 - \zeta_{SL})$ with a *decoherence* parameter ζ_{SL}, which represents a loss of coherence during the time evolution of the states and should be zero in Quantum Mechanics (QM). Final results obtained from KLOE with 1.5 fb^{-1} in 2004-2005 were [56] $\zeta_{SL} = (0.3 \pm 1.8(stat.) \pm 0.6(syst.)) \times 10^{-2}$ (Fig. 5) and, to the fit with the distribution in the $K^0 - \overline{K^0}$ basis, $\zeta_{0\overline{0}} = (1.4 \pm 9.5(stat.) \pm 3.8(syst.)) \times 10^{-7}$; no deviation from QM was observed. Decoherence in the $K^0 - \overline{K^0}$ basis results in the CP-allowed $K_S^0 K_S^0 \rightarrow \pi^+\pi^-\pi^+\pi^-$ decays and thus the value for the decoherence parameter $\zeta_{0\overline{0}}$ is much smaller. Since the measurement of non-zero ζ_{SL} is sensitive to the distribution in the small Δt region, the decay vertex resolution due to charged-track extrapolation ($\sim 1\tau_S \simeq 6$mm, to the vertex of a $K_S^0 \rightarrow \pi^+\pi^-$ decay close to the interaction point, in the KLOE detector) should be improved in future experiments. Other tests of CPT invariance and the basic principles of QM are discussed in [56, 57].

Kaon physics at the ϕ factory will continue with an upgraded KLOE detector, KLOE-2 [58], at an upgraded DAΦNE e^+e^- collider. During 2008 a new interaction scheme (*Crabbed Waist* collisions) was tested with the goal of reaching a peak luminosity of 5×10^{32} cm^{-2}s^{-1}, a factor of three larger than what previously obtained. In the first phase starting in 2010, the detector with minimal upgrade (two devices along the beam line to tag the scattered electrons/positrons from $\gamma\gamma$ collisions) restarts taking data for the integrated luminosity of 5 fb^{-1}. To the next phase, with the detector upgrades being planned for late 2011, an integrated luminosity of 20 fb^{-1} is expected. A cylindrical GEM detector [59] will be placed between the beam pipe and the inner wall of the drift chamber, as a new Inner Tracker, to improve the decay vertex resolution and to increase the acceptance for low transverse-momentum tracks.

6 Conclusions

The study of kaon physics continues to make great strides. The current program to study CP violation is being completed; the CP asymmetries in charged kaon decays have not been observed yet. The rare decays $K_L^0 \rightarrow \pi^0 \nu\bar{\nu}$, $K^+ \rightarrow \pi^+ \nu\bar{\nu}$ and the lepton flavor universality in $\Gamma(K^+ \rightarrow e^+\nu(\gamma))/\Gamma(K^+ \rightarrow \mu^+\nu(\gamma))$ will be measured with highly sophisticated detectors. A light neutral boson as a scalar/vector/pseudo-scalar particle was almost ruled out. CPT and QM tests will continue in a ϕ factory experiment. The kaon experiments, with ultra-high sensitivities and precisions, are essential and crucial as a probe of New Physics beyond the Standard Model.

Important topics of kaon physics: New Physics effects in ϵ_K and other meson-antimeson mixing observables [60, 61], V_{us} measurement with kaons and CKM unitarity test [62] (and the activities in the FlaviaNet Kaon Working Group [63, 64]), basic observables such as Δm, lifetimes, η_{+-}, and absolute branching ratios, radiative kaon decays, hadronic matrix elements and form factors, and $\pi\pi$ scattering (and the *cusp* effect) are not covered. The web site of

the 2009 Kaon International Conference (KAON09) [65] and the Proceedings [66] would be considered as a companion to this review.

Acknowledgments

References

[1] J.H. Christenson, J.W. Cronin, V.L. Fitch, and R. Turlay, Phys. Rev. Lett. **13** 138 (1964).

[2] V.L. Fitch, Rev. Mod. Phys. **53** 367 (1981); J.W. Cronin, Rev. Mod. Phys. **53** 373 (1981).

[3] L. Wolfenstein, Phys. Rev. Lett. **13** 562 (1964).

[4] M. Kobayashi and T. Maskawa, Prog. Theor. Phys. **49** 652 (1973).

[5] M. Kobayashi, Rev. Mod. Phys. **81** 1019 (2009); T. Maskawa, Rev. Mod. Phys. **81** 1027 (2009).

[6] CPLEAR collaboration, A. Angelopoulos *et al.*, Phys. Rep. **374** 165 (2003), and references therein.

[7] E.T. Worcester, arXiv:0909.2555 (2009) and arXiv:0910.3160 (2009).

[8] J. R. Batley *et al.*, Phys. Lett. **B544** 97 (2002).

[9] E.g., E. Blucher, B. Winstein, and T. Yamanaka, Prog. Theor. Phys. **122** 81 (2009).

[10] E.g., A. Ukawa, in these Proceedings.

[11] E.g., K. Anikeev *et al.*, *B Physics at the Tevatron: Run II and Beyond*, arXiv:hep-ph/0201071 (2002).

[12] NA48/2 Collaboration, J. R. Batley *et al.*, Eur. Phys. J. **C52** 875 (2007).

[13] NA48/2 Collaboration, J.R. Batley *et al.*, Phys. Lett. **B677** 246 (2009).

[14] R. Wanke, PoS KAON09 037 (2009); NA48/2 Collaboration, J.R. Batley *et al.*, arXiv:1004.0494 (2010).

[15] L.S. Littenberg, Phys. Rev. **D39** 3322 (1989).

[16] Y. Grossman and Y. Nir, Phys. Lett. **B398** 163 (1997).

[17] A.J. Buras, S. Uhlig, and F. Schwab, Rev. Mod. Phys. **80** 965 (2008), and references therein.

[18] F. Mescia and C. Smith, $K \to \pi\nu\nu$ *decay in the Standard Model*, `http://www.lnf.infn.it/wg/vus/content/Krare.html` (2010), and references therein.

[19] F. Mescia and C. Smith, Phys. Rev. **D76** 034017 (2007).

[20] A.J. Buras, M. Gorbahn, U. Haisch, and U. Nierste, JHEP **0611** 002 (2006).

[21] J. Brod and M. Gorbahn, Phys. Rev. **D78** 034006 (2008).

[22] D. Bryman, A.J. Buras, G. Isidori, and L. Littenberg, Int. J. Mod. Phys. **A21** 487 (2006).

[23] H. Watanabe *et al.*, Nucl. Instrum. Methods. Phys. Res. Sect. A **545** 542 (2005).

[24] E391a Collaboration, J.K. Ahn *et al.*, Phys. Rev. **D81** 072004 (2010).

[25] S. Adler *et al.*, Phys. Rev. **D77** 052003 (2008).

[26] E949 Collaboration, A.V. Artamonov *et al.*, Phys. Rev. Lett. **101** 191802 (2008) and Phys. Rev. **D79** 092004 (2009).

[27] `http://koto.kek.jp/`; H. Nanjo, PoS KAON09 047 (2009).

[28] http://j-parc.jp/.

[29] http://na62.web.cern.ch/NA62/; G. Ruggiero, PoS KAON09 043 (2009).

[30] Fermilab Proposal P996: *Measurement of the $K^+ \rightarrow \pi^+ \nu\bar{\nu}$ Decay at Fermilab* (2009).

[31] http://projectx.fnal.gov/.

[32] http://trek.kek.jp/; J. Imazato, PoS KAON09 007 (2009).

[33] E246 Collaboration, M. Abe *et al.*, Phys. Rev. **D73** 072005 (2006).

[34] HyperCP Collaboration, H.K. Park *et al.*, Phys. Rev. Lett. **94** 021801 (2005).

[35] D.G. Phillips, PoS KAON09 039 (2009).

[36] E391a Collaboration, Y.C. Tung *et al.*, Phys. Rev. Lett. **102** 051802 (2009).

[37] X.G. He, J. Tandean, and G. Valencia, Phys. Rev. Lett. **98** 081802 (2007).

[38] S. Oh and J. Tandean, JHEP **1001** 022 (2010), and references therein.

[39] BNL E871 Collaboration, D. Ambrose *et al.*, Phys. Rev. Lett. **81** 5734 (1998).

[40] A. Sher *et al.*, Phys. Rev. **D72** 012005 (2005).

[41] R. Appel *et al.*, Phys. Rev. Lett. **85** 2877 (2000).

[42] KTeV Collaboration, E. Abouzaid *et al.*, Phys. Rev. Lett. **100** 131803 (2008).

[43] T. Mori, in these Proceedings.

[44] V. Cirigliano and I. Rosell, Phys. Rev. Lett. **99** 231801 (2007).

[45] A. Masiero, P. Paradisi, and R. Petronzio, Phys. Rev. **D74** 011701(R) (2006).

[46] A. Masiero, P. Paradisi, and R. Petronzio, JHEP **0811** 042 (2008).

[47] http://pienu.triumf.ca/.

[48] http://pen.phys.virginia.edu/.

[49] KLOE Collaboration, F. Ambrosino *et al.*, Eur. Phys. J. **C64** 627 (2009) and **C65** 703(E) (2010).

[50] M. Moulson, PoS KAON09 035 (2009).

[51] E. Gooudzovski, PoS KAON09 025 (2009) and arXiv:1005.1192 (2010).

[52] KLOE Collaboration, F. Bossi *et al.*, Riv. Nuovo Cim. **031** 531 (2008), and references therein.

[53] The KLOE collaboration, G. D'Ambrosio and G. Isidori, JHEP **0612** 011 (2006).

[54] M. Palutan, Flavianet Kaon Workshop, Capri, Italy (2008).

[55] KLOE Collaboration, F. Ambrosino *et al.*, Phys. Lett. **B642** 315 (2006).

[56] A. Di Domenico and the KLOE collaboration, J. Phys.: Conf. Ser. **171** 012008 (2009).

[57] A. Di Domenico, PoS KAON09 038 (2009), and references therein.

[58] http://www.lnf.infn.it/kloe2/; P. Branchini, PoS KAON09 048 (2009); G. Amelino-Camelia *et al.*, arXiv:1003.3868 (2010).

[59] KLOE-2 Collaboration, G. De Robertis *et al.*, arXiv:1002.2572 (2010).

[60] E. Lunghi and A. Soni, Phys. Lett. **B666** 162 (2008).

[61] A.J. Buras and D. Guadagnoli, Phys. Rev. **D78** 033005 (2008).

[62] S. Prell, in these Proceedings.

[63] http://www.lnf.infn.it/wg/vus/.

[64] FlaviaNet Working Group on Kaon Decays, M. Antonelli *et al.*, arXiv:1005.2323 (2010).

[65] http://kaon09.kek.jp/.

[66] http://pos.sissa.it/cgi-bin/reader/conf.cgi?confid=83.

Discussion

Cheng-Ju Lin (LBNL Berkeley): What is the plan to measure $K^+ \to \pi^+ \nu \bar{\nu}$ at J-PARC?

Answer: A Letter of Intent to measure $K^+ \to \pi^+ \nu \bar{\nu}$ with K^+ decay at rest, as in BNL E949/E787, has been submitted, but the proposal is not prepared yet. To do the measurement at J-PARC we need a low-momentum K^+ beam line with good electrostatic K^+/π^+ separation, but such a beam line is not ready.

Physics of tau and charm

Yifang Wang[*]

Institute of High Energy Physics, Beijing 100049

The physics of tau and charm started in early 70's after J/ψ and τ were discovered. Since then several dedicated accelerators and experiments were built with increasing luminosities and studies on light hadron spectroscopy, charmonium, electroweak and QCD were never interupted. New interests and surprises are not rare in this area. With the newly built BEPCII/BESIII, an even brighter future is foreseen.

1 introduction: physics at tau-charm colliders

Since the successful test of ADA, several electron-positron colliders were built in late 60's and early 70's. The most successful one is SPEAR, which discovered both the ψ and tau, marking the beginning of the tau-charm physics. Many members of the charmonium family and charmed mesons were then discovered at SPEAR and Doris, and many unknowns and controversies were resolved up to 80's.

The precision physics at tau-charm energy region began from BEPC/BES, the first accelerator even built for high energy physics in China in early 90's. The luminosity were improved by an order of magnitude over SPEAR, and this record was surpassed by CESR-c in 2004, as shown in Fig. 1.
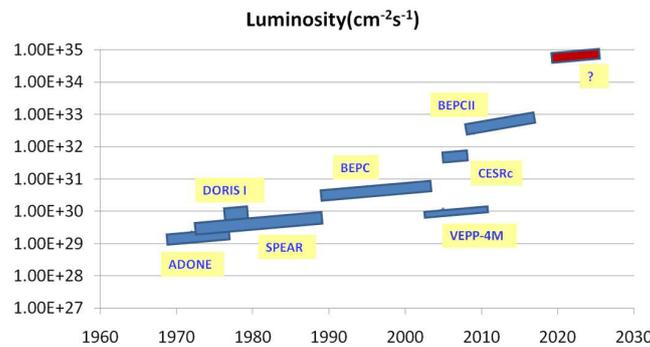
Figure 1: A history of accelerators running for tau-charm physics.

The newly built BEPCII/BESIII is an upgrade to the previous BEPC/BES [1, 2]. The designed peak luminosity is 1×10^{33} cm^{-2}s^{-1}, another order of magnitude over CESR-c. The

---

[*]yfwang@ihep.ac.cn

race may continue with the idea of a super-tau-charm factory with a luminosity of about $1 \times 10^{35} cm^{-2} s^{-1}$.

Why we are so interested in building tau-charm colliders in the last 40 years, even now in the era of LHC, and possibly in the future? In fact, J/ψ and its family can be produced at e^+e^- colliders with huge cross sections and abundant resonances, providing an ideal laboratory for charm, charmonium and QCD studies. Charm quark is actually a bridge between pQCD and non-pQCD, and relevant information becomes a ruler for Lattice QCD. Charmonium decays through the so-called three-gluon loop is one of the best channels to search for glueballs and hybrids. The threshold production of charmonia and taus has a lot of advantages on background suppression, kinematic constraints and quantum correlations. In the era of LHC, high precision flavor physics is complementary since new phenomena at high energies should also evident via virtual loops and secondary effects at lower energies.

The latest progress of tau-charm physics and prospects at the newly built high luminosity tau-charm collider, BEPCII, is summarized in the book "Physics at BESIII [3], which covers all the areas including the charm physics, charmonium physics, tau physics, QCD studies and light hadron spectroscopy. Examples of highlights include $D\bar{D}$ mixing, precision measurement of CKM matrix elements and the tau mass, charmonium transition and spectroscopy, exotic hadron searches, new hadrons above the open charm threshold, etc.

In this talk, I will select a few topics to report the progress in this field.

2 CLEOc: a fruitful short program on charm physics

CESRc started its charm program since 2004 and ceased operation in 2008. Although very short, it is a very fruitful program in charm and charmonium physics.

Threshold production of charmed mesons is of particular importance since D and $\bar{D}$ are doubly produced at $\psi(3770)$ at rest. $D\bar{D}$ mixing can then be studied in an almost background-free environment with quantum correlations. Even the statistics is low and there is no time-development, the double-tag technique allows to reduce systematic errors, hence a complementary to that at B-factories. CLEO reported a first determination of cosδ using the quantum correlation between two D's produced at rest from $\psi(3770)$ decays [4]. In fact, due to the mixing, tagging one D^0 in a CP eigenstate, the other side is a mixture of D^0 and $\bar{D}^0$ with an event rate proportional to $B_1 B_2 (1 + 2r cos\delta)$, where B_1 and B_2 are branching ratios of D's at each side, and cosδ is the quantum correlation, which is related to the mixing parameters. A global fit is performed for 8 hadronic D decay channels and δ is determined to be $(22^{+11+9}_{-12-11})^o$, limited by statistics. Clearly with BESIII, a significant improvement can be expected.

$D\bar{D}$ mixing has been firmly established, thanks mainly to B-factories with great statistical advantages. A global fit shows that mixing is established at 10.2 σ level, and consistent with CP conservation [5]. These results are consistent with the Standard Model as well as many New Physics models. In fact, Standard Model can not give a reliable prediction due to the complication at hadron level. In order to understand the origin of the mixing, we need to integrate all the flavor physics results, correlate them with other mixing results, have more data on rare decays and CP violation limits to constrain New Physics models. CLEO searched for the CP violation in many D and D_s decays [6]. BESIII at a high luminosity machine can in fact improve the limit significantly.

CKM matrix elements can be measured precisely via leptonic and semi-leptonic decays of

D mesons. In the leptonic case, the decay width follows

$$\Gamma(D_{(s)} \to l\nu) = f_{D_{(s)}}^2 |V_{cq}|^2 \frac{G_F^2}{8\pi} m_{D_{(s)}} m_l^2 (1 - \frac{m_l^2}{m_{D_{(s)}}^2})^2.$$

CLEO recently reported their measurements of $D^+ \to \mu^+\nu$, $D_s^+ \to \mu^+\nu$ and $D_s^+ \to \tau^+\nu$, giving $f_D = (205.8 \pm 8.5 \pm 2.5)$ MeV, $f_{D_s} = (259.5 \pm 6.6 \pm 3.1)$ MeV [7]. While f_D is in perfect agreement with the prediction of lattice QCD [8], i.e. (208 ± 4) MeV from the HPQCD-UKQCD group, f_{D_s} is 2.3 σ away from the prediction of (241 ± 3) MeV. BESIII may resolve this issue with a larger statistics and better precision.

In the semi-leptonic case, the differential decay width follows

$$\frac{d\Gamma(X \to X'l\nu)}{dq^2} = [f_+^{X \to X'}(q^2)|V_{Qq}|]^2 \frac{G_F^2}{24\pi^3} p_{X'}^3.$$

By fitting this formula with data and using LQCD prediction of $f_+^K(0)$ and $f_+^\pi(0)$, as shown in Fig. 2, CLEO obtained new CKM matrix element measurement [9], $|V_{cd}| = 0.234 \pm 0.007(stat.) \pm 0.002(syst.) \pm 0.025(LQCD)$, and $|V_{cs}| = 0.985 \pm 0.009(stat.) \pm 0.006(syst.) \pm 0.103(LQCD)$. Several new D and D_s semi-leptonic decay modes are observed for the first time by

decay mode	branching fraction
$D^+ \to \eta e^+ \nu$	$0.133 \pm 0.020 \pm 0.006$
$D^+ \to \eta' e^+ \nu$	<0.035
$D^+ \to \phi e^+ \nu$	< 0.016
$D_s^+ \to \eta e^+ \nu$	$2.48 \pm 0.29 \pm 0.13$
$D_s^+ \to \eta' e^+ \nu$	$0.91 \pm 0.33 \pm 0.05$
$D_s^+ \to \phi e^+ \nu$	$2.29 \pm 0.37 \pm 0.11$
$D_s^+ \to K^0 e^+ \nu$	$0.37 \pm 0.10 \pm 0.02$
$D_s^+ \to K^{*0} e^+ \nu$	$0.18 \pm 0.07 \pm 0.01$
$D_s^+ \to f_0(\to \pi^+\pi^-) e^+ \nu$	$0.13 \pm 0.04 \pm 0.01$

Table 1: Branching ratios of several new semi-leptonic decay modes measured by CLEO.

CLEO [10], as listed in Table 1. These new D decay modes are interesting for glueball searches, while new D_s decay modes are Cabibbo-suppressed and scalers.

Only a small fraction of charm physics results from CLEO are reported here. For more information, please refer to recent publications of the CLEO collaboration. Now let's turn to charmonium physics.
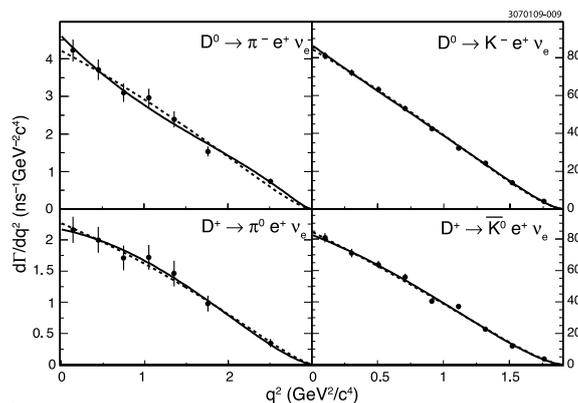
Figure 2: The momentum spectrum of semi-leptonic decays from CLEO experiment

Charmonium family, an interesting lab for pQCD and non-pQCD, can be used to calibrate LQCD. Their productions, transitions, decays and the spectroscopy are not fully understood

yet and examples of interesting and long-standing issues including the $\rho\pi$ puzzle, mixing state, missing states, and new XYZ states. For detailed discussion, please refer to reference [3].

η_c is the lowest state of the charmonium family, its mass and width are hence critical. However, current mass measurements are not consistent, and this problem is traced by CLEO to be the distorted line-shape of η_c [11] from a standard Breit-Wigner form,as shown in Fig 3. The reason is not known yet, and CLEO fitted the data with a modified empirical Breit-Wigner formula. We are waiting for results from BESIII on exclusive channels and energy dependent $\psi(1S, 2S) \rightarrow \gamma\eta_c$ matrix element measurements.
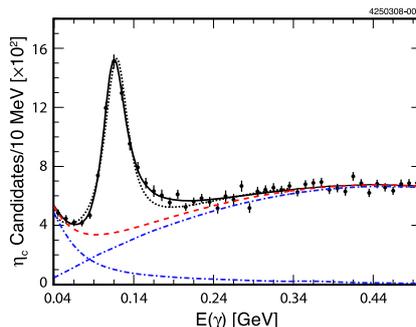
Figure 3: Fits to the photon spectrum in exclusive $J/\psi \rightarrow \gamma\eta_c$ decays using relativistic Breit-Wigner (dotted) and modified (solid) signal line shapes convolved with a 4.8 MeV wide resolution function.

χ_{cJ} from ψ' decays is ideal for the light hadron spectroscopy since they have clean and multiple J^{PC} states. In two body decays they can be used to study the role of the color octet mechanism and to probe the gluon content in final states. CLEO reported results for two-baryon final states previously [12], and two-meson final states recently including $\pi\pi$, $\eta\eta$, $\eta\eta'$, $\eta'\eta'$, KK, etc. [13]. Radiative decay processes of χ_{cJ} to light vectors, $\chi_{cJ} \rightarrow \gamma(\rho, \omega, \phi)$, similar to that of the glueball production of $J/\psi \rightarrow \gamma f_J$, have been searched for. For the first time, the decay modes of $\chi_{c1} \rightarrow \gamma\rho$ and $\chi_{c1} \rightarrow \gamma\omega$ are observed [14]. Figure 4 shows the observed signals and table 2 list the results in comparison with the prediction based on pQCD calculations [15]. However, the prediction is one order of magnitude below the observation.

decay mode	BR×10^6	U.L.[10^{-6}]	pQCD[10^{-6}]
$\chi_{c0} \rightarrow \gamma\rho^0$		<9.6	1.2
$\chi_{c1} \rightarrow \gamma\rho^0$	$243 \pm 19 \pm 22$		14
$\chi_{c2} \rightarrow \gamma\rho^0$	$25 \pm 10^{+8}_{-14}$	<50	4.4
$\chi_{c0} \rightarrow \gamma\omega$		<8.8	0.13
$\chi_{c1} \rightarrow \gamma\omega$	$83 \pm 15 \pm 12$		1.6
$\chi_{c2} \rightarrow \gamma\omega$		<7.0	0.5
$\chi_{c0} \rightarrow \gamma\phi$		<6.4	0.46
$\chi_{c1} \rightarrow \gamma\phi$	$12.8 \pm 7.6 \pm 1.5$	<26	3.6
$\chi_{c2} \rightarrow \gamma\phi$		<13	1.1

Table 2: Measured Branching ratios or up limits in comparison with pQCD calculations

CLEO also reported charmonia(J/ψ, $\psi(2S)$ and $\psi(3770)$) radiative decays to pesude-vectors, including π^0, η and η' [16]. Improvements over previous measurements on J/ψ and $\psi(2S)$ decays
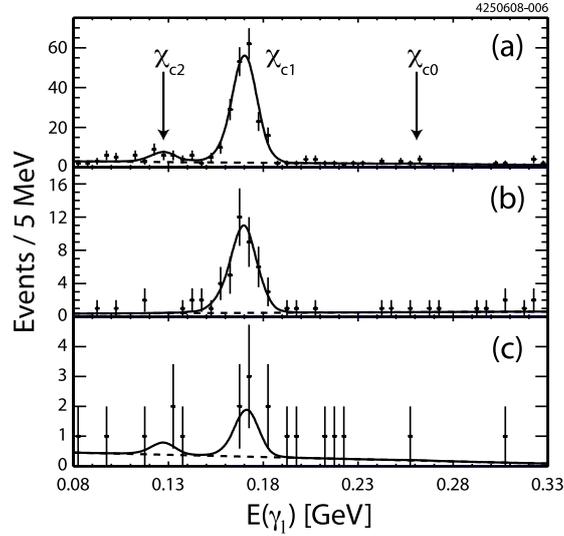
Figure 4: Observed signal of $\chi_{cJ} \to \gamma V$. The $\psi(2S) \to \gamma\chi_{cJ}$ transition photon (γ_1) energy distribution for (a) $\chi_{cJ} \to \gamma\rho^0$, (b) $\chi_{cJ} \to \gamma\omega$, and (c) $\chi_{cJ} \to \gamma\phi$ candidates. The data are shown by the points; the fit is shown as a solid line. The background component of the fit is indicated by the dashed line.

were observed, while no $\psi(3770)$ decays was observed. A new decay mode of $J/\psi \to \gamma\gamma\gamma$ was observed [17], and the branching fraction is measured to be $(1.2 \pm 0.3 \pm 0.2) \times 10^{-5}$. This is the quarkonium analogue of ortho-positronium decay, and no similar decays have been observed for any particles so far.

The last member of the charmonium family under the open charm threshold, h_c was discovered by CLEO [18] and an updated product branching fraction, $B(\psi(2s) \to \pi^0 h_c) \times B(h_c \to \gamma\eta_c)$, was reported to be $(4.19 \pm 0.32 \pm 0.45) \times 10^{-4}$ [19], averaging the inclusive and exclusive channels. Later I will report the first BESIII results which improves this measurements. In fact, with a much larger data sample and a great detector, BESIII will improve significantly all the results mentioned above, and new discoveries are expected.

3 KEDR: a special dedication to mass measurement

The VEPP-4M accelerator and the KEDR detector at Novosibirsk in Russia started operation in 2002 and the luminosity is about $1 \times 10^{30} cm^{-2} s^{-1}$. A special physics program was performed by calibrating the beam energy precisely. Two techniques are developed: Resonance Spin Depolarization with a precision better than 30 keV and Back Compton Scattering with a precision better than 150 keV. The mass of particles in the tau-charm

particles	mass(MeV)
tau	$1776.69^{+0.17}_{-0.19} \pm 0.15$
J/ψ	$3096.924 \pm 0.010 \pm 0.017$
$\psi(2s)$	$3686.125 \pm 0.010 \pm 0.015$
$\psi(3770)$	$3772.8 \pm 0.5 \pm 0.6$
$D^{\pm}$	$1869.32 \pm 0.48 \pm 0.21$
D^0	$1865.53 \pm 0.39 \pm 0.24$

Table 3: Recent mass measurements at KEDR

energy region, including tau, J/ψ,ψ', D mesons etc. are measured to an un-precedent precision. Table 3 lists their results[20]. Results are consistent with previous measurements and further improvements are expected. The Back Compton Scattering technique will be used at BESIII and an even more precised tau mass measurement is expected.

4 BESII: a final legacy

The partial upgrade of the BES detector, called BESII, stop operation in 2004, however, physics results on light hadron spectroscopy and QCD studies are still coming based on the existing data sample. Since the production cross section of J/ψ is huge, its decay is an ideal place for light hadron spectroscopy study. A few examples are given here.

κ is a very interesting particle needed by the Chiral Perturbative Theory. There was a hot debate since it was observed for the first time in $K\pi$ scattering. The E791 experiment found the evidence of neutral κ in 2004 from $D^+ \to K^-\pi^+\pi^+$ and BESII firmly established its existence in 2006 from $J\psi \to K^{*0}K\pi \to K\pi K\pi$ decays [21]. CLEO reported the necessity of charged κ in $D^0 \to K^+K^-\pi^0$, however, no $\kappa^\pm \to K^\pm\pi^0$ is needed in BABAR data. BESII recently observed charged κ in $J/\psi \to K^{*\pm}\kappa^\mp \to K_s\pi^\pm K^\mp\pi^0$, as shown in Fig. 5 [22]. The pole position is measured to be $(841\pm51^{+14}_{-28}) - i(288\pm101^{+64}_{-30})MeV/c^2$, in consistent with that of the neutral one.
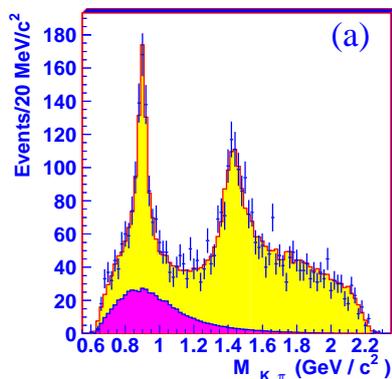
Figure 5: The observed $\kappa^\pm$ signal at BESIII from an invariant mass spectrum of $K^\pm\pi^0$. Shaded area are κ signals.

In addition to light hadron physics, QCD studies at the tau-charm energy region is of particular importance since it is at the boundary between pQCD and non-pQCD. Precision measurement of the R-value in this region will provide valuable input for vacuum polarization, improving the prediction of Higgs mass and g-2. BESII recently reported a new measurement of R at the center-of-mass energies of 2.6 GeV, 3.07 GeV and 3.65 GeV respectively, reducing the error from about 6% to 3.5% [23].

5 BESIII: a bright future

The newly completed upgrade of Beijing Electron-Positron Collider(BEPCII) and the new detector(BESIII) represents the future of the field [1]. BEPCII is a double-ring accelerator with a designed peak luminosity of 10^{33} cm$^{-2}s^{-1}$ at a beam current of 0.93 A. Both the machine and the detector worked remarkably well since beginning and world largest data samples of J/ψ and ψ' have been collected. It is believed that physics at the tau-charm region will be renewed dramatically and important discoveries will be possible.In the following I will gave a short summary about their performance and the initial results recently published.

5.1 Status of BEPCII/BESIII and data taking

The BEPCII/BESIII upgrade started in 2003 and successfully completed in 2008. BEPCII managed to accumulate a beam current of 500 mA in the storage ring, and obtained a collision luminosity close to 10^{32}cm^{-2}s^{-1} in March 2008. While the BESIII detector completed installation at the end of 2007 and the first full cosmic-ray event was recorded in March 2008. The detector was successfully moved to the interaction point on April 30, 2008. With a careful tuning of the machine, the first e^+e^- collision event was recorded by the BESIII detector on July 19, 2008, and a total of 14 million ψ' events was collected until Nov. 2008. Over this period, the BEPCII performance continued to improve by the lattice optimization, system debugging, and vacuum improvements. After a 1.5-month synchrotron radiation run and a winter maintenance, the machine resumed collision and its luminosity gradually improved from 1×10^{32} cm$^{-2}s^{-1}$ to 3×10^{32} cm$^{-2}s^{-1}$.

Starting from March of 2009, BES-III successfully collected 100 million $\psi(2S)$ events and 200 million J/ψ events, about a factor of 4 larger than the previous data samples from CLEO-c and BES-II, respectively. The peak luminosity was stable, typically at the level of 2×10^{32} cm^{-2}s^{-1} during the data taking at $\psi(2S)$, and 0.6×10^{32} cm^{-2}s^{-1} at J/ψ. An energy scan of the $\psi(2S)$ line-shape shows that the beam energy spread is about 1.4 MeV, and the effective peak cross section of $\psi(2s)$ is about 700 nb. The data taking efficiency of the detector is more than 85%.

The BESIII detector [1, 2], as shown in Fig. 6, consists of the following main components: 1) a main draft chamber (MDC) equipped with about 6500 signal wires and 23000 field wires arranged as small cells with 43 layers. The designed single wire resolution is 130 μm and the momentum resolution 0.5% at 1 GeV; 2) an electromagnetic calorimeter(EMC) made of 6240 CsI(Tl) crystals. The designed energy resolution is 2.5%@1.0 GeV and position resolution 6mm@1.0 GeV; 3) a particle identification system using Time-Of-Flight counters made of 2.4 m long plastic scintillators. The designed resolution is 80 ps for two layers, corresponding to a K/π separation (2σ level) up to 0.8 GeV; 4)a superconducting magnet with a field of 1 tesla; 5) a muon chamber system made of Resistive Plate Chambers(RPC).

The detector was calibrated using the $\psi(2S)$ events and the main performance parameters of the BES-III detector is shown in Fig. 7. Clearly, the detector is in a very good condition and all the design specifications have been satisfied.

A comprehensive Monte Carlo simulation code, largely based on the first principle of particles interacting with detector materials, was developed to model the performance of the BES-III detector. A good agreement was observed, not only on average numbers, but also on the details functional shape. This agreement ensures the well control of systematic errors and precision physics measurement.
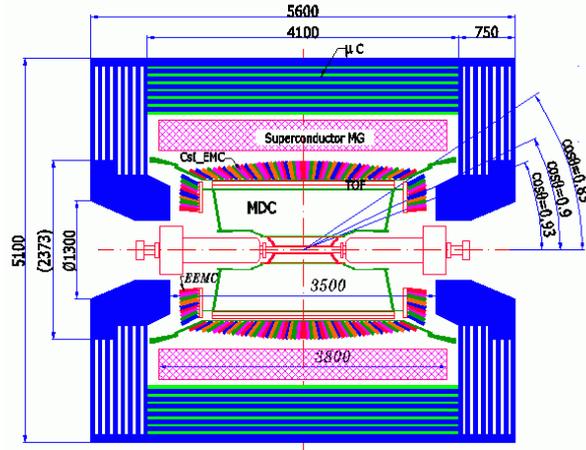
Figure 6: A schematic view of the BESIII detector.

5.2 Preliminary physics results

Physics at BESIII are very rich [3]. An initial physics program has been planned for the $\psi(2S)$ data set, including, but not limited to, the following topics:

- Spin-singlet studies(h_c, η_c, η_c');

- $\psi(2S)$ hadronic decays ($\rho\pi$ puzzle, new states);

- χ_c decays (search for new states and new decays).

A first glance of the $\psi(2S)$ data shows that a lot of resonances can be clearly seen. Fig. 8 shows the inclusive photon spectrum from the electromagnetic calorimeter. Signals from the electromagnetic transition between charmoniuum states can be well identified and they demonstrate the impressive performance of the CsI(Tl) crystal calorimeter.

Initial physics results have been obtained, ranging from the confirmation of BES-II and CLEO-c results, to completely new observations. Fig. 9 shows the prompt photon spectrum from $\psi(2S) \rightarrow \gamma\pi^0\pi^0$ (left) and $\psi(2S) \rightarrow \gamma\eta\eta$ (right) [24]. Signals from χ_{c0} and χ_{c2} are observed and their branching ratios are measured, which are consistent with recent results from CLEO-c [13].

The last member of the charmoniuum family below the open charm threshold called h_c was observed by CLEO-c in 2005 from $\psi(2S)$ decays to $\pi^0 h_c$, $h_c \rightarrow \gamma\eta_c$ [18] and an improved measurement was performed recently [19]. BESIII performed a similar analysis with a larger data sample, and a clear signal can be seen by tagging the prompt photon in the h_c decays [25], as shown in Fig. 10. In addition, BESIII tried to look for inclusive π^0 from $\psi(2S)$ decays and clear signals can be also seen. Branching fractions of $\psi(2S) \rightarrow \pi^0 h_c$, $h_c \rightarrow \gamma\eta_c$ can be individually measured for the first time, together with the width of h_c. Results are listed in the table 4 in comparison with recent CLEO results [19]. Good agreement can be seen.
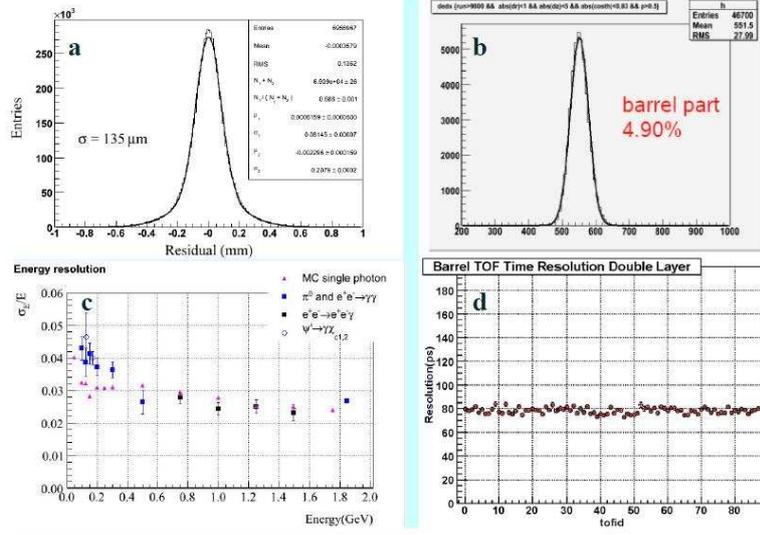
Figure 7: Main performance parameters of the calibrated BESIII detector: a) Single wire resolution of the drift chamber; b) dE/dx resolution of the drift chamber in the barrel part(w/ all wires); c) energy resolution of the CsI(Tl) crystal calorimeter as a function of photon energy from different physics processes; d) time resolution of TOF counters averaged over two layers for each counter ID in phi direction.
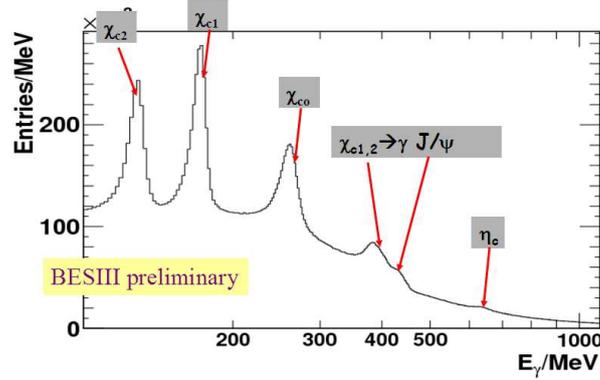
Figure 8: Measured inclusive photon spectrum from $\psi(2S)$ decays.

Parameters	BESIII result	CLEO results
M_{h_c}	$3525.40 \pm 0.13 \pm 0.18$ MeV	$3525.28 \pm 0.19 \pm 0.12$ MeV
Γ_{h_c}	$(0.73 \pm 0.45 \pm 0.28)$ MeV	-
$B(\psi' \to \pi^0 h_c$	$(8.4 \pm 1.3 \pm 1.0) \times 10^{-4}$	-
$B(h_c \to \gamma\eta_c)$	$(54.3 \pm 6.7 \pm 5.2)\%$	-
$B(\psi' \to \pi^0 h_c) \times B(h_c \to \gamma\eta_c)$	$(4.58 \pm 0.40 \pm 0.50) \times 10^{-4}$	$(4.19 \pm 0.32 \pm 0.45) \times 10^{-4}$

Table 4: Measured results of h_c in comparison with recent CLEO results. During the fit, Γ_{h_c} is floating at BESIII while CLEO fixes $\Gamma_{h_c} = \Gamma_{\chi c1} = 0.9 MeV$
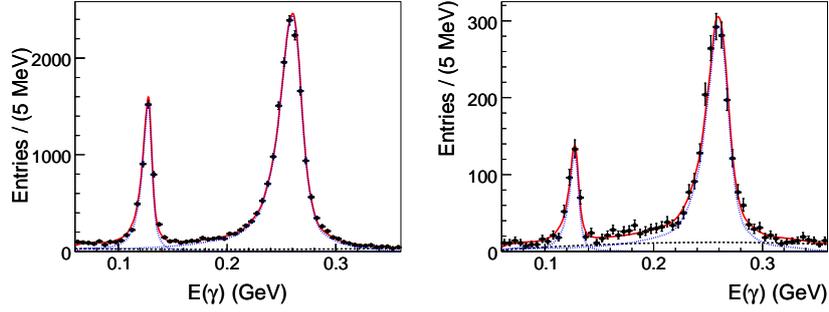
Figure 9: Observed χ_{c0} and χ_{c2} signal from $\psi(2S) \to \gamma\pi^0\pi^0$ (left) and $\psi(2S) \to \gamma\eta\eta$ (right) channels.
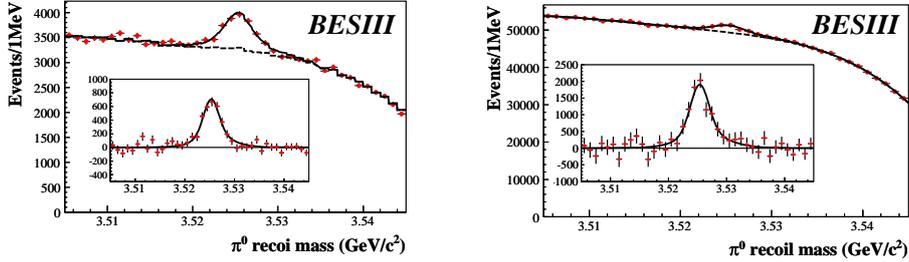
Figure 10: h_c observed in BES-III. Upper: tagging the prompt photon in the $h_c \to \eta_c$ decays, lower: tagging π^0 from $\psi(2s) \to \pi^0 h_c$ decays.

Other preliminary results of BESIII include, for example, the study of $\psi(2S) \to \gamma V V$, $V = \phi, \omega$, $\psi(2S) \to \gamma\gamma V$, $V = \rho, \phi, \omega$, $\psi(2S) \to \gamma P$, $P = \pi^0, \eta, \eta'$. New decay modes have been seen and results will be finalized soon.

BES-III also confirmed many observations by BES-II [26]. Fig. 11 shows the $p\bar{p}$ invariant mass from a) $\psi(2S) \to \pi\pi J/\psi$, $J/\psi \to \gamma p\bar{p}$, and b) $\psi(2S) \to \gamma p\bar{p}$ [27]. Clearly, a threshold enhancement can be seen in J/ψ decays, but not in $\psi(2S)$ decays, consistent with BES-II observations.

6 Summary

Charm physics will not stop at BEPCII/BESIII. The newly operational LHCb experiment, the upgrade of the B-factory at KEK to be operational in 2014, the PANDA experiment at FAIR planed to be operational in 2015, will all join the race. The super-flavor factory planed at FRASCATI and the super-tau-charm factory proposed at Novosirbisk, may substantial change the field. It is remarkable that tau-charm collider has a life time much more than 50 years.
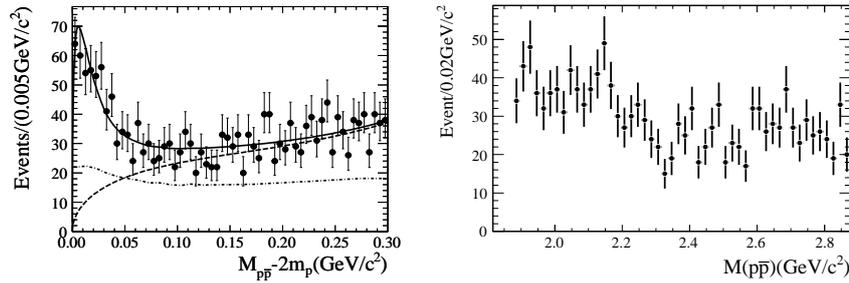
Figure 11: Invariant mass of $p\bar{p}$ from (left) $\psi(2s) \rightarrow \pi\pi J/\psi$, $J\psi \rightarrow \gamma p\bar{p}$, and (right) $\psi(2s) \rightarrow \gamma p\bar{p}$.

7   Acknowledgments

References

[1] Y.F. Wang, Int. J. Mod. Phys. A 21(2006)5371; Y. F. WANG, hex-ex:0711.4199, talk given at Charm07.

[2] M.Ablikim et al., BESIII coll., Nucl.Instrum.Meth.A614(2010)345.

[3] "Physics at BES-III", Edited by K. T. Chao and Y. F. Wang, Int. J. Mod. Phys. **A 24**, No.1(2009).

[4] J.L. Rosner *et al.*, CLEO coll., Phys.Rev.Lett.100 (2008) 221801;D. Asner *et al.*, CLEO coll., Phys. Rev. D78(2008) 012001.

[5] http://www.slac.stanford.edu/xorg/hfag/charm

[6] S. Dobbs *et al.*, CLEO coll., Phys.ReV.D 76 (2007) 112001; J.P. Alexander *et al.*, CLEO coll., Phys.ReV.Lett.100 (2008)161804; P. Rubin *et al.*, CLEO coll., Phys.Rev.D 78(2008)072003.

[7] B.I.Eisenstein *et al.*, CLEO coll., Phys.Rev.D78(2008)052003;J.P. Alexander *et al.*, CLEO coll., Phys.Rev.D79(2009)052001; P.U. Onyisi *et al.*, CLEO coll., PRD79(2009)052002.

[8] E. Follana *et al.*, HPQCD and UKQCD coll., Phys.Rev.Lett. 100(2008) 062002.

[9] D.Besson *et al.*, CLEO coll., Phys.Rev.D 80(2009) 032005.

[10] R.E. Mitchell et al.,CLEO coll., Phys.Rev.Lett.102(2009)081801; J.Yelton et al., CLEO coll., Phys.Rev.D.80(2009)052007.

[11] R.E. Michell *et al.*, CLEO coll., Phys.Rev.Lett. 102(2009) 011801.

[12] P. Naik *et al.*, CLEO coll., Phys.Rev.D 78(2008)031101(R).

[13] D. Asner *et al.*, CLEO coll., Phys.Rev.D 79(2009) 072007.

[14] J.V. Bennett *et al.*, CLEO coll., Phys.Rev.Lett. 101(2008)151801.

[15] Y. J. Gao *et al.*, Chin. Phys. Lett.23(2006)2376.

[16] T. K. Pdelar *et al.*, CLEO coll., Phys. Rev. D79(2009)111101.

[17] G. S. Adams *et al.*, Phys. Rev. Lett. 101(2008) 101801.

[18] J. L. Rosner *et al.*, CLEO Coll., Phys.Rev.Lett. 95(2005)102003; P. Rubin *et al.*, CLEO Coll.,Phys. Rev. D 72(2005)092004.

[19] S. Dobbs *et al.*,CLEO Coll.,Phys. Rev. Lett. 101(2008) 182003.

[20] V. V. Anashin *etal.*, arXiv:1001.2445 [hep-ex].

[21] M. Ablikim, *et al.*, BES collaboration, Phys. Lett. **B 633** (2006) 681.

[22] M. Ablikim, *et al.*, BES collaboration, arXiv:1002.0893 [hep-ex]

[23] M. Ablikim *et al.*, BESII collaboration, Phys.Lett.B677(2009)239.

[24] M. Ablikim *et al.*, BESIII collaboration, Phys. Rev. D 81, 052005 (2010).

[25] M. Ablikim *et al.*, BESIII collaboration, Phys.Rev.Lett. 104(2010) 132002.

[26] J. Z. Bai *et al.* [BES Collaboration], Phys. Rev. Lett., 2003, **91**: 022001; Phys. Rev. Lett., 2007, **99**: 011802.

[27] M. Ablikim *et al.*, BESIII collaboration, Chinese Phys. C 342010421.

Discussion

Sacha Kopp (University of Texas): I was confused about the distribution of the lineshape of the η_c in $J/\Psi \to \gamma\eta_c$ decays. Is it truly necessary to suggest it does not follow a Breit-Wigner, or can we just say that the shape is distorted due to an interference with another state in the decay?

Answer: It is not clear why the shape is distorted. There are suggestions that J/Ψ and ψ' decays does not follow Breit-Wigner, rather needs an $E_g^n amma$ correction, where n=3 for J/Ψ and n=7 for ψ'. However, even if J/Ψ can be fitted with this modified Breit-Wigner, Ψ' can not. Up to now there are no evidence for interference. We need more data to fit exclusive channels individually.

Sakue Yamada (KEK): It is a comment on your introduction. You did not mention about DORIS, which made the first confirmation of J/Ψ and also made other contributions like the discovery of χ_c states. I wish to remind of this history, particularly as this LP09 is being held in Hamburg.

Answer: Sorry about that. It should be mentioned.

Hans Bienlein (DESY): Do You plan to analyze $\gamma\gamma$ hadron production in BES-III? This could help you to identify gluonium states by comparing $\gamma\gamma$ production with γgg-production from J/Ψ decays.

Answer: Yes, we will do it. It is in our plans.

Neutrino Mass

Christian Weinheimer

Institut für Kernphysik, Westfälische Wilhelms-Universität Münster, Wilhelm-Klemm-Str. 9, D-48149 Münster, Germany

By the clear evidence of neutrino oscillations the existance of non-zero neutrinos masses is proven. With the various neutrino oscillation experiments their mixing angles and their squared mass differences but not the absolute neutrino mass scale are being determined. This absolute scale of neutrino masses is very important for understanding the evolution and the structure formation of the universe as well as for nuclear and particle physics beyond the present Standard Model. Complementary to deducing statements on the sum of all neutrino masses from cosmological observations two different methods to determine the neutrino mass scale in the laboratory are pursued: the search for neutrinoless double β decay and the direct neutrino mass search by investigating single β decays. For both methods currently experiments with a sensitivity of O(100) meV using quite different techniques are being set up or commissioned.

1 Introduction

The various oscillation experiments with solar, atmospheric, reactor and accelerator neutrinos have shown, that the different neutrino flavors mix and can oscillate during flight from one flavor state into another. The analysis of all neutrino oscillation experiments yields the mixing angles and the differences of squared neutrino mass eigenstates [1, 2]. Clearly these findings prove that neutrinos have non-zero masses, but they cannot determine the absolute neutrino mass scale. The huge abundance of neutrinos left over in the universe from the big bang ($\approx 336/\text{cm}^3$) and their contribution to structure formation and the evolution of the universe (*e.g.*[3]) as well as the key role of neutrino masses in finding the new Standard Model of particle physics (*e.g.* [4]) make the absolute value of the neutrino mass one of todays most urgent questions of astroparticle physics and cosmology as well as of nuclear and particle physics.

There exist 3 different approaches to the absolute neutrino mass scale:

- Cosmology
  Essentially, information on the sum of all neutrino masses $\sum m(\nu_i)$ is obtained by observing the size of cosmological fluctuations at different scales using cosmic microwave background and large scale structure data. Since light – and therefore relativistic at the time of structure formation – neutrinos would have smeared out fluctuations at small scales the power spectrum at small scales is sensitive to the sum of the neutrino masses. Up to now, no non-zero value but only limits on the sum of the 3 neutrino masses have been obtained around $\sum m(\nu_i) < 0.61$ eV/c^2 (*e.g.* [5]), which are to some extent model and analysis dependent [6].

- Neutrinoless double β decay ($0\nu\beta\beta$)

A neutrinoless double β decay[1] is forbidden in the Standard Model of particle physics. It could exist, if the neutrino is its own antiparticle ("Majorana-neutrino" in contrast to "Dirac-neutrino"). Furthermore, a finite neutrino mass is required in order to produce in the chirality-selective interaction a neutrino with a small component of opposite handedness on which this neutrino exchange subsists. The decay rate would scale with the absolute square of the so called effective neutrino mass m_{ee}. This effective neutrino mass takes into account the neutrino mixing matrix U and represents the coherent sum of the $m(\nu_i)$-components of the $0\nu\beta\beta$-decay amplitudes and hence carries their relative phases[2]:

$$\Gamma_{0\nu\beta\beta} \propto \left| \sum U_{ei}^2 m(\nu_i) \right|^2 := m_{ee}{}^2 \tag{1}$$

A significant additional uncertainty entering the relation of m_{ee} and the decay rate comes from the uncertainties of the nuclear matrix elements of the neutrinoless double β decay [10].

- Direct neutrino mass determination
  The direct neutrino mass determination is based purely on relativistic kinematics without further assumptions. Therefore it is sensitive to the neutrino mass squared $m^2(\nu)$. In principle there are two methods: time-of-flight measurements and precision investigations of weak decays. The former requires very long baselines and therefore very strong sources, which only cataclysmic cosmological events like a core-collapse supernova could provide. The non-observation of a dependence of the arrival time on energy of supernova neutrinos from SN1987a gave upper limits on the neutrino mass of about 6 eV/c^2 [8, 9]. Unfortunately nearby supernova explosions are too rare and too little understood to allow an improvement into the sub-eV range.

  Therefore, aiming for a sub-eV sensitivity, the investigation of the kinematics of weak decays and more explicitly the investigation of the endpoint region of a β decay spectrum is still the most sensitive model-independent and direct method to determine the neutrino mass. Here the neutrino is not observed but the charged decay products are precisely measured. Using energy and momentum conservation the neutrino mass can be obtained. In the case of the investigation of a β spectrum usually the "average electron neutrino mass" $m(\nu_e)$ is determined:

$$m(\nu_e)^2 := \sum |U_{ei}^2| m(\nu_i)^2 \tag{2}$$

  This incoherent sum is not sensitive to phases of the neutrino mixing matrix.

Figure 1 demonstrates that the different methods are complementary to each other and compares them. It shows, that the cosmological relevant neutrino mass scale $\sum m(\nu_i)$ has a nearly full correlation to $m(\nu_e)$ determined by direct neutrino mass experiments. The observable of neutrinoless double β decay, the effective neutrino mass m_{ee}, does not allow a very precise neutrino mass determination, $e.g.$ to determine $\sum m(\nu_i)$, due to the unknown CP and Majorana phases and the uncertainties of the nuclear matrix elements [10]. On the other hand

---

[1]Two β decays in the same nucleus at the same time with emission of two β electrons (positrons) while the (anti)neutrino emitted at one vertex is absorbed at the other vertex as a neutrino (antineutrino).

[2]These are the usual CP-violating phase of an unitary 3×3 mixing matrix and two so-called Majorana-phases, which only exist for Majorana particles.
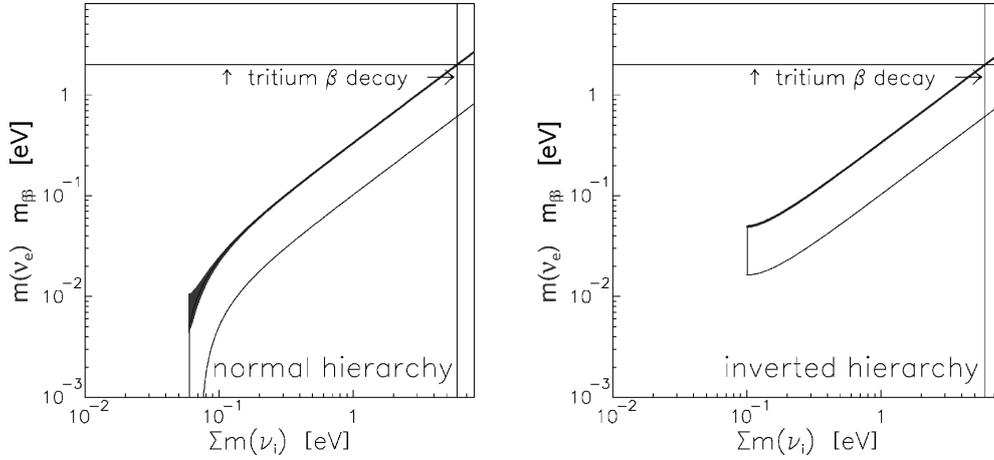
Figure 1: Observables of neutrinoless double β decay m_{ee} (open band) and of direct neutrino mass determination by single β decay $m(\nu_e)$ (gray band on upper boarder of m_{ee} band) versus the cosmologically relevant sum of neutrino mass eigenvalues $\sum m(\nu_i)$ for the case of normal hierarchy (left) and of inverted hierarchy (right) [7]. The width of the bands/areas is caused by the experimental uncertainties of the neutrino mixing angles [1] and in the case of m_{ee} also by the completely unknown Majorana- and CP-phases. Uncertainties of the nuclear matrix elements [10], which enter the experimental determination of m_{ee}, are not considered.

the combination of all three methods gives an experimental handle on the Majorana phases. Furthermore, the search for the neutrinoless double β decay is the only way to prove the Majorana character of neutrinos and one of the most promising ways to search for lepton number violation.

This article is structures as follows: Section 2 reports on the various searches for neutrinoless double β decay. In section 3 the neutrino mass determination from tritium and ^{187}Re β decay are presented. The conclusions are given in section 4.

2 Search for neutrinoless double β decay

There are more than 10 double β decay isotopes. For most of them the normal double β decay with neutrino emission has been observed. For neutrinoless double β decay there is only one claim for evidence at $m_{ee} \approx 0.4$ eV/c^2 by part of the Heidelberg-Moscow collaboration [11], all other experiments so far set upper limits. A couple of experiments with sensitivity O(100) meV are being set up to check this claim. Common to all these experiments is the use of ultrapure materials with very little radioactivity embedded in a passive and an active shield placed in an underground laboratory.

The most important signature of neutrinoless double β decay is, that the sum of the energy of both decay electrons (in case of double β^- decay, positrons for double β^+ decay) is equal to the Q-value of the nuclear transition. The experimental approaches can be classified into two methods (see Figure 2) [13]:
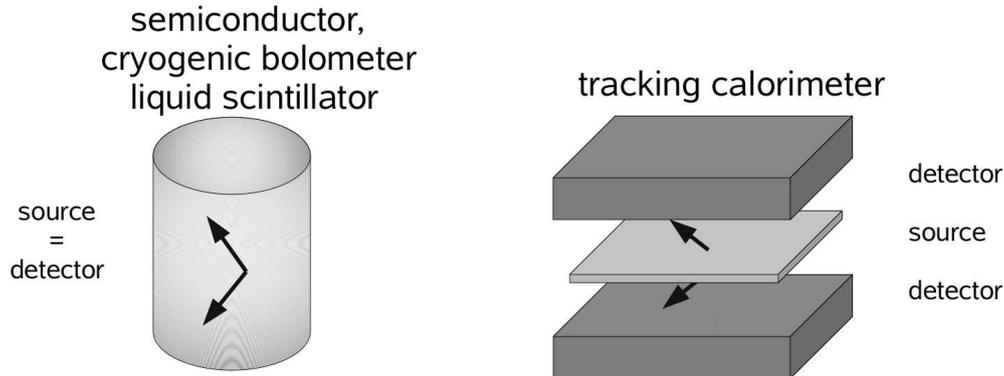
Figure 2: Two different experimental configurations in search for the neutrinoless double β decay.

2.1 "Source=detector" configuration

In the "source=detector" configuration the double β decay nuclei are part of the detector, which measures the sum of the energy of both β electrons. The experimental implementation of these calorimeters are semiconductors (*e.g.* isotopes: ^{76}Ge, ^{116}Cd, experiments: GERDA, MAJORANA, COBRA), cryo-bolometers (*e.g.* isotope: ^{130}Te, ^{82}Se, experiments: CUORICINO and its successor CUORE), LUCIFER and liquid scintillators (*e.g.* isotope: ^{48}Ca, ^{136}Xe, ^{152}Nd, experiments: EXO-200, SNO+. NEXT, KamLAND-Zen, CANDLE). In general, this method allows more easily to install a large target mass.

Currently the most sensitive limits comes from the CUORICINO experiment. which consisted of a tower of 62 tellurium oxide[3] cryo-bolometers with an active mass of 40.7 kg at the Gran Sasso underground laboratory LNGS yielding [12][4]:

$$t_{1/2}(^{130}\text{Te}) > 3 \cdot 10^{24} \text{ y} \qquad \text{and} \qquad m_{\text{ee}} < 0.19 - 0.68 \text{ eV} \tag{3}$$

The CUORICINO experiment has been completed and the installation of the nearly 20 times larger successor experiment CUORE has started.

The GERDA experiment [14] at Gran Sasso is being proceeded in two phases at the Gran Sasso underground laboratory with the option of a third phase together with the MAJORANA experiment [15]. GERDA uses enriched Germanium[5] embedded in a shielding cryostat filled with liquid argon, which itself sits in a water veto tank. This new shielding technique and the use of segmented or point-contact detectors in phase 2 should improve the background rate compared to the Heidelberg Moscow experiment by orders of magnitude. The commissioning of the GERDA experiment is nearly finished and the data taking will start in 2010.

The EXO collaboration starts with the EXO-200 detector [16], a liquid Xenon TPC with 200 kg of enriched Xenon (80 % enrichment of the double β decay isotope ^{136}Xe). The data

---

[3]The Cuoricino TeO$_2$ crystals are made out of natural tellurium with a 34 % fraction of the double β decay isotope ^{130}Te.

[4]The range of the effective neutrino mass limits originates from the different nuclear matrix elements calculated by different theory groups (see e.g. [10]).

[5]The enrichment of the double β decay isotope ^{76}Ge is about 86 %. The total mass of the phase 1 detectors amounts to 18 kg.

taking, first with natural xenon, will start in 2010.

The SNO+ experiment [17] is using the former solar neutrino detector SNO. The inner acrylic vessel will be filled with liquid scintillator, which will be doped by the double β decay isotope ^{152}Nd. Start of data taking is planned for 2013.

2.2 "Source$\neq$detector" configuration

In the this configuration the double β decay source is separated from two tracking calorimeters, which determine direction and energy of both β electrons separately (*e.g.* isotope ^{82}Se, ^{100}Mo, experiments: NEMO3 and its much larger successor SuperNEMO, ELEGANT, MOON).

By this method the most sensitive limit comes from the NEMO3 experiment [18] in the Modane underground laboratory LSM. NEMO3 is using thin source foils of a total area of 20 m^2. These foils contain 7 kg of the double β decay isotope ^{100}Mo and 1 kg of the double β decay isotope ^{82}Se. The foils are surrounded by a tracking chamber in a magnetic field composed of 6400 drift cells working in Geiger mode and calorimeter made out of 1940 plastic scintillators. The recent upper limits on neutrinoless double β decay from NEMO3 are [18][4]:

$$t_{1/2}(^{100}\text{Mo}) > 1.1 \cdot 10^{24} \text{ y} \qquad \text{and} \qquad m_{\text{ee}} < 0.45 - 0.93 \text{ eV}$$
$$t_{1/2}(^{82}\text{Se}) > 3.6 \cdot 10^{23} \text{ y} \qquad \text{and} \qquad m_{\text{ee}} < 0.89 - 1.61 \text{ eV}$$

Although it requires much larger detectors to accumulate similar large target masses as in the "source=detector" case, there is the advantage, that the independent information of both electrons allows to study double β decay processes with 2 neutrinos in detail. In case neutrinoless double β decay would be detected, the angular correlation of both electrons will allow to draw some conclusion on the underlying process [6].

3 Direct neutrino mass experiments

The signature of a non-zero neutrino mass is a tiny modification of the spectrum of the β electrons near its endpoint (see Figure 3), which has to be measured with very high precision. To maximize this effect, β emitters with low endpoint energy are favored.

3.1 "Source$\neq$detector" configuration: Tritium β decay experiments

Tritium is the standard isotope for this kind of study due to its low endpoint of 18.6 keV, its rather short half-life of 12.3 y, its super-allowed shape of the β spectrum, and its simple electronic structure. Tritium β decay experiments using a tritium source and a separated electron spectrometer have been performed in search for the neutrino mass for more than 50 years [7] yielding a sensitivity of 2 eV by the experiments at Mainz [20] and Troitsk [21]. The huge improvement of these experiments in the final sensitivity as well as in solving the former "negative $m^2(\nu_{\text{e}})$" problem with respect to previous experiments is mainly caused by the new spectrometers of MAC-E Filter type and by careful studies of the systematics.

The international KATRIN collaboration has taken the challenge set by the astrophysics and particle physics arguments to increase the sensitivity on the neutrino mass down to 0.2 eV.

---

[6]A theorem by Schechter and Valle [19] requests the neutrinos to have non-zero Majorana masses, if neutrinoless double β decay is proven to exist, but the dominant process could still be different, *e.g.* based on the exchange of a SUSY particle or by the contribution of right-handed weak charged currents.
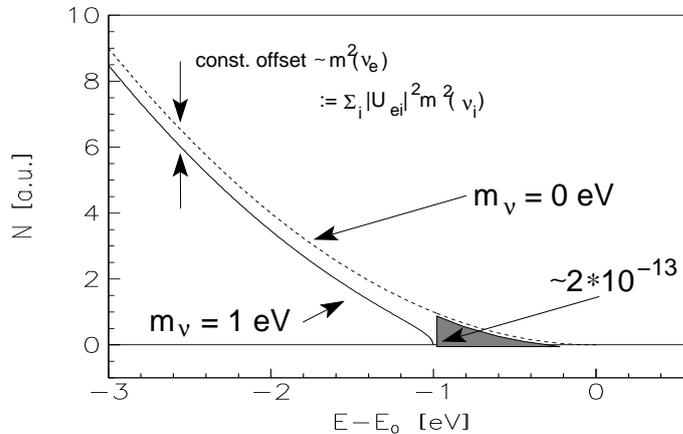
Figure 3: Expanded β spectrum around its endpoint E_0 for $m(\nu_{\mathrm{e}}) = 0$ (dashed line) and for an arbitrarily chosen neutrino mass of 1 eV (solid line). In the case of tritium, the gray-shaded area corresponds to a fraction of $2 \cdot 10^{-13}$ of all tritium β decays.

It is currently setting up an ultra-sensitive tritium β decay experiment based on the successful MAC-E-Filter spectrometer technique and a very strong Windowless Gaseous Tritium Source (WGTS) [22, 23] at the Karlsruhe Institute of Technology, Germany (formerly Forschungszentrum Karlsruhe). Improving tritium β-spectroscopy by a factor of 100 in the observable $m^2(\nu_{\mathrm{e}})$ evidently requires brute force, based on proven experimental concepts, and further improvements in many aspects. It was decided, therefore, to build a spectrometer of MAC-E-Filter type with a diameter of 10 m, corresponding to a 100 times larger analyzing plane as compared to the pilot instruments at Mainz and Troitsk, fed by β electrons from a high-luminosity windowless gaseous molecular tritium source. Figure 4 depicts a schematic plan of the whole 70 m long setup.

A decay rate of 10^{11} Bq is aimed for in a source with a diameter of 9 cm requiring extraordinary demands in terms of size and cryo-techniques to handle the flux of 10^{19} T_2-molecules/s safely and with per mille stability. T_2 is injected at the midpoint of a 10 m long source tube kept at a temperature of 30 K by a 2-phase liquid neon bath [24]. The integral column density of the source of $5 \cdot 10^{17}$ molecules/cm^2 has to be stabilized within 0.1 %. Owing to background considerations, the T_2-flux entering the spectrometer should not exceed 10^5 T_2-molecules/s. This will be achieved by differential pumping sections (DPS), followed by cryo-pumping sections (CPS) which trap residual T_2 on argon frost at about 3 K. Each system reduces the throughput by 10^7, which has been demonstrated for the cryo-pumping section by a dedicated experiment at Karlsruhe [25]. The T_2-gas collected by the DPS-pumps will be purified and recycled. All these components possess strong superconducting solenoids to guide the β electrons from the source to the spectrometer within a magnetic flux tube of 191 T cm^2. In summer 2009, the DPS arrived at Karlsruhe and is now being commissioned. As this chain of superconduction solenoids also guides ions from the source electrical barriers, radial drift fields and monitoring devices [28] will be installed in the DPS section.

A pre-spectrometer of MAC-E-Filter type will transmit only the uppermost part of the
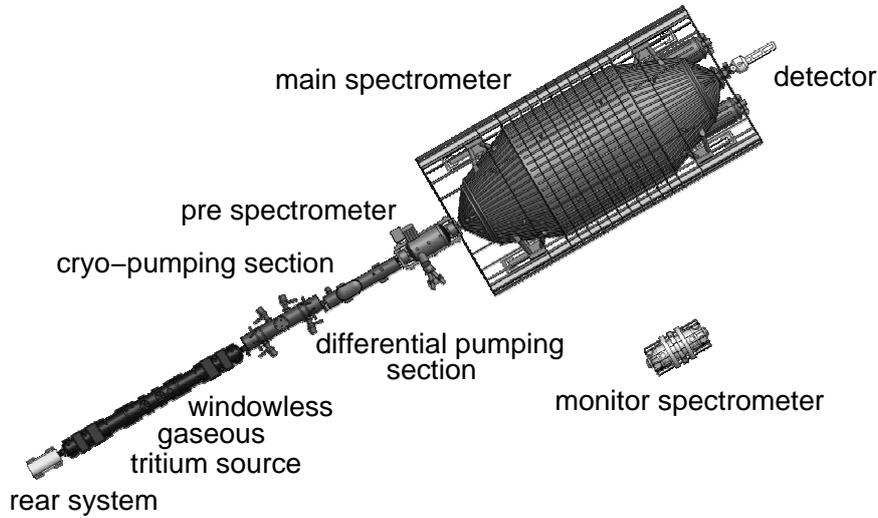
Figure 4: Schematic view of the 70 m long KATRIN experiment consisting of calibration and monitor rear system, windowless gaseous T_2-source, differential pumping and cryo-trapping section, small pre-spectrometer and large main spectrometer, segmented PIN-diode detector and separate monitor spectrometer.

β spectrum into the main spectrometer in order to reduce the rate of background-producing ionization events therein. Both pre- and main spectrometer will fulfill extreme vacuum conditions with a residual gas pressure of 10^{-11} mbar. The entire pre- and main spectrometer vessels will each be put on their respective analyzing potentials, which are shifted inside by about -200 V, however, due to the installation of a background reducing inner screen grid system (Fig. 5). A ratio of the maximum magnetic field in the pinch magnet over the minimum magnetic field in the central analyzing plane of the main spectrometer of 20000 provides an energy resolution of $\Delta E = 0.93$ eV near the tritium endpoint E_0. The residual inhomogeneities of the electric retarding potential and the magnetic fields in the analyzing plane will be corrected by the spatial information from a 148 pixel PIN diode detector [29]. Active and passive shields will minimize the background rate at the detector. Additional post-acceleration will reduce the background rate within the energy window of interest. Special care has to be taken to stabilize and to measure the retarding voltage. In addition to an ultra-precise HV divider [30], the spectrometer of the former Mainz Neutrino Mass experiment will be operated at KATRIN as a high voltage monitor spectrometer which continuously measures the position of the ^{83m}Kr-K32 conversion electron line at 17.8 keV [31], in parallel to the retarding energy of the main spectrometer. To that end its energy resolution has been refined to $\Delta E = 1$ eV.

The β electrons will be guided from the source through the spectrometer to the detector within a magnetic flux tube of 191 T cm^2, which is provided by a series of superconducting solenoids. This tight transverse confinement by the Lorentz force applies also to the 10^{11} daughter ions per second, emerging from β decay in the source tube, as well as to the 10^{12} electron-ion pairs per second produced therein by the β electron-flux through ionization of T_2 molecules. The strong magnetic field of 3.5 T within the source is confining this plasma strictly in the transverse direction such that charged particles cannot diffuse to the conducting wall of

Figure 5: A double-layer wire electrode module on the 3-axis measurement table for quality assurance. The fixing of the wires inside the ceramics holders (see inserted smaller photos right) with the connecting wires is checked with a high-resolution camera, whereas wire position and wire tension are monitored by a specially developed 2-dim. laser sensor [26].

the source tube for getting neutralized. The question how the plasma in the source becomes neutralized then or to which potential it might charge up eventually, has been raised and dealt with only recently [32]. The salient point is, however, that the longitudinal mobility is not influenced by the magnetic field. Hence the resulting high longitudinal conductance of the plasma will stabilize the potential along a magnetic field line to that value which this field line meets at the point where it crosses a rear wall. This provides a lever to control the plasma potential. Meanwhile the Troitsk group has performed a first experiment on the problem [33]. They have mixed ^{83m}Kr into their gaseous T_2 and searched for a broadening of the $L_{III}32$-conversion line at 30.47 keV which might be due to an inhomogeneous source potential. Their data fit is compatible with a possible broadening of 0.2 eV, which would not affect their results but suggests further investigation at KATRIN.

The sensitivity limit of KATRIN on the neutrino mass has been simulated on the basis of a background rate of 10^{-2} cts/s, observed at Mainz and Troitsk under optimal conditions. Whether this small number can also be reached at the so much larger KATRIN instrument – or even be lowered – has yet to be proven. At Mainz the main residual background originated from secondary electrons from the walls/electrodes on high potential caused by passing cosmic muons or by γs from radioactive impurities. Although there is a very effective magnetic shielding by the conservation of the magnetic flux, small violation of the axial symmetry and other inhomogeneities allowed a fraction of about 10^{-5} of these secondary electrons to reach the

detector and to be counted as background. After finishing tritium measurements in 2001, electrostatic solutions were developed at Mainz, which strengthened shielding of surface electrons by an additional factor of ≈ 10. This was achieved by covering the electrodes with negatively biased grids built from thin wires. Even more refined 2-layer wire electrode modules[27] have been developed and constructed for the KATRIN main spectrometer (Fig. 5) to achieve a background suppression of 2 orders of magnitude. They are currently being installed. In addition to secondary electrons from the walls/electrodes on high potential sneaking in from the outside, there is the danger of electrons created inside the spectrometers by little Penning discharges. By careful simulating all the electric and magnetic fields and redesigning the electrodes these discharges have been avoided completely at the pre spectrometer [34]. For the unavoidable Penning trap between pre and main spectrometer a solution by a sweeping wire has been tested [35]. The main spectrometer vessel has already passed successfully out-baking and out-gasing tests [36].

Since the KATRIN experiment will investigate only the very upper end of the β spectrum, quite a few systematic uncertainties will be small because of excitation thresholds. Others systematics like the inelastic scattering fraction or the source intensity will be controlled very precisely by measuring the column density online by an electron gun [37], by keeping the temperature and pressure within the tritium source at the per mille level constant and by determining the tritium fraction of the gas in the source by laser Raman spectroscopy to the per mille level [38]. Therefore each systematic uncertainty contributes to the uncertainty of $m^2(\nu_e)$ with less than $0.0075 \, \text{eV}^2$, resulting in a total systematic uncertainty of $\Delta m^2(\nu_e)_{sys} = 0.017 \, \text{eV}^2$. The total uncertainty will allow a sensitivity on $m(\nu_e)$ of 0.2 eV to be reached [23]. If no neutrino mass is observed, this sensitivity corresponds to an upper limit on $m(\nu_e)$ of 0.2 eV at 90 % C.L, or, otherwise, to evidence for (discovery of) a non-zero neutrino mass value at $m(\nu_e) = 0.3$ eV (0.35 eV) with 3σ (5σ) significance.

For the future there are some new proposals to improve the neutrino mass sensitivity with tritium β decay experiments even beyond KATRIN, *e.g.* cyclotron radiation from spiraling β decay electrons from a KATRIN-like tritium source could be detected by a set of radio antennas [39]. The Fourier analysis of the detected radio signal would result in a spectrum of the electron energy.

3.2 "Source=detector" configuration: ^{187}Re β decay experiments

^{187}Re is a second isotope suited to determine the neutrino mass. Due to the complicated electronic structure of ^{187}Re and its long half life of $4.3 \cdot 10^{10}$ y the advantage of the 7 times lower endpoint energy $E_0 = 2.47$ keV of ^{187}Re with respect to tritium can only be exploited if the β spectrometer measures the entire released energy, except that of the neutrino. This situation can be realized by using a cryogenic bolometer as the β spectrometer, which at the same time contains the β emitter.

One disadvantage connected to the rhenium bolometer method is the fact that one measures always the entire β spectrum. Even for the case of the very low endpoint energy of ^{187}Re, the relative fraction of ^{187}Re β decay events in the last eV below E_0 is of order 10^{-11} only (compare to Figure 3). Considering the long time constant of the signal of a cryogenic bolometer (typically several hundred μs) pile-up is a severe problem, since it changes the spectral shape near the endpoint. In order to limit the pile-up fraction to $\leq 10^{-4}$ only large arrays of cryogenic bolometers could deliver the signal rate needed. Another technical challenge is the energy resolution of rhenium bolometers. Although cryogenic bolometers with an energy resolution of

a few eV have been produced with other absorbers, this resolution has yet not been achieved with rhenium.

Two groups have started the field of ^{187}Re β decay experiments at Milan (MiBeta) and Genoa (MANU): The MANU experiment was using one metallic rhenium crystal of 1.5 mg working at a temperature of 100 mK and read out by Germanium doped thermistor. The β environmental fine structure was observed for the first time giving rise to a modulation of the shape of the β spectrum by the interference of the out-going β electron wave with the rhenium crystal [40]. The spectrum near the endpoint allowed to set an upper limit on the neutrino mass of $m(\nu_e) < 26$ eV. The MiBeta collaboration was using 10 crystals of AgReO$_4$ with a mass of about 0.25 mg each. The energy resolution of a single bolometer was about 30 eV. One year of data taking resulted in an upper limit on the "electron neutrino mass" of $m(\nu_e) < 15$ eV [41].

Both groups are now working together with other groups from different countries within the MARE collaboration [42]. The aim of MARE is to improve the energy resolution by new type of sensors (e.g. transition edge thermistors), to increase the thermalization and read-out speed and to increase the number of detectors significantly. In MARE phase 1 300 detectors with an energy resolution of 20 eV and a read-out time of 100 μs should provide a sensitivity on the neutrino mass of 2-3 eV. Although this is just the sensitivity which has already been reached in tritium β decay experiments this approach is interesting since it is very complementary in experimental techniques and systematic uncertainties. Presently a first array of detectors is being commissioned with 30 eV energy resolution and with a read-out time of 250 μs.

The goal is, to increase in MARE phase 2 the number of detectors to 50000. Together with the energy resolution goal of $\Delta E \leq 5$ eV and the aim to achieve a read-out and thermalization time of $\leq 5\mu$s the MARE could improve in phase 2 another order of magnitude in sensitivity on the neutrino mass. Of course this will only be possible if the very challenging improvements in detector performance will really be reached and if no other problem with the bolometer technique (like any tiny process giving rise of an energy leakage, e.g. by soft photons or meta-stable excitations) will appear when improving the sensitivity on the observable m_ν^2 by 4 orders of magnitude.

The MARE collaboration also considers to investigate the electron capture of ^{163}Ho instead of the β decay of ^{187}Re by an array of cryo-bolometers as an alternative for MARE phase 2. Here the detected Auger electrons and photons will give rise to a β-like spectrum, which in principle allows to determine the neutrino mass [43].

4   Conclusions

The absolute neutrino mass scale is addressed by three different methods. The analysis of large scale structure data and the anisotropies of the cosmic microwave background radiation are very sensitive but model dependent. The search for neutrinoless double β decay requires neutrinos to be their own antiparticles (Majorana neutrinos) and is measuring a coherent sum over all neutrino masses contributing to the electron neutrino with unknown phases. Therefore the value of the neutrino mass cannot be determined very precisely, but the discovery of neutrinoless double β decay would be the detection of lepton flavor violation. A few double β decay experiments of the second generation are currently being commissioned and will deliver data soon. Among the various ways to address the absolute neutrino mass scale the investigation of the shape of β decay spectra around the endpoint is the only model-independent method. The KATRIN experiment is being setup at Karlsruhe and will start data taking in 2012, whereas

the MARE experiment is commissioning a small array of detectors starting MARE phase 1. ¿From both laboratory approaches we expect in the coming years sensitivies on the neutrino mass of O(100) meV.

5   Acknowledgments

6   Bibliography

References

[1] K. Nakamura *et al.* (Particle Data Group), J. Phys. **G37**, 075021 (2010)

[2] S. Kopp, proceedings of the XXIV International Symposium on Lepton and Photon Interactions at High Energies, August 2009, Hamburg

[3] S. Hannestad, hep-ph/0404239

[4] M Lindner and W. Rohdejohann, JHEP 05 (2007) 089

[5] E. Komatsu *et al.*, (WMAP Collaboration) 2008 arXiv:0803.0547

[6] S. Hannestad *et al.*, J. Cosmol. Astropart. Phys. **08**, 015 (2007)

[7] E.W. Otten and C. Weinheimer, Rep. Prog. Phys. **71**, 086201 (2008)

[8] T.J. Loredo, D.Q. Lamb, Phys. Rev. **D65**, 063002 (2002)

[9] G. Pagliaroli, F. Rossi-Torres and F. Vissani, Astropart. Phys. **33** 287 (2010), [arXiv:1002.3349 [hep-ph]].

[10] F. Simkovic *et al.*, Phys. Rev. **C79** 055501 (2009)

[11] H.V. Klapdor-Kleingrothaus *et al.*, Phys. Lett. **B 586**, 198 (2004)

[12] C. Arnaboldi *et al.* (CUORICINO Collaboration), Phys. Rev. **C78** 035502 (2008)

[13] A. Guiliani, Acta Phys. Polnica **41** Issue 7, 1447 (2010)

[14] A. Smolnikov [GERDA Collaboration], J. Phys. Conf. Ser. **203**, 012059 (2010)

[15] C. E. Aalseth *et al.* [MAJORANA Collaboration], J. Phys. Conf. Ser. **203**, 012057 (2010) [arXiv:0910.4598 [nucl-ex]].

[16] L. J. Kaufman, J. Phys. Conf. Ser. **203**, 012067 (2010)

[17] C. Kraus and S. J. M. Peeters [SNO+ Collaboration], Prog. Part. Nucl. Phys. **64**, 273 (2010)

[18] F Mauger, J. Phys.: Conf. Ser. **203**, 012065 (2010)

[19] J. Schechter and J.W.F. Valle, Phys. Rev. **D25**, 2951 (1982)

[20] C. Kraus *et al.*, Eur. Phys. J. **C40**, 447 (2005)

[21] V.M. Lobashev, Nucl. Phys. **A719**, 153c (2003)

[22] A. Osipowicz *et al.* (KATRIN Collaboration), arXiv:hep-ex/0109033

[23] J. Angrik *et al.* (KATRIN Collaboration), KATRIN Design Report 2004, Wissenschaftliche Berichte FZ Karlsruhe 7090, http://bibliothek.fzk.de/zb/berichte/FZKA7090.pdf

[24] S. Grohmann, Cryogenics **49** 413 (2009)

[25] O. Kazachenko *et al.*, Nucl. Instr. Meth. **A587**, 136 (2008)

[26] M. Prall *et al.*, IEEE Trans. Nucl. Science **57** Issue 2, 787 (2010)

[27] K. Valerius, Prog. Part. Nucl. Phys. **64**, 291 (2010)

[28] M. Ubieto-Díaz *et al.*, Int. J. Mass. Spec. **288** 1 (2009)

[29] J. A. Dunmore and M. L. Leber [KATRIN Collaboration], J. Phys. Conf. Ser. **136**, 042056 (2008).

[30] Th. Thümmler *et al.*, New J. Phys. **11**, 103007 (2009)

[31] D. Vénos *et al.*, Measurement Techniques **53**, issue 3, 305 (2010)

[32] A.F. Nastoyashchii *et al.*, Fusion Science and Technology **48** 743 (2005)

[33] V.M. Lobashev, Proc. 11. Int. Workshop on Neutrino Telescopes, Venice/Italy, ed. B. Ceolin (Edizioni Papergraf) 507 (2005)

[34] S. Mertens [KATRIN Collaboration], Prog. Part. Nucl. Phys. **64**, 294 (2010)

[35] M. Beck *et al.*, Eur. Phys. J **A44** 499 (2010)

[36] J. Wolf , Journal of the Vacuum Sociecty of Japan **52** Issue 5, 278 (2009)

[37] K. Valerius *et al.*, New J. Phys. **11**, 063018 (2009)

[38] M. Sturm *et al.*, Las. Phys. **20**, 2 (2010)

[39] B. Monreal and J. A. Formaggio, Phys. Rev. D **80**, 051301 (2009)

[40] F. Gatti *et al.*, Nature **397**, 137 (1999)

[41] M. Sisti *et al.*, Nucl. Instr. Meth. **A520**, 125 (2004)

[42] A. Monfardini *et al.*, arXiv:hep-ex/0509038

[43] A. de Rújula , Nucl. Phys. **B188** 414 (1981)

Discussion

Poonam Metha (Bangalore): Comment on $0\nu\beta\beta$ process: The mass term depdends on the Majorana phases which could conspire in such a way that m_{ee} can become zero if we are very unlucky but this does not rule out the possibility that neutrinos are Majorana particles.

Answer: Yes, indeed. In the case that the non-zero neutrino masses are the only process responsible for neutrinoless double β decay this situation could exist in the non-inverted hierarchy scenario only, *i.e.* the three neutrino mass eigenstates are arranged as $m(\nu_1) < m(\nu_2) < m(\nu_3)$. The exact cancelation of the neutrinoless double β decay amplitude could in principle also happen, when another process (*e.g.* the exchange of a SUSY particle) adds destructively to the β decay amplitude of the non-zero neutrino masses, but such a lucky or unlucky coincidence is considered to be very unlikely.

Gianluca Introzzi (Padova, INFN): Why the detector had to travel 8800 km just to cover a distance of a few hundred kilometers?

Answer: The main spectrometer has to reach the very low residual gas pressure of 10^{-11} mbar to suppress the scattering of β electrons on the residual gas. Therefore, special welding techniques and surface treatments (*e.g.* electropolishing) had to be applied. This could not be done easily for a 10 m diameter vessel at Karlsruhe Institute of Technology as no extra hall was available. Therefore the big vessel was build completely at the company and had to be transported in one piece. A vessel of more than 23 m in length and 10 m in diameter can only be transported on big rivers or the sea but not on streets. A transport by air was not possible due to the weight of the vessel of 200 t.

Ahmed Ali (DESY): Measuring the neutrinoless double β decay will be a landmark measurement in particle physics. However, converting the half-life to the neutrino weighted mass m_{ee} will not be easy. It will become even more complicated in the presence of other competing mechanisms. Some help can come by measuring also the angular correlation coefficient of the two electrons in $0\nu\beta\beta$ decay. Which of the current and forthcoming experiments are sensitive to the angular measurements?

Answer: Especially the double β decay experiments with the "source $\neq$ detector" configuration are measuring both electrons separately and are able to do this. The experiment NEMO3 has shown excellent electron correlation data for $2\nu\beta\beta$ processes. NEMO3 and its successor SuperNEMO, which is under construction, are ideally designed to measure the angular correlation.

Hans Bienlein (DESY): Did you consider internal bremsstrahlung in β decay? It may influence the masurement of the endpoint of β spectrum.

Answer: In the analysis of the former Mainz Neutrino Mass Experiment as well as in KATRIN's simulation and analysis internal bremsstrahlung has been considered. The description by two different groups (W.W Repco, C.E. Wu, Phys. Rev. C **28**, 2433 (1983), S. Gardner, V. Bernard, U.G. Meissner, Phys. Lett. B **598**, 188 (2004)) were

applied. It was checked, that at KATRIN's sensitivity there is no significant difference using one or the other of the descriptions.

Status of Neutrino Theory

J. W. F. Valle[1]

[1] AHEP Group, Instituto de Física Corpuscular, C.S.I.C. – Universitat de València
Edificio de Institutos de Paterna, Apartado 22085, E–46071 València, Spain

A summary of neutrino oscillation results is given along with a discussion of neutrino mass generation mechanisms, including high and low-scale seesaw, with and without supersymmetry, as well as recent attempts to understand flavor. I argue that if the origin of neutrino masses is intrinsically supersymmetric, it may lead to clear tests at the LHC. Finally, I briefly discuss thermal leptogenesis and dark matter.

1   Status of neutrino oscillation experiments

The discovery of neutrino oscillations provides the first evidence of physics beyond the Standard Model (SM), marking the beginning of a new era in particle physics. Thanks to their brilliant confirmation by reactor and accelerator experiments, oscillations constitute the only viable explanation for the observed flavor conversion of "celestial" neutrinos [1–3], requiring both neutrino mass and mixing, as expected in theories without conserved lepton number [4,5].

Even in its simplest 3×3 unitary form, the lepton mixing matrix $K = \omega_{23}\omega_{13}\omega_{12}$ [5] differs from the quark mixing matrix in that each ω factor carries a physical phase: one is the KM-analogue and appears in oscillations, while the other two are Majorana phases and appear in lepton number (L)-violating processes. Current experiments are insensitive to CP violation, so that oscillations depend only on the three mixing angles $\theta_{12}, \theta_{23}, \theta_{13}$ and on the two squared-mass splittings $\Delta m_{21}^2 \equiv m_2^2 - m_1^2$ and $\Delta m_{31}^2 \equiv m_3^2 - m_1^2$ characterizing solar and atmospheric transitions. Setting $\Delta m_{21}^2 = 0$ in the analysis of atmospheric and accelerator data, and Δm_{31}^2 to infinity in the solar and reactor data analysis one obtains the neutrino oscillation parameters, as summarized in Figs. 1 and 2. Fig. 1 gives the allowed values of "atmospheric" and "solar" oscillation parameters, θ_{23} & Δm_{31}^2, and θ_{12} & Δm_{21}^2, respectively. The dot, star and diamond in the left panel of Fig. 1 indicate the best fit points of atmospheric, MINOS and global data, respectively. Similarly the "solar" oscillation parameters are obtained by combining solar and reactor neutrino data, as shown in the right panel. The dot, star and diamond indicate the best fit points of solar, KamLAND and global data, respectively. In both cases minimization is carried out with respect to the undisplayed parameters. One sees that data from artificial and natural neutrino sources are clearly complementary: reactor and accelerators give the best determination of squared-mass-splittings, while solar and atmospheric data mainly determine mixings. The right panel in Fig. 2 shows how data slightly prefer a nonzero θ_{13} value, though currently not significant, leading to an upper bound at 90%C.L. (3σ):

$$\sin^2\theta_{13} \leq \begin{cases} 0.060 \ (0.089) & \text{(solar+KamLAND)} \\ 0.027 \ (0.058) & \text{(CHOOZ+atm+K2K+MINOS)} \\ 0.035 \ (0.056) & \text{(global data)} \end{cases} \tag{1}$$
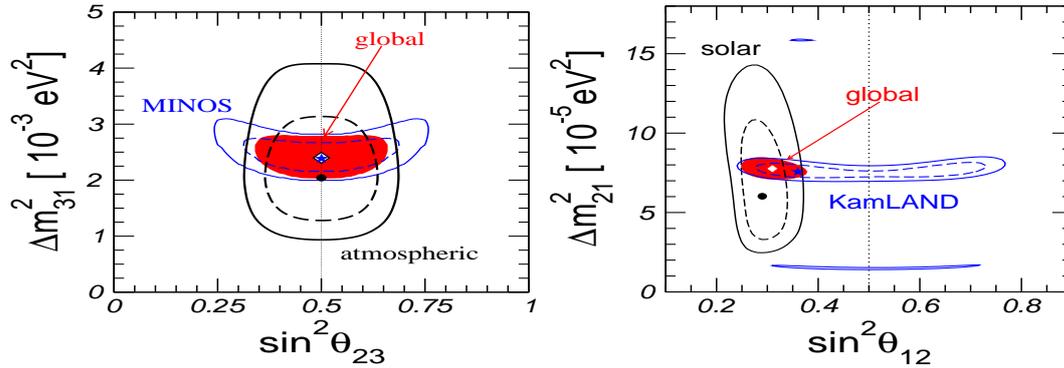
Figure 1: Current neutrino oscillation parameters, from a global analysis of the world's data [3].
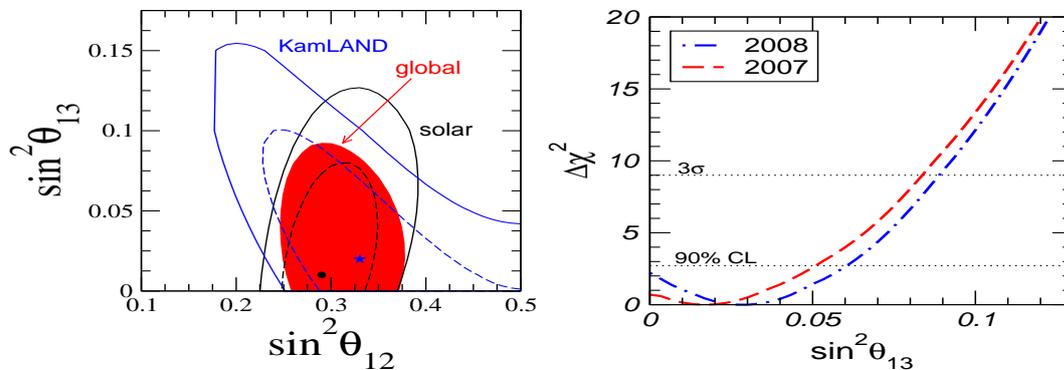
Figure 2: Constraints on $\sin^2 \theta_{13}$ from different neutrino oscillation data sets [3].

given for 1 dof, while the regions in Fig. 2 (left) correspond to 90% CL for 2 dof. The confirmation of a non-zero θ_{13} would strongly encourage the search for CP violation in upcoming neutrino oscillation experiments [6, 7]. Note that the small parameter $\alpha \equiv \frac{\Delta m_{21}^2}{|\Delta m_{31}^2|}$ is currently well-determined experimentally as $\alpha = 0.032$, $\quad 0.027 \leq \alpha \leq 0.038 \quad (3\sigma)$.

Before closing let us note that many effects may distort the "celestial" neutrino fluxes reaching our detectors, such as regular [8–10] and random [11, 12] solar magnetic fields. These would induce spin-flavor precession in the convective zone [13–15] as well as density fluctuations deep inside the Sun's radiative zone [16–18]. Although these can modify the solar neutrino survival probabilities [19, 20], they can not have an important impact on the determination of oscillation parameters, thanks to the KamLAND reactor neutrino spectrum data. The result is that oscillations remain robust against astrophysical uncertainties, and of all oscillation solutions allowed by solar data [21], only the large mixing angle solution survives KamLAND's measurements [22].

Often the generation of neutrino mass in gauge theories (left panel in Fig. 4) is accompanied by effective sub-weak strength ($\sim \varepsilon G_F$) flavour-changing (FC) or non-universal (NU) dimension-6 operators, as seen in the right panel. Such non-standard neutrino interactions (NSI) are expected in low-scale seesaw schemes, such as the inverse [23–25] and the linear [26] seesaw. In such schemes NSI would arise from the effectively non-unitary form of the corresponding lepton

mixing matrix [5] [65]. Relatively sizeable NSI strengths may also be induced in models with radiatively induced neutrino masses [66,67]. Current determination of solar neutrino parameters is not yet fully robust against the presence of large NSI, allowing for a new "dark side" solution that survives the inclusion of reactor data [27].

In contrast, thanks to the large statistics of atmospheric data over a wide energy range, the determination of atmospheric parameters Δm_{31}^2 and $\sin^2 \theta_{23}$ is fairly robust even in the presence of NSI, at least within the 2–neutrino approximation [28], a situation likely to improve with future neutrino factories [29]. However, NSI operators may have dramatic consequences for the sensitivity to θ_{13} at a neutrino factory [30] and may affect the interpretation of future supernova neutrino data in an important way [31–33]. Improved NSI tests will also shed light on the origin of neutrino mass, helping discriminate between high and low-scale schemes.

2   Neutrino mass and neutrinoless double beta decay

Neutrino oscillations can not probe absolute neutrino masses, for this we need cosmic microwave background and large scale structure observations [34], high sensitivity beta decay and $0\nu\beta\beta$ (neutrinoless double beta decay) studies [35]. The observation of neutrino oscillations suggests that light Majorana neutrino exchange will induce $0\nu\beta\beta$ as illustrated in the left panel of Fig. 3. This nuclear process would hold the key to probe the nature (Dirac versus Majorana) of neutrinos [36] since, in a gauge theory, it would imply a Majorana mass for at least one neutrino [36], as illustrated in the middle panel of Fig. 3.
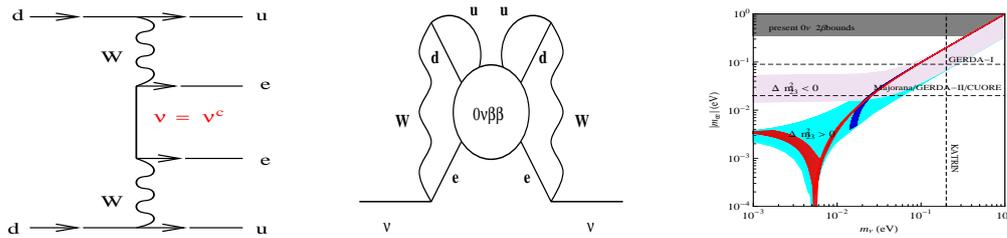
Figure 3: Neutrino mass mechanism (left), black box theorem (center) [36] and $0\nu\beta\beta$ decay parameter versus lightest neutrino mass for inverse and linear seesaw models (right), from [37].

Such "black-box" theorem [36] holds in any "natural" gauge theory, though its implications are rather difficult to quantify in general [38]. The $0\nu\beta\beta$ detection prospects were discussed in [39] and are summarized in the right panel in Fig. 3. The broad bands are allowed by current neutrino oscillation data [2, 3] for normal and inverse neutrino mass hierarchy, while the narrow bands correspond to the case of lepton mixing angles fixed to the tri-bimaximal values [37]. Note that for normal hierarchy there is in general no lower bound on $0\nu\beta\beta$ as there can be a destructive interference among the three neutrinos [1]. In contrast, the inverted neutrino mass hierarchy always gives a generic "lower" bound for the $0\nu\beta\beta$ amplitude. On the other hand, quasi-degenerate neutrino models [43, 44] give the largest possible $0\nu\beta\beta$ signal. Taking into account state-of-the-art nuclear matrix elements [45] one can determine the best current limit, which comes from the Heidelberg-Moscow experiment, as well as future experimental sensitivities [39], summarized in the right panel in Fig. 3 for GERDA, Majorana and CUORE.

---

[1]Specific flavor models may, however, lead to a lower bound on the $0\nu\beta\beta$ decay rate even for normal hierarchy neutrino spectra, as discussed in Refs. [37] [40–42].

3 Generating neutrino masses

Underpinning the origin of neutrino mass remains a challenge despite the tremendous progress we have achieved. Neutrino masses are markedly different from those of charged fermions in the SM. The latter arise by coupling the two chiral species to the Higgs scalar, hence linear in the electroweak symmetry breaking vacuum expectation value (vev) $\langle \Phi \rangle$ of the Higgs scalar doublet $\Phi \equiv H$. By contrast, being electrically neutral, neutrinos may get mass with just one chiral species: in other words, on general grounds they are of Majorana type [5]. The lowest-dimensional lepton number violating (LNV) operator has $\Delta L = 2$, namely $\lambda L \Phi L \Phi$, where L denotes a lepton doublet [4], see left panel in Fig. 4 [2].
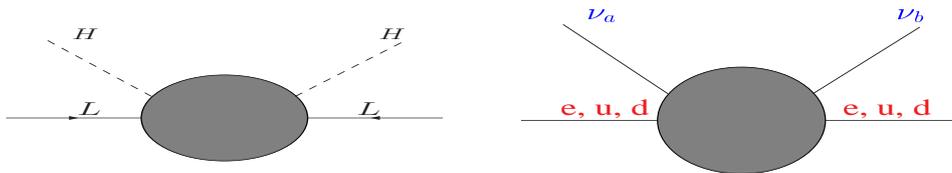
Figure 4: Neutrino mass [4] and non-standard neutrino interactions (NSI) operators [5].

Irrespective of their specific origin, the smallness of neutrino masses would come from the fact that they violate lepton number. The big issue is to identify which *mechanism* gives rise to the L-violating operator, its associated mass *scale* and its *flavor structure*. As for its magnitude, it may naturally be suppressed either by a high-scale M_X in its denominator, or may involve a low-mass-scale in its numerator.

It is often argued that gravity breaks global symmetries [48,49]. This would induce the L-violating operators suppressed by the Planck scale. The resulting Majorana neutrino masses are too small, hence the need for physics beyond the SM [50]. It is usual to assume that this physics lies at a large sub-Planck scale, say, associated to unification. However, λ may be suppressed by *small* scales, Yukawas and/or loop-factors [51]. There are three classes of mechanisms: (i) tree level, (ii) radiative, and (iii) hybrid, all of which may have high- or low-scale realizations, suggesting a fair chance that the origin of neutrino mass may be probed at accelerator experiments like the LHC. Depending on the nature of spontaneous lepton-number breaking there may be an extra neutral gauge boson [26,52] or a Nambu-Goldstone boson coupled to neutrinos [53].

3.1 Minimal high-scale seesaw

Weinberg's dimension-5 operator [4] may arise from the exchange of heavy fermion states with masses close to the "unification" scale. Depending on whether these are $SU(2)$ singlets or triplets the mechanism is called *type-I* [54–57], or *type-III* seesaw [58], respectively. Neutrino masses may also arise from the exchange of heavy triplet scalars, now called *type-II* seesaw [5] [53,59], as seen in the right panel in Fig. 5. The hierarchy of vevs required to account for the small neutrino masses $v_3 \ll v_2 \ll v_1$ is consistent with the minimization of the scalar potential. The resulting perturbative diagonalization of the seesaw mass matrix was given in Ref. [53] in the most general form that may be used in any model. From a phenomenological viewpoint, however, the most basic effective description of *any* seesaw is in terms of the SM $SU(3) \otimes SU(2) \otimes U(1)$ gauge structure with explicit L-violation [5].

---

[2]Note that neutrino masses may also arise from higher dimension effective operators [46,47].
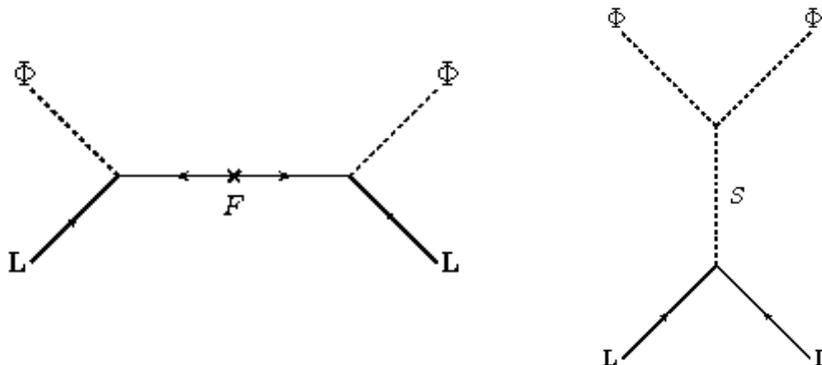
Figure 5: Type-I and III (left) and Type-II (right) realizations of the seesaw mechanism.

3.2   "Non-minimal" seesaw

The seesaw mechanism is not any particular *theory* but rather represents a broad *language* in terms of which to phrase neutrino mass model-building and many are its pathways. Indeed, it can be implemented non-minimally with lepton number broken explicitly or spontaneously, over a wide range of energy scales, in a variety of models with different gauge groups and multiplet contents, with or without supersymmetry. There is no point to attempt giving here a full taxonomy of seesaw schemes. However one should stress that any model must ultimately reduce to the SM. Hence what is phenomenologically most relevant, for example to describe neutrino oscillation data, is the effective structure of the SM seesaw mixing matrix, given in [5]. In addition to the mixing angles characterizing oscillations, the latter includes non-unitarity effects which will become an important topic in the agenda of future studies probing neutrino propagation beyond oscillations.

An attractive class of non-minimal seesaw schemes employs, in addition to the left-handed SM neutrinos ν_L, two $SU(3) \otimes SU(2) \otimes U(1)$ singlets ν^c, S [23] (see also e.g. [61–64]). The basic parameter characterizing the violation of lepton-number can be small [25,37] and may be calculable from supersymmetric renormalization group evolution effects [24].

3.3   Radiative neutrino masses

Neutrino masses may be radiatively calculable [66,67], with no need for a large scale. In this case the suppression comes from small loop-factors and Yukawa couplings. The same way as low-scale seesaw schemes, the states responsible for generating neutrino masses in radiative models may lie at the weak-scale, opening the door to phenomenology at the LHC [60].

4   Understanding and probing flavor

There is no reasonable doubt that flavor is violated in neutrino propagation [2, 3]. Current oscillation experiments indicate solar and atmospheric mixing angles which are unexpectedly large when compared to quark mixing angles. To a good approximation they are given by [68],

$$\tan^2\theta_{23} = \tan^2\theta_{23}^0 = 1 \quad \sin^2\theta_{\text{Chooz}} \quad = \sin^2\theta_{13}^0 = 0 \quad \tan^2\theta_{\text{SOL}} = \tan^2\theta_{12}^0 = 0.5. \quad (2)$$

Understanding the pattern of lepton mixing angles from first principles constitutes a big challenge to unified theories of flavor where quarks and leptons are related. Many less ambitious schemes have been suggested in order to reproduce the tri-bi-maximal pattern, at least partially, using various discrete flavor symmetry groups containing mu-tau symmetry, e. g. [43,44,69–76]. In general one expects the flavor symmetry to be valid at high energy scales. Deviations from tri-bi-maximal ansatz [77] may be calculable by renormalization group evolution [78–80]. A simple possibility is that, as a result of a given flavor symmetry such as A4 [43, 44], neutrino masses unify at high energies [81], the same way as gauge couplings do, due to supersymmetry. Such quasi-degenerate neutrino scheme predicts maximal atmospheric angle and vanishing θ_{13}, $\theta_{23} = \pi/4$ and $\theta_{13} = 0$, leaving the solar angle θ_{12} unpredicted, but Cabibbo-unsuppressed, $\theta_{12} = \mathcal{O}(1)$. If CP is violated θ_{13} becomes arbitrary and the Dirac phase is maximal [70]. The lower bound on the absolute Majorana neutrino mass scale $m_0 \gtrsim 0.3$ eV ensures that the model will be probed by future cosmological data and $0\nu\beta\beta$ searches.

It is natural to expect that, at some level, lepton flavor violation will also show up as transitions involving the charged leptons, since these sit in the same electroweak doublets as neutrinos. Rates for lepton flavour violating processes $l_j \rightarrow l_i + \gamma$ often lie in the range of sensitivity of coming experiments, providing an independent test. There are two basic mechanisms: (i) neutral heavy lepton exchange [82–84] and (ii) supersymmetry [85–87]. Both exist in supersymmetric seesaw-type schemes of neutrino mass, the interplay of both depends on the seesaw scale, and has been considered in [88]. Barring fine-tunings, high-scale seesaw models require supersymmetry in order to have sizeable LFV rates. The most interesting feature of these models is that they bring in the possibility of direct lepton flavour violation in the production of supersymmetric particles. As seen in Fig. 6 this provides the most direct way to probe LFV at the LHC in high-scale seesaw models.
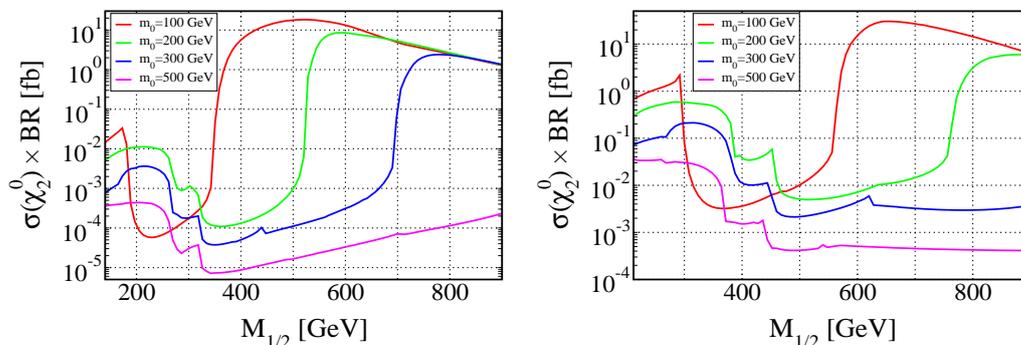
Figure 6: LFV rate for μ-τ lepton pair production from χ_2^0 decays versus $M_{1/2}$ for the indicated m_0 values, assuming minimal supergravity parameters: $\mu > 0$, $\tan\beta = 10$ and $A_0 = 0$ GeV, for type-I (left) and for type-II seesaw (right). Here $\lambda_1 = 0.02$ and $\lambda_2 = 0.5$ are Type-II seesaw parameters, and we imposed the contraint $\text{Br}(\mu \rightarrow e + \gamma) \leq 1.2 \cdot 10^{-11}$, from Ref. [89].

In low-scale seesaw schemes, by contrast, the sizeable admixture of "right-handed" (RH) neutrinos in the charged current (rectangular nature of the lepton mixing matrix [5]) induces
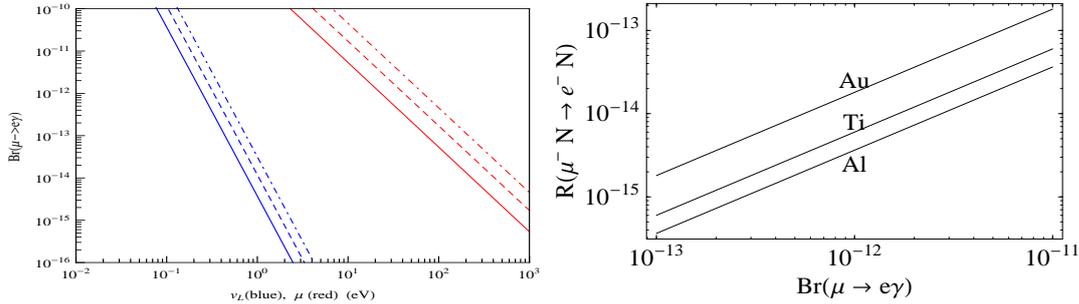
Figure 7: Left: $Br(\mu \to e\gamma)$ versus the LNV scale for inverse seesaw (top: red color) and linear seesaw (bottom, blue color). In both low-scale seesaw models we fix $M = 100\,GeV$ (continuous line), $M = 200\,GeV$ (dashed line) and $M = 1000\,GeV$ (dot-dashed line), from [37]. The right panel shows typical correlation between mu-e conversion in nuclei and $Br(\mu \to e\gamma)$, from [90].

potentially large LFV rates even in the absence of supersymmetry [82]. Indeed, an important point to stress is that LFV [82,83] and CP violation [91,92] can occur in the massless neutrino limit, hence their attainable magnitude is unrestricted by the smallness of neutrino masses. In Fig. 7 we display $Br(\mu \to e\gamma)$ versus the small LNV parameters μ and v_L for two different low-scale seesaw models, the inverse and the linear seesaw, respectively. Clearly the LFV rates are sizeable in both cases, the different slopes with respect to μ and v_L follow from the fact that $\Delta L = 2$ in the first case and $\Delta L = 1$, in the second.

Similarly [90] in low-scale seesaw models the nuclear $\mu^- - e^-$ conversion rates lie within planned sensitivities of future experiments such as PRISM [93]. Note that models with specific flavor symmetries, such as those in [25,37] relate different LFV rates. To conclude we mention that some seesaw schemes, like type-III with tiny Yukawas [58] or inverse type-III [25], may be directly probed at the LHC by directly producing the TeV states with gauge strength [60].

5   Probing neutrino properties at the LHC

In supersymmetric models lepton number can be broken together with the so-called R parity, leading to an intrinsically supersymmetric origin for neutrino masses [94–96]. This may happen spontaneously, driven by a nonzero vev of an $SU(3) \otimes SU(2) \otimes U(1)$ singlet sneutrino [97–99], leading to an effective model with bilinear violation of R parity [100,101]. The latter provides the minimal way to break R parity and add neutrino masses to the MSSM [101]. One finds that, typically, the atmospheric scale is generated at tree level by neutralino-exchange *weak-scale seesaw*, while the solar scale is radiatively induced [102]. Unprotected by any symmetry, the lightest supersymmetric particle (LSP) decays. Given the masses indicated by neutrino experiments these decays will happen inside typical detectors [102–104] but with a decay path that can be experimentally resolved, leading to a so-called displaced vertex [105], see left panel in Fig. 8. More strikingly, LSP decay properties correlate with the neutrino mixing angles. Indeed, as seen in the right panel in Fig. 8 the LSP decay pattern is predicted by the low-energy measurement of the atmospheric angle [103,106,107], allowing for a clear test at the LHC [60], namely a high-energy redetermination of θ_{23}. Similar correlations hold in variant models based on alternative supersymmetry breaking mechanisms, where other states appear as LSP [108].
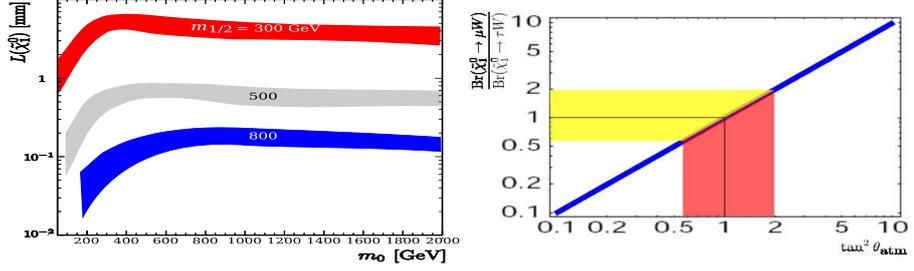
Figure 8: $\tilde{\chi}_1^0$ decay length versus m_0 for $A_0 = -100$ GeV, $\tan\beta = 10$, $\mu > 0$, and various $m_{1/2}$ values. The three shaded bands around $m_{1/2} = 300$, 500, 800 GeV correspond to the variation of the BRpV parameters in such a way that the neutrino masses and mixing angles fit the required values within 3σ. The right panel gives the ratio of branching ratios, $\mathrm{Br}(\chi_1^0 \to \mu q' \bar{q})$ over $\mathrm{Br}(\chi_1^0 \to \tau q' \bar{q})$ in terms of the atmospheric angle in bilinear R parity violation [103].

6 Neutrinos as cosmological probes

Neutrinos can probe very early epochs in the evolution of the Universe, previous to the electroweak phase transition. For example, the high-scale generation of neutrino masses through the seesaw mechanism may induce the observed baryon asymmetry of the Universe, as well as the dark matter, as I now discuss.

6.1 Thermal leptogenesis

The observed cosmological matter-antimatter asymmetry in the Universe may arise from the C/CP-violating out-of-equilibrium decays of the heavy RH neutrinos present in the seesaw. These take place before the electroweak phase transition [109] through the diagrams in the left panel in Fig. 9. The lepton asymmetry thus produced gets converted, through sphaleron processes, into a baryon asymmetry. This so-called leptogenesis scenario [110, 111] is a frame-
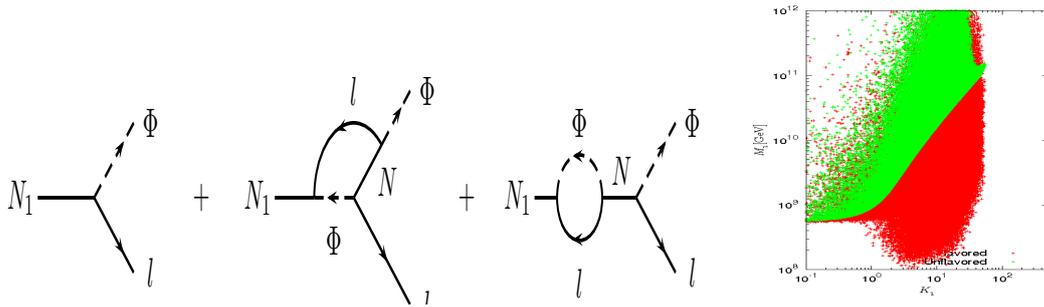
Figure 9: Diagrams (left), flavor effects on minimum required leptogenesis scale (right) [113].

work to explain just one number, namely the baryon asymmetry, currently well-determined by

WMAP [112]. It turns out that, as displayed in the right panel in Fig. 9, from Ref. [113], after taking into account carefully washout and flavor effects one finds that the required asymmetry can be achieved for a given range of model parameters which fits neutrino masses indicated by neutrino oscillation experiments. It did not have to be so, *a priori*, hence this may be taken as a success. The figure also shows how the inclusion of flavor effects lowers the minimum value of the lightest RH neutrino mass required for successful leptogenesis. Nevertheless, in order to avoid gravitino overproduction [114], which would destroy the standard Big Bang Nucleosynthesis predictions, one also requires an upper bound on the reheat temperature T_R after inflation, incompatible with Fig. 9 [115]. One way to prevent such *gravitino crisis* is to assume enhancement coming from resonant leptogenesis [116]. Alternatively, there are many ways to go beyond the minimal type-I supersymmetric seesaw [117–119]. For example one may add a small R-parity violating superpotential term $\lambda_i \hat{\nu}^c{}_i \hat{H}_u \hat{H}_d$, where $\hat{\nu}^c{}_i$ are RH neutrino supermultiplets [118]. In the presence of this term the produced asymmetry can be enhanced. In extended SO(10) supersymmetric seesaw schemes leptogenesis can occur at relatively low scales, through the decay of a new singlet, as illustrated in the left panel in Fig. 10. This not only avoids the gravitino crisis but also opens the possibility of detecting the new neutral gauge boson at the LHC [119, 120]. The right panel illustrates how a sizeable asymmetry may be achieved just with the leptonic CP violation parameter δ that characterizes neutrino oscillations.
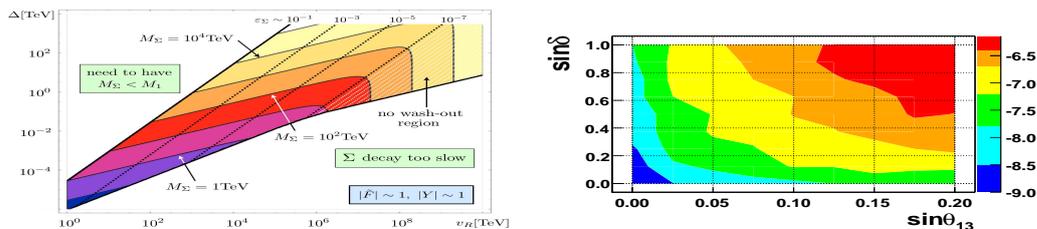
Figure 10: Low-scale leptogenesis in supersymmetric SO(10) models, from [119, 120].

6.2 Neutrino masses and dark matter

Neutrinos may get mass through the spontaneous breaking of ungauged lepton number. Due to quantum gravity effects the associated Goldstone boson - the majoron - is likely to pick up a mass, and play the role of late-decaying Dark Matter, decaying mainly to neutrinos [121, 122]. Cosmic microwave background observations place constraints on the majoron lifetime and mass, illustrated in left and middle panels of Fig. 11. This decaying dark matter scenario arises in type-II seesaw models, where the majoron couples to photons through the Higgs triplet and may be *tested* through the mono-energetic emission line from its sub-dominant decay to two photons, as illustrated in the right panel in Fig. 11.

Neutrino masses may also open new possibilities for "conventional" supersymmetric dark matter. For example, within the inverse seesaw mechanism minimal supergravity is more likely to have a *sneutrino* as the lightest superparticle than the conventional neutralino. Such schemes naturally reconcile the small neutrino masses with the correct relic sneutrino dark matter abundance and accessible direct detection rates in nuclear recoil experiments [125].

Acknowledgments
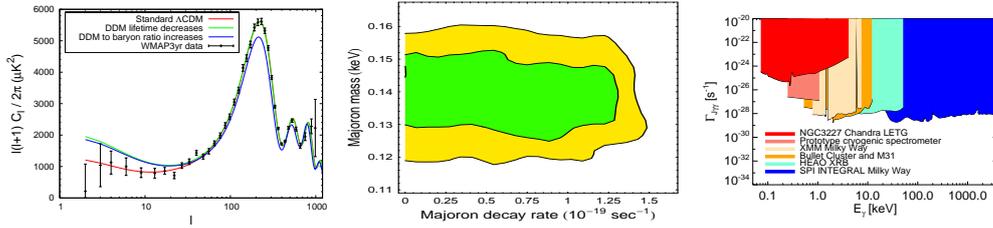
Figure 11: Late decaying majoron dark matter: decay parameters allowd by the CMB [123] (left-middle); probing sub-leading decay to two photons $J \to \gamma\gamma$ (right), from [124].

References

[1] Y Suzuki and S Kopp, talks presented at this Conference.

[2] M. Maltoni, T. Schwetz, M. A. Tortola, and J. W. F. Valle. *New J. Phys.*, 6:122, 2004.

[3] Thomas Schwetz, Mariam Tortola, and Jose W. F. Valle. *New J. Phys.*, 10:113011, 2008.

[4] Steven Weinberg. *Phys. Rev.*, D22:1694, 1980.

[5] J. Schechter and J. W. F. Valle. *Phys. Rev.*, D22:2227, 1980.

[6] A. Bandyopadhyay et al. *Rep. Prog. Phys.*, 72:106201, 2009.

[7] Hiroshi Nunokawa, Stephen J. Parke, and Jose W. F. Valle. *Prog. Part. Nucl. Phys.*, 60:338–402, 2008.

[8] O. G. Miranda et al. *Nucl. Phys.*, B595:360–380, 2001.

[9] M. Guzzo et al. *Nucl. Phys.*, B629:479–490, 2002.

[10] J. Barranco et al. *Phys. Rev.*, D66:093009, 2002.

[11] O. G. Miranda et al, *Phys. Rev. Lett.*, 93:051304, 2004.

[12] O. G. Miranda, T. I. Rashba, A. I. Rez, and J. W. F. Valle. *Phys. Rev.*, D70:113002, 2004.

[13] J. Schechter and J. W. F. Valle. *Phys. Rev.*, D24:1883, 1981. Err. D25, 283 (1982).

[14] E. Kh. Akhmedov. *Phys. Lett.*, B213:64–68, 1988.

[15] Chong-Sa Lim and William J. Marciano. *Phys. Rev.*, D37:1368, 1988.

[16] C. P. Burgess et al. *Mon. Not. Roy. Astron. Soc.*, 348:609, 2004.

[17] C. Burgess et al. *Astrophys. J.*, 588:L65, 2003.

[18] C. P. Burgess et al. *JCAP*, 0401:007, 2004.

[19] F. N. Loreti and A. B. Balantekin. *Phys. Rev.*, D50:4762–4770, 1994.

[20] H. Nunokawa et al. *Nucl. Phys.*, B472:495–517, 1996.

[21] M. C. Gonzalez-Garcia et al. *Phys. Rev.*, D63:033005, 2001.

[22] S. Pakvasa and J. W. F. Valle, Proc. of Indian Nat. Acad. Sci. 70A, No.1, 189 (2004) [hep-ph/0301061]

[23] R. N. Mohapatra and J. W. F. Valle. *Phys. Rev.*, D34:1642, 1986.

[24] F. Bazzocchi, D. G. Cerdeno, C. Munoz, and J. W. F. Valle. e-Print: arXiv:0907.1262 [hep-ph].

[25] D. Ibanez, S. Morisi, and J. W. F. Valle. *Phys. Rev.*, D80:053015, 2009.

[26] M. Malinsky, J. C. Romao, and J. W. F. Valle. *Phys. Rev. Lett.*, 95:161801, 2005.

[27] O. G. Miranda, M. A. Tortola, and J. W. F. Valle. *JHEP*, 10:008, 2006.

[28] N. Fornengo et al. *Phys. Rev.*, D65:013010, 2002.

[29] P. Huber and J. W. F. Valle. *Phys. Lett.*, B523:151–160, 2001.

[30] P. Huber, T. Schwetz, J. W. F. Valle. *Phys. Rev. Lett.*, 88:101804, 2002; *Phys. Rev.*, D66:013006, 2002.

[31] J. W. F. Valle. *Phys. Lett.*, B199:432, 1987.

[32] H. Nunokawa et al. *Phys. Rev.*, D54:4356–4363, 1996.

[33] A. Esteban-Pretel, R. Tomas, and J. W. F. Valle. *Phys. Rev.*, D76:053001, 2007.

[34] Julien Lesgourgues and Sergio Pastor. *Phys. Rep.*, 429:307–379, 2006;
S. Hannestad, *Ann. Rev. Nucl. Part. Sci.* 56: 137 (2006)

[35] C Weinheimer. Talk presented at this Conference.

[36] J. Schechter and J. W. F. Valle. *Phys. Rev.*, D25:2951, 1982.

[37] M. Hirsch, S. Morisi, and J. W. F. Valle. *Phys. Lett.*, B679:454, 2009.

[38] Martin Hirsch, Sergey Kovalenko, and Ivan Schmidt. *Phys. Lett.*, B642:106, 2006.

[39] III Avignone, Frank T., Steven R. Elliott, and Jonathan Engel. *Rev. Mod. Phys.*, 80:481–516, 2008.

[40] M. Hirsch et al. *Phys. Rev.*, D72:091301, 2005.

[41] M. Hirsch, S. Morisi, and J. W. F. Valle. *Phys. Rev.*, D79:016001, 2009.

[42] M. Hirsch, S. Morisi, and J. W. F. Valle. *Phys. Rev.*, D78:093007, 2008.

[43] K. S. Babu, Ernest Ma, and J. W. F. Valle. *Phys. Lett.*, B552:207–213, 2003.

[44] M. Hirsch et al. *Phys. Rev.*, D69:093006, 2004.

[45] A Faessler, G Fogli, E Lisi, V Rodin, A Rotunno, and F Simkovic. *Phys. Rev.*, D79:053001, 2009.

[46] Ilia Gogoladze, Nobuchika Okada, and Qaisar Shafi. *Phys. Lett.*, B672:235–239, 2009.

[47] Florian Bonnet, Daniel Hernandez, Toshihiko Ota, and Walter Winter. *JHEP*, 10:076, 2009.

[48] Sidney R. Coleman. *Nucl. Phys.*, B310:643, 1988.

[49] Renata Kallosh et al, *Phys. Rev.*, D52:912–935, 1995.

[50] Andre de Gouvea and J. W. F. Valle. *Phys. Lett.*, B501:115–127, 2001.

[51] J. W. F. Valle. Review lectures at Corfu, *J. Phys. Conf. Ser.*, 53:473–505, 2006.

[52] J. W. F. Valle. *Phys. Lett.*, B196:157, 1987.

[53] J. Schechter and J. W. F. Valle. *Phys. Rev.*, D25:774, 1982.

[54] Peter Minkowski. *Phys. Lett.*, B67:421, 1977.

[55] Murray Gell-Mann, Pierre Ramond, and Richard Slansky. Print-80-0576 (CERN).

[56] T. Yanagida. KEK lectures, 1979. ed. O. Sawada and A. Sugamoto (KEK, 1979).

[57] Rabindra N. Mohapatra and Goran Senjanovic. *Phys. Rev. Lett.*, 44:91, 1980.

[58] Robert Foot, H. Lew, X. G. He, and Girish C. Joshi. *Z. Phys.*, C44:441, 1989.

[59] G. Lazarides, Q. Shafi, and C. Wetterich. *Nucl. Phys.*, B181:287, 1981.

[60] P. Nath et al. The Hunt for New Physics at the Large Hadron Collider. e-Print: arXiv:1001.2693.

[61] D. Wyler and L. Wolfenstein. *Nucl. Phys.*, B218:205, 1983.

[62] M. C. Gonzalez-Garcia and J. W. F. Valle. *Phys. Lett.*, B216:360, 1989.

[63] Eugeni Akhmedov et al. *Phys. Rev.*, D53:2752–2780, 1996; Phys.Lett.B368:270-280,1996;
T. Appelquist and R. Shrock, *Phys. Lett.*, B548:204, 2002; *Phys.Rev.Lett.*, 90:201801,2003.

[64] S. M. Barr and Ilja Dorsner. *Phys. Lett.*, B632:527–531, 2006.

[65] B. W. Lee and R. E. Shrock, *Phys. Rev.* D16, 1444 ,1977.

[66] A. Zee. *Phys. Lett.*, B93:389, 1980;   D. Aristizabal Sierra and D. Restrepo, *JHEP*, 0608:036, 2006

[67] K. S. Babu. *Phys. Lett.*, B203:132, 1988;   D. Aristizabal Sierra and M. Hirsch, *JHEP* 0612, 052, 2006

[68] P. F. Harrison, D. H. Perkins, and W. G. Scott. *Phys. Lett.*, B530:167, 2002.

[69] P. F. Harrison and W. G. Scott. *Phys. Lett.*, B547:219–228, 2002.

[70] Walter Grimus and Luis Lavoura. *Phys. Lett.*, B579:113–122, 2004.

[71] Guido Altarelli and Ferruccio Feruglio. *Nucl. Phys.*, B720:64–88, 2005.

[72] A. Mondragon, M. Mondragon, and E. Peinado. *Phys. Rev.*, D76:076003, 2007.

[73] Federica Bazzocchi, Luca Merlo, and Stefano Morisi. *Phys. Rev.*, D80:053003, 2009.

[74] Guido Altarelli, Ferruccio Feruglio, and Luca Merlo. *JHEP*, 05:020, 2009.

[75] W. Grimus, L. Lavoura, and B. Radovcic. *Phys. Lett.*, B674:117–121, 2009.

[76] Anjan S. Joshipura, Bhavik P. Kodrani, and Ketan M. Patel. *Phys. Rev.*, D79:115017, 2009.

[77] S. F. King. *Phys. Lett.*, B675:347, 2009.

[78] Stefan Antusch, Joern Kersten, Manfred Lindner, and Michael Ratz. *Nucl. Phys.*, B674:401–433, 2003.

[79] Florian Plentinger and Werner Rodejohann. *Phys. Lett.*, B625:264–276, 2005.

[80] M. Hirsch et al. *Phys. Rev.*, D75:053006, 2007.

[81] P. Chankowski et al. *Phys. Rev. Lett.*, 86:3488, 2001.

[82] J. Bernabeu et al. *Phys. Lett.*, B187:303, 1987.

[83] M. C. Gonzalez-Garcia and J. W. F. Valle. *Mod. Phys. Lett.*, A7:477–488, 1992.

[84] A. Ilakovac and A. Pilaftsis. *Nucl. Phys.*, B437:491, 1995.

[85] Francesca Borzumati and Antonio Masiero. *Phys. Rev. Lett.*, 57:961, 1986.

[86] J. A. Casas and A. Ibarra. *Nucl. Phys.*, B618:171–204, 2001.

[87] S. Antusch, E. Arganda, M. J. Herrero, and A. M. Teixeira. *JHEP*, 11:090, 2006.

[88] F. Deppisch and J. W. F. Valle. *Phys. Rev.*, D72:036001, 2005.

[89] J. N. Esteves et al. *JHEP*, 05:003, 2009.

[90] F. Deppisch, T. S. Kosmas, and J. W. F. Valle. *Nucl. Phys.*, B752:80–92, 2006.

[91] G. C. Branco, M. N. Rebelo, and J. W. F. Valle. *Phys. Lett.*, B225:385, 1989.

[92] N. Rius and J. W. F. Valle. *Phys. Lett.*, B246:249–255, 1990.

[93] Y. Kuno. *AIP Conf. Proc.*, 542:220–225, 2000.

[94] Lawrence J. Hall and Mahiko Suzuki. *Nucl. Phys.*, B231:419, 1984.

[95] G. G. Ross and J. W. F. Valle. *Phys. Lett.*, B151:375, 1985.

[96] John R. Ellis and et al. *Phys. Lett.*, B150:142, 1985.

[97] A. Masiero and J. W. F. Valle. *Phys. Lett.*, B251:273–278, 1990.

[98] J. C. Romao, C. A. Santos, and J. W. F. Valle. *Phys. Lett.*, B288:311–320, 1992.

[99] J. C. Romao, A. Ioannisian, and J. W. F. Valle. *Phys. Rev.*, D55:427–430, 1997.

[100] Marco A. Diaz, Jorge C. Romao, and J. W. F. Valle. *Nucl. Phys.*, B524:23–40, 1998.

[101] M. Hirsch and J. W. F. Valle. *New J. Phys.*, 6:76, 2004.

[102] M. Hirsch et al. *Phys. Rev.*, D62:113008, 2000. Err-ibid. D65:119901,2002.

[103] W. Porod et al. *Phys. Rev.*, D63:115004, 2001.

[104] M. A. Diaz et al. *Phys. Rev.*, D68:013009, 2003.

[105] F. de Campos et al. *Phys. Rev.*, D71:075001, 2005; *JHEP*, 05:048, 2008.

[106] J. C. Romao et al. *Phys. Rev.*, D61:071703, 2000.

[107] Biswarup Mukhopadhyaya, Sourov Roy, and Francesco Vissani. *Phys. Lett.*, B443:191–195, 1998.

[108] M. Hirsch and W. Porod. *Phys. Rev.*, D68:115007, 2003.

[109] V. A. Kuzmin, V. A. Rubakov, and M. E. Shaposhnikov. *Phys. Lett.*, B155:36, 1985.

[110] M. Fukugita and T. Yanagida. *Phys. Lett.*, B174:45, 1986.

[111] W. Buchmuller, P. Di Bari, and M. Plumacher. *Ann. Phys.*, 315:305–351, 2005.

Discussion

Bennie Ward (Baylor University):

Could you comment on the degree of fine tuning in the prediction of θ_{ij} and Δm_{ij}^2 from high scale SUSY scenarios?

Answer: While supersymmetric seesaw schemes in unified gauge theories provide a potentially ideal framework to describe flavor, consistent predictions for neutrino properties as well as quark mass and mixing parameters are very hard to obtain in this context. We are still far from a unified description of flavor, hence we often play with flavor symmetries at lower scales.

Toru Iijima (Nagoya University):

You discussed about correlation to LFV. Can you comment on the relation to LFV in τ decays?

Answer: In many flavor-symmetry-based models one finds that the limits on muon-number violation are so stringent that they do not leave much room for sizable lepton-flavor-violation in tau decays.

Vali Huseynov (Nakhchivan State University):

At the beginning of your presentation you have mentioned about the see-saw mechanism. If I understood you correctly, you discuss the Majorana neutrinos. Does there exist the anormolous moment of a neutrino according to the theory presented by you?

Answer: When we studied the phenomenology of all types of seesaw mechanisms in early in 1980, Schecheter and I noted that neutrinos were expected to be Majorana-type in any natural gauge theory, irrespective of the mechanism that provides the neutrino mass. For this reason we never considered the neutrino anormalous moment.

Particle Physics in the LHC Era and beyond

Guido Altarelli

Dipartimento di Fisica 'E. Amaldi', Università di Roma Tre
INFN, Sezione di Roma Tre, I-00146 Rome, Italy
and
CERN, Department of Physics, Theory Unit
CH-1211 Geneva 23, Switzerland

I present a concise review of where we stand in particle physics today. First, I will discuss QCD, then the electroweak sector and finally the motivations and the avenues for new physics beyond the Standard Model.

1   Introduction

This concluding talk is not meant to be a summary of the Symposium. Rather it is a very concise overview (as implied by the severe page limit) of the status of particle physics at the start of the LHC time [1], as reflected at this Conference, together with a collection of personal thoughts stimulated by the excellent talks that I followed in their totality.

In a few words the general map of particle physics is as follows. The Standard Model (SM) is a low energy effective theory (nobody can believe it is the ultimate theory). It happens to be renormalizable, hence highly predictive and is extremely well supported by the data. However, one expects corrections from higher energies, in particular already from the TeV scale (LHC!), and also from the GUT/Planck scales and possibly from some additional intermediate scales. But even as a low energy effective theory the SM is not satisfactory. In fact while QCD and the gauge part of the EW theory are well established, the Higgs sector is so far just a conjecture. Not only it needs an experimental verification but it introduces serious theoretical problems, like the hierarchy problem, that demand some form of new physics at the electroweak scale. The most important goals of the experiments at the LHC [2, 3] are the clarification of the electroweak symmetry breaking mechanism, the search for signals of new physics at the TeV scale and, possibly, the identification of the unknown particles that make the dark matter in the Universe.

The future of particle physics very much depends on the outcome of the LHC. The LHC with the luminosity upgrade [4] will last for 15-20 years. Still the LHC cannot be all. A worldwide effort in neutrino physics is under way (T2K, DChooz, RENO, Daya Bay, NOνA......) [5], [6], [7]. The continuation of experiments on the CKM mixing and CP violation [8], [9] will take place at CERN with LHCb [10] and NA62..... [11] and at new improved B-factories [12]. "Small" experiments of capital importance will produce their results like those on τ and charm decays [13], neutrino mass (e.g. KATRIN) and neutrinoless double beta decay [14], EDM's [15] and the laboratory experiments on dark matter search [16]. A special mention deserves MEG, the on going search for the $\mu \to e\gamma$ decay at PSI [15], with a goal of improving the present

bound by one or two orders of magnitude. They are now at the level of sensitivity of the present bound and will soon release the results from the ongoing run. We look forward to seeing the results because a positive signal would be a great discovery and is predicted in plausible models, like in some supersymmetric extensions of the SM. Astroparticle experiments, like Fermi-LAT, PAMELA..... or AUGER, ICECUBE, ANTARES...., are more and more interesting for particle physics [17], [18], [19], also including the search for gravitational waves (VIRGO, LIGO....) [20] and experimental test of gravitation [21]. For planning the next big step (ILC, CLIC...) [22] we must wait for the LHC outcome in the first few years.

2   QCD

QCD stands as a main building block of the SM of particle physics. There are no essential problems of principle in its foundations and the comparison with experiment is excellent. For many years the relativistic quantum field theory of reference was QED, but at present QCD offers a more complex and intriguing theoretical laboratory. Indeed, due to asymptotic freedom, QCD can be considered as a better defined theory than QED. The statement that QCD is an unbroken renormalizable gauge theory, based on the $SU(3)$ colour group, with six kinds of triplets quarks with given masses, completely specifies the form of the Lagrangian in terms of quark and gluon fields. From the compact form of its Lagrangian one might be led to think that QCD is a "simple" theory. But actually this simple theory has an extremely rich dynamical content, including the striking properties of asymptotic freedom and of confinement, the complexity of the observed hadronic spectrum (with light and heavy quarks), the spontaneous breaking of (approximate) chiral symmetry, a complicated phase transition structure (deconfinement, chiral symmetry restoration, colour superconductivity), a highly non trivial vacuum topology (instantons, $U(1)_A$ symmetry breaking, strong CP violation,....), and so on.

So QCD is a complex theory and it is difficult to make its content explicit. Different routes have been developed over the years. There are non perturbative methods: lattice simulations (in great continuous progress), effective lagrangians valid in restricted specified domains, like chiral lagrangians, heavy quark effective theories, Soft Collinear Effective Theories (SCET), Non Relativistic QCD....) and also QCD sum rules, potential models (for quarkonium) etc. But the perturbative approach, based on asymptotic freedom and only applicable to hard processes, still remains the main quantitative connection to experiment. All of this is very important for the LHC preparation: understanding QCD processes is an essential prerequisite for all possible discoveries. Great experimental work on testing QCD has been accomplished over the years. In this respect it is very appropriate to pay here a tribute to HERA that has done a wonderful job in this domain. Great results are still coming out from HERA experiments [23, 24], like the measurements of the longitudinal structure function, of the diffractive structure functions, of the contribution of heavy quarks and so on. New interesting results have been found in heavy flavour spectroscopy [25]. Measurements of QCD processes at the Tevatron have also been of the utmost importance [26].

Due to confinement no free coloured particles are observed but only colour singlet hadrons. In high energy collisions the produced quarks and gluons materialize as narrow jets of hadrons. Our understanding of the confinement mechanism has much improved thanks to lattice simulations of QCD at finite temperatures and densities [27]. The potential between two colour charges, obtained from the lattice computations, clearly shows a linear slope at large distances (linearly rising potential). The slope decreases with increasing temperature until it vanishes at

a critical temperature T_C. Above T_C the slope remains zero. The phase transitions of colour deconfinement and of chiral restoration appear to happen together on the lattice. Near the critical temperature for both deconfinement and chiral restoration a rapid transition is observed in lattice simulations. In particular the energy density $\epsilon(T)$ is seen to sharply increase. The critical parameters and the nature of the phase transition depend on the number of quark flavours N_f and on their masses. For example, for $N_f = 2$ or 2+1 (i.e. 2 light u and d quarks and 1 heavier s quark), $T_C \sim 175\ MeV$ and $\epsilon(T_C) \sim 0.5 - 1.0\ GeV/fm^3$. For realistic values of the masses m_s and $m_{u,d}$ the phase transition appears to be a second order one, while it becomes first order for very small or very large $m_{u,d,s}$. At high densities the colour superconducting phase is probably also present with diquarks acting as Cooper pairs. The hadronic phase and the deconfined phase are separated by a crossover line at small densities and by a critical line at high densities. Determining the exact location of the critical point in T and μ_B is an important challenge for theory and is also important for the interpretation of heavy ion collision experiments.

A large investment is being done in experiments of heavy ion collisions with the aim of finding some evidence of the quark gluon plasma phase. Many exciting results have been found at the CERN SPS in the past years and more recently at RHIC [28]. At the CERN SPS some experimental hints of rapid variation of measured quantities with the energy density were found in the form, for example, of J/Ψ production suppression or of strangeness enhancement when going from p-A to Pb-Pb collisions. Indeed a posteriori the CERN SPS appears well positioned in energy to probe the transition region, in that a marked variation of different observables was observed. One impressive effect detected at RHIC, interpreted as due to the formation of a hot and dense bubble of matter, is the observation of a strong suppression of back-to-back correlations in jets from central collisions in Au-Au, showing that the jet that crosses the bulk of the dense region is absorbed. The produced hot matter shows a high degree of collectivity [29], as shown by the observation of elliptic flow (produced hadrons show an elliptic distribution while it would be spherical for a gas) and resembles a perfect liquid with small or no viscosity. There is also evidence for a 2-component hadronisation mechanism: coalescence [30] and fragmentation. Early produced partons with high density show an exponential falling in p_T: they produce hadrons by joining together. At large p_T fragmentation with power behaviour survives. Elliptic flow, inclusive spectra, partonic energy loss in medium, strangeness enhancement, J/Ψ suppression etc. are all suggestive (but only suggestive!) of early production of a coloured partonic medium with high energy density and temperature, close to the theoretically expected values, then expanding as a near ideal fluid. The experimental programme on heavy ion collisions will continue at the LHC where ALICE, the dedicated heavy ion collision experiment, is ready to take data [31].

As we have seen, a main approach to non perturbative problems in QCD is by simulations of the theory on the lattice [27], a technique started by K. Wilson in 1974 which has shown continuous progress over the last decades by going to smaller lattice spacing and larger lattices. A recent big step, made possible by the availability of more powerful dedicated computers, is the evolution from quenched (i.e. with no dynamical fermions) to unquenched calculations. Calculations with dynamical fermions (which take into account the effects of virtual quark loops) imply the evaluation of the quark determinant which is a difficult task. How difficult depends on the particular calculation method. There are several approaches (Wilson, twisted mass, Kogut-Susskind staggered, Ginsparg-Wilson fermions), each with its own advantages and disadvantages (including the time it takes to run the simulation on a computer). Another important progress is in the capability of doing the simulations with lighter quark masses (closer to the physical mass). As lattice simulations are always limited to masses of light quarks larger

than a given value, going to lighter quark masses makes the use of chiral extrapolations less important (to extrapolate the results down to the physical pion mass one can take advantage of the chiral effective theory in order to control the chiral logs: $\log(m_q/4\pi f_\pi)$). With the progress from unquenching and lighter quark masses an evident improvement in the agreement of predictions with the data is obtained. For example, modern simulations reproduce the hadron spectrum quite well. For lattice QCD one is now in an epoch of pre-dictivity as opposed to the post-dictivity of the past. And in fact the range of precise lattice results currently includes many domains: the QCD coupling constant (the value $\alpha_s(m_Z) = 0.1184(4)$ has been quoted [27]: the central value is in agreement with other determinations but I would not trust the stated error as a fair representation of the total uncertainty), the quark masses, the form factors for K and D decay, the B parameter for kaons, the decay constants f_K, f_D, f_{Ds}, the B_c mass and many more.

We now discuss perturbative QCD. In the QCD Lagrangian quark masses are the only parameters with dimensions. Naively (or classically) one would expect massless QCD to be scale invariant so that dimensionless observables would not depend on the absolute energy scale but only on ratios of energy variables. While massless QCD in the quantum version, after regularisation and renormalisation, is finally not scale invariant, the theory is asymptotically free and all the departures from scaling are asymptotically small and computable in terms of the running coupling $\alpha_s(Q^2)$ that decreases logarithmically at large Q^2. Mass corrections, present in the realistic case together with other non perturbative effects, are suppressed by powers of $1/Q^2$.

The measurements of $\alpha_s(Q^2)$ are among the main quantitative tests of the theory. The most precise and reliable determinations are from e^+e^- colliders (mainly at LEP: inclusive Z decays, inclusive hadronic τ decay, event shapes and jet rates) and from scaling violations in Deep Inelastic Scattering (DIS). There is a remarkable agreement among these different determinations. An all-inclusive average $\alpha_s(m_Z^2) = 0.1184(7)$ is obtained in [33], a value which corresponds to $\Lambda_{QCD} \sim 213(9)\ MeV$ ($\bar{M}S$, 5 flavours).

Since α_s is not too small, $\alpha_s(m_Z^2) \sim 0.12$, the need of high order perturbative calculations, of resummation of logs at all orders etc. is particularly acute. Ingenious new computational techniques and software have been developed and many calculations have been realized that only a decade ago appeared as impossible [34]. An increasing number of processes of interest for the physics at the LHC have been computed at NLO. Recent examples are the NLO calculations for $q\bar{q} \to t\bar{t}b\bar{b}$ [35] and for $W \to 3$ jets [36]. Methods for the automated calculation of NLO processes have been very much advanced, based on generalised unitarity [37] and algebraic reduction to basic integrals at the integrand level [38]. Powerful tools have been developed for automatic NLO calculations like HELAC, CutTools, BlackHat, Rocket [39].

Important work on jet recombination algorithms has been published by G. Salam and collaborators (for a review, see [40]). In fact it is essential that a correct jet finding is implemented by LHC experiments for an optimal matching of theory and experiment. A critical reappraisal of the existing cone and recombination methods has led to new improved versions of jet defining algorithms, like SISCone [41] and anti-k_T [42], with good infra red properties and leading to a simpler jet structure.

For benchmark measurements where experimental errors are small and corrections are large NNLO calculations are needed. A number of these extremely sophisticated calculations have been completed. In 2004 the complete calculation of the NNLO splitting functions has been published [43] $\alpha_s P \sim \alpha_s P_1 + \alpha_s^2 P_2 + \alpha_s^3 P_3 + \dots$, a really monumental, fully analytic, computation. More recently the main part of the inclusive hadronic Z and τ decays at $o(\alpha_s^4)$ (NNNLO!)

has been computed [44]. The calculation (which involves some 20.000 diagrams) is complete for τ decay, while for Z decay only the non singlet terms, proportional to $\Sigma_f Q_f^2$, are included (but singlet terms $(\Sigma_f Q_f)^2)$ are small at the previous order $o(\alpha_s^3)$). The calculation of the hadronic event shapes in $e^+ e^-$ annihilation at NNLO has also been completed [45], which involves consideration of 3, 4 and 5 jets with one loop corrections for 4 jets and two loop corrections for 3 jets. These calculations were applied in ref.[46] to the measurement of α_s from data on event shapes obtained by ALEPH with the result $\alpha_s(m_Z^2) = 0.1224 \pm 0.0039$.

Another very important example is Higgs production via $g + g \to H$ [47]. The amplitude is dominated by the top quark loop (if heavier coloured particles exist they also would contribute). The NLO corrections turn out to be particularly large. Higher order corrections can be computed either in the effective lagrangian approach, where the heavy top is integrated away and the loop is shrunk down to a point (the coefficient of the effective vertex is known to α_s^4 accuracy), or in the full theory. At the NLO the two approaches agree very well for the rate as a function of m_H. The NNLO corrections have been computed in the effective vertex approximation. Beyond fixed order, resummation of large logs were carried out. Also the NLO EW contributions are known by now. Rapidity (at NNLO) and p_T distributions (at NLO) have also been evaluated. At smaller p_T the large logarithms $[log(p_T/m_H)]^n$ have been resummed in analogy with what was done long ago for W and Z production.

The importance of DIS for QCD goes well beyond the measurement of α_s. In the past it played a crucial role in establishing the reality of quarks and gluons as partons and in promoting QCD as the theory of strong interactions. Nowadays it still generates challenges to QCD as, for example, in the domain of structure functions at small x or of polarized structure functions or of generalized parton densities and so on.

The problem of constructing a convergent procedure to include the BFKL corrections at small x in the singlet splitting functions, in agreement with the small-x behaviour observed at HERA, has been a long standing puzzle which has now been essentially solved. The naive BFKL rise of splitting functions is tamed by resummation of collinear singularities and by running coupling effects. The resummed expansion is well behaved and the result is close to the perturbative NLO splitting function in the region of HERA data at small x [48],[49].

In polarized DIS one main question is how the proton helicity is distributed among quarks, gluons and orbital angular momentum: $1/2\Delta\Sigma + \Delta g + L_z = 1/2$ [50]. The quark moment $\Delta\Sigma$ was found to be small: typically, at $Q^2 \sim 1~GeV^2$, $\Delta\Sigma_{exp} \sim 0.3$ (the "spin crisis") [51]. Either $\Delta g + L_z$ is large or there are contributions to $\Delta\Sigma$ at very small x outside of the measured region. Δg evolves like $\Delta g \sim log Q^2$, so that eventually should become large (while $\Delta\Sigma$ and $\Delta g + L_z$ are Q^2 independent in LO). For conserved quantities we would expect that they are the same for constituent and for parton quarks. But actually the conservation of $\Delta\Sigma$ is broken by the axial anomaly and, in fact, in perturbation theory beyond LO the conserved density is actually $\Delta\Sigma' = \Delta\Sigma + n_f/2\pi\alpha_s~\Delta g$ [51]. Note that also $\alpha_s\Delta g$ is conserved in LO, as $\Delta g \sim \log Q^2$. This behaviour is not controversial but it will take long before the log growth of Δg will be confirmed by experiment! But by establishing this behaviour one would show that the extraction of Δg from the data is correct and that the QCD evolution works as expected. If Δg was large enough it could account for the difference between partons $(\Delta\Sigma)$ and constituents $(\Delta\Sigma')$. From the spin sum rule it is clear that the log increase should cancel between Δg and L_z. This cancelation is automatic as a consequence of helicity conservation in the basic QCD vertices. Existing direct measurements by Hermes, Compass, and at RHIC are still very crude and show no hint of a large Δg [52] at accessible values of x and Q^2. Present data are consistent with Δg large enough to sizeably contribute to the spin sum rule but there is no indication that $\alpha_s\Delta g$ can explain

the difference between constituents and parton quarks.

Another important role of DIS is to provide information on parton density functions (PDF) [53] which are instrumental for computing cross-sections of hard processes at hadron colliders via the factorisation formula. The predictions for cross sections and distributions at pp or $p\bar{p}$ colliders for large p_T jets or photons, for heavy quark production, for Drell-Yan, W and Z production are all in very good agreement with experiment. There was an apparent problem for b quark production at the Tevatron, but the problem appears now to be solved by a combination of refinements (log resummation, B hadrons instead of b quarks, better fragmentation functions....)[54]. The QCD predictions are so solid that W and Z production are actually considered as possible luminosity monitors for the LHC.

The activity on event simulation also received a big boost from the LHC preparation (see, for example, [55] and the review [56]). General algorithms for performing NLO calculations numerically (requiring techniques for the cancellation of singularities between real and virtual diagrams) have been developed (see, for example, [57]). The matching of matrix element calculation of rates together with the modeling of parton showers has been realised in packages, as for example in the MC@NLO [58] or POWHEG [59] based on HERWIG. The matrix element calculation, improved by resummation of large logs, provides the hard skeleton (with large p_T branchings) while the parton shower is constructed by a sequence of factorized collinear emissions fixed by the QCD splitting functions. In addition, at low scales a model of hadronisation completes the simulation. The importance of all the components, matrix element, parton shower and hadronisation can be appreciated in simulations of hard events compared with the Tevatron data.

In conclusion, I think that the domain of QCD appears as one of great maturity but also of robust vitality (as apparent by the large amount of work produced for the LHC preparation) and all the QCD predictions that one was able to formulate and to test are in very good agreement with experiment.

3 The Higgs Problem

The Higgs problem is really central in particle physics today [61]. On the one hand, the experimental verification of the Standard Model (SM) cannot be considered complete until the structure of the Higgs sector is not established by experiment. On the other hand, the Higgs is directly related to most of the major open problems of particle physics, like the flavour problem and the hierarchy problem, the latter strongly suggesting the need for new physics near the weak scale, which could also clarify the dark matter identity. It is clear that the fact that some sort of Higgs mechanism is at work has already been established. The longitudinal degree of freedom for the W or the Z is borrowed from the Higgs sector and is an evidence for it. In fact the couplings of quarks and leptons to the weak gauge bosons W$^{\pm}$ and Z are indeed precisely those prescribed by the gauge symmetry. To a lesser accuracy the triple gauge vertices γWW and ZWW have also been found in agreement with the specific predictions of the $SU(2) \bigotimes U(1)$ gauge theory. This means that it has been verified that the gauge symmetry is unbroken in the vertices of the theory: all currents and charges are indeed symmetric. Yet there is obvious evidence that the symmetry is instead badly broken in the masses. The W or the Z with longitudinal polarization that are observed are not present in an unbroken gauge theory (massless spin-1 particles, like the photon, are transversely polarized). Not only the W and the Z have large masses, but the large splitting of, for example, the t-b doublet shows that even

the global weak SU(2) is not at all respected by the fermion spectrum. Symmetric couplings and totally non symmetric spectrum is a clear signal of spontaneous symmetry breaking and its implementation in a gauge theory is via the Higgs mechanism. The big remaining questions are about the nature and the properties of the Higgs particle(s).

The LHC has been designed to solve the Higgs problem. A strong argument indicating that the solution of the Higgs problem cannot be too far away is the fact that, in the absence of a Higgs particle or of an alternative mechanism, violations of unitarity appear in scattering amplitudes involving longitudinal gauge bosons (those most directly related to the Higgs sector) at energies in the few TeV range [62]. A crucial question for the LHC is to identify the mechanism that avoids the unitarity violation: is it one or more Higgs bosons or some new vector boson (like additional gauge bosons W, Z or Kaluza-Klein recurrences or resonances from a strong sector) [63, 64]?

It is well known that in the SM with only one Higgs doublet a lower limit on m_H can be derived from the requirement of vacuum stability (i.e. that the quartic Higgs coupling λ does not turn negative in its running up to a large scale Λ) or, in milder form, of a moderate instability, compatible with the lifetime of the Universe [65]. The Higgs mass enters because it fixes the initial value of the quartic Higgs coupling λ. For the experimental value of m_t the lower limit is below the direct experimental bound for $\Lambda \sim$ a few TeV and is $M_H > 130$ GeV for $\Lambda \sim M_{Pl}$. Similarly an upper bound on m_H (with mild dependence on m_t) is obtained, as described in [66], from the requirement that for λ no Landau pole appears up to the scale Λ, or in simpler terms, that the perturbative description of the theory remains valid up to Λ. The upper limit on the Higgs mass in the SM is clearly important for assessing the chances of success of the LHC as an accelerator designed to solve the Higgs problem. Even if Λ is as small as a few TeV the limit is $m_H < 600 - 800$ GeV and becomes $m_H < 180$ GeV for $\Lambda \sim M_{Pl}$.

In conclusion it looks very likely that the LHC can clarify the problem of the electroweak symmetry breaking mechanism. It has been designed for it!

4 Precision Tests of the Standard Electroweak Theory

The most precise tests of the electroweak theory apply to the QED sector. The anomalous magnetic moments of the electron and of the muon are among the most precise measurements in the whole of physics [15], [67]. Recently there have been new precise measurements of a for the electron [68] and the muon [69] ($a = (g - 2)/2$). The QED part has been computed analytically for $i = 1, 2, 3$, while for $i = 4$ there is a numerical calculation (see, for example, [71]). Some terms for $i = 5$ have also been estimated for the muon case. The weak contribution is from W or Z exchange. The hadronic contribution is from vacuum polarization insertions and from light by light scattering diagrams. For the electron case the weak contribution is essentially negligible and the hadronic term does not introduce an important uncertainty. As a result the a_e measurement can be used to obtain the most precise determination of the fine structure constant [70]. In the muon case the experimental precision is less by about 3 orders of magnitude, but the sensitivity to new physics effects is typically increased by a factor $(m_\mu/m_e)^2 \sim 4 \cdot 10^4$. The dominant theoretical ambiguities arise from the hadronic terms in vacuum polarization and in light by light scattering. If the vacuum polarization terms are evaluated from the e^+e^- data a discrepancy of $\sim 3\sigma$ is obtained (the τ data would indicate better agreement, but the connection to a_μ is less direct and recent new data have added solidity to the e^+e^- route)[72]. Finally, we note that, given the great accuracy of the a_μ measurement

and the estimated size of the new physics contributions, for example from SUSY, it is not unreasonable that a first signal of new physics would appear in this quantity.

The results of the electroweak precision tests also including the measurements of m_t, m_W and the searches for new physics at the Tevatron [74] form a very stringent set of precise constraints [73] to compare with the Standard Model (SM) or with any of its conceivable extensions [75]. When confronted with these results, on the whole the SM performs rather well, so that it is fair to say that no clear indication for new physics emerges from the data [76]. But the Higgs sector of the SM is still very much untested. What has been tested is the relation $M_W^2 = M_Z^2 \cos^2 \theta_W$, modified by small, computable radiative corrections. This relation means that the effective Higgs (be it fundamental or composite) is indeed a weak isospin doublet. The Higgs particle has not been found but in the SM its mass can well be larger than the present direct lower limit $m_H > 114.4$ GeV obtained from direct searches at LEP-2. The radiative corrections computed in the SM when compared to the data on precision electroweak tests lead to a clear indication for a light Higgs, not too far from the present lower bound. The exact upper limit for m_H in the SM depends on the value of the top quark mass m_t (the one-loop radiative corrections are quadratic in m_t and logarithmic in m_H). The measured value of m_t went down recently (as well as the associated error) according to the results of Run II at the Tevatron. The CDF and D0 combined value is at present $m_t = 173.1 \pm 1.3\ GeV$. As a consequence the present limit on m_H is quite stringent: $m_H < 186\ GeV$ (at 95% c.l., after including the information from the 114.4 GeV direct bound) [73].

In the Higgs search the Tevatron is now reaching the SM sensitivity. At this Symposium the quoted result for the SM Higgs is that the interval $160 < m_H < 170$ GeV is excluded at 95% c.l. [77]. But the most recent limit, reported near the end of 2009, is somewhat weaker: $163 < m_H < 166$ GeV [78]. The goal at Fermilab is to collect 12 fb^{-1} of luminosity by 2011 and possibly exclude $115 < m_H < 185$ GeV.

5   The Physics of Flavour

Another domain where the SM is really in good agreement with the data is flavour physics (actually too good in comparison with the general expectation before the experiments). In the last decade great progress in different areas of flavour physics has been achieved. In the quark sector, the amazing results of a generation of frontier experiments, performed at B factories and at accelerators, have become available. QCD has been playing a crucial role in the interpretation of experiments by a combination of effective theory methods (heavy quark effective theory, NRQCD, SCET), lattice simulations and perturbative calculations. The hope of the B-decay experiments was to detect departures from the CKM picture of mixing and of CP violation as signals of new physics. At present the available results on B mixing and CP violation on the whole agree very well with the SM predictions based on the CKM matrix [8], [11], [79]. A few interesting tensions at the 2-3 σ level should be monitored closely in the future [8], [9]: $\sin 2\beta$ from $B_d \rightarrow J/\Psi K^0$ versus ϵ_K and V_{ub} (which, however, in my opinion, is probably due to an underestimate of theoretical errors, particularly on the determination of V_{ub}), β_s measured by CDF, D_0 in $B_s \rightarrow J/\Psi \phi$ and $B \rightarrow \tau \nu$. But certainly the amazing performance of the SM in flavour changing and/or CP violating transitions in K and B decays poses very strong constraints on all proposed models of new physics [80], [81]. For example, if one adds to the SM effective non renormalizable operators suppressed by powers of a scale Λ one generally finds that experiments indicate very large values of Λ, much above the few TeV range indicated by

the hierarchy problem. Only if one assumes that the deviations from new physics occur at loop level and inherit the same SM protections against flavour changing neutral currents (like the GIM mechanism and small V_{CKM} factors) as, for example, in Minimal Flavour Violation models [81], that one obtains bounds on Λ in the few TeV range.

In the leptonic sector the study of neutrino oscillations has led to the discovery that at least two neutrinos are not massless and to the determination of the mixing matrix [7], [82]. Neutrinos are not all massless but their masses are very small (at most a fraction of eV). The neutrino spectrum could be either of the normal hierarchy type (with the solar doublet below), or of the inverse hierarchy type (with the solar doublet above). Probably masses are small because νs are Majorana fermions, and, by the see-saw mechanism, their masses are inversely proportional to the large scale M where lepton number (L) non conservation occurs (as expected in GUT's). Indeed the value of $M \sim m_{\nu R}$ from experiment is compatible with being close to $M_{GUT} \sim 10^{14} - 10^{15} GeV$, so that neutrino masses fit well in the GUT picture and actually support it. The interpretation of neutrinos as Majorana particles enhances the importance of experiments aimed at the detection of neutrinoless double beta decay and a huge effort in this direction is underway [14]. It was realized that decays of heavy ν_R with CP and L non conservation can produce a B-L asymmetry (which is unchanged by instanton effects at the electroweak scale). The range of neutrino masses indicated by neutrino phenomenology turns out to be perfectly compatible with the idea of baryogenesis via leptogenesis [83]. This elegant model for baryogenesis has by now replaced the idea of baryogenesis near the weak scale, which has been strongly disfavoured by LEP. It is remarkable that we now know the neutrino mixing matrix with good accuracy [84]. Two mixing angles are large and one is small. The atmospheric angle θ_{23} is large, actually compatible with maximal but not necessarily so. The solar angle θ_{12} (the best measured) is large, $\sin^2 \theta_{12} \sim 0.3$, but certainly not maximal. The third angle θ_{13}, strongly limited mainly by the CHOOZ experiment, has at present a 3σ upper limit given by about $\sin^2 \theta_{13} \leq 0.04$. It is a fact that, to a precision comparable with the measurement accuracy, the Tri-Bimaximal (TB) mixing pattern ($\sin^2 \theta_{12} \sim 1/3$, $\sin^2 \theta_{23} \sim 1/2$ and $\sin^2 \theta_{13} = 0$) [85] is well approximated by the data. If this experimental result is not a mere accident but a real indication that a dynamical mechanism is at work to guarantee the validity of TB mixing in the leading approximation, corrected by small non leading terms, then non abelian discrete flavor groups emerge as the main road to an understanding of this mixing pattern [86]. Indeed the entries of the TB mixing matrix are clearly suggestive of "rotations" by simple, very specific angles. In fact the group A_4, the simplest group used to explain TB mixing, is defined as the group of rotations that leave a regular rigid tetrahedron invariant. The non conservation of the three separate lepton numbers and the large leptonic mixing angles make it possible that processes like $\mu \to e\gamma$ or $\tau \to \mu\gamma$ might be observable, not in the SM but in extensions of it like the MSSM. Thus, for example, the outcome of the now running experiment MEG at PSI [15] aiming at improving the limit on $\mu \to e\gamma$ by 1 or 2 orders of magnitude, is of great interest.

6   Outlook on Avenues beyond the Standard Model

No signal of new physics has been found neither in electroweak precision tests nor in flavour physics [60]. Given the success of the SM why are we not satisfied with that theory? Why not just find the Higgs particle, for completeness, and declare that particle physics is closed? The reason is that there are both conceptual problems and phenomenological indications for physics

beyond the SM. On the conceptual side the most obvious problems are the proliferation of parameters, the puzzles of family replication and of flavour hierarchies, the fact that quantum gravity is not included in the SM and the related hierarchy problem. Among the main phenomenological hints for new physics we can list dark matter, the quest for Grand Unification and coupling constant merging, neutrino masses (explained in terms of L non conservation), baryogenesis and the cosmological vacuum energy (a gigantic naturalness problem).

We know by now [102], [16], [103] that the Universe is flat and most of it is not made up of known forms of matter: while $\Omega_{tot} \sim 1$ and $\Omega_{matter} \sim 0.3$, the normal baryonic matter is only $\Omega_{baryonic} \sim 0.044$, where Ω is the ratio of the density to the critical density. Most of the energy in the Universe is dark matter (DM) and Dark Energy (DE) with $\Omega_\Lambda \sim 0.7$. We also know that most of DM must be cold (non relativistic at freeze-out) and that significant fractions of hot DM are excluded. Neutrinos are hot DM (because they are ultrarelativistic at freeze-out) and indeed are not much cosmo-relevant: $\Omega_\nu \lesssim 0.015$. The identification of DM is a task of enormous importance for both particle physics and cosmology. The LHC has good chances to solve this problem in that it is sensitive to a large variety of WIMP's (Weekly Interacting Massive Particles). WIMP's with masses in the 10 GeV-1 TeV range with typical EW cross-sections turn out to contribute terms of $o(1)$ to Ω. This is a formidable hint in favour of WIMP's as DM candidates. By comparison, axions are also DM candidates but their mass and couplings must be tuned for this purpose. If really some sort of WIMP's are a main component of DM they could be discovered at the LHC and this will be a great service of particle physics to cosmology. Active searches in non-accelerator experiments are under way [16]. Some hints of possible signals have been reported: e.g. annual modulations (DAMA/LIBRA at Gran Sasso [104]), e^+ and/or e^+e^- excess in cosmic ray detectors, e.g. in PAMELA [105] and ATIC [106] (but the ATIC excess has not been confirmed by Fermi-LAT [107]). If those effects are really signals for DM they would indicate particularly exotic forms of DM [108]. But for the PAMELA effect an astrophysical explanation in terms of relatively close pulsars appears as a plausible alternative [102].

The computed evolution with energy of the effective gauge couplings clearly points towards the unification of the electro-weak and strong forces (Grand Unified Theories: GUT's) at scales of energy $M_{GUT} \sim 10^{15} - 10^{16}$ GeV which are close to the scale of quantum gravity, $M_{Pl} \sim 10^{19}$ GeV. One is led to imagine a unified theory of all interactions also including gravity (at present superstrings provide the best attempt at such a theory [109]). Thus GUT's and the realm of quantum gravity set a very distant energy horizon that modern particle theory cannot ignore. Can the SM without new physics be valid up to such large energies? One can imagine that some of the obvious problems of the SM could be postponed to the more fundamental theory at the Planck mass. For example, the explanation of the three generations of fermions and the understanding of the pattern of fermion masses and mixing angles can be postponed. But other problems must find their solution in the low energy theory. In particular, the structure of the SM could not naturally explain the relative smallness of the weak scale of mass, set by the Higgs mechanism at $\mu \sim 1/\sqrt{G_F} \sim 250$ GeV with G_F being the Fermi coupling constant. This so-called hierarchy problem [63], [64] is due to the instability of the SM with respect to quantum corrections. This is related to the presence of fundamental scalar fields in the theory with quadratic mass divergences and no protective extra symmetry at $\mu = 0$. For fermion masses, first, the divergences are logarithmic and, second, they are forbidden by the $SU(2) \bigotimes U(1)$ gauge symmetry plus the fact that at $m = 0$ an additional symmetry, i.e. chiral symmetry, is restored. Here, when talking of divergences, we are not worried of actual infinities. The theory is renormalizable and finite once the dependence on the cut-off Λ is

absorbed in a redefinition of masses and couplings. Rather the hierarchy problem is one of naturalness. We can look at the cut-off as a parameterization of our ignorance on the new physics that will modify the theory at large energy scales. Then it is relevant to look at the dependence of physical quantities on the cut-off and to demand that no unexplained enormously accurate cancellations arise. In fact, the hierarchy problem can be put in quantitative terms: loop corrections to the higgs mass squared are quadratic in the cut-off Λ. The most pressing problem is from the top loop. With $m_h^2 = m_{bare}^2 + \delta m_h^2$ the top loop gives

$$\delta m_{h|top}^2 \sim -\frac{3G_F}{2\sqrt{2}\pi^2} m_t^2 \Lambda^2 \sim -(0.2\Lambda)^2 \tag{1}$$

If we demand that the correction does not exceed the light Higgs mass indicated by the precision tests, Λ must be close, $\Lambda \sim o(1~TeV)$. Similar constraints also arise from the quadratic Λ dependence of loops with gauge bosons and scalars, which, however, lead to less pressing bounds. So the hierarchy problem demands new physics to be very close (in particular the mechanism that quenches the top loop). Actually, this new physics must be rather special, because it must be very close, yet its effects are not clearly visible in precision electroweak tests - the "LEP Paradox" [87] - now also accompanied by a similar "flavour paradox" [81]. Examples [63], [64] of proposed classes of solutions for the hierarchy problem are :

Supersymmetry. In the limit of exact boson-fermion symmetry [88] the quadratic divergences of bosons cancel so that only log divergences remain. However, exact SUSY is clearly unrealistic. For approximate SUSY (with soft breaking terms), which is the basis for all practical models, Λ is replaced by the splitting of SUSY multiplets, $\Lambda \sim m_{SUSY} - m_{ord}$. In particular, the top loop is quenched by partial cancellation with s-top exchange, so the s-top cannot be too heavy. An important phenomenological indication is that coupling unification is not exact in the SM while it is quantitatively precise in SUSY GUT's where also proton decay bounds are not in contradiction with the predictions. An interesting exercise is to repeat the fit of precision tests in the Minimal Supersymmetric Standard Model with GUT constraints added, also including the additional data on the muon $(g-2)$, the dark matter relic density and on the $b \rightarrow s\gamma$ rate. The result is that the central value of the lightest Higgs mass m_h goes up (in better harmony with the bound from direct searches) for moderately large $tan\beta$ and relatively light SUSY spectrum [89].

Technicolor. The Higgs system is a condensate of new fermions. There are no fundamental scalar Higgs sector, hence no quadratic devergences associated to the μ^2 mass in the scalar potential. This mechanism needs a very strong binding force, $\Lambda_{TC} \sim 10^3~\Lambda_{QCD}$. It is difficult to arrange that such nearby strong force is not showing up in precision tests. Hence this class of models has been disfavoured by LEP, although some special class of models have been devised a posteriori, like walking TC, top-color assisted TC etc [90].

Extra dimensions. One possibility is that M_{Pl} appears very large, or equivalently that gravity appears very weak, because we are fooled by hidden extra dimensions so that the real gravity scale is reduced down to a lower scale, even possibly down to $o(1~TeV)$ ("large" extra dimensions). This possibility is very exciting in itself and it is really remarkable that it is not directly incompatible with experiment but a realistic model has not emerged [91]. In fact, the most promising set of extra dimensional models are those with "warped" metric, which offer attractive solutions to the hierarchy problem [92, 93]. An important direction of development is the study of symmetry breaking by orbifolding and/or boundary conditions. These are models where a larger gauge symmetry (with or without SUSY) holds in the bulk. The symmetry is reduced on the 4 dimensional brane, where the physics that we observe is located, as an

effect of symmetry breaking induced geometrically by suitable boundary conditions (see, for example, the class of models in [94]). Also "Higgsless models" have been tried where it is the SM electroweak gauge symmetry which is broken at the boundaries [95] (then no Higgs should be found at the LHC but other signals, like additional vector bosons, should appear). Extra dimensions offer a rich and exciting general framework.

"**Little Higgs**" **models**. In these models extra symmetries allow $m_h \neq 0$ only at two-loop level, so that Λ can be as large as $o(10\ TeV)$ with the Higgs within present bounds (the top loop is quenched by exchange of heavy vectorlike new quarks with charge 2/3) [96]. Certainly these models involve a remarkable level of group theoretic virtuosity. However, in the simplest versions one is faced with problems with precision tests of the SM. These bad features can be fixed by some suitable complication of the model (see for example, [97]). But, in my opinion, the real limit of this approach is that it only offers a postponement of the main problem by a few TeV, paid by a complete loss of predictivity at higher energies. In particular all connections to GUT's are lost.

Effective theories for compositeness. In this approach [98] a low energy theory, left over by truncation of some UV completion, is described in terms of an elementary sector (the SM particles minus the Higgs) a composite sector (including the Higgs, massive vector bosons ρ_μ and new fermions) and a mixing sector. The Higgs is a pseudo Goldstone bosons of a larger broken gauge group, with ρ_μ the corresponding massive vector bosons. Mass eigenstates are mixtures of elementary and composite states, with light particles mostly elementary and heavy particles mostly composite. But the Higgs is totally composite (perhaps also the right-handed top quark). New physics in the composite sector is well hidden because light particles have small mixing angles. The Higgs is light because only acquires mass through interactions with the light particles from their composite components. This general description can apply to models with a strongly interacting sector as arising from little Higgs or extra dimension scenarios.

The anthropic solution. The apparent value of the cosmological constant Λ poses a tremendous, unsolved naturalness problem [99]. Yet the value of Λ is close to the Weinberg upper bound for galaxy formation [100]. Possibly our Universe is just one of infinitely many (Multiverse) continuously created from the vacuum by quantum fluctuations. Different types of physics are realized in different Universes according to the multitude of string theory solutions (10^{500}). Perhaps we live in a very unlikely Universe but the only one that allows our existence [101]. I find applying the anthropic principle to the SM hierarchy problem excessive. After all we can find plenty of models that easily reduce the fine tuning from 10^{14} to 10^2: why make our Universe so terribly unlikely? By comparison the case of the cosmological constant is a lot different: the context is not as fully specified as the for the SM (quantum gravity, string cosmology, branes in extra dimensions, wormholes through different Universes....).

¿From model building the following lessons can be derived. In all the new physics models we have mentioned there is a light Higgs ($\lesssim 200$ GeV), except in Higgsless models (if any) but new light new vector bosons exist in this case. In all models there is at least a percent fine tuning, so that fine tuning appears to be imposed on us by the data.

7 Conclusion

Supersymmetry remains the standard way beyond the SM. What is unique to SUSY, beyond leading to a set of consistent and completely formulated models, as, for example, the MSSM, is that this theory can potentially work up to the GUT energy scale. In this respect it is the most

ambitious model because it describes a computable framework that could be valid all the way up to the vicinity of the Planck mass. The SUSY models are perfectly compatible with GUT's and are actually quantitatively supported by coupling unification and compatible with proton decay bounds and also by what we have recently learned on neutrino masses. All other main ideas for going beyond the SM do not share this synthesis with GUT's. The SUSY way is testable, for example at the LHC, and the issue of its validity will be decided by experiment. It is true that we could have expected the first signals of SUSY already at LEP2, based on naturality arguments applied to the most minimal models (for example, those with gaugino universality at asymptotic scales). The absence of signals has stimulated the development of new ideas like those of extra dimensions and of "little Higgs" models. These ideas are very interesting and provide an important reference for the preparation of LHC experiments. Models along these new ideas are not so completely formulated and studied as for SUSY and no well defined and realistic baseline has sofar emerged. But it is well possible that they might represent at least a part of the truth and it is very important to continue the exploration of new ways beyond the SM. New input from experiment is badly needed, so we all look forward to the start of the LHC.

The most frequently asked questions are: is it possible that the LHC does not find the Higgs particle? Yes, it is possible, but then it must find something else. Is it possible that the LHC finds the Higgs particle but no other new physics (pure and simple SM)? Yes, it is technically possible but it is very unnatural. Is it possible that the LHC finds neither the Higgs nor new physics? No, it is "approximately impossible": that is it is impossible to the extent that the LHC energy and integrated luminosity are considered sufficient for a thorough exploration of the electroweak scale.

8 Acknowledgments

As the last speaker, on behalf of all participants, I thank the Organizers who have done really a great job, in particular Joachim Mnich. This Symposium presented a very complete picture of our field in a most confortable setting in the exciting background of the city of Hamburg.

References

[1] H. Burkhardt, these Proceedings.

[2] K. Jon-And, these Proceedings.

[3] R. Cousins, these Proceedings.

[4] M. Nessi, these Proceedings.

[5] S. Kopp, these Proceedings.

[6] Y. Suzuki, these Proceedings.

[7] J. Valle, these Proceedings.

[8] S. Prell, these Proceedings.

[9] T. Iijima, these Proceedings.

[10] A. Golutvin, these Proceedings.

[11] T. Komatsubara, these Proceedings.

[12] M. Giorgi, these Proceedings.

[13] Y. Wang, these Proceedings.

[14] C. Weinheimer, these Proceedings.

[15] T. Mori, these Proceedings.

[16] N. Smith, these Proceedings.

[17] M. Mostafa, these Proceedings.

[18] M. Punch, these Proceedings.

[19] P. Hulth, these Proceedings.

[20] F. Fidecaro, these Proceedings.

[21] S. Hoedl, , these Proceedings.

[22] E. Eisen, these Proceedings.

[23] A. Glazov, these Proceedings.

[24] M. Ruspa, these Proceedings.

[25] J. Brodzicka, these Proceedings.

[26] M. Wobisch, these Proceedings.

[27] A. Ukawa, these Proceedings.

[28] T. Peitzmann, these Proceedings.

[29] T. Renk, these Proceedings.

[30] See, for example, R.J. Fries et al Phys.Rev.**C68** 044902 (2003), ArXiv: nucl-th/0306027 and references therein.

[31] P. Braun-Munzinger, these Proceedings.

[32] G. Altarelli, Proceedings of the IFAE 2006, Pavia, Italy, ed. by G. Montagna *et al.*, Springer, 2007, pp. 3-22; ArXiv:hep-ph/0609097.

[33] S. Bethke, Eur.Phys.J. **C64** 689 (2009), ArXiv:0908.1135.

[34] N. Glover, these Proceedings.

[35] A. Bredenstein *et al.*, Phys.Rev.Lett.**103** 012002 (2009), ArXiv:0905.0110; ArXiv:1001.4006.

[36] C. F. Berger *et al.*, Phys.Rev. **D80** 074036 (2009), ArXiv:0907.1984.

[37] R. Britto, F. Cachazo and B. Feng, Nucl. Phys. **B725** 275 (2005), ArXiv:hep-th/0412103]. Z. Bern, L. J. Dixon and D. A. Kosower, Annals Phys. **322** 1587(2007), ArXiv:0704.2798.

[38] D. Forde, Phys. Rev. **D75** 125019 (2007), ArXiv:0704.1835; G. Ossola, C. G. Papadopoulos and R. Pittau, Nucl. Phys. **B763** 147 (2007), ArXiv: hep- ph/0609007; JHEP **0707** 085 (2007), ArXiv:0704.1271; JHEP **0805** 004 (2008), ArXiv:0802.1876; W.T. Giele, Z. Kunszt and K. Melnikov, JHEP **0804** 049 (2008), ArXiv:0801.2237 . R.K. Ellis, W.T. Giele and Z. Kunszt, JHEP **0803** 003 (2008), ArXiv: 0708.2398 R.K. Ellis *et al.*, Nucl.Phys. **B822** 270 (2009), ArXiv:0806.3467. C. Anastasiou *et al.*, Phys. Lett. **B 645** 213 (2007), ArXiv:hep-ph/0609191.

[39] For a review, see, for example, A. van Hameren, C.G. Papadopoulos and R. Pittau, JHEP **0909** 106 (2009), ArXiv:0903.4665.

[40] G.P. Salam, ArXiv:0906.1833.

[41] G.P. Salam and G. Soyez, JHEP **0705** 086 (2007), ArXiv:0704.0292.

[42] M. Cacciari and G.P. Salam, Phys. Lett. **B641** 57 (2006) ArXiv:hep-ph/0512210.

[43] A. Vogt, S. Moch, J.A.M. Vermaseren Nucl.Phys.**B691**129 (2004), ArXiv: hep-ph/0404111; Nucl.Phys.**B688** 101 (2004), ArXiv: hep-ph/0403192.

[44] P. A. Baikov, K.G. Chetyrkin and J.H. Kuhn, Phys.Rev.Lett. **101** 012002 (2008), ArXiv:0801.1821; ArXiv:0906.2987.

[45] A. Gehrmann-De Ridder *et al.* Phys. Rev. Letters**99**132002 (2007); ArXiv:0707.1285; JHEP **0712** 094 (2007), ArXiv:0711.4711; Phys.Rev.Lett. **100** 172001 (2008), ArXiv:0802.0813; JHEP **0905** 106 (2009), ArXiv:0903.4658.

[46] G. Dissertori *et al.*, JHEP **0802** 040 (2008), ArXiv:0712.0327; JHEP **0908** 036 (2009), ArXiv:0906.3436.

[47] S. Dawson, Nucl. Phys. **B359** 283 (1991); A. Djouadi, M. Spira and P.M. Zerwas, Phys. Lett. **B264** (1991) 440; M. Spira *et al.*, Nucl. Phys. **B453** 17 (1995); U. Aglietti *et al.*,JHEP **0701** 021 (2007); C. Anastasiou *et al.*, JHEP **0701** 082 (2007); M. Muhlleitner and M. Spira, Nucl.Phys. **B790** 1 (2008), ArXiv:hep-ph/0612254. R.V. Harlander, Phys. Lett. **B492** 74 (2000); V. Ravindran, J. Smith and W.L. van Neerven, Nucl. Phys. **B704** 332 (2005); T. Gehrmann, T. Huber and D. Maitre, Phys. Lett. **B622** 295 (2005); S. Catani, D. de Florian and M. Grazzini, JHEP **0105** 025 (2001); R.V. Harlander and W.B. Kilgore, Phys. Rev. **D 64** 013015 (2001); S. Catani, D. de Florian and M. Grazzini, JHEP **0201** 015 (2002); R.V. Harlander and W.B. Kilgore, Phys. Rev. Lett. **88** 201801 (2002); C. Anastasiou and K. Melnikov, Nucl. Phys. **B646** 220 (2002); V. Ravindran, J. Smith and W.L. van Neerven, Nucl. Phys. **B665** 325 (2003); C. Anastasiou, L.J. Dixon and K. Melnikov, Nucl. Phys. Proc. Suppl. **116** 193 (2003); C. Anastasiou, K. Melnikov and F. Petriello, Phys. Rev. Lett. **93** 262002 (2004), Nucl. Phys. B 724 (2005) 197; S. Catani and M. Grazzini, Phys.Rev.Lett. **98** 222002 (2007), ArXiv:hep-ph/0703012; C. Anastasiou, G. Dissertori and F. Stockli, JHEP **0709** 018 (2007), ArXiv:0707.2373; G. Bozzi *et al.* Nucl. Phys.**B791** 1 (2008), ArXiv:0705.3887; S. Marzani *et al.* Nucl.Phys. **B800** 127 (2008), ArXiv:0801.2544.

[48] G. Altarelli, R. D. Ball and S. Forte, Nucl.Phys. **B799** 199 (2008), ArXiv:0802.0032 and references therein.

[49] M.Ciafaloni et al, JHEP **0708** 046 (2007), ArXiv:0707.1453 and references therein.

[50] D. Hasch, these Proceedings.

[51] For reviews, see, for example S.D. Bass Rev.Mod.Phys.**77** 1257 (2005), ArXiv:hep-ph/0411005; Mod. Phys. Lett. **A24** 1087 (2009), ArXiv:0905.4619.

[52] For a recent analysis, see D. de Florian et al, Phys.Rev.Lett. **101** 072001 (2008), ArXiv:0804.0422; Phys.Rev. **D80** 034030 (2009), ArXiv:0904.3821.

[53] For a review and a list of references, see M. Dittmar et al, ArXiv:0901.2504.

[54] M. Cacciari et al JHEP**0407**033 (2004), ArXiv: hep-ph/0312132; M. Cacciari and P. Nason Phys.Rev.Lett. **89** 122003 (2002), ArXiv: hep-ph/0204025.

[55] F. Ambroglini *et al.*, ArXiv:0902.0293, ArXiv:0902.0180.

[56] J.M. Campbell, J.W. Huston and W.J. Stirling Rept.Prog.Phys. **70** 89 (2007).

[57] D. Kosower Phys.Rev.**D71**045016 (2005); S. Catani *et al.* Nucl.Phys.**B627**189(2002) and references therein.

[58] S. Frixione and B. Webber ArXiv: hep-ph/0612272, ArXiv:0812.0770 and references therein.

[59] S. Frixione, P. Nason and G. Ridolfi ArXiv:0707.3081; JHEP **0709**126 (2007), ArXiv:0707.3088.

[60] O.G. Lopez, these Proceedings.

[61] For a recent pedagogical review, see J.D. Wells, ArXiv:0909.4541.

[62] B. W. Lee, C. Quigg and H.B. Thacker Phys.Rev. **D16** 1519 (1977).

[63] C. Grojean, these Proceedings.

[64] S. Pokorski, these Proceedings.

[65] G. Isidori, G. Ridolfi and A. Strumia Nucl. Phys. **B609**387 (2001) and references therein.

[66] T. Hambye and K. Riesselmann Phys.Rev.**D55** 7255 (1997) and references therein.

[67] J. Jaeckel, these Proceedings.

[68] B. Odom *et al.* Phys. Rev. Lett. **97** 030801 (2006).

[69] Muon g-2 Collab., G.W. Bennett *et al.* Phys. Rev.**D73**072003 (2006) .

[70] G. Gabrielse et al Phys.Rev.Lett. **97** 030802 (2006); D. Hanneke, S. Fogwell, and G. Gabrielse, Phys. Rev. Lett. **100** 120801 (2008), ArXiv:0801.1134.

[71] T. Aoyama *et al.*, ArXiv:1001.3704 and and references therein.

[72] M. Passera, ArXiv: hep-ph/0702027; F. Jegerlehner, ArXiv: hep-ph/0703125; D.W. Hertzog *et al.*, ArXiv:0705.4617; K. Hagiwara *et al.*, Phys. Lett. **B649** 173 (2007), ArXiv:hep-ph/0611102; M. Davier *et al.*, ArXiv:0906.5443; M. Davier *et al.*, ArXiv:0908.4300.

[73] The LEP Electroweak Group, http://lepewwg.web.cern.ch/LEPEWWG/.

[74] F. Canelli, these Proceedings.

[75] S. Dittmaier, these Proceedings.

[76] G. Altarelli and M. Grunewald Phys.Rept. **189**403 (2004), ArXiv: hep-ph/0404165.

[77] G. Bernardi, these Proceedings.

[78] S. Jindariani, Proceedings of the Hadron Collider Physics Symposium, Evian, France, November 2009.

[79] For a recent review, see M. Antonelli *et al.*, ArXiv:0907.5386.

[80] G. Hiller, these Proceedings.

[81] For a recent review, see G. Isidori, ArXiv: 1001.3431.

[82] For reviews, see, for example, G. Altarelli and F. Feruglio, New J. Phys. **6** (2004) 106 ArXiv:hep-ph/0405048]; G. Altarelli, ArXiv:0905.3265; R.N. Mohapatra and A.Y. Smirnov, Ann. Rev. Nucl. Part. Sci. **56** 569 (2006) ArXiv:hep-ph/0603118; W. Grimus, PoS P2GC:001,2006. ArXiv:hep-ph/0612311; R.N. Mohapatra *et al.*, Rept.Prog.Phys. **70**1757 (2007), ArXiv:hep-ph/0510213; M.C. Gonzalez-Garcia and M. Maltoni, Phys. Rept. **460** 1 (2008) ArXiv:0704.1800.

[83] For a general review, see, for example, W. Buchmuller, R.D. Peccei and T. Yanagida, Ann.Rev.Nucl.Part.Sci.**55**311 (2005), ArXiv:hep-ph/0502169.

[84] G.L. Fogli *et al.*, Phys. Rev. Lett. **101** (2008) 141801 ArXiv:0806.2649; G.L. Fogli *et al.*, Nucl.Phys.Proc.Suppl.188:27,2009, ArXiv:0809.2936; T. Schwetz, M. Tortola and J.W. Valle, New J. Phys. **10** (2008) 113011 ArXiv:0808.2016; M. Maltoni and T. Schwetz, ArXiv:0812.3161.

[85] P.F. Harrison, D.H. Perkins and W.G. Scott, Phys. Lett. B **530**167 (2002), ArXiv:hep-ph/0202074; P.F. Harrison and W.G. Scott, Phys. Lett. B **535** 163 (2002), ArXiv:hep-ph/0203209; Phys. Lett. B **557** 76 (2003), ArXiv:hep-ph/0302025; ArXiv:hep-ph/0402006.

[86] For a review, see G. Altarelli and F. Feruglio, ArXiv:1002.0211.

[87] R. Barbieri and A. Strumia, ArXiv:hep-ph/0007265.

[88] For a pedagogical introduction see, for example, S.P. Martin, ArXiv: hep-ph/9709356.

[89] O. Buchmueller *et al.* Phys.Lett.**B657** 87 (2007), ArXiv: 0707.3447; JHEP 0809:117,2008, ArXiv:0808.4128; Eur.Phys.J.C64:391-415,2009, ArXiv:0907.5568 J. R. Ellis *et al.* JHEP**0708** 083 (2007), ArXiv:0706.0652.

[90] For recent overviews see, for example, K. Lane, ArXiv: hep-ph/0202255; R.S. Chivukula, ArXiv: hep-ph/0011264.

[91] For a review and a list of refs., see, for example, J.A. Hewett and M. Spiropulu Ann.Rev.Nucl.Part.Sci.**52** 397 (2002), ArXiv: hep-ph/0205106.

[92] L. Randall and R. Sundrum, Phys. Rev. Lett.**83** 3370 (1999), Phys. Rev. Lett.**83**4690 (1999); W.D. Goldberger and M. B. Wise Phys. Rev. Letters**83** 4922 (1999).

[93] For pedagogical reviews, see for example, R. Sundrum ArXiv: hep-th/0508134; R. Rattazzi ArXiv: hep-ph/0607055.

[94] K. Agashe *et al.* Nucl.Phys.**B719** 165 (2005); Nucl.Phys.**B742** 59 (2006); Phys.Lett.**B641** 62 (2006), ArXiv: hep-ph/0605341.

[95] See, for example, G. Cacciapaglia *et al.* Phys. Rev. **D70** 075014 (2004), ArXiv: hep-ph/0401160; Phys. Rev. **D71** 035015 (2005), ArXiv:hep-ph/0409126; ArXiv: hep-ph/0607146; R. Chivukula *et al.* Phys. Rev. **D71** (2005)115001, ArXiv: hep-ph/0502162; R. Casalbuoni *et al.* Phys. Rev.**D 71**075015 (2005), ArXiv: hep-ph/0502209.

[96] For reviews and a list of references., see, for example, M. Schmaltz and D. Tucker-Smith, ArXiv: hep-ph/0502182; M. Perelstein, ArXiv: hep-ph/0703138.

[97] H-C. Cheng and I. Low, ArXiv: hep-ph/0405243; J. Hubisz *et al.*, ArXiv: hep-ph/0506042.

[98] R. Contino *et al.*, JHEP **0705** 074 (2007), ArXiv: hep-ph/0612180; G.F. Giudice *et al.* JHEP**0706** 045 (2007), ArXiv: hep-ph/0703164.

[99] For orientation, see, for example, J.A. Frieman,M.S. Turner and D. Huterer, ArXiv: astro-ph/08030982 .

[100] S. Weinberg, Phys. Rev. Lett.**59** 2607 (1987).

[101] Examples of anthropic papers are: N. Arkani-Hamed, S. Dimopoulos and S. Kachru, ArXiv: hep-ph/0501082; G. Giudice and R. Rattazzi, Nucl.Phys.**B757** 19 (2006), ArXiv: hep-ph/0606105.

[102] B. Atwood, these Proceedings.

[103] K. Olive, these Proceedings.

[104] R. Bernabei *et al.* [DAMA Collab.], Eur. Phys. J. **205** 333 (2008).

[105] O. Adriani *et al.* [PAMELA Collab.], Nature **458** 607 (2009), ArXiv: 0810.4995.

[106] J. Chang *et al.* [ATIC Collab.], Nature **456** 362 (2008).

[107] A.A. Abdo *et al.* [Fermi-LAT Collab.], Phys. Rev. Lett. **102** 181101 (2009), ArXiv:0905.0025.

[108] V. Barger *et al.*, ArXiv: 0809.0162; M. Cirelli *et al.*, ArXiv:0802.3378; 0809.2409; N. Arkani-Hamed *et al.*, ArXiv:0810.0713; JHEP **0812** 104 (2008), ArXiv:0810.0714, E. Nardi *et al.*, ArXiv:0811.4153, G. Bertone *et al.*, ArXiv:0811.3744; E. Ponton and L. Randall, ArXiv:0811.1029; P. Meade *et al.*, ArXiv:0905.0480; M. Cirelli, P. Panci and P.D. Serpico, ArXiv:0912.0663 and references therein.

[109] S. Kachru, these Proceedings.

Discussion

Robert Lahman (Erlangen Centre for Astroparticle Physics): What evidence is there to support the idea that neutrinos are Majorana particles?

Answer: I said there there is an attractive explanation for the smallness of neutrino masses in comparison with other fermion masses, and also an explanation for the connection which appears from experiment with the GUT scale, where lepton number is violated, which suggests that neutrinos are Majorana particles. But I also said that the experimental proof would need the detection of neutrino-less double beta decay. Until this is not established the Majorana nature of neutrinos is only a conjecture. In generic grand unified models the proton decays, and lepton number is not conserved, so we expect that the neutrino is totally neutral and that there is no conserved quantum number that makes the difference between neutrino and anti-neutrino. So, in such theories the neutrino is a natural candidate to be a Majorana fermion, but only once lepton number violation is proven that will become completely established.

PROCEEDINGS OF THE

LEPTON PHOTON 2009
CONFERENCE

PART II: POSTER SESSION

Jets and α_s Measurements in DIS

Artem Baghdasaryan [1,2]

[1]DESY, Notketraße 85, 22607 Hamburg, Germany
[2]Yerevan Physics Institute, 2 Alikhanyan Brothers St., Yerevan 375036, Armenia

The inclusive, 2-jet and 3-jet jet cross sections at $5 < Q^2 < 100$ GeV^2 and the inclusive, 2-jet and 3-jet cross sections normalised to the NC DIS cross section at $150 < Q^2 < 15000$ GeV^2 are measured as function of Q^2 and P_T. The strong coupling is extracted.

1 Introduction

In contradiction to DIS cross section where α_s contributes indirectly (Fig. 1(a)), jet production cross sections directly depend on α_s through QCD Compton scattering (Fig. 1(b)) and boson-gluon fusion (Fig. 1(c)). This provides the possibility for an accurate determination of α_s from
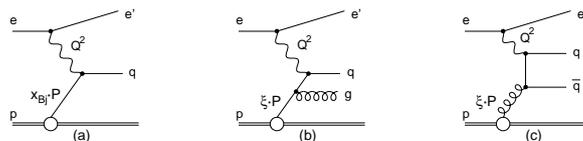
Figure 1: DIS at different order in α_s: (a) Born contribution, (b) QCD Compton scattering and (c) boson-gluon fusion

jet production data. The measurements are presented as both single and double differential cross sections in the variables Q^2 and jet transverse momentum P_T. The results agree well with NLO QCD calculations [1] corrected for hadronisation effects. The strong coupling α_s is extracted from a fit of the predictions to the data at low Q^2 ($5 < Q^2 < 100$ GeV^2) and at high Q^2 ($150 < Q^2 < 15000$ GeV^2). The running of α_s is tested in a wide range of μ_r.

2 Experimental methods and cross section measurements

The data presented in this paper were taken with the H1 detector at electron/positron and proton beam energies of 27.6 GeV and 920 GeV, respectively. The data samples were collected in 1999-2000 with an integrated luminosity of 43.5 pb^{-1} for low Q^2 and in 1999-2007 with an integrated luminosity of 395 pb^{-1} for high Q^2. The inelasticity y of the interaction is defined in the range $0.2 < y < 0.7$. Jets are defined with the inclusive k_t algorithm in the Breit frame. Cuts on the jet pseudorapidity η^L in the laboratory frame ($-1.0(-0.8) < \eta^L < 2.5(2.0)$ for low (high) Q^2) are applied to ensure that the jets are well contained within the acceptance of the calorimeter. To ensure the reliability of QCD predictions for the 2-jet and 3-jet sample [2], an additional cut on the invariant mass of the two leading jets ($M_{12} > 18(16)$ GeV for low (high)
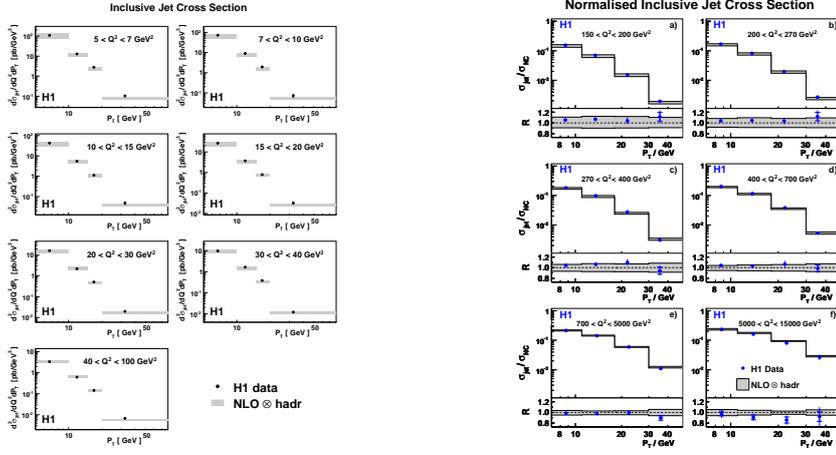
Figure 2: Inclusive (normalised) double differential jet cross sections as function of Q^2 and P_T compared with NLO QCD predictions corrected for hadronisation

Q^2) is applied. For the cross section extraction the experimental data is corrected for detector effects (resolution an efficiency) using Monte-Carlo event samples. The model uncertainties and the hadronic energy scale uncertainties are the dominant sources of experimental errors on the jet cross sections. The cross section normalisation to inclusive DIS data, applied to the high Q^2 data, allows to reduce systematic errors in most of the bins due to cancellation effects. Differential and double differential cross sections, corrected for detector and radiative effects are presented as function of Q^2 and P_T. Inclusive (normalised) double differential jet cross sections are presented in Fig.2 for low (high) Q^2. The band around the predictions shows the scale uncertainty of the NLO QCD calculations. In almost all the bins the scale uncertainty exceeds the total experimental error.

3 NLO QCD calculations. Strong coupling extraction

The data are compared with NLO QCD predictions, performed in the $\overline{\text{MS}}$ scheme for five massless quark flavors. The parton level calculations are corrected for hadronisation effects. The PDFs of the proton are taken from the CTEQ6.5M set. The factorisation scale is chosen as $\mu_f = \sqrt{(Q^2 + P_T^2)/2}$ ($\mu_f = Q$) for low (high) Q^2. The renormalisation scale is chosen as $\mu_r = \sqrt{(Q^2 + P_T^2)/2}$. Varying the scales μ_f and μ_r by factors in the range $1/2$ to 2, scale uncertainties up to 10% (30% at $P_T < 10$ GeV and 20% at $P_T > 20$ GeV) are observed for the data at high (low) Q^2. The uncertainties from PDFs and α_s are found to be small compared to these scale uncertainty. A fit of the (normalised) cross sections in bins of Q^2 and P_T to NLO predictions is performed, in order to extract α_s. The experimental errors and their correlations are taken into account using the Hesian method [3]. The results are consistent between different bins and combinations of bins. The same is true for combinations of inclusive, 2-jet or 3-jet measurements and for combining low and high Q^2 data. The theory error is estimated using the offset method, where the difference between α_s values obtained from fits under the variation of the theoretical uncertainties are studied.

α_s from Jet Cross Sections in DIS
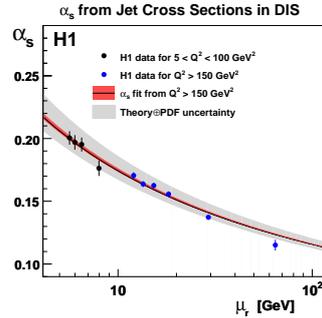
Figure 3: Comparison of $\alpha_s(\mu_r)$ values obtained by a fit in different bins to the two loop evolution.

4 Conclusion

Measurements of the inclusive, 2-jet and 3-jet (normalised) cross sections in the Breit frame in DIS with $0.2 < y < 0.7$ are presented for low (high) Q^2. Calculations in NLO QCD corrected for hadronisation effects agree well with single and double differential cross sections as functions of the jet transverse momentum P_T and the boson virtuality Q^2. It is observed that with a proper choice of the renormalisation scale, the theory is applicable for low P_T and low Q^2. The strong coupling $\alpha_s(M_Z)$ is extracted separately for low and high Q^2 as well as for both datasets together. The experimentally most precise determination of $\alpha_s(M_Z)$ is derived from a fit to the normalised jets cross sections at high Q^2 alone, as the normalisation leads to significant cancellations of systematic effects:

$$\alpha_s(M_z) = 0.1168 \pm 0.0007(\mathrm{exp})^{+0.0046}_{-0.0030}(\mathrm{th}) \pm 0.0016(\mathrm{pdf})$$

Determination of $\alpha_s(M_Z)$ from a fit to the jets cross sections at low Q^2 alone gives:

$$\alpha_s(M_z) = 0.1160 \pm 0.0014(\mathrm{exp})^{+0.0093}_{-0.0077}(\mathrm{th}) \pm 0.0016(\mathrm{pdf})$$

The combined fit of high and low Q^2 data has somewhat better experimental precision, but suffers from increased scale uncertainties. The running of α_s and the small experimental errors are visualised in Fig.3, where the measurements are displayed as a function of μ_r. It is remarkable that the total errors are essentially lower then theory prediction, hence setting a challenge for improved theoretical calculations.

References

[1] Z. Nagy and Z. Trocsanyi, Phys.Rev.Lett. **87** 082001 (2001).

[2] S. Frixione and G. Rudolfi, Nucl. Phys. **B507** 315 (1997).

[3] M. Botje, Eur.Phys.J. **C14** 285 (2000).

Recent Measurements of the Hadronic Final State from H1

Albert Knutsson[1] on behalf of the H1 Collaboration

[1]DESY, Notketraße 85, 22607 Hamburg, Germany

The poster summarizes recent measurements of the hadronic final state in photoproduction and neutral current deep inelastic scattering (NC DIS) data collected with the H1 detector at HERA. The photoproduction analyses cover measurements of prompt photon cross sections, and a study of the underlying event based on charge particle multiplicities in jet data. In low Q^2 DIS, strangeness production is studied through the production of K^*, K^0 and Λ baryons. A first measurement of the charge asymmetry in the hadronic final state in high Q^2 DIS is presented. The different measurements are compared to Monte Carlo models with parton showers as well as fixed order calculations.

1 Charged Particles and the Hadronic Final State Charge Asymmetry [1, 2]

The charge asymmetry of particles in the hadronic final state was investigated [1] in NC DIS in the kinematic range $100 < Q^2 < 8000$ GeV^2. Fig. 1a) shows the normalized distribution, $D(x_p)$, of the scaled particle momentum, $x_p = \frac{2p}{Q}$, for positive (*pos*) and negative (*neg*) charged particles as well as the sum of the two. Fig. 1b) shows the charge particle asymmetry, $(pos - neg)/(pos + neg)$, compared to various models. At large x_p, where the produced particles retain the information from the hard interactions with sea quarks and gluons, a large charge asymmetry is seen. At low x_p the particles produced in the fragmentation process play an important role, and the asymmetry is smaller. This is also seen in Fig. 1c) where the MC prediction with hadronization turned off (CDM-quark) maintain the charge asymmetry at low x_p. Also measured [2] is the average multiplicity and the normalised distribution of the scaled momentum of charged final state hadrons in different regions of x_p. The data agree with e^+e^-
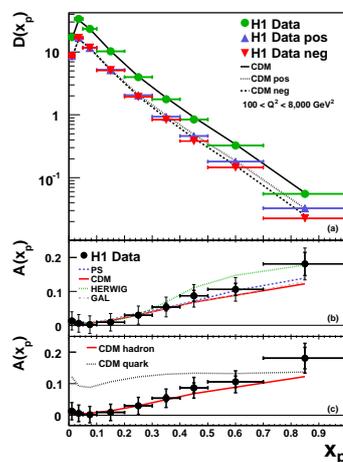

Figure 1: Scaled momentum distributions for positive and negative particles, and the asymmetry between these, compared to various MC models with parton showers.

data and are well described by MC with parton showers.

2   Prompt Photons in Photoproduction [3]

Final states with an isolated photon were analysed in photoproduction ($Q^2 < 1$ GeV^2). The analysis is based on data taken by the H1 experiment in the years 2004-2007, with a total integrated luminosity of 340 pb^{-1}. Cross sections are measured for photons with transverse momenta and pseudorapidities in the range $6 < E_T^\gamma < 15$ GeV and $-1.0 < \eta^\gamma < 2.4$, for events with and without an additional jet. The identification of the photons are based on shower shape variables and the isolation criteria is that the photon carries at least 90% of the energy of the jet containing the photon. A calculation based on the k_t-factorisation approach [7] describes the data better than a NLO QCD prediction [8], but both predictions undershoot the data at low E_T^γ and for backward photons (Fig. 2, left). The data are somewhat better described for events when an additional jet is explicitly required in the event (Fig. 2, right).
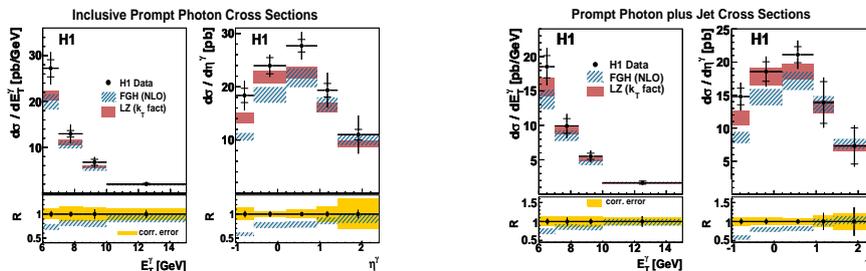
Figure 2: The inclusive prompt photon cross section (left), and the cross section for events with an additional jet (right) compared to theoretical calculations.

3   Strangeness Production at low Q^2 [4, 5]

Measurements on strangeness production give direct information about fragmentation parameters and knowledge of hadronization. $K^{*\pm}$, K_s^0 and Λ productions were analysed by using low Q^2 NC DIS events. One of the cross sections for $K^{*\pm}$ production [4], observed through the decay $K^{*\pm} \to K^0\pi^\pm$ is shown in Fig. 3 as a function of the transverse momentum of the $K^{*\pm}$ in laboratory frame. The MC prediction from DJANGO with the Color Dipole Model (CDM [9]) gives a decent description of the data, and also seen is that the largest contribution to the strange quark production comes from the fragmentation. The cross sections for K_s^0 and Λ production [5] are compared to Monte Carlo predictions with different values of the strangeness
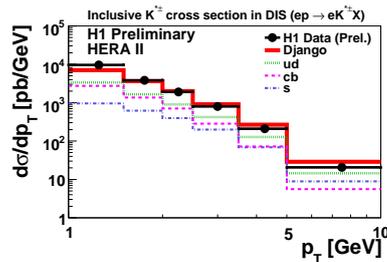
Figure 3: Cross section for $K^{*\pm}$ production as a function of the transverse momentum of the $K^{*\pm}$s. The MC predictions are decomposed into the contributions of the various quark flavours of the primarily incoming particles of the hard subprocess from the proton side.

suppression factor λ_s. Although no single combination of model and λ_s describes the data in all kinematic bins, the overall best description of the data is obtained with the CDM and $\lambda_s = 0.3$. Furthermore, the asymmetry between Λ and $\bar{\Lambda}$ production is flat within the errors of the measurement and thus no baryon number transfer from the proton beam to the hadronic final state is observed.

4   The Underlying Event in Photoproduction [6]

The underlying event (UE) in tagged photoproduction ($Q^2 < 0.01$) is analysed in a TEVATRON inspired way. The average multiplicity of charged particles in di-jet events with $E_{T,\mathrm{Jet}} > 5$ GeV is measured in different azimuthal regions with respect to the leading jet. When the energy fraction of the photon carried by the interacting parton, x_γ, is low the photon has a large hadronic-like substructure, and the contribution from multiparton interactions (MPI) is largest. In this kinematic region MPI simulations need to be included in PYTHIA [10] in order to describe the data. Remarkable is that the data description provided by CASCADE [11], a MC generator with parton showers based on the k_t-factorisation approach, but without any MPI simulated, is in competition with the predictions from PYTHIA with MPI.
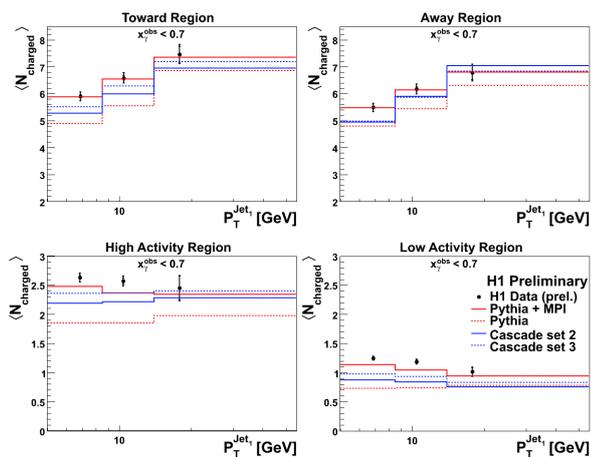
Figure 4: The average mulitplicity of charged particles as a function of the transverse momentum of the leading jet, in different azimuthal regions with respect to the leading jet.

References

[1] H1 Collaboration, F. D. Aaron *et al.*, Phys. Lett. B **681** 125 (2009)

[2] H1 Collaboration, F. D. Aaron *et al.*, Phys. Lett. B **654**, 148 (2007)

[3] H1 Collaboration, F. D. Aaron *et al.*, arXiv:hep-ex/0910.5631 (2009)

[4] D. Sunar, Proc. of 17th Int. Workshop on Deep-Inelastic Scattering and Related Subjects (DIS09), doi: 10.3360/dis.2009.91

[5] H1 Collaboration, F. D. Aaron *et al.*, Eur. Phys. J. C **61** 185 (2009)

[6] H1prelim-08-036, http://www-h1.desy.de/h1/www/publications/htmlsplit/H1prelim-08-036.long.html

[7] A. V. Lipatov and N. P. Zotov, Phys. Rev. D **72**, 054002 (2005).

[8] M. Fontannaz, J. P. Guillet and G. Heinrich, Eur. Phys. J. C **21**, 303 (2001)

[9] L. Lonnblad, Comput. Phys. Commun. **71**, 15

[10] T. Sjöstrand, S. Mrenna, and P. Skands, JHEP **05**, 026 (2006)

[11] H. Jung, Comput. Phys. Commun. **143**, 100 (2002)

Structure Functions Measurements at HERA

Alexey Petrukhin

DESY, Notkestraße 85, 22607 Hamburg, Germany
ITEP, B. Cheremushkinskaya 25, 117218 Moscow, Russia

Recent structure functions results from H1 and ZEUS are presented. The measurements cover a wide kinematic range of squared four-momentum transfers Q^2, from $0.2\,\mathrm{GeV}^2$ to $30000\,\mathrm{GeV}^2$, and Bjorken x between $5 \cdot 10^{-6}$ and 0.65. The results of QCD analyses based on these data and their impact on the parton density functions are presented.

1 DIS cross section measurements at low and medium Q^2

The measurements of the DIS cross sections at low Q^2 (from $0.2\,\mathrm{GeV}^2$ to $12\,\mathrm{GeV}^2$) [1] and medium Q^2 (from $12\,\mathrm{GeV}^2$ to $150\,\mathrm{GeV}^2$) [2] are based on data collected by the H1 Collaboration in 1999-2000. In order to access low values of Q^2 around 1 GeV^2 the interaction vertex, for short period of H1 2000 data taking, was shifted by approximately 70 cm along the proton beam direction. This data sample is also used for accessing larger values of x with Initial State Radiation (ISR) events. Data collected by the H1 Collaboration in 1999 with a nominal position of the interaction vertex are used for measurements in the region of high inelasticity y. These data are combined with H1 data taken in 1995-1997 following the prescription introduced in [3]. The H1 measurements at low and medium Q^2 are shown in Figure 1. These are the most precise results of the H1 Collaboration in the given kinematic domain. The accuracy of the combined measurements is typically at the level of 1-2%. The H1 data alone is used in a NLO QCD analysis to determine a new set of parton densities called H1PDF2009.

2 Measurements of the structure function F_L

Figure 2 shows the first measurements of the the structure function F_L performed by H1 [7] and ZEUS [8] Collaborations. They are based on inclusive deep inelastic e^+p scattering cross section measurements with a positron beam energy of 27.5 GeV and proton beam energies of 920, 575 and 460 GeV. Employing the energy dependence of the cross section, F_L is measured in the range $12 \leq Q^2 \leq 130\,\mathrm{GeV}^2$ and low Bjorken x $0.00024 \leq x \leq 0.007$. The F_L values agree with higher order QCD calculations based on parton densities obtained using cross section data previously measured at HERA.

3 Combined H1 and ZEUS results

A combination [9] is presented of the inclusive DIS cross sections measured by the H1 and ZEUS Collaborations in neutral and charged current unpolarised ep scattering at HERA during the
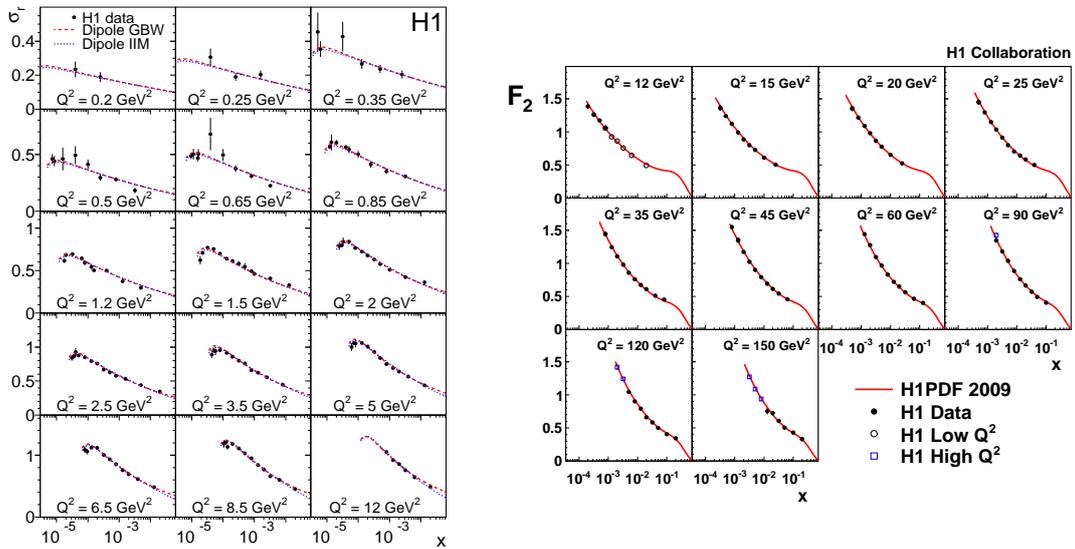
Figure 1: Left: reduced cross section σ_r from combined H1 1995-2000 data [1] compared to GBW [4] and IIM [5] models. Right: structure function F_2 from combined H1 1996-2000 data [2] compared to previously published H1 data [1], [6] and H1PDF2009 fit [2]. The errors represent the statistical and systematic uncertainties added in quadrature.

period 1994-2000. The data cover six orders of magnitude in Q^2, and in Bjorken x. The combination method used takes the correlations of systematic uncertainties into account, resulting in an improved accuracy. The combined data are the sole input in a NLO QCD analysis which determines a new set of parton distributions HERAPDF1.0 with small experimental uncertainties. This set includes an estimate of the model and parametrisation uncertainties of the fit result as explained in [9]. The combined results are shown in Figure 3.

References

[1] F. D. Aaron *et al.*, Eur. Phys. J. **C63** 625 (2009).

[2] F. D. Aaron *et al.*, arXiv:0904.3513v2 (2009).

[3] A. Glazov, AIP Conf. Proc. **792** 237 (2005).

[4] K. Golec-Biernat and M. Wusthoff, Phys. Rev. **D59**, 014017 (1999).

[5] E. Iancu, K. Itacura and S. Munier, Phys. Lett. **B590**, 199 (2004).

[6] C. Adloff *et al.*, Eur. Phys. J. **C30**, 1 (2003).

[7] F. D. Aaron *et al.*, Phys. Lett. **B665**, 139 (2008).

[8] S. Chekanov *et al.*, arXiv:0904.1092v1 (2009).

[9] F. D. Aaron *et al.*, arXiv:0911.0884v1 (2009).
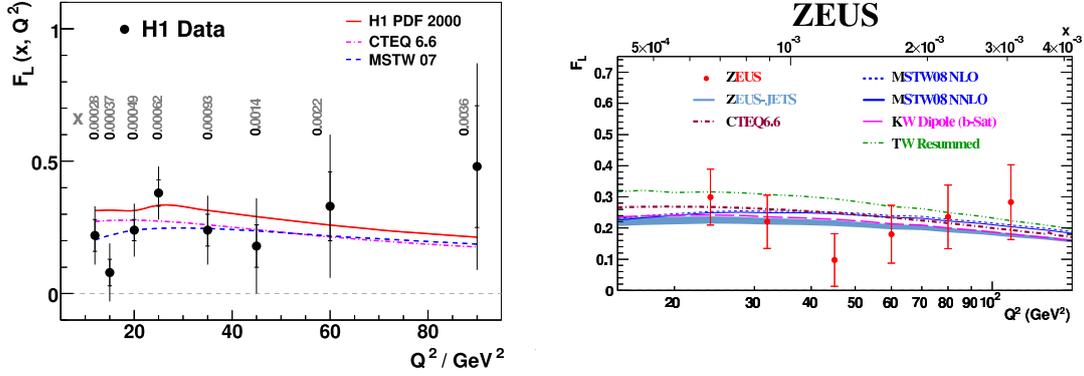
Figure 2: F_L from the H1 data [7] (left) and ZEUS data [8] (right) compared to the different theoretical predictions. The full error bars include the statistical and systematic uncertainties added in quadrature.
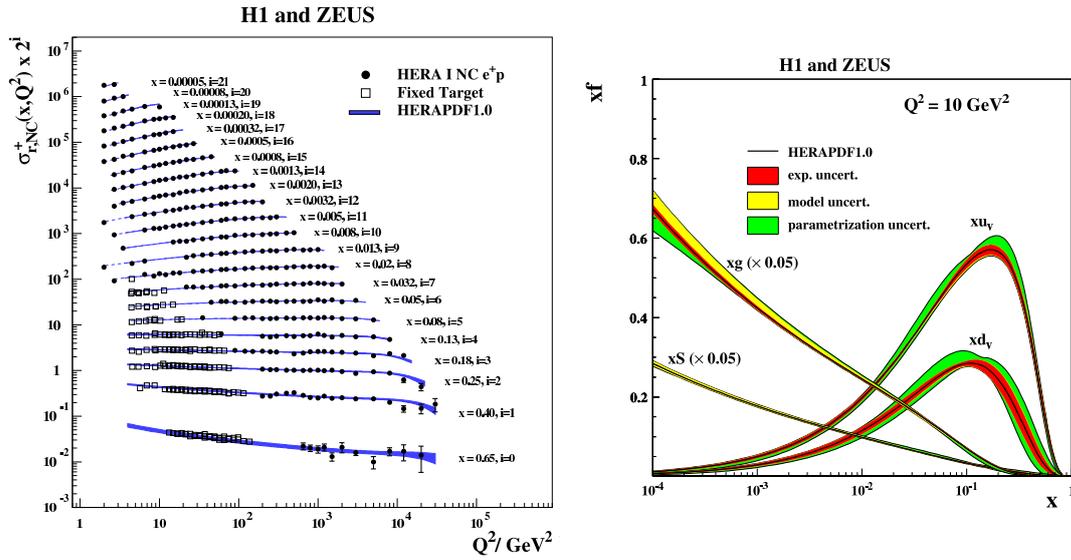
Figure 3: Left: HERA combined neutral current reduced cross section [9] and fixed-target data compared to the HERAPDF1.0 fit. The bands represent the total uncertainty of the fit. Right: the parton distribution functions from HERAPDF1.0 at $Q^2 = 10$ GeV^2. The gluon and sea distributions are scaled down by a factor 20. The experimental, model and parametrisation uncertainties are shown separately (see [9]).

Searches for New Physics at HERA

Gerhard Brandt[1]

[1]Deutsches Elektronen-Synchrotron DESY, Notketraße 85, 22607 Hamburg, Germany

HERA, the world's only $e - p$ Collider at DESY, Hamburg, running $1991 - 2007$, was ideally suited for searches for physics beyond the Standard Model due to its unique initial state. The H1 and ZEUS experiments with their asymmetric design provided 4π Coverage, excellent lepton ID and HFS reconstruction to detect any exotic signatures. The poster summarised here presents recent results on searches at HERA, most of them utilising the full HERA dataset of about 0.5 fb^{-1} per experiment and including the first combined H1+ZEUS results.

1 Signature Searches

1.1 General Search

A model-independent search for deviations from the Standard Model (SM) prediction is performed [1]. All event topologies involving isolated electrons, photons, muons, neutrinos and jets with transverse momenta above 20 GeV are investigated in a single analysis. Events are assigned to exclusive classes according to their final state. Figure 1 shows the event yields in each of the classes for e^+p (a) and e^-p (b) collisions separately. Overall the data (black dots) agree well with the SM expectation within the total uncertainties (shaded band). A dedicated algorithm is used to search for deviations from the SM in the distributions of the scalar sum of transverse momenta or the invariant mass of final state particles and to quantify their significance. Variables related to angular distributions and energy sharing between final state particles are also introduced to study the final state topologies. No signicant deviation from the SM expectation is observed in the phase space covered by the analysis. Many channels are also investigated in dedicated analyses, some of which are summarised below.

1.2 High-P_T Leptons

The first combined paper by H1 and ZEUS presents a study of events with at least two high transverse momentum leptons (electrons or muons) [2]. This signature is sensitive to physics beyond the SM. The overall agreement with the SM prediction is good, but at high invariant masses, more interesting events are observed than predicted. This is visible in distributions of the invariant mass of the two highest P_T leptons, M_{1_2}, and the sum of the lepton transverse momenta $\sum P_T$.

A search for events containing isolated leptons (electrons or muons) and missing transverse momentum is performed by the H1 and ZEUS experiments in a common phase space [3]. The observed event yields are compared to the prediction from the Standard Model which is
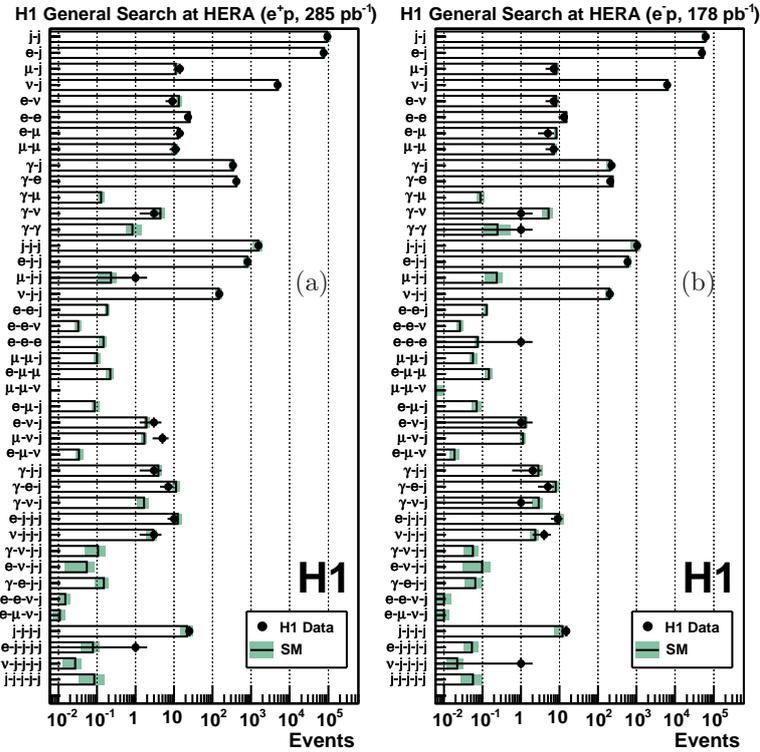
Figure 1: The data and the SM expectation for all event classes with observed data events or a SM expectation greater than 0.01 events for e^+p collisions (a) and e^-p collisions (b). The error bands on the predictions include model uncertainties and experimental systematic errors added in quadrature.

dominated by single W production. In general good agreement is found. The total single W boson production cross section is measured to be 1.07 ± 0.18 pb, in agreement with the SM expectation of 1.26 ± 0.19 pb.

At high hadronic transverse momentum P_T^X the isolated leptons signature is the same as for single top production. Inspired by events observed in the region $P_T^X > 25$ GeV by H1 [4] this is studied using anomalous effective FCNC couplings $\kappa_{tu\gamma}$, v_{tuZ} [5]. The resulting HERA limits on $\kappa_{tu\gamma}$ explore a domain not covered by other colliders.

2 Model Searches

2.1 Squarks in R-Parity Violating SUSY

A search for squarks in the Minimal Supersymmetric Standard Model with R-parity violation is performed [6]. The resonant production of squarks via a Yukawa-type coupling λ' is considered, taking into account direct and indirect R-parity violating decay modes. No evidence for squark production is found in the (multi-)lepton and (multi-)jet final state topologies investigated.

Squarks of the first and second generation with masses up to 275 GeV are excluded in the considered part of the parameter space for a Yukawa-type coupling of electromagnetic strength at 95% confidence level.

2.2 Contact Interactions

A search for deviations of the inclusive NC cross sections from the SM prediction at high Q^2 is performed [7]. Since no significant deviations are observed, various BSM models can be constrained. Limits are derived on the effective mass scale Λ in $eeqq$ contact interactions ($\Lambda > 3.8 - 8.9$ TeV), on the mass to the Yukawa coupling ratio for heavy-leptoquark models ($M_{LQ}/\Lambda_{LQ} > 0.41 - 1.88$ TeV), on the effective Planck-mass scale in models with large extra dimensions ($M_S > 0.94$ TeV) and on the quark charge radius ($R_q < 0.63 \cdot 10^{-16}$ cm).

2.3 Excited Fermions

A search for excited fermions (electrons, neutrinos and quarks) is performed [8, 9, 10]. The interactions are described by an effective Lagrangian for gauge mediated models where the excited fermions couple to the electroweak and strong gauge groups, parametrised by coupling parameters f, f' and f_s, respectively.

All decay channels are considered for all fermion types. No evidence for excited fermion production is found. Mass dependent exclusion limits on excited fermion production cross sections and on the ratio f/Λ of the coupling to the compositeness scale are derived. These limits extend the excluded region compared to previous excited fermion searches.

3 Bibliography

References

[1] F. D. Aaron *et al.* [H1 Collaboration], Phys. Lett. B **674** (2009) 257 [arXiv:0901.0507].

[2] F. D. Aaron *et al.* [H1 Collaboration and ZEUS Collaboration], JHEP **0910** (2009) 013 [arXiv:0907.3627].

[3] F. D. Aaron *et al.* [H1 Collaboration and ZEUS Collaboration], [arXiv:0911.0858].

[4] F. D. Aaron *et al.* [H1 Collaboration], Eur. Phys. J. C **64** (2009) 251 [arXiv:0901.0488].

[5] F. D. Aaron *et al.* [H1 Collaboration], Phys. Lett. B **678** (2009) 450 [arXiv:0904.3876].

[6] [H1 Collaboration], "Search for Squark Production in R-Parity Violating Supersymmetry at HERA", H1prelim-09-061.

[7] [ZEUS Collaboration], "Search for contact interactions at HERA ", ZEUS-prel-09-013.

[8] F. D. Aaron *et al.* [H1 Collaboration], Phys. Lett. B **678** (2009) 335 [arXiv:0904.3392].

[9] F. D. Aaron *et al.* [H1 Collaboration], Phys. Lett. B **666** (2008) 131 [arXiv:0805.4530].

[10] F. D. Aaron *et al.* [H1 Collaboration], Phys. Lett. B **663** (2008) 382 [arXiv:0802.1858].

Measurement of the Longitudinal Proton Structure Function with the ZEUS Detector at HERA

Julia Grebenyuk[1]

[1]DESY, Notketraße 85, 22607 Hamburg, Germany

The reduced cross sections for ep deep inelastic scattering have been measured with the ZEUS detector at HERA at three different centre-of-mass energies, 318, 251 and 225 GeV. From the reduced cross sections, measured double differentially in Bjorken x and the photon virtuality, Q^2, the proton structure functions F_L and F_2 have been extracted in the region $5 \times 10^{-4} < x < 0.007$ and $20 < Q^2 < 130$ GeV^2.

1 Introduction

The inclusive $e^{\pm}p$ deep inelastic scattering (DIS) cross section can, at low virtuality of the exchanged boson, Q^2, be expressed in terms of the two structure functions, F_2 and F_L, as

$$\frac{d^2\sigma^{e^{\pm}p}}{dxdQ^2} = \frac{2\pi\alpha^2 Y_+}{xQ^4}\left[F_2(x,Q^2) - \frac{y^2}{Y_+}F_L(x,Q^2)\right] = \frac{2\pi\alpha^2 Y_+}{xQ^4}\,\tilde{\sigma}(x,Q^2,y),$$

where α is the fine structure constant, x is the Bjorken scaling variable, y is the inelasticity and $Y_+ = 1 + (1-y)^2$. The quantity $\tilde{\sigma}$ is referred to as the reduced cross section. The kinematical variables are related via $Q^2 = xys$, where s is a centre-of-mass energy. The magnitude of F_L is proportional to the absorption cross section of longitudinally polarised virtual photons by protons, $F_L \propto \sigma_L$, while F_2 includes also the absorption cross section for transversely polarised virtual photons, $F_2 \propto (\sigma_T + \sigma_L)$. At low values of x, the ratio $R = F_L/(F_2 - F_L) \approx \sigma_L/\sigma_T$ gives the relative strengths of the two components. Within the DGLAP formalism, F_2 is dominated at low x by the $q\bar{q}$ sea distributions while the scaling violations of F_2 reflect the gluon distribution via a convolution with a splitting function. In contrast, the value of F_L is directly related to the gluon content regardless of the specific form of the scaling violation.

2 Experimental method

The values of F_2 and F_L were extracted at fixed x and Q^2 by fitting a straight line to the values of $\tilde{\sigma}$ against y^2/Y_+. The method relies on the relations $F_2(x,Q^2) = \tilde{\sigma}(x,Q^2,y=0)$ and $F_L(x,Q^2) = -\partial\tilde{\sigma}(x,Q^2,y)/\partial(y^2/Y_+)$, hence the need for data at fixed (x,Q^2) and different y. At HERA this was achieved by varying the centre-of-mass energy $\sqrt{s} = \sqrt{Q^2/xy}$.

Data were collected at $\sqrt{s} = 318$ GeV, $\sqrt{s} = 251$ GeV, and $\sqrt{s} = 225$ GeV, keeping the electron beam energy constant, $E_e = 27.5$ GeV, and varying the proton beam energy, E_p. Data were collected in 2006 and 2007 with $E_p = 920$, 575 and 460 GeV, referred to respectively as the HER (high-), MER (medium-) and LER (low-energy-running) samples. The corresponding integrated luminosities of the HER, MER and LER samples are 44.5, 7.1 and 13.9 pb^{-1}, respectively.

The event kinematics were evaluated based on the reconstruction of the scattered electron. At high y, the scattered electron tends to be low in energy and poorly separated from the hadronic final state which makes the measurement challenging. After the full event selection, the background consisted almost entirely of photoproduction events due to the misidentification of hadrons as electrons.

The reduced cross sections, $\tilde{\sigma}$, were measured from the HER, MER and LER samples in the kinematic region $0.09 < y < 0.78$ and $20 < Q^2 < 130$ GeV^2. The reduced cross sections in a given (x, Q^2) bin were calculated according to $\sigma(x, Q^2) = \frac{N_{\text{data}} - N_{\text{MC}}^{\text{bg}}}{N_{\text{MC}}^{\text{DIS}}} \tilde{\sigma}_{\text{SM}}(x, Q^2)$, where $\tilde{\sigma}_{\text{SM}}(x, Q^2)$ is the Standard Model

Figure 1: The points represent the ZEUS data for F_L ($\bullet$) and F_2 ($\blacktriangle$), respectively. The error bars on the data represent the combined statistical and systematic uncertainties. The predictions for F_L and F_2 using the ZEUS-JETS PDFs are also shown. The bands indicate the uncertainty in the predictions.

electroweak Born-level reduced cross section and N_{data}, $N_{\text{MC}}^{\text{bg}}$ and $N_{\text{MC}}^{\text{DIS}}$ denote, respectively, the number of observed events in the data and the expected number of background and DIS events from the MC.

3   Extraction of F_L, F_2 and R

In order to extract F_L, F_2 and R, bins were chosen in y such that, for each of the 6 Q^2 bins, there were 3 values of x at which the reduced cross sections were measured from all three data sets. Thus 54 cross sections were measured and the structure functions were extracted by performing a simultaneous fit to these cross section values.

To extract F_L and F_2, 48 parameters were fit simultaneously: 18 F_2 and 18 F_L values for the 18 (x, Q^2) points; 3 relative normalisation factors for the HER, MER and LER data sets and 9 global shifts of systematic uncertainties. The results are shown in Fig. 1. More details

can be found elsewhere [1].

Further fits to the data were performed to extract $F_L(Q^2)$ (evaluated for $y = 0.71$), $R(Q^2)$, and a single overall value of R for the full data set. Figures 2a and 2b show a comparison of the data with various predictions and models. All the models are consistent with the data. The overall value of R extracted from the fit is $R = 0.18^{+0.07}_{-0.05}$.

4 Summary

The first measurement of $F_L(x, Q^2)$ by the ZEUS collaboration is presented, as is the first measurement of $F_2(x, Q^2)$ at low x that does not include assumptions about F_L. The F_2 values are the most precise available from the ZEUS collaboration in the analysed kinematic region. The extraction of F_L and F_2 was based on the reduced double differential cross sections, $\tilde{\sigma}(x, Q^2)$, which were measured for $0.09 < y < 0.78$ and $20 < Q^2 < 130$ GeV^2 using data collected at $\sqrt{s} = 318$, 251 and 225 GeV. In addition, F_L and the ratio, $R = F_L/(F_2 - F_L)$, have been extracted as function of Q^2. An overall value of $R = 0.18^{+0.07}_{-0.05}$ was extracted for the entire kinematic region studied. A wide range of theoretical predictions agree with the measured F_L. The measurements provide strong evidence of a non-zero value of F_L.

References

[1] ZEUS Collab., S. Chekanov et al. Phys. Lett. **B 682** 8-22 (2009)
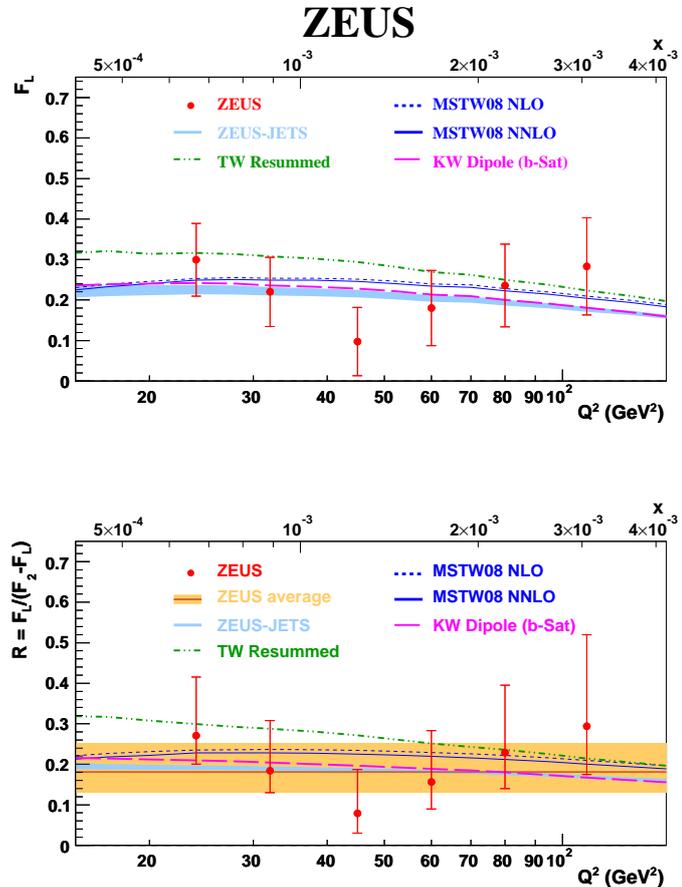
Figure 2: Values of (a) F_L and (b) R as a function of Q^2. The error bars on the data represent the combined statistical and systematic uncertainties. A $\pm 2.5\%$ correlated normalisation uncertainty is not included in the error bars. Various predictions and models are shown. The shaded band shown at (b) labelled ZEUS average represents the 68% probability interval for the overall R.

Measurements of Charm and Beauty in DIS via muon tags at ZEUS

Marcello Bindi[1], on behalf of ZEUS Collaboration

[1]University and INFN of Bologna, Italy

Charm and Beauty production were measured in deep inelastic scattering (DIS) with the ZEUS detector at HERA. Heavy quarks were reconstructed using their semi-leptonic decay into muons. The signal was separated from the background using lifetime information, the transverse momentum of the muon with respect to the axis of the associated jet and the missing transverse momentum parallel to the muon direction. Differential cross sections were measured and compared to next-to-leading order QCD predictions. The heavy quarks contribution to the proton structure function F_2, $F_2^{c\bar{c}}$ and $F_2^{b\bar{b}}$, were extracted and compared with theoretical predictions using different parametrizations of the proton PDFs.

1   Introduction

The measurement of charm and beauty production in deep inelastic scattering (DIS) provides a stringent test of quantum chromodynamics (QCD) since the large quark masses and the square of the four momentum transfer, Q^2, provide hard scales that make perturbative calculations applicable. At leading order, heavy quarks (HQ) are produced in DIS via boson–gluon fusion (BGF) ($\gamma^* g \rightarrow q\bar{q}$). A precise measurement of HQ production in DIS therefore provides a direct constraint on the gluon parton density function (PDF) of the proton.

Charm production in DIS at HERA has been measured previously using reconstructed charmed mesons or inclusively by exploiting the long lifetime of charmed hadrons[1]. Beauty production in DIS has been studied in events with muons and jets and from lifetime information[1]. The existing data are generally in good agreement with next-to-leading-order(NLO) QCD predictions.

We present here a recent measurement[2] of HQ production using semi-leptonic (SL) decays into muons. It is the first time that leptonic tags are used for charm measurements at HERA.

2   Selection cuts, fits and cross sections measurement

The data used in this analysis have been collected with the ZEUS detector in the 2005 running period during which HERA collided electrons of energy $E_e = 27.5$ GeV with protons of energy $E_p = 920$ GeV corresponding to a centre-of-mass energy $\sqrt{s} = 318$ Gev. The corresponding integrated luminosity was $\mathcal{L} = 126.0 \pm 3.3\ pb^{-1}$.

A sample of muon in DIS was selected and the accessible inelasticity $y = Q^2/(xs)$ and Q^2 were restricted to $0.01 < y < 0.7$ and $Q^2 > 20$ GeV^2. To remove background events with isolated muons ($\gamma\gamma \rightarrow \mu^+\mu^-$, J/ψ and Υ decays) and residual cosmic muons, an anti-isolation
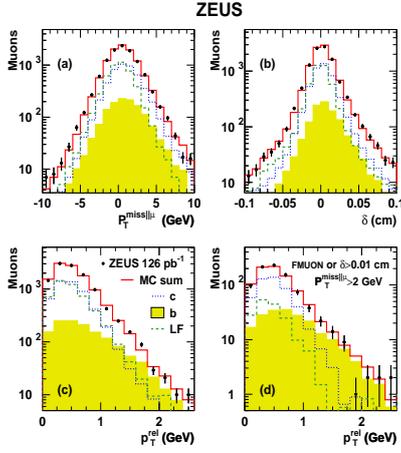
Figure 1: Distributions of (a) $p_T^{\mathrm{miss}||\mu}$, (b) δ, (c) p_T^{rel} for the selected sample of muons in DIS, and of (d) p_T^{rel} for a signal-enriched subsample with $p_T^{\mathrm{miss}||\mu} > 2$ GeV and either a muon in FMUON or $\delta > 0.01$ cm.
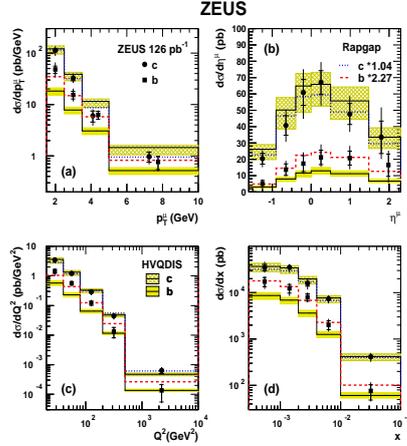
Figure 2: Differential muon cross sections for c and b as a function of (a) p_T^μ, (b) η^μ, (c) Q^2, and (d) x. The bands show the NLO QCD predictions (HVQDIS) and the corresponding uncertainties. The differential cross sections from RAPGAP are also shown.

cut was applied by requiring that the hadronic energy around the muon candidate was $E^{\mathrm{iso}} > 0.5$ GeV. A jet associated to the muon was required with $P_T^{jet} > 2.5$ GeV. The fractions of muons originating from charm, beauty or LF events were determined by fitting a combination of MC distributions to the measured three-dimensional distribution of the following discriminating variables [2] that are sensitive to different aspects of HQ decays:

· p_T^{rel}, the muon momentum component transverse to the axis of the associated jet,

· δ, the distance of closest approach of the muon track to the interaction point in the X, Y plane,

· $p_T^{\mathrm{miss}||\mu}$, the missing transverse momentum parallel to the muon direction, that has a distribution with a positive tail of events containing semileptonic HQ decays due to the presence of the neutrino.

A control sample of inclusive DIS data was used to test the quality of the simulation of these variables. The distributions of the three discriminating variables are shown in Fig. 1 (a-c) togheter with the distribution of p_T^{rel} for a signal-enriched subsample (Fig. 1 - d).

The global HQ fractions resulting from the fit are $f_c = 0.456 \pm 0.029$ (stat.) and $f_b = 0.122 \pm 0.013$ (stat.). The cross sections for muons from HQ decays were measured in the kinematic region $Q^2 > 20$ GeV^2, $0.01 < y < 0.7$, $p_T^\mu > 1.5$ GeV and pseudorapidities[1] $-1.6 < \eta^\mu < 2.3$ as a function of p_T^μ, η^μ, Q^2, and of the Bjorken scaling variable x and compared to QCD predictions. The differential cross sections as a function of p_T^μ, η^μ, Q^2, and x are compared in Fig.2 to the NLO QCD predictions based on HVQDIS.

---

[1] The ZEUS coordinate system is a right-handed Cartesian system, with the Z axis pointing in the proton beam direction, referred to as the "forward direction", and the X axis pointing towards the centre of HERA. The pseudorapidity is defined as $\eta = -\ln\left(\tan\frac{\theta}{2}\right)$, where θ is the polar angle.
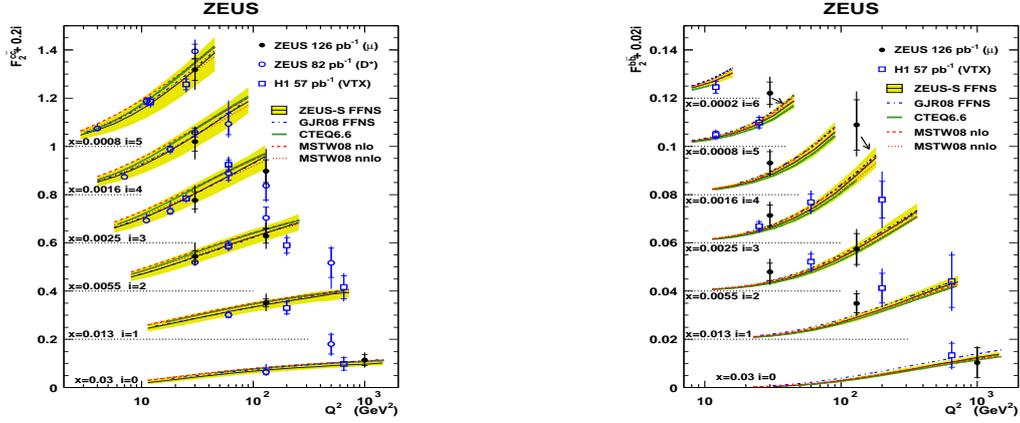
Figure 3: $F_2^{c\bar{c}}$(left) and $F_2^{b\bar{b}}$(right) extracted from the ZEUS muon[2](μ), and ZEUS charmed mesons [1](D^*) and from the H1 lifetime analysis[1](VTX). The data are shown as a function of Q^2 for fixed x values. The band represents the NLO FFNS calculation based on the ZEUS-S PDF fit and its uncertainty obtained from variations of the renormalisation and factorisation scales, of the HQ mass and of the PDFs. The different curves show the NLO FFNS calculation of GJR08 [3], the NLO and NNLO calculations in the GM-VFNS of MSTW08 [3] and the NLO GM-VFNS calculations of CTEQ6.6 [3] with $\mu_F^2 = Q^2 + m^2$.

3 Extraction of $F_2^{c\bar{c}}$ and $F_2^{b\bar{b}}$

The muon cross sections, σ^q, measured in bins of x and Q^2, were used to extract $F_2^{q\bar{q}}$ at a reference points in the x, Q^2 plane by: $F_2^{q\bar{q}}(x, Q^2) = \sigma^q \frac{F_2^{q\bar{q},\mathrm{th}}(x,Q^2)}{\sigma^{q,\mathrm{th}}}$, where $F_2^{q\bar{q},\mathrm{th}}(x, Q^2)$ and $\sigma^{q,\mathrm{th}}$ were calculated at NLO in the FFNS using the HvQDIS program. The largest uncertainty is related to the extrapolation to the full muon phase space. The theoretical uncertainty in the extraction of $F_2^{q\bar{q}}$ was evaluated by varying the HvQDIS parameters and by using a different PDF set (CTEQ5F). Figure 3 shows the extracted $F_2^{c\bar{c}}$ and $F_2^{b\bar{b}}$ from this analysis, as functions of Q^2 for fixed values of x, compared to previous ZEUS and H1 results [1] corrected to the same reference x used in the present analysis. Different QCD calculation are also shown. For $Q^2 \geq 60$ GeV^2 the present results are of comparable or higher precision than those previously existing.

References

[1] ZEUS Collaboration, Phys. Rev. D **69** (2004) 012004; H1 Collaboration, Eur. Phys. J. C **40** (2005) 349; H1 Collaboration, Eur. Phys. J. C **45** (2006) 23.

[2] ZEUS Collaboration, Eur. Phys. J. C **65** (2010) 65.;
M. Bindi, *Measurement of the Charm Production Cross Section in DIS Events at HERA*. PhD Thesis, Università di Bologna, Report DESY-THESIS-2008-026, 2008

[3] M. Gluck, P. Jimenez-Delgado and E. Reya, Eur. Phys. J. C **53** (2008) 355;
A. D. Martin, W. J. Stirling, R. S. Thorne and G. Watt, Eur. Phys. J. C **63** (2009) 188;
P. M. Nadolsky et al., Phys. Rev. D **78** (2008) 013004.

Measurement of Beauty Photoproduction from Inclusive Secondary Vertexing at HERA

Verena Schönberg

Physikalisches Institut der Universität Bonn, Nußallee 12, 53115 Bonn, Germany

Photoproduction of beauty quarks in events with two jets has been measured with the ZEUS detector at HERA using an integrated luminosity of $[128]pb^{-1}$. The beauty content was extracted using the decay-length significance of the b hadrons and the invariant mass of the decay vertices. Differential cross sections in $P_{\mathrm{T}}^{\mathrm{Jet}}$ and η^{Jet} are compared with the PYTHIA leading order plus parton shower (LO+PS) Monte Carlo and QCD predictions calculated at next-to-leading order. Furthermore the differential cross section as a function of η^{Jet} is compared to a previously published HERA I result.

1   Introduction

The production of beauty quarks in $e^{\pm}p$ collisions at HERA provides a good testing ground of perturbative Quantum Chromodynamics (QCD), as the large b-quark mass ($m_b \sim [5]GeV$) provides a hard scale that should ensure reliable predictions.

In contrast to previous measurements, in this analysis no requirements were imposed on the final state of the b decay. The measurement is therefore kept fully inclusive and benefits from the increase in statistics compared to the exclusive $b \to \mu$ and $b \to e$ analyses.

2   Event and candidate selection

A sample of photoproduction events ($Q^2 < [1]GeV$) was selected from e^+p collisions collected during 2006 and 2007 with the ZEUS detector, corresponding to an integrated luminosity of $\mathcal{L} \approx [128]pb^{-1}$. At least two jets with a pseudorapidity $|\eta^{\mathrm{Jet}}| < 2.5$ and a transverse momentum $P_{\mathrm{T}}^{\mathrm{Jet}} > [7(6)]GeV$ were required in the event. Standard cuts were applied to reject the contribution from deep inelastic scattering (DIS) events, corresponding to an effective cut of $Q^2 < [1]GeV^2$ and $0.2 < y < 0.8$, where y is the event inelasticity.

In order to reconstruct the b-hadron decay vertices, tracks were selected which had a transverse momentum $p_t \geq [0.5]GeV$ and were well reconstructed in the central tracking detector (CTD) and the microvertex detector (MVD). They were associated to one of the two highest energetic jets if they were within a cone of $\Delta R < 1$ with respect to the jet axis, with $\Delta R = \sqrt{\Delta\eta^2 + \Delta\phi^2}$. If two or more such tracks were associated to the selected jet, a candidate vertex was fitted from all associated tracks. Only vertices made of tracks with $\eta < 1.5$ were considered in the analysis. Finally, vertices with $\chi^2/\mathrm{dof} < 6$ and a distance from the interaction point $d_{XY} < [1]cm$ in the X-Y-plane (perpendicular to the beam axis) and $d_Z < [30]cm$ in Z (along the beam axis) were selected for the extraction of the beauty signal.

The same event and candidate selection was applied to Monte Carlo (MC) samples of beauty (b), charm (c) and light flavour (lf) events generated with PYTHIA 6.2 [1].

3   Determination of the b content

The heavy flavour content of the selected sample was determined by means of the decay-length significance, S, which is defined as the component of the decay length, d, projected on the X-Y-plane, along the jet-axis divided by its error δd. The decay-length significance distribution was divided into several bins of the invariant mass of the secondary vertex tracks providing almost pure beauty region at $[2]GeV \leq m_{vtx} < [7.5]GeV$, while the lower mass bins are dominated by charm. Figure 1 (left) shows S for the highest m_{vtx} range. In order to cancel potential systematic effects and to reduce the light flavour contribution, the left side of the significance (S^-, $S < 0$) was mirrored onto and subtracted from the right side (S^+, $S > 0$).

In order to extract the contributions from b and c quarks in the sample a binned χ^2 fit of the mirrored significance distributions ($S^+ - S^-$) was performed simultaneously in all three mass bins. The overall MC normalisation was constrained by adjusting the relative normalisation of the three MC subsamples to be consistent with the normalisation of the data in the unmirrored significance distribution. Figure 1 (right) shows $S^+ - S^-$ in three mass bins after the fit. The same fit was done in bins of $P_\mathrm{T}^\mathrm{Jet}$ and η^Jet for the extraction of the b content in the differential cross sections.

Requiring $m_{vtx} > [2]GeV$ and $S^+ - S^- > 8$ it was possible to obtain an almost pure beauty sample, for which good agreement between data and MC was found.
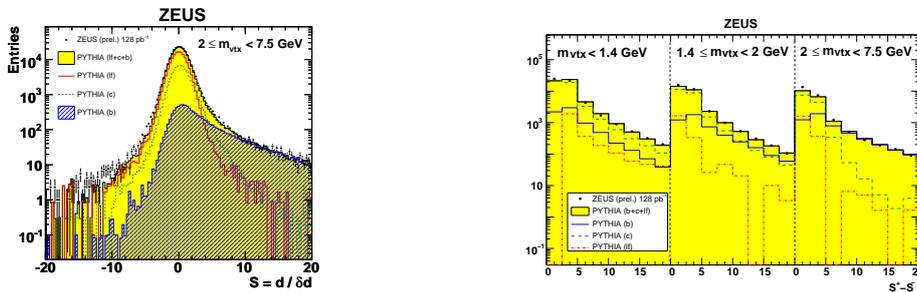
Figure 1: Distribution of decay-length significance, S, for $[2]GeV \leq m_{vtx} < [7.5]GeV$ (left) and mirrored decay-length significance in three mass bins (right) displaying the data and total MC distributions as well as the contributions from the three MC subsamples normalised according to the fractions obtained from the fit.

4   Results

The differential cross sections as a function of $P_\mathrm{T}^\mathrm{Jet}$ and η^Jet were measured for the process $e^+p \rightarrow e^+b\bar{b}X$ in the kinematic range $Q^2 < [1]GeV^2$, $0.2 < y < 0.8$, $P_\mathrm{T}^{\mathrm{Jet}\ 1(2)} > [7(6)]GeV$, $-2.5 \leq \eta^{\mathrm{Jet}\ 1(2)} < 2.5$ with at least one of the jets within $-1.6 \leq \eta^{\mathrm{Jet}\ 1(2)} < 1.3$. The results are compared to the PYTHIA LO+PS prediction as well as an NLO QCD prediction calculated
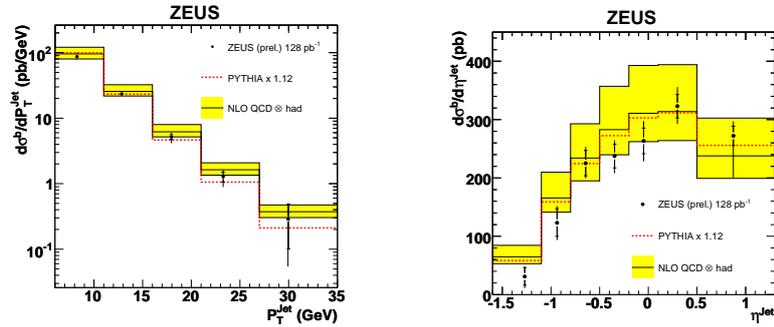
Figure 2: Differential cross section as a function of P_T^{Jet} (left) and η^{Jet} (right) for $Q^2 < [1]GeV^2$, $0.2 < y < 0.8$, $P_T^{Jet\ 1(2)} > [7(6)]GeV$ and $-2.5 \leq \eta^{\text{Jet}\ 1(2)} < 2.5$ using jets with $-1.6 \leq \eta^{\text{Jet}\ 1(2)} < 1.3$. The black points show the results from this analysis. The inner error bars are statistical uncertainties, while the outer error bars show the statistical and systematic uncertainties added in quadrature. The band represents the NLO QCD prediction with its uncertainties.

using the FMNR programme [2] as shown in Fig. 2. The FMNR settings were the same as in [3] with the default scale $\mu = \frac{1}{2}\sqrt{(p_t^b)^2 + m_b^2}$. Good agreement between the measurement and the predictions was observed. Furthermore, the cross sections as a function of η^{Jet} were compared to a previously published HERA I analysis [4]. The measurements agree well; the measurement presented here is much more precise than the previous analysis.

5   Conclusion

A measurement of beauty photoproduction using HERA II e^+p data collected in 2006 and 2007 has been presented. The decay-length significance, S, and the invariant mass, m_{vtx}, of the b hadron decay vertex have been used to determine the heavy quark contributions to the selected dijet sample. The production cross sections were found to be compatible with previous measurements and with NLO QCD predictions, while significantly improving the precision of the measurement.

References

[1] L. Lönnblad T. Sjöstrand and S. Mrenna. Pythia 6.2: Physics and manual, 2001.

[2] S. Frixione et al. Total cross sections for heavy flavour production at HERA. *Phys. Lett.*, B 348:633, 1995.

[3] ZEUS Collaboration; S. Chekanov et al. Measurement of beauty photoproduction using decays into muons in dijet events at hera. *JHEP*, 04:133, 2009.

[4] ZEUS Collaboration; S. Chekanov et al. Bottom photoproduction measured using decays into muons in dijet events in ep collisions at $\sqrt{s} = [318]GeV$. *Phys. Rev.*, D 70:12008, 2004.

Combined Limits on Anomalous Couplings at DØ

Jadranka Sekaric

Florida State University, 513 Keen Building, Tallahassee, FL 32306-4350, USA

We present the first combination of limits across different diboson production processes using 1 fb^{-1} of data collected by the DØ detector at the Fermilab Tevatron collider. We set the most stringent limits on anomalous values of the γ/ZWW couplings at a hadron collider and present the most stringent measurements to date for the W boson magnetic dipole and quadrupole moments.

1 Phenomenology

Study of the vector bosons interactions and the trilinear gauge boson couplings (TGCs) [1] provides a test of the electroweak sector of the Standard Model (SM). Any deviation from predicted SM values could indicate New Physics (NP). The TGCs contribute to diboson production via s-channel diagram. Thus, production of WW contains two trilinear vertices, γWW and ZWW, while the WZ production contains the ZWW vertex only. The effective lagrangian which describes γ/ZWW vertices contains 14 charged TGCs which are grouped according to the symmetry properties into C (charge conjugation) and P (parity) conserving couplings. In the SM all couplings vanish except $g_1^V = \kappa_V = 1$ ($V = \gamma/Z$). The value of g_1^γ is fixed by electromagnetic (EM) gauge invariance ($g_1^\gamma = 1$) while the value of g_1^Z may differ from its SM value. Considering the C and P conserving couplings only, five couplings remain, and their deviations from the SM values are denoted as the anomalous TGCs: Δg_1^Z, $\Delta\kappa_\gamma$, $\Delta\kappa_Z$, λ_γ and λ_Z. Couplings g_1^Z, κ_γ and λ_γ also relate to the W boson magnetic dipole moment μ_W and electromagnetic quadrupole moment q_W as $\mu_W = \frac{e}{2M_W}(g_1^\gamma + \kappa_\gamma + \lambda_\gamma)$ and $q_W = -\frac{e}{M_W^2}(\kappa_\gamma - \lambda_\gamma)$.

Anomalous TGCs could cause an unphysical increase in diboson production cross sections as the center-of-mass energy, $\sqrt{\hat{s}}$, approaches NP scale, Λ_{NP}. These divergences are controlled by a form factor $\Delta a(\hat{s}) = \Delta a_0/(1 + \hat{s}/\Lambda_{NP}^2)^n$ for which the anomalous coupling vanishes as $\hat{s} \to \infty$. The coupling a_0 is a low-energy approximation of the coupling $a(\hat{s})$ and $n = 2$ for γWW and ZWW couplings.

Because experimental evidence is consistent with the existence of an $SU(2)_L \times U(1)_Y$ gauge symmetry, it is reasonable to require the effective lagrangian to be invariant with respect to this symmetry. This gauge-invariant parametrization [2] gives the following relations between the $\Delta\kappa_\gamma$, Δg_1^Z and λ couplings: $\Delta\kappa_Z = \Delta g_1^Z - \Delta\kappa_\gamma \cdot \tan^2\theta_W$ and $\lambda = \lambda_Z = \lambda_\gamma$. We refer to this relationship as the $SU(2)_L \times U(1)_Y$ respecting scenario with three different parameters, $\Delta\kappa_\gamma$, λ and Δg_1^Z.

A second interpretive scenario, referred to as the equal couplings ($ZWW = \gamma WW$) scenario [3], specifies the γWW and ZWW couplings to be equal. In this case, $\Delta g_1^Z = \Delta g_1^\gamma = 0$ and the relations between the couplings become: $\Delta\kappa = \Delta\kappa_Z = \Delta\kappa_\gamma$ and $\lambda = \lambda_Z = \lambda_\gamma$.

2 Combined Final States

The TGC limits presented here are derived combining previously published measurements in four diboson final states: $W\gamma \to \ell\nu\gamma$, $WW/WZ \to \ell\nu jj$, $WW \to \ell\nu\ell'\nu$, and $WZ \to \ell\nu\ell'\bar{\ell}'$ [4]. The process $W\gamma \to \ell\nu\gamma$ is sensitive to the $WW\gamma$ coupling. The 0.7 fb^{-1} of data were analyzed to select events with an electron (muon) with $E_T > 25$ GeV (20 GeV), $\not{E}_T > 25$ (20) GeV and a photon with $E_T^\gamma > 9$ GeV. It is required that the photon and lepton are separated in space of $\Delta R = \sqrt{(\Delta\eta)^2 + (\Delta\phi)^2} > 0.7$. The final state radiation is suppressed requiring the transverse mass of the lepton, photon, and $\not{E}_T$ to be > 120 (110) GeV. In total 263 candidate events are observed. After subtracting backgrounds, the signal is measured to be $187 \pm 17_{\text{stat}} \pm 4_{\text{sys}}$ events and is consistent with the SM prediction of 197 ± 15 events. The photon spectra are input for the combination. For $W\gamma$ production in presence of anomalous TGCs, spectra were simulated using the Baur Monte Carlo (MC) event generator [5].

The $WW/WZ \to \ell\nu jj$ analysis probes both the ZWW and γWW vertex. We analyze 1.07 fb^{-1} of data selecting events with a lepton of $p_T > 20$ GeV, $\not{E}_T > 20$ GeV, and at least two jets with $p_T > 20$ GeV with the leading jet of $p_T > 30$ GeV. In total 26865 candidate events are observed which is consistent with the SM prediction of 26830 ± 828 events. The dijet p_T spectrum is used as input for the combination. Spectra with anomalous TGCs are generated by re-weighting the Pythia MC SM spectra to match spectra generated by a LO MC from Hagiwara, Zeppenfeld, and Woodside (HZW) [3].

The $WW \to \ell\nu\ell'\nu$ analysis uses 1 fb^{-1} of data. For all channels (ee, $e\mu$, and $\mu\mu$), the leading lepton must satisfy $p_T > 25$ GeV and the trailing lepton with $p_T > 15$ GeV. Both leptons must be of opposite charge. In the data 100 candidate events are observed, which is consistent with the prediction of 102.9 ± 4.4 events. Two-dimensional histograms of leading and trailing lepton p_T are used as input in the combination. Histograms are generated using the HZW MC.

Analysis of $WZ \to \ell\nu\ell'\bar{\ell}'$ final states uses 1 fb^{-1} of data. Four final states (eee, $ee\mu$, $\mu\mu e$, and $\mu\mu\mu$), require three leptons with $p_T > 15$ GeV and $\not{E}_T > 20$ GeV. To select Z candidates, like-flavor leptons must satisfy $71 < m_{ee} < 111$ GeV or $50 < m_{\mu\mu} < 130$ GeV. To reduce $t\bar{t}$ background events the magnitude of the vector sum of the charged lepton p_T and the $\not{E}_T$ must be less than 50 GeV. The sum over all channels yields 13 candidate events which is in agreement with the SM prediction of 13.7 ± 1.2 events. The p_T^Z of the Z boson is used in the combination and simulated using the HZW MC.

3 Results

The one-dimensional 68% and 95% C.L. limits for each coupling are shown in Table 1 for two scenarios. The measured values and the one-dimensional 68% C.L. intervals of the W boson magnetic dipole and electric quadrupole moments for $SU(2)_L \times U(1)_Y$ scenario (with $g_1^Z = 1$) are $\mu_W = 2.02^{+0.08}_{-0.09}$ $(e/2M_W)$ and $q_W = -1.00 \pm 0.09$ (e/M_W^2), respectively. Two-dimensional surfaces in $q_W - \mu_W$ space for both scenarios are shown in Figure 1.

4 Summary

Presented results are the most stringent limits on anomalous values of γWW and WWZ TGCs measured from hadronic collisions to date. The 95% C.L limits in both scenarios improve relative to the previous combined DØ [6] and CDF [7] results by a factor of ~ 3. Our measurements

Par.I	Min.	68% C.L.	95% C.L.	Par.II	Min.	68% C.L.	95% C.L.
$\Delta\kappa_\gamma$	0.07	-0.13, 0.23	-0.29, 0.38	$\Delta\kappa$	0.03	-0.04, 0.11	-0.11, 0.18
Δg_1^Z	0.05	-0.01, 0.11	-0.07, 0.16				
λ	0.00	-0.04, 0.05	-0.08, 0.08	λ	0.00	-0.05, 0.05	-0.08, 0.08

Table 1: One-dimensional minimum and combined 68% and 95% C.L. limits on anomalous γ/ZWW couplings for two scenarios: $SU(2)_L \times U(1)_Y$ (Par.I) and equal couplins (Par.II), both with $\Lambda_{NP} = 2$ TeV.
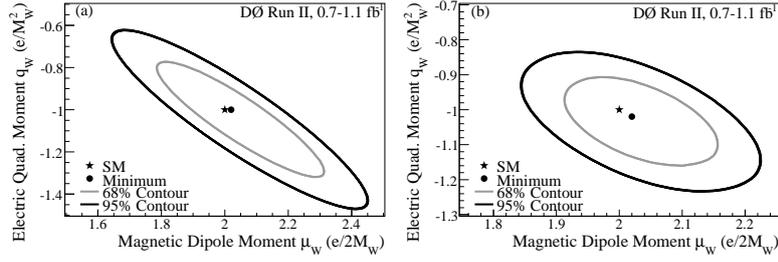
Figure 1: Two-dimensional 68% and 95% C.L. limits for the W boson electric quadrupole moment versus the magnetic dipole moment for (a) $SU(2)_L \times U(1)_Y$ scenario and (b) equal couplings scenario ($\Lambda_{NP} = 2$ TeV in both scenarios).

are comparable to that of an individual LEP2 experiments [8] even though all four analyses considered in this combination are limited by statistics. The DØ experiment also sets the most stringent measurements of μ_W and q_W moments to date.

References

[1] K. Hagiwara, J. Woodside, and D. Zeppenfeld, Phys. Rev. **D41** 2113 (1990).

[2] M. Bilenky, J. L. Kneur, F. M. Renard and D. Schildknecht, Nucl. Phys. **B 409** 22 (1993);
M. Bilenky, J. L. Kneur, F. M. Renard and D. Schildknecht, Nucl. Phys. **B 419** 240 (1994).

[3] K. Hagiwara, J. Woodside, and D. Zeppenfeld, Phys. Rev. **D41** 2113 (1990).

[4] V.M. Abazov *et al.*, (DØ Collaboration), Phys. Rev. Lett. **100** 241805 (2008);
V.M. Abazov *et al.*, (DØ Collaboration), Phys. Rev. **D80** 053012 (2009);
V.M. Abazov *et al.*, (DØ Collaboration), Phys. Rev. Lett. **103** 191801 (2009);
V.M. Abazov *et al.*, Phys. Rev. **D76** 111104(R) (2007).

[5] U. Baur and E.L. Berger, Phys. Rev. **D41** 1476 (1990);
U. Baur, T. Han, and J. Ohnemus, Phys. Rev. **D48** 5140 (1993).

[6] B. Abbott *et al.*, (DØ Collaboration), Phys. Rev. **D60** 072002 (1999).

[7] T. Aaltonen *et al.*, (CDF Collaboration), Phys. Rev. **D76** 111103(R) (2007).

[8] P. Abreu *et al.*, (DELPHI Collaboration), Phys. Lett. **B 502** 9 (2001);
G. Abbiendi *et al.*, (OPAL Collaboration), Eur. Phys. J. **C33** 463 (2004);
P. Achard *et al.*, (L3 Collaboration), Phys. Lett. **B 586** 151 (2004);
S. Schael *et al.*, (ALEPH Collaboration), Phys. Lett. **B 614** 7 (2005).

Search for ZH Production at D0 in $p\bar{p} \rightarrow \ell^+\ell^- b\bar{b}$ Events at $\sqrt{s} = 1.96$ TeV

John BackusMayes

University of Washington Department of Physics, Box 351560 Seattle, WA 98195-1560

We present a search for a low-mass standard model Higgs boson produced in association with a Z boson decaying to charged leptons at a center-of-mass energy of $\sqrt{s}$ =1.96 TeV with the D0 detector at the Fermilab Tevatron collider. The search is performed in a large data set of events containing two opposite-sign leptons (electron, muon, tau) and one or two b-tagged jets. Recent improvements to the sensitivity, from increased lepton acceptance to optimized signal-to-background discrimination, will be discussed.

1 Introduction

The mass of a standard model Higgs boson is constrained by direct searches performed at LEP and measurements of the top quark and W boson masses [1]. Combining these results, the Higgs mass m_H must be less than 186 GeV at 95% confidence level.

If $m_H < 135$ GeV, then Higgs bosons are expected to decay primarily to $b\bar{b}$. At hadron colliders, the inclusive $b\bar{b}$ cross section is six orders of magnitude larger than the cross section for Higgs production, so it is not feasible to find evidence for low-mass Higgs bosons produced alone. Instead, we search for associated production of vector (W, Z) and Higgs bosons. Requiring leptonic decay of the W or Z dramatically reduces the multijet background and increases our sensitivity to the Higgs signal. The analysis discussed here is concerned exclusively with ZH production in the $\ell^+\ell^- b\bar{b}$ final state; the D0 collaboration has also completed similar analyses using $\ell\nu b\bar{b}$ [2] and $\nu\bar{\nu} b\bar{b}$ [3] final states.

The irreducible backgrounds in this search are Z production with heavy-flavor jets, top quark pair production, and diboson final states. Instrumental backgrounds include jets faking charged leptons and light jets faking heavy-flavor jets.

A more detailed description of this analysis may be found in [4].

2 The Tevatron and the D0 detector

The Tevatron is a proton-antiproton collider located at Fermilab near Chicago, IL. Collisions have a center-of-mass energy of $\sqrt{s} = 1.96$ TeV. Fermilab's Accelerator Division continues to optimize the integrated luminosity produced by the Tevatron, and currently the accelerator is performing better than ever before. The total integrated luminosity delivered from RunII is over 7 fb^{-1}; results discussed here use up to 4.1 fb^{-1} of data.

D0 is a multi-purpose particle detector, one of two detectors located at collision points around the Tevatron. We have taken data with 90% average efficiency since the start of RunII. In this search, we employ every major component of D0 in order to identify muons, electrons, and heavy-flavor jets [5].

3 Event selection

3.1 Leptons

We strive for maximum Higgs signal acceptance, so our event selection is very loose. For muons, we require central track matches, $p_T > 10$ GeV, and $|\eta| < 2$. Electron requirements are $p_T > 15$ GeV and $|\eta| < 2.5$. All identified leptons are also required to pass various tracking and calorimeter isolation criteria, and the invariant mass of the dilepton pair must match the Z boson resonance: $70 < m_{\ell\ell} < 130$ GeV.

To be sure we accept as many Higgs events as possible, we select some electrons and muons that are not initially identified as such. In the inter-cryostat region (ICR) where there is little calorimeter coverage, we look for electrons that have been reconstructed as taus. In the various gaps in muon coverage, we look for isolated tracks. These additions improve our signal acceptance by 15%.

3.2 Jets

We select events with at least 2 jets, leading jet $p_T > 20$ GeV and second jet $p_T > 15$ GeV. Before tagging, $S/B = 0.0003$.

Using D0's neural net b-tagging algorithm [6], we require either two loose tags (inclusive) or one tight tag (exclusive), which improves S/B by factors of 20 and 10, respectively. The optimization of our final multivariate discriminant depends significantly on b-tag criteria, as do the expected signal and background yields, so we can improve our Higgs sensitivity by analyzing these orthogonal b-tag samples separately.

With the two highest-p_T tagged jets or the one tagged jet and highest-p_T untagged jet, we compute the invariant mass of the dijet system, which is the kinematical variable most sensitive to low-mass Higgs production.

3.3 Kinematic fit

With an ideal detector, we would have very little missing E_T in $ZH \to \ell^+\ell^- b\bar{b}$ events. Thus, events with a large p_T imbalance must result from either background processes or mismeasurement. Given our knowledge of the jet and lepton energy resolutions, we can make our measurements more precise and discriminate against backgrounds such as multijet production and $t\bar{t} \to \ell^+\ell^- \nu\bar{\nu} b\bar{b}$. To do this, we perform a constrained multi-dimensional fit on the p_T, η, and azimuthal angle ϕ of the two leptons and two candidate jets. We constrain the dilepton invariant mass to 91.2 ± 2.5 GeV and the vector sum of p_T to 0.0 ± 7.0 GeV.

Subsequently, we remove events with high kinematic fit χ^2 values to reduce instrumental background. As a result of the fit, the dijet mass resonance in Higgs events is more prominent, which translates directly to a 6-11% increase in Higgs sensitivity.

4 Results

We use boosted decision trees (BDT) [7] to combine the discrimination power of several kinematical variables: the dijet mass and p_T, the dilepton p_T and colinearity, and many others. No evidence for ZH production is seen, so we compute upper cross section limits based on the shape of the BDT output, using a modified frequentist approach [8, 9]. The leading sources of systematic uncertainty are the Z+heavy-flavor cross section (20%), the jet energy scale (10%), and b-tagging efficiencies (10%). Assuming a Higgs mass of 115 GeV, we exclude ZH production above 9.1 times the standard model expectation at 95% confidence level. Limits assuming other Higgs masses are shown in Fig. 1.

Upon comparison to previous results [10], our limits have improved roughly 12% beyond what is expected with more data. This is due to our use of more optimal selection criteria and more sophisticated analysis techniques. We are currently investigating further improvements to the analysis, including the use of matrix-element discriminants, improved b-tagging, and further optimization of our multivariate discriminant.
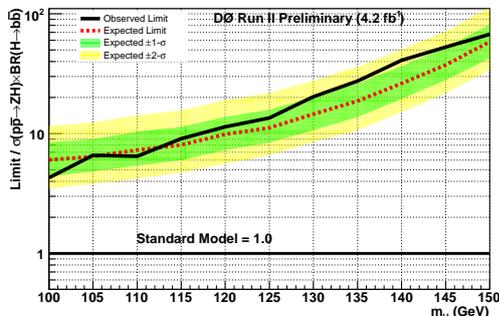
Figure 1: Expected and observed limits on ZH production, expressed as ratios to the standard model expectations.

References

[1] LEP, Tevatron and SLD Electroweak Working Groups, arXiv:0911.2604 [hep-ex] (2009).

[2] The D0 Collaboration, D0Note 5972-CONF (2009).

[3] The D0 Collaboration, arXiv:0912.5285 [hep-ex] (2010).

[4] The D0 Collaboration, D0Note 5876-CONF (2009).

[5] V. M. Abazov *et al.* (D0 Collaboration), Nucl. Instrum. Methods in Phys. Res. A **565**, 463 (2006); M. Abolins *et al.*, Nucl. Instrum. and Methods A **584/1**, 75 (2007); R. Angstadt *et al.*, arXiv:0911.2522 [physics.ins-det].

[6] T. Scanlon, FERMILAB-THESIS-2006-43.

[7] L. Breiman *et al.*, *"Classification and Regression Trees"* (Wadsworth, Belmont, CA, 1984); Y. Freund and R. E. Schapire, Machine Learning: Proceedings of the Thirteenth International Conference, Ed. L. Saitta (Morgan Kaufmann, San Francisco, 1996), p148.

[8] T. Junk, Nucl. Instrum. Methods in Phys. Res. A **434**, 435 (1999); A. Read, J. Phys. G **28**, 2693 (2002).

[9] W. Fisher, FERMILAB-TM-2386-E (2006).

[10] The D0 Collaboration, D0Note 5570-CONF (2008).

Combined Upper Limit on Standard Model Higgs Boson Production at DØ in $p\bar{p}$ Collisions at $\sqrt{s} = 1.96$ TeV

Ralf Bernhard

Physikalisches Institut, Albert-Ludwigs Universität Freiburg,
Hermann-Herder-Str. 3, 79104 Freiburg, Germany

The combination of the searches for the Standard Model Higgs boson at a center-of-mass energy of $\sqrt{s}$ =1.96 TeV, using up to 5.4 fb^{-1} of data collected with the D0 detector at the Fermilab Tevatron collider are presented. The major contributing processes include associated production ($WH \to l\nu bb$, $ZH \to \nu\nu bb$, $ZH \to llbb$, and $WH \to WWW^{(*)}$) and gluon fusion ($gg \to H \to WW^{(*)}$). As no significant excess is observed, we proceed to set limits on standard model Higgs boson production. The observed 95% confidence level upper limits are found to be a factor of 4.0 (1.5) higher than the predicted standard model cross section at $M_H = 115(165)$ GeV/c^2 while the expected limits are found to be a factor of 2.8 (1.4) higher than the standard model predicted cross section for the same masses.

1 Introduction

In the Standard Model (SM) of particle physics the Higgs mechanism is responsible for breaking electroweak symmetry, thereby giving mass to the W and Z bosons. It predicts the existence of a heavy scalar boson, the Higgs boson, with a mass that can not be predicted by the SM. Direct searches for the Higgs Boson were performed at the LEP experiments in the process $e^+e^- \to ZH$ with a centre of mass energy of 206.6 GeV. A direct mass limit at $m_H > 114.4$ GeV/c^2 [1] was set at the 95% confidence level (CL)[1]. The results from a combination of the two Tevatron experiments resulted in an exclusion in the mass range from 160 to 170 GeV/c^2[2].

The results of direct searches for SM Higgs bosons in $p\bar{p}$ collisions at $\sqrt{s} = 1.96$ TeV recorded by the DØ experiment are presented [3]. The analyses combined here seek signals of Higgs bosons produced in association with vector bosons ($q\bar{q} \to W/ZH$), through gluon-gluon fusion (GGF) ($gg \to H$), through vector boson fusion (VBF) ($q\bar{q} \to q\bar{q}H$), and in association with top quarks ($t\bar{t} \to t\bar{t}H$). The analyses utilize data corresponding to integrated luminosities ranging from 2.1 to 5.4 fb^{-1}, collected during the period 2002-2009. The Higgs boson decay modes studied are $H \to b\bar{b}$, $H \to W^+W^-$, $H \to \tau^+\tau^-$ and $H \to \gamma\gamma$. The searches are organized into 60 analysis subsets comprising different production, decay and final state particle configurations, each designed to isolate a particular Higgs boson production and decay mode. In order to facilitate proper combination of signals, the analyses were designed to be mutually exclusive after analysis selections. The 60 analyses used in this combination are outlined in Table 1. In the cases of $p\bar{p} \to W/ZH + X$ production, we search for a Higgs boson decaying to two bottom

---

[1]All limits given in this paper are at 95% CL

quarks, or two tau leptons. The decays of the vector bosons further define the analyzed final states. To isolate $H \to b\bar{b}$ decays, an algorithm for identifying jets consistent with the decay of a heavy-flavor quark is applied to each jet (b-tagging). Several kinematic variables sensitive to displaced jet vertices and jet tracks with large transverse impact parameters relative to the hard-scatter vertices are combined in a neural network (NN) discriminant trained to identify heavy-flavor quark decays and reject jets arising from light-flavor quarks or gluons. By adjusting a minimum requirement on the b-tagging NN output, a spectrum of increasingly stringent b-tagging operating points is achieved, each with a different signal efficiency and purity. For the $WH \to \ell\nu b\bar{b}$, $ZH \to \nu\nu b\bar{b}$ and $ZH \to \ell\ell b\bar{b}$ processes, the analyses are separated into two groups: one in which two of the jets were b-tagged with a loose tag requirement ($WH \to \ell\nu b\bar{b}$ and $ZH \to \ell\ell b\bar{b}$) or one loose and one tight tag requirement ($ZH \to \nu\nu b\bar{b}$) (hereafter called double b-tag or DT) and one group in which only one jet was tagged with a tight tag requirement (single b-tag or ST). The ST selection excludes additional loose-tagged jets, rendering the ST and DT selections orthogonal. The ST selection results in a typical per-jet efficiency and fake rate of about 50% and 0.5%, while the DT selection gives 60% and 1.5%. For these analyses, each lepton flavor of the W/Z boson decay ($\ell = e, \mu$) is treated as an independent channel. In the case of $WH \to \ell\nu b\bar{b}$ production, the primary lepton from the W boson decay may fall outside of the detector fiducial volume or may not be identified. Events of this type are selected by the $ZH \to \nu\nu b\bar{b}$ analysis. For $WH \to WW^+W^-$ production, we search for leptonic W boson decays with three final states of same-signed leptons: $WWW \to e^\pm\nu e^\pm\nu + X$, $e^\pm\nu\mu^\pm\nu + X$, and $\mu^\pm\nu\mu^\pm\nu + X$. In the case of $H \to W^+W^-$ and $q\bar{q}H \to q\bar{q}W^+W^-$ production via vector boson fusion, we search for leptonic W boson decays with three final states of opposite-signed leptons: $WW \to e^+\nu e^-\nu$, $e^\pm\nu\mu^\pm\nu$, and $\mu^+\nu\mu^-\nu$. In addition we also consider final states originating from Higgs boson production in association with a vector boson (WH or ZH), where leptons may originate from the vector boson or Higgs boson decay. In all $H \to W^+W^-$ decays with $M_H < 2M_W$, one of the W bosons will be off mass shell. In all cases, lepton selections include both electrons and muons ($\ell = e, \mu$), while τ leptons are included in the simulation and the selections necessarily have acceptance for secondary leptons from $\tau \to e/\mu$ decays. Finally, we include an analysis that searches for Higgs bosons decaying to two photons and produced via gluon-gluon fusion, vector boson fusion, and associated production mechanisms.

Table 1: List of analysis channels, corresponding integrated luminosities, and final variables. The final variable used for several analyses is a neural-network or boosted decision-tree discriminant output which is abbreviated as NN discriminant and DTree discriminant, respectively.

Production	Final State	Lumi. [fb^{-1}]	Final Variable	# Sub-Channels
WH	$\ell\nu b\bar{b}$ (ST/DT, 2/3 jet)	5.0	NN discriminant	16
$X + H$	$\tau\tau b\bar{b}/q\bar{q}\tau\tau$	4.9	DTree discriminant	2
ZH	$\nu\nu bb$ (ST/DT)	5.2	DTree discriminant	4
ZH	$\ell\ell bb$ (ST/DT)	4.2	NN discriminant	16
WH	$\ell^\pm\ell^\pm$	3.6	Likelihood	6
All	$\ell\nu\ell'\nu' + X$	5.4	NN discriminant	3
All	$\gamma\gamma$	4.2	Di-photon Mass	1
$t\bar{t}H$	$t\bar{t}bb$	2.1	Scaled H_T	12

2 Limit Combination

We combine results using the CLs method with a negative log-likelihood ratio (LLR) test statistic [4, 5]. The value of CLs is defined as CLs = CLs+b/CLb where CLs+b and CLb are the confidence levels for the signal-plus-background hypothesis and the background-only hypothesis, respectively. These confidence levels are evaluated by integrating corresponding LLR distributions populated by simulating outcomes via Poisson statistics. Separate channels and bins are combined by summing LLR values over all bins and channels. This method provides a robust means of combining individual channels while maintaining individual channel sensitivities and incorporating systematic uncertainties. Systematics are treated as Gaussian uncertainties on the expected number of signal and background events, not the outcomes of the limit calculations. This approach ensures that the uncertainties and their correlations are propagated to the outcome with their proper weights. The CLs approach used in this combination utilizes binned final-variable distributions rather than a single-bin (fully integrated) value for each contributing analysis. The exclusion criteria are determined by increasing the signal cross section until CLs = $1 - \alpha$, which defines a signal cross section excluded at 95% confidence level for $\alpha = 0.95$.

3 Systematic Uncertainties

The systematic uncertainties differ between analyses for both the signals and backgrounds. Here only the largest contributions are summarized. Most analyses carry an uncertainty on the integrated luminosity of 6.1%, while the overall normalization of other analyses is determined from the NNLO $Z/\gamma*$ cross section in data events near the peak of $Z \to \ell\ell$ decays. The $H \to b\bar{b}$ analyses have an uncertainty on the b-tagging rate of 2-6% per tagged jet. These analyses also have an uncertainty on the jet measurement and acceptances of 7%. All analyses include uncertainties associated with lepton measurement and acceptances, which range from 3-6% depending on the final state. The largest contribution for all analyses is the uncertainty on the background cross sections at 6-30% depending on the analysis channel and specific background. These values include both the uncertainty on the theoretical cross section calculations and the uncertainties on the higher order correction factors. The uncertainty on the expected multijet background is dominated by the statistics of the data sample from which it is estimated, and is considered separately from the other cross section uncertainties. The $H \to W^+W^-$ and $H \to \gamma\gamma$ analyses also assign a 11% uncertainty to the NNLO Higgs production cross section associated with the accuracy of the theoretical calculation and arising from uncertainty in PDF and scale. In addition, several analyses incorporate shape-dependent uncertainties on the kinematics of the dominant backgrounds in the analyses. These shapes are derived from the potential deformations of the final variables due to generator and background modeling uncertainties.

4 Derived Upper Limits

We derive limits on SM Higgs boson production $\sigma \times BR(H \to b\bar{b}/W^+W^-/\tau^+\tau^-)$ via the 60 individual analyses. To facilitate model transparency and to accommodate analyses with different degrees of sensitivity, we present our results in terms of the ratio of 95% C.L. upper

cross section limits to the SM predicted cross section as a function of Higgs boson mass[2]. The individual analyses described in Table 1 are grouped to evaluate combined limits over the range $100 \leq M_H \leq 200$ GeV/c^2. The $X + H \to \tau\tau b\bar{b}/q\bar{q}\tau\tau$ analysis contributes to the region $M_H \leq 145$ GeV/c^2, the $ZH \to \ell\ell b\bar{b}$, $ZH \to \nu\nu b\bar{b}$ $WH \to \ell\nu b\bar{b}$ and $H \to \gamma\gamma$ analyses contribute for $M_H \leq 150$ GeV/c^2, the $WH \to WW^+W^-$ analyses contribute for $M_H \geq 120$ GeV/c^2, the $t\bar{t}H \to t\bar{t}b\bar{b}$ analysis contribues for $M_H \geq 155$ GeV/c^2, and the $H \to WW$ analyses contribute for $M_H \geq 115$ GeV/c^2.

In Table 4 the expected and observed 95% C.L. cross section limit ratio to the SM cross sections for all analyses combined over the probed mass region ($100 \leq M_H \leq 200$ GeV/c^2) are shown.

Table 2: Combined 95% C.L. limits on $\sigma \times BR(H \to b\bar{b}/W^+W^-/\gamma\gamma/\tau^+\tau^-)$ for SM Higgs boson production. The limits are reported in units of the SM production cross section times branching fraction.

M_H (GeV/c^2)	100	105	110	115	120	125	130	135	140	145	150
Expected Limit	2.35	2.40	2.85	2.80	3.25	3.31	3.30	3.35	2.95	2.71	2.46
Observed Limit	3.53	3.40	3.47	4.05	4.03	4.19	4.53	5.58	4.33	3.86	3.20

M_H (GeV/c^2)	155	160	165	170	175	180	185	190	195	200	
Expected Limit	1.98	1.41	1.35	1.64	2.05	2.58	3.32	4.19	5.04	6.00	
Observed Limit	3.35	1.90	1.53	1.91	1.89	2.20	3.20	3.36	5.71	6.27	

5   Conclusion

Upper limits on standard model Higgs boson production derived from 60 Higgs search analyses including data corresponding to 2.1-5.4fb^{-1} were presetend. These analyses were combined and form new limits more sensitive than each individual limit. The observed (expected) 95% C.L. upper limit ratios to the SM Higgs boson production cross sections are 4.0 (2.8) at $M_H = 115$ GeV/c^2 and 1.5 (1.4) at $M_H = 165$ GeV/c^2.

6   Bibliography

References

[1] R. Barate et al. Search for the standard model Higgs boson at LEP. *Phys. Lett.*, B565:61–75, 2003.

[2] CDF and DØ Collaborations. Combined CDF and DØ Upper Limits on Standard Model Higgs-Boson Production with up to 4.2/fb of Data. hep-ex/0903.4001, 2009.

[3] DØ Collaboration. DØ Conference Note 6008, 2009.

[4] T. Junk. *Nucl. Intrum. Meth. A*, 435:434, 1999.

[5] A.Read. *CERN*, 2000-005, 2000.

---

[2]The SM prediction for Higgs boson production would therefore be considered excluded at 95% C.L. when this limit ratio falls below unity.

Search for Neutral Supersymmetric Higgs Bosons in $p\bar{p}$ Collisions at $\sqrt{s}=$ 1.96 TeV

Ken Herner[1], for the D0 Collaboration

[1]University of Michigan, 48109 Ann Arbor, MI, USA

We report results of searches for neutral supersymmetric Higgs Bosons in up to 2.7 fb^{-1} of data collected with the D0 detector at the Fermilab Tevatron. The final states include muons, taus, and jets from the decay of b hadrons. The searches observe no significant excess and set upper limits on neutral Higgs production cross sections. The limits are also translated into exclusions of MSSM parameter space.

1 Introduction

Supersymmetry (SUSY) [1] invokes a new symmetry between fermions and bosons and provides attractive solutions to some of the challenges to the Standard Model (SM) such as the hierarchy problem. In the Minimal Supersymmetric Standard Model (MSSM) there are two Higgs doublets, resulting in five physical Higgs bosons [2], two charged ($H^{\pm}$) and three neutral (h, H, A, collectively denoted ϕ). The ratio of the vacuum expectation values of the two doublets is denoted $\tan\beta$. The Higgs coupling to down-type fermions is enhanced by a factor $\propto \tan\beta$ meaning Higgs production in association with a b quark is enhanced by a factor $\propto \tan^2\beta$, giving potentially detectable signals at the Tevatron for large $\tan\beta$. Additionally, at least two of the three neutral Higgs bosons are nearly degenerate in mass, leading to a total cross section enhancement of $\sim 2 \times \tan^2\beta$. We report results of Higgs searches with the DØ detector at the Fermilab Tevatron in three main complementary search channels: $b\phi \rightarrow bb\bar{b}$, $b\phi \rightarrow b\tau\tau$, and $\phi \rightarrow \tau\tau$. The results have also been combined to yield additional exclusion in the MSSM parameter space.

2 Search Channels

2.1 $b\phi \rightarrow bb\bar{b}$ Search

The $b\phi \rightarrow bb\bar{b}$ channel offers the highest Higgs branching ratio (BR($H \rightarrow b\bar{b}) \approx 0.9$) in an accessible channel ($\phi \rightarrow b\bar{b}$ is obscured by background). DØ has performed this search in 2.6 fb^{-1} of data [3]. Events with at least three b-tagged jets are selected. A likelihood discriminant is formed to reject background before using the invariant mass of the two jets with the highest transverse momenta as the final discriminating variable. No significant excess is observed and 95% C.L. limits are set on the production cross section, which are then translated in to an

exclusion in the $\tan \beta$ vs. m_A plane for several MSSM benchmark scenarios, one of which is shown in Figure 1a.

2.2 $b\phi \rightarrow b\tau\tau$ Search

The $b\phi \rightarrow b\tau\tau$ channel has a lower branching ratio than the $b\phi \rightarrow b b\bar{b}$ channel but offers a much cleaner final state due to the lower multijet background. The b-jet requirement also reduces the $Z \rightarrow \tau\tau + X$ background making this channel the most sensitive when $m_\phi \simeq m_Z$. DØ has performed a search in 2.7 fb^{-1} of data [4]. The detector signature is one muon (assuming one tau decays to $\nu_\tau \mu \nu_\mu$), one hadronic tau, and one b-jet. The final discriminant variable is the product of two multivariate techniques designed to discriminate multijet and $t\bar{t}$ production. There is no significant excess and 95% C.L. limits are set in the $\tan \beta$ vs. m_A plane shown in Figure 1b.

2.3 $\phi \rightarrow \tau\tau$ Search

The $\phi \rightarrow \tau\tau$ search is complementary to the other two main search channels and combines three distinct final states: electron-hadronic tau, muon-hadronic tau, and electron-muon (when both taus decay to leptons). DØ has performed these searches in 2.2 fb^{-1} of data [5]. The visible mass (invariant mass of the visible leptons and missing transverse energy) is the final discriminant variable. Again there is no significant excess; Figure 1c shows the $\tan \beta$ vs. m_A parameter space exclusion.

3 Combination

DØ has combined results in the three aforementioned channels (the $b\tau\tau$ result used in the combination has 1.2 fb^{-1} of data) to extend the MSSM parameter space exclusion [6]. Figure 2a shows the combined exclusion. The $\phi \rightarrow \tau\tau$ search as also been combined with a similar analysis from the CDF collaboration [7]. Figure 2b shows the combined exclusion from these analyses.

4 Summary

The DØ Collaboration has performed searches for neutral supersymmetric Higgs bosons using up to 2.7 fb^{-1} of data in three complementary search channels. No significant excess above background predictions has been observed and D0 sets upper limits on the Higgs production cross section at 95% C.L. The results have also been translated into exclusion of MSSM parameter space.

References

[1] H. P. Nilles, Phys Rep. **110**, 1 (1984); H. E. Haber and G. L. Kane, Phys. Rep. **117**, 75 (1985).

[2] A. Djouadi, Phys. Rep. **459**, 1 (2008); and references therein.

[3] D0 Collaboration, V. Abazov *et al.*, D0 Note 5726-CONF (2008).

[4] D0 Collaboration, V. Abazov *et al.*, D0 Note 5985-CONF (2009).

[5] D0 Collaboration, V. Abazov *et al.*, D0 Note 5740-CONF (2008).

[6] D0 Collaboration, V. Abazov *et al.*, D0 Note 5935-CONF (2009).

[7] D0 Collaboration, V. Abazov *et al.*, D0 Note 5980-CONF (2009).
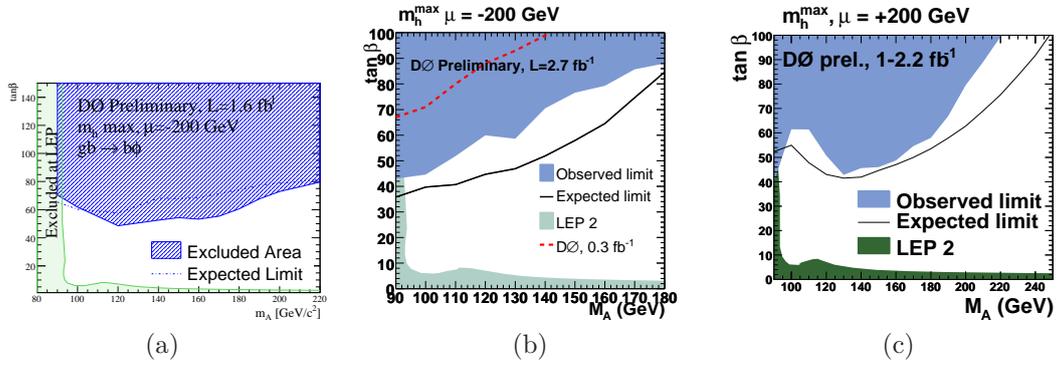
Figure 1: 95% C.L. limits in the $\tan\beta$ vs. m_A plane in the $b\phi \to b b\bar{b}$ (a), $b\phi \to b\tau\tau$ (b), and $\phi \to \tau\tau$ (c) analyses.
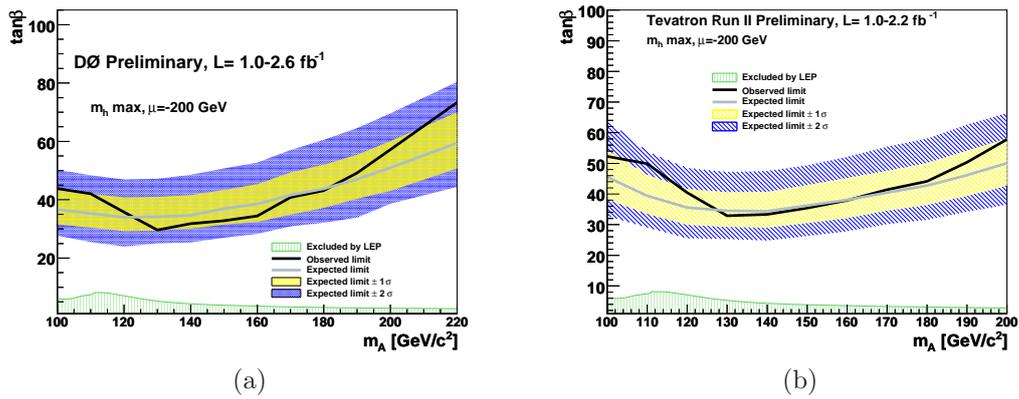

Figure 2: 95% C.L. limits in the $\tan\beta$ vs. m_A plane for DØ combination (a) and the DØ+ CDF $\phi \to \tau\tau$ combination (b) analyses.

Search for $H \to W^+W^- \to l^+l^-$ at DØ

Ruchika Nayyar[1] (for the DØ collaboration)

[1]University of Delhi, India

We present a search for the Standard Model Higgs boson produced via $H \to W^+W^- \to l^+l^-(ee, e\mu, \mu\mu, \tau \to e/\mu)$ process at $\sqrt{s} = 1.96$ TeV with the DØ detector at the Fermilab Tevatron collider. A Higgs particle with mass greater than 140 GeV decays primarily to a pair of W bosons and the leptonic decay modes provide a clean signature. This channel provides the greatest senstivity to the Higgs at Tevatron. Sophisticated multivariate techniques are used. No excess above the Standard Model is observed, hence upper limits on the Higgs production cross-section for m_H=115-200 GeV are set.

1 Introduction

A search for Higgs boson decyaing to WW* with the DØ detector [1] is presented. At Tevatron, the dominant production mechanism for a high mass ($m_H > 135 \text{ GeV}/c^2$) Higgs is gluon fusion with the dominant decay mode of the Higgs to two W bosons. In order to enhance signal to background significance, W's decaying to electrons and muons are used. Contributions from both vector boson fusion(VBF) and associated production (WH/ZH) have also been used.

2 Event Selection

Each event is characterized by two oppositely charged leptons and missing transverse energy $\not{E}_T$. Events are selected by using a three level trigger system with either a single or dilepton requirements. In the offline analysis, electrons are identified using calorimeter and tracking information, whereas muons are reconstructed from hits in the muon system along with a track match in the central tracker.

The leptons in each final state are required to be isolated, oppositely charged with a p_T greater than 15 GeV. Additionaly the invariant mass of each event is required to be greater than 15 GeV. This is referred to as the pre-selection. At this stage, the dominant backgrounds are the Drell-Yann production and the multijet/qcd background which are subsequently removed by applying requirements on the $\not{E}_T$ and the scaled $\not{E}_T$, defined as :

$$\not{E}_T^{\ scaled} = \frac{\not{E}_T}{\sqrt{\sum_{jets}(\Delta E^{jets} \cdot \sin \theta^{jet} \cdot \cos \Delta\phi(jet, \not{E}_T))^2}} \tag{1}$$

This quantity removes events where the $\not{E}_T$ could be a result of mis-measurement of jet energies.

A further requirement on the minimal transverse mass M_T between either of the leptons and $\not{E}_T$ reduces further variuos backgrounds.

$$M_T(\ell, \not{E}_T) = \sqrt{2p_T^\ell \not{E}_T(1 - \cos \Delta\phi(\ell, \not{E}_T))} \tag{2}$$

Lastly, a large fraction of remaining back to back $Z \to ll$ events are removed by rejecting events with large opening angle between the leptons ($\Delta\phi(l1, l2)$).
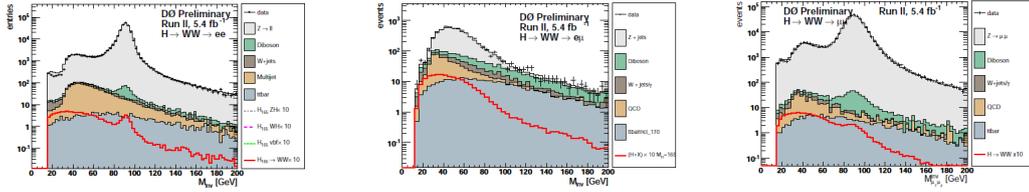

Figure 1: Invariant Mass for the each final state at the preselection stage.

	ee pre-selection	ee final	$e\mu$ pre-selection	$e\mu$ final	$\mu\mu$ pre-selection
$Z \to ee$	274746 ± 266	163.2 ± 2.3	306.4 ± 2.2	0.0 ± 0.0	–
$Z \to \mu\mu$	–	–	312.3 ± 1.0	6.5 ± 0.1	370375 ± 273
$Z \to \tau\tau$	1459 ± 15	0.7 ± 0.2	3858 ± 2	7.5 ± 0.1	2292 ± 3
$t\bar{t}$	158.1 ± 0.7	46.8 ± 0.4	321.3 ± 0.2	97.1 ± 0.1	158.3 ± 0.6
W+jets	302.8 ± 5.9	120.6 ± 4.0	274.2 ± 4.6	115.2 ± 3.3	150.9 ± 2.2
WW	202.6 ± 0.5	73.6 ± 0.3	495.5 ± 0.1	179.1 ± 0.1	235.6 ± 0.4
WZ	135.4 ± 0.1	11.5 ± 0.0	24.1 ± 0.0	7.7 ± 0.0	154.9 ± 0.1
ZZ	114.4 ± 0.1	73.6 ± 0.3	6.3 ± 0.0	0.8 ± 0.0	140.0 ± 0.1
Multijet	1370 ± 41	1.0 ± 1.1	461.7 ± 21.5	5.6 ± 2.4	332 ± 26
Signal ($M_H = 165$ GeV)	10.81 ± 0.01	7.30 ± 0.01	20.3 ± 0.0	14.7 ± 0.0	11.9 ± 0.0
Total Background	278489 ± 269	426.5 ± 4.8	6060 ± 22	419.6 ± 4.1	373838 ± 275
Data	277986	421	6123	403	376973

Figure 2: The event yield's for each final state at pre-selection and final cut stage. The errors shown are purely stastical only.

3   Neural Network

As a final discriminant, neural networks(NN) are used. The NNs are trained for each Higgs boson mass as well as for each final state against all Standard Model backgrounds. Gluon fusion as well as the vector boson fusion are fed as the signal to the NNs. The discriminating inputs used in the network are well described kinematic and topological variables that exploait the difference between the signal and the background, the network is trained and applied on all events passing the final selection requirements as descibed above.
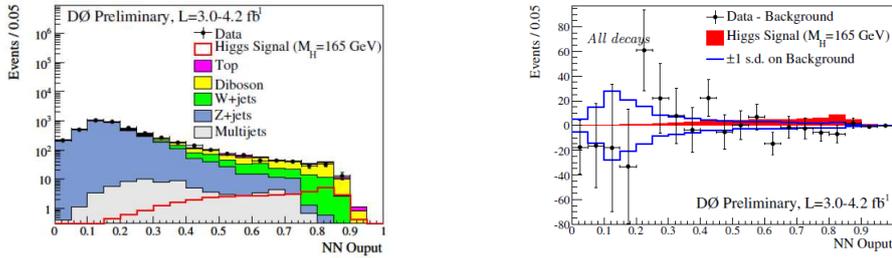
Figure 3: The NN output for all the channels combined(left) and the background subtracted(right).

4 Results and Conclusion

Limits on the cross sections for $\sigma \times BR(H \to W^+W^- \to l^+l^-)$ final states are derived at the 95% confidence level (C.L). The estimates for the expected number of background and signal events depend on numerous factors, and each of them introduce a systematic uncertainty.

Two kinds of systematics are considered in this analysis: flat systematics and shape systematics which modify the shape of the NN distribution. The total uncertainty on the background is approximately 13% and 10% for the Higgs signal. No evidence of Higgs boson is seen ans thus limts on the cross-section times the branching ratios are set. Limits for the combination of all the three channels are calculated using a modified frequentist method, the CL_s method with a log-likeihood ratio (LLR) test statistic.
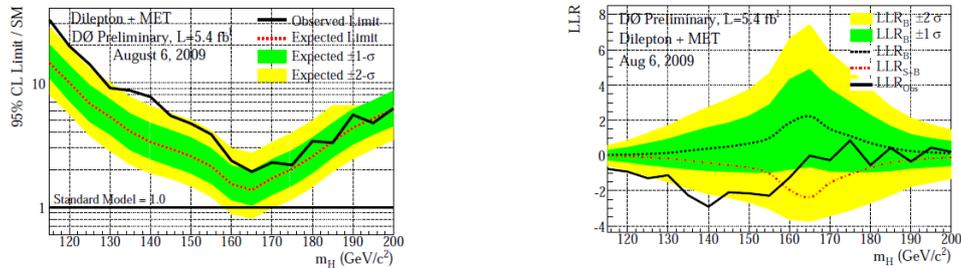
Figure 4: The NN output and the background subtracted nn output.

References

[1] DØ Collaboration, V. Abazov *et al.*, "The Upgraded DØ Detector," Nucl. Instrum. Methods Phys. Res. A **565**, 463 (2006).

Observation of Single Top Quark Production at DØ using Bayesian Neural Networks

Jyoti Joshi, Suman Beri (for the DØ Collaboration)

Panjab University, Chandigarh, India

We present observation of the electroweak production of single top quarks in 2.3 fb^{-1} of data recorded by the DØ experiment at the Fermilab Tevatron collider operating at 1.96 TeV center-of-mass energy. The cross section of single top quark production for the combined $tb+tqb$ channels measured is 4.70 $^{+1.18}_{-0.93}$ pb using Bayesian neural networks (BNN). The probability to measure a cross section at this value or higher in the absence of signal is 3.2 x 10^{-8}, corresponding to a 5.4 standard deviation significance for the observation.

1 Introduction

The standard model (SM) predicts top quarks being produced in pairs via strong interaction or singly via the electroweak interaction. In 1995, discovery of the top quark via strong interaction was announced by DØ and CDF experiments[1]. The electroweak single top quark production has been observed recently[2]. The two main production modes of single top are illustrated in Figure 1: the s-channel (tb) process which proceeds via the decay of virtual W boson, and the t-channel (tqb) process which proceeds via the exchange of virtual W boson. The sum of their predicted cross sections for a top quark mass of 170 GeV is 3.46 ± 0.18 pb[3].
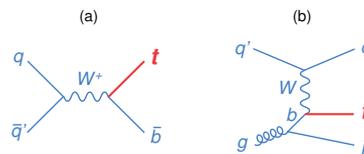
Figure 1: Feynman diagrams for s-channel (a) and t-channel (b) single top production.

2 Event Selection and Analysis Strategy

The 2.3 fb^{-1} dataset used in the analysis is collected from 2002 to 2007 using the DØ detector[4]. The events are selected with a final state consisting of one high transverse momentum (p_T) isolated electron or muon and missing transverse energy ($\not{E}_T$) together with a b-quark jet from the decay of the top quark ($t{\rightarrow}Wb \rightarrow \ell\nu b$), and an additional b antiquark in case of s-channel production, or an additional light-quark jet and a b-antiquark jet for t-channel production. Single top signal events are modeled using COMPHEP-based Monte Carlo (MC) event generator SINGLETOP[5]. $t\bar{t}$ and W+jets backgrounds are simulated using ALPGEN[6], and multijet background is modeled using data which contains non-isolated leptons. All MC events are passed through PYTHIA[7] and then through a GEANT-based full detector simulation. The

selection criteria[2] gives 4,519 events, which are expected to contain 223 ± 30 single top quark events. The analysis is split into 24 separate analysis channels based on lepton flavor (e or mu), jet multiplicity (2,3, or 4) and number of identified b jets (1 or 2), to increase the search sensitivity. Systematic uncertainties are considered for all corrections applied to the background model. The total uncertainty on the background is (8–16)% depending on the analysis channel.
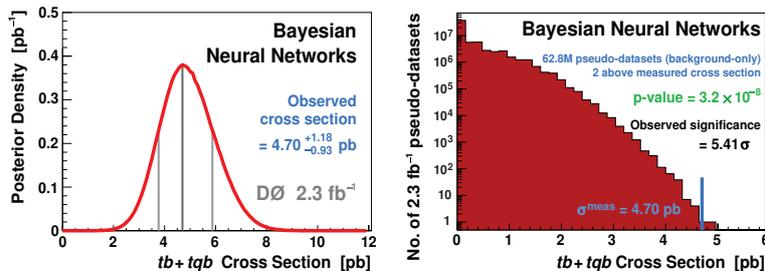
Figure 2: (Left)Posterior density distribution (Right)Cross section distributions on the pseudodatasets for BNN method.

3   Signal-background Separation using BNN

After event selection, we apply Bayesian neural networks (BNN)[8] to extract small single top signal from the large background. A BNN is an average over the output of many neural networks (NN) trained iteratively. Averaging makes the network training more efficient and less prone to overtraining.

We have improved and optimized BNN method from our previous analysis[9] in the choice of input variables and detailed tuning of some parameters. We started from 150 discriminating variables as input and then apply the RuleFitJF algorithm[10] to select the most sensitive kinematic variables, keeping between 18 and 28 of these as inputs, depending on the analysis channel.
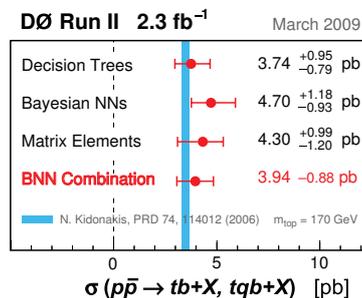
Figure 3: Summary of the measured cross sections compared to theoretical predictions.

4   Cross Section Measurement

We use the BNN output distributions of the 24 analysis channels to form a posterior probability density for the single top production cross section. The position of the peak of the resulting posterior density gives the cross section value and the 68% interval about the peak gives the ± 1 standard deviation (SD) uncertainty. We measure: $\sigma(p\bar{p} \to \mathrm{tb+X,tqb+X}) = 4.70^{+1.18}_{-0.93}$ pb. These measurements are consistent with the SM next-to-leading-order theory calculation.

The sensitivity of analysis to a contribution from single top quark production is estimated by generating an ensemble of pseudodatasets that samples the background model and its uncertainties in the absence of signal. We apply the BNN and measure the cross section for each pseudodataset in the same manner as for the real data which allows us to calculate the probability to measure the SM cross section ("expected significance") or the observed cross section ("observed significance"). The cross section measured by BNN has a $p-$value of 3.2 x 10^{-8} and a significance of 5.4 SD. Figure 2 shows (Left) the posterior density distribution and (Right) the cross section distributions on the pseudodatasets for the BNN method.

Along with BNN, two other MVA techniques are applied: boosted decision trees (BDT) and matrix elements (ME). As the methods are not 100% correlated, we combine them using additional BNN that take as input the output discriminants of the BNN, BDT and ME methods, and produces a single combination output discriminant. The combination leads to an increased expected sensitivity and a more precise measurement of the single top cross section. Figure 3 summarizes the cross sections measured by each of the analysis.

5   Summary

We have used Bayesian neural networks to separate single top quark signal from the background in a sample of lepton+jets events selected from 2.3 fb^{-1} of RunII data. The BNN output distributions across the 24 independent channels were combined using a Bayesian binned likelihood. The measured $tb+tqb$ single top quark production cross section is:

$$\sigma\left(p\bar{p} \rightarrow tb + X, tqb + X\right) \quad = 4.70^{+1.18}_{-0.93} \text{ pb}$$

The observed p-value is 3.2×10^{-8}, which corresponds to a 5.4 standard deviation significance.

References

[1] F. Abe *et al.* (CDF Collaboration), Phys. Rev. Lett. **74** 2626 (1995);
    S. Abachi *et al.* (D0 Collaboration), Phys. Rev. Lett. **74** 2632 (1995).

[2] V.M. Abazov *et al.* (D0 Collaboration), Phys. Rev. Lett. **103** 092001 (2009).

[3] N. Kidonakis, Phys. Rev. D**74** 114012 (2006).

[4] V.M. Abazov *et al.* (D0 Collaboration), Nucl. Instrum. Methods Phys. Res., Sect. **A565** 463 (2006).

[5] E.E. Boos *et al.*, Phys. Atom. Nucl. **69** 1317 (2006).

[6] M.L. Mangano *et al.*, J. High Energy Phys. 07 (2003) 001.

[7] T. Sjostrand, S. Mrenna and P. Skands, J. High Energy Phys. 05 (2006) 026.

[8] R.M. Neal, *Bayesian Learning for Neural Networks* **330** (Springer-Verlag, New York, 1996).

[9] V.M. Abazov *et al.* (D0 Collaboration), Phys. Rev. D**78** 012005 (2008).

[10] J.H. Friedman and B.E. Popescu, Ann. Stat. **2** 916 (2008).

First observation and measurement of the resonant structure of the $\Lambda_b^0 \to \Lambda_c^+ \pi^- \pi^+ \pi^-$ decay mode

P. Azzurri[1], P. Barria[2], M. A. Ciocci[2], S. Donati[3] and E. Vataga[1], for the CDF Collaboration.

[1]Scuola Normale Superiore, Piazza dei Cavalieri 7, 56126 Pisa, Italy
[2]Università di Siena, Dipartimento di Fisica, Via Roma 56, 53100 Siena, Italy
[3]Università di Pisa, Dipartimento di Fisica, Largo Bruno Pontecorvo 3, 56127 Pisa, Italy

We present the first observation of the $\Lambda_b^0 \to \Lambda_c^+ \pi^- \pi^+ \pi^-$ decay using data from an integrated luminosity of approximately 2.4 fb^{-1} of p$\overline{\text{p}}$ collisions at $\sqrt{s}$=1.96 TeV, collected with the CDF II detector at the Fermilab Tevatron. We also present the first observation of the resonant decays $\Lambda_b^0 \to \Sigma_c(2455)^0 \pi^+ \pi^- \to \Lambda_c^+ \pi^- \pi^+ \pi^-$, $\Lambda_b^0 \to \Sigma_c(2455)^{++} \pi^- \pi^- \to \Lambda_c^+ \pi^- \pi^+ \pi^-$, $\Lambda_b^0 \to \Lambda_c(2595)^+ \pi^- \to \Lambda_c^+ \pi^- \pi^+ \pi^-$ and $\Lambda_b^0 \to \Lambda_c(2625)^+ \pi^- \to \Lambda_c^+ \pi^- \pi^+ \pi^-$, and measure their relative branching ratios.

1 Introduction

Presented here is the observation of the $\Lambda_b^0 \to \Lambda_c^+ \pi^- \pi^+ \pi^-$ decay and resonant structure in analogy to the decay structure observed in the $\Lambda_b^0 \to \Lambda_c^+ \pi^+ \pi^- \mu^- \overline{\nu}_\mu$ channel [1]. All new measurements of the Λ_b^0 branching ratios can be compared to theoretical predictions in the heavy quark effective theory (HQEF) approximation [2].

This measurement is based on data from an integrated luminosity of approximately 2.4 fb^{-1} of p$\overline{\text{p}}$ collisions at $\sqrt{s}$=1.96 TeV, collected with the CDF II detector [3], using two-track impact parameter triggers. Unless stated otherwise, branching fractions, fragmentation functions, and lifetimes used in the analysis are obtained from the Particle Data Group world averages [4].

2 Event selection and signal yields

The event reconstruction and selection has been optimized in order to maximize the statistical significance of the total number of Λ_b^0 decays observed on the data. The Λ_c^+ candidates are reconstructed in the $\Lambda_c^+ \to$ pK$^- \pi^+$ channel requiring a vertex χ^2 probability in excess of 10^{-4}, a transverse decay length in excess of 200 μm, $p_\text{T}(\text{p}) > p_\text{T}(\pi^+)$, $p_\text{T}(\Lambda_c^+) > 4$ GeV/c and the Λ_c^+ invariant mass in the 2.24-2.33 GeV/c^2 mass range.

The Λ_b^0 candidates are reconstructed by further adding to the Λ_c^+ candidates three pion candidate tracks, with $\eta\phi$-opening $\Delta R(3\pi)$ smaller than 1.2. The Λ_b^0 candidate is required to have a vertex χ^2 probability in excess of 10^{-4}, a transverse decay length in excess of 200 μm and a significance in excess of 16, an impact parameter smaller than 70 μm, and a transverse momentum in excess of 9 GeV/c.

The resulting distribution of the invariant mass difference $m(\Lambda_c^+ \pi^- \pi^+ \pi^-) - m(\Lambda_c^+)$ with the $\Lambda_b^0 \to \Lambda_c^+ \pi^- \pi^+ \pi^-$ signal peak, is shown in Figure 1. A total signal yield of 848±93 candidates

is evaluated with an unbinned likelihood fit using a Gaussian distribution for the signal, an exponential distribution for the background, and Monte Carlo templates for B^0 and B^0_s backgrounds. In the following Λ^0_b candidates have been selected within 48 MeV/c^2 of the mass peak.
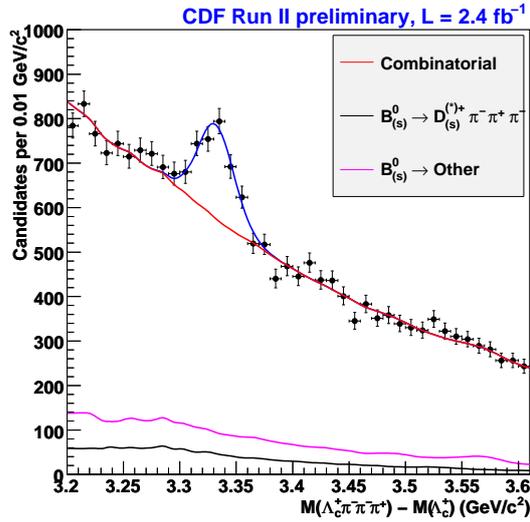
Figure 1: The reconstructed invariant mass difference $m(\Lambda^+_c \pi^- \pi^+ \pi^-) - m(\Lambda^+_c)$, after applying optimized cuts, showing the total $\Lambda^0_b \to \Lambda^+_c \pi^- \pi^+ \pi^-$ signal yield.
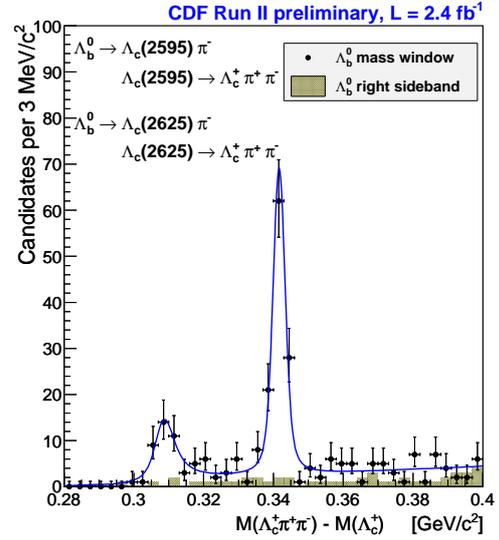
Figure 2: The reconstructed invariant mass difference $m(\Lambda^+_c \pi^- \pi^+) - m(\Lambda^+_c)$ within the Λ^0_b mass window, showing the $\Lambda^0_b \to \Lambda_c(2595)^+ \pi^- \to \Lambda^+_c \pi^- \pi^+ \pi^-$ and $\Lambda^0_b \to \Lambda_c(2625)^+ \pi^- \to \Lambda^+_c \pi^- \pi^+ \pi^-$ signal yields.

The mass difference $\Delta m^{-+} = m(\Lambda^+_c \pi^- \pi^+) - m(\Lambda^+_c)$ for selected Λ^0_b candidates is shown in Figure 2, with the two peaks from $\Lambda_c(2595)^+$ and $\Lambda_c(2625)^+$ decays. A fit performed with two signal peaks and a linear background yields 46.6 ± 9.7 $\Lambda^0_b \to \Lambda_c(2595)^+ \pi^-$ candidates and 114 ± 13 $\Lambda^0_b \to \Lambda_c(2625)^+ \pi^-$ candidates.

Finally the mass differences $m(\Lambda^+_c \pi^+) - m(\Lambda^+_c)$ and $m(\Lambda^+_c \pi^+) - m(\Lambda^+_c)$ are shown in Figure 2, for selected Λ^0_b candidates, after removing $\Lambda_c(2595)^+$ and $\Lambda_c(2625)^+$ decays with the $\Delta m^{-+} > 360$ MeV/c^2 requirement. Separate fits of the two signal contributions yield 41.5 ± 9.3 $\Lambda^0_b \to \Sigma_c(2455)^0 \pi^+ \pi^-$ candidates and 81 ± 15 $\Lambda^0_b \to \Sigma_c(2455)^{++} \pi^+ \pi^-$ candidates.

3 Results

Results are expressed in terms of relative branching fractions between the above resonant decay modes, correcting for the relative channel efficiencies with Monte Carlo simulations. Several sources of systematic effects have been considered, and the dominant uncertainties come from the Λ^0_b and Λ^+_c polarization uncertainty, and on the unknown fraction of non-resonant decays.

In summary the measured relative branching fractions are the following
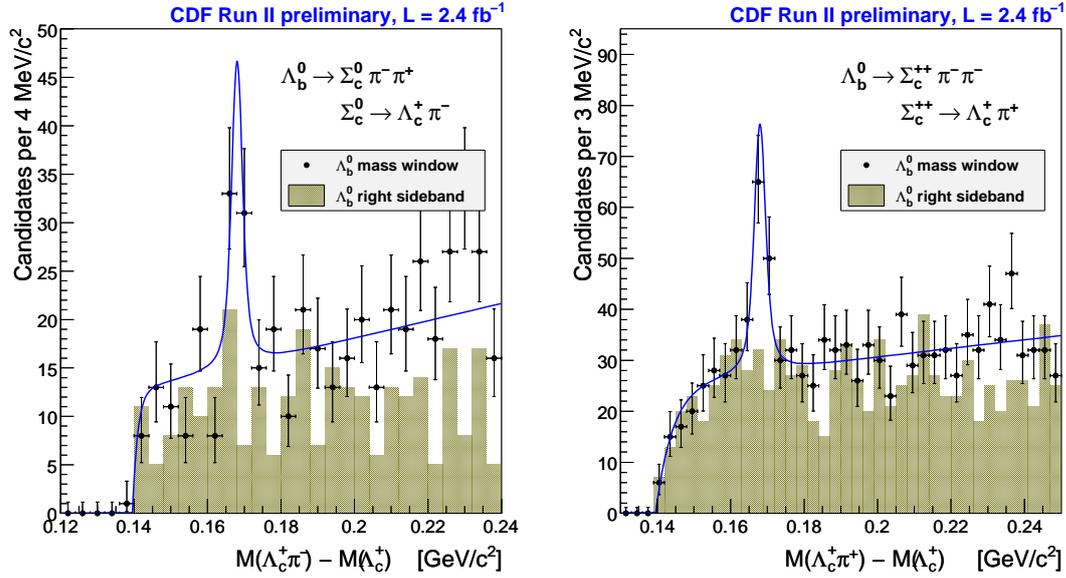
Figure 3: The invariant mass difference $m(\Lambda_c^+\pi^-) - m(\Lambda_c^+)$ (left) and $m(\Lambda_c^+\pi^+) - m(\Lambda_c^+)$ (right) for selected Λ_b^0 candidates, after removing events with $\Lambda_c(2595)^+$ and $\Lambda_c(2625)^+$ decays, and showing respectively the presence of $\Lambda_b^0 \to \Sigma_c(2455)^0\pi^+\pi^-$ and $\Lambda_b^0 \to \Sigma_c(2455)^{++}\pi^-\pi^-$ signals.

$$\frac{\mathcal{B}(\Lambda_b^0 \to \Lambda_c(2595)^+\pi^- \to \Lambda_c^+\pi^-\pi^+\pi^-)}{\mathcal{B}(\Lambda_b^0 \to \Lambda_c^+\pi^-\pi^+\pi^-)} = (2.5 \pm 0.6(\text{stat}) \pm 0.5(\text{syst})) \times 10^{-2}$$

$$\frac{\mathcal{B}(\Lambda_b^0 \to \Lambda_c(2625)^+\pi^- \to \Lambda_c^+\pi^-\pi^+\pi^-)}{\mathcal{B}(\Lambda_b^0 \to \Lambda_c^+\pi^-\pi^+\pi^-)} = (6.2 \pm 1.0(\text{stat})^{+1.0}_{-0.9}(\text{syst})) \times 10^{-2}$$

$$\frac{\mathcal{B}(\Lambda_b^0 \to \Sigma_c(2455)^{++}\pi^-\pi^- \to \Lambda_c^+\pi^-\pi^+\pi^-)}{\mathcal{B}(\Lambda_b^0 \to \Lambda_c^+\pi^-\pi^+\pi^-)} = (5.2 \pm 1.1(\text{stat}) \pm 0.8(\text{syst})) \times 10^{-2}$$

$$\frac{\mathcal{B}(\Lambda_b^0 \to \Sigma_c(2455)^0\pi^+\pi^- \to \Lambda_c^+\pi^-\pi^+\pi^-)}{\mathcal{B}(\Lambda_b^0 \to \Lambda_c^+\pi^-\pi^+\pi^-)} = (8.9 \pm 2.1(\text{stat})^{+1.2}_{-1.0}(\text{syst})) \times 10^{-2}$$

$$\frac{\mathcal{B}(\Lambda_b^0 \to \Lambda_c(2595)^+\pi^- \to \Lambda_c^+\pi^-\pi^+\pi^-)}{\mathcal{B}(\Lambda_b^0 \to \Lambda_c(2625)^+\pi^- \to \Lambda_c^+\pi^-\pi^+\pi^-)} = (40.3 \pm 9.8(\text{stat})^{+2.3}_{-1.8}(\text{syst})) \cdot 10^{-2}$$

$$\frac{\mathcal{B}(\Lambda_b^0 \to \Sigma_c(2455)^{++}\pi^-\pi^- \to \Lambda_c^+\pi^-\pi^+\pi^-)}{\mathcal{B}(\Lambda_b^0 \to \Sigma_c(2455)^0\pi^+\pi^- \to \Lambda_c^+\pi^-\pi^+\pi^-)} = (58.1 \pm 16.9(\text{stat})^{+6.3}_{-9.1}(\text{syst})) \cdot 10^{-2}$$

$$\frac{\mathcal{B}(\Lambda_b^0 \to \Lambda_c(2625)^+\pi^- \to \Lambda_c^+\pi^-\pi^+\pi^-)}{\mathcal{B}(\Lambda_b^0 \to \Sigma_c(2455)^{++}\pi^-\pi^- \to \Lambda_c^+\pi^-\pi^+\pi^-)} = 1.20 \pm 0.26(\text{stat})^{+0.05}_{-0.09}(\text{syst})$$

where the first error is statistical and the second is from systematic uncertainties.

References

[1] T. Aaltonen *et al.* (CDF Collaboration), Phys. Rev. **D79** 032001 (2009).

[2] A. V. Manohar and M. B. Wise, Cambr. Monogr. Part. Phys. Nucl. Phys. Cosmol. 10, 1 (2000); S. Godfrey and N. Isgur, Phys Rev. **D32**, 189 (1985); N. Isgur, D. Scora, B. Grinstein and M. B. Wise Phys Rev. **D39**, 799 (1989); A. K. Liebovich, I. W. Stewart, Phys. Rev. **D57**, 5620 (1998); A. K. Liebovich, Z. Ligeti, I. W. Stewart, M. Wise, Phys Lett **B586**, 337 (2004).

[3] D. Acosta *et al.* (CDF Collaboration), Phys. Rev. **D71** 032001 (2005).

[4] C. Amsler *et al.* (Particle Data Group), Phys, Lett. **B667** 1 (2008).

Commissioning the CMS Pixel Detector with Cosmic Rays

M. Dinardo[1]

[1]University of Colorado at Boulder - USA. On behalf of the CMS collaboration

The pixel detector of the Compact Muon Solenoid (CMS) experiment consists of three barrel layers and two endcap disks at each side of the barrel section. The detector was installed in summer 2008, commissioned with the readout chip internal pulse generator, and used in cosmic ray trigger data taking in a 3.8 T magnetic field. Despite the excellent detector performance some problems arose after installation. In about a year we went through a complete and important sequence of steps that go from the insertion of the detector in CMS, calibration, running, extraction, maintenance, to the re-insertion, re-calibration and final running. Currently 98.6% of the whole pixel detector is fully functional and results on detector performance are found to be in line with the design specifications.

1 Introduction

The CMS experiment [1] is designed to explore physics at the TeV energy scale exploiting the proton-proton collisions delivered by the Large Hadron Collider (LHC) [2]. The new energy frontier that is going to be attained by LHC requires the experiments to gather as much information as possible from each collision. To achieve such a challenging goal in the innermost, radiation hostile region, the high-precision and low-background tracking of CMS is based on the pixel detector [1].

2 Threshold, noise distributions and overall status

The thresholds are controlled at pixel level using two 8-bit DACs per ROC plus one 4-bit trim value per pixel. The readout thresholds and noise are measured by means of threshold scans.

Table 1: Mean noise and mean threshold for both barrel and endcap regions.

	Mean noise	RMS	Mean threhsold	RMS
Pixel barrel	141 e$^-$	35 e$^-$	3829 e$^-$	416 e$^-$
Pixel endcap	85 e$^-$	26 e$^-$	2941 e$^-$	237 e$^-$

The threshold is the value of injected charge where the efficiency is 50%. The noise is measured as the RMS of the curve. In Tab. 1 are reported the mean noise and mean threhsold, together with the their RMS value, for both barrel and endcap regions. The current detector status is: pixel barrel has ∼99% of working channels; pixel endcap has ∼97% of working channels (it's not at 99.5% because after re-insertion we experienced a bandwidth reduction on the analog output for some modules).

3 Cosmic ray data analysis

Approximately 85,000 tracks traversing the pixel detector volume were reconstructed with the Combinatorial Track Finder (CTF) algorithm in the 3.8 T field. For this set of tracks the average number of pixel hits is 3.01, for a total of about 257,000 clusters reconstructed in the pixel system. Pixel clusters are formed from adjacent pixels with a charge above the readout threshold. Both side and corner adjacent pixels are included in the cluster and a cut of 5,000 electrons is applied to the total charge. The cluster is projected along the sensitive directions by summing the charge collected in the pixels with the same coordinate. Residual charge miscalibration due to the pixel-to-pixel variation of the charge injection capacitor is modeled in the Montecarlo simulation. Figure 1 shows the simulated and measured cluster charge corrected for the track incident angle. To emulate the acceptance expected from collisions, tracks with angles in the transverse plane larger than 12° from normal are excluded from the study. Clusters are required to include at least two pixels and those with edge pixels are excluded from the sample. Finally, events with more than one cluster in the same sensor are excluded.
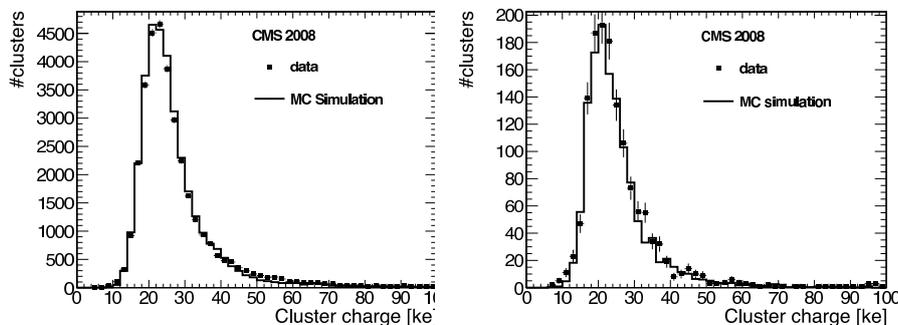
Figure 1: Charge distribution in kiloelectrons (ke) for clusters larger than one pixel measured with the barrel and endcap pixel detector in the first and second plot respectively. The data points show the measurement with cosmic rays and the solid line the simulation.

The residual distributions are measured as a function of the impact angles and cluster charge and a Gaussian fit is performed in each bin. The contributions to the width of the residual distribution are the track extrapolation error, the detector intrinsic resolution and multiple scattering contribution. The track extrapolation error is the largest contribution and includes the uncertainties due to residual misalignment of the sensors used in the trajectory extrapolation with respect to the measured sensor. Figure 2 shows the width from the Gaussian fit of the residual distribution as a function of the α and β angles and total cluster charge. For tracks normal to the sensor plane the Gaussian sigma is about 30 μm and 65 μm along the local x and y coordinates, respectively. The width strongly depends on the cluster charge and impact angles.

The intrinsic detector position resolution is measured using tracks traversing overlapping sensors in the barrel layers. Tracks passing through two overlapping modules in the same layer are used to compare the hit position with the expected position from the track trajectory. The difference in local hit position (ΔX_{hit}) of the track predictions is much more precisely known than the individual predicted positions. The double difference is formed by taking the difference between the hit position difference and the predicted position difference (ΔX_{pred}).
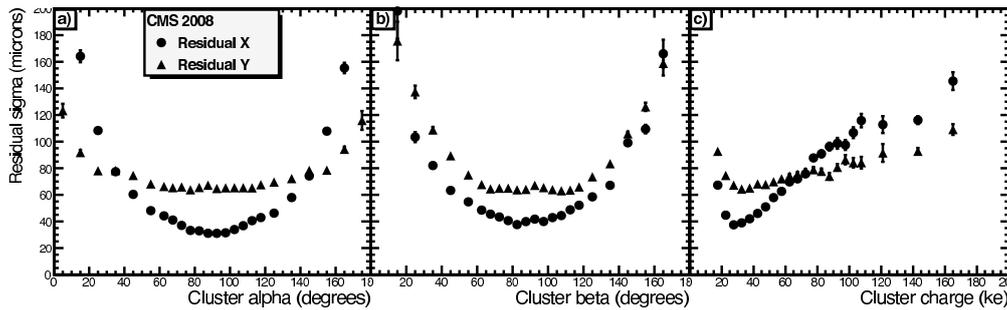
Figure 2: Pixel hit residuals as function of the transverse and longitudinal impact angles and cluster charge in kiloelectrons. The full circles correspond to the transverse coordinate and the full triangles to the longitudinal coordinate. Tracks have a momentum larger than 10 GeV/c. Impact angles of 90° correspond to normally incident tracks.

The width of this double difference distribution is insensitive to translational misalignment of the overlapping modules. The double difference widths are fit with a Gaussian and the uncertainty from the tracking prediction are subtracted to recover the hit resolution on the position difference. With the assumption of equal resolution for each of the modules in the overlap, the final fit values for the resolution for a single module is 18.6±1.9 μm along x and 30.8±3.2 μm along y. Events with the same range of impact angles as in the measured sample have been simulated in detail. The residual distributions are obtained comparing the true and reconstructed hit positions. A Gaussian fit to the simulated residual distribution gives a RMS of 22.1±0.2μm and 28.5±0.1μm along the x and y coordinates, respectively. The simulated values agree well with the measurements.

4 Conclusions

After installation in July 2008, the CMS Silicon pixel detector was rapidly commissioned and then operated in a month-long cosmic ray trigger run in October 2008. About 94% of the forward disks and 99% of the central barrel were included in this commissioning cosmic ray run. Online charge calibration permitted comparison of charge measurements with expectations from simulation, showing good agreement for charge distributions. Using tracks intersecting overlapping modules, hit resolutions of 20 μm ($r - \phi$) and 30 μm (z) are extracted from the small statistics available in the barrel detector. These results are in line with the expectations presented in Ref. [3]. Currently 98.6% of the whole pixel detector is fully functional. The thresholds are close to the minimum achievable. With the first data taken with the beam it is planned to time-align the different portions of the pixel detector with respect to the beam collisions and improve the spatial alignment.

References

[1] CMS Collaboration, *The CMS experiment at the CERN LHC,* JINST **0803** S08004 (2008).

[2] L. Evans and P. Bryant, *LHC machine,* JINST **3** S08001 (2008).

[3] CMS Collaboration, *CMS physics: Technical design report,* CERN-LHCC-2006-001 (2006).

First Alignment of the CMS Tracker and Implications for the First Collision Data

Johannes Hauk[1] on behalf of CMS Tracker Alignment Group

[1]Deutsches Elektronen-Synchrotron DESY, Notketraße 85, 22607 Hamburg, Germany

We present first results from the full alignment of the silicon tracking system of the CMS experiment. The alignment is done using about 3.2 million tracks from cosmic data taken during commissioning runs in 2008 with the detector in its final position named Cosmic Run at Four Tesla (CRAFT), in combination with survey measurements. Results are validated and tested against prediction with detailed detector simulation. The achieved resolution in all five track parameters is controlled. Implications for the CMS physics performance are discussed.

1 Design of the tracking system

The CMS tracker [1] is completely based on silicon pixel and strip modules (Fig. 1). They are mounted concentrically about the beam axis on different mechanical structures called subdetectors. Close to the beam pipe there is the pixel detector containing 1440 pixel modules in two subdetectors, which is surrounded by the strip detector. The 15 148 strip modules are divided among the subdetectors tracker inner barrel (TIB), outer barrel (TOB), inner disks (TID), and end caps (TEC). The modules are assembled into hermetic layers. The solenoid magnet provides an almost homogeneous magnetic field of 3.8 T throughout the tracker volume.

Figure 1: Upper right quarter of the longitudinal section of the CMS tracker. All strip subdetectors are illustrated (TIB, TID, TOB, TEC). Empty boxes show combined strip modules. Full Boxes show pixel modules or single strip modules. Further, the Laser Alignment System is visible (A, B, R).

The tracker is intended to reconstruct trajectories of charged particles ("tracks") based on a set of local coordinate measurements of traversed silicon modules ("hits"). The intrinsic resolution of the modules for hits is in the range 10–30 μm. For 100 GeV/c muons the tracker is expected to achieve a transverse momentum resolution of about 1.5 % and an impact parameter resolution of about 15 μm. The latter is necessary especially for efficient b-tagging. The values

are determined from simulation studies based on the design (ideal) geometry [1]. To reach this performance, it is crucial to know the alignment parameters $\mathbf{p}$ (positions x, y, z and orientations α, β, γ of all modules) to very high precision, so that the uncertainty of a measurement along a sensitive coordinate is less than $10\,\mu$m. The following studies are published in detail in [2].

2 Approaches and results of track-based alignment

2.1 Track-based alignment

The mounting precision of $O(100\,\mu\text{m})$ is by far not sufficient for the goals of physics analyses. The desired accuracy is gained with track-based alignment at the module level. It is based on the reconstruction of charged particle tracks:

Hit candidates are constructed from the induced charge distributions on the pixels or strips. For every hit measurement i, position coordinates x_{hit} and corresponding errors are estimated within the local coordinate frames of the modules. Hit candidates are assembled into track candidates by the pattern recognition procedure, and track parameters $\mathbf{q}$ for every track j are estimated by the track fit. This depends strongly on the alignment parameters $\mathbf{p}$.

The alignment procedure uses the constraints implied by the track model to estimate alignment corrections to the geometry. Deviations in geometry are reflected in the hit residual r, which is defined as the difference of the hit and the track prediction on the module's plane, x_{track}, for each independent measurement coordinate,

$$r_{ji} = x_{ji,\text{track}}\left(\mathbf{p}, \mathbf{q}_j\right) - x_{ji,\text{hit}}\,.$$

The distribution of residuals normalized by their errors is approximately Gaussian with a width of about 1, centered at 0, when there are no uncertainties in alignment parameters. Misalignment increases the spread of the residuals in general. This is reflected in an increase of the total χ^2-function, containing the goodness of all track fits,

$$\chi^2_{\text{tot}}\left(\mathbf{p}, \mathbf{q}\right) = \sum_j^{\text{tracks}} \sum_i^{\text{hits}} \frac{r_{ji}^2}{\sigma_{ji}^2}\,.$$

The algorithms estimate alignment parameters by minimizing this function using millions of tracks. This needs sophisticated statistical approaches, since the track fits depend on the alignment. Two algorithms are applied. The local method named HIP (Hits and Impact Points) estimates the parameters for each module. Then iterations are needed to take the correlations with the track fit into account. It uses the same track model as the reconstruction. The minimization is stabilized by including the survey information. The global method (Millepede II) fits all track and alignment parameters simultaneously. The advantage is that all correlations are considered, but its current implementation in CMS is restricted to a helical track model.

2.2 Input data

In 2008, the tracker was operated in its final position for one month to measure cosmic muons with the solenoid at the nominal magnetic field strength of 3.8 T. About 3.2 million tracks were considered to be useful for alignment. The selection contains tracks with at least eight hits and
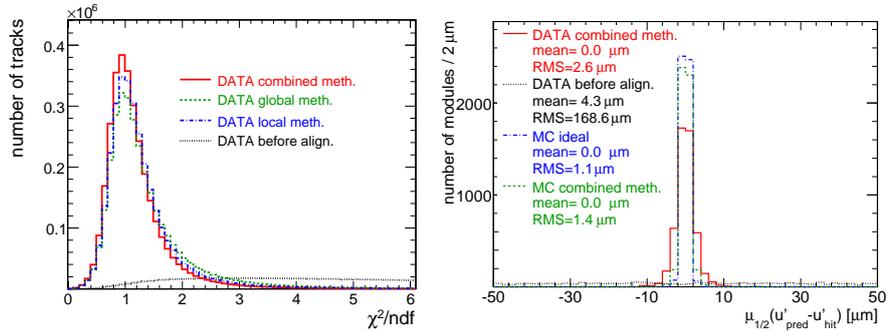
Figure 2: Distribution of normalized χ^2 of tracks (left) and distribution of module-wise medians of the hit residual distributions of TOB modules (right).

momentum $p > 4\,\mathrm{GeV/c}$. Furthermore, a defined measurement of the polar angle θ is required. Finally, only hits passing quality and outlier rejection criteria were used in the track fits.

For comparisons, a similar number of tracks was simulated using the standard Monte Carlo program. They show good agreement in the statistical distribution of the track parameters.

Survey measurements provide another source of alignment information. For all sub-detectors the mounting precision of sub-structures was estimated during integration. For TIB and TID the position of every module was also measured. The information can be used in the track-based alignment to set constraints by adding a term to the total χ^2-function.

2.3 Validation of alignment results

The first step of track-based validation is to analyze the distribution of values of track χ^2 normalized by its number of degrees of freedom (Fig. 2 (left)), and the hit residual distributions grouped per subdetector. While each algorithm applied individually leads to a respectable improvement of the goodness of fit, the best result is obtained by first running the global method and then applying the local method on the geometry based on the global method.

A sensible measure for the remaining misalignment is the distribution of module-wise medians of the residual distributions (DMR), as shown in Fig. 2 (right) for the TOB. Its broadening gives a lower limit for misalignment. Due to the largely vertical nature of the cosmic track data, the achieved alignment accuracy depends on the detector region. However, the observed performance is close to the expectation obtained by applying alignment algorithms to a simulated data sample of comparable statistics. The simulation gives also the smallest width achievable with present statistics for the case where the alignment parameters are fully known.

A particular challenge are weak modes. These are systematic distortions, which influence the χ^2-distribution only slightly, but can cause a significant bias in physics results (see Ref. [2]).

2.3.1 Overlap Residuals

Overlapping modules of the same layer can have hits from the same track. The difference in measured residuals for common tracks allows an understanding of relative misalignment within one layer. The mean of the distribution per pair can be indicative of shifts. Significant improvement is visible for all barrel detectors, as Fig. 3 (left) illustrates in case of the TIB.
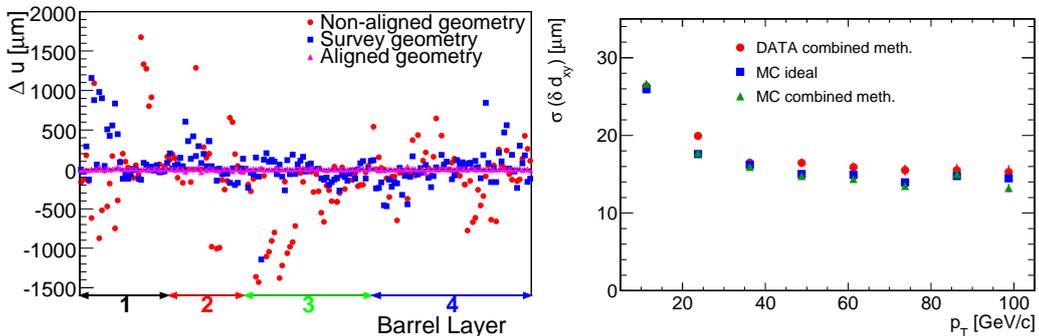
Figure 3: Mean values of overlap residuals for module pairs of TIB layers (left). RMS of the distribution of the difference between transverse impact parameters d_{xy} from track splitting with respect to transverse momentum p_{t} (right).

3 Tracking performance and impact on physics analyses

Misalignment causes a degradation of the tracking performance and influences the performance of many physics analyses. For example, b-tagging methods resolving lifetime signatures are sensitive to the spatial resolution and hence alignment accuracy. The impact parameter resolution is studied by splitting long tracks passing close to the interaction region at the point of closest approach related to the beam line. Both halves are reconstructed independently and their parameters are compared at the splitting point. The resolution of most parameters is almost as good as in the simulation. For the transverse impact parameter, d_{xy}, less than $20\,\mu$m is achieved for $p_{\mathrm{t}} > 20\,\mathrm{GeV/c}$ (Fig. 3 (right)). However, at this point effects from weak modes cannot be excluded. These can shift the track parameter values systematically and bias subsequent steps.

4 Conclusions

The first track-based alignment with the full tracker has been performed successfully. The local and global methods deliver similar results and show dramatic improvement in the alignment quality. However, a combined approach gives the best results. The cosmic track splitting shows that the resolution of track parameters is excellent, the RMS of the transverse impact parameter is less than $20\,\mu$m for transverse momenta above $20\,\mathrm{GeV/c}$. Updates on predicted misalignment uncertainties and scenarios, as well as studies on weak modes have been performed. An extensive discussion can be found in [2]. The alignment procedure is well advanced and ready for collision data taking.

References

[1] R. Adolphi et al. The CMS experiment at the CERN LHC. *JINST*, 0803:S08004, 2008.

[2] CMS Collaboration. Alignment of the CMS Silicon Tracker during Commissioning with Cosmic Rays. 2009.

Calibration of the CMS Magnetic Field using Cosmic Muon Tracks

Sara Bolognesi

CERN, 1211 Geneve 23, Switzerland

The CMS detector is designed around a large 4 T superconducting solenoid, enclosed in a 12 000-tonne steel return yoke instrumented with muon chambers. Using a large sample of cosmic muon events collected by CMS in 2008, the field in the steel of the barrel yoke has been determined with a precision of 3 to 8% depending on the location.

1 Magnetic field in CMS

The Compact Muon Solenoid (CMS) [1] is a general-purpose detector whose main goal is to explore physics at the TeV scale by exploiting the proton-proton collisions provided by the Large Hadron Collider (LHC) [2] at CERN. During October-November 2008, the CMS Collaboration conducted a data-taking exercise known as the Cosmic Run At Four Tesla (CRAFT) [3]: 270 million cosmic ray triggered events have been recorded with all installed detector systems participating and with the solenoid at a central magnetic flux density of 3.8 T. Using these data it was possible for the first time to probe the magnetic field in the steel of the barrel return yoke using reconstructed muon tracks.

The CMS silicon tracker is located inside the superconducting coil of the CMS magnet. Within that region, the field has a high strength, is relatively homogeneous and has been mapped with an accuracy better than 0.1%. This precision is crucial for physics analyses as it allows accurate measurements of charged particle track parameters near the interaction vertex.

The CMS barrel yoke is composed of five three-layered dodecagonal barrel wheels. The steel plates of the yoke return the flux of the solenoid and are interleaved with four layers of muon chambers. They serve as


Figure 1: Value of $|B|$ (left) and field lines (right) predicted on a longitudinal section of the CMS detector at a central magnetic flux density of 3.8 T. Each field line represents a magnetic flux increment of 6 Wb.

absorber and at the same time provide additional bending power for a measurement of the muon

momentum independent of the inner tracking system. The resolution in this case is limited by multiple scattering, by the finite resolution of the muon chambers, and by their alignment. To ensure that the systematic uncertainty due to the inaccuracy of the field map is negligible, the benchmark is set at 3% for the overall scale uncertainty and at 5% for the scale in individual plates in the barrel return yoke. These limits are conservative, as they are obtained for the extreme case of a fit with no vertex constraint. With a constrained fit the accuracy of the field in the return yoke can be relaxed by one order of magnitude.

A detailed map of the magnetic field is required for the accurate simulation and reconstruction of physics events. The CMS solenoid and yoke were modeled using the TOSCA finite element program [4]. The predicted magnetic flux density on a longitudinal section of the CMS detector is shown in Fig. 1.

Besides accuracy, computing efficiency of the map interface is a key requirement, as the map is accessed intensively during the on-line reconstruction in the High-Level Trigger. A compact field map of the entire CMS detector has been produced exploiting the 12-fold ϕ-symmetry of the yoke, with special treatment for the sectors affected by the main ϕ-asymmetric features (passages to route connections, supporting feet and carts, the steel plate on the floor).

2   Analysis method and results

The four stations of Drift Tube (DT) chambers which are interleaved with the three steel yoke layers can measure the direction of the track in the transverse plane (ϕ) with a resolution of about 1.8 mrad [5]. The track deflection in the transverse plane between two consecutive stations, i and $i + 1$, is related to the average axial component of the magnetic field along the track path in the steel plate (L):

$$(\phi_{i+1} - \phi_i)p_T = -0.3 \, q \int_i^{i+1} \vec{u}_\phi \cdot \vec{B} \times d\vec{l} \simeq -0.3 \, q \langle B_z \rangle L \tag{1}$$

where q is the muon charge, p_T is the muon transverse momentum in units of GeV/c, B is expressed in Tesla, and L in meters.

Given that the accuracy of the magnetic field map in the region inside the solenoid is very good, the momentum measured by the inner tracker can be taken as reference. The track parameters reconstructed there are extrapolated to the muon spectrometer, where they are compared with the measurements of the muon chamber. The extrapolation of track parameters and of their error matrices is performed taking into account multiple scattering and energy loss.

The correction that has to be applied to the magnetic field map B_z^{map}, in each point within the considered steel yoke plate, in order to obtain the best estimate of B_z^{true} that reproduces the measured track bending as observed in that plate is given by:

$$\frac{[(\phi_{i+1}^{\mathrm{prop}} - \phi_{i+1}^{\mathrm{data}}) - (\phi_i^{\mathrm{prop}} - \phi_i^{\mathrm{data}})] \cdot p_T}{(\phi_{i+1}^{\mathrm{prop}} - \phi_i^{\mathrm{prop}}) \cdot p_T} = \frac{\langle B_z^{\mathrm{map}} \rangle - \langle B_z^{\mathrm{true}} \rangle}{\langle B_z^{\mathrm{map}} \rangle}|_{i+1/i}. \tag{2}$$

where ϕ_i^{prop} and ϕ_i^{data} are the bending angles at the ith DT station for the propagated track and for the track segment reconstructed in the DT chamber, respectively.

Misalignment affects the measured angles of positive and negative muons in the same direction, while a distortion of the field map has an opposite effect on the propagated direction of tracks of opposite charge. The charge-antisymmetric combination of the numerator and denominator of the expression on the left side of Eq. 2 is therefore considered.

The results are listed in Tab. 1.

In order to search for possible biases the correction factors were averaged, grouping steel plates in different ways. For instance, given the propagation direction of the cosmic muons, inaccuracies in the energy loss estimation would be visible as an opposite bias in the scaling factors of upper and lower sectors. No biases are found to exceed the statistical uncertainties ($<1\%$).

	wheels ± 2	wheels ± 1	wheel 0
L1	0.99 ± 0.04	1.004 ± 0.004	1.005 ± 0.005
L2	0.96 ± 0.02	0.958 ± 0.003	0.953 ± 0.003
L3	0.92 ± 0.08	0.924 ± 0.003	0.906 ± 0.003

Table 1: Correction factors of the field map $\langle B_z^{\mathrm{true}} \rangle / \langle B_z^{\mathrm{map}} \rangle$ for each steel layer, from innermost one to outermost one, averaged between all the sectors in opposite wheels. Reported errors represent the statistical uncertainty only.

2.1 Systematics

Beside the effects of the misalignment and of the energy loss due to the material budget, which have been already mentioned, other systematic effects should be considered.

- The muon segment angle measured in each DT station can be affected by the imperfect knowledge of the internal geometry of the chambers (the assembly procedure can give an uncertainty of 1 mm in the chamber thickness [6]).

- A single correction factor is computed per each steel block for the average B field discrepancy, its local variations within the block are not considered.

- The measured correction factors for all sectors in each layer and wheel, as well as in opposite wheels, are compatible and can be averaged. However, residual differences of up to $\pm 1\%$ in the field integral for a radial path are predicted by the TOSCA model among the sectors where symmetry is assumed to hold.

- The radial component of the field is neglected but its presence affects both the real muon bending and the track extrapolation so a bias on the measured scaling factor is expected only if the ratio $B_r^{\mathrm{true}}/B_r^{\mathrm{map}}$ differs from the ratio $B_z^{\mathrm{true}}/B_z^{\mathrm{map}}$

Considering all the statistical and systematic uncertainties, the correction factors of the field map are determined with a precision better than 3% in the three inner wheels, while in the external wheels the precision is about 5% in the innermost yoke steel layer, 3% in the middle one and 8% in the outermost one.

References

[1] CMS Collaboration. The CMS experiment at the CERN LHC. *JINST*, 3:S08004, 2008.

[2] Lyndon Evans, (ed.) and Philip Bryant, (ed.). LHC Machine. *JINST*, 3:S08001, 2008.

[3] CMS Collaboration. Commissioning of the CMS Experiment and the Cosmic Run at Four Tesla. 2009.

[4] Vector Fields Ltd. Oxford, U. K. Tosca/opera-3d software. *http://www.vectorfields.com*.

[5] CMS Collaboration. Performance of the CMS Drift Tube Chambers with Cosmic Rays. 2009.

[6] CMS Collaboration. CMS Physics TDR: Volume I, Detector Performance and Software. *CERN-LHCC-2006-001*.

Electron and photon measurement with the CMS detector

Stefano Argirò[1] for the CMS Collaboration

[1]University of Torino, Italy, and INFN

Electrons and Photons play a crucial role at LHC in several fields. They provide important signatures for discovery of the Higgs Boson, for discovery of supersymmetry, or for the discovery of new heavy bosons like the Z'. Clean identification and excellent energy and momentum resolution where given high priority in the design of the CMS detector. The instrument, featuring a finely grained, high-resolution electromagnetic calorimeter and excellent tracking performances, is well equipped for the task of measuring these particles with high precision. In this contribution we will describe the CMS electron and photon identification and reconstruction capabilities.

1 Introduction

The CMS detector was designed giving great importance to the identification and measurement of photons and electrons. The goals of the experiment include the search for the Higgs boson, the search for new heavy bosons and the identification of possible supersymmetric particles. Two of the most promising discovery channels for the Higgs boson are $H \rightarrow \gamma\gamma$ and $H \rightarrow l^+l^-e^+e^-$ with $l = \mu, e$. For the first one, an excellent resolution of the photon energy is required in order to discern a possible invariant mass peak from the background. An hypothetical Z' boson could decay to an electron pair, which would be important to measure with high precision. Also, it is important to measure leptons in the final state of possible supersymmetric particles. The CMS detector relies on the Electromagnetic calorimeter (ECAL) to measure photons with high precision, and on the combination of the ECAL and tracking detectors to identify and reconstruct electrons.

2 The Electromagnetic Calorimeter (ECAL)

The ECAL is made of 76000 lead tungstate scintillating crystals, arranged in a *barrel* for the central region and an *endcap* for the forward regions. Crystals are equipped with avalanche photo diodes in the barrel and vacuum photo triodes in the endcaps. For energies above 100GeV the resolution is dominated by a constant term determined predominantly by the intercalibration precision. For lower energies the resolution is dominated by a stochastic term of around $2.8\% /\sqrt{E}$. Several studies have shown that it will be possible to intercalibrate each channel to a precision of 0.5%.

3   Energy reconstruction

97% of the shower produced by unconverted photons is contained in the 5x5 matrix of crystals in the η, ϕ plane. Nearly 50% of the photons will convert in the tracker material. For electrons the measurement is complicated by bremsstrahlung phenomena. Because of the 3.8 T solenoidal magnetic field, bremsstrahlung photons will deposit their energy in the calorimeter in the form of small clusters along the ϕ coordinate. This energy is recovered using appropriate clustering algorithms that identify superclusters, i.e. clusters of clusters including those produced by the original electron and its radiated photons. Starting with a seed crystal containing a local maximum of energy, superclusters are built within a narrow window in eta, following the energy spread by the magnetic field in the phi direction.

4   Photon identification and reconstruction

Excellent reconstruction of unconverted photons can be achieved in CMS. The energy of those photons is measured best using the energy contained in a 5×5 crystal matrix around the seed crystal, corrected for the lateral leakage correction $f(\eta)$ and for module border effects but otherwise uncorrected. Several criteria are used to identify true photons: tracker isolation, ECAL isolation, hadron calorimeter isolation, hadronic to electromagnetic ratio and R_9, which is the ratio of the energy contained in a 3×3 matrix and the supercluster energy. For example a π^0 will have a lower value of R_9 (Figure 1) when compared to an isolated photon.
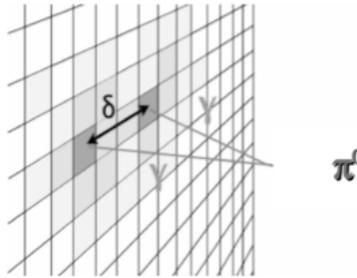
Figure 1: A π^0 produces a shower with a low value of R_9

5   Electron identification and reconstruction

Electron candidates are found when a supercluster can be associated to a track reconstructed in the silicon tracker detector, and in particular its innermost layers. The seeding strategy can be ECAL driven or tracker driven. The ECAL driven electron seeding is very efficient for $p_T^e > 10 GeV/c$. The tracker driven seeding uses a boosted decision tree to perform a preselection of the tracker clusters, in order to reduce the fake rate due to light hadrons. This strategy is more efficient for low p_T electrons and electrons within jets (non isolated). The electron track fit must account for the different energy loss mechanism of electrons compared to other charged particles, in particular the non gaussian nature of bremsstrahlung losses. This is accomplished using the Gaussian Sum Filter, that allows a good estimation of the track momentum both

at the ECAL surface and at the interaction point. The reconstruction efficiency measured on di-electron events using a tag and probe method is shown in Figure 2 .
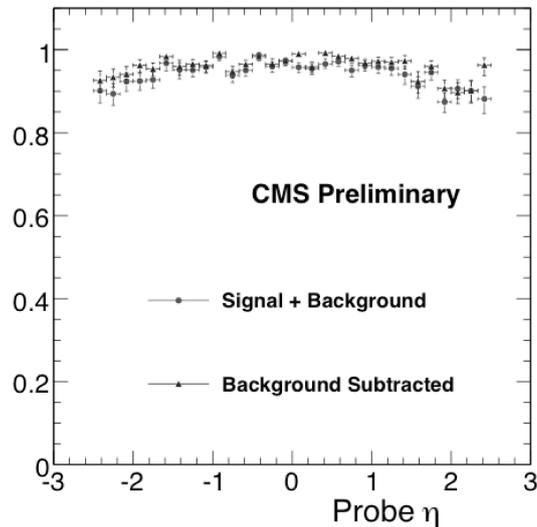
Figure 2: Electron reconstruction efficiency as a function of pseudorapidity studied on di-electron events

6   Conclusions

The CMS electromagnetic calorimeter is ready for data taking. It has been intercalibrated using cosmic rays stands and test beams to a level of 1% or 2% in the barrel and 10% in the endcaps. Cross checks have been performed using dE/dx measurements and beam dump events. Simulations show that the electron and photon reconstruction algorithms perform well. Of course much tuning work will be needed to understand the detector once real data are available.

References

[1] The CMS Collaboration, The CMS Experiment at the CERN LHC, JINST 3:S08004 (2008).

[2] The CMS Collaboration, The Electromagnetic Calorimeter Project Technical Design Report, CERN/ LHCC 97-33 (1997), ISBN 92-90831-122-1.

[3] The CMS Collaboration, Crystal ECAL Performance and Operation, CMS PAPER CFT-09-004.

[4] E. Meschi, T. Monteiro, C. Seez and P. Vikas, Electron Reconstruction in the CMS Electromagnetic Calorimeter, CMS NOTE 2001-034.

[5] The CMS Electromagnetic Calorimeter Group, Intercalibration of the barrel electromagnetic calorimeter of the CMS experiment at startup, CMS NOTE 2008/018.

[6] S. Baffioni et al., Electron reconstruction in CMS, CMS NOTE-2006/040.

Drift velocity and pressure monitoring of the CMS muon drift chambers

Lars Sonnenschein[1] on behalf of the CMS collaboration

[1]RWTH Aachen University, III. Physikalisches Institut A, 52056 Aachen, Germany

The drift velocity in drift tubes of the CMS muon chambers is a key parameter for the muon track reconstruction and trigger. It needs to be monitored precisely in order to detect any deviation from its nominal value. A change in absolute pressure, a variation of the gas admixture or a contamination of the chamber gas by air affect the drift velocity. Furthermore, the temperature and magnetic field influence its value. First data, taken with a dedicated Velocity Drift Chamber (VDC) built by RWTH Aachen IIIA are presented. Another important parameter to be monitored is the pressure inside the muon drift tube chambers. The differential pressure must not exceed a certain value and the absolute pressure has to be kept slightly above ambient pressure to prevent air from entering into the muon drift tube chambers in case of a leak. Latest drift velocity monitoring results are discussed.

1 Introduction

The muon drift tube chambers of the CMS detector rely crucially on the accurate knowledge of the drift velocity to reconstruct muon tracks as precise as possible. A monitor system for the direct measurement of the drift velocity is presented together with chamber gas pressure monitoring. In the first section the CMS muon drift tube chambers are explained, followed by two sections about their pressure and drift velocity monitoring, including latest measurements.

2 CMS muon drift tube chambers

The barrel of the CMS detector [1] consists of five wheels, each instrumented with 50 muon Drift Tube (DT) stations outside the 4 T solenoid magnet, arranged in four radial layers embedded in the iron return yoke of the solenoid. Each station is 29 cm thick and has a length along the beam axis of 2.5 m, given by the wheel width. Depending on the layer the station width varies between two and four meters. The three inner muon stations consist of three and the outermost of two superlayers which in turn consist of four layers of drift cells. The drift cells of the inner- and outermost superlayers are oriented parallel to the beam axis to measure the projection of muon tracks perpendicular to the beam axis. The middle superlayer (present in the three inner muon stations) is dedicated to the measurement of the track projection along the beam axis. The drift cells are arranged with a pitch of 42 mm × 13 mm. Field shaping strips (+1800 V) at the inner bottom and top of the drift cell are responsible for a very homogeneous electric field between the anode (+3600 V) and the cathode (-1200 V). The drift cells are operated with a

gas admixture of Ar (85% vol.) and CO_2 (15% vol.) at slight overpressure ($\sim$ 2 - 10 mbar). If a muon crosses a cell, ionised molecules drift to the cathode while electrons reach the anode sense wire. The crossing position of the muon can be computed by means of the drift velocity assuming linear behaviour due to a homogeneous electric field.

3 Pressure monitoring

The drift tubes are operated at slight overpressure of about 2 - 10 mbar. There are two gas manifolds at each chamber, one at the inlet and one at the outlet side. Each manifold is equipped with two pressure sensors, one with ±100 mbar and one with ±500 mbar relative pressure range, producing an analog signal of 0 - 4.5 V which is being digitised locally to ten bit precision, in modules called PADC's. The pressure monitoring allows one to limit the overpressure to the range of $0 < p < 20$ mbar. This is important to avoid contamination by ambient air and at the same time to stay well within the safety margin. Larger leakages can be detected by input - output differences. The drift velocity measurement in the Velocity Drift Chamber (VDC) can be corrected for the measured overpressure. Furthermore, each chamber is equipped with temperature sensors to allow for monitoring and corrections.

4 Drift velocity monitoring

A gas sample from the DT's is piped to the VDC monitoring system and to commercial oxygen and humidity analysers, to check for gas anomalies. The outlet of each of the 250 DT chambers, as well as the supply gas arriving at each barrel wheel can be individually sampled. Fig. 1 shows the working principle of a VDC. It consists of a small (one litre) single drift cell chamber equipped with anode (up to +1900 V), cathode (up to -15000 V) and field shaping electrodes. Two electron beams cross a sensitive region between anode and cathode. The sensitive region is characterised by a highly uniform electric field. The electrons are detected by a scintillating fibre and two silicon photomultipliers (SiPM's) in coincidence to provide a trigger. The drift times of the two beams are recorded with respect to the trigger. The average drift time between both parallel beams, separated by 4.8 cm is being measured and leads to a drift velocity distribution as e.g. shown in Fig. 2, left to 54.8 μm/ns with a width of 0.1 μm/ns by means of a single

Figure 1: Principle and geometry of the Velocity Drift Chamber (VDC).
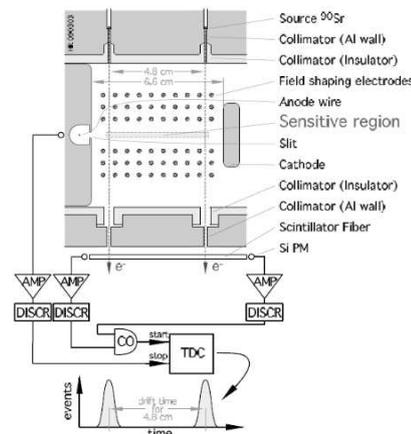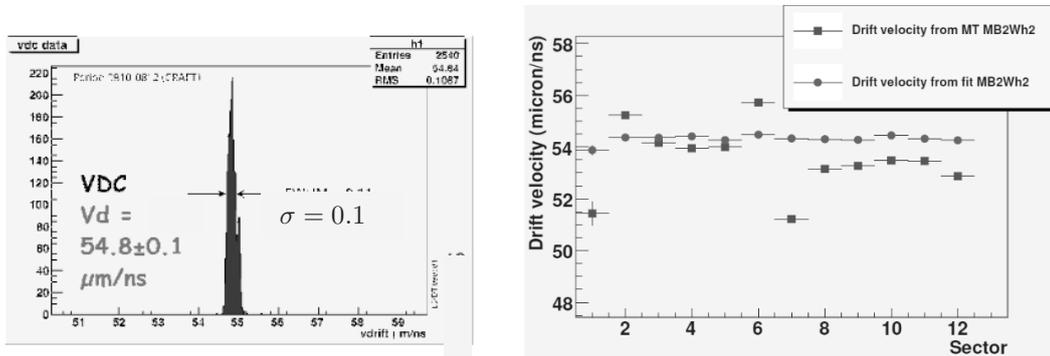
Figure 2: The drift velocity measured with a VDC at CMS (left) in comparison to the drift velocity of the drift tube chambers (right) determined by means of measured cosmic muon tracks with solenoid magnetic field switched off. The plots show average values of the different muon stations and wheels.

VDC which is in operation at CMS. The measured drift velocity corresponds to two days of data taking during the cosmic muon run period of CMS in August 2008. This can be compared to the indirectly determined drift velocity in the DT's of 54.5 μm/ns with a width of 0.1 μm/ns obtained from the cosmic muon data taking period 2008. The electric field of the VDC can be varied in a wide range without losing its homogeneity. The VDC measures the drift velocity directly for a given electric field while in the DT's the determined drift velocity is an effective parameter depending beside the gas admixture on the inhomogeneous electric field, muon track paths, software selection and fit algorithms. Therefore the drift velocity measured with the VDC can be exploited to verify the gas admixture and the indirectly determined drift velocity of a given muon station. Since January 2008 a single VDC unit is in operation at CMS, and it will be substituted by a larger system.

The complete VDC system consists of two racks. The first rack contains six VDC's (one for each wheel plus a spare one), flow controllers, pressure controllers and sensors, high voltage (HV) for the VDC's, a trigger for each VDC and a crate with dedicated VME modules. The second rack contains VME logics, a readout PC (Linux server), NIM modules, an UPS protection power supply and a gas crate.

Determination of the systematic uncertainties of the drift velocities measured by the six VDC's simultaneously while branched on one single gas circuit are on the way. Furthermore calibration runs for HV, PM voltage, gas admixtures, impurities (O_2, N_2), pressure and temperature dependencies are in the process of being accomplished.

In summary, gas admixture anomalies and the drift velocity of the DT's in the muon stations can be verified and validated by means of the VDC monitoring system which measures the drift velocity directly.

5 Bibliography

References

[1] CMS collaboration, *The CMS experiment at the CERN LHC*, JINST 3 (2008) S08004.

CMS: Cosmic muons in simulation and measured data

Lars Sonnenschein[1] on behalf of the CMS collaboration

[1]RWTH Aachen University, III. Physikalisches Institut A, 52056 Aachen, Germany

A dedicated cosmic muon Monte-Carlo event generator CMSCGEN has been developed for the CMS experiment. The simulation relies on parameterisations of the muon energy and the incidence angle, based on measured and simulated data of the cosmic muon flux. The geometry and material density of the CMS infrastructure underground and surrounding geological layers are also taken into account. The event generator is integrated into the CMS detector simulation chain of the existing software framework. Cosmic muons can be generated on earth's surface as well as for the detector located 90 m underground. Many million cosmic muon events have been generated and compared to measured data, taken with the CMS detector at its nominal magnetic field of 3.8 T.

1 Introduction

The parameterisation of the CMS cosmic muon generator CMSCGEN, including the normalisation to the cosmic muon flux measured in data is explained in detail. Furthermore the propagation of the muons through diverse materials from earth's surface to the CMS detector 90 m underground is elaborated. A comparison of the simulation to data measured with the CMS detector shows good agreement.

2 Muon flux parameterisation and normalisation

The cosmic muon generator of the CMS experiment [1] is based on a parameterised differential muon flux obtained by means of the air shower program CORSIKA [3] which in turn has been operated making use of the EPOS interaction model for high energy interactions and the GHEISHA interaction model for low energy hadronic interactions. The CORSIKA simulation results have been fitted with polynomials [4] to describe the differential flux at earth's surface as a function $\frac{d\Phi}{dp\,d\cos\theta\,d\phi}$ of the azimuth angle ϕ, the incidence angle θ and the muon momentum p. The flux is normalised to vertical muons from measured data with an energy of 100 GeV. The normalisation constant used amounts to

$$C_{\mathrm{norm}} = (2.59 \pm 0.18) \cdot 10^{-3} \mathrm{m}^{-2}\mathrm{s}^{-1}\mathrm{GeV}^{-1}\mathrm{sr}^{-1}. \qquad (1)$$

The maximally allowed phase space in azimuth angle is $\phi \in [0, 2\pi)$, whereas azimuthal isotropy has been assumed. The phase space for incidence angles is given by $0° < \theta < 84°$. For incidence angles of $\theta > 75°$ the parameterisation is extrapolated. In momentum the phase space is restricted to $3 < p_\mu < 3000$ GeV. The lower limit is driven by the existence of new physical processes which set in at such low momenta which makes the extrapolation invalid.

The upper limit of muon momenta is driven by strongly decreased flux in this regime. The muon momentum is approximated by a polynomial of the expression

$$L = \log_{10}(p/\text{GeV}) \tag{2}$$

which is slowly varying in muon momentum. The muon momentum spectrum is then fitted by a polynomial of the form

$$s(L) = a_0 + a_1 L + ... + a_6 L^6. \tag{3}$$

The momentum dependent zenith angle is taken into account by a polynomial of the cosine of the incident angle

$$z(\cos\theta, L) = b_0(L) + b_1(L)\cos\theta + b_2(L)\cos^2\theta. \tag{4}$$

Finally the differential flux is given by

$$\frac{d\Phi}{dp\,d\cos\theta\,d\phi} = C_{\text{norm}} \cdot \frac{1}{p^3} \cdot s(L) \cdot z(\cos\theta, L) \cdot \frac{1}{2\pi} \tag{5}$$

where the factor p^{-3} absorbs essentially the steeply falling momentum spectrum of cosmic muons. The charge ratio of positive over negative muons has been fixed to the constant value $R(\mu^+/\mu^-) = 1.28$ in the cosmic muon generator.

3   Muon energy loss in material

A random vertex on a disk at the surface is assigned to a generated single muon. The size of the disk which is centred around the vertical symmetry axis of the detector is determined by the chosen maximal incidence angle such, that a muon whose extrapolated direction does hit the CMS detector does necessarily have a vertex inside the disk. In the case the muon direction is pointing to the CMS detector the muon is propagated through the different material densities of the geological environment between the surface and the CMS detector, located at 90 m underground to obtain an integrated amount of water equivalents. This amount determines the energy loss of a given muon as a parameterised function [5] of the energy of the incident muon at surface. If the direction is not pointing to the CMS detector a new random vertex at the surface is chosen. A material map describes the diverse materials from earth's surface to the CMS detector. In concrete, the fundament of the hall at surface, the three vertical access shafts, a movable plug of the main shaft as well as the collision and service caverns including the adjacent parts of the LHC tunnel are taken into account. Two different average densities are assigned to the geological layers surrounding the CMS infrastructure. The upper half consists of sand, clay, gravels and water while the lower half consists of rock. In Fig. 1 the vertex position of the muons at the surface which reach the CMS detector are shown. Lower energetic muons are responsible for the enhanced intensities at the vertical access shafts. After the generated muons have been propagated to the CMS detector a full GEANT [2] simulation of the detector processes the muons further.

4   Simulation and data comparison

In the cosmic data taking period 2008 three hundred million events have been recorded with a solenoid magnetic field of $B = 3.8$ T. Global cosmic muons, which are reconstructed in the muon
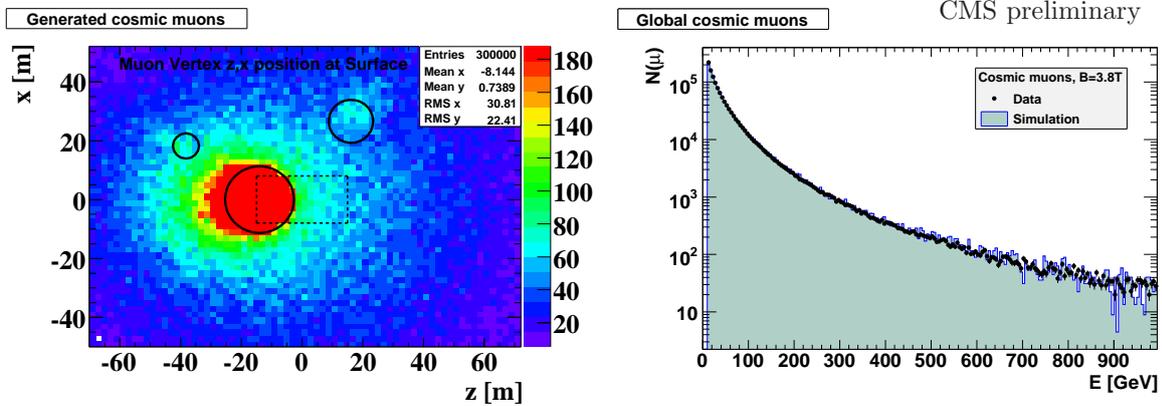
Figure 1: Left plot: Entrance vertex at the surface of the generated muons which arrive at the CMS detector (indicated by the dashed rectangle) 90 m underground. The three vertical shafts are indicated by black circles. There is clearly a correlation between muon intensity and shafts visible. Right plot: Energy spectrum of muons in data (black points) measured with the CMS detector. In comparison the GEANT simulation (green/blue histogram) is shown. The simulation has been normalised to the number of events of the data.

chambers and the central tracking system are chosen. A mixture of four different triggers is used in the simulation. The momentum of the reconstructed global muons is required to exceed a momentum threshold of $p = 10$ GeV. The incidence angle is restricted to the interval $0 \leq \theta < 60°$ to ensure that the parametrisation is applied far away from its regime of extrapolation. Fig. 1 right plot shows the energy spectrum of the cosmic muon data taken in 2008 in black points. The simulation is superposed as a green/blue shaded histogram and normalised to the number of entries in data. The decrease of the data distribution by the power of -2.7 is very well described by the simulation.

5 Bibliography

References

[1] CMS collaboration, *The CMS experiment at the CERN LHC*, JINST 3 (2008) S08004.

[2] S. Agostinelli *et al.*, *GEANT 4 - a simulation toolkit*, Nuclear Instruments and Methods in Physics Research A 506 (2003) 250-303 and IEEE Transactions on Nuclear Science 53 No. 1 (2006) 270-278.

[3] D. Heck *et al.*, Forschungszentrum Karlsruhe, Report FZKA 6019 (1998).

[4] Ph. Biallass, Th. Hebbeker, arXiv:0907.5514v1 [astro-ph.IM].

[5] Particle Data Group, p. 230, Phys. Lett. B, 592, 1-4 (2004).

Prospects for the First Top-Quark Pair-Production Cross-Section Measurement in the Semileptonic Channel at CMS

Jasmin Gruschke

on behalf of the CMS Collaboration
Institut für Experimentelle Kernphysik, KIT
Wolfgang-Gaede-Strasse 1, 76131 Karlsruhe, Germany

The advent of the LHC opens up a new era in top-quark physics. Given the large $t\bar{t}$ production cross-section and the high luminosity envisaged, the LHC can be considered a top-quark factory. We report on studies of early top-quark pair-production cross-section measurements with the CMS detector at a center-of-mass energy of 10 TeV. Of particular interest is the semileptonic channel in which the W boson from one top-quark decays into a charged lepton (electron/muon) and a neutrino, while the other decays into a quark and an anti-quark.

Introduction

More than one decade after its first observation in 1995 [1, 2], the top quark is to be rediscovered soon at the Large Hadron Collider. At a center-of-mass energy of $\sqrt{s} = 10$ TeV the $t\bar{t}$ production cross-section has been estimated to $\sigma(t\bar{t}) = 414 \pm 40(\text{scale}) \pm 20(\text{PDF})$pb [3].

This analysis addresses the potential of the CMS detector [4] to establish a top-quark signal within the first 20 pb^{-1} of LHC data. The experimental signature of the semileptonic $t\bar{t}$ decay is one high-energetic charged lepton (electron/muon), at least four jets and missing transverse energy. A more detailed review of the analyses can be found in [5, 6], where the μ+jets and the e+jets channel are treated separately.

Selection of $t\bar{t}$ Event Candidates

Striving for an early top-quark rediscovery, this analysis uses a simple and robust method able to identify top-quark pairs. Events are selected which contain exactly one high-energetic isolated lepton and at least four jets. The specific requirements on the muon are $p_\text{T} > 20$ GeV/c and $|\eta| < 2.1$, while for the electron $E_\text{T} > 30$ GeV and $|\eta| < 2.5$ are required. The momentum threshold for each jets is $p_\text{T} > 30$ GeV/c in the range $|\eta| < 2.4$.

The event selection yields about 320 $t\bar{t}$ signal and about 171 background events in the μ+jets channel. For the e+jets channel stricter requirements have to be applied in order to have comparable contributions of QCD events. Consequently, the statistics are reduced to 172 $t\bar{t}$ signal and 108 background events. The background in both channels is dominated by contributions originating from W+jets production. Figure 1 illustrates the expected event yield
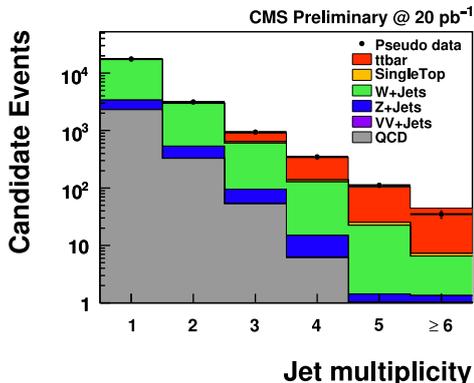
Figure 1: Expected event yield as a function of the jet multiplicity for the μ+jets channel. The *pseudo data* distribution is obtained by applying a bin-by-bin smearing based on Poisson statistics.
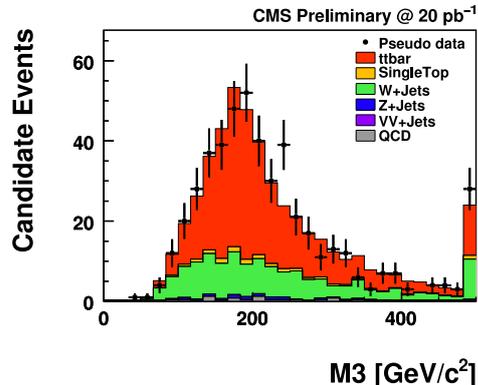
Figure 2: Invariant mass of the three jets with the highest vectorially summed transverse momentum for the μ+jets channel. The *pseudo data* distribution is obtained as in Figure 1.

as a function of the jet multiplicity for the μ+jets channel with the full event selection applied except the requirement on the number of jets.

Data-Driven Estimation of Background Contributions

We plan to employ data-driven techniques in order to reduce the dependence on the Monte Carlo modelling of background contributions. The estimation of QCD multi-jet contributions is investigated in both channels while in the μ+jets channels an additional method for the estimation of the W+jets contribution is studied.

For the estimation of the QCD contribution we studied two different methods which both yield a 50% systematic uncertainty. In the μ+jets channel, the ABCD method is investigated. Therein the phase space of two uncorrelated variables is divided into four regions (A, B, C and D). Among these three are highly enriched in QCD events while the fourth represents the signal region. Using the relation $N_{\mathrm{A}}/N_{\mathrm{B}} = N_{\mathrm{C}}/N_{\mathrm{D}}$ one can estimate the number of QCD multi-jet events N_{A} in the signal region A from measuring the number of events N_i in the three background enriched regions i. In the second method, which was studied in both lepton+jets channels, one single variable is investigated. This variable must exhibit a side-band region which is enriched in QCD multi-jet events, e.g. an isolation variable. After performing a fit to this variable in the side-band region and the subsequent extrapolation of the fitted function into the signal region, the number of QCD multi-jet events in the selected dataset can be estimated.

The estimation of the W+jets contribution utilizes the inverse of the charge asymmetry $R_{\pm} = \frac{N_{W^+} + N_{W^-}}{N_{W^+} - N_{W^-}}$, which will be calculated from predictions based on Monte Carlo simulations. Using this quantity we are able to estimate the number of charge asymmetric events—dominated by W+jets events—from the selected dataset via the number-difference of leptons (N^-) to anti-leptons (N^+): $(N^+ + N^-)_{\mathrm{data}} = R_{\pm} \cdot (N^+ - N^-)_{\mathrm{data}}$. For an integrated luminosity of 100 pb^{-1} this method yields a 30% uncertainty on the prediction of W+jets events among the selected event candidates dominated by the statistical uncertainty.

Extraction of the Cross Section

The extraction of the cross section is performed via a template fit to a discriminating variable using a binned likelihood procedure. Exemplarily the distribution of the M3 variable is shown in Figure 2 which is used as one possible discriminating variable for the fit. It represents the invariant mass of the three jets with the highest vectorially summed transverse momentum in the event. We employ ensemble tests (sets of 5k pseudo experiments) in order to estimate the sensitivity and the systematic uncertainties of the method. For the muon+jets channel we expect a statistical uncertainty of 12–18% and a systematic uncertainty of 19–25% depending on the discriminating variable investigated. Due to the smaller statistics, the electron+jets channel exhibits an increased statistical uncertainty of 23%, while the systematic uncertainty of 20% is comparable to the one estimated in the μ+jets channel. The dominating source for the systematic uncertainty of the method originates from the uncertainty on the jet energy scale. Additionally, for both channels the uncertainty arising from the uncertainty of the luminosity is estimated to be 10% and treated separately.

Conclusion

We demonstrated the early measurability of the $t\bar{t}$ cross-section within 20 pb^{-1} of LHC data at a center-of-mass energy of 10 TeV. The two feasibility studies presented investigate the μ+jets and the e+jets channel which both utilize data-driven techniques to estimate background contributions. For the measurement of the cross section a template fit is used leading to statistical as well as systematic uncertainties in the order of 20%. The dominating systematic uncertainty arises from the jet energy scale uncertainty.

Acknowledgements

References

[1] F. Abe et al. Observation of Top Quark Production in $p\bar{p}$ Collisions with the Collider Detector at Fermilab. *Phys. Rev. Lett.*, 74(14):2626–2631, Apr 1995.

[2] S. Abachi et al. Observation of the Top Quark. *Phys. Rev. Lett.*, 74(14):2632–2637, Apr 1995.

[3] Matteo Cacciari, Stefano Frixione, Michelangelo L. Mangano, Paolo Nason, and Giovanni Ridolfi. Updated predictions for the total production cross sections of top and of heavier quark pairs at the Tevatron and at the LHC. *JHEP*, 09:127, 2008.

[4] CMS Collaboration, R. Adolphi, et al. The CMS experiment at the CERN LHC. *JINST*, 0803:S08004, 2008.

[5] CMS Collaboration. Prospects for the first Measurement of the $t\bar{t}$ Cross Section in the Muon-plus-Jets Channel at $\sqrt{s} = 10$ TeV with the CMS Detector. *CMS Physics Analysis Summary*, CMS PAS TOP-09-003, 2009.

[6] CMS Collaboration. Plans for an early measurement of the $t\bar{t}$ cross section in the electron+jets channel at $\sqrt{s} = 10$ TeV. *CMS Physics Analysis Summary*, CMS PAS TOP-09-004, 2009.

Search for heavy narrow $t\bar{t}$ Resonances in Muon-plus-Jets final States with the CMS Detector

Thomas Peiffer[1]

on behalf of the CMS Collaboration
[1] Institut für Experimentelle Kernphysik, KIT
Wolfgang-Gaede-Straße 1, 76131 Karlsruhe, Germany

Many physics models beyond the Standard Model predict heavy new particles preferentially decaying to top pairs. Such new particles are searched for in proton-proton collisions at a centre-of-mass-energy of 10 TeV with the CMS detector as resonances in the top pair mass spectrum. New methods are presented for the selection and analysis of these events with two highly-boosted top quarks decaying into a final state with jets and a muon.

1 Introduction

The top quark, discovered in 1995 by the Tevatron experiments [1, 2], is the heaviest known elementary particle. Because its mass is of the order of the electroweak symmetry breaking scale, the top quark plays a special role in many theories beyond the Standard Model (SM). Many of those models predict new gauge bosons, for instance heavy gluons, axigluons, Z'-bosons, or gravitons, which couple strongly to top quarks [3]. In all these cases, the production of top pairs at hadron colliders through beyond SM mechanisms leads to resonances in the top pair invariant mass ($M_{t\bar{t}}$) spectrum. Because the centre-of-mass energy at the proton-proton collider LHC will be a factor 5–7 larger than at the Tevatron, the search for heavy resonances decaying into top quark pairs will be soon more effective than at the Tevatron.

In the analysis presented here [4] the experimental sensitivity to a narrow resonance in the $M_{t\bar{t}}$ distribution was studied, assuming an integrated luminosity of 200 pb^{-1} expected to be collected with the CMS detector [5] within the first year of operation at a centre-of-mass energy of 10 TeV. This study focuses on the search for new heavy particles with a mass above 1 TeV/c^2, which decay to top pairs, where one top quark decays leptonically into a muon, a neutrino and a b-quark, and the other hadronically. The branching ratio of this muon+jets channel is about 15%.

2 Event selection and reconstruction

In case of a high mass resonance which decays into a top pair, the event kinematic differs from the event topology of a $t\bar{t}$ event produced in a Standard Model process. In SM top-pair production the decay products of the top quarks are distributed isotropically since the top quarks are mainly produced with low transverse momenta. For the muon+jets decay channel one would therefore expect to observe one isolated muon and four jets, where two of the jets are

b-jets, which might be identified by a b-tagger. If the top quarks originate from the decay of a heavy particle, the top and the anti-top quarks are highly boosted. Their momenta are mostly in a back-to-back topology and the decay products of each top quark merge together. The hadronically decaying top quark will therefore often ends up in only one big jet instead of three well separated jets. The muon from the top quark which is assumed to decay leptonically will no longer be isolated, since it will be close to the b-jet from the top decay. Also the b-tagging requirements will work less optimal, due to decreasing b-tagging efficiency in case of highly boosted jets, for which it is more difficult to find secondary vertices, the main identification criterion for b-jets.

The event selection is therefore as follows: Only events accepted by a single-muon trigger are selected. At least one muon candidate is required to be reconstructed with a p_T larger than 15 GeV/c. Two jets are required to be reconstructed with a p_T larger than 50 GeV/c. The leading jet, possibly arising from the merging of the three quark jets from the hadronic top decay, is required to have a p_T above 260 GeV/c. No cut on the energy deposits in the calorimeters in a cone around the muon trajectory is applied, because the muon and the jet from the leptonic top decay might overlap for energetic top quarks. In place of this cut, events with $\Delta R_{\min} < 0.4$ and $p_T^{\mathrm{rel}} < 35$ GeV/c are vetoed to strongly reduce the QCD multi-jet background, where $\Delta R_{\min}$ indicates the minimum distance between the candidate muon and any reconstructed jet with $p_T > 30$ GeV/c and p_T^{rel} is the transverse momentum of the muon relative to the direction of the closest jet with $p_T > 30$ GeV/c. For further back-ground suppression, H_T^{lep}, defined as the sum of missing transverse energy and the transverse energy of the leading muon, has to exceed 200 GeV.

The invariant mass of the top pair is computed by reconstructing the four-vectors of the top quarks from the final state products: jets, muon and missing transverse energy due to the neutrino. The reconstruction method is adjusted to account for the special event kinematic of boosted top quark events. Particularly, the small angular separation of the decay products of the leptonically decaying top quark and the large separation of the two top quarks in a resonant decay are exploited. Details of the reconstruction are given in [4]. The result of event selection and reconstruction for backgrounds and signal is shown in Fig. 1. As signal, a Z' with masses of 1, 2 and 3 TeV/c² decaying to $t\bar{t}$ is presented for an assumed scenario of 200 pb⁻¹ integrated luminosity at $\sqrt{s}$=10 TeV of CMS data. The Z' cross section is assumed to be topcolor like [6].
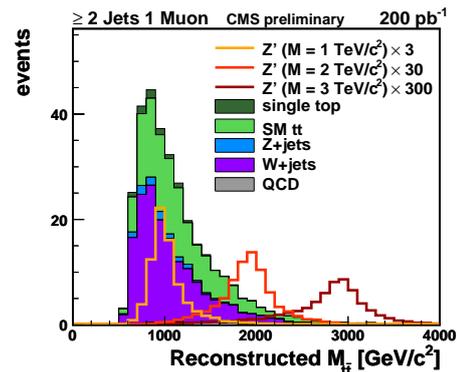
Figure 1: Distribution of reconstructed $M_{t\bar{t}}$ with superimposed Z' signals. The Z' cross sections used for this illustration purpose are given in multiples of the topcolor Z' cross section [6].

3   Statistical analysis

The extraction of the signal cross section is done by performing a likelihood fit of the $M_{t\bar{t}}$ distribution. As this distribution cannot separate different background processes well, a simultaneous fit to data is performed in a background enriched sideband. In the fit the rates for W+jets and QCD multi-jet backgrounds are kept as free parameters, while the rate of the

SM top pair background is constrained to the anticipated measured value within an statistical uncertainty of 20%.
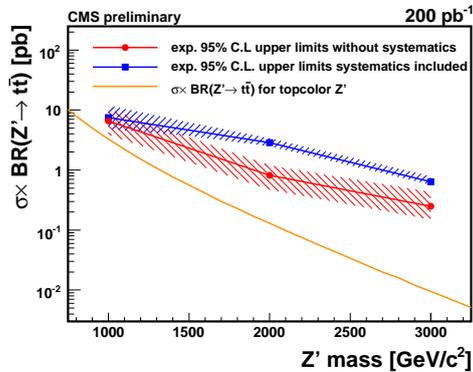
Figure 2: Expected limits on a narrow $t\bar{t}$ resonance with and without systematic uncertainties incorporated into the fit.
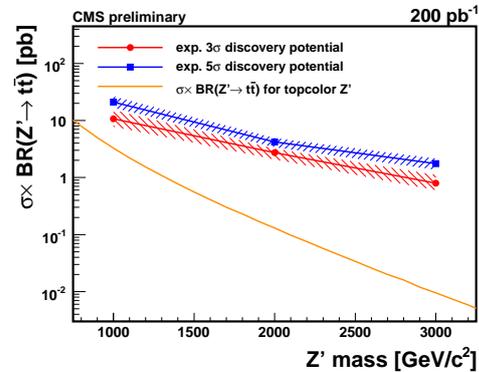
Figure 3: Expected cross sections of a $t\bar{t}$ resonance needed to claim a significance of 3 respectively 5σ with systematic uncertainties included.

Two physics aspects are exploited with the likelihood fit: A possible 95% C. L. exclusion limit on the cross section of a narrow resonance decaying to $t\bar{t}$ and the cross section, which would be required to claim a 3σ evidence or a 5σ discovery of such a signal (see Figures 2 and 3). Systematic uncertainties are incorporated into the fit and it has been found out, that the dominant systematic uncertainty is the uncertainty on the jet energy scale.

4   Conclusion

Assuming a scenario of 200 pb^{-1} collected at $\sqrt{s}$=10 TeV limits on heavy resonances decaying to top pairs in the multi-TeV range will be feasible for the first time. The cross section limits in reach are at the level of a few picobarn. While the obtained limits are not sufficient to exclude a topcolor Z', it is expected to set more stringent mass limits on models with heavy gluons or axigluons decaying to top pairs.

References

[1] F. Abe et al. Observation of top quark production in $\bar{p}p$ collisions. *Phys. Rev. Lett.*, 74:2626–2631, 1995.

[2] S. Abachi et al. Observation of the top quark. *Phys. Rev. Lett.*, 74:2632–2637, 1995.

[3] Rikkert Frederix and Fabio Maltoni. Top pair invariant mass distribution: a window on new physics. *JHEP*, 01:047, 2009.

[4] The CMS Collaboration. Search for heavy narrow $t\bar{t}$ resonances in muon-plus-jets final states with the CMS detector. CMS PAS EXO-09-008, 2009.

[5] R. Adolphi et al. The CMS experiment at the CERN LHC. *JINST*, 0803:S08004, 2008.

[6] Robert M. Harris, Christopher T. Hill, and Stephen J. Parke. Cross section for topcolor Z'(t) decaying to t anti-t. 1999.

Energy Weighting for the Upgrade of the Hadronic Calorimeter of CMS

Vladimir Andreev[1], Kerstin Borras[2], Dirk Krücker[2], Isabell Melzer-Pellmann[2], Matthias Stein[2], Peter Schleper[3]

[1]LPI – Lebedev Physical Institute, Leninskiy prospekt 53, Moscow
[2]DESY, Notketraße 85, 22607 Hamburg, Germany
[3]University of Hamburg, Notketraße 85, 22607 Hamburg, Germany

In these simulation studies an energy weighting method is applied to the signals of the CMS hadronic calorimeter with a possible readout scheme after the future upgrade. Tabulated weighting factors are used to compensate for the different response of hadronic and electromagnetic energy depositions of simulated pion showers in the hadronic calorimeter. The weighting improves the relative energy resolution from

$(\sigma_E/E)^2 \quad = [((92.5 \pm 0.6)\%/E)^2 + ((6.5 \pm 0.1)\%)^2] \text{ GeV}^2 \quad$ to
$(\sigma_{E,weight}/E)^2 = [((85.5 \pm 0.5)\%/E)^2 + ((4.4 \pm 0.1)\%)^2] \text{ GeV}^2.$

1   Introduction

The hadronic calorimeter (HCAL) of CMS is a non-compensating sampling calorimeter with an $e/\pi-$ratio of about 1.2 [1]. Consequently, the response for electromagnetic energy depositions is larger than for hadronic ones which affects the energy measurement. An energy weighting method to compensate for the $e/\pi-$ratio is possible if one can identify the electromagnetic- or hadronic-like origin of the energy deposition within a hadronic shower. For the CMS detector upgrade Phase I a longitudinal segmentation of the HCAL towers is discussed, improving its longitudinal granularity by a factor of four (see Fig. 1). This offers the possibility to resolve single parts of particle showers. A possible readout scheme ("1-4-4-8") is investigated here, where each digit represents the number of calorimeter cells which are read out in one channel.
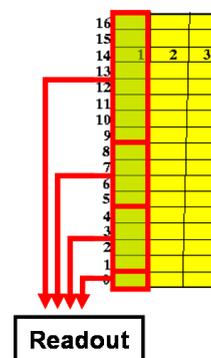
Figure 1: Sketch of a possible readout scheme ("1-4-4-8") for the CMS HCAL after the upgrade.

2   The Method and Realization

The method of the tabulated weighting factors [2] is software based. Its principle is to distinguish between electromagnetic and hadronic energy depositions in the HCAL and to find appropriate weighting factors for the compensation. The discrimination criterion is the *energy density*

$$\rho^i = E^i_{dep}/V^i, \qquad (1)$$

where E_{dep}^i is the deposited energy and V^i a measure for the volume in arbitrary units (number of layers per readout channel), both for a readout channel i, and

$$E_{dep}^i = E_{abs}^i + E_{sci}^i + E_{inv}^i, \tag{2}$$

where E_{abs}^i is the energy deposited in the absorber, E_{sci}^i the energy deposited in the scintillator and E_{inv}^i the invisible energy (from neutrinos, nuclear excitation, etc.).

The weighting is based on the fact that the average energy density of electromagnetic depositions is larger than for hadronic ones. In a MC simulation it is possible to obtain weighting factors w^i as a function of the energy density (see Figure 2)

$$w^i \left(\rho^i, E_{shower} \right) = \left\langle \frac{E_{dep}^i}{E_{meas}^i} \right\rangle, \tag{3}$$

where E_{shower} is the total shower energy received from a cluster algorithm of a $3 \times 3-$cluster and E_{meas}^i is the scintillator energy times a calibration factor.

These weighting factors are applied to data (here: simulated data) to yield a weighted energy

Figure 2: Weighting factors for the third channel of the readout scheme "1-4-4-8".

$$E_{weight}^i = E_{meas}^i \cdot w^i. \tag{4}$$

For the realization of the weighting method, a simulation of the CMS HCAL is necessary. This is done via a Geant3 [3] standalone simulation, as the deposited energy E_{dep}^i left in a readout channel i of the HCAL, including the absorber energy, is presently not available in the CMS software. In order to make the simulation as realistic as possible [4], *Gcalor* is chosen as shower generator. Since the weighting factors depend on the shower energy, it is necessary to create a set of them for multiple simulated test beam energies. This is done for the following energies: (10, 20, 30, 50, 100, 150, 225, 300) GeV. However, for any energy which does not correspond to one of these energies, an *interpolation* of the weighting factors is required. Here a linear interpolation is used.

3   Results

The relative energy resolution and linearity before and after weighting using the "1-4-4-8" design, are shown in Figure 3 and Figure 4, respectively. Both results are obtained from a Gaussian fit. The 80 GeV sample is a statistically independent test sample for which no weighting factors exist. The final result is obtained by interpolation between weighting factors of different energies only.

Figure 3: Energy resolution before (black) and after (red, dashed) the weighting with the 1-4-4-8 design.
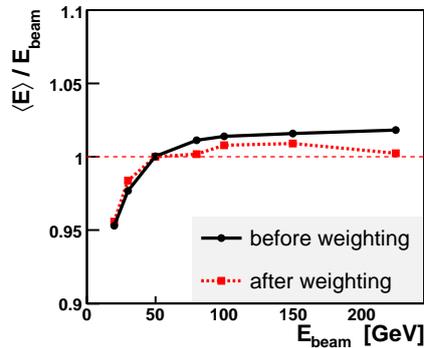
Figure 4: Linearity before (black) and after (red, dashed) the weighting with the 1-4-4-8 design.

The energy resolution is

$$
\begin{aligned}
(\sigma_E/E)^2 &= \left[((92.5 \pm 0.6)\%/E)^2 + ((6.5 \pm 0.1)\%)^2\right] \text{GeV}^2 &\text{(before weighting)}, \\
(\sigma_{E,weight}/E)^2 &= \left[((85.5 \pm 0.5)\%/E)^2 + ((4.4 \pm 0.1)\%)^2\right] \text{GeV}^2 &\text{(after weighting)}.
\end{aligned}
$$

4 Conclusion

Applying the weighting method to the CMS HCAL with the readout design "1-4-4-8", the sampling term and constant term of the energy resolution improve. As the energy distributions contain non-Gaussian tails (especially for lower energies), the improvement of the linearity is more pronounced for the mean of the distributions than for the mean of a Gaussian fit.

The entry at 80 GeV of the energy resolution (for which no weighting factors exist) is in good agreement with the other energies. This is an important consistency check. However, for the linearity there is a kink at 80 GeV. This can be explained by the *linear* interpolation of the weighting factors. In further investigations different interpolation methods should be studied systematically in order to avoid this effect.

Test beam results of the CMS HCAL can be found here [5].

References

[1] Arie Bodek. Performance of a prototype CMS hadron barrel calorimeter in a test beam. *IEEE Trans. Nucl. Sci.*, 46:407–409, 1999.

[2] C Issever, K Borras, and D Wegener. An improved weighting algorithm to achieve software compensation in a fine grained lar calorimeter. Technical Report physics/0408129. DESY-04-127. DESY-2004-127, DESY, Hamburg, 2004.

[3] Michel Goossens. *GEANT: Detector Description and Simulation Tool, long writeup W5013; March 1994.* CERN Program Library. CERN, Geneva, 1993.

[4] V. V. Abramov et al. Studies of the response of the prototype CMS hadron calorimeter, including magnetic field effects, to pion, electron, and muon beams. *Nucl. Instrum. Meth.*, A457:75–100, 2001.

[5] S. Abdullin et al. The CMS barrel calorimeter response to particle beams from 2-GeV/c to 350-GeV/c. *Eur. Phys. J.*, C60:359–373, 2009.

Standard Model Higgs search in the 4-lepton final state

Roberto Di Nardo[1], on behalf of the ATLAS Collaboration

[1] INFN & University of Rome "Tor Vergata"
Via della Ricerca Scientifica 1, 00133 Rome, Italy

The discovery potential of the ATLAS detector at the LHC for a neutral SM Higgs boson decaying to purely leptonic final states, that is $H \to ZZ^{(*)} \to 4$ leptons (electrons or muons), is presented. The signal is characterized by the presence of isolated leptons associated to the main proton-proton interaction vertex in the events, and constitutes one of the most promising channels for SM Higgs discovery in the mass region $130 < m_H < 700$ GeV/c^2. Analysis techniques for signal reconstruction and for background rejection are discussed.

1 Introduction

One of the main LHC physics goals is the understanding of Standard Model (SM) electroweak symmetry breaking mechanism, that requires the existence of a scalar Higgs boson to provide mass terms to fermions and gauge bosons. Precision electroweak measurements set an upper limit on the SM Higgs boson mass that is $m_H < 157$ GeV/c^2 at 95% Confidence Level (CL). This increases to $m_H < 186$ GeV/c^2 95%CL including the LEP2 direct search limit [1]. CDF and D0 experiments at Tevatron are directly searching the SM Higgs boson and the most recent combined results excludes the mass range between 163 GeV/c^2 and 166 GeV/c^2 at 95% CL [2]. The dominant production mechanism of the Higgs boson with proton-proton collisions at the LHC in the full m_H mass range is the gluon fusion mediated by the heavy quark loop. The vector boson fusion (VBF) process is one order of magnitude smaller than the gluon fusion but plays also an important role providing a good signature of two forward quark jets for which a forward jet tagging and a central jet veto allow better background rejection. Other production processes are: Higgs-strahlung and associated production with tt or W/Z bosons.

2 The $H \to ZZ^{(*)} \to 4l$ channel and backgrounds

Due to its experimentally clean signature, the $H \to ZZ^{(*)} \to 4l$ ($l = e, \mu$) is a "golden" decay channel for the Higgs boson discovery. In fact, after the signal selection, a clear peak in the four leptons invariant mass distribution on top of a smooth background is expected. The gluon fusion process is known at NNLO with an uncertainty of 10-20% coming from parton distribution functions and QCD scale while the vector-boson fusion at NLO with uncertainty smaller than 10%.

In Table 1 the $H \to ZZ^{(*)} \to 4l$ cross sections at NLO are shown for different values of the Higgs boson masses, corresponding to some of the event samples processed through the

ATLAS [3] full simulation and reconstruction chain.

The $qq, gg \rightarrow ZZ^{(*)} \rightarrow 4l$ process represents the irreducible background to Higgs decaying into four leptons and its cross section, rescaled to NLO, is $34.8 \cdot [K(M_{ZZ}) + 0.3]$ fb, with $K(M_{ZZ})$ being a mass dependent K-factor and 0.3 factor taking into account the gluon initiated process. The reducible background is given by the processes $qq \rightarrow Zb\bar{b} \rightarrow 4l$ and $qq, gg \rightarrow t\bar{t}$ with leptonic W and b decays and their cross section, including the $4l$ branching ratio, is 812.1 fb for the former and 6.1 pb for the latter. The signal cross section is several orders of magnitude

$m_H[\text{GeV}/c^2]$	$\sigma_{NLO} \cdot \text{BR[fb]}$
130	6.25
150	10.56
180	5.38
200	20.53
300	13.32
600	2.53

Table 1: $H \rightarrow ZZ^{(*)} \rightarrow 4l$ NLO cross section at 14 TeV

smaller than the reducible background so it is necessary to achieve large rejection factors against this background. Leptons from semileptonic b-decays, in contrast to those coming from Z decays, are less isolated, and are more likely to originate from a displaced vertex; hence, lepton isolation and the significance of the transverse impact parameter $d_0/\sigma(d_0)$ of final state leptons can be used as discriminating variables, as shown in Fig. 1.

Figure 1: Left: Normalized track isolation $\sum p_T/p_T$ (in a cone of ΔR=0.2) for the signal, the $Zb\bar{b}$ and $t\bar{t}$ backgrounds for the 4μ channel. Right: Transverse impact parameter significance for muons from signal and reducible background events [3].

3 Signal Selection and Results

In order to select the $H \rightarrow ZZ^{(*)} \rightarrow 4l$ signal, a single lepton trigger requiring a muon ($p_T > 20$ GeV) or an isolated electron ($E_T > 22$ GeV) is used. Events are further selected offline requiring that they contain at least 4 leptons with $p_T > 7$ GeV and $|\eta| < 2.5$, with at least two having $p_T > 20$ GeV. To reconstruct the $ZZ^{(*)}$ coming from the Higgs boson decay, two leptons with the same flavour and opposite charge are coupled in pairs. Lepton quality cuts are also applied:

- Electrons: if $m_H > 200$ GeV/c^2 a *loose electron* criteria [3] were implemented (containment in the middle sampling of the ATLAS EM Calorimeter and hadronic leakage); if $m_H < 200$ GeV/c^2 they have to satisfy a *medium electron* quality criteria, which corre-
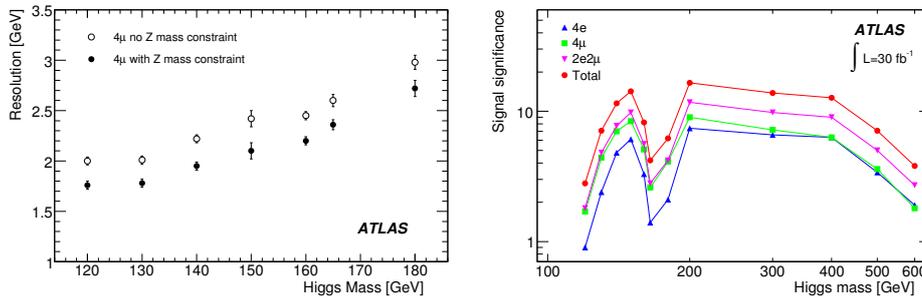
Figure 2: Left: $H \to 4\mu$ mass resolution as a function of the Higgs boson mass (open circles denote the resolution obtained without Z-mass constraint applied, while full circles show the resolution with the Z mass constraint). Right: Expected signal significances computed using Poisson statistics, for each of the three decay channels, and their combination.

sponds to *loose electron* requirements with additional lateral shower shape containment, and calorimetric isolation [3].

- Muons: are required to be either reconstructed by the *Combined* algorithm (Muon Spectrometer + Inner Detector (ID) track combination) or extrapolated from the ID.

To further filter the sample from the reducible backgrounds, isolation and vertexing cuts are applied (muon calorimetric isolation ($\sum E_T/p_T < 0.23$), lepton ID track isolation ($\sum p_T/p_T < 0.15$) and cuts on maximum lepton impact parameter $d_0/\sigma(d_0) < 3.5$ for muons and $d_0/\sigma(d_0) < 6.0$ for electrons). A Z mass constraint is applied to one or two ($m_H > 200$ GeV/c^2) lepton pairs to improve the resolution on the Higgs as shown in Fig. 2 (left). A set of kinematical cuts optimized using the expected signal and background distributions and the expected dilepton resolution is used for the Z invariant reconstructed mass. Events are finally selected within a $m_H \pm 2\sigma_{m_H}$ mass window where σ_{m_H} is the experimental 4-lepton mass resolution. The significance for the three different $H \to 4l$ decays, calculated using Poisson statistics, as a function of the Higgs boson mass is shown in Fig. 2 (right) where only statistical errors are taken into account while systematic errors on backgrounds are not included. For an integrated luminosity of 30 fb^{-1} at 14 TeV c.m. energy ATLAS will discover the SM Higgs in the $H \to ZZ^{(*)} \to 4l$ channel for Higgs masses between $130 - 500$ GeV/c^2 excepted the region around 160 GeV/c^2 where a 4σ significance is expected.

References

[1] http://lepewwg.web.cern.ch/LEPEWWG/ (August 2009), arXiv:0911.2604.

[2] CDF and D0 Collaborations, *Combined CDF and D0 Upper Limits on Standard Model Higgs-Boson Production with 2.1 - 5.4 fb^{-1} of Data*, FERMILAB-CONF-09-557-E, arXiv:0911.3930.

[3] ATLAS Collaboration, *Expected Performance of the ATLAS Experiment: Detector, Trigger and Physics*, CERN-OPEN-2008-020, arXiv:0901.0512.

[4] ATLAS Collaboration, *The ATLAS Experiment at the CERN Large Hadron Collider*, J. Instrum. 3(2008) S08003.

Tagging b-jets in ATLAS

Thomas Göpfert, on behalf of the ATLAS collaboration

Technische Universität Dresden, 01062 Dresden, Germany

The ability to identify jets containing b-hadrons is important for the high-p_T physics program of the ATLAS experiment at the LHC. This is in particular useful to select very pure top quark samples or for studying Standard Model or supersymmetric Higgs bosons which couple preferably to heavy objects. After a review of the algorithms used to identify b-jets, their anticipated performance is discussed as well as the impact of various critical ingredients such as the residual misalignments in the tracker. The prospects to measure the b-tagging performance in the first few hundreds of pb^{-1} of data with di-jet and $t\bar{t}$ events are presented. Finally two different physics use cases of b-tagging are summarised.

1 b-tagging algorithms in ATLAS

Bottom jets possess several characteristic properties that can be utilised to separate them from jets coming from the hadronisation of lighter quarks. The most important property is the relatively long lifetime of b-hadrons of about 1.5 ps. This leads to a measurable flight length of a few millimeters before their subsequent decay. The decay of the b-hadrons at a displaced secondary vertex can be identified inclusively by measuring the impact parameters (IP) of tracks coming from the decay, that is the distance from the point of closest approach of the track to the interaction vertex. The IP is a signed quantity, which is positive if the point of closest approach lies upstream with respect to the jet direction and negative in the other case. Apart from that, a secondary vertex can also be reconstructed explicitly. The various tagging methods studied in ATLAS can be divided into two main classes: the *spatial taggers* comprise methods that utilise lifetime information like impact parameters and decay vertices; the *soft-lepton taggers* are based on the reconstruction of the lepton in case the b-hadron decays semi-leptonically. These leptons have a sizable tranverse momentum as well as a large transverse momentum relative to the jet axis ($p_\mathrm{T}^\mathrm{rel}$). Detailed information on the presented results and b-tagging in ATLAS can be found in the chapter on b-tagging in [1] and references therein.

Apart from a few simple algorithms all tagging methods rely on a likelihood ratio to build a discriminating variable, called jet weight, for the separation of b-jets, c-jets and other jets. In the following only the separation between b-jets and light-jets is considered for simplicity. All jets having a jet weight above a certain cut value are then tagged as b-jets. This cut value determines the b-tagging efficiency ϵ_b, defined as the fraction of true b-jets that are tagged as b-jets. It also determines the rejection rate of light-jets R_u, defined as the inverse of the fraction of true light-jets that are falsely tagged. For a given cut on the weight the rejection of light jets as well as the efficiency, in general, strongly depend on η and p_T of the jet (c.f. Fig. 1).

A brief description of some of the ATLAS b-tagging algorithms follows. The *JetProb* algorithm uses the negative side of the transverse IP significance distribution as obtained from prompt tracks to calculate the probability of compatibility of the tracks with the primary vertex. More
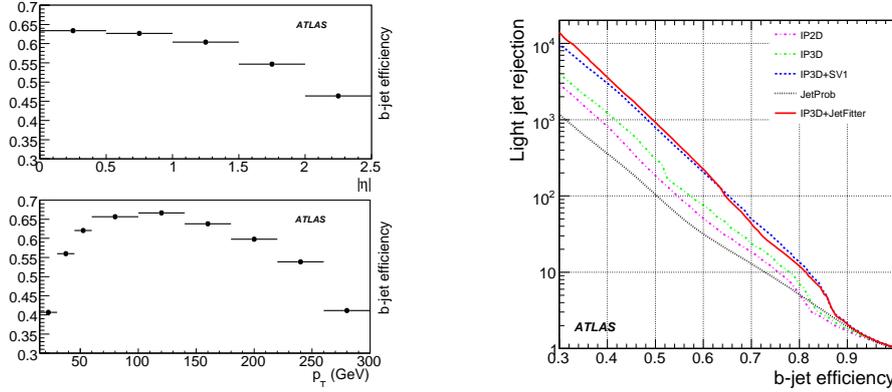
Figure 1: Left: *b*-tagging efficiency obtained with the IP3D+SV1 algorithm operating at a fixed cut on the *b*-tagging weight for $t\bar{t}$ events versus jet $|\eta|$ and p_T respectively [1]. Right: Rejection of light jets versus *b*-jet efficiency for $t\bar{t}$ events and for various tagging algorithms [1].

sophisticated tagging algorithms utilise the distribution of the IP significance as calculated in the transverse plane (*IP2D*) and in addition in the longitudinal projection (*IP3D*). One secondary-vertex tagger (*SV1/2*) fits inclusive secondary vertices and builds the jet weight from several one or more-dimensional variable distributions like e.g. the vertex mass. The tagger with the best single performance (*JetFitter*) fits the decay chain of *b*-hadrons, i.e. it fits a common *b/c*-hadron flight direction along with the position of additional vertices on it. The jet weight is calculated similarly to *SV1/2*, but taking different decay topologies into account.

Two soft-lepton tagger approaches are pursued in ATLAS. One uses soft muons and one or two dimensional reference histograms of the muons p_T and the muons $p_T^{\rm rel}$. The other uses electrons and relies on the challenging identification of soft electrons inside jets.

2 Performance in Monte Carlo simulations

The performance of the tagging methods is estimated on Monte Carlo simulated events. For the following results $t\bar{t}$ events were used. A snapshot of the expected light jet rejection as a function of the efficiency can be found in Fig. 1 for the spatial taggers. One can expect $R_u \sim 30$ for the *JetProb* tagger and up to $R_u \sim 200$ for the sophisticated *JetFitter* algorithm at a typical *b*-tagging efficiency of $\epsilon_b = 60\%$. The soft muon tagger for example gives $R_u \sim 300$ at $\epsilon_b = 10\%$, where ϵ_b includes semi-leptonic branching fractions.

An effort has been made to reach a realistic understanding of critical aspects of *b*-tagging. The studies summarised above were done assuming a perfect knowledge of all misalignments. More realistic studies take residual misalignments into account as well as the process of realignment including systematic uncertainties. Recent studies indicate a possible degradation of the light jet rejection of up to $\sim 30\%$ at most for fixed ϵ_b. Further degradations in rejection are seen in studies including pile-up events (~ 5 minimum bias events are expected at an instantaneous luminosity of $2 \cdot 10^{33}\,\mathrm{cm}^{-2}\mathrm{s}^{-1}$), where in a few percent of the cases a wrong primary vertex is reconstructed leading, among other things, to an artificial shift in the longitudinal IP and finally to a loss in rejection of $\sim 30 - 40\%$ for *IP3D* and *IP3D+SV1*. The taggers that take only the transverse impact parameter into account are minimally affected by pile-up however.

3 Prospects for performance measurements

It will be necessary to calibrate the b-tagging methods on data. This means that one has to measure the tagging efficiency as well as the rejection rate. Due to the dependence on p_T and η it is desirable to perform the calibration in bins of those variables. In addition one would also like to measure the reference histograms with data. For the efficiency measurement several methods have been studied in ATLAS that make use of either di-jet or $t\bar{t}$ events.

The $p_\mathrm{T}^\mathrm{rel}$ method is one approach that uses events with jets that include non-isolated muons. Templates of the muon $p_\mathrm{T}^\mathrm{rel}$ as obtained from simulated and reconstructed b-, c- and light-jets passing basic selection criteria are fitted to the measured distribution before and after applying the respective tagger, which preferably is a spatial tagger. By counting the number of muon jets before and after the tagging, the efficiency ϵ_b can be estimated. It was shown that an integrated luminosity of $\sim 50\,\mathrm{pb}^{-1}$ is sufficient to derive detailed calibration curves in p_T or η with a relative precision on ϵ_b of about 6%.

There are several methods that make use of $t\bar{t}$ events. One is an event counting method, that measures the average b-tagging efficiency and the cross section of $t\bar{t}$ production in the lepton+jets or the dilepton channel at the same time, by counting the number of events with 1, 2 or 3 tagged jets. With $\sim 100\,\mathrm{pb}^{-1}$ of data a relative precision on ϵ_b of $\sim (2.7(\mathrm{stat.}) \pm 3.4(\mathrm{sys.}))\%$ can be reached in the lepton+jets channel.

4 Physics use cases

There are various examples of use cases where b-tagging is a critical ingredient. One is the search for a Standard Model Higgs boson in the $t\bar{t}H(H \to b\bar{b})$ channel. Here b-tagging can be used to reduce or even eliminate large backgrounds like $t\bar{t}j\bar{j}$ or W+jets. For example the $t\bar{t}j\bar{j}$ background is reduced by two orders of magnitude by using b-tagging. Another example is the top quark mass measurement. There the highest precision can be reached in the $t\bar{t}$ lepton+jets channel by requiring two b-tagged jets using the hadronically decaying top as the mass estimator. Assuming a jet energy scale uncertainty of the order of one percent, a precision of $1\,\mathrm{GeV}$ can be reached with an integrated luminosity of $1\,\mathrm{fb}^{-1}$. A complementary approach relying on b-tagging infers the top quark mass from the mean transverse decay length of b-hadrons coming from the top decays. Here the uncertainty due to the jet energy scale is negligible.

5 Conclusion

Various algorithms for tagging b-jets have been studied in detail in ATLAS. The spectrum covers simple, robust taggers as well as sophisticated taggers, that make use of as much information as possible from the b-hadron decay chain. Several approaches for calibrating b-tagging algorithms with data were shown to be realisable with a few $100\,\mathrm{pb}^{-1}$ of data. b-tagging is essential for many physics analyses, like Higgs boson searches or top quark mass measurements.

References

[1] The ATLAS Collaboration, Expected Performance of the ATLAS Experiment, Detector, Trigger and Physics, CERN-OPEN-2008-020, Geneva, 2008.

Impact of the NLO Hadronic Effects on the Lepton-Nucleon Scattering

Aleksandrs Aleksejevs[1], Svetlana Barkanova[2]

[1]Division of Science, SWGC, Memorial University, Corner Brook, NL, Canada
[2]Physics Department, Acadia University, Wolfville, NS, Canada

The presented short paper outlines the importance of the careful theoretical examination of the Next-to-Leading Order (NLO) corrections for many processes. The special attention is paid to the case of the electron-nucleon scattering. The partially computerized procedure developed by our group, which has allowed accounting for the NLO hadronic degrees of freedom, is briefly described. Some ideas for future projects which could benefit from the use of our procedure, like electromagnetic form factors of nucleons, virtual Compton scattering, and hadron leptoproduction, are included.

Motivation and Introduction

Multi-loop effects in electroweak interactions play a crucial role in tests of the Standard Model, and require careful theoretical evaluation. The new generation of experiments needs the backgrounds and radiative effects calculated to a much higher precision than previously. According to [1], the radiative corrections can be as large as 30% of uncorrected cross section depending on the experiment conditions. Done by hand, the calculations usually lead to unavoidable approximations. We extended computational packages such as FeynArts [2] and FormCalc [3] for the evaluation of one-loop electroweak radiative corrections for lepton–nucleon scattering and obtained numerical results in good agreement with the current experimental data [4]. In lepton-nucleon interactions, it is important to include hadronic sector as well. So far, the best candidate for the phenomenological description of low-energy QCD processes has been Chiral Perturbation Theory (ChPBTh). In ChPBTh, determining the range of valid and contributing degrees of freedom to a given problem is often a challenge. However, the recent developments in the automatization of the NLO calculations in perturbative field theory give us the possibility to address this issue.

Lepton-Nucleon Scattering

Electroweak properties of the nucleon can be studied by parity-violating electron-nucleon scattering at low to medium energies. Resent and planned experiments like G0 [5, 6] or Q_{Weak} [7] can measure the asymmetry factor coming from the difference between cross sections of left-

and right-handed electrons very precisely. The asymmetry is calculated as:

$$A = \frac{d\sigma_R^{tot} - d\sigma_L^{tot}}{d\sigma_R^{tot} + d\sigma_L^{tot}} \cong A_{LO} + \frac{Re\left(M_{LO}^{\gamma}M_{NLO}^{Z}\right)_R - Re\left(M_{LO}^{\gamma}M_{NLO}^{Z}\right)_L}{|M_{LO}^{\gamma}|_{R(L)}^2},$$

where A_{LO} is a leading order asymmetry and the last term is a parity-violating NLO contribution. However, before physics of interest can be extracted, at least the NLO contribution to electroweak scattering needs to be carefully evaluated. The NLO corrections have been addressed by many researchers like [8, 9, 10] and [11], but more work still needs to be done. For example, the results of a study of two-boson (γ and Z) exchange corrections in parity-violating electron-proton elastic scattering including the intermediate states described by nucleons and delta resonance done in [12] differ significantly from those in [13]. Q_{Weak} [7], soon to be started at JLab, is a 2200 hour measurement of the PV asymmetry in elastic e-p scattering at $Q^2 = 0.026\, GeV^2$ which aims to carry out the first precision measurement of the proton's weak charge. With about 4% combined statistical and systematic errors, Q_{Weak} will either establish conformity with the Standard Model or point to New Physics. It is crucial that all the relevant corrections for such important experiment as Q_{Weak} are carefully accounted for, and preferably by several theory groups to allow comparing results.

The partially computerized procedure developed by our group allowed calculating large number of Feynman diagrams at different momentum transfers as well as performing an extensive analysis of the dependence on poorly constrained parameters to evaluate realistic uncertainties. We have included all the possible contributions arising from the Standard Model degrees of freedom and made some progress towards accounting for the hadronic degrees of freedom. For the lepton-hadron scattering, we can do the exact calculation of the model-independent corrections to the lepton current, and do model-dependent evaluation of hadronic current corrections, box graphs, self energies contribution and electromagnetic radiation of the charged particles (Soft and Hard Photon Bremsstrahlung). Our calculations are done in the on-shell renormalization scheme using Feynman gauge.

In [14], we computed the radiative corrections to the parity-violating asymmetries with accounting for the NLO effects using form factors for the hadronic currents. Dirac and Pauli form factors were taken in the dipole/monopole approximation and with no strange quark contribution. The final asymmetries were treated with both Soft and Hard-Photon Bremsstrahlung (SPB+HPB) contributions according to [15]. The computed results for the asymmetry agreed with theoretical predictions of G0 group [5]. With the NLO contributions to the parity-violating asymmetries found to be close to 20%, [14] yet again demonstrates the importance of the NLO effects for the lepton-nucleon scattering. An extension of FeynArts, called the CHM (the Computational Hadronic Model) was developed in [16] to include the hadronic sector using ChPBTh. The model included the octet of mesons, baryons, and the decuplet of resonances. One of the most interesting applications of the model shown in [16] were the studies of the dynamical dipole polarizabilities of the nucleon which produced both low energy and near-one-pion threshold behaviour in good agreement with [17].

Further Applications

Our computational approach can be used for a wide range of applications like electromagnetic form factors for nucleons, virtual Compton scattering, and hadron leptoproduction, just to

name a few. For example, in case of the electromagnetic form factors of nucleons calculated with ChPBTh, it is not completely clear what is responsible for deviations between theory and experiment at higher momentum transfers. The results obtained in [18] within ChPBTh describe the experimentally measured form factors quite well, but only with a momentum transfer up to $0.1\,GeV^2$. The authors [18] have suggested that higher-order effects may be very important and have to be studied in the framework of Next-to-NLO calculation or by including additional dynamical degrees of freedom. With our computational model, one should be able to run full calculations with the octet of pseudoscalar mesons, baryons and vector mesons and the decuplet of resonances included. The calculations up to two loops are possible, too. Another important application of our approach can be found in the analysis of the virtual Compton scattering, which can offer insights on the dynamical nucleon's structure over a wide kinematic range. The spin-independent part of Compton amplitude was evaluated in [19], for example, but the spin-dependent part needs more attention. The studies of semi-inclusive processes of hadron leptoproduction, an important tool for the testing QCD predictions of nucleon structure, could benefit from our model being used to better account for the radiative corrections to the hadronic tensor (i. e. hadron vertex corrections and the box diagrams). There are many packages developed for high-energy physics (see [20]), but the low-energy sector is not served nearly as well. We hope that our computational model can eventually serve a much larger community. At the moment, source files are available by request from the authors. In the future, we plan to make the files available though a website, complete with a manual, an automatic installer, the template codes for the selected processes, and the MC generators.

References

[1] L.C. Maximon, J.A. Tjon, Phys.Rev. C62 (2000) 054320, arXiv:nucl-th/0002058

[2] Hahn T 2001 arXiv:hep-ph/0012260v2

[3] Hahn T and Perez-Victoria M 1999 arXiv:hep-ph/9807565v1

[4] A Aleksejevs, S. Barkanova and P. Blunden, J. Phys. G: Nucl. Part. Phys. 36, 045101, (2009)

[5] G0 Collaboration, arXiv:nucl-ex/0506021v1

[6] G0 Collab., arXiv:0909.5107v1

[7] J. Bowman et al., Jefferson Lab Experiment, E02020, Proposal to PAC 21 at http://www.jlab.org/qweak/

[8] W. J. Marciano, A. Sirlin, Phys. Rev. D29, p. 75, (1984)

[9] M. J. Musolf, et al., Phys. Rep. 239, 1, (1994)

[10] Shi-Lin Zhu, et al., Phys. Rev. D 62, 033008, (2000)

[11] A. Afanasev, JLAB-THY-07-755, arXiv:0711.3065

[12] J. A. Tjon, P. G. Blunden, W. Melnitchouk, Phys.Rev.C79:055201, (2009)

[13] K. Nagata, H. Q. Zhou, C. W. Kao and S. N. Yang, arXiv:0811.3539

[14] A. Aleksejevs, S. Barkanova, V. Zykonov, to be publishaed in Yad. Fiz. (2010), ICHEP08 proceedings arXiv:0810.3688v1 (2008)

[15] A. Aleksejevs, S. Barkanova, P. Blunden and N. Deg, arXiv:0707.0657 (2007)

[16] A. Aleksejevs and M. Butler, to be published in J. Phys. G: Nucl. Part. Phys. 37 (2010)

[17] Bernard V, Kaiser N, Schmidt A and Meissner U-G, Phys. Lett. B 319 269 15 (1993)

[18] T. Fuchs, et al., arXiv:nucl-th/0305070v1, (2003)

[19] T. R. Hemmert, et al., Phys. Rev. D55, 55, (1997)

[20] The Physics Virtual Library at http://www.vifaphys.de/fi.php, Elementary Particles and Fields, Software

Renormalization of Fermion-Flavour Mixing

Andrea A. Almasy

Department of Mathematical Sciences, University of Liverpool, Liverpool L69 3BX, UK

We report on an explicit on-shell framework to renormalize the fermion-flavour mixing matrices in the Standard Model and its extensions, at one-loop level. It is based on a novel procedure to separate the external-leg mixing corrections into gauge-independent self-mass and gauge-dependent wave-function renormalization contributions.

1 Introduction

Renormalizability endows the Standard Model (SM) with enhanced predictive power due to the fact that ultraviolet (UV) divergences from quantum effects can be eliminated by a redefinition of a finite number of independent parameters, such as masses and coupling constants. Furthermore, it has been known for a long time that, in the most frequently employed formulations in which the complete bare mass matrices of quarks are diagonalized, the Cabibbo-Kobayashi-Maskawa (CKM) quark mixing matrix must be also renormalized. In fact, this problem has been the object of several interesting studies over the last two decades. A matter of considerable interest is the generalization of these considerations to minimal renormalizable extensions of the SM.

2 On-shell renormalization prescription

The on-shell renormalization framework we propose is a generalization of Feynman's approach in QED [1]. Recall that in QED the self-energy contribution to an outgoing fermion is given by

$$\Delta\mathcal{M}^{\text{leg}} = \overline{u}(p)\Sigma(\not{p})\frac{1}{\not{p}-m}, \quad \Sigma(\not{p}) = A(p^2) + B(p^2)(\not{p}-m) + \Sigma^{\text{fin}}(\not{p})$$

where $\Sigma(\not{p})$ is the self-energy, A and B are divergent constants, and Σ^{fin} is a finite part which is proportional to $(\not{p}-m)^2$ in the vicinity of $\not{p}=m$ and therefore does not contribute to $\Delta\mathcal{M}^{\text{leg}}$. The contribution of A to $\Delta\mathcal{M}^{\text{leg}}$ is singular at $\not{p}=m$ and gauge independent and that of B is regular but gauge dependent. They are called self-mass (sm) and wave-function renormalization (wfr) contributions. A is cancelled by the mass counterterm δm while B is combined with proper vertex diagrams leading to a finite and gauge-independent physical amplitude.

In the case of fermion-flavour mixing we encounter not only diagonal terms as in QED but also off-diagonal contributions. The self-energy corrections to an external fermion leg are now

$$\Delta\mathcal{M}^{\text{leg}}_{ij} = \overline{u}_i(p)\Sigma_{ij}(\not{p})\frac{1}{\not{p}-m_j},$$

where i denotes the external fermion of momentum p and mass m_i, and j the virtual fermion of mass m_j. Using a simple algorithm that treats i and j on an equal footing, we write the self-energy as:

$$\Sigma_{ij}(\not{p}) = A_{ij}(p^2) + (\not{p} - m_i)B_{1,ij}(p^2) + B_{2,ij}(p^2)(\not{p} - m_j) + (\not{p} - m_i)\Sigma_{ij}^{\text{fin}}(p^2)(\not{p} - m_j),$$

in analogy to QED. Similarly, we identify the contributions to $\Delta\mathcal{M}^{\text{leg}}$ coming from A as sm and those coming from $B_{1,2}$ as wfr contributions. Again, Σ^{fin} gives zero contribution.

We consider next the cancellation of the sm contributions with the mass counterterms. We start from the bare mass term in the Lagrangian, $-\overline{\Psi}' m_0' \Psi'$, and decompose the bare mass into a so-called renormalized mass and a corresponding counterterm, $m_0' = m' + \delta m'$. We then apply a bi-unitary transformation on the fermion fields $\overline{\Psi}', \Psi'$ that diagonalizes m' leading to the transformed mass term $-\overline{\Psi}(m + \delta m^{(-)}P_L + \delta m^{(+)}P_R)\Psi$. Here $P_{R,L} = (1 \pm \gamma_5)/2$ are the chiral projectors, m is real, diagonal and positive and $\delta m^{(\pm)}$ are arbitrary non-diagonal matrices subject to the Hermiticity constraint

$$\delta m^{(+)} = \delta m^{(-)\dagger}. \tag{1}$$

Further we adjust $\delta m^{(\pm)}$ to cancel, as much as possible, the sm contributions to $\Delta\mathcal{M}^{\text{leg}}$.

The diagonalization of the complete mass matrix $M = m + \delta m^{(-)}P_L + \delta m^{(+)}P_R$ by means of a bi-unitary transformation of the form:

$$\psi_{L,R} = U_{L,R}\hat{\psi}_{L,R} \approx (1 + ih_{L,R})\hat{\psi}_{L,R}, \tag{2}$$

naturally induces a mixing counterterm matrix. Note that the second equality holds only at one-loop level. The matrices $h_{L,R}$ are chosen such that $\hat{M}$ is diagonal and are found to be:

$$i(h_{L,R})_{ij} = -\frac{m_i\delta m_{ij}^{(\mp)} + \delta m_{ij}^{(\pm)}m_j}{m_i^2 - m_j^2}, \qquad (h_{L,R})_{ii} = 0. \tag{3}$$

Due to the transformation in Eq. (2) the $Vf_i\overline{f}_j$ bare interaction term in the Lagrangian transforms as well

$$\mathcal{L}_{Vf_i\overline{f}_j} \propto \overline{\psi}_L^{f_i} K_0 \gamma^\lambda \psi_L^{f_j} V_\lambda + H.c. \quad \xrightarrow{U_{L,R}} \quad \overline{\hat{\psi}}_L^{f_i}(K + \delta K)\gamma^\lambda \hat{\psi}_L^{f_j} V_\lambda + H.c.,$$

with $\delta K = i(Kh_L^{f_j} - h_L^{f_i}K)$. $K_0 = K + \delta K$ and K are explicitly gauge independent and preserve the basic properties of the theory. K is finite and identified with the renormalized mixing matrix. δK is identified with the mixing counterterm matrix.

3 Particular cases

Following the procedure outlined in Sec. 2, a CKM counterterm matrix was proposed in Ref. [2]:

$$\delta V = i\left(Vh_L^D - h_L^U V\right),$$

with $h_L^{D,U}$ given by Eq. (3). Both $V_0 = V + \delta V$ and V satisfy the unitarity condition and are explicitly gauge independent.

Some years later an alternative approach based on a gauge-independent quark mass counterterm expressed directly in terms of the Lorentz-invariant self-energy functions was proposed [3]. The mass counterterms so defined obey three important properties: (i) they are gauge independent, (ii) they automatically satisfy the Hermiticity constraint of Eq. (1) and thus are flavour-democratic, and (iii) they are expressed in terms of the invariant self-energy functions and thus useful for practical applications.

A comparative analysis of the W-boson hadronic widths in various CKM renormalization schemes, including the ones discussed above, and the study of the implications of flavour-mixing renormalization on the determination of the CKM parameters are presented in Ref. [4].

We have also considered the mixing of leptons in a minimal, renormalizable extension of the SM that can naturally accommodate heavy Majorana neutrinos. Here mixing appears both in charged- and neutral-current interactions and is described by the bare mixing matrices B_0 and C_0. Following ones more the prescription of Sec. 2, we found that the charged-lepton mass counterterm is identical to that of quarks, up to particle content. However, in the case of the Majorana-neutrino there are two important modifications due to the Majorana condition $\nu = \nu^C$ (here C denotes charge conjugation): (i) in addition to the Hermiticity constraint of Eq. (1) the mass counterterm should be symmetric, and (ii) now only one unitary transformation, $U^\nu = 1 + ih^\nu$, is needed to diagonalize the complete mass matrix $\hat{M}^\nu$. Keeping in mind the two changes, the mixing counterterm matrices are [5]

$$\delta B = i\left(Bh^\nu - h_L^l B\right) \qquad \text{and} \qquad \delta C = i\left(Ch^\nu - h^\nu C\right).$$

Once δB is fixed, δC is fixed as well. Note that both, the bare and renormalized mixing matrices, are gauge independent and preserve the basic properties of the theory.

4   Conclusions

We proposed an explicit on-shell framework to renormalize the fermion-flavour mixing matrices in the SM and its extensions, at one-loop level. It is based on a novel procedure to separate the external-leg mixing corrections into gauge-independent sm and gauge-dependent wfr contributions. An important property is that this formulation complies with UV finiteness and gauge-parameter independence, and also preserves the basic structure of the theory.

Acknowledgements

References

[1] R.P. Feynman, Phys. Rev. **76** 769 (1949).

[2] Bernd A. Kniehl and Alberto Sirlin, Phys. Rev. Lett. **97** 221801 (2006);
     Bernd A. Kniehl and Alberto Sirlin, Phys. Rev. **D74** 116003 (2006).

[3] Bernd A. Kniehl and Alberto Sirlin, Phys. Lett. **B673** 208 (2009).

[4] A.A. Almasy, B.A. Kniehl and A. Sirlin, Phys. Rev. **D79** 076007 (2009).

[5] Andrea A. Almasy, Bernd A. Kniehl and Alberto Sirlin, Nucl. Phys. **B818** 115 (2009).

Strong Scaling Ansatz of Flavor Neutrino Mass Matrix and Normal Mass Hierarchy

Teppei Baba, Masaki Yasué

Department of Physics, Tokai University, 1117 KitaKaname, Hiratsuka, Kanagawa, Japan

Considering Strong Scaling Ansatz (SSA) which predicts $U_{e3} = 0$ and the inverted mass hierarchy, we discover the possibility to realize the normal mass hierarchy by introducing tiny breakings of SSA. In this case, we can automatically reproduce the small mass squared difference ratio ($\Delta m_\odot^2 / \Delta m_{atm}^2 \ll 1$) instead of the suppressed U_{e3} ($|U_{e3}| \ll 1$).

1 Introduction

We start with the definition of the PMNS matrix U_{PMNS} [1], which gives the transformation of flavor eigenstate of neutrinos $\nu_f (f = e\text{А}\mu\text{А}\tau)$ into mass eigenstate of neutrinos $\nu_i (i = 1\text{А}2\text{А}3)$ as $\nu_f = \sum_{i=1}^{3} (U_{PMNS})_{fi} \nu_i$. We employ U_{PMNS} determined to be [2]:

$$U_{PMNS} = \Omega \begin{pmatrix} c_{13}c_{12} & c_{13}s_{12}e^{i\rho} & s_{13}e^{-i\delta} \\ -s_{12}e^{-i\rho}c_{23} - s_{13}e^{i\delta}c_{12}s_{23} & c_{12}c_{23} - s_{13}e^{i\delta}s_{12}e^{i\rho}s_{23} & c_{13}s_{23} \\ s_{12}e^{-i\rho}s_{23} - s_{13}e^{i\delta}c_{12}c_{23} & -c_{12}s_{23} - s_{13}e^{i\delta}s_{12}e^{i\rho}c_{23} & c_{23}c_{13} \end{pmatrix} K, \quad (1)$$

where $K = diag \begin{pmatrix} e^{i\beta_1} & e^{i\beta_2} & e^{i\beta_3} \end{pmatrix}$, $\Omega = diag \begin{pmatrix} 1 & e^{i\gamma} & e^{-i\gamma} \end{pmatrix}$ and θ_{ij} is the $\nu_i - \nu_j$ mixing angle. Assuming the seesaw model [3], we obtain the flavor neutrino mass matrix as

$$M_\nu = -\langle v \rangle^2 Y_\nu^T M_R^{-1} Y_\nu \tag{2}$$

through the higgs mechanism, where Y_ν is a coupling constant of the higgs interaction and $\langle v \rangle$ is a vacuum expectation value of the higgs boson. U_{PMNS} can be transformed from Eq.(1) into the Particle Data Group (PDG) version [4] by removing additional phases of ρ and γ. It should be noted that observable Dirac CP phase is given by $\delta_{CP} = \delta + \rho$ and Majorana CP phase β_1 is changed into $\beta_1' = \beta_1 - \rho$ in the case of U_{PMNS} of the PDG version. The experimental data [5] shows us atmospheric neutrino mass squared differences $\Delta m_{atm}^2 \equiv m_3^2 - (m_2^2 + m_1^2)/2$, solar neutrino mass squared differences $\Delta m_\odot^2 \equiv m_2^2 - m_1^2$ and mixing angles as follows:

$$\sin^2 \theta_{13} < 0.016^{+0.01}_{-0.01}, \ \sin^2 \theta_{23} \approx 0.466^{+0.073}_{-0.058}, \ \sin^2 \theta_{12} \approx 0.312^{+0.018}_{-0.019},$$
$$\Delta m_{atm}^2 \approx 7.67^{+0.16}_{-0.19} \times 10^{-5}, \ \Delta m_\odot^2 \approx 2.39^{+0.08}_{-0.11} \times 10^{-3}. \tag{3}$$

Strong Scaling Ansatz (SSA) [6] requires that all ratios of $M_{f\mu}/M_{f\tau}$ are equal as

$$\mathbf{c} \equiv -\sigma \frac{M_{e\mu}}{M_{e\tau}} = -\sigma \frac{M_{\mu\mu}}{M_{\mu\tau}} = -\sigma \frac{M_{\tau\mu}}{M_{\tau\tau}} \tag{4}$$

where $\sigma \equiv \pm 1$. There is an advantage of SSA that the condition of Eq.(4) is invariant under the renormalization running because its effects can be canceled between numerator and denominator [6]. Under the condition of Eq.(4), M_ν and also $\mathbf{M} \equiv M_\nu^\dagger M_\nu$ are determined as follows:

$$M_\nu^{(+)} = \begin{pmatrix} a & be^{i\chi} & \frac{-\sigma b}{\mathbf{c}}e^{i\chi} \\ be^{i\chi} & d & -\sigma\frac{d}{\mathbf{c}} \\ \frac{-\sigma b}{\mathbf{c}}e^{i\chi} & -\sigma\frac{d}{\mathbf{c}} & \frac{d}{\mathbf{c}^2} \end{pmatrix}, \quad \mathbf{M}^{(+)} = \begin{pmatrix} A & |B|\,e^{i\eta} & \frac{-\sigma|B|}{\mathbf{c}}e^{i\eta} \\ |B|\,e^{-i\eta} & D & \frac{-\sigma D}{\mathbf{c}} \\ \frac{-\sigma|B|}{\mathbf{c}}e^{-i\eta} & \frac{-\sigma D}{\mathbf{c}} & \frac{D}{\mathbf{c}^2} \end{pmatrix}. \quad (5)$$

We, respectively, use χ and η in Eq.(5) to denote phases of $e\mu$ and $e\tau$ elements of $M_\nu^{(+)}$ and $\mathbf{M}^{(+)}$, while $a, b, d, A, D, \mathbf{c}$ are real. We calculate the eigenvectors of $\mathbf{M}^{(+)}$, which does not contain the Majorana CP phases, and obtain

$$|\lambda_+\rangle = \begin{pmatrix} \cos\theta \\ -\sin\theta\frac{\mathbf{c}}{\sqrt{1+\mathbf{c}^2}}e^{-i\eta} \\ \sin\theta\frac{\sigma}{\sqrt{1+\mathbf{c}^2}}e^{-i\eta} \end{pmatrix}, |\lambda_-\rangle = \begin{pmatrix} \sin\theta e^{i\eta} \\ \frac{\mathbf{c}}{\sqrt{\mathbf{c}^2+1}}\cos\theta \\ -\frac{\sigma}{\sqrt{\mathbf{c}^2+1}}\cos\theta \end{pmatrix}, |\lambda\rangle = \frac{1}{\sqrt{1+\mathbf{c}^2}}\begin{pmatrix} 0 \\ \sigma \\ \mathbf{c} \end{pmatrix}, \quad (6)$$

where $\tan\theta = \frac{|B|\sqrt{1+\mathbf{c}^2}}{\mathbf{c}(\lambda_- - A)}$. Corresponding eigenvalues are given by $\lambda_\pm = \frac{1}{2}\left\{\left(D\left(1 + 1/\mathbf{c}^2\right) + A\right) \pm \omega\right\}$ and $\lambda = 0$, where $\omega = \sqrt{\left\{D\left(1 + 1/\mathbf{c}^2\right) - A\right\}^2 + 4\,|B|^2\left(1 + 1/\mathbf{c}^2\right)}$. We obtain $U_{e3} = 0$ if $|\lambda\rangle$ is assigned to the state of ν_3. In this case, we also obtain $\theta = \theta_{12}$, $t_{23} = \sigma/\mathbf{c}A$ $\rho = \eta$. This properties of SSA allow us to reproduce experimental data of Eq.(3) whose best fit values indicate the smallness of θ_{13} and the small deviation of θ_{23} from $\sigma\pi/4$. However, we couldn't have realized any hierarchy except for the inverted mass hierarchy [6].

We have discovered the possibility to realize the normal mass hierarchy in the paradigm of SSA when $|\lambda\rangle$ is assigned to the state of ν_2. In this proceedings, we call the former case (C1) and the latter case (C2). In (C2), we obtain $\theta_{12} = 0$ instead of $\theta_{13} = 0$ though it should be improved by introducing tiny breakings of SSA as well as $\theta = \theta_{13}$, $t_{23} = -\sigma\mathbf{c}$ and $\delta = -\eta$. In the next section, we consider a tiny breaking term to be added to M_ν in the case of (C2).

2   Effects of breakings of SSA

Breakings of SSA can be defined by adding mass matrix $M_\nu^{(-)}$ to $M_\nu^{(+)}$ as $M_\nu = M_\nu^{(+)} + M_\nu^{(-)}$ where

$$M_\nu^{(-)} = \varepsilon \begin{pmatrix} 0 & b' & \sigma b'/\mathbf{c} \\ b' & d' + d'' & \sigma d'/\mathbf{c} \\ \sigma b'/\mathbf{c} & \sigma d'/\mathbf{c} & (d' - d'')/\mathbf{c}^2 \end{pmatrix}. \quad (7)$$

The parameter ε denotes the tiny SSA breaking and $\tan\theta_{23}$ abbreviated as t_{23} is written as $t_{23} = -\sigma\mathbf{c}(1 - \Delta)/(1 + \Delta)$ in (C1) and $t_{23} = \sigma(1 - \Delta)/\mathbf{c}(1 + \Delta)$ in (C2), where Δ is also small because it induces to break SSA. We neglect the second order of breaking terms of SSA. Using formulas of [2], we easily compute the masses of neutrinos up to O(ε) as

$$m_1 e^{-2i\beta_1'} \approx \frac{1}{2}e^{2i\rho}a + d_0 - z_1, \quad m_2 e^{-2i\beta_2} \approx \frac{1}{2}e^{2i\rho}a + d_0 + z_1, \quad m_3 e^{-2i\beta_3} \approx 2\varepsilon d', \quad (8)$$

where $z_1 = \frac{2b_0 e^{i(\rho+\chi)}}{\mathbf{c}\sqrt{2}\sin 2\theta_{12}}$ in (C1),

$$m_1 e^{-2i\beta_1'} \approx \frac{1}{2}e^{2i\rho}a + \varepsilon d' - z_2, \quad m_2 e^{-2i\beta_2} \approx \frac{1}{2}e^{2i\rho}a + \varepsilon d' + z_2, \quad m_3 e^{-2i\beta_3} \approx 2d_0, \quad (9)$$

where $z_2 = \sqrt{2}e^{i\rho}\frac{\varepsilon b' + (i\gamma + \Delta)e^{i\chi}b_0}{\sin 2\theta_{12}}$ in (C2). As a result, we observe the new possibility of the normal mass hierarchy in (C2) though we need the condition of $|a| \ll 1$, whereas we are only allowed to have the inverted mass hierarchy in (C1) as have been already known.

The formulas enable us to readily understand the dependdence of mixing angles on flavor neutrino masses as

$$
\begin{aligned}
\tan 2\theta_{12}e^{i\rho} &\approx \frac{2\sqrt{2}b_0\left(a_0 e^{i\chi} + 2d_0 e^{-i\chi}\right)}{\mathbf{c}\left\{4\left(b_0^2 + d_0^2\right) - a_0^2\right\}}, \\
\tan 2\theta_{13}e^{-i\delta} &\approx \sigma 2\sqrt{2}\frac{b_0\left(a_0 e^{i\chi} + 2d_0 e^{-i\chi}\right)(\Delta - i\gamma) - \varepsilon\left(a_0 b' + b_0 d'' e^{-i\chi}\right)}{a_0^2 + 2b_0^2},
\end{aligned}
\tag{10}
$$

for (C1),

$$
\begin{aligned}
\tan 2\theta_{12}e^{i\rho} &\approx -2\sqrt{2}\frac{\varepsilon\left(a_0 b' + b_0 d'' e^{-i\chi}\right) + b_0(\Delta + i\gamma)\left(a_0 e^{i\chi} + 2d_0 e^{-i\chi}\right)}{a_0^2 + 2b_0^2}, \\
\tan 2\theta_{13}e^{-i\delta} &\approx -\sigma 2\sqrt{2}b_0\frac{a_0 e^{i\chi} + 2d_0 e^{-i\chi}}{\mathbf{c}\left(4d_0^2 - a_0^2\right)},
\end{aligned}
\tag{11}
$$

for (C2), where γ is also a small parameter because it obviously breaks SSA. We naturally obtain the smallness of θ_{13} in (C1), while we need $\left|b_0\left(a_0 e^{i\chi} + 2d_0 e^{-i\chi}\right)\right| \ll \left|4d_0^2 - a_0^2\right|$ for (C2). Moreover, Dirac CP phase $\delta_{CP} = \delta + \rho$ and Majorana CP phases β_1', β_2 and β_3 are found to large in both cases. Mass squared differences in (C2) are calculated from Eq.(9) as

$$
\begin{aligned}
\Delta m_\odot^2 &\approx \frac{2\sqrt{2}}{\sin 2\theta_{12}}\mathrm{Re}\left[\left(e^{-i\rho}a + 2\varepsilon d' e^{i\rho}\right)\left\{\varepsilon b' + (i\gamma + \Delta)e^{i\chi}b_0\right\}\right], \\
\Delta m_{atm}^2 &\approx 4d_0^2 - \tfrac{1}{4}a\left(a + 4\varepsilon d'\cos 2\rho\right).
\end{aligned}
\tag{12}
$$

Therefore, there is another virtue of SSA in (C2) that smallness of the ratio of the mass squared difference $\Delta m_{atm}^2/\Delta m_\odot^2 \ll 1$ is automatically satisfied as suggested by experiment because of the smallness of ε, γ and Δ, which serve as the SSA breaking parameters.

Acknowledgments

References

[1] Z. Maki, M. Nakagawa and S. Sakata, Prog. Theor. Phys. **28** 870 (1962).

[2] T. Baba and M. Yasuè, Phys. Rev. **D75** 055001 (2007).

[3] P. Minkowski, Phys. Lett. **B67** 421 (1977); T. Yanagida, in Proceedings of the Workshop on Unified Theories and Baryon Number in the Universe edited by A. Sawada and A. Sugamoto (KEK Report No.79-18, Tsukuba, 1979), p.95; Prog.Theor. Phys. 64 1870 (1980); M. Gell-Mann, P. Ramond and R. Slansky in Supergravity, North-Holland, Amsterdam 1979 edited by P. van Nieuwenhuizen and D. Freedmann, p.315; R. N. Mohapatra and G. Senjanovìc, Phys. Rev. Lett. 44, 912 (1980). See also, P. Minkowski, in Proceedings of the XI International Workshop on Neutrino Telescopes in Venice, Venice, 2005, edited by M. Baldo Ceolin (Papergraf S.p.A., Italy, 2005), p.7.

[4] S. Eidelman *et al*, Phys. Lett. **B592** 149 (2004). See also, L.-L. Chau and W.-Y. Keung, Phys. Rev. Lett. 53, 1802 (1984).

[5] G. L. Fogli, E. Lisi, A. Marrone, A. Melchiorri, A. Palazzo, A. M. Rotunno, P. Serra, J. Silk and A. Slosar, Phys. Rev. **D78** 033010 (2008).

[6] R. N. Mohapatra, W. Rodejohann Phys. Lett. **B644** 59 (2007); A. Blum1, R. N. Mohapatra2, and W. Rodejohann1, Phys. Rev. **D76** 053003 (2007).

Polarization effects in neutrino pairs production by electrons(positrons) in hot stellar magnetic fields

Rasmiyya E. Gasimova[a][1], Vali A. Huseynov (Guseinov)[ab][2], Yagut T. Shukurova[a][3]

[a]Nakhchivan State University, AZ 7000, Nakhchivan, Azerbaijan
[b]Nakhchivan Department of Azerbaijan National Academy of Sciences, AZ 7000, Nakhchivan, Azerbaijan
[1]vgusseinov@yahoo.com, [2]gasimovar@yahoo.co.uk, [3]yshukurova@yahoo.com

Polarization effects in neutrino pairs production by electrons (positrons) in hot stellar magnetic fields with allowance for the longitudinal polarizations of the initial and final electrons (positrons) are investigated. The asymmetry of the cooling in the process of electron neutrino pairs emission by electrons (positrons) is eight (four) times more than that one in the process of muon neutrino pairs emission by electrons (positrons) or in the process of tauon neutrino pairs emission by electrons (positrons).

1 Introduction

We investigate polarization effects in neutrino pairs production by electrons (positrons)

$$e^{\pm} \longrightarrow e^{\pm} + \nu_i + \widetilde{\nu}_i, \tag{1}$$

in hot stellar magnetic fields (e.g., in magnetars [1]) with allowance for the longitudinal polarizations of the initial and final electrons (positrons). Here $\nu_i = \nu_e, \nu_\mu, \nu_\tau$ and $\widetilde{\nu}_i = \widetilde{\nu}_e, \widetilde{\nu}_\mu, \widetilde{\nu}_\tau$. These processes were studied by numerous authors [2]-[9]. We present the analytic formula for the differential probability (DP) of the neutrino pairs emission by electrons (positrons) in hot stellar magnetic fields with allowance for the longitudinal polarizations of the initial and final electrons (positrons). It enables us to analyze the energy loss by electrons (positrons) having the different polarization states by means of neutrino pairs emission in hot stellar magnetic fields with allowance for the longitudinal polarizations of the initial and final electrons (positrons).

2 Differential probability of the processes and asymmetry of cooling of electrons (positrons) having different polarization states

We obtain for the DP per unit of time and per unit of volume

$$dw = (2\pi)^{-7} G_F^2 eH\omega^2\omega'^2 \sum_{\mathrm{n}=1}^{\infty} \sum_{\mathrm{n}'=0}^{\mathrm{n}-1} \sum_{\mathrm{i}} \frac{E_i E_i'}{|E_i' p_{zi} - E_i p_{zi}'|} Q f_e (1 - f_e') d\omega d\omega' d\Omega d\Omega'. \tag{2}$$

The meanings of the above indicated notations can be found in [10]. When electrons (positrons) are in different longitudinal polarization states, the asymmetry of the cooling of an electron (positron) gas by emission of neutrino pairs in a magnetic field can be determined by the general expression

$$A = \frac{dw_R - dw_L}{dw_R + dw_L}, \tag{3}$$

where $dw_R = dw(\zeta = 1, \zeta' = 1)$, $dw_L = dw(\zeta = -1, \zeta' = -1)$. Here $\zeta(\zeta')$ characterizes the orientation of the spin of the initial (final) electrons or positrons and $\zeta, \zeta' = +1(-1)$ corresponds to right-hand (left-hand) helicity.

3 Numerical estimations on asymmetry of cooling of electrons (positrons) having different polarization states

Let us consider two different types of an electron (positron) gas: the gas consisting of only the electrons (positrons) having a left-hand circular polarization and the gas consisting of only the electrons (positrons) having a right-hand circular polarization. We also assume that these two types of an electron (positron) gas are not mixed and the initial temperatures of the both of the gases are equal. After emission of neutrino pairs by electrons (positrons) the gases will be cooled at the expense of the energy transfer from electrons (positrons) to the emitted neutrino pairs. However, the gas consisting of only the electrons (positrons) having a left-hand circular polarization and the gas consisting of only the electrons (positrons) having a right-hand circular polarization will be cooled differently: $T_L \neq T_R$. Here T_L is the temperature of the gas (after neutrino pair emission) consisting of only the electrons (positrons) having a left-hand circular polarization and T_R is the temperature of the gas (after neutrino pair emission) consisting of only the electrons (positrons) having a right-hand circular polarization. Let us consider the case of $\vartheta = 0$, $\vartheta' = \pi/2$, $\alpha' = \varphi$ for numerical estimations, where $\vartheta(\vartheta')$ is the polar angle of the emitted antineutrino (neutrino) momentum, α' is the azimuthal angle of the emitted neutrino momentum, $tg\varphi = q_y/q_x$, $q = k + k'$, $k(k')$ is the 4-momentum of the emitted antineutrino (neutrino). If we consider the transition between the following Landau levels $n = 2 \longrightarrow n' = 1$ in magnetars ($H \cong 4.41 \times 10^{15}G$) and the (anti)neutrinos of energy $\omega, \omega' \cong 1MeV$, we obtain $A_{e^- \nu_e \widetilde{\nu}_e} \cong -0.80$ for the $e^- \longrightarrow e^- \nu_e \widetilde{\nu}_e$ process. Numerical estimations show that for the considered case of the magnetic field strength and the (anti)neutrino energy $A_{e^- \nu_\mu \widetilde{\nu}_\mu} = A_{e^- \nu_\tau \widetilde{\nu}_\tau} \cong -0.10$, i.e. $A_{e^- \nu_e \widetilde{\nu}_e} \cong 8A_{e^- \nu_\mu \widetilde{\nu}_\mu} \cong 8A_{e^- \nu_\tau \widetilde{\nu}_\tau}$.

Now we consider the process $e^+ \longrightarrow e^+ \nu_i \widetilde{\nu}_i$ and the case of $\vartheta = 0$, $\vartheta' = \pi/2$, $\alpha' = \varphi$ for numerical estimations of the asymmetry of the cooling. If we consider the transition $n = 2 \longrightarrow n' = 1$ in magnetars ($H \cong 4.41 \times 10^{15}G$) and the (anti)neutrinos of energy $\omega, \omega' \cong 1MeV$, we obtain $A_{e^+ \nu_e \widetilde{\nu}_e} \cong 0.84$ for the $e^+ \longrightarrow e^+ \nu_e \widetilde{\nu}_e$ process. Numerical estimations show that for the considered case of the magnetic field strength and the (anti)neutrino energy $A_{e^+ \nu_\mu \widetilde{\nu}_\mu} = A_{e^+ \nu_\tau \widetilde{\nu}_\tau} \cong 0.21$, i.e. $A_{e^+ \nu_e \widetilde{\nu}_e} \cong 4A_{e^+ \nu_\mu \widetilde{\nu}_\mu} \cong 4A_{e^+ \nu_\tau \widetilde{\nu}_\tau}$.

4 Conclusions

It is shown that the differential probabilities of the considered processes are sensitive to the spin variable of the initial and final electrons (positrons) and to the direction of the emitted neutrino pairs momenta. In general, the gas consisting of only the electrons (positrons) having

a left-hand circular polarization and the gas consisting of only the electrons (positrons) having a right-hand circular polarization are cooled at the expense of neutrino pairs emission by the electrons (positrons) in hot stellar magnetic fields asymmetrically. In the cooling process of the electron (positron) gas at the expense of neutrino pairs emission by the electrons (positrons) in hot stellar magnetic fields the dominant role belongs to the electron neutrino pairs emission process compared with the contribution of the muon (tauon) neutrino pairs emission process. The asymmetry of the cooling in the process of electron neutrino pairs emission by electrons is 8 times more than that one in the process of muon neutrino pairs emission by electrons or in the process of tauon neutrino pairs emission by electrons. The asymmetry of cooling in the process of electron neutrino pairs emission by positrons is 4 times more than that one in the process of muon neutrino pairs emission by positrons or in the process of tauon neutrino pairs emission by positrons.

5   Acknowledgments

References

[1] R.C. Duncan, C. Thompson, Ap.J. Letters **392** L9 (1992).

[2] V.N. Baier and V.M. Katkov, Sov. Phys. Doklady **171** 313 (1966).

[3] J.D. Landstreet, Phys. Rev. **153** 1372 (1967).

[4] V. Canuto, H.Y. Chiu and C.K. Chou, Phys. Rev. **D2** 281 (1970).

[5] A.V. Borisov, V.Ch. Zhukovskii and P.A. Eminov, Izv. Vuz. Fiz. **3** 110 (1978).

[6] A.D. Kaminker and D.G. Yakovlev, JETP **76** 229 (1993).

[7] A. Vidaurre *et al.*, Ap.J. **448** 264 (1995).

[8] D. G. Yakovlev *et al.*, Phys. Rep. **354** 1 (2001).

[9] A.D. Kaminker and D.G. Yakovlev, Mon. Not. Roy. Astroph. Soc. **371** 477 (2006).

[10] V.A. Guseinov, I.G. Jafarov and R.E. Gasimova, Phys. Rev. **D75** 073021 (2007).

Divergences in Particle Processes in Intense External Fields

Anthony Hartin[1]

[1]DESY, Notketraße 85, 22607 Hamburg, Germany

The study of fundamental interactions in intense external fields is a broad, interesting and incomplete area of study. Intense external fields are present in the charged bunch collisions at particle colliders, being responsible for the beamstrahlung, pair background processes and potentially affecting all collider physics processes. Pair annihilation in the intense fields near the surfaces of magnetars maybe responsible for intense gamma ray bursts. The intense colomb fields present in heavy ion collisions are also known to affect physics processes. In this paper I review the general QED in intense external fields, discuss the divergences present in the beamstrahlung transition rate and their potential mitigation.

1 QED in the Bound Interaction Picture

For Quantum Electrodynamical physics processes that take place in the presence of an external potential A^e the Lagrangian Density is written

$$\mathcal{L}_{QED} = -\tfrac{1}{4}\, F^{\mu\nu} F_{\mu\nu} + \bar{\psi}(i\slashed{\partial} + e\slashed{A} + e\slashed{A}^e - m)\psi \tag{1}$$

In the Interaction Picture (IP), the second term in Equation 1 is expanded and the term trilinear in Dirac and Maxwell field operators makes up the interaction Lagrangian $\mathcal{L}_I = e\bar{\psi}(\slashed{A} + \slashed{A}^e)\psi$. However if the external field is intense enough the coupling term arising from the external potential A^e approaches one, rendering the perturbation theory invalid. It is necessary to leave the external potential in the Dirac part of the Lagrangian so that, $\mathcal{L}_D = e\bar{\psi}(i\slashed{\partial} + \slashed{A}^e - m)\psi$.

In order to proceed in this Bound Interaction Picture (BIP) it is necessary to solve the Dirac Equation with the inclusion of the external potential. This Bound Dirac equation can be solved exactly for the case of the external potential being a plane wave electromagnetic field. The Bound Dirac Field Operator is a product of the normal free fermion solution with an extra phase and a magnetic moment term,

$$\Psi_p^V(x) = \left(1 + \frac{e\slashed{k}\slashed{A}^e}{2(kp)}\right) e^{iS(x)}\, u(p)$$

$$\text{where} \quad S(x) = -i\int_0^{(k\cdot x)} \left[\frac{e(A^e p)}{(kp)} - \frac{e^2 A^{e2}}{2(kp)}\right] d\phi$$
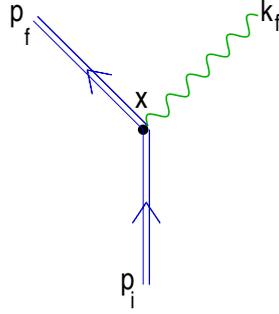
Figure 1: The Beamstrahlung Feynman diagram.

2 Beamstrahlung divergences

Photon radiation from a fermion scattering inelastically from the field of an oncoming charge bunch in a collider - the Beamstrahlung process (Figure 1) is considered in the BIP with Bound Dirac solutions in a constant crossed electromagnetic field. This form for external field leads to Bessel K functions of fractional order (which approach infinity as their argument tends to zero) in the transition probability,

$$W = \frac{\alpha m^2}{\pi\sqrt{3}\epsilon_i} \int_0^{(k\cdot p_i)} \frac{du}{(1+u)^2} \left[\int_{\xi(u)}^\infty K_{5/3}(y)dy - \frac{u^2}{1+u} K_{2/3}(\xi(u)) \right]$$

$$\text{where} \quad \xi(u) = \frac{2u}{3\nu(k\cdot p_i)}, \quad u = \frac{(k\cdot k_f)}{(k\cdot p_i)(k\cdot p_f)}$$

(2)

The Beamstrahlung Transition Rate (Equation 2) reaches infinity at the lower bound of the integration over the variable u which suggests that the beamstrahlung transition rate is divergence whenever the scalar product $(k\cdot k_f)$ is zero. The two apparent conditions for the infinity are when the radiated photon is soft (an IR divergence) or for radiation in the direction of the external field 4-momenta (a collinear divergence). The latter divergence is particularly glaring since it is known that the majority of radiated photons are emiited in a relativistic $1/\gamma$ cone about the initial fermion momentum (Figure 2).[1]

3 Divergence handling in the Bound Interaction Picture

In order to remove the divergence from the Beamstrahlung Transition Rate, it is tempting simply to follow the procedure of Regularization and Cancellation/Renormalization in the IP. However there are subtleties that need to be taken into account.

One such is that the regularization procedure doesnt lead to a cutoff-dependent logarithm, rather to a change in the lower bound of the integration over the parameter u. However this can be achieved using at least one of the usual at least methods - introducing a small photon mass to render $(k\cdot k_f)$ non-zero.

A second difficulty is that the Beamstrahlung process has one vertex with the emitted photon on the mass shell, whereas the usual Bremstrahlung process is second order with a virtual emitted photon. At the level of counting coupling constants, it can be seen that a correction to Bremstahlung can come from
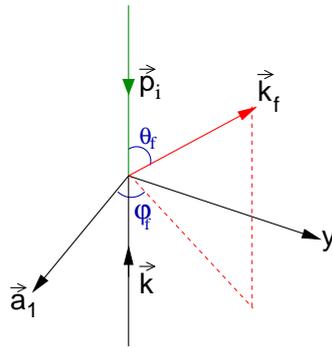
Figure 2: Coordinate system for the beamstrahlung process for a fermion (p_i) approaching an oncoming bunch field (k).
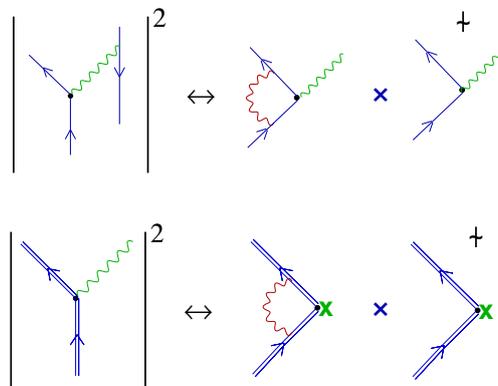
Figure 3: Equivalent Feynman diagrams for divergence cancellation in the IP (upper) and the BIP (lower).

the interference term of the vertex correction and elastic scattering. For the Beamstrahlung process it must be the interference term of the 1st and 3rd order elastic scattering in the BIP (Figure 3).

Work is under way to calculate the 3rd order BIP elastic scattering and to use it to remove the divergence from the Beamstrahlung transition rate. Beyond that it will be necessary to show explicitly that divergences in the BIP cancel to all orders.

4   Bibliography

References

[1] A.F. Hartin J.Phys.Conf.Ser.198 012004 (2009).

New distinguishing feature of a matter and an antimatter: asymmetry in the cooling of charged leptons and antileptons by means of neutrino pairs emission in a magnetic field

Vali A. Huseynov (Guseinov)[ab1], *Rasmiyya E. Gasimova*[a2], *Yagut T. Shukurova*[a3]

[a]Nakhchivan State University, AZ 7000, Nakhchivan, Azerbaijan
[b]Nakhchivan Department of Azerbaijan National Academy of Sciences, AZ 7000, Nakhchivan, Azerbaijan
[1]vgusseinov@yahoo.com, [2]gasimovar@yahoo.co.uk, [3]yshukurova@yahoo.com

The synchrotron emission of neutrino pairs by charged leptons (charged antileptons) in hot dense stellar magnetic fields is investigated in the work. It is shown that a matter and an antimatter are cooled at the expense of neutrino pairs emission asymmetrically. The dominant contribution to the asymmetry of the cooling of the collapsing stellar core is determined with the electron neutrino pairs emission by the electrons (positrons) having a left-hand (right-hand) circular polarization.

1 Introduction

At the neutrino cooling stage a neutron star (NS) cools mainly via neutrino emission from its interiors. In order to analyze the cooling mechanism of a NS it is important to investigate various neutrino reactions in a NS. Here we discuss the neutrino pairs emission by a charged lepton (antilepton) gas in hot dense stellar magnetic fields (e.g., in magnetars [1])

$$l^{\pm} \longrightarrow l^{\pm} + \nu_i + \widetilde{\nu}_i, \tag{1}$$

where $l^{\pm} = e^{\pm}, \mu^{\pm}, \tau^{\pm}$; $\nu_i = \nu_e, \nu_\mu, \nu_\tau$ and $\widetilde{\nu}_i = \widetilde{\nu}_e, \widetilde{\nu}_\mu, \widetilde{\nu}_\tau$. The considered processes are called the synchrotron emission of neutrino pairs (SEONP) by charged leptons (CL) (charged antileptons (CA)). They are responsible for a significant fraction of the energy loss by CL (CA) in the stellar medium and for the cooling of a NS. The SEONP by CL in a magnetic field (MF) and some aspects of polarization effects arising in these processes were studied by numerous authors [2]-[9]. However, the SEONP by CL in hot stellar MFs with allowance for the longitudinal polarizations (LP) of the initial and final CL has not been investigated completely. The main purpose of this paper is to present an analytic formula for the differential probability (DP) of the SEONP by CL (CA) in a MF with allowance for the LP of the initial and final CL (CA), to analyze polarization effects, to calculate the asymmetry of the cooling (AC) of the CL (charged lepton gas) and CA (charged antilepton gas) having the same polarization states by the emission of neutrino pairs in a MF and to show possible applications of the obtained results. Therefore, here we calculate the dependence of the DP of the SEONP by CL(CA) on

the polar and azimuthal angles of the momenta of the emitted neutrinos and antineutrinos in a MF.

2 Differential probability of the processes and asymmetry of cooling of charged leptons and charged antileptons having the same polarization states

In the low-energy approximation of the standard Weinberg-Salam-Glashow model we obtain for the DP per unit of time and per unit of volume

$$dw = (2\pi)^{-7} G_F^2 eH\omega^2\omega'^2 \sum_{n=1}^{\infty} \sum_{n'=0}^{n-1} \sum_{i} \frac{E_i E_i'}{|E_i' p_{zi} - E_i p_{zi}'|} Q f_l (1 - f_l') d\omega d\omega' d\Omega d\Omega'. \tag{2}$$

The meanings of the above indicated notations can be found in [10]. Let us consider two different types of a gas: the gas consisting of only CL and the gas consisting of only CA. We also assume that these two types of a gas are not mixed and the initial temperatures of both of the gases are equal: $T_{l^-} = T_{l^+} = T$. After neutrino pairs emission by CL and CA the gases will be cooled at the expense of the energy transfer from CL and CA to the neutrino pairs. Analyses show that $Q_- \neq Q_+$ and $dw_- \neq dw_+$, where $Q_-(Q_+)$ and $dw_-(dw_+)$ correspond to the $l^-(l^+)$-processes. So, the gas consisting of only CL and the gas consisting of only CA will be cooled asymmetrically: $T_{l^-}' \neq T_{l^+}'$. Here T_{l^-}' is the temperature of the gas consisting of only CL in the final state and T_{l^+}' is the temperature of the gas consisting of only CA in the final state. The AC of a charged lepton gas and a charged antilepton gas by neutrino pairs emission is explained by asymmetric energy transfer from CL and CA to the neutrino pairs. The AC of a charged lepton gas and a charged antilepton gas by neutrino pairs emission can be determined by the general expression

$$A = \frac{dw_- - dw_+}{dw_- + dw_+}. \tag{3}$$

3 Analyses and numerical estimations

Within the considered kinematics and conditions and in the limiting case of a very high temperature, $T \gg (eH)^{1/2}, \mu$, an influence of a medium leads to the constant statistical factors of $1/2$ both for the charged lepton gas and charged antilepton gas and the AC is determined as $A = (Q_- - Q_+)/(Q_- + Q_+)$. Here H is a magnetic field strength and μ is a chemical potential of a charged lepton (antilepton) gas. When initial CL and CA have a left-hand circular polarization, the AC $A_- = A(\zeta = -1) = (g_L^2 - g_R^2)/(g_L^2 + g_R^2)$. Here $g_L = 0.5 + sin^2\theta_w$, $g_R = sin^2\theta_w$ for ν_e−processes, $g_L = -0.5 + sin^2\theta_w$, $g_R = sin^2\theta_w$ for $\nu_\mu(\nu_\tau)$−processes and θ_w is the Weinberg angle. When initial CL and CA have a right-hand circular polarization, the AC is $A_+ = A(\zeta = +1) = -(g_L^2 - g_R^2)/(g_L^2 + g_R^2)$. The expressions for A_- and A_+ show that in the limiting case of a very high temperature $A_- = -A_+$ and the AC is sensitive to a neutrino flavour and spin variables of initial CL and CA. For $e^\pm \longrightarrow e^\pm \nu_e \widetilde{\nu}_e$ processes $A_{e\nu_e\widetilde{\nu}_e}(\zeta = \mp 1) \cong \pm 0.82$ and for $e^\pm \longrightarrow e^\pm \nu_\mu \widetilde{\nu}_\mu$ and $e^\pm \longrightarrow e^\pm \nu_\tau \widetilde{\nu}_\tau$ processes $A_{e\nu_\mu\widetilde{\nu}_\mu}(\zeta = \mp 1) = A_{e\nu_\tau\widetilde{\nu}_\tau}(\zeta = \mp 1) \cong \pm 0.16$. Comparison of the AC for $e^\pm \longrightarrow e^\pm \nu_e \widetilde{\nu}_e$ processes and $e^\pm \longrightarrow e^\pm \nu_\mu \widetilde{\nu}_\mu$ or $e^\pm \longrightarrow e^\pm \nu_\tau \widetilde{\nu}_\tau$ processes gives $A_{e\nu_e\widetilde{\nu}_e}/A_{e\nu_\mu\widetilde{\nu}_\mu} = A_{e\nu_e\widetilde{\nu}_e}/A_{e\nu_\tau\widetilde{\nu}_\tau} \cong 5.13$.

In case of $\zeta = -1$ we obtain for the $e^\pm \longrightarrow e^\pm \nu_e \widetilde{\nu}_e$ processes $dw_- \cong 10 dw_+$. It means that when electron neutrino pairs are emitted by the electrons and positrons having a left-hand circular polarization, $e^- \longrightarrow e^- \nu_e \widetilde{\nu}_e$ can contribute to the cooling process of the collapsing stellar core more essentially than $e^+ \longrightarrow e^+ \nu_e \widetilde{\nu}_e$. In case of $\zeta = +1$ we obtain for the $e^\pm \longrightarrow e^\pm \nu_e \widetilde{\nu}_e$ processes $dw_+ \cong 10 dw_-$. It means that when electron neutrino pairs are emitted by the electrons and positrons having a right-hand circular polarization, the $e^+ \longrightarrow e^+ \nu_e \widetilde{\nu}_e$ process can contribute to the cooling process of the collapsing stellar core more essentially than the $e^- \longrightarrow e^- \nu_e \widetilde{\nu}_e$ process. In principle, the formulae describing $e^- \longrightarrow e^- \nu_i \widetilde{\nu}_i$ and $e^+ \longrightarrow e^+ \nu_i \widetilde{\nu}_i$ can formally be applied to the $l^\pm \longrightarrow l^\pm \nu_i \widetilde{\nu}_i$ processes and to the processes of neutrino pairs emission by quarks (antiquarks). So, the obtained result for the AC of an electron gas and a positron gas by neutrino pairs emission is evidence for the AC of a matter and an antimatter by neutrino pairs emission. It is a new distinguishing feature of a matter and antimatter.

4 Conclusions

The obtained result for the AC of CL gas and CA gas by neutrino pairs emission shows that a matter and an antimatter are cooled at the expense of neutrino pairs emission asymmetrically. It is a new distinguishing feature of a matter and antimatter. The dominant contribution to the asymmetry of the cooling of the collapsing stellar core is determined with the electron neutrino pairs emission by the electrons (positrons) having a left-hand (right-hand) circular polarization. All these effects could contribute to the AC of the collapsing stellar core.

5 Acknowledgments

References

[1] R.C. Duncan, C. Thompson, Ap.J. Letters **392** L9 (1992).

[2] V.N. Baier and V.M. Katkov, Sov. Phys. Doklady **171** 313 (1966).

[3] J.D. Landstreet, Phys. Rev. **153** 1372 (1967).

[4] V. Canuto, H.Y. Chiu and C.K. Chou, Phys. Rev. **D2** 281 (1970).

[5] A.V. Borisov, V.Ch. Zhukovskii and P.A. Eminov, Izv. Vuz. Fiz. **3** 110 (1978).

[6] A.D. Kaminker and D.G. Yakovlev, JETP **76** 229 (1993).

[7] A. Vidaurre *et al.*, Ap.J. **448** 264 (1995).

[8] D. G. Yakovlev *et al.*, Phys. Rep. **354** 1 (2001).

[9] A.D. Kaminker and D.G. Yakovlev, Mon. Not. Roy. Astroph. Soc. **371** 477 (2006).

[10] V.A. Guseinov, I.G. Jafarov and R.E. Gasimova, Phys. Rev. **D75** 073021 (2007).

The Pancharatnam phase in two flavor neutrino oscillations

Poonam Mehta

Raman Research Institute, C. V. Raman Avenue, Bangalore 560 080, India.

We show existence of a topological phase in the phenomena of neutrino oscillations in vacuum and in matter for the minimal case of two flavors and CP conserving situation.

1 Introduction

In the ultra-relativistic limit, the Dirac equation for two flavor neutrinos (antineutrinos) can be reduced to a Schrödinger form written in terms of a two-component vector of positive (negative) energy probability amplitude. The two neutrino flavor states can be mapped to a two-level quantum system with distinct energy eigenvalues, $E_i \simeq p + m_i^2/2p$ in the ultrarelativistic limit under the assumption of equal fixed momenta (or energy). The mapping of the two flavor neutrino Hamiltonian to that of a two level quantum system straightforwardly leads to the identification of the topological component in the total phase, which is the central result of this article.

2 The Hamiltonian for the two flavor neutrinos

Ignoring the term proportional to the Identity, the neutrino Hamiltonian (both in vacuum and matter) can be cast in exactly the same form given by

$$\mathbb{H}_\nu \;=\; \frac{\omega}{2} \left[(\sin\vartheta)\sigma_x - (\cos\vartheta)\sigma_z \right] \;, \tag{1}$$

where $\omega = \delta m^2/2p$ and the mixing angle Θ is replaced by $\vartheta/2$ [1]. The mass eigenstates $|\,\vartheta, +\,\rangle$ and $|\,\vartheta, -\,\rangle$ are orthogonal antipodal points on the Poincaré sphere which always lie on the great circle formed by the intersection of the $x - z$ plane with the Poincaré sphere. And neutrino oscillations can be viewed as the neutrino flavor state precessing about the line joining the stationary mass eigenstates (analogous to elliptic axis) induced by the time-evolution operator $e^{-i\mathbb{H}_\nu t}$ on the Poincaré sphere. In the language of neutrino optics, both vacuum and matter exhibit elliptic birefringence property with different elliptic axes.

---

[1]In defining the Poincaré sphere, it is useful to work with half angles $\vartheta/2$ as it allows for a mapping of the entire set of states on to a two-dimensional sphere $\mathbb{S}_2$ as ϑ changes from 0 to 4π.

3 The Pancharatnam phase

In the context of two level system, if we consider three rays on the Poincaré sphere represented by $|\mathfrak{A}\rangle$, $|\mathfrak{B}\rangle$ and $|\mathfrak{C}\rangle$ such that the neighbouring ones are non-orthogonal, then the phase of the complex number $\langle\mathfrak{A}|\mathfrak{C}\rangle\langle\mathfrak{C}|\mathfrak{B}\rangle\langle\mathfrak{B}|\mathfrak{A}\rangle$ is given by $\Omega/2$ [1, 2] where Ω is equal to half the solid angle subtended by the geodesic triangle $\mathfrak{A}, \mathfrak{B}, \mathfrak{C}$ on the Poincaré sphere at its center. Pancharatnam's phase reflects the curvature of projective Hilbert space (ray space) and is independent of any parameterization or slow variation. Thus it can also appear in situations where the Hamiltonian is constant in time.

4 Applying Pancharatnam's idea to neutrino oscillations

In order to probe effects related to quantum phases (dynamical or geometric), one usually needs a split beam experiment. It is impossible to design a split-beam experiment in physical space for neutrinos due to their feeble interaction strength. However, the fact that neutrinos are produced and detected as flavor states allows us to think of the time evolution of neutrinos as a split-beam experiment in energy space as illustrated in [3]. Let us consider a neutrino created as a flavor state $|\nu_\alpha\rangle$,

$$|\nu_\alpha\rangle = \nu_{\alpha+}|\vartheta_1,+\rangle + \nu_{\alpha-}|\vartheta_1,-\rangle , \qquad (2)$$

where $|\vartheta_1,\pm\rangle$ are the eigenstates of $\mathbb{H}_\nu(\vartheta_1)$. Evolving the mass eigenstates adiabatically from $|\vartheta_1,\pm\rangle$ to $|\vartheta_2,\pm\rangle$ due to a slow enough variation of background density such that no mixing between the two eigenstates is ensured under time evolution leads to

$$|\vartheta_1,\pm\rangle \rightarrow e^{-i\mathcal{D}_\pm}|\vartheta_2,\pm\rangle \quad \text{with}$$

$$\mathcal{D}_\pm = \pm\frac{1}{2}\int_0^t \sqrt{(\omega\sin\vartheta)^2 + (V_C - \omega\cos\vartheta)^2}\,dt' + \int_0^t\left(p + \frac{m_1^2 + m_2^2}{4p} + \frac{V_C}{2} + V_N\right)dt'$$

as the dynamical phases, relevant both for the vacuum case ($V_C = V_N = 0$) and in the presence of varying matter density profile and t is the time of flight of the neutrino. $V_C = \sqrt{2}G_F n_e = 7.6 \times 10^{-14}Y_e\rho$ eV and $V_N = -\sqrt{2}G_F n_n/2 = -3.8\times 10^{-14}Y_n\rho$ eV are the respective effective potentials due to coherent forward scattering of neutrinos with electrons (via charged current interactions) and neutrons (via neutral current interactions). The oscillation probability for transition $\nu_\alpha \rightarrow \nu_\beta$ is given by

$$\begin{aligned}
\mathcal{P}(\nu_\alpha \rightarrow \nu_\beta) &= |\mathcal{A}(\nu_\alpha \rightarrow \nu_\beta)|^2 = \langle\nu_\alpha|\vartheta_1,+\rangle\langle\vartheta_2,+|\nu_\beta\rangle\langle\nu_\beta|\vartheta_2,+\rangle\langle\vartheta_1,+|\nu_\alpha\rangle \\
&+ \langle\nu_\alpha|\vartheta_1,-\rangle\langle\vartheta_2,-|\nu_\beta\rangle\langle\nu_\beta|\vartheta_2,-\rangle\langle\vartheta_1,-|\nu_\alpha\rangle \\
&+ [\langle\nu_\alpha|\vartheta_1,-\rangle e^{i\mathcal{D}_-}\langle\vartheta_2,-|\nu_\beta\rangle\langle\nu_\beta|\vartheta_2,+\rangle e^{-i\mathcal{D}_+}\langle\vartheta_1,+|\nu_\alpha\rangle + \text{c.c.}] .
\end{aligned} \qquad (3)$$

By closely inspecting the form of cross term appearing in the neutrino oscillation probability, we note that it is related to the interference term resulting from the two path interferometer [3]. Upon dropping the dynamical phase, we have $\langle\nu_\alpha|\vartheta_1,-\rangle\langle\vartheta_2,-|\nu_\beta\rangle\langle\nu_\beta|\vartheta_2,+\rangle\langle\vartheta_1,+|\nu_\alpha\rangle$ which can be viewed as a series of closed loop quantum collapses with intermediate adiabatic evolutions given by $|\nu_\alpha\rangle \rightarrow |\vartheta_1,+\rangle \rightarrow |\vartheta_2,+\rangle \rightarrow |\nu_\beta\rangle \rightarrow |\vartheta_2,-\rangle \rightarrow |\vartheta_1,-\rangle \rightarrow |\nu_\alpha\rangle$ that essentially covers a great circle in the $x-z$ plane as is shown in Fig. 1(a). This closed trajectory subtends a solid angle of $\Omega = 2\pi$ at the center of the great circle. Hence the phase of the
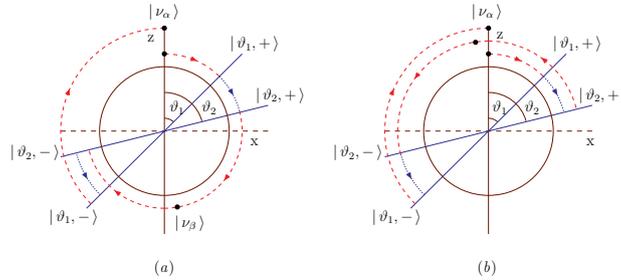
Figure 1: Direction of collapse processes (dashed, red) and adiabatic evolutions (dotted, blue) on the great circle in $x - z$ plane of the Poincaré sphere for appearance and survival probability.

interference term will be π (half the solid angle) due to Pancharatnam's prescription. For the case when $\alpha = \beta$, i.e. survival probability, it is easy to see that the collapses do not enclose the origin and therefore the interference term will not pick up any phase. This case is depicted in Fig. 1(b).

5   Conclusion

Our study provides the first clear prediction that a topological phase exists at the probability level even in the minimal case of two flavors and CP conservation. This is connected to the presence of an effective flux line of strength π (0) at the origin of ray space which is same as degeneracy point associated with the null Hamiltonian. It is shown that the topological phase is quite robust since it remains irrespective of evolution of neutrinos through vacuum or matter. The topological phase is built into the structure of the leptonic mixing matrix. The impact of CP violation is studied in [4] where it is shown that the phase can become geometric (different from π or 0) if the CP phase also varies as a function of time (space).

6   Acknowledgments

The author wishes to thank Joseph Samuel and Supurna Sinha for illuminating discussions.

References

[1] S. Pancharatnam. Generalized theory of interference and its applications. *Proc. Ind. Acad. Sci.*, A44:247–249, 1956.

[2] Joseph Samuel and Rajendra Bhandari. General setting for berry's phase. *Phys. Rev. Lett.*, 60:2339–2342, Jun 1988.

[3] P. Mehta. Topological phase in two flavor neutrino oscillations. *Phys. Rev. D*, 79:096013, 2009.

[4] P. Mehta. Geometric imprint of cp violation in two flavor neutrino oscillations. arXiv:0907.0562 [hep-ph].

Quasi-degenerate neutrinos and maximal mixing in hybrid seesaws

Joydeep Chakrabortty[1], *Anjan S. Joshipura*[2], *Poonam Mehta*[3*] *and Sudhir K. Vempati*[4]

[1]Harish-Chandra Research Institute, Allahabad 211 019, India
[2]Theory Group, Physical Research Laboratory, Ahmedabad 380 009, India
[3]Theoretical Physics Group, Raman Research Institute, Bangalore 560 080, India
[4]Centre for High Energy Physics, Indian Institute of Science, Bangalore 560 012, India.

We address the question of generating maximal neutrino mixing in the context of hybrid seesaw mechanisms with at least two sources (or two seesaws) in the neutrino mass matrix. In the case where both sources predict small mixing angles, we show that the total neutrino mixing can become maximal if the neutrinos have a quasi-degenerate pattern.

1 Introduction

The data from neutrino experiments is consistent with the presence of three light active neutrinos with one maximal, one large and one small mixing angle. The seesaw mechanism has been tremendously successful in giving tiny Majorana masses to neutrinos naturally. It also has the ingredients for generating the baryon asymmetry of the universe via leptogenesis. However, it predicts mixing angles which are small if quark-like angles are replicated in the leptonic sector. In this work we exploit the fact that in most models of grand unified theories (GUT), usually more than one seesaw mechanism is at work. It is then possible to obtain maximal mixing even if the individual seesaw mixings are small. Also, we point out that the enhancement of mixing from small to maximal is linked to quasi-degeneracy in the light neutrino mass spectrum.

2 Type I and Type II enhancement

Before we describe the idea of hybrid enhancement [1], let us briefly review the existing mechanisms of enhancement of mixing in the neutrino sector. It was shown [2] that by appropriate choice of flavor structure and the hierarchies in matrices m_D and M_R (stronger hierarchy in M_R compared to m_D), one could generate large mixing in m_ν in the Type I seesaw formula $m_\nu = -m_D M_R^{-1} m_D$. The mixing in individual matrices m_D and M_R was taken to be small (like the quark mixing). This was called the "seesaw effect (Type I enhancement)". This mechanism fails if the flavor structure of the right handed neutrinos is same as that of other fermions.

To overcome this problem, the authors in Ref. [3] exploited the interplay of the two terms in Type I plus II seesaw formula inorder to enhance the mixing in the neutrino mass matrix (even if the small mixing was of same order in the matrices m_D, M_R, m_L). For the case of normal

---

*Presenting author

hierarchy (NH) and degenerate contribution of two terms ($m_\nu^I = m_\nu^{II}$) in mass formula under suitable conditions (cancellation of dominant $\mathcal{O}(1)$ entries) it was possible to obtain large mixing. This was referred to as the "Type II enhancement". However, for inverted hierarchy (IH), such a procedure would require unnatural cancellations within several independent elements of m_ν. Without additional symmetries, it was impossible to accomodate maximal or zero mixing angles in their framework [3].

3   Hybrid enhancement of neutrino mixing

Clearly the enhancement mechanisms mentioned above worked in certain parameter regions and for NH but had limitations for example, the maximal mixing could not be explained easily. We analyse a general situation where we have two sources[1] of neutrino masses (both containing small mixings and of comparable magnitude) and phenomenologically find conditions under which enhancement of neutrino mixing can occur. The sources of neutrino mass can be independent seesaws like any two of the Type I, Type II or Type III seesaws or two copies of the same seesaw mechanism itself (infact sources other than seesaws can also contribute). We will refer to our proposed mechanism of generating maximal angles as "hybrid enhancement". The general texture analysis shows that this can only happen if the resulting pattern of neutrino masses is quasi-degenerate and this requires that the dominant elements in the submatrices are not cancelled in the total mass matrix (unlike in [3]), which in turn means that we have submatrices having NH and IH forms. Let us illustrate the idea for two and three generation cases below.

3.1   Two generations

Denoting the two terms contributing to the left-handed light neutrino mass matrix as

$$\mathbb{M}_\nu^{(1)} = \begin{pmatrix} m_{ee}^{(1)} & m_{e\mu}^{(1)} \\ m_{e\mu}^{(1)} & m_{\mu\mu}^{(1)} \end{pmatrix}, \qquad \mathbb{M}_\nu^{(2)} = \begin{pmatrix} m_{ee}^{(2)} & m_{e\mu}^{(2)} \\ m_{e\mu}^{(2)} & m_{\mu\mu}^{(2)} \end{pmatrix}, \tag{1}$$

we have the mixing angle θ of $\mathbb{M}_\nu = \mathbb{M}_\nu^{(1)} + \mathbb{M}_\nu^{(2)}$,

$$\tan 2\theta = \tan 2\theta^{(1)} \frac{1}{(1+d)} + \tan 2\theta^{(2)} \frac{d}{(1+d)}, \tag{2}$$

where $d = (m_{\mu\mu}^{(2)} - m_{ee}^{(2)})/(m_{\mu\mu}^{(1)} - m_{ee}^{(1)})$ and $\theta^{(1)}$ and $\theta^{(2)}$ are the mixing angles of $\mathbb{M}_\nu^{(1)}$ and $\mathbb{M}_\nu^{(2)}$ respectively. Given that $\theta^{(1)}$ and $\theta^{(2)}$ are small, θ would be maximal when $d = -1$. Assuming at least one of the diagonal entries in each of the matrix $\mathbb{M}_\nu^{(i)}$ is large, we have the following three solutions for $d = -1$:- (A) $m_{\mu\mu}^{(2)} = -m_{\mu\mu}^{(1)}$ (Both $\mathbb{M}_\nu^{(i)}$ NH), (B) $m_{ee}^{(2)} = -m_{ee}^{(1)}$ (Both $\mathbb{M}_\nu^{(i)}$ IH), and (C) $m_{ee}^{(2)} = m_{\mu\mu}^{(1)}$ or $m_{\mu\mu}^{(2)} = m_{ee}^{(1)}$ ($\mathbb{M}_\nu^{(1)}$ NH and $\mathbb{M}_\nu^{(2)}$ IH). For illustration, let us consider the (sub)-case of (C) with $m_{\mu\mu}^{(2)} = m_{ee}^{(1)}$,

$$\mathbb{M}_\nu = \mathbb{M}_\nu^{(1)} + \mathbb{M}_\nu^{(2)} = m_1 \begin{pmatrix} 0 & x \\ x & 1 \end{pmatrix} + m_2 \begin{pmatrix} 1 & -y \\ -y & 0 \end{pmatrix}, \tag{3}$$

where x, y are small entries. In the limit of exact degeneracy between m_1 and m_2, the mixing is maximal as is evident if both the m_1 and m_2 have the same CP parity. Thus to convert *one*

---

[1]The discussion of Ref. [3] is just a subcase of all possible cases.

small mixing angle in two matrices to *one* maximal mixing in the total matrix, we would require a *pair* of (quasi)-degenerate eigenvalues with the same CP parities, ordered oppositely in the sub-matrices. This count would be useful when we extend this *degeneracy induced large mixing* to three generations. The Left-Right Symmetric (LRS) model naturally has the ingredients for hybrid enhancement to work [1, 4].

3.2 Three generations

Extending the idea to three generations with two sources, we can find out the conditions when we can obtain only one maximal while the other two large and small respectively. From our arguments above, it appears that we can generate only one large mixing angle in the case when there are only two sub-matrices, because of the important constraint that the third mixing angle (θ_{13}) must not be large. Given that we can only generate one large mixing from the small mixing using the degenerate conditions, we will have to assume that at least one of the submatrices has intrinsically one maximal/large mixing angle. However, the presence of this mixing should not disturb the smallness of θ_{13} angle in the total mass matrix. In the following, we will consider one of the sub-matrices to have pseudo-Dirac structure and other one to have one large eigenvalue and all the three mixing angles small. This is because the pseudo-Dirac structure not only gives maximal mixing but also has the eigenvalues with opposite CP parities.

$$\mathbb{M}_\nu = m_1 \begin{pmatrix} x^2 & x & y^2 \\ x & 0 & 1 \\ y^2 & 1 & 0 \end{pmatrix} + m_2 \begin{pmatrix} 1 & z & t^3 \\ z & z^3 & t^3 \\ t^3 & t^3 & z^3 \end{pmatrix} , \qquad (4)$$

where x, y, z, t are small entries compared to m_1, m_2. There can be other textures such that the first of the matrices has only one large eigenvalue in a NH with maximal mixing and the second one has two large eigenvalues with one maximal mixing and two small mixings with IH [1].

4 Conclusion

In the present work, we have concentrated on the case with two seesaw mechanisms at work which occurs naturally in many examples like LRS models, SO(10) based GUT models *etc*. We have shown that if both these seesaw mechanisms result in mass matrices which only have small mixing in them, then the only pattern of mass eigenvalues which is *naturally* consistent with maximal/large mixing is the quasi-degenerate pattern for the total mass matrix. All the arguments presented in the present work are independent of the details of the sources of neutrino masses. While the present work is purely a phenomenological study, it is known that quasi-degeneracy in the neutrino sector would generally imply some symmetry in the Lagrangian. The details of such a symmetry are model dependent.

References

[1] J. Chakrabortty, A. Joshipura, P. Mehta and S. K. Vempati, arXiv:0909.3116 [hep-ph].

[2] A. Y. Smirnov, Phys. Rev. D **48**, 3264 (1993) [arXiv:hep-ph/9304205]. G. Altarelli, F. Feruglio and I. Masina, Phys. Lett. B **472**, 382 (2000) [arXiv:hep-ph/9907532].

[3] M. Lindner and W. Rodejohann, JHEP **0705**, 089 (2007) [arXiv:hep-ph/0703171].

[4] E. K. Akhmedov and M. Frigerio, Phys. Rev. Lett. **96**, 061802 (2006) [arXiv:hep-ph/0509299]; E. K. Akhmedov and M. Frigerio, JHEP **0701**, 043 (2007) [arXiv:hep-ph/0609046].

Yukawaon model and unified description of quark and lepton mass matrices

Yoshio Koide

Department of Physics, Osaka University, Toyonaka, Osaka 560-0043, Japan

In the so-called yukawaon model, where effective Yukawa coupling constants Y_f^{eff} ($f = e, \nu, u, d$) are given by vacuum expectation values of gauge singlet scalars (yukawaons) Y_f with 3×3 flavor components, it is tried to give a unified description of quark and lepton mass matrices. Especially, without assuming any discrete symmetry in the lepton sector, nearly tribimaximal mixing is derived by assumed a simple up-quark mass matrix form.

1 What is a yukawaon model?

First, let us give a short review of the so-called *yukawaon* model: We regard Yukawa coupling constants Y_f as effective coupling constants Y_f^{eff} in an effective theory, and we consider that Y_f^{eff} originate in vacuum expectation values (VEVs) of new gauge singlet scalars Y_f, i.e.

$$Y_f^{eff} = \frac{y_f}{\Lambda} \langle Y_f \rangle, \tag{1}$$

where Λ is a scale of an effective theory which is valid at $\mu \leq \Lambda$, and we assume $\langle Y_f \rangle \sim \Lambda$. We refer the fields Y_f as *yukawaons* [1] hereafter. Note that the effective coupling constants Y_f^{eff} evolve as those in the standard SUSY model below the scale Λ, since a flavor symmetry is completely broken at a high energy scale $\mu \sim \Lambda$.

In the present work, we assume an O(3) flavor symmetry. In order to distinguish each Y_f from others, we assume a U(1)$_X$ symmetry (i.e. *sector charge*). (The SU(2)$_L$ doublet fields q, ℓ, H_u and H_d are assigned to sector charges $Q_X = 0$.) Then, we obtain VEV relations as follows: (i) We give an O(3) and U(1)$_X$ invariant superpotential for yukawaons Y_f. (ii) We solve SUSY vacuum conditions $\partial W / \partial Y_f = 0$. (iii) Then, we obtain VEV relations among Y_f.

For example, in the seesaw-type neutrino mass matrix, $M_\nu \propto \langle Y_\nu \rangle \langle Y_R \rangle^{-1} \langle Y_\nu \rangle^T$, we obtain [2]

$$\langle Y_R \rangle \propto \langle Y_e \rangle \langle \Phi_u \rangle + \langle \Phi_u \rangle \langle Y_e \rangle \tag{2}$$

together with $\langle Y_\nu \rangle \propto \langle Y_e \rangle$ and $\langle Y_u \rangle \propto \langle \Phi_u \rangle \langle \Phi_u \rangle$, i.e. a neutrino mass matrix is given by

$$\langle M_\nu \rangle_e \propto \langle Y_e \rangle_e \left\{ \langle Y_e \rangle_e \langle \Phi_u \rangle_e + \langle \Phi_u \rangle_e \langle Y_e \rangle_e \right\}^{-1} \langle Y_e \rangle_e, \tag{3}$$

where $\langle \Phi_u \rangle_u \propto \text{diag}(\sqrt{m_u}, \sqrt{m_c}, \sqrt{m_t})$, and $\langle A \rangle_f$ denotes a form of a VEV matrix $\langle A \rangle$ in the diagonal basis of $\langle Y_f \rangle$ (we refer it as f basis). We can obtain a form $\langle \Phi_u \rangle_d = V(\delta)^T \langle \Phi_u \rangle_u V(\delta)$ from the definition of the CKM matrix $V(\delta)$, but we do not know an explicit form of $\langle \Phi_u \rangle_e$. Therefore, in a previous work [2], the author put an ansatz, $\langle \Phi_u \rangle_e = V(\pi)^T \langle \Phi_u \rangle_u V(\pi)$ by

supposing $\langle\Phi_u\rangle_e \simeq \langle\Phi_u\rangle_d$, and he obtained excellent predictions of the neutrino oscillation parameters without assuming any discrete symmetry. However, there is no theoretical ground for the ansatz for the form $\langle\Phi_u\rangle_e$.

The purpose of the present work is to investigate a quark mass matrix model in order to predict neutrino mixing parameters on the basis of a yukawaon model (2), without such the ad hoc ansatz, because if we give a quark mass matrix model where mass matrices (M_u, M_d) are given on the e basis, then, we can obtain the form $\langle\Phi_u\rangle_e$ by using a transformation $\langle\Phi_u\rangle_e = U_u\langle\Phi_u\rangle_u U_u^T$, where U_u is defined by $U_u^T M_u U_u = M_u^{diag}$.

2 Yukawaons in the quark sector

We assume a superpotential in the quark sector [3]:

$$W_q = \mu_u[Y_u\Theta_u] + \lambda_u[\Phi_u\Phi_u\Theta_u] + \mu_u^X[\Phi_u\Theta_u^X] + \mu_d^X[Y_d\Theta_d^X] + \sum_{q=u,d}\frac{\xi_q}{\Lambda}[\Phi_e(\Phi_X + a_qE)\Phi_e\Theta_q^X]. \quad (4)$$

Here and hereafter, for convenience, we denotes Tr[...] as [....] simply. From SUSY vacuum conditions $\partial W/\partial\Theta_u = 0$, $\partial W/\partial\Theta_u^X = 0$ and $\partial W/\partial\Theta_d^X = 0$, we obtain $\langle Y_u\rangle \propto \langle\Phi_u\rangle\langle\Phi_u\rangle$,

$$M_u^{1/2} \propto \langle\Phi_u\rangle_e \propto \langle\Phi_e\rangle_e\left(\langle\Phi_X\rangle_e + a_u\langle E\rangle_e\right)\langle\Phi_e\rangle_e, \quad (5)$$

$$M_d \propto \langle Y_d\rangle_e \propto \langle\Phi_e\rangle_e\left(\langle\Phi_X\rangle_e + a_d\langle E\rangle_e\right)\langle\Phi_e\rangle_e, \quad (6)$$

respectively. Here, $\langle\Phi_X\rangle_e$ and $\langle E\rangle_e$ are given by

$$\langle\Phi_X\rangle_e \propto X \equiv \frac{1}{3}\begin{pmatrix} 1 & 1 & 1 \\ 1 & 1 & 1 \\ 1 & 1 & 1 \end{pmatrix}, \quad \langle E\rangle_e \propto \mathbf{1} \equiv \begin{pmatrix} 1 & 0 & 0 \\ 0 & 1 & 0 \\ 0 & 0 & 1 \end{pmatrix}. \quad (7)$$

(Note that the VEV form $\langle\Phi_X\rangle_e$ breaks the O(3) flavor symmetry into S$_3$.) Therefore, we obtain quark mass matrices

$$M_u^{1/2} \propto M_e^{1/2}\left(X + a_u\mathbf{1}\right)M_e^{1/2}, \quad M_d \propto M_e^{1/2}\left(X + a_d e^{i\alpha_d}\mathbf{1}\right)M_e^{1/2}, \quad (8)$$

on the e basis. Note that we have assumed that the O(3) relations are valid only on the e and u bases, so that $\langle Y_e\rangle$ and $\langle Y_u\rangle$ must be real.

A case $a_u \simeq -0.56$ can give a reasonable up-quark mass ratios $\sqrt{m_{u1}/m_{u2}} = 0.043$ and $\sqrt{m_{u2}/m_{u3}} = 0.057$, which are in favor of the observed values [4] $\sqrt{m_u/m_c} = 0.045^{+0.013}_{-0.010}$, and $\sqrt{m_c/m_t} = 0.060 \pm 0.005$ at $\mu = M_Z$.

3 Yukawaons in the neutrino

However, the up-quark mass matrix (5) failed to give reasonable neutrino oscillation parameter values although it can give reasonable up-quark mass ratios. Therefore, we will slightly modify the model (2) in the neutrino sector.

Note that the sign of the eigenvalues of $M_u^{1/2}$ given by Eq.(8) is $(+, -, +)$ for the case $a_u \simeq -0.56$. If we assume that the eigenvalues of $\langle\Phi_u\rangle_u$ must be positive, so that $\langle\Phi_u\rangle_u$ in

Eq.(2) is replaced as $\langle\Phi_u\rangle_u \to \langle\Phi_u\rangle_u \cdot \mathrm{diag}(+1,-1,+1)$, then, we can obtain successful results except for $\tan^2\theta_{solar}$, i.e. predictions $\sin^2 2\theta_{atm} = 0.984$ and $|U_{13}| = 0.0128$ and an unfavorable prediction $\tan^2\theta_{solar} = 0.7033$.

When we introduce a new field P_u with a VEV $\langle P_u\rangle_u \propto \mathrm{diag}(+1,-1,+1)$, we must consider an existence of $P_u Y_e \Phi_u + \Phi_u Y_e P_u$ in addition to $Y_e P_u \Phi_u + \Phi_u P_u Y_e$, because they have the same $U(1)_X$ charges. Therefore, we modify Eq.(2) into

$$W_R = \mu_R[Y_R\Theta_R] + \frac{\lambda_R}{\Lambda}\left\{[(Y_e P_u \Phi_u + \Phi_u P_u Y_e)\Theta_R] + \xi[(P_u Y_e \Phi_u + \Phi_u Y_e P_u)\Theta_R]\right\}, \quad (9)$$

which leads to VEV relation $Y_R \propto Y_e P_u \Phi_u + \Phi_u P_u Y_e + \xi(P_u Y_e \Phi_u + \Phi_u Y_e P_u)$. The results at $a_u \simeq -0.56$ are excellently in favor of the observed neutrino oscillation parameters by taking a small value of $|\xi|$ (see Table 1):

Also, we can calculate the down-quark sector. We have two parameters (a_d, α_d) in the down-quark sector given in Eq.(8). (See Table 2 in Ref.[3]). The results are roughly reasonable, although $|V_{i3}|$ and $|V_{3i}|$ are somewhat larger than the observed values. Those discrepancies will be improved in future version of the model.

4 Summary

In conclusion, for the purpose of deriving the observed nearly tribimaximal neutrino mixing, a possible yukawaon model in the quark sector is investigated. Five observable quantities (2 up-quark mass ratios and 3 neutrino mixing parameters) are excellently fitted by two parameters. Also, the CKM mixing parameters and down-quark mass ratios are given under additional 2 parameters. The results are summarized in Table 1.

Sector	Parameters	Predictions		
		$\sin^2\theta_{atm}$	$\tan^2\theta_{solar}$	$|U_{13}|$
M_ν	$\xi = +0.0005$	0.982	0.449	0.012
	$\xi = -0.0012$	0.990	0.441	0.014
$M_u^{1/2}$	$a_u = -0.56$	$\sqrt{\frac{m_u}{m_c}} = 0.0425$	$\sqrt{\frac{m_c}{m_t}} = 0.0570$	
	two parameters	5 observables: fitted excellently		
M_d	$a_d e^{i\alpha_d}$	$\sqrt{\frac{m_d}{m_s}}$, $\sqrt{\frac{m_s}{m_b}}$, $|V_{us}|$, $|V_{cb}|$, $|V_{ub}|$, $|V_{td}|$		
	two parameters	6 observables: not always excellent		

Table 1: Summary of the present model.

It is worthwhile to notice that the observed tribimaximal mixing in the neutrino sector is substantially obtained from the up-quark mass matrix structure (8). Although the model for down-quark sector still need an improvement, the present approach will provide a new view to a unified description of the masses and mixings.

References

[1] Y. Koide, Phys. Rev. **D78** 093006 (2008); Phys. Rev. **D79** 033009 (2009).

[2] Y. Koide, Phys. Lett. **B665** 227 (2008).

[3] Y. Koide, Phys. Lett. **B680** 76 (2009).

[4] Z.-z. Xing, H. Zhang and S. Zhou, Phys. Rev. **D77** (2008) 113016. Also, see H. Fusaoka and Y. Koide, Phys. Rev. **D57** (1998) 3986.

Soft supersymmetry breaking terms from A_4 lepton flavor symmetry

Yuji Omura

Department of Physics, Kyoto University, Kyoto 606-8502, Japan

We study the supersymmetric model with the A_4 lepton flavor symmetry, in particular soft supersymmetry breaking terms, which are predicted from the A_4 lepton flavor symmetry. We evaluate soft slepton masses and A-terms within the framework of supergravity theory. Constraints due to experiments of flavor changing neutral current processes are examined.

1   Introduction

Recent experiments of the neutrino oscillation go into the new phase of precise determination of mixing angles and mass squared differences. Those indicate the tri-bimaximal mixing for three flavors in the lepton sector [1]. One of natural models realizing the tri-bimaximal mixing has been proposed based on the non-Abelian finite group A_4 [2].

On the other hand, the supersymmetric extension of the standard model is one of interesting candidates for physics beyond the weak scale. Flavor symmetries realizing realistic quark/lepton mass matrices would lead to specific patterns of squark and slepton mass matrices as their predictions, which could be tested in future experiments. The purpose of this paper is to study which pattern of slepton mass matrices is predicted from the A_4 model and to examine whether the predicted pattern of slepton mass matrices is consistent with the current FCNC experimental bounds, based on [3].

Now, we consider the supersymmetric A_4 model based on [4]. Under the A_4 symmetry, the chiral superfields for three families of the left-handed lepton doublets L_I ($I = e, \mu, \tau$) are assumed to transform as triplets, while the right-handed ones of the charge lepton singlets R_e, R_μ and R_τ are A_4 singlet, and non-trival singlets. The Z_3 and $U(1)_F$ charges are also assigned. The flavor symmetry is spontaneously broken by vacuum expectation values (VEV) of two triplets, χ_i, χ'_i, and by one singlet, χ, which are $SU(2)_L \times U(1)_Y$ singlets.

The superpotential is given by the effective one with the cut-off scale Λ. In order to obtain the natural hierarchy among lepton masses m_e, m_μ and m_τ, the Froggatt-Nielsen mechanism [5] is introduced as an additional $U(1)_F$ flavor symmetry under which only the right-handed lepton sector is charged.

The VEVs of gauge singlet scalar fields χ, χ_i and χ'_i are given by minima in the scalar potential. Actually, they are estimated as $\mathcal{O}(\tilde{\alpha})$ in the Ref.[3, 4], where $\tilde{\alpha}$ is the magnitude of the VEVs divided by Λ. The magnitude is estimated by the neutrino experimental data. That is, the scale $\Lambda \simeq 10^{14}$GeV gives $\tilde{\alpha} \sim \mathcal{O}(10^{-2})$ in the case with $\tan\beta = 3$ and yukawa couplings, $|y_\tau| \simeq |y_1| \simeq |y_2| \simeq 1$.

The charged lepton mass matrix becomes diagonal and the neutrino mass matrix can be simplified at the leading order as shown in ref.[4]. Then, the tri-bimaximal mixing is found for the lepton flavor mixing matrix. The next leading terms, $\mathcal{O}(\tilde{\alpha})$, modify the results. The lepton mixing angles are changed by $\mathcal{O}(\tilde{\alpha})$. For example, the deviations from the diagonal charged lepton mass matrix are estimated as $\theta_{R12} \sim \frac{m_e}{m_\mu}\mathcal{O}(\tilde{\alpha})$ and $\theta_{L12} \sim \mathcal{O}(\tilde{\alpha})$.

2 Soft SUSY breaking terms

We study soft SUSY breaking terms, i.e. soft slepton masses and A-terms, which are predicted from the A_4 model discussed in the introduction.

First, we study soft scalar masses. Within the framework of supergravity theory, soft scalar mass squared is obtained as [6]

$$m^2_{\bar{I}J}K_{\bar{I}J} = m^2_{3/2}K_{\bar{I}J} + |F^{\Phi_k}|^2\partial_{\Phi_k}\partial_{\bar{\Phi}_k}K_{\bar{I}J} - |F^{\Phi_k}|^2\partial_{\bar{\Phi}_k}K_{\bar{I}L}\partial_{\Phi_k}K_{\bar{M}J}K^{L\bar{M}}. \tag{1}$$

The flavor symmetry $A_4 \times Z_3$ requires the following form of Kähler potential for left-handed and right-handed leptons

$$
\begin{aligned}
K^{(0)}_{\text{matter}} &= a(Z, Z^\dagger)(L_e^\dagger L_e + L_\mu^\dagger L_\mu + L_\tau^\dagger L_\tau) \\
&\quad + b_e(Z, Z^\dagger)R_e^\dagger R_e + b_\mu(Z, Z^\dagger)R_\mu^\dagger R_\mu + b_\tau(Z, Z^\dagger)R_\tau^\dagger R_\tau ,
\end{aligned}
\tag{2}
$$

at the leading order, where $a(Z, Z^\dagger)$ and $b_I(Z, Z^\dagger)$ for $I = e, \mu, \tau$ are generic functions of moduli fields Z. This $K^{(0)}$ is the prediction of the A_4 model that three families of left-handed slepton masses are degenerate.

However, the flavor symmetry $A_4 \times Z_3$ is broken to derive the realistic lepton mass matrices and such breaking introduces corrections in the Kähler potential and the form of slepton masses. The correction terms of diagonal elements in the matter Kähler potential are estimated as $\mathcal{O}(\tilde{\alpha})$. Off-diagonal Kähler metric entries for both left-handed and right-handed leptons appear at $\mathcal{O}(\tilde{\alpha}^2)$. The leptonic FCNC is induced by off diagonal elements of scalar mass squared matrices in the diagonal basis of the charged lepton mass matrix. For example, $(\tilde{m}_L^2)_{12}$, which has a strong constraint on from FCNC experiments [7], is estimated as $(\tilde{m}_L^2)_{12}/m^2_{\text{SUSY}} = \mathcal{O}(\tilde{\alpha}^2)$, where m_{SUSY} denotes the average mass of slepton masses and it would be of $\mathcal{O}(m_{3/2})$. Because of $\tilde{\alpha} \sim 0.03$ for $y_\tau \simeq 1$, our prediction, $(\tilde{m}_L^2)_{12}/m^2_{\text{SUSY}} = \mathcal{O}(\tilde{\alpha}^2) = \mathcal{O}(10^{-3})$, would be consistent with the current experimental bound. Similarly, we can estimate $(\tilde{m}_R^2)_{12}/m^2_{\text{SUSY}}$ and results are the same. The D-term and radiative corrections are also discussed in Ref.[3].

Now, we examine the mass matrix between the left-handed and the right-handed sleptons, which is generated by the so-called A-terms. The A-terms are trilinear couplings of two sleptons and one Higgs field. After the electroweak symmetry breaking, these A-terms provide us with the left-right mixing mass squared $(m_{LR}^2)_{IJ} = h_{IJ}v_d$.

When we consider the leading order of Kähler potential $K^{(0)}_{\text{matter}}$, the (2,1) entry of $(\tilde{m}_{LR}^2)_{IJ}$, which has a strong constraint, vanishes at the leading order. However, such a behavior is violated at the next order, because the diagonal (1,1) and (2,2) entries of Kähler metric have non-degenerate corrections of $\mathcal{O}(\tilde{\alpha})$. Then, the h_{IJ} contribution to the (2,1) entry of $(\tilde{m}_{LR}^2)_{IJ}$ is estimated as $(\tilde{m}_{LR}^2)_{21} \sim \mathcal{O}(\tilde{\alpha}^2 m_\mu m_{3/2})$. Furthermore, the off-diagonal elements of Kähler metric have $\mathcal{O}(\tilde{\alpha}^2)$ of corrections, and these corrections also induce the same order of $(\tilde{m}_{LR}^2)_{21}$, i.e. $(\tilde{m}_{LR}^2)_{21} = \mathcal{O}(\tilde{\alpha}^2 m_\mu m_{3/2})$. Similarly, we can estimate the (1,2) entry and obtain the

same result, i.e., $(\tilde{m}_{LR}^2)_{12} = \mathcal{O}(\tilde{\alpha}^2 m_\mu m_{3/2})$ when $\tilde{\alpha} > m_e/m_\mu$. These entries have the strong constraint from FCNC experiments as $(\tilde{m}_{LR}^2)_{12}/m_{\mathrm{SUSY}}^2 \leq \mathcal{O}(10^{-6})$ and the same for the (2,1) entry for $m_{\mathrm{SUSY}} = 100$ GeV. However, the above prediction of the A_4 model leads to $(\tilde{m}_{LR}^2)_{12}/m_{\mathrm{SUSY}}^2 = \mathcal{O}(10^{-7})$ for $m_{\mathrm{SUSY}} = 100$ GeV and $\alpha \sim 0.03$, and that is consistent with the experimental bound.

Now, we discuss the contributions of F_Φ/Φ and F_{χ_i}/χ_i, where Φ is a Froggatt-Nielsen field. There is a possibility that F_Φ/Φ leads large off-diagonal elements because each right-handed charged lepton has a different $U(1)_F$ charge. The contribution to the (1,2) entry is estimated as $\mathcal{O}(\tilde{\alpha}^2 m_\mu m_{3/2})$. This result is the same as the above.

On the other hand, $F_{\chi_i}/\chi_i (\equiv A_i)$ contributes to $(\tilde{m}_{LR}^2)_{21}$ as $m_\mu \tilde{\alpha}(A_2 - A_1)$. That is, we estimate $(\tilde{m}_{LR}^2)_{21}/m_{\mathrm{SUSY}}^2 \sim 10^{-5} \times (A_2 - A_1)/m_{3/2}$ for $\tilde{\alpha} \sim \mathcal{O}(10^{-2})$. Thus, if $A_2 \neq A_1$ and $A_i = \mathcal{O}(m_{3/2})$, this value of $(\tilde{m}_{LR}^2)_{21}/m_{\mathrm{SUSY}}^2$ would not be consistent with the experimental bound for $m_{\mathrm{SUSY}} = 100$ GeV. Hence, a smaller value of $\tilde{\alpha}$ like $\tilde{\alpha} = \mathcal{O}(0.001)$ would be favorable to be consistent with the experimental bound and that implies a large $\mathcal{O}(1)$ coupling. Alternatively, for $\tilde{\alpha} \sim \mathcal{O}(10^{-2})$ it is required that $A_1 = A_2$ up to $\mathcal{O}(0.1)$. If the non-trivial superpotential leading to SUSY breaking does not include χ_i, i.e. $\langle \partial_{\chi_i} W \rangle = 0$, we can realize that situation. Hence, we obtain the degeneracy between A_i, i.e., $A_1 = A_2 = A_3$ up to $\mathcal{O}(\tilde{\alpha} m_{3/2})$. In this case, $(\tilde{m}_{LR}^2)_{21}$ is suppressed and we can estimate $(\tilde{m}_{LR}^2)_{21}/m_{\mathrm{SUSY}}^2 \sim \tilde{\alpha}^2 m_\mu/m_{3/2} = \mathcal{O}(10^{-6})$ for $\tilde{\alpha} \sim \mathcal{O}(10^{-2})$. This value is consistent with the experimental bound.

Similarly to slepton masses, radiative corrections to A-terms do not change drastically the above results. Note that Yukawa couplings are small, in particular the first and second families.

3 Conclusion

We have studied soft SUSY breaking terms, which are derived from the A_4 model. Three families of left-handed slepton masses are degenerate, while three families of right-handed slepton masses are, in general, different from each other. In the wide parameter region, the FCNCs predicted in the SUSY A_4 model are consistent with the current experimental bounds. Thus, the non-Abelain flavor symmetry in the A_4 model is useful not only to derive realistic lepton mass matrices, but also to suppress FCNC processes.

References

[1] P.F. Harrison, D.H. Perkins, and W.G. Scott, Phys. Lett. B **530**, 167 (2002);
P.F. Harrison and W.G. Scott, Phys. Lett. B **535**, 163 (2002).

[2] E. Ma and G. Rajasekaran, Phys. Rev. D **64**, 113012 (2001);
E. Ma, Mod. Phys. Lett. A **17**, 2361 (2002);
K.S. Babu, E. Ma, and J.W.F. Valle, Phys. Lett. B **552**, 207 (2003).

[3] H. Ishimori, T. Kobayashi, Y. Omura and M. Tanimoto, JHEP **0812**, 082 (2008) [arXiv:0807.4625 [hep-ph]].

[4] G. Altarelli and F. Feruglio, Nucl. Phys. B **741**, 215 (2006).

[5] C. D. Froggatt and H. B. Nielsen, Nucl. Phys. B **147**, 277 (1979).

[6] V. S. Kaplunovsky and J. Louis, Phys. Lett. B **306**, 269 (1993) [arXiv:hep-th/9303040].

[7] F. Gabbiani, E. Gabrielli, A. Masiero and L. Silvestrini, Nucl. Phys. B **477**, 321 (1996).

$\gamma + jet$ Final State as a Probe of q^* at the LHC

Satyaki Bhattacharya, Sushil S. Chauhan, Brajesh C. Choudhary, Debajyoti Choudhury

Department of Physics & Astrophysics, University of Delhi, Delhi 110007, India

If quarks are composite particles then its excited states are expected to play a role in the physics to be probed at the Large Hadron Collider (LHC). Concentrating on virtual effects and using CMS detection criteria we present a realistic examination of their effects at $\sqrt{s} = 14$ TeV in $\gamma + jet$ channel at the CERN LHC. The analysis shows that in the initial phase of the LHC operation, the discovery of $q*$ in the $\gamma + jet$ final state for $M_{q*} = 2(5)$ TeV is possible with an integrated luminosity of $200 pb^{-1} (\sim 140 fb^{-1})$.

1 Introduction

The replication of fermion families along with the mass hierarchies and mixings has led one to speculate about the possibility of quark-lepton compositeness. The fundamental matter constituents in such theories, very often termed *preons*[1], experience an hitherto unknown force on account of an asymptotically free but confining gauge interaction[2], which would become very strong at a characteristic scale Λ, thereby leading to bound states (composites) which are to be identified as quarks and leptons. Since our interest is in $q*$ contribution to the $\gamma + jet$ for their presence as a mass bump at hadron collider, it suffices to consider only the magnetic transition between ordinary and excited states. In general, it is often parameterized by

$$\mathcal{L}_{f*f} = \frac{1}{2\Lambda} \bar{f}_R^* \sigma^{\mu\nu} \left[\sum_i g_i\, c_i\, T_i^a\, G_{i\,\mu\nu}^a \right] f_L + h.c., \tag{1}$$

where the index i runs over the three SM gauge groups, viz. $SU(3)$, $SU(2)$ and $U(1)$, and g_i, $G_{i\,\mu\nu}^a$ and T_i^a are the corresponding gauge couplings, field strength tensors and generators respectively. The Λ and M_{q*} are the compositeness scale and mass of the excited state respectively.

2 $pp \rightarrow \gamma + jet$ via $q*$

To study this process, the event generation for signal and for different background processes was done using PYTHIA-v6.325 [3]. For signal event generation the matrix elements for $qg \rightarrow \gamma + jet(q^*)$ were implemented inside the PYTHIA framwork. We used CTEQ 5L as PDF and $Q^2 = \hat{s}$ with other default parameters. A number of points were generated for $M_{q*} = \Lambda$ with standard coupling value of f=1.0 and also with f=0.5. Signal and different backgrounds were generated above three $\hat{P}_T$ range, viz. 180GeV, 450GeV and 950GeV respectively. For final selection we used $P_T^{\gamma,jet} \geq 200$, 500 and 1000 GeV for analysis of different mass points. The photons were required to be in the $|\eta^\gamma| < 2.5$ where $1.444 \leq |\eta^\gamma| \leq 1.566$ is excluded on account

of the insensitive region between the barrel and endcaps[4]. The jets were required to be in $|\eta| \leq 3.0$ only.

We considered all the leading contributions for background processes and broadly categorize these into three classes viz.(i) where a direct photon and a hard jet is produced in the hard scattering (ii) QCD dijet, where one of the jets fragments into a high E_T $\pi^0(\rightarrow \gamma\gamma)$ which gets registered as a single photon (iii) photon + dijet production, where one of the jets is either lost or mismeasured such as $q\bar{q} \rightarrow q\bar{q}\gamma, gg\gamma$ processes or from $W/Z(\rightarrow jj) + \gamma$ production. To estimate the background reasonably at the generator level we have used a clustering algorithm to account for fake photons arising from jets [5]. For jet formation, we used Iterative Cone algorithm with jet size of $\Delta R = 0.5$.

Fake photon signals arising from a jet can be rejected by requiring either the absence of charged tracks above a certain minimum transverse momentum (P_{Tmin}^{trk}) associated with the photon or the absence of additional energetic particles in an annular cone (R_{iso}) around the photon candidate. We have considered two variables for the isolation purpose (a) the number of tracks (N_{trk}) and (b) the scalar sum of transverse energy (E_{TSUM}) inside a cone around the photon.
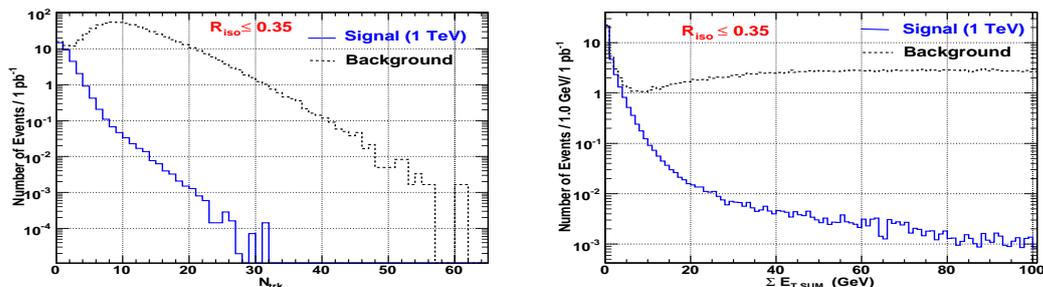

Figure 1: (Left) Number of tracks(N_{trk}) for the signal (1 TeV) and the background events around the photon. (Right) E_{TSUM} for the background and the signal events around photons for $M_{q*} = 1$ TeV Signal.

Fig. 1(Left) shows the distribution of number of charged tracks (N_{trk}) for signal ($M_{q*} = 1$ TeV) and the background around the leading photon within a cone size of $\Delta R \leq 0.35$. Since for the signal events the leading photon is the *true* photon, most of them have no associated tracks ($N_{trk} = 0$) and the distribution falls off very rapidly for larger N_{trk}. For background events though, the distribution peaks at $N_{trk} \sim 7$-8 and then falls slowly. The small rise at $N_{trk} = 0$ is due to the fact that $\gamma + jet$(SM) and $W/Z + \gamma$ backgrounds have true photons as the leading photon in the event and have no tracks around them, while the rising part along with the tail is mainly contributed by QCD dijet events with large number of tracks associated with fake photons. We also analyze the signal efficiency vs signal/background ratio (S/B) as a function of P_{Tmin}^{trk} to improve the selection efficiency for different signal mass points. We accept a photon to be an isolated one if there are no tracks with $P_{Tmin}^{trk} > 3.0$ GeV within $\Delta R = 0.35$. Figure 1(Right) shows the E_{TSUM} distribution for the leading photon in a cone of size $\Delta R = 0.35$ for $M_{q*} = 1$ TeV. It is evident that a large fraction of signal events have $E_{TSUM} < 5.0$ GeV whereas the background events typically have $E_{TSUM} \geq 5$ GeV. We used a threshold of $E_{TSUM} < 5$ GeV in $\Delta R = 0.35$ for this variable for photon selection.
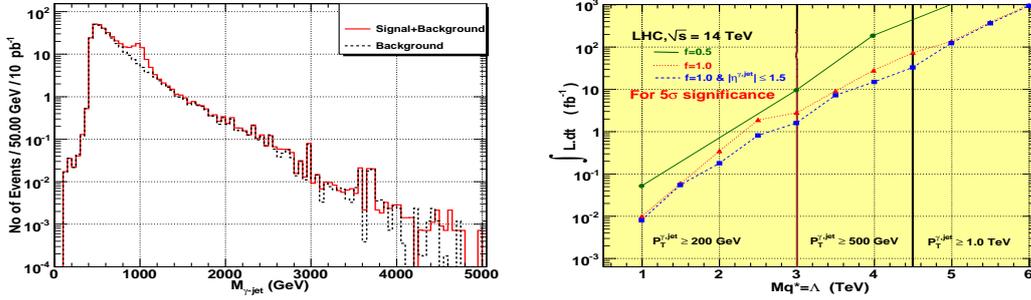
Figure 2: (Left)Invariant mass of $\gamma + jet$ system for signal+background and background only after applying the kinematic and isolation cuts for M_{q*} =1 TeV. (Right) Integrated luminosity distribution for 5σ significance as a function of M_{q*} for two different coupling strengths.

In Fig. 2(Left) we show invariant mass distribution for signal+background and background only after applying selection cuts to M_{q*} =1 TeV sample while Fig. 2(Right) shows the required luminosity needed for 5σ significance(calculated using *frequentist* approach) for the signal with different coupling strengths and pseudorapidity constraints. For estimating the luminosity we have exploited only the mass peak region of the signal over the SM background. We have used a mass window of $\pm \sim 3\Gamma(q*)$ around the mass peak. We also estimated various sources of systematic uncertainties and found that those arising from PDF, scale and luminoisty are the dominant ones.

3   Conclusions

To summarise, we have investigated the potential of using $\gamma + jet$ final state at the LHC for probing possible substructure of quarks. Presence of such a new state would alter the cross section for this process and the present analysis shows that a mass peak discovery for such excited states is possible in the initial phase of the LHC operation.

References

[1] H. Harari and N. Seiberg, Phys.Lett. **B98** (1981) 269; L. Lyons, Oxford University Publication 52/82 (June 1982).

[2] G. 't Hooft, in *Recent Developments in Gauge Theories*, G. 't Hooft *et al.*, eds. (Plenum Press, New York,1980).

[3] T. Sjostrand *et al.*, Comput. Phys. Commun. 135 (2001)238. [arXiv:hep-ph/9903282].

[4] CMS Collaboration, "CMS Physics Technical Design Report Vol-I",**CERN/LHCC 2006-001** (2006).

[5] Satyaki Bhattacharya, Sushil S. Chauhan, Brajesh C. Choudhary and Debajoyti Choudhury, Phys. Rev. D **76**(2007) 115017.

$b \to s\ell^+\ell^-$ in the high q^2 region at two-loops

Volker Pilipp, Christof Schüpbach

Albert Einstein Center for Fundamental Physics,
Institute for Theoretical Physics, University of Bern, Sidlerstrasse 5, 3012 Bern, Switzerland

We report on the first analytic NNLL calculation for the matrix elements of the operators O_1 and O_2 for the inlusive process $b \to X_s l^+ l^-$ in the kinematical region $q^2 > 4m_c^2$, where q^2 is the invariant mass squared of the lepton-pair.

1 Introduction

In the Standard Model, the flavor-changing neutral current process $b \to X_s l^+ l^-$ only occurs at the one-loop level and is therefore sensitive to new physics. In the kinematical region where the lepton invariant mass squared q^2 is far away from the $c\bar{c}$-resonances, the dilepton invariant mass spectrum and the forward-backward asymmetry can be precisely predicted using large m_b expansion, where the leading term is given by the partonic matrix element of the effective Hamiltonian

$$\mathcal{H}_{eff} = -\frac{4G_F}{\sqrt{2}} V_{ts}^* V_{tb} \sum_{i=1}^{10} C_i(\mu) O_i(\mu). \tag{1}$$

We neglect the CKM combination $V_{us}^* V_{ub}$ and the operator basis is defined as in [1]. In [2] we published the first analytic NNLL calculation of the high q^2 region of the matrix elements of the operators

$$O_1 = (\bar{s}_L \gamma_\mu T^a c_L)(\bar{c}_L \gamma^\mu T^a b_L), \qquad O_2 = (\bar{s}_L \gamma_\mu c_L)(\bar{c}_L \gamma^\mu b_L), \tag{2}$$

which dominate the NNLL amplitude numerically. Earlier these results were only available analytically in the region of low q^2 [3, 4].

2 Calculations
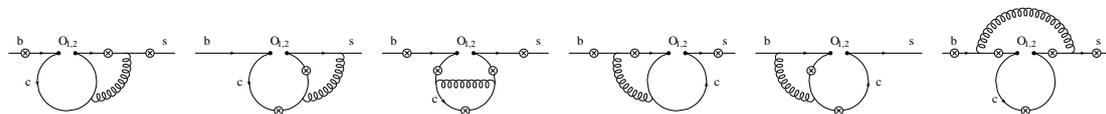
Figure 1: Diagrams that have to be taken into account at order α_s. The circle-crosses denote the possible locations where the virtual photon is emitted (see text).

The diagrams contributing at order α_s are shown in Figure 1. We set $m_s = 0$ and define $\hat{s} = q^2/m_b^2$ and $z = m_c^2/m_b^2$, where q is the momentum of the virtual photon. After reducing

occurring tensor-like Feynman integrals [5] the remaining scalar integrals can be further reduced to master integrals using integration by parts (IBP) identities [6]. Considering the region $\hat{s} > 4z$, we expanded the master integrals in z and kept the full analytic dependence in $\hat{s}$.

For power expanding Feynman integrals we use a combination of *method of regions* [7] and *differential equation techniques* [8, 9]: Consider a set of Feynman integrals $I_1, \ldots, I_n$ depending on the expansion parameter z and related by a system of differential equations obtained by differentiating I_α with respect to z and applying IBP identities:

$$\frac{d}{dz} I_\alpha = \sum_\beta h_{\alpha\beta} I_\beta + g_\alpha, \tag{3}$$

where g_α contains simpler integrals which pose no serious problems. Expanding both sides of (3) in ϵ, z and $\ln z$

$$I_\alpha = \sum_{i,j,k} I_{\alpha,i}^{(j,k)} \epsilon^i z^j (\ln z)^k, \qquad h_{\alpha\beta} = \sum_{i,j} h_{\alpha\beta,i}^{(j)} \epsilon^i z^j, \qquad g_\alpha = \sum_{i,j,k} g_{\alpha,i}^{(j,k)} \epsilon^i z^j (\ln z)^k, \tag{4}$$

and inserting (4) into (3) we obtain algebraic equations for the coefficients $I_{\alpha,i}^{(j,k)}$

$$0 = (j+1) I_{\alpha,i}^{(j+1,k)} + (k+1) I_{\alpha,i}^{(j+1,k+1)} - \sum_\beta \sum_{i'} \sum_{j'} h_{\alpha\beta,i'}^{(j')} I_{\beta,i-i'}^{(j-j',k)} - g_{\alpha,i}^{(j,k)}. \tag{5}$$

This enables us to recursively calculate higher powers of z of I_α, once the leading powers are known. In practice this means that we need the $I_{\alpha,i}^{(0,0)}$ and sometimes also the $I_{\alpha,i}^{(1,0)}$ as initial condition to (5). These initial conditions can be computed using method of regions. A non trivial check is provided by the fact that the leading terms containing logarithms of z can be calculated by both method of regions and the recurrence relation (5).

The summation index j in (4) can take integer or half-integer values, depending on the specific set of integrals I_α. In order to determine the possible powers of z and $\ln(z)$ we used the algorithm described in [9].

3   Results

In order to get accurate results we keep terms up to z^{10}. Our results agree with the previous numerical calculation [10] within less than 1% difference. The impact of our results on the perturbative part of the high q^2-spectrum [3]

$$R(\hat{s}) = \frac{1}{\Gamma(\bar{B} \to X_c e^- \bar{\nu}_e)} \frac{d\Gamma(\bar{B} \to X_s \ell^+ \ell^-)}{d\hat{s}} \tag{6}$$

is shown in Figure 2 (left), where we used the same parameters as in [2]. The finite bremsstrahlung corrections calculated in [4] are neglected. From Figure 2 (left) we conclude that for $\mu = m_b$ the contributions of our results lead to corrections of the order $10\% - 15\%$. Integrating $R(\hat{s})$ over the high $\hat{s}$ region, we define

$$R_{\text{high}} = \int_{0.6}^1 d\hat{s}\, R(\hat{s}). \tag{7}$$
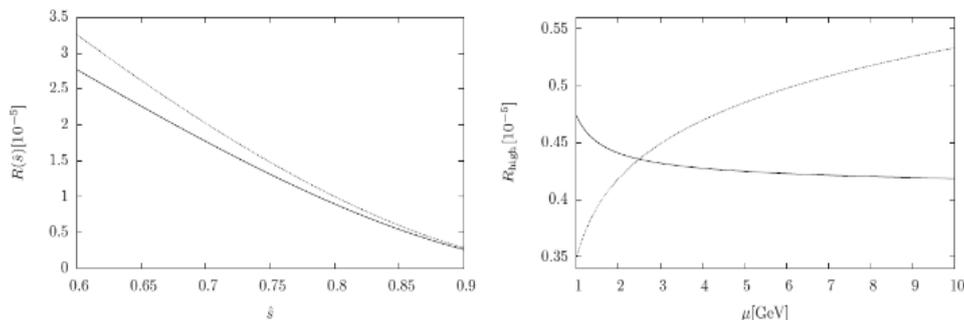
Figure 2: Perturbative part of $R(\hat{s})$ (left) and R_{high} (right) at NNLL. The solid lines represents the NNLL result, whereas in the dotted lines the order α_s corrections to the matrix elements associated with $O_{1,2}$ are switched off. In the left figure we use $\mu = m_b$. See text for details.

Figure 2 (right) shows the dependence of the perturbative part of R_{high} on the renormalization scale. We obtain

$$R_{\text{high,pert}} = (0.43 \pm 0.01(\mu)) \times 10^{-5},\tag{8}$$

where we determined the error by varying μ between 2 GeV and 10 GeV. The corrections due to our results lead to a decrease of the scale dependence to 2%.

References

[1] C. Bobeth, M. Misiak and J. Urban, Nucl. Phys. **B574**, 291 (2000).

[2] C. Greub, V. Pilipp and C. Schüpbach, JHEP **0812**, 040 (2008).

[3] H. H. Asatryan, H. M. Asatrian, C. Greub and M. Walker, Phys. Rev. **D65**, 074004 (2002).

[4] H. H. Asatryan, H. M. Asatrian, C. Greub and M. Walker, Phys. Rev. **D66**, 034009 (2002).

[5] G. Passarino and M. J. G. Veltman, Nucl. Phys. **B160**, 151 (1979).

[6] K. G. Chetyrkin and F. V. Tkachov, Nucl. Phys. **B192**, 159 (1981); F. V. Tkachov, Phys. Lett. **B100**, 65 (1981).

[7] M. Beneke and V. A. Smirnov, Nucl. Phys. **B522**, 321 (1998); S. G. Gorishnii, Nucl. Phys. **B319**, 633 (1989); V. A. Smirnov, Commun. Math. Phys. **134**, 109 (1990); V. A. Smirnov, Springer Tracts Mod. Phys. **177**, 1 (2002).

[8] R. Boughezal, M. Czakon and T. Schutzmeier, JHEP **09**, 072 (2007); A. V. Kotikov, Phys. Lett. **B254**, 158 (1991); V. Pilipp, Nucl. Phys. **B794**, 154 (2008); E. Remiddi, Nuovo Cim. **A110**, 1435 (1997).

[9] V. Pilipp, JHEP **09**, 135 (2008).

[10] A. Ghinculov, T. Hurth, G. Isidori and Y. P. Yao, Nucl. Phys. **B685**, 351 (2004).

Searching for tetraquarks on the lattice

S. Prelovsek[1], T. Draper[2], C.B. Lang[3], M. Limmer[3], K.-F. Liu[2], N. Mathur[4] and D. Mohler[5]

[1] Department of Physics, University of Ljubljana and Jozef Stefan Institute, Slovenia.
[2] Department of Physics and Astronomy, University of Kentucky, Lexington, KY 40506, USA.
[3] Institut für Physik, FB Theoretische Physik, Universität Graz, A-8010 Graz, Austria.
[4] Department of Theoretical Physics, Tata Institute of Fundamental Research, Mumbai, India.
[5] 4004 Wesbrook Mall Vancouver, BC V6T 2A3 Canada, Canada

We address the question whether the lightest scalar mesons σ and κ are tetraquarks. We present a search for possible light tetraquark states with $J^{PC} = 0^{++}$ and $I = 0$, $1/2$, $3/2$, 2 in the dynamical and the quenched lattice simulations using tetraquark interpolators. In all the channels, we unavoidably find lowest scattering states $\pi(k)\pi(-k)$ or $K(k)\pi(-k)$ with back-to-back momentum $k = 0$, $2\pi/L$, $\cdots$. However, we find an additional light state in the $I = 0$ and $I = 1/2$ channels, which may be related to the observed resonances σ and κ with a strong tetraquark component. In the exotic repulsive channels $I = 2$ and $I = 3/2$, where no resonance is observed, we find no light state in addition to the scattering states.

It is still not known whether the lightest observed nonet of scalar mesons σ, κ, $a_0(980)$ and $f_0(980)$ [2] are conventional $\bar{q}q$ states or exotic tetraquark $\bar{q}\bar{q}qq$ states. Tetraquark interpretation was proposed by Jaffe back in 1977 [1] and it is supported by many phenomenological studies, for example [2, 3]. The tetraquarks, composed of a scalar diquark and anti-diquark, form a flavor nonet and are expected to be light. The observed ordering $m_\kappa < m_{a_0(980)}$ favors tetraquark interpretation since the $I = 1$ state $[\bar{d}\bar{s}][us]$ with additional valence pair $\bar{s}s$ is naturally heavier than the $I = 1/2$ state $[\bar{s}\bar{d}][du]$.

It is important to determine whether QCD predicts any scalar tetraquark states below 1 GeV from a first principle lattice QCD calculation. Previous lattice simulations [4, 5] have not given the final answer yet. The strongest claim for σ as tetraquark was obtained using the sequential Bayes method to extract the spectrum [4] and needs confirmation using a different method. Our new results, given in this proceeding, are presented with more details in [6, 7].

We calculate the energy spectrum of scalar tetraquark states with $I = 0$, 2, $1/2$, $3/2$ in dynamical and quenched lattice simulations. Our dynamical simulation ($a \simeq 0.15$ fm, $V = 16^3 \times 32$) uses dynamical Chirally Improved u/d quarks [8] and it is the first dynamical simulation intended to study tetraquarks. The quenched simulation ($a \simeq 0.20$ fm, $V = 16^3 \times 28$) uses overlap fermions, which have exact chiral symmetry even at finite a.

The energies of the lowest three physical states are extracted from the correlation functions $C_{ij}(t) = \langle 0|\mathcal{O}_i(t)\mathcal{O}_j^\dagger(0)|0\rangle_{\vec{p}=\vec{0}} = \sum_n Z_i^n Z_j^{n*} e^{-E_n t}$ with tetraquark interpolators $\mathcal{O} \sim \bar{q}\bar{q}qq$, where $Z_i^n \equiv \langle 0|\mathcal{O}_i|n\rangle$. In all the channels we use three different interpolators that are products of two color-singlet currents [6]. In addition, we use two types of diquark anti-diquark interpolators in $I = 0$, $1/2$ channels [6].

When calculating the $I = 0$, $1/2$ correlation matrix, we neglect the so-called single and double disconnected quark contractions [5], as in all previous tetraquark studies. The resulting

states have only a $\bar{q}\bar{q}qq$ Fock component in this approximation, while they would contain also a $\bar{q}q$ component if single disconnected contractions were taken into account [5]. Since we are searching for "pure" tetraquark states in this pioneering study, our approximation is physically motivated.

All physical states n with given $J^{PC} = 0^{++}$ and I propagate between the source and the sink in the correlation functions. Besides possible tetraquark states, there are unavoidable contributions from scattering states $\pi(k)\pi(-k)$ for $I = 0$, 2 and scattering states $\pi(k)K(-k)$ for $I = 1/2$, $3/2$. Scattering states have discrete momenta $\vec{k} = \frac{2\pi}{L}\vec{j}$ on the lattice of size L and energy $(m_\pi^2 + \vec{k}^2)^{1/2} + (m_{\pi,K}^2 + \vec{k}^2)^{1/2}$ in the non-interacting approximation. Our main question is whether we find some light state in addition the scattering states in $I = 0$, $1/2$ channels. If such a state is found, it could be related to the resonances σ or κ with a strong tetraquark component.

The energies E_n are extracted from the correlation functions $C_{ij}(t)$ via the eigenvalues $\lambda^n(t) \propto e^{-E_n(t-t_0)}$ of the generalized eigenvalue problem $C(t)\vec{u}^n(t) = \lambda^n(t,t_0)C(t_0)\vec{u}^n$ at some reference time t_0 [9].
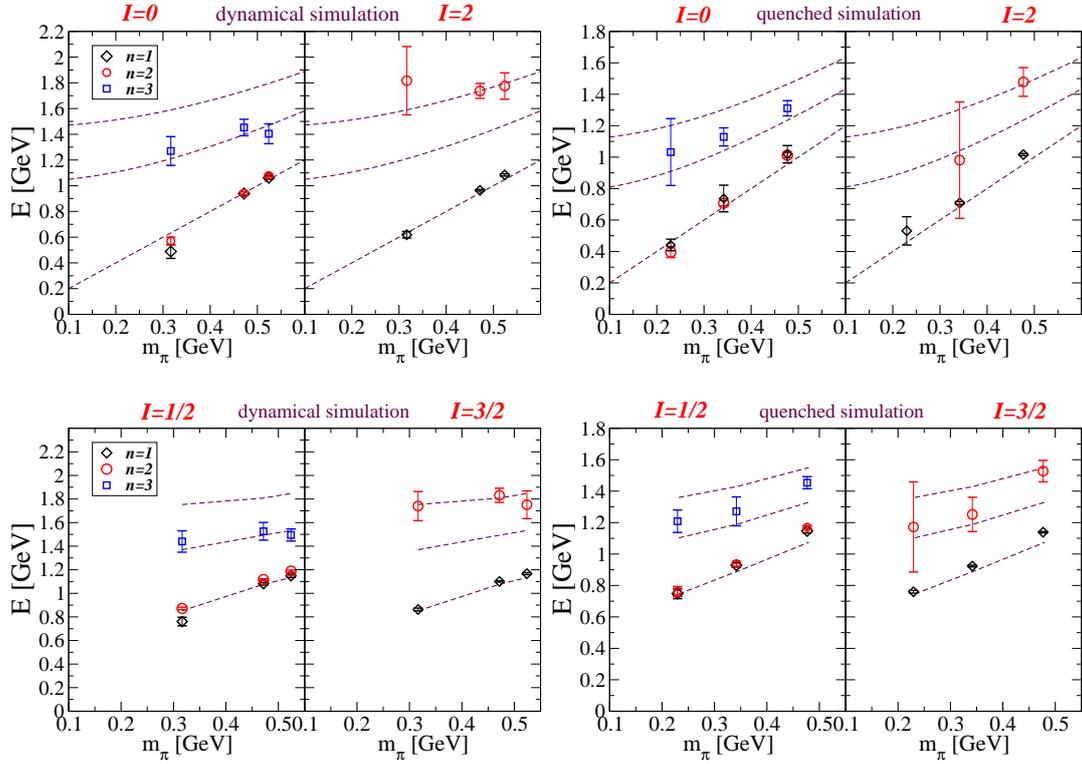

Figure 1: The resulting spectrum E_n for $I = 0$, 2, $1/2$, $3/2$ in the dynamical (left) and the quenched (right) simulations. Note that there are two states (black and red) close to each other in $I = 0$ and $I = 1/2$ cases. The lines at $I = 0$, 2 present the energies of non-interacting $\pi(k)\pi(-k)$ with $k = j\frac{2\pi}{L}$ and $j = 0, 1, \sqrt{2}$. Similarly, lines at $I = 1/2$, $3/2$ present energies of $\pi(k)K(-k)$.

The resulting spectrum E_n for all four isospins is shown in Fig. 1. The lines present the energies of the scattering states in the non-interacting approximation. Our dynamical and quenched results are in qualitative agreement.

In the repulsive channel $I = 2$, where no resonance is expected, we indeed find only the candidates for the scattering states $\pi(0)\pi(0)$ and $\pi(\frac{2\pi}{L})\pi(-\frac{2\pi}{L})$ with no additional light state. The first excited state is higher than expected due to the smallness of 3×3 basis. Similar conclusion applies for the repulsive $I = 3/2$ channel with πK scattering states.

In the attractive channel $I = 0$ we find two (orthogonal) states close to the threshold $2m_\pi$ and another state consistent with $\pi(\frac{2\pi}{L})\pi(-\frac{2\pi}{L})$, so we do find an additional light state. This leads to a possible interpretation that one of the two light states is the scattering state $\pi(0)\pi(0)$ and the other one corresponds to σ resonance with strong tetraquark component (see more general discussion in [10]). In the attractive $I = 1/2$ channel we similarly find the candidates for the lowest two $\pi(k)K(-k)$ scattering states and a candidate for a κ resonance with a large tetraquark component. These results have to be confirmed by another independent lattice simulation before making firm conclusions.

We investigate two criterion for distinguishing the one-particle (tetraquark) and two-particle (scattering) states in [7]. The first criteria is related to the time dependence of $C_{ij}(t)$ and $\lambda^n(t)$ at finite temporal extent of the lattice. The second is related to the volume dependence of the couplings $\langle 0|\mathcal{O}_i|n\rangle$.

The ultimate method to study σ and κ on the lattice would involve the study of the spectrum and couplings in presence of $\bar{q}\bar{q}qq \leftrightarrow \bar{q}q \leftrightarrow vac \leftrightarrow glue$ mixing, using interpolators that cover these Fock components. Such a study has to be done as a function of lattice size L in order to extract the resonance mass and width using the Lüscher's finite volume method [10, 11].

Acknowledgments

References

[1] R. L. Jaffe, Phys. Rev. D 15 (1977) 267 and 281; R. L. Jaffe, *Exotica*, hep-ph/0409065.

[2] *Note on the scalar mesons*, C. Amsler *et al.*, *Review of Particle Physics*, Phys. Lett. B667 (2008) 1.

[3] L. Maiani *et al.*, Phys. Rev. Lett. 93 (2004) 212002; G. 't Hooft *et al.*, Phys. Lett. B 662 (2008) 424; Hee-Jung Lee, N.I. Kochelev, Phys. Rev. D78 (2008) 076005.

[4] N. Mathur *et al.*, χQCD collaboration, Phys. Rev. D76 (2007) 114505.

[5] S. Prelovsek and D. Mohler, Phys. Rev. D79 (2009) 014503; M. Alford and R. Jaffe, Nucl. Phys. B578 (2000) 367; H. Suganuma *et al.*, Prog. Theor. Phys. Suppl. 168 (2007) 168; M. Loan, Z. Luo, Y. Y. Lam, Eur. Phys. J. C57 (2008) 579.

[6] S. Prelovsek, T. Draper, C.B. Lang, M. Limmer, K.-F. Liu, N. Mathur and D. Mohler, arXiv: 0909:5134, PoS LAT2009 (2009) 103.

[7] S. Prelovsek, T. Draper, C.B. Lang, M. Limmer, K.-F. Liu, N. Mathur and D. Mohler, to be published.

[8] C. Gattringer, C. Hagen, C.B. Lang, M. Limmer, D. Mohler and A. Schäfer, Phys. Rev. D79 (2009) 054501.

[9] M. Lüscher and U. Wolff, Nucl. Phys. B339 (1990) 222; B. Blossier *et al.*, JHEP 0904 (2009) 094.

[10] S. Sasaki and T. Yamazaki, Phys. Rev. D74 (2006) 114507, PoS LAT2007 (2007) 131.

[11] M. Lüscher, Comm. Math. Phys. 104 (1986) 177; Nucl. Phys. B354 (1991) 531; Nucl. Phys. B364 (1991) 237; Zhi-Yuan Niu, Ming Gong, Chuan Liu, Yan Shen, Phys. Rev. D80 (2009) 114509.

Gluon saturation effects at forward rapidities at LHC in pp collisions

Amir H. Rezaeian

Institut für Theoretische Physik, Universität Regensburg, 93040 Regensburg, Germany
Departamento de Física y Centro de Estudios Subatómicos,
Universidad Técnica Federico Santa María, Casilla 110-V, Valparaíso, Chile

We investigate hadrons and direct photon production in pp collisions at the LHC energy within the color-dipole approach. We show that greatest sensitivity to gluon saturation effects is reached at very forward rapidities in pp collisions at LHC ($\sqrt{s} = 14$ TeV). The discrepancies among various saturation models (fitted to HERA data) results can be about a factor of $2 - 3$ at forward rapidities. We found that the ratio of direct-photon to pion production can be about $20 - 10$ at forward rapidities $\eta = 7 - 8$. Therefore, direct photon production at forward rapidities should provide a rather clean probe as the background from radiative hadronic decays is significantly suppressed.

1 Introduction

At high energies/small Bjorken-x, QCD predicts that gluons in a hadron wavefunction form a new state, the so-called Color Glass Condensate (CGC) [1, 2], for a review see [3] and references therein. The cornerstone of the CGC is the existence of a hard saturation scale Q_s at which nonlinear gluon recombination effects become important and start to balance gluon radiation. The Color Glass Condensate (saturation) approach to QCD at high energy has been very successful to describe a variety of processes at Relativistic Heavy Ion Collider (RHIC) [3]. Nevertheless, the importance of saturation effects is still disputable given that other approaches offered alternative descriptions. In order to test saturation physics and its relevance, it seems therefore essential to consider various reactions in different kinematic regions at the Large Hadron Collider (LHC) and future collider experiments. Here, we address the role of gluon saturation at LHC energy $\sqrt{s} = 14$ TeV in hadrons and direct photon production in *pp* collisions within the light-cone color-dipole approach using various saturation models. Details of calculations can be found in Ref. [4].

2 Hadrons and photon at LHC within saturation models

The concept of saturation and the taming of the power-like rise of the gluon distribution at small Bjorken-x was first addressed in Ref. [1] in the double logarithmic approximation. The actual calculation of higher-order corrections to the non-linear small-x evolution equations still remains as a challenge [3], see also [5] and references therein. Thus, one may resort to a QCD-like model which incorporates the basic features of gluon saturation into the dipole-proton
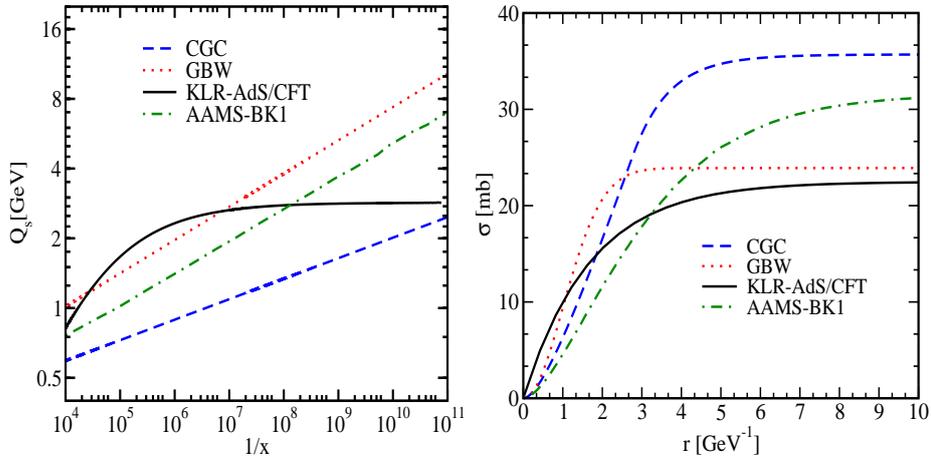
Figure 1: Left: Saturation scale as a function of $1/x$ for various color-dipole models labeled with CGC [6], GBW [7], KLR-AdS/CFT [5] and AAMS-BK1 [8]. Right: The total dipole-proton cross section $\sigma_{q\bar{q}}(r,x)$ at fixed $x = 10^{-5}$ in the various color-dipole models.

forward scattering amplitude, and provides predictions which will allow to test the validity of the treatment. There are several parametrizations proposed in the literature which all give a good description of HERA data but predict different saturation scales, see Fig. 1. The details of saturation models used in Fig. 1 can be found in Ref. [4]. The main feature of these models is that for decreasing x, the dipole amplitude saturates at smaller dipole sizes. Note that there is no unique definition for the saturation scale in literature. We define the saturation scale $Q_s^2 = 2/r_s^2$ as a energy scale at which the $q\bar{q}$ dipole scattering amplitude $\mathcal{N}_{q\bar{q}} \approx 0.4$ becomes sizable [4, 7].

The invariant cross-section of hadron and direct photon production can be calculated via the light-cone color-dipole factorization scheme [4], see also Ref. [9]. In Fig. 2, the differential cross-section of pion π^0 and direct photon γ (photons radiated in hadronic collisions not via hadronic decays) production at LHC are plotted versus rapidity at fixed transverse momenta $p_T = 1$ and 2 GeV within various color-dipole models (see Fig. 1). It is seen that the discrepancies among various saturation color dipole model results can be about a factor of $2-3$ at moderate rapidities. At the kinematic limit, i.e. at very forward rapidities and higher p_T where the differential cross-section approaches zero, kinematic constraints limit the parton phase space and saturation effects become less important. It is seen from Fig. 2 that for both hadron and photon production, away from the kinematic limit, at not very large η and p_T, a color-dipole model with larger saturation scale leads to a stronger peak at forward rapidity (having in mind that the saturation scale is a dynamical function of x, see Fig. 1).

In order to understand the *relative* importance of saturation effects at various rapidities, we employ the Semi-Sat model fitted to HERA data where the dipole-proton forward scattering amplitude is [10]:

$$\mathcal{N}_{q\bar{q}}^{\text{Semi-Sat}}(\vec{r},\vec{b},x) = 2\mathcal{N}_0 \left(\frac{rQ_s}{2}\right)^{2\gamma_{eff}}, \qquad Q_s = \left(\frac{x_0}{x}\right)^{\frac{\lambda}{2}} \left[\exp\left(-\frac{b^2}{2B_{\text{CGC}}}\right)\right]^{\frac{1}{2\gamma_s}}. \quad (1)$$
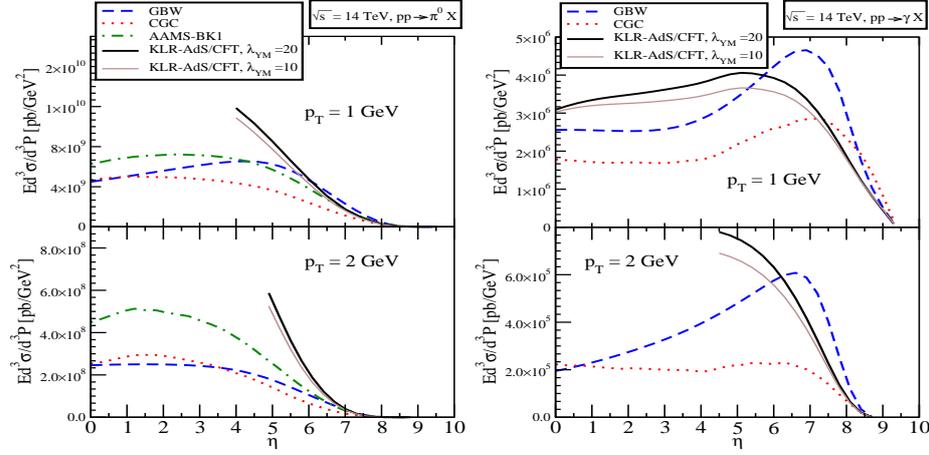
Figure 2: Invariant cross-section for pion (left) and direct photon (right panel) production in pp collisions at LHC as a function of rapidity η calculated with various color dipole models for various fixed p_T.

The parameter γ_{eff} is defined for $rQ_s \leq 2$ as $\gamma_{eff} = \gamma_s + \frac{1}{\kappa\lambda Y}\ln\frac{2}{rQ_s}$, and for $rQ_s > 2$ as $\gamma_{eff} = \gamma_s$. The value of other parameters of this model can be found in [10]. Surprisingly, the fit obtained with such an oversimplified model is as good as for the other models with $\chi^2/\text{d.o.f.} = 0.92$. In Fig. 3 we show, ratio of the two cross-sections for both pions and direct photon at LHC, calculated once with diffusion term and once without, i.e. $\gamma_{eff} = 0.43$. It is seen that at forward rapidities, the diffusion term in the anomalous dimension is not important, since it gives similar results as with a fixed $\gamma_{eff} = 0.43$. The preferred value of anomalous dimension $1 - \gamma_{eff} = 0.57$ at very forward rapidities is close to the one predicted from the BK equation [11]. It is well known that the saturation effects start being essential when the anomalous dimension reaches the value $\gamma_{cr} = 1 - \gamma_{eff} = 0.37$ which is the case for forward rapidities (see Refs. [1, 12]). This indicates that direct photon and hadron production at different rapidities at LHC are rather sensitive to saturation.

Direct photons can only be radiated from quarks, while hadrons can be produced by both gluons and quarks. At the LHC energy at midrapidity gluons dominate. Therefore the photon/pion ratio is significantly reduced toward midrapidity. However, at very forward rapidity, valence quarks become important and the photon/pion ratio rises. Moreover, at high p_T again valence quarks becomes important and we have a sharp rise of the photon/pion ratio. In Fig. 3 right panel, we show the photon/pion ratio γ/π^0 as a function of p_T at various rapidities within the GBW model and pp collisions. The ratio γ/π^0 can be as big as $10 - 20$ at very forward rapidities $\eta = 8 - 7$ at LHC energy. Therefore, direct photon production extends to higher rapidities for a fixed p_T, see Figs. 3. Note that suppression of hadrons at very forward rapidity also ensures significant suppression of radiative decays of those hadrons. Therefore, measurements of direct photons at forward rapidities should be rather clean, as the background from radiative hadronic decays is significantly suppressed.

The charged Higgs Boson of the two Higgs Doublet model type III

H. Cardenas[1], J. Duarte[2], J.-Alexis Rodriguez[2]

[1]Escuela de Física, Universidad Pedagógica y Tecnológica de Tunja, Duitama, Colombia
[2]Departamento de Física, Universidad Nacional de Colombia,2Bogotá, Colombia

Recently there are experimental reports from D0 and CDF collaborations searching for a particular signature of new physics in the framework of the Two Higgs Doublet Model (2HDM) type III, specifically looking for charged Higgs bosons. We present a review of the analysis done in the region $M_{H+} > m_t$ by D0 collaboration and we take into account the previous bounds obtained on the parameter space of the model. We use the ratio R_σ for the region $M_{H+} < m_t$.

One possible simple extension of the SM is by adding a new Higgs doublet and it is called the two Higgs Doublet Model (2HDM). This extension has the following direct consequences: it increases the scalar spectrum and it gives a more generic pattern of the Flavor Changing Neutral Currents (FCNC). FCNC at tree level can be consider a problem that was solved in the earlier versions of the two Higgs Doublet Model (2HDM type I and II) by imposing a discrete symmetry that restricts each fermion to be coupled at most to one Higgs doublet. But if the discrete symmetry is not imposed then FCNC at tree level remains, it is the so-called two Higgs Doublet Model type III. In the 2HDM-III, for each type quark, up or down type, there are two Yukawa couplings. One of the Yukawa couplings is in charge of generates the quark masses and the other one produces the flavor changing couplings at tree level. The two complex scalar fields correspond to eigth degrees of freedom, where three of them are identified as Goldstone bosons and are absorbed as longitudinal components to the $W^\pm$ and Z bosons giving mass to the weak bosons. The remaining degrees of freedom are interpreted as five physical states: two neutral scalars h^0 and H^0, a pseudo-scalar A^0, and a pair of charged Higgs bosons $H^\pm$.

While it may be hard to distinguish any one of these neutral Higgs bosons of the 2HDM-III from that one of the SM, the charged $H^\pm$ pair carry a distinctive hall-mark of this kind of new physics. Hence the charged Higgs boson plays a very important role in the search of new physics beyond the SM.

We will consider a general 2HDM-III where the Higgs doublets can couple with the up and down quark sector at the same time because there is not any discrete symmetry. In 2HDM-III there is a global symmetry which can make a rotation of the Higgs doublets and fix one VEV equal to zero. In such a way, $v_1 = v$ and $v_2 = 0$, and the mixing parameter $\tan\beta = v_2/v_1$ can be eliminated from the Lagrangian. If the parameter $\tan\beta$ is eliminated from the Lagrangian, we have the usual 2HDM type III [5], and the Lagrangian of the charged sector is given by

$$-\mathcal{L}^{III}_{H^\pm ud} = H^+\bar{U}[K\xi^D P_R - \xi^U K P_L]D + h.c. \tag{1}$$

where K is the Cabbibo-Kobayashi-Maskawa (CKM) matrix and $\xi^{U,D}$ the flavour changing matrices.
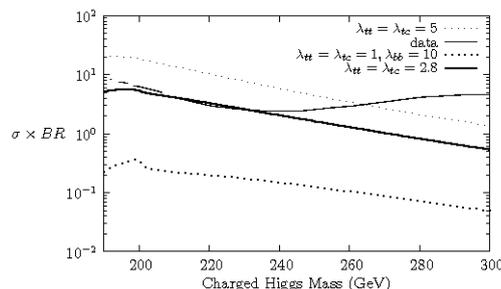
Figure 1: The cross section times branching fraction versus the charged Higgs boson for different scenarios in the type III 2HDM

For a better study of the FCNC processes, Cheng, Sher and Yuang (CSY) [2] propose an anzats for the Yukawa matrices. It is based on the SM $\phi f \bar{f}$ couplings and states that

$$\xi^{ij} \equiv \frac{\sqrt{m_i m_j}}{v} \lambda_{ij} .$$

This is an ansatz for the Yukawa texture matrices looking for a phenomenological similarity with SM couplings. This anzats obeys to the fact that couplings between fermions and the Higgs particle in the SM are proportional to the mass of the fermion. Parameters λ_{ij} could change the hierarchy between fermionic couplings and because of this it is expected that they would be ~ 1. Some restrictions over the λ_{ij} and the ξ_{ij} parameter sets have been found in literature, summarized in table 1 [3].

The analysis presented by D0 collaboration [1] for the type III 2HDM has followed the analysis done in reference [4] assuming that the parton level is important to enhance the cross section, if λ_{tc} is bigger than one. The experimental analisis have used $\lambda_{tc} = 5$. Further, they assumed the parameter λ_{tt} in the charged Higgs decay vertex, to be equal to λ_{tc}. About this last point, we should mention that Atwood, *et. al.* in reference [5] have already shown that the assumption $\lambda_{ij} = \lambda$ is not in agreement with the low energy phenomenology and on the other hand, it has been shown [3] that perturbation theory validity requires that

Parameter	Range
$\xi^2_{\mu\tau}$	$[7.62 \times 10^{-4} : 4.44 \times 10^{-2}]$
$\xi_{\tau\tau}$	$[-1.8 \times 10^{-2} : 2,2 \times 10^{-2}]$
$\xi_{\mu\mu}$	$[-0.12:0.12]$
$\xi_{\mu e}$	$[-0.39:0.39]$
λ_{bb}	$[-6:6]$
λ_{tt}	$[-\sqrt{8} : \sqrt{8}]$

Table 1: Experimental constraints over the ξ and λ matrices

$\lambda_{tc} \leq 2.8$. From this point we aim to explore scenarios allowed in the 2HDM-III space parameters, with the additional simplification that in this model $\tan\beta$ is a spureous parameter. The experimental D0 collaboration report the observed limits on the production cross section (pb) times the branching fraction $\sigma(q\bar{q}' \to H^+) \times B(H^+ \to t\bar{b})$. These limits are shown in Fig. 1 labeled as data. We have used the program CompHEP to evaluate the charged Higgs boson production and decays, $q\bar{q}' \to H^+ \to t\bar{b} \to W^+ b\bar{b} \to l^+\nu b\bar{b}$ where l represents an electron or muon. The expected limits using the same values of the λ_{ij} in the charged Higgs boson mass range 180 to 300 GeV are plotted in Fig. 1. In addition, in Fig. 1 are shown the predictions

Figure 2: The ratio R_σ with the experimental limits from D0 collaboration and different values of the space parameter in the framework of the type III 2HDM

taken $\lambda_{tc} = 2.8, 1$, $\lambda_{tt} = 2.8, 1$ and $\lambda_{bb} = 0, 10$. These values of λ_{ij} are allowed for the phenomenology according to the table 1. We conclude that restrictions on the parameter space of the type III 2HDM are not too stronger. We notice that in the case $\lambda_{ij} = 5$ only charged Higgs masses above around 264 GeV are allowed and for values $\lambda_{tt} = 2.8$ the charged Higgs boson mass should be bigger than 230 GeV. Finally, in the region $M_{H^+} < m_t$, we have used the reported measurements of the ratio $R_\sigma = \sigma(p\bar{p} \to t\bar{t})_{l+jets}/\sigma(p\bar{p} \to t\bar{t})_{dilepton}$. We have shown the results in Fig. 2.

1 Acknowledgments

References

[1] V. M. Abazov, *et. al*[D0 Collaboration], Phys. Rev. Lett.**102**191802 (2009) [arXiv:hep-ex/0807.0859]

[2] T. P. Cheng and M. Sher. *Phys. Rev.* **D35**, 3484 (1987).

[3] R. Martinez, J.-Alexis Rodriguez, S. Sanchez, Braz.J.Phys.38:507-510,2008 [arXiv:hep-ph/08104303]; C. Jimenez, R. Martinez, J.-Alexis Rodriguez, Braz.J.Phys.38:455-458,2008 [arXiv:hep-ph/0810.4313]; H. Cardenas, J. Duarte, J.-Alexis Rodriguez, arXiv:hep-ph/0810.3046 and references there in.

[4] H. He and C. P. Yuan, Phys. Rev. Lett. **83**, 28 (1999).

[5] D. Atwood, L. Reina and A. Soni,Phys. Rev. D **55**, 3156 (1997)[arXiv:hep-ph/9609279] and references there in.

On diffractive magnetic monopole production in pp collisions

I. Satsunkevich [1], *Dz. Shoukavy*[1], *P. Tsiareshka*[2],

[1]B.I. Stepanov Institute of Physics, National Academy of Sciences of Belarus, Nezalezhnasci Ave. 68, 220072 Minsk, Belarus.
[2]Joint Institute for Nuclear Research, Joliot-Curie 6, 141980, Dubna, Russia.

Here we propose diffractive production of the monopole pair via two-photon fusion. We used FPMC [1] for estimation of the total cross section for the spin 1 Dirac monopole diffractive production via the two-photon fusion.

1 Introduction, Motivation and Result

Over seventy years ago P.A.M. Dirac [2] proposed a model which postulated the existence of the isolated magnetic charge, presently known as the *Dirac magnetic monopole*. Since then massive theoretical and experimental efforts has been devoted to the problem. But up to now no experimental evidence of the monopole existence has been found. Nevertheless, the interest in magnetic monopole remains strong due to its elegance and the unifying nature of the model.

The strongest argument in favor of the existence of the magnetic monopole is the quantization of electric charge. In his paper Dirac established the relation between the elementary electric charge e and the basic magnetic charge g

$$eg = \frac{n\hbar c}{2}, \text{where } n = 0, \pm 1, \pm 2, ..., [1]$$

and $g_D = \hbar c/2e \simeq 68, 5e$ is the unit Dirac magnetic charge.

Secondly, the monopole's existence leads to the symmetrization of Maxwell's equations in classical electrodynamics. The introduction of magnetic charge density ρ_m and magnetic current density j_m would make the equations invariant under a global duality transformation.

And, finally, magnetic monopoles are predicted from field theories which unify the fundamental forces [4]-[5]. While most of the theoretical models tend to favor GUT monopoles with masses $\sim 10^{16} - 10^{17}$GeV and cannot discovered on the accelerators, in some Grand Unified models lower mass monopoles, with masses of order a few TeV, are allowed [5, 6].

These circumstances has stimulated the experimental searches for magnetic monopoles at accelerators [7]-[11] and in cosmic radiation experiments [12].

Now the favored model for monopole production has been Drell-Yan mechanism. This process was considered at Tevatron [8, 10] and LEP2 [11]. Maybe $\gamma\gamma$ direct production of the monopole-antimonopole pair was not considered at these experiments following an assumption of the small probability of usual particle-antiparticle pair production, for example e, μ, τ and so

---

[1]In the Schwinger approach [3] the the integer n takes on the values $n = 0, \pm 2, \pm 4, ...$

on. On the other hand, due to the large coupling constant for interaction with a photon α_g, the $\gamma\gamma$ fusion mode of monopole production, first pointed out by Cabibbo and Ferrari in 1962 [14], can be shown to be competitive with and, even in excess of, the Drell-Yan production cross-section.[2] We note that in the absence of the exactly schemes for calculating processes involving the magnetic monopoles, two-photon production and the Drell-Yan production, should be used concurrently. In paper [15] we have shown that $\gamma\gamma$ fusion (elastic case) at high energy pp-collisions could be more convenient mechanism. At present the diffraction in high energy physics has become a fashionable subject. Since the diffractive production of elementary particles is simply enough carried out experimentally. The main excellence of this method is consisted in a possibilities to obtain additional information on produced particles such as spins and parities at considerably reduced backgrounds. Therefore it seems to us interesting to propose and consider the diffractive production monopole pair via $\gamma\gamma$ fusion.

Here we consider the Dirac monopole for the case when $n = 1$ (see 1) with mass up to 2 TeV, a spin $s = 1$ only. It should be note that by the Dirac monopole means a pointlike particle without electric charge or hadronic interactions and with magnetic charge satisfying the Dirac charge quantization condition (1). As well known the dual symmetry of Maxwell's equations due to the existence of the magnetic monopole can be used to obtain the magnetic monopole versions of the Bethe-Bloch equation, Lorentz force and other relations. Milton [13] has shown that the electron-monopole scattering this cross section may be obtained from the Rutherford electron-electron scattering cross-section by substitution $\frac{e}{v} \to \frac{g}{c}$. Thus, to estimate the monopole production cross sections one uses the principle of the duality which require only replacement of electric charge with the monopole's effective charge $g\beta$, where β is the monopole speed. The photon-monopole coupling constant thus becomes: $\alpha_g = g^2\beta^2$, in the case $n = 1$.

The spin 1 Dirac monopole diffractive production via the two-photon fusion can be easily added into the FPMC generator. Just we need realize the following schema:

• You generate the diffractive W pair production $\gamma\gamma$ fusion. The WW production is switched on with a standard process IPROC=12030.

• Then you should replace mass of W on the monopole mass through RMASS(198)= monopole mass.D0.

• The next step is replacement the electromagnetic coupling constant α on the monopole coupling to photons α_g in the production subprocess cross section $\gamma\gamma -> W+W-$.

• And finally it is necessary to recompile and run ./module_reco < Datacards/dataQEDMonopole with following main parameters TYPEPR='EXC', TYPINT='QED', ECMS=14000, IPROC= 16030, NFLUX=15, AAANOM=10.

By varying the monopole mass in the `module_reco.f` file, we obtain the dependence of the $\gamma\gamma$ production cross-section on the monopole mass as shown in Fig. 1. In Fig. 2 – Fig. 4 we show representative distributions of the monopole-antimonopole pairs with masses of 500 GeV and 1500 GeV obtained with FPMC.

---

[2]It should be noted that in the experiment at HERA, a monopole–antimonopole pair was assumed to be produced by the process $e^+p \longrightarrow e^+M\overline{M}p$ via the interactions of photons emitted from each positron and proton [9].

References

[1] http://project-fpmc.web.cern.ch/project-fpmc/ .

[2] P.A.M. Dirac, Proc. Roy. Soc. Lond. A **A133**, 60 (1931).

[3] J. Schwinger, Phys. Rev. **144**, 1087 (1966).

[4] G.'t Hooft, Nucl. Phys. B **79**, 276 (1974); A.M. Polyakov, JETP Lett. **20**, 194 (1974).

[5] K.R. Dienes, E. Dudas and T. Gherghetta, Nucl. Phys. B. **537**, 47 (1999).

[6] T. W. Kephart and Q. Shafi, Phys.Lett. B **520**, 313 (2001).

[7] B. Abbott *et al.* (DØ Collab.), Phys. Rev. Lett. **81**, 524 (1998).

[8] G.R. Kalbfleisch, K.A. Milton, M.G. Strauss, L. Gamberg, E.H. Smith, and W. Luo, Phys. Rev. Lett. **85**, 5292 (2000); G.R. Kalbfleisch, W. Luo, K.A. Milton, E.H. Smith, M.G. Strauss, Phys Rev. D **69**, 052002 (2004).

[9] A. Aktas *et al.* (H1 Collab.), Eur. Phys. J. C **41**, 133 (2005).

[10] A. Abulencia *et al.* (CDF Collab.), Phys. Rev. Lett **96**, 201801 (2006).

[11] A. Atkas *et al.* (OPAL Collab.), Phys. Letts. B **663**, 37 (2008).

[12] M. Ambrosio *et al.* (MACRO Collab.), Eur. Phys. J. C **25**, 511 (2002); Eur. Phys. J. C **26**, 163 (2002); S. Balestra *et al.*, Eur. Phys. J. C, **55**, 57, (2008).

[13] K.A. Milton, Rept. Prog. Phys. **69**, 1637 (2006).

[14] N. Cabibbo and E. Ferrari, Nuovo Cim. **23**, 1147 (1962).

[15] Yu. Kurochkin, I. Satsunkevich, D. Shoukavy, N. Rusakovich and Yu. Kulchitsky, Mod. Phys. Lett. A **21**, 2873 (2006).
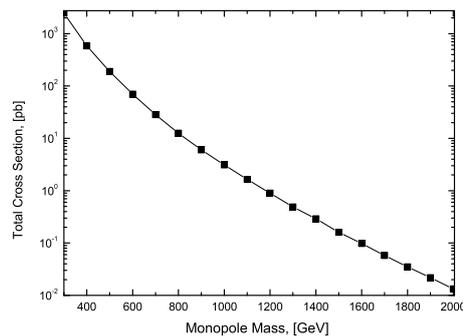
Figure 1: Diffractive monopole production via $\gamma\gamma$ fusion in pp-collisions at $\sqrt{s} = 14$TeV.
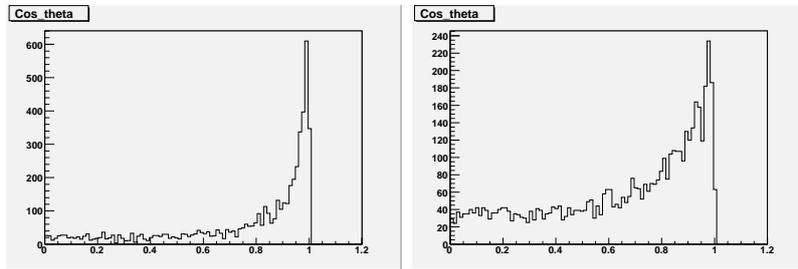
Figure 2: Monopole and antimonopole pair distributions as a function of $\cos\theta$ for monopole/antimonopole masses of 500 GeV (left) and 1.5 TeV (right).
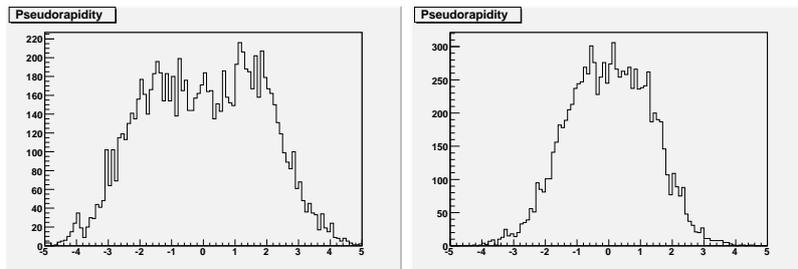

Figure 3: Monopole and antimonopole pair distributions as a function of pseudorapidity for monopole/antimonopole masses of 500 GeV (left) and 1.5 TeV (right).
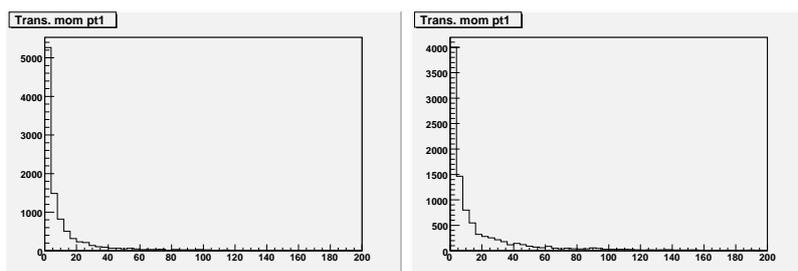

Figure 4: Monopole and antimonopole pair distributions as a function of p_T for monopole/antimonopole masses of 500 GeV (left) and 1.5 TeV (right). High p_T values for the given monopole masses would ensure high detection efficiency.

Baryonium in Confining Gauge Theory

Fumihiko Toyoda

Kinki University, Kayanomori, 820-8555 Iizuka, Japan

We show a new class of embedding solutions of D5 brane, which wraps on S^5 in the $AdS \times S^5$ space-time and contains fundamental strings as U(1) flux to form a baryon vertex. This configuration is regarded as a $D5 - \bar{D}5$ bound state, and we propose this as a baryonium state. We could also show their stability.

1   String Model

Quark confinement is well pictured by colored string confining quarks. The string has "orientation" because, when the string is cut by pair creation of quarks, the sequence of q and $\bar{q}$ is unique. When we define the orientation by the direction toward a confined quark, there should exist in the baryon a "singular point" from which the three strings emerge and where the three colors are neutralized. This point is called " junction" . In 1977 we proposed string junction model[1] (abbreviated as SJM), and investigated the nature of baryon and baryonium shown in Fig.1. The reason why they are so difficult to be observed was attributed to their complex structure, in particular, to the nature of junction.
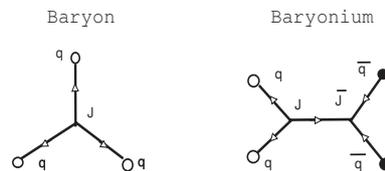

Figure 1: Baryon and baryonium in the string-junction model.

We try to explain the baryon and baryonium states in the framework of AdS/QCD. @They are expressed by D5($\bar{D}5$) brane in a 10D supergravity bavkground which is dual to a confining gauge theory.

2   D5 brane in $AdS_5 \times S^5$ space

We derive baryon and baryonium states from the equations of motion by the action of D5-brane which is embedded in a supersymmetric 10d background of type IIB theory. The background

solution should be dual to confining gauge theory and we consider the following background,

$$ds_{10}^2 = e^{\Phi/2}\left(\frac{r^2}{R^2}\eta_{\mu\nu}dx^\mu dx^\nu + \frac{R^2}{r^2}dr^2 + R^2 d\Omega_5^2\right) . \tag{1}$$

The dilaton Φ and the axion χ are given as

$$e^\Phi = 1 + \frac{q}{r^4} , \quad \chi = -e^{-\Phi} + \chi_0 , \tag{2}$$

and with self-dual Ramond-Ramond field strength

$$G_{(5)} \equiv dC_{(4)} = 4R^4\left(\text{vol}(S^5)d\theta_1 \wedge \ldots \wedge d\theta_5 - \frac{r^3}{R^8}dt \wedge \ldots \wedge dx_3 \wedge dr\right). \tag{3}$$

The D5-brane action is thus written as by the Dirac-Born-Infeld (DBI) plus WZW term

$$S_{D5} = -T_5\int d^6\xi e^{-\Phi}\sqrt{-\det\left(g_{ab} + \tilde{F}_{ab}\right)} + T_5\int d^6\xi \tilde{A}_{(1)} \wedge \mathcal{G}_{(5)} , \tag{4}$$

$$g_{ab} \equiv \partial_a X^\mu \partial_b X^\nu G_{\mu\nu} , \qquad \mathcal{G}_{a_1\ldots a_5} \equiv \partial_{a_1}X^{\mu_1}\ldots\partial_{a_5}X^{\mu_5}G_{\mu_1\ldots\mu_5} .$$

where $\tilde{F}_{ab} = 2\pi\alpha' F_{ab}$ and $T_5 = 1/(g_s(2\pi)^5 l_s{}^6)$ is the brane tension. And $\mathcal{G}_{(5)}$ denotes the induced five form field strength.

2.1 Baryon(D5 brane)

The D5 brane is embedded in the world volume $\xi^a = (t, \theta, \theta = 2, \ldots\theta = 5)$. Under the some assumptions, we obtain an energy functional from the above action,

$$U = \frac{N}{3\pi^2\alpha'}\int ds\, e^{\Phi/2}\sqrt{r^2\dot\theta^2 + \dot r^2 + (r/R)^4\dot x^2}\,\sqrt{V_\nu(\theta)}, \tag{5}$$

$$V_\nu(\theta) = D(\nu, \theta)^2 + \sin^8\theta. \tag{6}$$

Then, we obtain the following canonical equations of motion,

$$\dot r = p_r , \quad \dot p_r = \frac{2}{r^5}p_x^2 R^4 + \frac{p_\theta^2}{r^3} + \frac{1}{2}\left(V_\nu(\theta)\right)\,e^\Phi\partial_r\Phi, \tag{7}$$

$$\dot\theta = \frac{p_\theta}{r^2} , \quad \dot p_\theta = -6\sin^4\theta\left(\pi\nu - \theta + \sin\theta\cos\theta\right)\,e^\Phi, \tag{8}$$

$$\dot x = \frac{R^4}{r^4}p_x, \quad \dot p_x = 0 \tag{9}$$

Baryon is given by the classical solution with the boundary conditions[2],
$r(\theta_c) = r_c, \quad r(\pi) = r_{max}, \quad r(0) = r_0, \quad x(\theta_c) = 0.$

3 Baryonium(D5-anti D5 brane)

Baryonium is obtained by the classical solution by the same equations as baryon with the different boundary conditions,
$\theta'(0) = 0, \quad \theta(\pm x_c) = \pm\pi.$ We obtain the baryonium solutions numerically and calculate their energies[3].

3.1 Stability

In ordr to consider the fluctuations, we back to the action of D5 brane (4), and expand it with respect to the fluctuations, $\delta r(t,\theta) = r - \bar{r}, \delta x(t,\theta) = x - \bar{x}$ and $\delta A_t(\theta,t) = A_t - \bar{A}_t$, up to their quadratic terms. Here $\bar{r}$, $\bar{A}_t(\theta)$ and $\bar{x}$ are the solutions of the equations of motion. The modified quadratic term is obtained as

$$
\begin{aligned}
\tilde{L}_{(2)} &= \tilde{A}_{(2)}\delta r^2 + \frac{B_{(0)}}{2}\left[\left(\frac{R^4}{r^2} + x'^2\right)\left(-\delta\dot{r}^2 + \left(\frac{r}{R}\right)^4\frac{1}{Q_{(0)}}\delta r'^2\right) + 2x'r'\delta\dot{x}\delta\dot{r}\right. \\
&\quad + \left(r^2 + r'^2\right)\left(-\delta\dot{x}^2 + \left(\frac{r}{R}\right)^4\frac{1}{Q_{(0)}}\delta x'^2\right) - \left(\frac{r}{R}\right)^4\frac{1}{Q_{(0)}}2x'r'\delta x'\delta r'\right] \\
&\quad + Q_{(1)}r'\delta r'\delta r + Q_{(2)}x'\delta x'\delta r
\end{aligned}
\tag{10}
$$

By assuming the following form for the fluctuations,

$$
\delta r(t,\theta) = e^{i\omega t}\phi_r(\theta), \quad \delta x(t,\theta) = e^{i\omega t}\phi_x(\theta),
\tag{11}
$$

we estimate the value of frequency ω by solving the equations and obtain the stable regions($\omega^2 > 0$) shown in Fig.2[4].
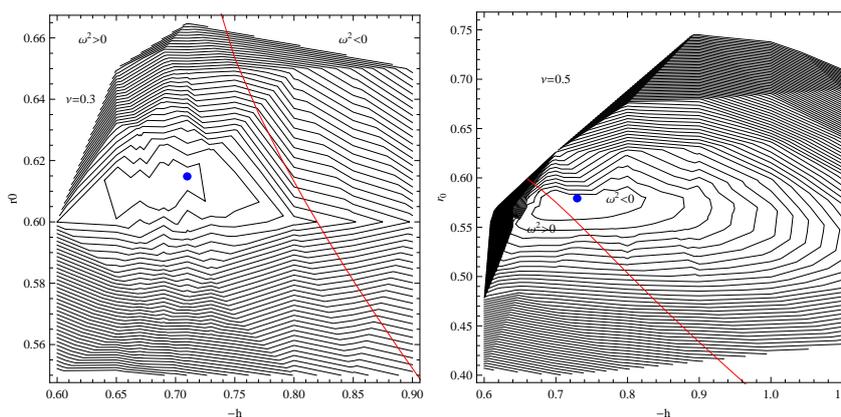

Figure 2: The equi-ω_2^2 curves in $(-h,r_0)$ plane. The equi-U curves in parameter plane. The lines express the border where the sign of ω^2 changes. And a blob denotes $U = U_{\min}$ point. The results for $\nu = 0.3$(left) and $\nu = 0.5$(right) are shown.

References

[1] M. Imachi,S. Otsuki and F. Toyoda, Prog.Theor.Phys.**57**,517 (1977).

[2] K. Ghoroku and M. Ishihara,Phys.Rev.D**77**,086003(2008) arXiv:hep-th/08060195.

[3] K. Ghoroku,M. Ishihara,A. Nakamura and F. Toyoda, JHEP**04**,041(2009) arXiv:hep-th/08091137.

[4] K. Ghoroku,M. Ishihara,A. Nakamura and F. Toyoda, arXiv:hep-th/09071170.

Estimation of Top Background to Supersymmetry Searches from Data

X. Zhuang[1*] on behalf of the ATLAS Collaboration
[1] Max-Planck-Instutut für Physik, München, Germany

The Standard Model process of $t\bar{t}$ production is one of the most important backgrounds in searches for Supersymmetry (SUSY) at the LHC. We describe some of the methods to estimate it with the first data of the ATLAS experiment. The performance of the methods has been evaluated with simulated data.

1 Introduction

High-energy jets, missing transverse energy (E_T^{miss}) and possibly leptons are the typical signature of R-parity conserved SUSY events at the LHC. The observation of deviations from the Standard Model may manifest the presence of SUSY. Due to the limited knowledge of Standard Model cross-sections, parton distribution functions, underlying event and parton showering at the LHC energy scale, as well as insufficient knowledge of the ATLAS detector itself, a reliable prediction of the Standard Model backgrounds should be derived mainly from the experimental data. In this note we present an overview of some of data-driven methods developed recently to estimate $t\bar{t}$ background in SUSY searches with zero, one or two isolated leptons, energetic jets and significant missing transverse energy. Due to lack high energy data, this note only deals with Monte Carlo simulations.

2 Data-driven methods

There are several kinds of data-driven methods in inclusive SUSY searches. One approach is the so called "ABCD" method, which is using a pair of uncorrelated variables with good signal versus background separation power and extrapolating the background from a background-dominated control region into the signal region. Another approach is called "Replacement Method". The example of this approach is the estimation of $Z \to \nu\nu$ background in the no-lepton mode from $Z \to \ell\ell$ ($\ell = e, \mu$) by replacement of leptons by neutrinos.

3 $t\bar{t} \to b\bar{b}l\nu l\nu$ in the two-lepton SUSY search mode

Monte Carlo studies show that $t\bar{t} \to b\bar{b}l\nu l\nu$ with both W bosons decaying leptonically is the dominant Standard Model background in the two-lepton SUSY search mode. The method of

---

* Current address: Ludwig-Maximilians-Universität, München, Germany
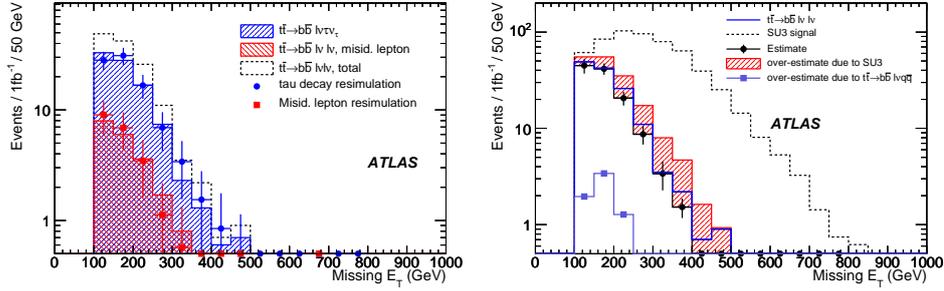
Figure 1: Left: $E_{\mathrm{T}}^{\mathrm{miss}}$ distribution of $t\bar{t} \to b\bar{b}l\nu l\nu$ events passing the one-lepton mode selection (open histogram) and fractions of events with a tau lepton (left hatching), a lost lepton (right hatching), compared to the estimate of these fractions from the data-like sample. Right: $E_{\mathrm{T}}^{\mathrm{miss}}$ distribution of $t\bar{t} \to b\bar{b}l\nu l\nu$ from MC prediction and from data-driven estimation with and without the presence of a SUSY signal with 1 fb^{-1} at 14 TeV (SU3 is a mSUGRA benchmark point with 650-700 GeV squark and gluino masses).

estimation of it is to select a control sample with pure $t\bar{t} \to b\bar{b}l\nu l\nu$ events by requiring at least one jet pair fulfilling the system of $t\bar{t} \to b\bar{b}l\nu l\nu$ kinematic equations.

$$
\begin{aligned}
m_W^2 &= (p_{l1} + p_{\nu 1})^2 \\
m_W^2 &= (p_{l2} + p_{\nu 2})^2 \\
m_t^2 &= (p_{l1} + p_{\nu 1} + p_{b1})^2 \\
m_t^2 &= (p_{l2} + p_{\nu 2} + p_{b2})^2 \\
E_x^{miss} &= p_{(\nu 1)x} + p_{(\nu 2)x} \\
E_y^{miss} &= p_{(\nu 1)y} + p_{(\nu 2)y}
\end{aligned}
\tag{1}
$$

Then "ABCD" method is applied with number of jet pairs satisfying the system of equation (1) and $E_{\mathrm{T}}^{\mathrm{miss}}$ as two uncorrelated variables.

4 $\quad t\bar{t} \to b\bar{b}l\nu l\nu$ in the one-lepton SUSY search mode

The dominant background in the one-lepton SUSY search mode is $t\bar{t}$ events with both W bosons decaying leptonically, where one lepton can be missing mainly because it is τ or not reconstructed electron or muon. The method of estimation of these two contributions is based on the "seed sample" with pure $t\bar{t} \to b\bar{b}l\nu l\nu$ extracted from data similar to the above section. The contribution from the events with W decaying into τ is estimated by replacing one of the lepton in the "seed sample" with a τ lepton and simulating the tau lepton decay. To estimate the contribution from the not reconstructed leptons, if the lepton is an electron, we replace the electron of the seed event by a jet reconstructed along with the electron, otherwise if the lepton is a muon, we remove the lepton from seed sample. Lepton identification efficiency is taken into account and all variables are recalculated. Fig. 1 (right) shows the $E_{\mathrm{T}}^{\mathrm{miss}}$ distribution of $t\bar{t}$ background compared to the data-driven estimates. The statistical (systematic) uncertainty of the method is estimated to be 12% (21%) for an integrated luminosity of 1 fb^{-1} [1].
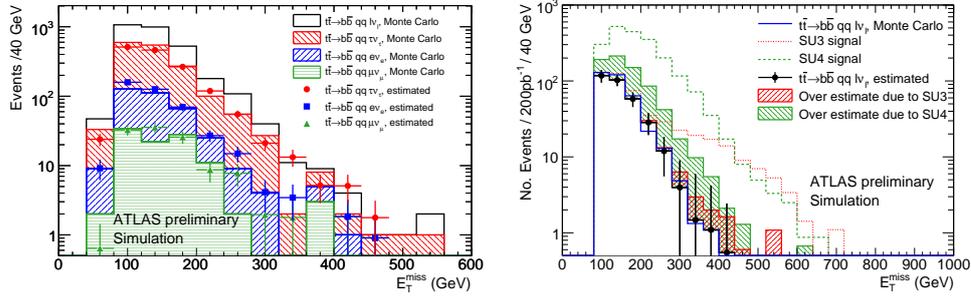
Figure 2: Left: $E_{\mathrm{T}}^{\mathrm{miss}}$ distribution of $t\bar{t} \to b\bar{b}l\nu q\bar{q}$ events (open histogram) and fractions of events with a tau lepton (left hatching), a lost electron (right hatching) and a lost muon (horizontal hatching), compared to the estimate of these fractions from the data-like sample. Right: $E_{\mathrm{T}}^{\mathrm{miss}}$ distribution of $t\bar{t} \to b\bar{b}l\nu q\bar{q}$ from MC prediction and from data-driven estimate with and without the presence of a SUSY signal with 200 pb^{-1} at 10 TeV (SU4 is a mSUGRA benchmark point with 400 GeV squark and gluino masses).

5 $t\bar{t} \to b\bar{b}l\nu q\bar{q}$ in the no-lepton SUSY search mode

Monte Carlo simulations show that the $t\bar{t} \to b\bar{b}l\nu q\bar{q}$ channel gives an important contribution to the Standard Model background in the no-lepton mode, where the lepton can be missing due to the lepton being a tau lepton or a non-identified electron or muon. The method of estimation of these two contributions is based on the "seed sample" enriched by the $t\bar{t} \to b\bar{b}l\nu q\bar{q}$ events extracted from the data. The replacement procedure is very similar to the above section. Fig. 2 (right) shows the $E_{\mathrm{T}}^{\mathrm{miss}}$ distribution of $t\bar{t} \to b\bar{b}l\nu q\bar{q}$ background compared to the data-driven estimates. The statistical (systematic) uncertainty of the method is estimated to be 8% (36%) for an integrated luminosity of 200 pb^{-1} [2].

6 Conclusion

Several complementary methods of background estimation are an important ingredient of SUSY discovery. Data-driven methods for top background estimation in the no, one and two-lepton SUSY search modes have been developed and tested with the Monte Carlo simulation.

References

[1] G. Akimoto *et al.*, *Expected Performance of the ATLAS Experiment - Detector, Trigger and Physics*, CERN-OPEN-2008-020, 1525-1561 (2009).

[2] Data-Driven Determination of $t\bar{t}$ Background to Supersymmetry Searches in ATLAS, ATLAS Public Note, ATL-PHYS-PUB-2009-083 (2009)

Top Quark Pair Production Cross Section Measurement at LHC with ATLAS

Alexander Doxiadis on behalf of the ATLAS Collaboration

Nikhef, Science Park 105, 1098 XG Amsterdam, the Netherlands

Several approaches for measuring the top quark pair production cross section with the ATLAS detector, designed for the early data taking period and therefore quite simple, are presented here, using decays with one or two leptons (electrons and muons) in the final state. Both in the single lepton and the dilepton channels the measurement is performed without identifying jets originated from a b-quark. The study aims to establish a top signal at the LHC.

1 Introduction

At the LHC, top quark pairs ($t\bar{t}$) will be produced mainly via gluon fusion ($\sim$87%). The cross section for $t\bar{t}$ production has been calculated at an approximate next-to-NLO (NNLO) with next-to-NLL (NNLL) resummation for $\sqrt{s}$=10 TeV, m_{top}=172.5 GeV and using the CTEQ6.5 PDF's [1]: $\sigma_{pp\to t\bar{t}}^{NNLOapprox} = 401.6$ $^{+3.6\%}_{-4.3\%}$ (scale) $^{+4.6\%}_{-4.5\%}$ (PDF) pb. Only decay channels of the $t\bar{t}$-pair that produce at least one electron or muon have been investigated. Presented here are commissioning analyses for $\sqrt{s}$=10 TeV and an integrated luminosity of 200 pb^{-1} that do not make use of b-tagging [2, 3].

2 Single Lepton Channel

2.1 Cut and Count method and fit method

The baseline analysis in the semi-leptonic channel consists of two complementary methods: the cut and count method and the fit method. Both methods analyze events that pass the following selection criteria: a single high-p_T lepton trigger, one isolated high-p_T lepton (e, μ) with $p_T > 20$ GeV, $\not{E}_T > 20$ GeV, four jets with $p_T > 20$ GeV of which three jets with $p_T > 40$ GeV. The hadronic top mass is then reconstructed by taking the invariant mass of the three jet combination, M_{jjj}, with the highest vector-summed p_T. At least one di-jet combination is required to be compatible with the W-boson mass: $|M_{jj} - M_W| < 10$ GeV.

In the cut and count method the cross section is calculated by counting the selected events in the three-jet invariant mass (M_{jjj}) plot, subtracting the expected number of background events and dividing by the expected efficiency and luminosity. In Figure 1 (left) the expected distribution of the three-jet invariant mass is shown. The main background for this analysis is

W+jets which can be determined from data. The largest systematic uncertainty, $\sim 10\%$, comes from the uncertainty in the jet energy scale (JES).

In the fit method, the M_{jjj} distribution is modeled by a Gaussian on top of a Chebychev polynomial. In Figure 1 (right) the likelihood fit of the three-jet invariant mass in the muon channel is shown. The cross section is then the number of events under the peak divided by the efficiency and the luminosity. The largest expected uncertainty, $\sim 13\%$, comes from the uncertainty in the amount of initial and final state radiation (ISR and FSR).
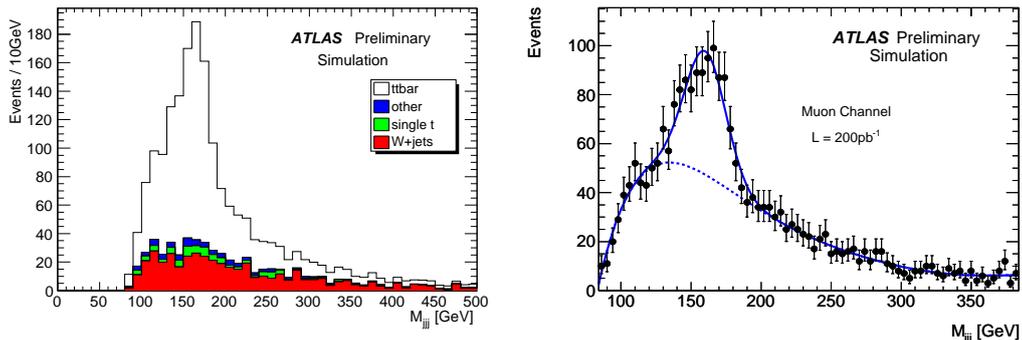

Figure 1: Left: expected distribution of the three-jet invariant mass in the electron channel after the standard selection and the M_W-cut, normalized to 200 pb^{-1}. Right: the likelihood fit in the three-jet invariant mass in the muon channel. The statistics correspond to an integrated luminosity of 200 pb^{-1}.

2.2 Variant analysis

The variant analysis does not rely on the $\not{E}_T$-variable. The selection requires: single high-p_T lepton trigger, one isolated central lepton (e, μ) with $p_T(e) > 40$ GeV or $p_T(\mu) > 30$ GeV, four jets with $p_T > 20$ GeV of which three jets with $p_T > 40$ GeV and HT2 > 160 GeV (the scalar sum of the p_T of the lepton, 2nd, 3rd and 4th jet). The cross section is determined by either a cut and count analysis or a template method. In the template method three templates are used to fit the data in M_{jjj}: $\mathcal{D}_{data} = A \times \mathcal{D}_{t\bar{t}} + B \times \mathcal{D}_{W,QCD} + C \times \mathcal{D}_{other}$, where $\mathcal{D}_{W,QCD}$ is the weighted sum of W+jets and QCD and $\mathcal{D}_{other}$ includes single top and Z+jets. The largest systematic uncertainty, $\sim 12\%$, comes from the uncertainty in the JES.

The expected uncertainties on the cross section for the muon channel (electron results are similar) are:

Cut&Count	3 (stat)	$^{+12}_{-15}$ (syst)	± 22 (lumi) %
Likelihood fit	15 (stat)	$^{+6}_{-15}$ (syst)	± 20 (lumi) %
Variant Cut&Count	3 (stat)	$^{+20}_{-20}$ (syst)	± 23 (lumi) %
Variant Template	6 (stat)	$^{+9}_{-15}$ (syst)	± 20 (lumi) %

3 Dilepton Channel

The following cuts are used: a single high-p_T lepton trigger, two oppositely charged isolated leptons (e, μ) with $p_T > 20$ GeV, $\not{E}_T > 35$ GeV ($\not{E}_T > 20$ GeV in the $e\mu$ channel) and two jets with $p_T > 20$ GeV. A Z-mass veto is used in the ee and $\mu\mu$ channels: $|M_{l^+l^-} - M_Z| > 5$ GeV. Any remaining backgrounds after the selection cuts will be estimated using data-driven methods. After selection the largest background is Z+jets ($\mu\mu$) and fake leptons from jets ($ee, e\mu$).

The method to extract the cross section is a cut and count method, where the result is given by a maximum likelihood estimate. All uncertainties are combined through a likelihood function for each channel. These are fitted and the final sensitivity is obtained from a profile likelihood ratio. In Figure 2 the log-likelihood curves for the ee channel is shown.

For the ee and $e\mu$ channels the largest expected uncertainty, $\sim 6 - 10\%$, is coming from the uncertainty in the fake rate. In the $\mu\mu$ channel uncertainty in the muon efficiency and the signal genera-


Figure 2: The log-likelihood curves for the ee channel. The solid dark curve is the log of the profile likelihood ratio - $\log\lambda(\sigma_{Sig})$, which includes all sources of systematics. The dotted light curve is the log of the likelihood ratio - $\log r(\sigma_{Sig})$, which was derived including only statistical uncertainties.

tor gives the largest expected uncertainty, $\sim 5\%$ each. The expected uncertainties on the cross section are:

ee channel	8 (stat)	$^{+14}_{-13}$ (syst)	$^{+26}_{-17}$ (lumi) %
$\mu\mu$ channel	6 (stat)	$^{+10}_{-9}$ (syst)	$^{+26}_{-17}$ (lumi) %
eμ channel	4 (stat)	$^{+10}_{-9}$ (syst)	$^{+26}_{-17}$ (lumi) %
combined	3 (stat)	$^{+10}_{-9}$ (syst)	$^{+26}_{-17}$ (lumi) %

4   Conclusions

It has been shown that with a luminosity of 200 pb^{-1} it is possible to measure the top quark pair production cross section with complementary analyses, both in the single lepton and dilepton channels, while being conservative in the evaluation of the systematic uncertainties assuming a detector not working yet at its best. Understanding top quark production is a stepping stone towards understanding the ATLAS detector, the Standard Model and finally new physics.

References

[1] Sven Moch and Peter Uwer. Theoretical status and prospects for top-quark pair production at hadron colliders. *Phys. Rev.*, D78:034003, 2008.

[2] The ATLAS collaboration. Prospects for the top pair production cross-section at $\sqrt{s}$=10 TeV in the single lepton channel in ATLAS. ATL-PHYS-PUB-2009-087.

[3] The ATLAS collaboration. Prospects for measuring top pair production in the dilepton channel with early ATLAS data at $\sqrt{s}$=10 TeV. ATL-PHYS-PUB-2009-086.

Top quark properties with ATLAS

Nuno Castro[1,2], on behalf of the ATLAS Collaboration

[1]Departamento de Física Teórica y del Cosmos, Universidad de Granada, 18071 Granada, Spain
[2]LIP, Departamento de Física, Universidade de Coimbra, 3004-516 Coimbra, Portugal

The top quark is unique in the Standard Model due to its large mass, possible role in electroweak symmetry breaking and rapid decay without forming bound states. Precise measurements of its properties offer both sensitive tests of the Standard Model and possible pathways of discovering new physics, and are an important and challenging part of the ATLAS physics program. The prospects, evaluated from Monte Carlo simulations, for precise measurements of the top quark mass, $t\bar{t}$ spin correlations, W polarization in top quark decays, anomalous Wtb couplings, as well as the expected sensitivity for rare top quark decays through flavour changing neutral currents and for $t\bar{t}$ resonances will be described for a centre-of mass energy of 14 TeV and an integrated luminosity of 1 fb^{-1}.

1 Introduction

Due to its unprecedented centre-of-mass energy and luminosity, the Large Hadron Collider (LHC) will be a top quark factory, opening a new era of precision measurements. Within the Standard Model (SM) the top quark has spin $1/2$, is the weak isospin partner of the b-quark and has charge $+2/3$. Although theory cannot predict the top quark mass, it was measured by the Tevatron experiments: $m_t = 173.1 \pm 1.3$ GeV [2]. The $t\bar{t}$ production cross-section is known from theory to next-to-leading order (NLO) in α_{s}, including next-to-leading logarithmic (NLL) contributions from soft gluon re-summation, and amounts to 833 ± 100 pb [3] for $m_t = 175$ GeV. This result is also supported by more recent calculations with lower theoretical uncertainties [4]. Due to a Cabibbo-Kobayashi-Maskawa matrix element V_{tb} close to one, the top quark decays dominantly to a b-quark and a W boson. The W longitudinal and right-handed helicity fractions in $t \rightarrow bW$ decays were measured by CDF and D0 experiments: $F_0 = 0.88 \pm 0.13$, $F_{\mathrm{R}} = -0.15 \pm 0.09$ and $F_0 = 0.49 \pm 0.14$, $F_{\mathrm{R}} = 0.11 \pm 0.08$ [5]. The on-shell decay width is $\Gamma(t \rightarrow bW)/|V_{tb}|^2 \sim 1.42$ GeV for $m_t = 175$ GeV, with a theoretical error below 1% [3]. The large top quark width translates into a short lifetime $\tau_t = 1/\Gamma \sim 10^{-25}$ s, shorter than the typical hadronization time scale ($\sim 10^{-24}$ s). This implies that the top quark decays before hadronization can take place and its spin information is transferred to the decay products, allowing the study of $t\bar{t}$ spin correlations at production. Top quarks can be produced at the LHC via strong interactions in pairs ($t\bar{t}$ production) or singly through electroweak processes. In the present report, the $t\bar{t}$ production at LHC pp collisions at $\sqrt{s} = 14$ TeV is considered, assuming an integrated luminosity of $L = 1$ fb^{-1}. The ATLAS [6] sensitivity to the measurements of top quark mass, $t\bar{t}$ spin correlations, W polarization and Wtb coupling structure, as well as the search for top quark decays through flavour changing neutral currents (FCNC) and $t\bar{t}$ resonances [7, 8] will be discussed.

2   Top quark mass

The expected precision for the top quark mass measurement was evaluated considering semilep-tonic $t\bar{t} \to bW^+\bar{b}W^-$ events, in which one of the W bosons decays hadronically and the other one decays in the leptonic channel. This topology is characterized by a final state with one charged lepton, missing transverse energy and four jets, two of them being originated by a b-quark [7]. The mass of the W boson candidate which decayed hadronically (m_{jj}) is recon-structed using the two closest light jets. The b-jet closest to this W boson is used to reconstruct the top quark. Its mass is shown in Fig. 1a. The statistical uncertainty of the top quark mass will be overwhelmed by the systematic error with a few fb^{-1}, and it is dominated by the un-certainties on the jets energy scales. In particular the b-quark (light quark) jets contribute 0.7 (0.2) GeV to the mass measurement uncertainty per percent of energy scale miscalibration [7]. If jet energies are calibrated within 1 to 5%, a precision of the order of 1 to 3.5 GeV should be achievable.
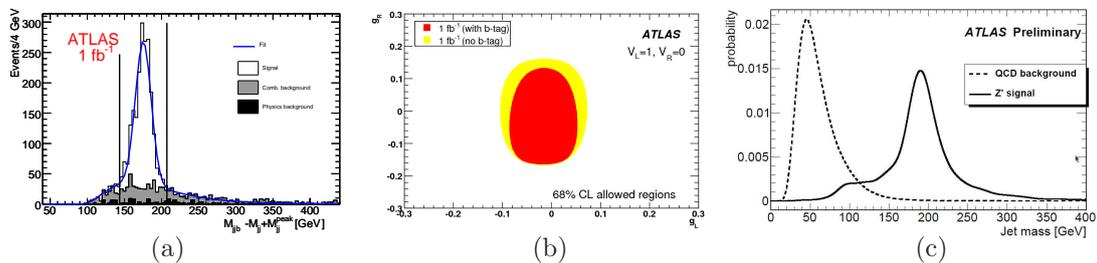

Figure 1: (a) reconstructed hadronic top quark mass; (b) two-dimensional 68% C.L. allowed regions for g_R versus g_L and (c) reconstructed mass of the jet from a boosted top quark for signal (plain line) and background (dashed line).

3 $t\bar{t}$ spin correlations

Although the top quarks in $t\bar{t}$ events are produced unpolarised at the tree level, the t and $\bar{t}$ spins are strongly correlated. Such correlations were studied by using semileptonic $t\bar{t}$ events with an electron or muon in the final state. Reconstructed angular distributions were used to estimate the expected absolute precision on the measurement of the spin correlation parameters A and A_D as 0.35 and 0.14, respectively. It should be noticed that these expectations were obtained by applying a cut on the $t\bar{t}$ mass distribution (required to be below 550 GeV) to enhance the spin correlations [7].

4 W polarization and Wtb anomalous couplings

Top quark pair production takes place through QCD interactions and it is, therefore, almost insensitive to the size and structure of the Wtb vertex. Nevertheless, the angular distributions of (anti)top quark decay products can give information about the structure of this vertex. The absolute uncertainty expected by ATLAS, for the measurements of the W boson longitudinal (F_0), left-handed (F_L) and right-handed (F_R) helicities is 0.045, 0.036 and 0.028, respectively.

The W boson polarization ratios ($\rho_\mathrm{R} = F_\mathrm{R}/F_0$ and $\rho_\mathrm{L} = F_\mathrm{L}/F_0$) together with the angular asymmetries (A_+ and A_-) were used to set limits on the anomalous couplings (g_R, g_L and V_R), using `TopFit` [9]. In Fig. 1b the expected two-dimensional 68% C.L. allowed region for g_R versus g_L is shown (assuming $V_\mathrm{R} = 0$ and $V_L = 1$).

5 Top quark rare decays through FCNC

Top quark rare decays through FCNC processes ($t \to qZ, q\gamma, qg$) are highly suppressed in the Standard Model [10]. These processes were studied by searching for $t\bar{t}$ events in which one of the top quarks decays to bW and the other one decays through FCNC. Expected limits on the branching ratios were set at 95% CL (in the absence of signal) to 6.8×10^{-4}, 2.8×10^{-3} and 1.2×10^{-2} for the $t \to q\gamma$, $t \to qZ$ and $t \to qg$ channels, respectively [7].

6 $t\bar{t}$ resonances

The discovery potential for the $t\bar{t}$ resonances decaying in the semileptonic channel, was studied as a function of the resonance mass. Using an analysis similar to the one used for the measurement of the top quark mass, ATLAS may be able to discover a $t\bar{t}$ resonance with $m_{t\bar{t}} = 700$ GeV if the product of the production cross-section and the branching ratio to a $t\bar{t}$ semileptonic final state is higher than 11 pb [7]. For higher $t\bar{t}$ masses, the t-quarks have higher boosts and the reconstruction efficiency drops, once the hadronic top quark decay products merge and are, therefore, reconstructed as a single jet (see Fig. 1c). Furthermore, the semileptonic top quark decays are no longer identified by the presence of an isolated lepton. A specific reconstruction was developed for this case [8] and a 95% C.L. expected limit was set at 550 (160) fb on the signal production cross-section times branching ratio to $t\bar{t}$ for a resonance mass of 2 (3) TeV.

Acknowledgements

References

[1] The ALEPH, CDF, D0, DELPHI, L3, OPAL and SLD Collaborations and LEP Electroweak Working Group, arXiv:0911.2604 [hep-ex] (2009).

[2] The Tevatron Electroweak Working Group, arXiv:0903.2503 [hep-ex] (2009).

[3] M. Beneke *et al.*, arXiv:hep-ph/0003033 (2000); R. Bonciani *et al.*, Nucl. Phys. B **529** 424 (1998).

[4] M. Cacciari *et al.*, JHEP **09** 127 (2008); S. Moch and P. Uwer, Nucl. Phys. Proc. Suppl. **183** 75 (2008).

[5] The CDF Collaboration, CDF note 10004 (2009); The D0 Collaboration, D0 Note 5722-CONF (2008).

[6] The ATLAS Collaboration, G. Aad *et al.*, JINST **3** S08003 (2008).

[7] The ATLAS Collaboration, G. Aad *et al.*, arXiv:0901.0512 (2009).

[8] The ATLAS Collaboration, ATL-PHYS-PUB-2009-081 (2009).

[9] J.A. Aguilar-Saavedra *et al.*, Eur. Phys. J. **C50** 519 (2007); J.A. Aguilar-Saavedra, Nucl. Phys. B **821** 215 (2009).

[10] J.A. Aguilar-Saavedra, Acta Phys. Polon. **B35** 2695 (2005).

Time Projection Chamber with triple GEM and highly granulated Pixel Readout

Jochen Kaminski[1], Christoph Brezina[1], Klaus Desch[1], Martin Killenberg[1], Frederik Klöckner[1], Thorsten Krautscheid[1], Martin Schultens[1]

[1]Universität Bonn, Nußallee 12, 53115 Bonn, Germany

A new readout consisting of a gas amplification stage made of three Gas Electron Multipliers (GEMs) and a highly granulated active anode was installed in a Time Projection Chamber (TPC). This setup was tested in various environments and an excellent spatial resolution close to the diffusion limit could be observed.

1 Introduction

Micro pattern gas amplification stages such as Gas Electron Multipliers (GEMs) [1] have many interesting features: high granularity, intrinsically suppressed ion back flow, almost no distortions due to $E \times B$ effects and a complete decoupling of the gas amplification and readout geometry. These devices improve the performance of Time Projection Chambers (TPCs) because they allow ungated operations and improve the spatial resolution. To fully exploit the potential of this combination the pad size in the readout plane has to be optimized according to the structure size of the gas amplification stage. The Timepix [2] is a suitable readout chip for the use in Micro Pattern Gas Detectors (MPGDs) by providing metalized pads to pick up the charge. The pitch of these pads is 55 µm and therefore of similar structure size as the holes of standard CERN GEMs having a pitch of 140 µm between holes and hole sizes of 60 to 70 µm. Each pad is connected to an on-chip readout chain, containing a preamplifier, discriminator and 14-bit counter. The pixel electronics can be operated in different modes. Some of these modes allow the measurement of the arrival time of the charge collected on the pad, or the "time-over-threshold" related to the amount of deposited charge.

2 Experimental Setup

To test the new readout structure with signals originating over a wide range of drift distances, we have designed and constructed a small and highly flexible TPC prototype with a cylindrical drift volume (maximum drift distance of 26 cm, inner diameter of 23 cm - see Fig. 1). The readout has been equipped with a stack of three GEMs with transfer gaps of 1 mm in between. The Timepix chip has been placed 1 mm below the last GEM. The pixels were operated in a checkerboard pattern of time and charge measurement. In Fig. 2 four charge depositions are shown and the two different modes are clearly visible: The pixels measuring the arrival time give the same value shown in black, while the pixels measuring the Gaussian charge distribution

Figure 1: Detector set up in the cosmic ray test stand.
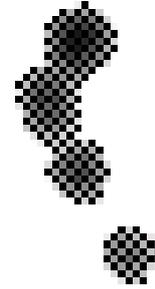
Figure 2: Charge depositions on the Timepix chip.

vary in shades of gray.

The detector was placed in a cosmic ray test stand at the Bonn lab. Here, two scintillators are used to trigger on cosmic rays and about 130,000 tracks have been recorded.

3 Results

The data was analyzed with MarlinTPC [3], a modular and flexible analysis tool. New algorithms had to be introduced to cope with the particular challenges of the readout method. For example great care was taken to split overlapping charge depositions and reconstruct the tracks from the single hits.

In Figs. 3 to 5 some results are shown that were obtained while using a gas mixture of He:CO_2 70:30. The average value of the size and the charge of a charge deposition are constant for drift distances larger than about 7 cm (see Figs. 3 and 4). This leads to the conclusion that charge depositions at these drift distances originate from single electrons in the
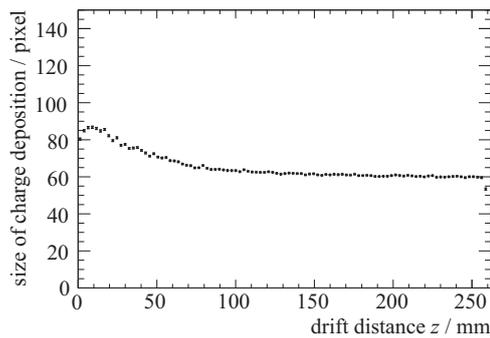

Figure 3: Number of pixels hit per charge deposition.
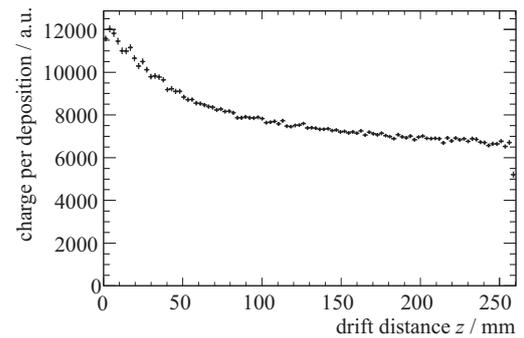
Figure 4: Charge per charge deposition in dependence on the drift distance.

drift region. For short drift distances the diffusion is insufficient to separate all electrons in the drift region. Therefore, an increasing number of charge depositions cannot be separated by the analysis algorithms leading to an increase in reconstructed charge and size.

The transverse spatial resolution is given in Fig. 5. For easier comparison the diffusion limit of single electrons is shown with a dashed line. The diffusion coefficient has been determined with the help of Magboltz 7.1 [4]. The fit function shown in a dark solid line is given by:

$$\sigma = \sqrt{\sigma_0^2 + \frac{D_t^2}{n_{ele}} z},$$

Figure 5: Transverse spatial resolution of the test detector.

where D_t is the transverse diffusion coefficient, σ_0 the intrinsic detector resolution and $n_{ele} = 1 + a\, e^{bz}$ takes into account the varying number of electrons per reconstructed charge deposition.

The result shows little deviation from the diffusion limit. For short drift distances the spatial resolution is below the diffusion limit due to $n_{ele} > 1$. In separate measurements quasi no dependence on the track inclination was observed and full functionality and excellent behavior in high magnetic fields with B up to 4 T could be demonstrated (see [5]).

4   Summary

For the first time the combination of a triple GEM and a Timepix chip was tested with signals drifting up to 26 cm. We have strong evidence that charge depositions seen on the chip originate from single electrons in the drift volume. The transverse spatial resolution of these charge depositions follows the diffusion limit with a small constant offset.

5   Acknowledgments

References

[1] F. Sauli, Nucl. Instrum. Meth. **A386** 531 (1997).

[2] X. Llopart *et al.*, Nucl. Instrum. Meth. **A581** 485 (2007).

[3] J. Abernathy *et al.*, *MarlinTPC, A Common Software Framework for TPC Development*, IEEE NSS MIC, Dresden, Germany (2008).

[4] S. F. Biagi, Nucl. Instrum. Meth. **A421** 234 (1999).

[5] C. Brezina, JINST **4** P11015 (2009).

Very Forward Detectors for ILC and LHC

*Sergej Schuwalow (on behalf of FCAL collaboration)*

DESY, Platanenallee 6, 15738 Zeuthen, Germany

Radiation hard solid state sensors are necessary to instrument the very forward region of LHC and future ILC detectors. We report the results of recent studies of GaAs, Diamond and Sapphire sensors and their applications for Beam Condition Monitor at LHC CMS Detector and Beam Calorimeter at ILD detector for ILC.

1 Radiation Hard Sensors

For the very forward region of ILC detectors special calorimeters are needed. They will be hit by a large fraction of e^+e^- pairs originating from beamstrahlung. Sensors have to withstand a very high radiation level up to several MGy per year. Similar conditions we face at LHC for detectors near the beam pipe. Radiation hardness of several sensor material candidates is tested experimentally and reported below.

Single crystal diamond sensors are grown using Chemical Vapor Deposition method by Diamond Detector Ltd company. They show very low leakage current (at pA level) and very good radiation hardness. Initial charge collection efficiency is close to 100%, after 10 MGy dose sensor still has above 10% of initial CCE (see Fig. 1).
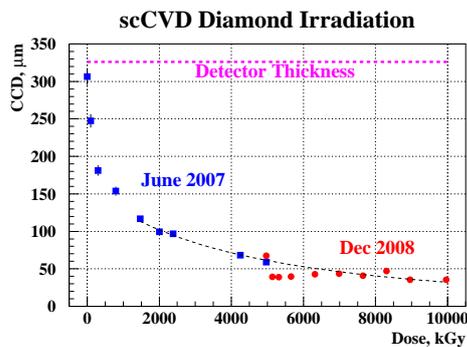

Figure 1: (Color online) Charge Collection Distance of single crystal Diamond sensor as a function of the absorbed dose. Two different irradiation periods are shown by different colors
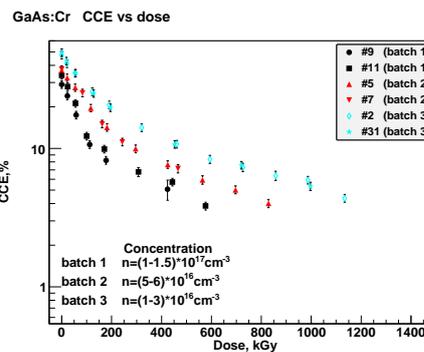
Figure 2: (Color online) Charge Collection Efficiency of GaAs sensor as a function of the absorbed dose for different Cr dopant concentration.

Large area GaAs sensors are obtained from Siberian Institute of Technology. They are produced using the liquid encapsulated Czochralski method and are doped with tin and tellur as shallow donors and chromium as a deep acceptor. Three batches with different concentration of the dopants are irradiated up to 1.2 MGy and the charge collection efficiency, CCE, is measured as a function of the absorbed dose (see Fig. 2). The sensors with a lower acceptor concentration show a larger initial charge collection efficiency and better radiation hardness.

**Sapphire Crb2 and Crb6 samples**
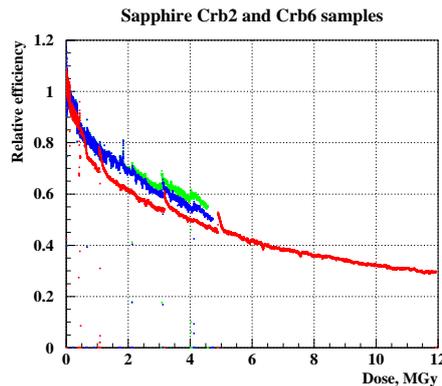
Figure 3: (Color online) Relative charge collection efficiency of single crystal Sapphire sensor as a function of the absorbed dose (see text).

Optical grade single crystal sapphire sensors are created using the Czochralski process. They show initially low (about 2%) CCE, but extremely high radiation tolerance (see Fig. 3). Since the signal from the detector is too small to observe it directly, CCE was extracted from the detector current measurements during irradiation. Crystals of better purity have to be tested.

2 Application examples at LHC and ILC

In the CMS detector at LHC a series of beam condition monitors [1] were installed and are in operation for measuring radiation doses and preventing possible damages to the detector in case of beam losses. The Fast Beam Condition Monitor, BCM1F, consists of two modules, with 4 scCVD diamond sensors each, located 1.8 m away from the IP, on both sides, and was designed to give a fast response measuring beam-halo on a bunch-by-bunch basis. Figure 4 shows a photo of one of the installed BCM1F stations and a photo of single module prototype.

Low polar angle Beam Calorimeter [2] for the detector at future Linear Collider is designed as a compact highly segmented sampling calorimeter with tungsten absorber (see Fig. 5). Thin sensor planes between absorber plates should provide a fast response and operate in the harsh radiation environment.

References

[1] A. Bell *et al.*, NIM **A614** 433 (2010).

[2] H. Abramowicz *et al.*, IEEE Trans.Nucl.Sci **51** (2004) 2983.
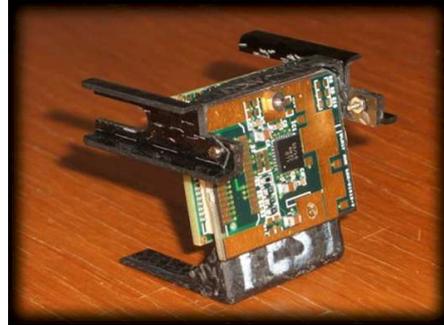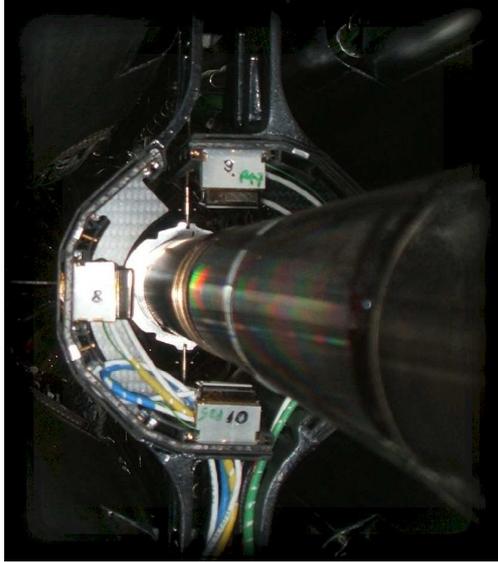
Figure 4: (Color online) Left: Photo of the Beam Condition Monitor (BCM1F) equipped with diamond sensors. Right: a single BCM1F module, containing preamplifier, laser optical link driver and power cirquits.
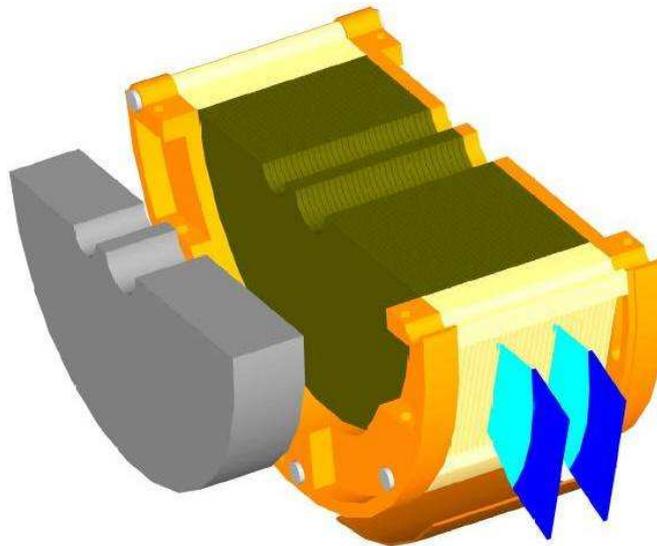

Figure 5: (Color online) Beam Calorimeter for the ILD detector is located at 3.5 m distance from the IP. Graphite block in front of BeamCal protects tracking detectors from backsplash particles.

Beam Test Results with Highly Granular Hadron Calorimeters for the ILC

F. Simon[1,2], for the CALICE Collaboration

[1]Max-Planck-Institut für Physik, München, Germany
[2]Excellence Cluster Universe, Garching, Germany

To evaluate different technologies for calorimetry at the International Linear Collider, the CALICE collaboration has constructed a highly granular analog hadron calorimeter with small scintillator cells, individually read out by silicon photomultipliers. This device has been extensively tested in particle beams. A digital hadron calorimeter based on RPC read-out is currently under construction, with first prototype beam test results already available. The high granularity allows detailed investigations of the substructure of hadronic showers, and can also be exploited for the development of sophisticated reconstruction algorithms.

1 Introduction

The physics program at a future high energy e^+e^- collider demands excellent reconstruction of multi-jet final states, originating for example from the production and decay of new heavy particles or the hadronic decays of gauge bosons. A promising technique to achieve the necessary jet energy resolution are Particle Flow Algorithms (PFA) [1, 2], which are based on the reconstruction of individual particles in jets. This approach requires excellent separation of particle showers, and thus extreme granularity, in the calorimeters. Two conceptually different options for PFA-optimized hadron calorimetry are being investigated by the CALICE collaboration, analog and digital sampling calorimetry. The analog option uses small scintillator tiles individually read out with silicon photomultipliers, while the digital option uses gas detectors with small readout pads, which are read out in digital (one bit per channel) or in semi-digital (two or three bits per channel, several amplitude thresholds) mode. Several gas detector technologies are under investigation, such as RPCs and the micro-pattern technologies Micromegas and GEM.

A 1 m^3 physics prototype of a scintillator-steel analog hadron calorimeter, with 7608 scintillator cells read out by SiPMs, ranging from 3×3 cm^2 to 12×12 cm^2 in size, has been tested extensively in particle beams at DESY, CERN and at Fermilab [3]. The imaging capabilities of this calorimeter provide detailed three dimensional information of the hadronic shower activity in the detector. The data recorded with the analog HCAL physics prototype has been used already for a wide range of detailed studies of hadronic showers, with an emphasis on the confrontation of data and simulations using a variety of different hadronic shower models. A digital hadron calorimeter based on RPC read-out is currently under construction and will be tested in the same absorber structure used for the analog HCAL. First test beam results from small prototypes are already available.

2   Selected results

The unprecedentedly granular information available on the topology of the hadronic showers allows the precise measurements of shower profiles, both longitudinally and laterally.

Particularly powerful for the comparison of longitudinal shower profiles with simulations is the possibility to directly identify the start point of the shower on an event by event basis. This allows to take the wide distribution of the depth of first interaction in the calorimeter out of the comparison, significantly improving the sensitivity of the profile studies to differences in the shower models. The position of the shower starting point is identified by increased activity extended over several detector cells, extracted from a specialized clustering algorithm.

Figure 1 shows the longitudinal shower profile for 10 GeV π^+, relative to the start of the shower, measured in the analog HCAL inclined by approximately 30° with respect to the beam axis. The inclination provides an increased depth of the detector, extending the range of the profile measurements. Also shown are simulations using several different physics lists in Geant4 [4]. In particular the theory driven model `QGSP_BERT`, favored by the LHC test beam campaigns, provides a satisfactory description of the observed profile, while other models show discrepancies in the energy density near the shower maximum and / or in the tails of the distribution. At higher beam energies, significantly increased discrepancies between data and all studied models have been observed, and are under further investigation.

The high granularity of the analog HCAL is also well suited for the use of software compensation algorithms to improve the hadronic energy resolution, by partially correcting for the difference in detector response to purely hadronic energy deposits and to electromagnetic subshowers. A classification of the different subcomponents can be achieved through the energy density in the shower, since electromagnetic showers tend to be denser than purely hadronic ones. In a first study, a weighting algorithm based on the local shower energy density, given by the amplitude in each individual cell, was developed [5]. Figure 2 shows the energy resolution for charged pions as a function of beam energy for the complete CALICE calorimeter setup (Silicon-Tungsten ECAL,
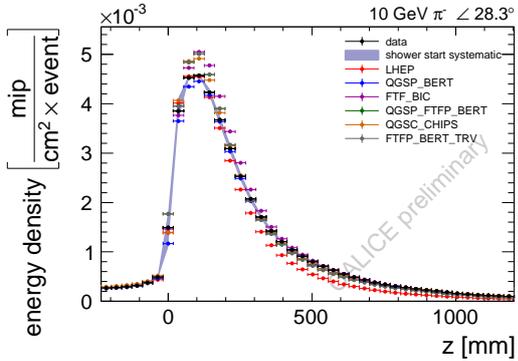
Figure 1: Longitudinal profile of hadronic showers of 10 GeV π^+, compared to various hadronic shower models.
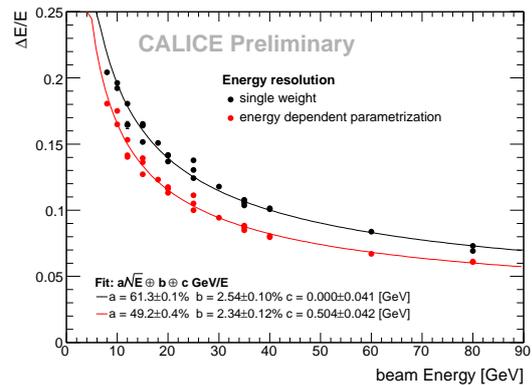

Figure 2: Energy resolution of the CALICE calorimeters for hadrons, with and without software compensation.

analog HCAL and tail catcher), both with and without the weighting algorithm. A 20% improvement in resolution was achieved with the software compensation, which also significantly improves the linearity of the detector response.

On the way to a full physics prototype for a digital HCAL, a small test detector consisting of 6 layers of 20×20 cm^2 RPCs with square 1 cm^2 readout pads, interleaved with 1.2 X_0 absorber plates consisting of 16 mm steel and 4 mm copper, has been tested with muons, electrons and hadrons at Fermilab. The total thickness of the prototype corresponds to 0.65 nuclear interaction lengths, limiting the studies possible with hadrons.

The electromagnetic data, compared to full detector simulations, demonstrate a good modeling of the detector in Geant4, shown by a satisfactory agreement of measurements and data [6]. Some discrepancies, in particular at higher energies in the region of the shower maximum, have been observed and are attributed to loss of efficiency in the RPCs due to high particle densities. Hadronic data has been analyzed in the energy range from 1 GeV to 16 GeV, and the number of observed hits has been compared to detector simulations. Reasonable agreement between data and simulations has been found [7], allowing the extrapolation of the performance of the small prototype to a full calorimeter. These studies demonstrate the potential of this new detector concept, which is now being prepared for experimental verification.

3   Outlook

The rich set of hadronic data taken with the physics prototype of a highly granular analog hadron calorimeter for future high energy colliders and the advanced data analysis produce now more and more refined results, demonstrating the capabilities for detailed tests of hadronic shower models as well as moving forward the development of sophisticated reconstruction algorithms. Further refinements of the data analysis and the simulation details promise to provide strong constraints for hadronic shower models within Geant4, and will help in their further development and validation. The first small-scale tests with an RPC based digital HCAL already demonstrated the potential of this new technique, which will be fully explored in the upcoming beam tests of a full physics prototype. This program will provide valuable additional data for the test of shower models, taking into account the insensitivity to neutrons of the used gas detectors, and will be crucial to identify the most promising technology for future experiments.

References

[1] J. C. Brient and H. Videau, "The Calorimetry at the Future e^+e^- Linear Collider", arXiv:hep-ex/0202004.

[2] V. L. Morgunov, "Calorimetry design with energy-flow concept (imaging detector for high-energy physics)", in 10th International Conference on Calorimetry in High Energy Physics (CALOR 2002), Pasadena, California, 25-30 Mar 2002.

[3] C. Adloff, et al. [CALICE Collaboration], "Construction and Commissioning of the CALICE Analog Hadron Calorimeter Prototype", submitted to JINST.

[4] J. Apostolakis, et al., "Geant4 Physics Lists for HEP", in 2008 IEEE Nuclear Science Symposium Conference Record.

[5] F. Simon [CALICE Collaboration], "Energy Reconstruction of Hadron Showers in the CALICE Calorimeters," arXiv:0911.4575 [physics.ins-det].

[6] B. Bilki *et al.*, "Measurement of Positron Showers with a Digital Hadron Calorimeter," JINST **4**, P04006 (2009).

[7] B. Bilki *et al.*, "Hadron Showers in a Digital Hadron Calorimeter," JINST **4**, P10008 (2009).

Engineering Prototypes for the CALICE Hadron Calorimeters

Angela Lucaci-Timoce[1]

[1]DESY, Notketraße 85, 22607 Hamburg, Germany

The engineering prototypes of the hadron calorimeters proposed by the CALICE collaboration as a solution for the physics requirements of the International Linear Collider (ILC) are presented. Two different technologies are currently under study: an analog hadronic calorimeter, based on scintillating tiles that are read out by silicon photo-multipliers (SiPMs), and a digital hadronic calorimeter, using gaseous detectors.

1   Introduction

The International Linear Collider [1] is a planned electron-positron collider, that will reach energies of up to 1 GeV, and which will perform precision measurements complementary to the Large Hadron Collider program. The goal for the jet energy resolution at ILC is to cleanly separate W and Z decays. The most promising approach to achieve this is considered to be the particle flow algorithm (PFA), that requires the reconstruction of all visible particles in an event, and imposes stringent requirements on the granularity of the ILC calorimeters.

Below, the work of the CALICE collaboration [2] towards a realistic mechanical structure and calibration concept of the hadron calorimeter prototypes for the ILC is presented. The hadron calorimeter (HCAL) consists of 48 layers in a cylindrical structure with an inner radius o 2.0 m, and an outer radius of 3.1 m, respectively, surrounded by a magnet. Inside the HCAL, the electromagnetic calorimeter will be placed. The front-end electronics has to be highly integrated. In section 2, the mechanical integration and the calibration procedure of the Analogue Hadron Calorimeter (AHCAL) are presented. In section 3, the options for the digital hadron calorimeter are shortly described.

2   The Analogue Hadron Calorimeter

A possible analogue realization of the hadron calorimeter for the ILC is using 3×3 cm^2 scintillator tiles, which are readout by novel silicon photomultipliers. The circular structure of the AHCAL will be divided into 16 sectors, one of which is shown in Fig. 1, with one detector layer. Each layer contains the scintillating tiles, the front-end electronics which is integrated into the absorber structure, and a 2 cm thick stainless stell absorber plate, such that the typical size of a sector's layer is 1×2.2 cm^2.

All electronics connections and interfaces can be placed at the two end-faces, which are thus easy to access for maintenance and service lines. In order to keep the single modules at reasonable size, the detector's electronics is divided into basic units (HCAL base unit: HBU), each with a typical size of 36×36 cm^2, integrating 144 tiles, together with the corresponding
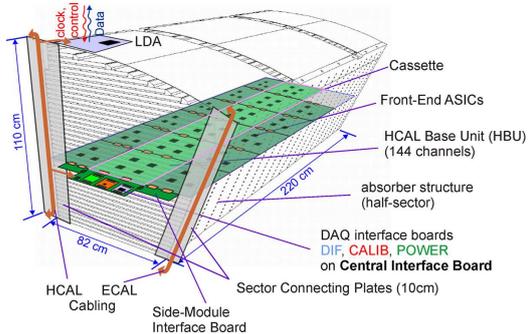
Figure 1: Structure of 1/16th part of the AHCAL's barrel, with only one detector layer shown. The electronics is integrated into the absorber structure.
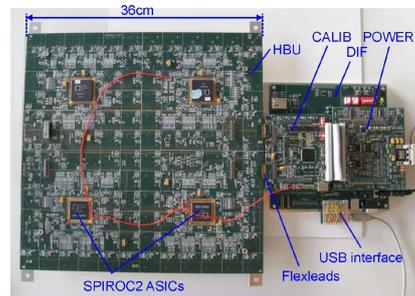
Figure 2: Top view of the HCAL Base Unit (left) connected to the data acquisitions modules (right). The scintillation tiles with SiPMs are assembled on the HBU back-side.

SiPMs, front-end electronics and the light calibration system. The analogue signals of the SiPMs are read out by 4 front-end ASICs of type SPIROC, developed by LAL/Omega.

The first prototype module with 144 detector channels connected to a preliminary data acquisition system has been realised within the EUDET framework (see Fig. 2). The interface to a Labview user PC is done via an USB module. The first results (see Fig. 3) indicate that the full operation chain of the system (including data taking with internal or external trigger, data read out, light calibration and preliminary data acquisition) has been established. More details can be found in [3]. The SiPMs response varies strongly with temperature and voltage:

$$\frac{dG}{dT} = \frac{-1.7\,\%}{K} \quad \text{and} \quad \frac{dG}{dV} = \frac{2.5\,\%}{100\,\text{mV}}, \tag{1}$$

therefore a gain calibration and monitoring system is needed. The calibration system offers several functionalities: at low light, the SiPMs show single photon peaks, and the distance between the peaks is a measure for the SiPM gain; at high light, the SiPM shows saturation behaviour, and the SiPM response function can be checked. For the calibration system, two concepts are currently under investigation: the first one, using one LED per tile (integrated into the detector gap), and a second one, developed by ASCR Prague, with strong LEDs outside the detector, which distribute the light via cleaved fibers [4]. For the first concept, an LED testboard has been realized, with ultraviolet LEDs mounted up-side down, and is being investigated at the University of Wuppertal.

In order to test the mechanical stability, tolerances and deformations, a real size prototype of 1/16th of an HCAL barrel structure was build at DESY Hamburg (see Fig. 4). The module consists of stainless steel plates of 16 mm thickness, which are supported only by 5 mm thick side pannels. Flatness measurements of the steel plate indicated deviations up to 8 mm. After roller leveling of the plate, the deviation reduced to less than 1 mm.

3 Digital Hadron Calorimeter

The high granularity of the ILC calorimeters required in the particle flow approach implies readout of a high number of channels, which is in general impractical. Monte Carlo simulations
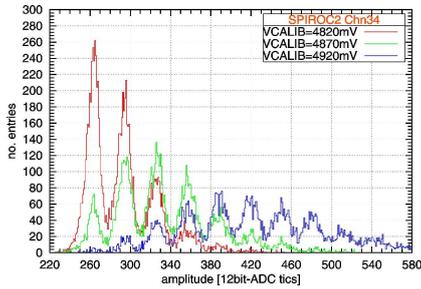
Figure 3: Single photon spectrum of a SiPM for three LED light intensities (VCALIB settings).

Figure 4: The vertical mechanical structure for the technical HCAL prototype.

have shown that it is possible to preserve the energy resolution of single hadronic particles using a simple discriminator with only one threshold. This lead to the idea of developing digital hadron calorimeters (DHCALs), with 1 bit per pad, and so-called semi-digital hadron calorimeters, with 2-3 bits per pad. The latter allows to distinguish between the simple case with one particle going through one pad of the detector, and the cases where several particles traverse the detector pad (important at high energies). The digital calorimeters are based on gaseous active layers with 1×1 cm^2 pad readout, and iron as absorber material. The CALICE DHCAL group investigates three different active media: rezistive plate chambers (RPCs) [5], gas electron multipliers (GEMs) and micromegas. In addition, two readout schemes, one based on the DCAL chip (developed by Argonne and Fermilab), and another one based on the HARDROC chip (developed by the French groups of LAL, LLR and IPNL) are developed.

4   Conclusions

The mechanical and electrical integrations of the hadron calorimeters for the ILC, proposed by the CALICE collaboration, have been presented. For the tile hadron calorimeter, mechanical tests of a real size module have been done. The various efforts provided valuable experience towards building an optimal calorimeter for the ILC environment.

References

[1] http://www.linearcollider.org/cms/

[2] https://twiki.cern.ch/twiki/bin/view/CALICE/CaliceCollaboration

[3] P. Goettlicher, *First Results of the Engineering Prototype of the CALICE Tile Hadron Calorimeter*, proceedings of the 2009 IEEE NSS conference

[4] Ivo Polak, *Calibration System of CALICE AHCAL Detector*, ALCPG 2009, Albuquerque, 29th Sept-3rd Oct 2009

[5] B. Bilki et al., *Hadron Showers in a Digital Hadron Calorimeter*, JINST **4**, P10008 (2009) [arXiv:0908.4236 [physics.ins-det]].

Test Beam Performance of CALICE Electromagnetic Calorimeter Physics Prototypes

Daniel Jeans (for the CALICE collaboration)

Laboratoire Leprince-Ringuet - Ecole polytechnique, CNRS/IN2P3

The CALICE collaboration develops calorimeter technology for future linear collider detectors, in particular for the Particle Flow approach to jet energy measurement. Two Electromagnetic calorimeter prototypes have been constructed and tested in test beams. Both are sampling calorimeters with Tungsten absorbers, and differ in their choice of active materiel. One is based on Silicon detectors with readout pads of size $1 \times 1cm^2$, while the other is based on $1 \times 4.5cm^2$ scintillator strips individually read out by MPPC devices. This paper reports on their performance in test beams, presenting the linearity and resolution of their energy response.

1 Introduction

A Linear Collider is widely proposed as the next accelerator to study the high energy frontier of particle physics at the TeV scale. The final state of many interesting physics processes will consist of one or more massive bosons. A particular challenge is the identification of hadronic W and Z boson decays, which requires an improvement of jet energy resolution by at least a factor of two with respect to current detectors.

A promising technique to achieve this is the so-called "Particle Flow" approach [1], which relies on the fact that around 65% of a jet's energy is in charged particles, around 25% in photons, and the remaining 10% in neutral hadrons. Particle Flow requires the topological separation of individual particles' calorimeter energy deposits, which allows the tracking system to be used to measure the charged energy, and the calorimeters to measure the neutral components. This topological separation requires a very highly granular calorimeter.

These considerations have led to the design, construction and testing of two EM calorimeter prototypes, both studied within the CALICE collaboration. Both are sampling calorimeters using Tungsten absorber due to its small Moliere radius, short radiation length, and relatively long hadronic interaction length. The two designs differ in the choice of technology for the active layers. One is based on Silicon sensors segmented into $10 \times 10mm^2$ readout pads (SiECAL), while the other uses $10 \times 45mm^2$ strips of plastic scintillator, individually read out by MPPC devices (ScECAL).

The ECAL prototypes were tested in various particle beams at DESY, CERN and FNAL. The detectors were exposed to beams of muons (largely for calibration purposes), electrons and positrons, and charged pions and protons, in the momentum range 1–180 GeV/c.

2 Silicon-Tungsten EM calorimeter

The Silicon-Tungsten prototype [2] has active sensors made of 525 micron thick high resistivity Si, segmented into 10×10mm^2 PIN diodes, fully depleted by a 200V bias voltage. 6 sensors are glued onto a PCB which channels signals to the very front end electronics. Two such PCBs are mounted on either side of a carbon-fibre composite structure, which also incorporates a layer of Tungsten. These slabs are then slid into an alveolar structure, constructed of carbon-fibre composite and additional Tungsten absorber layers. The first ten absorber layers are 1.4 mm thick (corresponding to 0.4 X_0), the next ten are at 2.8 mm, and the last ten have a thickness of 4.2 mm. In total, the calorimeter has a thickness of 20 cm/24 X_0, an active area of 18×18cm^2, and a total of around 10k readout channels.

The detector was calibrated using muon beams. These calibrations were very stable over the three year data taking period. The linearity and resolution of the detector's energy response to electrons and positrons was measured. Any non-linearity was shown to be at a level smaller than 1% in the energy range 1–45 GeV, and the energy resolution can be parameterised as $\sigma_E/E = 16.5/\sqrt{E} \oplus 1.1\%$, as shown in fig 2. A Geant4-based MOKKA [3] simulation of this ECAL prototype has been developed, and accurately describes the performance measured in the testbeam.

3 Scintillator-Tungsten EM calorimeter

This detector is based on 3.5 mm Tungsten absorber layers with active layers consisting of 45×10 $times$3mm^3 plastic scintillator strips [4]. The strips' orientation is alternated in successive layers. A Multi Pixel Photon Counting device (MPPC) [5] is placed at the end of each strip to measures the scintillation light. This device is very compact, insensitive to magnetic fields, inexpensive, and has excellent gain and quantum efficiency characteristics. The MPPC is coupled to the scintillator either directly or by means of a wavelength-shifting fibre (WLSF) running along the centre of the scintillator strip.

Two prototypes of such an ECAL have been constructed. The first small prototype had 26 layers with an active area of 9×9cm^2, and was used to test various types of scintillator and
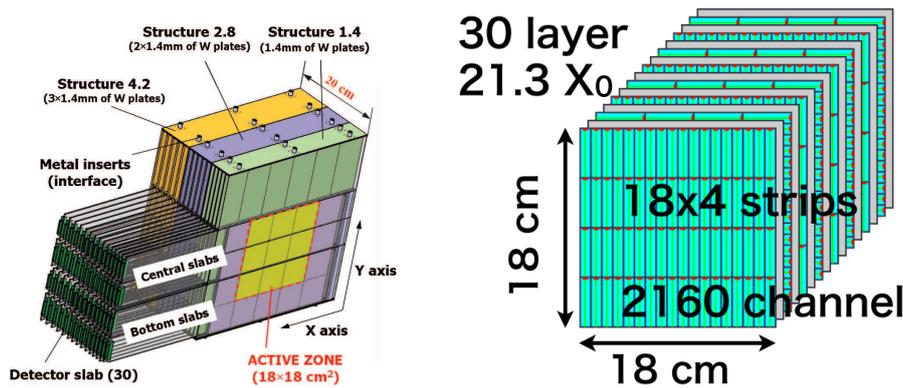

Figure 1: Structure of Silicon (left) and Scintillator-based (right) ECAL prototypes.

WLSF configurations, as well as gaining experience operating a large number of MPPCs. The second, larger, prototype consisted of 30 layers with active area 18×18cm^2, allowing the full containment of electromagnetic showers. Extruded scintillator strips with WLSF readout were used. This prototype was exposed to beams with a wider energy range and of different particle types. The collected data are being analysed. Figure 2 shows the energy response to electrons of different energies. By placing an iron target a few metres upstream of the calorimeter, tests of neutral pion reconstruction were also performed.
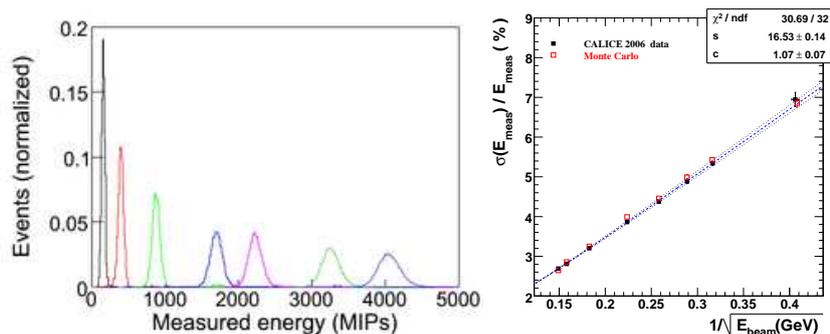

Figure 2: Response to electrons of ScECAL (left), and energy resolution of SiECAL (right)

4 Conclusions

The CALICE collaboration develops calorimetry for ILC detectors, based on the Particle Flow paradigm. This requires an ECAL with high granularity and excellent separation of hadronic and EM showers. Several different technological approaches have been proposed. Here we report on one based on Silicon active layers and a second based on scintillator strips read out by MPPCs. Prototype detectors of both types have been made, and exposed to a wide variety of particle beams in an intense test beam program. These data show that both technologies have sufficiently good energy resolution and linearity to meet the requirements for a LC ECAL. The results found are in good agreement with the results of detailed simulations.

References

[1] J.C. Brient, H. Videau, "The calorimetery at a future e+e- linear collider", arXiv:hep-ex/0202004 (2002).

[2] CALICE coll., "Design and Electronics Commissioning of the Physics Prototype of a Si-W Electromagnetic Calorimeter for the International Linear Collider", JINST 3:P08001,2008.
CALICE coll., "Response of the CALICE Si-W Electromagnetic Calorimeter Physics Prototype to Electrons", NIM A608 (2009) 372.

[3] http://polzope.in2p3.fr:8081/MOKKA

[4] CALICE coll., "The scintillator ECAL beam test at DESY, 2007", CALICE analysis note CAN-005.
CALICE coll., "The scintillator ECAL beam test at DESY, 2007 - Update 1", CAN-006.
CALICE coll., "The scintillator ECAL beam test at DESY, 2007 - Update 2", CAN-007.

[5] http://sales.hamamatsu.com/en/products/solid-state-division/si-photodiode-series/mppc.php

A Large Scale Prototype for a SiW Electromagnetic Calorimeter for the ILC - EUDET Module

Roman Pöschl[1]

[1]LAL Orsay, B.P. 34, 91898 Orsay, France
On behalf of the *CALICE* Collaboration

The CALICE collaboration is preparing large scale prototypes for highly granular calorimeters for detectors to be operated at the International Linear Collider, ILC. During the year 2010/2011 a prototype of a SiW electromagnetic calorimeter will be assembled which in terms of dimensions and layout meets already most of the requirements given by the ILC Physics Program and hence the detector design. In particular the very front end electronics will have to fit within alveolar layers with less than 1 cm in height. In this contribution the design of the prototype is presented and the steps towards the realisation will be presented.

1   Introduction

The next major worldwide project in high energy particle physics will be a linear electron positron collider a the TEV scale. This machine will complement and extend the scientific results of the LHC currently operated at CERN. The most advanced proposal for this linear collider is the International Linear Collider (ILC). Here, electron and positrons will be collided at centre-of-mass energies between 0.2 and 1 TeV. The detectors which will be installed around the interaction point are required to achieve a jet energy resolution of $30\%/\sqrt{E}$, thus a factor two better than the energy resolution achieved for a typical detector at LEP. The reconstruction of the final state of the e^+e^- will be based on so-called particle flow algorithms (PFA). The goal is to reconstruct every single particle of the final state which in turn demands a perfect association of the signals in the tracking systems with those in the calorimeters. As a consequence this requires a perfect tracking of the particle trajectories even in the calorimeters. To meet these requirements the detectors have to cover the whole solid angle and have to feature an unprecedented high granularity.

2   Towards a Technological Prototype for the SiW electromagnetic calorimeter

The application of PFA requires a perfect reconstruction of the particle trajectories in the calorimeter. For this the calorimeters have to be placed inside the coil of the super-conductive solenoid of the detectors. This puts tight constraints on the available space for the installation of the detectors. The design of the detector components and notably of the calorimeters have to take the following guidelines into account

- Optimisation of the number of calorimeter cells.

- Choice of the absorber material and the infrastructural components such as cooling, power supplies, readout cables and the very front end electronics.

For the electromagnetic calorimeter which surrounds the tracking chambers these criteria has lead to the choice of tungsten with a radiation length of X_0=3.5 mm,a Molière of R_M=9 mm and an interaction length of λ_I=96 mm.In the years 2005 and 2009 the CALICE collaboration has performed a test beam campaign at DESY, CERN and FNAL in order to demonstrate the principle of highly granular calorimeters and to confront the concept of Particle Flow with real data. The first results of the data analysis have been published in three articles [1, 2, 3]. The next prototype, also called EUDET Module, has been conceived during the year 2008 and enters now its construction phase. It addresses, more than the first prototype, the engineering challenges which come along with the realisation of highly granular calorimeters. The key parameters of the new prototype are

- Size of an individual cell of 5.5x5.5 mm^2.

- A depth of 24 X_0.

- Thickness of an individual layer of 3.4 mm and 4.4 mm according to the position within the calorimeter.

The Figures 1 and 2 show the mechanical housing and a cross section through two calorimeter layers which form a slab. The mechanical housing is realised by a tungsten carbon composite, which provides at the same the absorption medium and the mechanical rigidity of the detector. The silicon wafers are composed of high resistive silicon. While in principle the manufacturing of these wafers is a well known technique the challenge is to produce these wafers at small price in order to reduce the cost since a surface as large as 3000 m^2 will be needed for an ILC detector. The final calorimeter will comprise around 10^8 channels in total. In order to reduce the non-equipped space in the detector the very front end electronics (VFE) has to be integrated into the calorimeter layers, see Figure 2, which constitutes a major challenge for the construction of the calorimeter. The room available for the readout circuits (ASICs) and the interface boards between the ASICs and the silicon wafers is about a millimeter.

Each of the ASICs of the new prototype will readout 64 calorimeter cells and realises the measuring of the analog signal, the digitisation and the zero suppression such that only a limited number of channels are finally send to the data acquisition which is based on custom made components in order to allow for the employment of large quantities at reasonable prices for the experimentation at the ILC detector.

Due to the limited space available for cooling devices the heat dissipation of the ASICs has to be minimised. In addition to the cooling, the heat dissipation will be reduced by a novel technique called "Power Pulsing". Here, the VFE will only be switched on during the millisecond of a bunch train of particles. Such a bunch train contains about 3000 particle bunches separated by around 300 ns. During the around 200 ms between these bunch trains, the electronics will be switched off. Clearly, this novel technique will require detailed studies in order to assure that the signal quality of each channel remains constant after each powering cycle. The first ASICs which incorporate the power pulsing will be realised during 2009 and examined during the year 2010.

A calorimeter layer will have a length of about 1.5 m and will be composed by several units which carry silicon wafers as well as the VFE. The challenge is to integrate this fragile assembly into the alveolar structure which houses the calorimeter layers. The integration cradles are under development and a first integration test with a demonstrator has been successfully conducted in October 2010.
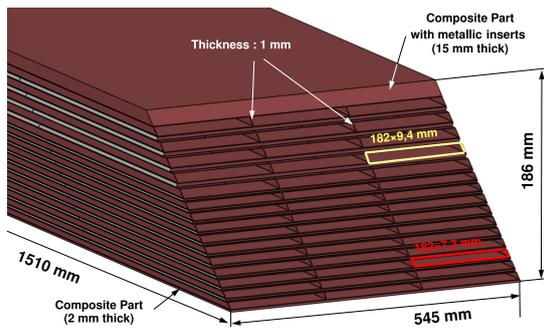

Figure 1: *Alveolar structure and its dimensions which houses the sensitive parts of the CALICE SiW electromagnetic calorimeter prototype.*
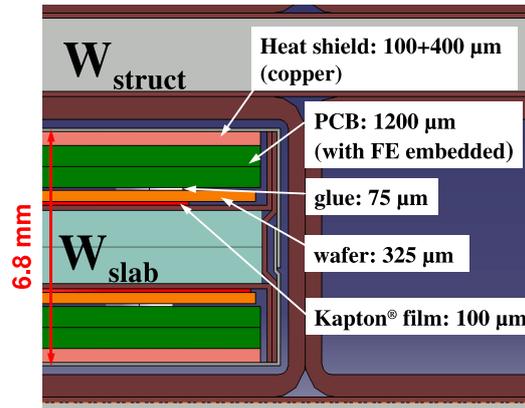

Figure 2: *Cross Section through a slab for the CALICE SiW electromagnetic calorimeter prototype.*

Acknowledgments

3   Bibliography

References

[1] CALICE Collaboration (J. Repond *et al.*), *Design and Electronics Commissioning of the Physics Prototype of a Si-W Electromagnetic Calorimeter for the International Linear Collider* Nucl.Instr. and Methods A608 (2009) 372 [arXiv:0811.2354].

[2] CALICE Collaboration (J. Repond *et al.*), *Response of the CALICE Si-W Electromagnetic Calorimeter Physics Prototype to Electrons*, Nucl.Instr. and Methods A608 (2009) 372 [arXiv:0811.2354].

[3] CALICE Collaboration, C. Adloff *et al.. Study of the interactions of pions in the CALICE silicon-tungsten calorimeter prototype.* 2010 JINST 5 P05007, arXiv:1003.2662v1 [physics.ins-det].
.

High Gradient SRF Research at DESY

Sebastian Aderhold[1], Detlef Reschke[1]

[1]DESY, Notketraße 85, 22607 Hamburg, Germany

Gradients exceeding 40MV/m have been multiply demonstrated in 9-cell SRF cavities that are foreseen for the International Linear Collider. The mass production of such cavities however remains a challenge. A new, in situ method for optical inspection, developed at KEK/Kyoto University allows to correlate surface features with e.g. quench locations. This and other tools are presented that enable a systematic approach to understanding the gradient limiting features in SRF cavities. Results from the large sample investigated at DESY are shown.

1   Reaching high accelerating gradients

One of the core parts of linear accelerators such as the European XFEL and the planned International Linear Collider (ILC) are the accelerating structures, in this case 9-cell RF resonators (cavities) made from Niobium and operated at 1.3 GHz. The design operating gradient for the ILC has been ambitiously chosen to be 31.5 MV/m [1].To reach high accelerating gradients, one has to demand high standards of the quality of the cavity's inner surface with respect to smoothness and cleanliness. In order to attain these conditions, about 200 μm of the surface material are removed by (electro-)chemical means. Before the test or assembly to an accelerator module the cavities are cleaned and handled in a clean room. The cavity preparation process is described in detail in [2] and [3]. Over the past 20 years, the maximum accelerating gradient of SRF cavities has been significantly improved. Several of the cavities that have been processed and tested at DESY have reached accelerating gradients higher than 35 MV/m in vertical test. A detailed analysis of recent nine-cell cavity results can be found in [4]. Even though high gradients are reached in many cases, the spread in the production is large with some cavities limited around 20 MV/m and below, so that series production with high yield needs a good understanding of the limiting effects. One feature limiting the gradient may be geometrical defects on the inner surface, like defects in the welding seams. Such defects can be detected via optical inspection of the inner surface of a cavity.
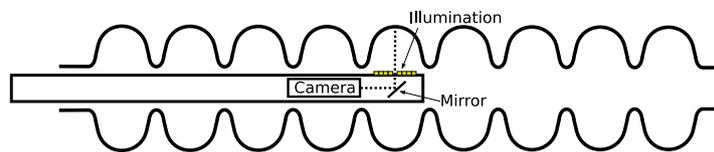

Figure 1: Schematic overview of optical inspection setup

2 Optical inspection of the inner surface of cavities

The properties of the Niobium make the optical inspection of the inner surface of SRF cavities very demanding. The smoothness of the surface after chemical treatment leads to bright reflections and low contrast. Since end of 2008 the prototype of an optical system, developed at KEK and Kyoto University [5], is available at DESY. It has been adapted to the situation inside a cavity and allows the inspection of the inner surface in situ. It consists of a high resolution digital camera in combination with a special lighting system. A schematic overview of the setup is shown in Fig. 1. The camera is situated inside a cylinder, looking to the inner cavity surface via a mirror. Illumination is done by a LED and 20 electroluminescent stripes. The stripes can be turned on and off individually to light the surface under different angles and thereby guarantee appropriate lighting for different structures on the surface.

2.1 Comparison between optical inspection and temperature mapping

During the RF measurement in the vertical test the surface temperature of the cavity can be monitored by an array of thermo-sensors (T-map) [6]. In case of a local breakdown of superconductivity (quench) the position can be identified by the increase in temperature at the outer surface. In several cases subsequent optical inspection of the corresponding areas on the inner surface revealed visible defects, e.g. in the welding seam. One example for such a correlation is shown in Fig. 2. The cavity Z130 was limited at 17.3 MV/m by quench in the first vertical test and was cut out of its He-vessel for further investigation. The second test was donet with T-map. The $3\pi/9$–mode was limited at 22 MV/m and heating of the quench was observed on the equator of cell 5 (left part of Fig. 2). Optical inspection of the corresponding area revealed a circular pit of about 700 μm diameter on the edge of the welding seam (right part of Fig. 2).
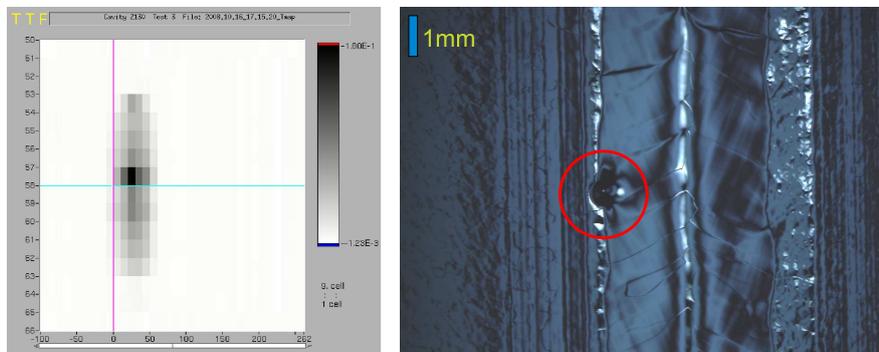

Figure 2: Heating of quench detected by T-map in Z130 (left) and defect in optical inspection picture of corresponding area (right)

2.2 Inspection in different stages of preparation

Optical inspections in consecutive stages of the surface treatment process allow the study of formation and evolution of surface defects. The series of pictures in Fig. 3 shows the evolution

of an area on the equator of cell 1 in the cavity Z137. The left picture is taken after welding before any further chemical treatment of the surface. The welding seam looks normal and similar to all the other eight welding seams. After the main surface removal of 108 μm by electro-polishing (EP) (center picture) rough areas and steep edges at the grain boundaries are visible on the equator and in the heat affected zone of cell 1, in contrast to the other eight cells. The final EP has smoothened out the edges a bit (right picture) and the equator is shinier, but the steep grain boundaries remain. The accelerating gradient of Z137 was limited by quench at 25.2 MV/m in the vertical test. Heating of the quench was located by T-map next to the equator of cell 1. It is not yet understood why cell 1 reacted differently under EP.

Figure 3: Equatorial welding seam of cell 1 in Z137: before EP (left), after main-EP (center) and after final-EP (right)

3 Summary

SRF cavities already exceed the specifications for future accelerator projects, but production suffers from a scatter in accelerating gradient. One reason for limitation of a cavity at lower gradients are geometrical defects on the inner surface that can be detected by optical inspection. Correlations between heating at the quench location found by T-map and visible defects in the optical inspection were found in several cases. Studies on the evolution of defects during the different stages of surface preparation are carried out. The goal is to categorize structures on the inner surface, in order to understand, which defects keep a cavity from reaching high accelerating gradients. The ability to detect and remove such limiting features in early stages of the processing may help to improve the yield in a large scale production.

References

[1] ILC Reference Design Report, www.linearcollider.org/rdr/

[2] B. van der Horst *et al.*, TUP30, p. 196, Proc. of 13th Workshop on RF Superconductivity, Beijing, China (2007).

[3] B. van der Horst *et al.*, THPPO072, p. 791, Proc. of 14th Workshop on RF Superconductivity, Berlin, Germany (2009)

[4] D. Reschke *et al.*, TUPPO051, p. 316, ibid. ref. [3].

[5] Y. Iwashita *et al.*, Phys. Rev. ST Accel. Beams 11, 093501 (2008).

[6] Q.S. Shu *et al.*, 11th CEC/ICMC Conference, TU-A3-6, pp. 895-904, Columbus, USA (1995)

Electron-Nucleon Scattering at the Tera Scale

Max Klein[1]

[1]University of Liverpool, Oxford Street, L69 7ZE Liverpool, United Kingdom

The following paper briefly summarizes a poster, which describes the design and the physics of the Large Hadron Electron Collider (LHeC). The poster may be viewed at the LHeC webpage http://cern.ch/lhec, which leads to talks, papers and references too.

1 Introduction

The Large Hadron Electron Collider is a new colliding beam facility under study, which is based on the LHC at CERN. It exploits very high cms energies of $s = 4E_e E_p \simeq 4 \cdot 60 \cdot 7000 \simeq 2 \cdot 10^6$ GeV^2 in order to pursue a rich programme of inelastic, polarised electron/positron-proton, deuteron and heavy ion scattering measurements. Reaching momentum transfer values squared of Q^2 above 10^6 GeV^2 and correspondingly low values of Bjorken $x \propto Q^2/s \sim 10^{-6}$ in the region of deep inelastic scattering (DIS), at luminosities of 10^{33}cm^{-2}s^{-1}, the LHeC surpasses the HERA kinematic reach and performance by about two orders of magnitude. In a plot of past, current and future DIS projects, in terms of luminosity versus energy, the LHeC stands out as a unique possibility for deep inelastic scattering to explore the high energy frontier, alongside with the LHC and a future pure lepton collider, much as HERA, with the TeVatron and LEP, explore the Fermi energy scale of $\sqrt{s} \sim M_W$.

This poster illustrates part of the still ongoing work on the machine, interaction region and detector designs as well as on the physics potential of the LHeC at high mass scales, high parton densities and with high precision. The study is pursued in a wide international collaboration under the auspices of CERN, ECFA, NuPECC and a Scientific Advisory Committee. It is directed to a Conceptual Design Report by 2010, as a contribution to the deliberations of the HEP community on its future programme of exploring the energy frontier with accelerators. If further supported, the LHeC may come into operation in the early twenties, constituting a new experiment at the LHC in the high luminosity running phase.

2 Machine and Detector

The biggest challenge of the *ep* collider is its luminosity. At TeV energies one becomes sensitive to so far unobserved processes. A scale is set perhaps by the $WW \to H$ fusion process, which has a cross section of order 100 fb in charged current scattering at the LHeC for masses of $m_H \sim 150$ GeV. To explore the highest Q^2 and large Bjorken x region, the luminosity can hardly be large enough because the (photon exchange) cross section diminishes like Q^{-4} and the parton distributions tend like $(1-x)^3$ to $x \to 1$. For the LHeC a ring-ring (RR) and a linac-ring (LR) configuration are designed. The choice between these for a next phase, the Technical Design Report, has many aspects, technology, cost, infrastructure, accelerator strategy, schedule etc.,

but their comparison and design starts with the luminosity potential. In ep collisions the beams have to be matched. The luminosity in a ring-ring (RR) configuration can be approximated as

$$L = \frac{N_p \gamma}{4\pi e \epsilon_{pn}} \cdot \frac{I_e}{\sqrt{\beta_{px}\beta_{py}}} = 8.2 \cdot 10^{32} cm^{-2} s^{-1} \cdot \frac{I_e}{50\text{mA}} \cdot \frac{N_p 10^{-11}}{1.7} \cdot \frac{\text{m}}{\sqrt{\beta_{px}\beta_{py}}} \qquad (1)$$

with the electron beam current given as $I_e = 0.35 \cdot P[\text{MW}]/50 \cdot (100/\text{E}_e[\text{GeV}])^4$ mA. With the so-called ultimate LHC proton beam parameters, $N_p = 1.7 \cdot 10^{11}$, $\epsilon_{pn} = 3.75\,\mu$m and $\beta px(y) = 1.8(0.5)$ m, and assuming $P = 40$ MW synchrotron radiation induced power loss, one obtains a luminosity, for 60 GeV of electron beam energy, of about $2 \cdot 10^{33}$ cm^{-2}s^{-1}. The corresponding formula for the linac-ring (LR) configuration is

$$L = 8 \cdot 10^{31} cm^{-2} s^{-1} \cdot \frac{I_e}{1\text{mA}} \cdot \frac{N_p 10^{-11}}{1.7} \cdot \frac{0.2\text{m}}{\beta^*} \qquad (2)$$

where the current now is given as $I_e = P[\text{MW}]/\text{E}_e[\text{GeV}]$. With a possibly reachable β^* of 10 cm one obtains for the ultimate beam a luminosity of $1.6 \cdot 10^{32} \cdot P/E_e \simeq 0.7 \cdot 10^{32}$ cm^{-2} s^{-1} for $P = 25$ MW and $E_e = 60$ GeV. This is a factor of about two higher than the HERA II value. There are two ways for increasing the luminosity further: the LHC high luminosity upgrade programme envisages up to about $N_p = 4 \cdot 10^{11}$ protons per bunch which yet requires upgrades and refurbishment of the LHC injector chain. Such a high value is currently not included in the LHeC luminosity estimates. This leaves the power as a main source. Given a design power limit of 100 MW wall-plug, as compared to a 400 MW power limit of CLIC, one finds that energy recovery techniques are the only viable method to effectively increase P to $P_b/(1-\eta)$. Assuming a recovery efficiency of $\eta = 94\,\%$ and an available beam power of about $P_b = 25$ MW, aside with cryogenic power and efficiency considerations, one estimates a LR luminosity figure of about 10^{33} cm^{-2}s-1. The design is based on about ten work packages for each of the options, as on the beam optics, interaction regions, cryogenics, magnets, rf. or infrastructure.

The CDR on the LHeC comprises a detector design concept. This must cope with a a number of demands: i) polar angle acceptance for electrons, backwards, and hadrons, forward, to 179° and 1°, respectively; ii) calibration uncertainties about twice smaller than achieved with H1, in order to perform high precision QCD and electroweak measurements; iii) high modularity and minimum dimensions for optimum installation and maintenance and iv) integration of beam separation (of 3 beams) and focussing functions combined with efficient screening from direct and backscattered synchrotron radiation. For the present design status see the LHeC web page.

3 Physics Programme

The physics programme of the LHeC naturally is extremely rich. One may summarize it with four items, for which illustrations are on the poster, HERA, precision, BSM and low x/eA:

- HERA's achievements lead further: While there are large logarithmic terms $\propto \ln(1/x)$ in the perturbative evolution, yet, no deviations from the linear DGLAP evolution had been observed so far, despite some indications from recent precision measurements. The saturation of the gluon density remains to be observed. Parton densities at high x have not been accurately measured due to lack of luminosity. The neutron and the nuclear structure were not studied, a unique omission in the history of DIS experiments. New concepts

have been introduced with parton amplitudes, diffractive partons and uninegrated parton distributions, which require much deeper exploration. No instantons, no odderons, no leptoquarks have been observed, which calls for larger phase space and luminosity.

- The LHeC is a unique precision machine for electron-quark and photon-gluon interactions. With Q^2 exceeding M_Z^2 by a factor of 100, the electroweak interactions become very large, i.e. weak neutral (NC) and charged currents (CC) explore the partonic structure in a unique way: for the first time the complete set of parton distributions can be measured, including for example the strange and anti-strange quark density from $e^{\pm}p$ CC scattering, and one eventually overcomes the many assumptions used in today's extractions of parton distributions. The LHeC is a single top and anti-top quark factory with the single t production cross section in CC of about 10 pb. Per mille accuracy may be achieved for the strong coupling constant, α_s, and the light quark weak NC couplings, etc.

- Owing to the very high energy and luminosity the LHeC complements ideally the search for and interpretation of possibly observed new physics at the LHC. With precision pdf measurements it disentangles new effects from variations of proton structure. By itself the ep machine has unique sensitivity to singly produced new states, as there possibly are excited electrons or neutrinos, RPV SUSY or leptoquark states. With its high precision the LHeC explores $eeqq$ contact interactions up to 50 TeV. One measures the $H \to b\bar{b}$ coupling, and a new level of accuracy for the gluon and the beauty density will determine the production cross sections of the SM or MSSM Higgs particles, respectively.

- The high energies lead into the regime of saturated parton distributions, which is one of the most intensely studied problems of modern strong interaction theory, related to non-linear parton interactions or superhigh energy neutrino physics. The LHeC is bound to find new physics as it surpasses the unitarity limit both in ep and in eA scattering at very low x and $Q^2 > 1\,\mathrm{GeV}^2$ where α_s is small. Parton distributions in nuclei may be studied in a range of DIS extended by nearly four orders of magnitude, thus accompanying AA physics at the LHC and studying a plethora of effects related to the quark-gluon plasma, shadowing and its relation to diffraction etc. If there were new states diffractively produced at the LHC, precision diffraction measurements at the LHeC are of possibly crucial value. With variations of charge and polarisation, generalised parton distributions can be studied.

The CDR of the LHeC will be available in spring 2011. At that time one will have obtained some first reliable information from the LHC about the TeV mass range. Difficult decisions on the direction of particle physics and the future of CERN are ahead. Building an affordable ep/A collider for the exploration of the Terascale so far is an attractive possibility, not to exploit the hadron beams at the LHC for a combination with high energy electron beams would appear to be a waste of resources and exploration potential. Besides ATLAS, CMS, LHCb and ALICE, the LHeC appears to be worth being the 5th element of experimentation at the LHC.

4 Acknowledgments

Radiative Decays of B Hadrons at LHC*b*

Fatima Soomro
Imperial College London
Email: f.soomro07@imperial.ac.uk

LHC*b* is a dedicated *B* physics experiment at the Large Hadron Collider (LHC) at CERN. The experiment aims to look for New Physics at energy scales much higher than those reachable through direct production, by measuring effects from the New Physics particles in rare beauty and charm decays. Radiative penguin decays of *B* mesons are an important part of the LHC*b* physics programme, and the detector is well positioned to harness the large statistics of these decays available at the LHC luminosity. Even with a small integrated luminosity of 100 pb^{-1}, 5% of what LHC*b* would collect in one nominal year of LHC, it can make a competitive measurement of the *CP* asymmetry in the decay $B_d \to K^*\gamma$.

1   Introduction

Radiative pengiun decays of *B* mesons are an example of Flavour Changing Neutral Currents, which are forbidden at tree level in the Standard Model (SM). Such decays can only occur due to loop diagrams, and the one corresponding to $b \to s\gamma$ is shown in Fig. 1. The contribution of all the known particles to the loop can be calculated, and hence the branching ratio of such decays can be predicted in the SM.

The current average experimental value of the inclusive $\mathcal{B}(B \to X_s\gamma)$ is $3.56 \pm 0.26 \times 10^{-4}$

Figure 1: The loop diagram for a $b \to s\gamma$ transition

[1], which is in agreement with the latest theoretical predication of $3.15 \pm 0.23 \times 10^{-4}$ [2]. The newest measurement by the *Belle* colaboration [3] is also in agreement with theory.

However, New Physics (NP) can have more subtle effects than a change in the branching ratio, for example the *CP* asymmetry in the decay $B_d \to K^*\gamma$. Another interesting way to look for deviations from the SM is to probe the chiral structure of the possible NP operator in $b \to s\gamma$ decays, by measuring the photon polarization.

The decays $B_u \to K^*\pi\gamma$, $B_u \to \phi K\gamma$, and $\Lambda_b \to \Lambda\gamma$ can provide sensitivity to the photon polarization by an angular analysis of the decay products. The decays $B_s \to \phi\gamma$ and $B_d \to K^*\gamma$ can also be used for such a study, but $B_s \to \phi\gamma$ offers much more sensitivity than $B_d \to K^*\gamma$ due to the large decay width difference ($\Delta\Gamma$) between the B_s and $\overline{B}_s$ mesons, as compared to the B_d system. Further, it is a flavour blind final state, so the photon polarization analysis can be done without flavour tagging aswell [4]. The decays $B_d \to \rho\gamma$ and $B_d \to \omega\gamma$ are very useful in constraining the ratio of $|V_{td}|$ and $|V_{ts}|$ [5] [6].

In 2010, the first year of physics operation of the LHC, an integrated luminosity of $100\,\mathrm{pb}^{-1}$ is foreseen. In the following, we focus on $B_d \to K^*\gamma$ and $B_s \to \phi\gamma$, in particular the very early measurements possible with these decays, at LHCb.

2 $B_d \to K^*\gamma$ at LHCb

With quite modest integrated luminosities, LHCb can perform measurements competitive to the current B Factory results, as the statistics available to the experiment are quite large. Table 1 lists the expected number of triggered and selected $B_d \to K^*\gamma$ and $B_s \to \phi\gamma$ decays for a range of luminosities.

Decay mode	$100\,\mathrm{pb}^{-1}$	$500\,\mathrm{pb}^{-1}$	$2\,\mathrm{fb}^{-1}$
$B_d \to K^*\gamma$	4×10^3	2×10^4	7×10^4
$B_s \to \phi\gamma$	550	3×10^3	1.1×10^4

Table 1: Expected number of triggered and selected $B_d \to K^*\gamma$ and $B_s \to \phi\gamma$ decays at LHCb

The direct CP asymmetry in $B_d \to K^*\gamma$ decay $\mathcal{A}^{\mathrm{dir}}_{\mathrm{K}^*\gamma}$, is predicted to be less than 1% in the SM. It is defined as

$$\mathcal{A}^{\mathrm{dir}}_{\mathrm{K}^*\gamma} = \frac{\mathcal{B}_{\mathrm{B}_d \to \mathrm{K}^*\gamma} - \mathcal{B}_{\bar{\mathrm{B}}_d \to \bar{\mathrm{K}}^*\gamma}}{\mathcal{B}_{\mathrm{B}_d \to \mathrm{K}^*\gamma} + \mathcal{B}_{\bar{\mathrm{B}}_d \to \bar{\mathrm{K}}^*\gamma}}.$$

which can be experimentally measured by counting the number of reconstructed $\mathrm{B}_d \to \mathrm{K}^*\gamma$ and $\bar{\mathrm{B}}_d \to \bar{\mathrm{K}}^*\gamma$ decays. The systematics introduced due to production and detector asymmetries can be cancelled, to leading order, using $\mathrm{B}_d \to \mathrm{K}^*\mathrm{J}/\psi$ as a control channel and building the ratios $\mathcal{R}$ and $\bar{\mathcal{R}}$:

$$\mathcal{R} = \frac{\mathcal{N}_{\mathrm{B}_d \to \mathrm{K}^*\gamma}}{\mathcal{N}_{\mathrm{B}_d \to \mathrm{K}^*\mathrm{J}/\psi}}, \quad \bar{\mathcal{R}} = \frac{\mathcal{N}_{\bar{\mathrm{B}}_d \to \bar{\mathrm{K}}^*\gamma}}{\mathcal{N}_{\bar{\mathrm{B}}_d \to \bar{\mathrm{K}}^*\mathrm{J}/\psi}}, \quad \text{and} \quad \mathcal{A}_{\mathcal{R}} = \frac{\bar{\mathcal{R}} - \mathcal{R}}{\bar{\mathcal{R}} + \mathcal{R}}.$$

In the ratios $\mathcal{R}$ and $\bar{\mathcal{R}}$, the production and detector asymmetries cancel to first order, and the asymmetry $\mathcal{A}_{\mathcal{R}}$ is a function of the direct asymmetries $\mathcal{A}^{\mathrm{dir}}_{\mathrm{K}^*\gamma}$ and $\mathcal{A}^{\mathrm{dir}}_{\mathrm{K}^*\mathrm{J}/\psi}$.

The explicit expression for $\mathcal{A}^{\mathrm{dir}}_{\mathrm{K}^*\gamma}$ becomes

$$\mathcal{A}^{\mathrm{dir}}_{\mathrm{K}^*\gamma} = \frac{\mathcal{A}_{\mathcal{R}} + \mathcal{A}^{\mathrm{dir}}_{\mathrm{K}^*\mathrm{J}/\psi}}{1 + \mathcal{A}_{\mathcal{R}}\mathcal{A}^{\mathrm{dir}}_{\mathrm{K}^*\mathrm{J}/\psi}}.$$

With $100\,\mathrm{pb}^{-1}$, $\mathcal{A}_{\mathcal{R}}$ can be measured to less than 2% accuracy, hence the measurement of $\mathcal{A}^{\mathrm{dir}}_{\mathrm{K}^*\gamma}$ will be limited by the current $\mathcal{A}^{\mathrm{dir}}_{\mathrm{K}^*\mathrm{J}/\psi}$ measurement [7].

3 $B_s \to \phi\gamma$ at LHCb

The decay $B_s \to \phi\gamma$ can be used to extract the photon polarization in the $b \to s\gamma$ transition. With $500\,\mathrm{pb}^{-1}$, it is possible to perform an unbinned maximum likelihood fit on $B_s \to \phi\gamma$ events. With that data sample, the uncertainty on the photon polarization result will be comparable to the the present one, if the parameter is computed from the current results of the CP violating parameters [7]. However, even with $100\,\mathrm{pb}^{-1}$, an interesting measurement of the ratio of $\mathcal{B}_{\mathrm{B}_s \to \phi\gamma}$ to $\mathcal{B}_{\mathrm{B}_0 \to \mathrm{K}^*\gamma}$ can be made.

Here the important uncertainties arise from various trigger efficiencies which can be different

for the two channels, and also from the uncertainty on the production rates of B_s and B_d mesons (due to the poor knowledge of the fragmentation constants f_b and f_s). Again, one can use $B_s \to \phi J/\psi$ and $B_d \to K^* J/\psi$ as normalization channels to reduce these uncertainties, and construct the ratio

$$\mathcal{R}^{B_s \to \phi\gamma} = \frac{\mathcal{B}_{B_s \to \phi\gamma}/\mathcal{B}_{B_s \to \phi J/\psi}}{\mathcal{B}_{B_d \to K^*\gamma}/\mathcal{B}_{B \to K^* J/\psi}}. \tag{2}$$

Most systematic uncertainties are expected to cancel in this ratio, and the statistical error is about 5% for $100\,\mathrm{pb}^{-1}$.

4 Conclusion

Radiative decays of B mesons are loop processes and are extremely sensitive to NP phenomena. In this area, the existing experimental measurements agree with the theoretical predications of the SM, and act as efficient constraints of NP models.

Large statistics of radiative decays will help in making these constraints even more strict, and LHCb will contribute to the improvements in the current B Factory results and make new measurements in the field of radiative decays. In this document, an overview of the radiative physics programme of LHCb was given with emphasis on early measurements which may already be feasible in the 2010 run of the LHC.

The physics reach of LHCb can surpass that of the B Factories with only $100\,\mathrm{pb}^{-1}$. With this integrated luminosity, the experiment can make interesting and important measurements of the direct CP asymmetry in $B_d \to K^*\gamma$ decay and also of a ratio of the branching fractions of $B_s \to \phi\gamma$ and $B_d \to K^*\gamma$.

References

[1] C.Amsler *et al.* [Particle Data Group], Phys. Lett. B **667**, 1 (2008)

[2] M.Misiak *et al.*, Phys. Rev. Lett. **98**, 022002 (2007); See also T.Becher and M.Neubert, Phys.Rev.Lett. **98**, 022003 (2007)

[3] The Belle Colaboration, *Measurement of Inclusive Radiative B-meson Decays with a Photon Energy Threshold of 1.7 GeV*, `Phys. Rev. Lett.103:241801 (2009)`

[4] F.Muheim, Y.Xie, R.Zwicky, *Exploiting the width difference in $B_s \to \phi\gamma$*, `Phys. Lett. B 664, 174 (2008)`

[5] A.Ali, E.Lunghi, A.Ya.Parkhomenko, *Implication of the $B \to (\rho, \omega)\gamma$ Branching Ratios for the CKM Phenomenology* , `Phys. Lett. B 595:323-338 (2004)`

[6] A. Ali, A.Ya.Parkhomenko, *Branching Ratios for $B \to K^*\gamma$ and $B \to \rho\gamma$ Decays in Next-to-Leading Order in the Large Eneregy Effective Theory*, `Eur.Phys.J. C23 (2002) 89-112`

[7] The LHCb Collaboration, B. Adeva et al, *Roadmap for selected key measurements of LHCb*, `LHCb-PUB-2009-029, arXiv:0912.4179v1 [hep-ex]`

Searches for Leptonic B Decays at *BABAR*

Silke Nelson, Representing the BABARCollaboration

SLAC, 2575 Sand Hill Rd, 94025 Menlo Park, CA, USA

Measurements of the branching fractions of purely leptonic decays of B-mesons translate into constraints in the plane of the charged Higgs mass versus $\tan\beta$ which are relatively insensitive to the particular theoretical model. Using the full *BABAR* dataset of 450 million B-decays we search for these decays. No significant signal is found in the decays into electrons or muons and we set upper limits on the branching fractions of the order of a 10^{-6} at 90% confidence level. We measure the branching fraction of $B \to \tau\mu$ to be $(1.7 \pm 0.6) \times 10^{-4}$.

1 Theoretical Motivation

In the Standard Model, the purely leptonic decay of a charged B-meson proceeds through the annihilation of the two constituent quarks through a virtual W-Boson. The branching fraction (BF) of this decay can be expressed as follows:

$$\mathcal{B}(B \to l\nu) = \frac{G_F^2 m_B}{8\pi} m_l^2 \left(1 - \frac{m_l^2}{m_B^2}\right)^2 f_B^2 V_{ub}^2 \tau_B.$$

The dependence of $\mathcal{B}(B \to l\nu)$ on the lepton mass arises from helicity suppression. The ratio between the rates for the lepton species $\tau : \mu : e$ is $\sim 1 : 5 \times 10^{-3} : 10^{-7}$ which makes the τ channel the most abundant. The hadronic uncertainties contained in the decay constant f_B are calculable only in lattice theory and their direct measurement is solely possible through leptonic B-decays.

The $B \to \tau\nu$ decay has also an important impact in model beyond the Standard Model because it allows to constraint parameter of the New Physics. When adding an extended Higgs sector [1] the decay may also proceed via the exchange of a charged Higgs at tree level, so the branching fraction expression becomes

$$\mathcal{B}_{(B \to \tau\nu)} = \mathcal{B}_{SM} \times \left(1 - \frac{m_{B^\pm}^2}{m_{H^\pm}^2} \frac{\tan^2\beta}{(1 + \epsilon_0 \tan\beta)}\right)^2.$$

In the 2HDM type-II scenario without contributions from other SUSY particles, ϵ_0 is one.

2 *BABAR* Datasample and Results

The data used in this analysis were collected with the *BABAR* detector at the PEP-II storage ring at the SLAC National Accelerator Laboratory. We use the full *BABAR* dataset, corresponding to an integrated luminosity of $417.6\,\text{fb}^{-1}$ with center-of-mass (CM) energy equal to the $\Upsilon(4S)$

rest mass. These data contain $(458.9 \pm 5.1) \times 10^6$ $\Upsilon(4S) \to B\overline{B}$ pairs. In the BABAR detector is described in detail elsewhere [2].

$B^\pm \to \tau\nu$

While this decay has the highest branching fraction of the purely leptonic B decays, the presence of multiple neutrinos in the final state results in the lack of kinematic constraints for reconstruction of the signal-decay. We overcome this obstacle by fully reconstructing one the two B-decays, called tag B in the following, and subsequently search in the remainder of the event for the signal decay. We reconstruct the tag B two different classes of decays: semileptonic (SL) decays $B \to D^{(*)0}l\nu$ and fully hadronic decays $B \to D^{(*)0}X$, where X is a combination of pions and kaons. The presence of a well reconstructed tag B reduces the background from non-B decays greatly at the price of the tag reconstruction efficiency which is of order of a percent for the SL tag or about 0.2% for the hadronic tag. To further reject continuum events we employ event shape variables using the fact that the B-mesons are produced nearly at rest in the $\Upsilon(4S)$ decay and thus decay isotropically, while the products of other $\Upsilon(4S)$ decays are boosted and lead to di-jet like events. The most important variable for the rejection of both continuum and B-background is the extra energy (E_{extra}), which is the total energy of charged and neutral particles that cannot be directly associated with the reconstructed daughters of the tag B or the signal B. The left plot of Figure 2 shows the final E_{extra} for the hadronic tag samples in data and MC [3].

$B^\pm \to l\nu(l = e, \mu)$

The full hadronic reconstruction of one of the B decays determines the signal-B rest frame, allowing to extract the BF of the signal decay via a fit to the lepton momentum which exhibits a peak at 2.65 GeV due to the two-body nature of the signal-B decay. The fit to data is shown in the right plot of Figure 2[5]. The determination of the signal-B rest frame in SL-tagged events has an azimuthal ambiguity which leads to a less distinct peak.In the CM frame, the shapes of the lepton momentum of signal and background events are still different enough to allow for an inclusive analysis in addition to the tagged analyses. Here the less distinct signature is being balanced by the higher statistics avaliable without the tag-requirement and related inefficiency. We combine all particles besides signal candidate lepton into a B candidate and fit its mass and the lepton-momentum in the CM-system simultaneously[4].

The results of the BABAR searches for purely leptonic decays of charged B-mesons are summarized in Table 1.

Analysis method	$B \to e\nu$ 90% CL limit	$B \to \mu\nu$ 90% CL limit	$B \to \tau\nu$ 90% CL limit	$B \to \tau\nu$ central BF in 10^{-4}
Inclusive [4]	1.0×10^{-6}	1.9×10^{-6}	n/a	n/a
Hadronic Reco. [5, 3]	5.6×10^{-6}	5.2×10^{-6}	3.4×10^{-4}	$(1.8^{+0.9}_{-0.8} \pm 0.4 \pm 0.2)$
SL Reco. [6]	11×10^{-6}	8×10^{-6}	2.7×10^{-4}	$(1.7 \pm 0.8 \pm 0.2)$

Table 1: Results of the BABAR searches for purely leptonic decays of charged B-mesons.
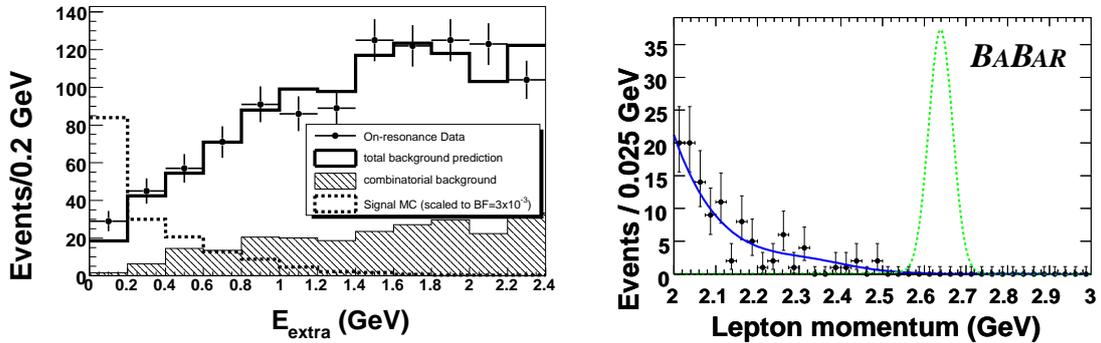
Figure 1: E_{extra} for the hadronic tag $B \to \tau\nu$-samples (left) and the muon momentum (right) in data (dots), signal (dashed line) and background prediction (histograms) (left).

3 Conclusions

The BABAR measurements of $\mathcal{B}(B \to \tau\nu)$ have reached a significance of 2.3 or 2.2 σ in for the SL-tag and hadronic tag analyses respectively. The current world average of (1.73 ± 0.35)[7] has a $\approx 2\sigma$ disagreement with the SM prediction. It can be used to exclude parameter space in the $m_{H^\pm} - \tan\beta$ plane as shown in Figure 2. With currently available luminosity we can only set limits for $\mathcal{B}(B \to [e,\mu]\nu)$, but the muon channel with its striking signature will reach measurement levels at future B-factories [8].
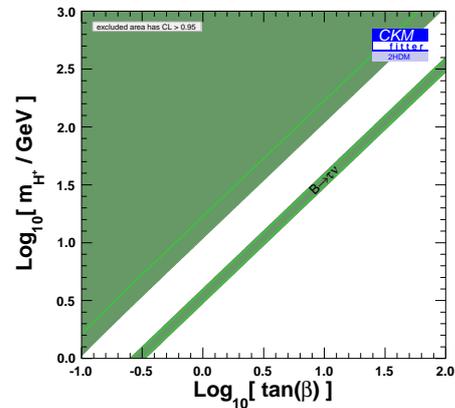

Figure 2: Constraints on the 2HDM parameter space $(m_{H^\pm}, \tan\beta)$ from $B \to \tau\nu$ decays [7].

References

[1] G. Isidori and P. Paradisi, Phys. Lett. **B 639**, 499 (2006).

[2] BABAR Coll. (B. Aubert *et al.*), Nucl. Instrum. Methods Phys. Res., Sect. A **479**, 1 (2002); W. Menges, IEEE Nucl. Sci. Symp. Conf. Res. **5**, 1470 (2006).

[3] BABAR Coll. (B. Aubert *et al.*), Phys. Rev. **D 77**, 011107(2008).

[4] BABAR Coll. (B. Aubert *et al.*), Phys. Rev. **D 79**, 90101(2009).

[5] BABAR Coll. (B. Aubert *et al.*), Phys. Rev. **D 77**, 091104(2008).

[6] BABAR Coll. (B. Aubert *et al.*), PRD-RC **81**, 051101(2010).

[7] UTFit Collab., arXiv:0908.3470 (2009); CKMfitter Collab., arXiv:0907.5135 (2009).

[8] M. Bona *et al.* hep-ex/0709.0451 (2007); S. Hashimoto *et al.*, KEK-2004-4 (2004).

The Belle-II Pixel Vertex Detector at the SuperKEKB Flavor Factory

F. Simon[1,2], K. Ackermann[1], L. Andricek[3], C. Heller[1], C. Kiesling[1], A. Moll[1,2], H-G. Moser[3], J. Ninkovic[3], K. Prothmann[1,2], B. Reisert[1], R. Richter[3], M. Ritter[1], S. Rummel[3], A Wassatsch[3]
for the DEPFET Collaboration

[1]Max-Planck-Institut für Physik, München, Germany
[2]Excellence Cluster Universe, Garching, Germany
[3]Max-Planck-Institut für Physik, Halbleiterlabor, München, Germany

An upgraded asymmetric e^+e^- flavor factory, SuperKEKB, is planned at KEK. It will deliver a luminosity of 8×10^{35}cm^{-2}s^{-1}, allowing precision measurements in the flavor sector which can probe new physics well beyond the scales accessible to direct observation. The increased luminosity also requires upgrades of the Belle detector. Of critical importance here is a new silicon pixel vertex tracker, which will significantly improve the decay vertex resolution. This new detector will consist of two detector layers close to the interaction point, using DEPFET pixel sensors with 50 μm thick silicon in the active area.

1   Introduction

The study of B meson systems at the asymmetric energy e^+e^- flavor factories KEKB and PEP-II, running predominantly at the $\Upsilon(4s)$ resonance, has helped to firmly establish the CKM picture of quark mixing and CP violation in the Standard Model. In addition, new mesonic states involving heavy quarks have been discovered and have been investigated in detail. Despite the success of the current experiments, which have collected 553 fb^{-1} in the case of BaBar and more than 1 ab^{-1} in the case of Belle, many questions yet remain to be answered. With a significant increase in statistical precision, flavor factories have the potential to probe new physics through the deviation of observables from the Standard Model predictions, most spectacularly illustrated by the potential observation of a non-closing unitarity triangle. Such precision measurements thus provide sensitivity to high mass scales, complementary to the direct searches at high energy colliders [1, 2].

To provide the required increase in statistics, a next generation machine, the super flavor factory SuperKEKB, is planned at KEK [3]. This upgrade of the existing KEKB collider will provide an instantaneous luminosity of up to 8×10^{35}cm^{-2}s^{-1}, enabling the collection of an integrated luminosity of 50 ab^{-1} in less than a decade of operation. This increase in luminosity by a factor of 40 over the present world record, held by KEKB, will be achieved by extreme focusing of the beams in the interaction region, so-called nanobeams, and by a moderate increase of the beam currents. The increased interaction rates and larger background levels require significant upgrades of the existing Belle detector. For the Belle-II experiment, all major detector subsystems will be replaced or upgraded [3, 4, 5].
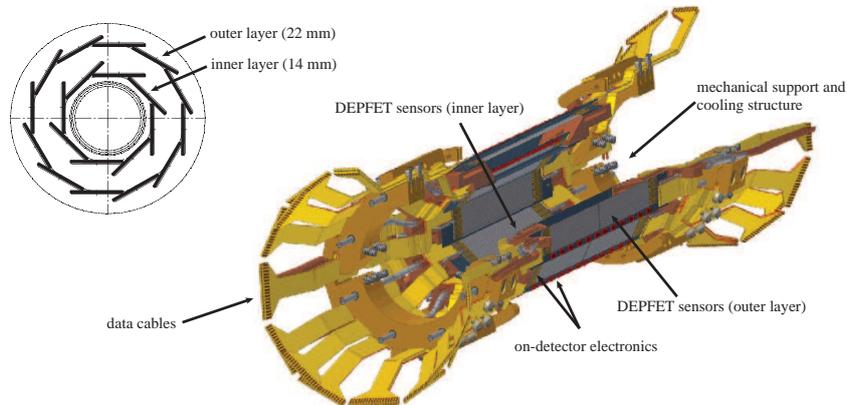
Figure 1: Illustration of the Belle-II PXD, showing the arrangement of the modules of the inner and outer layers (inset upper left), and a the schematic of the overall mechanical design, including support and cooling structures and data cables.

2 The pixel vertex tracker PXD

Improved secondary vertex resolution will be provided by a new silicon pixel vertex tracker, the PXD. Excellent vertexing is crucial for time dependent CP violation studies, where the time difference between the decays of two B mesons is measured by the spatial separation of their decay vertices. This exploits the forward boost of the meson rest frame, provided by the energy asymmetry of the two colliding beams. In the case of B^0 pairs, the decay time differences are typically of the order of 1.5 ps, corresponding to flight distances of around 200 μm.

The PXD uses DEPFET [6] active pixel sensor technology, developed at the semiconductor laboratory of the MPI for Physics in Munich. It consists of two layers, at a radius of 14 mm and 22 mm, respectively, arranged around the thin straight section of the Beryllium beam pipe in the interaction region of the Belle-II detector, as illustrated in the inset in the upper right corner of Figure 1. The inner layer uses 8, the outer layer 12 individual detector modules, with an active length


Figure 2: Illustrative cross section through a PXD module. The silicon in the active area is thinned to 50 μm, 450 μm thick silicon rims are left on the module sides for stability.

of 120 mm for the outer layer, sufficient to cover the full acceptance of the Belle-II detector from 17° to 150°, relative to the high energy beam axis. The modules of the inner layer are designed as monolithic silicon structures, while the outer layer modules consist of two joined sensors, required by the size of the 6" wafers used for production. To minimize the amount of material, crucial for the precise reconstruction of low momentum tracks, the modules themselves are thinned down to a thickness of 50 μm in the active area, with 450 μm thick silicon rims to provide structural stability, as illustrated in Figure 2. Thus, no additional mechanical support within the detector acceptance is necessary.

Both inner and outer layer sensors will have 1600 by 250 pixels, which are continuously read

out in a rolling shutter mode, with a readout time of 20 μs. The pixels on the inner modules have a size of roughly $50 \times 50 \, \mu\mathrm{m}^2$, while the outer modules have slightly elongated pixels with a size of $75 \times 50 \, \mu\mathrm{m}^2$. The read out electronics are located on the module ends, with additional chips for the addressing of individual pixel rows mounted on one side of the stave. The total power consumption is around 7 W per module side, with about 0.5 W dissipated over the active area, and 0.5 W dissipated in the switcher electronics on the stave edges. The required cooling capacity imposes strict constraints on the detector support. The still evolving design is based on support rings on both detector ends made of copper, chosen for the excellent thermal conductivity, which hold the silicon modules. The rings themselves contain cooling channels for active cooling, and through-going air channels to provide cooling for the sensor surfaces with a cold air flow. Several options for the cooling of the support rings are under investigation, including water cooling and evaporative cooling schemes using C_3F_8 or CO_2. The current mechanical design of the PXD, including support structures and data cables, is illustrated in Figure 1.

The DEPFET sensors used in the PXD combine particle detection and amplification of the signal by embedding a field effect transistor into fully depleted silicon. The low noise due to the low capacity of the pixels and the internal amplification provides very high signal to noise ratios. With non-thinned 450 μm thick sensors using an ILC-like pixel geometry of $24 \times 24 \, \mu\mathrm{m}^2$ pixels, a signal to noise ratio of around 130 and a spatial resolution of better than 2 μm has been achieved in beam tests [7]. For the thinned sensors, signal to noise ratios in excess of 20 are expected.

Due to the high number of pixels and the continuous readout in a background dominated environment, the zero suppressed data rate of the PXD is expected to be on the order of 20 GB/s. A data reduction scheme using fast online tracking in the silicon strip detector to select regions of interest in the PXD for further data processing is being developed to reduce the PXD data output to a manageable level.

3 Outlook

A test production of thinned DEPFET sensors with the Belle-II PXD pixel geometry is well advanced, and will undergo thorough testing in the summer of 2010. Prototypes of the mechanical support and cooling structures are under construction. In parallel, the final detector parameters are being determined with detailed single track and physics simulation studies. The assembly and installation of the PXD in the Belle-II detector and the beginning of data taking at the SuperKEKB flavor factory is envisaged for the year 2013.

References

[1] T. E. Browder, T. Gershon, D. Pirjol, A. Soni and J. Zupan, Rev. Mod. Phys. **81**, 1887 (2009).

[2] T. Browder, *et al.*, JHEP **0802**, 110 (2008).

[3] S. Hashimoto *et al.*, KEK-REPORT-2004-4.

[4] I. Adachi *et al.* [sBelle Design Group], arXiv:0810.4084 [hep-ex].

[5] Z. Dolezal [Belle Collaboration], arXiv:0910.0388 [hep-ex].

[6] J. Kemmer and G. Lutz, Nucl. Instrum. Meth. A **253**, 365 (1987).

[7] C. Marinas, arXiv:0901.4639 [physics.ins-det].

The Project NICA/MPD at JINR: Status of Design and Construction

N.B.Skachkov, on behalf of NICA Collaboration,

JINR, 141980, Joliot Curie 6, Dubna, Russia

The new project, named NICA/MPD, was proposed at the Joint Institute for Nuclear Research in 2006. It includes the Nuclotron-based Ion Collider fAcility (NICA) and the multi-purpose detector (MPD). The main goal of the project is to start in the coming years experimental study of hot and dense strongly interacting QCD matter. This goal is proposed to be reached by: 1) development of the existing accelerator facility Nuclotron; 2) design and construction of heavy ion collider (NICA) with maximum collision energy of $\sqrt{s}_{NN} = 11$ GeV (gold) and average luminosity of $10^{27} cm^{-2} s^{-1}$ and 3) design and construction of MPD at intersecting beams. Realization of the project will provide unique conditions for the world community research activity because the highest nuclear (baryonic) density under laboratory conditions can be reached in the NICA energy region. Generation of intense polarized proton and deuteron beams aimed at investigation of polarization phenomena at the Nuclotron M and NICA facilities is foreseen. The maximum c.m. energy of colliding polarized protons is planning to be reached of $\sqrt{s}_{NN} = 27$ GeV and of $\sqrt{s}_{NN} = 12.7$ GeV for deuteron collisions. Average luminosity will reach of $10^{30} - 10^{31} cm^{-2} s^{-1}$ in the both modes. The possibility of realization proton - ion and deuteron ion head-on and merging beam collision modes are under consideration also.

1 NICA/MPD Goals and Physics Problems

Theoretical and experimental investigations of the QCD phase diagram are among the most prominent research directions in modern physics. The investigations at NICA are relevant to understanding of the evolution of the Early Universe after Big Bang, formation of neutron stars, and the physics of heavy ion interactions. The new JINR facility will make it possible to study in-medium properties of hadrons and nuclear matter equation of state, including a search for possible signatures of deconfinement and/or chiral symmetry restoration phase transitions and QCD critical endpoint in the region of $\sqrt{s}_{NN} =4$ -11 GeV (gold) by means of careful scanning in beam energy and centrality of excitation functions.

The first stage measurements includes: 1) Multiplicity and global characteristics of identified hadrons including multi-strange particles; 2) Fluctuations in multiplicity and transverse momenta; 3) Directed and elliptic flows for various hadrons; 4) HBT and particle correlations.

Electromagnetic probes (photons and dileptons) are supposed to be added at the second stage of the project. The beam energy of the NICA is very much lower than the region of the RHIC and the LHC but it sits right on top of the region where the baryon density at the freeze-out is expected to be the highest. In this energy range the system occupies a maximal space-time volume in the mixed quark-hadron phase (the phase of coexistence of hadron and

quark-gluon matter similar to the water-vapor coexistence-phase). The net baryon density at LHC energies is predicted to be lower. The energy region of NICA will allow analyzing the highest baryonic density under laboratory conditions (see the phase diagram below). The
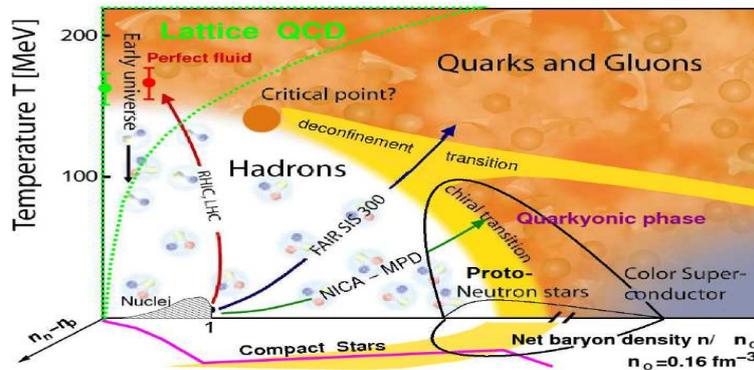

Figure 1: *Phase diagram .*

conditions similar to NICA are expected to be reproduced at FAIR facility in Darmstadt after put the synchrotron SIS300 into operation (in 2015). For more information about Physics at NICA see http://nica.jinr.ru and http://theor.jinr.ru/twiki-cgi/view/NICA/WebHome sites which contain the material of Round Table discussions in 2005-2009 (" NICA White Paper").

2   MPD for Mixed Phase experiments

The experimental set-up of proposed MPD (see its schematic picture below) has to detect the high multiplicity events and perform particle identification in 4 geometry. The MPD consists of a central detector (CD) and two forward spectrometers (FS-A and FS-B) situated along the beam line symmetrically with respect to the centre of MPD. The CD consists of the time projection chamber (TPC) supplemented by the inner tracker (IT) surrounding the interaction region, and two end cap trackers (ECT). The CD aimed to reconstruct and identify both charged and neutral particles in the pseudorapidity region $|\eta| < 2$. The high performance time-of-flight (TOF) system based on RPC allows pion, kaon and proton identification in the broad rapidity range and up to total momentum of 2 GeV/c. The energy loss (dE/dx) measurements in the TPC gas will give an additional capability for particle identification in low momentum region. For the electron/positron and gamma detection and their energy measurement the electromagnetic calorimeter (ECal) is considered. Two ECTs are located on both sides of the TPC. The ECT is designed to provide tracking information for particles traveling at small radii and for which the TPC has poor reconstruction ability. The fast forward detectors (FD), beam-beam counters (BBC) and zero degree calorimeter (ZDC) are used for trigger definition, centrality determination and reconstruction of the position of the interaction point in the ion-ion collision. The FS-A and FS-B cover the pseudorapidity region from 2.0 to 3.0. They are considered as optional.

Here are some basic MPD parameters: 1) we expect that interaction rate of Au+Au events at luminosity of 1027 cm-2s-1 is 10 kHz. (Interaction rate of central events is of 5kHz); 2) The accuracy of vertex reconstruction by means of IT is better then 0.2 mm; 3) The TPC produces
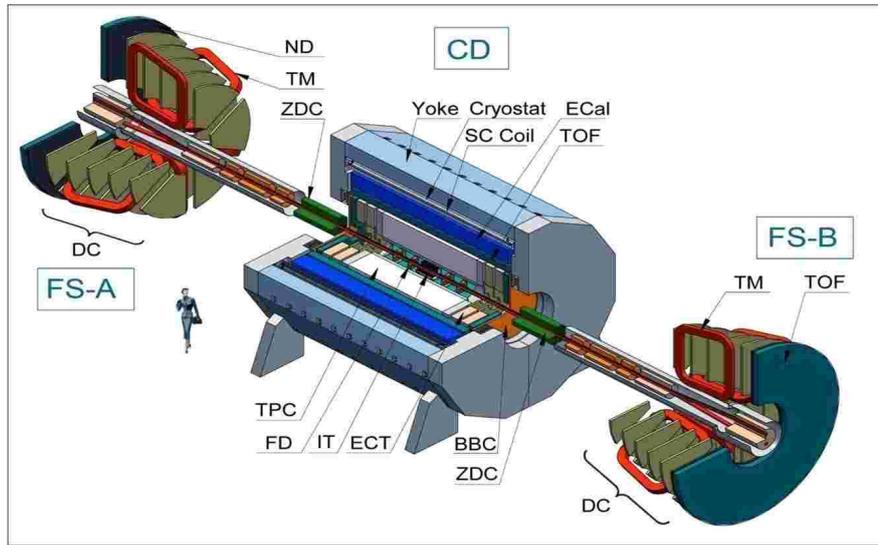
Figure 2: Schematic picture of the MPD detector

50 hits per track and provides the momentum measurement with an accuracy of 1 % in the range of p = 0.2 2 GeV/c. Time of flight system has resolution of 100 ps and provides pion and kaon separation with probability less than 5 % for p< 2 GeV/c.

2.1 NICA General Layout

Construction of the new facility is based on the existing buildings and infrastructure of the synchrophasotron/Nuclotron of the JINR Veksler-Baldin Laboratory of High Energy Physics. Therefore, the total collider ring length is limited to 0.8 of the Nuclotron orbit length and is approximately equal to 202 m. There are two long and two intermediate straights of 34 m and 17 m each respectively in the ring. Four magnetic arcs FODO structure have dense enough magnetic structure. In order to have the collider magnetic rigidity of 45 Tm the bending magnets field has to be increased up to 4 T or higher. The collider option based on 2 T Nuclotron-type dipoles is under consideration also nevertheless, the ring perimeter should be taken not less then 350 m in this case that exclude any possibilities to install it within the existing building. The accelerator chain includes: heavy ion source RFQ injector linac booster ring Nuclotron Superconducting collider rings. The collider NICA will have two interaction points. The MPD, aimed for studies of hot and dense strongly interacting matter and search for possible manifestation of signs of the mixed phase, and the Spin Physics Detector (SPD). The peak design kinetic energy of Au79+ ions in the collider is 4.5 AGeV. Beam cooling and bunching systems are foreseen. The collider magnetic system is fitted to the existing building. The project design presumes realization of some fixed target experiments. Collider operation with polarized deuteron and light ion beams is foreseen as the second stage of the project development.

3   The Project Milestones

The stages of the NICA/MPD project realization proposed in 2006 were fixed as the following: 2007-2009: - Development of the Nuclotron facility, preparation of Technical Design Report, start prototyping of the MPD and NICA elements; 2008-2011: - Design and Construction of NICA and MPD; 2010-2012: - Assembling; 2013: - Commissioning.

INSPIRE - The Next-Generation HEP Information System

Annette Holtkamp[1,2]

[1]CERN, 1211 Geneve 23, Switzerland
[2]on leave of absence from DESY, Notkestraße 85, 22607 Hamburg, Germany

CERN, DESY, Fermilab and SLAC have joined forces to build INSPIRE, the next-generation HEP information platform offering innovative tools for information discovery and communication. Representing a natural community-based evolution of SPIRES, INSPIRE provides fast access to the entire body of HEP literature. As a subject repository it will host fulltexts of preprints, Open Access journal articles and supplementary material like conference slides and multimedia, enabling novel text- and data mining applications. In the spirit of Web2.0 INSPIRE will also supply tools for collaboration and user-enriched content.

1 Introduction

Since decades, the SPIRES [1] database of High-Energy Physics (HEP) literature and related information, maintained by DESY, Fermilab and SLAC, is serving as the dominant information resource for particle physicists [2]. To adapt current technological advances to the workflow of HEP scientists SPIRES is moving to a new platform, Invenio [3], a modern open-source multimedia digital library platform developed at CERN. The three SPIRES partners DESY, Fermilab and SLAC have joined forces with CERN to build INSPIRE, the next-generation gateway to all HEP relevant information. Based on hosting the entire body of HEP literature metadata and the fulltext of all open access publications, it will empower scientists with state-of-the-art discovery tools. This paper highlights some of the innovations INSPIRE will offer in the near future.

2 Extended content

A survey launched in 2007 [2] revealed the need of the HEP community for access to material beyond the current scope of SPIRES. Following these wishes INSPIRE will over time significantly broaden the spectrum of covered material.

Since highest priority was given in the survey to the access to fulltext, INSPIRE will host the fulltext of all freely accessible preprints, journal articles, conference contributions, theses as well as research notes of experimental collaborations. The indexing of conference talks will be accompanied by long-term archiving of the corresponding slides. In addition, INSPIRE will act as repository for all kinds of supplementary material, like data, software or multimedia, which authors may want to supply to increase the usability of their scientific results. Thus it

will serve as a long-term archive for material that is in danger of getting irrevocably lost over time.

Another explicit wish of the HEP community is seamless access to older material. Complementing the role of arXiv [4] as the place where particle physicists deposit their new material, INSPIRE will ingest pre-arXiv articles wherever possible, aiming to cover the complete historical corpus of HEP literature.

3   Extended functionality

In addition to reproducing SPIRES' successful functionality on a modern platform, INSPIRE profits from Invenio's advanced technology to offer new features.

Searches are not only much faster and more efficient, but also, besides supporting the SPIRES specific syntax, INSPIRE enables Google-like free-text searches across metadata and fulltext.

For each article, a detailed page shows abstract, keywords and links to different fulltext versions, supplementary material and a growing wealth of additional information. A new feature to be expected on the detailed article page in the near future is the display of figures extracted from the fulltext. In parallel, figure captions will become independently searchable.

Citation analysis is supplemented by a citation history, visualizing the citation counts of an article over time. The "co-cited with" feature opens up new paths to find related articles.

Author pages provide a citation summary and comprehensive information on affiliation history, research subjects, frequent coauthors, research output. Work is under way to disambiguate authors and correctly attribute articles and in the future other scientific output to their creators.

Personal accounts will enable options like private bookshelves, alerts or RSS feeds, personalized display formats or tools for sharing information within a collaboration. Web2.0 functionality will allow scientists in the future to submit material, to attach comments, to tag content or to aggregate related objects.

Semantic techniques for information retrieval are under development that, based on a taxonomy of HEP concepts, will allow e.g. to translate a search for "SQCD" into a query for "supersymmetry" and "quantum chromodynamics", to search for material of similar content or to facilitate broadening and narrowing searches. Another application currently being refined is the automatic categorization of material on ingestion, so that a paper is automatically recognized e.g. as a conference talk on Higgs search or as an internal note on detector calibration. Automatic assignment of keywords from the HEP taxonomy will allow unified searches across different materials.

4   Outlook

At the forefront of information technology, INSPIRE will continuously develop innovative tools to put at the disposal of particle physicists.

Moving beyond the paper-centric paradigm, INSPIRE provides a platform not only to store supplementary material as attachments to an article but to treat all kinds of scientific output as independent objects, be it a dataset, a video or a software program. A user friendly search interface and a standardized set of metadata will allow comprehensive searches over all database content. Through the assignment of unique identifiers (similar to DOI's [5]) to non-article objects they will become independently citable. Measuring their usage will contribute to the

development of new metrics creating more comprehensive profiles for researchers and allowing to track the impact of ideas and retrieve the most relevant material.

INSPIRE's capacity to handle non-article objects blends in perfectly with initiatives towards data preservation whose importance is increasingly recognized by the HEP community [6, 7]. Thanks to its role as central HEP information system, INSPIRE is ideally placed to become an essential partner in digital preservation e.g. by hosting high-level data files and making them discoverable and citable, by ingesting and preserving documentation in the form of internal notes or wikis under the protection of a flexible access control system, and by participating in the development of standards.

To exploit synergies with other information providers and neighboring fields, collaboration will be intensified among others with the Astrophysics Data System (ADS)[8] and the Particle Data Group (PDG) [9] with the aim of providing seamless access to related information resources. Thus, finding an astroparticle physics paper on INSPIRE will smoothly lead to the underlying data sets indexed at ADS. An experimental or phenomenological paper on leptonic Z decay will be linked to corresponding information on the PDGlive website [10], and searches using PDG codes are planned to be enabled in INSPIRE. Projects undertaken in cooperation with publishers aim e.g. to improve ingestion of metadata or to enable fulltext searches of articles predating arXiv.

INSPIRE will thus continue and develop further the role that SPIRES has played as "the" reference HEP scientific information platform, providing inspiration for information management in other fields of science.

INSPIRE will go into production in Spring 2010. A public beta version is already available for testing.

References

[1] http://spires.slac.stanford.edu

[2] A. Gentil-Beccot *et al.*, J. Am. Soc. Inf. Sci. Technol. **60** (2009) 150, arXiv:0804.2701

[3] http://cdsware.cern.ch/invenio/index.html

[4] http://arXiv.org

[5] http://www.doi.org

[6] A. Holzner *et al.*, arXiv:0906.0485

[7] R. Mount *et al.*, arXiv:0912.0255;
    https://www.dphep.org

[8] http://adswww.harvard.edu

[9] http://pdg.lbl.gov

[10] http://pdglive.lbl.gov